Astrophysics and Space Science Proceedings 53

Banibrata Mukhopadhyay
Sudipta Sasmal *Editors*

# Exploring the Universe: From Near Space to Extra-Galactic

## A Collection of Research Reviews on Contemporary Astrophysics and Space Science

Springer

**Astrophysics and Space Science Proceedings**

Volume 53

More information about this series at http://www.springer.com/series/7395

Banibrata Mukhopadhyay • Sudipta Sasmal
Editors

# Exploring the Universe: From Near Space to Extra-Galactic

## A Collection of Research Reviews on Contemporary Astrophysics and Space Science

Springer

*Editors*
Banibrata Mukhopadhyay
Department of Physics
Indian Institute of Science
Bangalore, India

Sudipta Sasmal
Department of Ionospheric Sciences
Indian Centre for Space Physics
Kolkata, India

ISSN 1570-6591 ISSN 1570-6605 (electronic)
Astrophysics and Space Science Proceedings
ISBN 978-3-319-94606-1 ISBN 978-3-319-94607-8 (eBook)
https://doi.org/10.1007/978-3-319-94607-8

Library of Congress Control Number: 2018956293

© Springer International Publishing AG, part of Springer Nature 2018
This work is subject to copyright. All rights are reserved by the Publisher, whether the whole or part of the material is concerned, specifically the rights of translation, reprinting, reuse of illustrations, recitation, broadcasting, reproduction on microfilms or in any other physical way, and transmission or information storage and retrieval, electronic adaptation, computer software, or by similar or dissimilar methodology now known or hereafter developed.
The use of general descriptive names, registered names, trademarks, service marks, etc. in this publication does not imply, even in the absence of a specific statement, that such names are exempt from the relevant protective laws and regulations and therefore free for general use.
The publisher, the authors and the editors are safe to assume that the advice and information in this book are believed to be true and accurate at the date of publication. Neither the publisher nor the authors or the editors give a warranty, express or implied, with respect to the material contained herein or for any errors or omissions that may have been made. The publisher remains neutral with regard to jurisdictional claims in published maps and institutional affiliations.

This Springer imprint is published by the registered company Springer Nature Switzerland AG
The registered company address is: Gewerbestrasse 11, 6330 Cham, Switzerland

# Foreword



Prof. Gennady S. Bisnovatyi-Kogan

Sandip Chakrabarti is 60!

It is impossible to believe, but the jubilee is coming. Sandip is almost the same as he was 30 years ago, when I first met him: bright, energetic, and open for discussion of new and interesting scientific problems.

I am happy to write this introduction to a volume which is contributed by the members of a school established by Sandip, who seem to be the most numerous and

active in Indian astrophysical science. During the past 20 years or so, almost forty Ph.D.s were supervised by Prof. Sandip K. Chakrabarti and another ten or so are in the making. The passed out students have already produced another ten or so Ph.D. students, in turn.

An important characteristic of his school is that not only the number of students is large, by any standard in astrophysics, the subjects vary from space exploration with balloons to Dirac equations in Kerr black hole geometry, from black hole astrophysics to earthquake prediction using the Earth as a gigantic detector, and from exo-planet search with optical telescope to the formation of prebiotic molecules. And if that's not enough, Prof. Chakrabarti founded a brand new space research institute named the Indian Centre for Space Physics as a bonus which has now become a hotbed of intense research activities by young talents.

The diverse nature of the articles in this volume, all written by the Ph.D. students of Prof. Chakrabarti, testifies to the diverse topics that came out of this school. In the Part I, we see the general relativistic studies around black holes in sufficiently wide fields, such as the formation of disks and jets in Kerr geometry, measurements of spins, images of black hole horizon with modern disks, and outflows even touching gravitational wave emission due to inspiraling of two black holes, *in the presence of accretion flows*.

In the Part II, various aspects of relativistic astrophysical flows around black holes are described, such as effects of radiative transfer, heating and cooling processes, spectral and timing properties, numerical simulations of hydrodynamics, Monte-Carlo approaches applied to spectral and timing studies, etc. A wide variety of topics such as the models of triggering of outbursts, size variation of accretion disks, and effects of magnetic flux tubes are also included. Some chapters cover the accretion flows around neutron stars and their spectral properties as well.

In the Part III, diverse directions in observational astronomy have been taken up which had links to this group's research activities. Discussions on the evolution of observational astronomy in X-rays have been made. The data fitting procedure used the Chakrabarti–Titarchuk model of two-component advective flows (TCAF) developed in this group. It is shown how this solution extracts physical flow parameters, including masses of the black holes for stellar mass, intermediate mass, and super-massive black holes. Similarly, radio astronomy and optical astronomy have been covered. Near and far space explorations by low-cost balloon-borne instruments have been initiated by this group as well. Some studies in these directions are also presented.

In the Part IV, a very emerging field of astrochemistry has been covered. The problem of the origin of life on Earth is one of the most intriguing research areas. It is becoming clear that the complex biomolecules, which are the precursors of life, had to be formed through a generic process, perhaps during the collapse of star forming clouds using gas and grain chemistry. The chapters herein describe the time evolution of chemical composition of the gas cloud and analyse what the study of isotopomers could tell us about the age of the star forming region. Historically, search of interstellar molecules used to yield simple and abundant molecules. Today, using large area detectors such as ALMA, we can look for amino acids and other

life-giving complex molecules or at least for their precursors. This interesting Part offers glimpses of research areas in astrochemistry which are in focus today.

The final Part treats the science that can be done assuming Earth's ionosphere as a huge detector. The study of the ionosphere has found new applications in the form of prediction of seismic activities due to lithosphere–atmosphere–ionosphere coupling which is now firmly believed to take place on Earth. Ionospheric changes due to cosmic radiations are reflected in perturbations on very low frequency (VLF) radio waves which can be used to study the injected spectra. It becomes apparent that even solar X-ray spectra could be detected from ground-based VLF observations, which are very interesting, indeed. Another exciting finding seems to be the estimates of ice spread in Antarctica from attenuation of VLF signals. These new directions in addition to the studies of changes in VLF signal amplitudes due to solar flares and eclipses have been described in this Part.

This book touches a large number of areas of research which have been triggered and are being pursued by this group of researchers. They have positively contributed to our knowledge base in these very important areas of astronomy, astrophysics, and space science, and I firmly believe they will continue to do in future. I am sure this book would be of great value to future researchers in a wide variety of fields.

Space Research Institute
Moscow, Russia

Prof. Gennady Bisnovatyi-Kogan



Sandip Kumar Chakrabarti. Born: Malda, November 15, 1958



S.K. Chakrabarti with Prof. S. Chandrasekhar at Lindau (1994)



Left to Right: Lev Titarchuk, Rashid Sunyaev, Upendra Desai and S.K. Chakrabarti at a tree planting event at the Indian Centre for Space Physics



S.K. Chakrabarti explaining principles of Fresnel zone plate-based imager of RT-2 payload to W.D. Arnett and R.P. Kerr (extreme tight) at the X-ray laboratory of ICSP



S.K. Chakrabarti with Prof. K.S. Thorne

# Preface

Festschrifts are written to celebrate special occasions, often to mark a theoretical advancement or a historical event or simply to celebrate a milestone of a scholar. One of the reasons we have decided to bring this book out is that we felt in our heart that some perceptible and welcome scientific progress took place in the Eastern India led almost single-handedly by one man which we directly witnessed. Till around the middle of the 1990s, when one of us (BM) was still a master's student, there was no institution within about a thousand miles of the Kolkata (then Calcutta) region where we could pursue serious research in astronomy, astrophysics, and space science. However, this region was the cradle of these subjects in the pre-independence era when J.C. Bose discovered microwave communications, M.N. Saha gave Saha equation, and S.K. Mitra carried out important research in ionospheric layers. Even in the post-independence era, A.K. Raychaudhuri had a fundamental theoretical contribution to cosmology with an equation which is the genesis of singularity theorem. Due to several factors, a vacuum was created and the young scholars of the region were compelled to leave the region in search of space-related research environment, often crowding visa offices. Surprisingly, when the other of us (SS) was a master's student, merely a decade later, this problem disappeared. Something new had happened in less than a decade interval. Not only one could carry out researches in these areas, but besides black hole astrophysics, diverse fields of astrochemistry, ionospheric research, space exploration through satellites, low-cost balloon launching, and optical astronomy opened up in a little new school of learning manned by just one person. This, by now, expanded to a bigger school and a hotbed of activities.

In less than two decades, Professor Sandip Kumar Chakrabarti (SKC hereinafter) produced about forty Ph.D. students and another ten are in the making. A natural question would be: coming from a single individual, how diverse can their training be, so as to call for a Festschrift? Well, this book will give the answer to that. If the readers find that it is as diverse as that of a full-fledged institution, they have a reason to do so: Although SKC's formal training was at the University of Chicago and Caltech, he is largely self-taught and he does not believe in any topical boundary. He uses expertise gained in one topic to another one with equal dexterity. Thus,

Poisson's equation applied to rings around Saturn and Einstein's equation in massive disk around a black hole became one and the same problem. Nuclear reactions in accretion flows around a black hole and molecular reactions in a collapsing proto-stellar cloud became the same problem. Issues arising from fabrication of payloads for a satellite and those of indigenously developed balloon program became comparable. Application of GEANT4 for payload response and using Monte-Carlo on Earth's ionosphere treated as a gigantic detector became similar. Such versatility is uncommon. Underlying all these was of course an urge that the students coming out of his supervision should not compete among themselves while in search of further opportunities. Therefore, diversification was not an option, but a necessity. Not surprisingly, students coming out of SKC's school are now spread around all over the world often presenting talks in diverse sessions of the same general assemblies. Conversely, very well-attended international conferences on Observational Evidences for Black Holes in the Universe (1998, 2008), Propagation Effects of Very Low Frequency Radio Waves (2010), Chemical Evolution of Star Forming Region and Origin of Life (2012), etc., were organized by him so that the students may be exposed to the stalwarts in these topics. He edited proceedings of all of them as well.

As a consequence, for the sake of streamlining the thoughts, we had to classify fifty odd articles of SKC's former and present Ph.D. students into five sections and divided each section into (not so homogeneous) chapters. The size of each section is very much different, consisting of four to fifteen chapters. Optical astronomy and balloon program being relatively new, though they deserve separate sections, were put together with X-ray observation to have an Observational Astronomy section. For obvious reason, some articles are more professionally written than others.

Broadly speaking, the first section includes certain formal problems in general relativity and relativistic astrophysics. Although they are presented here as applications around a black hole, they could equally well be used for other related problems around compact objects of strange equation of states, even in other theories of gravity, and also white dwarfs in principle. In the second section, we have put together all the chapters specifically related to the theoretical studies and numerical simulations of accretion processes mainly around black holes and neutron stars. The two-component advective flow (TCAF) solutions and their properties are discussed here. In the third section, we have put the observational astronomy chapters. Many of these chapters show how one can understand the observational data in their entirety, i.e., both the spectral and temporal properties without changing the underlying paradigm solution. This section includes fitting data of galactic, extragalactic, and intermediate mass black hole sources, balloon-borne space exploration, radio astronomy, etc. Even initial results of a newly installed 0.61m optical telescope by SKC at the Indian Centre for Space Physics (ICSP hereinafter), a Institute he founded almost 20 years ago from now, are included for the sake of completeness. In the fourth section, we have included astro-chemistry which was initiated at ICSP from scratch. Special emphasis that is given in this school is the formation of complex organic and prebiotic molecules in star forming regions which may lead to the origin of life. In the fifth and final

section, we have put together the chapters which treat the entire Earth as a single detector. The study of the response of the ionosphere due to impinging UV, X-ray, and gamma-ray radiations is included here. Several works concentrate on the propagation characteristics of very low frequency (VLF) radio waves in the Earth-ionosphere waveguide and how the deviation from ideal response of the ionosphere could be used as a tool to detect terrestrial and extraterrestrial energetic phenomena. Since the research topics discussed in this volume are not only diverse but also have a universal appeal, we believe that the entire scientific community would be benefited immensely by this volume.

A teacher also has teachers. Therefore, we have decided that a few photographs of SKC, with those who influenced him, could be in order. We have included his photos with Prof. Subrahmanyan Chandrasekhar (with whom he worked at the University of Chicago), Prof. W. David Arnett (his formal Ph.D. supervisor at the University of Chicago), and Prof. Kip S. Thorne (his mentor at Caltech where he was a Tolman Fellow). He was deeply drawn to the studies of Kerr black holes when he found that Prof. Chandrasekhar wanted to put Prof. Roy P. Kerr's photo in the front page of his book on black holes. At the University of Chicago, physics or astronomy groups did not have any accretion disk-related expertise. Hence, in the early 1980s, hot, off the press, classics of R.A. Sunyaev, B. Paczynski, and M.A. Abramowicz gave him the required directions. At Caltech, he was inspired by the way Prof. Thorne could handle so many students at a time with passion and how he used to discuss weekly progress with all of them together at the Interaction Room of the Bridge Annex. Meeting Prof. Lev Titarchuk at NASA changed the direction of all that he was doing to date. Masters of hydrodynamics and radiative transfer joined hands to create one of the most successful models in accretion physics, the TCAF solution. Dr. Upendra Desai of NASA/GSFC visited ICSP several times to demonstrate how lightweight instruments could be fabricated and sent to space. As a consequence, and especially after attending Sputnik's golden jubilee event in Moscow in 2007, SKC's imagination rose to a new level which led him to develop his own space program at ICSP. As many as a record 109 number balloon missions were launched so far by his team. Not surprisingly, SKC was present directing payload fabrication to launch, communication with airport controller, and finally to chase the descending parachutes till recovering the payloads (mostly X-ray detectors) of all of these missions. Some results are there in this volume. With his engineers he also applied for three patents in this very technologically challenging subject. These are not included in this volume for technical reasons.

We thank all our colleagues, whom SKC supervised and has been supervising, to come up most enthusiastically with 50 odd articles to celebrate his 60th birthday on November 15th, 2018. Prof. Gennady S. Bisnovatyi-Kogan has written a wonderful summary of this volume in his foreword. Dr. V. Shantha (the senior most living member of Prof. S. Chandrasekhar's family), Prof. K.S. Thorne, Prof. W.D. Arnett, Prof. R.P. Kerr, Prof. L. Titarchuk, and Dr. U. Desai all gave their permissions to include their photos in this volume. We thank them profusely. We also thank the editors of all journals who gave their kind permission to reproduce several figures in different chapters. Dr. Suman Chakraborty and Dr. Tamal Basak have spent their

valuable hours helping us with editorial corrections, and they deserve our special gratitude. Last but not least, we thank Dr. Ramon Khanna (Executive Editor at Springer) and Ms. Christina Fehling and the entire team of Springer for having patience and helping us at every step to make this publication possible.

Bangalore, India — Banibrata Mukhopadhyay
Kolkata, India — Sudipta Sasmal
1st June 2018

# Contents

**Part I General Relativity and Relativistic Astrophysics**

**Spinning Black Holes, Spinning Flows and Spinors** ..... 3
Banibrata Mukhopadhyay

**Relativistic Flows in Astrophysics** ..... 17
Indranil Chattopadhyay

**Evolution of Imaging of Black Hole Accretion-Outflow System over Half a Century** ..... 29
Arka Chatterjee

**Gravitational Wave Emission from Binary Mergers: Ideal Versus Real Picture** ..... 39
Prasad Basu

**Part II Solutions of Model Flows Around Compact Objects**

**My Experiences and Experiments with Transonic Flows Around Compact Objects** ..... 53
Santabrata Das

**Transonic Flow Solutions with Explicit Cooling and Viscosity** ..... 67
Santanu Mondal

**On the Nature of Outflows from Low Angular Momentum Inflows Around Black Holes** ..... 85
Chandra Bahadur Singh

**Generalized Flows Around Neutron Stars** ..... 93
Ayan Bhattacharjee

**Radiation Characteristics of Two-Component Accretion Flow Paradigm Around Black Holes** ..... 109
Samir Mandal

**How Are the Outbursts Around Black Holes Triggered?** ..... 121
Shreeram Nagarkoti

**Formation of Two Component Flows by Numerical Simulations Around Black Holes** ..... 131
Kinsuk Giri

**Outbursts in Stellar Black Hole Candidates: A Time-Dependent Study of Viscous Accretion Flow** ..... 145
Abhishek Roy

**Monte-Carlo Simulation as a Defining Tool to Diagnose Timing and Spectral Properties of Flows Around Black Holes** ..... 157
Himadri Ghosh

**Sensitivity of Spectral and Temporal Properties of Accretion and Outflows on Space Time Geometry, Viscosity and Cooling** ..... 171
Sudip K. Garain

**Dynamics of Magnetic Flux Tubes in an Advective Flow Around Black Hole** ..... 183
Arnab Deb

**A Pseudo-Newtonian Approach to Study the Accretion Processes Around Kerr Black Holes** ..... 195
Soumen Mondal

**Part III Observational Astronomy**

**Observational Aspects of Black Holes: Past Challenges and Future Prospects** ..... 215
Anuj Nandi

**Evolution of Flow Properties Around Black Holes from Observations: Developments over the Past Decades** ..... 229
Dipak Debnath

**Do Spectral and Timing Properties Carry Information About Flow Geometry?** ..... 245
Partha Sarathi Pal

**Variability Properties of Galactic Black Holes** ..... 257
Broja Gopal Dutta

**Spectral and Timing Analysis of Transient, Persistent and Variable Black Hole X-Ray Binaries: The Present Viewpoint** ..... 271
Anuvab Banerjee

**Measurement of Masses of Galactic Black Holes from Spectral Analysis** ..... 283
Debjit Chatterjee

**Disk-Jet Connection in Black Holes** ..... 299
Arghajit Jana

**A Dynamic Photon Index Probes into TCAF** ..... 311
Arindam Ghosh

**Study of Broadband Spectra of AGNs Using Two Component Advective Flow Paradigm** ..... 329
Prantik Nandi

**Spectral Study of Ultraluminous X-ray Sources with XMM-Newton** ..... 339
Piklu Santra

**Radio Observations of Galactic Compact Objects** ..... 347
Sabyasachi Pal

**From Black Holes to Earthquakes: Saga of a Long and Lovely Journey** ..... 357
Asit K. Choudhury

**Detector Development and Optimization for Space Based Astronomy from Satellites and Balloons** ..... 371
Ritabrata Sarkar

**Science with Small Telescopes** ..... 387
Shyam Sarkar, Ashim Sarkar, and Pabitra Sil

**A Classic Problem in Newtonian Dynamics: How Thick Are Saturn's Rings?** ..... 395
Abhijit Bhattacharyya

**From Test and Evaluation Till Onboard Performance of Indian Payloads: RT-2 Onboard CORONAS-PHOTON and LAXPC Onboard AstroSat** ..... 409
Tilak Katoch

**Part IV Astrochemistry of Biomolecules**

**Renaissance of Astro-Chemistry in Indian Context** ..... 427
Ankan Das

**The Interstellar Molecular Complexity** ..... 439
Liton Majumdar

**One Supervisor and Three Different Topics to Choose from: My Choice and Subsequent Progress** ..... 453
Kinsuk Acharyya

**Explaining Major Sources of Sulfur-Bearing Molecules in the Interstellar Medium** ..... 467
Prasanta Gorai

**Role of Interstellar Molecules on Evolution of Cosmic Deuteration: An ALMA Observation as a Case in Point** ..... 477
Dipen Sahu

**Binding Energy and Isomerism: Two Important Aspects of Astrochemistry** ..... 491
Milan Sil

**Radiative Transfer Modeling of Some Relevant Interstellar Species** ..... 503
Bratati Bhat

**Part V Earth's Ionosphere as a Gigantic Detector**

**Renaissance of VLF Science in Indian Context** ..... 513
Sudipta Sasmal

**Remote Sensing of the Ignorosphere: Need for a Complete Earth-Ionosphere Radio Wave Propagation Model** ..... 527
Sujay Pal

**Ground-Based and Space-Based Studies of Lower Ionospheric Irregularities: Observation and Modeling** ..... 545
Suman Chakraborty

**Quantitative Modeling of Lower Ionospheric Response Due to Solar X-ray Flare: A Propagating Radio Wave Simulation Approach** ..... 561
Tamal Basak

**Numerical Simulation of Equatorial Ionospheric Response to Extra-Terrestrial High Energy Phenomena Using Ion Chemistry Models** ..... 571
Sourav Palit

**Earth's Ionosphere as a Detector for High Energy Extra-Solar Radiation** ..... 585
Sushanta Kumar Mondal

**Study of Seismo-Ionosphere Coupling Using Perturbation in Very Low Frequency Radio Signal** ..... 597
Suman Ray

**Pre- and Co-seismic Irregularities in Ionosphere and Troposphere and Precursory Studies with Various Techniques** ..... 611
Soujan Ghosh

**Observation and Modeling of Ionospheric Response of Annular Solar Eclipse** ..... 625
Surya K. Maji

**Space Weather: Response of the Atmosphere to Solar Activity and Its Implications for LEO Satellites Aerodynamic Drag** ..... 637
Victor U. J. Nwankwo

**Estimation of Wait's Empirical D-Region Model Parameters Based on Standard IRI Model** ..... 645
Subrata Kundu and Swati Chowdhury

# Part I
# General Relativity and Relativistic Astrophysics

# Spinning Black Holes, Spinning Flows and Spinors




**Banibrata Mukhopadhyay**

**Abstract** Angular momentum is an indispensable quantity perhaps in describing all the astrophysical phenomena. This is because all the cosmic objects are expected to be rotating, however be the magnitude of angular speed. The generalized astrophysical black hole is the rotating one (the Kerr black hole) which often accretes matter from its surrounding (e.g. from its binary companion) forming an accretion disk (namely X-ray binary). This accretion disk is the continuous infall of rotating matter towards a centrally located black hole (it, however, could also form around a neutron star, a white dwarf and in protoplanetary systems etc.). Hence, the flow and thus universe around a black hole is rotating/spinning in general (non-rotating accretion is a special case of it with zero angular momentum, called Bondi accretion). As black holes can not be seen directly, accretion flow around them plays indispensable roles to detect them. Now the infalling matter in accretion disks predominantly consists of protons, heavier ions, in general baryons; and electrons, neutrinos, in general leptons; all are fermions. Therefore, infalling matter predominantly consists of spinors (or spin-half particles), apart from photons which are of spin-one. In this Chapter, I aim at displaying a global picture of the interplay between three rotating/spinning entities: central black hole, accretion disk, and particles (having intrinsic spin) consisted by the disk. I show that how the underlying interplay governs important physics influencing astrophysical and gravitational phenomena remarkably.

## 1 Introduction

One of the most celebrated discoveries in the last century was Einstein's general relativity: Einstein's equation and, subsequently, its solution for a rotating black hole by Kerr. As a black hole does not reflect any light, the accretion disk formed

B. Mukhopadhyay (✉)
Department of Physics, Indian Institute of Science, Bangalore, India
e-mail: bm@iisc.ac.in

© Springer International Publishing AG, part of Springer Nature 2018

B. Mukhopadhyay, S. Sasmal (eds.), *Exploring the Universe: From Near Space to Extra-Galactic*, Astrophysics and Space Science Proceedings 53,
https://doi.org/10.1007/978-3-319-94607-8_1

around it by the inspiralling matter from the surrounding environment (e.g. from a companion star or stars in the galaxy for a super-massive black hole) plays indispensable roles to identify its existence and properties. Shakura and Sunyaev [47] proposed a Keplerian disk model explaining observed thermal multi-color blackbody spectra. However, it does not work to explain non-thermal power-law spectra observed in many sources, e.g. Cyg X-1, GRS 1915+105. One of the successful models to explain the same is Two Component Advective Flow (TCAF) proposed and promoted by Chakrabarti and his collaborators [6, 8–10, 14], first by (pseudo-)Newtonian framework and then by general relativistic formalism. I was fortunate enough to begin my research career to study such hot accretion flows, with ion temperature $\gtrsim 10^9$ K, under the leadership of Chakrabarti. In this context, I then mainly worked on possible nucleosynthesis and production of heavier elements (often called metal in astrophysics) in such hot flows [12, 35], following Chakrabarti's earlier initiation in a simpler model [15, 21]. I showed that even within 10 Schwarzschild radius, metals like $^{46}$Ti, $^{32}$S, $^{30}$S, $^{50}$Cr etc. form with mass fraction $\sim 10^{-4}$–$10^{-3}$, though very close to the black hole they destroy again. Interestingly, as the accretion was assumed to be occurring from a sun-like star, all were insignificant to start with. Similarly, neutrons form therein which remain survived till the matter reaches the black hole event horizon. See Fig. 1 capturing some basic nucleosynthesis, outlined here, in TCAF. Of course this is rather a representative example, depending on the disk hydrodynamics and thermodynamics

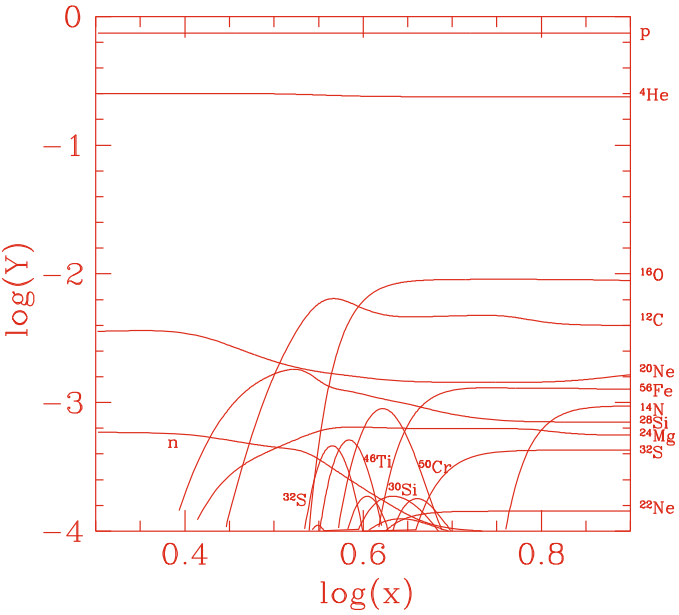



**Fig. 1** Variation of nuclear element mass fraction as a function radial coordinate from the black hole in units of Schwarzschild radius [35]

there are many possibilities of nucleosynthesis in TCAF. Once outflow/jet forms, as predicted in TCAF [10], in near vicinity of a black hole, these synthesized elements come out and contaminate the surrounding universe influencing the metallicity of the underlying galaxy.

TCAF is a powerful model, and is perhaps Chakrabarti's one of the most (if not the most) successful work. It's theory and simulation not only explain emitted photons and corresponding spectra of an accretion disk flow, in particular its harder spectral state, but also related features, like observed quasi-periodic oscillations (QPOs) [11, 26], outflows (which might turn out to jets) [10] etc. This Chapter and the subsequent Chapters devoting high energy astrophysics part of this volume have been mainly devoting to uncover the excellence of TCAF by demonstrating its variety of applications. It has been demonstrated in subsequent Chapters, based on the basic building block established here and next few Chapters, how useful TCAF is in uncovering multiple observations in compact object astrophysics.

A rotating/spinning accretion flow consists of neutrons (however small number be to start with), protons, heliums and heaver ions, in general all sorts of baryon, and electrons, neutrinos, in general some leptons, apart from photons, supplied, e.g., by the companion star. All of them are fermions (except photons) with intrinsic spin half obeying Pauli's exclusion principle. They are the basic building block of infalling matter in the accretion disk which is however influenced by the central rotating/spinning black hole. Hence, the properties of all fermions therein are also influenced by the black hole, which determine furthermore astrophysical features.

Chandrasekhar, in a series of work, explored the behavior of spin-half particles in Kerr geometry (along with other black hole geometries) and investigated the underlying effective potentials and radial parts of the solution of Dirac equation in Kerr geometry; see the Monograph by Chandrasekhar [16]. Subsequently, Chakrabarti, under the mentorship of Chandrasekhar, explored in detail the angular solution of Dirac equation in Kerr metric [5], for the first time in the literature to the best of my knowledge. Subsequently, there was a gap of one and half decades in this continuous exploration before I joined Chakrabarti to work in this topic in very last few years of previous century. In a series of papers, along with Chakrabarti I explored the complete solutions (radial and angular, and combined results) of Dirac equation in Schwarzschild (whose angular solution is simply the spherical harmonics) [34], Kerr [13, 36] and Reissner-Nordström [27] geometries and their applications. In fact, my Ph.D. thesis under the supervision of Chakrabarti had two parts: nucleosynthesis in TCAF and solutions of Dirac equation in various black hole geometries, under the remarkable caliber of Chakrabarti and me (!). Interestingly, either of the fields Chakrabarti himself inherited during his Ph.D. research period, which more interestingly he did not pursue much in the post-Ph.D. period (though read the Chapters of this volume devoted to astrochemistry which are apparently inspired by Chakrabarti's original exploration of nucleosynthesis in space). This is because he prioritized other topics of his interest, which are discussed in the latter Chapters. Once introduced by him, I however took the responsibility to

continue exploring both the topics, along with the topics I myself opened later on, which all could not be touched upon in the limited scope of present article.[1]

In early years of this century, I decided to explore astrophysics and cosmology applications of the solutions of Dirac equations. Particular emphasis was supernova disk with enormous neutrino production during the formation of a black hole [25], baryogenesis and leptogenesis [19, 24], degenerate stars [17, 48], neutrino oscillations in curved spacetime [30] etc. In the accretion front, a part of my exploration, related to what I commenced during Ph.D., has been proposing a new pseudo-Newtonian description [28], and subsequent elaboration [38–40], for relativistic accretion flows around a rotating black hole [29], high frequency QPOs [33] in accreting sources, two-temperature general advective accretion flows [44, 45], nucleosynthesis in supernova disks [1, 2] etc.

In the present chapter, I will uncover tremendous roles of angular momentum of black holes, underlying accretion process and fundamental particles therein in order to understand observables. I will show, certain features, even lying with TCAF, only arise if angular momentum is non-zero and in a specific range.

## 2 Effect of Spin Black Hole on Critical Points in Accretion Flows

At least one critical point/radius ($r_c$), which is often the same as the sonic point/radius, is unavoidable in a black hole accretion. Technically speaking, at this radius, the velocity gradient of accreting matter turns out to be of indeterminant (zero-by-zero) form. This is because, far away from the black hole matter is subsonic but close to the black hole event horizon it becomes supersonic, hence matter must be transonic; see [7], for details. A critical point serves as one the boundaries in accretion flows, where the flow energy (E) and accretion rate ($\dot{M}$) become functions of $r_c$ solely [29]. Here, one also obtains the magnitude of Mach number and the sound speed as a function of $r_c$. Hence, by specifying flow E (which is same as E at $r_c$ for the inviscid flow) one can obtain $r_c$ (or $r_c$-s).

It is known that multiple critical points and subsequently shock in TCAF around a black hole are possible only in the presence of general relativistic effect. For the ease of discussion, here we present the set of inviscid advective accretion flow equations in the pseudo-Newtonian formalism [28, 29] around a rotating black hole as

$$\dot{M} = 4\pi r v_r \rho h(r), \quad \mathrm{E} = \frac{1}{2}v_r^2 + nc_s^2 + \frac{\lambda^2}{r^3} + V, \tag{1}$$

[1] See, however, the work on origin of turbulence and transport in accretion disks [31, 41–43]; super-Chandrasekhar white dwarfs [3, 17, 18], which are very important ones.

where $v_r$ is the radial velocity of accretion flow, $\rho$ the density, $h(r)$ the disk scale height, $c_s$ the sound speed, $n$ the polytropic index, $\lambda$ the specific angular momentum, $V$ the pseudo-Newtonian gravitational potential for the flow around a Kerr black hole established earlier [28] given by

$$\frac{dV}{dr} = F = \frac{(r^2 - 2a\sqrt{r} + a^2)^2}{r^3(\sqrt{r}(r-2) + a)^2}, \tag{2}$$

where $a$ is the specific angular momentum of black hole (Kerr parameter) and $r$ the radial distance from black hole. We express the length in units of $GM/c^2$, speed by $c$ and other variables accordingly, when $G$ is the Newton's gravitation constant, $c$ the speed of light and $M$ the mass of black hole. Note further that the differential form of E equation above is the Euler's equation describing the momentum balance of flow leading to $dv_r/dr = 0/0$ at $r_c$ and, hence, the energy and entropy at $r_c$ are respectively given by

$$\mathrm{E}_c = 2(n+1)\left[\left(\frac{\lambda^2}{r_c^3} - F_c\right) / \left(\frac{1}{F_c}\frac{dF}{dr}|_c - \frac{3}{r_c}\right)\right] + V_c + \frac{\lambda^2}{2r_c^2}, \tag{3}$$

$$\dot{\mu}_c = (K(1+n)/n)^n \dot{M} = r_c^{3/2} F_c^{-1/2} \{(2n+1)/n\}^{(2n+1)/4} \times \left[\left(\frac{\lambda^2}{r_c^3} - F_c\right) / \left(\frac{1}{F_c}\frac{dF}{dr}|_c - \frac{3}{r_c}\right)\right]^{n+1}, \tag{4}$$

where $K = P/\rho^{1+1/n}$ carrying information of entropy, where $P$ is the flow pressure.

Variations of $\mathrm{E}_c$ and $\dot{\mu}_c$ with $r_c$ indicate the existence of critical/sonic points and the possible formation of shock. For example, at a given $\mathrm{E}_c$, a positive slope of the $\mathrm{E}_c - r_c$ curve indicates a center-type critical point (through which matter never passes) and a negative slope indicates a saddle-type critical point. Formation of a shock requires two saddle-type critical points in either sides of a center-type critical point in a flow. See [8], for details; also see [50].

Figure 2 (left-panel) shows that for a nonrotating or low spinning black hole, two saddle-type and one center-type sonic points are possible to form depending on the energy. However, with the increase of spin of a corotating black hole, the inner saddle-type sonic points disappear as shown in Fig. 2 (left-panel). Therefore, general relativity favors and disfavors both the formation of multiple critical/sonic points in a flow, depending on the angular momentum of black hole (and also $\lambda$). This is because, the presence of black hole's event horizon at $r > 0$ renders dominating gravitational force over centrifugal force in the vicinity of black hole as well as far away of it, resulting in multiple critical points and a possible formation of shock, when at an intermediate distance centrifugal force dominates. However, when a corotating black hole's spin increases, it increases an angular drag in the spacetime around it, partly opposing radial gravitational force and reducing dramatic radial infall of matter compared to the situation of a nonrotating black hole. This also

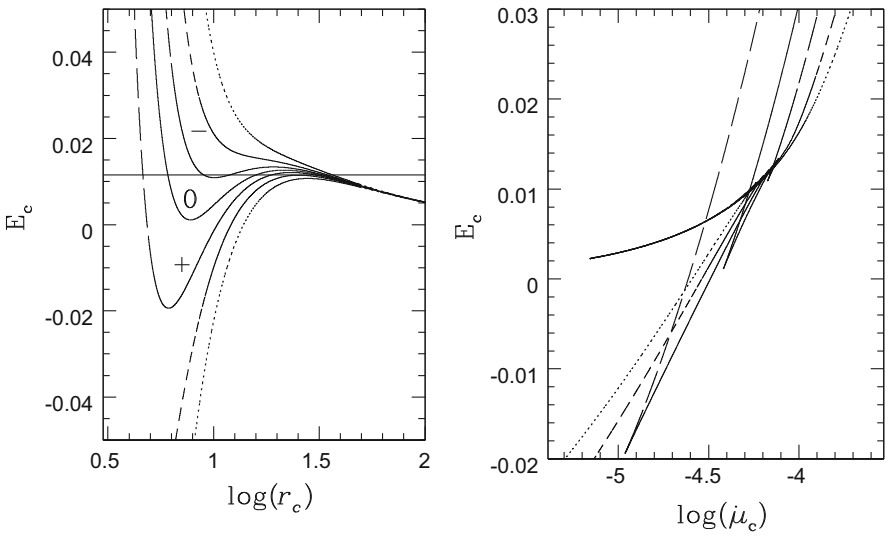



**Fig. 2** Left-Panel: Energy at critical points as a function of critical radius at various Kerr parameters for $\lambda = 3.2$. Central solid line, marked as '0', is for $a = 0$. The lines below it (zone demarked as '+') from top to bottom respectively are for $a = 0.2$ (long-dashed), 0.5 (dashed) and 0.998 (dotted) and the lines above it (zone demarked as '−') from bottom to top respectively are for $a = -0.2$ (long-dashed), $-0.5$ (dashed) and $-0.998$ (dotted). Right-Panel: Energy at critical points as a function of entropy at critical points. Others are same as Left-Panel

prompts in reducing maximum allowed angular momentum (and minimum required angular momentum for shock) and hence centrifugal force in the accreting matter, resulting in disappearance of inner saddle-type critical points, in particular at a given $\lambda$. For a counterrotating black hole, on the other hand, situation is opposite when the angular drag in the spacetime is in the opposite direction to the flow angular velocity and hence partly cancels it. This prompts in increasing the maximum allowed angular momentum (and minimum required angular momentum for shock) and hence centrifugal force in the accreting matter. Therefore, the multiple critical points and shock are more favored at higher angular momentum of the flow. Therefore, depending on the orientation of black hole's spin, inner saddle-type critical/sonic points may or may not appear at a given $\lambda$. This has been demonstrated explicitly in next section.

Figure 2 (right-panel) confirms that for a given $\lambda$, the closed region demarked by the loci of inner and outer saddle-type and center-type critical points is possible or favored only at low Kerr parameters. The occurrence of this region leads to the possible transition of flow from outer to inner critical point branches by increasing entropy at a fixed energy (hence satisfying Rankine-Hugoniot shock conditions) resulting in shock formation.

Therefore, we can summarize the following:

1. Advective accretion disks around a nonrotating or slowly rotating black hole can have inner, outer and center-type critical points, if the net angular momentum of flow is in a certain range.
2. Pure Newtonian description of advective accretion flows is misleading, which does not predict the formation of shock (as there is no singularity at $r = 2$).
3. As the spin of corotating black hole increases, gravitational strength becomes softer compared to the net centrifugal effect at a given $r$, while event horizon forms more and more close to the black hole. This also shrinks the size of horizon to inner most stable circular orbit radius, where the inner saddle-type sonic point forms generally. As a result, the possibility of formation of shock decreases around faster spinning black holes, unless the flow angular momentum is suitably reduced.
4. For a fast counterrotating black hole, however, the size of horizon to inner most stable circular orbit increases and the lower and upper bounds of flow angular momentum giving rise to two saddle-type critical points and shock increase.

Note that the formation of multiple critical points and shock are the basic building block to explain important observables in TCAF, e.g. outflow, QPO etc. Interestingly, disappearance and/or instability of critical points was also shown in very hot flows consisting of significant nuclear burning [37]. In such a situation, a significant nuclear energy generates/absorbs which is comparable to viscous energy released in the flow.

## 3 Interplay Between Disk Angular Momentum and Kerr Parameter to Form Critical Points in Accretion Flows

Bondi flow, which is a class of spherical accretion, exhibits only one saddle-type critical point in a flow and hence no shock around a black hole; see, however, [20]. It is the disk angular momentum and the flow centrifugal force which leads to two saddle-type and one center-type critical points and hence shock formation. However, as the centrifugal is a quadratic effect, it does not depend on the orientation of disk rotation, unlike the effect due to spin of black hole. Figure 3 (left-panel) shows how with the increase of disk angular momentum, two more critical points emerge in a flow which has had only one saddle-type critical point at lower angular momenta. However, at a very high angular momentum, even though three critical points exist there is no formation of shock (e.g. $\lambda = 3.6$). This is because there is no possibility of transition from outer to inner critical point branches by increasing entropy in the flow at a fixed energy (hence not satisfying Rankine-Hugoniot shock conditions).

Nevertheless, for a rotating black hole, the range of angular momentum giving rise to multiple $r_c$ and hence shock changes. Figure 3 (middle-panel) shows that even at $\lambda = 2.8$ multiple $r_c$ exist for $a = 0.5$, which however produces only one

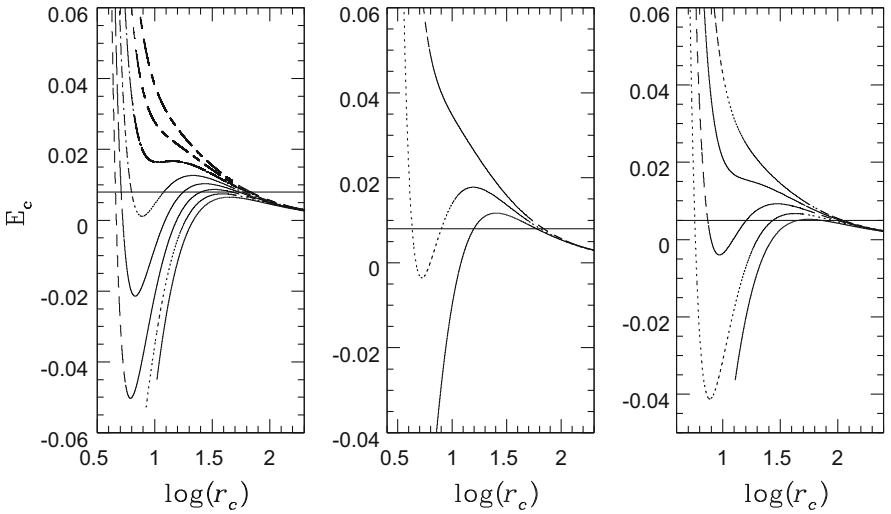



**Fig. 3** Left-Panel: Energy at critical points as a function of critical radius for a nonrotating black hole. The lines from top to bottom are respectively for $\lambda = 2.6, 2.8, 3, 3.2, 3.4, 3.6, 3.8$ and 4. Middle-Panel: Same as Left-Panel but for a black hole with $a = 0.5$ when the lines from top to bottom are respectively for $\lambda = 2.4, 2.8$ and 3.2. Right-Panel: Same as Left-Panel but for a black hole with $a = -0.05$ when the lines from top to bottom are respectively for $\lambda = 2.8, 3.2, 3.6, 4$ and 4.4

$r_c$ for $a = 0$. On the contrary, at $\lambda = 3.2$, there are only two $r_c$ (one saddle- and center-type each) for $a = 0.5$, whereas an additional $r_c$ is there, and hence shock is possible, for $a = 0$. Figure 3 (right-panel), on the other hand, shows that even at $\lambda$ as high as 3.6 multiple $r_c$ exist for $a = -0.5$, whereas $\lambda = 3.2$ reveals only one $r_c$ which has two more $r_c$ for $a = 0$, hence $\lambda$ range giving rise to shock shifts to higher side. Like the case of nonrotating black holes, at a very high $\lambda$, say at 4, although there are multiple $r_c$ for $a = -0.5$, Rankine-Hugoniot conditions do not satisfy to form a shock. Even at a higher $\lambda$, e.g. at 4.4, the locus of inner saddle-type $r_c$ disappears, as shown in Fig. 3 (right-panel).

Therefore, we summarize that the rotation of black hole and disk angular momentum (around $r_c$ in viscous flows) both control TCAF solutions, their consequences and the underlying physically viable parameter space to explain observation. This may be useful to extract fundamental characters (mass, spin) of black holes. Hence, accretion around a corotating black hole appears to be more quasi-spherical in the near vicinity with lower specific angular momentum compared to that around a counterrotating black hole. Hence, effectively the black hole's spin determines the flow geometry.

## 4 Consequence of Spinors in Curved Spacetime

Now we turn our focus into more fundamental level, in quantum level, in order to understand the constituents of disk/flow matter, e.g. individual particles therein, accreting towards a black hole. Naturally they are influenced by the underlying spacetime curvature.

Baryons and leptons, being spin-half particles, interact with background spacetime curvature while propagating in accretion disks towards a rotating central black hole; see, e.g., [30, 32]. This effect, namely coupling of spinors with background spin connections, is expected to have astrophysical consequences in, namely, neutrino-dominated accretion disks forming during the formation of a black hole [23]; cosmological consequences in, namely, leptogenesis and baryogenesis in early universe [19]; consequences in the astroparticle sector, e.g. effective CPT violation in neutrinos [49], a black hole's behaving as a mass-spectrograph [34, 36], etc.

Nevertheless, here we touch upon a newer consequence, when spinors' propagating in a curved spacetime is shown leading to "gravitational Zeeman splitting" in their energy and a geometric phase.

### *4.1 Gravitational "Zeeman Effect"*

One has to start with the Dirac equation in curved spacetime, which I have been working on since the beginning of research career. Dirac equation in the presence of background gravitational fields is known to have the form [4, 22, 32, 46]

$$\left[i\gamma^{\mu}\partial_{\mu} - m + i\gamma^{\mu}A^{g}_{\mu} + \gamma^{5}\gamma^{\mu}B^{g}_{\mu}\right]\psi = 0, \tag{5}$$

where $A^{g}_{\mu}$ and $B^{g}_{\mu}$ are the gravitational covariant 4-vector potentials (gravitational coupling with the spinor), $m$ is the mass of the spinor, and $\gamma^5 = \gamma_5 = i\gamma^0\gamma^1\gamma^2\gamma^3$ as usual, when the Dirac $\gamma$-matrices have their usual meaning. Here we choose $\hbar = c = 1$ ($\hbar$ being reduced Planck's constant). For simplicity, in rest of the discussion we retain and explore the consequence of the axial-vector-like term in equation which suffices for the present purpose. Nevertheless, the vector-like term might be anti-hermitian as well (depending on the spacetime nature) and can be removed from the total Lagrangian when adding with its complex conjugate part.

Now like the case of standard electromagnetic fields known to produce Zeeman effects, for a nontrivial solution of $\psi$, the Hamiltonians of spin-up and spin-down particles are given by

$$(H + \boldsymbol{\sigma}.\mathbf{B}^{g})^2 = \mathbf{p}^2 + {B^{g}_{0}}^2 + m^2 - 2B^{g}_{0}\boldsymbol{\sigma}.\mathbf{p}, \tag{6}$$

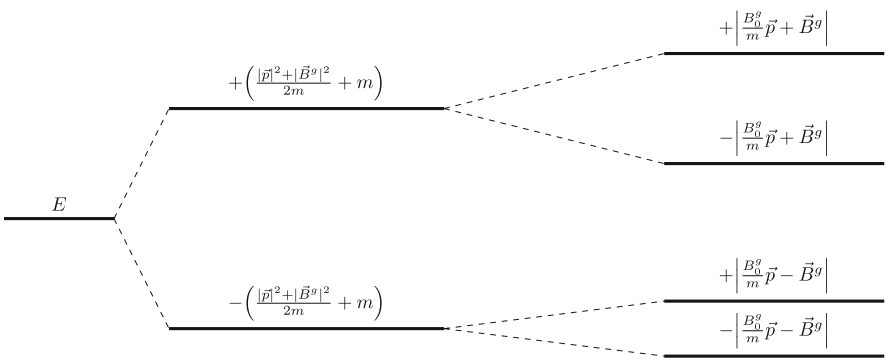



**Fig. 4** Gravitational "Zeeman-splitting"

where $B_0^g$ is the temporal component of $B_\mu^g$. In the regime of weak gravity and when $m$ is much larger than the rest of the terms in the R.H.S. of Eq. (6), it reduces to

$$H = -\boldsymbol{\sigma}.\mathbf{B}^g \pm \left[\frac{\mathbf{p}^2 + B_0^{g\,2}}{2m} + m - \frac{B_0^g \boldsymbol{\sigma}.\mathbf{p}}{m}\right]. \tag{7}$$

Figure 4 represents the energy splitting given by Eq. (7). Here the splittings are different than those in electromagnetic case. Both the splittings are involved with the interaction between the spin and background gravitational fields, hence, called the gravitational "Zeeman-effect". The two-fold splitting in dispersion energy between up and down spinors for positive and negative energy spinors induced by gravitational fields is governed by two terms associated with the Pauli spin matrix, whether the field is weak or strong.

## *4.2 Gravitational Geometric/Berry Phase*

The terms associated with Pauli matrix in Eq. (7) are also responsible for geometric phase for up or down spinors, similar to the case in electromagnetic fields, which in spherical polar coordinates with $\mathbf{R} \equiv (r, \tilde{\theta}, \tilde{\phi})$ is given by

$$\Phi_g = i \oint \langle\psi|\nabla|\psi\rangle.d\mathbf{R} = \frac{\tilde{\phi}}{2}(1 - \cos\tilde{\theta}). \tag{8}$$

Interestingly, even if $B_\mu^g$ is constant (in a local inertial frame) but nonzero, as $\mathbf{p}$ is varying—at least expected to change the momentum direction due to the propagation of spinor, $\Phi_g$ survives, as seen from the last term in Eq. (7). Hence, while in electromagnetic fields the magnetic potential and hence field has to be varying, in gravitational field even the constant (but nonzero) gravitational potential still could produce geometric phase.

### 4.3 Condition for Nonzero $B^g_\mu$ and Its Computation in Various Spacetimes

The gravitational potential $B^g_\mu$ can be computed in various spacetime metrics. Very importantly, in order to have nonzero $B^g_\mu$, the spherical symmetry has to be broken and hence in Schwarzschild geometry (and hence for the spacetime around a nonrotating black hole), it vanishes. On the other hand, in Kerr geometry (and hence for the spacetime around a rotating black hole), it survives. Also it survives in other natural spacetimes breaking spherical symmetry, e.g. in early universe under gravity wave perturbation, Bianchi II, VIII and IX anisotropic universes, in Fermi-normal coordinate up to second order correction. Note that in an expanding universe, gravitational potential $B^g_\mu$ turns out to be constant at a given epoch which could act as a background effect.

In the Kerr-Schild coordinate, after putting $\hbar$ and $c$ appropriately, the temporal part of $B^g_\mu$ reads as [32]

$$B^g_0 = -\frac{4az}{\bar{\rho}^2\sqrt{2r^3}}\frac{\hbar c}{r_g}, \tag{9}$$

where $\bar{\rho}^2 = 2r^2 + a^2 - x^2 - y^2 - z^2$. Naturally, $B^g_0$ survives (and is varying with space coordinates) for any non-spinning black hole leading to gravitational Zeeman effect and geometric phase independent of the spatial part $\mathbf{B}^g$. The contribution to geometric phase from nonzero $\mathbf{B}^g$ arises only if it is varying.

In Bianchi II spacetime with, e.g., even equal scale-factors in all directions, $B^g_0$ survives as [19]

$$B^g_0 = \frac{4 + 3y^2 - 2y}{8 + 2y^2}\hbar c, \tag{10}$$

leading to a geometric phase even though $\mathbf{B}^g = 0$ (provided $\mathbf{p}$ varying) when $y$ is the size of universe at a given epoch.

## 5 Summary

In this brief article, I have attempted to establish the importance of angular momentum, classical as well as quantum, in astrophysical and cosmological systems. The article has been compiled based on a part of my work in last two decades, since I started my research career under the supervision of Sandip K. Chakrabarti.

One of the fundamental entities lying with many astrophysical and cosmological phenomena is matter accretion or accretion disk. It forms around a highly dense body, e.g. compact star, massive star in a binary system, etc. I have elaborated, in the classical level, that the existence of angular momentum in accretion flows

forming accretion disks and its specific magnitude is expected to control many observed features, like outflows, QPOs around compact sources. This is because disk angular momentum determines flow critical/sonic points which furthermore determine shock formation, leading to many observed features.

However, the range of disk angular momentum controlling flow geometry and subsequently predicting observed data is determined by the angular momentum of compact object, e.g. the Kerr parameter of a black hole in the present discussion, at the center of the flow. It is the combined effects of flow and black hole angular momenta which determine flow critical points and geometry. Moreover, shock in an accretion disk is a general relativistic phenomenon (in a Newtonian formalism it does not work, at least a pseudo-Newtonian formalism has to be considered for it). Therefore, the black hole accretion disk is a class of (general) relativistic astrophysical feature. In the premise of TCAF, several observations related to accretion disk flow have been explored and underlying astrophysics are uncovered in the subsequent Chapters. This Chapter is to be considered as a basic building block of underlying physics.

Another related exploration, which requires a quantum description, is the properties of fundamental particles in accretion disks around a black hole, when particles are influenced by general relativistic effects. As many astrophysical and cosmological phenomena are involved with particle dynamics, in particular the behavior of spin-half particles, in curved spacetime, I have undertaken this mission. While it controls models with collapsar disks, baryogenesis etc., what I explored earlier, in this article I have targeted a different and unique physics. I have shown that spinors in a curved spacetime, e.g. in the geometry of rotating black hole spacetime, have revealed in splitting in their energy: gravitational "Zeeman effects", and also have acquired a geometric phase during their propagation.

Both the explorations of the effects of angular momenta in their respective classical and quantum realms have many far reaching implications, some of which have been touched upon here. More attention needs to be paid in them.

**Acknowledgements** I am indebted to my Ph.D. adviser Sandip Kumar Chakrabarti for considering me as his student and introducing me into the fascinating field of black hole astrophysics two decades back. His advices, suggestions and criticisms furthermore have helped me to shape my independent research career and to branch out into various other fields. I dedicate this Chapter to him.

## References

1. Banerjee, I., Mukhopadhyay, B.: ApJ **778**, 8 (2013)
2. Banerjee, I., Mukhopadhyay, B.: RAA **13**, 1063 (2013)
3. Bhattacharya, M., Mukhopadhyay, B., Mukerjee, S.: MNRAS **477**, 2705 (2018)
4. Birrell, N.D., Davies, P.: Quantum Fields in Curved Space. Cambridge University Press, Cambridge (1982)
5. Chakrabarti, S.K.: Proc. Roy. Soc. Lon. **391**, 27 (1984)

6. Chakrabarti, S.K.: ApJ **347**, 365 (1989)
7. Chakrabarti, S.K.: Theory of Transonic Astrophysical Flows. World Scientific, Singapore (1990)
8. Chakrabarti, S.K.: ApJ **464**, 664 (1996)
9. Chakrabarti, S.K.: MNRAS **283**, 325 (1996)
10. Chakrabarti, S.K.: A&A **351**, 185 (1999)
11. Chakrabarti, S.K., Manickam, S.G.: ApJ **531**, L41 (2000)
12. Chakrabarti, S.K., Mukhopadhyay, B.: A&A **344**, 105 (1999)
13. Chakrabarti, S.K., Mukhopadhyay, B.: MNRAS **317**, 979 (2000)
14. Chakrabarti, S.K., Titarchuk, L.G.: ApJ **455**, 623 (1995)
15. Chakrabarti, S.K., Jin, L., Arnett, W.D.: ApJ **313**, 674 (1987)
16. Chandrasekhar, S.: The Mathematical Theory of Black Holes. Clarendon, London (1983)
17. Das, U., Mukhopadhyay, B.: Phys. Rev. Lett. **110**, 071102 (2013)
18. Das, U., Mukhopadhyay, B.: JCAP **05**, 045 (2015)
19. Debnath, U., Mukhopadhyay, B., Dadhich, N.: MPLA **21**, 399 (2006)
20. Dhang, P., Sharma, P., Mukhopadhyay, B.: MNRAS **461**, 2426 (2016)
21. Jin, L., Arnett, W.D., Chakrabarti, S.K.: ApJ **336**, 572 (1989)
22. Kaku, M.: Quantum Field Theory. Oxford University Press, Oxford (1993)
23. Kohri, K., Narayan, R., Piran, T.: ApJ **629**, 341 (2005)
24. Kolb, E.W., Turner, M.S.: The Early Universe. Levant Books, Kolkata (1989)
25. MacFadyen, A.I., Woosley, S.E.: ApJ **524**, 262 (1999)
26. Molteni, D., Sponholz, H., Chakrabarti, S.K.: ApJ **457**, 805 (1996)
27. Mukhopadhyay, B.: CQG **17**, 2017 (2000)
28. Mukhopadhyay, B.: ApJ **581**, 427 (2002)
29. Mukhopadhyay, B.: ApJ **586**, 1268 (2003)
30. Mukhopadhyay, B.: MPLA **20**, 2145 (2005)
31. Mukhopadhyay, B.: ApJ **653**, 503 (2006)
32. Mukhopadhyay, B.: CQG **24**, 1433 (2007)
33. Mukhopadhyay, B.: ApJ **694**, 387 (2009)
34. Mukhopadhyay, B., Chakrabarti, S.K.: CQG **16**, 3165 (1999)
35. Mukhopadhyay, B., Chakrabarti, S.K.: A&A **353**, 1029 (2000)
36. Mukhopadhyay, B., Chakrabarti, S.K.: Nuc. Phys. B **582**, 627 (2000)
37. Mukhopadhyay, B., Chakrabarti, S.K.: ApJ **555**, 816 (2001)
38. Mukhopadhyay, B., Ghosh, S.: ApJ **667**, 367 (2003)
39. Mukhopadhyay, B., Ghosh, S.: MNRAS **342**, 274 (2003)
40. Mukhopadhyay, B., Misra, R.: ApJ **582**, 347 (2003)
41. Mukhopadhyay, B., Afshordi, N., Narayan, R.: ApJ **629**, 383 (2005)
42. Nath, S.K., Mukhopadhyay, B.: Phys. Rev. E **92**, 023005 (2015)
43. Nath, S.K., Mukhopadhyay, B.: ApJ **830**, 86 (2016)
44. Rajesh, S.R., Mukhopadhyay, B.: New Astron. **15**, 283 (2010)
45. Rajesh, S.R., Mukhopadhyay, B.: MNRAS **402**, 961 (2010)
46. Schwinger, J.: Particles, Sources, and Fields I. Addison-Wesley, Reading (1989)
47. Shakura, N., Sunyaev, R.: A&A **24**, 337 (1973)
48. Shapiro, S.L., Teukolsky, S.A.: Black Holes, White Dwarfs, and Neutron Stars: The Physics of Compact Objects. Wiley-VCH, Weinheim (1983)
49. Sinha, M., Mukhopadhyay, B.: Phys. Rev. D **77**, 025003 (2008)
50. Thompson, J.M.T., Stewart, H.B.: Nonlinear Dynamics and Chaos. Wiley, New York (1985)

# Relativistic Flows in Astrophysics




**Indranil Chattopadhyay**

**Abstract** Most of the matter accreting onto a compact object, or emanating from its vicinity, can be satisfactorily modeled as a fluid. These fluids are different from terrestrial versions. The temperature can range from relativistic values to non-relativistic ones and at high temperature, the fluid is composed of charges and not neutral particles as is the case in the terrestrial version.

We use relativistic equation of state to describe trans-relativistic fluid, around compact objects and at regions far from it. For steady state investigation we took the help of generalized Bernoulli parameter which acts as a constant of motion. We also exploited the fact that the global solution should be of higher entropy and correct boundary conditions. This approach is considered for dissipative accretion flow in curved geometry around black holes, magnetosphere around neutron stars or white dwarfs, and also for magnetically driven outflows. We show that the flow geometry close to a black hole is quite different from a neutron star because of the strong magnetic field around the latter, which has implication on the radiative processes dominant nearby. We also obtained shock solutions for lepton dominated accretion flow around neutron stars, but not around black holes, this is again due to the different flow geometry around the two different types of compact objects. Magnetically driven flows in the special relativistic domain, are able to produce flows which connect both the Alfven and fast sonic points. Numerical simulation of the fluid with relativistic equation of state, shows distinct differences depending on the composition of the flow.

I. Chattopadhyay (✉)
ARIES, Manora Peak, Nainital, Uttarakhand, India
e-mail: indra@aries.res.in

© Springer International Publishing AG, part of Springer Nature 2018

B. Mukhopadhyay, S. Sasmal (eds.), *Exploring the Universe: From Near Space to Extra-Galactic*, Astrophysics and Space Science Proceedings 53,
https://doi.org/10.1007/978-3-319-94607-8_2

## 1 Introduction

Examples of relativistic flows in astrophysics are invariably linked to matter flow into or out of a compact object. Generally a flow is called relativistic when the fluid moves from one spatial position to the other with a speed (i.e., bulk speed) close to the speed of light. Such insane speed can be achieved by accreting matter close to a black hole (BH) [37], or, when matter around a compact object like BH or neutron star (NS) is violently ejected in the form of astrophysical jets [38]. Since, an accretion disk around a compact object has never been directly observed, but jets have been observed, majority of investigations on relativistic fluid were applied to the studies of jets [2, 5–8, 13, 33]. By relativistic fluid mechanics, the general trend had been to either use relativistic equations of motion or, use Newtonian equations of motion with pseudo potentials, and use the adiabatic index to be $\Gamma = 4/3$ in the equation of state of the fluid. However, the thermal speed of the particles that constitute an astrophysical fluid, may also approach the speed of light at some regions of the flow but non-relativistic elsewhere, and thereby make the fluid thermally trans-relativistic. In such cases $\Gamma$ is no more constant, but a function of temperature and composition of the fluid [1, 31, 32].

The exact equation of state (EoS) for relativistic gas has been used in relativistic hydrodynamics tentatively [18, 19]. The major stumbling block is that the perfect EoS is expressed as the ratio of modified Bessel's function of the second kind of order one, two and three, or two and three, or one and two [1, 15, 31], which depends on the recurrence relation used and are equivalent to each other [36]. An extremely close but algebraic approximation of the perfect EoS was proposed [3, 12, 27] and was used to study relativistic jets in flat metric and jets and accretion flow near a BH and NS in strong gravity.

In the next section, we introduce the relativistic EoS and its properties. In Sect. 3, we discuss application of this equation of state on the dynamics of relativistic outflows in flat metric as well as, curved metric. In Sect. 4.1, we discuss the accretion flow onto magnetized compact objects with hard surface. In Sect. 4.2 we discuss accretion on to black holes, and possible precursor of jets. In the last section we summarize and point out to some future direction and issues.

## 2 Equation of State

The closure relation between the thermodynamic quantities like the internal energy, pressure and mass density, is called equation of state (EoS) of a fluid, and it helps to solve the equations of hydrodynamics. If the thermal speed of constituent particles are non-relativistic then the internal energy can be computed by obtaining the expression of average energy of the particles in the momentum or configuration space and is given by $e_{\rm th} = p/(\Gamma - 1)$, where $p$ is the isotropic pressure [30]. However, if the constituent particles are identical and executing relativistic motion,

then the EoS obtained independently by [1, 15, 31] was shown to be equivalent by [36], and are given by

$$e = \rho c^2 \frac{3K_3(1/\Theta) + K_1(1/\Theta)}{4K_2(1/\Theta)} = \rho c^2 \frac{K_3(1/\Theta)}{K_2(1/\Theta)} - p = \rho c^2 \left(3\Theta + \frac{K_1(1/\Theta)}{K_2(1/\Theta)}\right).$$

Here $\Theta$ is proportional to temperature and $c$ is the speed of light in vacuum. We may use the acronym RP (relativistic perfect) to represent the above EoS. The problem is the presence of the ratios of modified Bessel's function, which are difficult to implement in numerical schemes. Primarily motivated by this fact, we proposed a new EoS which was an extremely close approximate of the exact relativistic EoS, in addition it also satisfies the fundamental Taub's inequality [32] and is given by [3, 12, 27],

$$e = n_{e^-} m_e c^2 f; \quad f = (2-\xi)\left[1 + \Theta\left(\frac{9\Theta+3}{3\Theta+2}\right)\right] + \xi\left[\frac{1}{\eta} + \Theta\left(\frac{9\Theta+3/\eta}{3\Theta+2/\eta}\right)\right] \tag{1}$$

where, $\xi = n_{p^+}/n_{e^-}$ is the relative proportion of protons w.r.t electrons, $\eta = m_e/m_p$ is the ratio of electron to proton rest mass and $\Theta = kT/m_e c^2$, where $k$ is the Boltzmann constant. We may use the acronym CR to represent the EoS represented by Eq. (1), from the initials of the original proposers. Figure 1 shows how closely CR mimics RP, even for fluids with different composition. The temperatures corresponding to the electron and proton rest mass are marked on the $T$ axis. It is clear if the flow temperature is higher than the proton temperature then $\Gamma \to 4/3$. However, for purely leptonic flow, $\Gamma \to 4/3$ at temperatures greater than electron rest mass.

## 3 Relativistic Fluids: Outflows

The energy-momentum tensor of a fluid is given by

$$T^{\mu\nu} = T^{\mu\nu}_{\rm M} + T^{\mu\nu}_{\rm R} + T^{\mu\nu}_{\rm EM}, \tag{2}$$

where, the suffix M, R and EM represent the three components for matter, radiation and electro-magnetic field of the energy-momentum tensor, that describes a relativistic fluid. The composite form of the equation of motion of the fluid is given by,

$$T^{\mu\nu}_{;\nu} = 0 \tag{3}$$

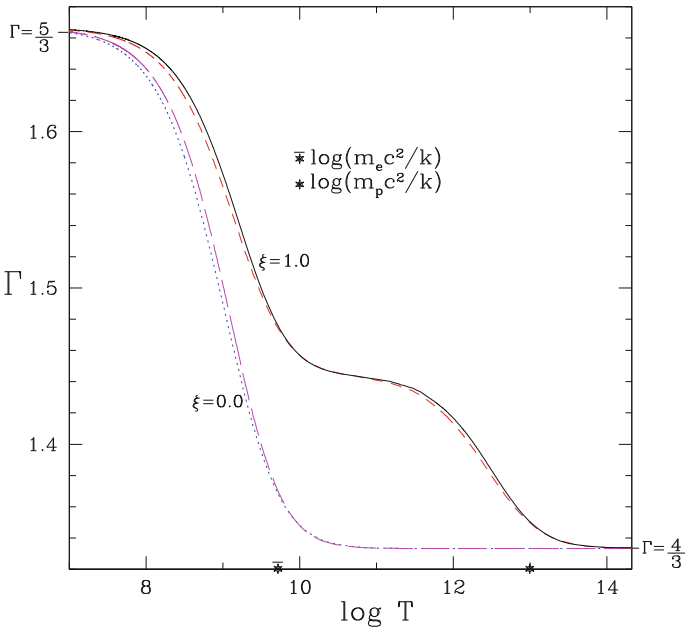



**Fig. 1** Comparison of $\Gamma$ as a function of $T$, between that computed from RP (solid/black, long-dashed/magenta) and CR (dashed/red, dotted/blue) EoS. The two different distributions are for electron-proton flow ($\xi = 1$) and electron-positron flow ($\xi = 0$) (Ref: Fig. C1 a of [36]) (Color figure online)

and the particle number (of matter) conservation equation

$$(nu^{\nu})_{;\nu} = 0. \tag{4}$$

In the above, the Greek alphabets signify space-time components in four space, $u^{\mu}$ components of four velocity, and $n$ the number density measured in fluid rest frame. One needs to solve Eqs. (3), (4) in a given space-time metric, whose general form is $ds^2 = g_{\mu\nu}dx^{\mu}dx^{\nu}$.

## *3.1 Time Dependent Relativistic Hydrodynamics*

We developed a relativistic hydrodynamic code ($T^{\mu\nu}_{\rm R} = T^{\mu\nu}_{\rm EM} = 0$) in special relativity (i.e., $g_{\mu\mu} = (-1, 1, 1, 1)$, $g_{\mu\nu}|_{\mu\neq\nu} = 0$). The energy momentum tensor of the matter is given by $T^{\mu\nu}_{\rm M} = (e + p)u^{\mu}u^{\nu} + pg^{\mu\nu}$. The fluxes were calculated by using Eq. (1). In Fig. 2, we plot density contour and velocity vectors of relativistic jet launched with Lorentz factor $\gamma_{\rm inj} = 10$. In the computational set up we assumed $c = 1$. We showed the jet profile and shock positions differ if we change the composition parameter [4, 14].

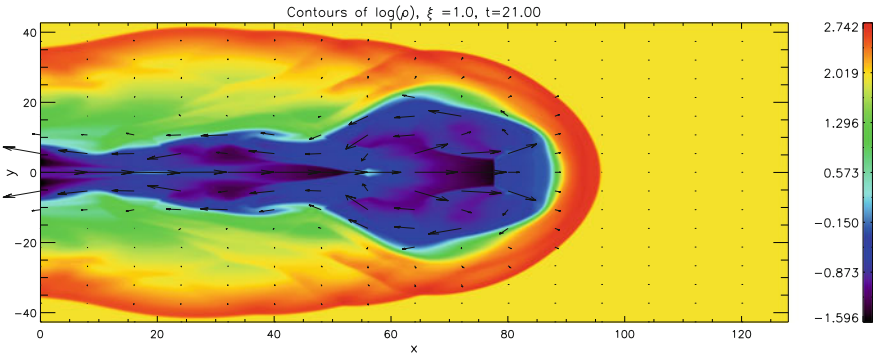



**Fig. 2** Density contour and velocity vector of an astrophysical jet launched with $\gamma_{\rm inj} = 10$, $\rho_{\rm inj} = 0.1$ pressure $p = 0.01$ and ambient density $\rho_{\rm amb} = 100$. The jet is composed of electron-proton plasma

## *3.2 Radiatively Driven Stationary Jets in Curved Space Time*

If we consider $T^{\mu\nu}_{\rm EM} = 0$, $g_{tt} = -(1 - 2GM/rc^2) = -1/g_{rr}$; $g_{\theta\theta} = r^2, g_{\phi\phi} = r^2\sin^2\theta$; $g_{\mu\nu}|_{\mu\neq\nu} = 0$, and $\partial/\partial t = \partial/\partial\phi = 0$, we are in the realm of radiatively driven axisymmetric, stationary flow. For $u^r > 0$ therefore we are in the regime of radiatively driven jets. The radiative stress tensor is given by $T^{\mu\nu}_{\rm R} = \int I l^\mu l^\nu d\Omega$. The momentum balance equation becomes,

$$u^r \frac{du^r}{dr} + \frac{1}{r^2} = -\left(1 - \frac{2}{r} + u^r u^r\right)\frac{1}{e+p}\frac{dp}{dr} + \rho_e \frac{\sigma\sqrt{g^{rr}}\gamma^3}{m_e(e+p)}\Im^r \tag{5}$$

$$\sigma = \chi_c \sigma_T = \left[\frac{1}{1 + \left(\frac{T_e}{4.5\times10^8}\right)^{0.86}}\right]\sigma_T \tag{6}$$

$\sigma_T$ is Thomson scattering cross section, for $\chi_c = 1$ it is the Thomson scattering cross section. $\Im^r$ is a function of radiation moments, and $T_e$ is the electron temperature. The entropy equation is given by

$$\frac{de}{dr} - \frac{e+p}{\rho}\frac{d\rho}{dr} = -\frac{\gamma\rho_e(1-\chi_c)R_t}{\sqrt{g^{rr}}}. \tag{7}$$

Here $R_t$ is radiative contribution representing energy exchange between radiation and fluid:

$$R_t = \frac{\sigma}{m_e}\left[\frac{g^{rr}\mathscr{R}_0}{v} + \frac{v\mathscr{R}_2}{g^{rr}} - 2\mathscr{R}_1\right]$$

where, $\mathscr{R}_0$, $\mathscr{R}_1$, $\mathscr{R}_2$ are the zeroth, first and second moments of radiation field.

Integrating Eqs. (5) and (7) we obtain the generalised Bernoulli parameter

$$E = -hu_t e^{-X_f}, \tag{8}$$

where

$$X_f = \int dr \frac{\gamma(2-\xi)}{(f+2\Theta)\sqrt{g^{rr}}} [\Im - (1-\chi_c)R_t] .$$

It is to be remembered that $E$ is a constant of motion, even if radiation imparts momentum and energy to the jet. It was shown that a jet can suffer from stationary internal shocks due to the change in flow geometry, and also due to the radiation field from a moderately thick accretion disk [34, 35]. However, in the Compton scattering regime because a part of the radiation energy is absorbed by the matter, it increases the thermal energy of the jet and produces faster jets. In Fig. 3a, c, d we plot the jet three-velocity $v$ with radial distance $r$ for the disk with same disk luminosity. The jet generalized Bernoulli parameter $E$ is reduced from 1.2 to 1.07 to 1.04. In Fig. 3a, b we compare the three velocity and temperature of the jet with $E = 1.2$, and show that both the velocity and temperature of the jet is more in the Compton regime than the Thomson scattering regime by about 20%. Figure 3c shows the existence of an internal shock in the jet.

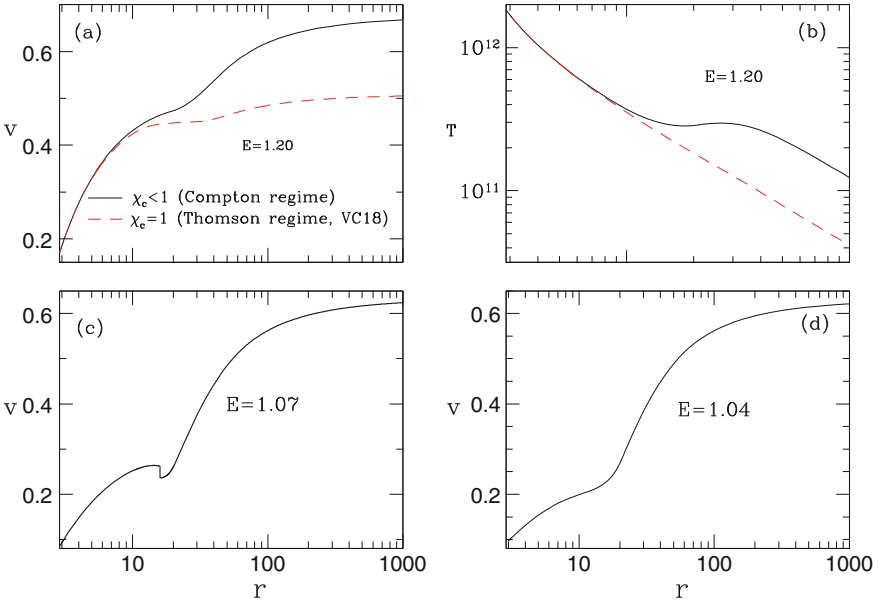



**Fig. 3** Comparison of radiatively driven jet for (**a**), (**b**) $E = 1.2$, (**c**) $E = 1.07$ and (**d**) $E = 1.04$. The solutions presented are electron-proton flow or $\xi = 1$

### 3.3 Relativistic MHD

Magnetically driven outflow was also studied with relativistic EoS. The electromagnetic component of the energy momentum tensor is

$$T^{\mu\nu}_{\rm EM} = F^{\mu}_{\sigma} F^{\nu\sigma} - \frac{g^{\mu\nu} F^{\lambda\sigma} F_{\lambda\sigma}}{4}. \tag{9}$$

Along with this, one has to also solve the electro-magnetic Maxwell's equations which are,

$$\partial_\mu F_{\nu\lambda} + \partial_\nu F_{\lambda\mu} + \partial_\lambda F_{\mu\nu} = 0; \ \& \ F^{\mu\nu}_{;\nu} = -J^{\mu},$$

here, $F_{\mu\nu}$ is the electro magnetic field tensor. We followed the methodologies of [33], but used CR EoS instead of fixed $\Gamma$ EoS and obtained trans Alvenic and trans-fast MHD outflows in flat metric (see Fig. 4). The slow critical point is not obtained without gravity.

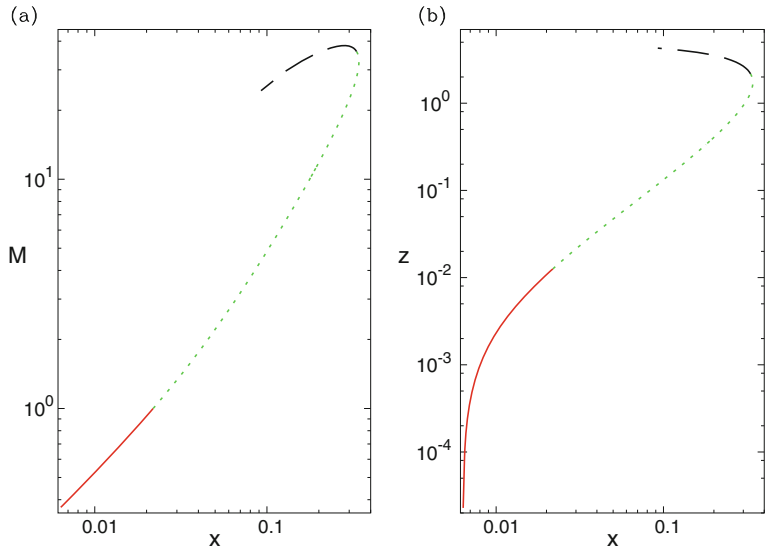



**Fig. 4** (**a**) The Alven Mach number $M$ with cylindrical radial distance in units of light cylinder radius. (**b**) Cylindrical radial coordinate $x$ with the axial coordinate $z$ is plotted. Junction between solid and dotted curve is the Alfven point, while between dotted and dashed curve is the fast sonic point. The solutions presented are electron proton flow or $\xi = 1$

# 4 Accretion Flows

## 4.1 Around Black Holes

Our investigation on accretion flows around black holes started mainly with fixed $\Gamma$ EoS [10, 16, 17, 21, 25, 26]. Since the temperature distribution of an accretion flow varies by 3–4 order of magnitude, therefore from Fig. 1 it is clear that, the relativistic EoS has to be considered for correct physics. We used the CR EoS on accretion flow on to black holes in the inviscid as well as in the viscous regime [3, 9, 11, 12, 22–24]. Inviscid solutions are relatively easy to obtain, simply because, for a given specific energy and angular momentum, the sonic or critical points can be found out uniquely. However, for dissipative flow, the critical points cannot be known apriori. We integrated all the equations of motion in steady state to obtain the generalized Bernoulli parameter, and used it to generate the global solutions. The generalized Bernoulli parameter is expressed as,

$$E = h\gamma_v \exp X_f \tag{10}$$

$$X_{f1} = \int \left[ \frac{1 - a_s^2/r^2}{r^2(1 - 2/r + a_s^2/r^2)} + \frac{l^2}{2r^3 \mathscr{D} \gamma_v^2} - \frac{(0.5r^3\mathscr{A} + r^3 - a_s^2)(l^2/\mathscr{A} + \omega\gamma\sqrt{\frac{\mathscr{A}}{\mathscr{D}}})}{r^2\gamma_v^2} \right] dr$$

$$X_{f2} = \int \left[ \frac{g^{\phi\phi} g_{rr} \tilde{\tau} \rho u^r (L - L_0)^2}{2\eta(f + 2\Theta)} - \frac{\Lambda}{(e + p)u^r g^{rr} \gamma_v^2} - \frac{S^r}{(e + p)\mathscr{D}} \right] dr$$

and

$$X_f = X_{f1} + X_{f2},$$

$S^r = u^r t_{\phi r} \sigma^{r\phi}$, $t_{\mu\nu}$ are the components of viscous stress tensor, and $\sigma_{\mu\nu}$ are components of shear tensor, $\Lambda$ is the combined radiative cooling term, $\tilde{\tau}$ is the composition function, $L = hu_\phi$, $\gamma_v$ is the Lorentz factor related to three velocity along the radial direction, $\gamma$ is the total Lorentz factor, $\mathscr{A} = 1 + a_s^2/r^2 + 2a_s^2/r^3$, and $\mathscr{D} = 1 - 2/r + a_s^2/r^2$, where $a_s$ is the Kerr parameter. $E$ is constant of motion even in presence of viscosity and cooling. We use this constant of motion to obtain all possible accretion solutions.

We found that, accretion solutions may admit shock solutions, but in addition to energy or angular momentum of the flow, the fluid has to contain significant protons to make it hot enough. Accretion flows are convergent flows and become hotter as they accrete towards the central object. Due to the property of the space-time around a black hole, the inflow geometry is approximately a radial flow, independent of the nature of flow geometry further out. Lepton dominated flows are not hot, and even in convergent flow on to a black hole, it only becomes hot enough to produce a sonic point close to the horizon and not hot enough to form a shock. Therefore, lepton

dominated accretion flow around a black hole cannot produce a shock or very high energy radiation, and this is true for inviscid as well as viscous accretion flow as well.

We also estimated formation of bipolar jets from accretion flows around black holes. We solved the equations of Von-Zeipel surfaces to obtain the jet streamlines. We showed that for Kerr parameter $a_s > 0.6$, shocks can even form in jets. Interestingly, the shock in jets imposed by the curved space-time of a highly spinning black hole, is stronger than shock in accretion flow. The related radiative properties is yet to be worked out.

### *4.2 Accretion Around Compact Objects with Hard Surface*

Accretion flow onto a neutron star or a white dwarf is different from that around a black hole, essentially on two accounts—(1) neutron stars or white dwarfs have hard surfaces, while a black hole has none, and (2) space time around a neutron star or white dwarf has intrinsic magnetic field anchored to the star itself, but a black hole has no intrinsic magnetic field.

We solved the equations of motion in the strong field approximation and showed that in addition to the shock formed close to the star surface, there is a possibility of a second shock forming further away from the surface. Moreover, we also showed that the temperature profile considered is distinctively different if one considers a fixed $\Gamma$ EoS or CR EoS [28, 29]. Another major difference is in the flow geometry around a neutron star, controlled by the magnetic field around it. The cross-section decreases at a steeper rate than a radial flow geometry, such that shocks may form even for lepton dominated accretion flow. The major advancement in this field is in consideration of cooling processes in order to obtain a solution which matches the inner boundary condition on the surface of the star.

## 5 Summary and Future Direction

In this paper we showed, how our understanding of relativistic fluid-mechanics as applied to astrophysics has affected our understanding of the physics related to compact objects. We showed that, the composition indeed affects the flow structure. The choice of $\Gamma$ in fixed $\Gamma$ EoS is critical to obtain a magnetically driven outflow which passes through both the Alfven and fast points. But using CR EoS relieves us from such constraints. In relativistic simulations we obtained flow structure which depend on composition of relativistic jets, which is not seen in simulations with fixed $\Gamma$ EoS. Accretion of lepton dominated flows around a black hole is distinctly different from that around a neutron star. We also showed that if some protons are present in the accretion flow then high energy phenomena like shocks will occur for some choice of flow parameters. Some workers have used relativistic EoS and

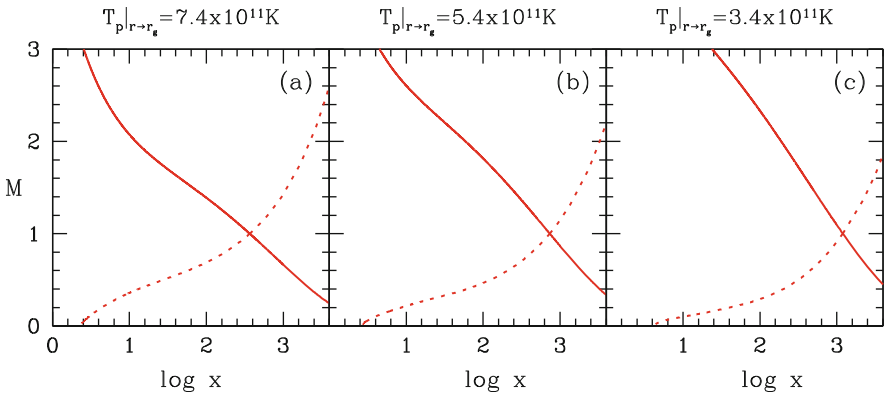



**Fig. 5** Transonic Bondi two-temperature solution in Schwarzschild metric for the same $E = 1.0001$, $\dot{M} = 0.1$ and $M_{BH} = 10$ but multiple transonic solutions. Here $\xi = 1$, accretion rate $\dot{M}$ is in units of Eddington rate and black hole mass, in units of solar mass

failed to detect accretion shock around black holes [20]. Their limitation was that they used electron-positron flow, which will not only not show shocks but also fail to produce multiple sonic points even in the inviscid limit.

Two major aspects remains to be investigated, (1) two temperature accretion solution with CR EoS, (2) treating $\xi$ as a flow variable rather than a constant. The problem with two temperature solution is that, there is another increase in flow variable i.e., instead of one temperature $\Theta$, we now have two temperatures $\Theta_e$ and $\Theta_p$, without any increase of the number of governing equations. Therefore, one can construct multiple transonic solutions for the same generalized Bernoulli parameter. In Fig. 5 we show three transonic two temperature Bondi solution in general relativity, all corresponds to the same $E$ and $\dot{M}$. One needs to find a principle to try and obtain the unique two temperature solution. In addition, one has also to consider how a variable $\xi$ would affect the solutions.

**Acknowledgements** The author acknowledges Mr. Mukesh K. Vyas, Mr. Kuldeep Singh and Ms. Shilpa Sarkar for their help in preparing the plots.

## References

1. Chandrasekhar, S.: An Introduction to the Study of Stellar Structure. Dover, New York (1938)
2. Chattopadhyay, I.: MNRAS **356**, 145 (2005)
3. Chattopadhyay, I.: In: Chakrabarti, S.K., Majumdar, A.S. (eds.) AIP Conference Series, vol. 1053, pp. 353–356. Proceedings of 2nd Kolkata Conference on Observational Evidence of Back Holes in the Universe and the Satellite Meeting on Black Holes Neutron Stars and Gamma-Ray Bursts. American Institute of Physics, New York (2008)

4. Chattopadhyay, I.: In: Chattopadhyay, I., Nandi, I., Das, S., Mandal, S. (eds.) Proceedings of Recent Trends in the Study of Compact Objects (RETCO-II): Theory and Observation. Astronomical Society of India Conference Series, vol. 12, pp. 131–132 (2015)
5. Chattopadhyay, I., Chakrabarti, S.K.: IJMPD **9**, 57 (2000)
6. Chattopadhyay, I., Chakrabarti, S.K.: IJMPD **9**, 717 (2000)
7. Chattopadhyay, I., Chakrabarti, S.K.: BASI **30**, 313 (2002)
8. Chattopadhyay, I., Chakrabarti, S.K.: MNRAS **333**, 454 (2002)
9. Chattopadhyay, I., Chakrabarti, S.K.: Int. Journ. Mod. Phys. D **20**, 1597–1615 (2011)
10. Chattopadhyay, I., Das, S.: New A. **12**, 454–460 (2007)
11. Chattopadhyay, I., Kumar, R.: MNRAS **459**, 3792–3811 (2016)
12. Chattopadhyay, I., Ryu, D.: ApJ **694**, 492 (2009)
13. Chattopadhyay, I., Das, S., Chakrabarti, S.K.: MNRAS **348**, 486 (2004)
14. Chattopadhyay, I., Ryu, D., Jang, H.: In: Khare, P., Ishwara-Chandra, C.H. (eds.) In: Proceedings 31st ASI Meeting, BASI. Astronomical Society of India Conference Series, vol. 9, pp. 13–16 (2013)
15. Cox J.P., Giuli, R.T.: Principles of Stellar Structure, vol. 2. Gordon and Breach Science Publishers, New York (1968)
16. Das, S., Chattopadhyay, I.: New A. **13**, 549–556 (2008)
17. Das, S., Chattopadhyay, I., Nandi, A., Molteni, D.: MNRAS **442**, 251–258 (2014)
18. Falle, S.A.E.G., Komissarov, S.S.: MNRAS **278**, 586–602 (1996)
19. Fukue, J.: PASJ **39**, 309 (1987)
20. Gammie, C.F., Popham, R.: ApJ, **498**, 313–326 (1998)
21. Kumar, R., Chattopadhyay, I.: MNRAS **430**, 386–402 (2013)
22. Kumar, R., Chattopadhyay, I.: MNRAS **443**, 3444–3462 (2014)
23. Kumar, R., Chattopadhyay, I.: MNRAS **469**, 4221–4235 (2017)
24. Kumar, R., Singh, C.B., Chattopadhyay, I., Chakrabarti, S.K.: MNRAS **436**, 2864–2873 (2013)
25. Kumar, R., Chattopadhyay, I., Mandal, S.: MNRAS **437**, 2992–3003 (2014)
26. Lee, S.-J., Chattopadhyay, I., Kumar, R., Hyung, S., Ryu, D.: ApJ **831**, 33 (2016)
27. Ryu, D., Chattopadhyay, I., Choi, E.: ApJS **166**, 410–420 (2006)
28. Singh, K., Chattopadhyay, I.: JoAA **39**, 10 (2018)
29. Singh, K., Chattopadhyay, I.: MNRAS, **476**, 4123–4138 (2018)
30. Spitzer, L.: Physics of Fully Ionized Gas. Wiley, New York (1956)
31. Synge, J.L.: Relativisitc Gas. North Holland, Amsterdam (1957)
32. Taub, A.H.: Phys. Rev. **74**, 328 (1948)
33. Vlahakis, N., Konigl, A.: ApJ **596**, 1080 (2003)
34. Vyas, K.M., Chattopadhyay, I.: MNRAS **469**, 3270–3285 (2017)
35. Vyas, K.M., Chattopadhyay, I.: A&A (2018, in press). https://doi.org/10.1051/0004-6361/201731830
36. Vyas, K.M., Kumar, R., Mandal, S., Chattopadhyay, I.: MNRAS **453**, 2992–3014 (2015)
37. Wald, R.M.: General Relativity. University of Chicago Press, Chicago (1984)
38. Zensus, J.A., Cohen, M.H., Unwin, S.C.: ApJ **443**, 35 (1995)

# Evolution of Imaging of Black Hole Accretion-Outflow System over Half a Century




**Arka Chatterjee**

**Abstract** Light bending around black holes has a beautiful consequence on the image of accretion disks around black holes. The nature of disks around black holes has evolved from a static Keplerian disk to modern days dynamic advective flow models. As a result, the images of black holes have changed. Major efforts of producing simulated black hole images are briefly presented. Distinguishing event horizon from the disk will be one of the major discoveries of this century. Event Horizon Telescope (EHT) is getting prepared to discern the horizon of Sgr A* where radio interferometry technique has been deployed. For Galactic black holes, the required resolution is much higher and X-ray interferometry is essential.

## 1 What to See?

A black hole is by definition a region where the *"space is falling faster than light"*—Hamilton. A singularity in space-time is covered by the event horizon. Classical [41] general relativity debunks the idea of seeing inside a black hole horizon. However, the mathematical simplicity involving the intrinsic properties of a black hole allows us to extract information on mass and spin without penetrating the horizon itself. Schwarzschild [62] radius $R_s = \frac{2GM_{bh}}{c^2} \sim 3 \times \frac{M_{bh}}{M_\odot}$, where $G$ is universal gravitational constant, $M_{bh}$ is the mass of black holes, $M_\odot$ is the mass of sun and $c$ is the speed of light, defines the extent of the horizon region of any black hole. As $M_{bh}$ increases, the size of the horizon increases linearly and more region disappears from the outside universe. For a non-spinning black hole, $R_s$ is single valued and thus, it is a spherical region. However for a Kerr black hole [44], $R_H = \frac{R_s \pm \sqrt{R_s^2 - 4a^2}}{2}$ has two solutions and distorts from its spherical shape depending on the spin parameter. So, the quest of observing a black hole can be narrated down to resolving the shape and size of the horizon. There is more to

A. Chatterjee (✉)
Indian Centre for Space Physics, Kolkata, India

© Springer International Publishing AG, part of Springer Nature 2018

B. Mukhopadhyay, S. Sasmal (eds.), *Exploring the Universe: From Near Space to Extra-Galactic*, Astrophysics and Space Science Proceedings 53,
https://doi.org/10.1007/978-3-319-94607-8_3

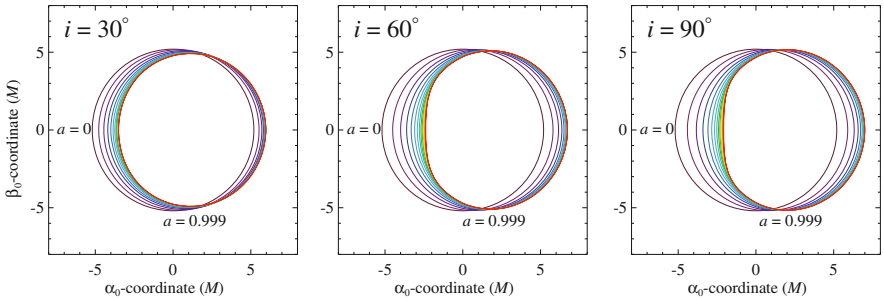



**Fig. 1** Black hole shadows for different spin and inclination angle are presented in [11]. Distortion in the shadows moves with the inclination angle only when the spin is present

the story. Photons cannot escape from the surface of the horizon. The last orbit of photons after which all photons must be absorbed by the black hole is known as photon orbit. This is a highly unstable orbit. Photons can either escape or fall into the black hole. For a spin less black hole the orbit occurs at $r_{po} = \frac{3R_s}{2}$ and for a spinning black hole $r_{po} = R_s\left[1+\cos\left(\frac{2}{3}\cos^{-1}\left(\pm\frac{a}{M}\right)\right)\right]$. In case of a Kerr black hole, not only the shape of the photon sphere deviates from spherical shape it also changes with the inclination angle. Figure 1 (adopted from [11]) represents the theoretical shape of the photon sphere for various spin parameters seen from three different inclination angles. The distortion is found to be maximum at edge on situation. Beyond this photon sphere, the region is perfectly dark and known as the black hole shadow. Essentially, distinguishing this region is the holy grail of seeing a black hole. It is to be noted that various space-time geometries will generate numerous structures (see [5, 43, 65] for details) of this shadow region and is the most perfect place where the theories of curved space time are subjected to extreme tests.

However, the problem of seeing the horizon remained disturbingly fascinating as a black hole does not radiate by itself. So, catching photons from a region as close as to horizon was declared unphysical. But, the story of black hole imaging started with the flourishing subject of accretion physics (see [8, 63]). Accretion disks are formed during matter infall on the black hole from nearby stellar body. While the matter flowing inside the hole, it loses gravitational potential energy which is transferred into radiation. This radiation comes out spreading all over the electromagnetic spectrum. Depending on mass of the black hole and proximity of the emitting region from black hole, the radiation can be in radio or in X-rays. The more matter falls into the potential well of the black hole, it radiates more. But, there is a limit on how much matter can accrete into the black hole per unit time and the matter will not block the radiation. The limit is known as Eddington limit. Beyond this limit radiation may drive away the inflowing matter in outward directions causing outflows.

The geometry of the accretion disk depends on the spin parameter of the black hole. Accretion disk configuration in the region close to the black hole deviates more

with the spin. Without falling onto a black hole, the closest possible orbit is at $2R_s$ also known as marginally bound orbit $r_{mb}$ (see [1]) where binding energy vanishes. With increasing spin, for prograde orbits $r_{mb}$ approaches the horizon (see [12]) with the condition $r_{mb} \geq r_{po}$. Thus, theoretically, it is possible to detect photons emitted from $r_{mb}$. The current situation of observing a black hole is by catching photons emitted from the accretion disk from a very close region to the central black hole and to significantly extract the information of the shadow region by resolving the region with the best possible SNR instrumentation.

However, interpretation of the observed photons emitted from a close region of black holes demands the understanding of modern accretion mechanism like, Two Component Advective Flow (see [17] for details) (TCAF) solution. Two components, namely, Keplerian and sub-Keplerian form a shock at specified location depending on the energy and angular momentum of the inflow (see [13, 15]). Matter slows down due to the outward centrifugal force and hence the post-shock region is known as the CENtrifugal pressure supported BOundary Layer or CENBOL. Effects of viscosity on the shock formation are prescribed (see [14, 16]). Formation of shock and luminosity variation due to shock oscillation are presented in the literature (see [51, 52]). The sub-Keplerian flow or the halo sandwiches Keplerian disk which acts as soft-photon source. Together, the flow forms a complete set of solutions which simulates spectral and temporal variabilities present in the outbursting or persistent black holes. As the flow solution is independent of the mass of the compact object, similar results found from the TCAF are applicable to supermassive black holes also. However, with the mass of the central black holes the dominating radiative property may change keeping the similar disk structure. Hydrodynamic simulations confirmed the formation of Keplerian disk (see [40]) while the effect of Compton cooling on the hydrodynamics and spectra of TCAF showed spectral softening (see [36]) due to cooling. Images of accretion disks in TCAF paradigm are reported (see [19–21, 37] for details) where Comptonization of the seed photons and the self-consistent outflows produced by TCAF are shown for various inclination angles and disk accretion rates.

## 2 How to See?

The basic process of visualizing an accretion disk is by allowing the photons to reach the observer following the curved geometry. The rest is to take the projection of received photons on the source plane keeping the black hole at the centre. Theoretical initiatives to simulate the images of accretion disk started with [23]. They plotted iso-radial curve which is a distorted view of photons coming from a particular radius situated on equatorial plane. Pineault and Roeder [58] extended the iso-radial curves for various spin parameters. Luminet [46] first produced the image of Keplerian disk around a Schwarzschild black hole by calculating the bolometric flux emitted by the disk using [57] flux profile. First colored images of an accretion disk around a non-rotating black hole was published by Fukue and Yokoyama [35].

The development of images in early years (1972–1988) is available from Luminet's own blog. Viergutz [66] first produced images of accretion disk around a Kerr black hole. A few years later, [47] produced images of accretion disks using Ray-Tracing mechanism. At this point, it is important to discuss the solution processes involving the emitter-observer imaging techniques.

## 2.1 Semi Analytical Approach

Using the symmetries of space-time around black holes and restricting the origin of a photon in a particular plane (equatorial plane mostly), one arrives at the integrals which can connect the photons from end of observer to a particular point on the accretion disk plane. By generating a decent amount of such curves, the entire disk can be obtained. This process is known as semi-analytic approach. This is a rather computationally inexpensive process and most of the earlier works in this field followed similar ways. The following discusses the process to arrive at the integral.

Using the metric, the *interval* can be written as

$$ds^2 = g_{\mu\nu} dx^\mu dx^\nu,$$

where, $g_{\mu\nu}$ is the metric tensor which depends on the intrinsic properties of central object and $x^\mu = t, r, \theta, \phi$ for $\mu = 0, 1, 2, 3$.

For null geodesics, we can set the interval to be zero, restrain the photons on the equatorial plane and letting $u = 1/r$. Thus, we have a simple relationship

$$\left(\frac{du}{d\phi}\right) \sim \xi(u)\ (say).$$

So, the deviation angle at infinite $\phi_\infty$ can be evaluated as

$$\phi_\infty \sim \int_0^u \frac{du}{\xi(u)},$$

which can be transformed in the classical Jacobi elliptic integrals of first and second kind (see [18, 46] for details). Using proper geometric transformations, one can arrive at the iso-radial curves. Following this method, various packages were developed to visualize the disk hole system (see [55, 67, 70]).

## 2.2 Ray Tracing

With the advent of computational facility, people started to integrate the geodesic equations to extract more information and to find other possible ways to generate

images. It often appeared in the literature that rather than using the exact geodesic equations which are second order coupled differential equations Lagrangian or Hamiltonian techniques are being used to solve the problem. This form of Ray-Tracing involves lot less computational steps as the equations are in first order.

In curved space-time, photon trajectories are governed by geodesic equations,

$$\frac{d^2x^\mu}{dp^2} + \Gamma^\mu_{\nu\lambda}\frac{dx^\nu}{dp}\frac{dx^\lambda}{dp} = 0,$$

with $\mu = [0, 1, 2, 3]$; $x^0 = t$, $x^1 = r$, $x^2 = \theta$ and $x^3 = \phi$, where $p$ is Affine parameter, $\Gamma^\mu_{\nu\lambda}$ changes with the intrinsic parameters of black hole. Using tetrad formalism [68], one can transfer the velocities to obtain the image on the observer plane.

With proper choice of accretion disk geometry, it is possible to construct images shooting rays from the end of the observer and finding whether they arrive on the plane of accretion disk. This is *Backward Ray-tracing* process (see [69]). Following this method, one can anticipate the disk configurations having simple geometric models. However, computational time substantially reduces as most of the photons intersects the plane of the accretion disk.

The basic process of Ray-Tracing involves with *Forward Ray Tracing*. The source or the accretion disk produces photons which interacts with the ambient hot medium. After that, photons leaves the system to reach a distant observer following the geodesic equations for a given space-time. Interactions of photons with electrons present in the disk are easier to incorporate in this process. There are no restrictions on the disk geometry. Any hydrodynamically obtained solution for an accretion disk can be implemented in this process. However, it requires rather large computational time which can be minimized by utilizing the symmetries of space-time (see [19, 20] and [21] for details).

## 3 Images of Accretion Disk-Outflow

Due to the increase in Doppler effect, the Keplerian disk gets brighter on one side and dimmer on the other side. Polarization of emitted photons from the disk was measured from simulation and were articulated (see [10, 24, 45, 61] for details). Hydrodynamic simulation of Keplerian disk was first performed by Armitage and Reynolds [3]. Simulated images of force-free Jets for M87 were presented by Broderick and Loeb [9]. Images of thick disk having various disk parameters have been reported in the literature (see [34, 71]) and references therein. However, inverse Comptonization dominates (see [64]) in the power-law part of the spectra of GBHs and the images of accretion disk around them should contain the Compton cloud or CENBOL.

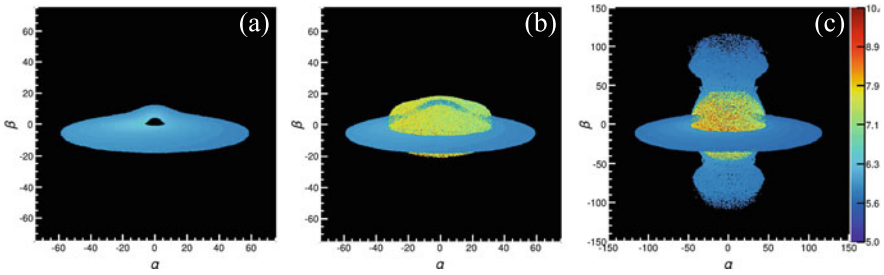



**Fig. 2** Images of accretion disk around a Schwarzschild black hole are presented for (**a**) a pure soft state; (**b**) a hard state with a CENBOL and (**c**) a flaring states where outflows are self-consistently produced from the CENBOL region. Disk rate $\dot{m}_d = 0.1$ is kept constant for all images. For panel (**c**), the halo rate is $\dot{m}_h = 0.1$. For details see [19, 21]

Images were constructed (see [19]) where relativistic thick disks act as the Compton cloud and Keplerian disk supplies the soft seed photons required for inverse Comptonization. Due to bending, the spectra hardens with the inclination angle. Figure 2 shows the three spectral states of an accretion disk. A pure soft state is shown in panel (a) where only Keplerian disk is seen. In the presence of the CENBOL, hard photons are produced via Comptonization and the image is shown in Fig. 2b. Thus, Fig. 2b corresponds to hard state. Hydrodynamic simulations of TCAF (see [40]) have been included where resultant images show time dependent outflow structures (see [21]). However, time dependence may be smeared out during the time convolved image formation. Figure 2c represents the image of accretion disk where outflows are self-consistently generated from the CENBOL region. Disk rates are kept constant through out all the simulations.

## *3.1 Observed Spectra of TCAF*

Spectral variation with respect to inclination angle is shown in Fig. 3 (see [19] for more details on inclination dependent spectra). The disk rate is kept constant. With increasing inclination angle more and more soft photons from the Keplerian disk enter into the CENBOL region. Gravitational lensing bends the trajectories of photons such that the number of photons which are passing through the CENBOL region increases. This is how a gravitational bending of photons enhances the spectral hardening in higher inclination angle objects.

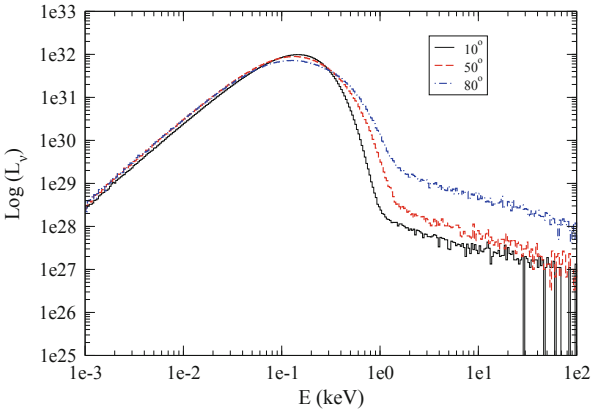



**Fig. 3** Variation of observed spectrum with inclination angles 10°, 50° and 80° where disk rate fixed at $\dot{m}_d = 10^{-1}$. For details see [19, 21]

## 4 Sgr A*: The Prime Candidate

At the centre of our Galaxy, we have a supermassive black hole with mass $M_{bh} \sim 4 \times 10^6$. Surrounding the black hole, there is not enough matter to accrete which means the geometry to be halo dominated and hence synchrotron radiation dominates even in X-rays. Recent simulations (see [30]) constrained the accretion rate to a much smaller value than that of the earlier prediction done by Coker and Melia [22]. The peak luminosity in radio frequency is observed around 300 GHz. Being the closest super-massive black hole, it is the best bet to find the event horizon. Still, the angular resolution required to resolve the horizon demands an Earth sized telescope. A few information on Sgr A* are given in Table 1.

However to this relative closeness, resolving Sgr A* is quite a challenging job. The technical difficulties were somewhat reduced by closure phase measurements (see [28, 33]). Numerous GRMHD simulations targeted for Sgr A* have been reported (see [25–27, 29, 30, 53, 54, 56, 60] and references therein). Falcke and Markoff [32] presented a detailed review on the process of observing Sgr A* using EHT.

**Table 1** Basic parameters of Sgr A*

| Parameters | Values | References |
|---|---|---|
| Mass | $\sim 4.3(\pm 0.4) \times 10^6\ M_\odot$ | [38] |
| Distance | $\sim 8.3(\pm 0.15)$ kpc | [38, 59] |
| Gravitational radius | $GM/c^2 \sim 6.3 \times 10^6 \sim 5\,\mu$as | [32] |
| Schwarzschild radius | $2GM/c^2 \sim 13 \times 10^6 \sim 10\,\mu$as | [32] |
| Accretion rates | $10^{-7} M_\odot$/year $\geq \dot{m} \geq 10^{-9}\ M_\odot$/year | [2, 49] |
| Eddington luminosity | $L_{edd} = 4\pi GMm_p c/\sigma_T \sim 5 \times 10^{44}$ erg/s | [32] |
| Radio luminosity | $\nu L_\nu(350\,\text{GHz}) \sim 2 \times 10^{-10}\ L_{edd}$ | [42] |
| X-ray luminosity | $L(2\text{–}10\,\text{keV}) \sim 4.6 \times 10^{-12}\ L_{edd}$ | [4] |

### *4.1 Spectral States*

To actually extract images from radio-interferometry, one requires to identify the spectral states of the sources. Spectral shape generally provides the morphology (see [17]) of the system. Sgr A* showed quiescent and flaring states (see [27]). An inverted spectrum which rises with the peak at $10^{12}$ Hz has been observed. After that, at sub-mm wavelength the spectrum cuts-off. Jet activity of Sgr A* (see [48] and references therein) in radio is quite popular. Also, X-rays flairs are reported [6] which have the luminosity compared to radio band.

This points to the requirement of X-ray interferometry. In closer region, all types of black holes radiate in X-rays. For low luminosity supermassive black holes, radio luminosity dominates. In this respect, Sgr A* is a special kind. Apart from the LLAGNs, X-ray interferometric images will produce very similar results that are obtained considering TCAF solution.

## 5 Discussions and Conclusions

Imaging of accretion disks around black holes have evolved in the last 47 years (1972–2018). Concept of the images is shifted from the standard Keplerian disk images to modern advective flow models. Spectral line studies combined with the image processing successfully fitted [31] the profiles of the iron lines of GBHs and AGNs. However, the source structure of the iron lines is still debated (see [50]). In this current review, we have briefly reported the current situation accretion disk images and future possibilities of X-ray imaging of black hole candidates. Two Component Advective Flow (TCAF) solution has been used to describe the geometry of the accretion disk. Both hydrostatic (see [19]) and hydrodynamic [21] aspects were investigated under TCAF paradigm. Images of pure Keplerian disk and CENBOL in presence and absence of the outflows are presented.

Apart from the GBHs, the accretion rates of RL Quasars, Seyfert galaxies are high enough (see [7]) for Comptonization and cooling features to play crucial role in the formation of disk structure. For, Sgr A*, the "G2" like events (see [39]) may introduce massive inflow onto the black hole where the disk-outflow images presented by Chatterjee et al. [21] will corroborate with the observable X-ray images.

To resolve Galactic black holes, one requires to explore further deep into the X-ray regime. The resolution of telescopes for such objects must be $10^{-9}$–$10^{-12}$ arcsec. It is like measuring the width of an human hair on the moon using a ground based telescope. Currently, EHT is operating on $\sim 10^{-6}$ arcsec resolution utilizing the ground based radio interferometric technique. However, understanding of the outbursting and persistent microquasars, which are nearby, demands a space based X-ray interferometric observatory. AGNs and GBHs both exhibit X-Ray emissions from a closer region to the central black hole. Thus, the X-ray interferometer will be operational for both these classes of black holes.

**Acknowledgements** AC acknowledges Prof. Sandip K. Chakrabarti for introducing him to the fascinating subject of Black Hole Astrophysics and Indian Centre for Space Physics (ICSP) for financial support during the research.

## References

1. Abramowicz, M.A., Jaroszynski, M., Sikora, M.: A&A **63**, 221 (1978)
2. Agol, E.: ApJL **538**, L121–L124 (2000)
3. Armitage, P.J., Reynolds, C.S.: MNRAS **341**, 1041 (2003)
4. Baganoff, Y., et al.: ApJ **591**, 891 (2003)
5. Bambi, C., Freese, K.: Phys. Rev. D **79**(4), 043002 (2009)
6. Barrìre, N.M., Tomsick, J.A., Baganoff, F.K., Boggs, S.E., Christensen, F.E.: ApJ **786**, 46 (2014)
7. Bian, W.H., Zhao, Y.H.: PASJ **55**, 599 (2003)
8. Bondi, H.: MNRAS **112**, 195 (1952)
9. Broderick, A.E., Loeb, A.: ApJ **697**, 1164 (2009)
10. Bromley, B.C., Melia, F., Liu, S.: ApJ **555**, 83 (2001)
11. Chan, C.K., Psaltis, D., Özel, F.: ApJ **777**, 13 (2013)
12. Chakrabarti, S.K.: ApJ **288**, 1 (1985)
13. Chakrabarti, S.K.: ApJ **347**, 365 (1989)
14. Chakrabarti, S.K.: MNRAS **243**, 610 (1990)
15. Chakrabarti, S.K.: Theory of Transonic Astrophysical Flows. World Scientific, Singapore (1990)
16. Chakrabarti, S.K.: ApJ **464**, 664 (1996)
17. Chakrabarti, S.K., Titarchuk, L.G.: ApJ **455**, 623 (1995)
18. Chandrasekhar, S.: The Mathematical Theory of Black Holes. Oxford University Press, Oxford (1985)
19. Chatterjee, A., Chakrabarti, S.K., Ghosh, H.: MNRAS **465**, 3902 (2017)
20. Chatterjee, A., Chakrabarti, S.K., Ghosh, H.: MNRAS **472**, 1842 (2017)
21. Chatterjee, A., Chakrabarti, S.K., Ghosh, H., Garain S.K.: MNRAS **478**, 3356 (2018)
22. Coker, R., Melia, F. ApJ **488**, L149 (1997)
23. Cunningham, C.T., Bardeen, J.M.: ApJ **183**, 237 (1973)
24. Dexter, J.: MNRAS **462**, 115 (2016)
25. Dexter, J., Agol, E., Fragile, P.C., McKinney, J.C.: ApJ **717**, 1092 (2010)
26. Dibi, S., Drappeau, S., Fragile, P.C., Markoff, S., Dexter, J.: MNRAS **426**, 1928 (2012)
27. Dibi, S., Markoff, S., Belmont, R., Malzac, J., Barrìre, N., Tomsick, J.: MNRAS **441**, 1005 (2013)
28. Doeleman, S.S., Weintroub, J., Rogers, A.E.E., et al.: Nature **455**, 78 (2008)
29. Dolence, J.C., Gammie, C.F., Shiokawa, H., Noble, S.C.: ApJ **746**, L10 (2012)
30. Drappeau, S., Dibi, S., Dexter, J., Markoff, S., Fragile, P.C.: MNRAS **431**, 2872 (2013)
31. Fabian, A.C., Rees, M.J., Stella, L., White, N.E.: MNRAS **238**, 729 (1989)
32. Falcke, H., Markoff, S.: CQGra **30**(24), 244003 (2013)
33. Fish, V.L., Doeleman, S.S., Beaudoin, C., et al.: ApJ **727**, L36 (2011)
34. Fuerst, S.V., Wu, K.: A&A **424**, 733 (2004)
35. Fukue, J., Yokoyama, T.: PASJ **40**, 15 (1988)
36. Garain, S.K., Ghosh, H., Chakrabarti, S.K. ApJ **437**, 1329 (2012)
37. Ghosh, H., Garain, S.K., Giri, K., Chakrabarti, S.K.: MNRAS **416**, 959 (2011)
38. Gillessen, S., et al.: ApJ **692**, 1075 (2009)
39. Gillessen, S. et al.: Nature **481**, 51 (2012)
40. Giri, K., Chakrabarti, S.K.: MNRAS **430**, 2836 (2013)

41. Hamilton, A.J.S.: General Relativity, Black Holes, and Cosmology. https://jila.colorado.edu/~ajsh/astr3740_17/grbook.pdf
42. Haubois, X., et al.: A&A **540**, A41 (2012)
43. Johannsen, T., Psaltis, D.: ApJ **718**, 446 (2010)
44. Kerr, R.P.: Phys. Rev. Lett. **11**, 237 (1963)
45. Krawczynski, H.: ApJ **754**, 133 (2012)
46. Luminet, J.P.: A&A **75**, 228 (1979)
47. Marck, J.A.: CQGra **13**, 393 (1995)
48. Markoff, S., Bowler, G.C., Falcke, H., MNRAS **379**, 1519 (2007)
49. Marrone, D.P., Moran, J.M., Zhao, J.H., Rao, R.: ApJ **640**, 308 (2006)
50. Mizumoto, M., Moriyama, K., Ebisawa, K., Mineshige, S., Kawanaka, N., Tsujimoto, M.: PASJ (2018). https://doi.org/10.1093/pasj/psy032
51. Molteni, D., Lanzafame, G., Chakrabarti, S.K.: ApJ **425**, 161 (1994)
52. Molteni, D., Sponholz, H., Chakrabarti, S.K.: ApJ **457**, 805 (1996)
53. Móscibrodzka, M., Gammie, C.F., Dolence, J.C., Shiokawa, H., Leung, P.K.: ApJ **706**, 497 (2009)
54. Móscibrodzka, M., Falcke, H., Shiokawa, H.: A&A (2016). https://doi.org/arXiv:1510.07243v3
55. Müller, T., Frauendiener, J.: Eur. J. Phys. **33**, 955 (2012)
56. Noble, S.C., Leung, P.K., Gammie, C.F., Book, L.G.: CQGr **24**, 259 (2007)
57. Page, D.N., Thorne, K.S.: Astrophys. J. **191**, 499 (1974)
58. Pineault, S., Roeder, R.C.: Astrophys. J. **212**, 541 (1977)
59. Reid, M., Menten, K.M. et al.: ApJ **783**, 130 (2013)
60. Roelofs, F., Johnson, M.D., Shiokawa, H., Doeleman, S.S., Falcke, H.: ApJ **847**, 55 (2017)
61. Schnittman, J.D., Krolik, J.H.: ApJ **712**, 908 (2010)
62. Schwarzschild, K.: Sitzungsberichte der Königlich Preussischen Akademie der Wissenschaften zu Berlin. Phys.-Math. Klasse **7**, 189–196 (1916)
63. Shakura, N.I., Sunyaev, R.A.: A&A **24**, 337 (1973)
64. Sunyaev, R.A., Titarchuk, L.G.: A&A **143**, 374 (1985)
65. Takahashi, R.: ApJ **611**, 996 (2004)
66. Viergutz, S.U.: Astron. Astrophysics **272**, 355 (1992)
67. Vincent, F.H., Paumard, T., Gourgoulhon, E., Perrin, G.: CQGra **28**, 22501 (2011)
68. Weinberg, S.: Gravitation and Cosmology. Wiley, London (1972)
69. Whitted, T.: Commun. ACM **32**(6), 343 (1980)
70. Yang, X., Wang, J.: ApJS **207**, 6 (2013)
71. Younsi, Z., Wu, K., Fuerst, S.V.: A&A **545**, 13 (2012)

# Gravitational Wave Emission from Binary Mergers: Ideal Versus Real Picture




**Prasad Basu**

**Abstract** We give here a brief review of the works studying the signatures of accretion disks on the gravitational wave signals generated by extreme mass ratio binary systems of compact objects. An example of such a system is a stellar mass compact star (typically a neutron star or a black hole) orbiting a central super-massive black hole embedded in a massive accretion disk. We particularly focus on the effects produced by hydrodynamic drag of the disk on the orbiting companion and find that the drag effects produced by the disk matter are indeed capable of modifying the companion's motion and, hence, the gravitational wave signal emitted from the system. The nature and significance of the effect depends crucially on the flow parameters of the disk, e.g. velocity, density profiles of the flow. Therefore, on one hand, one needs to incorporate these effects while theoretically modelling the gravitational wave signal emitted from such systems. On the other hand, by studying the emitted gravitational wave signals profile, one could infer about the nature of the accretion disk, which has been, till date, done only by observing the electro-magnetic signals coming from it. This multi-messenger astronomy was for the first time conceived and worked out during our research work.

## 1 Introduction

Binary systems of compact objects (black hole, neutron star and white dwarf) are the most important sources for the gravitational wave (GW) detectors, both for the ground based (LIGO, VIRGO, TAMA) and the future space based detectors of GW. One of the important classes of such systems, particularly for the future space based detector, is the so called extreme mass ratio inspirals (EMRI) which basically consists of a stellar mass compact object (CO) of mass 10–100$M_{\odot}$ orbiting

P. Basu (✉)
Department of Physics, Cotton University, Guwahati, Assam, India

© Springer International Publishing AG, part of Springer Nature 2018

B. Mukhopadhyay, S. Sasmal (eds.), *Exploring the Universe: From Near Space to Extra-Galactic*, Astrophysics and Space Science Proceedings 53,
https://doi.org/10.1007/978-3-319-94607-8_4

a central super-massive black hole (SMB) of mass $10^5$–$10^9 M_\odot$ [25]. Such systems are believed to exist at the center of our Galaxy [10, 23].

For such binaries the lighter COs can be considered as test particles moving through the geodesic of the background space-time metric generated by the central super-massive black hole. By analyzing the GW waveform emitted from them, one could extract information about the nature of CO's trajectory, hence check various predictions of general relativity both in the weak and strong field limits [1]. Again the detectors of GW depend on the use of matched filtering technique which requires a bank of theoretically produced GW templets to be cross-correlated with the incoming GW signal. Hence an accurate theoretical modelling of the dynamics of such systems are required both for the detection and analysis purposes. A major part of the studies is, therefore, devoted to accurately model the CO's trajectories and the emitted GW profile form EMRIs [16, 21, 27].

The COs, in particular SMBs in galactic centres, are believed to be endowed with an accretion disk which could be as massive as the central supper-massive black hole [8]. The presence of an accretion disk can modify the GW signal by influencing the dynamics of an orbiting companion independent of whether the disk is gravitating or not. In particular, a compact star orbiting in a Keplerian orbit through a sub-Keplerian accretion disk will experience a hydrodynamic drag force due to the accretion of matter from the disk. As a result, the companion dynamics and emitted GW signal will also get modified [10, 11]. However, though the GW emission processes from binary systems consisting of two point-like systems are studied quite extensively, not much of the work has been done incorporating the effect of accretion flows in the system, and the results vary considerably depending upon the choice of disk models. By not-incorporating this effect, one could end up extracting wrong parameters from gravitational wave signals.

In this chapter, we would like to discuss the current status of this issue as well as the future prospective of these studies. In the next section, we will briefly discuss the basic formalism relating the GW emission from the binary systems and the hydrodynamic drag. In Sect. 3, we will give a short account of the work that have been already done in this area and discuss how the various information about the SMB and CO in the binary systems can be extracted from the observed GW. We will discuss extensively the case where the disk's hydrodynamics is given by transonic accretion flow with the presence of accretion shock in details. Because of the strong non-Keplerian nature of such a flow, the drag force due to angular momentum exchange between the companion and the disk becomes more prominent. Also the sudden changes of the drag force in the shock region produce glitches in the GW signal. Thus such systems are observationally more important than others. Finally, as a part of concluding remark, we will discuss the prospect of simultaneous observations of disks by gravitational and electromagnetic waves.

## 2 EMRI Dynamics

Here and for the rest of the chapter, we choose $G = c = M = 1$. Here, $G$, $c$ and $M$ are the universal gravitational constant, speed of light and the mass of the central super-massive black hole respectively. Distance, specific angular momentum and time are measured in units of $GM/c^2$, $GM/c$ and $GM/c^3$ respectively.

### *2.1 GW Emission*

As the mass of the CO is much smaller than the mass of the SMB in EMRI systems, the CO essentially moves as a test particle on the geodesic of the background metric created by the central SMB. As the CO moves in an accelerated motion, the system emits gravitational wave and loses energy and angular momentum. A general bound orbit in general relativity is a precessing ellipse [14]. For such an orbit, the energy and angular momentum emission rates due to GW can be computed in terms of the eccentricity $e$ and the length of semi-major axis $r$ as [5]

$$\dot{E}_{GW} = \frac{32}{5} M_c^2 \frac{g_1(e)}{r^5} \quad \text{and} \quad \dot{l}_{GW} = \frac{32}{5} M_c \frac{g_2(e)}{r^{7/2}}. \tag{1}$$

Here $M_c$ is the mass of the CO and $g_1(e)$, $g_2(e)$ are given by

$$g_1(e) = \frac{1 + \frac{73}{24}e^2 + \frac{37}{96}e^4}{(1-e^2)^{7/2}}, \quad \text{and} \quad g_2(e) = \frac{1 + \frac{7}{8}e^2}{(1-e^2)^2}. \tag{2}$$

As the system loses its binding energy and angular momentum, the length of semi major axis $r$ and the eccentricity $e$ decrease according to the formulae

$$\dot{r}_{GW} = -\frac{64}{5} m g_1(e) r^{-3} \quad \text{and} |\dot{e}_{gw}| = \frac{304}{15} m g_3(e) r^{-4}, \tag{3}$$

where $g_3(r) = \dfrac{e\left(1 + \frac{121}{304}e^2\right)}{\left(1-e^2\right)^{5/2}}$. As the emission rates $\dot{E}_{GW}$ and $\dot{l}_{GW}$ are much smaller than the specific binding energy $E$ and the specific angular momentum $l$ of the system, one can assume that due to loss of energy and momentum, the companion moves on a time-dependent geodesic defined by the instantaneous value of the semi-major axis $r(t)$ and eccentricity $e(t)$. Such an approximation is called adiabatic approximation. Given the initial value of $r$ and $e$, one can compute their values at any instant $t$ from the knowledge of $\dot{r}(t)$ and $\dot{e}(t)$.

## 2.2 Hydrodynamic Drag

As the companion moves through the accretion disk, it experiences a drag force. The drag force arises due to two mechanisms. First, due to accretion of matter by the companion from the accretion disk, and second, due to dynamical friction caused by the deflection of disk matter by the gravitational field of the moving companion. If we assume that the accretion by the secondary black hole is of Bondi-Hoyle-Lyttleton type, the rate of mass accretion by the secondary would be given by Shapiro and Teukolsky [33],

$$\dot{M}_c = \frac{4\pi\bar{\lambda}\rho_0 M_c^2}{(v_{rel}^2 + a_s^2)^{3/2}}, \tag{4}$$

where $\rho_0$ is the local density of the disk matter, $a_s$ is the sound speed in the disk ($a_s^2 = p/rho_0$, $p$ being the pressure) and $v_{rel}$ is the relative velocity of disk matter with respect to the orbiting companion. Here $\bar{\lambda}$ is a constant of the order unity. Therefore, the rate of loss of specific angular momentum due to the accretion is given by Chakrabarti [10], Basu and coworkers [26], PhD Thesis as,

$$\left(\frac{dl}{dt}\right)_{acc} = \dot{M}_c(l_c - l_{disk}). \tag{5}$$

Here $l_c$ is the specific angular momentum of CO and $l_{disk}(r)$ is the specific angular momentum distribution of the fluid disk. In general relativistic terminology, $l$ would be computed from $-u_\phi/u_t$ with usual meaning for $u_\mu$.

The angular momentum loss due to dynamical friction can be calculated from the tangential component of dynamical frictional force given by Chandrasekhar [13], Ostriker [31], Barausse and Rezzolla [3] as,

$$\frac{dp}{d\tau} = \frac{4\pi\rho_0 h(1+v_{rel}^2)^2 M_C^2 \gamma^2}{v_{rel}^2} I, \tag{6}$$

where $h$ is the specific enthalpy of the fluid and $\gamma = -(u^\mu)_{fluid}(u_\mu)_{companion}$ is the Lorentz factor (contraction between fluid's and companion's four velocity). The value of $I$ depends on the Mach number and the radius of the orbit and can be computed numerically [3].

Thus one can compute drag forces due to both accretion and dynamical friction from the knowledge of flow parameters $\rho_0$, $p$, $v_{rel}$. These values depend on the choice of flow model, hence the drag effects corresponding to accretion disks having different flow characteristics are found to be different.

## 3 Explorations So Far

Both the accretion disks and binary systems are common astrophysical systems that have well studied in the literature, but it is relatively recent that the effect of disks on GW sources have been discussed. The study was initiated by Chakrabarti [9–11] by assuming EMRI system predictions of which were tested by numerical simulations [28]. These studies considered an EMRI embedded in an accretion disk, where the CO accretes in the Bondi-Hoyle-Lyttleton (BHL) approximation [6, 17, 20]. Since the gas velocity is in general different from the CO's velocity for a non-Keplerian disk, the CO either losses the angular momentum (hastening the coalescence) for a sub-Keplerian disk, or gains it (delaying the coalescence) if the disk has a super-Keplerian distribution of angular momentum. In the extreme situation, when the accretion rate is very high, the flow is highly super-Keplerian, and the angular momentum gain due to accretion could supersede the angular momentum loss via GW emission, resulting in a stalled orbit. Giampieri [19] studied the case of equal mass black hole and Narayan [30] examined the effect for radiatively-inefficient accretion flows (ADAF). He computed the ratio of the timescales on which the EMRI loses angular momentum due to hydrodynamic torques and GW emission. He found that for all reasonable values of ADAF parameters, GW phase is changed by an order of $10^{-2}$ rad, which is well below the sensitivity of LISA. Since ADAF is for extremely low accretion rates, such conclusion is expected. A realistic sub-Keplerian halo rate on the CO in an EMRI could be much larger than ADAF rates.

Subr and Karas [22, 34] considered a general elliptical orbit inclined to the plane of the disk and studied the evolution of its eccentricity and inclination. They chose the accretion disk to be a thin radiatively-efficient Keplerian $\alpha$ disk [32] and found that for the outer part of the disk, if the CO's motion does not perturb the disk significantly, an initial elliptical and off equatorial orbit gradually circularizes itself and aligns with the plane of the disk. Later, in a follow up work, they extended their study to the inner parts of the Shakura-Sunyaev disks, where the radiation pressure significantly modifies the density profile. They estimated the relative timescales for both the effects and concluded that GW emission drives the evolution interior to $\sim 100GM/c^2$.

Following the line of Karas and Subr [22], Levin [24] considered a thin self-gravitating, radiatively-efficient disk, including optically thick and thin regimes. He did an order of magnitude estimation of the timescales of hydrodynamic drag and planetary migration, including the effect of azimuthal winds, and concluded that in spite of the fact that the GW emission drives the evolution inside $\sim 100\, GM/c^2$, such disk effects may be important for LISA EMRIs.

The hydrodynamic drag on the CO moving through a thick accretion torus was examined by Barausse and Rezzolla [3]. In this case, they found that depending upon the values of system parameters the drag effect may become important in a few cases. However, such stationary thick massive tori with constant specific angular momentum are unstable to non-axisymmetric perturbations, making their existence rather uncertain.

Recently, Bence et al. [5] studied the effects for a radiation pressure dominated thin accretion disk and found that the non-axisymmetric gravitational effect occurring due to the formation of a spiral density wave in the disks (analogous to planetary migration) plays the dominant effect to the motion of CO and could be observable by LISA.

## 4 The Case of Transonic Accretion Flow

Here we study the disk whose hydrodynamics is given by sub-Keplerian transonic accretion flow. Such flows are specially important as the disk matter in this case has higher radial velocity and lower angular momentum than a Keplerian disk. Both the properties are expected to enhance the drag-effects on the CO, as the drag forces depend on the differences of velocity and angular momentum between the CO and the disk matter Eqs. (3)–(4). Furthermore, hydrodynamic shock is likely to form in such flows resulting in discontinuity in the flow parameters (e.g. velocity, density, pressure etc. [7, 18]). This produces sudden changes of the CO's motion which may be reflected in the glitches observed in the GW waveform [4]. Discussion of this section is based on the work in [4].

### *4.1 Nature of Disk Flow*

We consider the central super-massive black hole to be a rotating black hole. We use Pseudo-Kerr potential [12] to incorporate the general relativistic effect and solve the accretion flow using the method given in [29] corresponding to different values of Kerr-parameter ($a$) and viscosity ($\alpha_\pi$). The variations of the flow Mach number and specific angular momentum are shown in Fig. 1a, b. One can see that the flow is significantly sub-Keplerian and a shock forms at $r = 13.75$.

### *4.2 Drag Effects on the Companion Black Hole*

We consider the CO initially in a circular orbit. As it loses the energy and angular momentum, the orbital radius shrinks and CO slowly inspirals towards the center maintaining the adiabatic condition. Here only the drag effect due to the accretion matter by CO is considered. The total rates of changes of energy and angular momentum are then given by

$$\dot{E}_{tot} = \dot{E}_{acc} + \dot{E}_{gw} \quad \text{and} \quad \dot{l}_{tot} = \dot{l}_{acc} + \dot{l}_{gw}. \tag{7}$$

The accretion rates of CO from the disk of the central SMB is shown in Fig. 2a, b. Figure 2c shows the ratio of angular momentum loss rate due to accretion drag and

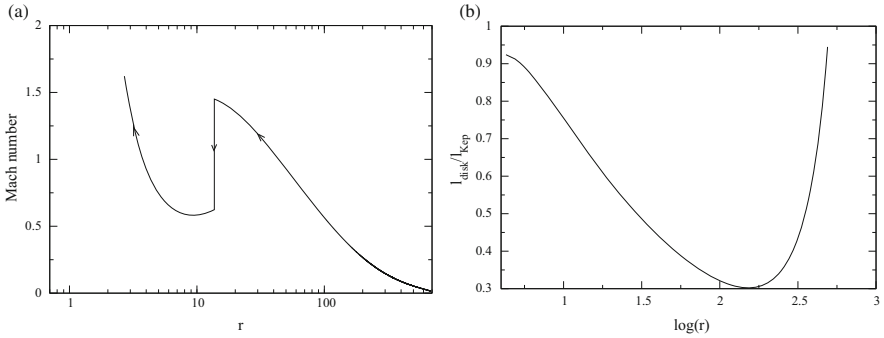



**Fig. 1** (**a**) A typical example of the variation flow Mach number as a function of radial distance, with $\alpha_{\Pi} = 0.05$ and $a = 0.5$. The location of shock of is at $r_s = 13.75$ and is denoted by a vertical arrow. The outer and inner sonic points are located at $r_o = 50.6$ and $r_i = 3.99$ respectively. In (**b**), the plot of the ratio of the disk's specific angular momentum and Keplerian angular momentum is shown. At very large distance from the black hole ($r_{tr} = 500.1$), the flow starts deviating from that of a Keplerian disk and remain sub-Keplerian throughout its way to horizon. The parameter values are chosen as ($a = 0.5,\ \alpha_{\Pi} = 0.05$) (From [4])

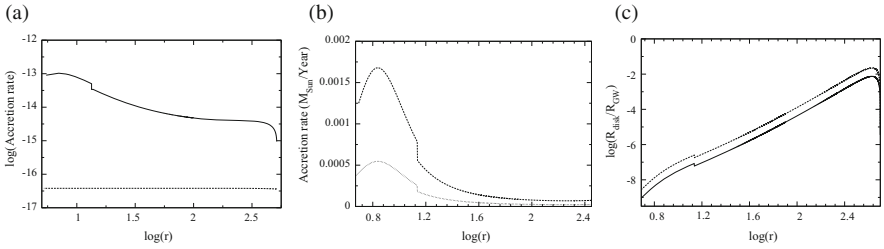



**Fig. 2** Comparison of the Bondi accretion rate (solid) and the Eddington rate (horizontal line) on the companion as it spirals into the central SMB while remaining submerged inside the accretion disk of the primary. In (**b**) plot of the accretion rates of the CO from the accretion disk of the central SMB as a function of the radial distance from the SMB, when the latter accretes at (**a**) one solar mass per year (dotted), and (**b**) three solar mass per year (dashed). In (**c**), the ratio of the angular momentum loss rates due to the accretion by the CO from the disk of the SMB ($R_{disk}$) and that due to GW emission ($R_{GW}$) is plotted when the central black hole is accreting at one solar mass per year (solid) and at three solar mass per year (dashed). The sudden changes observed in the region where shock forms, which can be reflected as glitches in the emitted GW profile (From [4])

due to GW emission. One can see a sudden jump in the accretion rate at the location of shock.

## *4.3 Effects on GW Emission*

Due to additional loss of angular momentum because of the accretion drag, there is a reduction in infall time. The variation of infall time with spin parameter of the

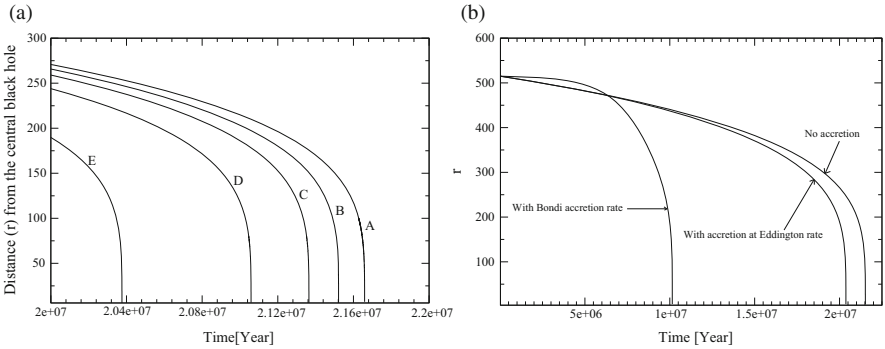



**Fig. 3** (**a**) Infall time of the CO is plotted against the radial distance from the center (From [4]). Curves (A) and (B) correspond to the case when accretion disk is not present in the system, for Kerr parameter $a = 0$ and $a = 0.5$ respectively. Curves (C) and (D) represent the case when the accretion disk is present and the CO is accreting at Bondi rates corresponding to respectively $1M_{\odot}$ year$^{-1}$ and $3M_{\odot}$ year$^{-1}$ accretion rates on the primary. The curve (E) corresponds to the case when the CO is accreting at one Eddington rate. Here the value of the viscosity parameter is $\alpha_{\Pi} = 0.05$. In (**b**) another comparison of infall time is shown in the presence and absence of the accretion disk

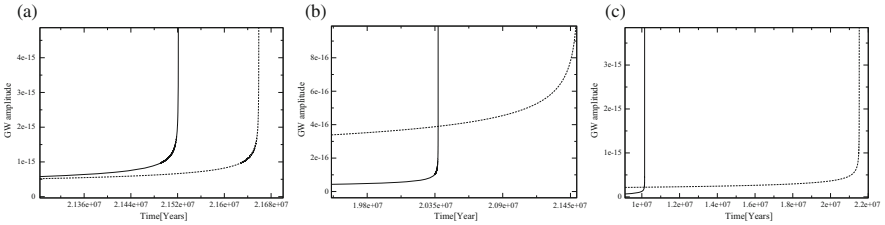



**Fig. 4** In (**a**), the effect of the Kerr parameter on the gravitational wave amplitude: $a = 0$ (dashed curve) and $a = 0.5$ (solid curve) are compared. The spin-orbit coupling term in the potential ensures a rapid infall in the Kerr geometry (From [4]). In (**b–c**), another comparison of the final stages of the chirp amplitude profiles with (solid) and without (dashed) the disk when the companion is accreting at (**a**) an Eddington rate, and (**b**) at the Bondi rate, is shown. The coalescence takes place much faster when the disk is present

central SMB ($a$), without the presence of accretion disk, and for different accretion rates when the disk is present, is shown in Fig. 3a, b. Rapid infall resulted in an enhancement in the amplitude of GW which is shown in Fig. 4a–c.

## *4.4 Issue of the Formation of Gap*

Because of the non-axisymmetric gravitational interaction of binary system with the disk, a torque is generated by the binary on the disk matter. This, in some case, may result in to the formation of a gap in the disk [2, 15]. In case of the Keplerian

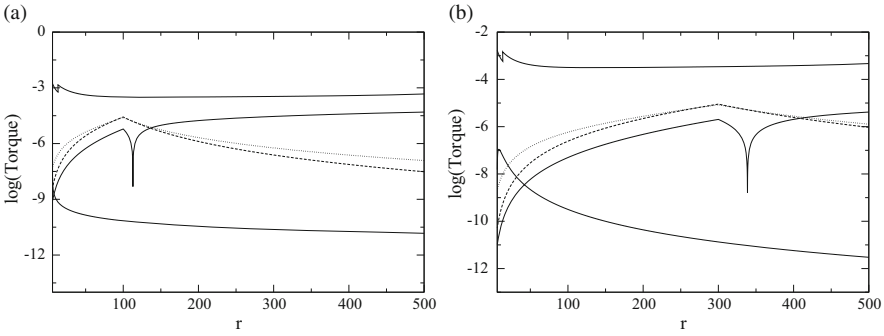



**Fig. 5** Amplitudes of the binary-torque and the viscous torque is compared in **a** and **b**. The logarithm of the amplitudes of first three harmonics ($a_1$, $a_2$, $a_3$) of the binary-torque is plotted as a function of distance from the SMB with the viscous torque of the accretion disk. In (**a**) The dotted and dashed curves represent $\log(a_2)$ and $\log(a_3)$ respectively, while $\log(a_1)$ is represented by the solid curve with singular point. The singularity of $\log(a_1)$ occurs at the point where $a_1 = 0$. The topmost solid curve represents the viscous torque in an advective accretion disk while the lowermost solid curve represent the same for a Keplerian disk. Here the accretion rate is equal to one Eddington rate of SMB ($0.2 M_\odot$ year$^{-1}$) and $\alpha = 0.05$. Viscous torque of the accretion disk does not depend on accretion rate. The mass and the location of the CO is given by $M_c = 10^5 M_\odot$ and $r = 100$. In (**b**), the same results are shown for $r = 300$ (From [4])

disk, where the viscous torque of the accretion flow is much smaller compared to the torque generated by the binary, such gaps may form. But in this case, due to the strong sub-Keplerian nature of the flow, the viscous torque is much higher than the torque generated by the binary. Hence, no gap forms. Figure 5a, b compare the viscous torque and the torque due to binary.

## 5 Discussion and Conclusion

A real EMRI is not a system of two isolated compact stars. An important third component namely, the accretion disk of the primary, is very likely to be present in the system. The studies, so far made, have not come to a general consensus about the effect of the accretion disk on the emitted gravitational wave profile. Various hydrodynamic models of disks give different results. For the Keplerian $\alpha$-disk, which is the most popular candidate for describing radiatively efficient accretion flow around AGNs, the disk driven migration of CO, occurring due to angular momentum loss of CO through spiral density wave formed in the disk, has a dominant effect on CO's motion and its imprint on the GW profile could be detected by LISA. On the other hand, the effects of dynamical-friction and accretion-drag are not so important in this case.

Another case of special interest is the disk flow modelled by transonic accretion flows. The strong non-Keplerian nature of the accretion is responsible for higher

radial and tangential drags. Discontinuities in the flow parameters due to the formation of shock may produce sudden changes in the trajectory of the CO, effect of which could be observable through the glitches in the emitted GW. Although in this case the effects estimated are still feeble, these can be used to set an upper limit on the flow parameters, e.g. accretion rate, velocity etc.

Till date, accretion disks are observed only through the electromagnetic signals coming from it. However, since the effects of the disk on the emitted GW signal crucially depend on the choice of hydrodynamic models of the disk, GW also has the potential to serve as another medium by which the disk can be observed [11]. Thus simultaneous observations of the disk by both gravitational and electromagnetic waves would provide more information about the nature of the disk, which in turn helps to constrain the values of flow parameters and test the various paradigms of the disk. We believe that this multi-messenger astronomy would be very important in the present century.

**Acknowledgements** I am thankful to Prof. S.K. Chakrabarti for developing the subject of GWs from EMRIs and multi-messenger astronomy. This needs to be explored further with various disk parameters.

## References

1. Amaro-Seoane, P., Gair, J.R., Freitag, M., Miller, M.C., Mandel, I., Cutler, C.J., Babak, S.: Class. Quantum Gravity **24**, 113 (2007). arXiv:astro-ph/0703495
2. Armitage, P.J., Natarajan, P.: ApJ **567**, L9 (2002)
3. Barausse, E., Rezzolla, L.: Phys. Rev. D **77**, 104027 (2008). arXiv:0711.4558 [gr-qc]
4. Basu, P., Mondal, S., Chakrabarti, S.K.: MNRAS **388**, 219 (2008). http://csp.res.in/ICSP-WEB/thesis.html
5. Bence, K., Nicols, Y., Loeb, A.: Phys. Rev. D **84**, 024032 (2011). arXiv:1104.2322 [astro-ph.GA]
6. Bondi, H., Hoyle, F.: Mon. Not. R. Astron. Soc. **104**, 273 (1944)
7. Chakrabarti, S.K.: Astrophys. J. **347**, 365 (1989)
8. Chakrabarti, S.K.: Theory of Transonic Astrophysical Flows. World Scientific, Singapore (1990)
9. Chakrabarti, S.K.: (1992). arXiv:astro-ph/9208006
10. Chakrabarti, S.K.: ApJ **411**, 610 (1993)
11. Chakrabarti, S.K.: Phys. Rev. D **53**, 2901 (1996). arXiv:astro-ph/9603117
12. Chakrabarti, S.K., Mondal, S.: Mon. Not. R. Astron. Soc. **369**, 976 (2006)
13. Chandrasekhar, S.: Astrophys. J. **97**, 255 (1943)
14. Chandrasekhar, S.: The Mathematical Theory of Black Holes. Clarendon Press, London (1983). ISBN-13: 978-0198512912
15. Dotti, M., Colpi, M., Haardt, F., Mayer, L.: MNRAS **379**, 956 (2007)
16. Drasco, S., Hughes, S.A.: Phys. Rev. D **73**, 024027 (2006)
17. Edgar, R.: New A Rev. **48**, 843 (2004). arXiv:astro-ph/0406166
18. Fukue, J.: Publ. Astron. Soc. Japan **39**, 309 (1987)
19. Giampieri, G.: (1993). arXiv:astro-ph/9305034
20. Hoyle, F., Lyttleton, R.A.: Proceedings of the Cambridge Philosophical Society, vol. 35, p. 405 (1939)
21. Hughes, S.A., Drasco, S., Flanagan, E.E., Franklin, J.: Phys. Rev. Lett. **94**, 221101 (2005)

22. Karas, V., Subr, L.: A&A **376**, 686 (2001). arXiv:astro-ph/0107232
23. Kormendy, J., Richstone, D.: Ann. Rev. Astron. Astrophys. **33**, 581 (1995)
24. Levin, Y.: MNRAS **374**, 515 (2007). arXiv:astro-ph/0603583
25. http://lisa.nasa.gov/, http://sci.esa.int/home/lisa/
26. Mandal, S., et al.: Ph.D. Thesis. Indian Centre for Space Physics, Kolkata. http://csp.res.in/ICSP-WEB/thesis.html
27. Mino, Y.: Phys. Rev. D **67**, 084027 (2003)
28. Molteni, D., Gerardi, G., Chakrabarti, S.K.: ApJ **436**, 249 (1994)
29. Mondal, S., Basu, P., Chakrabarti, S.K.: Mon. Not. R. Astron. Soc. **396**, 1038 (2009)
30. Narayan, R.: Astrophys. J. **536**, 663 (2000). arXiv:astro-ph/9907328
31. Ostriker, E.C.: Astrophys. J. **513**, 252 (1999)
32. Shakura, N.I., Sunyaev, R.A.: Astron. Astroph. **24**, 337 (1973)
33. Shapiro, S., Teukolsky, S.: Black Holes, Neutron Stars and White Dwarfs. Wiley, New York (1983)
34. Subr, L., Karas, V.: A&A **352**, 452 (1999). arXiv:astro-ph/9910401

# Part II
# Solutions of Model Flows Around Compact Objects

# My Experiences and Experiments with Transonic Flows Around Compact Objects




**Santabrata Das**

**Abstract** In this work, we discuss the transonic properties of the accretion flow considering the black hole (hereafter BH) as the central object. During accretion, before crossing the horizon, flow passes through the saddle-type critical point located outside the event horizon. Depending on the input parameters of the flow, namely specific energy and angular momentum for adiabatic flow, advective accretion flow may possess multiple saddle type critical points and, in such cases, flow may experience discontinuous transition in the flow variables as an imprint of shock waves. Considering the generalized accretion flow that includes viscosity, magnetic field and radiative cooling mechanisms, we compute the global transonic accretion solutions containing shocks and examine the influence of flow parameters on the shock properties. We find that shocks form for widespread flow parameters and, subsequently, we calculate the critical values of both viscosity and accretion rate that cater shocks. We continue the search of shocked accretion solutions for two-temperature flow and obtain such solutions for the first time in the literature. Finally, we discuss the possible origin of mass loss from the accretion disk and show that launching of outflow continues to take place around rotating BHs having wide range of spin parameters ($a_k$).

## 1 Introduction

The topic of accretion flow around compact objects draws significant attention to the astrophysical community since several decades simply because it successfully demonstrates the spectral and temporal properties of the accreting systems. It was Hoyel and Lyttleton [1], who for the first time examined the issues of axisymmetric particle acceleration across the shock in order to estimate the amount of matter piles up on the stellar surface while accreting from the interstellar medium. Unfortunately,

S. Das (✉)
Indian Institute of Technology Guwahati, Guwahati, Assam, India
e-mail: sbdas@iitg.ac.in

© Springer International Publishing AG, part of Springer Nature 2018

B. Mukhopadhyay, S. Sasmal (eds.), *Exploring the Universe: From Near Space to Extra-Galactic*, Astrophysics and Space Science Proceedings 53,
https://doi.org/10.1007/978-3-319-94607-8_5

dissatisfied results emerged as the effect due to pressure was largely neglected. Bondi [2] carried out his pioneering work where inflowing matter is accreted spherically symmetrically on to a isolated star because of influence of gravitational attraction. He investigated the effect of finite pressure in detail and pointed out that the temperature of the accreted matter has a crucial role in spherical accretion process.

In the early days of accretion disk physics, accretion in a binary system was first investigated, where angular momentum is being transported towards the outer edge of the disk due to viscosity that eventually admits matter to fall into the BH potential while forming a disk like depository called as accretion disk. Following this notion, a self-consistent study of the astrophysical flow around BHs considering disk accretion comes in the literature in the late eighties. Chakrabarti [3] presented a generalized *hybrid model* flow model, that opened up a new window in accretion theory around BHs. It was pointed out that matter deviates from Keplerian to sub-Keplerian distributions because of the fact that flow must be supersonic at the BH horizon, according to the inner boundary conditions. Overall, the theoretical modeling of the accretion flow around BH was done by considering the flow to be geometrically thin, axisymmetric, and advection dominated in nature [3–6]. In addition, for simplicity, the flow was assumed to maintain hydrostatic equilibrium in the direction transverse to the flow motion. With this, the hydrodynamic equations are constructed assuming the flow to be confined in the disk equatorial plane, where vertically integrated pressure and density at the equatorial plane identify their exact values at the disk surface. By solving these governing equations, stationary accretion flow solutions are obtained by employing the appropriate boundary conditions. These flow solutions are directly dependent on the initial flow parameters, such as specific energy, specific angular momentum, accretion rate and successfully illustrate the different properties of the astrophysical flow.

However, since magnetic fields are expected to be present in every astrophysical environments, it is noteworthy that accretion flows around BHs are also supposedly magnetized. In reality, magnetic fields inside the disk are in general migrated either from the companion star or from the interstellar medium [7], which remain 'frozen' with the accreting matter or by the dynamo action [8]. Moreover, the existence of magnetic fields in accretion theory is immensely important as it has the potential to transport angular momentum and also provide the satisfactory description of the origin of the disk viscosity. Several group of researchers conclusively pointed out that magnetic fields play vital role in deciding the accretion flow dynamics around BHs. Interestingly, magnetic fields act in an accretion disk in various ways. In general, the turbulent magnetic fields yield Maxwell stress that induces the angular momentum transport outward causing the inflowing matter to sink into the BH [9]. Further, it can account for the origin of the outflowing matter in the form of highly collimated bipolar jets commonly observed in BH systems [10]. In addition, energy dissipation processes, namely heating and cooling of the accreting matter, are directly resulted by the dissipation of magnetic energy [11–13] and synchrotron radiation, respectively.

What is more, the outflows and jets are also generated from the accretion flow itself [14, 15]. When matter with sufficient angular momentum accretes towards the BH, centrifugal force becomes comparable to gravity. This causes a puffed up torus like structure to form where the flow suffers a discontinuous shock transition. At the shock, an excess of thermal pressure gradient force is generated due to the compression of matter which drives some parts of accreting matter in vertical direction in the form of outflows or jets.

Considering all these aspects, in the following sections, we describe the generalized advective accretion disk theory around BHs and discuss the various aspects of the global accretion solutions around BHs. Further, we compute the highest value of the mass outflow rate from the disk that is directly associated with the kinetic jet power commonly observed in BH systems.

## 2 Global Accretion Solution

### *2.1 Critical Point Analysis*

We begin with a steady, thin, axisymmetric, advective accretion disk on to a Schwarzschild BH of mass $M_{\rm BH}$. To express the flow variables, we choose an unit system as $2G = M_{\rm BH} = c = 1$, where $G$ and $c$ represent the Gravitational constant and speed of light. With this, length, time and angular momentum of the flow are written in terms of $r_g$ $(= 2GM_{\rm BH}/c^2)$, $r_g/c$ and $r_g c$, respectively.

During course of accretion on to BH, inflowing matter with almost zero radial velocity at the outermost edge of the accretion disk (i.e., subsonic) crosses the BH horizon with velocity similar to the speed of light (i.e., super-sonic). This clearly indicates that while falling on to BH, at some point, flow radial velocity must exactly match with the sound speed and accordingly accreting matter smoothly transit from subsonic to supersonic state. This specific point is commonly known as critical point and depending on the flow parameters, a flow may have single or multiple critical points [3, 4, 6]. Interestingly, the radial velocity gradient $(dv/dx)$ takes $0/0$ form at the critical point and, hence, we use the l'Hospital rule to compute $dv/dx$ at the critical point $(x_c)$ [4]. It may be noted that non-dissipative flow may possess maximum of four critical points and, among these, one always remains inside the horizon and others, if they at all exist, remain outside the horizon [5]. Similar features are also seen to be present for dissipative flow as well [16]. The nature of critical points is decided based on the value of $dv/dx$ at $x_c$. In general, $dv/dx$ owns two values at the critical point. When $dv/dx$ are real and of opposite sign, the critical point is called as saddle-type or X-type. A nodal-type critical point is obtained, when gradients are real and of same sign. If the gradients are complex, the critical point belongs to the class of spiral-type or O-type [6, and references therein]. In the astrophysical context, the saddle-type critical point is considered to be a matter of special interest as the accretion solutions on to BHs only pass

through it. In addition, in order to form a standing shock, accretion flow must contain multiple saddle-type critical points, among them the closest and furthest points are corresponding to the inner ($x_{\rm in}$) and outer ($x_{\rm out}$) saddle-type critical points respectively.

In order to understand the nature of critical points with more clarity, we consider the viscous accretion flow and ignore the presence of magnetic field for the time being. Fixing a viscosity parameter ($\alpha_B = 0.1$), we calculate the profile of specific angular momentum ($\lambda_c$) measured at $x_c$ and it is depicted in Fig. 1 [16]. Here, various curves denote the Results for different energies ($\mathscr{E}_c$) at $x_c$. From the uppermost to the lowermost curves, we choose $\mathscr{E}_c$ = 0.0007, 0.001, 0.003, 0.005, 0.007, 0.011, 0.015, 0.019, 0.023 and 0.027, respectively. In addition, the long-dashed curve is drawn for the reference purpose that corresponds to the Keplerian angular momentum distribution ($\lambda_{\rm Kep}$). It may be noted that $\lambda_{\rm Kep}$ remains totally independent on the flow parameters, however, depends on the flow geometry. In the plot, solid, dotted and short-dashed curves denote the results obtained for saddle, nodal and spiral type critical points respectively.

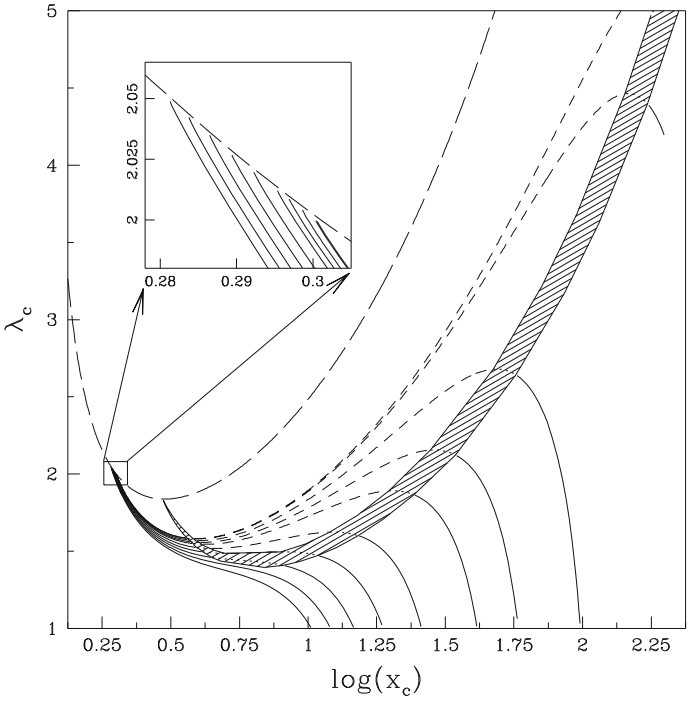



**Fig. 1** Profile of specific angular momentum ($\lambda_c$) with logarithmic critical point location [$\log(x_c)$] for viscous accretion flow. Results plotted with solid, dotted and short-dashed curves are for saddle, nodal and spiral type critical points and long-dashed curve refers to Keplerian angular momentum distribution. Here, effect due to magnetic field is ignored and viscosity parameter is considered as $\alpha_B = 0.1$. Shaded region indicates the domain of nodal-type critical points [16]

Notice that critical points always form at a sub-Keplerian value. Moreover, it may be noted that when $\mathscr{E}_c$ is small, critical points appear in a sequence as saddle—nodal—spiral—nodal—saddle with the increase of $x_c$. As $\mathscr{E}_c$ is increased, the domain of spiral-type critical points reduces which is apparently occupied by the nodal-type critical points. Shaded region indicates the domain of nodal-type critical points. For a given $\lambda_c$, when $\mathscr{E}_c$ again increases, the nodal-type points are eventually disappeared leaving the flow to have only single saddle-type critical point. This clearly indicates that for a given $\lambda_c$, we have a energy range $\mathscr{E}_{\rm min} < \mathscr{E}_c < \mathscr{E}_{\rm max}$ that provides multiple critical points. In the inset, it is shown that $\lambda_c$ never exceeds Kelperian value although it may closely approach towards it.

The most general behavior of the flow at a critical point is clearly visualized in a three-dimensional plot depicted in Fig. 2. In the plot, the surface $F(\mathscr{E}_c, \lambda_c, x_c) = 0$ for $\alpha_B = 0.01$ is drawn, where $x_c$, $\lambda_c$ and $\mathscr{E}_c$ are plotted along X, Y and Z-axes [16]. Note that, multiple critical points appear at relatively higher values of angular momentum whereas single critical point solutions are obtained for lower angular momentum values. Therefore, flow with $\lambda < \lambda^{\rm cri}$ fails to possess multiple critical points, where $\lambda^{\rm cri}$ denotes critical angular momentum.

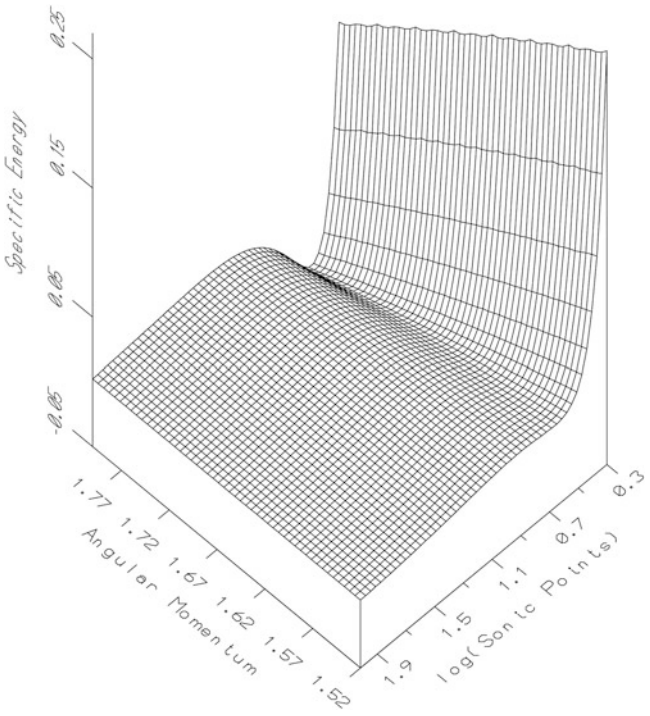



**Fig. 2** Display of how the number of critical points changes in 3D view of $F(\mathscr{E}_c, \lambda_c, x_c) = 0$ surface. Here, we choose $\alpha_B = 0.01$. See text for details [16]

Overall, although the above analysis of critical point is carried out only for viscous flows, it would be reasonable to use the similar concept for generalized accretion flows (i.e., including radiative cooling, magnetic fields etc.) as well and, therefore, we would like to do so in the subsequent sections while obtaining the generalized accretion solutions around BHs.

## 2.2 Accretion Solutions Containing Shocks

To calculate a global accretion solution for a magnetized flow, we simultaneously solve the governing equations by supplying the boundary values of angular momentum ($\lambda$), plasma$-\beta$ (defined as the ratio of the gas pressure to magnetic pressure), accretion rate ($\dot{m}$) and viscosity parameter ($\alpha_B$) at a given radial distance ($x$) [17]. Since the BH solutions must be transonic, inflowing matter must cross the critical point ($x_c$) and, therefore, it is very convenient to supply the boundary values of the flow at $x_c$. With this, we integrate the governing equations from $x_c$ once up to just outside the BH horizon and then up to the large distance from the horizon (i.e., outer edge of the sub-Keplerian disk, $x_{\rm edge}$) and finally join them to obtain a complete global transonic advective accretion solution [17]. Needless to mention that a given set of input parameters solely decide the number of the critical points (single or multiple) present in the flow (see Figs. 1 and 2).

In Fig. 3a, we display a complete global magnetized accretion solutions around a BH where the flow in injected from $x_{\rm edge} = 1000$ with $\lambda_{\rm edge} = 0.1170\lambda_K$ ($\lambda_K$ being the Keplerian value of specific angular momentum at that location), $\mathscr{E}_{\rm edge} = 4.4112 \times 10^{-5}$, $\beta_{\rm edge} = 2207.51$, $\alpha_B = 0.02$ and $\dot{m} = 0.004$. After passing through $x_{\rm out}$ ($= 369.98$), inflowing matter becomes supersonic and continues to accrete towards the BH as depicted using thick-solid curve. It may be possible for flow to remain supersonic up to the horizon as indicated by thick-dotted curve, but some interesting thing may also happen here. Close to the BH, as the timescale due to viscosity is larger than the infall time scale, the transport of angular momentum becomes feeble that strengthen the centrifugal repulsion against gravity. Because of that accretion flow slows down as it feels a virtual barrier causing the accumulation of matter there. As a consequence, turbulence is developed and local entropy is increased that eventually leads to the triggering of shock transition when the shock conditions are fulfilled. Evidently, shock conditions are the manifestation of conservation laws of mass, momentum, energy and magnetic field [18]. It may be noted that accretion solutions with shock are thermodynamically preferred over the shock free solutions [19]. We observe that at $x_s = 22.36$, shock conditions are fulfilled, where supersonic flow jumps to the subsonic branch which is shown by vertical arrow. Because of fatal attraction of gravity, subsonic flow gradually proceed inwards and inevitably dives in to the BH supersonically after crossing $x_{\rm in}$ ($= 2.41$). In the figure, thin-solid curve represents

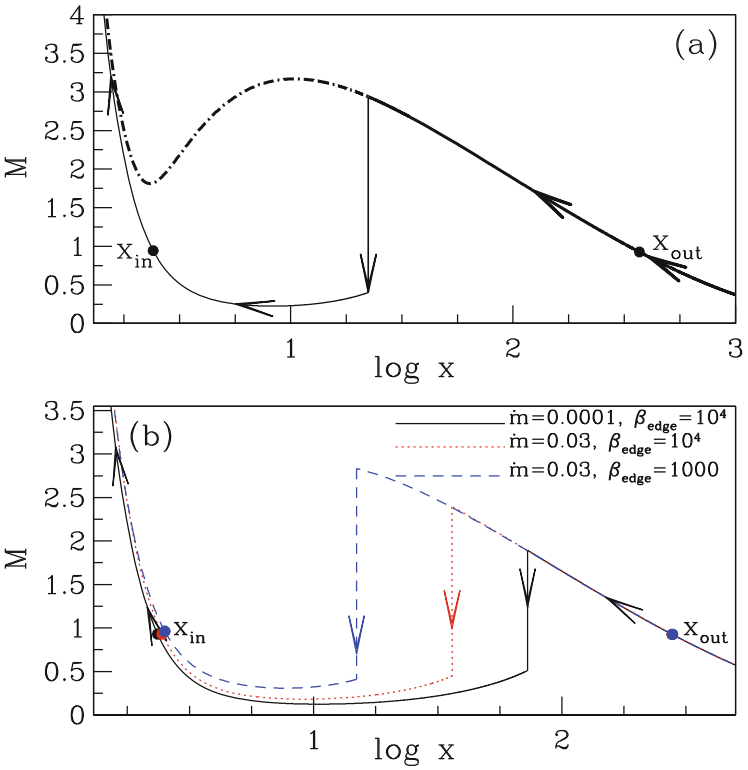



**Fig. 3** (**a**) Example of a shock induced global accretion solution. Vertical arrow indicates the shock transition and arrows show how flow moves towards BH [17]. (**b**) Dynamics of shock location with respect to $\dot{m}$ and plasma-$\beta$. Shock front settles down to a closer distance as the level of dissipation is increased [17]

this part of the solution. Overall, arrows show the direction of the flow as it proceeds towards the BH.

Next, we study how the dynamics of shock wave is tuned by the dissipation parameters, such as $\beta_{\rm edge}$ and $\dot{m}$. In the upper panel of Fig. 3b, flow is injected with parameters such as $x_{\rm edge} = 500$, $\mathscr{E}_{\rm edge} = 1.025 \times 10^{-3}$, $\lambda_{\rm edge} = 0.1386\lambda_K$ and $\alpha_B = 0.02$, respectively. When we choose $\dot{m} = 0.0001$ and $\beta_{\rm edge} = 10^4$ at $x_{\rm edge}$, shock transition takes place at $x_s = 72.79$ which is indicated using solid vertical arrow. Considering $\dot{m} = 0.03$ and keeping rest of parameters fixed at $x_{\rm edge}$, we find that shock front is moved inward at $x_s = 36.11$ shown by dotted vertical arrow [17]. In the latter case, since the density and temperature are enhanced in the post shock flow (equivalently, post-shock corona (PSC)), cooling becomes stronger at PSC reducing its thermal pressure. This compels the shock to settle down at smaller radius for establishing the pressure balance on both sides of the shock. Next, we set $\beta_{\rm edge} = 1000.00$ and $\dot{m} = 0.03$, keeping rest of the flow variables fixed at $x_{\rm edge}$ and calculate the position of

shock transition at $x_s = 14.88$ shown by dashed vertical arrow. Decrease of $\beta_{\rm edge}$ results the increase of turbulent magnetic fields indicating the increases of Maxwell stress as well. Accordingly, the transport of angular momentum towards the disk edge is also increased. This is effectively weaken the centrifugal repulsion at the inner part of the disk. In addition, increase of magnetic fields enhances the rate of synchrotron cooling. Due to these physical processes, position of the shock transition moves even closer to the BH [17]. Overall, the above investigation clearly indicates that in addition to $\dot{m}$, $\beta_{\rm edge}$ is also play vital role in deciding the shock dynamics.

In the quest of global accretion solutions, we compute the critical viscosity parameter ($\alpha_B^{\rm cri}$) as a function of $\beta_{\rm in}$ that admits shocked accretion solution. Since the limiting values of the adiabatic index is $5/3 \leq \gamma \leq 4/3$, we obtain $\alpha_B^{\rm cri}$ for $\gamma \sim 4/3$ (for thermally ultra-relativistic flow) and $\gamma \sim 1.5$ (for thermally semi-non-relativistic flow) and the results are depicted in Fig. 4a. Here, $\dot{m} = 0.01$ is considered and $\gamma$ values are marked. In a magnetized accretion flow, the angular momentum transport is increased as $\beta_{\rm in}$ is decreased. Since shocks are mainly centrifugally

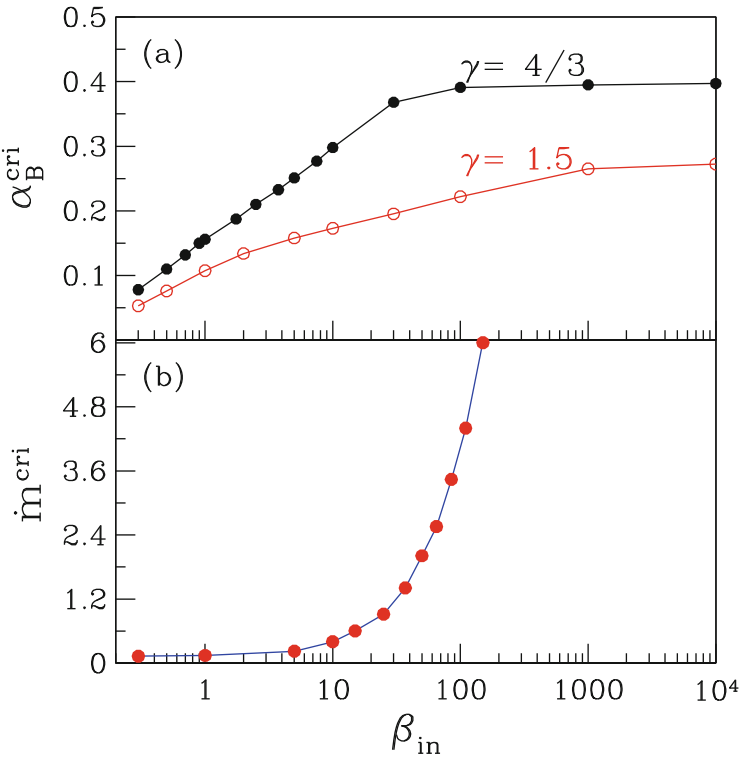



**Fig. 4** (**a**) Variation of critical viscosity parameter ($\alpha_B^{\rm cri}$) with $\beta_{\rm in}$ that admits shocks. Here, we set $\dot{m} = 0.01$. (**b**) Profile of critical accretion rate ($\dot{m}^{\rm cri}$) that permits shocks. Here, we choose $\alpha_B = 0.01$ and $\gamma = 4/3$ [17]

driven, when $\beta_{\rm in}$ is small, a modest $\alpha_B$ is good enough to transport the angular momentum needed for shock. Hence, when flow is magnetized, $\alpha_B^{\rm cri}$ owns smaller value. As $\beta_{\rm in}$ is monotonically increased, $\alpha_B^{\rm cri}$ is also follow the increasing trend and ultimately tends to the saturation limit that corresponds to the gas pressure dominated flow. It is observed that $\gamma = 4/3$ corresponds to $\alpha_B^{\rm cri} \sim 0.4$ [16] and $\gamma = 1.5$ corresponds to $\alpha_B^{\rm cri} \sim 0.27$ [18, 20]. Note that $\alpha_B^{\rm cri}$ is always small for $\gamma = 1.5$ which indicates that shock transition is less likely as flow approaches to the non-relativistic domain. This is not surprising because, for $\gamma \to 5/3$, accretion flow contains single critical point only [4, 16], that effectively reduces the shock transition possibility.

Similarly, we compute the critical accretion rate ($\dot{m}^{\rm cri}$) that allows shock transition in accretion flow around a BH [17]. We show the obtained results in Fig. 4b considering $\alpha_B = 0.01$. For $\beta_{\rm in} < 1$, the inner region of the disk becomes magnetically dominated and since synchrotron cooling is active in the disk, flow experiences significant cooling even when $\dot{m}$ is small. Thus, when flow is considered to be magnetically dominated ($\beta < 1$), we find small $\dot{m}^{\rm cri}$. When $\beta_{\rm in}$ is increased, the magnetic activity becomes weaker and thus the cooling is reduced. Therefore, flow continue to harbor shock even with large $\dot{m}$. For $\beta \gg 1$ (i.e., gas pressure dominated flow), magnetic fields become insignificant yielding a negligible cooling. Hence, $\dot{m}^{\rm cri}$ apparently tends to become independent of $\beta_{\rm in}$ [17].

### *2.3 Shocks in Two-Temperature Accretion Flow*

Very recently, to the best of our knowledge, Dihingia et al. [21] for the first time have shown that two-temperature accretion flow (hereafter TTAF) harbor shock waves. Moreover, they have argued that these solutions are very much viable as they have the potential to describe the spectral states of BHs. While modeling, we consider low angular momentum, viscous, two-temperature accretion flow that suffers various radiative cooling namely, bremsstrahlung, synchrotron and Compton cooling, respectively. In addition, during accretion, ions are heated due to the dissipation caused by viscosity. To take care the viscous effect, we adopt a well established viscosity prescription of [22]. In order to possess the shock in TTAF, inflowing matter containing multiple critical points must satisfy the standing shock conditions (see Sect. 2.2). In addition to that, since $t_{ei} > t_{ee}$ and $t_{ei} > t_{ii}$ [23, 24], where $t_{ei}$, $t_{ee}$ and $t_{ii}$ denote the time scales for electron-ion collision, electron-electron collision and ion-ion collision, respectively, it is quite justified to consider that electron temperature mostly remains unaffected within the shock width ($\Delta x_s$). In this work, since we consider $\Delta x_s \to 0$ (i.e., shock is thin), we assume $T_{e+} = T_{e-}$ immediately just before and after the shock.

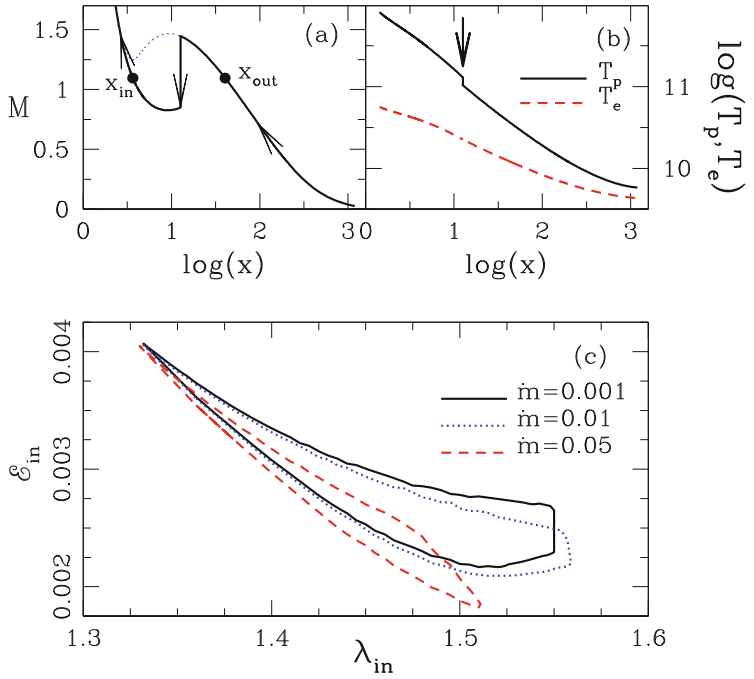



**Fig. 5** Illustration of a typical two-temperature global accretion solution that contains shock. Variation of (**a**) Mach number $M$ and (**b**) electron and ion temperatures ($T_e$, $T_i$) as functions of radial distance. (**c**) Modification of parameter space in $\lambda_{\rm in} - \mathscr{E}_{\rm in}$ plane that admits shocks. See text for details [21]

In Fig. 5a, we illustrate the two-temperature global accretion solution where subsonic accreting matter from the outer edge of the disk crosses $x_{\rm out}$ (=40.594) to change its sonic character from subsonic to supersonic and keep accreting to the BH. Supersonic TTAF indeed may safely cross the BH horizon (shown using dotted curve), but it is found that TTAF makes a shock jumps at $x_{\rm s} = 12.6370$ to join with the subsonic branch. Subsequently, subsonic flow enters in to the BH after crossing $x_{\rm in}$ (=3.6529). The other flow variables at $x_{\rm in}$ are calculated as $\lambda_{\rm in} = 1.3947$ and $T_{\rm e,in} = 4.074 \times 10^{10}$ K, respectively. In the figure, arrows point the overall direction of flow motion towards the BH and, in particular, the vertical arrow refers shock position [21]. Figure 5b demonstrates the profiles of ion ($T_i$, solid) and electron ($T_e$, dashed) temperatures for the same solution as presented in Fig. 5a. We find that ions and electrons are weakly coupled and electrons are cooled faster than ions. Due to this, inflowing matter maintains two-temperature distribution. Moreover, because of shock compression, ion temperature jumps up just after the shock which is indicated using vertical arrow. Note that $T_e$ remains unaffected across the shock front as $t_{ei} > t_{ee}, t_{ei}$ [23, 24].

In order to establish the fact that the shock solutions are not the discrete solution, we identify the region in $\lambda_{\rm in} - \mathscr{E}_{\rm in}$ plan that permit shocks [21]. Here, $\lambda_{\rm in}$ and $\mathscr{E}_{\rm in}$ are the angular momentum and energy of flow measured at $x_{\rm in}$. Note that shock parameter space is calculated at $x_{\rm in}$ as in general we have $1.2 \lesssim \lambda_{\rm in} \lesssim 2$ and $2 \lesssim x_{\rm in} \lesssim 4$ [4, 16]. Thus, it is reasonable to assume that the flow crosses the horizon with $\lambda$ and $\mathscr{E}$ similar to the values measured at $x_{\rm in}$. We choose $\alpha_B = 0.01$ and $T_{\rm e,in} = 6.75 \times 10^9$ K and the obtained results are presented in Fig. 5c where the regions separated using solid, dotted and dashed curves are calculated for $\dot{m} = 0.001, 0.01$ and $0.05$, respectively. We observe that parameter space is shrunk and shifted to the lower energy domain with the increase of $\dot{m}$. This is obvious because inflowing matter always loses energy as it accretes on to the BH. In reality, beyond a critical limit of $\dot{m}$, shock parameter space vanishes as shock conditions do not satisfy there.

## 2.4 Accretion-Ejection Solutions

One of the promising aspects of the shock induced accretion solution is that the post-shock region of the disk is hot and dense and, eventually, becomes puffed up that behaves like a Comptonizing cloud (PSC). In the course of accretion, inflowing matter experiences excess thermal gradient force at PSC that deviates a fraction of the accreting matter in the vertical direction to produce bipolar outflows. This mechanism enables us to establish the coupling of outflow generation with the accretion dynamics. Following this appealing mechanism of outflow formation, we self-consistently compute the rate of mass-loss ($R_{\dot{m}}$) from the disk around a rotating BH of spin parameter $a_k$ [25]. In this work, we simulate the general relativistic effect by considering the pseudo-potentials prescribed by [26] (see, Soumen Mondal, this volume). Further, we compute the rate of maximum mass-loss ($R_{\dot{m}}^{\rm max}$) for a given value of adiabatic index ($\gamma$). To do that, we freely vary the flow parameters of the adiabatic flow, such as energy ($\mathscr{E}$) and angular momentum ($\lambda$), that cater maximum $R_{\dot{m}}$. The significance of this study relies on the fact that $R_{\dot{m}}^{\rm max}$ is directly associated with the jet kinetic power observed in BH systems. In Fig. 6, we display the variation of $R_{\dot{m}}^{\rm max}$ with $a_k$ where upper, middle and bottom panels are for thermally ultra-relativistic ($\gamma = 4/3$), thermally trans-relativistic ($\gamma = 1.4$) and semi-non-relativistic flows ($\gamma = 1.5$), respectively. First of all, we observe that the mass-loss continues to happen from the disk around a rotating BH having wide range of $a_k$ values. In all the panels, $R_{\dot{m}}^{\rm max}$ shows gradual increase with $a_k$. Moreover, we find that thermally ultra-relativistic flow produces more outflows in comparison with flow having high $\gamma$ value. This happens because the outflows we study here are mainly thermally driven [25].

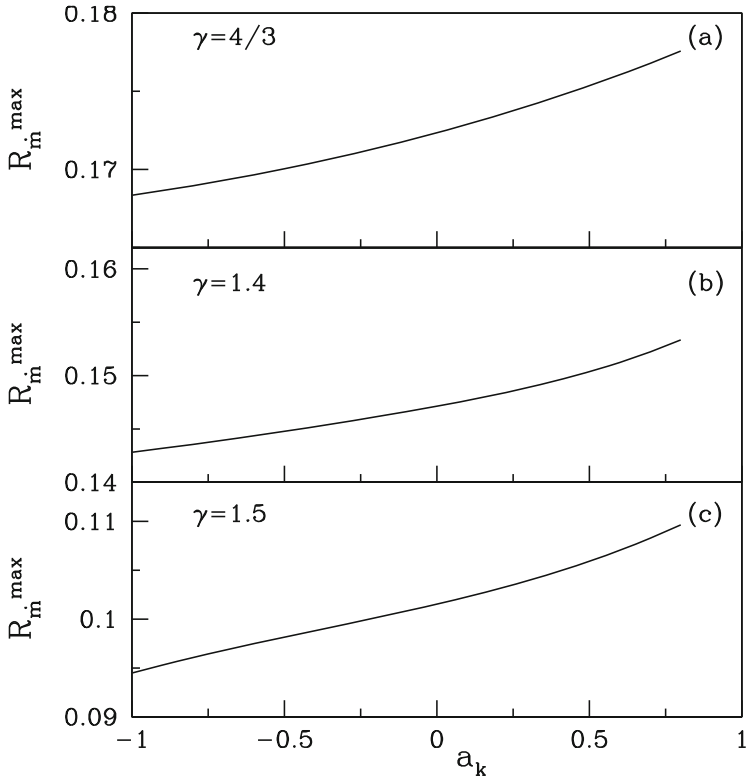



**Fig. 6** Variation of maximum outflow rates ($R_{\dot{m}}^{max}$) with BH spin ($a_k$). Panels (**a**), (**b**) and (**c**) are for $\gamma = 4/3$, $\gamma = 1.4$ and $\gamma = 1.5$, respectively [25]

## 3 Conclusion

Global accretion solutions in the BH system are necessarily transonic in nature and they are definitely sub-Keplerian in the vicinity of the BH. It is seen that depending on the parameters, inflowing matter possesses single or multiple critical points. Although the nature of the critical point may be of saddle-, nodal-, and spiral-type, astrophysical flows can pass through the saddle-type critical point only. Accretion flow containing multiple saddle-type critical points carries special importance as it may harbor shock waves [3, 4, 6]. In the context of generalized accretion flow including viscosity, magnetic fields etc., we investigate the various aspects of the shock induced accretion flow and our findings are summarized below.

1. The presence of shock in the accretion flow around a BH seems to be unavoidable in astrophysical context. We obtain the global shock solutions in gas-pressure and magnetic-pressure dominated flows and observe that the evolution of shock front is purely regulated by $\dot{m}$ and plasma-$\beta$ Further, we

calculate the critical viscosity parameter ($\alpha_B^{\rm cri}$) that permits shocks and find that global shock solutions are pretty common even when $\alpha_B$ is large. Moreover, we compute the critical accretion rate ($\dot{m}^{\rm cri}$) for shock as well. It is seen that $\dot{m}^{\rm cri}$ is small for magnetically dominated flow: the fact is that smaller $\dot{m}$ is sufficient to produce the maximum cooling limit for shock transition. With the decrease of the magnetic fields, $\dot{m}^{\rm cri}$ gradually increases and eventually becomes independent for the gas-pressure dominated flow [16].

2. For the first time, we self-consistently calculate the solutions of TTAF that contain shocks in presence of radiative cooling and viscosity. In TTAF, it is seen that shock solutions are not the discrete solutions, instead it exists for a ample rage of input flow parameters. We identify the effective region in $\lambda_{\rm in} - \mathscr{E}_{\rm in}$ plane for different $\dot{m}$-s that admit shocks. We observe that with the increase of cooling (i.e. increase of $\dot{m}$), shock parameter space is decreased that eventually reduces the possibility of shock formation [21].
3. Finally, we compute the maximum rate of mass loss ($R_{\dot{m}}^{\rm max}$) from the disk by freely varying energy and angular momentum and examine its dependency on BH spin ($a_k$). We find that thermally ultra-relativistic flow ($\gamma = 4/3$) exhibits the maximum mass loss rate as $\sim$17–18%. Moreover, we observe that $R_{\dot{m}}^{\rm max}$ weakly depends on $a_k$ irrespective to the choice of $\gamma$ values [25].

**Acknowledgements** Author expresses sincerest gratitude to Sandip K. Chakrabarti for his continuous encouragement, motivation and valuable suggestions during Ph.D. period that helped him to acquaint with the fabulous world of astrophysics especially to the subject of black holes. Author also thanks Anuj Nandi, Samir Mandal, Biplob Sarkar, Ramiz Aktar and Indu Kalpa Dihingia, as the present article is based on the collaborative works carried out with them.

## References

1. Hoyel, F., Lyttleton, R.A.: Proc. Comp. Phil. Soc. **35**, 405 (1939)
2. Bondi, H.: MNRAS **112**, 195 (1952)
3. Chakrabarti, S.K.: ApJ **347**, 365 (1989)
4. Chakrabarti, S.K.: Theory of Transonic Astrophysical Flows. World Scientific, Singapore (1990)
5. Das, S., Chattopadhyay, I., Chakrabarti, S.K.: ApJ **557**, 983 (2001)
6. Das, S.: MNRAS **376**, 1659 (2007)
7. Bisnovatyi-Kogan, G.S., Ruzmaikin, A.A.: Ap&SS **28**, 45 (1974)
8. Torkelsson, U., Brandenburg, A.: A&A **283**, 677 (1994)
9. Balbus, S., Hawley, J.F.: ApJ **376**, 214 (1991)
10. Miller, J.M., Raymond, J., Fabian, A., Steeghs, D., Homan, J., Reynolds, C., van der Klis, M., Wijnands, R.: Nature **441**, 953 (2006)
11. Machida, M., Nakamura, K.E., Matsumoto, R.: PASJ **58**, 193 (2006)
12. Hirose, S., Krolik, J.H., Stone, J.M.: ApJ **640**, 901 (2006)
13. Krolik, J.H., Hirose, S., Blaes, O.: ApJ **664**, 1045 (2007)
14. Chakrabarti, S.K.: A&A **351**, 185 (1999)
15. Das, S., Chattopadhyay, I., Nandi, A., Chakrabarti, S.K.: A&A **379**, 683 (2001)
16. Chakrabarti, S.K., Das S.: **349**, 649 (2004)

17. Sarkar, B., Das, S., Mandal, S.: MNRAS **473**, 2415 (2018)
18. Sarkar, B., Das, S.: MNRAS **461**, 190 (2016)
19. Becker, P.A., Kazanas, D.: ApJ **546**, 429 (2001)
20. Das, S., Becker, P.A., Le, T.: ApJ **702**, 649 (2009)
21. Dihingia, I.K., Das, S., Mandal, S.: MNRAS **475**, 2164 (2018)
22. Chakrabarti, S.K., Molteni, D.: MNRAS **272**, 80 (1995)
23. Colpi, M., Maraschi, L., Treves, A.: ApJ **280**, 319 (1984)
24. Frank, J., King, A., Raine, D.J.: Accretion Power in Astrophysics, 3rd edn., p. 398. Cambridge University Press, Cambridge (2002)
25. Aktar, R., Das, S., Nandi, A.: MNRAS **453**, 3414 (2015)
26. Chakrabarti, S.K., Mondal, S.: MNRAS **369**, 976 (2006)

# Transonic Flow Solutions with Explicit Cooling and Viscosity




**Santanu Mondal**

**Abstract** In this chapter, we discuss about the transonic flows around black hole binaries in presence of explicit cooling and viscosity and their observational aspects. Accreting compact objects are powerful X-ray emitters. The X-ray flux arises from two key accretion flow components: the geometrically thin standard accretion disk and an inner X-ray corona. The flow that feeds these objects is transonic in nature and the structure of the flow appears to depend on the heating and cooling mechanisms, where the whole system can flatten to a disk or puff up into a sphere, radiate efficiently or advect all of its energy. Sometimes the inner region varies quasi-periodically without changing much its total accretion rates. Thus the phenomenology of X-ray observations of accreting compact object is very rich and intensely studied. To go beyond the standard model of a stable accretion flow, with no corona and only a parametric viscosity of unknown origin, it is necessary to rely on a promising physical solution. In a Two Component Advective Flow solution, a high-viscosity Keplerian disk is flanked by a low angular momentum and low-viscosity flow that forms a centrifugal pressure-supported shock. The post-shock region which behaves as a Compton cloud, upscatters soft photons from the Keplerian disk. The shock wave forms under the satisfaction of Rankine-Hugoniot conditions. This shock may be steady or oscillating depending on whether flow has cooling or not. To get the full transonic solution we coupled hydrodynamics and radiative transfer in presence of cooling, heating and viscosity mechanisms.

S. Mondal (✉)
Instituto de Física y Astronomía, Facultad de Ciencias, Universidad de Valparaíso, Valparaíso, Chile

Indian Centre For Space Physics, Kolkata, India

© Springer International Publishing AG, part of Springer Nature 2018

B. Mukhopadhyay, S. Sasmal (eds.), *Exploring the Universe: From Near Space to Extra-Galactic*, Astrophysics and Space Science Proceedings 53,
https://doi.org/10.1007/978-3-319-94607-8_6

# 1 Introduction

X-ray binaries are systems consisting of compact objects which are gravitationally bound to a normal companion star. The compact object can be either a neutron star or a black hole candidate. X-ray binaries are all powered by accretion of matter on to the compact star. The companion star donates matter to the compact star either via Roche lobe overflow or by stellar wind outflows. It is believed that accreting matter forms a disk like structure around the compact star and falls onto the compact object only after dynamically reducing its angular momentum. Viscosity is responsible to transport all the angular momentum outwards, allowing most of the matter to be transported to the inner regions of the disc. As the matter moves through the accretion disc, approximately half of its gravitational potential energy is radiated away. The wavelength of the observed radiation is determined by the position of the radiating matter in the disc. In the outer region of the disk the temperatures are of the order of a few thousand degrees and therefore the radiation will be in the IR. In the inner regions of the disk the temperature can reach several million degrees producing X-ray and other high energy emissions. An accretion disk produces multi-wavelength spectrum. Thus, studying accretion disk is very important to understand the dynamics and radiation mechanism inside it.

## *1.1 Accretion onto Black Holes*

Black holes are the simplest celestial objects. It cannot be directly visualized but from observational point of view their existence may be inferred. Different telescopes, and X-ray, gamma-ray observations point to their existence. Stellar mass black holes are considered to be end products of massive stars. Because of its strong gravity, surrounding gas and matter from other stars are pulled by a black hole causing a rush of matter from the star to the black hole. In an astrophysical context, accretion is a process by which matter gathers around a central object and falls into it. In binary systems, matter may fall through the Roche lobe which is a region where matter is gravitationally bound with the star. Winds, especially in high mass X-ray binaries, may also be transferred from one star to another. In case of active galaxies and quasars, matter may be supplied to the central black hole very intermittently, and the angular momentum of the supplied matter at the outer edge may not be as high as Keplerian. This is because matter may originate from winds of star clusters and the supersonic wind may pass through shock waves which randomize some of their velocity components. These flows have very little viscosity. Therefore, radiation efficiency is in between a spherical flow and a thin Keplerian disk.

The simplest solution of axisymmetric particle flow through shock front was carried out by [33]. Pressure was not included in the flow. In 1952, Bondi [2] solved the spherically symmetric accretion flow problem where he considered that the gas is at rest at infinity. Bondi did not consider any perturbation in the flow such as,

rotation, magnetic field, Comptonization and pair production etc. In 1963, the first Quasar QSO 3C272 was discovered [32] and the high luminosity was promptly attributed to high gravitation field. In 1964, Salpeter [61] using the solution of [62], concluded that luminosity is due to Bondi accretion flow on super-massive black holes. The importance of the accretion process as a source of power was realized specially in case of X-ray binaries wherein the black hole accreted matter from its companion star through Roche lobe overflow or stellar wind accretion.

It is believed that matter accreting onto the black holes forms a disk like structure [42] and enters into the black hole only after dramatically reducing its angular momentum. In [60] scientists first realized the importance of angular momentum loss in accretion disks. In 1973, Shakura and Sunyaev [63] (hereafter SS73) proposed an accretion disk model in Newtonian geometry where the viscous stress needed to transport the angular momentum was simply assumed to be proportional to the pressure and [57] presented the solution in a general relativistic framework. In all these models, the infalling matter moves in Keplerian orbits and minimizes its energy by settling down at the equatorial plane and forming a thin disk where the height of the disk is much less than the radial distance. Heat generated by the viscosity is radiated away from the disk surface as thermal emission which can be modelled as a multi-temperature black body. These models indeed predict the correct luminosity of these sources and fit the observed spectrum for a limited wavelength range.

This kind of disk, however, does not predict the non-thermal high energy X-ray emission, routinely observed in accreting black hole systems. Observers realized that a complete picture of the accretion flow feeding stellar mass black holes must have the standard Keplerian disk (SS73), which produces the soft photons, and a hot corona [66, 68] which Comptonized some of these soft-photons into hard X-rays. This latter component is called the Compton cloud and its origin is a matter of intense theoretical research. At the same time [39] showed using a pseudo-Newtonian flow that the accretion flow is necessarily transonic. In 1989, [5] showed extensively that before reaching the black hole, matter forms a shock and then passes through the inner sonic point. According to Two Component Advective Flow (TCAF) solution by Chakrabarti and Titarchuk [16] (hereafter CT95), the second hot component at the inner region of the disk is nothing but the low viscous and low angular momentum halo, or to be more precise the innermost region supported by centrifugal barrier is identified with the Compton cloud.

## *1.2 Two Component Advective Flow Model Description*

Though historically various disk models came before the generalized equation was found by Chakrabarti and collaborators, we start with the most general solution so that we can demonstrate how the other disk models constitute special cases.

In a binary system, as the matter starts from secondary to the compact primary object, several physical processes become very important. First among them is viscous dissipation of angular momentum of the flow which helps matter to be

accreted and the second is the radiative processes, where the emitted radiation interacts with the disk matter itself before being released. These cause accreted matter to have an energy and angular momentum distribution inside the flow. This matter settles down on the equatorial plane of the central gravitating object. If the viscosity is high the angular momentum distribution quickly becomes [9]. Depending on the accretion rate and the optical depth of the disk, the temperature may be very low and the disk becomes a thin, cold, Keplerian disk. When the accretion rate is very high or very low, the pressure could be very high, due to radiation pressure or ion pressure respectively which naturally affect angular momentum distribution as well. Such a pressure also increases the thickness of the inner flow. Some matter may be accreted by the black hole from the winds of the companion star, or even the outflows generated by the inner part of the flow. Therefore, a flow could be sub- or super-Keplerian close to the black hole when advection, pressure, cooling terms etc. are present. These effects must come out self-consistently from the flow equations. In general, the flow close to the compact object will be a mixture of Keplerian and sub-Keplerian matter. During the accretion, the infalling matter is accreted quasi-spherically having an infall time similar to the free fall time until the specific angular momentum become comparable with the Keplerian angular momentum. At this point, the flow virtually stops and piled up matter produces a standing shock. This shock may be produced anywhere in the disk 10–$10^4\, r_g$, depending on the specific energy and angular momentum. The post shock region is puffed up due to the conversion of kinetic energy into thermal energy. According to CT95 this post-shock pile-up region behaves like a Compton cloud and produces hard radiation of the emitted spectrum, be in a stellar mass black hole or in the case of super-massive black hole. In the frame work of CT95, it is clear that the black hole accretion, in general, contains two components: one component has a viscosity higher than a critical value (which depends on other flow parameters) is Keplerian. The sub-critical viscous low angular momentum component remains sub-Keplerian, which is relatively hot and optically thin. Observational evidences also show that most of the accretion processes indeed have two components (e.g., [65]). Recently, numerical simulations by Giri and Chakrabarti [29] showed that indeed TCAF solution is obeyed and the flow configuration is stable in nature. Numerical simulation by Molteni et al. [45], showed that considerable winds are produced from the post-shock region. Numerical simulations by Garain et al. [28], show that the amount of matter in the outflow depends on accretion rates. They also found emitted spectra from their numerical simulations. These are similar to what TCAF predicted. Thus TCAF solution can be regarded as a grand unified model as it encompasses all the other known solutions in the literature as special cases. This will be discussed the next section of this chapter. Not only from the theoretical ground, it is supported by the observation as discussed in several works (see, e.g., [17, 19, 24–26, 34, 50, 52]). It is to be noted that unlike other models in the literature, where Compton cloud is an ad hoc component, our picture includes components which are the actual solutions of a series of governing equations. In the next section we will discuss about that in details. The TCAF reduces the number of parameters, but identifying the outer edge of Compton cloud at the inner edge of the Keplerian disc.

The halo and disk rates together with the compression ratio give the optical depth and temperature of the Compton cloud. Similarly the shock oscillation gives the QPO frequency.

## 2 Transonic Solution in Dissipative Flows

So far, several analytical studies have been done in presence of viscosity and energy dissipation [13, 22, 64] and also in numerical simulations as discussed above in order to understand accretion onto black holes in the framework of TCAF. However all the works considered cooling as a parameter, which should come from Comptonization of soft photons from the Keplerian disk by the hot electron cloud in a self-consistent way.

### *2.1 Effects of Compton Cooling in Transonic Flow*

In this section, we will concentrate on how the behavior of transonic solution changes when there is an energy dissipation (mainly Compton cooling) in the flow. We consider a rotating, thin, axisymmetric and adiabatic flow around a black hole. The flow behavior depends on the initial flow parameters, namely, energy ($\varepsilon$), angular momentum ($\lambda$), disk accretion rate ($\dot{m}_d$) etc. For a suitable set of flow parameters, the flow possesses multiple sonic points and forms a shock depending on whether Rankine-Hugoniot (R-H) shock conditions [37] are satisfied or not. Our motivation comes from both analytical and observational points of view. In the first case, there is a large number of non-linear equations and finding a solution from there is a challenging job. On the other hand, the centrifugal pressure supported shock could be an essential component for the explanation of outbursting black hole candidates (BHCs). One can model using specific energy and specific angular momentum ($\varepsilon$ and $\lambda$ respectively) or Keplerian and sub-Keplerian rates from TCAF. Therefore it is important to study hydrodynamic properties including radiative transfer self-consistently. However, till date, no transonic flow [8, 39, 58] solution has been obtained in presence of Thermal Comptonization.

In [47] (hereafter MC13), for the first time, analytical solution was obtained of the transonic flow with Compton cooling calculated explicitly from radiation spectrum. This solution satisfies earlier predictions and different aspects of TCAF solution. Furthermore, the post-shock region, known as the CENBOL (CENtrifugal pressure dominated BOundary Layer) could be responsible for the outflows or jets, like any other boundary layers [11, 49]. In Fig. 1, we show the complete transonic solution of accretion flows in presence of Compton cooling. The amount of cooling is calculated from integrating the emitted spectrum, where soft photons from the disk gain energy by repeated scattering with the hot electron inside the CENBOL. As the accretion rate increases, number of soft photon increases, increasing the cooling rate which shrinks the size of the CENBOL. The inner edge of the truncated

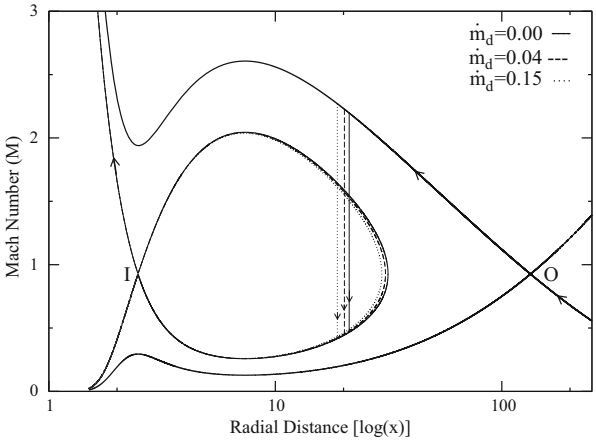



**Fig. 1** A complete transonic flow solution in the M−log(x) plane in presence of Compton cooling. As the accretion rate increases, the shock drifts closer to the black hole. Solid line shows the solution of [6], dashed and dotted lines show the transonic solution for different accretion rates ($\dot{m}_d = 0.04,\ 0.15$) of [47]

Keplerian disk also moves inward. Solid line shows the location of the shock when there is no cooling, dashed and dotted lines show the movement of shock waves for different accretion rates. The points "O" and "I" denote the outer and the inner sonic points of the flow, which comes after solving conservation equations (e.g. energy, mass accretion etc., [5]) with physical cooling.

In Fig. 2, we show variation of spectral index ($\alpha$) with accretion rates ($\dot{m}_d$ and $\dot{m}_h$ are disk and halo rates respectively). The curves are generally shifted upward, since the spectra become softer due to cooling. For example, when $\dot{m}_h = 1.0$, a hard to soft transition ($\alpha = 1$) takes place at $\dot{m}_d = 0.011$ instead of at 0.033 valid for a non-dissipative transonic flow (CT95). If we decrease the halo rate, the optical depth of the post-shock region is decreased, thereby decreasing the number of hot electrons in the post-shock region to process the intercepted soft photons which makes the spectrum softer. At very low accretion rates, the spectral index is very insensitive to the disk rate. However, since thermal Comptonization process becomes effective when the optical depth of the CENBOL is above $\sim 2/3$, the cooling takes effect suddenly and forms the soft state. With the rise in the disk rate, cooling rate becomes higher and thus the shrinking in the parameter space forming shocks is also rapid (see, [47]).

## *2.2 Effects of Viscosity in Transonic Flows*

The most important process governing the accretion of rotating matter is the action of viscous stress within the flow. Viscous stress drive accretion by transporting

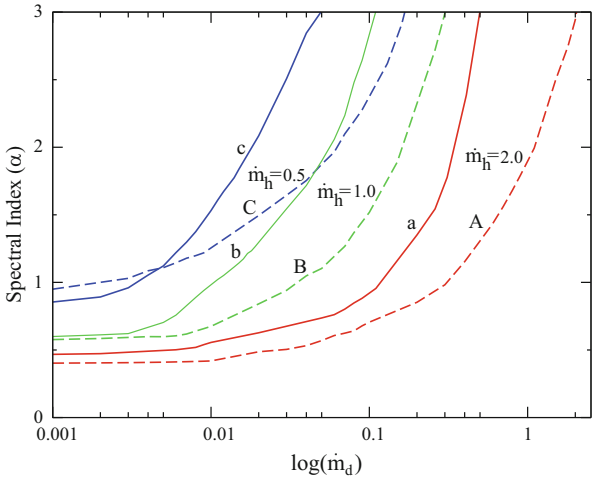



**Fig. 2** Energy spectral index ($\alpha$) variation with accretion rate ($\dot{m}_d$) for different halo rates (0.5, 1.0, 2.0). A, B, and C are the spectral index variation with disk accretion rate when cooling is present and a, b, and c are the variation of spectral index when no cooling is there i.e. [16] results. The slope is measured in the 2–50 keV energy band. Figure is adopted from [47]

angular momentum outward and mass inward: it is also a way to convert gravitational energy of matter into heat. The matter accreting through the Roche lobe is Keplerian in nature, but it requires a large viscosity to transport the angular momentum. In case such a viscous process is not available, low angular momentum sub-Keplerian matter from wind accretion can rapidly accrete with different rate. This does not require high viscosity and due to the transonicity condition at the inner sonic point [9], the flow will form a shock [6, 7, 41]. In the original standard disk model (SS73), the turbulent disk matter is described by a viscous stress tensor assumed to be proportional to the total pressure. The proportionality constant is viscosity parameter $\alpha$. The sub-Keplerian halo viscosity ($\alpha_h$) can be very low compared to Keplerian viscosity ($\alpha_K$) as it is tenuous and largely supersonic and turbulence free.

There are large number of analytical and numerical simulation results in the literature containing the shock solutions in adiabatic and inviscid flows [8, 14, 31]. There is a critical viscosity ($\alpha_c$) of the flow, below which the flow converges to a shock solution and above that limit, the disk is Keplerian passing through the inner sonic point to the black hole. Analytical solutions by Chakrabarti [9], Chakrabarti and Das [13], and Das and Chakrabarti [20] showed the details about the critical viscosity parameters and the flow topology for different viscosity values. They showed that depending on the viscosity parameter, the flow topology changes. According to TCAF solution, flow is divided into two component when it approaches a black hole. This effect is due to the variation of viscosity in the vertical direction. Higher viscosity in the equatorial plane region produces Keplerian

disks while lower viscosity farther out keeps the sub-Keplerian flows without much transport of angular momentum. Numerical simulation of [30] clearly shows the segregation of the two components in a flow where $\alpha$ monotonically decreases in the vertical direction. Thus the viscosity of both the components can be calculated using SS73 disk prescription and angular momentum transport mechanism. The angular momentum transport takes place according to the following equation [8]:

$$\dot{M}(\lambda - \lambda_e) = -r^2 W_{r\phi}, \tag{1}$$

where, $W_{r\phi} = -\alpha P$, is the viscous stress, $\alpha$ being SS73 viscosity parameter and $\lambda_e$ is the angular momentum at the inner edge of the disk. This transport process depends on the viscosity prescription. At the shock, Mach number $M$ varies from supersonic to sub-sonic, the rate of transport of angular momentum would be quite different on both sides of the shock. Angular momentum at the shock must be discontinuous. If the viscosity is very small, angular momentum on both sides of the shock match and produces a steady shock. In this case, the shock forms far away from the black hole.

The formation of shock and change in spectral states not only depends on the heating and cooling mechanisms but also on the ejection mechanism associated with the accretion. In the next section we discuss about how spectral shape could changes due to the presence of jet in the system.

## *2.3 Spectral Signature of Presence of Jet*

The problems of mass loss, and the origin, acceleration, collimation of jets, and its relation with the rest of the accreting system still remained unclear even after several decades of research. Since magnetic field is ubiquitous, it is expected to play a key role in transporting matter out of the disk and in deciding the outflow velocity. Collimation may also be done by hoop stress [12, 36] of toroidal fields escaping from accretion flow due to buoyancy effects. So it may not be essential to have strong and large scale aligned magnetic field in the disk itself. There is no convincing evidence that the magnetic field is dynamically important in accretion disks. In the rotating wind solution of [4], the flow was assumed to be coming out of the thick accretion disk [3] which happened to be the post-shock region or CENBOL in the transonic flow solution of [5]. Some models [1, 59] postulated that the black hole spin could be responsible to accelerate jets. However it has been found that there is no evidence that the jets are powered by black hole spin [27] at least in the case of X-ray binary and such conclusion can be valid for active galaxies and quasars as well. In [10, 11] proposed that perhaps the entire outflow is produced by this post-shock region, either steadily, as in a hard state, or episodically, when this region collapses due to enhance tension of toroidal magnetic field [55]. However, what should be the spectral shape and how it will change with the presence of jet are not shown till date.

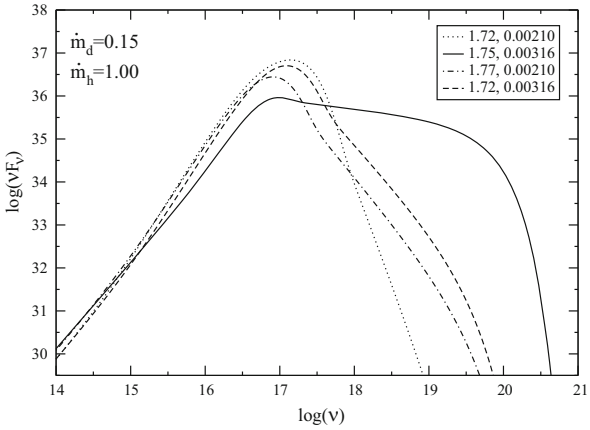



**Fig. 3** Spectral shape for different sets of energy and angular momentum of the flow. It shows from transonic solution in presence of mass loss and cooling, that the size of the Compton cloud increases with increase in angular momentum and the spectrum becomes harder. On the other hand, the increase in outflow rate makes the spectrum softer [49]. Details are discussed in the text

In this section we summarize the results of [49], where authors self consistently solved the transonic solution and showed the signature of jet on the emitted spectra from the accretion disk. Figure 3 shows spectral variation for a different sets of energy ($\varepsilon$) and angular momentum ($\lambda$) of the flow. Dotted curve shows the variation when angular momentum is low (1.72). For this set of flow parameters, the system is in the soft state (size of the post-shock region is very small) and the outflow rate is also low, $\sim$0.63%. The solid line shows the spectrum when both energy and angular momentum are high and shock forms far from the black hole, thus the emitted spectrum is hard. From out self-consistent solution, it is clear that the spectral index and the outflow rate change significantly with a change in energy and angular momentum of the flow, when disk (0.15) and halo (1.0) accretion rates are kept fixed. We also observed that in the hard and intermediate states jet emission rate is higher and change in spectral shape is more significant than soft state [11, 49]. In the hard and intermediate states, thermal pressure at the post-shock region is sufficiently higher to drive the matter out, thus the outflow rate is also higher.

Here, we put some key points that make the work of [47, 49] different from earlier works [11, 21, 64]:

1. Compression ratio $R$ is allowed to vary from 7 to 1, obtained from initial energy and angular momentum of the flow. This $R$ is used to calculate the optical depth of the post-shock region.
2. Height of the shock, shock temperature and outflow rates are obtained from hydrodynamic solution.
3. Inner boundary of the Keplerian disk is neither a parameter nor a constant. It changes according to shock condition.
4. The modified R-H shock condition includes cooling, which is neither a parameter nor an assumption. It is estimated directly from the emitted spectrum.
5. In summary, whole solution including hydrodynamics and radiative transfer come out once the energy, angular momentum, disk rate and halo rate are supplied.

The above variation in spectrum is on the basis of change in R-H condition due to the presence of outflows. The presence of jets can make the spectrum harder, when soft photons from the disk are also upscattered by the jet. On the other hand, when Comptonized photons from the CENBOL pass through the diverging jet medium, show bulk motion effects, that can also change the shape of the overall spectra [48].

Thus the solution not only explains the theoretical understandings but also explains observational evidences such as heating, cooling, viscosity and outflows. In the next section we will discuss about how theoretical understandings directly explains observational evidences satisfactorily in the framework of transonic solution.

## 3 Fitting of Satellites Data with TCAF

Different physical mechanisms and theoretical understanding of TCAF model have been discussed in the earlier sections. Here we will discuss about the model fitting of the observed data. Very recently in 2014, TCAF model has been incorporated in NASA's XSPEC software as a local additive Table model [25] to fit the observed data. The model, has five input parameters including mass of the black hole. The parameters are (1) mass of the black hole, (2) disk accretion rate, (3) halo accretion rate, (4) location of the shock, and (5) shock compression ratio. The original [16] source code which used strong shocks for illustration purposes, was modified to include the possibility of weaker shocks, Debnath et al. [25] generate around millions of model spectra to make a model *fits* file, which is used in XSPEC as *atable* command to fit the data. Since then series of papers [19, 26, 34, 44, 50, 52] have been published which successfully explain the outburst features of black hole candidates from the observed data of different satellites (e.g., RXTE, *Swift*, NuSTAR etc.). From the model fitted parameters one can explain the cause of rising and declining phases of an outburst, evolution of QPOs, cause of accretion rate change, and the explanation for different spectral states change etc.

### *3.1 Presence of Double Horn Iron Line and Estimation of Spin*

The observed X-ray spectrum in compact objects is complex and contains several components due to the accreting material (specifically the inner hot region) which reprocesses, absorbs and scatters photons from the Keplerian disk. The main three components are (1) disk blackbody, (2) power law component, and (3) iron line around, 6.4 keV energy. The combination of the strong iron abundance in the disk matter and the associated high Fe fluorescence makes the Fe K-shell fluorescence lines the strongest emission features to be detected in the X-ray wave band. Thus they automatically became one of the prior targets of X-ray observers. However, this iron line may not be symmetric around 6.4 keV, it could be asymmetric and

distorted due to (1) Doppler effects, (2) relativistic effects, and (3) reprocessing and transmission of radiation from the surrounding medium. The $K_\alpha$ line for low mass X-ray binaries can be emitted by a hot Compton cloud in a photoionization equilibrium [35], or it could be produced by fluorescence from an X-ray-irradiated cold gas [40]. This emission line profile helps to constrain essential parameters of the accreting BH system. The main physical parameters such as disk inclination, inner and outer radius of the disk, and Kerr rotational parameter of the central object. Laor [38] studied the line emission from a disk of a rotating black hole and the effects of strong gravity on the emitted profile.

Mondal et al. [52] observed the same asymmetric feature of iron line emission for the BHC GX 339-4 during its 2013 outburst. Authors fitted the combined *Swift* and NuSTAR data with TCAF and LAOR models. Figure 4 shows the unfolded spectra of the model fit. It is also observed that the intensity of the iron line is maximum when the location of the shock is minimum. This is also an indication of relativistic broadening. From the LAOR model fitted parameters we can estimate the disk inclination angle and inner edge of the disk. It is well known that once we have the inner edge ($r_{in}$) of the disk one can estimate the Kerr parameter ($a$) of the central object using:

$$r_{in} = M + (M^2 - a^2)^{1/2}. \tag{2}$$

Our estimated spin parameter for GX 339-4 is $\sim 0.99$ using LAOR model as a phenomenological model.

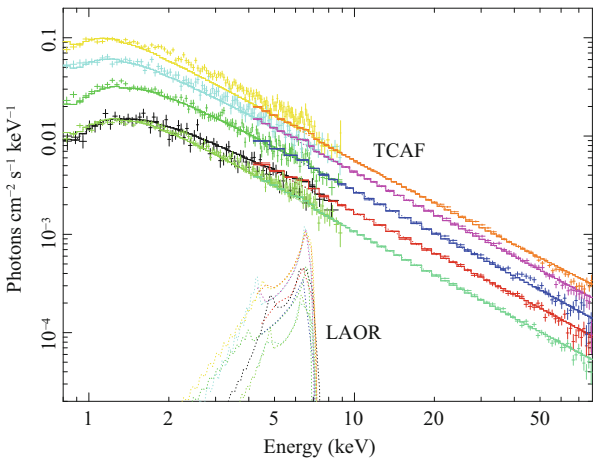



**Fig. 4** Unfolded spectra of BHC GX 339-4 fitted with the TCAF model and the LAOR model of double peaked iron line. The data covers the energy range from 0.8–79 keV observed by Swift and NuSTAR. Variation of $Fe\ K_\alpha$ line intensity of all the observations are also shown [52]

### 3.2 *Observational Signatures of Cooling and Viscosity*

It is observed that the variability in both spectro-temporal domain is a very common feature of accretion [24, 43, 56, 67]. The signature of variability is observed from spectral shape change and also from quasi periodic oscillation (QPO) frequency variation. It is believed that the oscillation of shock, which is also the boundary of the Compton cloud supposed to originate low frequency QPOs (LFQPOs). This oscillation occurs when resonance condition satisfies i.e. cooling time scale roughly matches with the infall timescale [46]. Recently, Chakrabarti et al. [18] applied the resonance condition for H 1743-322 BHC and showed that LFQPOs are produced when cooling time scale roughly matches with infall time scale. During the outburst, as the day progresses size of the Compton cloud/shock changes, during the rising phase it decreases and opposite scenario occurs in the decline phase and spectral state changes from hard (soft) to soft (hard) through intermediate states. However, which physical mechanisms are responsible for that and what are their pattern of variation are not discussed so far. Recently, Mondal et al. [51, 53] studied the accretion behavior of the outbursting candidates both in presence of cooling and viscosity. Here we discuss those results briefly. Authors showed that during the rising phase, cooling and viscosity parameter increases on a daily basis. The amount of cooling is mainly the amount of energy gained by the low energy photons due to repeated scattering, which is estimated from the area under the power law component of the radiation in the observed spectra. For our solution, we consider that the accretion starts at the outer boundary of the disk with some value of energy and angular momentum, as the cooling is present in the system, the flow moves in transporting angular momentum outwards via viscosity. Thus the required change in angular momentum will give us an idea of how much amount of viscosity was needed in a particular observation. It is to be noted that, the final value of the angular momentum of the flow is decided by the QPO frequency observed on that day. In Fig. 5a, shows the variation of amount of Compton cooling for a transient source

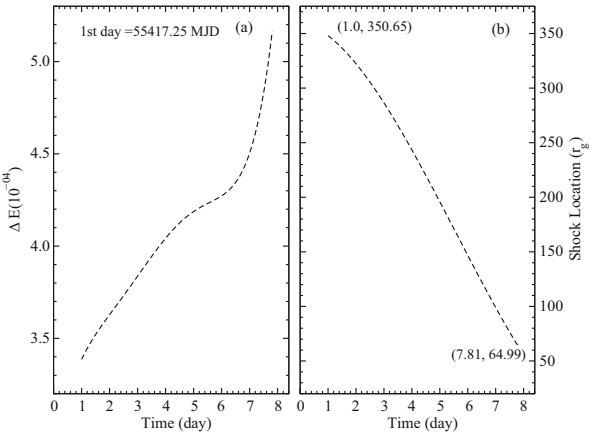



**Fig. 5** (**a**) Variation of energy loss as a function of days. As the day progresses, amount of cooling increases. (**b**) Movement of the shock location in progressive day of H 1743-322 during its 2010 outburst

H 1743-322 during the raising phase of its 2010 outburst. The amount of cooling required in both theory and observation are calculated from the observed spectral energy distribution (SED). This is estimated using [49], $\sum_{i=\nu_l}^{\nu_u} \nu_i F_{Comp}(i)$, where $\nu_l$ and $\nu_u$ are the lower and upper frequency range in the spectrum. $F_{Comp}(i)$, is the Comptonized flux, which comes from the power-law component of the spectrum.

In Fig. 5b, shows the corresponding movement of the shock, which moves inward towards the black hole due to the presence of progressively increasing cooling. At the first day (MJD = 55417.2) of the outburst, shock was at $\sim$351 $r_g$, whereas at the end of the rising phase (MJD = 55424.1) of the outburst shock reaches at $\sim$65 $r_g$, which is due to the loss of energy from the CENBOL. From the movement of the shock we estimate the velocity of shock movement, which is a few meters/s.

The movement of shock in presence of cooling has been well established by several authors both from theoretical and observational ground [17, 23, 46, 47, 50]. This movement of shock is responsible for the evolution of observed QPOs of different frequencies. Propagatory oscillating shock solution can explain such frequency drifts very well [17, 24, 56]. These phenomenological models are found to be justified when we actually compute shock drifts from radiated energy loss from a self-consistent transonic solution. We find that in order to have Rankine-Hugoniot conditions satisfied on each day, viscosity parameter must be evolving too. If one keeps the outer boundary condition fixed, and increase the viscosity parameter that causes the shock to move outward [15], but keeping the inner boundary condition fixed, the shock moves inward [8, 13]. We find support of the latter phenomenon in an outbursting source where matter supply is changing and viscosity enhancement steadily brought the shock closer to the black hole. Cooling is found to rise day by day (see, Fig. 5a) and so is viscosity. This movement of the shock increases QPO frequency as is observed. Figure 6a shows the variation of QPO frequency on a daily basis for several BHCs during their raising and declining phases of different outbursts. The dashed lines show the variation of theoretically calculated QPO frequency using Compton cooling from the observed spectral energy distribution (SED).

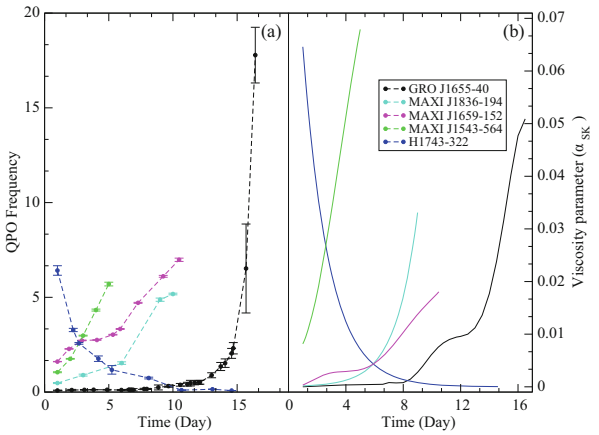



**Fig. 6** Variation of (**a**) QPO frequency with progressive days during different outbursts of the candidates, obtained from observation (circles) and analytical solution (dashed lines), and (**b**) viscosity parameter ($\alpha_{SK}$) with time (in day) during the outburst of the BHCs are shown [53]

For the estimation of sub-Keplerian viscosity, we use the physical parameters at the shock, which turns Eq. (1), as below:

$$\dot{M}_h(l^{'} - l) = -X_s^2 W_{r\phi} \tag{3}$$

where, $\dot{M}_h$ and $W_{r\phi} = -\alpha_h P$, are the sub-Keplerian mass accretion rate and viscous stress respectively, $\alpha_h$ being (SS73) viscosity parameter of the sub-Keplerian halo component. We assume that the flow satisfies SS73 prescription at a given point of the flow so that viscous stress is proportional to the local pressure. Angular momentum variation from Eq. (3) can be written as [8],

$$\Delta l = \frac{\alpha_h X_s a^2}{v} \tag{4}$$

where, $v$ is the radial flow velocity, $X_s$ is the location of the shock in $r_g (= 2GM/c^2$ where G, M and c are the gravitational constant, mass of the black hole and speed of light respectively) unit, and $\Delta l = (l^{'} - l)$ is the change in specific angular momentum ($l$) between the specific angular momentum at some radius, from which the flow starts, as compared to the radius where shock forms, for a given cooling. Specific angular momentum at the radius where the flow starts is $l^{'}$ and it is $l$ at the shock location, where the observed QPO matches with the theoretical value. During the estimation of $\alpha_h$ we are not using the accretion rate directly, we are considering only the physical quantities such as the $a$, $v$ and $X_s$ etc., which come from basic input parameters for the sub-Keplerian component. The observed QPOs give us an handle on where the shock forms. That gives us the input parameters for the sub-Keplerian flow. The above estimation is recently made by Mondal et al. [51, 53]. It is to be noted that [53, 54] also estimated the disk viscosity for outbursting candidates and all possible QPO formations from hydrodynamic solution. Figure 6b shows the corresponding variation in viscosity. This shows how viscosity should vary in each day during the outburst. The transonic flow solution also implicates that the variation of viscosity is responsible for the change in accretion rate daily basis, redistributing Keplerian matter to sub-Keplerian and completes the outburst cycle. This conclusion is also in the same line of SS73 prescription. In future we aim to apply these solutions for other compact objects mainly for active galactic nuclei to study their outburst evolution, disc structure and dynamics of the flow. From different time scales (e.g., viscous, free fall, cooling etc.) estimation, we will be able to understand the variability nature of the sources.

## 4 Concluding Remarks

Black hole accretion and it's dynamics are different from other compact objects in space. Here flow enters super-sonically with the velocity of light passing through the inner sonic point, whereas in case of Neutron star there is a hard surface where the

flow has zero velocity. Another important point is that black holes can not radiate, thus the radiation which we observe is purely from the accreting disk. To study the outgoing radiations and flow dynamics, one needs to solve transonic flow equations, which consist both hydrodynamic and radiative transfer mechanisms.

In this chapter, we discuss about the transonic solution of black hole accretion using two component advective flow (TCAF) model as a basic model. In original TCAF model shock location was chosen as a parameter which was not computed from *ab initio* calculation. Even though while fitting with TCAF, the shock properties are used as parameters since the total number of unknowns remains the same, it may be instructive to find the transonic solution (say, for the halo component) when cooling is present and the location of the shock is calculated from the initial energy and angular momentum of the flow. The height and temperature of the shock is also calculated from the initial flow parameters. We also estimated the viscosity parameter for both the Keplerian and sub-Keplerian flows. For Comptonization, we need to have the source of seed photons. For this, we assume a two component advective flow (TCAF) of [16] where a viscous, standard Keplerian disk in the equatorial plane supplies the seed photons in the form of soft X-rays. We compute the energy loss due to Comptonization from the radiative transfer code and couple it with the hydrodynamic equations. The energy loss increases due to the increase in accretion rate, which decreases the size of the post-shock region. As a result, the shock moves towards the black hole softening the emitted spectrum.

We also estimated the viscosity variation during the outburst phase of the transient sources. Our solution tells about how viscosity and cooling are responsible for the evolution of QPOs. Transonic solution confirms that viscosity is responsible for the change in accretion rate during the outburst and the evolution of whole outburst cycle. Our solution also explains the rise and decay of outburst from the rise and fall of cooling and viscosity. For the origin of QPOs, Compton cooling is the main physical process, even if the viscosity is negligibly small. We fit the data from different satellites for different black holes with TCAF and study their flow dynamics and accretion states during their outburst phases. From the model fitted spectrum and parameters we also estimate the Kerr parameter. In future we hope to incorporate effects of iron line broadening and radiative transfer mechanism in jet, not only for stellar mass black holes but also for other compact objects.

**Acknowledgements** I am thankful to my Ph.D. advisor Prof. Sandip K. Chakrabarti for his continuous support, encouragement and discussions during my work. I also acknowledge all my collaborators for their useful discussions and suggestions. I acknowledge FONDECYT postdoctoral grand (#3160350) for the article.

## References

1. Blandford, R.D., Znajek, R.L.: MNRAS **179**, 433 (1977)
2. Bondi, H.: MNRAS **112**, 195 (1952)
3. Chakrabarti, S.K.: ApJ **288**, 1 (1985)

4. Chakrabarti, S.K.: In: Audouze, J., Tran Thanh Van, J. (eds.) Accretion Processes in Astrophysics. Editions Frontiers, Paris (1986)
5. Chakrabarti, S.K.: ApJ **347**, 365 (1989)
6. Chakrabarti, S.K.: PASJ **41**, 1145(1989)
7. Chakrabarti, S.K.: MNRAS **243**, 61 (1990)
8. Chakrabarti, S.K.: Theory of Transonic Astrophysical Flows. World Scientific, Singapore (1990)
9. Chakrabarti, S.K.: ApJ **464**, 664 (1996)
10. Chakrabarti, S.K.: IJP **72**, 183 (1998)
11. Chakrabarti, S.K.: A&A **351**, 185 (1999)
12. Chakrabarti, S.K., Bhaskaran, P.: MNRAS **255**, 255 (1992)
13. Chakrabarti, S.K., Das, S: MNRAS **349**, 649 (2004)
14. Chakrabarti, S.K., Molteni, D.: ApJ 417, 671 (1993)
15. Chakrabarti, S.K., Molteni, D.: MNRAS **272**, 80 (1995)
16. Chakrabarti, S.K., Titarchuk, L.G.: ApJ **455**, 623 (1995)
17. Chakrabarti, S.K., Debnath, D., Nandi, A., et al.: A&A **489**, L41 (2008)
18. Chakrabarti, S.K., Mondal, S., Debnath, D.: MNRAS **452**, 3451 (2015)
19. Chatterjee, D., Debnath, D., Chakrabarti, S.K., et al.: ApJ **827**, 88 (2016)
20. Das, S., Chakrabarti, S.K.: IJMPD **14**, 933 (2004)
21. Das, S., Chattopadhyay, I., Nandi, A., et al.: A&A **379**, 683 (2001)
22. Das, S., Chakrabarti, S.K., Mondal, S.: MNRAS **401**, 2053 (2010)
23. Debnath, D., Chakrabarti, S.K., Nandi, A., et al.: BASI **36**, 151 (2008)
24. Debnath, D., Chakrabarti, S.K., Nandi, A.: AdSpR **52**, 2143 (2013)
25. Debnath, D., Chakrabarti, S.K., Mondal, S.: MNRAS **440**, L121 (2014)
26. Debnath, D., Mondal, S., Chakrabarti, S.K.: MNRAS **447**, 1984 (2015)
27. Fender, R.P., Gallo, E., Russell, D.: MNRAS **406**, 1425 (2010)
28. Garain, S.K., Ghosh, H., Chakrabarti, S.K.: ApJ **758**, 114 (2012)
29. Giri, K., Chakrabarti, S.K.: MNRAS **430**, 2836 (2013)
30. Giri, K., Garain, S.K., Chakrabarti, S.K.: MNRAS **448**, 3221 (2015)
31. Hawley, J.W., Smarr, L.L., Wilson, J.R.: ApJ **277**, 296 (1984)
32. Hazard, C., Mackay, M.B., Shimmins, A.J.: Nature **197**, 1037 (1963)
33. Hoyle, F., Lyttleton, R.A.: PCPS **35**, 405 (1939)
34. Jana, A., Debnath, D., Chakrabarti, S.K., et al.: ApJ **819**, 107 (2016)
35. Kallman, T., White, N.E.: ApJ **341**, 955 (1989)
36. Konigl, A.: ApJ **342**, 208 (1989)
37. Landau, L., Lifshitz, E.M.: Fluid Mechanics. Pergamon Press, New York (1959)
38. Laor, A.: ApJ **376**, 90 (1991)
39. Liang, E.P.T. Thompson, K.A.: ApJ **240**, 271 (1980)
40. Lightman, A.P., White, T.R.: ApJ **335**, 57 (1988)
41. Lu, Ju-Fu., Yuan, F.: MNRAS **295**, 66 (1998)
42. Lynden-Bell, D.: Nature **223**, 690 (1969)
43. McClintock, J.E., Remillard, R.A.: arXiv, 036213 (astro-ph/0306213v4) (2006)
44. Molla, A.A., Debnath, D., Chakrabarti, S.K., et al.: MNRAS **460**, 3163 (2016)
45. Molteni, D., Lanzafame, G., Chakrabarti, S.K.: ApJ **425**, 161 (1994)
46. Molteni, D., Sponholz, H., Chakrabarti, S.K.: ApJ **457**, 805 (1996)
47. Mondal, S., Chakrabarti, S.K.: MNRAS **431**, 2716 (2013)
48. Mondal, S., Chakrabarti, S. K.: (2018, submitted)
49. Mondal, S., Chakrabarti, S.K., Debnath, D.: Ap&SS **353**, 223 (2014)
50. Mondal, S., Debnath, D., Chakrabarti, S.K.: ApJ **786**, 4 (2014)
51. Mondal, S., Chakrabarti, S.K., Debnath, D.: ApJ **798**, 57 (2015)
52. Mondal, S., Chakrabarti, S.K., Debnath, D.: Ap&SS **361**, 309 (2016)
53. Mondal, S., Chakrabarti, S.K., Nagarkoti, S., et al.: ApJ **850**, 47 (2017)
54. Nagarkoti, S., Chakrabarti, S.K.: MNRAS **462**, 850 (2016)
55. Nandi, A., Chakrabarti, S.K., Vadawale, S., et al.: A&A **380**, 245 (2001)

56. Nandi, A., Debnath, D., Mandal, S., et. al.: A&A **542**, 56 (2012)
57. Novikov, I.D., Thorne, K.S.: In: DeWitt, C., DeWitt, B. (eds.) Black Holes. Gordon and Breach, New York (1973)
58. Paczyński, B., Witta, P.J.: A&A **88**, 23 (1980)
59. Penrose, R.: Nuovo Cemento **1**, 252 (1969)
60. Prendergast, K.H., Burbridge, G.R.: ApJ **151**, L83 (1968)
61. Salpeter, E.: ApJ **140**, 796 (1964)
62. Schwarschild, K.: SpaW **50**, 189–196 (1916)
63. Shakura, N.I., Sunyaev, R.A.: A&A **24**, 337 (1973)
64. Singh, C.B., Chakrabarti, S.K.: MNRAS **410**, 2414 (2011)
65. Smith, D.M., Heindl, W.A., Markwardt, C.B., et al.: ApJ **554**, 41 (2001)
66. Sunyaev, R.A., Titarchuk, L.G.: ApJ **86**, 121 (1980)
67. Tomsick, J.A., Kaaret, P., Kroeger, R.A., et al.: ApJ **512**, 892 (2000)
68. Zdziarski, A.A., Lubinski, P., Gilfanov, M., et al.: MNRAS **342**, 355 (2003)

# On the Nature of Outflows from Low Angular Momentum Inflows Around Black Holes




**Chandra Bahadur Singh**

**Abstract** Black holes capture matter from surroundings which form disk-like structures. These so-called accretion disks, under suitable conditions, give rise to jets and outflows which are also important components of black hole system. In recent times it has been reported that beside spin of the black hole, another parameter may be playing crucial role in determining the origin and acceleration of outflows and jets. The strength of centrifugal pressure supported shock wave in case of low angular momentum flow around black holes may be responsible for jets and outflows. The energy dissipation as well as mass loss rate across the shock may happen at the base of the jets and outflows. The outflow properties are determined by these parameters close to the black hole.

## 1 Introduction

Outflows and jets are seen in different types of astrophysical objects like active galactic nuclei (AGN), young stellar objects (YSOs), high mass X-ray binaries (HMXB) and low mass X-ray binaries (LMXB). Usually the accretion disks are related to the production of outflows and jets. A 'boundary layer' is taken as an important ingredient in the formation of outflows and jets [2, 3]. Several astrophysical objects ranging from YSOs to AGN seem to have a boundary layer between the accretion disk and the central object. In case of black hole accretion, subsonic region between sonic location and standing shock called CENtrifugal pressure dominated BOundary Layer or CENBOL can be responsible for the outflows and jets [1].

Using hydrodynamic equations to address conical flows in Newtonian potential, [3] calculated the mass outflow rate as a function of mass inflow rate. In the study, quasi-spherical dense region having size of few tens of Schwarzschild radius around

C. B. Singh (✉)
The Raymond and Beverly Sackler School of Physics and Astronomy, Tel Aviv University, Tel Aviv, Israel

© Springer International Publishing AG, part of Springer Nature 2018

B. Mukhopadhyay, S. Sasmal (eds.), *Exploring the Universe: From Near Space to Extra-Galactic*, Astrophysics and Space Science Proceedings 53,
https://doi.org/10.1007/978-3-319-94607-8_7

a black hole or neutron star was considered. The existence of such region is possible when there is a constant angular momentum flow, quite low compared to Keplerian value, close to the compact object. At the outer boundary of such region, standing shock may or may not form. One interesting property was seen in the study that the mass outflow rate $R_{\dot{m}}$, ratio of mass outflow and inflow rate, was found to depend on property of standing shock i.e., compression ratio $R$ which is the ratio of height integrated density in the post-shock and pre-shock regions.

Subsequently, Das et al. [4] studied the outflow behaviour around black hole by adding angular momentum in the flow and using the Paczynski-Wiita pseudo-Newtonian potential [11]. Such potential mimics the space-time around the non-rotating black hole. In the inner region around the black hole, when the Rankine-Hugoniot condition is satisfied standing shock is formed. It was found that $R_{\dot{m}}$ is comparatively low in case of weak and strong shocks having $R \sim 1$ and $R \sim 4$–$7$ respectively while it is highest possible for shock of intermediate strength when $R \sim 2$–$3$. This happens because in the case of $R \sim 2$–$3$ size of CENBOL and its temperature conspire to enhance the ejection of higher amount of matter. Such property of outflows around black holes is independent of equation of state, adiabatic or isothermal.

Based on the foundation of above mentioned works, I was assigned by Prof. Sandip K. Chakrabarti to extend the semi-analytical studies of origin of outflows taking into account dissipative flows around black holes. In next section, I will briefly describe about the work which was done in the period August 2008–March 2012 as a PhD student.

## 2 Theoretical Predictions

The cartoon diagram showing the accretion-ejection phenomena around black hole is shown in Fig. 1. The flow is likely to undergo loss of energy ($\Delta\mathscr{E}$ energy per unit mass) and matter ($\dot{M}_J$ gram of matter per unit time) at the boundary of CENBOL which happens to be location of standing shock. In the study three types of flow models were considered for axisymmetric flow without viscosity: vertical equilibrium where the gravity is balanced by thermal pressure gradient in vertical direction, conical with wedge shape and constant height. The loss of energy were prescribed accordingly as proportional to (A) temperature difference between the pre-shock and the post-shock regions ($\Delta\mathscr{E} = fn(a_+^2 - a_-^2)$), (B) average of energies in the regions ($\Delta\mathscr{E} = fn\frac{(a_+^2+a_-^2)}{2}$) and (C) thermal energy content of post-shock region ($\Delta\mathscr{E} = fn(a_+^2)$) [16]. The subscripts "$-$" and "$+$" refer to pre-shock and post-shock quantities respectively. $f$ is a fraction which is chosen arbitrarily, while $a$ and $n$ are sound speed and polytropic index respectively.

With increase in $R$ the outflow rate decreases as seen in Fig. 2. This can be explained as: for higher value of $R$, as shock shifts towards the black hole the temperature of post-shock region (in other words, jet base or CENBOL surface)

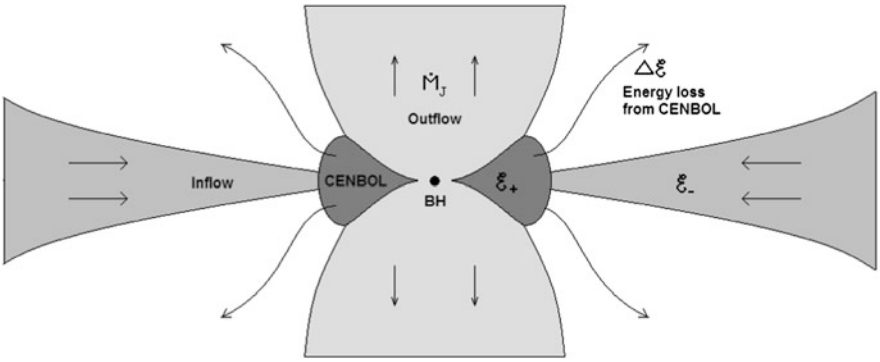



**Fig. 1** A cartoon diagram of the system under consideration. The axi-symmetric accretion flow forms a centrifugal pressure supported boundary layer or CENBOL where the Rankine-Hugoniot condition is satisfied. At the CENBOL, the flow losses an energy of $\Delta\mathscr{E}$ per unit gram and $\dot{M}_J$ matter in the outflow. Figure adopted from [16]

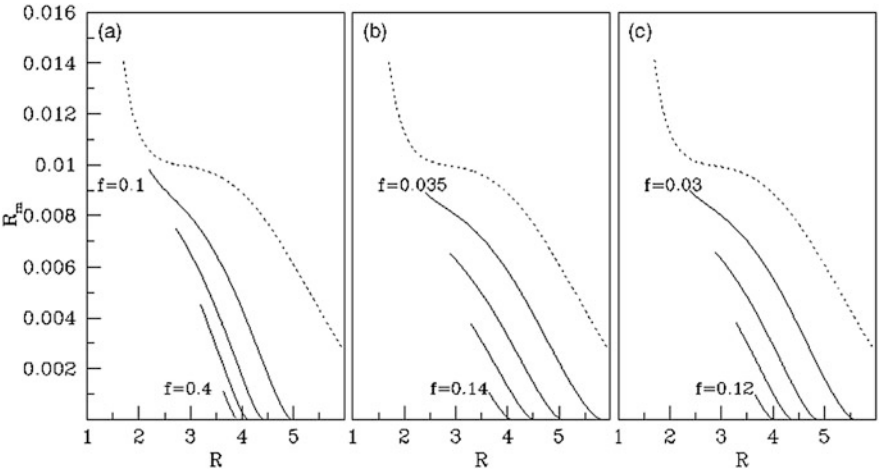



**Fig. 2** Variation of $R_{\dot{m}}$ as a function of compression ratio $R$ for different Models of energy loss in case of vertical equilibrium flow model: (**a**) Model (A): $f$ varies from 0.1 (top curve) to 0.4 (bottom curve) with an interval of 0.1; (**b**) Model (B): $f$ varies from 0.035 (top curve) to 0.14 (bottom curve) with an interval of 0.035; (**c**) Model (C): $f$ varies from 0.03 (top curve) to 0.12 (bottom curve) with an interval of 0.03. The dashed curve in all the cases represents the outflow rates without any energy dissipation. Note that the outflow rate goes down when the compression ratio increases. Below a certain compression ratio, depending on the energy loss, no self-consistent solution exists. Also, the higher the fractional loss is, the lower is the outflow rate, as the post-shock flow losses thermal drive. Figure adopted from [16]

rises but its area shrinks rapidly at the same time. No self-consistent solution was found below a certain value of $R$ [16] unlike the non-dissipative solution where such solution exists [3]. This may correspond to the physical scenario where CENBOL can no longer lose matter and energy when the shock strength is quite weak. The

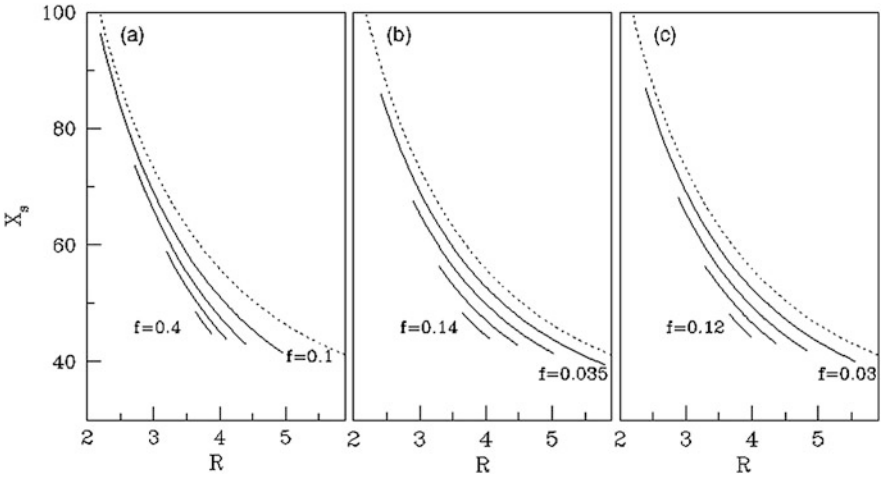



**Fig. 3** (**a**–**c**) Shock location $X_s$ as a function of compression ratio $R$ in all the three models as in Fig. 2a–c. The dashed curve represents the shock locations without any energy dissipation. Figure adopted from [16]

support for theoretical predictions come from the observational evidences that hot Compton clouds capable of driving outflows and jets are not available in soft spectral states [7] and references therein.

As the shock starts moving towards the black hole, the outflow rate goes down. This happens because the post-shock region is same as the base of outflow. In case of higher fractional dissipation $f$, the shock forms at comparatively larger distance from the black hole for a given value of $R_{\dot{m}}$. The accretion flow having higher value of specific energy show tendency of higher amount of mass outflow. Although flows with lower energy can lose higher fraction of energy, the outflow rates are comparatively smaller [16].

Figure 3 shows that the post shock region shrinks in size as there is increase in energy loss. This is caused by the fact that the CENBOL region gets cooler as the energy loss happens. So the shock has to adjust itself such that the Rankine-Hugoniot condition is satisfied. However the Rankine–Hugoniot condition cannot be fulfilled and stable shock cannot form at all beyond a certain limit of energy loss from the system [16].

The model governing the flow geometry decides the amount of mass outflow rate from the post-shock region [15]. In case of vertical equilibrium and conical flow models, on increasing the cooling rate the parameter space of specific energy and specific angular momentum shrinks in size. However the parameter space increases with increase in cooling up to a certain limit in case of constant height model then on further increase in cooling the parameter space starts to shrink as well [17]. The generic property of flow seems to be the parameter space can completely disappear beyond a certain limit of cooling. This also supports the observational signature that no significant outflow can be expected from the spectrally soft states. In presence

of energy and mass loss, the transonic properties of inflows and outflows are model dependent.

Fluid composition of flow can play an important role in determining the outflow properties. An equation of state can be formulated which can truly represent the flow properties around black holes: thermally relativistic in the inner region near black hole while non-relativistic at large distance from the black hole. The flow containing only electron-positron pairs can never form a standing shock while presence of some amount of baryons can facilitate the formation of the standing shock. This indicates that the protons are necessary for the system to show some outflow behaviour. In case of flow containing proton number density as 27% of the electron number density, $R_{\dot{m}}$ achieves the highest possible value. So it can be speculated that jet with electron-positron pair only may not form at all [10].

## 3 Observational Signatures

Theoretically predicted outflow behaviours can be compared with observational signatures. For various observational constraints it is not easy to compute both the inflow and out flow rates from the observations. The luminosity of the disk obtained by fitting the spectrum often gives an estimate of the disk rate. The rate (at least the lower limit) of the jet may also be obtained from the amount of energy released. Below we present an example of the stellar mass black hole candidate and an example from the super massive black hole to show that the rates computed by us falls in the right range. Conversely, if one knows one of the rates, it is possible to estimate the other rate using our calculation of $R_{\dot{m}}$.

Though SS433 is not confirmed to be a black hole, it is one of the very few cases where the ejection and propagation of jets from supercritical accretion disk could be studied clearly. The jets of SS433 excite the radio nebulae W50. In SS433, narrow jets of gas propagate from the inner regions of the disk perpendicular to the disk plane. The donor star fills its critical Roche lobe and provides a powerful and almost continuous flow of gas at a rate of $\simeq 10^{-4}$ solar mass/year [14, 18]. The mass loss rate in SS433 jets has been estimated to be $\simeq 5 \times 10^{-7}$ solar mass/year [6, 9] based on observations. The mass outflow rate $R_{\dot{m}}$ appears to be $\simeq 0.005$, which lies in the range of the value obtained by our theoretical calculation which is at most $\simeq 0.013$. The base of the jet is estimated to be $\simeq 100$ Schwarzschild radii [5] which is in agreement with the size of the CENBOL acting as base of jet in our model. Thus the observational results appear to be supporting our theoretical estimates regarding the mass outflow rate and size of the base of the jet in case of stellar mass black holes like SS433.

In case of systems containing supermassive black holes like M87, it has been found that the mass accretion rate appears to be $\simeq 1.34 \times 10^{-1}$ solar mass/year [12] and the rate of energy release through jets is $\simeq 10^{43}$ erg/s [13] so the mass outflow rate $R_{\dot{m}}$ turns out to be $\simeq 0.0033$, which also lies in the range of the value obtained by our theoretical results. The base of the jet in case of M87 has been found to be

within 100 Schwarzschild radii [8]. It can be concluded that our theoretical results agree well with the observational results of systems containing stellar mass as well as supermassive black holes. The results also confirm that the base of the jet should correspond to the size of CENBOL region.

## 4 Numerical Studies

The works included in previous section are semi-analytical which focussed on accretion-ejection model. Further in recent time, we performed special relativistic simulation of hydrodynamical accretion flow around black hole in order to extend our results for the case of rotating black holes. Two typical values of specific angular momentum of accreting matter were considered: one which forms standing shock and other which does not form in case of non-rotating black hole as predicted by theoretical solutions.

In case of low value of specific angular momentum of accretion flow, with slight increase of black hole spin $a$ like from 0 to 0.25 in prograde sense the shock location is pushed away from the black hole and bigger post shock region is formed which leads to outflow rate as 50% of inflow rate, while in case of $a = 0$ it is only 10%. On further increase of $a$ like 0.5 and 0.75, the shock leaves the domain and negligible amount of matter is able to escape as outflow. On the other hand in case of retrograde $-0.5$, the shock is formed closer to the black hole compared to non-rotating case, relatively smaller amount of matter leaves the domain and the outflow rate is only 4% of the inflow rate.

In case of quite lower value of specific angular momentum of accretion flow, no axisymmetric standing shock is supposed to form based on theoretical solutions and the flow behaves as expected however an oblique shock forms quite close to black hole causing small outflow rates from the post-shock region. It continues to behave in the similar manner unless black hole spin $a$ is increased to 0.5. For $a = 0.5$ and 0.75, axisymmetric shocks are formed with increased location and outflow rates as $a$ is increased. The retrograde case with $a = 0.5$ shows similar results as that of non-rotating black hole case.

In all cases of accretion flow studied with different $a$, the outflows are quite sub-relativistic and at most reaches few % of speed of light driven by thermal pressure gradient. It is also seen that formation of standing shock leads to ejection of larger amount of mass compared to the case where no formation of standing shock takes place so it is astrophysically relevant in case of advective flow close to black hole (Singh, Vaidya, and Okuda, in preparation). The value of $R_{\dot{m}}$ remains in the range of 0.01–0.1 as expected and the post shock region size is in the order of some tens of black hole horizon radius.

Furthermore, we added magnetic field and could see formation of outflows with two-components, extra component arises in funnel wall region most likely driven by magnetic pressure gradient. In such scenario, there is also sub-relativistic outflows outside the funnel wall. The relativistic outflows reach even 40% of speed of light inside the funnel wall and may continue to accelerate.

## 5 Outlook

Based on the above mentioned results from theoretical, observational and numerical studies, there is certain level of confidence that the physical picture presented here can help us understand the properties of inflows and outflows in case of stellar mass and supermassive black holes. Future works need to include additional physics for theoretical studies and larger computational domain in case of numerical studies.

## References

1. Chakrabarti, S.K.: Astrophys. J. **347**, 365 (1989)
2. Chakrabarti, S.K.: Indian J. Phys. **72(B)**, 183 (1998)
3. Chakrabarti, S.K.: Astron. Astrophys. **351**, 185 (1999)
4. Das, S., Chattopadhyay, I., Nandi, A., Chakrabarti, S.K.: Astron. Astrophys. **379**, 683 (2001)
5. Fabrika, S.: Astrophys. Space Phys. Rev. **12**, 1 (2004)
6. Fabrika, S.N., Borisov, N.V.: Sov. Astron. Lett. **13**, 279 (1987)
7. Fender, R.P., Gallo, E., Russell, D.: Mon. Not. R. Astron. Soc. **406**, 1425 (2010)
8. Junor, W., Biretta, J.A., Livio, M.: Nature **401**, 891 (1999)
9. Königl, A.: Mon. Not. R. Astron. Soc. **205**, 471 (1983)
10. Kumar, R., Singh, C.B., Chattopadhyay, I., Chakrabarti, S.K.: Mon. Not. R. Astron. Soc. **436**, 2864 (2013)
11. Paczyński, B., Witta, P.: Astron. Astrophys. **88**, 23 (1980)
12. Reynolds, C.S., DiMatteo, T., Fabian, A.C., Hwang, U., Canizares, C.R.: Mon. Not. R. Astron. Soc. **283**, L111 (1996)
13. Reynolds, C.S., Fabian, A.C., Celotti, A., Rees, M.J.: Mon. Not. R. Astron. Soc. **283**, 873 (1996)
14. Shklovskii, I.S.: Sov. Astron. **25**, 315 (1981)
15. Singh, C.B., Chakrabarti, S.K.: Int. J. Mod. Phys. D **20**, 2507 (2011)
16. Singh, C.B., Chakrabarti, S.K.: Mon. Not. R. Astron. Soc. **410**, 2414 (2011)
17. Singh, C.B., Chakrabarti, S.K.: Mon. Not. R. Astron. Soc. **421**, 1666 (2012)
18. van den Heuvel, E.P.J.: Vistas Astron. **25**, 95 (1981)

# Generalized Flows Around Neutron Stars




**Ayan Bhattacharjee**

**Abstract** In this chapter, we present a brief and non-exhaustive review of the developments of theoretical models for accretion flows around neutron stars. A somewhat chronological summary of crucial observations and modelling of timing and spectral properties are given in Sects. 2 and 3. In Sect. 4, we argue why and how the Two-Component Advective Flow (TCAF) solution can be applied to the cases of neutron stars when suitable modifications are made for the NSs. We showcase some of our findings from Monte Carlo and Smoothed Particle Hydrodynamic simulations which further strengthens the points raised in Sect. 4. In summary, we remark on the possibility of future works using TCAF for both weakly magnetic and magnetic Neutron Stars.

## 1 Introduction

In this chapter, we present a brief and non-exhaustive review of the developments of theoretical models for accretion flows around neutron stars (NSs). A somewhat chronological evolution of crucial observations and modelling of timing and spectral properties are given in Sects. 2 and 3, respectively. In Sect. 4, we discuss the prospect of the Two-Component Advective Flow (TCAF) solution given by Chakrabarti and Titarchuk in [19] (hereafter, CT95), around NSs, with certain modifications required for NS. In Sect. 5, we highlight some of our findings from Monte-Carlo simulation of spectra of an accreting NS ([4], hereafter BC17). In Sect. 6, we discuss the recent results from Smoothed Particle Hydrodynamics simulations in presence of cooling where we studied the time evolution of accretion around NSs. Finally, we summarise the key results to argue that the generalized flows around NSs, are likely to be some form of TCAF.

A. Bhattacharjee (✉)
S. N. Bose National Centre for Basic Sciences, Salt Lake, Kolkata, India
e-mail: ayan12@bose.res.in

© Springer International Publishing AG, part of Springer Nature 2018

B. Mukhopadhyay, S. Sasmal (eds.), *Exploring the Universe: From Near Space to Extra-Galactic*, Astrophysics and Space Science Proceedings 53,
https://doi.org/10.1007/978-3-319-94607-8_8

The modelling of accreting neutron stars were largely prompted by significant observational findings in the last 50 years. Although many of the models are of great phenomenological importance, it is impossible to cover all of those and their modified versions, in this text. We take a separate approach to address the evolution of such theories: we point to the observational evidence that either proved the validity of a theory, prompted a modification or refuted a theory in light of new results. This approach lets us to touch upon the relevant models as well as compare them in terms of predictions of observational results.

## 2 Evolution of Theories: Timing Properties

The temporal variations of accreting NSs (both magnetic and weakly-magnetic) are reflected in the Power Density Spectra (PDS) of the lightcurves at different energies. The presence and evolution of Quasi-Periodic Oscillations (QPOs) reveal significant details about both the hydrodynamic and radiative transfer processes. In order to discuss the chronological developments in timing studies, we briefly define (Wang [80]) different classes of QPOs and their observed properties.

- **Low-Frequency QPOs (LFQPO):** Low-frequency QPOs are observed in the range of 5–60 Hz, with Quality Factor $Q \geq 2$, and amplitudes of 1–10%. The Horizontal-, Normal-, and Flaring Branch Oscillations all lie in this domain and are respectively abbreviated as HBO, NBO and FBO.
- **hecto-Hz QPOs (hHz QPO):** The hecto-hertz (hHz) QPO is usually a peaked noise. If the peak is coherent enough to have a quality factor $Q > 2$, it is classified as a QPO. The frequency $\nu_{hHz}$ is seen in the range of 100–200 Hz. It has rms amplitude between 2% and 20%.
- **Kilo Hz QPOs (kHz QPO):** These are defined as the QPOs in the range $200\,\text{Hz} < \nu_{kHz} < 1300\,\text{Hz}$.

The first detailed study of a magnetic neutron star, with almost radial accretion, was carried out by Elsner and Lamb [25]. They studied the formation of magnetosphere, its scale and structure, the stability of its boundary and the plasma flow into the magnetosphere and Alfven surface. Ghosh et al. [31] studied the spin-up and spin-down mechanism of the star due to this. Ghosh and Lamb [29, 30] focused on the radial and vertical structures of the transition region and the changing of period of the pulsating stars. Van der Klis et al. [77] studied the power density spectra of the source GX 5-1, and found intensity dependence of the centroid frequency, width and power of the observed QPOs (20 and 40 Hz) and low-frequency noises ($< 15$ Hz). Lamb et al. [40] found QPOs in 5–50 Hz range for Sco X-1. They proposed that a clumpy disc, while interacting with a weak magnetosphere,

produced the modulation in accretion rate and oscillations in X-ray flux. Priedhorsky et al. [56] found a bimodal behavior in the response of QPO frequency with intensity. The 6 Hz QPO, in quiescent state, was anti-correlated with intensity. The QPO in the active state, however, was correlated with intensity and varied from 10–20 Hz. Two modes of spectral behaviors were also identified for Sco X-1. Paczynski [54] suggested the luminosity variations of the boundary might be a result of a unsteady flow with low viscosity. Van der Klis et al. [78] studied the atoll source 4U 1636-53. Correlation between spectral shape, fast variability, burst duration and temperature with accretion rate $\dot{M}$ hinted that the source state is determined by the accretion rate $\dot{M}$. The persistent intensity varied independent of other characteristics, indicating that intensity was not probably a good measure of accretion rate. Strohmayer et al. [68] studied the burst and quiescent states of the LMXB 4U 1728-34 to find pulsations of 363 Hz and twin QPOs, respectively. The twin kHz QPOs varied between 650–1100 Hz, with count rate till reaching a maximum, while maintaining a constant separation of 363 Hz. The magnetospheric beat frequency model was used to explain the X-ray variability. Van der Klis et al. [79] found the twin kHz QPO frequency separation is not constant, rather varied from 310 to 230 Hz, for Sco X-1. It was concluded that any beat frequency model or photon bubble model was unlikely to explain the origin of these peaks. Authors also found HBOs near 45 and 90 Hz, both of which increased with accretion rate. In Méndez et al. [44], the energy dependent study of twin kHz QPO and band limited noise revealed different behaviors, suggesting the two processes are generated at two different radii. It was remarked that the kHz QPOs were due to oscillations of the boundary layer, very close to the surface and the broad noise was generated from near the inner edge of a disc. It was also mentioned that QPO frequency and the noise cut-off frequencies tracked $\dot{M}$ better than the count rate. Wijnands et al. [83] found the coexistence of HBOs and kHz QPOs for GX 17+2. This suggested that the magnetospheric beat frequency model could not address both the phenomena simultaneously. The rms and FWHM of the upper kHz QPO varied with the change in frequency, whereas the similar quantities remained almost constant for lower kHz QPO with the change of frequency. Wijnands et al. [84] found both kHz QPOs and HBOs for the Z-source Cyg X-2. Jonker et al. [38] showed that the twin kHz QPO frequencies moved to higher values with the increase of accretion rate for the Z-source GX 340+0. However, the rms and FWHM of lower QPO remained consistently constant, whereas the ones corresponding to upper kHz QPO decreased. Simultaneous HBO was also detected along with its second harmonic between 20 to 50 Hz and 38 and 69 Hz. It was also concluded from the study of FWHM of HBOs with states, that something other than $\dot{M}$ determined the timing properties. Wijnands et al. [84] found very similar results for the object GX 5-1, where simultaneous kHz QPOs and HBOs were observed.

In [73], hereafter TLM98 a super-Keplerian transition layer (TL) was invoked to explain the kHz QPOs (a detailed discussion to be followed in the next section). Méndez et al. [45] showed that the LMXB 4U 1608-522 had twin kHz QPOs and the frequency separation is not constant with the change of centroid frequencies, contradicting a simple beat-frequency interpretation. The authors compared differ-

ent models for the accretion onto this atoll source having 10% average luminosity of Sco X-1, a Z-source showing similar features, and concluded that the photon-bubble model, the transition layer model nor any modified beat frequency model were able to explain the phenomena. Méndez and van der Klis [43] found simultaneous existence of burst oscillations and twin kHz QPOs for the source 4U 1728-34. The frequency separation always remained smaller than the burst frequency, for varying accretion rates. For the same object, Titarchuk and Osherovich [72] used the transition layer model to identify the low-Lorentzian frequency to be due to radial oscillation in viscous time-scale and the break frequency to be associated with radial diffusion time-scale. Psaltis et al. [57] studied many non-pulsating NSs and black holes (BHs) of varying luminosities and source types. A correlation between (1) the NS: kHz QPOs and HBOs, (2) BH: QPOs and noises, of same type but varying three orders of magnitude in frequency and coherence was found. This suggested that the variations are systematic and related by similar processes in the two types of sources, further constraining the theoretical models of these phenomena. Titarchuk et al. [74] added the effects of coriolis forces and interaction of magentosphere with flow to explain the different modes of QPOs observed for 4U 1728-34. Dieters et al. [23] remarked that the position on the Z-track or the spectral state was not the only parameter that governs the behavior of Sco X-1. Jonker et al. [39] discovered a new broad component in the PDS of GX 340+0 between 9 to 14 Hz. Yu et al. [86] studied the source Sco X-1 and found that the upper kHz QPO frequency and the ratio of lower to upper kHz QPO amplitude was anti-correlated with the count rate that varied in the NBO timescale (6–8 Hz). This suggested that some of the NBO flux was generated from inside the inner disk radius and the radiative stress modulated the NBO frequency. Muno et al. [50] did a longterm study of a total of 13 Z and atoll sources to remark that the atoll sources trace out the color-color diagram over a larger range of luminosity, on a much longer timescale and have a harder spectra when they are faint as compared to the Z-sources. But, both types trace out similar three branched color-color patterns, suggesting a similarity, which was previously not recorded because of incomplete sampling.

Belloni et al. [8] conducted a detailed analysis of PDS of multiple BHCs and NSs, by decomposing the PDS onto four primary Lorentzians. They showed that this not only provides a better statistics, but also yields a better phenomenology which tracked the evolution of different QPO frequencies with spectral states. It was found that a one-on-one correspondence can be found between different QPOs in NSs and BHs, which obey similar correlations. This suggested that, apart from the mass dependence of the dynamical timescale, the physical processes governing the phenomena could be the same and the high-frequency components might not require the NS surface as black holes also show similar features with weaker amplitude. Mauche [41] drew a similar conclusion by studying the correlations between two QPOs in BHCs, NSs and White Dwarfs (WDs) which showed that the correlated nature can be extended another two orders of magnitude with WDs. The author discussed several models in light of the observed QPOs and dwarf-nova oscillations (DNOs). All models that relied on the presence of strong magnetic fields or a stellar surface to explain the high frequency oscillations were ruled out. The only one

which produced the observed frequencies was the TL model where Keplerian orbital frequencies are suggested as the origin of QPOs.

Wijnands et al. [85] studied multiple accreting neutron stars which had burst oscillations. It was found that any simple beat frequency model or any model which relied on general relativistic effects very close to the rotating star is unlikely to explain the phenomena. The authors stated that the QPOs can be understood in terms of resonances at privileged radii in an accretion disc, but pointed towards general relativistic epicyclic motions to be the cause of such resonance. Barret et al. [3] studied the Q factor and coherence time variation of both the kHz QPOs to reveal that the Q factor follow different pattern in the two. From their analysis of the LMXB 4U 1608-52, that any model involving clumps orbiting within or above the accretion disk were ruled out, and disc/shock oscillations were suggested as the more likely mechanism. Belloni et al. [9] showed that the ratio of upper and lower kHz QPO frequencies was found to be 3/2 only because of a biased sampling. A simple resonance model of a Keplerian disc, thus, is unlikely to address the kHz QPOs. Cassella et al. [11] studied the continuous transition from FBO to NBO in $\sim$100 s timescale, for Sco X-1. From the one-to-one correspondence between the LFQPOs in BHs and NSs, it was inferred that the physical mechanisms that determine these oscillations, which are present in both, are in favor of a disk origin of oscillation and rules out models involving interaction with the surface or magnetosphere.

Méndez [42] studied, for multiple NSs, the maximum Q factor and rms power associated with upper and lower kHz QPOs. For the lower one, $Q_{max}$ increased at first and decreased exponentially with increasing luminosity. For the upper one, the Q value remained almost independent of luminosity of the sources. The author suggested that one possible mechanism of generation of kHz QPOs would be that the mass accretion rate sets the size of the inner radius of the disk which determines the QPO frequency as well as the relative contribution of the high-energy part of the spectrum to the total luminosity. Boutloukos et al. [10] also pointed towards high radial accretion instead of a Keplerian disc, to explain the relatively lower value of kHz QPO frequencies found in the source Cir X-1. Wang et al. [81] studied the energy dependence of the low-frequency NBOs for Sco X-1. They concluded that in near Eddington luminosities, the oscillations in the TL, the region between inner edge of disk and neutron star, might be responsible for the NBOs. It was noted that the centroid frequency varried non-monotonically with energy indicating a radial oscillation.

## 3 Evolution of Theories: Spectral Properties

The understanding and modelling of spectral properties of NSs was mainly dictated by the advent of new satellites with finer energy resolution and broader range. As background subtraction methods improved, more and more intrinsic features came

into prominence from a spectral data. For a detailed discussion on the evolution of spectral modelling, see BC17. We summarise the key points below.

The soft state spectra of NSs was explained with the presence of a blackbody emission from the boundary layer of a neutron star [46]. The harder states had a power-law tail in the energy spectrum. It was evident that it originated from Compton scattering process [47, 82]. The two models differed in terms of the origin of seed photons and their temperature. The former assumed a cooler boundary layer along with Comptonized photons from a hotter disk. The latter assumed a hotter boundary layer, compared to the disk, whose seed photons were Comptonized. Sunyaev and his collaborators [34, 37, 55] assume that the flow forms a Keplerian disk and reaches all the way to the NS surface. This disk is connected with the boundary layer where the thickness increases due to higher temperature. An arbitrarily placed Compton cloud near the star was assumed to be responsible for the hardening of the boundary layer emission [34]. Most of these studies addressed the soft state spectra of neutron stars. Another problem was faced while addressing the state transition of neutron stars in LMXBs. The fact that disk accretion rate was not the single factor that controlled the size or temperature of the Compton cloud, used to model the hard state spectra, lead to the conclusion that some unknown parameter, related to the truncation radius of the disc, is responsible for the hard X-ray tail [1, 2, 22]. Paizis et al. [53] found a systematic positive correlation between the X-ray hard tail and the radio luminosity, suggesting that the Compton cloud might serve as the base of radio jets (which was proposed for black holes by Chakrabarti and his group. See [16] and references therein for a review). A TL or Compton cloud has been placed between the Keplerian disk and the boundary layer in recent phenomenological studies ([27, 76], hereafter TSS14). Chakrabarti has argued in the past [13, 14, 18] that in black hole accretion, the flow passes through the inner sonic point ensuring that the flow becomes sub-Keplerian just outside the horizon. In the case of NSs, even if the flow became Keplerian, the velocity must slow down to match with the sub-Keplerian velocity at the surface [13, 14, 18]. Numerical simulations [17] clearly showed that transition from a Keplerian disk to a sub-Keplerian disk is mediated by a super-Keplerian region.

To generate and understand the emergent spectra from (inverse-) Comptonization processes, which are highly non-local, usage of Monte-Carlo simulations were essential. Seon et al. [64] used toy models of spherical Compton clouds of constant temperature and optical depth, surrounding a weakly magnetic neutron star to generate hard X-ray tails. The accretion column geometry, for neutron stars with strong magnetic fields ($B \sim 10^{10-12}$ Gauss), was successfully used as background of Monte Carlo simulation to explain the spectral properties in certain cases [51, 52]. These studies provide some answers in terms of spectral fitting. However, these were based on phenomenological models which used arbitrarily placed Compton clouds. Many cartoon models were inspired in the community of black holes and neutron stars by the transonic flow solution of CT95 which have been used for the explanation of both spectral properties and the for the explanation of QPOs.

The COMPTT and COMPTB models, used successfully for spectral analysis of accreting NSs, used an extended TL. Many NS LMXBs are studied using the

COMPTB framework, such as 4U 1728-34 [59], GX 3+1 [60], GX 339+0 [61], 4U 1820-30 [75], Scorpius X-1 (TSS14), 4U 1705-44 [62] etc. The HMXB 4U 1700-37 has also been examined, recently, using the same model [63]. This model, in general, required two COMPTB components. The one corresponding to a cloud closer to the Keplerian disk typically had higher temperature and the one closer to the star had relatively lower temperature (works cited above). The one corresponding to Comptonization of NS surface photons, showed a saturation in COMPTB model's spectral index [26]. This index is, however, different from the spectral index found by fitting the power-law portion of the spectrum, which can have continuous range of values depending on the halo and disk accretion rates (BC17).

## 4 Two-Component Advective Flows Around Neutron Stars

For a more involved review of TCAF around NSs, refer to [16]. We summarise the points raised in this regard from BC17. A standard Keplerian disk alone was unable to explain the spectral and timing properties of a black hole (20, 36, 69–71, 87, CT95; 15). There are mainly two components of a spectrum: a thermal component resembling of a multi-colour blackbody radiation [65], and another component, which is similar to a power-law, produced by inverse Comptonization of the thermal or non-thermal electrons [70, 71]. There are many models that deal with the production of a Compton cloud that generates the power-law. In many cases, the possible scenarios required excessive fine-tuning of accreting matter and are not physical or not self-consistent (for a review, see [16]). However, the transonic flow solution based TCAF is a unique self-consistent solution. It addresses all the aspects of spectral and temporal properties at the same time. The low viscosity advection component produces a centrifugal barrier supported boundary layer or CENBOL very close to a compact object, in this scenario. A shock transition occurs at the boundary of CENBOL. This shock surface may be stationary, oscillating or propagatory [16]. The post-shock region acts as a natural reservoir of hot electrons. The flow component near the equatorial plane, with higher viscosity, becomes a Keplerian disk [35]. This disk emits a multi-colour blackbody radiation which are intercepted and re-radiated by the CENBOL to create the power-law-like component [28]. This component normally has an exponential cut-off where recoil becomes important.

The shock can oscillate due to resonance ([48], hereafter MSC96) or non-satisfaction of Rankine-Hugoniot condition [58]. The variation in the size of the CENBOL results in modulation of hard X-ray intensity. It manifests as the low-frequency quasi-Periodic oscillations (LFQPOs). The CENBOL also acts as the source of outflows and jets. When the CENBOL is cooled down due to excessive soft photons, the jet also disappears. There are clear observational evidence of two-component advective flows in several black hole candidates [7, 21, 24, 49, 66, 67].

The independently obtained advective flow 'TCAF' naturally explains the phenomenological Compton cloud without any drastic modification of the earlier

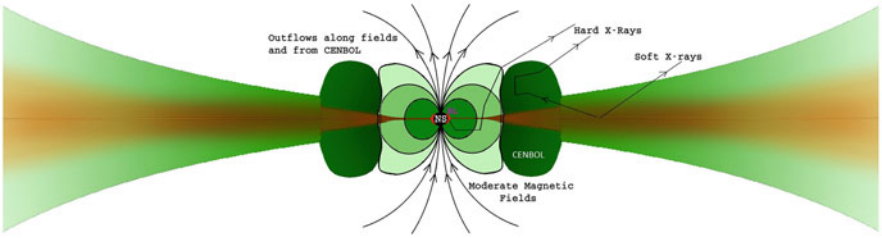



**Fig. 1** A schematic diagram of accretion dynamics and radiation processes in a Two Component Advective Flow solution with a centrifugal barrier supported shock front close to a neutron star with moderate magnetic field. The original artwork ([16], Fig. 2) has been reused here with the permission from the author, SKC. The Normal Boundary Layer (NBOL) on the star surface (BL, in the figure) as a result of a shock, and a secondary Compton cloud in the magnetosphere apart from the possible presence of CENBOL make the spectra complex [16]

models. The flow at the outer edge of the disk has little knowledge of the nature of the compact source, except near the innermost boundary. When the magnetic field is weak ($<10^8$ Gauss), one does not expect a vastly different flow configuration between the two cases. The advective matter almost freely falls under gravity till it hits the surface of the star. In reality, there are two such layers simultaneously present in a neutron star accretion (see Fig. 1): One is similar to the normal boundary layer (NBOL), and the other is similar to the CENBOL in a black hole accretion (CT95). In a black hole accretion, only CENBOL is present. In the next segment, we point out some of the major similarities between the flow configuration demanded by observation and the TCAF scenario. The following points strengthen the conclusion of [18] that the boundary condition of the gravitating object (BH or NS) modifies the solutions of the transonic flows only in the last few Schwarzschild radii.

### *4.1 Prospect of TCAF as the Generalized Flow Around NS*

We list some properties of a 'generalized' flow around NS which are present in the TCAF:

- $\nu_{LF}$ bimodal behaviour: Two separate accretion rates control the intensity. One reduces the oscillation radius, another increases it.
- Correlated QPOs seen in BHs, NSs and WDs: The generalized model should not require the presence of a stellar surface or magnetosphere.
- Similar $\nu_{kHz}$ in sources of varying intensity: QPOs are controlled by more than one accretion rates.

(continued)

- Long coherence time of kHz QPOs: Clumpy disk models with azimuthal asymmetry to generate QPOs in Keplerian orbital time-scale are unlikely. Radial and vertical oscillation would be preferred.
- A 'mass' accretion rate which controls both the inner edge of the disk that generates kHz QPOs also decides the relative contribution to high energy part of the spectrum.
- The Compton cloud acts as the base of the jet.
- The state transition was not controlled by a single accretion rate.
- Low $\nu_{kHz}$ in some NSs: Radial accretion (advective flow) is preferred over a Keplerian disc.

## 5 Spectral Modelling

We explored the spectral properties of TCAF around an NS in BC17 which we discuss below. We had computed the effects of thermal Comptonization of soft photons emitted from a Keplerian disk and the boundary layer of the NS by the post-shock region of a sub-Keplerian flow [12, 32], formed due to the centrifugal barrier. In the simulations, the shock location $X_s$ was also the inner edge of the Keplerian disc. A series of realistic spectra were computed after taking care of the photoelectric absorption by the interstellar medium. We assigned a set of electron temperatures of the post-shock region $T_{CE}$, the temperature of the normal boundary layer (NBOL) $T_{NS}$ of the neutron star and the shock location $X_s$. These parameters depend on the cooling due to intercepted soft photons by the CENBOL region and thus controlled by the flux (or temperature) of the two black body emitting regions: NBOL and the disk. The disk and halo accretion rates ($\dot{m}_d$ and $\dot{m}_h$, respectively) controlled the resultant spectra. The computed spectra were similar to those of weakly magnetic neutron stars in hard states (Fig. 2, left panel). We also studied the case of cooling of the CENBOL when $T_{CE}$ value is high (250 keV) and it is shown in Fig. 2 (right panel).

**Key Findings (BC17):**

1. The spectrum became harder when $\dot{m}_h$ was increased.
2. We showed the evidence of spectral hardening as the inclination angle of the disk is increased.
3. The absorption due to ISM was used to convolve the computed spectrum, in 0.1–250 keV range. We found the spectra to be very similar to realistic hard-state spectra of accreting neutron stars (see Fig. 2).

(continued)

4. An increase in accretion rates cools the CENBOL down. It also creates an outward shift of the hottest region. A cooler cloud near NBOL and a hotter cloud near the disc, having equal optical depth $\tau_0/2$ (see Fig. 2), is created.

## 6 Hydrodynamics

We have used the Smoothed Particle Hydrodynamics (SPH) method (MSC96) to simulate the behavior of inviscid flow accreting on an NS. During the hard spectral state, the incoming flow has a negligible viscosity, leading to the absence of any disk blackbody emission. In such a state, the flow can be assumed to be purely inviscid for the computational purpose. We have shown that for a purely inviscid advective

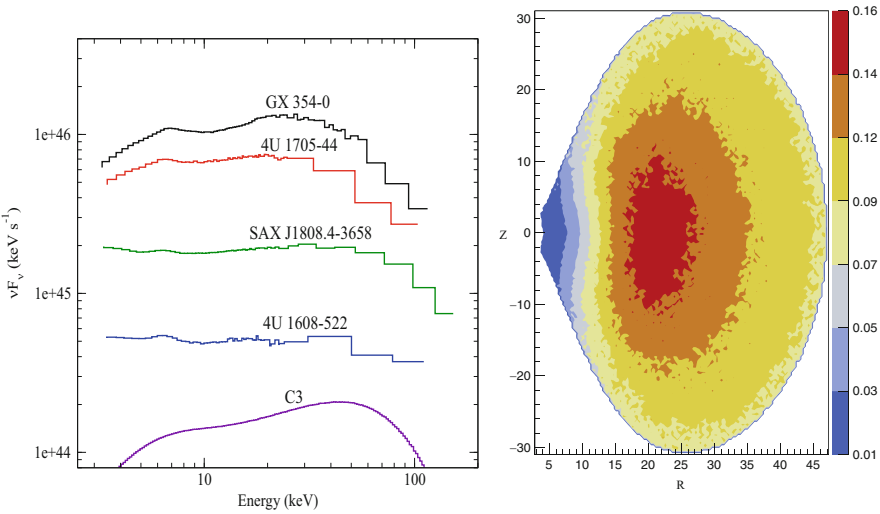



**Fig. 2** Left panel: The spectra of a few weakly magnetized neutron stars. For comparison, we put the spectrum of Case C3 ($\dot{m}_d = 0.1$, $\dot{m}_h = 0.5$, $X_s = 46.8\, r_S$, $T_{CE} = 25.0\,\text{keV}$) of our simulation. The simulations generally reproduced the hard state spectral features. These plotted spectra of different objects were obtained by RXTE observations and are adapted from [33]. Right panel: The temperature (in dimensionless unit ($kT_e/mc^2$)) contours after Compton cooling, from the simulation (for initial $T_{CE} = 250.0\,\text{keV}$, $X_s = 46.8\, r_S$, $\dot{m}_h = 0.5$). We observed that with the increase of $\dot{m}_h$, the temperature of CENBOL closer to NBOL, $T_e(\tau_0/2)^{NS}$ decreased. Here $\tau_0$ is the total optical depth of CENBOL calculated along the equatorial plane. The temperature of CENBOL closer to disc, $T_e(\tau_0/2)^{KD}$, also decreased, but remained greater than the corresponding $T_e(\tau_0/2)^{NS}$. The modified contours show the effective region of Compton scattering changes due to higher temperature of CENBOL. The contour in red shows the most effective region for Compton scattering and it is similar to the proposed geometry of TSS14 (adopted from BC17) (Color figure online)

flow having angular momentum, the solution allows two shocks in the flow. The outer one, forms due to strong centrifugal barrier (CENBOL), which is a common feature for both neutron stars and black holes. The inner shock (NBOL) forms very close to the surface of a neutron star, due to the presence of the hard physical boundary. The oscillations in TCAF solution can be of different types depending on the competing forces in play. We have found that an advective flow in presence of cooling can generate many modes of such oscillations in 2D and the numerical values tend to agree with observational results (see Figs. 3, 4). It is to be noted that the infall time scale from CT95 (and subsequent work in the TCAF paradigm) has the same $r^{3/2}$ dependence with the radial distance $r$ and differ from Keplerian orbital time scale by a factor of $R_{comp}/2\pi$, where $R_{comp}$ is the shock strength. This suggests that the TCAF scenario, in principle, would produce the same numerical values of frequencies for all such sources, even when the viscosity is low to form a TL and flow is not-Keplerian to begin with. The pre-shock and post-shock regions of NBOL are orders of magnitude denser than CENBOLs near its outer edge and contribute to oscillations. In the TCAF scenario, the presence of NS surface aids the shock formation but a similar oscillatory features near the compact object are seen in BHs as well since an artificial surface is produced due to the centrifugal barrier.

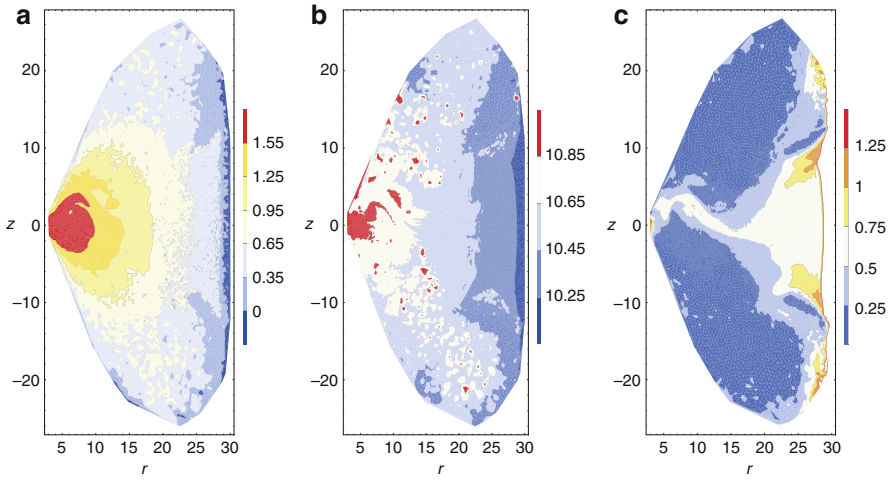



**Fig. 3** The density (log scale) in (**a**), temperature (log scale) in (**b**) and Mach number contours in (**c**) for accreting inviscid flow when specific angular momentum $\lambda = 1.8$, at $t = 0.269$ s (adopted from [6], hereafter BC18). Notice that the Mach number contours near the edge of the star are supersonic and no subsonic contours are plotted. This is due to the fact that in the plotted case, the shock surface was very close to the boundary and the subsonic pseudo particles were absorbed at the surface, before being written out, within the code. The situation, however, is different when viscosity is added, which makes the shock more diffused and a clear supersonic to subsonic transition, comprising of multiple layers of particles are seen [5]. The contours in (**a**) and (**b**) are very similar to the thick disk approximation made in BC17, apart from the presence of outflows

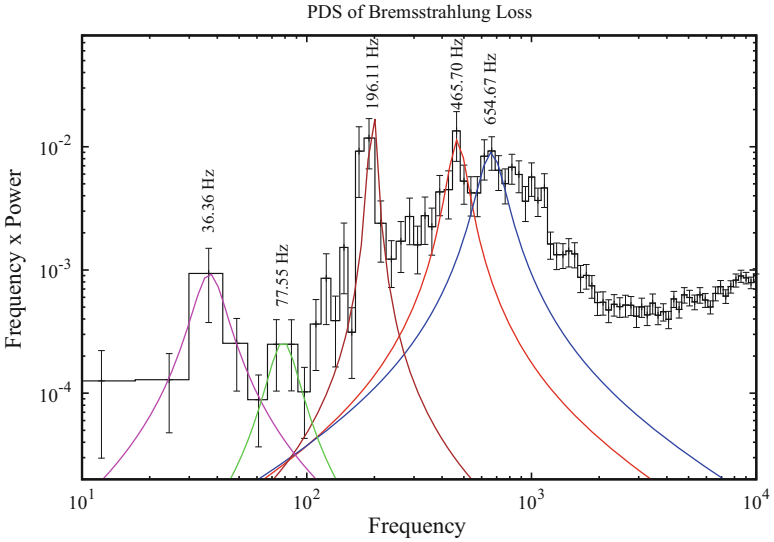



**Fig. 4** The ($frequency \times Power$) vs frequency curve (power density spectrum) obtained from the light curve of the bremsstrahlung loss, is plotted here (adopted from BC18). Five distinct peaks have been fitted with Lorentzian profiles, having centroid frequencies 36.36 Hz (magenta), 77.55 Hz (green), 196.11 Hz (brown), 465.70 Hz (red), and 654.67 Hz (blue) are also plotted. For this simulation $\lambda = 1.7$, $R_{ns} = 4.0\ R_s$. It is to be noted that even without invoking any magnetic field and strong viscosity to create a Keplerian disc, our simulations capture the LFQPOs, the hecto-Hz QPO and the twin kHz QPOs (Color figure online)

**Key Findings (BC18):**

1. The formation of the two shocks in 2D.
2. The formation and variation of outflow rate from the post-shock region when the angular momentum of the inflow varied.
3. Shock formation in strong winds.
4. The radial oscillation of shocks when cooling effects are added.
5. Formation of asymmetries w.r.t. the Z = 0 plane and instabilities due to the interaction of inflow and outgoing strong winds which leads to vertical oscillations (Fig. 3c).
6. The oscillation of NBOL and CENBOL manifested as the LFQPOs, hecto-Hz QPO and twin kHz QPOs in the power density spectra of Bremsstrahlung loss (Fig. 4).

## 7 Concluding Remarks

The discussions of Sects. 4.1, 5 and 6 prove that the TCAF is at the core of the most generalized flow structure around NS. Since the nature of the companion remains generally similar irrespective of whether the compact object is a BH or an NS, it is natural that we use the TCAF solution for the NSs as well, specifically when the magnetic field is not very strong. As suggested in [16] (see Fig. 1), the presence of strong magnetic field will modify the flow configuration from standard TCAF and matter would eventually accrete along the field lines onto the poles, in extreme cases. But, the two components, Keplerian and sub-Keplerian, of accretion would still extend to the magnetosphere, making the flow more complex than what is typically found in the literature so far.

The results of BC17 and BC18 were thought of long ago by Chakrabarti in [14], where a grand unified solution for advection onto compact objects was discussed. In his own words, if one were to summarise his contributions within a couple of words, it would be realizing the importance of 'angular momentum' in accretion. There is no *a priori* reason to assume that companion would eject matter in a fine-tuned Keplerian distribution. The assumption that the flow would have sufficient viscosity which is required to get rid of angular momentum before it reaches a compact object, is also not right. The presence of strong centrifugal force forms shocks and instabilities in the flow without the requirement of extra parameters such as magnetic fields. The sub-Keplerian component of accretion and the effects of cooling have not yet been rigorously implemented in the models of accretion flow around NS. We wish to explore further on this in future.

**Acknowledgements** I would like to acknowledge the constant support and motivation provided by Prof. Sandip K. Chakrabarti. The work we have been doing for the past 2 years on the numerical simulation of spectral and timing properties of accreting neutron stars, was inspired by his work in the domain of stellar mass and supermassive black holes; conceived by him for the cases of neutron stars due to his unparalleled physical insight into the subject and flexibility to adapt in the face of new observations; implemented by his steadfast approach in supervising our work. I would personally like to thank him for tolerating and answering any and all of my academic questions, irrespective of time or place, for the past 4 years, I have worked under his supervision.

## References

1. Barret, D.: Adv. Space Res. **28**, 307 (2001)
2. Barret, D., Olive, J.-F.: ApJ **576**, 391 (2002)
3. Barret, D., Olive, J.-F., Miller, M.C.: MNRAS **361**, 855 (2005)
4. Bhattacharjee, A., Chakrabarti, S.K.: MNRAS **472**, 1361 (2017)
5. Bhattacharjee, A., Chakrabarti, S.K.: (2018, in preparation)
6. Bhattacharjee, A., Chakrabarti, S.K.: ApJ (2018, submitted, Ref: AAS12515)
7. Bhattacharjee, A., Banerjee, I., Banerjee, A., Debnath, D., Chakrabarti, S.K.: MNRAS **466**, 1372 (2017)
8. Belloni, T., Psaltis, D., van der Klis, M.: ApJ **572**, 392 (2002)

9. Belloni, T., Méndez, M., Homan, J.: AAP **437**, 209 (2005)
10. Boutloukos, S., van der Klis, M., Altamirano, D., et al.: ApJ **653**, 1435 (2006)
11. Casella, P., Belloni, T., Stella, L.: AAP **446**, 579 (2006)
12. Chakrabarti, S.K.: ApJ, **288**, 1 (1985)
13. Chakrabarti, S.K.: MNRAS **240**, 7 (1989)
14. Chakrabarti, S.K.: ApJ **464**, 664 (1996)
15. Chakrabarti, S.K.: ApJ **484**, 313 (1997)
16. Chakrabarti, S.K.: In: Ruffini, R., Jantzen, R., Bianchi, M. (eds.) Proceedings of the 14th Marcel Grossmann Meeting, pp. 369–384. World Scientific Press, Singapore (2017). https://doi.org/10.1142/9789813226609_0020
17. Chakrabarti, S.K., Molteni, D.: MNRAS **272**, 80 (1995)
18. Chakrabarti, S.K., Sahu, S.A.: AAP **323**, 382 (1997)
19. Chakrabarti, S., Titarchuk, L.G.: ApJ **455**, 623 (1995)
20. Chakrabarti, S.K., Wiita, P.J.: ApJ **411**, 602 (1993)
21. Debnath, D., Chakrabarti, S.K., Nandi, A.: Adv. Space Res. **52**, 2143 (2013)
22. Di Salvo, T., Stella, L.: arXiv:astro-ph/0207219 (2002)
23. Dieters, S. W., van der Klis, M.: MNRAS **311**, 201 (2000)
24. Dutta, B.G., Chakrabarti, S.K.: ApJ **828**, 101 (2016)
25. Elsner, R.F., Lamb, F.K.: ApJ **215**, 897 (1977)
26. Farinelli, R., Titarchuk, L.: AAP **525**, A102 (2011)
27. Farinelli, R., Titarchuk, L., Paizis, A., Frontera, F.: ApJ **680**, 602–614 (2008)
28. Garain, S.K., Ghosh, H., Chakrabarti, S.K.: MNRAS **437**, 1329 (2014)
29. Ghosh, P., Lamb, F.K.: ApJ **234**, 296 (1979)
30. Ghosh, P., Lamb, F.K.: ApJ **232**, 259 (1979)
31. Ghosh, P., Lamb, F.K., Pethick, C.J.: ApJ **217**, 578 (1977)
32. Ghosh, H., Chakrabarti, S.K., Laurent, P.: Int. J. Mod. Phys. D **18**, 1693 (2009)
33. Gilfanov, M.: The Jet Paradigm. Lecture Notes in Physics, vol. 794, p. 17. Springer, Berlin (2010)
34. Gilfanov, M.R., Sunyaev, R.A.: Physics Uspekhi **57**, 377–388 (2014)
35. Giri, K., Chakrabarti, S.K. MNRAS **430**, 2836 (2013)
36. Haardt, F., Maraschi, L.: ApJ **413**, 507 (1993)
37. Inogamov, N.A., Sunyaev, R.A.: Astron. Lett. **25**, 269 (1999)
38. Jonker, P.G., Wijnands, R., van der Klis, M., et al.: ApJL **499**, L191 (1998)
39. Jonker, P.G., van der Klis, M., Wijnands, R., et al.: ApJ **537**, 374 (2000)
40. Lamb, F.K., Shibazaki, N., Alpar, M.A., Shaham, J.: NAT **317**, 681 (1985)
41. Mauche, C.W.: ApJ **580**, 423 (2002)
42. Méndez, M.: MNRAS **371**, 1925 (2006)
43. Méndez, M., van der Klis, M. ApJL **517**, L51 (1999)
44. Méndez, M., van der Klis, M., van Paradijs, J., et al.: ApJL **485**, L37 (1997)
45. Méndez, M., van der Klis, M., Wijnands, R., et al.: ApJL **505**, L23 (1998)
46. Mitsuda, K., Inoue, H., Koyama, K., et al.: PASJ **36**, 741 (1984)
47. Mitsuda, K., Inoue, H., Nakamura, N., Tanaka, Y.: PASJ **41**, 97 (1989)
48. Molteni, D., Sponholz, H., Chakrabarti, S.K.: ApJ **457**, 805 (1996)
49. Mondal, S., Debnath, D., Chakrabarti, S.K.: ApJ **786**, 4 (2014)
50. Muno, M.P., Remillard, R.A., Chakrabarty, D.: ApJL **568**, L35 (2002)
51. Odaka, H., Khangulyan, D., Tanaka, Y.T., et al.: ApJ **767**, 70 (2013)
52. Odaka, H., Khangulyan, D., Tanaka, Y.T., et al.: ApJ **780**, 38 (2014)
53. Paizis, A., Farinelli, R., Titarchuk, L., et al.: AAP **459**, 187 (2006)
54. Paczynski, B.: NAT **327**, 303 (1987)
55. Popham, R., Sunyaev, R.: ApJ **547**, 355 (2001)
56. Priedhorsky, W., Hasinger, G., Lewin, W.H.G., et al.: ApJL **306**, L91 (1986)
57. Psaltis, D., Belloni, T., van der Klis, M.: ApJ **520**, 262 (1999)
58. Ryu, D., Chakrabarti, S.K., Molteni, D.: ApJ **474**, 378 (1997)
59. Seifina, E., Titarchuk, L.: ApJ **738**, 128 (2011)

60. Seifina, E., Titarchuk, L.: ApJ **747**, 99 (2012)
61. Seifina, E., Titarchuk, L., Frontera, F.: ApJ **766**, 63 (2013)
62. Seifina, E., Titarchuk, L., Shrader, C., Shaposhnikov, N.: ApJ **808**, 142 (2015)
63. Seifina, E., Titarchuk, L., Shaposhnikov, N.: ApJ **821**, 23 (2016)
64. Seon, K.-I., Choi, C.-S., Nam, U.-W., Min, K.-W.: J. Korean Astron. Soc. **27**, 45 (1994)
65. Shakura, N.I., Sunyaev, R.A.: AAP **24**, 337 (1973)
66. Smith, D.M., Heindl, W.A., Swank, J.H.: ApJ **569**, 362 (2002)
67. Smith, D.M., Heindl, W.A., Markwardt, C.B., Swank, J.H.: ApJL **554**, L41 (2001)
68. Strohmayer, T.E., Zhang, W., Swank, J.H., et al.: ApJL **469**, L9 (1996)
69. Sunyaev, R.A., Truemper, J.: NAT **279**, 506 (1979)
70. Sunyaev, R.A., Titarchuk, L.G.: AAP **86**, 121 (1980)
71. Sunyaev, R.A., Titarchuk, L.G.: AAP **143**, 374 (1985)
72. Titarchuk, L., Osherovich, V.: ApJL **518**, L95 (1999)
73. Titarchuk, L., Lapidus, I., Muslimov, A.: ApJ **499**, 315 (1998)
74. Titarchuk, L., Osherovich, V., Kuznetsov, S.: ApJL **525**, L129 (1999)
75. Titarchuk, L., Seifina, E., Frontera, F.: ApJ **767**, 160 (2013)
76. Titarchuk, L., Seifina, E., Shrader, C. ApJ **789**, 98 (2014)
77. van der Klis, M., Jansen, F., van Paradijs, J., et al.: NAT **316**, 225 (1985)
78. van der Klis, M., Hasinger, G., Damen, E. et al.: ApJL **360**, L19 (1990)
79. van der Klis, M., Wijnands, R.A.D., Horne, K., Chen, W.: ApJL **481**, L97 (1997)
80. Wang, J.: Int. J. Astron. Astrophys. **6**, 82 (2016)
81. Wang, J., Chang, H.-K., Liu, C.-Y.: AAP **547**, A74 (2012)
82. White, N.E., Peacock, A., Hasinger, G., et al.: MNRAS **218**, 129 (1986)
83. Wijnands, R., Homan, J., van der Klis, M., et al.: ApJL, **490**, L157 (1997)
84. Wijnands, R., Méndez, M., van der Klis, M., et al.: ApJL **504** L35 (1998)
85. Wijnands, R., van der Klis, M., Homan, J., et al.: NAT **424** 44 (2003)
86. Yu, W., van der Klis, M., Jonker, P.G.: ApJL **559**, L29 (2001)
87. Zdziarski, A.A., Lubiński, P., Gilfanov, M., Revnivtsev, M.: MNRAS **342**, 355 (2003)

# Radiation Characteristics of Two-Component Accretion Flow Paradigm Around Black Holes




**Samir Mandal**

**Abstract** We discuss different radiation processes in a general ($2^3$ *flow*) accretion disk around a black hole and present the radiation spectra. The spectrum calculation includes a hybrid flow due to acceleration of electrons across the shock wave. We discuss different Comptonization scenarios in the hybrid plasma. The local radiation emissivity is calculated including self-absorption. Radiation spectra are used to model the emission from black hole X-ray binaries and to explain the state transitions. A comparison is made to understand the differences in spectral characteristics between stellar mass and supermassive black holes. Also, two-component advective solutions can be used to understand the triggering of outburst events in compact X-ray sources due to sudden surge of viscosity or mass accretion at the outer boundary.

## 1 A General Accretion Flow ($2^3$ *Flow*)

The general accretion scenario around compact objects consists of **two-component** flow due to the nature of surroundings. In compact binary systems, the flow of matter from the companion may be due to stellar wind (low-angular momentum matter: [1–5]) or Roche lobe overflow (Keplerian matter: [6, 7]) or a combination of the both [8–10]. A similar scenario may exist around a supermassive black hole (BH) as well: a low-angular momentum flow due to mutual cancellation of angular momentum of the gravitationally captured matter from the interstellar medium or stellar winds and a Keplerian flow by the transfer of angular momentum due to turbulence in the medium. The possibility of a single component (either Keplerian or sub-Keplerian) accretion flow is equally valid as well in special cases.

A Keplerian flow is governed by a small radial flow velocity. Hence accreting matter gets sufficient time to radiatively cool down and the accretion disk tem-

S. Mandal (✉)
Indian Institute of Space Science and Technology, Thiruvananthapuram, India
e-mail: samir@iist.ac.in

© Springer International Publishing AG, part of Springer Nature 2018

B. Mukhopadhyay, S. Sasmal (eds.), *Exploring the Universe: From Near Space to Extra-Galactic*, Astrophysics and Space Science Proceedings 53,
https://doi.org/10.1007/978-3-319-94607-8_9

perature distribution can be well approximated by a multi-colour blackbody. A low-angular momentum (sub-Keplerian) flow has significantly higher infall velocity and the accreting matter may or may not get enough time to maintain a single temperature distribution. In an ionized plasma, protons are heated due to viscous dissipation and Coulomb coupling tries to maintain the energy exchange between electrons and protons due to collisions. Since the electron-electron and proton-proton collision time scales are smaller than the electron-proton collision time scale [11], flow may manage to maintain **two-temperature**, [8, 12, 13] separately for electrons and protons, unless the infall time scale is much larger than the electron-proton collision time. Of course at a high accretion rate with equipartition magnetic field, MHD instabilities or magnetic field reconnection [14, 15] may be important to heat up the electrons, and resulting in a single temperature flow.

Another important property of sub-Keplerian matter is that the radial flow velocity must be supersonic at the vicinity of the BH and the flow may pass through shock transitions [5, 16] depending on the strength of the centrifugal barrier. The accretion flow which contains shocks is radiatively efficient and potentially very important to explain many observed features as the flow kinetic energy is being converted into thermal energy. Also acceleration of particles [17–20] is possible due to diffusive back and forth motion of particles across shock by the Fermi acceleration mechanism. This makes **two different velocity distributions** of particles in the post-shock region (POSR), majority of them still follow a thermal distribution and the rest, a small fraction, are non-thermal particles. In this chapter, we are going to understand the radiation characteristics of a $2^3$ *flow*: two-component, two-temperature flow having two different distributions of particles (electrons).

## 2 Radiation Processes in $2^3$ *Flow*

The radiation processes in a $2^3$ *flow* can be characterized into two categories, namely production of seed photons and the interactions of these soft photons with high energy electrons in the POSR producing high energy radiations. The relevant physical processes are discussed in the following sub-sections.

### *2.1 Multi-Colour Blackbody Radiation*

The optically thick Keplerian disk is radiatively efficient due to conversion of viscous dissipated energy into radiation and the radiation characteristic is assumed to be locally blackbody. The local blackbody temperature [11] can be estimated from the viscous dissipated flux as

$$T(r) = \left\{ \frac{3GM\dot{M}}{8\pi\sigma r^3} \left[ 1 - \frac{r_{in}}{r} \right]^{1/2} \right\}^{1/4}, \tag{1}$$

where $r$ represents the radial coordinate, $M$ is the mass of the central object, $\dot{M}$ is the mass accretion rate and $r_{in}$ is the inner radius of the disk. Here $G$ stands for universal gravitational constant and $\sigma$ is Stefan constant. The temperature has $M^{-1/4}$ dependency for a constant dimensionless accretion rate. This temperature distribution is derived under the Newtonian prescription of gravity and it depends on the sources of opacity in the disk (see [6] for more detail description of temperature at different regions of the disk). For an extension of this work in general relativity see, [7, 21]. Hence the Keplerian disk produces multi-colour blackbody photons and the local emitted intensity of radiation is given as,

$$I_\nu(r) = \frac{2h\nu^3}{c^2[e^{h\nu/kT(r)} - 1]}, \tag{2}$$

where $h$ is Planck constant, $c$ is speed of light, $k$ is Boltzmann constant and $\nu$ is the frequency of radiation. The integrated radiation spectrum has a Rayleigh-Jeans characteristic at low frequency (corresponds to the emission from outer part of the disk) and exponential cutoff at high frequency (from the inner part of the disk), whereas in the intermediate frequency, the spectrum behaves as $\nu^{1/3}$ due to combination of peaks of blackbody spectra of different temperatures.

## 2.2 Free-Free Emission

A hot plasma is completely, ionized and the free electrons undergo accelerated motion due to random encounter in the Coulomb field of protons. This process emits radiation which is known as free-free emission. These emissions are very common in astrophysical systems and are extended from radio to X-ray range depending on the density and temperature of the system. In compact HII region, it appears as a continuum radio emission, whereas in X-ray binaries, AGNs, intergalactic gas in cluster of galaxies, the emissions are dominant in X-rays. The low-angular momentum accretion flow around compact X-ray binaries is usually optically thin and geometrically thick, unless the accretion rate is extremely high. Such flows around compact objects are hot enough ($\geq 10^9$ K) that the flow is completely ionized and produce thermal free-free emission. The free-free emissivity [22] due to non-relativistic thermal electrons can be written as,

$$j_{fT}(\nu) = \frac{2^5\pi q^6 Z^2}{3m_e c^3} n_i n_e \left(\frac{2\pi}{3km_e}\right)^{1/2} T_e^{-1/2}\, e^{-h\nu/kT_e}\, \bar{g}_{ff}, \tag{3}$$

where $q$ is electron change, $m_e$ is mass of electron, $T_e$ is temperature of electron, $n_e$ and $n_i$ are number densities of electrons and ions respectively. $\bar{g}_{ff}$ is a velocity averaged Gaunt factor. The exponential fall in the spectrum keeps the signature of thermal distribution. In a similar way, ions emit radiation due to encounter with

electrons but this is $\sqrt{\frac{m_e T_e}{m_i T_i}}$ times smaller than that of electrons, where $m_i$ and $T_i$ are mass and temperature of ions respectively. The electron-electron or proton-proton interactions do not emit free-free radiation under dipole approximation [22]. The radiation has a flat spectrum with exponential cutoff which is the characteristic of the temperature of the medium.

Non-thermal free-free emissions could be observed as low energy gamma-ray/hard X-ray emissions in the objects such as supernova remnants [23], in the interstellar medium due to cosmic ray interactions, cluster of galaxies in which accretion or merger shocks [24, 25] are present. Non-thermal free-free emissions are rarely considered in accretion/ejection systems around compact objects. But here we include the emissivity due to a power-law distribution of particles for the purpose of completeness. We consider a non-thermal distribution of electrons as,

$$n_e(E)dE = K_e E^{-n} dE, \tag{4}$$

where, $E$ is the electron energy and $n$ is the powerlaw index. The non-thermal free-free emissivity [26] is given as,

$$j_{fN}(\nu) = \frac{2^5 \pi q^6 Z^2}{3 m_e^2 c^4} n_i K_e \begin{cases} \left(2m_e c^2\right)^{1-n/2} \frac{X}{4} e^{Q(n-2)/2} (\zeta_e h\nu)^{-n/2}; & h\nu < \frac{2m_e c^2}{\zeta_e} \\ \frac{X + ln\left(1+\frac{\zeta_e h\nu}{2m_e c^2}\right)}{2} e^{Q(n-3)/2} (\zeta_e h\nu)^{1-n}; & h\nu > \frac{2m_e c^2}{\zeta_e}, \end{cases} \tag{5}$$

where $Q = \frac{1-2n}{n(n-1)}$, $X = [ln(1.368\zeta_e) - Q]$ and $\zeta_e$ is the fraction of electron kinetic energy converted to photon energy. The free-free emissivity due to a powerlaw distribution of electrons has a powerlaw spectral signature.

Every emission process is balanced by an absorption of the same physical process—*principle of detailed balance*. The absorption coefficient is frequency dependent and is determined [22] as,

$$a_\nu = -\frac{c^2}{8\pi \nu^2} \int dE\, j(\nu, E) E^2 \frac{\partial}{\partial E}\left[\frac{N(E)}{E^2}\right], \tag{6}$$

where $j(\nu, E)$ is the emissivity of the process and $N(E)$ is the distribution of the electrons. For a thermal medium Eq. (6) becomes,

$$j_{fT}(\nu) = a_{fT}(\nu) B(\nu), \tag{7}$$

where, $a_{fT}(\nu)$ is thermal free-free absorption coefficient and $B(\nu)$ is the blackbody intensity. The turnover frequency ($\nu_{fa}$) can be determined by the condition,

$$a_{fT}(\nu_{fa})R = 1, \tag{8}$$

where, $R$ is the characteristic size of the medium. Hence, for $\nu < \nu_{fa}$, the medium is optically thick and has a characteristic Rayleigh-Jean spectrum, whereas for $\nu > \nu_{fa}$, the medium shows optically thin free-free emission.

## 2.3 Synchrotron Emission

Magnetic fields are ubiquitous in the universe and the motion of charge particles under the influence of magnetic field produces synchrotron radiation. It can be both thermal and non-thermal in nature depending on the distribution of the underlying particles which produce the radiation. Non-thermal synchrotron emission is more widely observed in astrophysical systems such as, Herbig-Haro objects [27], microquasar jets [28, 29], AGN jets [30, 31] etc. An analytical expression of synchrotron emissivity for ultra-relativistic power-law electrons is simple to describe and mostly the interest in radio astronomy. Also, thermal synchrotron in non-relativistic domain [32] as well as ultra-relativistic limit are well developed. But an analytical prescription of thermal synchrotron emission in the semi-relativistic range ($T_e \sim 10^8 - 10^{10}$ K) is very hard and a number of studies in literature [33–37] have contributed towards this. A magnetized and hot sub-Keplerian matter around compact objects would be an important source of both thermal and non-thermal synchrotron radiations under optically thin condition. The radiation emissivity of synchrotron emission [13] from a semi-relativistic thermal distribution of electrons is expressed in CGS unit as

$$j_{sT}(\nu) = 4.43 \times 10^{-30} \frac{4\pi n_e \nu}{K_2(1/\theta_e)} I(x_m), \tag{9}$$

where $x_m = \frac{2\nu}{3\nu_0 {\theta_e}^2}$, $K_2$ is the modified Bessel function of second kind, $\theta_e = kT_e/m_e c^2$, $\nu_0$ is cyclotron frequency and an isotropic pitch angle integrated

$$I(x_m) = \frac{4.0505}{{x_m}^{1/6}} \left(1 + \frac{0.40}{{x_m}^{1/4}} + \frac{0.5316}{{x_m}^{1/2}}\right) exp(-1.8899 {x_m}^{1/3}).$$

As we have mentioned in Sect. 1 that an accretion flow in the presence of shock wave can produce a non-thermal distribution of electrons (Eq. (4)) and the

non-thermal synchrotron emissivity [20]

$$j_{sN}(\nu) = \frac{3-n}{2} \mathscr{A}\, \mathscr{G}\, B^{(n+1)/2}\, \nu^{(1-n)/2}, \tag{10}$$

$$\text{where} \quad \mathscr{A} = \frac{(3\pi)^{1/2} K_e q^3}{m_e c^2 (1+n)(3-n)} \left( \frac{2\pi m_e^3 c^5}{3q} \right)^{(1-n)/2},$$

$$\mathscr{G} = \frac{\Gamma(\frac{3n+19}{12})\, \Gamma(\frac{3n-1}{12})\, \Gamma(\frac{n+5}{4})}{\Gamma(\frac{n+7}{4})},$$

and $B$ is the strength of magnetic field. The above result averages over an isotropic distribution of pitch angles.

Emission and absorption are simultaneous processes in any medium and synchrotron photons interact with a charge in a magnetic field and get absorbed, giving up its energy to the charge. The self-absorption coefficient due to synchrotron process can be determined using Eq. (6). An equation similar to Eq. (8) can be used to numerically calculate the synchrotron self-absorption turnover frequency $\nu_{sa}$ [37, 38]. In case of a hybrid medium (thermal+non-thermal), $\nu_{sa}$ can be determined [13, 20] as

$$[j_{sT}(\nu) + j_{sN}(\nu)] \times \mathscr{V} = \pi [(1-\zeta) s_{sT}(\nu) + \zeta s_{sN}(\nu)] \times \mathscr{S}, \tag{11}$$

where $\zeta$ is the percentage of electrons having a power-law energy distribution, $\mathscr{V}$ and $\mathscr{S}$ are the volume and surface encompassing by the medium. $s_{sT}(\nu)$ and $s_{sN}(\nu)$ are source functions for thermal and non-thermal synchrotron respectively. The synchrotron source function below $\nu_{sa}$ has a $\nu^2$ characteristic for thermal medium, whereas a $\nu^{5/2}$ dependency for a non-thermal medium.

## 2.4 Comptonization: Source of High Energy Radiation

The interactions of photons with free electrons result in an exchange of energy [39]:

$$\frac{\nu'}{\nu} = \frac{1 - \mu v/c}{1 - \mu' v/c + (h\nu/\gamma m_e c^2)(1 - cos\,\alpha)}, \tag{12}$$

where, $\nu$ and $\nu'$ are photon frequency before and after scattering respectively, $\mu$ and $\mu'$ are cosine angles of photon before and after scattering with the initial direction of electron and $\alpha$ is the angle of scattering. The electron is moving with velocity $v$ and Lorentz factor $\gamma$. Thus for an electron at rest, the energy transfer, $\frac{\Delta\nu}{\nu} = \frac{\nu'-\nu}{\nu} = -h\nu/m_e c^2(1-cos\,\alpha)$. As long as the electron is moving with non-relativistic speed, i.e. the photon energy in the electron rest frame $\gamma h\nu < m_e c^2$, the scattering can be

described by Thomson cross-section. For a relativistic electron $\gamma^2-1 >> h\nu/m_ec^2$, the photon energy after scattering is enhanced (inverse-Compton) by $\gamma^2$ and the scattering is described by Klein-Nishina cross-section [22].

In a hot plasma, the mean enhancement of seed photon energy due to inverse-Compton scattering (multiple scattering) depends on both the distribution of seed photons as well as relativistic electrons. Below, we discuss the photon enhancement factor ($\mathscr{F}$) for the following scenarios.

- Comptonization of thermal photons by thermal electrons [20, 40]:

$$\mathscr{F}_{TT} = \eta_1 \left\{ 1 - \left( \frac{x_a}{3\theta_e} \right)^{\eta_2} \right\}, \tag{13}$$

  where $\eta_1 = \frac{P(A-1)}{(1-PA)}$, and $P = 1-e^{-\tau}$, is the probability of photon scattering. The electron scattering optical depth $\tau = n_e \sigma_T R$, where $\sigma_T$ is Thomson cross-section and $R$ is the size of Comptonizing cloud. The mean amplification factor per scattering $A = 1+4\theta_e+16\theta_e^2$, and $\eta_2 = -1-lnP/lnA$. Here $x_a = h\nu_a/m_ec^2$, is the average input photon energy and $\theta_e = KT_e/m_ec^2$, is dimensionless electron temperature.

- Comptonization of non-thermal (Eq. (4)) seed photons by the thermal electrons [20, 40]:

$$\mathscr{F}_{NT} = \eta_1 \left\{ 1 - \left( \frac{s}{\phi_s} \right) \frac{x_{max}^{\phi_s} - x_a^{\phi_s}}{(3\theta_e)^{\eta_2} \, (x_{max}^s - x_a^s)} \right\}, \tag{14}$$

  where $x_{max} = h\nu_{max}/m_ec^2$, $s = 2 - n$ and $\phi_s = \eta_2 + s$.

- Comptonization of non-thermal (Eq. (4)) seed photons by non-thermal electrons [22]:

$$\mathscr{F}_{NN} = \frac{4}{3}\sigma_T R K_e \frac{(E_{max}^{3-n} - E_{min}^{3-n})}{(3-n)}, \tag{15}$$

  where $E_{max}$ and $E_{min}$ represent the maximum and minimum energies of the power-law electrons, respectively. In case of sub-Keplerian flow with a hybrid distribution of electrons due to acceleration across shock, $E_{min}$ can be calculated from the average temperature of the flow whereas $E_{max}$ is computed from the number of scattering that the electrons undergo inside the disc before they escape [20].

The inverse-Compton spectrum in a thermal medium depends on both $\tau$, $T_e$ and, hence, Compton parameter $y = (A-1)(\tau + \tau^2)$ can be used to describe the significance of the process. For $y << 1$, the emergent spectrum is mostly determined by single scattering and has a powerlaw signature, whereas $y >> 1$ forms a Wien spectrum determined by $T_e$ only. The intermediate region, $y \sim 1$,

is most important for an X-ray emitting medium and most difficult to address analytically. In this case, two distinct possibilities may arise: sufficiently high $T_e$ and $\tau < 1$ medium produces a powerlaw spectrum, whereas semi-relativistic $T_e$ with $\tau \sim 1$ results in a cutoff powerlaw spectrum.

An optically thin non-thermal medium produces a powerlaw inverse-Compton spectrum due to single scattering and the spectral index $p = (n-1)/2$, whereas an optically thick non-thermal medium shows hardly any difference from a thermal medium, provided the mean electron energy is same [41].

Hence, in general, the inverse-Compton emissivity can be expressed as a combination of cutoff powerlaw and Wien spectrum, given by,

$$j_c(\nu) = j_P \left(\frac{x}{\theta_e}\right)^{-p} e^{-x/\theta_e} + j_W \left(\frac{x}{\theta_e}\right)^{3} e^{-x/\theta_e}, \tag{16}$$

where $j_P$ and $j_W$ are normalizations related to the contributions from power-law and Wien components, respectively. For low/moderate optical depth, using source volume averaged [42, 43] scattering probability, the spectral index can be approximated [22] as $\alpha = -lnP/lnA$. Whereas for high scattering optical depth, a kinetic Fokker-Planck equation [44–47] is required to describe the Comptonization process. The geometry (and hence $\tau$) and particle distribution dependence of the Comptonization process are responsible for existing many Comptonization models [44, 45, 48–50, and referrence therein] available in the literature. Most of these models assume a static uniform Compton cloud/corona on top of the Keplerian disk, whereas in $2^3$ *flow*, the dynamic POSR region acts as a Compton cloud which is a natural extension of the sub-Keplerian flow. In the next section, we discuss the methodology for calculating the radiation spectrum using hydrodynamics.

## 3 Radiation Hydrodynamic Solutions in $2^3$ *Flow*

We consider a two-component axisymmetric accretion disk in vertical equilibrium [5]. Here, the Keplerian disk (KD) is static and the dynamics of sub-Keplerian disk (SKD) determines the accretion disk radiation properties. The two mass accretion rates (KD rate: $\dot{m}_d$, SKD rate: $\dot{m}_h$) are expressed in the unit of Eddington accretion rate. The radial distance ($x$) is measured in the unit of $r_g = 2GM/c^2$ and the mass of BH is expressed in solar mass ($M_\odot$). The other flow parameters are shock location ($x_s$), compression ratio ($R$) and $\zeta$, fraction of non-thermal electrons. The hydrodynamics of an accretion disk is described by the continuity equation, energy conservation equation and the entropy generation equation. The details of these governing equations can be found in [5, 51, and references therein] for single temperate flows, whereas [20, 52, 53, and referrences therein] for two-temperature flows. The solutions of the hydrodynamic equations in the presence of radiative processes (discussed in Sect. 2) allow to calculate the flow variables $n_e(x)$, $T_e(x)$, $T_i(x)$, $B(x)$ [52, 53]. These local variables are used to calculate the

local radiation emissivity (Sect. 2) from individual annuli of the disk due to different radiation processes [20, 53–55]. Finally, we combine these local contributions to evaluate the total spectrum for different radiative processes. Figure 1 shows a representative spectrum of various radiative contributions (the details are mentioned in the figure caption). The major flow parameters, $\dot{m}_h = 0.3$, $\dot{m}_d = 0.5$, $x_s = 5.0$ and $\zeta = 0.07$, are chosen such that Fig. 1a represents a soft state. It has characteristic signature of strong peak at a few keV and a steep powerlaw spectrum, extending without cut-off up to hundreds of keV. Whereas Fig. 1b represents a hard state with signature of weaker soft component below 1 keV and harder powerlaw extending upto few hundreds of keV with exponential cutoff. The parameters for hard state are $\dot{m}_h = 1.47$, $\dot{m}_d = 0.001$, $x_s = 19.0$ and $\zeta = 0.067$. Hence, spectral state transition can be understood by changing the flow parameters. A higher Keplerian rate is associated with a soft state, whereas the same for sub-Keplerian rate corresponds to hard state. This result has been applied [54] to Cyg X-1 to explain both soft and hard spectral states and the inclusion of non-thermal synchrotron emission due acceleration of a small fraction of electrons across shock provides a natural explanation of extended non-thermal tail in the soft state. A similar study has been done by [56–58], but without providing an origin of non-thermal electrons.

Accretion process around supermassive BHs should be a natural extension of the study around a stellar mass BHs. Figure 2 shows a comparison of accretion disk spectral characteristics between a stellar mass BH and a supermassive BH. The important parameters are $\dot{m}_h = 0.1$, $\dot{m}_d = 0.5$, $x_s = 20.0$ and $\zeta = 0.01$, which are same for both the cases except the mass of the central sources. The result

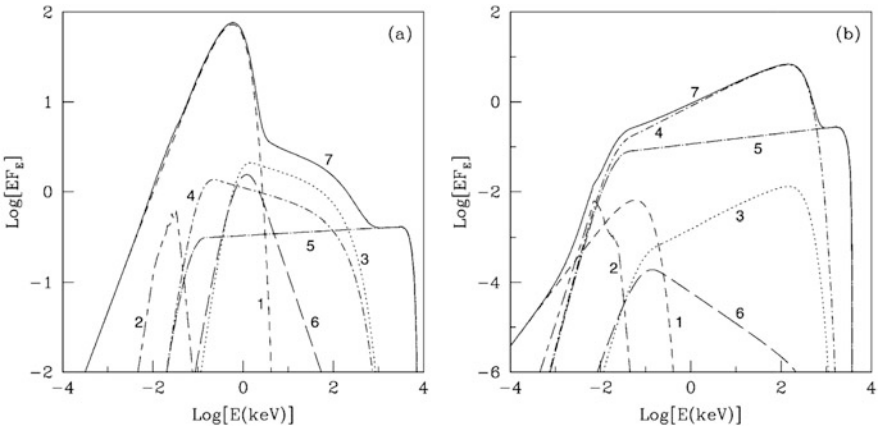



**Fig. 1** The general nature of the spectra in a $2^3$ *flow*. We show two representative cases (**a**) soft state and (**b**) hard state (reproduced from [54]) for different choice of parameters given in the text. Various components are (1) multi-colour blackbody contribution from the Keplerian disk, (2) synchrotron radiation from POSR, (3) Comptonization of soft photons from Keplerian disk by POSR, synchrotron self-Comptonization of POSR soft photons by (4) the thermal and (5) the non-thermal electrons, (6) bulk motion Comptonization of the POSR soft photons due to convergent nature of the flow, and (7) the overall spectrum

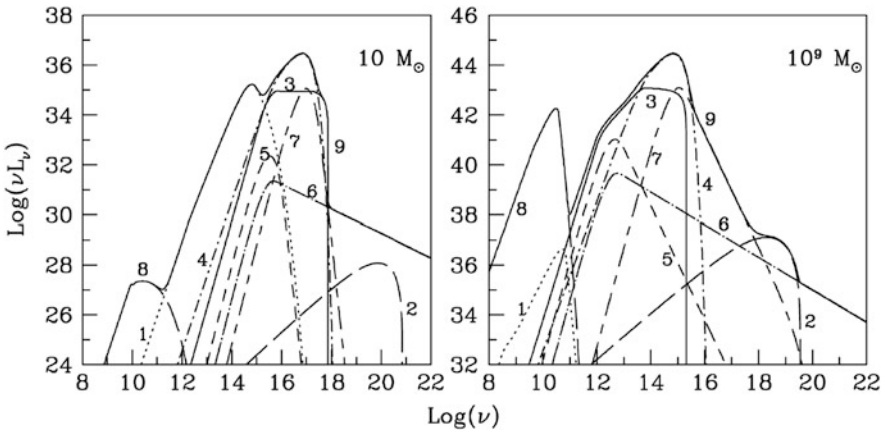



**Fig. 2** Comparison of different spectral components around stellar mass and supermassive BHs (marked). The different curves represent: (1) thermal synchrotron radiation from the preshock sub-Keplerian flow and (2) the same for bremsstrahlung radiation. (3) shows the synchrotron contribution from non-thermal electrons in the POSR and (4) is due to blackbody radiation from the Keplerian disk. (5) and (6) represent the synchrotron self-Comptonization of soft photons emitted by the thermal and non-thermal electrons, respectively. The Comptonization of intercepted blackbody photons by POSR is given by (7) and (8) shows the synchrotron emission from the jet. Finally, (9) represents the overall spectrum. This figure is reproduced from [55]

shows that the bremsstrahlung radiation is negligible for a stellar mass BH, but it is important for a supermassive BH. However, the synchrotron contribution is more important in the case of a stellar mass BH. The Comptonized spectrum of the blackbody radiation becomes harder with the increase of BH mass. An application of this result to M87 [55] shows a non-thermal synchrotron origin of so called big blue bump in the contrary to the common claim of Keplerian origin.

Two-component flow solution can be used to explain the outburst profile (Hardness-intensity diagram) of X-ray binaries. In this model [59], an outburst is triggered either because of a sudden change in mass supply rate from the binary companion or a sudden surge in viscosity (mostly turbulence) at the outer boundary which gradually converts sub-Keplerian matter into Keplerian matter. This increase in Keplerian rate enhances the X-ray luminosity gradually and spectral state becomes softer. In outbursting X-ray binary systems, the infall time scale for sub-Keplerian matter is typically $\sim$ days, whereas Keplerian matter responds in viscous time scale $\sim$ few tens of days. Hence, once an outburst is triggered, the typical rise time of a few days can be explained by the viscous time scale and the decline phase of the outburst starts as the Keplerian region recedes back and the hard state is regained.

The radiation spectra from two-component accretion solutions have been implemented [60, 61] in *XSPEC* and could successfully explain the spectral modelling of several X-ray binary systems. Also [61, 62] have determined the mass of the central BHs in X-ray binary systems using broadband spectral modeling.

## 4 Conclusions

We discuss the most general scenario of accretion flow around BHs. In Sect. 2, we describe different processes of soft photon sources as well as Comptonization of both thermal and non-thermal photons in a two-component flow. A hybrid distribution of electrons may originate in an accretion flow in presence of a shock. The absorption processes modify the emissivity and we calculate the absorption (self/turnover) frequency in a hybrid plasma. The medium is optically thick below the turnover frequency and optically thick above this. We highlight various Comptonization models (Sect. 2.4) exist in the literature and discuss their differences with the two-component model. In Sect. 3, the radiation characteristics around a stellar mass and a supermassive BHs (Fig. 2) are discussed. We see importance of different radiative processes depending on the mass of the central source. We explain the state transitions (Fig. 1) in BH X-ray binary systems by changing the model parameters. The triggering of outburst events in compact X-ray binary systems can occur due conversion of sub-Keplerian matter into Keplerian matter in two-component flow model paradigm. The two-component flow model has been implemented in *Xspec* as a local model to study the spectral behaviour and mass of the central compact object in BH X-ray binary system can be determined using broadband spectral modeling.

## References

1. Liang, E.P., Thompson, K.A.: ApJ **240**, 271 (1980)
2. Paczyński B., Wiita, P.J.: A&A **88**, 23 (1980)
3. Paczyński B., Bisnovatyi-Kogan, G. Acta Astron. **31**, 283 (1981)
4. Abramowicz, M., Czerny, B., Lasota, J.P., Szuskiewicz, E.: ApJ **332**, 646 (1988)
5. Chakrabarti S.K.: ApJ **347**, 365 (1989)
6. Shakura, N.I., Sunyaev, R.: A&A **24**, 337 (1973)
7. Novikov, I. D., Thorne, K.S.: In: Dewitt, C., Dewitt, B. (eds.) Black Holes. Gordon & Breach, New York (1973), p. 343
8. Chakrabarti, S.K., Titarchuk, L.: ApJ **455**, 623 (1995)
9. Giri, K., Chakrabarti, S. K.: MNRAS **430**, 2836 (2013)
10. Liu, B.F., Taam, R.E., Qiao, E., Yuan, W.: ApJ **806**, 223 (2015)
11. Frank, J., King, A., Raine, D.: Accretion Power in Astrophysics. Cambridge University Press, Cambridge (2002)
12. Shapiro, S.L., Lightman, A.P., Eardley, D.M.: ApJ **204**, 187 (1976)
13. Narayan, R., Yi, I.: ApJ **452**, 710 (1995)
14. Bisnovatyi-Kogan, G.S., Lovelace, R.V.E.: ApJ **486**, L43 (1997)
15. Quataert E., Gruzinov A.: ApJ **520**, 248 (1999)
16. Das S., MNRAS **376**, 1659 (2007)
17. Bell, A.R., MNRAS **182**, 147 (1978)
18. Bell, A.R.: MNRAS **182**, 443 (1978)
19. Ghisellini G., Haardt F., Svensson R.: MNRAS **297**, 348(1998)
20. Mandal, S., Chakrabarti, S.K.: A&A **434**, 839 (2005)
21. Page, D.N., Thorne, K.S.: ApJ **191**, 499 (1974)

22. Rybicki, G.B., Lightman, A.P.: Radiative Processes in Astrophysics. Wiley-Interscience, New York (1979)
23. Vink, J.: A&A **486**, 837 (2008)
24. Sarazin, C. L., Kempner, J.C.: ApJ **533**, 73 (2000)
25. Nevalainen, J., Oosterbroek, T., Bonamente, M. et al.: ApJ **608**, 166 (2004)
26. Zekovic, V., Arbutina, B., Dobardzic, et al.: IJMPA **28**, 1350141 (2013)
27. Vig, S., Veena, V.S., Mandal, S., Tej, A., et al.: MNRAS **474**, 3808 (2018)
28. Mirabel, I.F., et al.: Nature **358**, 215 (1992)
29. Mirabel, I.F., Rodriguez, L.F.: Nature **371**, 46 (1994)
30. Liang, R.A., Bridle, A.H.: MNRAS **228**, 557 (1987)
31. Bridle, A.H., et al.: AJ **108**, 775 (1994)
32. Chanmugam G., Barrett P. E., Wu K., Courtney M.W.: ApJS **71**, 323 (1989)
33. Jones, T.W., Hardee, P.E.: ApJ **228**, 268 (1979)
34. Petrosian V.: ApJ **251**, 727 (1981)
35. Takahara F., Tsuruta S.: Prog. Theor. Phys. **67**, 485 (1982)
36. Robinson, P.A., Melrose, D.B.: Aust. J. Phys. **37**, 675 (1984)
37. Mahadevan, R., Narayan, R., Yi I.: ApJ **465**, 327 (1996)
38. Zdziarski A. A., Poutanen J., Mikolajewska, J. et al.: MNRAS **301**, 435 (1998)
39. Pozdniakov, L., Sobol, I., Syunyaev, R.: ASPR **2**, 189 (1983)
40. Dermer, C.D., Liang, E.P., Canfield, E.: ApJ **369**, 410 (1991)
41. Ghisellini, G., Haardt, F., Fabian, A.C.: MNRAS, **263**, L9 (1993)
42. Osterbrock D.E.: Astrophysics of Gaseous Nebulae. Freeman, San Francisco (1974)
43. Zdziarski, A.A., Fabian, A.C., Nandra K. et al.: MNRAS **269**, L55 (1994)
44. Sunyaev, R.A., Titarchuk L.G.: A&A **86**, 121 (1980)
45. Sunyaev, R.A., Titarchuk, L.G.: A&A **143**, 374 (1985)
46. Zdziarski A.A.: ApJ **289**, 514 (1985)
47. Lightman A.P., Zdziarski A.A.: ApJ **319**, 643 (1987)
48. Haardt F., Maraschi L., Ghisellini G.: ApJ **432**, L95 (1994)
49. Poutanen J., Svensson R.: ApJ **470**, 249 (1996)
50. Poutanen J., Coppi P.: Phys. Scr. **T77**, 57 (1998)
51. Das, S., Chakrabarti, S.K.: IJMPD **13**, 1955 (2004)
52. Dihingia, I. K., Das, S. Mandal, S.: MNRAS **475**, 2164 (2017)
53. Mandal, S., Mondal, S.: JApA **39**, 19 (2018)
54. Chakrabarti, S.K., Mandal, S.: ApJL **642**(1), 49 (2006)
55. Mandal, S., Chakrabarti, S.K.: ApJL **689**, L17 (2008)
56. Lin, D., Liang, E.P.: A&A **341**, 954 (1999)
57. Wardziński G., Zdziarski, A.A.: MNRAS **325**, 963 (2001) [Erratum: 2001, MNRAS,327, 351]
58. Zdziarski, A.A., Grove, J.E., Poutanen, J. et al.: ApJ **554**, L45 (2001)
59. Mandal, S., Chakrabarti, S.K.: ApJL **710**, L147 (2010)
60. Debnath, D., et al.: MNRAS **440**, L121 (2014)
61. Iyer, N., Nandi, A., Mandal, S.: ApJ **807**, 108 (2015)
62. Nandi, A. et al.: Ap&SS **363**, 90 (2018)

# How Are the Outbursts Around Black Holes Triggered?




**Shreeram Nagarkoti**

**Abstract** We study accretion processes under two component accretion flow paradigm where an accretion flow has Keplerian and sub-Keplerian components. Here, observational studies carried out by authors in earlier studies using this approach are revisited. Using various methods, Shakura and Sunyaev's viscosity parameter, $\alpha$ values in both sub-Keplerian and Keplerian components are obtained during outbursts of various sources. The values of $\alpha$ were found to be supercritical in Keplerian component and subcritical in sub-Keplerian component always (as suggested in previous studies). Subsequently, a study of variation of sub-Keplerian values of $\alpha$ was then carried out which confirms that this value rose gradually in rising phase and decreased in declining phase for all outbursting sources. Spectral state transitions took place for some particular limits of sub-Keplerian values of $\alpha$. For its values less than 0.008, all sources were categorized in hard spectral state. When it was in the ranges 0.008–0.035 and 0.035–0.01, hard and soft intermediate states were observed respectively. Soft spectral state would be expected for any larger values of $\alpha$ in the sub-Keplerian component. Thus the concept of viscosity enhancement being responsible for triggering the outbursts and spectral state changes around black holes has been strengthened. A study with more outbursts of larger number of sources should be carried out to confirm this value of $\alpha$ which triggers these outbursts and spectral state transitions, predict various line parameters relevant for their future astronomical detection.

## 1 Introduction

It has now become a standard practice to study accretion processes under two component advective flow (TCAF) paradigm. The approach stresses on two distinct (Keplerian and sub-Keplerian) components to accrete. For a black hole accretion, the viscous process is held responsible to transport matter inwards and angular

S. Nagarkoti (✉)
St. Xavier's College, Maitighar, Kathmandu, Nepal

© Springer International Publishing AG, part of Springer Nature 2018

B. Mukhopadhyay, S. Sasmal (eds.), *Exploring the Universe: From Near Space to Extra-Galactic*, Astrophysics and Space Science Proceedings 53,
https://doi.org/10.1007/978-3-319-94607-8_10

momentum outwards. Chakrabarti and Titarchuk [9] explained the accretion flow as having a Keplerian component with supercritical values of Shakura and Sunyaev's [45] viscosity parameter $\alpha$ ($>\alpha_{cr}$, a critical value above which shock formation is not possible) in the equatorial plane, enveloped by a sub-Keplerian component with subcritical values of $\alpha$. The idea of Compton cloud or Corona [46, 47] and several phenomenological models were already in the literature. The sub-Keplerian component forms the centrifugal pressure supported boundary layer or shocks which behaves as the Compton cloud in TCAF paradigm. Through an extended period of time with a large number of collaborative work with different generations of authors, Chakrabarti has proven the ubiquity of these shocks ([8] and references in the Volume).

Thermal-viscosity instability [5, 6, 29, 48] is held responsible for repeated outbursting events observed from dwarf novae. Accretion rate in the Keplerian component is understood to shoot up triggering the outbursting event. Enhancement of convective viscosity [3] in the outer parts of disk that occurs after enough pile-up of matter could be the reason for such rise in accretion rate in Keplerian component (might contribute to enhancements of sub-Keplerian component as well). Many recent observational analyses [2, 12, 13, 17, 23, 31, 34] have indicated gradual increase of matter accretion rate in both these components. As a rule, all sub-Keplerian accretion rates were found to peak a few days before Keplerian rates peaked (caused clearly due to difference in $\alpha$, [32, 33, 35, 36]).

Scrutinizing these observational analyses further along history, all outbursting events could generally be divided into hard (HS), soft (SS) and intermediate states (HIMS, SIMS, [1, 16, 28, 37]). Actually, a sequence of $HS \rightarrow HIMS \rightarrow SIMS \rightarrow SS \rightarrow SIMS \rightarrow HIMS \rightarrow HS$ transitions is observed from the beginning to end of the outburst cycle before each source becomes quiescent. An established practice in the community is the study of hardness-intensity diagram [1, 19]. It shows the hysteresis behaviour during each outburst. This whole cycle is said to be divided into rising, full outburst and declining phases. From the observational analyses [2, 12, 13, 17, 23, 31, 34] completed in the past, it is possible to find the details about accretion rates in the two components of the flow, as well as shock properties and viscosity parameter. The spectral fit of an outbursting source are used to extract four physical parameters, including the time lag between the peaks of the accretion rates of Keplerian and sub-Keplerian components. This in turn provides $\alpha_K$ (in the Keplerian component); using the POS model, the shock location, (which indicates the size of the Compton cloud) is obtained; from the QPO using the transonic flow solution $\alpha_{SK}$ (in the sub-Keplerian component) is obtained. Such investigation of several black hole candidates with outbursting properties during both rising and declining phases led to some interesting results which were published in [33]. We elaborate those understandings here.

In [8] and references therein, topology of the accretion flow was shown to change with $\alpha$. Particularly, the concept of $\alpha_{cr}$ was introduced which would separate flow solutions in sub-Keplerian and Keplerian components. Spectral states are determined by the radiation from these components and hence, $\alpha$ clearly plays a crucial role in determination of various spectral states and their transitions. Roy

and Chakrabarti [43] have demonstrated that Keplerian disk form easily in the rising phase due to higher viscosity. But due to withdrawal of viscosity, the matter accretion rates do not vary in the same timescale. Assuming that the viscosity enhancement is responsible for high accretion rates close to the inner disk edge, we found that there is certain minimum value of viscosity required from spectral state transition.

## 2 Calculations

We found various values of $\alpha_{SK}$, the viscosity parameter in the sub-Keplerian component for all observations of rising or declining phase of the outbursts of various sources. In this undertaking, we follow TCAF paradigm. During the quiescent stage, stronger shocks form comparatively far from the central object resulting in large CENBOL (CENtrifugal pressure supported BOundary Layer). As viscosity changes, the shocks weaken (compression ratios at shocks drop) and the shock location decreases likewise. This results in decrease in CENBOL size. The Comptonizing role of the CENBOL diminishes and hence, the spectral state of the source changes from HS $\rightarrow$ HIMS $\rightarrow$ SIMS. The first of such transitions, HS$\rightarrow$HIMS marks the triggering of the outburst. As the process ensues gradually, a time is reached when such shock vanishes completely resulting in a complete SS. Full outburst is said to have occurred. Depending on the phenomena responsible for viscosity enhancements, these rising phase transitions might be incomplete. After sufficient matter is flushed in and the viscosity values go back to lower number, the states backtrack to HS again. During this overall rising/declining phase, using cooling at the shock due to inverse Comptonization obtained from the fitted spectra, $\alpha_{SK}$ was calculated. Such method was used in [33] based on earlier works [7, 8, 10, 27].

For a comparative study, $\alpha_K$ was also calculated for each case [33, 36]. As mentioned earlier, during the rising phase of the outbursts, Keplerian accretion rates were found to peak few days after sub-Keplerian rates peak. If we assume that both these components started from the outer edge of the disk at the same time and sub-Keplerian component takes no time (comparatively) to traverse the disk, then it becomes safe to consider this peak to peak time delay as the viscous infall time of the Keplerian component. This key assumption was used in our $\alpha_K$ calculations.

### *2.1 $\alpha_{SK}$ Calculation*

The formalism for the calculation of $\alpha_{SK}$ is borrowed from the work of [33]. The discussions in this chapter summarise most of the results from this work. To calculate QPO frequency using shock location $X_s$, we use the relation $\nu_{QPO} = M_{BH} \times 10^{-5}/[R\ X_s(X_s - 1)^{1/2}]$, where $R$ is shock compression ratio [11] and

$M_{BH}$ is the mass of the central black hole. For the details of the calculation of $\alpha_{SK}$ for a given cooling such that the observed QPO matches with theoretical value, the readers are referred to [33]. During such a calculation of $\alpha_{SK}$, only physical parameters obtained from basic input parameters using observed values of QPO frequencies viz. $a$, $v$ and $X_s$ were used.

### 2.2 $\alpha_K$ Calculation

We use the approach described in [36]. We obtain viscous timescale as $t_{visc} \approx \frac{r^2}{\alpha_K a h} \approx \frac{r^{1/2}(r-1)}{\alpha_K (\frac{h}{r})^2}$, [42] where the ratio,

$$\frac{h}{r} = 2.4 \times 10^{-3} \alpha_K^{\frac{-1}{10}} \dot{M}^{\frac{3}{20}} m^{\frac{-3}{8}} r^{\frac{1}{8}} r_*^{\frac{1}{8}} f^{\frac{3}{5}},$$

[20] and, $\alpha_K$, $a$, $r$ and $h$ stand for the Keplerian viscosity parameter, the adiabatic sound speed, radius of the outer edge and the scale height of the accretion disk (in units of $r_* = \frac{Gm}{c^2}$) respectively. $\dot{M}$ is accretion rate in the units of $10^{17}$ erg s$^{-1}$, $m$ is mass of the black hole (in solar mass units) and $f = \left(1 - \frac{1}{r^{\frac{1}{2}}}\right)^{\frac{1}{4}}$. We calculate $t_{visc}$ for multiple values of $\alpha_K$ until the calculated value matches the observed viscous timescale (gap between Keplerian and sub-Keplerian accretion rate peaks).

### 2.3 $\alpha_{cr}$ Calculation

Nagarkoti and Chakrabarti [36] have described a method to estimate $\alpha_{cr}$ which we follow here. We create a database using the values of possible $X_s$ all over the parameter space and integrate inwards from the shock location to find the infall timescale, $t_{infall} = \int dt = \int \frac{dx}{v}$. We then use the formalism [30] to calculate QPO frequencies. The relation is, $\nu_{QPO} = \frac{1}{t_{QPO}} = \frac{1}{t_{infall}}$. Then, we select all QPO values and $X_s$ relevant for the particular outburst of interest and the maximum $\alpha$ thus found is $\alpha_{cr}$ for the specific case.

## 3 Results

We selected five different outbursting sources with different masses (of overall range of LMXBs). This selection was also based on the availability of earlier TCAF analysis of outbursts such that above anticipated calculations could be carried out. The details of the selected sources are given in Table 1.

**Table 1** Details about the selected sources

| Source | Mass $M_{\odot}$ | Distance kpc | $i$ degree | Orbital period (h) | Outburst year | Spectral *states*[a] | Discovery year |
|---|---|---|---|---|---|---|---|
| GRO J1655-40 | $7.02 \pm 0.22$[1] | $3.2 \pm 0.2$[2] | $69.5 \pm 0.1$[1] | $62.920 \pm 0.003$[3] | 2005 | HS, HIMS, SIMS | 1994[4] |
| H 1743-322 | 9.0–13.0[5] | $8.5 \pm 0.8$[6] | $75 \pm 3$[6] | – | 2010 | HS, HIMS, SIMS | 1977[7,8] |
| MAXI J1543-564 | 12.6–14.0[9] | 8.5[10] | – | – | 2011 | HIMS, SIMS | 2011[11] |
| MAXI J1836-194 | 7.5–11.0[13] | $7 \pm 3$[14] | 4–15[14] | $< 4.9$[14] | 2011 | HS, HIMS | 2011[12] |
| MAXI J1659-154 | 4.7–7.8[15,16] | $8.6 \pm 3.7$[17] | $70 \pm 10$[17] | $2.414 \pm 0.005$[17] | 2010 | HS, HIMS, SIMS | 2010[18] |

References: (1) Orosz and Bailyn [40], (2) Hjellming and Rupen [22], (3) van der Hooft et al. [51], (4) Zhang et al. [53], (5) Pétri [41], (6) Steiner et al. [49], (7) Kaluzienski and Holt [24], (8) Doxsey et al. [18], (9) Chatterjee et al. [13], (10) Stiele et al. [50], (11) Negoro et al. [38], (12) Negoro et al. [39], (13) Jana et al. [23], (14) Russell et al. [44], (15) Molla et al. [34], (16) Yamaoka et al. [52], (17) Kuulkers et al. [25], (18) Mangano et al. [26]

[a]Observed spectral states Adopted from Mondal et al. [33]

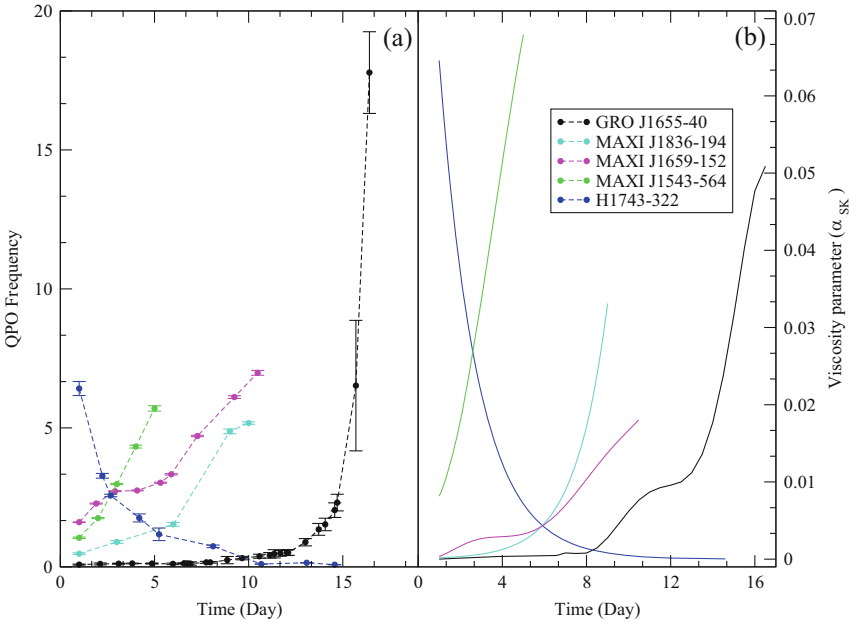



**Fig. 1** Variation of (**a**) QPO frequency with days during different outbursts of the candidates, obtained from observation (circles) and analytical solution (dashed lines), and (**b**) viscosity parameter ($\alpha_{SK}$) with time (in day) during the outburst of the BHCs are shown. Adopted from [33]

The generalization of the overall findings shown in Fig. 1 is that $\alpha_{SK}$ in the sub-Keplerian component was always $< 0.008$ in pure HS. It took values in the range of 0.008–0.035 in HIMS and 0.035–0.01 in SIMS. Values of about 0.01 are expected during SS. On the basis of such calculations, Fig. 2 was obtained which implies that 0.008, 0.035 and 0.01 are the $\alpha_{SK}$ values at spectral state transitions HS→HIMS, HIMS→SIMS and SIMS→SS respectively. Values of $\alpha_{cr}$ and $\alpha_K$ were calculated as well. The parameters used and sources are enlisted in Table 2. These helped us verify $\alpha_{SK} < \alpha_{cr} < \alpha_K$. Giri and Chakrabarti [21] found that super-critical viscosity in equatorial plane led to de-segretation of the accretion flow into TCAF. This work led to numerical verification of the theoretical understanding expressed in [9]. With above observational verification of the same, the TCAF paradigm appears to be very close to describing the black hole accretion process accurately.

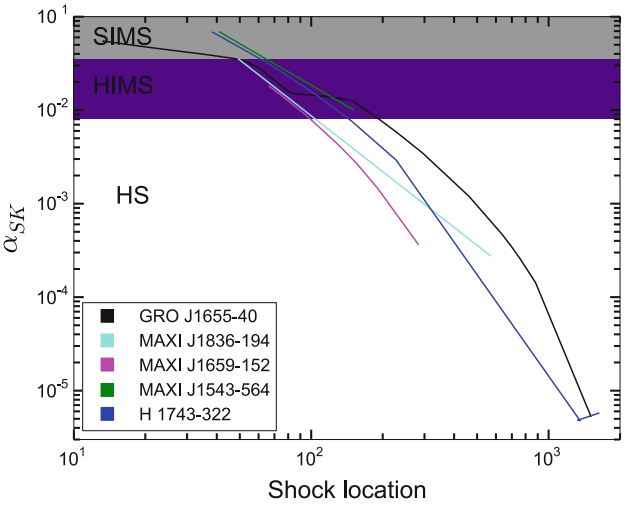



**Fig. 2** Variations of $\alpha_{SK}$ with shock location are shown. The lines are for MAXI J1543-564 (top green); H 1743-322 (second top blue); GRO J1655-40 (middle black); MAXI J1836-194 (last but bottom light blue); MAXI J1659-152 (bottom magenta). Adopted from [32]

**Table 2** Parameters and calculated $\alpha_K$ values

| Source | $m$ ($M_\odot$) | $\dot{m}_d$ ($\dot{M}_{Edd}$) | $t_{visc}$ (days) | $\alpha_K$ | $\alpha_{cr}$ | $\alpha_{SK}$ |
|---|---|---|---|---|---|---|
| H 1743-322 | 11.4 | 3.600 | 13.6 | 0.18 | 0.13 | 0.068 |
| GRO J1655-40 | 7.02 | 1.740 | 7.3 | 0.25 | 0.16 | 0.018 |
| MAXI J1543-564 | 13.2 | 0.656 | 7.7 | 0.29 | 0.14 | 0.055 |
| MAXI J1836-194 | 8.0 | 2.395 | 10.0 | 0.18 | 0.11 | 0.068 |
| MAXI J1659-154 | 6.0 | 1.328 | 7.2 | 0.22 | 0.10 | 0.035 |

References: Mondal et al. [31], Orosz and Bailyn [40], Debnath et al. [15], Chatterjee et al. [13], Jana et al.[23], Molla et al. [34]
Adopted from Mondal et al. 2017[33]

## 4 Discussion

The conjecture of enhancement of viscosity being responsible for triggering outbursts around black holes has been strengthened in this paper with several evidences. Early works such as the limit cycle model of dwarf novae outbursts [4] assume that the accreting gas accumulates in quiescence and then suddenly accretes onto the central object during outbursts (e.g., [4]). In outbursting black hole sources the main triggering is done by enhancement of viscosity such that higher viscosity ([11, 14] and references therein) removes piled up matter then rushes to the black hole causing an outburst. This continues until the stored, piled up matter is exhausted. At the low

density quiescent state, there is advective flow with a shock and the Keplerian disk remains at the piling radius. With the rise of viscosity, the Keplerian disk enters inside the piling radius and eventually high density soft states are produced. When viscosity does not exceed the critical value, the Keplerian disk will not form, the soft-intermediate state or the soft state may not be seen. When the storage of matter at the piling radius is exhausted, viscosity is also reduced and the Keplerian disk previously formed at the piling radius is washed out by the interaction with the advective component. This has been reported to take a long time and decide the duration of the soft state [43] during which the flux steadily decreases. However, the soft-intermediate state in the rising phase is decided by the viscous time to create the Keplerian disk. Hence, when studying the size of the Keplerian disk, the duration of the soft-intermediate states in the rising and declining phases along with the soft state can become a good indicator. Total amount of accumulated matter at the piling radius is guided by two physical processes: the steady transfer of matter from the companion through the Roche Lobe superposed by anomalous rate due to the intrinsic (magnetic or otherwise) activity of the companion. This modulation of supply rate of matter could be due to companion's activity.

Overall, an estimate for $\alpha_{SK}$ values during spectral state transitions are now available. An extension to this work is warranted so as to check how stringent these limits are. Besides, the number (five) of outbursts studied is very small and similar study of many more similar cases needs to be carried out to establish the mechanism discussed above. The most important of all such state transitions is HS→HIMS (or SIMS). This transition practically marks the start of the outbursts.

## References

1. Belloni, T., Homan, J., Casella, P., et al.: A&A **440**, 207 (2005)
2. Bhattacharjee, A., Banerjee, I., Banerjee, A., Debnath, D., Chakrabarti, S.K.: MNRAS **466**, 1372 (2017)
3. Bisnovatyi-Kogan, G.S., Blinnikov, S.I.: A&A **59**, 111 (1977)
4. Cannizzo, J.K.: In: Wheeler J.C. (ed.) Accretion Disks in Compact Stellar Systems, vol. 6 (C93a). World Scientific, Singapore (1993)
5. Cannizzo, J.K., Chen, W., Livio, M.: ApJ **454**, 880 (1995)
6. Cannizzo, J.K., Still, M.D., Howell, S.B., Wood, M.A., Smale, A.P.: ApJ **725**, 1393 (2010)
7. Chakrabarti, S.K.: ApJ **347**, 365 (1989)
8. Chakrabarti, S.K.: Theory of Transonic Astrophysical Flows. World Scientific, Singapore (1990)
9. Chakrabarti, S.K., Titarchuk, L.G.: ApJ **455**, 623 (1995)
10. Chakrabarti, S.K., Manickam, S.G.: ApJ **531**, L41 (2000)
11. Chakrabarti, S. K., Nandi, A., Debnath, D., et al.: IJP **79**, 841 (2005). arXiv:astro-ph/0508024
12. Chakrabarti, S.K., Debnath, D., Nagarkoti, S.: MNRAS (2018, under review)
13. Chatterjee, D., Debnath, D., Chakrabarti, S.K., Mondal, S., Jana, A.: ApJ **827**, 88 (2016)
14. Dutta, B.G., Chakrabarti, S.K., Pal, P.S.: AIPC **1053**, 165 (2008)
15. Debnath, D., Chakrabarti, S.K., Nandi, A., et al.: BASI **36**, 151 (2008)
16. Debnath, D., Chakrabarti, S.K., Nandi, A., et al.: AdSpR **52**, 2143 (2013)
17. Debnath, D., Chakrabarti, S.K., Mondal, S.: MNRAS **440**, L121 (2014)

18. Doxsey, H., Bradt, G., Fabbiano, R.: IAU Circ., 3113 (1977)
19. Fender, R.P., Belloni, T.M., Gallo, E.: MNRAS **355**, 1105 (2004)
20. Frank, J., King A., Raine, D.: Accretion Power in Astrophysics, 3rd edn. Cambridge University Press, New York (2002)
21. Giri, K., Chakrabarti, S.K.: MNRAS **430**, 2836 (2013)
22. Hjellming, R.M., Rupen, M.P.: Nature **375**, 464 (1995)
23. Jana, A., Debnath, D., Chakrabarti, S.K., et al.: ApJ **819**, 107 (2016)
24. Kaluzienski, L.J., Holt, S.S.: IAU Circ., 3104 (1977)
25. Kuulkers, E., Kouveliotou, C., Belloni, T., et al.: A&A **552**, 32 (2013)
26. Mangano, V., Baumgartner, W.H., Cummings, J.R., et al.: GCN, 11294 (2010)
27. Matsumoto, R., Kato, S., Fukue, J., Okazaki, A.T.: PASJ **36**, 71 (1984)
28. McClintok, J. E., Remillard, R.A.: arXiv:astro-ph/0306213 (2006)
29. Meyer, F., Meyer-Hofmeister, E.: A&A **132**, 143 (1984)
30. Molteni, D., Sponholz, H., Chakrabarti, S.K.: ApJ **457**, 805 (1996)
31. Mondal, S., Debnath, D., Chakrabarti, S.K.: ApJ **786**, 4 (2014)
32. Mondal, S., Chakrabarti, S.K., Debnath, D.: ApJ **798**, 57 (2015)
33. Mondal, S., Chakrabarti, S.K., Nagarkoti, S.: ApJ **850**, 47 (2017)
34. Molla, A.A., Debnath, D., Chakrabarti, S. K., et al.: MNRAS, **460**, 3163 (2016)
35. Nagarkoti, S., Chakrabarti, S.K.: ApJ **816**, 7 (2016)
36. Nagarkoti, S., Chakrabarti, S.K.: MNRAS **462**, 850 (2016)
37. Nandi, A., Debnath, D., Mandal, S., et. al.: A&A **542**, 56 (2012)
38. Negoro, H., Nakahira, S., Ueda, Y., et al.: ATEL, 3330 (2011)
39. Negoro, H., Nakajima, M., Nakahira, S., et al.: ATEL, 3611 (2011)
40. Orosz, J., Bailyn, C.: ApJ **477**, 876 (1997)
41. Pétri, J.: Ap&SS **318**, 181 (2008)
42. Pringle, J.E.: ARA&A **19**, 137 (1981)
43. Roy, A., Chakrabarti, S.K.: MNRAS **472**, 4689 (2017)
44. Russell, T. D., Soria, R., Motch, C., et al.: MNRAS **439**, 1381 (2014)
45. Shakura, N.I., Sunyaev, R.A.: A&A **24**, 337 (1973)
46. Sunyaev, R.A., Titarchuk, L.G.: A&A **86**, 121 (1980)
47. Sunyaev, R.A., Titarchuk, L.G.: A&A **143**, 374 (1985)
48. Smak, J.: Acta. Astron. **34**, 161 (1984)
49. Steiner, J.F., McClintock, J.E., Reid, M.J.: ApJL **745**, L7 (2012)
50. Stiele, H., Munoz-Darias, T., Motta, S., Belloni, T.M.: MNRAS **422**, 679 (2012)
51. van der Hooft, F., Heemskerk, M. H. M., Alberts, F., van Paradijs, J.: A&A **329**, 538 (1998)
52. Yamaoka et al.: PASJ **64**, 32 (2012)
53. Zhang, S.N., et al.: IAU Circ., 6046 (1994)

# Formation of Two Component Flows by Numerical Simulations Around Black Holes




**Kinsuk Giri**

**Abstract** In this article, the results of our numerical simulations of a transonic flow having various viscosity parameters and cooling processes are discussed. In our simulation, for each of the cases, the sub-Keplerian matter is injected at outer boundary. Advection of matter towards a black hole is allowed. As a result, we got a complete solution in which the meridional part behaves like a thin and cool Keplerian disk. However, the other part which is away from the equatorial plane behaves like a transonic flow with standing and oscillating shocks. Finally, we observed that, our solution is consistent with the Chakrabarti-Titarchuk two-component advective flow configuration as the flow approaches to a black hole.

## 1 Introduction

Unlike other astronomical objects, accretion disks are made of rapidly rotating gas which spirals slowly onto a central gravitating object (such as the black holes, neutron stars, white dwarfs etc). The releasing of gravitational energy of the infalling mass in accretion disks is one of the most important mechanism for astronomical objects to get powered. So, the accretion of matter onto compact massive stars is the source of the observed X-rays and gamma-rays. As black holes are actually 'black', there could not be any direct observational evidence of them. The only way to observe a black hole is to analyze radiations emitted by accreting matter or in broadly 'accretion process' around the same black hole. To study on accretion process, it is very significant to study the hydrodynamics of the flow as it emits radiation that is detected by various telescopes. Hydrodynamic properties of the matter come from the basic fluid equations, viz, continuity equation, momentum conservation equations and energy equations. Thus, we got a boundary value problem (BVP) from the system of equations. However, in each of the cases, it is not

K. Giri (✉)
National Institute of Technical Teachers' Training and Research, Salt Lake, Kolkata, India
e-mail: kinsuk@nitttrkol.ac.in

© Springer International Publishing AG, part of Springer Nature 2018

B. Mukhopadhyay, S. Sasmal (eds.), *Exploring the Universe: From Near Space to Extra-Galactic*, Astrophysics and Space Science Proceedings 53,
https://doi.org/10.1007/978-3-319-94607-8_11

possible to solve all simultaneous equations analytically. Therefore, it is necessary to use several numerical methods to solve these equations. This is the cause that how numerical simulation is important to study this subject. Since last three decades, many numerical simulations have been done on accretion process around a black hole.

One of the significant contributions in the theory of accretion process was made by Shakura and Sunyaev in 1973 [24], hereafter SS73, which is widely known as the 'Keplerian disc' successfully explaining the multi-colour black body component of the spectrum observed in galactic and extra-galactic systems. In SS73 the so-called $\alpha$-parameter was first proposed to measure the turbulent viscosity. Later, Lynden-Bell and Pringle [3], Pringle [22] etc. analytically did several works on the basis of SS73 model. However, unfortunately SS73 disc is unable to produce power-low emissions commonly observed at the higher energy band. Various ad-hoc models for hot accretion disc are given by various groups to explain the power-law component. In this regard, in 1995, Chakrabarti and Titarchuk (hereafter CT95), however, nicely explained the spectra using a global *solution*. In this global solutionn (CT95) they mentioned about a sub-Keplerian flow that produces a centrifugal barrier close to a black hole and surrounds an SS73 disc which is corrected at the inner edge of the disc, which plays a key role. Later, many workers including [4, 9, 20, 25–28] and others found evidences of two components in many of the black hole candidates.

On the theoretical and numerical side, in order to incorporate viscosity in huge amount, the so-called turbulent or $\alpha$-viscosity has been implemented successfully to several numerical works on accretion processes, viz. Robertson and Frank [23], Chakrabarti [5, 6], Chakrabarti and Molteni [7], McKinney and Narayan [19], Igumenshchev et al. [15], Yuan et al. [29], Kumar and Chattopadhyay [16], Giri and Chakrabarti [10] (hereafter GC12), Giri et al. [13], Das et al. [8].

The basic issue is that due to centrifugal barrier of an inviscid flow shocks form close to a black hole. This shock slowly becomes weaker and ultimately disappears as the viscosity is larger than it's critical value. This was predicted in theoretical models, but it was needed to see that this is the case, through numerical simulations. We emphasize on the injection of sub-Keplerian (low angular momentum) flow which others emphasize on injecting near Keplerian flow. So the results are totally different. They produce Keplerian disc, we produce sub-Keplerian puffed up torus unless the viscosity is very high. In this present article, based on my two published papers, viz., Giri and Chakrabarti [10] and Giri et al. [13], I will discuss the effects of viscosity and cooling in transonic flows.

## 2 Model Equations with Viscosity and Cooling

In all of our simulations, an axisymmetric flow around a Schwarzschild black hole in two dimensions has been considered. In the place of general relativity, we use the well known pseudo-Newtonian potential which is given by Paczyński and Wiita

([21], hereafter PW80) . In order to implement the geometry, we use the cylindrical polar coordinates $(r, \phi, z)$. The set of equations those are used in our system is basic conservation laws, viz., Conservation of Mass, Conservation of Momentum, Conservation of Energy.

Assuming the pseudo-Newtonian potential (PW80), following are the *Euler equations* ([17], hereafter LL59):

$$\rho[\frac{\partial \mathbf{v}}{\partial t} + \mathbf{v}.\nabla \mathbf{v}] = \nabla P + \rho \mathbf{G}, \tag{1}$$

where,

$$\mathbf{G} = -\frac{1}{2(R-1)^2 R}\frac{\mathbf{R}}{R},$$

with the components,

$$G_r = -\frac{1}{2(R-1)^2 R}\frac{r}{R},$$

$$G_z = -\frac{1}{2(R-1)^2 R}\frac{z}{R}.$$

Here, $R = \sqrt{r^2 + z^2}$ in cylindrical coordinate system $(r, \theta, z)$.

In order to add viscosity, we concentrate on the momentum component equations. Explicitly, the $\phi$ component equation is given by,

$$\frac{\partial}{\partial t}(\rho v_\phi) + \frac{1}{r}\frac{\partial}{\partial r}(r\rho v_\phi v_r) = -\frac{\rho v_\phi v_r}{r}. \tag{2}$$

$$\Rightarrow \rho\frac{\partial v_\phi}{\partial t} + \rho v_r\frac{\partial v_\phi}{\partial r} + [v_\phi\frac{\partial \rho}{\partial t} + \rho v_\phi\frac{\partial v_r}{\partial r} + \frac{\rho v_\phi v_r}{r}] = -\frac{\rho v_\phi v_r}{r}. \tag{3}$$

From the continuity equation (1) we obtain,

$$\frac{\partial \rho}{\partial t} + \frac{1}{r}\frac{\partial}{\partial r}(r\rho v_r) = 0,$$

$$\Rightarrow v_\phi\frac{\partial \rho}{\partial t} + \rho v_\phi\frac{\partial v_r}{\partial r} + \frac{\rho v_\phi v_r}{r} = 0. \tag{4}$$

Replacing (4) in (3), we have

$$\rho\frac{\partial v_\phi}{\partial t} + \rho v_r\frac{\partial v_\phi}{\partial r} = -\frac{\rho v_\phi v_r}{r}. \tag{5}$$

As in [2], the general form of the equations of the flow is given by

$$\rho[\frac{\partial \mathbf{v}}{\partial t} + \mathbf{v}.\nabla \mathbf{v}] = -\nabla P + \mathbf{F_b} + \nabla.\tau, \tag{6}$$

where, $\mathbf{v}$ be the flow velocity, $\rho$ represents fluid density, $P$ is pressure, $\boldsymbol{\tau}$ is represented by stress tensor, and $\mathbf{F_b}$ is denoted as body forces per unit volume acting on the flow and $\nabla$ represents the square of gradient operator.

Now, in cylindrical coordinates, the $\phi$-component of Navier-Stokes equation (LL59 and [1]) is given by

$$\rho[\frac{\partial v_\phi}{\partial t} + v_r\frac{\partial v_\phi}{\partial r} + \frac{v_\phi v_r}{r} + \frac{v_\phi}{r}\frac{\partial v_\phi}{\partial \phi} + v_z\frac{\partial v_\phi}{\partial z}] =$$

$$-\frac{1}{r}\frac{\partial P}{\partial \phi} + \mu[\frac{\partial^2 v_\phi}{\partial r^2} + \frac{1}{r}\frac{\partial v_\phi}{\partial r} - \frac{v_\phi}{r^2} + \frac{1}{r^2}\frac{\partial^2 v_\phi}{\partial \phi^2} + \frac{\partial^2 v_\phi}{\partial z^2} + \frac{2}{r^2}\frac{\partial v_\phi}{\partial \phi}] + F_\phi, \tag{7}$$

where $\mu$ is denoted as dynamic viscosity defined by $\mu = \eta\rho$ and $\eta$ is called the kinematic viscosity. Here, $F_\phi$ is so-called body force. As we have chosen the axisymmetric case, we have neglected the terms with $\frac{\partial}{\partial \phi}$. Thus, $F_\phi = \rho G_\phi$. However, for the axisymmetric case, $G_\phi = 0$ and, thus, $F_\phi = 0$. In our system, we integrate along $r$ as well as the $z$ direction separately, not simultaneously. Considering the $r$ direction first, Eq. (7) takes the form

$$\rho\frac{\partial v_\phi}{\partial t} + \rho v_r\frac{\partial v_\phi}{\partial r} = -\frac{\rho v_\phi v_r}{r} + \mu[\frac{\partial^2 v_\phi}{\partial r^2} + \frac{1}{r}\frac{\partial v_\phi}{\partial r} - \frac{v_\phi}{r^2}]. \tag{8}$$

Therefore, the viscous term for this equation is

$$\mu[\frac{\partial^2 v_\phi}{\partial r^2} + \frac{1}{r}\frac{\partial v_\phi}{\partial r} - \frac{v_\phi}{r^2}]. \tag{9}$$

We can write this term as ([18])

$$\frac{1}{r^2}\frac{\partial}{\partial r}(r^2\tau_{r\phi}), \tag{10}$$

where

$$\tau_{r\phi} = \mu r\frac{\partial \Omega}{\partial r}. \tag{11}$$

Here, $\Omega$ is angular velocity and defined as

$$\Omega = \frac{v_\phi}{r}.$$

Initially, in our cases, we start with a simple power-law cooling with a cooling rate of

$$\Lambda_{br} = 1.4 \times 10^{-27}\,\mathrm{N}^2(r,z)T^{\beta}(r,z)\,\mathrm{erg\,cm^{-3}\,s^{-1}}, \tag{12}$$

where $N(r,z)$ is represented as number density and $T(r,z)$ is flow-temperature at $(r,z)$. Also, it is clear that for $\beta = 0.5$, this formula reduces to bremsstrahlung cooling which is well known to us. At any $(r,z)$, the gas temperature is given by

$$T = \frac{p}{\rho}\frac{\mu m_p}{k_b}, \tag{13}$$

where, $k_b$ = Boltzmann constant, $\mu = 0.5$, for purely hydrogen gas. At the beginning of the run of our simulations, in our cases, in order to increase cooling efficiency, $\beta$ is chosen as 1.0.

## 3 Our Simulation Setup

The setup of our simulation is presented in [10–12]. We will not repeat those here. Please, go through these papers for details. In order to describe the gravitational field of the black hole, to mimic the effects of general theory of relativity, as mentioned earlier, the so-called pseudo-Newtonian potential (PW80) is used. The potential term in the form of PW80 is given by,

$$\phi(r,z) = -\frac{GM_{BH}}{(R - R_g)}, \tag{14}$$

where, $R = \sqrt{r^2 + z^2}$.

The main cause of obtaining shocks or no shocks in any kind of accretion flow simulations depends on the way the boundary conditions are selected. In various simulations, some groups mainly concentrated on the time evolution of the flow injected with almost Keplerian rotation. The free outflow boundary condition was used there. The injected matter had zero radial and zero vertical components of velocity, and approximately the Keplerian angular velocity. However, the flows mentioned above do not have energy to become supersonic, so no question of any shock formation.

The above stated hydrodynamic equations are numerically solved by using a grid based a finite difference method. This method is developed on the basis of Total Variation Diminishing (TVD). In mathematical context TVD concept was originally developed by Ami Harten on 1983 [14].

## 4 Concept of Critical Viscosity Parameter: Simulation Results

Initially, during the several runs of our simulations, the outer boundary of the simulation grid is chosen at $r = 50$. Even if we chose very far, say $300r_g$, the result would be the same. The point is that when the Rankine-Hugoniot condition cannot be fulfilled, the shock will propagate to infinity. Only the sub-sonic and Keplerian flow will remain. This is our well known Shakura-Sunyaev disc. On the way the shock will be stuck at the numerical boundary, since boundary condition is not dynamically changed to let the shock pass through. That is why we do not see the complete disappearance of the shocks. For this case, we have taken the specific angular momentum ($\lambda = 1.66$) and the specific energy $= 0.0035$. Let us discuss a few important results.

In Fig. 1a, b Mach number and density distributions of the flow are shown respectively along radial direction at equatorial plane. For the curves as in Fig. 1a, b the values of $\alpha$ are (left to right in Fig. 1a and bottom to top in Fig. 1b, respectively): 0.0, 0.0175, 0.035, 0.0525, 0.06125, 0.07, 0.0735. Theoretically when the viscosity is high enough there is no way the Rankine-Hugoniot conditions can be satisfied (C90). So above the critical viscosity the shock has to move away to infinity and only the sub-sonic flow is left behind. In a numerical simulation the boundary is at a finite distance and the injected flow itself is supersonic, so this 'actual disappearance' cannot be seen. As there will always be a Mach number jump near the boundary. It requires a dynamical boundary condition to avoid such problems. However, this does not affect the outcome of the simulation. We see that the shock moves out as

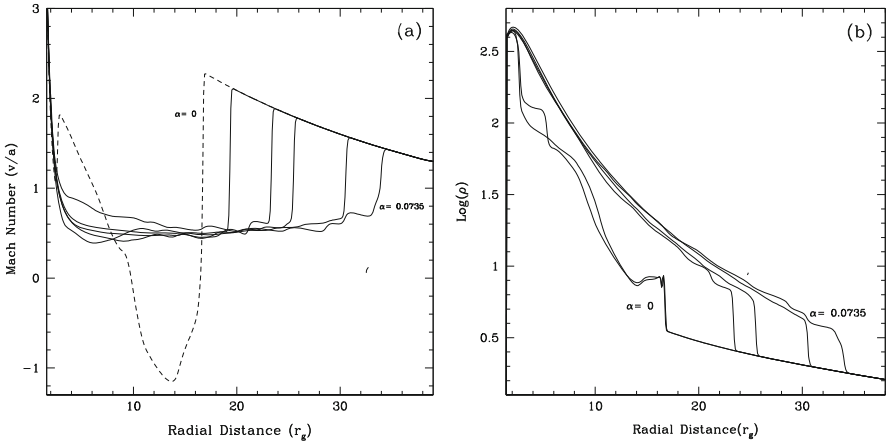



**Fig. 1** Radial variation of (**a**) Mach number and (**b**) density in a viscous transonic flow on the equatorial plane. For details regarding parameters and others please see text [10]

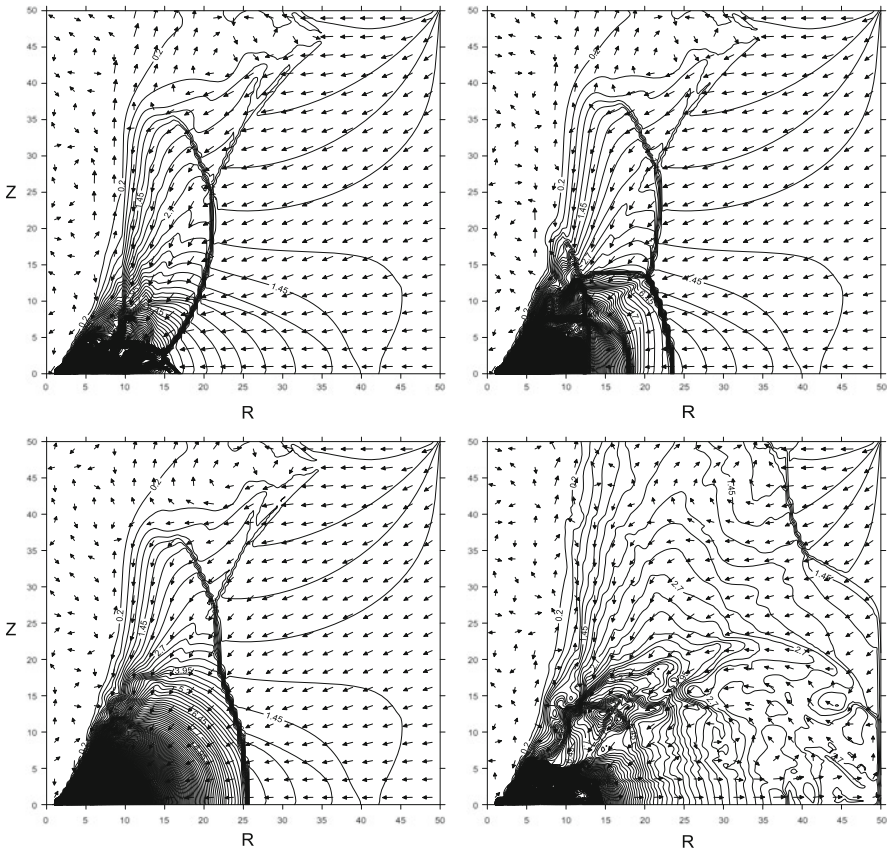



**Fig. 2** Variations in the density and velocity distribution when viscosity varies. Here, densities are in normalized unit, radius and velocity are in Schwarzschild unit. For details see the text [10]

$\alpha$ increases and it gets weaker and weaker. To actually show the disappearance one has to keep a boundary very far and with a sub-sonic injection.

In Fig. 2, we show density of matter and the velocities vary with viscosity. The results are for $t = 24.75$ s and $\alpha = 0.0$ (a: top left), 0.0525 (b: top right), 0.0735 (c: bottom left) 0.074 (d: bottom right) respectively. The contour having minimum density has $\rho_{min} = 0.2$. The maximum density is (a) $\rho_{max} = 450$, (b) $\rho_{max} = 395$, (c) $\rho_{max} = 354$ and (d) $\rho_{max} = 286$. The contour interval is $\delta\rho = 0.25$. In our all cases with near constant angular momentum, $v_\phi$ goes as $\frac{1}{r}$, and thus the differential motion is more than that in a Keplerian disc where $v_\phi$ goes as $\frac{1}{r^{1/2}}$.

## 5 Numerical Simulations of Formation of Keplerian Disc from Sub-Keplerian Halo

In this study [13], we started our simulation with a power-law cooling term which is analogous to bremsstrahlung. As soon as optically thick disc starts forming i.e., a single component flow starts segregating in two components, we assume cooling due to black body emission from the surface of optically thick component, whereas optically thin advective flow continues to cool with power-law cooling term. In this case, we did not consider the Compton scattering of the black body photons, emitted from the cold disc surface, by the hot sub-Keplerian flow.

We have run several cases. We will present a standard case where the parameters are chosen as following. The specific energy $\mathcal{E} = 0.001$ in unit of $c^2$, the specific angular momentum $\lambda = 1.70$ in unit of $r_g c$, At the outer boundary of the simulation box, the matter injection rate is assumed as $\dot{M} = 2.0$. This accretion rate is measured in the units of mass Eddington rate, the value of this rate is $1.44 \times 10^{17} M_{BH}$ gm/s. Also, we select for this case the value of viscosity parameter, a dimensionless number $\alpha = 0.012$.

We assume that optically thick disc emits black body emission as is in the case of a standard disc (SS73). We do not explicitly track each and every photon and Comptonize it till it is diffused from the surface to the hot halo region as a black body photon. That would be tremendously time consuming. Instead, in our simulation, we compute optical depth of accretion flow along vertical direction starting from infinity to the equatorial plane. As soon as we find a sudden increase in optical depth, we know the optically thick disc has formed and we assume black body cooling from that surface. Thus we effectively replace the property inside an optically thick disc by its surface property. This surface is clearly dynamically obtained and is automatically changing.

In Fig. 3, we compare the distribution of simulated specific angular momentum at $r - z$ plane and corresponding Keplerian distribution for the same case. Our simulation results are shown in Fig. 3a. In order to analyze at simulated Keplerian disc, in Fig. 3b the close region to the equatorial plane is zoomed while the same is shown in Fig. 3c for theoretical Keplerian distribution in linear scale. Figure 4a shows the velocity variation and density distributions of the flow and Fig. 4b temperature distributions.

The Keplerian disc component that is formed in our simulation is not advection dominated as a slim disc. Its radial velocity is small as in a SSD73 disk. So, our disc temperature distribution should not be affected by advection to show that the temperature distribution in our simulated Keplerian disc is proportional to that of the SSD73 theoretical shape. On the other hand, the temperature distribution for advection dominated hot sub-Keplerian flow is affected by the advection and in our simulation we also found these variations. This is well studied by transonic astrophysical flow work of Chakrabarti and his group. But, in this work we wanted to show how our disk compares with the SS73 disc.

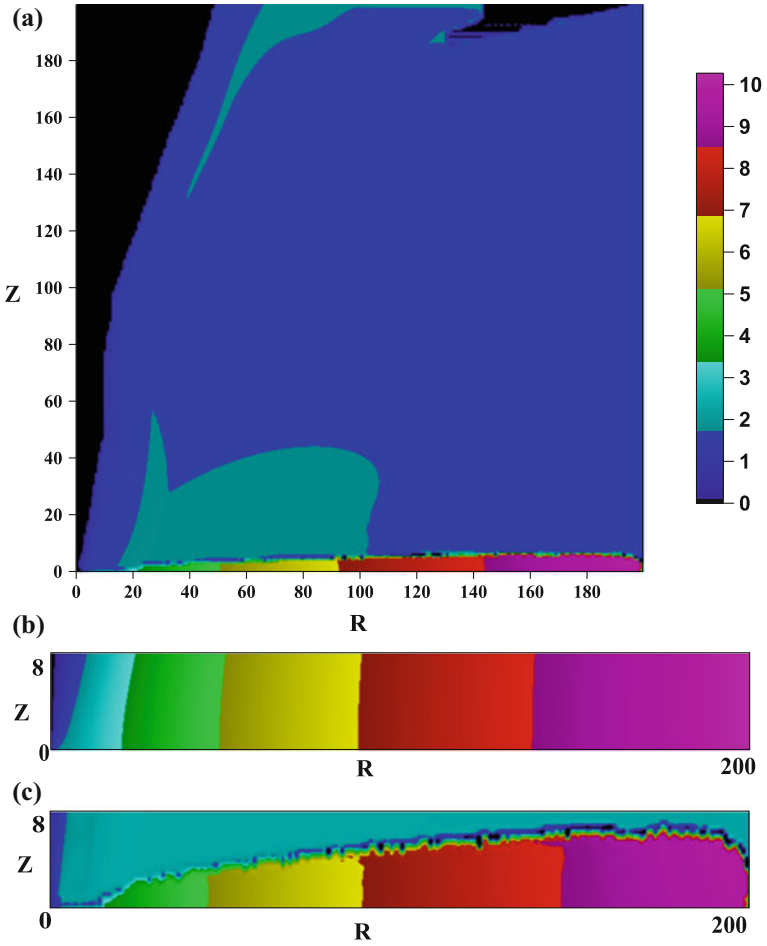



**Fig. 3** (**a**) Specific angular momentum distribution at $r - z$ plane in our simulation (Top panel) for this case. To compare with analytical results, region close to the equatorial plane is zoomed in to show (**b**) distribution in our simulated result, and (**c**) Keplerian distribution [13]

We calculated mass flow rate of hot sub-Keplerian component. In each case, mass flow rate of hot component is a bit lesser than difference between injected mass flow rate and disc rate. The reason of being lesser is loss of matter by the outflow and absorbtion (sucking) of matter by black hole itself. A few percentage of matter is going away from the hot flow as outflows while a very few percentage of hot matter also is being sucked by the black hole. We show that density of matter at the Keplerian disc is extremely high as compared to the density of hot flow although at the beginning of our simulation, entire grid was empty, hence no Keplerian disc was there initially. So, it is evident from our simulation that condensation plays a

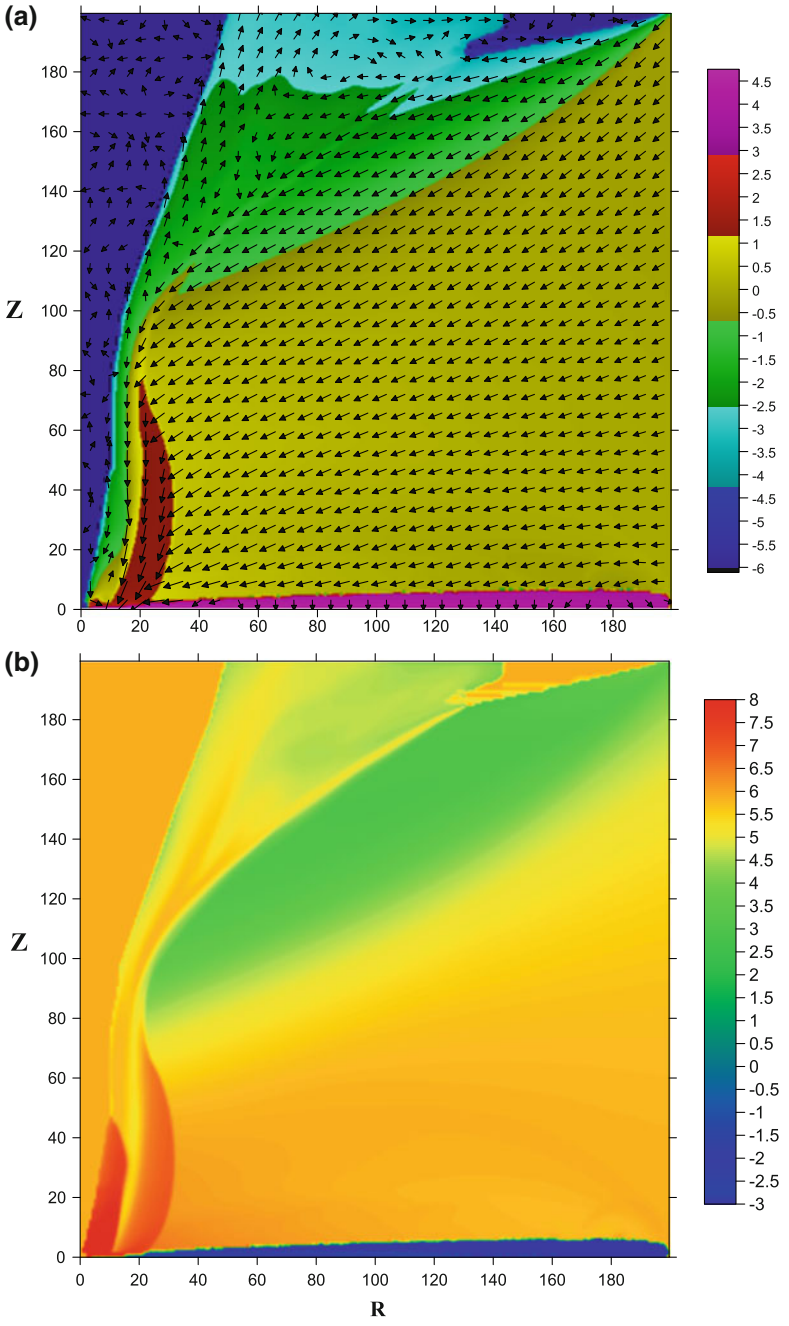



**Fig. 4** (**a**) Density and velocity distributions, and (**b**) temperature distribution in logarithmic scale at $r - z$ plane for this case. Densities in normalized units are shown in logarithmic scale as in the scale on the right. A two component flow is clearly seen [13]

significant role to gradually shift a part of the injected hot flows to the cool Keplerian disc component while the rest part of hot component forms sub-Keplerian flow and the outflow.

## 6 Discussions

Theoretically when the viscosity is high enough there is no way the Rankine-Hugoniot conditions can be satisfied (C90). Therefore, above the critical viscosity the shock has to move away to infinity and only the sub-sonic Keplerian flow is left behind which passes through the inner sonic point. In a numerical simulation, the boundary is at a finite distance and the injected flow itself is supersonic, so this 'actual disappearance' cannot be seen. It requires a dynamical boundary condition to avoid such problems. However, this does not affect the outcome of the simulation. We see that the shock moves out as $\alpha$ increases and it gets weaker and weaker. To actually show the disappearance, one has to keep a boundary very far and with a sub-sonic injection.

In all the problems boundary conditions play a role. What we showed is that when the viscosity is increased, the shock propagates outwards and should have actually left the boundary and go to infinity if it is more than the critical value, otherwise settled in a place outside the boundary. However, since we have chosen a boundary condition where the matter is injected at the outer boundary, it will not allow anything to go out and thus the outgoing shock halts near the boundary, instead of leaving the computational grid.

A standard Keplerian disc forms in two steps: (a) viscosity must be sufficiently high to produce a Keplerian distribution, and (b) cooling must be sufficiently efficient to enhance optical depth so that it emits a black body locally. Initially in our simulation the whole gas is assumed to be hot and sub-Kepelerian. But, gradually, due to cooling, a part of injected hot flow condenses at the equatorial plane. On the other hand, turbulent viscosity transports angular momentum so that the new born condensed flow achieves the Keplerian angular momentum distribution. As the cooled flow archives a Keplerian angular momentum, its radial velocity goes down. This helps the condensed flow to become more denser. This is a dynamic process.

We calculated the mass flow rate of hot sub-Keplerian component. In each case, the mass flow rate of hot component is a bit lesser than the difference between injected mass flow rate and disc rate. The reason of being lesser is the loss of matter by the outflow and absorbtion (sucking) of matter by black hole itself. A few percentage of matter is going away from the hot flow as outflows, while a very few percentage of hot matter also is being sucked by the black hole. We show that density of matter at the Keplerian disc is extremely high as compared to the density of hot flow, although at the beginning of our simulation, entire grid was empty, hence no Keplerian disc was there initially. Therefore, it is evident from our simulation that condensation plays a significant role to gradually shift a part of the injected hot flows to the cool Keplerian disc component, while the rest part of hot component forms sub-Keplerian flow and the outflow.

From the literature of the formation of accretion disc theory, it is believed that the Maxwell stress in magnetically turbulent accretion disc is several times larger than the turbulent viscous stress which I have used my hydrodynamic simulation. So, we would like to extend my viscous hydrodynamic model to magnetohydrodynamic models. In order to predict the evolution of accretion discs, we will evaluate the angular momentum transport rate more quantitatively through direct 3D magnetohydrodynamics simulations. The ultimate goal is to understand the magnetic field strengths and topologies in the central regions of the accretion disc and how the shocks behave near the event horizon. Our main queries will be following. (a) Are the conclusions based on analytical considerations continued to remain valid for a three dimensional flow? (b) Do the shocks survive for magneto hydrodynamic accretion flows? (c) How does the shock funnel wall shock oscillate in both vertical and horizontal directions ? (d) How does the outflow rate depend on viscosity and magnetic field? (e) How does magnetic field work on the stability of the accretion as well as shock? (f) Finally, how does those affect on calculated spectra? Our future research activities will aim at investigating from all kinds of discs upto AGNs and related physical phenomena by modeling them using the technique of numerical simulations. Till now, we have done this work for a Schwarzschild (non-rotating) black hole. It will be interetsting to find how the simulation results differ for a rotating black hole. With the help of numerical experiments, in near future we will perform it.

It is expected that the effect of magnetic field as well as viscosity together plays an important role of standing and oscillating shocks near black holes. It is a debatable issue in the science community that how angular momentum is transported outward such that the matter can advect towards the central object. In my work, we will specifically differentiate the roles of viscous stress components and magnetic stress components in the accretion disc formation. In future, we will simulate the timing and spectral properties of black hole candidates with the coupling of both hydrodynamics and radiation hydrodynamics. We will also carry out satellite data analysis and use our model to explain observed results. So in future, as we will compare my simulated results with observations, we expect it to reveal many queries in the vogue of this subject.

**Acknowledgements** KG acknowledges Prof. Sandip K. Chakrabarti for introducing him to the fascinating subject of Black Hole Astrophysics and S. N. Bose National Center for Basic Science (SNBNCBS) for financial support during the research.

## References

1. Acheson, D.J.: Elementary Fluid Dynamics. Oxford Applied Mathematics and Computing Science Series. Oxford University Press, Oxford (1990)
2. Batchelor, G.K.: An Introduction to Fluid Dynamics. Cambridge University Press, Cambridge (1967)
3. Bell, B.L., Pringle, J.E.: MNRAS **168**, 603 (1974)

4. Cambier, H.J., Smith, D.M.: ApJ **767**, 46 (2013)
5. Chakrabarti, S.K.: ApJ **347**, 365 (C89) (1989)
6. Chakrabarti, S.K.: Theory of Transonic Astrophysical Flows. World Scientific, Singapore (1990)
7. Chakrabarti, S.K., Titarchuk, L.G.: ApJ **455**, 623 (CT95) (1995)
8. Das S., Chattopadhyay I., Nandi A., Molteni D.: MNRAS **442**, 251 (2014)
9. Dutta, B.G., Chakrabarti, S.K.: MNRAS **404**, 2136 (2010)
10. Giri, K., Chakrabarti, S.K.: MNRAS **421**, 666 (2012)
11. Giri, K., Chakrabarti, S.K.: MNRAS **430**, 2836 (2013)
12. Giri, K., Chakrabarti, S. K., Samanta, M., Ryu, D.: MNRAS **403**, 516 (2010)
13. Giri, K., Garain, S., Chakrabarti, S.K.: MNRAS **448**, 3221 (2015)
14. Harten, A.: J. Comp. Phys. **49**, 357 (1983)
15. Igumenshchev, I.V., Abramowicz, M.A., Narayan, R.: ApJ **537**, 27 (2000)
16. Kumar R., Chattopadhyay, I.: MNRAS **430**, 386 (2013)
17. Landau, L.D., Lifshitz, E.M.: Fluid Mechanics. Pergamon Press, Oxford (1959)
18. Lanzafame, G., Molteni, D., Chakrabarti, S.K.: MNRAS **299**, 799 (1998)
19. McKinney, J.C., Narayan, R.: MNRAS **375**, 513 (2007)
20. Miller, J.M., Wijnands, R., Homan, J., Belloni, T., Pooley, D., Corbel, S., Kouveliotou, C., van der Klis, M., Lewin, W.H.G.: ApJ **563**, 928 (2001)
21. Paczyński, B., Wiita, P.J.: A & A **88**, 23 (1980)
22. Pringle, J.E.: A R A & A **19**, 137 (1981)
23. Robertson, J.A., Frank, J.: MNRAS **221**, 279 (1986)
24. Shakura, N.I., Sunyaev, R.A.: A & A **24**, 337 (SS73) (1973)
25. Smith, D.M., Heindl, W. A., Markwardt, C., Swank, J.H.: ApJ **554**, L41 (2001)
26. Smith, D.M., Heindl, W.A., Swank, J.H.: AAS **33**, 1473 (2001)
27. Soria, R., Risaliti, G., Elvis, M., Fabbiano, G., Bianchi, S., Kuncic, Z.: ApJ **695**, 1614 (2009)
28. Soria, R., Broderick, J. W., Hao, J., Hannikainen, D.C., Mehdipour, M., Pottschmidt, K., Zhang, S.N.: MNRAS **415**, 410 (2011)
29. Yuan, F., Maochun, W., Bu, D.: ApJ **761**, 129 (2012)

# Outbursts in Stellar Black Hole Candidates: A Time-Dependent Study of Viscous Accretion Flow




**Abhishek Roy**

**Abstract** In the accretion process around compact objects, matter needs a considerable amount of viscosity to take away its angular momentum and maintain the flow towards the compact object. There are two components that dominate the accretion flow onto black holes, one having Keplerian angular momentum distribution near equatorial plane, another low angular momentum sub-Keplerian flow surrounding the Keplerian flow. A sudden rise in viscosity in the accretion disk at a very large distance from the compact object is generally responsible for the X-ray outbursts of some stellar mass black holes. When viscosity reduces, the object tends to return to its pre-outburst quiescence stage. We have tried to mimic the rise and fall of viscosity parameter as a part of the outer boundary condition by numerical simulation procedure to study the pattern of formation and disappearance of the Keplerian disk inside an advective halo. We believe that, for the first time, our results are able to simulate the two-component advective flow dynamics during an entire X-ray outburst of a black hole candidate. Also, we see, the hysteresis effect of an outburst is caused mainly for the difference in the time duration in the formation and disappearance of the Keplerian component in the two-component flow.

## 1 Introduction

Numerical simulations help us to understand the behavior of accretion flow around a black hole in real time-scales. Early low angular momentum inviscid flow simulations by Hawley et al. [16] and others [13, 18, 22] indicated the possibility of the formation of shock waves for the rapid rise of centrifugal barrier as matter approaches a black hole. Giri and Chakrabarti [11, 12] and Giri et al. [14] showed the effects of viscosity and cooling on the nature of change in topology. It was also shown that if the ([28], hereafter SS73) viscosity parameter $\alpha$ is above a

A. Roy (✉)
S. N. Bose National Center for Basic Sciences, Kolkata, India
e-mail: abhishek12@bose.res.in

© Springer International Publishing AG, part of Springer Nature 2018

B. Mukhopadhyay, S. Sasmal (eds.), *Exploring the Universe: From Near Space to Extra-Galactic*, Astrophysics and Space Science Proceedings 53,
https://doi.org/10.1007/978-3-319-94607-8_12

critical value, an advective flow with specific pairs of injected parameters (energy and angular momentum per unit mass) can form a standard Keplerian disk which is consistent with the theoretical work for isothermal and adiabatic advective flows [5, 6]. When the viscosity parameter goes down with vertical distance, two component advective flow (TCAF) is obtained where a Keplerian disk is submerged inside a low-angular momentum sub-Keplerian flow. Both Keplerian and halo rates are controlled by the viscosity parameter [6]. There are suggestions from NASA satellite data that TCAF can explain the observed properties of time variation of flux and spectral index [29, 30].

X-ray spectra of black hole candidates are explained by two types of radiations, a soft multi-color thermal blackbody component and a single power-law component produced by Compton scatterings [31, 32]. In the TCAF scenario, the post-shock region behaves as the Compton cloud, responsible for scattering [7]. A black hole candidate in outbursting stage goes through several spectral states such as Hard, Hard-Intermediate, Soft-Intermediate, Soft during its rising phase and in a reverse order in the declining phase [8, 19, 23]. Detailed fitting of spectral data with a TCAF solution shows that both the Keplerian disk and the advective components increase in the rising phase at different rates. In the declining phase, it happens in the other way around. Interestingly, in declining phase, the time scale is found to be much longer than that in rising phase. The dwarf novae outbursts are generally thought to be the result of thermal limit-cycle instability [2–4, 20, 21] where a constant switching of accretion rate between a high and low viscosity level happens for repeated outburst cases. Also, it is believed that outburst in stellar mass black holes occurs due to a sudden rise in turbulence or viscosity. In these cases, the viscosity must be time-dependent and must rise significantly in order to trigger the outburst. As there is no detailed model of viscous transport, it is assumed that for the outburst in dwarf novae, the $\alpha$ parameter has radial dependence.

We try to answer a very important and unresolved problem in our work. If the viscosity is allowed to vary both radially and temporally, would the flow pass through the stages found in the fittings of observational data using TCAF solution? Would the $\alpha$ parameter be only responsible for these or the entire viscous stress is modified throughout the process? To study that, we carried out numerical simulations of an advective flow with $\alpha = \alpha(r, z, t)$, where $r$ and $z$ being the radial and vertical coordinates. We have shown that in these situations, initially, the advective flow breaks down into two distinct components of Keplerian and sub-Keplerian flows corresponding to the rising phase of an outburst. If the viscosity is withdrawn, the system tends to return to its original advective flow configuration without any Keplerian component, taking a much longer time than the creation of the disk. So, our simulation answers one problem of why the declining phase does not retrace the same path through the parameter space as that of the rising phase.

## 2 Governing Equations for Viscous Accretion Flow

A Schwarzschild black hole has been considered surrounded by an axisymmetric advective (low angular momentum compared to Keplerian angular momentum everywhere in the disk) flow around it. Paczyński and Wiita [24] potential has been used which is pseudo-Newtonian in nature. The coordinate system is cylindrical polar coordinates $(r, \phi, z)$. The mass of the black hole $(M_{bh})$ is assumed to be 10 $M_{\odot}$ and considered as the unit of mass. The Schwarzschild radius $r_g = 2GM_{bh}/c^2$ is the unit of distance and $c$, the velocity of light, is unit of velocity.

### *2.1 Basic Equations*

In viscous flows, the magnitude of the shear stress is proportional to the symmetric components of velocity gradient. The viscous stress-tensor is described by Landau and Lifshitz [17] given by

$$\tau = -\zeta\theta\mathbf{g} - 2\eta\sigma. \tag{1}$$

$\zeta$ is bulk velocity, and $\eta$ is the shear viscosity. For an inertial frame of reference, the equation of the flow can be expressed in general form [1] as

$$\rho\left[\frac{\partial \mathbf{v}}{\partial t} + \mathbf{v}.\nabla\mathbf{v}\right] = -\nabla P + \mathbf{F}_b + \nabla.\tau, \tag{2}$$

where $\mathbf{v}$, $P$ and $\rho$ are flow velocity, pressure and fluid density respectively. The body force per unit volume acting on the fluid is $\mathbf{F}_b$ and $\tau$ is the viscous stress tensor having six independent components, $\tau_{rr}$, $\tau_{r\phi}$, $\tau_{rz}$, $\tau_{\phi\phi}$, $\tau_{\phi z}$, $\tau_{zz}$ in cylindrical polar coordinate system.

Dynamic viscosity is $\mu = \eta\rho$. For an axisymmetric case, $\phi$ components of body forces are zero, we can neglect $\frac{\partial}{\partial\phi}$ term, and for a thin accretion flow, $\tau_{r\phi}$ plays the major role for the transportation of angular momentum along the radial direction. The shear stress is proportional to the total pressure $p$. Transport is done through exchange of angular momentum between two adjacent rotating layers. From $SS\alpha$ prescription, $\tau_{r\phi} = -\alpha P$. The proportionality factor $\alpha$ may vary throughout the flow depending on involved physical processes. If $\alpha$ varies radially, we get the reduced viscous term as,

$$\mu = \frac{1}{r^2}\frac{\partial}{\partial r}(-r^2\alpha P) = -\left(\frac{2p\alpha}{r} + \alpha\frac{\partial p}{\partial r} + p\frac{\partial \alpha}{\partial r}\right). \tag{3}$$

## 2.2 Inclusion of Time Varying Viscosity

We have chosen the viscosity parameter ($\alpha$) having explicit dependence on both radial and vertical direction where the temporal variation has been introduced in the radial dependence part as,

$$\alpha(\bar{r}, \bar{z}, t) = \alpha_0(t) f(\bar{r}, t) g(\bar{z}), \tag{4}$$

where $\bar{r} = \frac{r}{r_0}$ and $\bar{z} = \frac{z}{z_0}$.
For $t_0 \leq t < t_m$,

$$\alpha_0(t) = \alpha_0, \tag{5}$$

where $\alpha_0 = 0.12$, $t_0$ is the time when viscosity is triggered on and $t_m$ is the time at which $\alpha$ attains its maximum value.
For $t \geq t_m$,

$$\alpha_0(t) = \alpha_0 e^{q(t-t_m)}, \tag{6}$$

where $q = -9.39 \times 10^{-3}$ is a constant.

$$g(z) = 1 - (\bar{z})^{1.6} \tag{7}$$

is vertical distribution as used in [11]. Here, $r_0 = z_0 = 200 r_g$, limits of simulation box or outer boundary.
$f(\bar{r}, t)$ has been considered in two different ways.

(1) Power-law distribution

$$\alpha = \alpha_0 \bar{r}^{\epsilon(t)}. \tag{8}$$

When $t_0 \leq t < t_m$, then

$$\epsilon(t) = \epsilon_0 e^{-p(t-t_0)}, \tag{9}$$

where, $\epsilon_0 = 650$, $p = 2.55 \times 10^{-3}$ are constants.
When $t \geq t_m$, $\alpha_0(t)$ varies as Eq. (6).

(2) Gaussian Distribution

$$\alpha = \alpha_0 e^{-\frac{(\bar{r}-r_0)^2}{2[c(t)]^2}}. \tag{10}$$

When $t_0 \leq t < t_m$, then

$$c(t) = c_0 e^{p(t-t_0)}, \tag{11}$$

where, $c_0 = 1.1$ and $p = 2.55 \times 10^{-3}$ are constants.

When $t \geq t_m$, $\alpha_0(t)$ varies as Eq. (6).

Thus, calculating $\alpha$ we compute dynamic viscosity coefficient $\mu$.

$$\alpha = \alpha_0(t)\bar{r}^{\epsilon(t)}, \quad \text{(Case I)} \tag{12}$$

and

$$\alpha = \alpha_0(t)e^{-\frac{(\bar{r}-r_0)^2}{2[c(t)]^2}}. \quad \text{(Case II)} \tag{13}$$

## 3 Numerical Simulations Mimicking an Outburst

In these simulations, an axisymmetric, viscous flow in a pseudo-Newtonian gravitational field [24] has been considered. We have considered a cylindrical coordinate system, at the centre of which a point mass $M_{bh}$ is located ($M_{bh} = 10M_{\odot}$). The matter can fall from any directions towards the black hole. We have considered only the first quadrant with reflection symmetries along $r$ and $z$ directions. The stretch of the computational box is $0 \leq r \leq r_0$ and $0 \leq z \leq r_0$, where $r_0$ is the outer boundary radius where matter is being injected. Our simulation distance is chosen only up to $200r_g$ and the results can be scaled till the distance $R_t$. The time will be scaled by $(R_t/r_0)^{3/2}$. The simulation region can be scaled till the triggering distance $R_t$. When $\alpha$ is introduced to the flow, Keplerian matter will enter for $r < R_t$. An absorbing boundary $r_i$ at $2.5r_g$ has been placed beyond which no information comes out as matter is completely absorbed. The surroundings of the black hole is filled with a plasma of density $\rho_{bg} = 10^{-6}$ and the temperature as that of the incoming material to start with to avoid nonphysical singularities dividing by zero. The density of incoming matter is $\rho_{in} = 1$ injected through the outer edge at $r = r_0$.

The polytropic equation of state for accreting matter is, $P = K\rho^{\gamma}$, where $\rho$ and $P$ are matter density and isotropic pressure of the matter. The adiabatic index $\gamma = 1 + \frac{1}{n}$, where $n$ is the polytropic index. Here, for all the simulations $\gamma = 4/3$. For all our cases, the simulation box and each grid is square shaped and $r_0 = 200r_g$, which gives grid size 0.39 in units of Schwarzschild radius.

We have varied the $\alpha$ parameter with time in a way that after the start of the simulation, as time evolves, initially viscosity increases at the outer boundary and then enters into the interior grids of the simulation box. When $\alpha$ reaches its maximum value ($\alpha_0$) at the inner edge ($r_i$), then we gradually diminish $\alpha_0$ with time to decrease $\alpha$ and then viscosity eventually vanishes from the system.

The initial value of $\alpha_0$ has been chosen as 0.12 and we have used the same flow parameters as studied by Giri and Chakrabarti [12] where the critical $\alpha$ parameter is $\alpha_c = 0.074$ above which the disk remains Keplerian.

The simulations have been carried out for several hundreds of dynamical timescale which corresponds to a few seconds in physical unit, $2\,GM/c^3$ being the conversion unit which scales with the mass of the black hole. We initially ran

the simulation up to a time of $t = 19.8$ s without viscosity to avoid the effects of transients which would correspond to an advective flow with a standing shock without any Keplerian disk. We used this as our initial condition to run all our model cases.

For case I, $\alpha = \alpha_0(t)\bar{r}^{\epsilon(t)}$, initially we choose $\epsilon(t) = \epsilon_0 = 650$. When viscosity is turned on at $t_0 = 19.8$ s, $\epsilon(t)$ starts to vary as Eq. (9) up to $t_m = 69.3$ s, where $\alpha_0(t)$ reaches its maximum value $\alpha_0$. Then $\alpha_0(t)$ starts to diminish as Eq. (6) and at 89.11 s, $\alpha$ vanishes entirely from the system [25].

For case II, $\alpha = \alpha_0(t)e^{-\frac{(\bar{r}-r_0)^2}{2[c(t)]^2}}$, the peak of the Gaussian is at the outer boundary ($r_0 = 200r_g$). Before the viscosity is turned on, $c(t)$ is set to $c_0$. From $t_0 = 19.8$ s to $t_m = 69.3$ s, $c(t)$ varies as Eq. (11). Then $\alpha_0(t)$ starts to diminish as Eq. (6) and at 89.11 s, $\alpha$ diminishes to zero [25].

We have used the total variation diminishing (TVD) method [15] to incorporate hydrodynamic simulations in order to deal fluid dynamics which Ryu et al. [26, 27] developed to study astrophysical flows around black holes. The same code has been used by Giri et al. [13] and Giri and Chakrabarti [11, 12]. For concreteness, we have concentrated only on a set of specific energy and angular momentum pair, namely $\widetilde{\lambda} = 1.7$ and $\mathscr{E} = 0.001$ respectively.

## 4 Phases of an Outburst

If we introduce viscosity in the accretion flow, we will observe that initially the advective flow is segregated in Keplerian and Sub-Keplerian components which corresponds to the rising phase of the outburst. After Keplerian component is fully formed (up to the outer boundary of our simulation box), if we withdraw the viscosity, we will find that the Keplerian components are being diffused at time proceeds, and the system tends to return to its original configuration.

### *4.1 Rising Phase: Creation of Disk*

For the inclusion of viscosity in the accretion flow, the centrifugal pressure supported shock becomes weaker and weaker and ultimately the shock disappears resulting flow becomes Keplerian for large enough viscosity [5, 6]. This theoretical expectation was checked by Giri and Chakrabarti [11, 12] with a constant $\alpha$ at all radial distance for the entire simulations and only $z$ variation was introduced ($\alpha$ decreasing with height). In our case, the time dependence is introduced such a way that we could mimic rapid rise and fall of viscosity. We 'turned on' the viscosity at $t = 19.8$ s and 'turned it off' at $t = 89.11$ s for both Case I and Case II. The simulations were terminated at $t = 99.01$ s. Here, we present the results only for Case I.

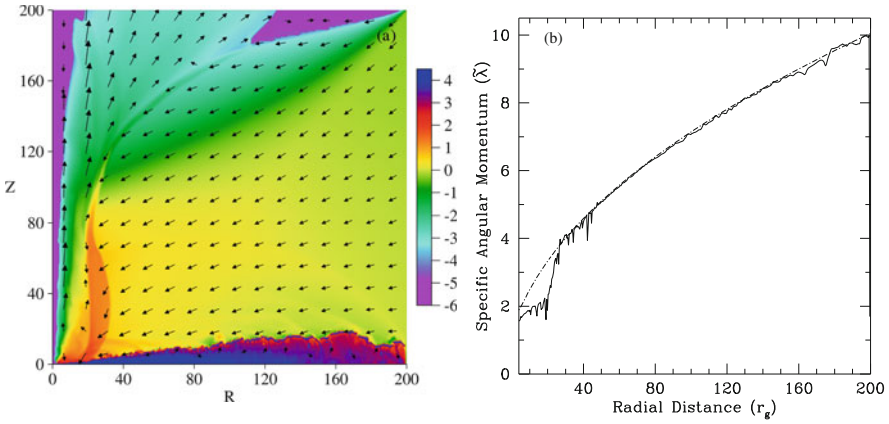



**Fig. 1** (**a**) Density and velocity vectors, (**b**) specific angular momentum distribution ($\tilde{\lambda}$) of accretion flow at $t = 98.80$ s for Case I. The viscosity has been brought down to zero after the Keplerian disk is fully-formed. The outflow remains strong without quenching [25]

To obtain a standard disk, we need to cool the Keplerian distribution region efficiently. To achieve this, we follow a well established procedure to use a power-law cooling ($\propto T^{\beta}$) as in [12]. The cooling rate is $\propto \rho^2 T^{\beta}$, where, $\beta > 0$ is the cooling index. For $\beta = 0.5$ the process is bremsstrahlung. We start with $\beta = 0.5$ throughout, but, when the region with Keplerian distribution is optically thick, the index was raised to 0.6.

As we turn on the viscosity, as the matter is accreted, initially the viscous stress near the inner edge is near zero. As $\alpha$ increases with time, $-\alpha P$ becomes significant close to the inner edge due to high pressure and angular momentum transport starts efficiently. On equatorial plane, this result is similar to what was seen in [7]. In Fig. 1, we see that Keplerian disk is fully-formes when viscosity just diminished to zero after reaching its maximum value near inner edge [25].

## *4.2 Declining Phase: Annihilation of Disk*

Due to the presence of viscosity, Keplerian disk has been formed and the advective component above and below remained similar to the original flow of sub-Keplerian angular momentum which formed CENtrifugal pressure dominated BOundary Layer, or CENBOL (the post-shock region). If we withdraw the viscous process, the Keplerian disk cannot sustain the distribution and the disk must diffuse out till it get mixed with the advective component and accrete more efficiently off the equatorial plane. So, Keplerian disk is gradually washed off and in the long run we expect to have the configuration we started with at $t = 19.8$ s when viscosity was turned on. For long time behavior study, our simulation run time is 1980.55 s for both the cases.

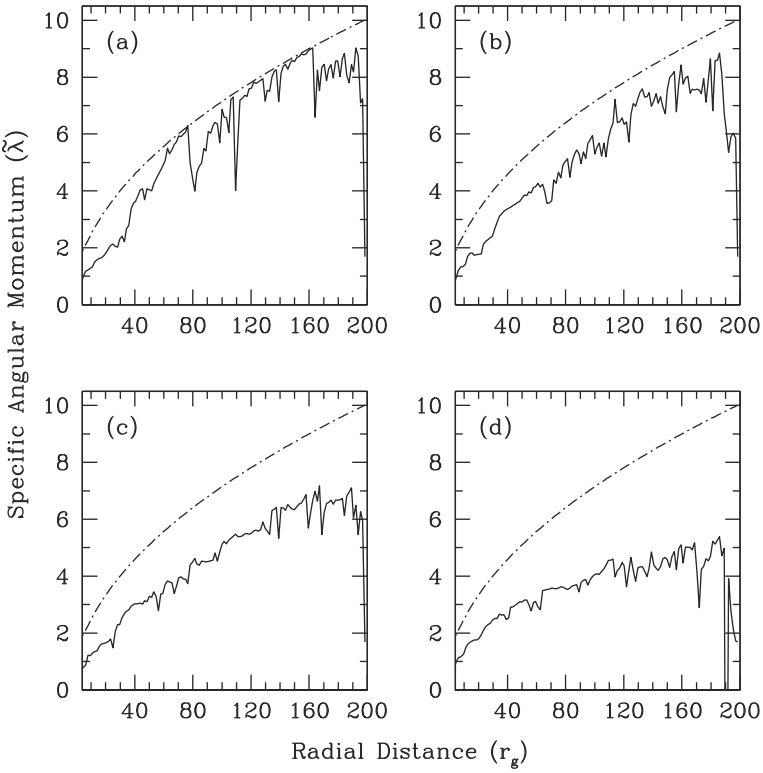



**Fig. 2** The decreasing trend of specific angular momentum ($\widetilde{\lambda}$) long after viscosity is turned off. Here, the Case I was chosen. The distributions are plotted at $t$ = (**a**) 229.68 s, (**b**) 870.59 s, (**c**) 1129.30 s, and (**d**) 1946.76 s respectively [25]

Here in Fig. 2a–d we present the angular momentum distribution of the flow on the equatorial plane for Case I at $t$ = (a) 229.68 s, (b) 870.59 s, (c) 1129.30 s and (d) 1946.76 s long after the viscosity is turned off at $t = 89.1$ s [25]. We can see that the distribution very slowly reverts back to the original distribution. We had to stop the simulation earlier due to computational time constraints.

## 5 Comparison with Observational Data

In Fig. 3a $\alpha$ (solid, scaled up by a factor of 30), $\tau$ (dotted, scaled up by a factor of $2.5 \times 10^3$) and $\widetilde{\lambda}$ (dashed) have been averaged over inner $40r_g$ on the equatorial plane as they evolved from the beginning till the end of the simulation [25]. Viscosity parameter ($\alpha$) rises and falls in a shorter time scale, but the implication of the change in $\alpha$ continued 25 times longer.

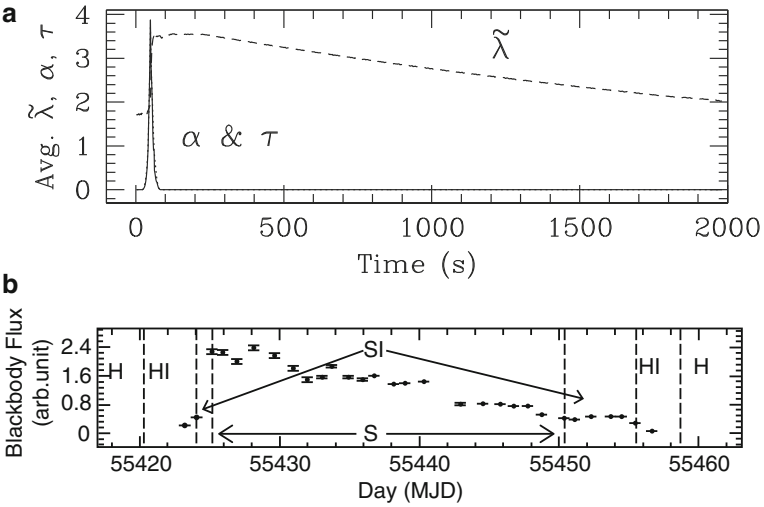



**Fig. 3** (**a**) Variation of $\alpha$ (solid, scaled up by a factor of 30) and $\tau$ (dotted, scaled up by a factor of $2.5 \times 10^3$) and $\tilde{\lambda}$ averaged over inner $40r_g$ for Case I. Viscosity parameter rises and falls within $\sim$ 100 s but the effect of change in viscosity remains longer. Extrapolated time when the average angular momentum is $\sim$ 1.7 is about 2500 s, about a factor of $\sim$ 25 longer than the formative period. (**b**) Variation of Blackbody flux observed from data for 2010 outburst of H1743-322 source showing identical profile with specific angular momentum dissipation in (**a**) as it goes from Hard-Intermediate to Soft-Intermediate to Soft state and comes back to Hard-Intermediate again due to formation and destruction of Keplerian disk [25]

Figure 3b shows the change in blackbody flux from observed data for 2010 outburst of H1743-322 [8]. Comparing Fig. 3a, b, we note a significant point that the variation of averaged specific angular momentum dissipation obtained from simulation in Fig. 3a matches with the change in blackbody flux observed from data for 2010 outburst of H1743-322. For the rising phase of outburst, a Keplerian disk is formed and blackbody flux increases and the system moves from Hard-Intermediate to Soft-Intermediate to Soft state. For the declining phase of outburst, blackbody flux decreases and again goes through Soft-Intermediate and comes back to Hard-Intermediate and then to Hard state. The same happens also for specific angular momentum distribution in our simulation, as it reaches its maximum value in Soft state when Keplerian disk is fully formed and then comes back to its initial value of 1.7 when disk starts to disappear and system comes back to hard state.

## 6 Conclusion

Two component advective flows successfully explain spectral state evolution of outbursting sources. This was theoretically established by Chakrabarti and Titarchuk [7] and observational verifications were done by Smith et al. [29, 30] among

others. But, the exact physical processes which govern the evolution of the flow configurations in the accretion disk remained illusive. In their breakthrough work, Giri and Chakrabarti [11, 12] and Giri et al. [14] showed that even if $\alpha$ were chosen to be a constant number throughout the disk, as long as it decreases vertically, an advective viscous transonic flow will be divided into two components, a Keplerian equatorial component and a sub-Keplerian off-equatorial halo. However, fitting of spectral data in hard, hard-Intermediate, soft-intermediate and soft states in the rising phase and the reverse sequence of states in the declining phase clearly shows that the relative importance of the Keplerian and the sub-Keplerian components are changing. The initialization and culmination of outburst occurs in hard states with primarily sub-Keplerian matter. In the soft state, the rising state ends and the declining state begins, where Keplerian matter dominates. Moreover, the rising and declining do not take place in the same time scale. In analogy of dwarf novae outbursts, we expect that a sudden rise in viscous process is the cause of triggering an outburst in black hole candidates as well.

In our work, we have assumed a couple of typical time dependence of viscosity parameter which rises sharply at the outer edge of the simulation grid and then falls off with time. We chose the outer edge only at $200r_g$ and the whole time scale of a full outburst is scaled down due to computational time constraint in carrying out high resolution runs for a long time. In that process, a few months of the whole outburst was brought down to a few hundreds of seconds by introducing and withdrawing $\alpha$ very rapidly. As $\alpha$ variation changed the rate of angular momentum transport, the high optical depth region needed to be cooled down to have true standard Keplerian disk. This was taken account with a power-law cooling rate faster than the bremsstrahlung process. We indeed noticed that the flow configuration gradually changed from totally advective (hard state) to a truncated Keplerian disk state (intermediate states) and then to finally a fully-formed Keplerian disk spread through the grid (soft state). It has also been found that the process of building up of the Keplerian disk is much faster than the process of disappearance of the Keplerian disk by at least a factor of about 25. This explains clearly the reason of the rising phase in a real outburst being almost shorter by a factor of 10 than the declining phase. What we find here rising phase is shorter than declining phase by a factor of 25 where in the actual case, the factor is 10. There could be a small amount viscosity all along and this could dissipate the Keplerian disk faster once the enhanced amount is withdrawn which we have not incorporated in our simulations. Else, It is possible that the matter density and temperature rises at the outer edge at the time of outburst which were not taken into account in the present scenario. Here we concentrated only on the viscosity parameter $\alpha$ variation, but not on the stress as a whole.

In our simulation, we showed the evolution of the two component advective flows during an outburst. We have added the cooling in the Keplerian Component but the Comptonization was not incorporated. If Comptonization is introduced, that would remove some of the shortcomings of this simulation. Like, the collapse of jet in presence of a dominant Keplerian disk [9, 10]. This happens since soft photons cool down the base of the outflow through inverse Comptonization helping to quench the outflows. In the absence of Comptonization, we can see some outflows still

present in soft states as well. Incorporation of Comptonization would require to couple Monte-Carlo simulations with hydrodynamic studies.

## References


1. Batchelor, G.K.: An Introduction to Fluid Dynamics. Cambridge University Press, Cambridge (1967)
2. Cannizzo, J.K.: ApJ **419**, 318 (1993)
3. Cannizzo, J.K., Chen, W., Livio, M.: ApJ **454**, 880 (1995)
4. Cannizzo, J.K., Still, M.D., Howell, S.B., Wood, M.A., Smale, A.P.: ApJ **725**, 1393 (2010)
5. Chakrabarti, S.K.: MNRAS **243**, 610–619 (1990)
6. Chakrabarti, S.K.: ApJ **464**, 664–683 (1996)
7. Chakrabarti, S.K., Molteni, D.: MNRAS **272**, 80 (1995)
8. Debnath, D., Chakrabarti, S.K., Nandi, A.: AdSpR **52**, 2143 (2013)
9. Garain, S.K., Ghosh, H., Chakrabarti, S.K.: ApJ **758**, 114 (2012)
10. Garain, S.K., Ghosh, H., Chakrabarti, S.K.: MNRAS **437**, 1329 (2014)
11. Giri, K., Chakrabarti, S.K.: MNRAS **421**, 666 (2012)
12. Giri, K., Chakrabarti, S.K.: MNRAS **430**, 2836 (2013)
13. Giri, K., Chakrabarti, S.K., Samanta, M.M., Ryu, D.: MNRAS **403**, 516 (2010)
14. Giri, K., Garain, S.K., Chakrabarti, S.K.: MNRAS **448**, 3221 (2015)
15. Harten, A.: J. Comp. Phys. **49**, 357 (1983)
16. Hawley, J.F., Smarr, L.L., Wilson, J.R.: ApJS **55**, 211 (1984)
17. Landau, L.D., Lifshitz, E.M.: Fluid Mechanics. Pergamon Press, Oxford (1959)
18. Lanzafame, G., Molteni, D., Chakrabarti, S.K.: MNRAS **299**, 799 (1998)
19. McClintock, J.E., Remillard, R.A.: In: Lewin, W., van der Klis, M. (eds.) Compact Stellar X-ray Sources. Cambridge Astrophysics Series, vol. 39. Cambridge University Press, Cambridge (2006)
20. Meyer F., Meyer-Hofmeister E.: A&A **104**, L10 (1981)
21. Meyer F., Meyer-Hofmeister E.: A&A **132**, 143 (1984)
22. Molteni, D., Ryu, D., Chakrabarti, S. K.: Astrophys. J. **470**, 460 (1996)
23. Nandi, A., Debnath, D., Mandal, S., Chakrabarti, S.K.: Astron. Astrophys. **542**, A56 (2012)
24. Paczyński, B., Wiita, P.J.: Astron. Astrophys. **88**, 23 (1980)
25. Roy, A., Chakrabarti, S.K.: MNRAS **472**, 4689 (2017)
26. Ryu, D., Brown, G.L., Ostriker, J.P., Loeb, A.: ApJ **452**, 364 (1995)
27. Ryu, D., Chakrabarti, S.K., Molteni, D.: ApJ **474**, 378 (1997)
28. Shakura, N.I., Sunyaev, R.A.: Astron. Astrophys. **24**, 337 (1973)
29. Smith, D.M., Heindl, W.A., Markwardt, C.B., Swank, J.H.: ApJ **554**, L41 (2001)
30. Smith, D.M., Heindl, W.A., Swank, J.H.: ApJ **569**, 362 (2002)
31. Sunyaev, R.A., Titarchuk, L.G.: Astron. Astrophys. **86**, 121 (1980)
32. Sunyaev, R.A., Titarchuk, L.G.: Astron. Astrophys. **146**, 374 (1985)

# Monte-Carlo Simulation as a Defining Tool to Diagnose Timing and Spectral Properties of Flows Around Black Holes




**Himadri Ghosh**

**Abstract** In this chapter we discuss the development and application of a Monte-Carlo radiative transfer code. Monte-Carlo simulation has been proven to be very useful for cases where exact or near exact analytical solutions are impossible. Radiative processes occurring in case of advective accretion mechanism is a classic example where Monte-Carlo simulation has been found to be very useful. This Chapter deals with the schematics that have been utilized. Spectral variations with various parameters are shown.

## 1 Introduction

Monte-Carlo simulation is an essential tool to understand the formation of spectrum in compact bodies [17]. Sunyaev and Titarchuk ([19, 20]; hereafter ST80 and ST85) showed that the power-law component of a blackbody spectrum forms due to inverse Comptonization. Hua and Titarchuk [13] studied the Monte-Carlo simulation for various known geometries and temperatures of the electron clouds and confirmed the conclusions drawn in ST80, ST85 and Titarchuk [21] using a Monte-Carlo simulation. Laurent and Titarchuk [14, 15] showed the effects of the bulk motion Comptonization which was predicted to produce a power-law spectrum even in the soft states ([3]; hereafter CT95).

The two component advective model is around for over decades, and there are more and more evidences that the flows around the galactic black holes are of two components. In this chapter, we attempt to carry out Monte-Carlo simulations in such systems. In Sect. 2, we give a brief description of simulation procedure using the Monte-Carlo method. We have shown two applications of this Monte-Carlo code in Sects. 3 and 4. Mainly the spectral analysis is presented in this chapter. Temporal

H. Ghosh (✉)
Heritage Institute of Technology, Department of Physics, Kolkata, India
e-mail: himadri.ghosh@heritageit.edu

© Springer International Publishing AG, part of Springer Nature 2018

B. Mukhopadhyay, S. Sasmal (eds.), *Exploring the Universe: From Near Space to Extra-Galactic*, Astrophysics and Space Science Proceedings 53,
https://doi.org/10.1007/978-3-319-94607-8_13

properties of the emitted hard photons from an accretion disk are discussed in the chapter written by Sudip Garain.

## 2 Simulation Procedure

In a simulation, we follow the following steps. (a) We randomly generate a photon out of the Keplerian disk. (b) Using another set of random numbers we obtain its injected direction. (c) Another random number is used to obtain a target optical depth $\tau_c$ at which the scattering takes place. (d) The photon is followed within CENBOL till the optical depth reached $\tau_c$. (e) A scattering is allowed to take place. (f) Energy exchange between the photon and electron is computed through Comptonization or inverse Comptonization assuming the electrons to obey relativistic Maxwell's distribution. (g) Photon frequencies are also gravitationally red-shifted or blue shifted depending on its relative location change with respect to the black hole. (h) The process is continued till the photon either leaves the CENBOL or is absorbed by the black hole.

## 3 Spectral Properties of a Static Thick Accretion Disk

In the present section, we use a thick accretion disk of toroidal geometry as the Compton cloud which is produced by the sub-Keplerian inflow. The outer boundary of the thick accretion disk is considered to be the inner edge of the Keplerian disk. One positive aspect in treating the CENBOL in this manner is that the distributions of electron density and temperature can be obtained totally analytically. The results of this section are adapted from [8]; hereafter GCL09.

### *3.1 The Electron Cloud and the Soft Photon Source*

The cartoon diagram of our simulation set up is shown in Fig. 1. The Keplerian disk is truncated and the inner edge is extended till the outer boundary of the CENBOL (shock location). However, in the soft states when the post-shock region is cooled down, the Keplerian disk can extend till the last stable circular orbit.

The hot electrons in the puffed up CENBOL intercept the soft photons and reprocess them via inverse Compton scattering. A soft photon emitted towards the CENBOL may undergo a single, multiple or no scattering with the hot electrons.

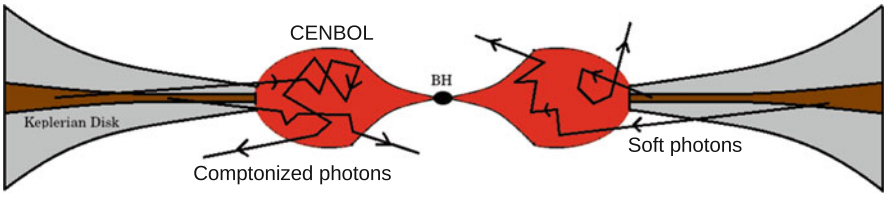



**Fig. 1** A cartoon diagram of the geometry of the Compton cloud used for the Monte-Carlo simulations presented in this section (figure adapted from GCL09)

## 3.2 Thermodynamic Conditions Inside the Compton Cloud

Using the prescription given in [4] we compute the matter density and temperature distributions in this section. Assuming the disk is adiabatic and the specific angular momentum and specific entropy are constant throughout the disk, the equation of state is given by $p = K\rho^{\gamma}$, where $\rho$ and $p$ are the matter density and isotropic pressure, respectively. Here, $\gamma$ is the adiabatic index and $K$ is the entropy constant. We calculated an effective electron temperature $T_{eff}$ of the CENBOL using the prescription given in Sec. 2.4 of CT95.

The Keplerian disk has a inner edge at the outer edge ($R_{out}$) of the CENBOL, and the outer edge is at $500r_g$, where $r_g$ is Schwarzschild radius. The soft photons have a multi-color blackbody spectrum coming from a standard ([18]; hereafter SS73) disk.

For the sake of completion of a simulation using a reasonable amount of computer time, we take a constant fraction of the number of photons from each annulus of the Keplerian disk. Because of the number of photons we select is way below the actual number, the absolute value of accretion rate itself is not very meaningful. However, the relative number of the intercepted photons and the number density of electrons inside CENBOL appears to be more important.

In Fig. 2, we show the distribution of the temperature (in keV) in the Keplerian disk and that in the CENBOL which we have used in our simulations. Different panels are for different values of the outer edge $R_{out}$ (marked) of the CENBOL radius. We provide the effective temperature ($T_{eff}$) within the post-shock region in $R_{out}$ in Table 1. These were obtained by changing the central density of the thick disk, which gave a temperature distribution inside CENBOL. Subsequently, CT95 was followed to obtain an effective temperature. In simulations, however, the actual temperature distribution was used.

## 3.3 Results and Discussions

In Table 2, we summarize all the cases for which the simulations have been presented in this section. In column 1, various cases are marked. In column 2, $R_{out}$

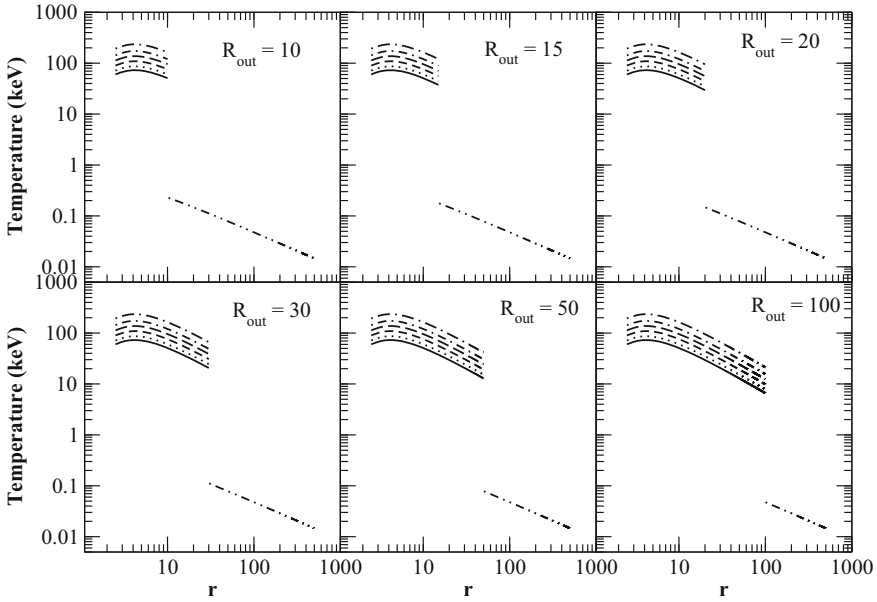



**Fig. 2** Temperature distribution (in keV) inside the disk and the CENBOL region for different CENBOL outer boundaries ($R_{out}$) and various central densities. Table 1 gives the relation between the central densities and the line styles (figure adapted from GCL09)

**Table 1** (Adapted from GCL09) Central electron number densities ($n$ in cm$^{-3}$) and the effective temperatures (in keV) for various outer edge $R_{out}$ of the CENBOL used in this section

| | $R_{out}$ | | | | | | |
|---|---|---|---|---|---|---|---|
| $n$ (cm$^{-3}$) | 10 | 15 | 20 | 30 | 50 | 100 | Line style |
| $7 \times 10^{19}$ | 61 | 54 | 50 | 46 | 43 | 42 | Solid |
| $1 \times 10^{20}$ | 73 | 64 | 59 | 54 | 51 | 50 | Dotted |
| $2 \times 10^{20}$ | 91 | 80 | 74 | 68 | 65 | 63 | Short dashed |
| $5 \times 10^{20}$ | 115 | 101 | 93 | 86 | 81 | 79 | Big dashed |
| $9 \times 10^{20}$ | 145 | 128 | 118 | 109 | 102 | 99 | Dash-dotted |
| $2 \times 10^{21}$ | 197 | 173 | 160 | 147 | 139 | 135 | Big dash-dotted |

and $T_{eff}$ in keV are listed. In column 3, we calculate the percentage $p$ of the total injected photons that have suffered scattering through CENBOL. In column 9, we present the energy spectral index $\alpha$ ($I(E) \sim E^{-\alpha}$) obtained from our simulations.

In Fig. 3, we summarize the results of all the cases, bunching them in groups with the same CENBOL size. Different cases are marked in each panel. Curves (a) to (f) are from bottom to top respectively. Note that as $T_{eff}$ is raised (a $\rightarrow$ f), the spectrum becomes harder. Also, as $R_{out}$ is increased, the percentage $p$ of photons intercepted is also increased as the CENBOL becomes bigger. However, as the CENBOL size is increased, it becomes increasingly difficult to soften the

**Table 2** Summary of all the simulation cases presented in this chapter (adapted from GCL09)

| Case | $R_{out}, T_{eff}$ | $p$ | $\alpha$ | Case | $R_{out}, T_{eff}$ | $p$ | $\alpha$ | Case | $R_{out}, T_{eff}$ | $p$ | $\alpha$ |
|---|---|---|---|---|---|---|---|---|---|---|---|
| 1a | 10, 61 | 2.627 | 2.10 | 2a | 15, 54 | 3.955 | 1.12 | 3a | 20, 50 | 4.625 | 0.85 |
| 1b | 10, 73 | 2.627 | 1.90 | 2b | 15, 64 | 3.955 | 0.99 | 3b | 20, 59 | 4.623 | 0.75 |
| 1c | 10, 91 | 2.627 | 1.65 | 2c | 15, 80 | 3.957 | 0.82 | 3c | 20, 74 | 4.626 | 0.64 |
| 1d | 10, 115 | 2.630 | 1.40 | 2d | 15, 101 | 3.958 | 0.70 | 3d | 20, 93 | 4.623 | 0.54 |
| 1e | 10, 145 | 2.628 | 1.15 | 2e | 15, 127 | 3.953 | 0.57 | 3e | 20, 118 | 4.623 | 0.44 |
| 1f | 10, 197 | 2.627 | 0.90 | 2f | 15, 173 | 3.957 | 0.45 | 3f | 20, 160 | 4.623 | 0.34 |
| 4a | 30, 46 | 5.648 | 0.65 | 5a | 50, 43 | 6.930 | 0.56 | 6a | 100, 42 | 9.562 | 0.42 |
| 4b | 30, 54 | 5.645 | 0.56 | 5b | 50, 51 | 6.931 | 0.50 | 6b | 100, 50 | 9.615 | 0.30 |
| 4c | 30, 68 | 5.645 | 0.46 | 5c | 50, 65 | 6.931 | 0.44 | 6c | 100, 63 | 9.633 | 0.24 |
| 4d | 30, 86 | 5.650 | 0.40 | 5d | 50, 81 | 6.931 | 0.38 | 6d | 100, 79 | 9.642 | 0.19 |
| 4e | 30, 109 | 5.647 | 0.35 | 5e | 50, 102 | 6.929 | 0.32 | 6e | 100, 99 | 9.648 | 0.17 |
| 4f | 30, 147 | 5.652 | 0.29 | 5f | 50, 139 | 6.929 | 0.28 | 6f | 100, 135 | 9.650 | 0.13 |

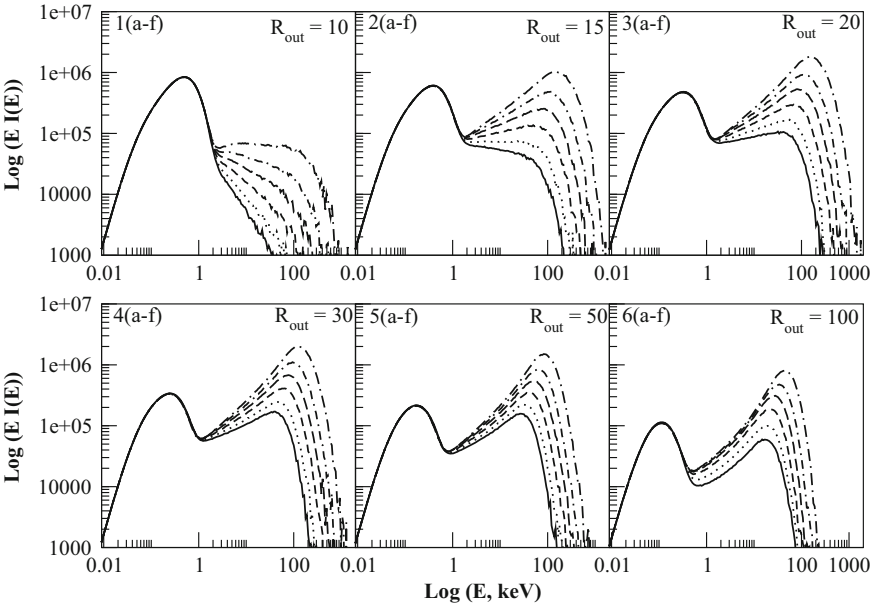



**Fig. 3** Variation of the spectrum with the increase of effective temperature ($T_{eff}$) of the CENBOL for a fixed CENBOL size $R_{out}$. Each panel marks the cases for which the spectrum is drawn. Curves for (a) to (f) are from bottom to top respectively along the direction of increasing density and effective temperature (figure adapted from GCL09)

spectrum with the same number of injected photons. Thus the spectrum becomes harder. This behavior matches with the earlier theoretical predictions (Fig. 6 of [2]). All the spectra are angle-averaged.

## 4 Effects of Thermal and Bulk Motion Comptonizations in the Presence of an Outflow

In this section, we see the effects of bulk velocity of the Compton cloud on the emitted spectrum from an accretion disk. Here ([9]; hereafter GGC10) obtain the outgoing spectrum in the presence of both inflows and outflows. We show how the spectrum depends on the flow parameters of the inflow, such as the accretion rates of the two components and the shock strength. In our result, we see the effects of the bulk motion Comptonization (CT95), because of which even a cooler CENBOL produces a harder spectrum. At the same time, the effect of down-scattering due to the outflowing electrons is also seen, because of which even a hotter CENBOL causes the disk-jet system to emit lesser energetic photons. Thus, the net spectrum is a combination of all these effects.

## 4.1 Simulation Set Up

To simplify the geometry of the inflow-outflow configuration without sacrificing the salient features, we assume the flow geometry as depicted in the cartoon diagram presented in Fig. 4. The components of the hot electron clouds, namely, the CENBOL, the outflow and the sub-Keplerian flow, intercept the soft photons emerging out of the Keplerian disk and reprocess them via inverse-Compton scattering. We have chosen a spherical shape of the CENBOL for simplicity. The sub-Keplerian inflow in the pre-shock region is assumed to be of wedge shape of a constant angle $\Psi$. The outflow, which emerges from the CENBOL in this picture, is also assumed to be of constant conical angle $\Phi$.

## 4.2 Compton Cloud and Its Temperature, Density and Its Internal Bulk Velocity Components

We assume the black hole to be non-rotating and we use the pseudo-Newtonian potential ([16]; hereafter PW80) to describe the geometry around the black hole. The

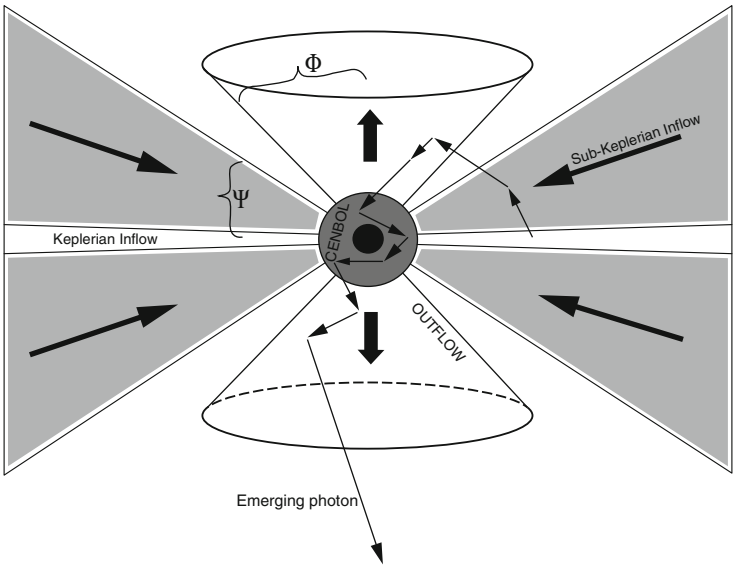



**Fig. 4** A cartoon diagram of the geometry of our Monte-Carlo simulation presented in Sect. 4. The spherical inflowing post-shock region (CENBOL) surrounds the black hole. The Keplerian disk is on the equatorial plane and a sub-Keplerian halo is above and below. A diverging conical outflow is formed from the CENBOL. The zig-zag path of a typical photon is shown (figure adapted from GGC10)

velocity components and angular momenta are measured in units of $c$, the velocity of light, and $r_g c$ respectively.

The flow is supersonic in the pre-shock region and sub-sonic in the post-shock (CENBOL) region. We chose this surface at a location ($R_s$), where the pre-shock Mach number $M = 2$. This location depends on the specific energy $\epsilon$ [1]. Inside the CENBOL, both the Keplerian and the sub-Keplerian components are mixed together. The velocity variation of the matter inside the CENBOL is assumed to be the same as the Bondi accretion flow solution reduced by the compression ratio due to the shock.

In our simulation, we have used the jet angle $\Phi = 58°$. This is the highest value of $\Phi$ we can choose for our system, because, for $\Phi$ more than 58° the disk would be evacuated. Thus we have chosen $\Phi$ to be smaller than this in order that steady jets are produced. The velocity variation inside the jet is obtained from the outflow branch of Bondi solution. Using the prescription described in Section 2.1 of GGC10, we compute the density variation inside the jet.

## *4.3 Source of Soft Photons*

The soft photons are produced from a Keplerian disk whose inner edge coincides with the CENBOL surface, while the outer edge is located at $500 r_g$. The source of soft photons has the multi-color blackbody spectrum coming from a standard SS73 disk. The soft photons are generated isotropically between the inner and outer edges of the Keplerian disk but their positions are randomized using the distribution function of black body temperature $T(r)$. All the results of the simulations presented here have used the number of injected photons to be $6.4 \times 10^8$. The mass of the black hole $M_{bh} = 10 M_{\odot}$.

## *4.4 Simulation Procedure*

In a given simulation, we assume a Keplerian disk rate ($\dot{m}_d$) and a sub-Keplerian halo rate ($\dot{m}_h$). The specific energy ($\epsilon$) of the halo determines hydrodynamic properties (such as number density of the electrons and the velocity variation) and the thermal properties of matter. Here we chose the PW80 potential. So the radial velocity is not exactly unity at $r = 1$, the horizon, but it becomes unity just outside. In order not to over-estimate the effects of bulk motion Comptonization which is due to the momentum transfer of the moving electrons to the horizon, we shift the horizon just outsize $r = 1$ where the velocity is unity. The shock location of the CENBOL is chosen where the Mach number $M = 2$ and the compression ratio at the shock is assumed to be a free parameter. Soft photons are generated from a standard Keplerian disk (SS73) andare injected into the sub-Keplerian halo, the CENBOL and the outflowing jet. The simulation procedure is same as mentioned

in Sect. 2. To highlight our point, we are especially choosing the cases when the jet could play a major role in shaping the spectrum.

## 4.5 Results

In Fig. 5a–c, we have shown the velocity, electron number density and temperature variations inside the CENBOL and the jet for the parameters $\epsilon = 0.015$, $\dot{m}_d = 0.01$ and $\dot{m}_h = 1$. We varied the compression ratio $R$ for these simulations. The solid, dotted and dashed curves are for $R = 2$ (Case 1a), 4 (Case 1b) and 6 (Case 1c) respectively. The velocity variation within the jet does not change with $R$, but the density (in the unit of $\text{cm}^{-3}$) does (middle panel) as the amount of matter inside the jet changes with $R$. The doubledot-dashed line gives the velocity variation of the matter within the jet for all the above cases. The direction of the bulk velocity (radial direction in accretion, vertical direction in jets) is shown by the arrows.

In Table 3, we summarize the parameters of all the cases. In column 1, various cases are marked. In column 2, $R$ and percentage $P_m$ of the total matter that is going out as outflow are listed. In column 3, we show the total number of photons (out of the total injection of $6.4 \times 10^8$) intercepted by the CENBOL and jet ($N_{int}$) combined. Column 4 gives the number of photons ($N_{cs}$) suffered scattering inside the flow. Columns 5, 6 and 7 show the number of scatterings taken place in the CENBOL ($N_{cenbol}$), in the jet ($N_{jet}$) and in the pre-shock sub-Keplerian halo ($N_{subkep}$) respectively. The number of photons captured ($N_{cap}$) by the black hole

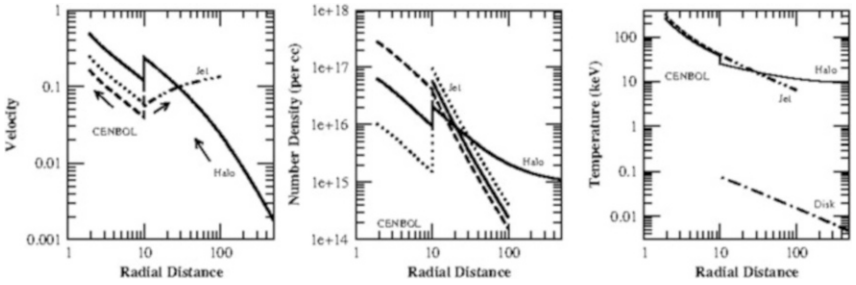



**Fig. 5** (**a**)–(**c**) The velocity (left), density (middle) and temperature (right) profiles of Cases 1(a-c) as described in Table 3 are shown with solid ($R = 2$), dotted ($R = 4$) and dashed ($R = 6$) curves. $\dot{m}_d = 0.01$ and $\dot{m}_h = 1$ were used (GGC10)

**Table 3** Summary of the simulation parameters (adapted from GGC10)

| Case | R, $P_m$ | $N_{int}$ | $N_{cs}$ | $N_{cenbol}$ | $N_{jet}$ | $N_{subkep}$ | $N_{cap}$ | $p$ | $\alpha$ |
|---|---|---|---|---|---|---|---|---|---|
| 1a | 2, 58 | 2.7E8 | 4.0E8 | 1.4E7 | 7.5E7 | 8.4E8 | 3.4E5 | 63 | 0.43 |
| 1b | 4, 97 | 2.7E8 | 4.1E8 | 2.4E6 | 1.3E8 | 8.6E8 | 3.3E5 | 65 | 1.05 |
| 1c | 6, 37 | 2.7E8 | 4.0E8 | 5.4E7 | 4.8E7 | 8.3E8 | 3.1E5 | 62 | −0.4 |

is given in column 8. In column 9, we give the percentage $p$ of the total injected photons that have suffered scattering through CENBOL and the jet. The energy spectral index $\alpha$ ($I(E) \sim E^{-\alpha}$) obtained from our simulations is listed in column 10 (for more details please see GGC10).

In Fig. 6, we show the variation of the spectrum in the three simulations presented in Fig. 5a–c. The difference in the spectrum is mainly due to the CENBOL and the jet since the density, velocity and temperature profiles of the pre-shock, sub-Keplerian region and the Keplerian flow are the same in all these cases. In the case of the strongest shock (compression ratio $R = 6$), only 37% of the total injected matter goes out as the jet. At the same time, due to the shock, the density of the post-shock region increases by a factor of 6, so the effective density and temperature of the matter inside the CENBOL is highest and that inside the jet is lowest in this case. Hence the spectrum is the hardest for $R = 6$. Similar effects are seen for $R = 4$ and for $R = 2$ also. For $R = 4$ almost 97% of total injected matter goes out as the jet, reducing the matter density of the CENBOL significantly. The spectrum is the softest in this case. We can understand this from Table 3 also, where we find that $N_{cenbol}$ is the lowest and $N_{jet}$ is the highest in this case (Case 1b). If number of scattering increases in jet, up-scattering decreases and down-scattering increases. When the shock strength $R = 2$, 57% of the inflowing matter goes out as jet. The density in the post-shock region increases by a factor of 2, due to shock. This makes

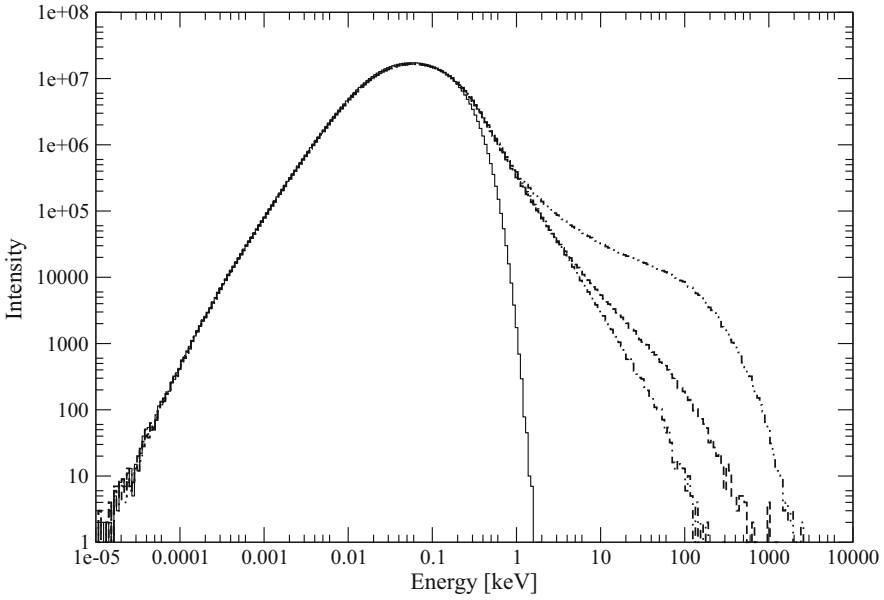



**Fig. 6** Variation of the emerging spectrum for different compression ratios. The solid curve is the injected spectrum from the Keplerian disk. The dashed, dash-dotted and doubledot-dashed lines are for $R = 2$ (Case 1a), $R = 4$ (Case 1b) and $R = 6$ (Case 1c) respectively (figure adapted from GGC10)

this case similar to a non-shock case as far as the density is concerned, but with a little higher temperature of the CENBOL due to the shock. Therefore, the spectrum with the shock would be harder than when the shock is not present (this result is adapted from GGC10).

In Fig. 7a–c, we show the components of the emerging spectrum for all the three cases presented in Fig. 6. The solid curve is the intensity of all the photons which suffered at least one scattering. The dashed curve corresponds to the photons with last scattering from the CENBOL region and the dash-dotted curve is for the photons with their last scattering in the jet region. The spectrum from the jet region is found to be softer than the spectrum from the CENBOL. The jet spectrum becomes softer when $N_{jet}$ increases and $N_{cenbol}$ decreases. This happens because of two reasons. First, the jet is cooler than the CENBOL, so the photons get lesser amount of energy

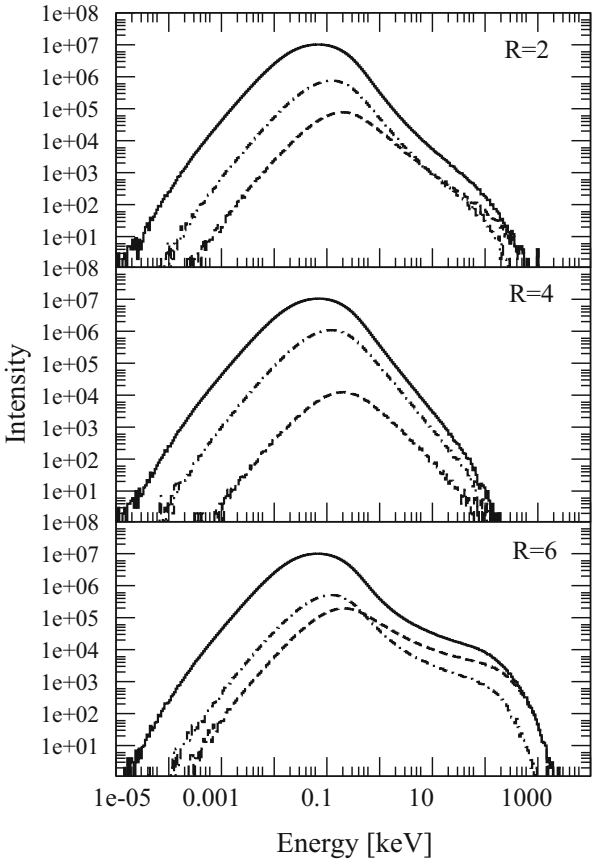



**Fig. 7** (a)–(c) Variation of the components of the emerging spectrum with the shock strength ($R$). Contribution of photons coming out of the CENBOL (dashed) and the jet (dash-dotted) regions are plotted (figure adapted from GGC10)

from jet due to thermal Comptonization making the spectrum softer. Second, the photons are down-scattered by the outflowing jet which makes the jet spectrum softer. The effect of down-scattering is maximum when $R = 4$ then it is for $R = 2$ and for $R = 6$ this is minimum. This happens as $N_{cenbol}$ is much larger than $N_{jet}$ for $R = 6$ case, so most of the photons get up-scattered. This result is adapted from GGC10.

We now turn our attention to the effect of the variation of jet-angle on the output spectrum. In Fig. 8b, we have plotted the spectra for three different jet angles [$\Phi = 30°$ (dashed curve), 50° (dash-dotted curve) and 58° (solid curve)], keeping $\Psi = 32°$ and $R = 4$, fixed. Parameters used for the simulation: $\epsilon = 0.015$. $\dot{m}_d = 0.01$ and $\dot{m}_h = 1$. The temperature and velocity distributions remain same for all these three cases, only difference the change in $\Phi$ makes is in the density of the matter inside the CENBOL. In Fig. 8a, we plot the density variation with radial distance. The line styles for $\Phi = 30°$, 50° and 58° are same as Fig. 8b. Here, dotted plot gives the density inside the jet for all the three cases. With the decrease in jet angle, the density of the infalling matter inside the CENBOL increases, thus increasing the number of upscattered photons which makes the spectrum harder.

## 5 Discussions and Conclusions

In this chapter, we have discussed the results we found in GCL09 and GGC10, where we considered steady state geometries of the accretion disk and the simulated the spectral behaviour for them. In reality, one should do a time-dependent simulation, where the hydrodynamics of the flow changes due to the radiative transfer in the accretion disk and the time dependence of the output spectra can be observed. In a series of papers [10–12], we have shown the time-dependent

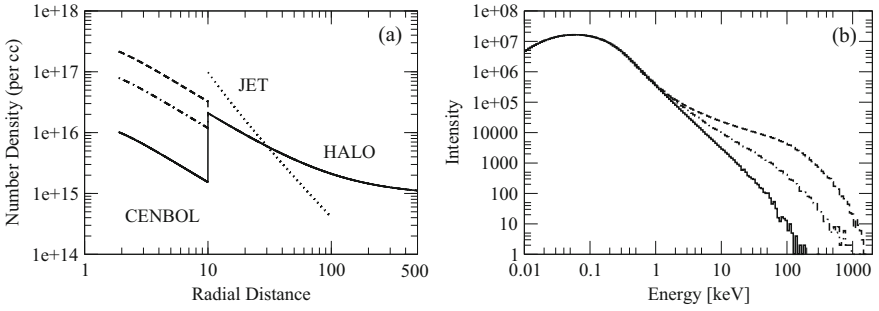



**Fig. 8** (**b**) The variation of the output spectrum if we vary the jet angle is shown. Here, the dashed, dash-dotted and solid curves are for $\Phi = 30°$ and 50° and 58°, respectively. Compression ratio $R$ is 4 in all three cases. (**a**) The density variation with the change in $\Phi$ is shown. Parameters and the line styles are same as the right panel. The dotted plot shows the density variation inside the outflow

simulation results, which include both hydrodynamics and radiative transfer. We use the low angular momentum halo along with a Keplerian disk. We find how the Comptonization affects the temperature distribution of the flow and how this in turn affects the dynamics of the flow as well. These timing features have been discussed in the Chapter written by Sudip Garain.

We have also studied the time-dependent images of advective flows around a black hole by coupling the Monte-Carlo code with a ray tracing code [5–7].

## References

1. Chakrabarti, S.K.: Theory of Transonic Astrophysical Flows. World Scientific, Singapore (1990)
2. Chakrabarti, S.K.: ApJ **484**, 313 (1997)
3. Chakrabarti, S.K., Titarchuk, L.G.: ApJ **455**, 623 (CT95) (1995)
4. Chakrabarti, S.K., Jin, L., Arnett, W. D.: ApJ **313**, 674 (1987)
5. Chatterjee, A., Chakrabarti, S.K., Ghosh, H.: MNRAS **472**, 1842 (2017)
6. Chatterjee, A., Chakrabarti, S.K., Ghosh, H.: MNRAS **465**, 3902 (2017)
7. Chatterjee, A., Chakrabarti, S.K., Ghosh, H., Garain, S.K.: MNRAS (2018). arXiv:1802.10296
8. Ghosh, H., Chakrabarti, S.K., Laurent, P.: IJMPD **18**, 1693 (GCL09) (2009)
9. Ghosh, H., Garain, S.K., Chakrabarti, S.K., Laurent, P.: IJMPD **19**, 607 (GGC10) (2010)
10. Ghosh, H., Garain, S., Giri, K., Chakrabarti, S.K.: MNRAS **416**, 971 (2011)
11. Garain, S., Ghosh, H., Chakrabarti, S.K.: ApJ **758**, 114 (2012)
12. Garain, S., Ghosh, H., Chakrabarti, S.K.: MNRAS **437**, 1329 (2013)
13. Hua, J.M., Titarchuk, L.G.: ApJ **469**, 280 (1996)
14. Laurent, P., Titarchuk, L.: ApJ **511**, 289 (1999)
15. Laurent, P., Titarchuk, L.: ApJ **562**, 67 (2001)
16. Paczyński, B., Wiita P.J.: A&A **88**, 23 (PW80) (1980)
17. Poznyakov, L., Sobol, I., Sunyaev, R.: A & Sp Physics Reviews, **2**, 189 (1983)
18. Shakura, N.I., Sunyaev, R.A.: A& A **24**, 337 (SS73) (1973)
19. Sunyaev, R.A., Titarchuk, L.G.: A&A **86**, 121 (ST80) (1980)
20. Sunyaev, R.A., Titarchuk, L.G.: A&A **143**, 374 (ST85) (1985)
21. Titarchuk, L.: Astrophys. J. **434**, 570 (1994)

# Sensitivity of Spectral and Temporal Properties of Accretion and Outflows on Space Time Geometry, Viscosity and Cooling




**Sudip K. Garain**

**Abstract** In this chapter, we describe the development of a radiation hydrodynamic simulation code and discuss the results obtained when we use it to study the dynamics of an accretion disk around a galactic black hole. For the first time, we are able to consider the presence of both the components of the two component advective (TCAF) model, namely, the Keplerian disk and sub-Keplerian halo, in a single simulation. These simulations give us the opportunity to study simultaneously the time dependence of the disk structure and its spectral as well as temporal properties. We prove several of the conjectures that were made earlier based on theoretical studies and other simulations. We also discuss the current developments in this simulation code and the future scopes.

## 1 Introduction

The spectral and the timing properties of the two-component advective flow (TCAF) 'model' have been extensively studied since it was proposed by Chakrabarti and Titarchuk in 1995 [13]. By the time I started working with Prof. S.K. Chakrabarti in 2008, this model for the accretion disk around the compact objects was already very well established. It clearly answered several questions of this subject. The review articles by Chakrabarti [5–8] document the state of the understanding of the subject around that time. The spectral and timing properties of the accretion disk were explained very satisfactorily by this model [9, 10, 15, 16, 21, 23, 40, 44, 47, 50].

In addition to theoretical developments, several numerical experiments were also performed using hydrodynamics simulations, even including radiative transfer processes ([11, 12, 41]; [38, 42, 43]; hereafter MSC96, [14]; hereafter CAM04). The results of the numerical simulations provided additional insights in understanding many observations from several black hole candidates. Usually, the analytical

S. K. Garain (✉)
Department of Physics, University of Notre Dame, Notre Dame, IN, USA
e-mail: sgarain@nd.edu

© Springer International Publishing AG, part of Springer Nature 2018

B. Mukhopadhyay, S. Sasmal (eds.), *Exploring the Universe: From Near Space to Extra-Galactic*, Astrophysics and Space Science Proceedings 53,
https://doi.org/10.1007/978-3-319-94607-8_14

methods help in understanding the steady state solutions of the advective accretion disk. Moreover, many times simplifying assumptions are made to handle the non-linear dissipative processes present inside the disk. Therefore, many 'details' of the system and their time-dependent behaviour are buried under those assumptions. Time dependent numerical solutions allow us to avoid many such assumptions and hence, help us in understanding the time dependent features of the disk dynamics in much better way.

The goal in my thesis work was to advance the numerical works by incorporating realistic radiative process into the hydrodynamic simulations. One of the important radiative processes taking place inside the accretion disk is the inverse-Comptonization (or Comptonization). This process is believed to be responsible for producing the observed hard radiation ([51], [13]; hereafter CT95) from the black hole binaries. One way to study this process numerically is to use Monte-Carlo method. Therefore, the aim of our work was to couple the hydrodynamic simulation with the Monte-Carlo simulation to result in a radiation hydrodynamic simulation code. The idea was to study simultaneously the time dependence of disk configuration and resulting the spectral properties of the disk.

In Sect. 2, we provide a very brief description of the radiation hydrodynamic code that we develop. More details can be found in [30]; hereafter GGGC11, [27]; hereafter GGC12, [28]; hereafter GGC14, [26]; hereafter G14. In Sect. 3, we discuss some results of our study of spectral properties using this code. In Sect. 4, we discuss the timing properties of the disk. All the discussions provided in this chapter are mainly based on the results published in the aforementioned articles. Finally, in Sect. 5, we provide some discussion based on our further research including viscosity and general relativistic simulations.

## 2 Brief Description of the Radiation Hydrodynamic Code

In this section, we describe the development of the time dependent radiation hydrodynamic simulation code. This code is basically the coupling of two different codes. The hydrodynamic properties of the accretion disk are simulated using a hydro-solver which uses second order accurate finite difference numerical scheme based on total variation diminishing (TVD) property [34, 48]. This solver uses pseudo-Newtonian ([45]; hereafter PW80) potential to simulate the accretion flow around a non-rotating black hole. On the other hand, the radiative properties are studied using a Monte-Carlo code which simulates the generation of photons, their propagation and inverse-Compton (or Compton) scattering inside the accretion disk [29, 39, 46].

Following these steps, we couple these two codes:

(1) Using the non-radiative hydro-code, we evaluate the hydrodynamic properties (density, velocity components and temperature) of the sub-Keplerian disk interior.

(2) Using Monte-Carlo code, the spectrum is computed from this hydrodynamic configuration.
(3) During the Monte-Carlo step, the local cooling/heating from each zone is also explicitly computed. The new temperature profile for the disk interior is supplied to the hydro-code.
(4) The hydro-code is run for a short duration much less than the local infall time scale. Thus, we find a new hydrodynamic state and go back to step (1)

Clearly, this is a two step procedure. Since the calculation of Compton process is via Monte-Carlo code (which is highly non-linear) while the hydrodynamic simulation is by finite difference method, they cannot be coupled directly (G14). However, using this resulting coupled radiation hydrodynamic code, we are able to see how the disk properties and the resulting spectra modify with time.

## *2.1 Modelling of Keplerian Disk Photon Packets*

The hydrodynamic part in the above resulting radiation hydrodynamic code is non-viscous and hence, we are unable to generate Keplerian disk self-consistently (more recent version includes viscosity and generates Keplerian disk self-consistently). Therefore, we assume the presence of a standard Shakura-Sunyaev Keplerian disk [49] at the equatorial plane of the sub-Keplerian halo. This Keplerian disk only serves as the source of soft photons. We use Monte-Carlo technique to model these soft photons. Each photon is tracked beginning from its generation at the disk surface till it leaves the sub-Keplerian accretion disk or absorbed by the black hole.

From a Keplerian disk of a given disk rate $\dot{m}_d$, we can always analytically compute the number of soft photons $n_\gamma(r)$ per unit surface area per unit time at a given radius $r$. Thus, once we set our computational domain, we can evaluate the total disk emission rate $N$/s by integrating radially. This number $N$ comes out to be very large (e.g. $\sim 10^{46}$/s for a disk extending from $3r_g$ to $300r_g$ and disk accretion rate $\dot{m}_d = 0.1$; here $r_g$ represents the Schwarzschild radius). In practice, it is nearly impossible to handle these many number of photons in a Monte-Carlo simulation because of the limitation of computational resources and timely computation. Therefore, we replace the actual large number of photons $n_\gamma(r)$ at a given radius $r$ by a smaller number of bundles of photons, say, $N_{comp}(r)$ and calculate a weightage factor,

$$f_W = \frac{n_\gamma(r)}{N_{comp}(r)}.$$

Therefore, in true sense, each 'photon' of our Monte-Carlo simulation actually represents a bundle consisting of $f_W$ number of true photons. We assume that all the photons of a bundle behave in the similar way. Thus, if an injected 'photon' is scattered by an electron inside a volume element of size $dV$, it is assumed that

all $f_W$ number of true photons of that bundle have suffered similar scattering with the electrons inside the volume element $dV$. Furthermore, if the energy exchange per electron in this inverse-Compton (or, Compton) scattering is $\Delta E$, we multiply this amount by $f_W$ and distribute this energy loss (gain) among all the electrons inside that particular volume element. This procedure is followed for all the $N_{comp}$ number of 'photons' and the revised energy distribution of the electrons is obtained. Typically, we use $\sim 10^7$ number of 'photons' in each of our Monte-Carlo steps. We conducted rigorous tests to conclude that this number provides converged results (GGC12; G14).

To accelerate the computation, we parallelize the Monte-Carlo step using MPI. This significantly helped in studying the time dependence of the radiative properties for longer time. In the next few sections, we provide some results of our numerical simulations.

## 3 Spectral Properties of the TCAF

In this section, we briefly mention some results of our study of the spectral properties of the TCAF using our code. Usually, for our simulations, we take a hydro-steady state as the initial condition. Please see Fig. 1 which shows typical initial configuration (with an axi-symmetric sub-Keplerian halo component) of our simulations. On this hydrodynamic configuration, we run the Monte-Carlo step and compute the spectrum. This is the first approximation of the spectrum. As the iterations proceed, the disk converge to another steady state with lower average temperature and converged spectrum.

We consider TCAF with spherically symmetric as well as axi-symmetric sub-Keplerian accretion component (GGGC11; GGC12; GGC14; G14). For a given simulation run, we assume a Keplerian disk rate ($\dot{m}_d$) and a sub-Keplerian halo rate ($\dot{m}_h$). The specific energy ($\epsilon$) and specific angular momentum ($\lambda$) of the halo provide the hydrodynamic (e.g., number density of the electrons and the velocity distribution) and the thermal properties of matter. For nearly all cases, we find that in presence of cooling, the system achieves its final steady state within a dynamical time ($\sim 0.1$ s for our simulation domain).

For our experiment with initially spherically symmetric [1] halo component, we find that in the presence of an axi-symmetric soft photon source (e.g., a Keplerian disk) on the equatorial plane, the structure of the halo becomes axi-symmetric in the final steady state. This happens because, due to the higher optical depth, there is a significant cooling near the axis of the intervening accreting halo between the disk and the axis (GGGC11). The final emitted spectrum is also found to be direction dependent. When the disk is viewed from top, the spectrum shows a large soft bump, while the edge on view shows the spectrum to be harder. Further analysis of the resulting final spectra reveal even more interesting properties. The photons which suffer moderate number of scatterings and hence, spend moderate amount of time inside the halo (typically less than 100 ms) contribute more to the

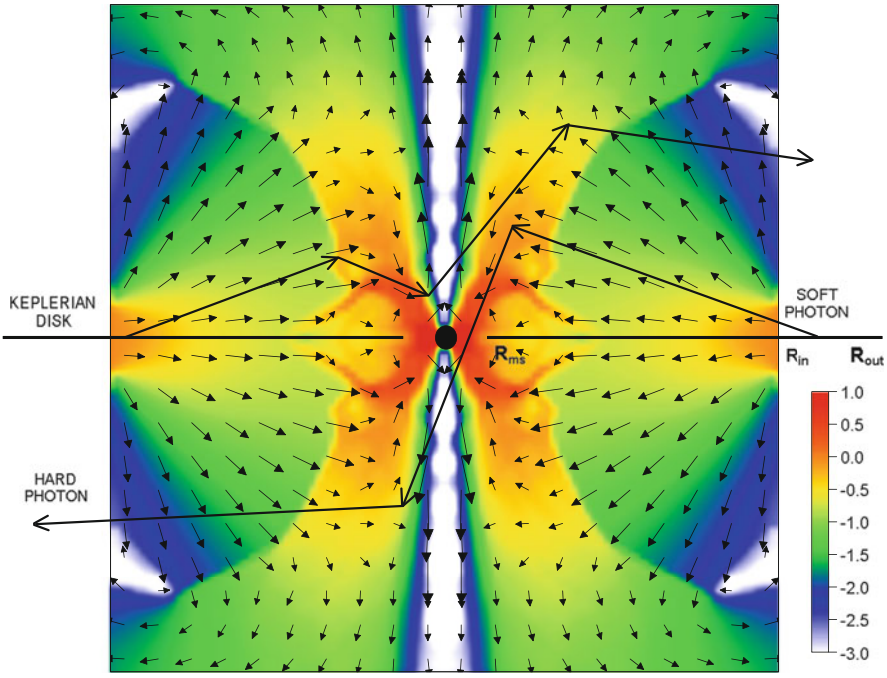



**Fig. 1** The schematic diagram of our simulation set up. The velocity vectors of the infalling matter are shown. The colors show the normalized density in a logarithmic scale. The zig-zag trajectories are the typical paths followed by the photons. Velocity vectors are drawn for $\lambda = 1.73$ (GGC14) (Color figure online)

harder spectrum part. If the photons suffer larger scattering and spend more time inside the halo (more than 100 ms), they loose their energies because they transfer their energies back to the cooler electrons before escaping. Bulk motion of the accreting halo is also found to affect the final spectra. The accreting matter push the photons towards the hotter, denser inner regions to suffer more and more scatterings (GGGC11) and make the resulting spectrum harder. Also, we find that the photons which are scattered close to the black hole horizon and escape without any further scattering, produce the high energy tail in the output spectrum (G14). This shows a clear signature of the presence of bulk motion Comptonization (CT95) near the black hole horizon.

When the infalling halo has angular momentum, its structure changes significantly. Because of the centrifugal force, the matter slows down and as a result, they pile up close to the black hole before being accelerated again towards the black hole. The density and the temperature of the halo increases in this region and the so-called 'Compton cloud' is formed. A shock may or may not form in the infalling halo depending on $\epsilon$, $\lambda$ as well as the radiative and viscous properties. The outflow is also found to be formed self-consistently from this region. The radiation spectrum is determined by the collective effects of the inflow and outflow. For our simulations

**Table 1** List of parameters and a summary of results (adopted from G14)

| Case ID | $\epsilon, \lambda$ | $\dot{m}_d$ | $\dot{m}_h$ | $< R_{sh} >$ | $\nu_{QPO}$ | $< \alpha >$ | $\frac{t_{in}}{t_{cool}}$ |
|---|---|---|---|---|---|---|---|
| C1 | 0.0021, 1.73 | 1e−4 | 0.1 | 25.75 | No QPO | 0.826 | 0.694 |
| C2 | 0.0021, 1.73 | 2e−4 | 0.1 | 22.82 | 10.63 | 0.853 | 0.844 |
| C3 | 0.0021, 1.73 | 3e−4 | 0.1 | 20.39 | 12.34 | 0.868 | 0.954 |
| C4 | 0.0021, 1.73 | 4e−4 | 0.1 | 18.62 | 14.63 | 0.873 | 0.944 |
| C5 | 0.0021, 1.73 | 5e−4 | 0.1 | 18.33 | 22.74 | 0.901 | 1.071 |
| C6 | 0.0021, 1.73 | 1e−3 | 0.1 | 15.02 | 18.2 | 1.074 | 0.993 |
| C7 | 0.0021, 1.73 | 1e−2 | 0.1 | 3.4 | No QPO | 1.139 | 3.558 |
| C8 | 0.0021, 1.73 | 1e−1 | 0.1 | 3.6 | No QPO | 1.102 | 33.236 |
| C9 | 0.0021, 1.73 | 3e−4 | 0.05 | 23.53 | 10.74 | 0.998 | 0.859 |
| C10 | 0.0021, 1.73 | 3e−4 | 0.15 | 18.37 | 22.80 | 0.797 | 1.031 |
| C11 | 0.0021, 1.73 | 3e−4 | 0.2 | 16.78 | No QPO | 0.757 | 1.049 |

with axi-symmetric sub-Keplerian accretion flow, as an initial condition, we choose a configuration where the infalling halo has a shock. We choose $\dot{m}_d$ and $\dot{m}_h$ as our parameters of the simulations. In Table 1, we present results of our simulation which is reproduced from GGC14 and G14. As we increase $\dot{m}_d$ keeping $\dot{m}_h$ fixed, we generally find the shock to move closer to the black hole in the final steady state and even disappear for some very higher values of $\dot{m}_d$ (see Column 5 of Table 1). This is understandable because, higher $\dot{m}_d$ supplies more soft photons to the Compton cloud. Because of inverse-Compton scattering, they extract more thermal energy from this region, thereby reduce the thermal pressure of this region and the shock moves closer to the black hole. This results in a softer spectrum in the final steady state. The spectral slopes can be found in Column 7. Since the outflow also partially depends on the thermal energy content of this region, it is found to be quenched for higher $\dot{m}_d$. These results clearly demonstrate the correlation between the spectral states and outflow rates from the accretion disks [3, 4, 20, 24, 25]. We also perform the other set of tests, namely, increasing $\dot{m}_h$ with keeping $\dot{m}_d$ fixed. For such simulations, we again find that the shock moves closer to the black hole with increasing $\dot{m}_h$. This is due to the enhanced number of scatterings inside the halo because of the higher optical depth, which in turn increases the cooling in this region. However, the final resulting spectra are found to be harder with increasing $\dot{m}_h$ because more photons get inverse-Comptonized and hence, the number of high energy photons in a given energy band increases.

## 4 Temporal Properties of the TCAF

The advantage of Monte-Carlo simulation is that we can track each photon beginning from its origin to detection. Thus, we can compute exactly how much time it spent in between. This is very useful because this helps us in constructing

the light curves using our simulation result. These simulated lightcurves carry the signature of the time variation of the hydrodynamic properties inside the disk.

In our two-step simulation procedure, we time-advance the hydro state by an amount of time, let's say, $\delta t$. Then, in the Monte-Carlo step, we process all the photons which are produced in this time interval $\delta t$. As soon as a photon leaves the computational domain (i.e., it is 'detected'), it is saved in an energy bin as well as in a time bin. For our typical simulations presented in GGC14; G14, we divide the energy range 0.01–5000 keV in 300 logarithmic energy bins. The time resolution is of 5 ms. After the run is completed, we rebin these photons with a time bin of 0.01 s to compute the lightcurves. To count the photons in a given energy band, we add up the photon numbers in each energy bin which fall in the required energy band. In Fig. 2, we show a few light curves (taken from GGC14, G14) for the simulation runs with parameters presented in Table 1. Case IDs are marked on each panel. The disk accretion rates and halo rates were chosen to be on the lower side so as to have fewer number of photons to be used in Monte-Carlo simulations.

We are able to analyze these lightcurves in the formal way. For example, we can construct the power density spectrum (PDS) of these light curves using the NASA

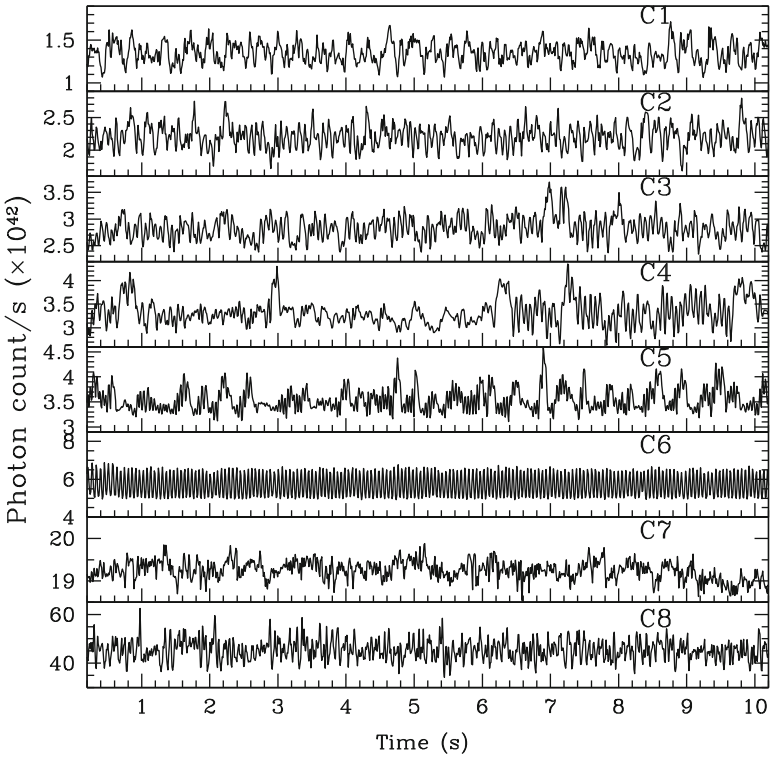



**Fig. 2** The simulated light curves in 0.5–100 keV range are shown. Here, $\dot{m}_d$ is increased keeping $\dot{m}_h = 0.1$ constant (GGC14). See Table 1 for the parameters used for these cases

HEAsoft package and we can find whether any quasi-periodic oscillations (QPOs) are formed or not. In fact, such analysis shows that we find several cases where low frequency (LF) QPOs are indeed formed in our simulations. The observed frequencies are listed in column 6 of Table 1. These simulation results further helped us in verifying even more conjectures that were made earlier based on other simulations and observations (MSC96; CM00; CAM04; [21]). First, the oscillation in the centrifugal barrier dominated post-shock region (CENBOL) is responsible for the LFQPOs observed in the black hole candidates. This is easily verified by taking the Fourier transform of the time variation of shock location. Clearly, the oscillation frequency matches with the QPO frequency that are listed in Table 1. Second, LFQPOs are found to be present when the infall time scale of post-shock matter roughly matches with the cooling time scale. This is also verified by evaluating the required time scales from our simulations. For the simulation runs presented in GGC14; G14, we find the shape of this hot post-shock region to be mostly paraboloid with the base to be oblate spheroid sometimes. In most cases, the post-shock region is found to have lots of turbulent flow of matter. Therefore, it is not always straightforward to evaluate the exact infall time scale. However, we can approximately evaluate the infall time scale, as is done in GGC14; G14. In order to calculate the infall time scale in the post-shock region, first we need to know the radial velocity profile of infalling matter in this region. Since the post-shock matter has turbulence and back flow, we evaluate an average radial velocity $v_{avg}(R)$ of the matter at each radial zone with the zone-center location of $R$. In our grid based simulation, we already know the radial velocity component of matter in each zone. Thus, at a given $R$, we calculate the average of the radial velocity component over 20 vertical grids starting from the equatorial plane and calculate $v_{avg}(R)$ as follows:

$$v_{avg}(R) \sim \frac{\sum_{iz=1}^{20} v_R(R, iz)}{20},$$

where, $v_R(R, 1)$ represents the radial velocity component on the first vertical grid (i.e., on the equatorial plane), $v_R(R, 2)$ represents the same on the second vertical grid and so on. Once we know $v_{avg}(R)$ at each radial zone, we can evaluate the infall time scale as (GGC14),

$$t_{in} = \sum_{R=R_{sh}}^{1.5} \frac{dR}{v_{avg}(R)},$$

where, the summation is done starting from the shock location $R_{sh}$ to the inner boundary 1.5 of the computational domain. The cooling timescale $t_{cool}$, on the other hand, is easy to compute as it includes only the scalar quantities, namely, the total thermal energy content $E_{th}$ in the post-shock region and the cooling rate $\dot{E}$ in the

same region. Thus, we have

$$t_{cool} = \frac{E_{th}}{\dot{E}}.$$

Please note that $\dot{E}$ is calculated directly from the Monte-Carlo simulation. In Table 1, we present the ratio $\frac{t_{in}}{t_{cool}}$ in the last column. We see that this ratio is nearly 1 for all the cases when LFQPOs are seen.

## 5 Discussions and Further Studies

The results from the analytical methods and the numerical simulations helped to conjecture (or even prove) many of the findings about the spectral and timing properties of the black holes. These were: The variations of the accretion rates of the two components, namely disk and halo, of a TCAF are responsible for state transitions (CT95; [2]); The spectral states must be directly correlated to the outflow rates [3, 4, 20]; The oscillation of the CENBOL generates the Low Frequency Quasi-Periodic Oscillations (LFQPOs) and the oscillations are produced when there is a resonance between the cooling and infall time scales (MSC96; CAM04). In our work, with the help of the radiation hydrodynamic simulations, we rigorously prove that indeed the spectral and timing properties of a TCAF are exactly as conjectured before.

Parallel to the above work, development has also been made to include the effect of viscosity in the hydrodynamic simulations [31, 32]. These simulations show that inclusion of viscosity and radiative process can generate stable TCAF configuration self-consistently. However, in our simulations presented above, instead of generating the disk self-consistently, we assume its presence to serve as the source of soft photons. Therefore, it is obvious that we further improve our simulation technique to include viscosity in the radiation hydrodynamic simulation and self-consistently generate the disk and the photons from it. Towards that step, we improve the radiative processes in the viscous hydrodynamic simulation code as shown in [33]. In this work, instead of assuming simple power-law cooling ($\sim T^{\beta}$, with $\beta = 0.6$) everywhere in the disk, we include the cooling rate consistent with black body radiation ($\sim T^4$) from the surface of the optically thick regions in our simulation domain. These simulations, with improved cooling prescription, show the formation of a stable TCAF configuration. Thus, in this work, we prove that the standard disk, emitting black body on the equatorial plane, can indeed survive the fast moving sub-Keplerian flow above and below. Moreover, in this paper, we show that the surface temperature of the resulting cooler, denser Keplerian component behaves like a standard [49] disk. More work currently being done to study the spectral and timing properties from this self-consistently produced TCAF solution.

In a TCAF scenario (CT95), the Keplerian disk evaporates inside the post-shock region due to heating and turbulence, and mix up with the sub-Keplerian

component. However, in a non-viscous hydrodynamic simulation, achieving this mix up is numerically challenging since we don't have a mechanism to transport angular momentum. For that reason, in all our simulations presented in Sects. 3 and 4, we assume the presence of a Keplerian disk extending till the inner most stable circular orbit ($3r_g$ for a non-rotating black hole). This assumption, in turn, resulted in very efficient cooling for lower $\dot{m}_d$ (please see Table 1). We hope that in a self-consistently simulated TCAF solution, we will find improved values of accretion rates consistent with observed results [17, 18, 22, 35].

Further improvements in this subject aim to completely replace the use of pseudo-Newtonian potential and study the TCAF solution and its spectral, timing properties as well as the images from the disk in full general relativistic (GR) framework. Towards that goal, hydrodynamic simulations have been performed in full general relativity, using Schwarzschild as well as Kerr spacetime [36, 37]. We have been able to show that, even in two-dimension, centrifugal force supported steady shock waves formation is possible in presence of strong dragging of inertial frames. Simultaneously, to study the propagation of photons in these space-time, ray tracing algorithm has been developed (G14; [19]). These ray tracing code has been used in the Monte-Carlo simulations to study the spectral properties as well as the images of the disk. In future, we have plan to couple all these isolated pieces and construct a general relativistic viscous radiation hydrodynamic simulation code which will allow us to self-consistently simulate the TCAF solution in presence of strong gravity and study its spectral, temporal properties as well as image the disk configuration.

## References

1. Bondi: MNRAS **112**, 195 (1952)
2. Chakrabarti, S.K.: ApJ **484**, 313 (1997)
3. Chakrabarti, S.K.: Ind. Jour. of Phys. **72B**, 565 (1998). astro-ph/9810412
4. Chakrabarti, S.K.: A&A **351**, 185 (1999)
5. Chakrabarti, S.K.: Astrophys. Space Sci. **297**, 131 (2005)
6. Chakrabarti, S.K.: Bull. Astr. Soc. India **35**, 271 (2007)
7. Chakrabarti, S.K.: AIP Conference Proceedings of Observational Evidence for Black Holes in the Universe, vol. 1053, p. 325 (2008)
8. Chakrabarti, S.K.: AIP Conference Proceedings of 4th Gamow International Conference on Astrophysics and Cosmology After Gamow, vol. 1206, p. 244 (2010)
9. Chakrabarti, S.K., Mandal, S.: ApJ **642**, L49 (2006)
10. Chakrabarti, S.K., Manickam, S.G.: ApJ **53**, L41 (CM00) (2000)
11. Chakrabarti, S.K., Molteni, D.: ApJ **417**, 671 (1993)
12. Chakrabarti, S.K., Molteni, D.: MNRAS **272**, 80 (1995)
13. Chakrabarti, S.K., Titarchuk, L.G.: ApJ, 455, 623 (CT95) (1995)
14. Chakrabarti, S.K., Acharyya, K., Molteni D.: A&A **421**, 1 (2004)
15. Chakrabarti, S.K., Debnath, D., Nandi, A., Pal, P.S.: A&A **489**, L41 (2008)
16. Chakrabarti, S.K., Dutta, B.G., Pal, P.S.: MNRAS **394**, 1463 (2009)
17. Chakrabarti, S.K., Mondal, S., Debnath, D.: MNRAS **452**, 3451 (2015)
18. Chatterjee, D., Debnath, D., Chakrabarti, S. K., Mondal, S., Jana, A.: ApJ **827**, 88 (2016)

19. Chatterjee, A., Chakrabarti, S.K., Ghosh, H., Garain, S.K.: MNRAS **478**, 3356 (2018)
20. Das, S., Chattopadhyay, I., Nandi, A., Chakrabarti, S.K.: A&A **379**, 683 (2001)
21. Debnath, D., Chakrabarti, S.K., Nandi, A.: A&A **520**, 98 (2010)
22. Debnath, D., Molla, A.A., Chakrabarti, S.K., Mondal, S.: ApJ **803**, 59 (2015)
23. Dutta, B.G., Chakrabarti, S.K.: MNRAS **404**, 2136 (2010)
24. Fender, R.P., Belloni, T.M., Gallo, E.: MNRAS **355**, 1105 (2004)
25. Gallo, E., Fender, R.P., Pooley, G.: NuPhS **132**, 363 (2004)
26. Garain, S.K.: PhD thesis (2014)
27. Garain, S.K., Ghosh, H., Chakrabarti, S.K.: ApJ **758**, 114 (GGC12) (2012)
28. Garain, S.K., Ghosh, H., Chakrabarti, S.K.: MNRAS **437**, 1329 (GGC14) (2014)
29. Ghosh, H., Chakrabarti, S.K., Laurent, P.: Int. J. Mod. Phys. D **18**, 1693 (2009)
30. Ghosh, H., Garain, S.K., Giri, K., Chakrabarti, S.K.: MNRAS **416**, 959 (GGGC11) (2011)
31. Giri, K., Chakrabarti, S.K.: MNRAS **421**, 666 (2012)
32. Giri, K., Chakrabarti, S.K.: MNRAS **430**, 2836 (2013)
33. Giri, K., Garain, S.K., Chakrabarti, S.K.: MNRAS **448**, 3221 (2015)
34. Harten, A.: Jour. of Comp. Phys. **49**, 357 (1983)
35. Jana, A., Debnath, D., Chakrabarti, S.K., Mondal, S., Molla, A.A.: ApJ **819**, 107 (2016)
36. Kim, J., Garain, S.K., Balsara, D.S., Chakrabarti, S.K.: MNRAS **472**, 542 (2017)
37. Kim, J., Garain, S.K., Chakrabarti, S.K., Balsara, D.S.: MNRAS (2018, submitted)
38. Lanzafame, G., Molteni, D., Chakrabarti, S.K.: MNRAS **299**, 799 (1998)
39. Laurent, P., Titarchuk L.: ApJ **511**, 289 (1999)
40. Mandal, S., Chakrabarti, S.K.: ApJ **689**, L17 (2008)
41. Molteni D., Lanzafame, G., Chakrabarti, S.K.: ApJ **425**, 161 (1994)
42. Molteni, D., Ryu, D., Chakrabarti, S.K.: ApJ **470**, 460 (MRC96) (1996)
43. Molteni, D., Sponholz, H., Chakrabarti, S.K.: ApJ **457**, 805 (MSC96) (1996)
44. Nandi, A., Manickam, S.G., Rao, A.R., Chakrabarti, S.K.: MNRAS **324**, 267 (2001)
45. Paczyński, B., Wiita P.J.: A&A **88**, 23 (PW80) (1980)
46. Poznyakov, L., Sobol, I., Sunyaev, R.: A & Sp Physics Reviews **2**, 189 (1983)
47. Rao, A.R., Naik S., Vadawale, S.V., Chakrabarti, S.K.: A&A **360**, 25L (2000)
48. Ryu, D., Ostriker, J.P., Kang, H., Cen, R.: ApJ **414**, 1 (1993)
49. Shakura, N.I., Sunyaev, R.A.: A& A **24**, 337 (1973)
50. Smith, D., Heindl, W., Swank, J.: ApJ **569**, 362 (2002)
51. Sunyaev, R.A., Titarchuk, L.G.: A&A **86**, 121 (1980)

# Dynamics of Magnetic Flux Tubes in an Advective Flow Around Black Hole




**Arnab Deb**

**Abstract** Observational studies in the two spectral regions of the electromagnetic spectrum, in the domain of the hard X-rays on one hand, and in the domain of radio wavelengths on the other hand, revealed the existence of new stellar sources of relativistic jets known as micro-quasars (Mirabel et al. Nature 358(6383):215–217, 1992; Mirabel and Rodriguez, Nature 371(6492):46–48, 1994). It is seen that the relativistic jets with significant matter content are produced when the inner part of the disk is destroyed and evacuated (Chakrabarti and D'Silva, ApJ 424:138, 1994; Nandi et al. Astron. Astrophys. 380:245–250, 2001). Clearly, magnetic field has to play a major role in origin, acceleration and collimation of these relativistic jets. Due to predominantly rotating accretion flows close to the inner edge of a disk, entangled magnetic fields advected through the flow would be toroidal. This is particularly true for weakly viscous, low angular momentum transonic or advective discs. We focus our study to the trajectories of toroidal flux tubes inside a geometrically thick flow which undergoes a centrifugal force supported shock and also the effects of these flux tubes on the dynamics of the inflow and the outflow. Finite difference method (Total Variation Diminishing) is used for this purpose and specifically focussing on whether these flux tubes significantly affect the properties of the outflows such as its collimation and the rate. It is seen that depending upon the cross-sectional radius of the flux tubes which control the drag force, these field lines may move towards the central object or oscillate vertically before eventually escaping out of the funnel wall (pressure zero surfaces) along the vertical direction. A comparison of results obtained with and without flux tubes show these flux tubes indeed could play pivotal role in collimation and acceleration of jets and outflows.

A. Deb (✉)
S.N. Bose National Centre for Basic Sciences, Salt Lake, Kolkata, India

© Springer International Publishing AG, part of Springer Nature 2018

B. Mukhopadhyay, S. Sasmal (eds.), *Exploring the Universe: From Near Space to Extra-Galactic*, Astrophysics and Space Science Proceedings 53,
https://doi.org/10.1007/978-3-319-94607-8_15

## 1 Introduction

The process in which matter due to gravity accumulates in the vicinity of a compact object is called accretion. In case of black holes, the inner boundary condition states that matter must fall onto the black hole with velocity of light and this requires all the accretion flow to be transonic in nature. The centrifugal pressure causes the inflowing matter to slow down and this results in piling up of the matter near the inner part of the disk causing an increase in temperature and the matter is puffed up creating a torus like structure. This structure is called the Centrifugal Pressure supported Boundary layer or CENBOL ([4], hereafter C89, 1999, [5]; MLC94, [6]; [7]). As shown by MLC94, in the limit of no radial velocity, the CENBOL has a property similar to as that of a thick accretion disk [35]. Due to this CENBOL region, a fraction of inflowing matter gets ejected as the outflow and this outflow eventually gets collimated and accelerated creating relativistic jets. However, a clear understanding of formation, acceleration, and collimation of these jets has been eluding the astrophysicists. Early theoretical approach to study collimation and acceleration of jets consisted of studies of thin as well as geometrically thick accretion discs as it was believed that the properties of accretion discs are somehow connected to the origin of bipolar jets. Numerous theoretical models [1, 2, 8, 21, 27, 28] showed that in the context of thin disk hydromagnetic processes play a enigmatic role in collimation and acceleration of outflows/jets.

Blandford and Payne [1] (BP) assumed an axially symmetric, self-similar, cold magnetospheric flow originating from the Keplerian disc and asserted that a centrifugal pressure driven outflow is possible if the poloidal component of the magnetic field makes an angle less than 60°. At large distances from the disc, the toroidal component of the magnetic field becomes important and aides in collimation the outflow. Königl [27] in his work obtained radial self-similar configuration of magnetic field inside a cold and partially ionized disc and showed that for certain set of parameters BP type wind can be produced. Chakrabarti and Bhaskaran [8] provided more general approach to the solution of the field and obtained well collimated bipolar outflows and radio jets from magnetized accretion discs in self-consistent manner.

Another genre of magnetized disk solutions are present in the literature where the background flow is assumed to be the standard Keplerian disks and the magnetic field is assumed to be sheared and advected by the flow [24, 29, 41]. These works showed that discs with sufficient magnetic flux tube can eventually launch cosmic jets as the field structure close to disc surface becomes Blandford-Payne type. There exist few works that extends to Kerr black holes. The gravitomagnetic potential of a rotating black hole in the presence of a differentially rotating disk is seen to generate poloidal loop structures close to and in the ergosphere that may support extraction of rotational energy from the black hole [22, 23]. In principle the Kerr hole may even drive a self-excited dynamo and amplify weak (even axisymmetric) magnetic field to a higher field strength [25, 26]. A large body of

literature is present that explores many aspects of the effects of buoyancy and shear amplification on these magnetic flux in the paradigm of thin accretion disk (e.g., [9–11, 15, 16, 27, 40]).

All the works discussed above are in the paradigm of thin accretion disk or standard Keplerian disc. But now, we shall turn our attention to magnetized thick disc where due to the combined effect of magnetic tension and buoyancy, toroidal fields are ejected from the disc and may produce jets without having any significant poloidal component. If accretion rate is high ($\dot{M} >> \dot{M}_{Edd}$), the radiation emitted by the in-falling matter exerts a significant pressure on the gas which inflates the disc making it geometrically 'thick' [$H(r) \sim r$]. Thick accretion discs have very little angular momentum and matter may fall into the central object without any need for a viscosity and also the thick accretion disks have funnels like openings or chimneys where the anisotropic radiation field could be sufficiently strong to accelerate radio jets. But still, magnetic fields can be observed in jets and this makes the 'chimney' region magnetically active. A thorough analytical study of the behaviour of toroidal magnetic flux tubes in the backdrop of thick accretion discs has been studied by Chakrabarti and D'Silva ([9]; hereafter CD94(I) and [12]; hereafter, CD94(II)). They showed that depending upon the various flows and field parameters, such as, initial position of release, cross-sectional radius of the flux tubes, angular momentum distribution, etc. flux rings injected into thick disk will emerge into the "chimney" (funnel like opening at the inner part of the disc) or will be expelled away. The magnetic fields are cannibalized along with the accreting matter from the companion and are sheared into forming toroidal flux tubes. From this study it can be observed that firstly, for sufficiently high disc temperature ($T_p > 4 \times 10^{10}$ K), the magnetic tension dominates over all other effects and the tube collapses catastrophically towards the axis and thus squeezing out matter in the disk along the axis of the black hole in the process to form radio jets. The sudden collapse of fields in the funnel would cause destruction of the inner part of the disc forming blobby radio jets. Detailed observation of GRS1915+105 shows these features (Mirabel and Rodriguez [32], Mirabel et al. [33], Nandi et al. [34]). Secondly, for proper entropy condition coronal structure is possible to form as flux tubes can oscillate inside the disc creating an internal structure similar to the solar interior. So far, no study of the flux tube behaviour and its possible effects on the flow dynamics and on the jet formation in the context of a self-consistent, time dependent, geometrically thick transonic flow has been performed. Hence, we first simulate a time dependent inviscid accretion disk using finite difference grid based numerical method. We, then, inject toroidal thin magnetic flux tube into the inviscid flow and follow its trajectory, its effect on the flow dynamics and its role in the collimation and acceleration of the outflow and jet.

## 2 Governing Equations for Hydrodynamic Flow and Flux Tubes

### 2.1 Hydrodynamic Equations

Equations governing hydrodynamic flow is comprised of the conservation laws, namely, the mass, momentum, and energy conservation. These equations can be written as, using dimensionless units that are presented in Ryu et al. [37, 38], Molteni et al. ([31], hereafter, MRC96), Giri et al. ([17], hereafter, GC10) and Giri [18] in great detail. For inviscid flow, hydrodynamic equations can be obtained from Navier-Stokes equation by ignoring viscous stress tensor. The equations are given as,

$$\frac{\partial \rho}{\partial t} + \nabla.(\rho \mathbf{v}) = 0 \tag{1}$$

$$\rho \frac{\partial \mathbf{v}}{\partial t} + \rho(\mathbf{v}.\nabla).\mathbf{v}) = -\nabla p + \mathbf{f_{grav}} + \mathbf{f_{mag}} + \nabla.\tau \tag{2}$$

$$\frac{\partial E}{\partial t} + \nabla.\left[\left(H + \frac{1}{2}v^2\right).\rho \mathbf{v}\right] = 0. \tag{3}$$

$H$ is the enthalpy of the system, $\mathbf{f_{grav}}$ and $\mathbf{f_{mag}}$ are the gravitational force and the force due to magnetic field respectively. These two forces come under the broader classification of body forces. $\tau$ is the viscous stress tensor that has six mutually independent components but for thin accretion flow the most dominant contributor is $\tau_{r\phi}$ component (in cylindrical co-ordinate system) and thus we can ignore other components. For non magnetized inviscid flow we put $\tau = 0$ and $f_{mag} = 0$. Equations (1)–(3) can be written in terms of conservative variables in a compact form,

$$\frac{\partial \mathbf{q}}{\partial t} + \frac{1}{r}\frac{\partial (r\mathbf{F}_1)}{\partial r} + \frac{\partial \mathbf{F}_2}{\partial r} + \frac{\partial \mathbf{G}}{\partial z} = \mathbf{S}, \tag{4}$$

where the state vector is

$$\mathbf{q} = \begin{pmatrix} \rho \\ \rho v_r \\ \rho v_\theta \\ \rho v_z \\ E \end{pmatrix}, \tag{5}$$

the flux functions are

$$\mathbf{F}_1 = \begin{pmatrix} \rho v_r \\ \rho v_r^2 \\ \rho v_\theta v_r \\ \rho v_z v_r \\ (E+p)v_r \end{pmatrix} , \mathbf{F}_2 = \begin{pmatrix} 0 \\ p \\ 0 \\ 0 \\ 0 \end{pmatrix} , \mathbf{G} = \begin{pmatrix} \rho v_z \\ \rho v_r v_z \\ \rho v_\theta v_z \\ \rho v_z^2 + p \\ (E+p)v_z \end{pmatrix}, \tag{6}$$

and the source function is

$$\mathbf{S} = \begin{pmatrix} 0 \\ \frac{\rho v_\theta^2}{r} - \frac{\rho r}{2\left(\sqrt{r^2+z^2}-1\right)^2\sqrt{r^2+z^2}} - f_{mag,r} \\ -\frac{\rho v_r v_\theta}{r} \\ -\frac{\rho z}{2\left(\sqrt{r^2+z^2}-1\right)^2\sqrt{r^2+z^2}} + f_{mag,z} \\ -\frac{\rho(r v_r + z v_z)}{2\left(\sqrt{r^2+z^2}-1\right)^2\sqrt{r^2+z^2}} \end{pmatrix}. \tag{7}$$

Here, the energy density (without potential energy) is given as(GC10, MRC96),

$$E = p/(\gamma - 1) + \rho(v_r^2 + v_\theta^2 + v_z^2)/2,$$

where $\rho$ is the mass density, $\gamma$ is the adiabatic index, $p$ is the pressure, $v_r$, $v_\theta$ and $v_z$ are the radial, azimuthal and vertical components of velocity respectively.

## *2.2 Equation of Motion of the Flux Tubes*

We consider an azimuthally symmetric flux ring with the approximation that the cross sectional radius of the flux ring is smaller compared to local pressure scale height. This enables us to assume that variation of different physical quantities inside the tube is negligible. Here, following CD94(I), the equations of motion for

thin axisymmetric flux tube are given as,

$$\ddot{\xi} - \xi\dot{\theta} + \frac{X}{(1+X)}[-\xi\dot{\phi}^2 \sin^2\theta - 2\xi\omega\dot{\phi}\sin^2\theta] = \frac{X}{(1+X)}\left\{\frac{M}{X}[g - \xi\omega^2\sin^2\theta] - T_{ens}\sin\theta - \frac{D_r}{\pi\sigma^2\rho_e}\right\}, \tag{8}$$

$$\xi\ddot{\theta} + 2\dot{\xi}\dot{\theta} + \frac{X}{(1+X)}[-\xi\dot{\phi}^2\sin\theta\cos\theta - 2\xi\omega\dot{\phi}\sin\theta\cos\theta] = -\frac{X}{(1+X)}\left\{\frac{M}{X}\xi\omega^2\sin\theta\cos\theta + T_{ens}\cos\theta + \frac{D_\theta}{\pi\sigma^2\rho_e}\right\}, \tag{9}$$

$$\xi\sin\theta\ddot{\phi} + 2\dot{\xi}\sin\theta(\dot{\phi}+\omega) + 2\xi\cos\theta\dot{\theta}(\dot{\phi}+\omega) + \xi\sin\theta\left\{\dot{\xi}\frac{\partial\omega}{\partial r} + \dot{\theta}\frac{\partial\omega}{\partial\theta}\right\} = 0, \tag{10}$$

where, $(\xi, \theta, \phi)$ is the position of a point inside a flux ring having magnetic field $B$. Here, $\xi$ is measure of radial distance in the unit of Scwarzschild radius ($r_g$). Here, $X$ is defined as $X = m_i/m_e$ where, $m_i = \rho_i\pi\sigma^2 \cdot 2\pi r\sin\theta$ is the mass inside the flux tube of radius of cross section (in the meridional plane) $\sigma$ and $m_e = \rho_e\pi\sigma^2\cdot 2\pi r\sin\theta$ is the mass of the external flow displaced by the flux tube. The flux $\psi = B\pi\sigma^2$ through the ring remains constant. The flux tube experiences buoyancy and the buoyancy factor is given by,

$$M = \frac{\rho_e - \rho_i}{\rho_e} = \frac{m_e - m_i}{m_e}$$

where $\rho_e$ and $\rho_i$ represent external and internal densities respectively. In case of flux tubes moving adiabatically with its surrounding we solve for $\rho_i/\rho_e$ from the equation,

$$k_1\left(\frac{\rho_i}{\rho_e}\right)^{4/3} + k_2\left(\frac{\rho_i}{\rho_e}\right)^2 - 1 = 0, \tag{11}$$

where,

$$k_1 = \frac{(1-\beta_e M_0)}{(1-M_0)^{4/3}},$$

$$k_2 = \beta_e\frac{M_0}{(1-M_0)^2}\left(\frac{T_e}{T_{e,0}}\right)^2\left(\frac{\xi\sin\theta}{\xi_0\sin\theta_0}\right)^2.$$

From the ratio $\rho_i/\rho_e$ we calculate the magnetic buoyancy. The effective acceleration due to gravity is,

$$\mathbf{g}_{eff} = (g - \xi\omega^2 \sin^2\theta)\hat{\xi} - \xi\omega^2 \sin\theta\cos\theta\hat{\theta} \tag{12}$$

where, $g$ is given as $g = 1/2(\xi - 1)^2$ in Schwarzschild unit. The drag force per unit length is given as,

$$\mathbf{D} = -0.5C_D\rho_e\sigma|(\dot{\xi} - v)\hat{\xi} + \xi\dot{\theta}\hat{\theta}|(\dot{\xi} - v)\hat{\xi} + \xi\dot{\theta}\hat{\theta} \tag{13}$$

where, $C_D = 0.4$ is a dimensionless coefficient that has constant value of 0.4 for high Reynold's number, [19]. Magnetic tension force is given by

$$T_{ens} = \frac{4\pi M_0 T_e(\xi_0)}{\mu_e A(1 - M_0)\xi_0 \sin\theta_0}$$

is a dimensionless measure of the magnetic tension (CD94(I)) where, $T_e(\xi_0)$ is the initial of the external fluid, $(\xi_0, \theta_0)$ is the initial position of the flux tube, $A$ is area increment factor given as $A = (\sigma/\sigma_0)^2$, where $\sigma_0$ is the initial cross sectional radius, $\sigma$ is the instantaneous radius and $M_0$ is the initial buoyancy factor, which is calculated to be $M_0 = B^2/8\pi p_{g,e}$ where, $p_{g,e}$ is external gas pressure. As $A(t) = \sigma^2(t)/\sigma_0^2$, this gives the evolution of the flux tubes over the course of the simulation. Explicit form of this area expansion factor is given as (CD94(I)),

$$A = \left(\frac{T_e(\xi_0, \theta_0)}{T_e(\xi, \theta)}\right)^3 \left(\frac{\xi_0 \sin\theta_0}{\xi \sin\theta}\right)\left(\frac{1 - M_0}{1 - M}\right)$$

where, $T_e(\xi, \theta)$ is directly coming from our simulation at each instant of time.

For the purpose of simulation, we have considered the black hole to be a stellar mass black hole with the mass $10M_\odot$. Outer boundary of the disc is assumed to be at $200r_g$ although the actual size of the disc is much larger than what we have considered. Since we have considered an inviscid disc the angular momentum remains constant throughout the disc. For the detail description of the numerical setup for the inviscid disc simulation refer to [13]. For schemes, basic properties of the code, and different test results, please refer to [20], [38] and [37]. We inject the magnetic flux rings at the outer boundary near the equatorial plane ($\theta = 89°$) with a initial magnetic buoyancy ($M_0$) which we calculate by taking the ratio between the magnetic pressure and external gas pressure. We use the injected flow to have constant specific angular momentum of (1) $\lambda = 1.6$, and (2) $\lambda = 1.7$ and for each of these cases we use the specific total energy $\varepsilon = 0.001,\ 0.002,\ 0.006$. For detailed set up of the magnetized disc refer to [14]. We couple the equations of motions for the flux tube with the hydrodynamic Total Variation Diminishing (TVD) code. We modify the source function as given in Eq. (7) by adding Lorentz force term. This will include flux tube's effect on the fluid. We calculate the density, velocity, pressure and temperature distribution using time dependant TVD code based on the

boundary values and the equation of state only. These flow parameters are used as the input parameters for computing a flux tube's evolution inside the disc since the drag, buoyancy etc. depend on the environment in which the tube is moving and those in turn are plugged in Eqs. (8)–(10) and we numerically solve them using the fourth order Runge-Kutta method.

## 3 Effects of Magnetic Flux Tube

The trajectories of the flux tubes are obtained in our simulations by solving the Eqs. (8)–(10) described in the Sect. 2.2 and are plotted in $r - z$ plane. Figure 1 shows the trajectories for the flux tubes injected with initial cross sectional radii $0.001,\ 0.005,\ 0.01,\ \&\ 0.1\ r_g$ respectively released from the outer boundary with two different flow energies, namely, $\varepsilon = 0.001, 0.002$ (marked). For both the energies, flux tubes having initial $\sigma < 0.1 r_g$ emerge in the chimney. Flux tubes with

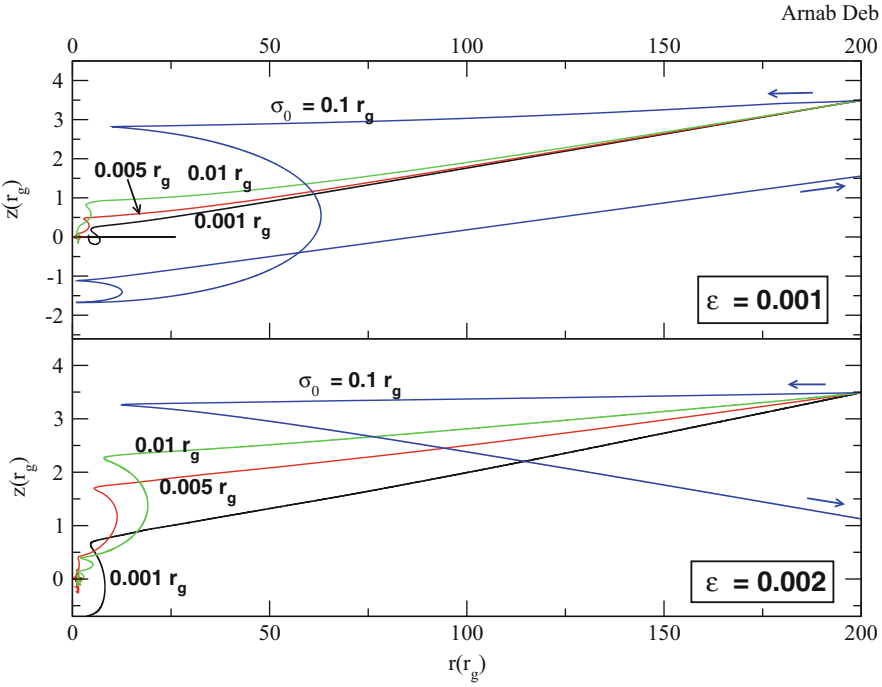



**Fig. 1** Trajectories of flux tubes injected from the outer boundary i.e., $r = 200 r_g$ and $\theta = 89°$ with zero initial velocity. Trajectories are in $r = R \sin\theta$ vs. $z = R \cos\theta$ plane. The trajectories are drawn for a flow with angular momentum $\lambda = 1.6$ and energies 0.001 (upper panel) and 0.002 (lower panel). $\sigma$ is the cross sectional radii of the injected flux tubes. Here $\sigma$ values are 0.001 $r_g$, 0.005 $r_g$, 0.01 $r_g$ and 0.1 $r_g$ (Deb et al. [14])

$\sigma \geq 0.1 r_g$ are expelled for the lower energy case. As we increase the energy of the flow, the flux rings tend to oscillate more as they will have more kinetic energy than the lower flow energy configuration. Since this is an inviscid flow, Coriolis force will not play any part in this and flux tubes will move inwards along the direction of local pressure gradient.

Jets can be categorized into two classes: (a) sustained and slow moving outflow originating from the post shock region and (b) blob of fast moving matter that squirted out due to sudden collapse of the inner part of the disc. The type (a) outflows are accelerated indirectly and the collimation of this jet reduces its lateral expansion retaining its initial energy. The cross-sectional area increases slowly with distance (along Z axis) and thus they are accelerated. Figure 2 shows the radial distribution of outflow rate for magnetized and non-magnetized flow having angular momentum 1.6 and from the plots it is quite evident that outflow coming out of magnetized flow is collimated by the presence of magnetic flux tube. Figure 3 shows the z-velocity difference of magnetized and non magnetized flow and it can be observed that in case of magnetized flow the velocity has increased significantly and thus it can be inferred that the outflow has been accelerated in presence of magnetic flux tube. If we increase the angular momentum to 1.7 only the limit for expulsion of flux tubes changes but overall nature of the outcome remains same. Here, we have only summarized our results but for detailed analysis refer to [14]

## 4 Conclusion

In earlier studies, such as CD94(I), CD94(II), simulations were carried out to study the dynamics of flux tubes in the backdrop of time independent thick disk [3, 35, 36]. In those earlier works, the conclusions can be summarized as, depending upon the position of release flux tubes can emerge into the chimney making it highly magnetically active region or can be expelled away. It is also possible to construct favourable entropy condition so that flux tubes can oscillate inside the disc around equipotential surface and thus consequently storing the flux tubes until they become enough buoyant to leave the system. In this present study, we inject a toroidal flux tube and follow its dynamics and its effect inside a time dependent two quadrant accretion flow after removing the reflection symmetry. In our simulation depending on its initial cross sectional radius and flow parameters such as angular momentum and energy flux tubes move toward the "chimney" or oscillate till it gets expelled away. We also find that in case of certain angular momenta and energies, firstly, the outflow rates ($\dot{M}(r)$) from both upper and lower quadrants increase significantly in comparison to the outflow rates with respect to the non-magnetic cases and secondly, the outflow rate is reaching its maximum value at much smaller radius, i.e., the spread of the outflow at the upper and lower boundaries has reduced significantly. We find that the difference of z component of velocity of magnetized and non magnetized flow becomes positive in a very narrow zone of outflowing region indicating the increase of velocity in the presence of magnetic field.

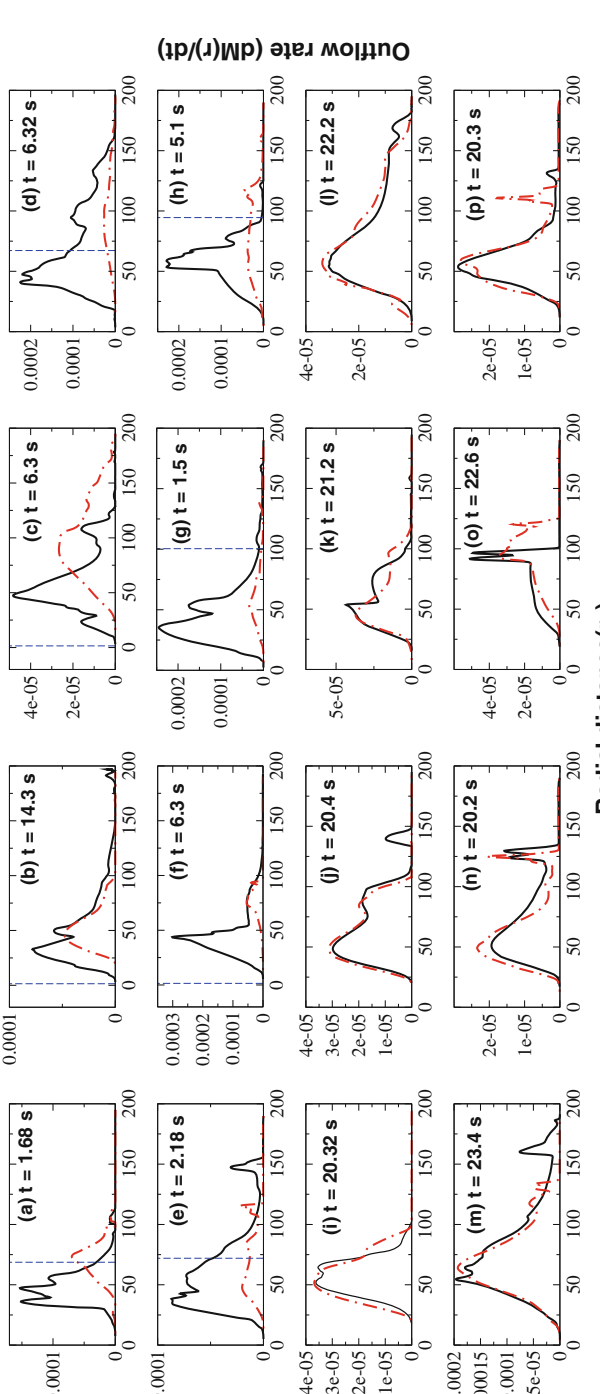



**Fig. 2** Radial distribution of the outflow rate ($\dot{M}_{out}$) of the flow having the specific angular momentum ($\lambda$) = 1.6 and energy ($\varepsilon$) = 0.002. The black solid curve represents the outflow rate for the flow with magnetic field and red solid curve (dot-dashed in hard copies) denotes the result in non-magnetic case. The upper two rows (**a**)–(**h**) of the plot show the collimation of the outflow from upper and lower quadrants respectively for different flux tubes with different $\sigma$. The lower two rows (**i**)–(**p**) depict the dissipation of the collimating effect once the flux tube has escaped or fallen into the black hole. The vertical dashed lines drawn in panels of first two rows depict the position of the flux tube at time for which the outflow rates are drawn (Deb et al. [14]) (Color figure online)

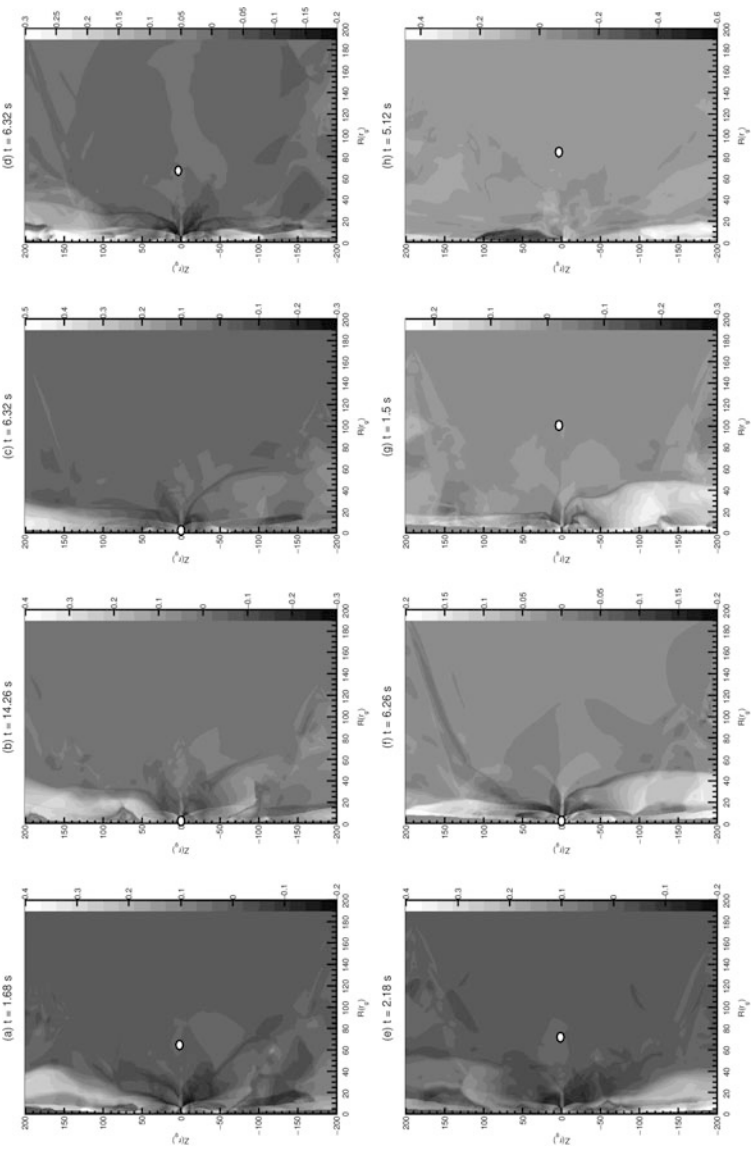



**Fig. 3** Map of the difference between z-velocity of magnetized and non-magnetized flow. (**a**)–(**d**) represent the upper quadrant and (**e**)–(**h**) represent the lower quadrant of a two quadrant flow. Each pair of panels (upper and lower) represent different cross sectional radius. Here, $\sigma$ (= 0.001, 0.005, 0.01, 0.1 $r_g$). Angular momentum ($\lambda$) is 1.6 and specific energy ($\varepsilon$) is 0.002. Each panel is drawn for different times were as the Fig. 2. The circles drawn in the panels give the position of flux tube at times for which the panels are drawn (Deb et al. [14])

## References


1. Blandford, R.D., Payne, D.G.: MNRAS **199**, 883 (1982)
2. Camenzind, M.: In: Belvedere, G. (ed.) Astrophysics and Space Science Library. Accretion Disks and Magnetic Fields in Astrophysics, vol. 156, pp. 129–143 (1989). https://doi.org/10.1007/978-94-009-2401-714
3. Chakrabarti, S.K.: ApJ **288**, 1 (1985)
4. Chakrabarti, S.K.: ApJ **347**, 365 (C89) (1989)
5. Chakrabarti, S.K.: Astron. Astrophys. **351**, 185–191 (1999)
6. Chakrabarti, S.K., Titarchuk, L.G.: Astrophys. J. **455**, 623 (1995)
7. Chakrabarti, S.K., Titarchuk, L., Kazanas, D., Ebisawa, K.: Astron. Astrophys. Suppl. **120**,163–166 (1996)
8. Chakrabarti, S.K., Bhaskaran, P.: MNRAS **255**, 255 (1992)
9. Chakrabarti, S.K., D'Silva, S.: ApJ **424**, 138 (1994)
10. Chakrabarti, S.K., Rosner, R., Vainshtein, S.I.: Nature **368**, 434 (1994)
11. Coroniti, F.V.: ApJ **244**, 587 (1981)
12. D'Silva, S., Chakrabarti, S.K.: ApJ **424**, 149 (1994)
13. Deb, A., Giri, K., Chakrabarti, S.K.: MNRAS **462**, 3502 (2016)
14. Deb, A., Giri, K., Chakrabarti, S.K.: MNRAS **472**(2), 1259–1271 (2017)
15. Eardley, D.M., Lightman, A.P.: ApJ **200**, 187 (1975)
16. Galeev, A.A., Rosner, R., Vaiana, G.S.: ApJ **229**, 318 (1979)
17. Giri, K., Chakrabarti, S.K., Samanta, M.M., Ryu, D.: MNRAS **403**, 516 (2010)
18. Giri, K.: In: Giri, K. (ed.) Numerical Simulation of Viscous Shocked Accretion Flows Around Black Holes. Springer Theses. Springer, Berlin (2015). ISBN 978-3-319-09539-4
19. Goldstein, S.: Modern Developments in Fluid Mechanics, vol. 1. Clarendon Press, Oxford (1938)
20. Harten, A.: J. Comp. Phys. **49**, 357 (1983)
21. Heyvaerts, J., Norman, C.: ApJ **347**, 1055 (1989)
22. Khanna, R.: ASPC **178**, 57 (1999)
23. Khanna, R.: (1999). arXiv:astro-ph/9903091
24. Khanna, R., Camenzind, M.: Astron. Astrophys. **263**, 401 (1992)
25. Khanna, R., Camenzind, M.: A & A **307**, 665 (1996)
26. Khanna, R., Camenzind, M.: A & A **313**, 1028 (1996)
27. Königl A.: ApJ **342**, 208 (1989)
28. Lovelace, R.V.E.: Nature **262**, 649 (1976)
29. Lovelace, R.V.F., Wang, J.C.L., Sulkanen, M.E.: Astrophys. J. **315**, 504 (1987)
30. Molteni, D., Lanzafame, G., Chakrabarti, S.K.: ApJ **425**, 161 (1994)
31. Molteni D., Ryu D., Chakrabarti, S.K.: ApJ **470**, 460 (1996)
32. Mirabel, I.F.; Rodríguez, L.F.: Nature **371**(6492), 46–48 (1994)
33. Mirabel, I.F., Rodriguez, L.F., Cordier, B., Paul, J., Lebrun, F.: Nature **358**(6383), 215–217 (1992)
34. Nandi, A., Chakrabarti, S.K., Vadawale, S.V., Rao, A.R.: Astron. Astrophys. **380**, 245–250 (2001)
35. Paczyński, B., Wiita, P.J.: Astron. Astrophys. **88**, 23 (1980)
36. Rees, M.J., Begelman, M.C., Blandford, R.D., Phinney, E.S.: Nature **295**, 17 (1982)
37. Ryu, D., Brown, G.L., Ostriker, J.P., Loeb, A.: ApJ **452**, 364 (1995)
38. Ryu D., Chakrabarti, S.K., Molteni, D.: ApJ **474**, 378 (1997)
39. Sakimoto P.J., Coroniti, F.V.: ApJ **342**, 49 (1989)
40. Shibata, K., Tajima, T., Matsumoto, R.: ApJ **350**, 295 (1990)
41. Wang, J.C.L., Sulkanen, M.E., Lovelace, R.V.: Astrophys. J. **355**, 38 (1990)

# A Pseudo-Newtonian Approach to Study the Accretion Processes Around Kerr Black Holes




**Soumen Mondal**

**Abstract** Successive developments of the Newtonian approaches are presented to study the accretion processes around black holes. A number of ways the potentials are proposed simply to avoid the complexity of the general relativistic (GR) framework. We carefully review those pseudo-potentials. The constraints and limitations, success and failure, have also been addressed. We find the pseudo-Kerr potential in Mondal and Chakrabarti (Mon Not R Astron Soc 371:1418, 2006) is one of the best for GR predictions. Using this pseudo-Kerr potential, the particle dynamics and the accretion flow hydrodynamics have also been carried out. The results are compared with the GR and percentage of accuracy are also presented briefly.

## 1 Introduction

The Keplerian accretion disk around a black hole namely the standard disk [32] provides enormous information about the accretion disk around the black holes in a non-relativistic framework. A simple minded model of the geometrically thick accretion disk (Paczyǹski and Wiita [28], hereafter PW) or Advective accretion flows [5, 35] do usually adopt a modified gravitational potential simply to reduce the complexity of the general relativistic(GR) treatment. The well known Paczyński and Wiita potential or the 'pseudo-Newtonian' approach also pretty accurately describes the complex scenarios of the hydrodynamics containing heating, cooling and radiative transfer processes. The results obtained in—hydrodynamic or magneto-hydrodynamic numerical simulations employing pseudo-Newtonian geometry—are quite satisfactory [10, 17, 21, 29, 30]. So far, using these potential a number of investigations and theoretical predictions are made. These are proven reasonably accurate, at least qualitatively, whenever any postdiction have been made success-

S. Mondal (✉)
Department of Physics, Jadavpur University, Kolkata, India

© Springer International Publishing AG, part of Springer Nature 2018

B. Mukhopadhyay, S. Sasmal (eds.), *Exploring the Universe: From Near Space to Extra-Galactic*, Astrophysics and Space Science Proceedings 53,
https://doi.org/10.1007/978-3-319-94607-8_16

fully using full general relativity. Interestingly one notices, the most of the photons coming to the detectors arise out the disk away from the inner regions, therefore, the discrepancies in this approach are small, order of few percent. Thus the idea of pseudo-Newtonian' approaches have been successfully continued often around a non rotating black holes. Almost at the same time, there is indeed a need of extension of the concept of 'pseudo-Newtonian' treatment in case of rotating black holes. So far several attempts have been made in this regard; e.g., [2, 7, 16, 26, 31]. It is being observed that to include the most, if not all of the properties of Kerr space time, one can always find a reasonable accuracy by suitably choosing an effective potential in Kerr geometry. Keeping that in mind a number of such potentials have been proposed. A few of them have been derived under a certain constraints and are used to work out a specific problem. The spirit of 'ad hoc'-ness in choosing a suitable a pseudo-potential in Kerr geometry first proposed by Chakrabarti and Khanna [7] considering the basic predictions of the Kerr geometry remain almost same. Among the all a major achievement was finally made in [23]. Henceforth, the GR scenarios could be mimicked in Newtonian framework. A close comparisons have also been made carefully. In the forthcoming sections this would be discussed in great details.

Here we plan to review a few important pseudo-potentials and the developments made so far in the recent past. In the next, we study the particle dynamics in GR and pseudo-Kerr potentials. Finally, we review the hydrodynamic solutions of accretion flows. The errors and accuracies are also presented in each section.

## 2 Pseudo-Potentials in Schwarzschild and Kerr Space-Times

We measure the distance, mass, time and the specific angular momentum etc. in the unit of $GM/c^2$, $M$, $GM/c^3$ and $GM/c$ respectively, where $G$, $c$ and $M$ are the universal gravitational constant, velocity of light in free space and the mass respectively.

### *2.1 Paczyński and Wiita Potential (1980)*

The most simple and successful potential in the Schwarzschild geometry proposed so far is that of [28]. The gravitational potential $\Phi_N(r) = -\frac{1}{r}$ is replaced by $\Phi(r)_{PW} = -\frac{1}{(r-2)}$ where $r = 2$ is the black hole's event horizon radius. One of the reason behind the major success is that it reproduces the Keplerian distribution exactly: $\frac{l^2(r)}{r^3} = \frac{1}{(r-2)^2}$ and, therefore, $l_{Kep}(r) = \frac{r^{\frac{3}{2}}}{(r-2)}$ for the circular orbit of radius $r$ having the specific angular momentum $l(r)$. Because of its simple form, it is easy to handle the complexity of the problems without distorting the salient features of the space-time of a non-rotating Schwarzschild black hole. Thus, the

errors are also small. It is the most frequently used potential when the rotational effects are negligible.

## 2.2 Chakrabarti and Khanna Potential (1992)

To extend the pseudo-Newtonian concept in the Kerr geometry [7], in a very important step, first proposed a suitable potential to describe the motion of a test particle around a rotating black hole: $\phi_k = 1 - \frac{1}{r-r_0} + \frac{1}{2}\omega^2 r^2$, where $r_0 =$ constant, a function of the Kerr parameter $a$, $\omega$ is the angular velocity of zero angular momentum observer (ZAMO). The last term is the frame dragging term. Therefore, the effective potential of a test particle having angular momentum $l$ is: $\phi = \phi_k + \frac{r_1 a l}{r^3} + (1 - \frac{2}{r})\frac{l^2}{2r^2}$. The second term indicates a coupling between the angular momentum ($l$) of the particle and the spin of the black hole which is just analogous to the spin-orbit coupling. Last term indicates the contribution of rotational potential energy. The expression of the potential for $a = 0$ is derived by linearizing the Schwarzschild effective potential (see, e.g., [33]): $[V(r)]^{\frac{1}{2}} = \sqrt{1 - \frac{2}{r} + (1 - \frac{2}{r})\frac{l^2}{r^2}} = 1 - \frac{1}{r} + (1 - \frac{2}{r})\frac{l^2}{2r^2}$. This potential reproduces with reasonable accuracy most of the relevant physical effects that occur near a Kerr black hole, such as

1. the location of $r_{mb}$ and $r_{ms}$ orbits, also the angular momenta at these orbits and binding energy ($\phi_{ms}$) of the particle at the marginally stable orbit, the evolution of the ellipticity of the orbits,
2. the particle and fluid dynamics; though this potential is derived for describing particle and fluid accretion but it surprisingly reproduces the locations of the horizon and ergo-sphere in the neighborhood of $a = 0.5$.

Apart from the general similarity of the results, the actual number matches to better than 10% over almost the entire range of $a$. This potential was planned for orbits on the equatorial plane, and thus cannot be used to describe the motion in the non-equatorial plane. Some of the physics is expected to breakdown on the horizon, as expected.

## 2.3 Lu and Chakrabarti Potential (1995)

The non-equatorial motion of a test particle in Newtonian approach first was proposed by Lu and Chakrabarti [19], around a rotating black hole. The potential $\phi = 1 - \frac{1}{r-r_0} + \frac{r_1 a l}{r^3} + \frac{(1-\frac{2}{r})l^2}{2r^2 \sin^2\theta}$, successfully projects the marginally bound orbit of a particle on the equatorial plane. For a thick disk, distribution of the equipotential surfaces is studied using this potential. Although by this potential one can simulate

the orbits in the non-equatorial plane, there remain some problems unsolved such as Frame-dragging effects. Also Carter constant is not calculated yet.

## 2.4 Semerak and Karas Potential (1999)

Semerak and Karas [31], proposed a potential including a Newtonian part and a frame-dragging part: $\Phi = -\frac{r}{\Sigma}(1 - \frac{a\sin^2\theta}{m}\dot{\phi})^2 + \frac{r\Sigma}{(r^2+a^2)\Delta}\frac{\dot{r}^2}{m^2}$. This effective potential accounts for the frame-dragging effects and especially in the intermediate and large distances provides a good fit to GR result, whereas it does not describe correctly the inner most region where the horizon and the important circular orbits lie. Also the radial epicyclic frequency is not reproduced with a good accuracy (the same goes with the Paczyński and Wiita Potential).

## 2.5 Artemova, Björnsson and Novikov Potential (1996)

Considering the free fall acceleration as a basis, a number of potentials were proposed by Artemova et al. [2] for non-rotating and rotating black holes.

**(a) Potential for Non-rotating a Black Hole** Their first potential is based on the free-fall acceleration of a test particle, $F_1 = -1/r^2(1 - \frac{2}{r})^{\frac{1}{2}}$. From the expression they proposed their first potential: $\phi_1 = -1 + (\frac{r-2}{r})^{\frac{1}{2}}$. The second potential is also obtained by considering the three-dimensional free-fall acceleration vector of a test particle that is at rest in the Schwarzschild reference frame, given by: $F_2 = -1/r^2(1 - \frac{2}{r})$ and, therefore, the potential is: $\phi_2 = \frac{1}{2}\ln(\frac{r-2}{r})$. They studied different potentials in modeling the relativistic solutions for the accretion disk structure around a non-rotating black hole. They found that their proposed potentials give better approximation in describing the radial dependence of $\eta$ (total energy dissipated at a given radius) for optically thick disk solutions, scattering optical depth ($\tau_0$), as functions of radius and the temperature structure ($\theta$), than that of the Newtonian potential. Also efficiency ($e$) can be calculated as $e = \frac{(r\Omega)^2}{2} + \phi$. Using their potentials the respective values of $e$: $e_1$ and $e_2$ respectively are $-0.081$ and $-0.078$, whereas the relativistic value is $-0.057$. Finally, they proposed a unique form for the free-fall accelerations given by, $F_i = -\frac{1}{r^{2-\alpha_i}(r-2)^{\alpha_i}}$, with $\alpha_0 = 0$, which gives free-fall acceleration for the Newtonian potential.

**(b) Potential for a Rotating Black Hole** Two more potentials have also been proposed to model the space time around a rotating black hole. They are obtained in a similar way, namely, free-fall acceleration of a test particle, given by $F_3 = -\frac{1}{r^{2-\beta}(r-r_1)^{\beta}}$, where $r_1$ is the radius of even horizon, $\beta = \frac{r_{in}}{r_1} - 1$, which is deter-

mined by the exact expression of general relativity. The acceleration corresponding to second potential is: $F_4 = -\frac{1}{r^2(1+\frac{a^2}{r^2}-\frac{2}{r})^\gamma}$, where $\gamma = \frac{r_{in}^2+a^2-2r_{in}}{2(r_{in}-a^2)}$. It is a claim that these potentials successfully reproduce (1) horizon and also approximate the important orbits, (2) with a good approximation to the relativistic solutions at any value of $a$, (3) the accretion disk solutions ($\eta$, $\tau_0$, $\theta$) with deviations from the pure general relativistic ones of the order of 10–20%.
The efficiency for the both of the potentials corresponding to the free-fall accelerations agrees very well with GR results for all the values of $a$, and deviation is less than 5%.

## 2.6 Mukhopadhyay Potential (2002)

In 2002, Mukhopadhyay proposed a new potential in Kerr Geometry with a new method. Taking the Keplerian distribution of angular momentum $l_k = \frac{l}{E}$ of a circular orbit of radius $r$ on the equatorial plane (see, [33]), the centrifugal force was extracted in the Kerr geometry by equating, $\frac{l_k^2}{r^3} = F_r = \frac{(r^2-2a\sqrt{r}+a^2)^2}{r^3[\sqrt{r}(r-2)+a]^2}$. Thus, $F_r$ identifies as the gravitational force of the black hole at the Keplerian orbit and finds the potential $V_r = \int F_r dr$. It (1) reproduces the location of last stable circular orbit ($r_s$) exactly and marginally bound orbit ($r_b$) in GR with maximum error 5%, (2) also reproduces the energy ($E_s$) at the last stable circular orbit in a fairly good agreement with GR values with maximum possible error 10%, (3) reveals total energy dissipation ($\eta$) up to error 10% with respect to GR values, (4) is also valid for both co-and counter-rotating black holes, which is not the case for Artemova potential. However, this potential can not describe the motion in non-equatorial planes. Later, three more potentials were also proposed with his collaborators, including the one describing the motion in non-equatorial planes [14, 27].

## 2.7 Chakrabarti and Mondal [9]: Pseudo-Kerr Potential

One of the successful potentials proposed so far in Kerr geometry is that by Chakrabarti and Mondal [9]: pseudo-Kerr or PK-potential. The potential is valid not only in the equatorial and the non-equatorial motions, but also in the co- and contra- rotation motions [8]. Further, it could be used in studying both the particle and fluid dynamics around a rotating black hole. The error is not more than 5% for the Kerr parameters $-1 \leq a \leq 0.8$. It is well known that in relativity the energy components such as gravitational, centrifugal, Coriolis etc., are not simply additive, PK-potential also is proposed in ad-hoc manner, is not derived using any general

relativistic formalism. It is given by

$$\Phi\,(r,\theta) = 1 - \frac{1}{r - r_0} + \frac{2a\left(\tilde{l} + \omega r^2\right)}{r^3 sin\theta} + \alpha^2 \frac{\left(\tilde{l} + \omega r^2\right)^2}{2r^2 sin^2\theta}, \tag{1}$$

where $\theta$ is measured from the axis of rotation of the black hole and $r_0 = 0.04 + 0.97a + 0.085a^2$. The red-shift factor $\alpha = \frac{\rho}{\Sigma}\sqrt{\Delta}$, and the dragging term, $\omega = \frac{2ar}{(r^2+a^2)^2 - \Delta a^2 \sin^2\theta}$, $\rho^2 = r^2 + a^2 cos^2\theta$, $\Sigma^2 = \left(r^2 + a^2\right)^2 - a^2 \Delta sin^2\theta$ and $\Delta = r^2 + a^2 - 2r$, have been borrowed from general relativity. The specific angular momentum $\tilde{l}$ here has the same meaning as $u_\phi$ in GR [8].

Given the form of the potential presented above, it is not hard to identify the meaning of the individual terms. For example, first term indicates to the rest mass energy and the second one corresponds to a Newtonian potential similar to $-1/r$. The mathematical 'singularity' at $r = r_0$ falls well inside the black hole horizon radius. The third term indicates to the spin-orbit coupling term consists of a product of $a\tilde{l}$ which encounters the Lense-Thirring effect. Since the objects get dragged even when its angular momentum is zero, virtually the same dragging effect introduced through $\omega$ and just adding a term $\tilde{l}$ with it. The last term is rotational energy term carefully taken and thus justified with the previous consideration. Further we see that the kinetic energy of a test particle would appear to persist even when $\tilde{l}$ is zero. Using the present form of the potential the results on both the particle and fluid dynamics are presented in great details. Here we follow the same line of arguments given in [9] to discuss the basic properties.

## 3 Particle Dynamics in GR and Newtonian Approach

To speak about any Newtonian treatment the Kerr geometry one needs to first follow up its silent relativistic features. Those could be derived taking the well known form of the stationary and axi-symmetric metric given in the Boyer-Lindquist co-ordinate $(t,\ r,\ \theta,\ \phi)$ as

$$ds^2 = -(1-\frac{2}{\Sigma})dt^2 - \frac{4ar\sin^2\theta}{\Sigma}dtd\phi + \frac{\Sigma}{\Delta}dr^2 + \Sigma d\theta^2 + (r^2 + a^2 + \frac{2ra^2\sin^2\theta}{\Sigma})\sin^2\theta d\phi^2,$$

where $\Delta = r^2 - 2r + a^2$, $\Sigma = r^2 + a^2\cos^2\theta$ and $a = J/M$ is the Kerr parameter varying in $-1 \leq a \leq 1$. From the Lagrangian expression $\mathscr{L} = g_{\mu\nu}\dot{x}^\mu\dot{x}^\nu$ on the equatorial plane $(\theta = \frac{\pi}{2})$, one can obtain the equations of motion of a test particle introducing two conserved quantities namely, the energy $\mathrm{E}'$ and the angular momentum $l'$ of the test particle, i.e., $p_t = \frac{\partial\mathscr{L}}{\partial\dot{t}} = -\mathrm{E}'$ and $p_\phi = \frac{\partial\mathscr{L}}{\partial\dot{\phi}} = l'$. Now, using the fact that $g_{\alpha\beta}p^\alpha p^\beta = -m^2$, where $m$ is the mass of the test particle, one

finds the radial equation of motion on the equatorial plane as,

$$r^3\dot{r}^2 = R(E', l', r) = V_K = E^2(r^3+a^2r+2a^2)-4aEl'-(r-2)l'^2-m^2r\Delta \quad (2)$$

where $R(E', l', r) = V_K$ is known as the effective potential in the Kerr geometry. The effective potential is an entity that a particle always respects to form a equatorial orbits, whether circular (marginally bound and marginally stable), elliptical, hyperbolic or parabolic etc. This is because the extrema of an effective potential give the locations of circular orbits, while the intersections between a constant energy line and a potential curve of constant $l'$ give the turning points of an elliptical orbit. Note that for circular orbits, $\dot{r} = 0$, and $\ddot{r} = 0$. This implies $R = 0$ and $\frac{\partial R}{\partial r} = 0$. Both the conditions give expression for the specific energy $\tilde{E} = \frac{E'}{m}$ and the specific angular momentum $\tilde{l} = \frac{l'}{m}$, of a test particle moving in a circular orbit. Importantly, marginally bound and marginally stable circular orbits are considered as the mile-stones in the Kerr geometry. Introduction of any new potential do respect these space-time mile-stones. The location of a marginally bound circular orbit occurs at $\tilde{E} = \frac{E'}{m} = 1$, implying $r_{mb} = 2 \mp a + 2\sqrt{(1 \mp a)}$, for $a = 0$, $r_{mb} = 4$; for $a = 1$, $r_{mb} = 1$ for prograde orbit and 5.83 for retrograde orbit. The marginally stable circular orbits occur at the point of inflexion of the curve, which requires $\frac{\partial^2 R}{\partial r^2} = 0$. For $a = 0$, $r_{ms} = 6$; for $a = 1$, $r_{ms} = 1$ for prograde orbit or 9 retrograde orbit; for details see [33].

In a very similar way one also finds the circular, elliptical and other orbits in PK-geometry. Using Newton's Law, $m\ddot{r} = F_r = -\frac{\partial \Phi_{PK}}{\partial r}$, and one obtains the circular orbit by putting: $\ddot{r} = 0$, and $\dot{r} = 0$, i.e., $r$ is constant. For the marginally bound orbits, $\frac{d\Phi_{PK}}{dr}|_{r_{mb}} = 0$ and $\Phi_{PK}|_{r_{mb}} = 1$, whereas for the marginally stable orbit (an inflexion point) $\frac{d\Phi_{PK}}{dr}|_{r_{ms}} = 0$, and $\frac{d^2\Phi_{PK}}{dr^2}|_{r_{ms}} = 0$. The angular momentum for which both the equations are satisfied is known as marginally bound angular momentum $l_{mb}$ and marginally stable angular momentum $l_{ms}$ respectively. For a given $\Phi(r, \tilde{l})$ and a constant energy line, there could be two intersections $r_1$ and $r_2$ at virtually identical locations which correspond to apoastron and periastron. Thus the elliptical orbits are also trivially reproduced.

### *3.1 The Effective Potentials and Orbits*

In Fig. 1a, we plot simultaneously the three potentials (1) the relativistic effective Kerr potential $V_K$ or $R(r)$, the solid lines, (2) the dashed lines for PW potential and (3) the dotted lines drawn for the PK-potential when black hole rotation is taken to be zero. The various values of angular momentum $\tilde{l}$ is also considered. The $\tilde{l}$ values are gradually increasing from the bottom to the top of the curves. We see that PK-potential is slightly more accurate with respect to the PW-potential. In Fig. 1b, we compare the potentials for $a = 0.5$ and in Fig. 1c, d, we plot the

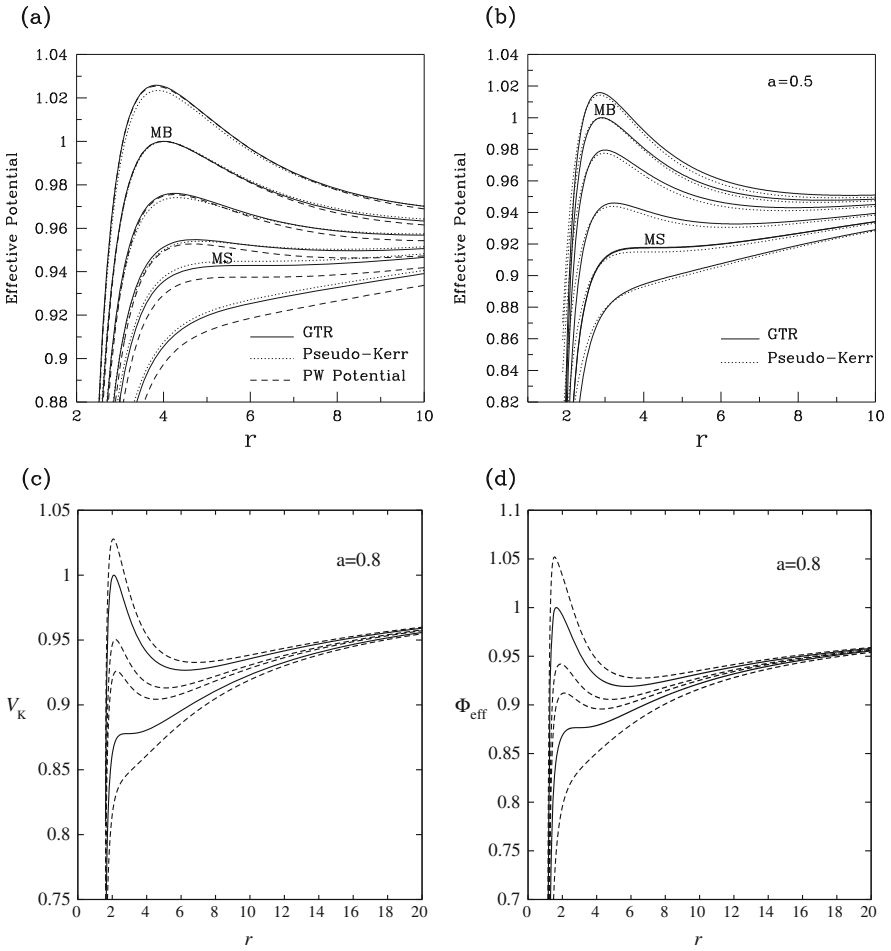



**Fig. 1** (**a**) A simultaneous plot of three effective potentials (1) GR (solid) (2) Pseudo-Kerr (dotted) (3) PW (dashed) are presented. The specific angular momentum are chosen $\tilde{l} = 3.2,\ 3.4,\ 3.6,\ 3.8,\ 4.0$ and 4.2 respectively from bottom to topmost for the three nearly close spaced curves. (**b**) The second plot of the potentials are shown for $a = 0.5$ taking different $\tilde{l} = 2.7, 2.90, 3.1, 3.3, 3.4142$ and 3.5 values, where the solid curves are for GR and dashed curves are for the PK-potential. The marginally stable(MS) and bound(MB) curves are plotted with their respective values (from [9]). We show the potential profiles even for a higher Kerr parameter values say, $a = 0.8$ in (**c**) the GR effective Kerr potential $V_K$ and in (**d**) the PK-potential $\Phi_{eff}$ separately. The lower solid curve is plotted for MS and the upper solid curve is for the MB angular momentum respectively. The comparison has been made for the other curves having same $\tilde{l}$ values (from [9])

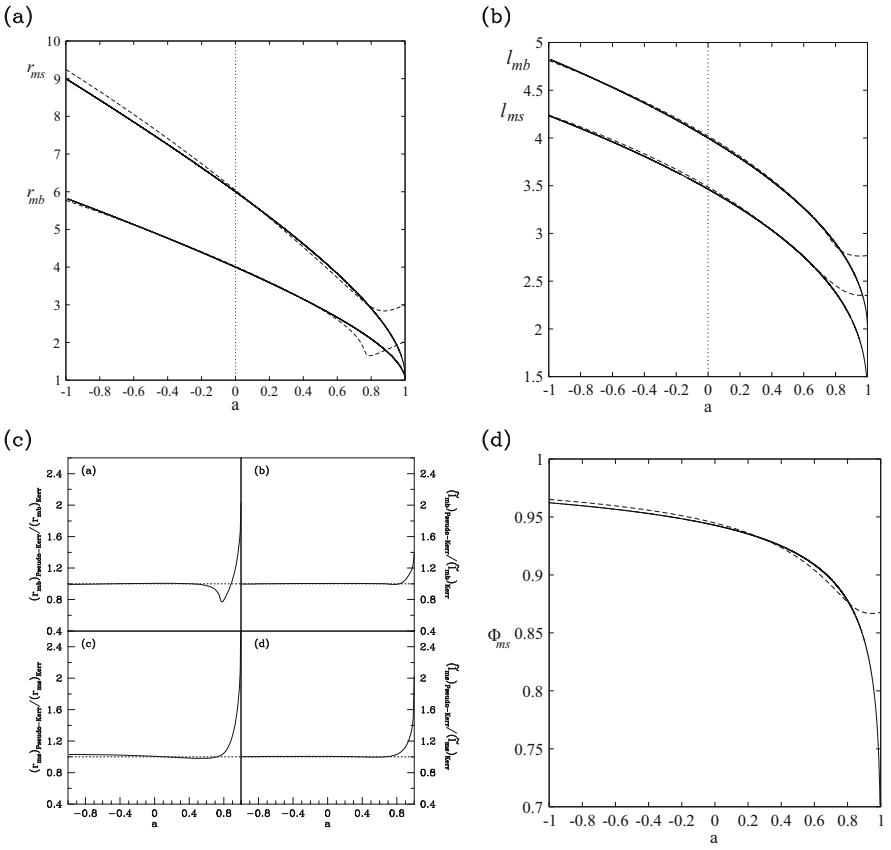



**Fig. 2** (**a**–**d**) The salient features of the Kerr geometry are compared with respect to the $r_{ms}$ and $r_{mb}$ (top left), radii and $l_{ms}$ and $l_{mb}$ (top right) values. As before we follow in GR, a solid line and in the PK-potential, a dashed line. In the bottom left plot we show the ratios in the two different approaches and the errors are being also measured using a unity line (dashed curve) in each case. In the bottom right panel $\Phi_{ms}$ are plotted at the marginally stable radii taking both the PK-potential (dashed) and Kerr Geometry (solid). Note that this $\Phi_{ms}$ counts maximum energy release (the rest mass energy minus the $\Phi_{ms}$) from a black hole sources (from [9])

different potential profiles both in GR and PK respectively for $a = 0.8$. From Fig. 1a–d we see that there is indeed a very little difference in potentials at all radial distances for various angular momentum and spin of the black hole. Therefore, one concludes that the for the same parameter values PK-potential describes GR profile more accurately.

Figure 2a–d is plotted to compare the (a) $r_{ms}$ and $r_{mb}$, values (b) $l_{ms}$ and $l_{mb}$ values respectively, is obtained using the PK-potential and in GR. We also calculate the ratios in the two approaches in Fig. 1c. It shows that the ratios indeed reasonably close to unity in the wide span $-1 < a < 0.8$. We see that $a \sim 0.8$, the discrepancies in $r_{ms}$, $r_{ms}$ and $l_{mb}$ are well below 5%. Since the $r_{mb}$ is located near by the horizon,

the error is $> 7.26\%$ for $a > 0.7$. It could be up to about 20% when $a = 0.9$. Therefore, the PK-potential gives satisfactory results when $a < 0.8$.

Further, the rest mass energy minus the potential energy $\Phi_{ms}$ at radii $r = r_{ms}$, is a measure of amount of maximum energy that can release as when a particle approaches towards a black hole. For instance, for a Schwarzschild black hole, $\Phi_{ms} \sim 0.943$. Hence a maximum of about 5.7% energy may be released. For an extreme Kerr black hole, this number is almost 40%. In Fig. 2d, we present the binding energies obtained from GR and PK potentials. Comparison shows both closely agree in the range $-1 < a < 0.8$. Beyond $a > 0.8$, the applicability in the linear approach suddenly breaks down because the non-linearities become very strong and important when $r_{ms}$ and $r_{mb}$ forms close to the horizon and thus the region must be excluded as $a \to 1$. This region must be treated separately and therefore, needs a special attention.

## 3.2 Orbits in Equatorial and Non-equatorial Planes

To find the orbits in equatorial and non-equatorial planes, the Lagrangian formulation $\mathscr{L} = T - \Phi(r, \theta)$ is used, where $T = \frac{1}{2}\dot{r}^2 + \frac{1}{2}r^2\dot{\theta}^2$, is the kinetic energy of the test particle and which helps to find out the equation of motion corresponding to $\ddot{r}$ and $\ddot{\theta}$. Defining two types of azimuthal co-ordinates, one $\phi_d = -\frac{\partial \mathscr{L}}{\partial(\tilde{l}+\omega r^2)}$, a co-ordinate viewed from a distant observer, and the other $\phi$ attached to ZAMO, namely, with the dragged frame with an angular velocity $\omega$. Figure 3a–d show the particle trajectories for co- and contra-rotation of the black hole, and for a distant observer. The parameters are mentioned in the panel. We see in Fig. 3d, the effect of the dragging of the inertial frame is also imprinted.

In Fig. 4, we present a few examples of the orbits of a test particle having vertical oscillations when it is released away from the equatorial plane. Here we have shown the projections of those trajectories in the meridional plane. The parameters are

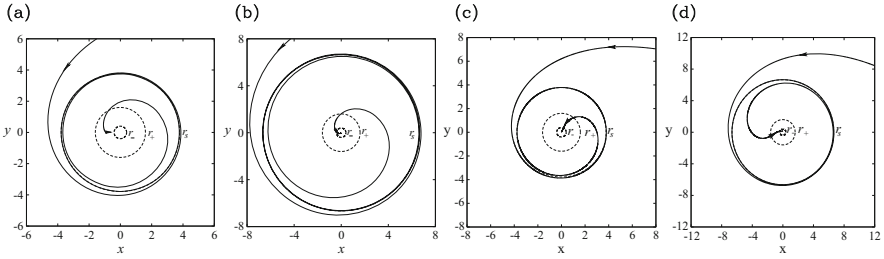



**Fig. 3** The trajectories of a test particle is plotted taking (**a**) $a = 0.8$, $\tilde{l} = 3.9$, and (**b**) $a = -0.8$, $\tilde{l} = 3.9$ using PK-potential, as observed from a dragged frame. In (**c**–**d**) is plotted for a distant observer for same parameters. The effect of frame dragging could also be noticed in the inertial frame

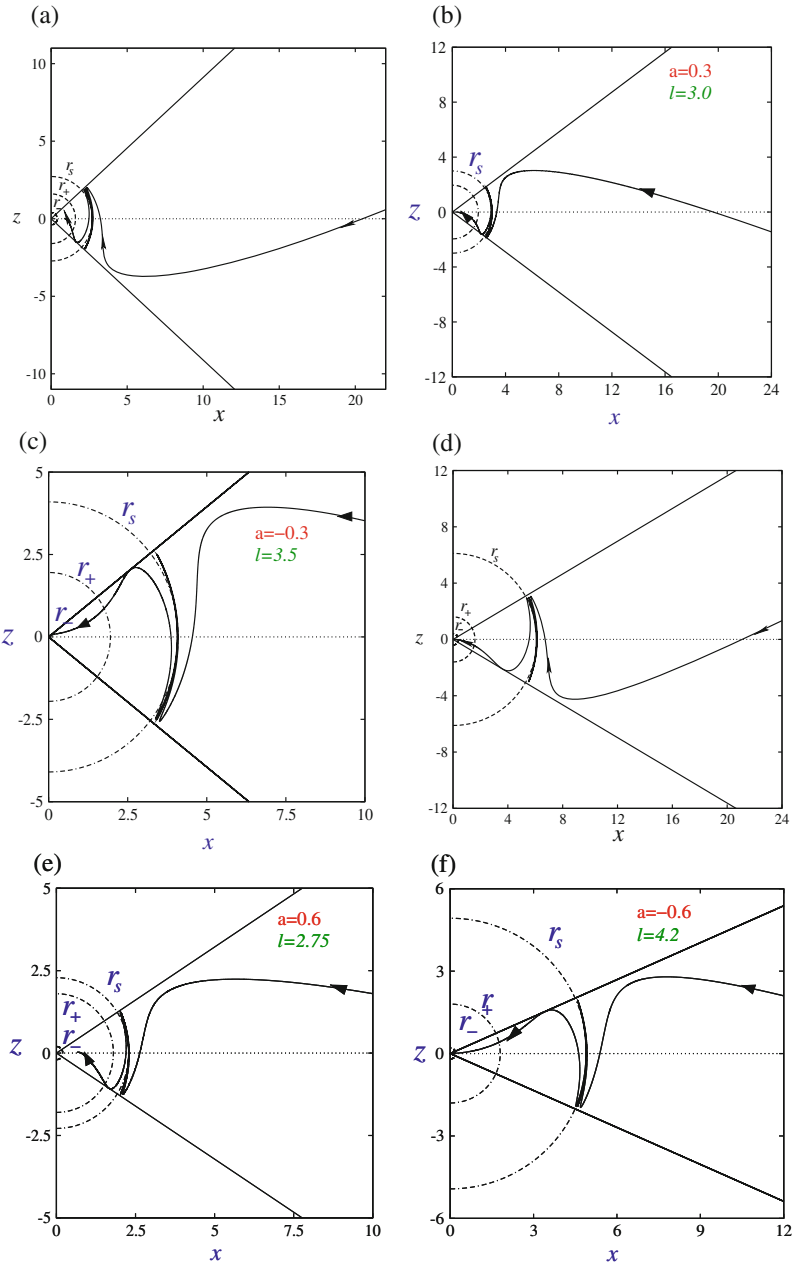



**Fig. 4** (**a**–**f**) We plot the off-equatorial particle orbits and its projections are shown in the X-Z plane using PK-potential. In left top panel $a = 0.8, \tilde{l} = 2.7, \dot{\theta} = 0.00336657$ where as in the left bottom panel $a = -0.8, \tilde{l} = 4.5\ \dot{\theta} = 0.0031929$ having energy $= 1$ respectively. The radii of the both the horizons are also drawn with dashed circles. $r_s = 3.1$, 6.1 and $\theta_s = 47.6$, and 60 in degrees, respectively. The radial velocity is equals to zero at $r = r_s$, and the injected velocity is $\dot{\theta}$ [9]. On the right panels we plot a few other trajectories. Parameters are shown inside the panel

(top left) $a = 0.8$, $\tilde{l} = 2.7$, and (bottom left) $a = -0.8$, $\tilde{l} = 4.5$. Energy is chosen to be 1 (free particle) and $\dot{\theta}$ with which the particle has been injected is (top left) 0.00336657, and (bottom left) 0.0031929, respectively. The corresponding $r_s$ (where the radial velocity of the particle is zero) is 3.1, and 6.1 and $\theta_s$ is 47.6°, and 60° respectively. The horizontal axis gives the absolute value of the axial distance and the vertical axis gives the distance from the equatorial plane. The location $r_s$, in each case, is indicated by a dashed circle. The outer and inner horizons ($r_+$ and $r_-$ respectively) are also marked properly. A few more plots are also shown for different parameters marked inside the boxes. The nature of these trajectories is to be compared with those in [11]. In Fig. 5a, b, we plot the (a) $r_s$ and (b) $\theta_s$ and its variation as functions of particle angular momenta $\tilde{l}$. The solid line shows the variation are obtained in GR and the triangles are in our potentials. This shows that results match very well with the exact GR results.

Next, it is important to discuss whether the Carter constant (e.g. [3]) in Kerr geometry remains a constant or not. To check it one finds [15] $p_\theta^2 + \frac{p_\phi^2}{\sin^2\theta} + 2mV_\theta(\theta) = L^2 + 2mV_\theta = \alpha_\theta^2$, which needs to be a constant, in case of a $\theta$-dependent potential (assumed here). Notice the present form of the PK-potential does not match with the above. Thus, we expand the potential to find out the constant $\alpha_\theta$. We see up to a term $\frac{\tilde{l}^2}{r^3 sin^2\theta}$, the net angular momentum is constant, i.e., $V_\theta$ remains constant. Further, Fig. 5b indicates that for the highly off equatorial motions ($\theta \sim 50$), the important features of the particle trajectories well match with the GR predictions and numerical results including the off-equatorial orbits indicate the net angular momentum is constant.

Finally, $\nu_{LT} = \frac{2a}{r^3 sin\theta}$; on the equatorial plane $\theta = \frac{\pi}{2}$, $\nu_{LT} = 2a/r^3$ which exactly matches as in [18] in the weak-field [34] limit. Note that [18] derived $\Delta\Omega =$

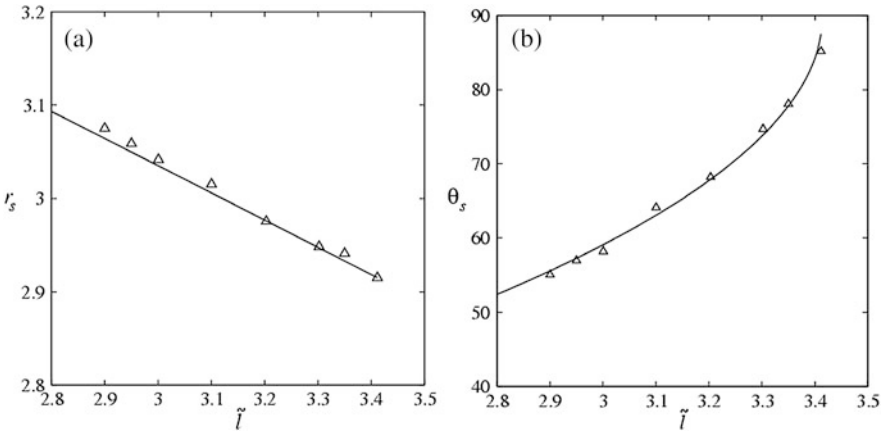



**Fig. 5** (**a**–**b**) The $r_s$ and $\theta_s$ with specific angular momentum $\tilde{l}$ for $a = 0.5$ is plotted for both GR (solid) and PK-potential (triangle) (from [9])

$2a/r^{3/2}$ per revolution and a revolution for such a Keplerian orbit takes place in $2\pi/\Omega = r^{3/2}$ time. Thus, these two frequencies are same in the Newtonian limit.

## 4 Review on the Hydrodynamic Solutions in Accretion Flows

To study the accretion processes around black holes three basic hydrodynamic equations are required. They are namely, (1) the Euler equation, (2) the continuity equation and (3) the entropy generation equation or the equation of state. In the absence of dissipation in the flows two entity namely, the specific energy, the specific angular momentum together with the mass flux remains conserved in the flows. One can extract the conserved quantities namely, the specific energy, the specific angular momentum in the absence of dissipation, and the mass flux of the flow. Thus, three conserved quantities and the equation of state governs the basic hydrodynamics of the accretion disk [23].

**(a) Energy Conservation Equation** The specific energy $\mathscr{E} = \frac{1}{2}u^2 + \frac{\gamma}{\gamma-1}\frac{P}{\rho} + \Phi_{eff}$, is obtained from the radial Euler equation, where $\Phi_{eff}(r, a, l)$ is the PK-potential, $\gamma = \frac{c_p}{c_v}$, $P$, $\rho$ and $u$ are adiabatic index, isotropic pressure, mass density and radial velocity of the flow respectively. The specific angular momentum $l = u_\phi/u_t$ of the flow is also conserved, and could be obtained from the azimuthal part of it.

**(b) Mass Conservation Equation** $\dot{m} = -2\pi\,\rho\,u\,x\,h(x)$, is obtained from the Continuity equation, where $x = rsin\theta$ is the radial distance and $h(x) = a_s x^{1/2}(\frac{\partial \Phi_{eff}}{\partial z})_{z=0}$ denotes the disk height and is estimated by equating the pressure gradient force with the vertical component of the gravitational force ($z$-component of the Euler equation). Here $a_s$ is the adiabatic sound speed, i.e., $a_s^2 = \gamma P/\rho$.

**(c) Entropy Generation Equations** The above two equations are not sufficient to find a complete solutions and one more equation is required. The entropy generation equation $\frac{u}{\gamma-1}(\frac{dP}{dx} - \frac{\gamma P}{\rho}\frac{d\rho}{dx}) = \Lambda - \Gamma$, considered for this purpose, where $\Lambda$ and $\Gamma$ are cooling and heating terms. When $\Lambda = \Gamma = 0$, the integration of the above equation one finds $P = K\rho^\gamma$, the adiabatic equation of state, where $K$ is an entropy constant. For inviscid flows we deal with an adiabatic equation of state, however to study the radiation properties, one must take the above entropy generation equation.

**(d) Sonic Point Conditions and Hydrodynamic Solutions** The steady state solutions of the flow variables namely, $u(r)$ and $a_s(r)$ can be found by integrating the differential equation $\frac{du}{dx} = \frac{N}{D}$, obtained by differentiating and eliminating of the above equations. Depending on the boundary conditions, the nature of the solution would be different. For example, the accretion onto a black hole is transonic in nature, i.e., subsonic matter crosses the sonic point becoming supersonic at the horizon. At the sonic point where subsonic to supersonic transition occurs

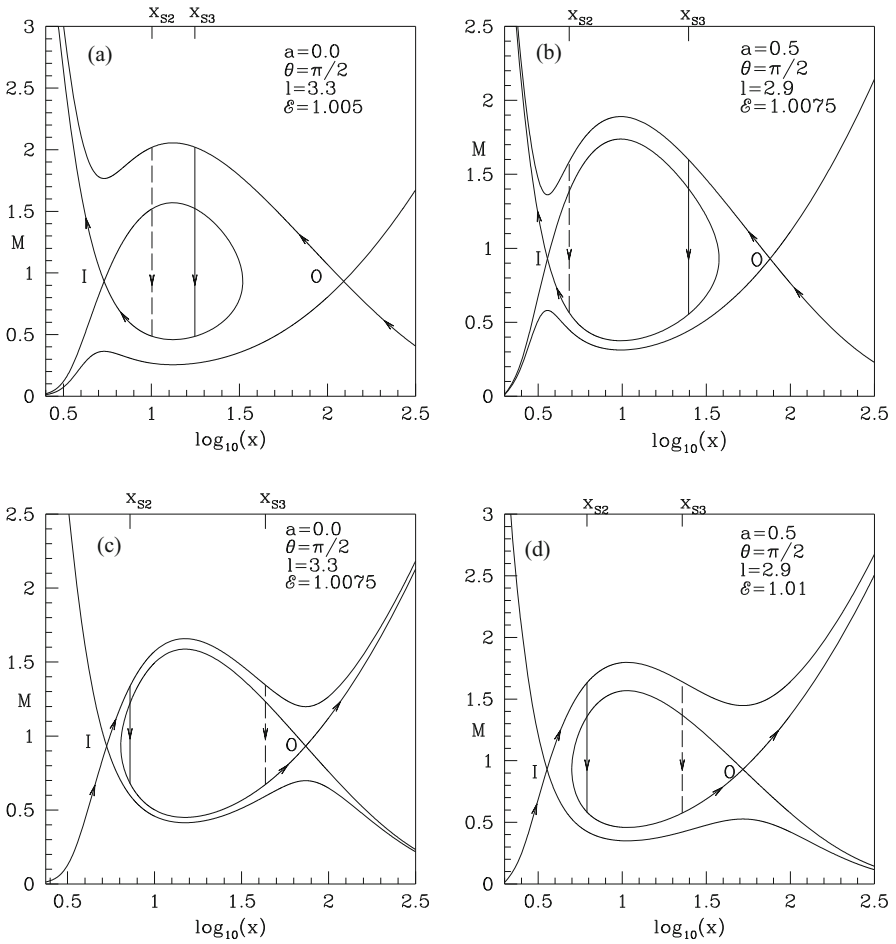



**Fig. 6** The accretion and wind solutions having shocks are plotted. The Kerr parameters are (**a**) $a = 0$, and (**b**) $a = 0.5$ for accretion, whereas (**c**) $a = 0$ and (**d**) $a = 0.5$ for wind flows. Flow passes through the arrow indicated lines as shown in the figure. The unstable shock is also presented through a vertical dashed line (from [23])

$N = D = 0$. This additional feature in this problem helps one to determine the distinct hydrodynamic solutions for different boundary conditions uniquely, for details see [4]. We plot such exact hydrodynamic solutions so called the flow topologies for accretion and wind (out flows) flows in Fig. 6. The Kerr parameter and flow parameters are given in the figure.

**(e) Hydrodynamic Shocks in the Accretion and Wind Flows** Depending on the angular momentum of the flow, hydrodynamic solutions possess one or two saddle

type sonic point(s) [4, 13]. Further, the transonic solutions may have shocks if the following Rankine-Hugoniot conditions are satisfied,

1. energy flux: $\mathscr{E}_+ = \mathscr{E}_-$
2. mass flux: $\dot{m}_+ = \dot{m}_-$
3. pressure balance: $W_+ + \Sigma_+ u_+^2 = W_- + \Sigma_- u_-^2$,

where '+' and '−' represent the flow variables evaluated just after and just before the shock. Here $W$ and $\Sigma$ is the vertically averaged pressure and density respectively. In Fig. 6, the locations of the accretion and wind shocks are shown. They are significantly important in determining the spectral properties of the accretion flows and therefore their characterization are also necessary. This is because soft photons associated with the relatively cooler pre-shock flows get inverse Comptonize by the hot thermal electrons in the post-shock region and produces high energy power law tail. Further, the presence of these shocks provide a suitable environment to accelerate those electrons which can produce non-thermal spectrum at very high energies. The non-steady or oscillations of shocks at the transition boundary can cause quasi-periodic oscillations observed in hard X-rays. We therefore, classify the different regions of the flow parameters available for the standing shocks and oscillating shocks [24]. In Fig. 7a, b, the separate boundaries of the regions of the parameter space are plotted taking the specific energy $\mathscr{E}$, specific angular

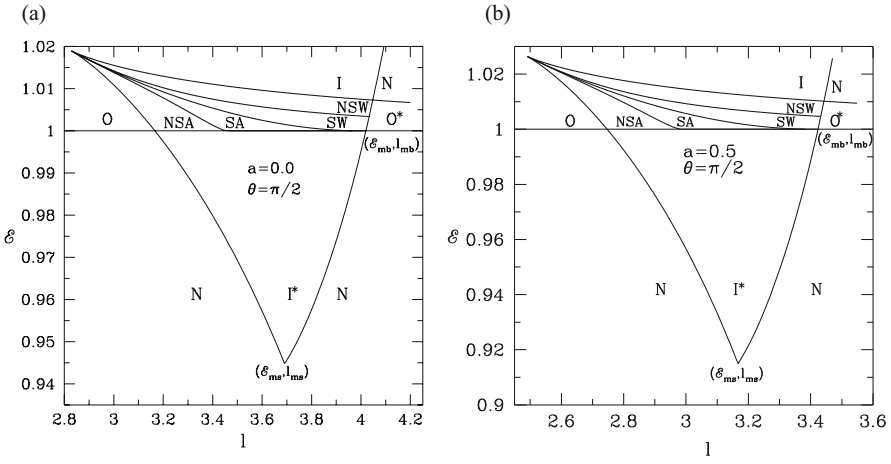



**Fig. 7** The boundaries of different regions of parameters space are plotted for (**a**) $a = 0$ and (**b**) $a = 0.5$ values. Depending on the specific energy $\mathscr{E}$ and specific angular momentum $l$ one or more sonic points could be present. In the presence of multiple sonic points shocks may also form. The short symbolic representation of the different regions of the parameters are—O(outer sonic point only), I(inner sonic point only), SA(shocks in accretion ), SW(shocks in wind), NSA(no shocks in accretion), NSW(no shocks in wind ), $I^*$(inner $\alpha$ topology only), $O^*$ (outer $\alpha$ type topology) and $N$ (having no solution) etc. The marginally bound and marginally stable values are represented by $ms$ and $mb$ respectively (from [23])

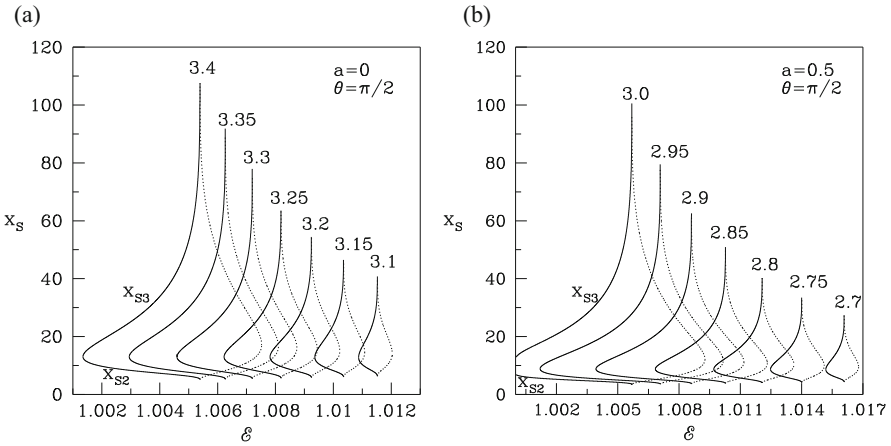



**Fig. 8** The stable shocks $x_{s3}$ and unstable shocks $x_{s2}$ are plotted as a function of energy and angular momentum taking Kerr parameter (**a**) $a = 0$ and (**b**) $a = 0.5$. The solid curves are drawn with the parameters taken from the shock in accretion (SA) region, and the dotted curves from the shock in wind (SW) region [23]

momentum $l$ and different values of Kerr parameter within which multiple sonic points are present [23].

The variations of the both the shock locations of inner $x_{s2}$ and outer $x_{s3}$ (see Fig. 6) as functions of energy, angular momentum $l$ and Kerr parameter are presented in Fig. 8. Each parameters are also marked on the curves. Employing the full GR formalism in the inviscid flows the hydrodynamic shocks have already been investigated by Chakrabarti [6], and thereafter [22]. The results agree fairly well and errors less than $\sim$5% have been detected. Thus, considering above facts, we think that the PK-potential is just ready to investigate a few important issues; (1) viscous dissipative flows, (2) spectral properties and effect of rotation of the black hole. Meantime, a number of such attempts have already been made, for example, [25] for the viscous dissipative flow, [1, 12] for dissipative shocks, and [20] for spectral properties etc. (see Santabrata Das, this volume).

## 5 Conclusion

In this Chapter, I proposed a pseudo-Newtonian approach to study particle and fluid dynamics around a Kerr black hole. Following the successive development of the pseudo-Kerr potentials and a careful investigation it revels that the PK-potential provides more successful description in reproducing GR results very closely. Any discrepancies from the actual GR values are less than 5% in most of the cases. Hence the potential is capable in obtaining the characteristics of particle trajectories very accurately as long as the Kerr parameter lies $a < 0.8$ for co-rotating motion and

($a < 1$) for contra-rotating motion. The radii of the marginally bound orbit and the marginally stable orbits are also accurately obtained. Further, particle trajectories are compared both in the equatorial and the non-equatorial motions. Interestingly the PK-potential is found to reproduce more accurate results in comparison to [28], in Schwarzschild geometry. In addition, full accretion hydrodynamics have also been reviewed. A comparative studies are also made in the inviscid accretion and wind flows. The hydrodynamic solutions associated with the different boundary conditions are also verified. The identification of the flow parameters and their classification are found correctly. Moreover, the accretion and wind shocks are also nicely obtained with a minimal error. Thus, using the proposed potential, a series of studies in accretion hydrodynamics have already been carried out, even when heating, cooling and radiative processes are present. Therefore, we think that PK-potential would be extremely helpful to study various phenomena such as the spectra, time-dependent solutions through numerical simulations, effect of the black hole rotation on accretion hydrodynamics, Quasi-Periodic Oscillations of observed X-ray fluxes etc. up to a reasonable accuracy.

**Acknowledgements** We are thankful to Prof. SKC for making a sustained effort to have a simple minded potential for the Kerr geometry and I am proud to be a part of it. I acknowledge Mouli Chaudhuri while preparing this brief review.

## References

1. Aktar, R., Das, S., Nandi, A., Sreehari, H.: Mon. Not. R. Astron. Soc. **471**, 4806 (2017)
2. Artemova, I.V., Bj$\ddot{o}$rnsson, G., Novikov I.D.: Astrophys. J. **461**, 565–571 (1996)
3. Carter, B.: Phys. Rev. **174**, 1559 (1968)
4. Chakrabarti, S.K.: Astrophys. J. **347**, 365 (1989)
5. Chakrabarti, S.K.: Theory of Transonic Astrophysical Flows. World Scientific, Singapore (1990)
6. Chakrabarti, S.K.: Astrophys. J. **464**, 664 (1996)
7. Chakrabarti, S.K., Khanna, R.: Mon. Not. R. Astron. Soc. **256**, 300–306 (1992)
8. Chakrabarti, S.K., Mondal, S.: Ind. J. Phys. **79**(11), 1237 (2005)
9. Chakrabarti, S.K., Mondal, S.: Mon. Not. R. Astron. Soc. **369**, 976 (2006)
10. Chakrabarti, S.K., Acharyya, K., Molteni, D.: Astron. Astrophys. **421**, 1 (2004)
11. Chandrasekhar, S.: Mathematical Theory of Black Holes. Oxford University Press, Oxford (1983)
12. Das, S., Chakrabarti, S.K., Mondal, S.: Mon. Not. R. Astron. Soc. **401**, 2053 (2010)
13. Fukue, J.: Publ. Astron. Soc. Japan **39**, 309 (1987)
14. Ghosh, S., Mukhopadhyay, B.: Astrophys. J. **667**, 367 (2007)
15. Goldstein, H., Poole, C., Saiko, J.: Classical Mechanics, 3rd edn. Pearson Education, Singapore (2004)
16. Ivanov, R.I., Prodanov, E.M.: Phys. Let. B **611**, 34 (2005)
17. Lee, T., Becker, P.A.: Astrophys J. **632**, 476 (2005)
18. Lense, J., Thirring, H.: Physik. Z. **19**, 156 (1918)
19. Lu, J.F., Chakrabarti, S.K.: Chin. Astron. Astrophys. **19**, 7 (1995)
20. Mandal, S., Mondal, S.: J. of Astrophysics and Astronomy **39**, 19 (2018)
21. Molteni, D., Sponholz, H., Chakrabarti, S.K.: Astrophys. J. **457**, 805 (1996)

22. Mondal, S.: Astrophys J. **708**, 1442 (2010)
23. Mondal, S., Chakrabarti, S.K.: Mon. Not. R. Astron. Soc. **371**, 1418 (2006)
24. Mondal, S., Chakrabarti, S.K.: Int. J. Mod. Phys. D. **16**, 1381 (2007)
25. Mondal, S., Basu, P., Chakrabarti, S.K.: Mon. Not. R. Astron. Soc. **396**, 1038 (2009)
26. Mukhopadhyay, B.: Astrophys. J. **581**, 427 (2002)
27. Mukhopadhyay, B., Misra, R.: Astrophys. J. **582**, 347 (2003)
28. Paczyǹski, B., Wiita, P.: Astron. Astrophys. **88**, 23 (1980)
29. Ryu, D., Brown, G.L., Ostriker, J.P., Loeb, A.: Astrophys. J. **452**, 364 (1995)
30. Ryu, D., Chakrabarti, S.K., Molteni, D.: Astrophys. J. **474**, 378 (2004)
31. Semerak, O., Karas, V.: Astron. Astrophys. **343**, 325 (1999)
32. Shakura, N.I., Sunyaev, R.A.: Astron. Astrophys. **24**, 337 (1973)
33. Shapiro, S., Teukolsky, S.: Black Holes, Neutron Stars and White Dwarfs. Wiley, New York (1983)
34. Wilkins, D.C.: Phys. Rev. D **5**, 814 (1972)
35. Yang, R., Kafatos, M.: Astron. Astrophys. **295**, 238 (1994)

# Part III
# Observational Astronomy

# Observational Aspects of Black Holes: Past Challenges and Future Prospects




**Anuj Nandi**

**Abstract** This article focuses on the observational aspects of Galactic Black Hole (GBH) sources, since the first confirmation of 'astrophysical' BH by *UHURU* Satellite, followed by discovery of X-ray emission from Cygnus X-1 with sounding rocket experiments. Most of the GBH sources show rich 'spectro-temporal' variabilities as observed by several instruments on-board space-based observatories. We present a few interesting observational results to understand the accretion dynamics around a BH. We also highlight the importance of a *spectro-temporal-polarimetric* mission to probe the extreme gravity region of BH sources.

## 1 Introduction

Astrophysical Galactic Black Holes (GBHs; $3M_{\odot} \leq M_{BH} \leq 20M_{\odot}$, where, $M_{BH}$ being the mass of BH) are the end-products of stellar evolution of massive stars of mass $\gtrsim 15M_{\odot}$. It is a challenging task to identify a BH that may be present in a compact X-ray binary system. Since BHs are by definition 'black', as light can not escape from them, a 'true' identification of a BH by observing the electromagnetic (EM) radiation is not possible. Therefore, the best way to 'see' or to identify a BH is to study how matter behaves around these compact objects and what type of EM radiation it emits.

GBH X-ray binaries considered to be a coupled system of a primary BH with a companion star of variable mass. In general, the primary accretes matter from its companion via Roche lobe overflow in Low-Mass X-ray Binary (LMXB) system, and from stellar winds in High-Mass X-ray Binary (HMXB) system, to form an accretion disk around a BH [16]. The accretion disk gets heated-up due to viscous dissipation with high temperature ($\sim 10^7$ K) to emit radiation in X-rays via the release of immense gravitational potential energy of the infalling matter.

A. Nandi (✉)
Space Astronomy Group, ISITE Campus, U. R. Rao Satellite Centre, Bangalore, India
e-mail: anuj@isac.gov.in

© Springer International Publishing AG, part of Springer Nature 2018

B. Mukhopadhyay, S. Sasmal (eds.), *Exploring the Universe: From Near Space to Extra-Galactic*, Astrophysics and Space Science Proceedings 53,
https://doi.org/10.1007/978-3-319-94607-8_17

The observed emissions play a major role for the identification of a BH in the X-ray binary system as well to investigate the accretion dynamics around BH.

A more direct evidence of a BH in binary systems is obtained by measuring the mass of the compact object by knowing the 'actual' binary parameters (i.e., orbital period, mass of the companion etc.). Several techniques have been used to study binary parameters, and hence to constrain the mass of the central object. Till date, 77 GBH sources have been reported [32] including three extragalactic stellar mass BH candidates. Most of the sources are bright in X-rays, and hence it is possible to study various observational aspects, which are considered to be the unique features of the BH sources [26]. The detection of BH sources in our Galaxy was not possible till the first detection of 'non-solar' X-rays sources, which led to the beginning of new branch in Astronomy.

The results presented in this article are based on archival data[1] from various space-based X-ray observatories, namely *RXTE*, *XMM-Newton*, *Swift*, *NuSTAR*, and from the all sky monitor *MAXI* on-board ISS.

## 2 X-Ray Astronomy

X-ray astronomy is an arena/branch of astronomy, which mostly focuses on the study of astronomical objects/sources at X-ray wavebands, in the range of 0.1 keV to few 100s of keV. As the Earth atmosphere is opaque to X-rays, X-ray astronomical observations are carried out using sounding rockets, Balloons and Satellites. Satellite observation is the most viable option for doing the X-ray astronomy experiments, as other two options have some limitations. But the X-ray astronomy began with the sounding rocket experiments only. At the same time, several balloon-borne experiments were also attempted to provide position, angular size of the sources in higher energies up to 300 keV [14, 15].

### *2.1 Beginning of X-Ray Astronomy*

The first astronomical X-ray experiments were performed in the US in 1948 and 1949 using captured World War II (WWII) V2 rockets. X-rays were detected from the Solar corona by Herb Friedman and his team at the US Naval Research Lab (NRL), which marks the *Beginning of X-ray Astronomy*.

The Sun produced X-ray flux $\sim 10^6$ photons/cm$^2$/s at Earth, which could be easily detected during the 1948–1949 with then-available detectors/counters. But, it took more than 10 years (decade delay!) to detect X-ray emissions from the 'non-solar' X-ray sources. This is because of the limitation of the sensitivity of the instrument.

[1] https://heasarc.gsfc.nasa.gov/cgi-bin/W3Browse/w3browse.pl.

The breakthrough experiment was carried out in 1962 by Riccardo Giacconi, Bruno Rossi and his collaborators at American Science & Engineering (AS&E) in Cambridge, Massachusetts. An experiment was designed with capability of detecting 0.1–1.0 X-ray photons/cm$^2$/s, and with sensitivity more than 50–100 times of any previous experiment. The larger detection area and wide field of view (FOV) of the experiment increase both sensitivity and observational duration of any source during the rocket flight. The experiment carried out on June 12, 1962, was successful in detecting first 'non-solar' X-rays from a source in the direction of constellation of Scorpius. The source was very intense in the night sky ($\sim$28 counts/cm$^2$/s) and was designated as Sco X-1. A follow-up campaign identified the X-ray source as a binary with a compact primary object (i.e., a Neutron Star). The discovered result is shown in Fig. 1 with maximum counts observed near 195° azimuth, the direction of the constellation Scorpius.

**Cyg X-1: First Galactic Black Hole** The X-ray source, Cygnus X-1, was discovered during a survey conducted with sounding rockets in 1964 by several groups from GSFC and MIT [4]. As a result of the survey study, Cyg X-1 (initially Cyg XR-1) was found to be located in the constellation Cygnus with right ascension (*RA*) 19 h 53 min and declination (*dec*) 34.6°. Later, the X-ray source Cyg X-1 was confirmed to be a BH owing to the rapid variability observed by *UHURU* satellite.

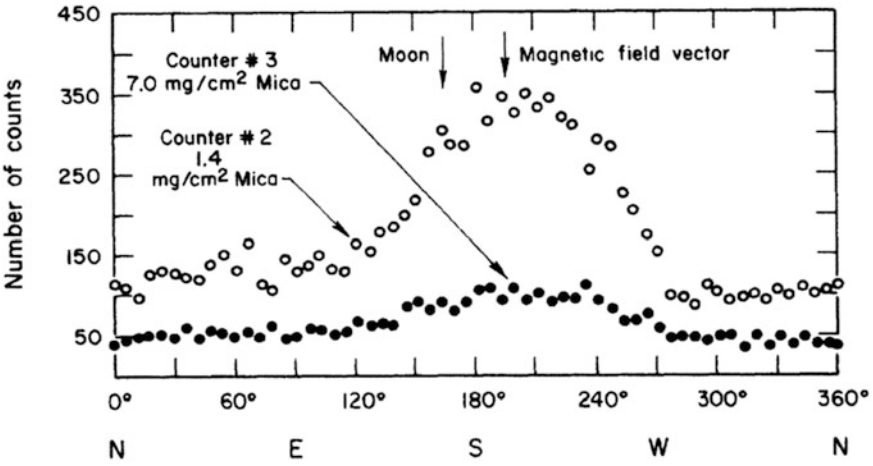



**Fig. 1** The first detection of 'non-solar' X-ray source was observed on June 12, 1962 with Aerobee rocket carrying three Geiger counters. The excess X-ray counts observed near 195° azimuth, as shown in the plot was from the direction of the constellation Scorpius. Later, the source was identified as Sco X-1. Adapted from [11]

## 2.2 Space-Based Observations

Within one decade, the first dedicated X-ray satellite *UHURU* ('Freedom') was developed and was launched on December 12, 1970 to place the satellite well above the Earth's atmosphere for long duration observations. *UHURU* discovered more than 300 new X-ray sources which include X-ray binary sources, supernovae, active galaxies, quasars etc. The observed data from the detectors on-board *UHURU* satellite revealed the pulsations from the X-ray binaries (e.g., Her X-1, Cen X-3) including Cyg X-1. Cyg X-1 was observed to flicker in erratic manner with characteristic time scale of milliseconds [23]. The rapid X-ray variability, which was chaotic in nature, led to the confirmation that Cyg X-1 could be a BH source rather than a Neutron Star in a X-ray binary system [27].

With the advancement of new technologies, several space based missions were planned as a follow-up of *UHURU* satellite. Since 1970, several successful missions, which were launched by NASA, ESA including Russia, Japan and India paved the way to revolutionize the field of Astronomy and Astrophysics to study the compact objects, especially BHs in great detail. In Table 1, we summarize the capabilities of various instruments of some of the 'great' missions, which are now either in decommissioned phase or in operational condition. In the same table, we also mention some of the approved upcoming missions, which are expected to further revolutionize the astrophysical study of BH sources in our Galaxy.

**Table 1** Summary of X-ray astronomy missions with comparative capabilities of the instruments

| Mission (agency) | Instrument (type) | Energy range (keV); energy resolution (eV@keV) | Remarks |
|---|---|---|---|
| *Past missions* | | | |
| UHURU (NASA) | Proportional counters (survey-timing) | 2–20 | Discovered 300 X-ray sources, including variability of Cyg X-1 |
| EXOSAT (ESA) | (Imaging, timing and spectroscopy) | 0.05–50 | Discovered QPO in GX 5-1 source |
| Ginga (Japan) | LAC (spectroscopy) | 1.5–37; 1080@6 | Discovery of transient BH candidates |
| ROSAT (ESA) | PSPC, HRI (survey-imaging) | 0.1–2.5; 500@1.0 | First all sky scan in soft X-rays |
| ASCA (JAXA) | GIS, SIS (imaging, spectroscopy) | 0.4–10; 472@5.9 | Discovery of broadening of iron lines in AGN |
| RXTE (NASA) | ASM, PCA, HEXTE (timing, spectroscopy) | 2–250; 1200@6.0 | Discovered HFQPOs in Neutron Stars and BH |
| IRS-P3 (ISRO) | IXAE (timing) | 2–20 | Time variability in BH sources |

(continued)

**Table 1** (continued)

| Mission (agency) | Instrument (type) | Energy range (keV); energy resolution (eV@keV) | Remarks |
|---|---|---|---|
| *Operational missions* | | | |
| Chandra (NASA) | ACIS, HRC | 0.1–10; 30@6.0 | Imaged X-ray emission from SN, AGN etc. |
| XMM-Newton (ESA) | EPIC-PN (imaging, timing, spectroscopy) | 0.1–15; 32@6.5 | Detected emission line features in AGN, variability in low energies |
| Integral (ESA) | SPI, IBIS, JEM-X (imaging, timing, spectroscopy) | 3–10,000; 8000@100 | High energy X-ray emission from BH |
| Suzaku (Japan) | XRT, XRS, XIS (imaging, spectroscopy) | 0.2–600; 50@1.0 | X-ray emission from BH binaries |
| Swift (NASA) | BAT, XRT, UVOT (imaging, timing, spectroscopy) | 0.2–150; 70@1.0 | GRBs and origin of BHs |
| AstroSat (ISRO) | LAXPC, CZTI, SXT, SSM, UVIT (imaging, timing, spectroscopy) | 0.3–150; 3000@30 | Multi-wavelength study of BH binaries |
| *Approved missions* | | | |
| Spectrum X-Gamma (Russia) | eROSITA, Lobster, ART, GRB | 0.2–30; 130@6.0 | Hard X-ray survey for obscured BH and quest for dark energy |
| XpoSat (ISRO) | POLIX, XSPECT (polarimetry, timing, spectroscopy) | 5–30 and 1–10 | Polarization along with spectroscopy studies of X-ray sources |
| IXPE (NASA) | (Polarization-sensitive imaging) | 2–8; 540@2.0 | X-ray polarimetric imaging |
| XARM (JAXA) | Resolve, Xtend (spectroscopy and imaging) | 0.3–13; 7@0.3–12 | Recovery mission of Hitomi, study of formation of BH |
| eXTP (China) | SFA, LAD, PFA, WFM (spectroscopy, timing and polarimetry) | 0.5–50; 180 eV | State of matter under extreme conditions of density, gravity and magnetism |

## 3 Observational Windows for BH Astrophysics and Implications

Most of the GBH candidates, if not all, are transient (or outbursting) in nature [9, 32]. Persistent BH sources have almost uniform intensity ($\sim 10^{37}$ erg s$^{-1}$ in X-rays) over a long period, while the transient sources show varying intensities (i.e., X-ray flux) with different time scales (days to months) resulting in outburst (of few mCrab to 12 Crab; [33]). Since its discovery, Cyg X-1 remains active by changing spectral states over longer time scale, whereas GRS 1915+105 show persistent emission

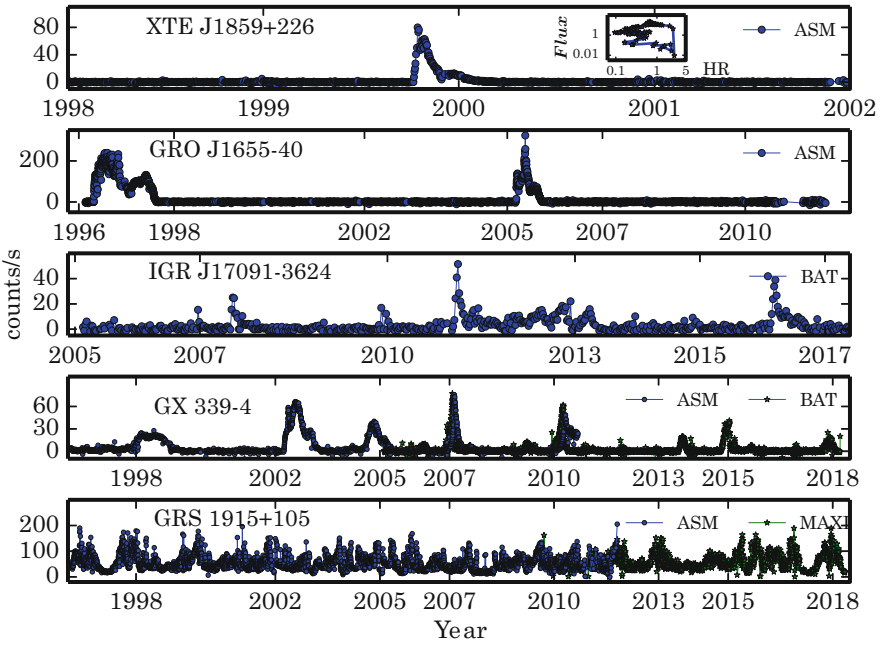



**Fig. 2** Lightcurve profiles of BH X-ray binaries are shown with the frequency of outburst. During the RXTE era, XTE J1859+226 showed outburst activity only once, whereas GRO-J1655-40 has undergone two outburst phases with activity for long duration. GX 339-4 has gone into frequent outbursts with recurrence time scale of 2–3 years, while IGR J17091-3624 has shown multiple outbursting activity during 2007, 2011 and 2016. In comparison, GRS 1915+105 has shown persistent emission over longer time scale with aperiodic and 'structured' variabilities in shorter time scale of secs to days. Outbursting sources follow a q-profile in the HID, shown in the inset of the top panel. Adapted from [30] with modification

with aperiodic variability in shorter time scales (few secs to days). Few sources like GX 339-4 undergo multiple outburst phases with recurrence time scale of 2–3 years and are well separated by quiescent phases. Another interesting source GRO J1655-40 remains mostly in-active (i.e., quiescent phase) for long duration and goes into outbursting phase once in a decade or so. In Fig. 2, we show the variation of X-ray count rate with time (MJD) over a long duration of two decades of several BH sources, highlighting the nature and frequency of the outburst in comparison with the persistent source. Observational data of all the sources were extracted from *ASM/RXTE*, *BAT/Swift* and *MAXI* instruments. During an outburst, the GBH sources follow a typical q-shape profile in the Hardness-Intensity Diagram (HID) [12, 20], which is shown in the inset of the top panel of Fig. 2.

Therefore, the Galactic transient and persistent BH candidates are the most interesting X-ray sources to study the peculiar temporal and spectral changes that occur during their activity phases. The BH states, namely LHS (low-hard state), HIMS (hard-intermediate state), SIMS (soft-intermediate state) and HSS (high-soft state) are identified in outbursting sources based on the evolution of spectral and

timing properties that are associated with different branches of the q-profile (see top panel of Fig. 2).

Below, we present the X-ray observational characteristics which are unique features of BH sources.

**Temporal Variability** All types of BH X-ray binaries emit X-ray photons that show variability on a wider range of timescales from microseconds to days, depending on the origin of the variability. These variabilities are the fastest astrophysical phenomena observed in compact objects that are discovered through the X-ray astronomy missions (*EXOSAT* and *RXTE*).

The Fourier transform of the X-ray variabilities results in a Power Density Spectrum (PDS) as a function of frequency. In general, PDS consists of band-limited noise along with a narrow component representing the 'fastest' variability. The narrow component which has finite width and is usually represented by a Lorentzian, termed as a Quasi-periodic Oscillation or QPO feature (see top-left panel of Fig. 5). QPOs are categorized into Low Frequency QPOs (LFQPOs) which belong to the range 0.1–30 Hz and High Frequency QPOs (HFQPOs) which are found to oscillate at frequencies from 40 Hz to a few hundreds of Hz for BH systems. Till now, the highest QPO observed, in GRO J1655-40, is ∼450 Hz (see top-left panel of Fig. 5). LFQPOs are further divided into A, B and C types [6]. In general, C-type QPO frequencies are observed to increase monotonically during the rising phase of the outburst, whereas it has been found that the A- and B-type QPOs are possibly linked with jet ejection from the BH systems [10, 24]. On the other hand, it is generally believed that the HFQPOs are originated from the inner part of the disk and has been used to constrain the spin of the BH systems [1] (also see [18]).

*GRS 1915+105: Is the Source Unique?* The enigmatic Galactic BH source GRS 1915+105 showed very complex X-ray variability (at least 13 types) during the RXTE era [3, 19]. Each X-ray variability 'class' has different spectro-temporal characteristics that are very much dynamic in nature. In some classes, QPO frequencies vary from 0.01 to 10 Hz, and are associated with hard spectral state. On the other hand, some other classes do not show QPO features and spectra are generally soft in nature. Sometimes, these classes show signature of HFQPOs at frequency of ∼42 and ∼67 Hz [26].

In addition to GRS 1915+105, several other BH sources show similar type of X-ray variabilities but with different time scale as shown in Fig. 3. It has been identified that the X-ray variabilities observed in XTE J1859+226 (1999 outburst), IGR J17091-3624 (2016 outburst), and GX 339-4 (2002, 2007 and 2010 outbursts) are coupled with SIMS of the outburst phase of the sources [5, 13, 25]. It could be possible that GRS 1915+105 is 'locked' in one of its intermediate states and exhibits all peculiar variabilities. Transition from one class to another class also takes place in a matter of hours, whereas the spectral state transitions in some of the classes take place in a matter of few seconds. Further, we argue that the unique variability observed in these sources could be due to the local variation of mass accretion rate, as the global variation of accretion rate in the disk takes place in the viscous time scale, which could be order of days.

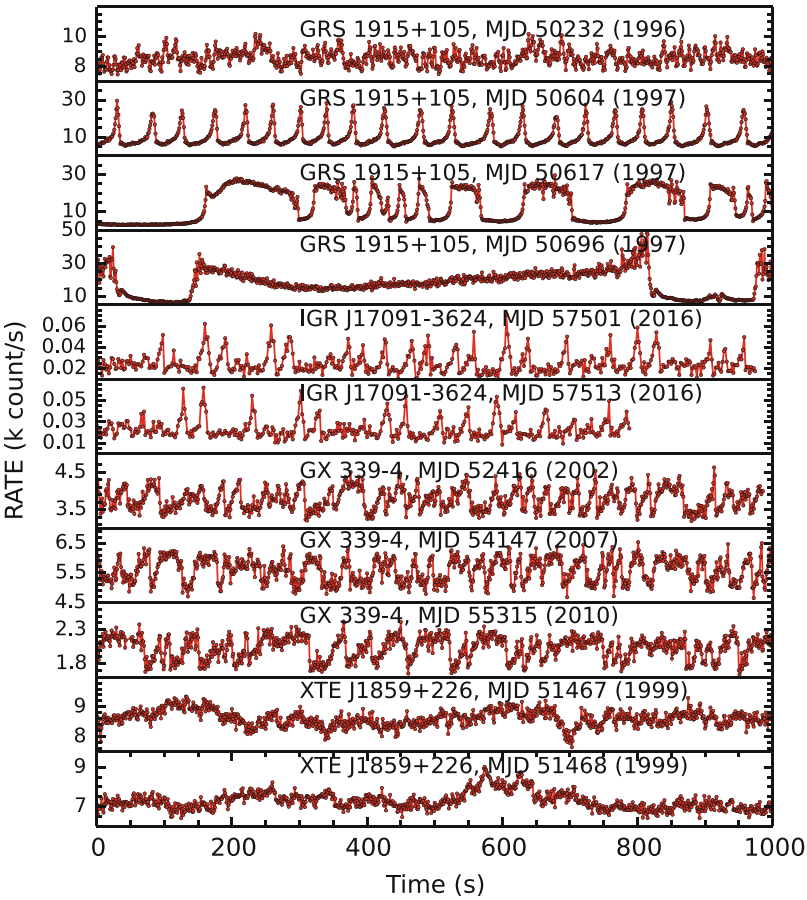



**Fig. 3** The aperiodic and 'structured' X-ray variabilities exhibited by various BH sources during their activity phases are presented. Top four panels show only four peculiar X-ray variabilities ($\phi$, $\rho$, $\kappa$ and $\theta$ classes) observed in GRS 1915+105. In the bottom panels, we show the variabilities observed in IGR J17091-3624 (2016), in GX 339-4 (2002, 2007 and 2010) and in XTE J1859+226 (1999) to compare with the variabilities observed in GRS 1915+105. The variabilities observed in the latter three sources were associated with SIMS of their outbursting phases, which provide an indication that GRS 1915+105 may be 'locked' in one of its intermediate states. Adapted from [30] with modification

**Spectral Variability** In general, X-ray binaries emit radiations in wide-band of X-ray energy ranges, varying from low energy to high energy (∼0.1 keV to few 100 keV). The energy spectral distributions, that are observed in the X-ray binaries, are composed of blackbody and power-law components. In general, the nature of the energy spectra of the accretion disk is modeled using a standard Keplerian disk [29] coupled with the 'Compton corona' (often a sub-Keplerian flow) [7, 31]. Usually, the hot 'Compton corona' inverse-Comptonizes the soft photons (i.e., thermal emission)

emitted from the Keplerian disk to produce the high energy component of the radiation spectrum.

In addition, the energy spectrum shows the signature of asymmetric feature of iron line at 6.4 keV and the reflection bump in the energy range of 20–40 keV [17]. Both these features are also found to be variable and highly depend on the accretion states of BH. This observational studies seem to be directly linked with the relativistic nature of the accretion disk.

It has also been observed that the energy spectrum as well as the spectral parameters (disk temperature, power-law index etc.) evolve along with the outburst profile. This indicates the dynamical nature of the accretion disk. During LHS, the spectrum is dominated by power-law component with high energy emission, whereas in HSS the thermal emission dominates at low energies showing the strong presence of a Keplerian disk. Typical energy spectra of different spectral states of a BH system during its outburst are shown in Fig. 4.

**Imaging and Polarimetry** Unprecedented X-ray imaging quality of *Chandra* and *XMM-Newton* below 10 keV was useful for studying the spectral nature in the low energy 0.3–10 keV with high signal to noise ratio. On the other hand, the *NuSTAR* mission, which is designed with hard X-ray focusing telescope (3–79 keV) with unprecedented spatial (see bottom-left panel of Fig. 5) and spectral resolution revolutionized the understanding of nature of accretion disk in the presence of rotating BH by probing the iron line feature (∼6.4 keV) and reflection bump on top of the Comptonized spectrum.

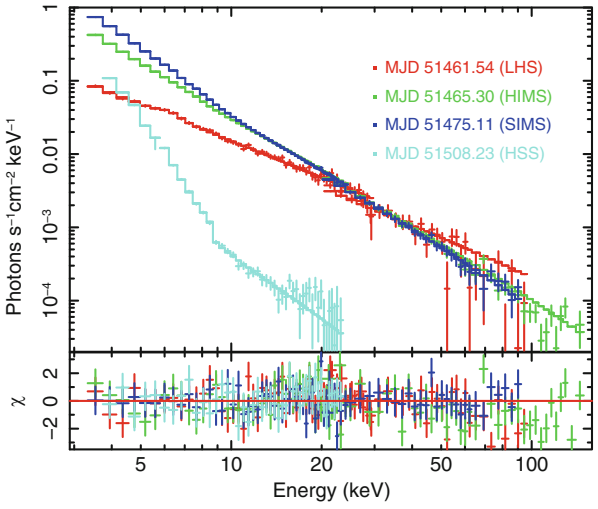



**Fig. 4** The energy spectra (3–150 keV) of four spectral states (i.e., LHS, HIMS, SIMS and HSS) of the 1999 outburst of XTE J1859+226 are shown. The energy spectra are modeled with phenomenological models of *XSPEC* (i.e., *diskbb*, *Gaussian* and *powerlaw* components) as well with two-component flow model. Residuals (in bottom panel) are within $2\sigma$. Adapted from [21]

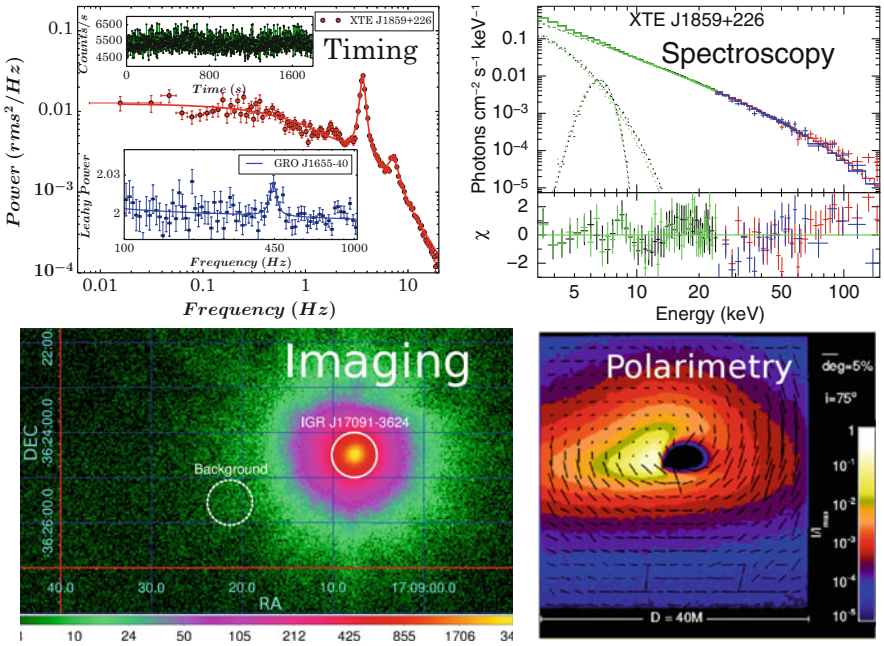



**Fig. 5** Composite representation of temporal, spectroscopic, imaging results from BH sources, whereas the polarimetric result is based on simulation in the thermal state of BH. Reproduced from [1, 2, 25, 28, 30]. See text for details

Measurement of polarization in X-rays is a photon eating process and has not been possible to design space-based instruments due to lack of required sensitivity for such type of measurements. However, experiments were performed with Aerobee-350 rockets using Lithium scattering polarimeter and Bragg crystals. A new window in X-ray astronomy has been opened up by the detection of X-ray polarization signature from the Crab pulsar [22].

## 4 Future Prospects of BH Astrophysics

Since the beginning of X-ray astronomy in early 1960s, our understanding about the BH sources has increased many-folds with the spectroscopy, timing and the imaging studies in X-rays. Over last five decades, several space missions have been realized (see Table 1) in order to observe compact BH X-ray sources with energy resolution improved by several factors and the time resolution has increased by a few orders of magnitude. At the same time, theoretical models have improved considerably from the accretion of spherical flows to multi-component accretion flows in the presence of magnetic fields including coronal and jet physics.

Considering that several models are degenerate with respect to timing and spectroscopic information, the polarimetric measurement along with timing and spectroscopy would break the degeneracy and greatly improve the understanding of the energetic phenomena around the vicinity of a BH. The polarimetry measurement adds two more dimensions to our understanding, the degree of polarization and the angle of polarization, and thus provides an excellent diagnostic tool to understand the emission processes from the compact objects.

With the advancement of X-ray optics along with the high sensitivity in X-ray polarimetric instrumentation, the field of X-ray polarimetry is opened again after 40 years. A dedicated mission in soft X-rays is planned by NASA (IXPE: Imaging X-ray Polarimetric Emission) to be launched by 2020. ESA has planned XIPE (X-ray Imaging Polarimetry Explorer) to be flown in 2024. In parallel to that, India's AstroSat-CZTI has provided the polarization variation of Crab pulsar over its off-pulse in the energy range of 100–380 keV [34].

In Fig. 5, we have shown a composite picture showing the results from four branches (i.e., Timing, Spectroscopy, Imaging and Polarimetry) of X-ray astronomy for BH sources. In the top-left panel of Fig. 5, we show the timing analysis results using *RXTE* data, highlighting the 'fastest' variability observed as LFQPO (∼3.6 Hz) and HFQPO (∼450 Hz). The broadband energy spectrum in the energy range of 3–150 keV is shown in top-right panel of Fig. 5. The spectrum shows the signature of disk emission, iron-line feature and high-energy cutoff, which clearly indicate that emission mechanism is complex in nature in a disk around a BH [30]. The hard X-ray imaging capability of *NuSTAR* is shown in the bottom-left panel of Fig. 5, highlighting the source and background region [25]. Further, lightcurve and spectrum are generated from the desired regions to do temporal and spectral studies with better statistics. The image that is shown in the bottom-right panel of Fig. 5 is the simulation of X-ray polarization signature expected from BHs in the thermal state [28]. Here, the accreting material on the left is moving towards the observer who is at an inclination of 75° with respect to the rotation axis of the BH. Both direct radiation as well as the return radiation that is deflected by the strong field gravity of the BH before scattering off the disk are shown.

Considering the present understanding of BH astrophysics, it is the need of the hour to design a 'spectro-temporal-polarimetric' mission to probe the extreme gravity as well as the true nature of the accretion dynamics around the BH sources. Keeping this in mind, we propose a multi-wavelength *Spectro-Temporal-Polarimetric* Observatory, coined as *IMAP* (ISRO's Multi-wavelength Astronomy Probe) for focused and dedicated observation of compact objects.

## 5 Conclusion

Since 1960, the spectral and timing studies have enhanced our understanding of different astrophysical processes around compact objects. Worldwide many coordinated attempts have been made for simultaneous multi-wavelength and long

term temporal and spectral observations. Our understanding have greatly improved with numerous data available with advanced techniques of data analysis. New theoretical models as well as various techniques of analyzing data have also been developed.

Still, there are many open questions yet to be answered—The true characteristics of matter and radiation in the close vicinity of event horizon is not known. Why do compact objects show outburst? What is the nature of accretion flow (single component vs. multi-component)? What is the origin and nature of jets (electron-positron, electron-proton or something else), and so on.

Even after many observations of variability classes as observed in many BH sources, the origin of the classes and transition from one class to another are poorly understood. The fundamental question—are these variabilities coupled with viscous time scale (global) or free-fall time scale (local) of the accretion dynamics? In order to address this question, it is very important to have continuous observation of the sources. Using *RXTE* and *IXAE* data, we have found some evidences of class transition (e.g. $\chi$ to $\theta$; $\kappa$ to $\rho$) that are happening within 3–5 h (see [8] for details). This rules out the possibility of dynamical change at the outer edge of the disk (i.e., viscous time scale). Therefore, fast transitions of/within classes could be due to change in accretion dynamics at an intermediate distance of the disk, where Keplerian and sub-Keplerian flows play major role.

Keeping in mind the complex nature of accretion dynamics, it is further required to study the correlation between the energy dependent QPO features with iron-line. The evolution of reflection features along with wide-band spectra is required to investigate in detail to probe the nature of relativistic accretion disk around BHs.

Compact objects (especially BHs) are considered to be the 'ideal' astrophysical laboratories to test the extreme gravity effect as well as the accretion-ejection phenomena by providing spectro-temporal-polarimetric characteristics of the observed electromagnetic emission in the IR ($\sim$1 μm) to $\gamma$-ray ($\sim$1 MeV) band. In this context, we propose a multi-wavelength *Spectro-Temporal-Polarimetric* Observatory to probe extreme gravity region around a BH for future studies.

**Acknowledgements** The author would like to express sincerest gratitude to Sandip K. Chakrabarti for his constant encouragement, and setting ambitious goals during Ph.D. work, which paved the way to continue research in the fascinating world of astronomy. This article is based on the collaborative works carried out over the years with Dipak Debnath, Radhika D., Nirmal Iyer and Sreehari H.—special thanks to all of them. The author also personally thanks all the *IMAP* team members towards the contribution for writing the proposal.

*A scientist without knowledge of social science is not a philosopher.*
– Anonymous philosopher's view

## References


1. Aktar, R., Das, S., Nandi, A., Sreehari, H.: MNRAS (2017). https://doi.org/10.1093/mnras/stx1893
2. Aktar, R., Das, S., Nandi, A., Sreehari, H.: J. Astrophys. Astron. (2018). https://doi.org/10.1007/s12036-017-9507-0
3. Belloni, T., Klein-Wolt, M., Méndez, M., van der Klis, M., van Paradijs, J.: Astron. Astrophys. **355**, 271–290 (2000)
4. Bowyer, S., Byram, E.T., Chubb, T.A., Friedman, H.: Cosmic X-ray Sources. Science (1965). https://doi.org/10.1126/science.147.3656.394
5. Capitanio, F., Del Santo, M., Bozzo, E., Ferrigno, C., De Cesare, G., Paizis, A.: MNRAS (2012). https://doi.org/10.1111/j.1365-2966.2012.20834.x
6. Casella, P., Belloni, T., Stella, L.: Astrophys. J. (2005). https://doi.org/10.1086/431174
7. Chakrabarti, S.K., Titarchuk, L.G.: Astrophys. J. (1995). https://doi.org/10.1086/176610
8. Chakrabarti, S.K., Nandi, A., Chatterjee, A.K., Choudhury, A.K., Chatterjee, U.: Astron. Astrophys. (2005). https://doi.org/10.1051/0004-6361:20041662
9. Chen, W., Shrader, C.R., Livio, M.: Astrophys. J. (1997). https://doi.org/10.1086/304921
10. Fender, R.P., Homan, J., Belloni, T.M.: MNRAS (2009). https://doi.org/10.1111/j.1365-2966.2009.14841.x
11. Giacconi, R., Gursky, H., Paolini, F.R., Rossi, B.B.: Phys. Rev. Lett. (1962). https://doi.org/10.1103/PhysRevLett.9.439
12. Homan, J., Belloni, T.: Astrophys. Space Sci. (2005). https://doi.org/10.1007/s10509-005-1197-4
13. Iyer, N., Nandi, A., Mandal, S.: Astrophys. J. (2015). https://doi.org/10.1088/0004-637X/807/1/108
14. Jacobson, A.S., Jerde, R.L., Peterson, L.E.: AIAA J. (1967). https://doi.org/10.2514/3.4341
15. Lewin, W.H.G., McClintock, J.E., Ryckman, S.G., Smith, W.B.: https://doi.org/10.1086/180741
16. Longair, M.S.: Cambridge University Press, Cambridge (2011). ISBN: 9781139494540
17. Miller, J.M., Reynolds, C.S., Fabian, A.C., Cackett, E.M., Miniutti, G., Raymond, J., Steeghs, D., Reis, R., Homan, J.: Astrophys. J. Lett. (2008). https://doi.org/10.1086/589446
18. Mukhopadhyay, B.: Astrophys. J. (2009). https://doi.org/10.1088/0004-637X/694/1/387
19. Nandi, A., Manickam, S.G., Chakrabarti, S.K.: ArXiv Astrophysics e-prints (2000) astro-ph/0012523
20. Nandi, A., Debnath, D., Mandal, S., Chakrabarti, S.K.: Astron. Astrophys. (2012). https://doi.org/10.1051/0004-6361/201117844
21. Nandi, A., Mandal, S., Sreehari, H., Radhika, D., Das, S., Chattopadhyay, I., Iyer, N., Agrawal, V.K., Aktar, R.: Astrophys. Space Sci. (2018). https://doi.org/10.1007/s10509-018-3314-1
22. Novick, R., Weisskopf, M.C., Berthelsdorf, R., Linke, R., Wolff, R.S.: Astrophys. J. Lett. (1972). https://doi.org/10.1086/180938
23. Oda, M., Gorenstein, P., Gursky, H., Kellogg, E., Schreier, E., Tananbaum, H., Giacconi, R.: Astrophys. J. Lett. (1971). https://doi.org/10.1086/180726
24. Radhika, D., Nandi, A., Agrawal, V.K., Seetha, S.: MNRAS (2016). https://doi.org/10.1093/mnras/stw1239
25. Radhika, D., Sreehari, H., Nandi, A., Iyer, N., Mandal, S.: Astrophys. Space Sci. (2018, under review)
26. Remillard, R.A., McClintock, J.E.: Annu. Rev. Astron. Astrophys (2006). https://doi.org/10.1146/annurev.astro.44.051905.092532
27. Rothschild, R.E., Boldt, E.A., Holt, S.S., Serlemitsos, P.J.: Astrophys. J. Lett. (1974). https://doi.org/10.1086/181452
28. Schnittman, J.D., Krolik, J.H.: Astrophys. J. (2009). https://doi.org/10.1088/0004-637X/701/2/1175
29. Shakura, N.I., Sunyaev, R.A.: Astron. Astrophys. **24**, 337–355 (1973)

30. Sreehari, H., Nandi, A., Radhika, D., Iyer, N., Mandal, S.: J. Astrophys. Astron. (2018). https://doi.org/10.1007/s12036-018-9510-0
31. Tanaka, Y., Lewin, W.H.G.: Black hole binaries. In: X-ray Binaries, pp. 126–174. Cambridge University Press, Cambridge (1995)
32. Tetarenko, B.E., Sivakoff, G.R., Heinke, C.O., Gladstone, J.C.: Watchdog. Astrophys. J. Suppl. (2016). https://doi.org/10.3847/0067-0049/222/2/15
33. Tsunemi, H., Kitamoto, S., Okamura, S., Roussel-Dupre, D.: Astrophys. J. Lett. (1989). https://doi.org/10.1086/185383
34. Vadawale, S.V., Chattopadhyay, T., Mithun, N.P.S., Rao, A.R., Bhattacharya, D., Vibhute, A., Bhalerao, V.B., Dewangan, G.C., Misra, R., Paul, B., Basu, A., Joshi, B.C., Sreekumar, S., Samuel, E., Priya, P., Vinod, P., Seetha, S.: Nat. Astron. (2018). https://doi.org/10.1038/s41550-017-0293-z

# Evolution of Flow Properties Around Black Holes from Observations: Developments over the Past Decades




**Dipak Debnath**

**Abstract** To find direct observational evidences of accretion flows around black holes, one needs to study them with a physical model. Although there are many phenomenological and theoretical models available in the literature, observational astronomy of black holes has changed significantly after the successful implementation of the two component advective flow solution (TCAF) into XSPEC as an additive table model to fit energy spectra. Accretion flow dynamics around black holes are now more transparent, since a spectral fit with this most generalized accretion flow solution directly provides us information about the flow parameters. Prediction of quasi-periodic oscillation frequencies, which is a timing feature, is also a reality from the TCAF model fitted shock parameters. One can also estimate black hole mass, spin, etc., which are intrinsic source parameters from spectral analysis with the TCAF solution. Estimation of X-ray contribution from jets or outflows are also possible from spectral analysis with the TCAF solution.

## 1 Introduction

Observation of black hole sources in X-rays was started by Giacconi and his collaborators more than 50 years ago in 60s (e.g., [2, 29, 35, 46]). Theoretical model for accretion flows around black holes and understanding various observational features, also started more than 40 years ago in early 70s (e.g., [43, 47]). Until now many astronomical satellites, starting from Uhuru to ASTROSAT are launched to see deeper inside of systems with these mysterious compact objects. However, we feel that the observational astronomy on black holes has progressed significantly, specially after the launch of RXTE (Rossi X-ray Timing Explorer) in December 1995.

D. Debnath (✉)
Indian Centre for Space Physics, Kolkata, India

© Springer International Publishing AG, part of Springer Nature 2018

B. Mukhopadhyay, S. Sasmal (eds.), *Exploring the Universe: From Near Space to Extra-Galactic*, Astrophysics and Space Science Proceedings 53,
https://doi.org/10.1007/978-3-319-94607-8_18

It is well established that in a black hole binary (BHB) system, primary compact object black hole (BH) can accrete matter from its companion star by two processes. When the BH and the companion star are sufficiently close, outer surface matter from the companion is captured by the compact object (here BH) by Roche lobe overflow. The compact object can accrete matter also via wind of massive secondary star. For a wind accretion, the matter flows towards the BH in a free fall time scale since it carries matter with no or very less angular momentum. If the matter possesses significant amount of angular momentum then it accumulates to form an optically thick and geometrically thin disk around the compact object and proceeds toward the BH by transferring its angular momentum. The disk emits electromagnetic radiation when its swirling matter falls into it from its companion star. Emission spectrum contains radio waves to $\gamma$-rays.

Stellar mass black hole binaries can exhibit rapid evolution in their spectral and temporal properties in short duration. These BH candidates (BHCs) are of mainly two types, namely, outbursting or transient (GX 339-4, GRO J1655-40, H 1743-322, XTE J1118+480, XTE J1817-330, etc.) and persistent (Cyg X-1, 4U 1957+115, GRS 1915+105, etc.). There are also few sources, which may be called semi-persistent (IGR J17091-3624, Swift J1753.5-0127, etc.). These BHCs start as a typical outbursting source before moving into the persistent nature, and finally after few years they move into the quiescent phase. During an outburst, a transient BHC shows evolutions in its both spectral and timing features, whereas persistent sources could stay in one spectral state for a long duration. The transient BHCs are interesting sources to study in high energy X-ray band as they show rapid evolution in their spectral and timing properties during outbursts. During an outburst, strong correlation between spectral and timing properties are seen. Several works are found in literature (see, e.g., [20, 22, 24–26] and references therein), which explain variations of the timing and the spectral properties of these compact objects during their X-ray outbursts. In general, it has been found that these transient compact objects exhibit different spectral states, such as *hard* (HS), *hard-intermediate* (HIMS), *soft-intermediate* (SIMS), and *soft* (SS) during their outbursts in the sequence of: HS$\rightarrow$HIMS$\rightarrow$SIMS$\rightarrow$SS$\rightarrow$SIMS $\rightarrow$HIMS$\rightarrow$HS to form a hysteresis loop (see, e.g., [22, 24] and references therein). They also show signature low and high frequency quasi-periodic oscillations (QPOs) in some of these spectral states (see, [22] and references therein). The frequencies of the low frequency QPOs are found to evolve with time during the rising and the declining phases (more precisely, during HS and HIMS) of the outbursts. It has been observed by several authors (see, [22, 24–26, 31] and references therein) that extracted physical flow parameters undergo a hysteresis loop during their spectral evolution through entire phase of an outburst of these BHCs. One can also find a strong correlation between spectral and timing properties, such as different spectral states, observation of QPOs, strong outflows, etc. in the different branches of these hysteresis plots, e.g., *hardness-intensity diagram* (HID; [20] and references therein) or *accretion rate ratio intensity diagram* (ARRID; [31]). According to the nature of the variations of temporal and spectral properties during outbursts, Debnath et al. [26] classified transient BHCs into two types: (1) *type-I* or *classical-type*, where all four main

spectral states are observed (HS $\rightleftharpoons$ SS via two intermediate, HIMS and SIMS spectral states), and (2) *type-II* or *harder-type*, where SS (sometimes even SIMS) could not be observed. The type-II type of outbursts are generally termed as 'failed' outbursts.

In the literature, one may find large number of phenomenological and theoretical models, which claim to explain physics of accretion processes around black holes. However, we believe that a correct theoretical model must address all the aspects (both spectral and temporal) of observational data and that true for all the black holes. We also believe that for a true physical model, total number of model parameters should be minimum, otherwise anything could be fitted after addition of one after another parameter. In general practice, we see that to explain any new observed feature, some of the observers add-up extra model(s) on ad-hoc basis (without any physical connection) while fitting spectra, which indeed increases number of total model input parameters.

It is well known that emitted spectrum of the radiation coming from black holes is a *multi-color* in nature, and it contains both *thermal* and *non-thermal* components. One component is basically the multi-color blackbody radiation from the standard Keplerian disk [47], and the other is a non-thermal power-law component, which is generally originated from the 'Compton' cloud [49] composed of hot electrons. In *two component advective flow (TCAF) solution* of Chakrabarti and Titarchuk [12] (hereafter CT95), the role of so-called *'Compton cloud'* or *'hot corona'* of earlier models is replaced by the CENtrifugal pressure supported BOundary Layer (CENBOL), which automatically forms behind the centrifugal barrier due to piling up of the low viscosity (sub-critical), low angular momentum and optically thin matter known as sub-Keplerian (halo) accretion component. In TCAF, the other component of accretion flow is the high viscous, geometrically thin and optically thick Keplerian (disk) matter which is submerged inside the sub-Keplerian halo component. Keplerian disk is naturally truncates at the shock location since in general CENBOL is much hotter. Keplerian disk settles down to a standard Shakura-Sunyaev disk when cooling is efficient. Low energy (soft) thermal photons from the Keplerian disk intercept with the CENBOL (composed of hot electrons) and emit as high energy (hard) photons by cooling down CENBOL through repeated Compton scatterings.

To get direct estimation of the accretion flow parameters from spectral fits of the black hole sources, Debnath et al. [23] have successfully implemented TCAF solution into HEASARC's spectral analysis software package XSPEC [1] as an additive table model. After that, Debnath and his collaborators have been quite successful to explain accretion flow properties of a few stellar mass BHCs (such as, H 1743-322, GX 339-4, Swift J1753.5-0127, XTE J1118+480, MAXI J1659-152, MAXI J1836-194, MAXI J1543-564, Cygnus X-1) during their X-ray active phases [4, 16, 17, 23–26, 31, 36, 37, 39–42]. The evolution of different spectral as well as temporal features are now more clearly understandable. They also have estimated intrinsic physical parameters, such as mass, spin of the BH from spectral analysis with the TCAF model *fits* file. The estimation of the amount of X-rays coming from jets or outflows are also done from TCAF model fitted spectral analysis.

## 2 TCAF Model and Its Implementation as an Additive Table Model in XSPEC

The theory of the TCAF model (CT95; Chakrabarti [7], hereafter C97) has been introduced and described in detail in the literature more than two decades ago. The configuration of this generalized transonic flow solution has been found stable by Giri and Chakrabarti [30] in their recent extensive numerical simulations. A simple cartoon diagram of the TCAF solution is presented in CT95, where as in [10], generalized cartoon diagram is shown. In the later paper, more physical facts/processes associated with the accretion flows around black holes are presented. This model requires two accretion rates: Keplerian disk and sub-Keplerian halo rates. The Keplerian disk forms at the equatorial plane and is immersed in the sub-Keplerian halo. Other two essential parameters are location and compression ratio of the shock at shock location outside the CENBOL. These two parameters provide the height of the shock, calculated using the pressure balance condition [6]. The density and the temperature distribution of the accretion flow and especially matter in the post-shock region are calculated using two-temperature hydrodynamic flow equations and continuity equation as presented in CT95. The original CT95 code also self-consistently computes optical depth, average electron temperature of the CENBOL, spectral index of the emerging spectrum, etc. by adding relevant cooling and heating processes, such as those arising due to physical processes of bremsstrahlung, Comptonization, inverse bremsstrahlung and inverse Comptonization. In the current version of the TCAF model, synchrotron cooling process was not included. Original CT95 considered only strong shock case for demonstration purpose of their model. But, in order to take care of weaker shocks needed for actual fitting of data from different spectral states, Debnath et al. [24] generalized the expression for the shock height ($H_{shk}$) and shock temperature ($T_{shk}$) in the following way:

$$H_{shk} = \left[\frac{\gamma(R-1){X_s}^2}{R^2}\right]^{\frac{1}{2}} \tag{1}$$

and the shock temperature is given by,

$$T_{shk} = \frac{m_p(R-1)c^2}{2R^2 k_B(X_s-1)}, \tag{2}$$

where, $m_p$, $k_B$, $c$, $\gamma$, $X_s$, and $R$ are the mass of the proton, Boltzmann constant, velocity of light, adiabatic constant, shock location, and compression ratio of the flow respectively. They also incorporated the spectral hardening correction depending on the accretion flow rate as in Shimura and Takahara [48]. Paczyński and Wiita [44] pseudo-Newtonian potential $\Phi_{PN} = -\frac{1}{2(r-1)}$ also has been used to describe the geometry around the black hole.

In a summary, to generate the model spectra (which are used as inputs for generating TCAF model *fits* file), Debnath et al. [23, 24], modified original CT95 code as follows.

1. Compression ratio $R$ is varied from 4 (strong) to 1 (weak) to fit data from all spectral states. In original CT95 code, strong shock with $R = 4$ was assumed for illustration purpose.
2. Temperature of the post-shock region was computed with these variable $R$ values.
3. Radial velocity was considered as of C97 after assuming flow to be rotating.
4. Spectral hardening correction as of Shimura and Takahara [48] was incorporated. This correction depends on the accretion flow rates. Debnath et al. [24] uniformly considered the correction factor ($f$) as 1.8 to calculate effective temperature of the emitted spectrum.

The successful implementation of the TCAF solution as an additive table model in XSPEC [1] was done recently by Debnath et al. [23]. HEASARC's spectral analysis software package XSPEC is the common user-friendly platform, which is generally used by astrophysicists to fit energy spectrum with models. It consists of a large number of inbuilt theoretical or phenomenological models. One may also fit energy spectra in XSPEC with a local table model, after generating model fits file compatible with it. Debnath et al. [23] have done that for the TCAF solution. To generate a model *fits* file of version $v0.1$, they first generated huge number ($\sim$1 million) of theoretical model spectra by varying five basic model input parameters: Keplerian rate (disk rate $\dot{m}_d$), sub-Keplerian rate (halo rate $\dot{m}_h$), mass of the black hole ($M_{BH}$), location of the shock $X_s$, and the compression ratio $R$ in different grid values as mentioned below. (1) $\dot{m}_d$ in $0.001–10\dot{M}_{Edd}$, (2) $\dot{m}_h$ in $0.001–10\ \dot{M}_{Edd}$, (3) $M_{BH}$ in 3–20 Solar mass ($M_\odot$), (4) $X_s$ in 6–460 $r_s$, and (5) $R$ in 1–4. Here, $\dot{M}_{Edd}$ is the Eddington rate, which is equal to $L_E c^2$, where $L_E$ is the Eddington luminosity and $c$ is the velocity of light. Beside not generating model *fits* file using huge number of theoretical model spectra, one may use the model code directly in XSPEC to fit energy spectrum. But, direct fitting of the spectrum with the model is a bit time consuming, since TCAF model is not based on simple analytical equations, rather it is a solution of iterative processes of radiative transfer equations. So to fit one spectrum directly with code in XSPEC (where in every step it generates model spectra inside the XSPEC and tries to fit it with least-square fit technique), it may take hours to find best fit. Due to this time issue, it is better to use model *fits* file as a local model.

So at present, to fit BH spectra after keeping TCAF model *fits* file into the local hard-drive and using it as a local additive table model, one needs to supply six model initial guess parameters: (1) mass of the black hole ($M_{BH}$) in units of $M_\odot$, (2) Keplerian rate ($\dot{m}_d$ in units of $\dot{M}_{Edd}$), (3) sub-Keplerian rate ($\dot{m}_h$ in units of $\dot{M}_{Edd}$), (4) location of the shock ($X_s$ in units of Schwarzschild radius $r_s = 2GM_BH/c^2$), (5) compression ratio ($R = \rho_+/\rho_-$, where $\rho_+$ and $\rho_-$ are densities of the post- and pre- shock matters) of the shock, and (6) the model normalization value ($N$). For a known BHC, one only needs four input parameters, since $M_{BH}$ and $N$ are constants.

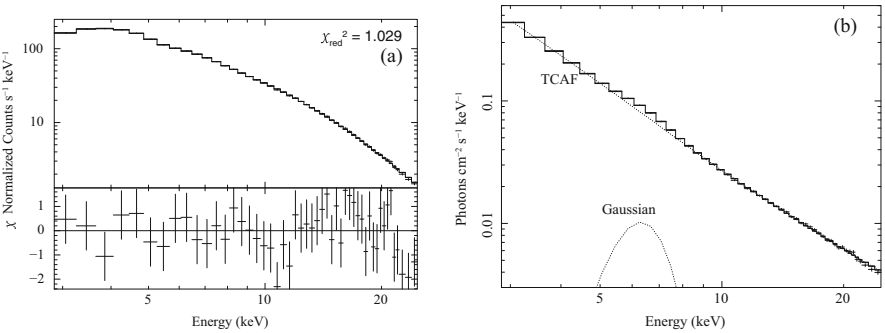



**Fig. 1** (**a**) TCAF model fitted 2.5–25 keV PCA spectrum of GX 339-4 (Observation ID = 95409-01-14-04; MJD = 55300) with variation of $\Delta\chi$ is shown in the left panel. The value of the model fitted reduced $\chi^2$ is written down. (**b**) The unfolded model components of the spectral fit are shown on the right panel. Adapted from [23]

The model normalization $N$ should not vary for a particular BHCs on a daily basis, since it is a function of intrinsic source parameters such as, mass of the BH, distance and disk inclination angle.

In Fig. 1, we show a typical spectra (observation ID: 95409-01-14-04, UT date: 2005 Apr. 01 and MJD = 53000) of GX 339-4, fitted with the TCAF solution in combination with a Gaussian profile of ∼6.4 keV for Fe emission line and interstellar absorption model *'wabs'* in the form of: "$wabs \times (TCAF + Gaussian)$".

## 3 TCAF Model as a Complete Solution for Black Hole Accretion: Useful Tool to Explain Various Observational Aspects

As stated earlier, TCAF model is a global solution of radiative transfer equations by considering two component of viscous flows (separated by critical viscosity) around the black holes. Here, no assumptions are made on ad-hoc basis. So, one can expect proper theoretical explanation of various observational facts such as, different temporal as well as spectral features in active phases of black holes. The model was introduced by Chakrabarti and his collaborators in mid-90s (CT95, C97). Until 2010, no direct observational fitting using TCAF model was done, only different observational aspects are explained based on the knowledge of the TCAF solution. In Dutta and Chakrabarti [27], a manual fitting of the TCAF model was done for Galactic BHC XTE J1550-564 during its 1998–1999 outburst. Mandal and Chakrabarti [34] also fitted the data of outburst source GRO 1655-40 and showed that two components rate vary with days. Debnath and his collaborators have successfully implemented this solution into XSPEC as an additive table model to fit energy spectra with the model *fits* file in an user-friendly manner [23, 24]. Now

one can explain different observational (spectral and timing) aspects of black hole accretion directly from spectral fits. One can also estimate different intrinsic source parameters (for e.g., mass of the BH, spin, etc.) from spectral analysis. Estimation of X-ray contribution of jets or outflow rates are also possible from spectral fitting with the current version of the TCAF model *fits* file. All these recent prospect of the observational black hole astronomy with TCAF model, makes this model as a complete solution for black hole accretion. In the following sub-Sections brief summary of the above mentioned observational evidences with the TCAF solution will be discussed.

## *3.1 Spectral Analysis to Study Accretion Flow Properties Around Black Holes*

After the successful implementation of the TCAF solution as an additive table model in XSPEC [23, 24], till now Debnath and his collaborators have studied number of transient (H 1743-322, GX 339-4, MAXI J1659-152, MAXI J1836-194, MAXI J1553-564, XTE J1118+480), persistent (Cygnus X-1), and semi-persistent (Swift J1753.5-0127) BHCs during their X-ray active phases using archival data of various astronomy satellites (RXTE, Swift, NuSTAR, MAXI, etc.). New more sources are in pipe-line. The detailed spectral analysis with the TCAF model *fits* file, directly provides us with information about the flow rate of the two types of inflowing matters, location and size of the 'hot Compton cloud', i.e., CENBOL, and mass of the black hole (if unknown).

Low frequency QPOs (LFQPOs) in the range of 0.01–30 Hz are common temporal features in black hole binaries, when fast Fourier transformed power density spectra are generated from low time binned (for example 0.01 s) lightcurves (see, [22] and references therein). These QPOs are periodic variations of the intensity. Generally QPOs are of three types: A, B, and C [5]. These QPOs (generally type 'C') are commonly found to evolve monotonically in rising/declining HS and HIMS spectral states [13, 14, 21, 22]. The type 'C' QPOs are originated due to resonance oscillation of the shock, i.e., as a whole oscillation of the CENBOL when resonance condition satisfies, i.e., when cooling time scale roughly matches with infall time scale. The signature of LFQPOs are absent during SS, while during SIMS one may see sporadic (on and off) observations of the QPOs, roughly on around same observed frequency.

Based on the variation of the TCAF model fitted/derived flow parameters ($\dot{m}_d$, $\dot{m}_h$, $X_s$, R, and ARR) and nature (frequency, width, Q-factor, rms, etc.) of QPOs (if observed), one may find a better understanding about the properties and evolution of different observed spectral states during an outburst of a BHC. During an outburst of a classical or type-I BHC, four observed spectral states generally form a hysteresis loop in the sequence of: HS→HIMS→SIMS→SS→SIMS→HIMS→HS. In general, one may see a local maximum of the ARR on the HS⇌HIMS transition day and of evolving QPO frequency on the transition day of HIMS⇌SIMS. During the

rising HS, ARR is generally found to increase with a monotonically rise in the halo rate and reaches at its local maximum on the HS-HIMS transition day. During this phase of the outburst, the shock moves inward with gradually weakening strength.

In the rising HIMS, the shock further moves in rapidly due to the rise in Keplerian disk rate which shrinks the CENBOL in-size. On the transition day of HIMS-SIMS, shock compression ratio ($R$) becomes approximately unity. During this period of the outburst, due to rise in Keplerian disk rate and decrease in sub-Keplerian halo rate, the ARR rapidly reduces to a lower value on the transition day. During the rising SIMS, ARRs are observed at a lower value and generally type 'B' or 'A' QPOs are observed sporadically on and off. The origin of these QPOs is assumed to be due to non-satisfaction of Rankine-Hugoniot condition to form a stable shock location [15, 45] or due to weak resonance phenomenon (either a weakly resonating CENBOL for type 'B' or a shockless centrifugal barrier for type 'A'). A strong jet may be found during both intermediate phases of the outburst which may be due to the cooling down of the CENBOL (according to TCAF solution, which acts as base of the jet) with a sudden rise in the contribution of the Keplerian matter. The cooling reduces matter sound speed, which makes the upper part of the jet supersonic quite abruptly. In the SS, the ARR is reduced further with a clear dominance of the Keplerian flow.

In the declining SIMS, the contribution of the Keplerian component starts to decrease and sporadic appearances of QPOs are seen again. The ARR varies in a similar way as of SIMS (rising). On the declining SIMS-HIMS transition day, the maximum value of the monotonically evolving, i.e., decreasing QPO frequency could be seen. In the process, during the declining HIMS, the ARR rises rapidly and reaches its local maximum of the declining phase on the HIMS-HS transition day. The QPO frequencies are observed to decrease continuously in a rapid manner with the outward movement of the shock and rise in the compression ratio. In the declining HS, both ARR and QPO frequency decrease with time due to rapid outward movement of shock. At the same time, a decrease in both the flow components and jet or outflow rates (if present) may be observed.

The evolution of 'hot Compton cloud', i.e., CENBOL, two component (Keplerian and sub-Keplerian) accretion rates during four different (HS, HIMS, SIMS and SS) spectral states in an outburst of a transient BHC, are pictured in Fig. 2. Similarly in Fig. 3, evolution of the TCAF model fitted/derived parameters and observed QPOs during 2010 outburst of Galactic transient BHC H 1743-322 are shown.

## *3.2 ARRID: A Correlation Between Spectral and Temporal Properties*

From a self-consistent understanding of the accretion flow, such as with the TCAF solution, it is clear that the spectral and temporal properties must be correlated. During an outburst of a transient BHC, one can observe the general correlation, though, due to viscous effects as obtained from simulations, the curves in rising and declining phases are different and a hysteresis loop is seen. One can plot

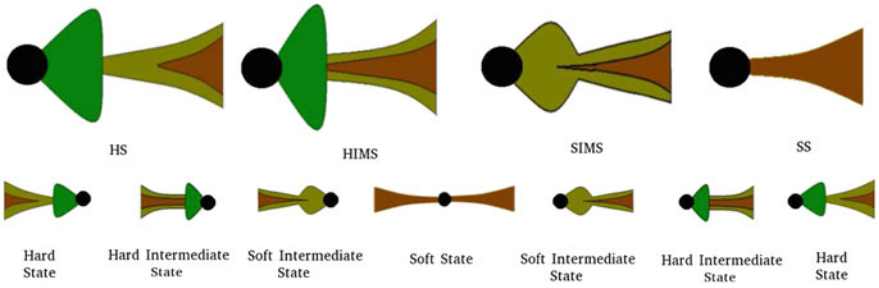



**Fig. 2** Cartoon diagrams showing the evolution of the CENBOL and the Keplerian disc in a Two Component Advective Flow (TCAF) solution. When the sub-Keplerian halo accretion rate is high, the shock front remains far away from the BHC. As the Keplerian component is formed and moves inward during the rising phase of the outburst, the shock starts to move inward. As the disc accretion rate gets higher, the spectrum becomes softer. The peak flux is observed in the soft state of the outburst when effectively the Keplerian component remains. When the viscosity goes down and disc starts to evaporate into halo component, the shock front starts moving outward. This goes on till the object finally comes back to its initial hard state. Adapted from [11].

total photon counts, i.e., intensity from the light curves with the hardness ratios (HRs; ratio between high to low energy band photon counts), namely, hardness-intensity diagram (HID) or 'q'-diagram (see, [20] and references therein), where different branches are supposed to be correlated with different spectral states and other features (e.g., types of QPOs, jets, etc.). But main problem for this type of diagram is the selection of energy ranges for HRs, where high energy photons of the pre-selected fixed energy band are supposed to be non-thermal and other low energy part from thermal component. In TCAF model, where one can directly obtain rates of Keplerian and sub-Keplerian components and plot accretion rate ratio intensity diagram (ARRID), which is more physical. In Jana et al. [31], clearly it has been shown that in ARRID, transitions between different spectral states and their properties are more prominent than HID (for e.g., see point 'D' of Fig. 4 of Jana et al. [31], when transition between declining HIMS-HS occurs). ARRID clearly shows a hysteresis effect and its different branches are associated with the different spectral states, though model independent HID does not contain these precise information.

### *3.3 Prediction of Frequency of the Dominating Type 'C' QPOs: Yet Another Correlation to Spectral and Temporal Properties*

In Debnath et al. [23], for the first time in literature, direct estimation and prediction of a temporal feature, such as frequency of the dominating type 'C' QPOs were done from spectra analysis with the TCAF model. This was possible because the same

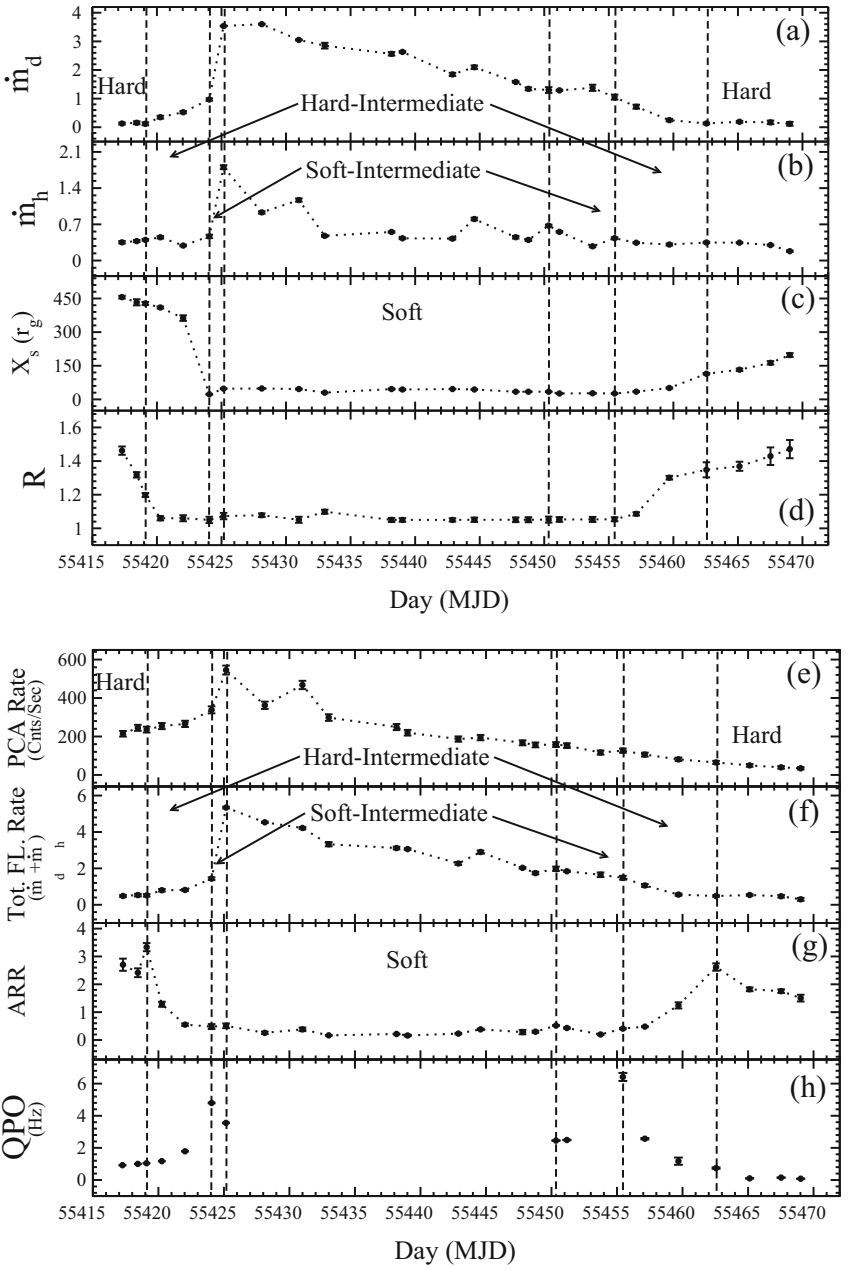



**Fig. 3** In left panel, variations of TCAF model fitted parameters : (**a**) Keplerian disk rate $\dot{m}_d$ (in $\dot{M}_{Edd}$), (**b**) sub-Keplerian halo rate $\dot{m}_h$ (in $\dot{M}_{Edd}$), (**c**) shock location $X_s$ (in Schwarzschild radius $r_s$), and (**d**) compression ratio $R$ with time (in day) for 2010 outburst of H 1732-322 are shown. In right panel, variation of (**e**) 2–25 keV PCA (PCU2) rate (in counts/sec), (**f**) total accretion rate (in $\dot{M}_{Edd}$), (**g**) ARR ($\dot{m}_h/\dot{m}_d$), and (**h**) observed QPO frequency (in Hz) are shown. Adapted from [39]

shock which defines the boundary of the CENBOL, i.e., the size of the Compton cloud in TCAF solution, also causes low frequency QPOs as it oscillates. The frequency of oscillation is inversely proportional to the infall time ($t_{infall}$) in post-shock region when resonance condition between cooling and infall time scales is satisfied [15, 38]. The frequency ($\nu_{QPO}$) of the observed QPOs is determined by the relation,

$$\nu_{QPO} \sim t_{infall}^{-1} = \frac{c^3}{2GM_{BH}} \frac{1}{[RX_s(X_s-1)^{1/2}]} = \frac{C}{[R\ X_s(X_s-1)^{1/2}]}, \tag{3}$$

where, $C$ is a constant = $M_{BH} \times 10^{-5}$.

Debnath and his collaborators [4, 16, 23] have successfully calculated and verified dominating type 'C' QPOs for GX 339-4, GRO J1655-40, H 1743-322, MAXI J1543-564 from TCAF model fitted shock parameters (location $X_s$ and compression ratio $R$).

### *3.4 Mass Estimation of Unknown Black Hole Candidates*

In the present TCAF model *fits* file, mass of the BH is an important input parameter. If it is well known for a BHC, then while fitting energy spectra of a BHC, one may freeze it at that known value or one could estimate it from spectral fits by keeping it as a variable. Each spectral fit with the TCAF model *fits* file, provide us one best fitted mass value of the BH. It may vary in a narrow range from one spectrum to other (observed in different time frames) of the same BHC, since it is a measured quantity. So it should contain errors due to various factors. For example, instrumental errors in different observations should not be same on each day. Also, $M_{BH} \sim T^4$, and in TCAF solution, the spectral fits are highly sensitive to the temperature $T$, a small error in determination of T gives rise to a significant error in $M_{BH}$. Apart from all these error contributing factors, by taking average of the fitted mass values from different observations, one may get an estimation of the probable value of the mass of a BH and also its range, which is basically the lower and the upper limits of the observed mass values from different observations.

Recently, Debnath and his collaborators have successfully estimated masses of a few BHCs, such as MAXI J1659-152, MAXI J1836-194, MAXI J1543-564, H 1742-322, Swift J1753.5-0127, XTE J1118+480, Cygnus X-1 from spectral analysis with the TCAF model [16, 17, 26, 31, 36, 37] from spectral analysis with the TCAF solution. They also verified their estimated mass values with that of the other, measured with conventional or dynamical methods. They sometimes found that their estimated mass values are more accurate than others, at-least in terms of estimated ranges. Mass of the Galactic BHC MAXI J1659-152 was estimated in the range of 4.7–7.8 $M_\odot$ or $6^{+1.8}_{-1.3}$ $M_\odot$ [36]. Then this was verified from that obtained (in between 5.1 and 7.4 $M_\odot$) from the evolution of the QPO frequencies fitted with propagating oscillatory shock (POS) model ([13, 14, 21, 22]

and references therein). After that, Debnath and his collaborators have extended this mass estimation method to other well known BHCs: MAXI J836-194 (7.5–11 $M_{\odot}$, or $9.54^{+1.47}_{-2.03}$ $M_{\odot}$; [31]), MAXI J1543-564 (12.6–14.0 $M_{\odot}$, or $13^{+1.0}_{-0.4}$ $M_{\odot}$; [16]), H 1743-322 (9.25–12.86$M_{\odot}$, or $11.21^{+1.65}_{-1.96}M_{\odot}$; [37]), Swift J1753.5-0127 (4.75$M_{\odot}$ to 5.90$M_{\odot}$, or $5.35^{+0.55}_{-0.60}M_{\odot}$; [26]), XTE J1118+480 (6.25–7.49 $M_{\odot}$, or $6.99^{+0.50}_{-0.74}$ $M_{\odot}$; [17]), Cygnus X-1 ($14.57 \pm 0.68M_{\odot}$; [3]).

### *3.5 Estimation of Jet X-Ray Fluxes and Study of the Nature of Jets*

Generally, normalization is a multiplicative factor that converts the observed spectrum to match it with the theoretical model spectrum coming from the source. Disk brightness varies with observation times. Hence, while fitting spectra with a phenomenological or theoretical model other than TCAF, it varies with time (day), since these models are concerned only about the shape of the spectrum. But, TCAF solution takes care of both shape and intensity/flux changes. In TCAF model, model fitted flow parameters such as disk rate, halo rate, shock location, and compression ratio change in such a way from one to another observations, the effect of the changes of brightness as well as spectral shape automatically get included. This is because unlike other models, according to TCAF, the model normalization $N$ should be constant for a particular BHC observed by a given instrument.

According to TCAF, $N$ is a factor which only depends on the intrinsic source parameters, such as mass of BH, distance and inclination angle of the system. Thus it must remain constant throughout the outburst for a BHC. Although, one may see deviation of the constancy of the $N$ values, when disk processes (it indeed changes effective disk area) or dominance of any other physical processes (such as effect of jets or outflows), whose effects have not been included in the present version of the TCAF model *fits* file.

The deviation of the constancy of $N$ values are observed during 2005 outburst of Swift J1753.5-0127 [26] and MAXI J1836-194 [31]. While compared with the variation of the $N$ values with the observed radio fluxes ($F_R$), it has been found that the region of the outbursts, where higher $N$ values are required to fit spectra, radio fluxes were also high. This allowed us to make a guess that requirement of the higher $N$ values may be due to excess contribution of X-rays from jets (since jet also contributes in X-rays), whose effect has not been included in the current version of the TCAF model *fits* file. Jana et al. [32], introduced a new method to separate jet X-ray fluxes from total observed X-rays, where disk also contributes. After comparison with $N$ and $F_R$ values, they make assumption that on the lowest observed $N$ value (if $F_R$ also low), total X-rays ($F_X$) are only contributed by the accretion disk and CENBOL, i.e., from inflowing matter alone. Now, to estimate X-ray flux contribution only from the inflow ($F_{inf}$), they refitted all spectra after freezing $N$ at its lowest observed value. Now, one can easily get contribution of

X-rays coming from jets/outflows ($F_{ouf}$) by taking differences of $F_{inf}$ from $F_X$, i.e.,

$$F_{ouf} = F_X - F_{inf}. \tag{4}$$

With the above mentioned method, Jana et al. [32, 33] estimated jet X-ray fluxes for two Galactic BHCs: Swift J1753.5-0127, and MAXI J1836-194. X-ray jets are found to be higher in intermediate spectral states (here HIMS) compared to HS, which is consistent with our theoretical understanding [8, 9, 19]. It has been found that the jet contributes in X-rays up to a maximum of 32% during 2005 outburst of Swift J1753.5-0127, and 86% during 2011 outburst of MAXI J1836-194.

To find properties of the jets, Jana et al. [32, 33] also make correlation study i.e., with the relation of $F_R \sim F_X^b$, where $b$ is the correlation index in between $F_{ouf}$, $F_X$, and $F_{inf}$ with $F_R$. As reported by others, they also observed steeper correlation indices of $F_X$ vs. $F_R$ for the two BHCs. But while they correlated $F_R$ with $F_{ouf}$, they found correlations in the form of $F_R \sim F_{ouf}^{0.61\pm0.08}$ for MAXI J1836-194 and $F_R \sim F_{ouf}^{0.59\pm0.11}$ for Swift J1753.5-0127. These correlation values (0.61 and 0.59) are well within the limit of standard correlation index range ∼0.6–0.7 [18, 28]. Thus $F_R \sim F_{ouf}^{0.6}$ could be said as universal correlation, but to firmly confirm it more observations are required. If jets are compact then a tight correlation is expected in between $F_R$ and $F_{ouf}$, whereas for discrete or blobby ejections, tight correlation may not be found. Based on these ideas, Jana et al. [32, 33] reported compact jets during HS of the 2005 outburst of Swift J1753.5-0127 and entire period i.e., during both HS and HIMS of the 2011 outburst of MAXI J1836-194, while during the HIMS of the 2005 outburst of Swift J1753.5-0127 they reported jets as partially blobby in nature.

## 4 Concluding Remarks

The transonic black hole accretion flow model, two-component advective flow (TCAF) model was introduced by Chakrabarti and his collaborators in mid-90s [7, 12]. Almost after around two decades (in 2014), it has been successfully implemented into HEASARC's spectral analysis software package XSPEC as an additive table model, after generation of a large size *fits* file using $\sim 10^6$ theoretical model spectra, which are made by varying five model input parameters: mass of the BH $M_{BH}$ in $M_\odot$, Keplerian disk rate $\dot{m}_d$ in $\dot{M}_{Edd}$, sub-Keplerian halo rate $\dot{m}_h$ in $\dot{M}_{Edd}$, shock location $X_s$ in $r_s$, shock compression ratio R. Now, by fitting spectral data with the current version of the TCAF model *fits* file, one directly gets information about the accretion flow parameters, which not only control spectral shape but also take care of the intensity/flux variations. This is the reason that unlike other models, according to TCAF, the model normalization $N$ should be constant for a particular BHC observed by a given satellite instrument. This is because the TCAF

model normalization only depends on the intrinsic source parameters, such as mass of BH, distance and inclination angle. Since TCAF model is a global solution of radiative transfer equations for accretion flows around black holes, so it is quite expected that spectral fits with the model should not only explain evolution of spectral properties but also evolution of timing properties of black hole sources. For details of how TCAF was successfully used, readers may consult the papers of Debnath and collaborators mentioned above. To make this model more accurate, it is necessary to include more physical processes such as effect of jets, bulk motion Comptonization, spin, etc. Iron and other prominent line profiles may come up from spectral fits, if chemical abundances of the inflowing matter are considered.

**Acknowledgements** I want to express my heartiest gratitude to Prof. Sandip K. Chakrabarti for allowing me to work under his supervision during Ph.D. (2005–2010) and even after Ph.D. I am thankful to Prof. A.R. Rao, Dr. Anuj Nandi, my students and other colleagues for their constant support to me. I also want to thank Indian Center for Space Physics, for allowing to me work there for more than 13 years, first as a Ph.D. student and then as a faculty member. I am also thankful to NASA/GSFC scientist, Prof. Keith A. Arnaud for his kind help to write FORTRAN programs for the generation of model *fits* file by using theoretical (TCAF) model spectra. I should not forget to acknowledge national funding agencies CSIR (NET JRF and SRF fellowships), DST (projects: SR/FTP/PS-188/2012, EMR/2016/003918 and GITA/DST/TWN/P-76/2017), and ISRO (project: ISRO/RES/2/388/2014–15) for their constant financial support to me and my students for carrying forward our research works. Finally I would like to thank my loving parents, wife and son for their moral support to me.

## References

1. Arnaud, K.A., In: Jacoby, G.H., Barnes, J. (eds.) Astronomical Data Analysis Software and Systems V. ASP Conference Series, vol. 101, p. 17 (1996)
2. Bahcall, N.A., Bahcall, J.N., Schmidt, M.: ApJ **183**, 777 (1973)
3. Banerjee, I., Bhattacherjee, A., Banerjee, A., Debnath, D., Chakrabarti, S.K.: Ap&SS (2018, submitted)
4. Bhattacharjee, A., Banerjee, I., Banerjee, A., et al.: MNRAS **466**, 1372 (2017)
5. Casella, P., Belloni, T., Stella, L.: ApJ **629**, 403 (2005)
6. Chakrabarti, S.K.: ApJ **347**, 365 (1989)
7. Chakrabarti, S.K.: ApJ **484**, 313 (1997) (C97)
8. Chakrabarti, S.K.: A&A **351**, 185 (1999)
9. Chakrabarti, S.K.: Ind. J. Phys. **73B**(6), 931 (1999)
10. Chakrabarti, S.K.: In: Das, S. et al. (eds.) ASI Conference Series, vol. 8, p. 1 (2013)
11. Chakrabarti, S.K.: In: Ruffini, R., Jantzen, R., Bianchi, M. (eds.) MG14 Conference Proceedings, p. 369. World Scientific Press, Singapore (2017)
12. Chakrabarti, S.K., Titarchuk, L.G.: ApJ **455**, 623 (1995) (CT95)
13. Chakrabarti, S.K., et al.: IJP **78**, 841 (2005). ArXiv:astro-ph/0508024
14. Chakrabarti, S.K., Debnath, D., Nandi, A., Pal, P.S.: A&A **498**, L41 (2008)
15. Chakrabarti, S.K., Mondal, S., Debnath, D.: MNRAS **452**, 3451 (2015)
16. Chatterjee, D., Debnath, D., Chakrabarti, S.K., et al.: ApJ **827**, 88 (2016)
17. Chatterjee, D., Debnath, D., Jana, A., Chakrabarti S.K.: ApJ (2018, submitted). arXiv:1803.09438
18. Corbel, S., Nowak, M.A., Fender, R.P., et al.: A&A **400**, 1007 (2003)
19. Das, T.K., Chakrabarti, S.K.: CQGra **16**, 3879 (1999)

20. Debnath, D., Chakrabarti, S.K., Nandi, A., Mandal, S.: BASI **36**, 151 (2008)
21. Debnath, D., Chakrabarti, S.K., Nandi, A.: A&A **520**, 98 (2010)
22. Debnath, D., Chakrabarti, S.K., Nandi, A.: AdSpR **52**, 2143 (2013)
23. Debnath, D., Chakrabarti, S.K., Mondal, S.: MNRAS **440**, L121 (2014)
24. Debnath, D., Mondal, S., Chakrabarti, S.K.: MNRAS **447**, 1984 (2015)
25. Debnath, D., Molla, A.A., Chakrabarti, S.K., et al.: ApJ **803**, 59 (2015)
26. Debnath D., Jana A., Chakrabarti S.K., et al.: ApJ **850**, 92 (2017)
27. Dutta, B.G., Chakrabarti, S.K.: MNRAS **404**, 2136 (2010)
28. Gallo, E., Fender, R.P., Pooley, G.G.: MNRAS **344**, 60 (2003)
29. Giacconi, R., et al.: ApJ **148**, 119 (1967)
30. Giri, K., Chakrabarti, S.K.: MNRAS **430**, 2836 (2013)
31. Jana, A., Debnath, D., Chakrabarti, S.K., et al.: ApJ **819**, 107 (2016)
32. Jana, A., Chakrabarti, S.K., Debnath, D.: ApJ **850**, 91 (2017)
33. Jana, A., Debnath, D., Chakrabarti, S.K., et al.: ApJ (2018, submitted)
34. Mandal, S., Chakrabarti, S.K.: ApJ **710**, L147 (2010)
35. Merkert, T.H., et al.: ApJ **184**, 67 (1978)
36. Molla, A.A., Debnath, D., Chakrabarti, S.K.: MNRAS **460**, 3163 (2016)
37. Molla, A.A., Chakrabarti, S.K., Debnath, D., et al.: ApJ **834**, 88 (2017)
38. Molteni, D., Sponholz, H., Chakrabarti, S.K.: ApJ **457**, 805 (1996)
39. Mondal, S., Debnath, D., Chakrabarti, S.K.: ApJ **786**, 4 (2014)
40. Mondal, S., Chakrabarti, S.K., Debnath, D.: Ap&SS **353**, 223 (2014)
41. Mondal, S., Chakrabarti, S.K., Debnath, D.: ApJ **798**, 57 (2015)
42. Mondal, S., Chakrabarti, S.K., Debnath, D.: Ap&SS **361**, 309 (2016)
43. Novikov, I., Thorne, K.S.: In: DeWitt, C., DeWitt, B.S. (eds.) Black Holes, vol. 343. Gordon & Breach, New York (1973)
44. Paczyński, B., Witta, P.J.: A&A **88**, 23 (1980)
45. Ryu, D., Chakrabarti, S.K., Molteni, D.: ApJ **474**, 378 (1997)
46. Schmidt, M.: The Observatory **91**, 985 (1971)
47. Shakura, N.I., Sunyaev, R.A.: A&A **24**, 337 (1973) (SS73)
48. Shimura, T., Takahara, F.: ApJ **445**, 780 (1995)
49. Sunyaev, R.A., Titarchuk, L.G.: ApJ **86**, 121 (1980)

# Do Spectral and Timing Properties Carry Information About Flow Geometry?




**Partha Sarathi Pal**

**Abstract** X-ray binaries are enigmatic sources for their interesting variability properties. The variabilities are believed to be due to change in Two Component Accretion Flows. The accretion flow evolution also results in the change in geometry of the accretion discs. The results of LMXBs (e.g. GRS 1915+105, IGR J17091-3624, GRO J1650-44, GX 339-4 etc.) are analysed in dynamically determined energy bands instead of fixed energy bands as used in traditional hardness ratios. This approach revealed the geometry of accretion flow variation near the compact object through a mass independent general picture.

## 1 Introduction

Stellar cycle is a process in which a star evolves through a series of radical changes during its lifetime. Depending on the stellar mass, this lifetime ranges from a few million years (for the most massive stars) to trillion years (for the least massive). Rapid advancement in Astronomy and Astrophysics over the past several decades has been made possible because of advancements in our understanding of fundamental physics and improvement in the observational equipments like telescopes (both ground based and space-borne), remote sensing systems, computers etc. With the advent of modern technology and the space-borne telescopes, satellites are capable of seeing the objects in $\gamma$-rays, X-rays, Ultraviolet (UV) and Infrared (IR) radiations and thus the focus has been intensified to understand the physical processes which are going on around or inside various objects. Sophisticated ground-based telescopes are also used as an effective tool for receiving the optical and radio signals which are coming out from the same source.

As X-ray observations of astronomical objects cannot be carried out from the ground based facilities due to photoelectric absorption of X-rays by the atoms

P. S. Pal (✉)
School of Physics & Astronomy, Sun Yat-sen University, Guangzhou, China
e-mail: parthasp@mail.sysu.edu.cn

© Springer International Publishing AG, part of Springer Nature 2018

B. Mukhopadhyay, S. Sasmal (eds.), *Exploring the Universe: From Near Space to Extra-Galactic*, Astrophysics and Space Science Proceedings 53,
https://doi.org/10.1007/978-3-319-94607-8_19

and molecules of the Earth's atmosphere, space based X-ray missions are the only methods for these observations. As the X-ray sky is transparent to the observers (telescopes) at very high altitudes, the observation should be conducted above the Earth's atmosphere. The first on-board experiment with the sounding rocket V2 which enabled significant research, was carried out after the Second World War in 1949. This experiment was able to reveal that the Sun is a powerful source of X-ray radiations [12]. In 1962, Giacconi and his team first discovered the X-ray source outside the solar system. This source subsequently became known as Sco X-1. Cyg X-1, the first black hole candidate was also discovered in these early attempts in 1962 [13]. The first Earth-orbiting satellite which was completely devoted to the study of cosmic X-ray sources was the UHURU satellite, launched in 1970 [14]. The major three discoveries by the UHURU satellite bare the underlying nature of many galactic and extra-galactic X-ray sources. The discovery of two eclipsing X-ray pulsars with Doppler-shifting periods, Her X-1 and Cen X-1, demonstrated a type of binary X-ray sources consisting of a normal star and a spinning magnetized Neutron Star. However, the most successful and productive era of X-ray astronomy began with the launch of Rossi X-ray Timing Explorer (RXTE) in December 30, 1995 which was decommissioned in January 5, 2012. The study of time variability phenomenon got a major boost from RXTE mission due to its unique time resolution (1 μs) capability. Discovery of kHz quasi-periodic oscillations (QPOs) from low mass X-ray binaries, high frequency quasi-periodic oscillations (HFQPO) from Galactic black holes and the spectral study in wide energy range (2–200 keV) of many X-ray sources (e.g., black holes, Neutron Stars, X-ray pulsars, extra-galactic objects etc.) have changed our understandings of what goes on in the most active regions of the Universe. The superior spectral resolution and sensitivity of the XMM-Newton Observatory of the European Space Agency (ESA) and spectacular X-ray imaging capability of Chandra X-ray Observatory, both of which were launched at the end of the last millennium, have already contributed to the advancement and understandings of high energy astrophysical processes in X-ray sources. The best available evidence for the existence of BHs is dynamical, and the evidences for the twenty systems are generally very strong, with cautions for only two cases: LMC X-1 and XTE J1859+226 [21]. Their variability is obvious: there are binary systems containing hot and cool supergiants (Cyg X-1 and GRS 1915+105) and many compact systems consisting of K-dwarf secondaries. Considering all 20 black hole candidates (BHCs), only 3 are persistently bright X-ray sources (Cyg X-1, LMC X-1 and LMC X-3). The 17 transient sources include 2 that are unusual. GRS 1915+105 is persistently bright since its first known outburst in August, 1992. GX 339-4 undergoes frequent outbursts followed by very quiet states, but it has never been reached quiescent state [18]. There are a few compact objects discovered which used to lack an optical counterpart, and very few of them have known orbital periods. They are considered as BHCs because they closely resemble X-ray spectral and temporal behavior of other black holes candidates in binaries [21, 32]. The observational evidences from LMXBs were attempted to explain with color-color diagrams obtained with fixed energy bands similarly obtained for Neutron Star analysis [16, 17, 30]. The Neutron Star analysis with

color-color diagrams obtained from fixed energy bands was successful because the Neutron Stars belong to smaller mass range but the LMXBs fall in the mass range 3–20$M_{\odot}$ [21]. To explain the observational evidences from LMXBs, a new parameter, Comptonizing Efficiency (CE), is introduced. CE is a ratio of seed photons and comptonized photons with each energy bands dynamically determined from the diskbb plus powerlaw fitting analysis. This is a ratio of unabsorbed photons to understand the variation before the absorption due to Inter-Stellar medium. This parameter gives the geometry of the inner part of the accretion disc as CE gives us an idea about the amount of the soft photons interacting with the hot-electron cloud [24–27]. Some LMXB candidates (e.g. GRS 1915+105, IGR J17091-3624, GRO J1655-40, 4U 1630-47, XTE J1550-564, H 1743-322, XTE J1118+480, XTE J1859+226 etc.) have been chosen by us to calculate CE dynamically to explain their variability in light of geometry variation of the accretion disc close to the compact objects through a mass independent general picture.

To explain the light curve and spectral properties of black holes, we have adopted a widely accepted picture, based on the Two Component Advective Flow (TCAF) solution [3]. The most interesting and exciting X-ray features of black holes are the complex variabilities of light curves, Quasi-Periodic Oscillations (QPOs), sporadic spectral state variations among Hard, Soft and Intermediate states. According to TCAF, the flow in the disc, in general, is a combination of a Keplerian flow which resides in equatorial plane and a sub-Keplerian flow. The latter moves above and below the Keplerian flow and after passing through a possible shock near the centrifugal barrier, forms the inner 'hot' region or the CENBOL. The oscillation of CENBOL or the shock is thought to be the natural explanation of QPO frequencies. The variation of the Keplerian and the sub-Keplerian components and their interaction with the CENBOL and the outflowing matter are believed to be the explanation for the complex variability of the light curves and the spectral features observed in X-ray satellite data. During my research work, we tried to explain the observational results in light of accretion disc geometry evolution with the help of TCAF model.

## 2 X-Ray Data Analysis and CE Calculation

We have analyzed the archival data of RXTE, SWIFT-XRT Satellite of the LMXBs, i.e., GRS 1915+105, IGR J17091-3624, GRO J1655-40, XTE J1550-564, GX 339-4 etc., which are available in High Energy Astrophysics Science Archive Research Center (HEASARC), NASA.

### *2.1 Timing Analysis*

Temporal studies of the X-ray sources are done using the Event and Binned mode data. The observed X-ray flux variations with time is known as the 'light curve'

and their Fourier transformation in the Power-Frequency plane is known as the Power Density Spectra (PDS). The flux variation (photon counts/sec) is highly quasi-periodic in nature. The ftools task powspec calculates the power spectrum density using the Fast Fourier Transformation (FFT) algorithm.

## 2.2 Spectral Analysis

The reduction and analysis of X-ray spectra involve several steps, namely: data selection, background estimation, response-matrix generation and finally analysis with the XSPEC package. During analysis the spectra are fitted with diskbb model to get evolution of Keplerian photons and power-law model/ COMPST model to get idea about the sub-Keplerian photons along with inter-stellar absorption model.

## 2.3 Dynamic Analysis

We adopted the dynamic representation technique in our analysis procedure which can depict the continuous variation of the compact object during the observation span. This technique is applied for both timing and spectral analysis. Figure 1 shows the dynamic variation of the light curve of $\lambda$ class of GRS 1915+105. For timing analysis PDSs are generated for the 10 s time span with 0.01 s time bin and each PDS precedes by 10 s from its previous PDS. This shows a pictorial representation of variation of QPO during the observation span. The middle panel of Fig. 1 shows the evolution of QPO during the observation span. For spectral analysis, PCA spectra are generated for 16 s time span with 16 s time bin and each PCA spectrum precedes by 16 s from its previous spectrum. The bottom panel of Fig. 1 shows the spectral evolution of the compact object during the observation span. Both of the dynamic representations are similar with the flux variation during that span. This represents the signature of evolution of the compact object in the order of a few seconds.

## 2.4 Comptonizing Efficiency (CE) Calculation

The spectra are fitted within XSPEC environment with the models and constraints mentioned before. The fitting parameters are used to calculate the blackbody photon counts from the Keplerian component and the powerlaw photon counts from the Compton cloud (CENBOL). The number of blackbody photons are obtained from the fitted parameters of the multi-color disc blackbody model [20]. The blackbody flux in cts/s/keV is integrated between 0.1 keV to the maximum energy in keV obtained from fitting up to which the diskbb model fits with the spectra as done in Ref. [31] to calculate $\gamma_{BB}$, the number of the blackbody photons in cts/s.

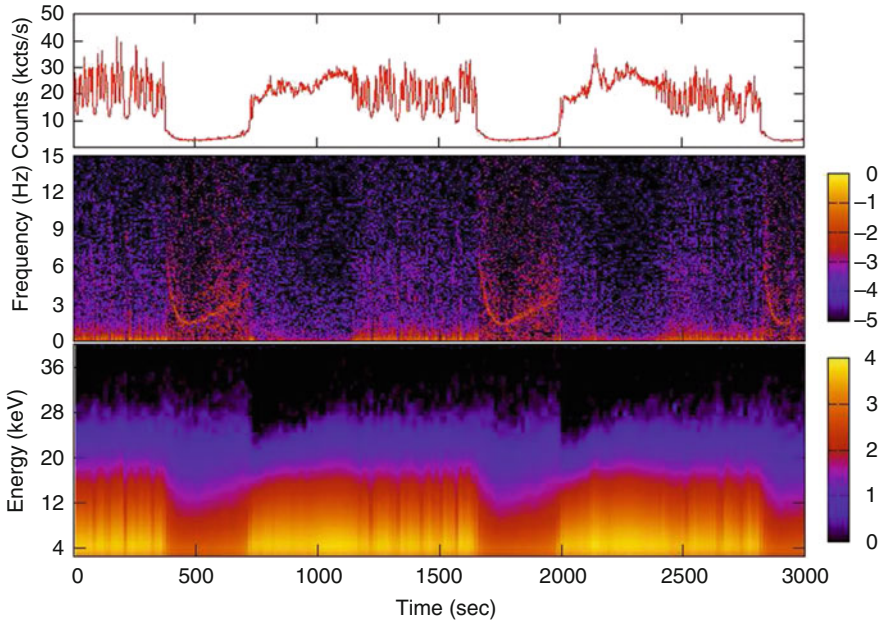



**Fig. 1** A dynamical representation of λ class light curve of black hole candidate GRS 1915+105. The middle panel shows the dynamical QPO variation and bottom panel shows the dynamic spectral variation of the data set

The Comptonized photons $\gamma_{PL}$ that are produced due to inverse-Comptonization of the soft blackbody photons by 'hot' electrons in CENBOL are calculated by using the powerlaw equation. It is reported in Ref. [33]; that the Comptonization spectrum will have a peak around $3 \times t_{in}$. The powerlaw equation is integrated from $3 \times t_{in}$ to 40 keV to calculate total number of Comptonized photons in cts/s. From the number of blackbody and powerlaw photons we compute a simple parameter obtainable directly from observations. This parameter, which we term as Comptonizing Efficiency or CE, is simply the ratio between the number of photons in the powerlaw component and the blackbody component. The variation of the Comptonizing Efficiency (CE) with time is plotted to have an idea of how the CENBOL may be changing its geometry. In the calculation, we exclude the inter-stellar absorption while calculating the number of blackbody and powerlaw photons. This is because we are interested in the photons which were emitted from the disc before suffering any absorption. Thus the variation of CE along with other features (e.g. spectral and QPO frequency variations) will reflect the actual radiative properties of the flow near a black hole. The Comptonizing Efficiency (CE) is a concept: it is basically the hardness ratio where the ranges of the soft and hard photons are determined from the spectral fits. We find that, when averaged over a full cycle (whenever possible) or over a sufficiently long time period, every class is

characterized by more or less a unique CE. When these CE values are lined up, we get a sequence in which the variability class transitions are expected to occur.

## 3 Results and Discussions

In the RXTE era, GRS 1915+105 was monitored thousands of times in the X-ray band and the scientific results reveal a unique nature of this compact object. Continuous X-ray observation of GRS 1915+105 reveals that the X-ray intensity of the source changes peculiarly in a variety of time scales ranging from seconds to days [15, 22]. The light curves of GRS 1915+105 was classified in different classes depending on the nature of color-color diagram, i.e. ratio of photons from two fixed energy bands [1]. Quasi-Periodic Oscillations (QPOs) were observed in a wide range of frequencies. QPOs in this source were associated with different types of X-ray variabilities and their timing properties were correlated with spectral features [23, 29, 31]. The origin of QPO frequencies between 0.5 and 10 Hz was identified to be due to the oscillation of the Comptonized photons, presumably emitted from the post-shock region of the low angular momentum (sub-Keplerian) flow [2, 28]. The dynamic analysis result, shown in Fig. 1, encouraged us to carry out the dynamical analysis of both the temporal and the spectral properties for the compact objects showing variation in the order of seconds. Indian Satellite IXAE had observed class transitions for GRS 1915+105 [4, 5]. The reported transition sequence of classes were $\kappa \rightarrow \rho$, $\chi \rightarrow \rho$, $\chi \rightarrow \theta$, $\rho \rightarrow \alpha$. The average value of CE for these transiting classes are calculated and it was found that the observed transitions follow smooth variation of the $\langle CE \rangle$, which in turn indicates the geometry of the Compton cloud. The $\alpha$ class was explained as a mixture of $\rho$ and $\chi$ class. The $\theta$ class was termed as anomalous class due to presence of magnetic effect during this class [26].

The analysis was further extended for all the classes for GRS 1915+105 with more than one datasets for each class. A sequence of the classes, shown in Fig. 2, depending upon the $\langle CE \rangle$ was proposed. There $\phi, \gamma, \delta, \omega$ classes were mentioned as softer classes as very few Keplerian disk photons (e.g., 0.05%) interacted with the hot electron cloud. This indicated that during the softer classes the Keplerian flow was very high and QPOs were also absent as the CENBOL size was very small. Then all $\chi$ classes were mentioned as harder classes as greater number Keplerian disk photons interacted with the hot electron cloud. This indicated that during the harder classes the sub-Keplerian flow was very high and QPOs were also present as the CENBOL size was bigger. Rest of the classes (e.g. $\alpha, \beta, \lambda, \theta, \kappa, \nu, \rho$) were termed as intermediate classes as we could see spectral variations during these classes within one observation epoch. The dynamic analysis of these classes showed the harder to softer transitions in order of seconds. The evolution of CE during burst-on and burst-off states also indicated the geometry evolution of hot electron cloud in smaller time span [27].

The outburst sources showed the evolution of accretion flow during their active states i.e. outbursts [6–10]. After successful explanation of the geometry evolution

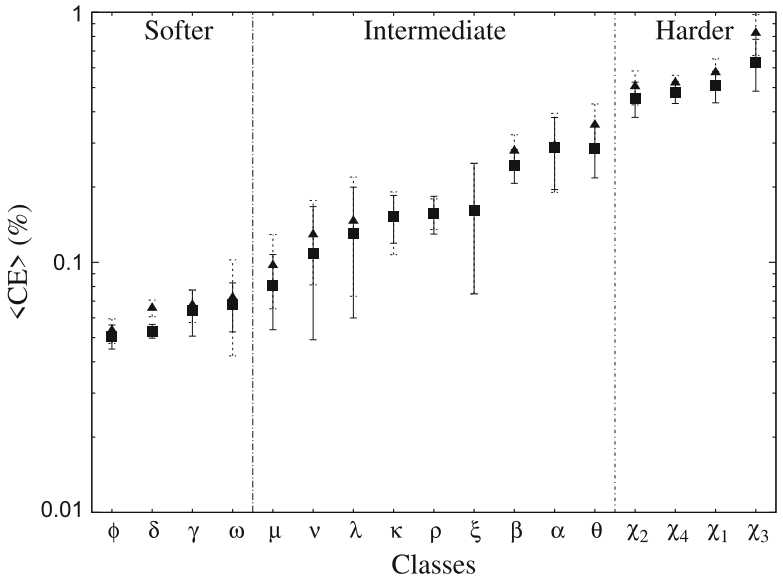



**Fig. 2** Variation of the average Comptonizing Efficiency ($\langle CE \rangle$) for different variability classes of GRS 1915+105 from harder to softer state [27]

of accretion disc for GRS 1915+105 [26, 27], the analysis and $\langle CE \rangle$ calculation for outburst sources (i.e. XTE J1550-564, GX 339-4, GRO J1655-40, H 1743-322) was performed to understand the geometry evolution of the accretion disc [24]. It was observed that all outbursts start and end with large CENBOL but not necessarily with highest optical depth. As the outburst progresses the CENBOL size decreases. The evolution of CE for outburst sources varied from 0.0% to 3%. But in case of GRS 1915+105 the CE ranged between 0.005% and 0.8% along with high luminosity. This implied that GRS 1915+105 was in its intermediate state or usually the peak of the outburst. Then it was postulated that eventually when the viscosity in the system would reduce the declining part of the outburst for GRS 1915+105 could be observed. In Ref. [24] a correlation between the timing and spectral analysis results was reported. It had been seen that CE is higher when the CENBOL size is bigger. During the harder state the location and height of shock location was large. It was observed that the LF-QPOs are due to the oscillation of shock waves and frequency is inversely proportional to the infall time scale in the post-shock region up to inner sonic point [2]. The relation between the shock oscillation frequency along with CE was studied and observed that CE is inversely proportional to the QPO frequency. But the relation was not tightly followed because of the presence of jet. The range of CE was different for various objects in the context of duration of outbursts, QPO frequency range, etc. There was also a considerable variability in CE which may be due to outflows from the CENBOL [24].

In 2011 another outburst source IGR J17091-3624 started showing similar variabilities like GRS 1915+105. The lower luminosity of this source could be due to either smaller mass of central engine or larger distance. During 2011 outburst, similar light curves such as $\mu, \nu, \lambda, \kappa, \rho, \beta, \chi$ classes of GRS 1915+105 were observed with shorter time scales. RXTE and Swift-XRT data were analysed. Both hardness-ratio with fixed energy band as described in Ref. [1] and $\langle CE \rangle$ with dynamically determined energy bands were calculated for these similar light curves. This is to perform a comparative study between IGR J17091-3624 and GRS 1915+105. The color-color diagram of $\rho$ class of GRS 1915+105 light curve and the similar light curve from IGR J17091-3624 appeared as spots in different regions. This is shown in Fig. 3. The light curves of the two objects having a similar variation end-up with different values of hardness ratio due to different black hole

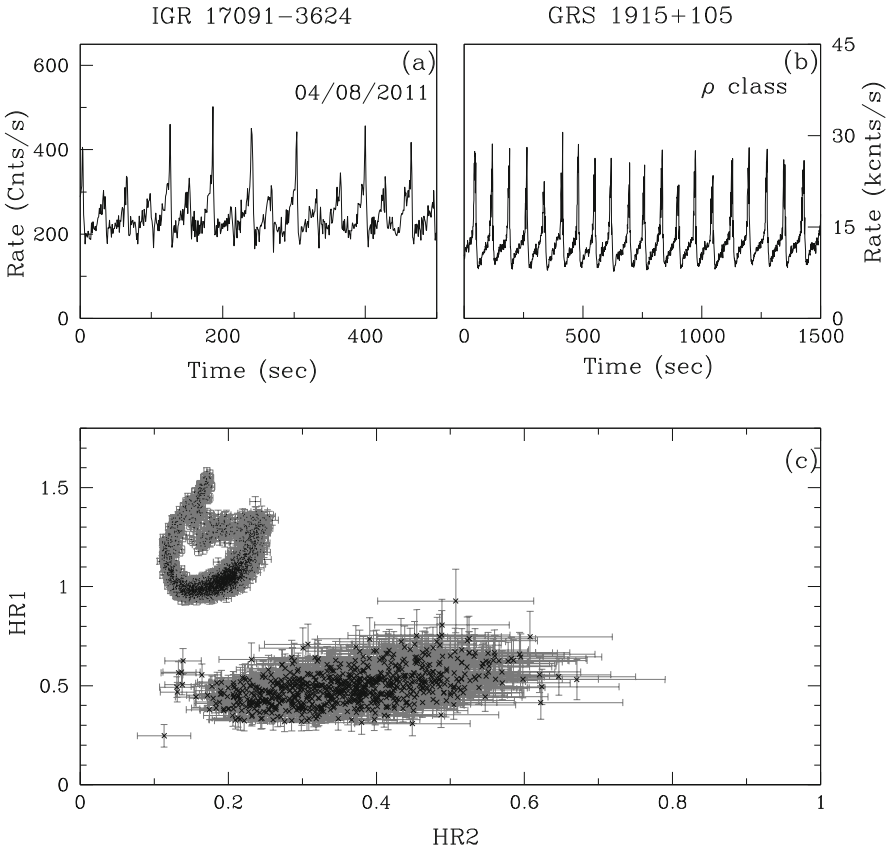



**Fig. 3** Comparative study between hardness ratio from similar light curves of IGR 17091-3624 and GRS 1915+105 [25]. (**a**) 1 s time bin light curve of IGR 17091-3624 on 04/08/2011. (**b**) 1 s time bin light curve of GRS 1915+105 $\rho$ class data. (**c**) Comparison of color-color diagrams along with error bar from (**a**) and (**b**)

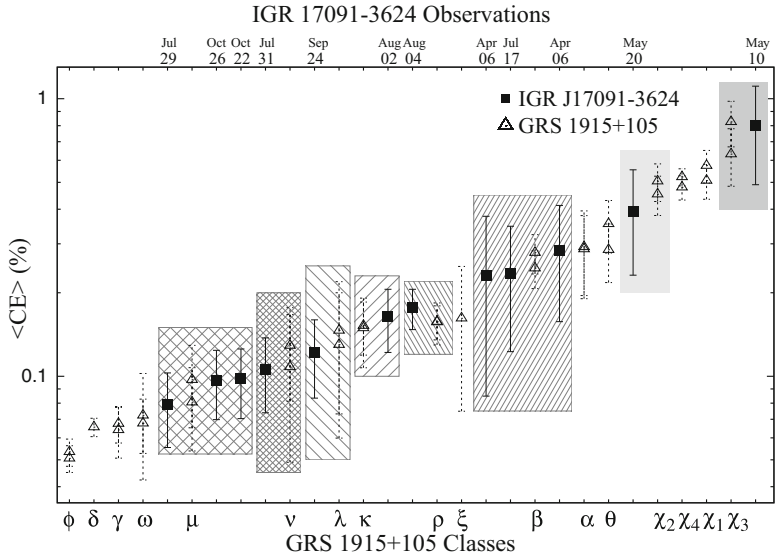



**Fig. 4** Comparative study between $\langle CE \rangle$ of IGR 17091-2634 (filled square) for the 2011 outburst drawn in ascending order and GRS 1915+105 (hollow triangles) [25]. $\langle CE \rangle$ of GRS 1915+105 are adopted from Ref. [27]

masses. However, similar light curves were observed to have $\langle CE \rangle$ values. This is shown in Fig. 4. Thus it was understood that the evolution of the Comptonizing cloud in presence of seed photons of the standard disc, takes place exactly the same way in both the objects. The absence of light curves in IGR 17091-3624, similar to the softer classes of GRS 1915+105 (e.g. $\phi$, $\gamma$, $\delta$), was explained as the smaller accretion rate of the compact object. This comparative work established the Comptonizing Efficiency (CE), as a mass independent parameter which indicate about the geometry evolution of accretion disc for all different compact objects [25].

Inside CENBOL, the amount of inverse comptonization of seed photons depends both upon size and optical depth of the electron cloud. The degree of interaction of soft photons inside CENBOL also gives rise to the time-lag of the harder photons from soft photons [10, 26, 27]. The relation between time-lag variation of comptonized photons w.r.t. seed photons and CE, is studied to understand the inverse comptonization process and matter distribution inside the CENBOL. It is clear that not only the CENBOL but the base of jet also take part in production of the hard photons. It can be seen that time-lag is negative when $CE \leq 0.85\%$ but when $0.85 \leq CE \leq 1.0\%$ then time lag becomes positive. This explains when lag is negative only CENBOL is generating the hard photons. But as the base of jet is formed and started producing the hard photons the time-lag becomes positive as the optical depth of the hot electron cloud is increased due to the presence of CENBOL and base of jet. It was mentioned earlier in Ref. [24, 25] that GRS 1915+105 is probably undergoing a very long outburst and it is now in

its intermediate state. We tried to understand the similarities in GRS 1915+105 and other outburst sources. In this process the QPO frequency variation with CE for GRS 1915+105 during the $\chi$ states is studied. The variation of GRS 1915+105 and the evolution of similar parameters obtained from XTE J1550-564 outburst analysis were done in Ref. [24]. We observed a similar evolution of QPO frequency with CE. QPO frequency roughly indicates the shock location hence the size of the CENBOL while CE represents the amount of seed photons interacting with the CENBOL. We find that the variation of CE with QPO are similar for both persistent sources and outburst sources [11].

## 4 Conclusions

Not long ago, LMXBs, both persistent and outburst sources, were termed as enigmatic sources due to spectral and temporal variabilities [1, 19]. They were fascinating because they have shown variabilities in different time scales. The observational evidences of LMXBs were explained as a continuation of Neutron Star analysis although LMXBs fall in a wide mass range than Neutron Stars [16, 17, 30]. During my research period the parameter Comptonizing Efficiency (CE), calculated with dynamic energy band obtained from analysis, explained evolutions of geometry of accretion flows around different LMXB candidates. It has been established that all the variabilities in observational evidences are geometry variation of accretion disc due to inflow and outflow variations [26, 27]. The mass-independence of the parameter CE was also verified for IGR J17091-3624 and GRS 1915+105 whereas the traditional hardness ratio could not show similar characteristics. The reason behind the limitation of traditional hardness ratio is actually choice of the fixed energy bands for all cases. It is already established that the physical processes behind the same energy band photons from two different mass black holes are different. For instance the 2–10 keV photons from stellar mass black holes are considered as the seed photons emitting from the Keplerian disc whereas for super-massive black holes the same energy band photons represent Comptonized photons. Again the study of propagation of oscillatory shock during outbursts was explained as the movement of inner edge of the Keplerian disc [6, 7]. Comparison of CE evolution along with the shock propagation explained the idea about the geometric shape evolution of the CENBOL during outbursts. It is established that the base of Jet is also responsible for the inverse-comptonization of the soft photons along with CENBOL. For this reason during hard states CE represents the photons interacting with the CENBOL and base of jet. This is a limitation of the parameter CE that it cannot distinguish between the hard photons emitting from the CENBOL and base of Jet [24]. Their contributions could be separated later by Jana and collaborators (this volume). It is observed that the hard photons show time-lag from soft photons and the amount of time-lag of hard photons is related with the propagatory oscillatory shock [10]. The simultaneous studies of time-lag with CE will definitely overcome the present limitation of the parameter

in future publications [11]. Throughout my research period a unification is done for both persistent and outburst sources variabilities as functions of geometry of inner region of the accretion disc irrespective of their masses [24, 25]. Further studies are required to understand the accretion flow mechanism in varying mass ranges of compact objects (e.g. active galaxies and Neutron Stars) to get an overall mass independent general picture of matter accretion around compact objects.

**Acknowledgements** P. S. Pal acknowledges the Post-Doctoral Fellowship at Sun Yat-sen University, China.

## References

1. Belloni, T., Klein-Wolt, M., Méndez, M., van der Klis, M., van Paradijs, J.: A model-independent analysis of the variability of GRS 1915+105. Astron. Astrophys. **355**, 271–290 (2000)
2. Chakrabarti, S.K., Manickam, S.G.: Correlation among quasi-periodic oscillation frequencies and quiescent-state duration in black hole candidate GRS 1915+105. Astrophys. J. Lett. **531**, L41–L44 (2000). https://doi.org/10.1086/312512
3. Chakrabarti, S., Titarchuk, L.G.: Spectral properties of accretion disks around galactic and extragalactic black holes. Astrophys. J. **455**, 623 (1995). https://doi.org/10.1086/176610
4. Chakrabarti, S.K., Nandi, A., Choudhury, A., Chatterjee, U.: Evidence of class transitions in GRS 1915+105 from Indian x-ray astronomy experiment data. Astrophys. J. **607**, 406–409 (2004). https://doi.org/10.1086/383235
5. Chakrabarti, S.K., Nandi, A., Chatterjee, A.K., Choudhury, A.K., Chatterjee, U.: Class transitions and two component accretion flow in GRS 1915+105. Astron. Astrophys. **431**, 825–830 (2005). https://doi.org/10.1051/0004-6361:20041662
6. Chakrabarti, S.K., Debnath, D., Nandi, A., Pal, P.S.: Evolution of the quasi-periodic oscillation frequency in GRO J1655-40 - implications for accretion disk dynamics. Astron. Astrophys. **489**, L41–L44 (2008). https://doi.org/10.1051/0004-6361:200810136
7. Chakrabarti, S.K., Dutta, B.G., Pal, P.S.: Accretion flow behaviour during the evolution of the quasi-periodic oscillation frequency of XTE J1550-564 in 1998 outburst. Mon. Not. R. Astron. Soc. **394**, 1463–1468 (2009). https://doi.org/10.1111/j.1365-2966.2008.14328.x
8. Debnath, D., Chakrabarti, S.K., Nandi, A.: Properties of the propagating shock wave in the accretion flow around GX 339-4 in the 2010 outburst. Astron. Astrophys. **520**, A98 (2010). https://doi.org/10.1051/0004-6361/201014990
9. Dutta, B.G., Chakrabarti, S.K.: Evidence for two-component flows around the black hole candidate XTEJ1550-564 from spectral features during its 1998–1999 outburst. Mon. Not. R. Astron. Soc. **404**, 2136–2142 (2010). https://doi.org/10.1111/j.1365-2966.2010.16428.x
10. Dutta, B.G., Chakrabarti, S.K.: Temporal variability from the two-component advective flow solution and its observational evidence. Astrophys. J. **828**, 101 (2016). https://doi.org/10.3847/0004-637X/828/2/101
11. Dutta, B.G., Pal, P.S., Chakrabarti, S.K.: Evolution of accretion disc geometry of GRS 1915+105 during its $\chi$ state as revealed by TCAF solution. Mon. Not. R. Astron. Soc. **479**, 2183–2192 (2018)
12. Friedman, H., Lichtman, S.W., Byram, E.T.: Photon counter measurements of solar x-rays and extreme ultraviolet light. Phys. Rev. **83**, 1025–1030 (1951). https://doi.org/10.1103/PhysRev.83.1025
13. Giacconi, R., Gursky, H., Paolini, F.R., Rossi, B.B.: Evidence for x rays from sources outside the solar system. Phys. Rev. Lett. **9**, 439–443 (1962). https://doi.org/10.1103/PhysRevLett.9.439

14. Giacconi, R., Kellogg, E., Gorenstein, P., Gursky, H., Tananbaum, H.: An x-ray scan of the galactic plane from UHURU. Astrophys. J. Lett. **165**, L27 (1971). https://doi.org/10.1086/180711
15. Greiner, J., Morgan, E.H., Remillard, R.A.: Rossi x-ray timing explorer observations of GRS 1915+105. Astrophys. J. Lett. **473**, L107 (1996). https://doi.org/10.1086/310402
16. Hasinger, G.: A classification of fast quasi-periodic X-ray oscillators - Is 6 HZ a fundamental frequency? Astron. Astrophys. **186**, 153–158 (1987)
17. Hasinger, G., van der Klis, M.: Two patterns of correlated X-ray timing and spectral behaviour in low-mass X-ray binaries. Astron. Astrophys. **225**, 79–96 (1989)
18. Hynes, R.I., Steeghs, D., Casares, J., Charles, P.A., O'Brien, K.: Dynamical evidence for a black hole in GX 339-4. Astrophys. J. Lett. **583**, L95–L98 (2003). https://doi.org/10.1086/368108
19. Klein-Wolt, M., Fender, R.P., Pooley, G.G., Belloni, T., Migliari, S., Morgan, E.H., van der Klis, M.: Hard X-ray states and radio emission in GRS 1915+105. Mon. Not. R. Astron. Soc. **331**, 745–764 (2002). https://doi.org/10.1046/j.1365-8711.2002.05223.x
20. Makishima, K., Maejima, Y., Mitsuda, K., Bradt, H.V., Remillard, R.A., Tuohy, I.R., Hoshi, R., Nakagawa, M.: Simultaneous X-ray and optical observations of GX 339-4 in an X-ray high state. Astrophys. J. **308**, 635–643 (1986). https://doi.org/10.1086/164534
21. McClintock, J.E., Remillard, R.A.: Black Hole Binaries, pp. 157–213 (2006). ArXiv:astro-ph/0306213
22. Morgan, E.H., Remillard, R.A., Greiner, J.: RXTE observations of QPOs in the black hole candidate GRS 1915+105. Astrophys. J. **482**, 993–1010 (1997). https://doi.org/10.1086/304191
23. Muno, M.P., Morgan, E.H., Remillard, R.A.: Quasi-periodic oscillations and spectral states in GRS 1915+105. Astrophys. J. **527**, 321–340 (1999). https://doi.org/10.1086/308063
24. Pal, P.S., Chakrabarti, S.K.: A study of the variation of geometry of accretion flows of compact objects through timing and spectral analysis of their outbursts. Mon. Not. R. Astron. Soc. **440**, 672–682 (2014). https://doi.org/10.1093/mnras/stu319
25. Pal, P.S., Chakrabarti, S.K.: Comptonizing efficiencies of IGR 17091-3624 and its similarity to GRS 1915+105. Adv. Space Res. **56**, 1784–1792 (2015). https://doi.org/10.1016/j.asr.2015.07.016
26. Pal, P.S., Chakrabarti, S.K., Nandi, A.: Evidence of variation of the accretion flow geometry in GRS 1915 + 105 from IXAE and RXTE data. Int. J. Mod. Phys. D. **20**, 2281–2289 (2011). https://doi.org/10.1142/S0218271811020329
27. Pal, P.S., Chakrabarti, S.K., Nandi, A.: Comptonization efficiencies of the variability classes of GRS 1915 + 105. Adv. Space Res. **52**, 740–759 (2013). https://doi.org/10.1016/j.asr.2013.04.016
28. Rao, A.R., Naik, S., Vadawale, S.V., Chakrabarti, S.K.: X-ray spectral components in the hard state of GRS 1915+105: origin of the 0.5–10 Hz QPO. Astron. Astrophys. **360**, L25–L29 (2000)
29. Rodriguez, J., Durouchoux, P., Mirabel, I.F., Ueda, Y., Tagger, M., Yamaoka, K.: Energy dependence of a low frequency QPO in GRS 1915+105. Astron. Astrophys. **386**, 271–279 (2002). https://doi.org/10.1051/0004-6361:20020218
30. Schulz, N.S., Hasinger, G., Truemper, J.: Spectral classification of low-mass X-ray binary (LMXB) energy spectra with color-color diagrams. Astron. Astrophys. **225**, 48–68 (1989)
31. Sobczak, G.J., McClintock, J.E., Remillard, R.A., Bailyn, C.D., Orosz, J.A.: RXTE spectral observations of the 1996–1997 outburst of the microquasar GRO J1655-40. Astrophys. J. **520**, 776–787 (1999). https://doi.org/10.1086/307474
32. Tanaka, Y., Lewin, W.H.G.: Black hole binaries. In: X-Ray Binaries, pp. 126–174. Cambridge University Press, Cambridge (1995)
33. Titarchuk, L.: Generalized comptonization models and application to the recent high-energy observations. Astrophys. J. **434**, 570–586 (1994). https://doi.org/10.1086/174760

# Variability Properties of Galactic Black Holes




**Broja Gopal Dutta**

**Abstract** In X-ray binaries, fast variability in X-ray emission on time-scales of milli-seconds to seconds is a common and very complex phenomenon. The variability of astronomical sources is usually expressed as a time series. The study of variability property implies the time series analysis of the light curve obtained from various sources. These study includes the study of Power Density Spectrum (PDS) and time/phase lag spectrum. Studies of energy dependent temporal properties (i.e.,variability properties) in different variability time scale for the nearly edge on (high inclination) and nearly face on (low inclination) compact binary sources could through-light the detail structure of the accretion geometry. Again, the evolutionary picture of variability parameters, such as QPO frequency, time lag and energy dependent lag for transient and persistent sources can be studied with the simplified framework of Two Component Advective Flow (TCAF) solution. However, even with this simplified model and employing Monte-Carlo simulation technique, the simulated spectral behavior can be tested with the observational results. Thus it is possible to answer the cause of hard and soft lag and their transitions in higher inclination sources within the framework of a single TCAF solution. Also the evolution of the low frequency quasi-periodic oscillations (LFQPOs) and associated time lag in transient and persistently variable black hole sources as a function of time can be explained by variation of the Compton cloud size in a Two Component Advective Flow solution (TCAF).

B. G. Dutta (✉)
Department of Physics, Rishi Bankim Chandra College, Naihati, West Bengal, India

Indian Centre for Space Physics, Kolkata, India

© Springer International Publishing AG, part of Springer Nature 2018

B. Mukhopadhyay, S. Sasmal (eds.), *Exploring the Universe: From Near Space to Extra-Galactic*, Astrophysics and Space Science Proceedings 53,
https://doi.org/10.1007/978-3-319-94607-8_20

## 1 Introduction

The outburst features of the Galactic black holes (GBHs) are of great interest because they allow the study of low mass X-ray binaries (LMXBs) under a wide range of accretion rates and conditions. GBHs are a class of astrophysical sources with X-ray emission that is powered by accreting matter from a companion star. The outbursts are the keys to develop a complete understanding of the accretion physics in black hole candidates and provide insights to the accretion disk dynamics. In order to investigate the intriguing aspects of the accretion processes, it is necessary to study the accretion disk structure and the nature of variability in Galactic black hole binaries during their outbursts, both theoretically as well as observationally.

In X-ray binaries, rapid variability in X-ray emission on time-scales of seconds to milliseconds is a common and a very complex phenomenon. It was proposed quite early that the rapid variability observed in XRBs was produced by instabilities in the 'standard' accretion disc [31, 54]. The disc can produce variations over a broad range of time-scales, i.e., on viscous time scale. The degree of variability mainly depends on the energy of the photons. Low Frequency Quasi-periodic oscillations (LFQPOs) with frequencies ranging from a few mHz to ∼30 Hz have been discovered in most observed black hole X-ray binaries (BHBs) [34]. The complex timing behavior certainly challenges models which predict both the X-ray variability and the X-ray spectra [42]. It is suggested that these LFQPOs must be linked to the properties of the accretion disc since their centroid frequencies are correlated with the disc flux [32] while the emitted luminosity itself varies, for example due to changes in mass accretion rate [1, 59]. In [3, 5, 50, 60] it was shown that the Comptonized photons take part in QPOs and thus they are intrinsically related to spectral states.

There are several models in the literature which attempt to explain origins of QPOs. A possible origin of the type-C QPOs for the geometric oscillations could be Lens-Thirring precession of the Comptonizing medium, due to misalignment of the black hole spin and the binary orbit [29, 57, 58]. Heil et al. [27], Motta et al.[41] confirmed that the QPO amplitude depends on the inclination of the binary orbit, strongly suggesting a geometric origin [53]. Ingram and van der Klis [28] found that the iron line equivalent width changes over a QPO cycle in GRS 1915+105, also strongly pointing towards a geometric origin. Ingram and van der Klis [28] studying QPO phase-resolved spectra, found that the iron line equivalent width changes over a QPO cycle in GRS 1915+105, strongly pointing to a geometric origin. Meanwhile [4, 8, 24, 38] suggested that these QPOs could be related to the resonance oscillation of the Compton clouds since their occurrences strongly depend on the accretion rates which in turn change the cooling time scale. This latter solution was demonstrated by complete hydrodynamic simulations and does not require a spinning black hole.

Despite these efforts to explain the LFQPOs and their evolution and origin of the lags, none of those models appears to be able to explain the cross over of lags for a particular source at the fixed QPO frequency, such as, ∼2.3–2.5 Hz in GRS 1915+105 or ∼3.2 Hz in XTE J1550-564 both of which have a similar

(high) inclination angle [45]. Earlier, the Two Component Advective Flow (TCAF) solution was used to explain the QPO behavior ([7, 14, 36, 37, 44, 50], etc.), spectral properties ([2, 9, 11, 16, 39, 49, 55, 56, 62], etc.), CE variation [46, 48] and time-lag properties [19] in BH binary systems during outbursts. In TCAF paradigm which originates from self-consistent transonic flow solution, the equatorial plane has a standard Keplerian disc and the sub-Keplerian (i.e., lower angular momentum) halo surrounds it. CENtrifugal pressure supported BOundary Layer or CENBOL is also formed between inner and outer sonic points which plays the role of the Compton cloud. Only in TCAF, the Compton cloud (i.e., CENBOL) is self-consistently reduced in size as the soft state is approached and QPO frequency is increased, and thus the time lag properties are self-consistently linked to the spectral properties. Other models, such as the disc corona model [26, 63] and the lamp-post models [33, 35] are yet to address all the observed complex aspects within a single framework.

In the POS model [6, 7, 14, 24], the resonance oscillation of the post-shock region, i.e., the Compton cloud, causes the observed low-frequency quasi-periodic oscillations (QPOs). The evolution of QPO frequency is explained by the systematic variation of mean size of the Compton cloud, i.e., the steady radial movement of the shock front. It moves inwards when the CENBOL is cooled down. Opposite is true when it is heated [40]. As the shock moves in with the increase in disc accretion rate, the density and optical depth also generally increases. Thus, analysis of the energy-dependent temporal properties in different variability timescales can diagnose the dynamics and geometry of accretion flows around black holes. This has been shown for the high inclination transient black hole source XTE J1550-564 during its 1998 outburst and the low-inclination black hole transient source GX 339-4 during its 2006–2007 outburst using RXTE/PCA data [19]. However, the dependence of lag on photon energy is more intriguing. GX 339-4 was found to exhibit only the positive lag for all QPO frequencies, while in XTE J1550-564, the lag switches sign and becomes negative at a crossing frequency of $\sim$3.2 Hz. It was explained qualitatively by adding up variations of the lag components at different length scales [19]. The lag is observed in one band with respect to the other band. But in each energy band the photons are coming as the outcome of difference physical processes such as Compton scattering, reflection, focusing by curved space time, even due to down-scattering by jets or shock surfaces, etc. Whether it would be soft or hard lag will depend on the dominating process in that energy bin. In a soft-lag, the soft photons are delayed due to their using a longer path or the delayed hard photons are down scattered to softer region. In a high inclination system it can be the reflected component also. This effect is opposite in a low inclination system. Thus the delay will depend on the inclination angle [10, 19]. The dependence on QPO frequency comes because the frequencies are dependent on CENBOL size which in turn decide which photons can reach observers when inclination is high (obscuration effect). At this length scale ($R_{tr}$) the lag changes its sign. This frequency is not universal as the dominating lag would depend on inclination angles and the mass of the black holes which determine the length scales of the Compton cloud.

## 2 Mathematical Formulation to Quantify the Variability

The Fourier quantities to evaluate the short term variability in the light curves of black hole system can be calculated by using time series analysis technique. The archival data of *RXTE* Satellite of the Galactic black hole sources, e.g., XTE J1550-564, GRO J1655-40, GX 339-4 GRS 1915+105 etc. which are available in *High Energy Astrophysics Science Archive Research Center (HEASARC)*, NASA.

### *Time Series Analysis*

The variability of astronomical sources is usually expressed as a time series, $x_h$, of observed count rate in certain energy band, where $h$ denotes the number of time bin during which the count rate was measured [61]. The cross spectrum is defined as $C(j) = f_1^*(j) \times f_2(j)$, where $f_1$ and $f_2$ are the complex Fourier coefficients for the two energy bands at a frequency $\nu_j$ and here $f_1^*(j)$ is the complex conjugate of $f_1(j)$ [61]. The phase lag between two band signals at Fourier frequency $\nu_j$ is $\phi_j = arg[C(j)]$ and the corresponding time lag is $\phi_j/2\pi\nu_j$. The 'Power' of the signal in a Power Density Spectrum (PDS) is a non-complex quantity obtained by

$$P_j = f_j^* f_j = |f_j|^2. \tag{1}$$

## 3 Evolution of Accretion Flow Geometry in TCAF

It is already stated in [23] that in the TCAF model, the POS solution has been successfully applied to study the evolution of QPO frequencies and to explain the variation of accretion flow geometry during the rising and the declining phases of the outbursts of a few transient BHCs, such as GRO J1655-40 [5, 6], XTE J1550-564 [7], GX 339-4 [14, 44], H 1743-322 [15] and IGR J17091-3624 [30], MAXI J1659-152 [36] and also applied to a persistent source GRS 1915+105 [23]. In the shock oscillation model of QPOs, the oscillation of X-ray intensity is actually due to the oscillation of the post-shock (CENBOL) region [3, 38]. The physical reason for the oscillation of shocks is as follows: Imagine that the shock is receding at a moment. From the frame co-moving with the shock, the upstream flow would appear to be faster, and the post-shock region downstream would therefore be hotter and would cool down faster. This reduction of post-shock pressure causes the shock to return towards the black hole, and the process will continue till it overshoots the equilibrium region and comes much closer. Here, from the shock frame the incoming flow would be slower and the post-shock cooling diminishes and compressional heating pushes the shock outward. Thus these two opposite effects cause the shock to oscillate only if the cooling time scale and

the compressional heating time scale (infall time scale) are similar. Thus what we observe is a resonance. Furthermore, by moving back and forth, the CENBOL expands and shrinks and the number of intercepted photons, and therefore the processed hard photon number is modulated. With a power-law cooling [4, 38] this was demonstrated. With a dynamical cooling such as a strong outflow, (e.g., [52]) is present, which is true when the shock condition is not satisfied, the CENBOL oscillates. In outbursting sources, an enhancement of the accretion rate increases the local density and thus the cooling rate. The resulting drop of the post-shock pressure reduces the shock location and increases the oscillation frequency [40] during the phase leading to a softer state. Once the resonance sets in, it would continue to be locked into resonance till accretion rates change considerably, causing evolution of QPOs as the object goes to softer and harder states respectively. Most interestingly, this condition allows one to obtain QPO frequency from the shock location or the size of the Compton cloud (CENBOL).

Figure 1 shows the evolution of accretion Geometry in different phases (a–e) of the outburst in XTE J1550-564 during the 1998 outbursts [7]. A physical picture of the accretion geometry which emerges out that at the beginning of the rising phase [panel (a)], the flow is dominated by a sub-Keplerian flow with a shock at a largest distance from the source. The shock propagates towards the black hole with a constant velocity and at the same time, the Keplerian disc moves in viscous time scale and the spectrum becomes softer. The QPO frequency also rises [panel (b)] and the shock strength decreases. Subsequently [panel (c)], the shock becomes weaker and stopped while a reverse shock formed and propagated outward to initiate the declining phase. The Keplerian component is strongest in this case. The reverse shock propagated outward at almost constant velocity as QPO frequency also started to decrease [panel (d)]. The supply of Keplerian flow also ceased and the flow broke into two parts, the inner part is moving in while the other part stayed back. The segment moving in is eventually drained in viscous timescale ($\sim$11 days) [panel (e)]. The lowest panel shows the corresponding cartoon diagrams of the Mach number (M) vs. radial distance (r) of the Keplerian (thick curve) and the sub-Keplerian (thin curve) flow [7].

## 4 Observational Evidences

Typical evolutions of the QPOs in transient black-hole sources during outburst has already been established for a long time [5–7, 14, 15, 18, 20]. These evolutions suggest that certain specific physical mechanisms are in place which are responsible for the generation of QPOs for days after days [5–7, 14, 15]. These authors found that the Comptonization region gradually shrinks in the rising phase of an outburst when QPO frequencies go up and the reverse is true in the declining phase.

In general, it is expected that there would be a monotonically decreasing lag with increasing QPO frequency and a monotonically increasing lag with shock location. This is precisely what happens in Galactic black hole sources [19, 21–23]. The net

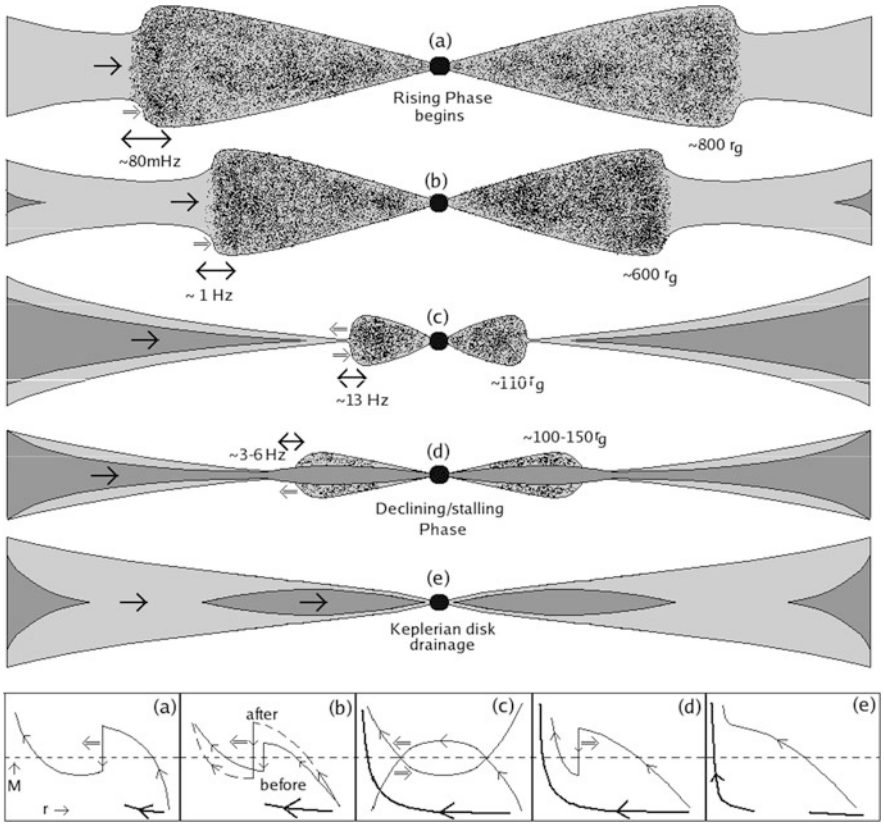



**Fig. 1** A physical picture [7] which emerges out of the spectral and temporal analysis of the 1998 outburst of XTE J1550-564: (**a**) beginning of the rising phase when QPO was first detected, (**b**) middle of the rising phase, where the Keplerian disc also started to move in, (**c**) end of the rising phase and the beginning of the declining phase, (**d**) stalling of the outgoing shock wave due to interaction with the incoming Keplerian disc and finally (**e**) the draining of the part of the Keplerian component which ended the first phase of outburst. The lower most panel gives a cartoon diagram of the Mach numbers of the Keplerian and the sub-Keplerian components

time lag due to Comptonization is the sum over light crossing times of the mean free paths $l_{Comp}$ between two successive Compton scattering, i.e., $t^c_{lag} = \sum l_{Comp}/c \propto X_s/c$. However, when one considers the energy dependence, the picture is more complex. Since energy is expected to rise, after each successive scattering, higher energies are expected to have higher lags. As pointed out by earlier works [12, 13, 51] and also Refs. [19, 22, 23] explained that the energy dependence of the time lag is not straightforward to understand.

In XTE J1550-564 [13, 17] the lag first increases with frequency, peaks at some characteristic frequency, and then decreases and moves toward to negative (soft) lag at frequency ∼3.4 Hz. This pattern of the phase lag associated with the QPO bears

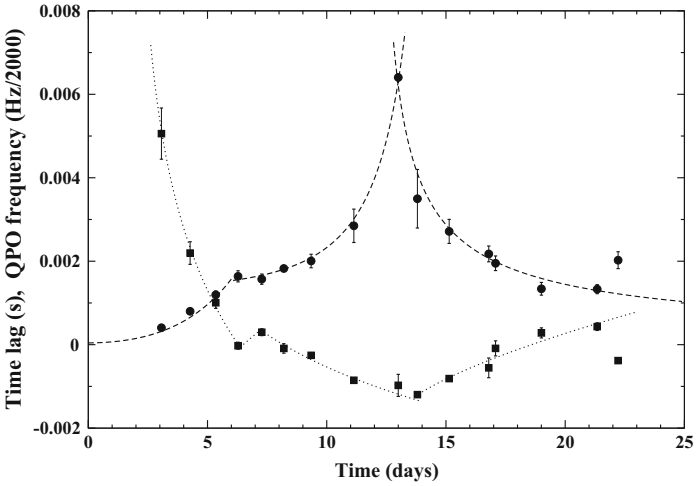



**Fig. 2** Evolution of time lag (filled squares) and QPO frequency (filled circles) are plotted with time (days) during rising (MJD 51065 to MJD 51076) and declining (MJD 51076 to MJD 51084) phases of XTE J1550-564 in the 1998 outburst. Time lag is calculated at QPO frequency ($f_Q$) integrated over the width which is equal to FWHM ($F_w$) of the QPO itself [19]

a remarkable resemblance to that observed in GRS 1915+105 [12, 51], albeit with 'zero-lag' occurring at a different QPO frequencies. This is due to the very nature of the emission process in both the Keplerian and sub-Keplerian components.

Figure 2 [19] shows the systematic variation of the time lag (filled squares), which is QPO frequency-dependent and the QPO frequency (filled circles) as a function of time (days) during the onset (MJD 51076-MJD 51084) and declining (MJD 51076-MJD 51084) phases of the 1998 outburst in XTE J1550-564. Here, the 0th day (i.e., MJD 51065) means the day when the first QPO was detected. In the onset phase, the time lag variation was fitted with a curve where the time lag $\sim t^{-0.423\pm.02}$ and the reduced $\chi^2$ is close to 1.3 ($\chi^2/10$). It is also found that time lag decreases with the increase of both the QPO frequency and time (day) during the onset phase. In the declining phase, a systematic variation of the same time lag was observed. The declining phase starts after observing the highest value of $\nu_{QPO} = 13.1$ Hz on MJD 51076. The fitted curve represents time lag $\sim t^{0.663\pm.03}$ with a reduced $\chi^2$ close to 1.6 ($\chi^2/7$).

Figure 3 shows a systematic variation of the frequency dependent time lag as a function of day during the rising (MJD 51076 to MJD 51084) and the declining (MJD 54133 to MJD 54145) phases of GX 339-4 during the 2007 outburst. Time lag was calculated at the QPO frequency ($f_Q$) in the same way as before [19].

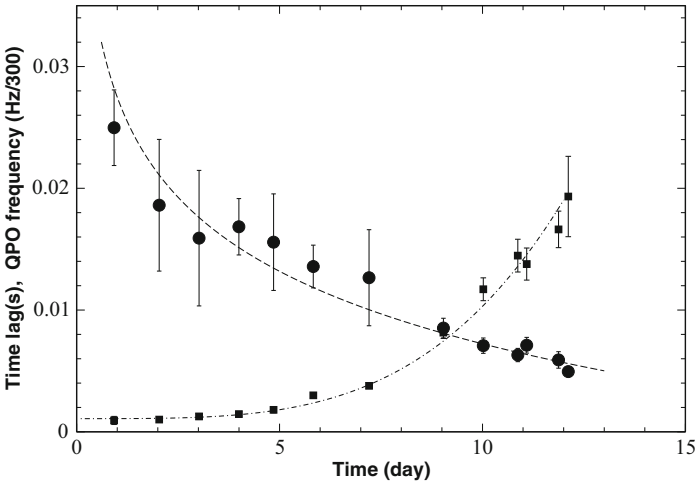



**Fig. 3** Evolution of time lag and QPO frequency are plotted as a function of time in days during the rising (MJD 54133 to MJD 54145) phases of GX 339-4 in the 2007 outburst. Time lag is calculated at the QPO frequency ($f_Q$) by integrating over the range of the FWHM ($F_w$) of the QPO [19]

## 5 Effects of Inclination on Variability Properties

In very recent work, Refs.[27, 43] showed that in higher inclination systems, there are systematically harder X-ray power-law emissions. Properties of low frequency QPOs are also inclination dependent. On the other hand, Ref. [27] found that the amplitude of the broad-band noise (subtracting the low-frequency QPOs) is no longer dependent on inclination, implying its correlation with the source structure of the emitting regions. Using Monte-Carlo simulations, Ref. [25] also finds that for the same disc flow properties, the spectrum changes with inclination angle.

References [19, 23] have found that the time lag is not only a function of the average energy of the emitted photons, it is also a function of the inclination angle of the binary system and explained the time lag behavior within the framework of a single two-component advective flow model. What is clear in both high and low inclination systems is that the lag increases when QPO frequency goes down, i.e., the Comptonizing region whose oscillation causes QPOs goes up. What is not obvious is the cause of change of sign at a specific QPO frequency, i.e., at a specific size. They discussed that the most possible major processes that contribute the lag are (1) repeated Compton scattering, (2) reflection and (3) focusing due to gravitational bending and possible reason of why the sign change occurs only in high inclination systems i.e., hard to soft lag.

The physical processes contributing to lags may be understood from Fig. 4 [19] where it is shown that how the radiations from an accretion disc and Comptonizing cloud (CENBOL) may reach observers located at an angle $\theta < 60°$ and $\theta > 60°$

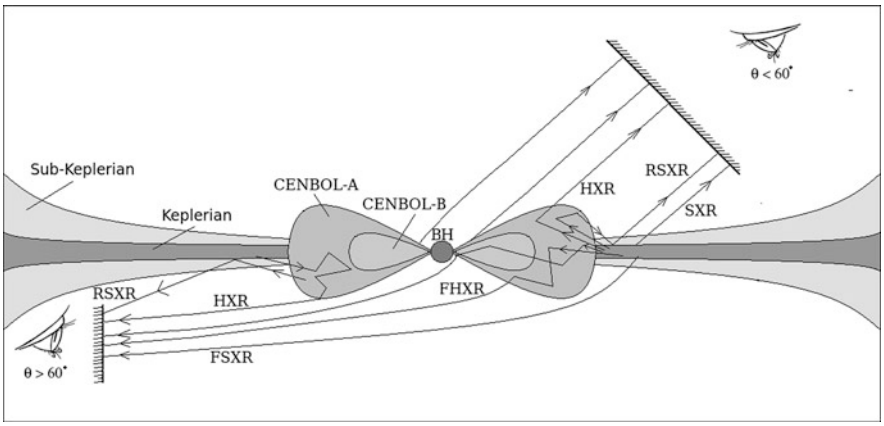



**Fig. 4** Cartoon diagram of two component advective flows where soft photons (SIR) from Keplerian discs are inverse Comptonized by the post-shock region, namely, Centrifugal pressure supported BOundary Layer (CENBOL) and hard X-rays (HER) are produced. Radiations could directly reach the observer, or reach through focusing effects (FSXR, FHXR). Harder radiations from the inner regions of CENBOL (CENBOL-B), would be more focused than the Comptonized photons which had undergone lesser number of scattering from outer CENBOL (CENBOL-A). Reflected component (RSXR) from a Keplerian disc would primarily affect softer X-rays and may delay soft X-ray travel time. Observers with $\theta < 60°$ will see lesser focusing effects [19]

through various paths. As already mentioned, the time of travel is proportional to the number of scattering at the CENBOL and one expects harder X-rays (HXR) to come at later times. However, radiations emitted from inner CENBOL (CENBOL-B) are also focused due to gravitational bending of lights and may be further delayed. Hard photons reflected from the Keplerian disc as softer radiation (RSXR) also takes a longer route, especially for high inclination sources. Thus, while each soft photon may have a range of time lag (high and low) depending on whether it is focused and/or reflected before reaching the observer, hard X-rays are always expected to be delayed. This causes non-monotonicity of the lag with energy when the inclination angle is high [19].

Figure 5 shows energy dependent time lag for QPO centroid frequencies $f_Q = 6.87\,\text{Hz}$, $f_Q = 4.34\,\text{Hz}$, $f_Q = 4.14\,\text{Hz}$, $f_Q = 1.297\,\text{Hz}$, $f_Q = 0.436\,\text{Hz}$ of low inclination source GX 339-4 [19]. It is clearly observed that hard lag to be monotonically increasing with energy of the photons for all the QPO frequencies. This behavior suggests that as the location of shock (i.e., QPO frequencies) changes, the contribution in total time lags which is from different mechanisms also changes. Furthermore, all the lags are positive, unlike the case of XTE J1550-564 which was of high inclination and contributions cancel to change sign at a particular shock location for a given object

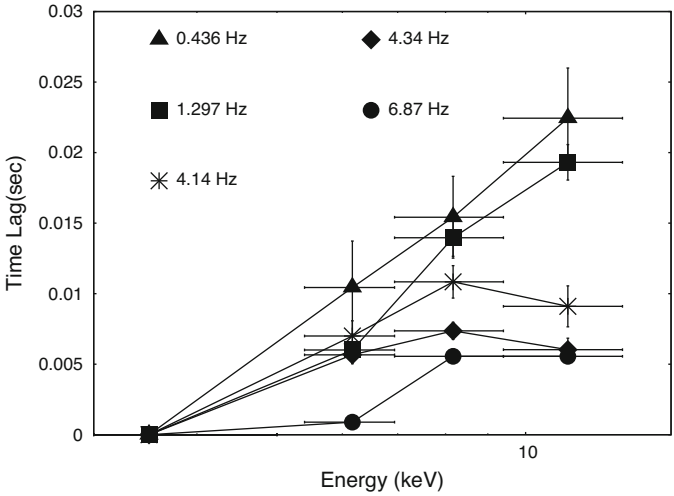



**Fig. 5** Energy dependence of time lag for different QPO centroid frequencies ($f_Q = 6.87$ Hz, $f_Q = 4.34$ Hz, $f_Q = 4.14$ Hz, $f_Q = 1.297$ Hz, $f_Q = 0.436$ Hz). Here we choose 2.0–5.4 keV (0–12, channels) as a reference energy band. The other energy bands are 5.4–6.9 keV (13–16, channels), 6.9–9.4 keV (17–22, channels), 9.4–13.1 keV (23–31, channels). Clearly varies on QPO frequency. We find that the hard lag is directly related to the energy of photons for different QPO frequencies [19]

## 6 Variability Properties in Transient and Persistent Sources

A coherent evolutionary picture of QPO frequency and time lag was observed for the persistent source GRS 1915+105 and the transient source XTE J1550-564. Within POS models, the initial decrease of QPO frequency as a function of time (declining QPO frequency and hardening of spectrum) is consistent with a shock steadily receding for both the sources [7, 19, 23]. Subsequent increase of QPO frequency (rising QPO frequencies and softening of spectrum) can be explained in terms of the shock moving towards the black hole with a constant velocity for both the sources. The fit also requires the shock to be time dependent in both the objects, and to become weaker as it propagates towards the black hole. Hence, the observed variations of QPO frequency with time resemble the variation in size of the CENBOL. We find in both the sources that the time lag increases when the QPO frequency decreases, i.e., when the size of the Comptonizing region (i.e., CENBOL) increases, and that at a specific QPO frequency, i.e., at a specific size of the Comptonizing region, the lag changes from hard to soft (i.e., switches sign). We also find for both the objects that the CE (Comptonizing Efficiency) vs. QPO frequency evolution looks similar [46, 47], independently of the fact that one is a persistent source and the other is a transient source.

With regard to the evolution of LFQPO properties and time lag within the POS solution, the persistent source GRS 1915+105 and the transient source XTE J1550-564 do not show significant differences. Just as in the declining phase of an outburst the spectrum is hardened and QPO frequency is decreased, the first part of a $\chi$ state in GRS 1915+105 also show exactly the same behavior. Similarly, just as in the rising phase of an outburst, the spectrum is softened and QPO frequency is increased, the second part of a $\chi$ state shows the same behavior. The shock location also decreases monotonically in the softening part of the $\chi$ state and exactly opposite behavior is seen in the hardening part of the state. We see that the geometry of the CENBOL evolves in the same way in the two types of sources. More generally, this conclusion might apply to any source belonging to the two different classes, with most of the observed differences being ascribable to different inclination angles. In other words, the apparently persistent class variable source such as GRS 1915+105 behaves as though it is made up of a large number of weak outbursts, nature of which is dictated by viscous processes which, in turn, decide the accretion rates.

## 7 Simulated Lag Spectra and Observational Evidences

X-Ray time lag of black hole candidates contains important information regarding the emission geometry. The real cause of the lag behavior with energy, geometry of the accretion disk and spectral states can be realized with the study photon paths inside a Two Component Advective Flow (TCAF) which appears to be a satisfactory model to explain the spectral and timing properties. Recently, Ref. [10] were employed Monte-Carlo simulation technique to carry out the Comptonization process and relativistic thick disk in Schwarzschild geometry as the CENtrifugal pressure supported BOundary Layer (CENBOL) which is the Compton cloud. They compute the cumulative time taken by a photon during Comptonization, reflection and following the curved geometry on the way to the observer. They found the variation of time lags with accretion rates, CENBOL size and inclination angle of the source. Time lags for different energy channels are plotted for different inclination angles. The general trend of variation of time lag with QPO frequency, inclination and energy is similar to the observational results. Thus, the time dependent aspects of time lag behavior and its origin can be explained satisfactorily with simplified TCAF solution [10].

## 8 Conclusion

A coherent evolutionary picture of variability parameters, such as QPO frequency, time lag and energy dependent lag for transient and persistent sources were observed and explained with the simplified framework of TCAF solution. However, even with this simplified model and employing Monte-Carlo simulation technique, the

simulated spectral behavior is similar to observational results. It is also clearly found that variability property depends on the inclination of the source. The low inclination sources exhibit only positive lag for all QPO frequency, while in higher inclination sources the time lag switches sign and it becomes negative above certain frequency.

References [19, 23] were discussed all possible effects namely, (1) repeated Compton scattering, (2) reflection and (3) focusing due to gravitational bending which control the lag and possible reason of why the sign change occurs only in high inclination systems. Specifically, they showed that in order to get net lag, it is necessary to add up the qualitative variations of lags for the above processes. The high inclination objects could have negative time lags, i.e., soft photons appearing before hard photons due to reflection and focusing effects. This effect was seen in XTE J1550-564 and GRS 1915+105 at frequencies higher than $\sim$3.2 Hz. It is observed that if focusing by gravitational photon bending is important in deciding the lag, low inclination sources are not likely to be affected by this effect and the energy dependence of lag would look significantly different. With regard to the evolution of LFQPO properties and time lag with time within the POS solution, the persistent source GRS 1915+105 and the transient source XTE J1550-564 do not show significant differences. The geometry of the CENBOL evolves in the same way in the two types of sources. More generally, this conclusion might apply to any source belonging to the two different classes, with most of the observed.

**Acknowledgements** I like to thank Prof. S. K. Chakrabarti for his continuous advice and guidance during and as well as after the PhD work. I acknowledge T. Belloni for providing the timing analysis software GHATS.

## References

1. Cabanac, C., Henri, G., Petrucci, P.O., Malzac, J., Ferreira, J., Belloni, T.M.: Mon. Not. R. Astron. Soc. **404**, 738–748 (2010). https://doi.org/10.1111/j.1365-2966.2010.16340.x
2. Cambier, H.J., Smith, D.M.: Astrophys. J. **767**, 46 (2013). https://doi.org/10.1088/0004-637X/767/1/46
3. Chakrabarti, S.K., Manickam, S.G.: Astrophys. J. Lett. **531**, L41–L44 (2000). https://doi.org/10.1086/312512
4. Chakrabarti, S.K., Nandi, A., Choudhury, A., Chatterjee, U.: Astrophys. J. **607**, 406–409 (2004). https://doi.org/10.1086/383235
5. Chakrabarti, S.K., Nandi, A., Chatterjee, A.K., Choudhury, A.K., Chatterjee, U.: Astron. Astrophys. **431**, 825–830 (2005). https://doi.org/10.1051/0004-6361:20041662
6. Chakrabarti, S.K., Debnath, D., Nandi, A., Pal, P.S.: Astron. Astrophys. **489**, L41–L44 (2008). https://doi.org/10.1051/0004-6361:200810136
7. Chakrabarti, S.K., Dutta, B.G., Pal, P.S.: Mon. Not. R. Astron. Soc. **394**, 1463–1468 (2009). https://doi.org/10.1111/j.1365-2966.2008.14328.x
8. Chakrabarti, S.K., Mondal, S., Debnath, D.: Mon. Not. R. Astron. Soc. **452**, 3451–3456 (2015). https://doi.org/10.1093/mnras/stv1566
9. Chatterjee, D., Debnath, D., Chakrabarti, S.K., Mondal, S., Jana, A.: Astrophys. J. **827**, 88 (2016). https://doi.org/10.3847/0004-637X/827/1/88
10. Chatterjee, A., Chakrabarti, S.K., Ghosh, H.: Mon. Not. R. Astron. Soc. **472**, 1842–1849 (2017). https://doi.org/10.1093/mnras/stx1916

11. Choudhury, M., Rao, A.R.: Astrophys. J. Lett. **616**, L143–L146 (2004). https://doi.org/10.1086/426543
12. Cui, W.: Astrophys. J. Lett. **524**, L59–L62 (1999). https://doi.org/10.1086/312296
13. Cui, W., Zhang, S.N., Chen, W.: Astrophys. J. Lett. **531**, L45–L48 (2000). https://doi.org/10.1086/312520
14. Debnath, D., Chakrabarti, S.K., Nandi, A.: Astron. Astrophys. **520**, A98 (2010). https://doi.org/10.1051/0004-6361/201014990
15. Debnath, D., Chakrabarti, S.K., Nandi, A.: Adv. Space Res. **52**, 2143–2155 (2013). https://doi.org/10.1016/j.asr.2013.09.002
16. Debnath, D., Molla, A.A., Chakrabarti, S.K., Mondal, S.: Astrophys. J. **803**, 59 (2015). https://doi.org/10.1088/0004-637X/803/2/59
17. Dutta, B.G.: In: Das, S., Nandi, A., Chattopadhyay, I. (eds.) Astronomical Society of India Conference Series, vol. 8, pp. 41–44 (2013)
18. Dutta, B.G., Chakrabarti, S.K.: Mon. Not. R. Astron. Soc. **404**, 2136–2142 (2010). https://doi.org/10.1111/j.1365-2966.2010.16428.x
19. Dutta, B.G., Chakrabarti, S.K.: Astrophys. J. **828**, 101 (2016). https://doi.org/10.3847/0004-637X/828/2/101
20. Dutta, B.G., Chakrabarti, S.K., Pal, P.S.: In: Chakrabarti, S.K., Majumdar, A.S. (eds.) American Institute of Physics Conference Series, vol. 1053, pp. 165–170 (2008). https://doi.org/10.1063/1.3009476
21. Dutta, B.G., Belloni, T., Motta, S.: Astronomical Society of India Conference Series, vol. 9 (2013)
22. Dutta, B.G., Sarathi Pal, P., Chakrabarti, S.K.: In: Astronomical Society of India Conference Series, vol. 12 (2015)
23. Dutta, B.G., Pal, P.S., Chakrabarti, S.K.: Mon. Not. R. Astron. Soc. **479**, 2183-2192 (2018). https://doi.org/10.1093/mnras/sty1572
24. Garain, S.K., Ghosh, H., Chakrabarti, S.K.: Mon. Not. R. Astron. Soc. **437**, 1329–1336 (2014). https://doi.org/10.1093/mnras/stt1969
25. Ghosh, H., Garain, S.K., Giri, K., Chakrabarti, S.K.: Mon. Not. R. Astron. Soc. **416**, 959–971 (2011). https://doi.org/10.1111/j.1365-2966.2011.19090.x
26. Haardt, F., Maraschi, L.: Astrophys. J. **413**, 507–517 (1993). https://doi.org/10.1086/173020
27. Heil, L.M., Uttley, P., Klein-Wolt, M.: Mon. Not. R. Astron. Soc. **448**, 3348–3353 (2015). https://doi.org/10.1093/mnras/stv240
28. Ingram, A., van der Klis, M.: Mon. Not. R. Astron. Soc. **446**, 3516–3525 (2015). https://doi.org/10.1093/mnras/stu2373
29. Ingram, A., Done, C., Fragile, P.C.: Mon. Not. R. Astron. Soc. **397**, L101–L105 (2009). https://doi.org/10.1111/j.1745-3933.2009.00693.x
30. Iyer, N., Nandi, A., Mandal, S.: Astrophys. J. **807**, 108 (2015). https://doi.org/10.1088/0004-637X/807/1/108
31. Lightman, A.P., Eardley, D.M.: Astrophys. J. Lett. **187**, L1 (1974). https://doi.org/10.1086/181377
32. Markwardt, C.B., Swank, J.H., Taam, R.E.: Astrophys. J. Lett. **513**, L37–L40 (1999). https://doi.org/10.1086/311899
33. Martocchia, A., Matt, G.: Mon. Not. R. Astron. Soc. **282**, L53–L57 (1996). https://doi.org/10.1093/mnras/282.4.L53
34. McClintock, J.E., Remillard, R.A.: Annu. Rev. Astron. Astrophys. **44**, 49-92 (2006). https://doi.org/10.1146/annurev.astro.44.051905.092532
35. Miniutti, G., Fabian, A.C.: Mon. Not. R. Astron. Soc. **349**, 1435–1448 (2004). https://doi.org/10.1111/j.1365-2966.2004.07611.x
36. Molla, A.A., Debnath, D., Chakrabarti, S.K., Mondal, S., Jana, A.: Mon. Not. R. Astron. Soc. **460**, 3163–3169 (2016). https://doi.org/10.1093/mnras/stw860
37. Molla, A.A., Chakrabarti, S.K., Debnath, D., Mondal, S.: Astrophys. J. **834**, 88 (2017). https://doi.org/10.3847/1538-4357/834/1/88
38. Molteni, D., Sponholz, H., Chakrabarti, S.K.: Astrophys. J. **457**, 805 (1996). https://doi.org/10.1086/176775

39. Mondal, S., Debnath, D., Chakrabarti, S.K.: Astrophys. J. **786**, 4 (2014). https://doi.org/10.1088/0004-637X/786/1/4
40. Mondal, S., Chakrabarti, S.K., Debnath, D.: Astrophys. J. **798**, 57 (2015). https://doi.org/10.1088/0004-637X/798/1/57
41. Motta, S.E., Casella, P., Henze, M., Muñoz-Darias, T., Sanna, A., Fender, R., Belloni, T.: Mon. Not. R. Astron. Soc. **447**, 2059–2072 (2015). https://doi.org/10.1093/mnras/stu2579
42. Muno, M.P., Remillard, R.A., Morgan, E.H., Waltman, E.B., Dhawan, V., Hjellming, R.M., Pooley, G.: Astrophys. J. **556**, 515–532 (2001). https://doi.org/10.1086/321604
43. Muñoz-Darias, T., Coriat, M., Plant, D.S., Ponti, G., Fender, R.P., Dunn, R.J.H.: Mon. Not. R. Astron. Soc. **432**, 1330–1337 (2013). https://doi.org/10.1093/mnras/stt546
44. Nandi, A., Debnath, D., Mandal, S., Chakrabarti, S.K.: Astron. Astrophys. **542**, A56 (2012). https://doi.org/10.1051/0004-6361/201117844
45. Orosz, J.A., Steiner, J.F., McClintock, J.E., Torres, M.A.P., Remillard, R.A., Bailyn, C.D., Miller, J.M.: Astrophys. J. **730**, 75 (2011). https://doi.org/10.1088/0004-637X/730/2/75
46. Pal, P.S., Chakrabarti, S.K.: Mon. Not. R. Astron. Soc. **440**, 672–682 (2014). https://doi.org/10.1093/mnras/stu319
47. Pal, P.S., Chakrabarti, S.K.: Adv. Space Res. **56**, 1784–1792 (2015). https://doi.org/10.1016/j.asr.2015.07.016
48. Pal, P.S., Chakrabarti, S.K., Nandi, A.: Adv. Space Res. **52**, 740–759 (2013). https://doi.org/10.1016/j.asr.2013.04.016
49. Pottschmidt, K., Chernyakova, M., Zdziarski, A.A., Lubiński, P., Smith, D.M., Bezayiff, N.: Astron. Astrophys. **452**, 285–294 (2006). https://doi.org/10.1051/0004-6361:20054077
50. Rao, A.R., Naik, S., Vadawale, S.V., Chakrabarti, S.K.: Astron. Astrophys. **360**, L25–L29 (2000)
51. Reig, P., Belloni, T., van der Klis, M., Méndez, M., Kylafis, N.D., Ford, E.C.: Astrophys. J. **541**, 883–888 (2000). https://doi.org/10.1086/309469
52. Ryu, D., Chakrabarti, S.K., Molteni, D.: Astrophys. J. **474**, 378–388 (1997). https://doi.org/10.1086/303461
53. Schnittman, J.D., Homan, J., Miller, J.M.: Astrophys. J. **642**, 420–426 (2006). https://doi.org/10.1086/500923
54. Shakura, N.I., Sunyaev, R.A.: Mon. Not. R. Astron. Soc. **175**, 613–632 (1976). https://doi.org/10.1093/mnras/175.3.613
55. Smith, D.M., Heindl, W.A., Swank, J.H.: Astrophys. J. **569**, 362–380 (2002). https://doi.org/10.1086/339167
56. Smith, D.M., Dawson, D.M., Swank, J.H.: Astrophys. J. **669**, 1138–1142 (2007). https://doi.org/10.1086/521822
57. Stella, L., Vietri, M.: Phys. Rev. Lett. **82**, 17–20 (1999). https://doi.org/10.1103/PhysRevLett.82.17
58. Stella, L., Vietri, M., Morsink, S.M.: Astrophys. J. Lett. **524**, L63–L66 (1999). https://doi.org/10.1086/312291
59. Tagger, M., Pellat, R.: Astron. Astrophys. **349**, 1003–1016 (1999)
60. Vadawale, S.V., Rao, A.R., Chakrabarti, S.K.: Astron. Astrophys. **372**, 793–802 (2001). https://doi.org/10.1051/0004-6361:20010574
61. van der Klis, M., Hasinger, G., Stella, L., Langmeier, A., van Paradijs, J., Lewin, W.H.G.: Astrophys. J. Lett. **319**, L13–L18 (1987). https://doi.org/10.1086/184946
62. Wu, K., Soria, R., Campbell-Wilson, D., Hannikainen, D., Harmon, B.A., Hunstead, R., Johnston, H., McCollough, M., McIntyre, V.: Astrophys. J. **565**, 1161–1168 (2002). https://doi.org/10.1086/324328
63. Zdziarski, A.A., Lubiński, P., Gilfanov, M., Revnivtsev, M.: Mon. Not. R. Astron. Soc. **342**, 355–372 (2003). https://doi.org/10.1046/j.1365-8711.2003.06556.x

# Spectral and Timing Analysis of Transient, Persistent and Variable Black Hole X-Ray Binaries: The Present Viewpoint




**Anuvab Banerjee**

**Abstract** We discuss the spectral and timing analysis, and the mass determination of transient sources using a few phenomenological models other than TCAF solution (like photon index and QPO frequency correlation method). Then we discuss the relative feasibility of TCAF solution in determining the same quantities, and the additional information and insight that our method can provide. Taking forward from that, we will discuss how the spectral and timing properties of persistent sources generally agree with those of the transient sources under TCAF paradigm. Thus from the perspective of the accretion flow dynamics, there is really not much difference between these two types of objects. Finally, we will discuss how the variability of the class variable sources such as GRS 1915+105 can also be explained under the purview of TCAF solution and therefore this paradigm provides a common platform for the analysis of all such objects.

## 1 Introduction

The black holes not being self-radiating objects, study of spectral and timing properties associated with the accretion flow around black holes is a productive way to detect them and extract the associated physical parameters. Several attempts have been made in that front since about 1973 [38]. Establishment of a paradigm capable of explaining observational findings in a single framework was accomplished by Chakrabarti and his co workers [6, 8, 9]. They came up with a global advective flow solution by considering simultaneously the two types of accretion flows (Keplerian and sub-Keplerian), and had taken into account physical processes associated with the flow. The Two Component Advective Flow (TCAF) solution was obtained by solving the hydrodynamic and radiative transfer equations [9], unlike the previous attempts which were model based approaches. The crux of their findings was the

A. Banerjee (✉)
S. N. Bose National Centre for Basic Sciences, Salt Lake, Kolkata, India

© Springer International Publishing AG, part of Springer Nature 2018

B. Mukhopadhyay, S. Sasmal (eds.), *Exploring the Universe: From Near Space to Extra-Galactic*, Astrophysics and Space Science Proceedings 53,
https://doi.org/10.1007/978-3-319-94607-8_21

natural emergence of the shock front based on the initial flow parameters. It the most significant feature of TCAF solution; which at one stroke explained the tail end of the spectrum being produced as a result of inverse Comptonization of soft seed photons in the hot post-shock region, and the appearance of Quasi Periodic Oscillation (QPO) as a result of the tug of war between the cooling time-scale in the post-shock region and the infall time-scale from the shock front. In short, the properties of the CENtrifugal pressure supported BOundary Layer (CENBOL), i.e. the post shock region as we have mentioned earlier is mainly responsible for the production of high energy radiation and producing outflow. In the following sections we will provide a glimpse of how this solution treats different kinds of black hole sources in an equal footing.

## 2 Spectral and Timing Analysis of Transient Source: H1743-322

The hall mark of the transient sources is their existence in the quiescent state for a significant amount of time, and occasional excursions to the outbursting phases, i.e. the order of magnitude intensification of the peak X-ray luminosity. It was shown earlier that such a source transits through a number of spectral states, which are typically the hard state (HS), hard-intermediate state (HIMS), soft-intermediate state (SIMS) and soft state (SS) ([21, 30]). The Power Density Spectra (PDS) also divulge the presence of low frequency Quasi Periodic Oscillation. The correlation of the different spectral states with the branches of Hardness Intensity Diagram (HID) have been reported previously (see [3] for an extensive discussion). The transition between the different spectral states would generally follow the sequence as HS $\rightarrow$ HIMS $\rightarrow$ SIMS $\rightarrow$ SS, and then would retrace the path to revert back to the original hard state.

Studying the spectral and temporal behaviour of the outbursting sources, the extraction of the intrinsic properties such as the mass and the normalization of the concerned object is quite an involved task. There are large number of models available in the literature dedicated towards this objective. Substantial progress on that using the Two Component Advective Flow (TCAF) solution has been made on that front and the flow parameters such as the accretion rates, shock location etc. has been determined alongside. However, before discussing the results as obtained by the TCAF model, it would be a better idea to present the whiff of some other models and their key conclusions. This will reveal the relative superiority of TCAF solution over those models in determining such parameters. For that, we would use the transient source H 1743-322 to be a case in point

H1743-322 is a low mass, Galactic X-ray binary. Its mass has not been measured yet through dynamical method. However, several attempts have been made to determine the most feasible mass range which we are summarizing below.

Shaposhnikov and Titarchuk [39] determined the mass of this object with the aid of their QPO frequency-photon index correlation method on the 2003 outburst. Here one requires one primary reference source whose mass, distance and the inclination angle are measured using dynamical method. Considering the theoretical conjecture that the QPO frequency should be inversely proportional to the mass of the black hole, scaling laws are devised in terms of the ratio of QPO frequency and the ratio of fluxes. For this particular black hole, GRO J1655-40 was used as a reference source, and the mass of H1743-322 was determined to be $13.3 \pm 3.2\, M_{\odot}$. However, the requirement of another source is a serious drawback in this scheme. McClintock et al. [22] estimated its mass to be $\sim 11\, M_{\odot}$ using their high-frequency QPO correlation method, but that also requires another reference source.

From the model of high-frequency QPOs based on the spin of the black hole, the mass predicted by Pétri [35] lies in the range of 9–13 $M_{\odot}$. According to this method, the oscillation of the accretion disk and the rotating background field associated with the compact object under consideration is an essential ingredient for the explanation of the High frequency QPOs in Low Mass X-ray Binaries. Obviously since the mass determination heavily relies on the intrinsic parameter of the concerned black hole, the error in the measurement of spin will inevitably creep in the determination of mass.

Now let us come down to the corresponding analysis using the TCAF solution. In case of this object, from the sequence of outbursts as shown in the RXTE/ASM light curve, it had become clear that the one in 2003 took place about 20 years after its first flaring. Subsequent quasi-regular outburst like flares includes are of moderate or small intensity. The 2010 outburst was analyzed by Mondal et al. [25] and was found that the flow parameters extracted from the TCAF fitting agree with the variation of diskbb and power-law fluxes. The 2.5–25.0 keV spectra were fitted keeping the systematic error within 1%, and the normalization was kept free. Ideally, if the mass and the distance of the object is fixed, the normalization should not vary. However, since these quantities are not known in absolute certainty, it would be operationally more feasible to let it vary within a narrow range. Later, the 2010 and 2011 outbursts were analyzed by Molla et al. [24]. Firstly, the fitting was done by constraining the normalization in a narrow window, and then keeping it frozen at the average value $N = 15.55$. The mass from all the estimates turned out to be in the range 9.25–12.86 $M_{\odot}$, and it was compared with the photon index versus QPO frequency correlation method using GRO J1655-40 as a reference. The obtained mass from the second method turned out to be $11.65 \pm 0.65\, M_{\odot}$, which is within the acceptable limit as obtained in other methods formerly.

The same task was repeated on the 2004 outburst (the first stereotypical outburst after 2003) and the entire 117 day long data was fitted first using wabs*(diskbb+power-law) model and then using TCAF solution in [4], and we are now summarizing the key conclusions obtained there. Using the shock location ($X_s$), the compression ratio (R) and the mass obtained from the fitting, the QPO

frequency was determined using the relation [11]

$$\nu_{qpo} = \frac{c^3}{2GM_{BH}} \frac{1}{[RX_s(X_s - 1)^{1/2}]} \tag{1}$$

and the obtained QPO frequency was in agreement with the one obtained from the PDS. Finally, using the Propagatory Oscillatory Shock (POS) model, the velocity of the shock front could be determined.

The variation of diskbb and power-law fluxes implies that the object transits from HIMS to HS during the entire period of observation. This was confirmed from the TCAF fitting, where during the first 13 days of observation, the disk rate is greater than the halo rate, after that the case is exactly opposite (Fig. 1). From the varying and the constant normalization, the mass of the object could be constrained to be 10.31–14.07 $M_{\odot}$. This falls into the correct ballpark obtained in the previous attempts.

This method of studying the spectral and temporal behaviour of the outbursting sources and extracting the mass has been employed on a number of sources such as

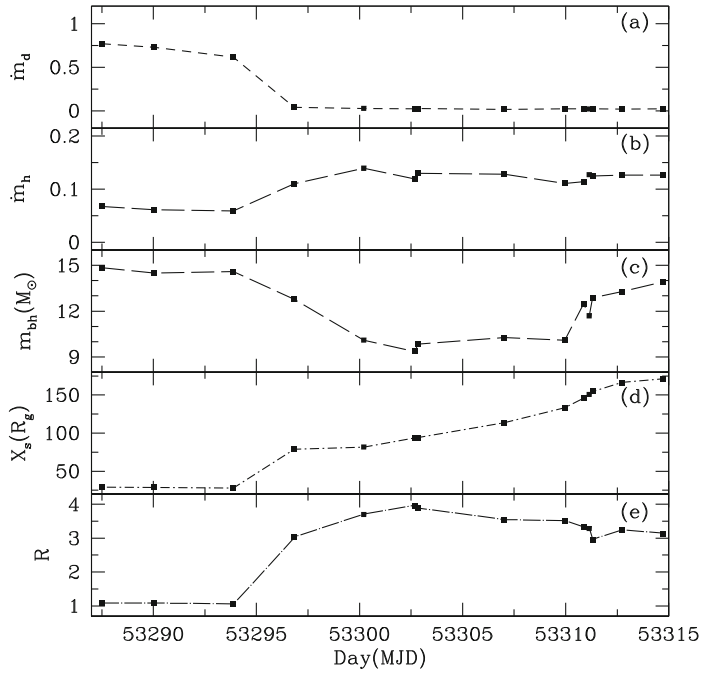



**Fig. 1** Variation of (**a**) the disk accretion rate (in Eddington units), (**b**) halo rate (in Eddington units), (**c**) Mass of the black hole (in unit of solar mass), (**d**) shock location (in unit of $2GM/c^2$) and (**e**) the compression ratio

GX 339-4 [30], MAXI J1543-564 [12], MAXI J1836-194 [19], MAXI J1659-152 [23] with considerable success.

Hence, spectral fitting using TCAF solution reasonably constrains the mass, and in addition, this does not require the reference of other sources and their details. In does not also require any additional intrinsic parameter such as spin for its mass determination, rather the feasible value of another intrinsic parameter like normalization comes out quite naturally. As a bonus, we can also predict the shock velocity, provided the QPO is observed in the PDS. This velocity of about a meter or so per second is a hall-mark of all outbursting sources. This movement is again due to Comptonization cooling (Mondal, this volume). Hence, the legitimacy of this method in studying the accretion flow dynamics during an outburst and mass determination is apparent.

## 3 Spectral and Timing Analysis of the Persistent Source: Cygnus X-1

These sources are characterized by their persistent luminosity in X-rays and the relatively more massive (20–30 $M_\odot$ or more) companions. It was reported by Grinberg et al. [16, 17] that such sources typically attempt to transit to a soft state once or twice in a year, but ultimately the predominant hard state is restored. It was further reported that during the spectral transition, unlike the transient sources, they generally do not traverse the entire q-diagram or the Hardness Intensity Diagram (HID) [5]. The companions release masses $\sim 10^{-5}$–$10^{-7}\ M_\odot\ \mathrm{year}^{-1}$ in the form of the winds, which in turn is captured by the central object.

Cygnus X-1 is a well studied Galactic black hole X-ray binary. The long term behaviour of Cygnus X-1 was studied by Wilms et al. [42] using the RXTE data from early 1999 to late 2004. The X-ray spectra were studied using the phenomenological broken power-law model endowed with an exponential cutoff factor. This work was further extended by Grinberg et al. [16, 17] using the RXTE-ASM, swift-BAT, MAXI and FERMI-GBM data to classify the spectral states for the entire period from 1996 (year of launching of RXTE) to early 2015. The spectral states as reported were given by (as shown in Fig. 2):

- A predominant soft state from the onset of 1996 to late 1996 (phase I).
- A hard state with bouts of softening from late 1996 to early 1998 (phase II).
- A substantially long presence of soft state for a span of about 6 years between early part of 1998 to mid-2006, interspersed by a string of failed state transitions (phase III).
- A dominant presence of hard state from mid-2006 to mid-2010 (phase IV).
- A prolonged presence of soft state from mid 2010 to 2015 (phase V).

To summarize, Cyg X-1 exhibits state transition like behaviours [43]. However, the phenomenological model such as a broken power-law model does not capture

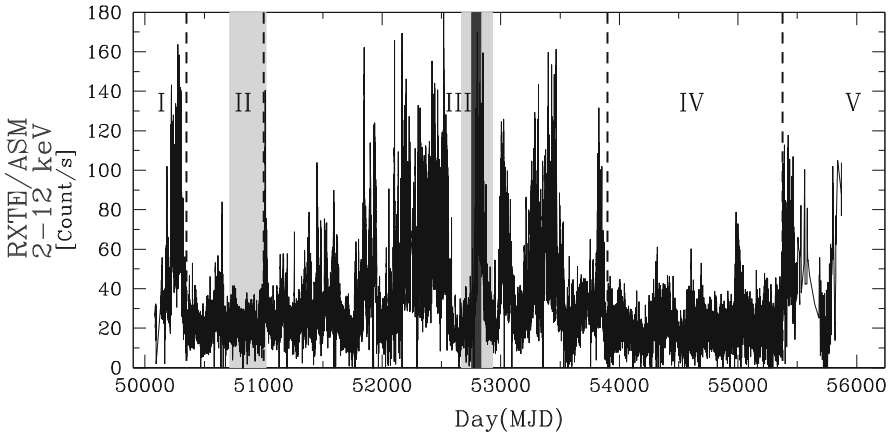



**Fig. 2** RXTE/ASM light curve of Cygnus X-1 in the 2.0–12.0 keV energy range illustrating the five phases through which the object has transited from early 1996 to late 2015. The shaded region in phase II represents the hard state which has been fitted with TCAF solution. In phase III, the lighter shaded region implies the domain in which outburst like behaviour was observed and TCAF solution was employed. The darker shaded region in that strip represents the region where due to enhanced flux, the fit could not be obtained [16] (adapted from [1])

the underlying physics of the accretion flow dynamics. Since the flow behaviour is ultimately dependent on the rate of the release of companion mass and other related flow parameters, and should be independent of the details of the central object, hence on the perspective of the underlying flow behaviour, transient and persistent sources should be treated on the same platform. This consideration motivated us to study the spectral behaviour in the light of TCAF solution as well, and carry out the similar analysis as has been done for transient sources (Fig. 3).

The mass of this object as predicted by Gies and Bolton [13] lies in the range 7–16 $M_{\odot}$, where the companion mass of 16 $M_{\odot}$ was assumed. Considering the companion mass to be $\sim$20 $M_{\odot}$, the mass estimated by Ninkov et al. [31] was around the range $10 \pm 1$ $M_{\odot}$. Herrero et al. [18] constrained the mass in the range 5–15 $M_{\odot}$. However, all such measurements crucially relied upon the measurement of the source distance, and there were high degree of errors regarding the measurement of the distance [37]. Using the distance measured by Reid et al. [37], Orosz [32] was able to constrain the mass within 13.8–15.8 $M_{\odot}$. However, all such methods required external parameters such as mass of the companion and the distance of the source for the mass determination, and thus the similar sort of problem as in the case of transient sources crop up here as well. Hence, spectral study using TCAF would be a big plus even on that front because it would reasonably predict the mass without these extra constraints.

Before going into the results, Let us try to first understand what we would naively expect. In case of outbursting sources, as we have discussed before, the source predominantly lives in the quiescent state. The sub-Keplerian matter is accreted

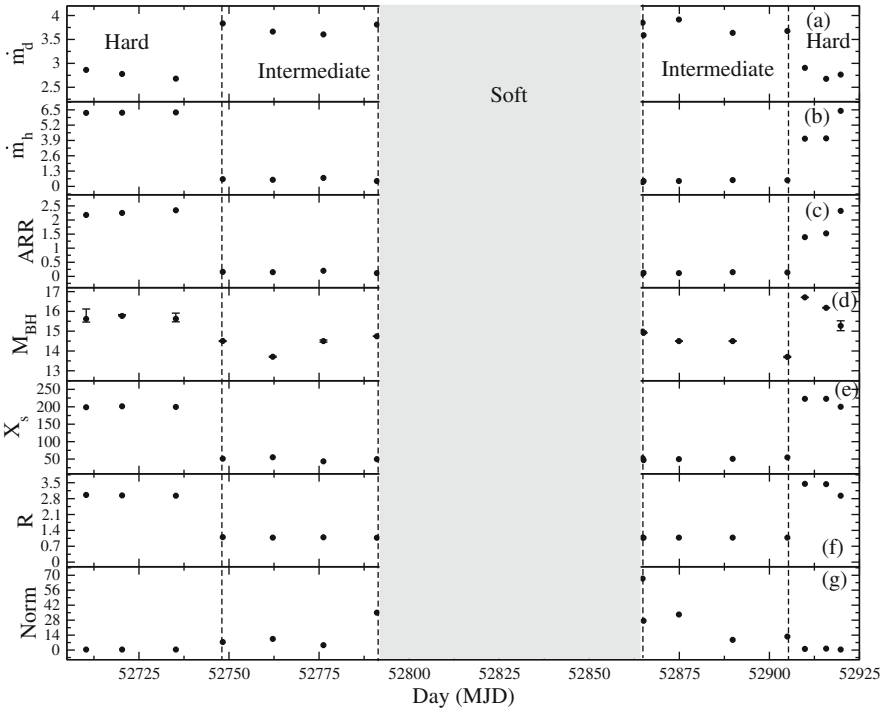



**Fig. 3** Variation of (**a**) disk accretion rate (in Eddington unit), (**b**) halo rate (in Eddington unit), (**c**) the accretion rate ratio ARR ($= \dot{m}_h/\dot{m}_d$), (**d**) the mass of the black hole (in unit of solar mass), (**e**) location of the shock from (in unit of $2GM/c^2$), (**f**) shock strength and (**g**) normalization

through the wind. It was shown by extensive hydrodynamic simulation by Giri and Chakrabarti [14] that if the flow viscosity climbs above a critical value, then the sub-Keplerian matter is converted to radiatively efficient soft Keplerian matter, i.e. of lower radial velocity and higher angular momentum flow. Subsequently, as the viscosity parameter again drops below the critical value, the flow settles down to the initial quiescent state. This is the mechanism of triggering an outburst. Now, there is considerable time lag between the sub-Keplerian and Keplerian flow due to the difference in the radial velocity. However, in case of persistent sources, the flow is mostly sub-Keplerian, the size of the Keplerian disk is smaller in this case. As we will analyze the outburst like phases using *Diskbb+Power-law* model, we would expect the simultaneous increase of diskbb and power-law fluxes, and the subsequent TCAF fitting will affirm the outburst like feature from the vantage point of the accretion rates.

With this basic proposition in mind, let us try to understand the observational results. Here we are now going to summarize the work done by Banerjee et al. [1] in this regard. We have analyzed the phase II and phase III of the spectral transition using RXTE archival data. The background subtracted spectra in the 2.5–45.0 keV energy window were fitted using TCAF solution with 1% systematic error.

During the phase II of the source activity, which is reportedly a prolonged hard state [16, 17], the fitted parameters were in agreement with the hard state type behaviour. The disk accretion rate varies from 0.68–0.75 $\dot{M}_{Edd}$, and the halo rate was obtained in the range 1.72–1.84 $\dot{M}_{Edd}$. Thus, the disk rate is considerably smaller than the halo rate, which is a signature of the hard state like behaviour. The mass obtained in this period of observation lies in the bound $14.12 \pm 0.51\, M_{\odot}$. Shock location varies in the range 70.37–73.35 $R_s$, and the compression ratio was in the range 1.18–1.25. Hence all the parameters vary in a very narrow range, and corroborate to the hard state type behaviour. Thus, from the vantage point of accretion flow dynamics, the properties of transient and persistent sources are alike.

During the phase III of the source activity, which is reportedly a flaring phase [16, 17], the spectral fitting yielded positive results. During the first ∼25 days, the object seems to reside in the hard state as is suggested by the diskbb+power-law fitting, where the diskbb flux is one order of magnitude lesser than the power-law flux. In the TCAF fitting, the average disk accretion rate is ∼2.78 $\dot{M}_{Edd}$ and the average halo rate is ∼6.26 $\dot{M}_{Edd}$, and the shock location is roughly 199 $R_s$, which are in agreement with the hard state like behaviour. After that, for about 45 days, the spectral fitting yielded different results. From the fitting using diskbb+power-law, the diskbb flux and power-law flux started increasing simultaneously, which is the signature of persistent sources. This is indicative of outburst like behavior. We then fitted the spectra using TCAF+Gaussian model. There the disk rate was greater than the halo rate (∼3.73 $\dot{M}_{Edd}$ and ∼0.59 $\dot{M}_{Edd}$), and the shock location also came down (∼50 $R_s$); implying softer state like behaviour. Then, during ∼65 days, the flux was so high that reasonable fit could not be obtained, and after that, the previous sequence followed. Hence, the proposed outburst like behaviour is confirmed by TCAF spectral fitting and in addition, it is providing the flow parameters in each of the observations. The mass of the source obtained from all observations was obtained to be $M_{avg} = 14.57 \pm 0.68\, M_{\odot}$. This lies well within the ballpark predicted by the previous observation.

Hence, the variation of the parameters during the state transition follows quite the same trend as that of transient sources; only difference being in this case the numerical values of the accretion rates are higher compared to transient sources ($\dot{m}_d$ and $\dot{m}_h$ were respectively ∼2 and 6 $\dot{M}_{Edd}$ during the hard state). Except that, the one-to-one correspondence between these two kinds of sources are quite apparent.

## 4 Class Variable Sources Under TCAF Paradigm

These are somewhat enigmatic sources as compared to the objects we have discussed earlier, upon which continuous X-ray observations show that the peak X-ray intensity changes in a variety of timescales from a few seconds to a few days. GRS 1915+105 is such a stellar mass black hole binary which shows the peculiar time variability [15, 26]. This variability was a real puzzling aspect at that point of time, and several attempts were being made in the direction of a full classification

of all such variabilities for a better understanding of the phenomenon. Belloni et al. [2] analyzed 163 observation of RXTE during the period of 1996–1997, and put the variabilities into 12 separate classes based on the photon count in different energy bands and the conventional color-color diagram. Subsequently, the existence of new classes were reported [20, 27, 28, 40, 41].

However, at that point there was hardly any clue regarding the emergence of such a large variety of classes. Significant development along that direction was first made by Nandi et al. [29] who tried to group these variabilities under the paradigm of black hole accretion including a shock. The post-shock region being hot enough compared to the pre-shock region, that serves as the base of outflows and winds, and the soft seed photons emanating from the disk are intercepted by the CENBOL region and the outflow. Considering the proportionality of the inverse-Comptonized photons by the CENBOL region with the soft seed photons, they defined the softness diagrams (where (B/C) is plotted against (A/C); A, B, C being the number of photons in the (0–3), (3–17) and (17–60) keV respectively). Those were then classified into four classes: HARD, SOFT, SEMI-SOFT and INTERMEDIATE. All the Hardness-Intensity Diagrams (HID) could be grouped under these four classes. Almost linear plots in all the cases is an affirmation of the proportionality of the number of photons in different energy bands.

Under the purview of advective-flow, Chakrabarti and Manickam [7] explained the variabilities quite succinctly by considering the interception of the seed photons with the outflow, and subsequent fall-back mechanism. The crux of their explanation may be summarized as follows. It implies that the base of the outflow within the sonic sphere being optically thick enough to be cooled down catastrophically by the inverse-Comptonization of the injected soft seed photons, it loses its outward drive and falls back upon the accreting matter, thereby momentarily increasing the accretion rates. The outflow collapses in this process and the enhancement of thermal energy of the post-shock region and consequent build up of the vertical pressure gradient force for triggering the outflow starts all over again. This collapse of outflow and re-injection of matter is responsible for the burst-on and burst-off phenomena (increase and decrease of the photon count respectively) and the formation of blobby jets.

This conjecture was further made by Chakrabarti et al. [10] where the fitting using Diskbb+power-law on GRS 1915+105 and GRO 1655-40 demonstrated that during the burst on state, the photon index and inner disk temperature much higher compared to the burst-off state. This makes sense, since during the burst-on state the softer state like behaviour would be apparent. Furthermore, it was demonstrated by Chakrabarti and Manickam [7] using the correlation between the QPO frequency and duration of the quiescent state, that during the off state if QPO is at all present, only the higher energy photons (those being scattered from the post-shock region and not emerging from the disk) should capture the signature of it. They found that there was no signature of QPO in the (0–4) keV PDS, but distinct signature of QPO in the (4–13) keV PDS. Rao and his collaborators [36] using the RXTE data in the $\chi_3$ state of GRS 1915+105, fitted the spectra in the 3–190 keV energy band (using both PCA and HEXTE data into account) using Diskbb+CompST+power-law model, and

reported the origin of (0.5–10) Hz QPO to be predominantly due to the variations in the Comptonized component. In the TCAF paradigm, the post-shock region serves as the Comptonizing component.

All such findings are very clearly pointing to the fact that all the apparently different and enigmatic classes should ultimately be explained under the consideration of the changes in accretion rates. If that is the case, these classes cannot pop out arbitrarily, but will emerge out in a definite sequence as an offshoot of the smooth changes in the accretion rates. Decisive stride in that direction was made by [34] where a quantity called "Comptonizing Efficiency (CE)" (ratio of photon count from the power-law and the blackbody components) was defined, and the different classes were sequenced vis-a-vis CE in the ascending order. They found that the classes with harder states are endowed with more CE. It was further concluded that since the sub-Keplerian flow does not involve viscous effects, the transition from harder to softer states could be attained very swiftly, which would not have been possible just by the Keplerian flow. These conclusions made these whole set of affairs understandable within TCAF framework. Later on, the CE for IGR 17091-3624 was found to be similar to GRS 1915+105 as well [33].

What would be the way forward from here? So far, the spectra of the small time segments as the object moves from one class to another, or even when within a class, the light curve transits from burst-on to the burst-off states, were not fitted using TCAF solution. Therefore how the accretion rates and shock location evolve during such dynamical process remains to be seen. On the classes with lower count rate and lower activity, i.e., which demonstrate hard state like behaviour ($\chi_2$ and $\chi_4$ classes), the spectra could be fitted with TCAF solution alone, whereas on the radio loud classes additional components (like cutoff power-law model) would be required in order to account for the enhanced hard photons from the outflow (in the form of Synchrotron radiation and Comptonization from the outflow). In the classes with higher variability, as we move from burst-off to burst-on states, the disk accretion rate should also increase, with higher normalization and lower shock location. This is what we expect to report elsewhere.

## 5 Summary

The triggering of an outburst and the subsequent evolution being entirely governed by the flow parameters like viscosity, the explanation of outburst should not be dependent on the exclusive nature of the black hole, whether transient or persistent. That has been in fact demonstrated from the analysis on these two kinds of objects. The same conclusion should ultimately translate to the explanation of the transition of different classes in case of class variable sources. The crucial features of outburst and variability for all such cases are the same, and hence TCAF solution brings them on a common platform.

## References


1. Banerjee, I., Bhattacharjee, A., Banerjee, A., Debnath, D., Chakrabarti, S.K.: (2018, submitted). Reference no. AAS05179R2
2. Belloni, T., Klein-Wolt, M., Mendez, M., et al.: A&A **355**, 271–290 (2000)
3. Belloni, T., Homan, J., Casella, P., et al.: A&A **440**, 207 (2005)
4. Bhattacharjee, A., Banerjee, I., Banerjee, A., Debnath, D., Chakrabarti, S.K.: MNRAS **466**, 1372 (2017)
5. Böck, M., et al.: A&A **533**, A8 (2011)
6. Chakrabarti, S.K.: MNRAS **243**, 610 (1990)
7. Chakrabarti, S.K., Manickam, S.G.: ApJ **531**(1), L41 (2000)
8. Chakrabarti, S.K., Molteni, D.: ApJ **417**, 671 (1993)
9. Chakrabarti, S.K., Titarchuk, L.G.: ApJ **455**, 623 (1995)
10. Chakrabarti, S.K., Nandi, A., Manickam, S.G., Mondal, S., Rao, A.R.: ApJ **579**, L21 (2002)
11. Chakrabarti, S.K., Debnath, D., Nandi, A., et al.: A&A **489**, L41–L44 (2008)
12. Chatterjee, D., Debnath, D., Chakrabarti, S.K., Mondal, S., Jana, A.: ApJ **827**, 88 (2016)
13. Gies, D.R., Bolton, C.T.: ApJ **304**, 371 (1986)
14. Giri, K., Chakrabarti, S.K.: MNRAS **430**, 2836 (2013)
15. Greiner, J., Morgan, E.H., Remillard, R.A.: ApJ **473**, 107–110 (1996)
16. Grinberg, V., et al.: A&A **554**, A88 (2013)
17. Grinberg, V., et al.: A&A **565**, A1 (2014)
18. Herrero, J., Kudritzki, R.P., Gabler, R., Vilchez, J.M., Gabler, A.: A& A **297**, 556 (1995)
19. Jana, A., Debnath, D., Chakrabarti, S.K., Mondal, S., Molla, A.A.: ApJ **819**, 107 (2016)
20. Klein-Wolt, M., Fender, R.P., Pooley, G.G., et al.: MNRAS **331**, 745–764 (2002)
21. McClintock, J.E., Remillard, R.A.: In: Lewin, W., van der Klis, M. (eds.) Compact Stellar X-ray Sources, vol. 39, p. 157. Cambridge University Press, Cambridge (2006)
22. McClintock, J.E., Remillard, R.A., Rupen, M.P., et al.: ApJ **698**, 1398 (2009)
23. Molla, A.A., Debnath, D., Chakrabarti, S.K., Mondal, S., Jana, A.: MNRAS **460**, 3163 (2016)
24. Molla, A.A., Chakrabarti, S.K., Debnath, D., Mondal, S.: ApJ **834**, 88 (2017)
25. Mondal, S., Debnath, D., Chakrabarti, S.K.: ApJ **786**, 4 (2014)
26. Morgan, E.H., Remillard, R.A., Greiner, J.: ApJ **482**, 993–1010 (1997)
27. Naik, S., Rao, A.R.: A&A **362**, 691–696 (2000)
28. Naik, S., Rao, A.R., Chakrabarti, S.K.: JApA **23**, 213–234 (2002)
29. Nandi, A., Manickam, S.G., Chakrabarti, S.K.: Ind. J. Phys. **74B**(5), 331 (2000)
30. Nandi, A., Debnath, D., Mandal, S., Chakrabarti, S.K.: A&A **542**, 56 (2012)
31. Ninkov, Z., Walker, G.A.H., Yang, S.: ApJ **321**, 425 (1987)
32. Orosz, J.A., et al.: ApJ **742**, 84 (2011)
33. Pal, P.S., Chakrabarti, S.K.: Adv. Space Res. **56**, 1784–1792 (2015)
34. Pal, P.S., Chakrabarti, S.K., Nandi, A.: Adv. Space Res. **52**, 740–759 (2013)
35. Pétri, J.: Ap&SS **318**, 181–186 (2008)
36. Rao, A.R., Naik S., Vadawale, S.V., Chakrabarti, S.K.: A&A **360**, L25 (2000)
37. Reid, M.J., McClintock, J.E., Narayan, R., et al.: ApJ **742**, 83 (2011)
38. Shakura, N.I., Sunyaev, R.A.: A&A **24**, 337 (1973)
39. Shaposhnikov, N., Titarchuk, L.G.: ApJ **699**, 453 (2009)
40. Vadawale, S.V., Rao, A.R., Nandi, A., Chakrabarti, S.K.: A&A **370**, 17–21 (2001)
41. Vadawale, S.V., Rao, A.R., Naik, S., et al.: ApJ **597**, 1023–1035 (2003)
42. Wilms, J., Nowak, M.A., Pottschmidt, K., Pooley, G.G., Fritz, S.: A&A **447**, 245 (2006)
43. Zhang, S.N., Cui, W., Harmon, B.A., Paciesas, W.S., Remillard, R.E., et al.: ApJ **477**, L95 (1997)

# Measurement of Masses of Galactic Black Holes from Spectral Analysis




**Debjit Chatterjee**

**Abstract** Mass is one of the intrinsic properties of black holes. In this article, some methods of measuring the mass of the black hole and a brief comparison of these methods is discussed. We show that Two Component Advective Flow (TCAF) model is capable of computing masses quite accurately even with a few seconds of spectral data.

## 1 Introduction

Mass is one of the fundamental properties of a black hole. According to *no hair* theorem there are three fundamental properties of a generalized black hole: mass, charge and spin. When a massive object is collapsed due to the fuel exhaustion and particle (electron or neutron) degeneracy pressure could not stop the shrinking, the end phase of this collapse is a black hole. After the creation of black hole it is hard to infer about its intrinsic properties, since no information can come out from the event horizon. But the matter orbiting around a black hole can dissipate its orbital energy and release electromagnetic radiation, which could be detected to predict the properties of the black hole. In fact, mass is the best indicator to predict if an X-ray transient is a black hole or not. Mass of the black hole can vary in a vast range. Mass is one of the scaling factors which determine some of the astrophysical phenomena around black holes. Depending on the mass range there are three types of black holes—stellar massive (e.g., Cyg X-1, GRS 1915+115), intermediate (e.g., GCIRS 13E, M82-X1, HLX-1) and supermassive (e.g., Sagittarius $A^*$). Here, we will mainly focus on the mass measurement of stellar mass black holes.

D. Chatterjee (✉)
Indian Centre for Space Physics, Kolkata, India

© Springer International Publishing AG, part of Springer Nature 2018

B. Mukhopadhyay, S. Sasmal (eds.), *Exploring the Universe: From Near Space to Extra-Galactic*, Astrophysics and Space Science Proceedings 53,
https://doi.org/10.1007/978-3-319-94607-8_22

## 2 Dynamical Method

The best way to measure the mass is when the system is in a binary configuration. Fortunately, most of the systems are in binaries. A large number of these binaries happen to be X-ray transients [57]. The best opportunity to measure the mass of a black hole is when it is in its quiescent state. In this time the companion star is often observable in optical, which allows to measure the radial velocity of the donor star and also predicts its nature. In case of spectroscopic binaries, the radial velocity can be measured from the cross-correlation of spectral type of the donor star and stellar template. Analyzing the Doppler shifted spectra from the companion star its semi-amplitude of radial speed ($v_{1r}$) and orbital period (P) can be calculated. The mass of the black hole can be calculated by using Newtonian two body problem and Kepler's third law. Suppose the mass of the companion star and the black hole is $M_1$ and $M_2$ respectively, and their orbital period around the common center of mass is $P$. Then, the *mass function* $f(M)$ is,

$$f(M) = \frac{(M_2 sin\, i)^3}{(M_1 + M_2)^2} = \frac{P}{2\pi G}\, v_{1r}^3, \tag{1}$$

where 'i' represents the inclination angle of the orbital plane to the line of sight. 'G' is the gravitational constant. $v_{1r}$ is the amplitude of the observed velocity curve of the companion star and it is equal to $v_1 sin\, i$, where $v_1 = 2\pi a_1/P$ is the orbital velocity and $a_1$ is the radius of the semi-major axis of the companion star. If 'i'=90°, then it means observing the orbital plane edge-on. This *mass function* is a lower limit on the compact object's mass ($M_2$) since $M_1 > 0$ and $sin\, i \leq 1$. This dynamical method can be used for the mass determination of any binary object provided all the necessary information (radial velocity $v_{1r}$, orbital period $P$, inclination angle $i$ of the system and the companion's mass $M_1$) are available.

## 3 Mass from Spectroscopic and Temporal Analysis

After the launch of different multi-wavelength satellites, the observational astronomy has been progressed tremendously. Pringle and Rees [77] constructed an accretion model around black holes and neutron stars considering Kepler's laws. In 1973, Shakura and Sunyaev [88] proposed a plausible model for black hole accretion process, known as the *standard thin disk* model. But, this model explains the spectra up to a certain energy range. Subsequent theories and observations reveal that the full observed X-ray spectrum has two components. A standard type cool disk can produce approximately a thermal blackbody type spectrum, while a hotter Compton cloud is required to inverse Comptonize the soft photons which contribute to the power-law component of the spectrum. Several phenomenological and theoretical

models have been developed to infer the accretion properties of black holes. Some of these models also try to estimate mass of the black holes in an indirect way.

### 3.1 Disk Blackbody Model

*Multi-color disk blackbody* (diskbb) model [50, 60] is an upgraded version of standard disk model to explain the low energy, soft X-ray part of the black hole spectra. The obtained parameters of this model are inner disk temperature ($T_{in}$) and normalization ($N$), which are used to predict the mass of a black hole. The disk blackbody normalization corresponds to

$$N = (\frac{R_{km}}{D_{10}})^2 cos\theta, \tag{2}$$

where $D_{10}$ represents the source distance (in 10 kpc), $R_{km}$ denoted as the disk inner radius (in km), and '$\theta$' is the inclination of the disk. The spectral fitted parameters ($T_{in}$ and $N$) can be used to predict the mass of black hole, if the inner disk temperature is very high and the value of normalization is low. Now, this high temperature and low normalization correspond to high accretion rate, high distance, high inclination and low black hole mass and probably very high spin. Lower mass increases the disk temperature, since $M_{BH} \sim T^4$. Again, lower mass corresponds to low inner radius ($R_{in}$), which decrease the normalization value ($N$). Furthermore, high spin also decreases the inner radius and gives higher temperature. Though, the mass prediction by this model is not very reliable because this is a phenomenological model and the inner edge of the disk which comes out of fits may not be realistic.

### 3.2 QPO-Photon Index Correlation

For neutron stars and black holes, the accretion process has many similarities. Part of the accreting matter with large angular momentum forms a disk and the other part free falls toward the compact object until centrifugal barrier stops it [14]. These two part of the matter contributes to the resulting spectra of a compact object (See, Ayan Bhattacharjee, this volume). Titarchuk et al. [96] proposed the dynamical adjustment of Keplerian disk at neutron star surface. Similar to Molteni et al.'s [64] work on black holes, they demonstrated that the kHz oscillations is from the mechanical oscillation of the centrifugal boundary. Psaltis et al. [78] suggested that the low and high frequency QPOs follow a tight correlation for neutron stars and black holes. They also proposed that the correlation indicates a weak dependency on the properties of the source, such as the mass, magnetic field and the presence of a hard surface. Mauche [56] extended this work to the dwarf nova. The study of this correlation of QPOs for this broad range of compact objects leads to the question

whether there is a way to distinguish black holes from other compact objects using this observational relation. A comprehensive study on the correlation between QPO frequency and photon index for different black hole candidates [32, 45, 98] show a strong correlation between the index and the frequency. They also noticed a saturation in photon index when the state transition occurs. Following the persistent correlation of QPO frequency and photon index over time for many sources suggest that the low frequency QPOs are related to the corona which gives rise to a strong correlation with the photon index. Titarchuk and Fiorito [95] proposed how the photon index of their corona model changes as a function of mass accretion rate. In their paper, they also proposed that the frequency of QPO is inversely proportional to the black hole's mass and offered a scaling method for estimating the mass of a black hole from the QPO frequency-photon index correlation ($\Gamma(\nu_{low})$). Where $\nu_{low}$ is the frequency of QPO. They also show observational evidence, how the mass of one known black hole candidate can be used to estimate another black hole's mass which has same QPO frequency-photon index correlation. If for a given source the mass ($M_1$) and the index-frequency dependence $\Gamma(\nu_{low})$ is known, then for another black hole candidate with a similar index-frequency dependence ($\Gamma(\nu'_{low})$ a simple frequency shift $\nu'_{low} = (M_1/M_2)\nu_{low}$ with respect to $\nu_{low}$ allows to estimate the mass ($M_2$) of that source. The detailed formalism is described in [89].

According to their model description [95, 96] the normal mode volume oscillations of the outer boundary of Compton cloud is the reason for the low frequency QPOs. As a ratio of magneto-acoustic velocity and size, the QPO frequency should be inversely proportional to size of the Compton cloud. Again, this oscillation occurs at the adjustment radius (outer boundary of the Compton cloud) where the transition from Keplerian disk to sub-Keplerian Compton cloud occurs. This adjustment radius can be stated in terms of Schwarzschild radius. Hence, the size of the Compton cloud is proportional to the mass of the black hole. Thus, the QPO frequency is inversely proportional to the mass of the black hole. The spectral index is nothing but a measure of up-scattering efficiency of the Compton cloud. The formulated version of this method (as given in [89]) is

$$f(\nu) = A - D\ B\ ln[exp(\frac{\nu_{tr} - \nu}{D}) + 1]. \tag{3}$$

$A$ and $B$ are the values of the index saturation level and slope of the function. $D$ is a constant parameter which controls how fast the transition occurs, generally assumed to be '1'. For, $\nu < \nu_{tr}$ the slope $B$ is proportional to the black hole's mass. Following this method, Shaposhnikov and Titarchuk [89] estimated masses for Cyg X-1 and GRS 1915+105 (see, Fig. 1) using the correlation with the known source GRO J1655-40. The advantage of this method is that it is independent of the system geometry and the distance of the source. Though to determine the mass of a black hole in this method, the black hole must have a clear QPO frequency-photon index correlation pattern. Also, a reference known (mass) source is needed with a similar QPO-index correlations and with same saturation index.

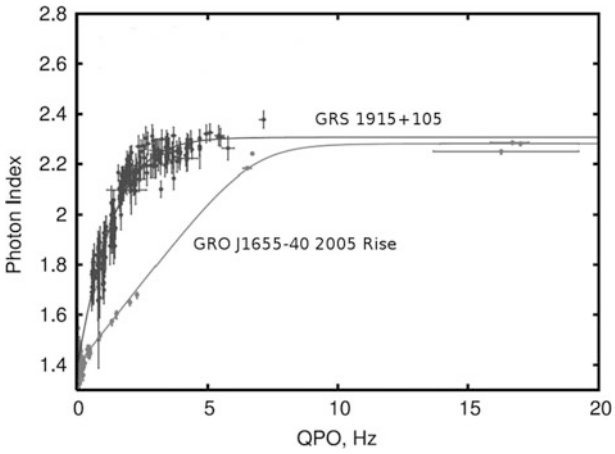



**Fig. 1** $\Gamma$-QPO frequency correlations for GRS 1915+115 and GRO J1655-40 during the 2005 outburst. Here, GRO J1655-40 is used as a reference source to estimate the mass of GRS 1915+105 (adapted from [89])

## *3.3 Propagating Oscillatory Shock (POS) Model*

Observation and prediction of the possible origin of low frequency QPOs have been done in many articles. It was proposed [13, 15, 18, 63] that QPOs are due to oscillation of standing or propagating shock waves near the near edge of a transonic (advective) flow. The frequency of the QPO ($\nu_{QPO}$) is inversely proportional to the infall time ($t_{infall}$) scale in the post shock region. It has been noticed that type-C QPOs are generally observed in hard and hard intermediate spectral states of the rising or the declining phases of an outburst, and the frequency of these QPOs evolves as the outburst progresses. Type-A or B QPOs are sporadically observed generally in the soft-intermediate spectral states [25, 27, 67]. In [18, 63], they proposed that, the shock oscillations occur when resonance condition satisfies, i.e., when the cooling time scale of post-shock region roughly matches with the infall time scale. The shock oscillation may also happen due to the non-satisfaction of Rankine-Hugoniot [86] shock condition. This gives rise to type-A QPOs also. According to Chakrabarti et al. [18], less sharper i.e., low 'Q'-valued QPOs (types B and A) may also due to resonance phenomenon, either a weakly resonating CENBOL (type B) or a shockless centrifugal barrier (type A).

To study monotonic evolutions of the QPO frequencies during rising and declining (HS & HIMS) of an outburst of a black hole candidates, Chakrabarti and his collaborators have introduced a model, namely propagating oscillatory shock (POS) model in 2005 [16, 17, 26, 27, 67]. According to POS model, in rising phase, with the increasing rate of soft Keplerian matter the shock strength decreases as outburst progresses and the post-shock region starts to shrink (i.e. shock moves inwards to the black hole), resulting in a monotonic increase in QPO frequency.

In the declining phase, the opposite scenario occurs and the QPO frequencies monotonically decreases as shock recedes. The basic governing equations of POS model [16, 17] are as follows.

The instantaneous measure of the QPO frequency ($\nu_{QPO}$ in Hz) is

$$\nu_{QPO} \sim t_{infall}^{-1} = \frac{\nu_{s0}}{R[X_s(X_s-1)^{1/2}]} = \frac{c^3}{2GM_{BH}} \frac{1}{[RX_s(X_s-1)^{1/2}]}. \quad (4)$$

For a black hole of mass $M_{BH}$, $\nu_{s0}$=$c/r_s$=$c^3/2GM_{BH}$ denotes the inverse of the light crossing time (in $s^{-1}$), and $c$ is the velocity of light.

The shock strength $\beta$ is defined as

$$\beta = 1/R = 1/R_0 \pm t_d^2\alpha. \quad (5)$$

'$R_0$' represents the value of compression ratio ($R$) on the 0th (first) day, the time in days is denoted by $t_d$. $\alpha$ is a constant number, which accounts for the strength of $R$ (i.e. how it becomes stronger or weaker) during QPO evolution period.

The instantaneous shock location is defined as,

$$X_s(t) = X_{s0} \pm Vt/r_s, \quad (6)$$

where, $X_{s0}$ is the shock location ($X_s$) on the first observation and $r_s = 2GM_{BH}/c^2$ is the Schwarzschild radius.

Acceleration or deceleration could be present in the shock movement. The instantaneous shock velocity is formulated as,

$$V(t) = V_0 \pm ft_d, \quad (7)$$

where, $V_0$ represents the velocity of the first observation (0th day) and the acceleration/deceleration of the shock is denoted by '$f$'. The '$\pm$' sign symbolizes the accelerating or decelerating shock respectively.

The study of the evolution of the QPO frequency with the POS model has been done for several objects [16, 17, 26, 27, 67]. By fitting evolution of the QPO frequencies with the POS equations, one can estimate instantaneous shock parameters ($X_s$ and $R$), velocity, etc. One can also estimate mass of the black hole from Eq. (4). In [3, 19, 61] masses of Galactic black hole candidates MAXI J1659-152, MAXI J1543-564 and H 1743-322 respectively are measured with the POS model fitted QPO frequency evolution studies. The error limits i.e., probable ranges of the measured masses could be estimated from the POS model fitted $M_{BH}$ vs. $\chi^2_{red}$ parabolic variations (For example, see Molla et al. [61] and Chatterjee et al. [19]). Figures 2 and 3 [19] show the POS model fitted QPO evolution and $M_{BH}$ vs. $\chi^2_{red}$ variations for black hole candidate MAXI J1543-564 during the rising phase of its 2011 outburst.

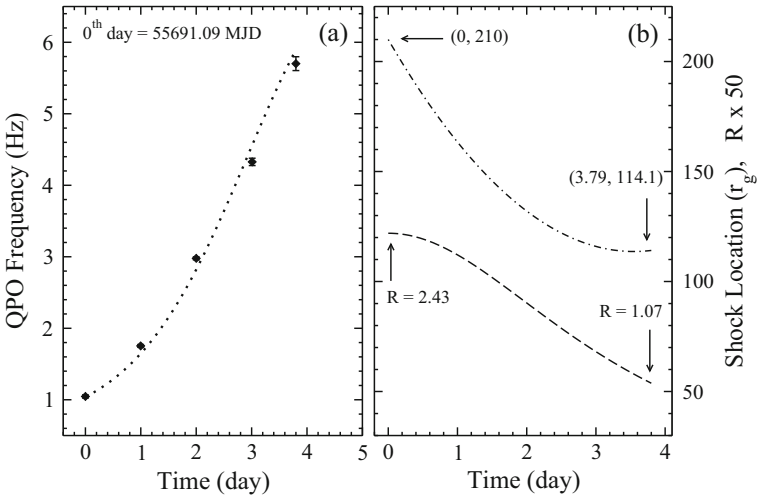



**Fig. 2** Variation of (**a**) type-C QPO frequency with day, (**b**) shock location and compression ratio from POS model (adapted from [19])

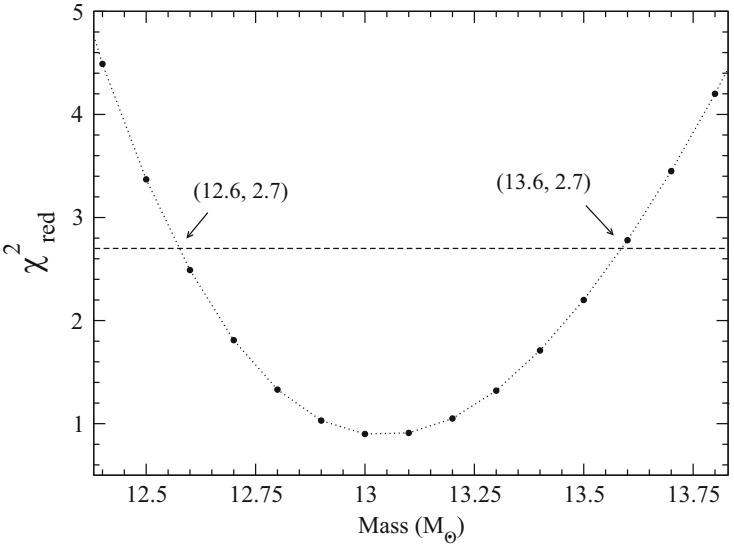



**Fig. 3** POS model fitted $\chi^2_{red}$ with variation of mass allows to predict probable mass range (90% confidence) if we restrict ourselves to $\chi^2_{red} \leq 2.7$ (adapted from [19])

### 3.4 Two Component Advective Flow (TCAF) Model

Chakrabarti and Titarchuk [14] came up with an accurate model to explain the physical processes occurring around the accretion disk which is known as the Two Component Advective Flow (TCAF) solution. They proposed two component in the flow categorized by the value of viscosity parameter $\alpha$. For a lower viscosity parameter value ($\alpha < \alpha_{cr}$), the flow becomes subsonic and moves with a significant amount of radial velocity. This is called the *sub-Keplerian* component. The other component consists of high angular momentum and high viscosity ($\alpha > \alpha_{cr}$) matter. Here, $\alpha_{cr}$ is a critical viscosity parameter. This component is optically thick in nature and moves very slowly (in viscous time scale) towards the black hole. The sub-Keplerian matter gains its velocity approaching towards the event horizon till the centrifugal force makes the flow stop suddenly and forms the shock wave due to piling up of matter. The post-shock region is called the CENtrifugal pressure dominated BOundary Layer (or CENBOL). This post-shock region is geometrically thick and very hot in nature. It acts as the 'hot Compton cloud', where soft photons from the Keplerian disk gain their energy and become hard by inverse-Comptonization process. The flow in the accreting matter continues its journey towards the event horizon and enters the black hole supersonically. The Keplerian disk is the origin of lower energy multicolor black body spectrum. The CENBOL region contributes to the higher energy part of the spectrum. CENBOL is also considered as the base of outflows and jet emission [11, 12]. In 2014, this solution has been included as an additive table model into HEASRAC's spectral analysis software package XSPEC to fit energy spectra of black holes [28, 29]. Basically one needs to supply four input flow parameters (two types of accretion rates: disk rate and halo rate; two types of shock parameters: shock location and compression ratio) to fit one spectrum with the TCAF solution if mass and model normalization (which are supposed to be constant for a known source) values are known. The model normalization is a function of mass of the black hole, distance of the system from the observer, and inclination angle of the system. So, for a non-precessional black hole this normalization must be almost constant if observed by a given instrument. Recently, Jana et al. [44] showed if deviation of the constancy of the model normalization is seen, then it could be due to extra contribution of X-rays coming from jets or outflows.

If mass of the black hole is not known, then from the best fitted spectrum, one can estimate it, since it is an important model input parameter while fitting spectrum with the TCAF model *fits* file in XSPEC. Each spectral fit with the TCAF solution, gives us one best fitted mass of the black hole. It may vary in a narrow range for a number of fitted spectrum of one black hole, since it is a measured quantity. So it must contain errors due to various factors. For example, instrumental errors in observations should not be same on every day. Also, mass of the black hole is proportional to the fourth power of the disk temperature ($M_{BH} \sim T^4$), and in TCAF solution, the spectral fits are highly sensitive to the temperature $T$, a small error in determination of T gives rise to a significant error in $M_{BH}$. Beside of all these

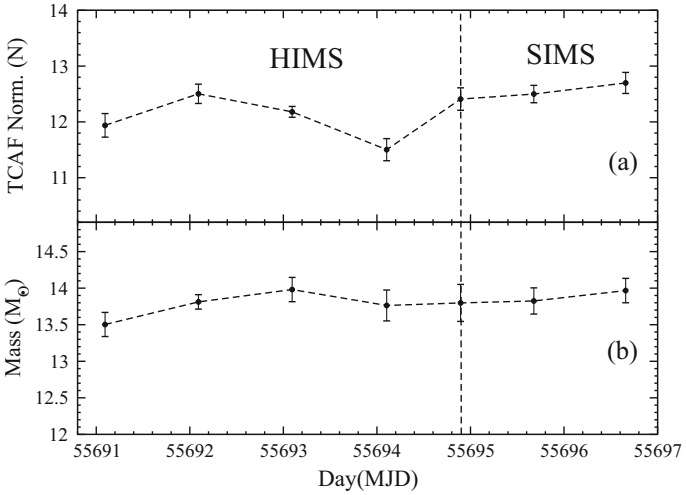



**Fig. 4** Variations of the mass and TCAF normalization with days for MAXI J1543-564 (adapted from [19]

error contributing factors, by taking average of the fitted mass values from different observations, one may get a good estimation of the probable value of the mass of a black hole and also its range, which are basically the lower and the upper limits of the observed mass values from different observations.

Recently, Debnath and his collaborators have been successfully estimated masses of a few black holes, such as MAXI J1659-152, MAXI J1836-194, MAXI J1543-564, H 1742-322, Swift J1753.5-0127, XTE J1118+480, Cygnus X-1 [19, 20, 30, 43, 61, 62] from spectral analysis with the TCAF solution. Variations of the mass and TCAF normalization are shown in Fig. 4 for MAXI J1543-564 for its 2010 Outburst (Details are in [19]).

## 4 Discussion and Concluding Remarks

Dynamical measurement of mass is the most direct method for estimating mass of any binary system provided the companion object is bright and not so distant for determination of its orbital period and the radial peak velocity. The information of the mass of the companion and the inclination of the system give a fair estimation of the other (primary) objects mass. Other indirect methods based on spectral and timing analysis, do not have these constraints. Although, measurement of mass from spectral results by phenomenological *diskbb* model is not so reliable because of it is not based on the physical properties of the black hole accretion processes. In contrast, QPO-photon index correlations model's advantage compare to dynamical measurement is that the source need not to be bright and nearby. However, to

estimate the mass from this method, the black hole under study must have a clear index-QPO correlation up to the saturation level, and the correlation must be similar to that of the reference known black hole candidate. The mass of the reference black hole must be known. These information are very rarely available in literature, and so it is the limitations of this method. On the other hand, POS model is free from such problems. Although, the origin of some QPOs may be different from that proposed by the POS model, observation of monotonic evolution of QPOs on a daily basis can give a rough estimate of the mass of the black hole. On the other hand, measurement of the mass of a black hole from the spectral analysis using TCAF solution is not constrained by QPO observation. Each spectral fits gives one best fitted mass value for the black hole. Analyzing the spectral properties of a few observations is enough to predict the mass of the black hole within a narrow range. TCAF model has successfully estimated the masses of several black holes (H 1743-322, MAXI J1659-152, MAXI J1836-194, MAXI J1543-564, Swift J1753.5-0127, XTE J1118+480, Cygnus X-1) beside studying physical explanations of their accretion flow dynamics.

H 1743-322 is a black hole candidate which showed X-ray outbursts in 1 or 2 years interval. The mass of H 1743-322 was not been measured dynamically. Petri [76] estimated the mass of the black hole from high frequency QPO model to be in the range of 9–13 $M_{\odot}$. McClintock et al. [59] measured the inclination of the system to be $\theta = 75 \pm 3°$. The distance of the system is reported by Steiner et al. [93] as $8.5 \pm 0.8$ kpc. Using the photon index ($\Gamma$)-QPO frequency correlation method [90] predicted the mass of H 1743-322 to be $13.3 \pm 3.2\ M_{\odot}$. They used RXTE PCA data of 2003 outburst and took GX 339-4 as the reference black hole of known mass. Debnath et al. [27] studied the spectral and temporal properties of 2010 and 2011 X-ray activities for this black hole candidate using disk blackbody (*DBB*) and powerlaw *PL* model. Molla et al. [62] investigated both 2010 and 2011 outbursts by restricting the normalization parameter to a narrow range, which has been varied in the previous work on this source of its 2010 outburst by Mondal et al. [65]. They predicted the mass of the black hole from this two consecutive outburst to be 9.25–12.86 $M_{\odot}$. They also estimated the mass using spectral and temporal correlation method (described in Sect. 3.2 or see Shaposhnikov and Titarchuk [90] for this source) to be $11.65 \pm 0.67\ M_{\odot}$ using GRO J1655-40 as a reference source. Combining these two methods, they estimated the most probable mass of the source to be $11.21^{+1.65}_{-1.96}\ M_{\odot}$ (For details, see Molla et al. [62]). Recently, Bhattacharjee et al. [3] follow the same constant normalization technique as described in Molla et al. [61] to estimate the mass of H 1743-322 for its 2004 outburst. The measured the mass range to be $10.31–14.07 M_{\odot}$. They also verified this estimated mass from POS model Eq. (4) (see Sect. 3.3) for two observations.

MAXI J1659-152 is another transient black hole candidate, which has been studied in multi-wavelength. The dynamical mass measurement for this source has not been done yet, although there are several predictions of its mass. Kennea et al. [46] estimated its mass to be in the range $2.2–3.1 M_{\odot}$ where Yamaoka et al. [102] predicted that to be $3.6–8.0 M_{\odot}$. The orbital period of this source has been estimated as $\sim$2.42 h [51, 52]. They also predicted the mass of the companion as

0.15–0.25$M_\odot$. Shaposhnikov et al. [91] measured the mass to be $20 \pm 3$ $M_\odot$. Molla et al. [61] estimated the mass of this source using two methods: TCAF model fitted constant normalization method (4.7–7.8$M_\odot$) and from POS model (5.1–7.4$M_\odot$) by studying the QPO evolution. From these two methods, the estimates of the most probable mass of MAXI J1659-152 appears to be 4.7–7.8$M_\odot$ or $6^{+1.8}_{-1.3}$ $M_\odot$, which is in a narrow range.

The mass of transient black hole candidate MAXI J1836-194 has been suggested by Russel et al. [85] from spectroscopic study to be in the range 4–12$M_\odot$. They also predicted the distance of the system to be 4–10 kpc. The mass and radius of the companion star are computed as $<0.65M_\odot$ and $<0.59$ $R_\odot$. Cenko et al. [10] predicted this system as a high mass X-ray binary with a high massive Be star. The spin parameter suggested for this source by Reis et al. [81] is $a = 0.88 \pm 0.03$. Jana et al. [43] find the mass of this source to be in the range of 7.5–11$M_\odot$ from the spectral study using TCAF solution.

MAXI J1543-564 is a transient black hole candidate, which has been poorly studied because of its faintness. The companion of this candidate is not confirmed due to the fact that there is no significant variation in the optical spectrum [84]. Stiele et al. [94] reported a minimum distance of the source to be 8.5 kpc during its 2011 outburst. Chatterjee et al. [19] predicted the probable mass of this black hole candidate from the spectral and temporal properties to be in the range of 12.6–14.0$M_\odot$.

Transient black hole candidate Swift J1753.5-0127 is one of the sources which exhibits a long active period. The orbital period is predicted to be ∼2.85 h [68] to ∼3.2 h [103]. The mass of the primary and the companion are also reported by them to be $<5$ $M_\odot$ and 0.17–0.25$M_\odot$. The disk inclination is suggested to be $>40°$. Shaw et al. [92] suggested even bigger mass ($>7.4$ $M_\odot$) for this black hole candidate. The donor star is predicted to be a K or M spectral type main sequence star [4]. The distance of this source is estimated as 4–8 kpc [4]. On the other hand, Froning et al. [33] predicted the distance to be $<3.7$ kpc for inclination of $i = 55°$ or $<2.8$ kpc for inclination of $i = 0°$. Debnath et al. [30] investigated the accretion flow properties of this source during its 2005 outburst. They classified and explained the state transition during this 2005 outburst and also estimated the probable mass of this black hole to be 4.75–5.90 $M_\odot$ or $5.35^{+0.55}_{-0.60}M_\odot$. Recently, Jana et al. [44] extracted the contribution of jet using the TCAF solution.

XTE J1118+480 is one of the widely studied Galactic transient black hole binary (BHB) for its unique location in the Galactic halo. Due to its location in Lockman Hole, this source suffers very low interstellar absorption and for this reason, it is an interesting object to extensively study in multi-wavelength. The optical counterpart has been identified by Uemura et al. [97] and the source was categorized as a typical X-ray novae in outburst [34]. Optical observation near its quiescent state reveals a higher mass function, $f(M) = 6.1 \pm 0.3$ $M_\odot$ [99], confirmed it as a black hole. Mass of this source is estimated as 6.0–8.2 $M_\odot$ [48, 99]. The distance of this source is measured to be $1.8 \pm 0.6$ kpc [58, 99]. The companion is reported as a K5 V-M0 V spectral type dwarf star of mass 0.09–0.5 $M_\odot$ [99]. This is suggested to be a low mass X-ray binary system with a short orbital period of

4.1 h [22, 75]. This BHB is also identified as a highly inclined (68–79°) system [48]. Quasi Periodic Oscillations have been found in its Power Density Spectrum (PDS) in X-ray, optical, and IR wavebands [37, 101]. Several groups [21, 54, and references therein] have studied this source in multiwavelength. Chatterjee et al. [20] studied the spectral and temporal properties of this source during its 2000 outburst using TCAF solution. From the variation of normalization parameter they extracted the X-ray jet parameters during that period. They conclude the 'outburst' to be an abnormal X-ray activity induced by jet. They also estimated the probable range of the mass of the black hole to be 6.25–7.49$M_{\odot}$ or $6.99^{+0.50}_{-0.74}$ $M_{\odot}$ (Table 1).

**Table 1** Mass of some Galactic black holes

| Name | Mass | References |
|---|---|---|
| GRO J0422+32 | 3–5 | [5, 35] |
| | $>9M_{\odot}$ | [1, 7, 31, 83, 100] |
| 1A 0620-00 | $6.60 \pm 0.25$ | [6, 49] |
| | 10 | [87] |
| 4U 0538-641 | $6.95 \pm 0.33$ | [71] |
| 4U 0540-697 | $10.91 \pm 1.41$ | [74] |
| 4U 1543-475 | >3 | [69, 70] |
| | 8.45–10.39 | [53, 74] |
| Cyg X-1 | $14.8 \pm 1$ | [72] |
| GRO J1655-40 | $5.4 \pm 0.3$ | [2, 38] |
| GRS 1009-45 | $5.95 \pm 0.89$ | [41, 49] |
| GRS 1915+105 | 12.4 | [80] |
| | $14 \pm 4$ | [40] |
| GS 1124-684 | 6.47–8.18 | [8, 49, 53] |
| GS 1354-64 | 7.47 | [8, 9, 49, 53] |
| GS 2000+251 | 7.2–7.8 | [7, 31] |
| GX 339-4(1H 1659-487) | $\geq 6$ | [42, 66] |
| H 1705-250 | 5.64–8.30 | [82] |
| H 1743-322 | 9.25–12.86 | [62] |
| | 10.31–14.07 | [3] |
| | 9–13 | [76] |
| MAXI J1543-564 | 12.6–14 | [19] |
| MAXI J1659-152 | 4.29–7.93 | [61] |
| | 2.2–3.1 | [46] |
| | 3.6–8 | [102] |
| MAXI J1836-194 | 7.5–11 | [43] |
| Swift J1357.20933 | >9.3 | [24, 55] |
| Swift J1753.5-0127 | 4.7–5.7 | [30] |
| V404 Cyg | $12 \pm 2$ | [87] |
| | 8.4–9.2 | [47] |
| XTE J1118+480 | 6.00–8.2 | [20, 36, 48, 99] |

(continued)

**Table 1** (continued)

| Name | Mass | References |
|---|---|---|
| XTE J1550-564 | 8.36–10.76 | [49, 53, 73] |
| XTE J1650-500 | $4.72 \pm 2.16$ | [39, 49, 53] |
| XTE J1859+226 | 10.83 | [23, 79, 90] |

References: [1] Beekman et al., [2] Beer et al., [3] Bhattacharjee et al., [5] Callanan et al., [6] Cantrell et al., [7] Casares et al., [8] Casares et al., [9] Casares et al., [19] Chatterjee et al., [20] Chatterjee et al., [23] Corral-Santana et al., [24] Corral-Santana et al., [30] Debnath et al., [31] Filippenko et al., [36] Gelino et al., [35] Gelino et al., [38] Hjellming and Rupen, [39] Homan et al., [40] Hurley et al., [42] Hynes et al., [41] Hynes et al., [43] Jana et al., [46] Kennea et al., [47] Khargharia et al., [48] Khargharia et al., [49] Kreidberg et al., [53] Liu et al., [55] Mata Sanchez et al., [61] Molla et al., [62] Molla et al., [66] Muñoz-Darias et al., [70] Orosz et al., [69] Orosz, [71] Orosz, [72] Orosz et al., [74] Ozel et al., [76] Petri et al., [79] Radhika and Nandi, [80] Reid et al., [82] Remillard et al., [83] Reynolds et al., [87] Shahbaz et al., [90] Shaposhnikov and Titarchuk, [99] Wagner et al., [100] Webb et al., [102] Yamaoka et al.

**Acknowledgements** I am highly indebted to my supervisors Dr. Dipak Debnath and Prof. Sandip K. Chakrabarti for their guidance and constant supervision as well as for providing necessary information regarding the review and also for their support in completing the review. I would also like to thank my departmental colleagues for their constant motivations and suggestions to complete this review. I acknowledge the support of DST/SERB sponsored Extra Mural Research project (EMR/2016/003918).

## References

1. Beekman, G., Shahbaz, T., Naylor, T., Charles, P.A., Wagner, R.M., Martini, P.: MNRAS **290**, 303 (1997)
2. Beer, M., Podsiadlowski, P.: MNRAS **331**, 351 (2002)
3. Bhattacharjee, A., Banerjee, I., Banerjee, A., Debnath, D., Chakrabarti, S.K.: MNRAS **466**, 1372 (2017)
4. Cadolle Bel, M., Ribó, M., Rodriguez, J., et al.: ApJ **659**, 549 (2007)
5. Callanan, P.J., Garcia, M.R., Filippenko, A.V., McLean, I., Teplitz, H.: ApJ **470L**, 57 (1996)
6. Cantrell, A., Bailyn, C., Orosz, J., et al.: ApJ **710**, 1127 (2010)
7. Casares, J., Martin, A.C., Charles, P.A., Martin, E.L., Rebolo, R., Harlaftis, E.T., Castro-Tirado, A.J.: MNRAS **276**, 35 (1995)
8. Casares, J., Martin, E.L., Charles, P.A., Molaro, P., Rebolo, R.: New Ast. **1**, 299 (1997)
9. Casares, J., Orosz, J.A., Zurita, C., et al.: ApJS **181**, 238 (2009)
10. Cenko, S.B., Miller, A.A., Bloom, J.S.: ATel **3614**, 1 (2011)

11. Chakrabarti, S.K.: A&A **351**, 185 (1999)
12. Chakrabarti, S.K.: Ind. J. Phys. **73B**(6), 931 (1999)
13. Chakrabarti, S.K., Manickam, S.G.: ApJ **531**, L41 (2000)
14. Chakrabarti, S.K., Titarchuk, L.G.: ApJ **455**, 623 (CT95) (1995)
15. Chakrabarti, S.K., Acharyya, K., Molteni, D.: A&A **421**, 1 (2004)
16. Chakrabarti, S.K., Nandi, A., Debnath, D., et al.: IJP **79**, 841 (2005). arXiv:astro-ph/0508024
17. Chakrabarti, S.K., Debnath, D., Nandi, A., et al.: A&A **489**, L41 (2008)
18. Chakrabarti S.K., Mondal, S., Debnath, D.: MNRAS **452**, 3451 (2015)
19. Chatterjee, D., Debnath, D., Chakrabarti, S.K., Mondal, S., Jana, A.: ApJ **827**, 88 (2016)
20. Chatterjee, D., Debnath, D., Chakrabarti, S.K., Jana, A.: ApJ (2018, in communication)
21. Chaty, S., Haswell, C.A., Malzac, J., Hynes, R.I., Shrader, C.R., Cui, W.: MNRAS **346**, 689 (2003)
22. Cook, L., Patterson, J., Buczynski, D., Fried, R.: IAUCirc, **7397**, 2 (2000)
23. Corral-Santana, J.M., et al.: Mon. Not. R. Astron. Soc. **413**, 15 (2011)
24. Corral-Santana, J.M., Casares, J., Munoz-Darias, T., Rodriguez-Gil, P., Shahbaz, T., Torres, M.A.P., Zurita, C., Tyndall, A.A.: Sci **339**, 1048 (2013)
25. Debnath, D., Chakrabarti, S.K., Nandi, A., Mandal, S.: BASI **36**, 151 (2008)
26. Debnath, D., Chakrabarti, S.K., Nandi, A.: A&A **520**, 98 (2010)
27. Debnath, D., Chakrabarti, S.K., Nandi, A.: AdSpR **52**, 2143 (2013)
28. Debnath, D., Mondal, S., Chakrabarti, S.K.: MNRAS **440**, L121 (2014)
29. Debnath, D., Mondal, S., Chakrabarti, S.K.: MNRAS **447**, 1984 (2015)
30. Debnath, D., Jana, A., Chakrabarti, S.K., Chatterjee, D., Mondal, S.: ApJ **850**, 92 (2017)
31. Filippenko, A.V., Matheson, T., Ho, L.C.: ApJ **455**, 614 (1995)
32. Fiorito, R., Markwardt, C., Swank, J.: BAAS **35**, 11.07 (2003)
33. Froning, C.S., Maccarone, T.J., France, K., et al.: ApJ **780**, 48 (2014)
34. Garcia, M., Brown, W., Pahre, M., McClintock, J., Callanan, P., Garnavich, P.: IAUCirc **7392**, 2 (2000)
35. Gelino, D.M., Harrison, T.E.: ApJ **599**, 1254 (2003)
36. Gelino, D., Balman, S., et al.: ApJ **642**, 438 (2006)
37. Haswell, C.A., Hynes, R.I., King, A.R., Stull, J., Ioannou, Z., Webb, N.A.: IAUCirc 7407 (2000)
38. Hjellming, R., Rupen, M.: Nature **375**, 464 (1995)
39. Homan, J., Wijnands, R., Kong, A., et al.: MNRAS **366**, 235 (2006)
40. Hurley, D.J., Callanan, P.J., Elebert, P., Reynolds, M.T.: MNRAS **430**, 1832 (2013)
41. Hynes, R.I.: ApJ **623**, 1026 (2005)
42. Hynes, R.I., Steeghs, D., Casares, J., et al.: ApJ **583**, L95 (2003)
43. Jana, A., Debnath, D., Chakrabarti, S.K., et al.: ApJ **819**, 107 (2016)
44. Jana, A., Chakrabarti, S.K., Debnath, D.: ApJ **850**, 91 (2017)
45. Kalemci, E.: Ph.D. thesis, UC San Diego (2002)
46. Kennea, J.A., et al.: ApJ **736**, 22 (2011)
47. Khargharia, J., Froning, C.S., Robinson, E.L.: ApJ **716**, 1105 (2010)
48. Khargharia, J., Froning, C.S., Robinson, E.L., Gelino, D.M.: AJ **145**, 21 (2013)
49. Kreidberg, L., Bailyn, C., Farr, W., Kalogera, V.: ApJ **757**, 36 (2012)
50. Kubota, A., Tanaka, Y., Makishima, K., et al.: PASJ **50**, 667 (1998)
51. Kuulkers, E., et al.: Astron. Tel. **2912**, 1 (2010)
52. Kuulkers, E., et al.: A&A **552**, A32 (2013)
53. Liu, Q.Z., van Paradijs, J., van den Heuvel, E.P.J.: A&A **469**, 807 (2007)
54. Markoff, S., Falcke, H., Fender, R.: A&A **372L**, 25 (2001)
55. Mata Sanchez, D., Munoz-Darias, T., Casares, J., Corral-Santana, J.M., Shahbaz, T.: MNRAS **454**, 2199 (2015)
56. Mauche, C.: ApJ **580**, 423 (2002)
57. McClintock, J.E., Remillard, R.A.: In: Lewin, W.H.G., van der Klis, M. (eds.) Compact Stellar X-ray Sources, vol. 39, p. 157. Cambridge University Press, Cambridge (2006)

58. McClintock, J.E., Garcia, M.R., Caldwell, N., Falco, E.E., Garnavich, P.M., Zhao, P.: ApJL **551**, L147 (2001)
59. McClintock, J.E., Remillard, R.A., Rupen, M.P., et al.: ApJ **698**, 1398 (2009)
60. Mitsuda, K., Inoue, H., Koyama, K., Makishima, K., et al.: PASJ **36**, 741 (1984)
61. Molla, A.A., Debnath, D., Chakrabarti, S.K., et al.: MNRAS **460**, 3163 (2016)
62. Molla, A.A., Chakrabarti, S.K., Debnath, D.: ApJ **834**, 88 (2017)
63. Molteni, D., Sponholz, H., Chakrabarti, S.K.: ApJ **457**, 805 (1996)
64. Molteni, D., Tóth, G., Kuznetsov, O.A.: ApJ **516**, 411 (1999)
65. Mondal, S., Debnath, D., Chakrabarti, S.K.: ApJ **786**, 4 (2014)
66. Muñoz-Darias, T., Casares, J., Martínez-Pais, I.G.: MNRAS **385**, 2205 (2008)
67. Nandi, A., Debnath, D., Mandal, S., Chakrabarti, S.K.: A&A **542**, A56 (2012)
68. Neustroev, V.V., Veledina, A, Poutanen, J., et al.: MNRAS **445**, 2424 (2014)
69. Orosz, J.A.: IAUS **212**, 365 (2003)
70. Orosz, J.A., Jain, R.K., Bailyn, C.D., McClintock, J.E., Remillard, R.A.: ApJ **499**, 375 (1998)
71. Orosz, J., Steeghs, D., McClintock, J., et al.: ApJ **697**, 573 (2009)
72. Orosz, J.A., McClintock, J.E., Aufdenberg, J.P., et al.: ApJ **742**, 84 (2011)
73. Orosz, J., Steiner, J., McClintock, J., et al.: ApJ **730**, 75 (2011)
74. Ozel, F., Psaltis, D., Narayan, R., McClintock, J.: ApJ **725**, 1918 (2010)
75. Patterson, J.: IAUCirc **7412**, 2 (2000)
76. Petri, J.: Ap&SS **318**, 181–186 (2008)
77. Pringle, J., Rees, M.J.: A&A **21**, 1 (1972)
78. Psaltis, D., Belloni, T., van der Klis, M.: ApJ **520**, 262 (1999)
79. Radhika, D., Nandi, A.: AdSpR **54**, 1678 (2014)
80. Reid, M., McClintock, J., Steiner, J., et al.: ApJ **796**, 2 (2014)
81. Reis, R.C., Miller, J.M., Reynolds, M.T., et al.: ApJ **751**, 34 (2012)
82. Remillard, R.A., Orosz, J.A., McClintock, J.E., Bailyn, C.D.: ApJ **459**, 226 (1996)
83. Reynolds, M.T., Callanan, P.J., Filippenko, A.V.: MNRAS **374**, 657 (2007)
84. Russell, D., Lewis, F., Roche, P., et al.: ATel **3359**, 1 (2011)
85. Russell, T.D., Soria, R., Miller-Jones, J.C.A., et al.: MNRAS **439**, 1390 (2014)
86. Ryu, D., Chakrabarti, S.K., Molteni, D.: ApJ **474**, 378 (1997)
87. Shahbaz, T., Ringwald, F.A., Bunn, J.C., Naylor, T., Charles, P.A., Casares, J.: MNRAS **271**, L10 (1994)
88. Shakura, N.I., Sunyaev, R.A.: Astron. Astrophys. **24**, 337 (1973)
89. Shaposhnikov, N., Titarchuk, L.: ApJ **663**, 445 (2007)
90. Shaposhnikov, N., Titarchuk, L.: ApJ **699**, 453 (2009)
91. Shaposhnikov, N., Swank, J.H., Markwardt, C., Krimm, H.: Astrophysics (2011). Preprint. arXiv:1103.0531
92. Shaw, A.W., Charles, P.A., Casares, J., et al.: MNRAS **463**, 1314 (2016)
93. Steiner, J.F., McClintock, J.E., Reid, M.J.: ApJL **745**, L7 (2012)
94. Stiele, H., Munoz-Darias, T., Motta, S., Belloni, T.M.: MNRAS **422**, 679 (2011)
95. Titarchuk, L., Fiorito, R.: ApJ **612**, 988 (2004)
96. Titarchuk, L., Lapidus, I., Muslimov, A.: ApJ **499**, 315 (1998)
97. Uemura, M., et al.: PASJ **52**, L15 (2000)
98. Vignarca, F., Migliari, S., Belloni, T., Psaltis, D., vander Klis, M.: A&A **397**, 729 (2003)
99. Wagner, R.M., Foltz, C.B., Shahbaz, T., Casares, J., Charles, P.A., Starrfield, S.G., Hewett, P.: ApJ **556**, 42 (2001)
100. Webb, N.A., Naylor, T., Ioannou, Z., Charles, P.A., Shahbaz, T.: MNRAS **317**, 528 (2000)
101. Wood, K.S., et al.: ApJL **544**, L45 (2000)
102. Yamaoka, K., et al.: PASJ **64**, 32 (2012)
103. Zurita, C., Torres, M.A.P., Durant, M., et al.: ATel **1130**, 1 (2007)

# Disk-Jet Connection in Black Holes




**Arghajit Jana**

**Abstract** It is well established that the accretion disk and jet are coupled. Jet and accretion disk arise self-consistently from any transonic flow solution and clearly from its generalized version, the two-component advective flow (TCAF) solution. Observationally, strong signatures of disk-jet connections are seen for many black hole binaries. The nature and evolution of jets depend on accretion flows. Correlation between X-ray and radio fluxes is also seen, which indicates a coupling between accretion disk and jet. In this review, we discuss developments of theoretical models to describe the origin of the jets or outflows and the nature of the disk-jet coupling on the basis of the transonic flows around black holes. Then we discuss the observational evidences of the disk-jet connections.

## 1 Introduction

Astrophysical jets are examples of some of the extreme physical processes in the universe. They are generally observed in systems like black holes (BH), neutron stars and protostars. Most powerful jets are associated with active galactic nuclei (AGN), where super massive black holes act as central engines. Jets are ubiquitous but it is still not clear how they are produced, collimated and accelerated. Several theoretical models were introduced to explain the jets. It is clear that accretion disk and jets are connected. In this review, we will discuss the connection between the accretion and jets on the basis of transonic flows. Observational signatures of disk-jet coupling will be presented. The jet intensity variations in terms of accretion rates and spectral states will be discussed. The nature (compact or blobby) of the jets or outflows from our analysis will also be discussed.

A. Jana (✉)
Indian Centre for Space Physics, Kolkata, India

© Springer International Publishing AG, part of Springer Nature 2018

B. Mukhopadhyay, S. Sasmal (eds.), *Exploring the Universe: From Near Space to Extra-Galactic*, Astrophysics and Space Science Proceedings 53,
https://doi.org/10.1007/978-3-319-94607-8_23

## 2 Disk-Jet Solution in Transonic Flow

It is well accepted that jets are coupled with accretion disks around black holes. They are produced from the inflowing accreting matter from the companion. Hence, it is very important to understand the nature of the accretion flow from physical point of view. Accretion disk and jet are the transonic solutions of the same set of equation with opposite boundary conditions. Early theory of an accretion disk did not include jets or outflows [7, 83]. In Shakura-Sunyaev standard (SS73) disk model, viscosity was introduced to remove the angular momentum, so that matter can fall into the black hole. Later, it is realized that jet or outflow can extract angular momentum from the accretion in a very efficient way. Magnetized disk was considered to be the origin of the jet. Since 1973, some theoretical models were developed to explain various observational properties of accretion disks [2, 3, 86, 87]. Some models were also introduced to explain jets based on hydrodynamic or hydromagnetic framework [5, 6, 92]. It is generally accepted that magnetic field is responsible for the collimation of jets [8, 22].

### *2.1 Transonic Flow Solution*

Study of jets and outflows in the context of accretion is not new. Wind solution arises in a self-consistent way from the spherical Bondi accretion flow. Charkabarti [9] presented a rotating wind solution. Standing shock solution of rotating isothermal accretion and wind were studied for dissipative [14, 15] and non-dissipative flows [10–12, 14, 16]. Both axisymmetric [1, 10–13] and non-axisymmetric shock solution for accretion and wind were studied for rotating adiabatic flows [17].

In 1992, Chakrabarti and Bhaskaran [22] showed that the jets can be produced easily with the low angular momentum sub-Keplerian flow than from a Keplerian disk. They showed that it is possible to obtain a collimated bipolar jets and outflows from a magnetized disk in a self consistent way. Chakrabarti and D'Silva [23, 47] studied magnetized thick disk in detail and they showed that the toroidal magnetic flux tube could be the reason behind the collimation of jets. This is also shown by numerical simulation [40] and A. Deb (this volume). Nandi et al. [75] explained blobby jets with the magnetic rubber band effect based on transonic flow solution.

### *2.2 Accretion-Jet Coupling*

In mid-90s, Chakrabarti and his collaborators introduced the most generalized accretion flow solution based on transonic flow solution [18, 24]. The proposed *'two components advective flow' (TCAF)* solution is quite successful to explain various temporal and spectral properties observed in the black hole X-ray binaries

[4, 21, 27–29, 42–45, 55, 70, 72–74]. TCAF also can explain disk-jet connection observed in black holes [56, 57].

Evolution of jet is strongly related to the spectral states (please see, Chakrabarti [21] for a recent review). During a typical outburst, generally a type-I or classical black hole goes through several spectral state transition in the sequence as: hard (HS) → hard-intermediate (HIMS) → soft-intermediate (SIMS) → soft (SS) → soft-intermediate (SIMS) → hard-intermediate (HIMS) → hard (HS) (see, [41, 78] and references therein). Different types of jets are observed in different spectral states. The evolution of jets and their properties could be well explained with the TCAF solution. The spectral states are generally controlled by the accretion rates and the properties of the shocks. In the hard state, the sub-Keplerian flow is dominated over the Keplerian disk. A strong shock is formed at centrifugal barrier. The post-shock region is known as the CENBOL (CENtrifugal pressure supported BOundary Layer). CENBOL is 'hot' and puffed-up region of the advective flow. It also acts as the base of the jet. Soft photons from the Keplerian disk become hard due to inverse Comptonization inside the CENBOL. In the soft state, more Keplerian matter comes in and cools down the CENBOL. Hence, soft radiation dominates in the observed spectra. In between, source stays in the intermediate states, i.e. in the HIMS and the SIMS.

The evolution of jets with the spectral states were studied extensively [25, 76, 90, 91]. In the hard state, above CENBOL, the outflowing matter moves subsonically up to the sonic surface, before moving away in supersonic speed. In the HS, compact or continuous jets are observed. In the intermediate states, more matter comes in, resulting cooling of CENBOL. As a result of temperature drop, subsonic matter near the sonic surface suddenly becomes supersonic. The supersonic matter separates from the CENBOL and moves away. In the intermediate state (HIMS and SIMS), we may observe discrete ejections or blobby jets. In the soft state, more Keplerian matter comes in and cools down the CENBOL completely. Hence, the jet is quenched.

## 2.3 *Outflow Rate*

Chakrabarti and his collaborators showed that the radiative pressure is sufficient to launch and accelerate the jet from low to moderate Lorentz factors [19, 20, 39]. They have calculated the outflow rate from the inflow rate with the TCAF solution. Chakrabarti [19] showed that the mass outflow rate can be calculated from the inflow rate i.e. accretion rate and shock strength. The outflow rate is given by (Eqn. 16 of Chakrabarti [19]).

$$R_{\dot{m}} = \frac{\dot{M}_{out}}{\dot{M}_{in}} = \frac{\theta_{out}}{\theta_{in}} \frac{R}{4} \left(\frac{R^2}{R-1}\right)^{3/2} \exp\left(\frac{3}{2} - \frac{R^2}{R-1}\right), \tag{1}$$

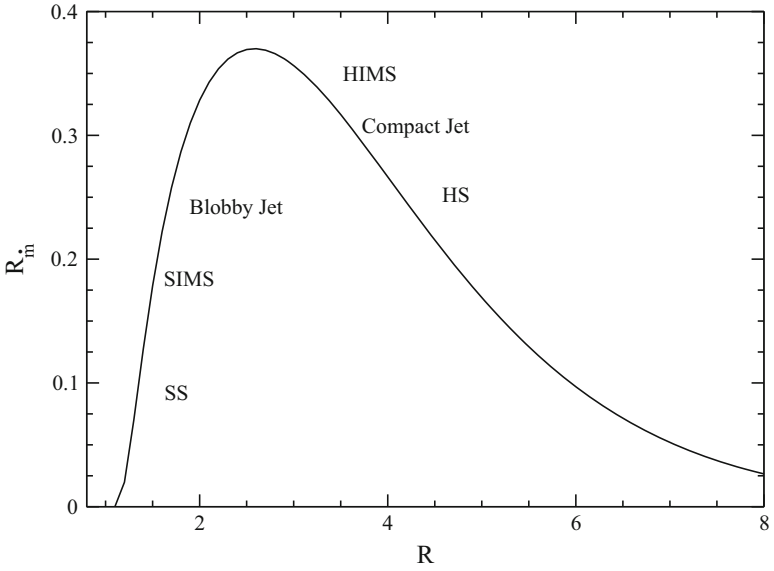



**Fig. 1** Variation of the ratio between outflow and inflow rates ($R_{\dot{m}}$) as a function of the compression ratio at the shock $R$ is shown [19]. It shows a peak at intermediate shock strength. Adapted from [19, 56]

where, $\dot{M}_{out}$ and $\dot{M}_{in}$ are the mass outflow and accretion rate respectively. $\theta_{out}$ and $\theta_{in}$ are the solid angle subtended by outflowing and inflowing matter respectively. $R$ is the shock compression ratio. In Fig. 1, we plot $R_{\dot{m}}$ as a function of $R$. For simplicity, we assume $\theta_{out} = \theta_{in}$. From Fig. 1, we see $R_{\dot{m}}$ is maximum when the shock is not strongest, rather it has intermediate strength. From observational point of view, $R_{\dot{m}}$ is maximum in the intermediate states and not in the hard state. In the intermediate state, accretion rate ($\dot{M}_{in}$) increases, thus outflow rate ($\dot{M}_{out}$) will also increase (see also, [25]). Precisely this is observed in black holes which will be discussed in Sect. 3 in details.

## 3 Observation of Disk-Jet Connection

A possible jet was first time observed in M87 back in 1918 in optical wavebands. Heber Curtis of Lick Observatory reported that "curious straight rays, which were apparently connected with the nucleus by a thin line of matter." [30]. Later, with the emerging of radio astronomy, several active galactic nuclei (AGN) were discovered and they exhibited strong radio jets. Later, jets were observed in other wavebands too.

### 3.1 Jets in Galactic Stellar Mass Black Holes

Radio jets are common features in AGNs. However, jets have not been observed in Galactic black holes until 1992 when it was observed in Galactic stellar mass black hole 1E 1740.7-2942 for the first time [69]. Galactic black hole X-ray binaries mimic several properties of AGN in smaller length scale and shorter timescale. AGN jets have length scale about $\sim Mpc$, where Galactic black holes exhibit jet up to about $1 - 3$ pc. Soon after the discovery of two-sided radio jets in 1E 1740.7-2942, GRS 1758-258 is also reported to have radio jets [80]. These Galactic black holes showed relativistic jets in much smaller scale (0.02–0.06 pc) than AGN. GRS 1915+105 [68], GRO J1655-40 [54, 88] are also observed to exhibit superluminal jet which is very common in AGN. Another type of jet is observed in Galactic black holes with very small scale $\sim 10^{-4}$ pc. They are called compact jet. In general, two types of jets are observed in Galactic black holes: continuous or *compact jet* and discrete ejection or *blobby jet*.

Compact radio jets have been detected in many Galactic black holes such as, GRS 1915+105 [46], Cygnus X-1 [85]. SS 433 is known to have blobby jet with blobs moving at a speed of 0.26c ([25, 26, 77] and references therein). GRS 1915+105 is also observed to have discrete ejections [50].

Traditionally jets are observed in radio wavebands. However, AGN showed jets in optical, UV and X-ray band. X-ray jet study became popular after the launch of Chandra satellite. Chandra observation discovered several black holes jets with X-rays. A large scale X-ray jet is observed in BHC XTE J1550-564 [32, 33, 61, 89]. Corbel et al. [32, 33] showed that the jet in XTE J1550-564 is relativistic and decelerating. The radio blobs are ejected at relativistic speed with emitting X-rays. Similar types of jets were observed in H 1743-322 [36]. They observed that the radio blobs were moving away from the black holes with ATCA observation. Later, Chandra observation discovered the X-ray emission associated with the radio blobs. Kaaret et al. [62] reported a similar jet was observed in 4U 1755-33 with size 3–8 kPc. This is larger than those in XTE J1550-564 and H 1743-322. High energy $\gamma$-ray jets are observed in Cygnus X-1 [60, 65] and in the recent outburst of V 404 Cyg [66].

### 3.2 Correlation of Jets in Different Wavebands

Base of the jet is a 'hot' region, hence it emits in the X-ray via inverse-Comptonization of the soft photons from Keplerian disk or via synchrotron cooling. As the jet moves away from the central black hole, its temperature falls due to adiabatic expansion. Hence, it emits photons in low energy wavebands, i.e., in UV, optical, IR and radio. Since, the same jet emits radiations in IR, radio and in X-ray, we can expect a correlation among them. A strong correlation between IR and radio is found in GRS 1915+105 [48]. Eikenberry et al. [48] observed that IR

flux is delayed by 30 min from X-ray flux. Fender et al. [49] found radio and IR correlation for this black hole. They found radio is delayed by 7 or 33 min. The delay is expected since emitting region of X-ray, IR and radio are at the different locations of the jet. Eikenberry et al. [48] also confirmed that IR and radio is synchrotron emission from the jet. A similar observation was also reported by Lasso-Cabrera and Eikenberry [64].

### *3.3 X-Ray/Radio Correlation*

Traditionally, it is assumed that the radio flux is emitted from the jet while the tracer of the accretion disk is X-ray flux. Empirically, a correlation between radio ($F_R$) and X-ray ($F_X$) fluxes has been observed in the form,

$$F_R \sim F_X^b, \tag{2}$$

where $b$ is the correlation index. Hannikainen et al. [53] first observed the correlation between radio and X-ray flux in GX 339-4. Corbel et al. [31, 34] reported the correlation between radio and X-ray fluxes with correlation index $b$ ∼0.6–0.7 for GX 339-4. This correlation study was extended with a larger sample of black holes. The correlation index was found to be ∼0.7 [51]. The correlation with an index of 0.6–0.7 is called the 'standard correlation'. The correlation study is extended to the quiescent state for V404 Cyg, A 0620-00 and GX 339-4 [34, 37, 51, 52]. Remarkably, the same relation is obtained over a large range of X-ray luminosities in some of these BHCs.

This correlation index was thought to be universal. However, later a steeper correlation with powerlaw index ∼1.4 is observed in many black holes such as XTE J1908+094 [58], H 1743-322 [38] in hard state. These black holes are radiatively efficient or radio-quite sources. Some black holes are observed to follow dual correlation track. Galactic black holes such as GRO J1655-40 [35], H 1743-322 [38], MAXI J1659-152 [59], XTE J1752-223 [79] are observed to lie in the steeper correlation track (i.e. $b \sim 1.4$) in the hard state, however they move to the standard correlation track (i.e. $b \sim 0.6$–0.7) when the source enters into the quiescent or low X-ray luminosity state. This indicates that the quiescent state is radiatively inefficient.

However, later a few black holes were discovered to have other correlation indexes. BHC Swift J1753.5-0127 is found to have $b \sim 1.13$ [56, 81]. BHC MAXI J1836-194 showed more peculiar correlation with power law index ∼1.8 [57, 82]. The reason behind this unusual index is that the system may be surrounded by a cloud or a jet having variable Lorentz factors.

An attempt was made to connect AGN with Galactic black hole by Merloni et al. [67]. They extended the observed correlation to the active galactic nuclei by including the mass in the fundamental plane of black hole activity. They obtain the

relation in the form,

$$\log L_R = (0.60^{+0.11}_{-0.11}) \log L_X + (0.78^{+0.11}_{-0.09}) \log M + 7.33^{+4.05}_{-4.07}. \quad (3)$$

In this relation, only the mass is fundamental. $L_X$ can be treated as fundamental since it is assumed to be a good tracer of accretion dynamics. However, $L_R$ represents only a fraction of total jet luminosity. The validity of correlation over decades of $M$ and $L_X$ indicates the robustness of jet physics. Though attempts were made to replace $L_R$ with more fundamental quantity, namely, the accretion rate [63].

In these correlation of radio and X-ray fluxes, X-ray flux is assumed to be originated from the accretion flow. However, the jet also contributes in the X-ray energy band. Thus the total observed X-ray comes from both accretion flow and jet. Hence, to find good correlation, one must separate the jet X-ray flux from the total X-ray flux. It can be done easily with the TCAF solution which will be discussed in the next section.

## 4 X-Ray Jet with TCAF Solution

One requires four input parameters for spectral analysis with TCAF solution if mass of the BH is known (for more details see, [42, 43]). The basic input parameters are two types (Keplerian and sub-Keplerian) of accretion rates, mass of the black hole (if not known) and shock parameters (location and strength). The model normalization ($N$) is a function of intrinsic source parameters such as mass, distance and inclination angle of the source. Thus the model normalization must be constant for a particular BHC observed by a given instrument (for details, see, [56, 70, 71]). However, if jet is present, higher values of $N$ may be required, since the jet also contributes in the X-ray waveband. So, it may be considered that no or negligible contribution of the jet in X-rays, when the lowest $N$ value was required to fit the spectral data with the current version of the TCAF model *fits* file. Generally, in the late HS of an outburst of an outbursting BHC, we see this situation. Based on this assumption, X-ray contribution from the jet can be separated from the total observed X-ray ($F_X$). This method has been applied for Galactic black holes MAXI J1836-194; Swift J1753.5-0127 and XTE J1118+480 and the jet X-ray fluxes ($F_{ouf}$) are calculated [29, 56, 57].

Jana et al. [56] have done spectral analysis with the TCAF model based fits file keeping $N$ free. They obtain the flux from these fits which is the total X-ray flux ($F_X$), contributed by both the accretion disk and the jet. As stated before, when the minimum value of $N$ is required to fit the data, they assumed only accretion disk contributed to the X-ray band on that particular observation. Then they refitted all the observed spectra after freezing $N$ at its minimum value. These fixed $N$ value fits allow them to calculate X-ray flux coming only from accretion disk and CENBOL, i.e., from the inflowing matter ($F_{inf}$). Taking the difference of $F_X$ and $F_{inf}$, they

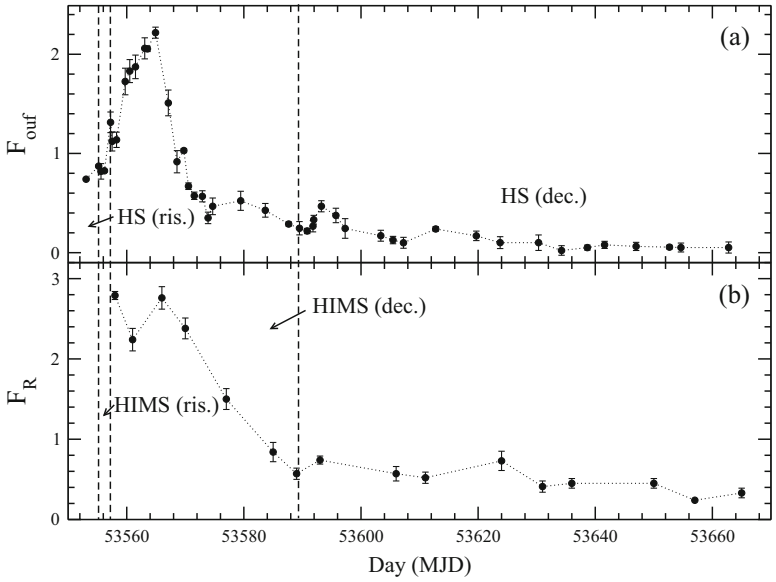



**Fig. 2** Variation of (**a**) $F_{ouf}$ and (**b**) $F_R$ is shown as a function of day (MJD) for Swift J1753.5-0127 during its 2011 outburst. X-ray jet flux $F_{ouf}$ is in the energy range of 3–25 keV and in unit of $10^{-10}$ $ergs/s$. $F_R$ is observed in 4.8 GHz frequency band in units of mJy. X-ray data are taken from [56] and radio data are taken from [84]

calculated X-ray flux contribution of jet or outflow $F_{ouf}$, as stated below (Eqn 1 of [56]),

$$F_{ouf} = F_X - F_{inf}. \tag{4}$$

Using this method, the jet fluxes have been calculated successfully for three Galactic black holes, namely, Swift J1753.5-0127 (during its 2005 outburst), MAXI J1836-194 (during its 2011 and 2012 outbursts), and XTE J1118+480 (during its 2000 outburst). In Fig. 2a, variation of jet X-ray flux ($F_{ouf}$) for Swift J1753.5-0127 is shown during its 2005 outburst. For comparison, observed radio flux ($F_R$) is also plotted in Fig. 2b. From this plot, we can see the evolution of $F_{ouf}$ is similar to the $F_R$. MAXI J1836-194 and XTE J1118+480 also showed a similar behavior [29, 57].

Jana et al. [56, 57] finds some interesting result when they correlated radio fluxes ($F_R$) with jet X-ray fluxes ($F_{ouf}$). They find correlation index $b \sim 0.59$ for Swift J1753.5-0127 and $b \sim 0.61$ for MAXI J1836-194. This indicates that there could exist an universal correlation in the form of $F_R \sim F_{ouf}^{0.6}$. However, more sample is required to check if this relation holds. Jet contribution in the X-ray flux is also calculated. It is found that $F_{ouf}/F_X$ has maximum value in the intermediate state (here HIMS) not in the hard state [56, 57]. These observations are also consistent with the theoretical prediction by Chakrabarti [19, 20] (Fig. 1).

## 5 Summary and Outlook

In this article, we have discussed about the disk-jet connections around black holes with the TCAF solution. Jana et al. [56] have used the same transonic accretion flow solution to estimate X-ray contribution coming from the jets or outflows and studied the nature of the emitting jets. The estimation and correlation of the jet X-ray fluxes ($F_{ouf}$) with the observed radio fluxes ($F_R$) are made for two Galactic BHCs Swift J1753.5-0127 and MAXI J1836-194. The correlation index was found to be $b \sim 0.6$ for both sources. To conclude that this correlation index is universal between $F_{ouf}$ vs. $F_R$ for Galactic BHCs, we need to consider a few more black holes. The nature of outflowing jets are also studied for these BHCs. During HS, both the sources showed compact jets, since a tight correlation between $F_{ouf}$ and $F_R$ were observed. But during HIMS, although MAXI J1836-194 showed compact jets, Swift J1753.5-0127 showed partially blobby or discrete ejections. In future, the study of disk-jet connection can be extended to AGNs with transonic flow based TCAF solution.

**Acknowledgements** I would like to thank Prof. Sandip K. Chakrabarti and Dr. Dipak Debnath for guiding me in my academic career. I would also like to thank ICSP, ISRO, DST and CSIR for their financial assistance to me.

## References

1. Abramowicz, M.A., Chakrabarti, S.K.: ApJ **350**, 281 (1990)
2. Abramowicz, M., Jaroszynski, M., Sikora, M.: A&A **63**, 221 (1978)
3. Abramowicz, M.A., Czerny, B., Lasota, J.P., Szuzkiewicz, E.: ApJ **332**, 646 (1988)
4. Bhattacharjee, A., Banerjee, I., Banerjee, A., et al.: MNRAS **466**, 1372 (2017)
5. Blandford, R.D., Payne, D.G.: MNRAS **194**, 883 (1982)
6. Blandford, R.D., Znajek, R.L.: MNRAS **179**, 433 (1977)
7. Bondi, H.: MNRAS **112**, 195 (1952)
8. Camenzind, M.: ASSL **156**, 129 (1989)
9. Chakrabarti, S.K.: ApJ **303**, 582 (1986)
10. Chakrabarti, S.K.: ApJL **337**, L89 (1989)
11. Chakrabarti, S.K.: MNRAS **238**, 1381 (1989)
12. Chakrabarti, S.K.: MNRAS **240**, 7 (1989)
13. Chakrabarti, S.K.: ApJ **347**, 365 (1989)
14. Chakrabarti, S.K.: Theory of Transonic Astrophysical Flows. World Scientific, Singapore (1990)
15. Chakrabarti, S.K.: MNRAS **243**, 610 (1990)
16. Chakrabarti, S.K. ApJ **350**, 275 (1990)
17. Chakrabarti, S.K.: ApJ **362**, 406 (1990)
18. Chakrabarti, S.K.: ApJ **484**, 313 (1997)
19. Chakrabarti, S.K.: A&A **351**, 185 (C99a) (1999)
20. Chakrabarti, S.K.: Ind. J. Phys. **73B**(6), 931 (C99b) (1999)
21. Chakrabarti, S.K.: In: Ruffini, R., Jantzen, R., Bianchi, M. (eds.) Proc. 14th Marcel Grossman Meeting, p. 369. World Scientific, Singapore (2016)
22. Chakrabarti, S.K., Bhaskaran, P.: MNRAS **255**, 255 (1992)

23. Chakrabarti, S.K., D'Silva, S.: ApJ **424**, 138 (1994)
24. Chakrabarti, S.K., Titarchuk, L.G.: ApJ **455**, 623 (CT95) (1995)
25. Chakrabarti, S.K., Goldoni, P., Wiita, P.J., et al.: ApJL **576**, L45 (2002)
26. Chakrabarti, S.K., Pal, S., Nandi, A., et al.: ApJL **595**, L45 (2003)
27. Chakrabarti, S.K., Mondal, S., Debnath, D.: MNRAS **452**, 3451 (2015)
28. Chatterjee, D., Debnath, D., Chakrabarti, S.K., et al.: ApJ **827**, 88 (2016)
29. Chatterjee, D., Debnath, D., Jana, A., Chakrabarti, S.K.: Ap&SS (2018, submitted)
30. Curtis, H.D.: PLicO **13**, 9 (1918)
31. Corbel, S., Fender, R.P., Tzioumis, A.K., et al.: A&A **359**, 251 (2000)
32. Corbel, S., Fender, R., Tzioumis, A.: IAU Circ. 7795 (2002)
33. Corbel, S., Fender, R., Tzioumis, A.: Science **298**, 196 (2002)
34. Corbel, S., Nowak, M.A., Fender, R.P., Tzioumis, A.K., Markoff, S.: A&A **400**, 1007 (2003)
35. Corbel, S., Fender, R.P., Tomsick, J.A., Tzioumis, A.K., Tingay, S.: ApJ **617**, 1272 (2004)
36. Corbel, S., Kaaret, P., Fernder, R.P., et al.: ApJ **632**, 504 (2005)
37. Corbel, S., Koerding, E., Kaaret, P.: MNRAS **389**, 1697 (2008)
38. Coriat, M., Corbel, S., Prat, L., et al.: MNRAS **414**, 677 (2011)
39. Das, T.K., Chakrabarti, S.K.: CQGra **16**, 3879 (1999)
40. Deb, A., Giri, K., Chakrabarti, S.K.: MNRAS **472**, 1259 (2017)
41. Debnath, D., Chakrabarti, S.K., Nandi, A.: AdSpR **52**, 2143 (2013)
42. Debnath, D., Chakrabarti, S.K., Mondal, S.: MNRAS **440**, L121 (2014)
43. Debnath, D., Mondal, S., Chakrabarti, S.K.: MNRAS **447**, 1984 (2015)
44. Debnath, D., Molla, A.A., Chakrabarti, S.K., et al.: ApJ **803**, 59 (2015)
45. Debnath, D., Jana, A., Chakrabarti, S.K., et al.: ApJ **850**, 92 (2017)
46. Dhawan, V., Mirabel, I.F., Rodríguez, L.F.: ApJ **543**, 373 (2000)
47. D'Silva, S., Chakrabarti, S.K.: ApJ **424**, 149 (1994)
48. Eikenberry, S.S., Matthews, K., Morgan, H., et al.: ApJ **494**, L61 (1998)
49. Fender, R.P., Pooley, G.G.: MNRAS **300**, 573 (1998)
50. Fender, R.P., Garrington, S.T., McKay, D.J., et al.: MNRAS **304**, 865 (1999)
51. Gallo, E., Fender, R.P., Pooley, G.G.: MNRAS **344**, 60 (2003)
52. Gallo, E., Fender, R.P., Miller-Jones, J.C.A., et al.: MNRAS **370**, 1351 (2006)
53. Hannikainen, D.C., Hunstead, R.W., Campbell-Wilson, D., Sood, R.K.: A&A **337**, 460 (1998)
54. Hjellming, R.M., Rupen, M.P.: Nature **375**, 464 (1995)
55. Jana, A., Debnath, D., Chakrabarti, S.K., et al.: ApJ **819**, 107 (2016)
56. Jana, A., Chakrabarti, S.K., Debnath, D.: ApJ **850**, 91 (2017)
57. Jana, A., Debnath, D., Chakrabarti, S.K., Chatterjee, D.: ApJ (2018, submitted)
58. Jonker, P.G., Gallo, E., Dhawan, V., et al.: MNRAS **351**, 1359 (2004)
59. Jonker, P.G., Miller-Jones, J.C.A., Homan, J., et al.: MNRAS **423**, 3308 (2012)
60. Jourdain, E., Roques, J.P., Chauvin, M., Clark, D.J.: ApJ **761**, 27 (2012)
61. Kaaret, P., Corbel, S., Tomsick, J.A., et al.: ApJ **582**, 945 (2003)
62. Kaaret, P., Corbel, S., Tomsick, J.A., et al.: ApJ **641**, 410 (2006)
63. Kording, E.G., Fender, R.P., Migliari, S.: MNRAS **369**, 1451 (2006)
64. Lasso-Cabrera, N.M., Eikenberry, S.S.: ApJ **775**, 82 (2013)
65. Laurent, P., Rodriguez, J., Wilms, J., et al.: Sci. **332**, L438 (2011)
66. Loh, A., Corbel, S., Dubus, G., et al.: MNRAS **462**, L111 (2016)
67. Merloni, A., Heinz, S., di Matteo, T.: MNRAS **345**, 1057 (2003)
68. Mirabel, I.F., Rodríguez, L.F.: Nature **371**, 46 (1994)
69. Mirabel, I.F., Rodríguez, L.F., Cordier, B., Paul, J., Lebrun, F.: Nature **358**, 215 (1992)
70. Molla, A.A., Debnath, D., Chakrabarti, S.K., et al.: MNRAS **460**, 3163 (2016)
71. Molla, A.A., Chakrabarti, S.K., Debnath, D., Mondal, S.: ApJ **834**, 88 (2017)
72. Mondal, S., Chakrabarti, S.K., Debnath, D.: Ap&SS **353**, 223 (2014)
73. Mondal, S., Chakrabarti, S.K., Debnath, D.: ApJ **798**, 57 (2015)
74. Mondal, S., Chakrabarti, S.K., Debnath, D.: Ap&SS **361**, 309 (2016)
75. Nandi, A., Manickam, S.G., Rao, A.R., Chakrabarti, S.K.: MNRAS **324**, 267 (2001)
76. Nandi, A., Chakrabarti, S.K., Vadawale, S.V., Rao, A.R.: A&A **380**, 245 (2001)

77. Nandi, A., Chakrabarti, S.K., Belloni, T., et al.: MNRAS **359**, 629 (2005)
78. Nandi, A., Debnath, D., Mandal, S., Chakrabarti, S.K.: A&A **542**, 56 (2012)
79. Ratti, E.M., Jonker, P.G., Miller-Jones, J.C.A., et al.: MNRAS **423**, 2656 (2012)
80. Rodríguez, L.F., Mirabel, I.F., Marti, J.: ApJ **401**, L15 (1992)
81. Rushton, A.P., Shaw, A.W., Fender, R.P., et al.: MNRAS **463**, 628 (2016)
82. Russell, T.D., Miller-Jones, J.C.A., Curran, P.A., et al.: MNRAS **450**,1745 (2015)
83. Shakura, N.I., Sunyaev, R.A.: A&A **24**, 337 (SS73) (1973)
84. Soleri, P., Fender, R.P., Tudose, V., et al.: MNRAS **406**, 1471 (2010)
85. Stirling, A.M., Spencer, R.E., de la Force, C.J., et al.: MNRAS **327**, 1273 (2001)
86. Sunyaev, R.A., Titarchuk, L.G.: ApJ **86**, 121 (1980)
87. Sunyaev, R.A., Titarchuk, L.G.: A&A **143**, 374 (1985)
88. Tingay, S.J., Jauncey, D.L., Preston, R.A., et al.: Nature **374**, 141 (1995)
89. Tomsick, J.A., Corbel, S., Fender, R., et al.: ApJ **582**, 983 (2003)
90. Vadawale, S.V., Rao, A.R., Chakrabarti, S.K.: A&A **372**, 3 (2001)
91. Vadawale, S.V., Rao, A.R., Nandi, A., Chakrabarti, S.K.: A&A **370**, 17 (2001)
92. Znajek, R.L.: MNRAS **182**, 639 (1978)

# A Dynamic Photon Index Probes into TCAF




**Arindam Ghosh**

**Abstract** Five successive outbursts in each of the two transient low-mass X-ray binaries (LMXBs), viz. GX 339-4 and H 1743-322, during 1997–2010 and 2003–2008 respectively, are analyzed using (1.5–12 keV) data of All Sky Monitor (ASM) in Rossi X-ray Timing Explorer (RXTE) satellite. In LMXBs, a big Keplerian disc having high viscosity and high angular momentum is likely to form via Roche-lobe overflow amid the advective sub-Keplerian halo. However, in high-mass X-ray binaries (HMXBs), almost inviscid and wind-dominated sub-Keplerian flow carrying low angular momentum rushes inwards virtually freely. Two travel timescales in these two components bring about a longer delay of the standard Keplerian disc heading for the black hole in LMXBs than that in HMXBs. Disc and halo components are respectively behind the emission of black-body and power-law photons. A direct cross-correlation between these two fluxes of photon (or energy), in dearth of a linear mutual dependence, may never reveal this arrival time delay; rather these two are interlinked via viscous modulations, which usher the accreting matter to the interior. In order to compute a relative time delay between the two radiation fluxes emitted by the aforesaid two flow components, RXTE/ASM photon counts (GX 339-4) and average energy fluxes (H 1743-322) are cross-correlated with respect to a dynamic photon index ($\Theta$) proposed by Professor Sandip K. Chakrabarti. This viscous time delay dictates the fate of any outburst in all respects, while $\Theta$ acts as a dynamical indicator to trace the spectral states throughout the duration of the outburst. It is also found in GX 339-4 that the Keplerian disc varies in size from an outburst to another, whereas the disc size is biggest during the brightest outburst of H 1743-322 in 2003 and diminishes during its subsequent weaker outbursts. Moreover, the time delay and hysteresis property of the disc, as well as the failure of a potential outburst can be evident from the behaviour of $\Theta$ alone. All results confirm two dynamical flows in accretion onto a black hole, as proposed in the TCAF paradigm.

A. Ghosh (✉)
S. N. Bose National Centre for Basic Sciences, Kolkata, India
e-mail: arindam.ghosh@bose.res.in

© Springer International Publishing AG, part of Springer Nature 2018

B. Mukhopadhyay, S. Sasmal (eds.), *Exploring the Universe: From Near Space to Extra-Galactic*, Astrophysics and Space Science Proceedings 53,
https://doi.org/10.1007/978-3-319-94607-8_24

## 1 Introduction

In this layered article, a temporal analysis of five successive outbursts in each of GX 339-4 [8] and H 1743-322 [9] with RXTE/ASM (1.5–12 keV) data, within the framework of Two-Component Advective Flow (TCAF; Chakrabarti and Titarchuk [5, hereafter CT95]) is discussed so as to show the signature of its two flow components, among other outcomes. These two hydrodynamic flows generally govern two radiation components of the observed spectra, though in a nonlinear way. A thin Keplerian disc having high angular momentum and high viscosity dissipates gravitational energy and emits multi-colour blackbody (soft) photons Shakura and Sunyaev [14, hereafter SS73]. A geometrically thick, hot, and advective sub-Keplerian flow, haloing the disc vertically, carries low angular momentum and low viscosity. This gets bulged while approaching the black hole, due to the centrifugal boundary (known as 'CENBOL'). Its dissipation via recurrent inverse Comptonization produces high-energy (hard) photons exhibiting a power-law distribution. A generic Compton cloud possesses this emission property [16, 17]. Any significant change in X-rays radiated from both disc and halo reveals the variation of the corresponding two mass accretion rates in the inner region. Unlike a viscous SS73 disc, an advective sub-Keplerian flow does not require viscosity for accretion. On the contrary, the disc matter moves inwards by spatially and temporally varying viscosity. However, even if the accretion rate in the Keplerian disc increases suddenly, the disc matter with high angular momentum would fail to cross a radial distance, $X_a$, where the viscosity is low. The matter had better pile up in an annular region around $X_a$, until the flow becomes highly viscous, presumably due to convective viscosity exceeding the critical viscosity parameter [3, 4]. This brings about a swift inrush of disc matter and an outburst would result in. The aforesaid radial distance $X_a$ away from the black hole is termed as *accumulation radius* or *pile-up radius*. If the viscosity is sufficient so that the spectrum eventually achieves the soft state, it is called a normal (canonical) outburst. If the viscosity fails to rise to an adequate degree, and only an intermediate spectral state is reached, then the outburst will appear to be anomalous or *failed*. The region between $X_a$ and the outer edge of the CENBOL is filled during the outburst following a shock. However, the viscous disc matter will take more time than the advective halo matter in traveling from $X_a$ to the CENBOL. As a consequence, the disc component arrives later than the halo component. The difference in their arrival times is defined in the following:

**Arrival Time Delay:** $\tau = t_{disc} - t_{halo}$, where, $t_{halo}$ and $t_{disc}$ are the travel (from $X_a$) timescales of the halo and the disc respectively. $\tau > 0$ implies that the disc lags behind the halo. Both advance simultaneously, if $\tau = 0$.

During an outburst in transient low-mass X-ray binaries (LMXBs), the soft (low-energy or black-body) radiation shows a peak belated by a few days to a few weeks following the peaking of the hard (non-thermal power-law) radiation. Moreover, the total radiated energy can vary from an outburst to the other in a frequently transient source because the accumulation radius ($X_a$) itself is different for each outburst [6, 8–10]. The accumulation radii $X_a$s represent the sizes of the Keplerian disc in multiple outbursts exhibited by a transient LMXB such as GX 339-4 or H 1743-322. The total energy liberated per outburst appears to be proportional to the time elapsed in the quiescent state prior to the outburst [6]. This can be evident from the histograms in Fig. 1, where total mean hard (blue/dashed) and soft (red/continuous) energy fluxes released per outburst (OB) are represented by the bar heights. Equal bar width (≠duration) is not to scale. The triangles represent the central points of OB1-OB5 marked with Calendar years. The quiescent time elapsed before OB2 and OB5 in GX 339-4 or OB4 in H 1743-322 is longer than that before other

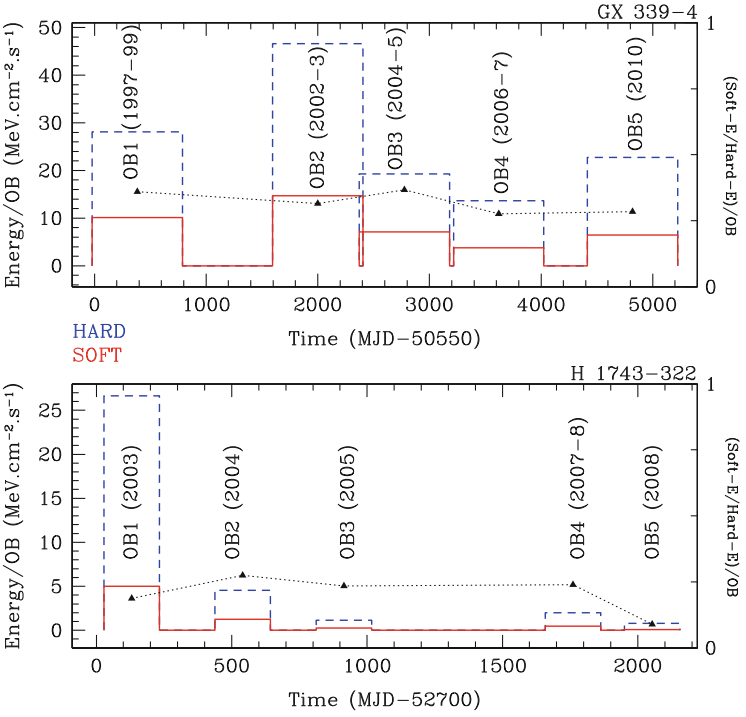



**Fig. 1** Histograms: (top) GX 339-4 and (bottom) H 1743-322: Total mean hard (blue/dashed) and soft (red/continuous) energy fluxes released in $n$th outburst (OBn, n = 1,. . . ,5) are represented by the bar heights. Equal bar width (≠duration) is not to scale. The dotted curve with triangles (central points of OB1–OB5 marked with Calendar years) represents the soft-to-hard energy ratio on a (0,1) scale; soft energy never exceeds ∼35% of hard energy in proportion. The quiescent time elapsed between any two consecutive outbursts is responsible for an increase in both fluxes during the latter (color online)

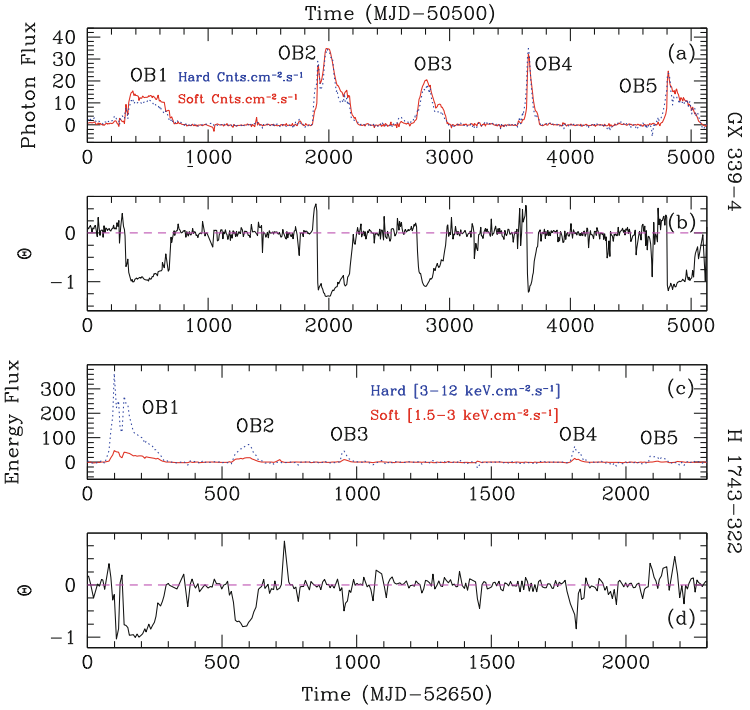



**Fig. 2** Hard (blue/dotted) and soft (red/continuous) photon counts in (**a**) GX 339-4, and energy fluxes in (**c**) H 1743-322 are drawn with weekly average data for a quick look on the five successive outbursts in both (marked as OBn, n = 1, . . . , 5 as in Fig. 1) and also for clarity. The corresponding long time behaviour of the dynamic photon index $\Theta$ is shown in (**b**) and (**d**), where the outbursts are manifested by the strong dips. The horizontal line (magenta/dashed) ($\Theta \rightarrow 0$) and the minimum in the dips ($\Theta \rightarrow -1$) approximately represent HS and SS respectively (color online)

outbursts. This can be estimated from Fig. 2a, c, where hard (blue/dotted) and soft (red/continuous) photon counts in (a) GX 339-4, and energy fluxes in (c) H 1743 are drawn with weekly average data. It is seen from Figs. 1 and 2c that both the fluxes drop drastically in OB3 (2005) from their highest values in OB1 (2003); a sufficiently long time (>2 years) of quiescence followed thereafter is instrumental behind the brighter OB4 (2007-8) and the following weak outburst (OB5). We shall see that the arrival time delay, the accumulation radius, the disc size, and this quiescent time gap are consistent with one another. In particular, a much bigger disc size during the brightest/longest outburst OB1 (2003) in H 1743-322 than those observed in its subsequent four weak outbursts [9] is consistent with its preceding long time (∼25 years) quiescence [6]. Smith et al. [15] found a distinct time lag of several weeks between a suitably defined power-law index and hard photon flux (in RXTE/ASM and /PCA) in the quiescent LMXBs, GRS 1758-258 and 1E 1740.7-2942, however, no significant lag (∼0d) in the HMXBs, Cyg X-1 and Cyg X-3. This led them to infer the evidence for two accretion flows as proposed in TCAF.

## 2 Observation with Temporal Data Analysis

### 2.1 RXTE/ASM 3-Channel X-Ray Data

Despite the presence of negative counts due to background subtraction and stringent energy binning, RXTE/ASM data is still useful for its availability for a long duration of time. These negative counts become minimal during outbursts. Therefore, the archived RXTE/ASM ASCII data during five outbursts of both GX 339-4 and H 1743-322 are analyzed. RXTE/ASM, operated over (1.5–12) keV energy range, consists of three energy bands, viz. A = 1.5–3) keV, B = (3–5) keV, and C = (5–12) keV. Let $a$, $b$, and $c$ respectively be the number of photons in A, B, and C bands. Their mean energies are $E_A = 2.25$ keV, $E_B = 4$ keV, and $E_C = 8.5$ keV respectively. A-band represents soft photon flux $a$ or low-energy flux $aE_A$; B and C bands together represent the total hard (3–12 keV high-energy) photon flux $(b + c)$ or energy flux $(bE_B + cE_C)$. But, a direct cross-correlation between the two fluxes will not give the arrival time delay $(\tau_r)$ between the two accretion flow components, as these do not independently emit soft and hard fluxes of radiation. Indeed, the hard flux depends not only on the soft flux, but also on the size, density, and optical depth of the CENBOL (Compton cloud). Moreover, the hard flux is always observed to increase with the soft flux during an outburst. So, no significant ($\gg 0$) time delay can be obtained from such a direct flux-flux correlation.

### 2.2 Dynamic Photon Index $\Theta$ (Proposed by Prof. Chakrabarti)

In view of the aforesaid difficulty, Professor Chakrabarti prescribed me a dynamic photon index $(\Theta)$ in a Winter afternoon of 2015 during our binary academic discussion. The way he discovered such a physical parameter is depicted in Fig. 3a. This is given by Ghosh and Chakrabarti [8, 9],

$$\Theta = \tan^{-1}[\frac{(c-b)}{(E_C - E_B)}].$$

As $\Theta$ represents relative change of one flux with respect to the other it can be used as a reference parameter for cross-correlation with individual fluxes. Here, $\Theta$ is defined to be the slope of the hard region of the spectrum drawn in *linear scale*. If the power-law photon index $\Gamma$ is given by $\phi(E) \sim E^{-\Gamma}$, then

$$dlog(\phi(E))/dlogE = -\Gamma.$$

$\Gamma \leq 2$ indicates a hard state (HS) while $\Gamma > 2$ indicates a soft state (SS). However, with ASM data, we use $tan\Theta = d\phi(E)/dE = -\Gamma\phi(E)/E$ in order to define the spectral state, as logarithmic scale is inapt when ASM count is negative. Therefore,

$$\phi(E) \sim (-\frac{tan\Theta}{\Gamma})^{\beta},$$

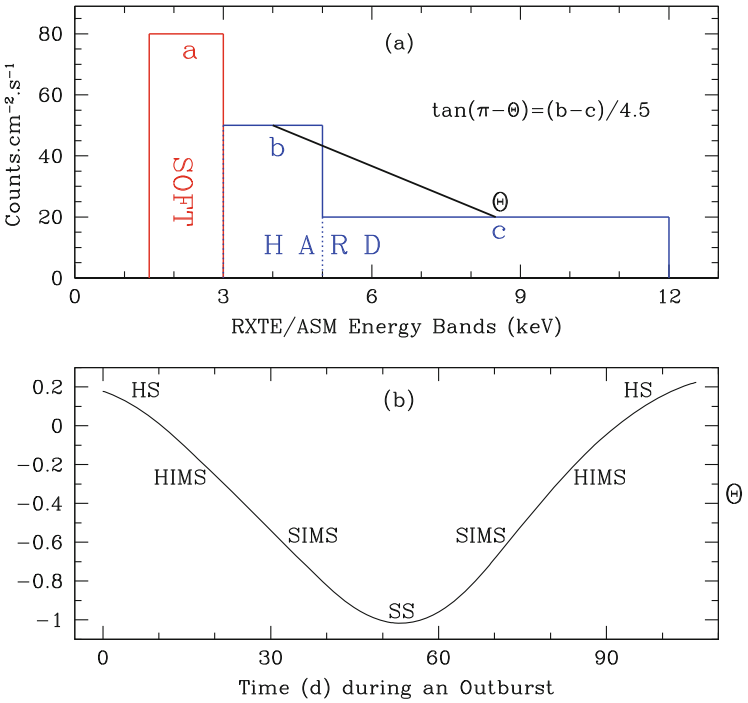



**Fig. 3** Cartoon diagrams: (**a**) The way $\Theta$ is extracted by Prof. Chakrabarti from RXTE/ASM energy bands. $\Theta$ is susceptible to changes in both fluxes of photon and energy. (**b**) Typical behaviour of $\Theta$ during any normal outburst is approximately shown by the well-like schematic curve. Hard state (HS), hard-intermediate state (HIMS), soft-intermediate state (SIMS), and soft state (SS) are intuitively marked along the well-like schematic curve. $\Theta$ is highest at the commencement (HS) and culmination (HS) of an outburst. $\Theta \geq 0$ in HS, $\Theta \rightarrow -1$ in SS, and $\Theta_{\pm} \sim -0.5$ in HIMS/SIMS

where, $\beta = \Gamma/(\Gamma + 1)$. By definition, $-1.57 < \Theta < 1.57$. In general, $tan\Theta$ must be negative only since $c < b$ for equal energy binning. In the SS, $\phi(E)$ is high and $\Theta \rightarrow -1.57$. In the HS, low $\phi(E)$ approaches a constant, hence $\Theta \rightarrow 0$. Soon we shall see that $\Theta$ is a *dynamic dummy* of the usual photon index $\Gamma$; however, it will appear to be more effective than the latter. This is also evident from Fig. 2b, d, where long time behaviour of $\Theta$ is shown for GX 339-4 and H 1743-322 respectively with weekly average data; strong dips ($\Theta \sim -1$) indicate the outbursts, while the horizontal line (magenta) represents the hard states with $\Theta \sim 0$. As the size of the C band in RXTE/ASM is largest, so the possibility of $c > b$ often gives rise to $\Theta > 0$ indicating a *harder* state. In fact, in such a case, our desired $\tau_r$ can be estimated from $\Theta$-behaviour alone, as shown in Fig. 5. Moreover, it can account for the *hysteresis* property of the Keplerian disc pertaining to the outbursts with varying features (see Sect. 3). This also makes a manifestly empirical parameter, $\Theta$, a physical parameter of a mind-blowing spectral reference, only with TCAF at hand (see Sect. 2.4).

### 2.3 Relative Arrival Time Delay $\tau_r$

The relative arrival time delay between the hard and the soft fluxes (of photon or energy) is defined, with reference to $\Theta$, as

$$\tau_r = t_{CC(\Theta,Soft)} - t_{CC(\Theta,Hard)} \rightarrow \tau.$$

$\tau_r > 0$ implies that the disc radiation (black body) lags behind the halo radiation (power law). Otherwise, both evolve simultaneously if $\tau_r = 0$. The cross-correlation (CC) between $\Theta$ and two fluxes can be done by the standard CROSSCOR task of HEASOFT/XRONOS package [8, 9], or otherwise.

Arrival time delay $\tau$ or $\tau_r$ can be computed from:

**Lightcurves:** Soft photon flux peaks later than the hard photon flux. The difference in their peaking instants of time gives $\tau_r$ [10].

**Accretion Rates:** TCAF fits with high energy X-ray data provide two mass accretion rates. The disc rate shows a belated peak as compared to the halo rate. $\tau_r \sim \tau$ is just their peaking time difference [10].

**Dynamic Photon Index $\Theta$:** At the commencement of an outburst, $\Theta \sim 0$ in HS; but it increases gradually to a *harder* value ($\sim 0.5$) before retaining fast to $\sim 0$. The time elapsed in this 'spectral hardening' is roughly equal to $\tau_r > 0$ [8, 9].

**Cross-Correlation with $\Theta$:** Either the fluxes of soft and hard photon or the fluxes of soft and hard energy, when cross-correlated with reference to $\Theta$, result in $\tau_r$ [8, 9].

### 2.4 Physical Significance of $\Theta$

An increase in advective halo matter can increase $c$ (5–12 keV) more over $b$ (3–5 keV) without affecting the overall hard flux of photons ($b + c$) or radiation ($(bE_B + cE_C)$) or soft fluxes ($a$ and $aE_A$) abruptly. The spectrum would then get hardened gradually until the Keplerian disc matter rushes inwards leaving the accumulation radius $X_a$. Then $\Theta$ would rise from $\sim 0$ to $\gg 0$ (0.5, say). As soon as the disc matter comes close to the CENBOL and increases the soft flux, power-law branch becomes softened and $\Theta \rightarrow 0$. The time elapsed during this spectral hardening is our desired $\tau_r$, which can be evident from $\Theta$-behaviour alone at the commencement of the outburst if $X_a$ is far away, i.e. $\tau_r$ is long or the disc is big in size. In such cases, the well-like symmetry depicted in Fig. 3b will be distorted. This will also be reflected from the lightcurves, 'radiation-curves', and

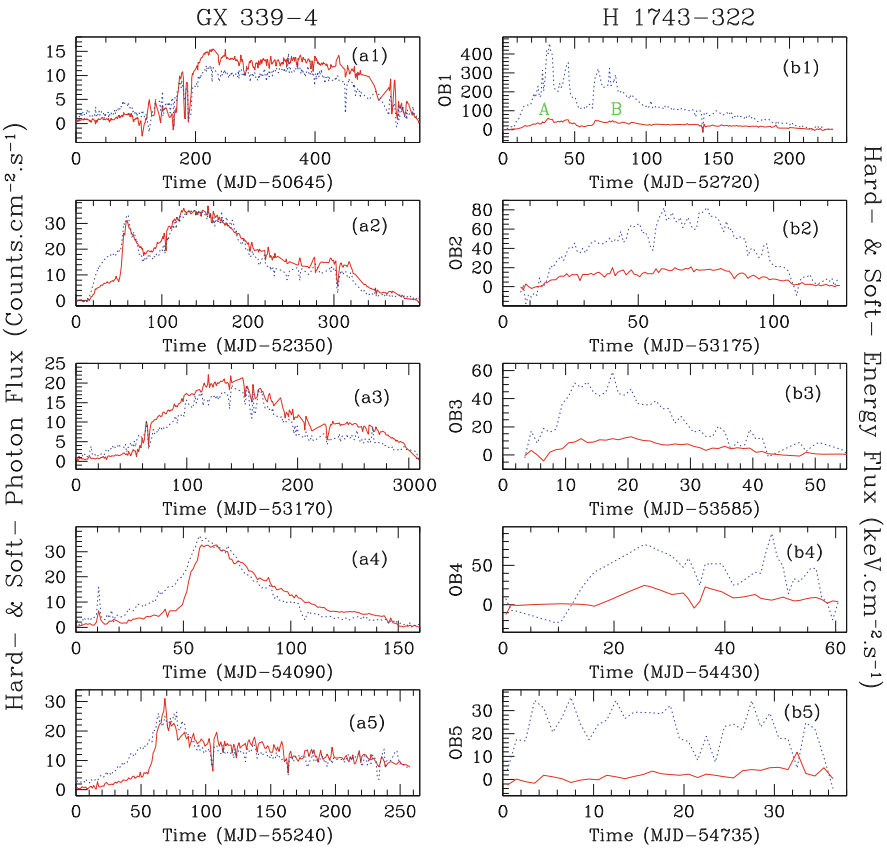



**Fig. 4** Average hard flux (blue/dotted) and average soft flux (red/continuous) of photons in (**a**) GX 339-4 and energy in (**b**) H 1743-322 during the outbursts of Figs. 1 and 2 are zoomed with daily average data. Two peaks in (**b1**) are marked as A and B. Outbursts in (**a1**), (**a3**), (**b2**), and (**b3**) are examples of OB-I type, and those in (**a2**), (**a4**), (**a5**), and (**b1**) conform to OB-II type (see the gray box in Sect. 3). In (**b5**), the lower soft flux seems to be anti-correlated with the hard flux. However, both fluxes are apparently strongly correlated with each other in all other outbursts (color online)

accretion rates about the peak outburst followed by a declining phase longer than the rising phase. Otherwise, i.e. when $X_a$ is nearby, $\tau_r$ is negligibly small to be detected, and a small disc is obvious; then $\Theta$ may initially fluctuates at $\sim$0 before following Fig. 3b ideally. In such a case, the lightcurves or 'radiation-curves' will be roughly symmetric about the peak outburst, flanked by a rising phase and a declining phase of comparable duration (see Fig. 4). So, the physical parameter $\Theta$ acts as a dynamical indicator which traces any outburst like clockwork. Note : The behaviour of $\Theta$ with time is almost similar to that of the Comptonization efficiency (CE) [8, 11]. Both the physical indices, $\Theta$ and CE, can therefore replace the popular Hardness Ratio(s), HR1, HR2, etc. for a far better understanding of the spectra observed due to accretion onto a black hole. Such a simple yet stunning

*spectro-temporal* index can be extended to analysis with data of any recent multi-channel satellite, which, especially, receives both blackbody and power-law photons simultaneously.

## 3 Results of Observation

Any normal outburst is characterized by four spectral states, viz. hard state (HS), hard-intermediate state (HIMS), soft-intermediate state (SIMS), and soft state (SS). Spectral transition must go through HS→HIMS→SIMS →SS→SIMS→HIMS→HS for a normal (canonical) outburst. This is depicted in Fig. 3b. $\Theta$ should attain its highest value at the beginning (HS) and at the end (HS) of a normal outburst. Approximately, $\Theta \geq 0$, $\Theta_{\pm} \sim -0.5$, and $\Theta \rightarrow -1$ can be respectively assigned to HS, HIMS/SIMS, and SS. $\Theta_{max}$ either fluctuates about 0, or exceeds 0 in the HS at the commencement of an outburst; $\Theta_{min}$ does not go below $-1.5$ in a typical SS at the peak outburst. This is congruent with its theoretical limit. The possibility of having more than one distinct SS or an interim HS in the well of Fig. 3b would indicate a multiplicity in the outburst (twin, trinity, etc.). Also, a few *minuscule* outbursts can occur back to back; or, only intermediate state(s) may be present instead of the achievement of the SS, within the two generic HSs limiting the outburst. All these can be generalized as *anomalous* outbursts. $\Theta$ may not clue the corresponding lightcurves in about such spectral deviations.

The hard flux (blue/dotted) and soft flux (red/continuous) of photon (GX 339-4) or energy (H 1743-322) during the outbursts considered here are zoomed in Fig. 4 with daily average data. Two major peaks of the brightest (twin) outburst OB1 (2003) of H 1743 are marked as A and B, which are examined separately. Figure 5 shows the behaviour of $\Theta$ during all outbursts considered here. Their average envelopes are drawn (magenta) with running-mean data. Green horizontal lines define a *plateau* and HS, where $\Theta \sim 0$. $\Theta$ drops down from its highest value following the commencement (HS) of an outburst and rises again at its culmination (HS). Due to the spectral hardening because of $\tau_r(d) > 0$, as discussed in Sect. 2.4, the desired arrival time delays are approximately marked in the relevant boxes. Multiple wells indicate more than one SS or interim HS/HIMS/SIMS in Figs. 5a1 and b1, and mini outbursts in Fig. 5b4. The outburst OB5 (2008) in H 1743 is reported to be a *failed* [2] or an *almost successful* [18] since the spectrum transits from HS to HIMS before marginally culminates upon HS with decreased luminosity. This is directly reflected from Fig. 5b5, where $\Theta$ is seen to be decreasing slowly from HS to HIMS, and marginally attains an expected HS at the end of this *failed* outburst. All numbers estimated approximately from $\Theta$ alone are in agreement with those obtained from the $\Theta$-flux correlations shown in Fig. 6, where both direct hard-soft correlation (black), and indirect $\Theta$-hard (blue/dotted), and $\Theta$-soft (red/continuous) correlation curves are drawn at once. A strong anti-correlation between the fluxes directly or via $\Theta$ in Fig. 6b5 indicates that the spectrum of OB5 in H 1743 was never softened, thereby corroborating its *failure*. The classic hard-soft correlation curves

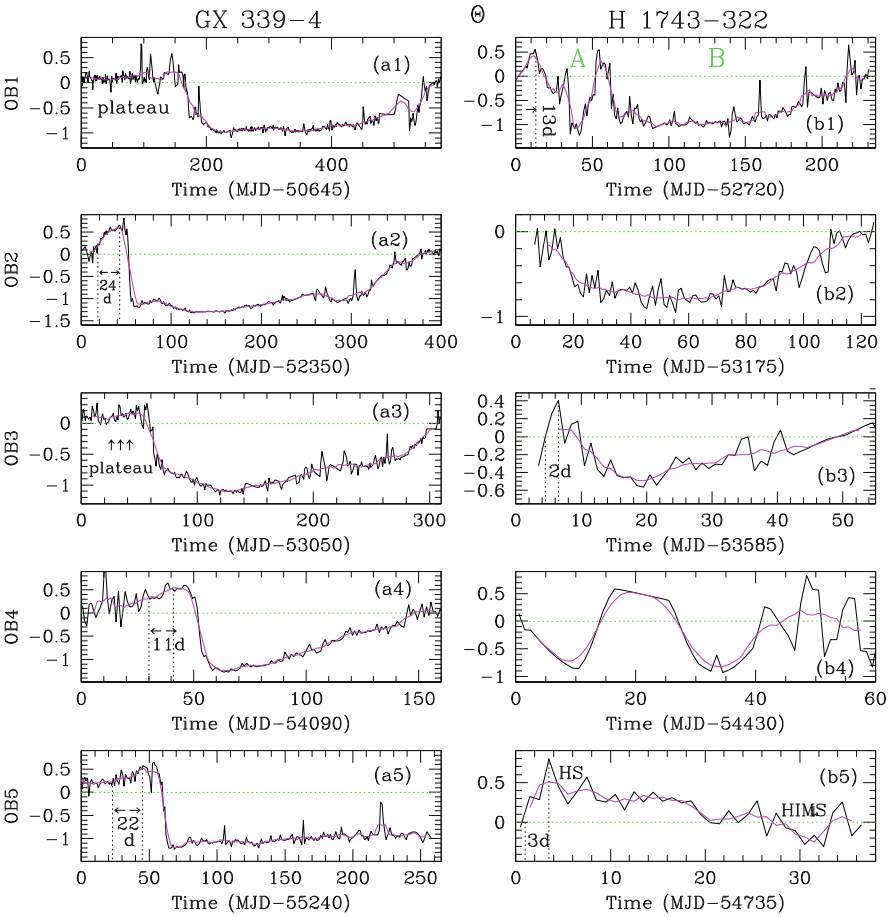



**Fig. 5** $\Theta$-behaviour in all outbursts: Average envelopes are drawn (magenta/bold) with running-mean data. $\Theta \rightarrow 0$ (green/dotted lines) defines a plateau in the HS; $\Theta$ drops down from its highest value following the commencement of outbursts and rises again at their end. Numbers in boxes are approximate $\tau_r(d)$ due to a spectral transition from HS to a harder state. In (**b5**), $\Theta$ decreases slowly from HS to HIMS, and marginally attains a HS at the end of this *failed* or *anomalous* outburst. Multiple wells indicate more than one SS or interim HS/HIMS/SIMS in (**a1**) and (**b1**), and $\geq$2 *minuscule* outbursts in (**b4**) (color online)

(black) show a strong correlation between the two fluxes in all other outbursts but without any tangible time delay, as expected. $\Theta$ is seen to be responsive equally to the fluxes of photon or energy and gives the desired time delays. All numerical estimates pertaining to the outbursts are summarised in Table 1.

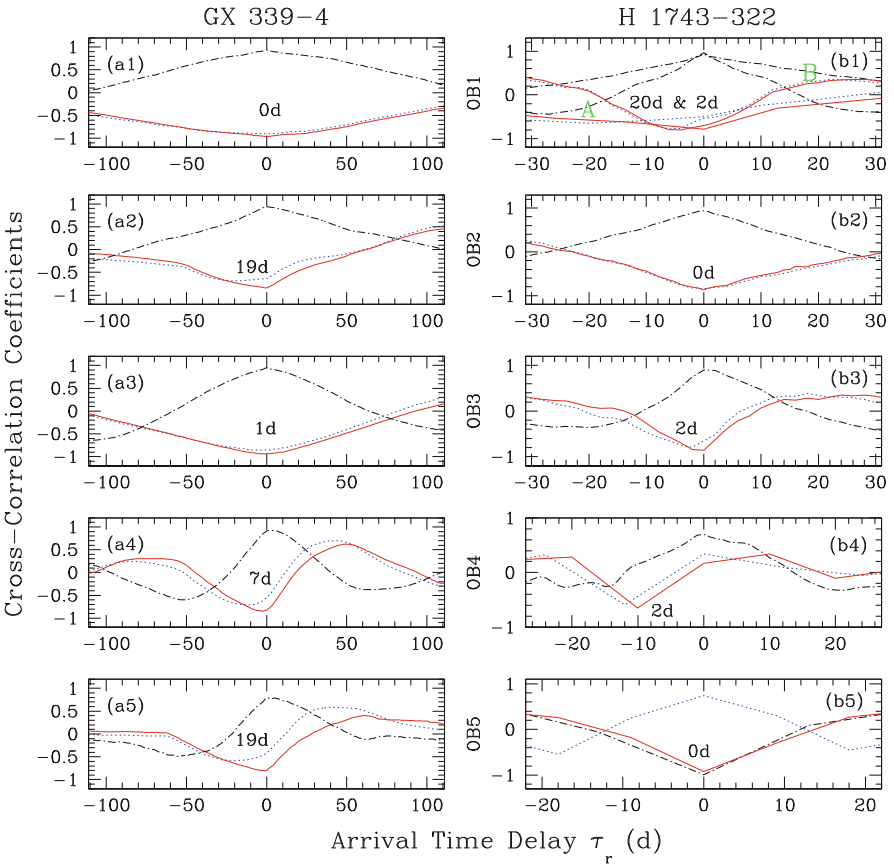



**Fig. 6** Cross-Correlation Profiles: Classic hard-soft correlation curves (black/dot-dashed) show a strong correlation (except for (**b5**)) between the two fluxes; both fluxes evolve simultaneously as expected. But, $\Theta$ is responsive equally to hard (blue/dotted) and soft (red/continuous) fluxes of photon or energy and gives our desired time delays, written in each box. In agreement with Fig. 5**b5**, a strong anti-correlation between the fluxes directly or with respect to $\Theta$ also indicates that the spectrum of OB5 in (**b5**) was never softened appreciably (color online)

All outbursts (OB) are divided into two classes with the following features:

1. **OB-I Type Outbursts:**
   a. Both soft and hard fluxes change in a similar manner throughout the duration of the outburst. Shape of the lightcurves and $\Theta$-curve is roughly symmetric about the peak outburst (SS: $\Theta \rightarrow -1$), and so

(continued)

the duration of their rising phase is comparable to that of the declining phase.
   b. $\Theta$ (along with CE) fluctuates rapidly about its mean highest value ($\Theta \sim 0$) along a broad plateau at the commencement of the outburst (HS) before dropping quickly to its lowest value in SS ($\Theta \rightarrow -1$).
   c. CENBOL may be squeezed before the shock.
   d. Arrival time delay $\tau$ or $\tau_r \sim 0d$.
   e. Accumulation radius $X_a$ is nearby.
   f. Disc size is small and hysteresis is less.

2. **OB-II Type Outbursts:**

   a. Hard flux increases first and faster than soft flux in the rising phase. Shape of the lightcurves and $\Theta$-curve is not symmetric about the peak outburst (SS: $\Theta \rightarrow -1$), and so the duration of their declining phase is few times longer than that of the rising phase.
   b. Fluctuations in $\Theta$ (and CE) are less in HS along a narrow plateau, where $\Theta \sim 0$, whence $\Theta$ increases steadily to a 'harder' state value of $\sim 0.5$ before falling off sharply to its lowest value in SS ($\Theta \rightarrow -1$).
   c. CENBOL may be inflated before the shock.
   d. Arrival time delay $\tau$ or $\tau_r \gg 0d$.
   e. Accumulation radius $X_a$ is far away.
   f. Disc is big in size and hysteresis is strong.

Transient LMXBs exhibiting sporadic outbursts are most likely to form either an OB-I type disc, or a disc with moderate size.

**Table 1** Relative arrival time delay ($\tau_r$) in GX 339-4 and H 1743-322 during outbursts (OBn)

| Transient LMXB | OBn | $\tau_r(d)$ $\Theta$-Flux | Fluxes | $\Theta(\sim)$ | Type | Disc size | Remarks on OB |
|---|---|---|---|---|---|---|---|
| GX 339-4 | OB1 | $0 \pm 1.4$ | $0 \pm 1$ | 0 | OB-I | Small | Normal |
| | OB2 | $19 \pm 1.4$ | $0 \pm 1$ | 24 | OB-II | Big | Normal |
| | OB3 | $1 \pm 1.4$ | $0 \pm 1$ | 0 | OB-I | Small | Normal |
| | OB4 | $7 \pm 1.4$ | $3 \pm 1$ | 11 | OB-II | Moderate | Normal |
| | OB5 | $19 \pm 4.1$ | $0 \pm 1$ | 22 | OB-II | Big | Normal |
| H 1743-322 | OB1-A | $20 \pm 8$ | $0 \pm 1$ | 13 | OB-II | Big | Anomalous |
| | OB1-B | $2 \pm 0.7$ | $0 \pm 1$ | 0 | OB-I | Small | Normal |
| | OB2 | $0 \pm 1.1$ | $0 \pm 1$ | 0 | OB-I | Small | Normal |
| | OB3 | $2 \pm 1.4$ | $0 \pm 1$ | 2 | OB-I | Small | Normal |
| | OB4 | $2 \pm 7.8$ | $0 \pm 1$ | 0 | OB-I | Small | Anomalous |
| | OB5 | $0 \pm 6.4$ | $0 \pm 7$ | 3 | – | Small | Anomalous |

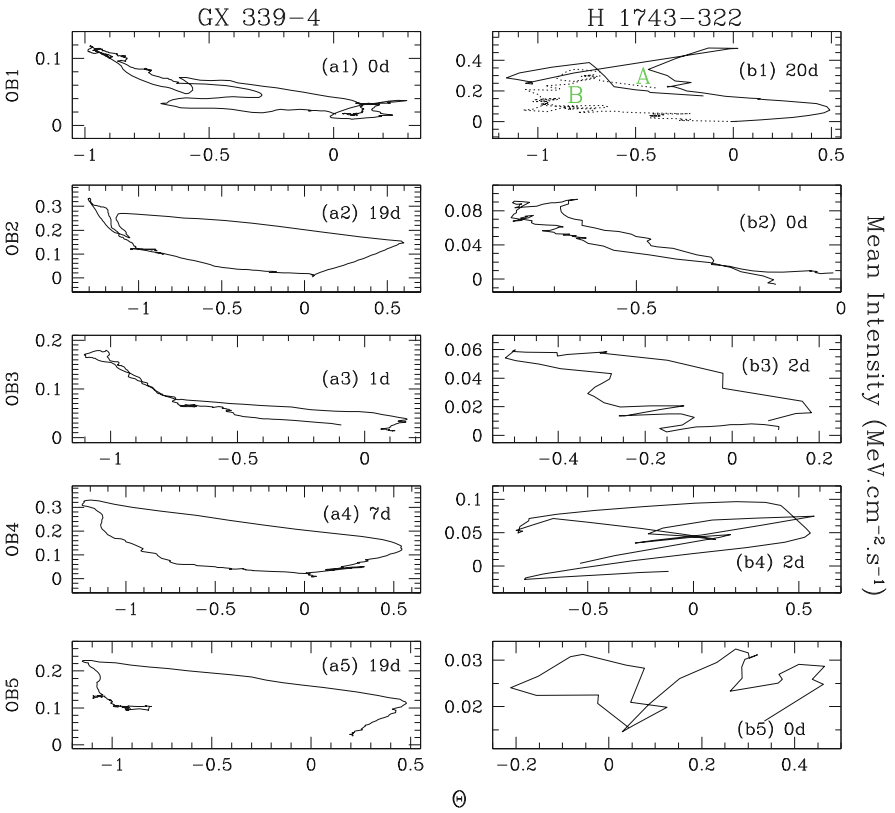



**Fig. 7** Hysteresis loop (a better alternative to q-track pattern of HR-intensity plot): twofold loop for OB1-A, and dotted loop for OB1-B in (**b1**) indicate a twin or a trinity in OB1; the bigger loop area in (**b1**) is consistent with higher $\tau_r(d)$ or larger disc size than those in its other OBs. Small area with $\tau_r(d) \rightarrow 0$ indicates a small disc due to a nearby $X_a$. An incomplete loop in (**a5**) is due to a lack of data in declining phase. In consistence with Fig. 5b4 and b5, multiple loops in (**b4**) hint at mini outbursts within OB4, while a closed loop in (**b5**) indicates that OB5 was *almost successful*

Figure 7 represents the mean intensity in all ten outbursts considered here as a function of $\Theta$. However, running-mean data are used for clarity and comparison. Loops account for the *hysteresis* property, in relation with the changes in both fluxes, as a measure of inability to retrace the rising phase track by the declining phase. This is due to an inability of the Keplerian disc to be dissipated away quickly in the absence of viscosity following the peak outburst (SS). In general, a closed loop ensures a normal (canonical) outburst. The loop area is a measure of *hysteresis loss*, i.e. the amount of matter dissipated away. 'Manifold' loops indicate either multiple mini outbursts, as in Fig. 7b4, or a twin outburst as in Fig. 7b1. It is trivial (Fig. 4b1) that the brightest outburst OB1 in H 1743 is a twin outburst; but, in view of both Figs. 5b1 and 7b1, any discerning reader might feel a thrill in observing that OB1-A itself is a twin outburst due to an interim HS and prefer a trinity. The wiggles in

the disrupted loop of Fig. 7a1 are due to multiple interim hardening/softening of the spectrum, justifying the fluctuations observed in the plateau region (Figs. 4a1 and 5a1). The statement that the outburst OB5 (2008) in H 1743 is *almost successful* [18] is true because of the closed loop in Fig. 7b5; but this is also a *failed* one as its narrow horizontal stretch ($\Theta \geq -0.2$) ascertains a lack of proper softening. In Roy and Chakrabarti [13] it was concluded that a large Keplerian disc (with strong hysteresis) in an outburst would take a long time to disappear. Thus the retracing track deviates more for a large Keplerian disc and vice versa. This is justified by the vertical stretch of the loops in Fig. 7. A large $\tau_r$ also means a large accumulation radius $X_a$. Hence, $\tau_r$, together with the loop area, indicates the size of the Keplerian disc. Clearly, the size of the disc is different in different outbursts. So, the magnificent *spectro-temporal* dynamic photon index $\Theta$, appropriate for two dynamic flows, basically scans every bit of an outburst.

In order to see the signature of TCAF also in HMXBs, we consider Cyg X-1 and Cyg X-3, along with an extra LMXB but a class-variable source, GRS 1915+105, with an observation by RXTE/ASM for a long time (5000 days). The responses of these three objects are instantaneous in terms of their photon fluxes, $\Theta$, and also CE [8]. Here, only the correlation profiles are given in Fig. 8. Hard and soft fluxes have no relative arrival time delay at all. Reig et al. [12] obtained similar flux-flux cross-correlation profiles in Cyg X-1 and GRS 1915+105 by using the three bands of long-term RXTE/ASM data separately and hardness ratios. This implies that the size of the Keplerian disc cannot be large in both; the disc in Cyg X-1, particularly in its *flare*s, is similar to that in OB-I type of outbursts in LMXB [8, 10]. However, Cyg X-3 behaves differently, in spite of its partial resemblance to both class-variable GRS 1915+105 and persistent Cyg X-1 in terms of otherwise segregated two components of radiation. The response of $\Theta$ with the fluxes is very weak. So, Cyg X-3 is quite different from Cyg X-1. Statistically weak peaks ($\Theta$-flux) at $\tau_r(d) = 0$ could possibly be explained, if Cyg X-3 is really a ternary system with 'double black hole' (BH-BH) or black-hole-and-neutron-star (BH-NS) progenitor [1], which must endow the flows with an additional nonlinearity, which could ruin the fine-tuning observed in both Cyg X-1 and GRS 1915+105. It could also be possible that no accumulation radius is needed at all in forming a disc in the inner region of all these three X-ray sources.

## 4 Summary

In several types (transient, persistent, or class-variable) of sources, pertaining to LMXBs and HMXBs, the soft fluxes either lag hard fluxes or both change simultaneously. This can be easily interpreted if there are two components in the accretion flow (CT95); the advective component, which is mainly responsible for the hard flux, always accretes faster than the viscous component, which primarily controls the soft flux. The Keplerian disc lags behind the sub-Keplerian halo because of its higher angular momentum, which is transported in a longer viscous timescale.

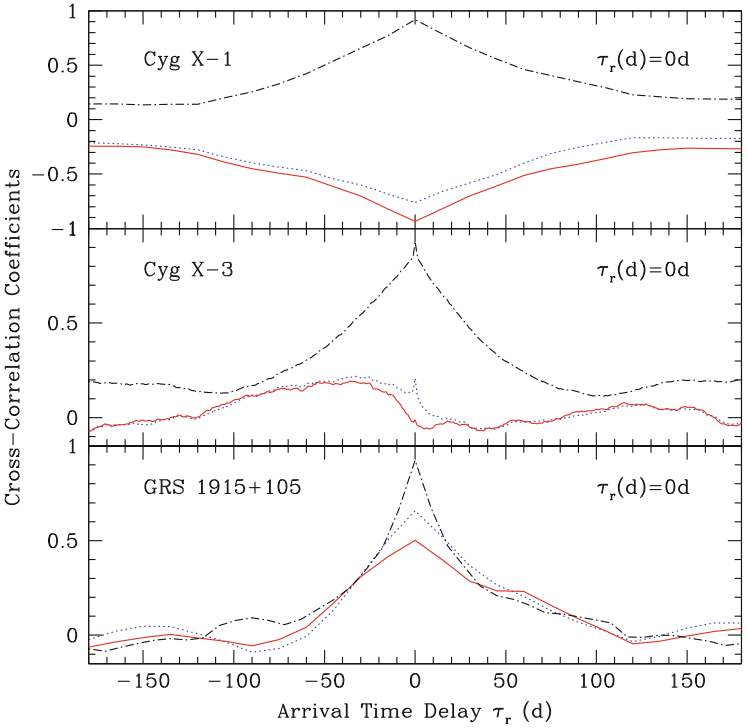



**Fig. 8** Correlations in Cyg X-1, Cyg X-3 and GRS 1915+105 with >13 years RXTE/ASM daily data: Colour/line stamps are same as in Fig. 6. No time delay is observed in all objects. This should be attributed to a small Keplerian disc in them. Behaviour of $\Theta$ with the photon fluxes in Cyg X-1 is similar to OB-I type of outbursts. Weak peaks of $\Theta$-flux correlations in Cyg X-3 are not wanting in physical significance, as it could be a ternary system with a doubly compact progenitor (BH-BH or BH-NS), which endues the overall accretion flow with an additional nonlinearity

The advective component having lower angular momentum does not require any viscosity in general. Our works reveal that the two components in an accretion flow are separable with or without a time delay between them in all sources considered here. Transient sources exhibiting outbursts reveal that no delay is necessary in order to trigger an outburst in LMXBs with a small disc; however, a significant time delay of few days to few weeks in LMXBs with big disc prevails. Moreover, our dynamic photon index $\Theta$ alone helped us classify all outbursts into two types, based on the difference in several distinct features, which are also consistent with the implications of CT95. Ghosh and Chakrabarti [7] inferred a similar result based on the smearing effect on the tidal perturbation at the outer edge of the disc due to viscosity. RXTE/ASM total photon flux above its average gave rise to a distinct peak in the Fourier spectra at quasi-orbital periods (QOPs)—a very sharp peak for HMXBs (Cyg X-1 and Cyg X-3) and a broad peak for LMXBs (e.g., GRS 1758-258 and 1E 1740.7-2942), thereby implying similar conclusions about the disc size.

Thus, the contributions of the two dynamic flow components of CT95 are proved to be indispensable for understanding both spectral and temporal properties pertaining to the accretion onto a black hole.

**Tailpiece:** Having evolved into an observational data analyst, I am fond of magic numbers. The date of birth of Professor Sandip Kumar Chakrabarti, i.e. 15th November '58, gives rise to a basic number 6 in two ways: (i) 1+5 = 6, and (as November = 11), (ii) $11 + 58 = 69 \Rightarrow 6 + 9 = 15 \Rightarrow 1 + 5 = 6$. I encountered him for the first time in 2003, i.e. 15 years ago. He is popularly known by all as SKC; S, K, and C respectively being the 19th, 11th, and 3rd letter of the alphabet: $19 + 11 + 3 = 33 \Rightarrow 3 + 3 = 6$. Are 15 or 6 trivial? Wait. Consider the two transient black holes studied here, i.e., GX 339 and H 1743. Now, G and H, respectively being the 7th and 8th letter, also result in $15 \Rightarrow 6$ when added. Furthermore, X = 24th letter, and $2 + 4 = 6$. Strangely enough, $1 + 7 + 4 + 3 = 15$ and $3 + 3 + 9 = 15$; both gives 6 ultimately! 6 is also the number of decades so far traveled by him with a reservoir of quests throughout the cosmos! Perhaps, he knows exactly what is happening out there or, why are the things the way they are there. I always take pride in the fact that I was destined to be pursuing research with such a great scientist like Him.

**Acknowledgements** I am grateful, for anything, to Professor Sandip Kumar Chakrabarti, who is far more in my life as a man, as an ideal scientist, and also for his magnetic personality, than merely the Supervisor of my PhD Thesis.

## References

1. Belczynski, K., Bulik, T., Mandel, I., Sathyaprakash, B.S., Zdziarski, A.A., Mikołajewska, J.: ApJ **764**, 96 (2013)
2. Capitanio, F., Belloni, T., Del Santo, M., Ubertini, P.: MNRAS **398**, 1194 (2009)
3. Chakrabarti, S.K.: MNRAS **243**, 610 (1990)
4. Chakrabarti, S.K.: ApJ **464**, 664 (1996)
5. Chakrabarti, S.K., Titarchuk, L.G.: ApJ **455**, 623 (1995)
6. Chakrabarti, S.K., Debnath, D., Nagarkoti, S.: (2018, submitted)
7. Ghosh, A., Chakrabarti, S.K.: ApSS **361**, 310 (2016)
8. Ghosh, A., Chakrabarti, S.K.: MNRAS **479**, 1210 (2018)
9. Ghosh, A., Chakrabarti, S.K.: (2018, submitted)
10. Ghosh, A., Banerjee, I., Chakrabarti, S.K.: (2018, submitted)
11. Pal, P.S., Chakrabarti, S.K.: ASR **56**, 1784 (2015)
12. Reig, P., Papadakis, I., Kylafis, N.D.: A&A **383**, 202 (2002)
13. Roy, A., Chakrabarti, S.K.: MNRAS **472**, 4689 (2017)
14. Shakura, N.I., Sunyaev, R.A.: A&A **24**, 337 (1973)
15. Smith, D.M., Heindl, W.A., Swank, J.H.: ApJ **569**, 362 (2002)

16. Sunyaev, R.A., Titarchuk, L.G.: A&A **86**, 121 (1980)
17. Sunyaev, R.A., Titarchuk, L.G.: A&A **143**, 374 (1985)
18. Zhou, J.N., Liu, Q.Z., Chen, Y.P., Li, J., Qu, J.L., Zhang S., Gao, H.Q., Zhang, Z.: MNRAS **431**, 2285 (2013)

# Study of Broadband Spectra of AGNs Using Two Component Advective Flow Paradigm




**Prantik Nandi**

**Abstract** We describe the spectral properties of Active Galactic Nuclei (AGNs) using TCAF. TCAF is two component advective flow solution based on proper hydrodynamics and radiative transfer equations. It is established that this is very successful to study stellar-mass black holes. Here we show that it is applicable for AGNs as well. We present the X-ray properties of AGNs and discuss our model with observational data of two nearby well known AGNs: NGC 4151 and NGC 7469. We fit the spectra with TCAF and find the corresponding parameters and compare them with other results.

## 1 Introduction

Active Galactic Nucleus (AGN) are the one of the most energetic and violent phenomena ever observed in the Universe. Sometimes the luminosity produced by AGNs is as high as $10^{44}$ erg $s^{-1}$ from a very compact region (probably less than 1 $pc^3$). These large energies have been hypothesised to be gravitational in origin: "The accretion of matter onto a massive black hole" [26]. It is remarkable that, 26 years later, it has been found that massive black hole does exist in almost all galactic centres [12]. The main point is to properly understand the accretion physics in relation to the observations for different types of AGNs and how they are related to each other and it is very complex to understand the proper accretion dynamics around a supermassive black hole ($M_{BH} \geq 10^6 M_{\odot}$). To comprehend of this accretion process, a full analysis is required from very low luminosity AGNs (low accretion rate and high mass) to high luminosity AGNs (high accretion rate and high mass).

P. Nandi (✉)
S. N. Bose National Centre for Basic Sciences, Kolkata, India
e-mail: prantiknandi@bose.res.in

© Springer International Publishing AG, part of Springer Nature 2018

B. Mukhopadhyay, S. Sasmal (eds.), *Exploring the Universe: From Near Space to Extra-Galactic*, Astrophysics and Space Science Proceedings 53,
https://doi.org/10.1007/978-3-319-94607-8_25

On the other hand, due to their extreme brightness (luminosity $\sim 10^{44} erg/s$), AGNs can be detected up to very high redshifts (upto z ∼4–5), making them optimal tracers of the large-scale structure of the universe [4]. Thus, they offer the possibilities to get the crucial information on how galaxies form and evolve at very early epochs during the evolution of the Universe.

To explain the spectral and timing properties of AGNs, scientists have proposed different models, such as, thin disk model (Lynden-Bell [18]) [27]; ADAF model [22] etc. by considering the complex accretion flow dynamics around a black hole. But each model has its own deficiencies as they are not all comprehensive. Chakrabarti and his co-workers [5–7] proposed a global advective flow solution on the base of radiative transfer equations with proper hydrodynamics of the flow. According to this model, there are two types of accretion flows (Keplerian and sub-Keplerian) which move towards the central object. The advective flow is puffed up due to its slowing down by the centrifugal barrier which, under some favourable conditions, can even produce a standing or oscillating shock in the vicinity of the black hole horizon. The region between the shock and the innermost sonic point close to the horizon is known as the CENtrifugal pressure supported BOundary Layer (CENBOL) and plays a major role by reprocessing injected low energy (soft) photons on it to produce high energy radiations including those observed in the X-ray band.

## 2 X-ray Study for AGNs

It is observed that AGNs are among the most powerful sources in X-rays. In most cases, the central X-ray source is covered by a huge cloud of a very large column density ($N_H > 10^{22}\,\mathrm{cm}^{-2}$) to explain absorbed X-ray emission. This allows one to study AGNs through X-rays.

The broadband spectral energy distribution (SED) of AGNs is shaped by the black hole properties as well as the nature of the infalling matter. In optical-UV band, the SED comprises a 'big blue bump', which is broadly consistent with optically thick and geometrically thin accretion disk proposed by Shakura and Sunyaev [27]. In X-ray band, AGN consists a primary continuum, which is approximated by a cut off power law with a reflection component. In general, the spectrum also show a significant photo-electric absorption, Fe fluorescence [13, 19] and inverse Compton scattering by hot, optically thin coronal region [15]. Along with this components, a cold and/or warm absorption can influence the AGN's X-ray spectrum and an additional soft excess is observed in most cases. The origin of this soft X-ray excess bump is poorly understood. It may be caused by further X-ray reflection off the accretion disk [8], partially ionised absorption [14], or warm Compton upscattering within the accretion disk [11]. Sometimes the X-ray, coming from the central part of AGNs may be absorbed by a cloud. Thus, the soft part of X-ray cannot be seen directly, leading to a classification of less active type 2 Seyfert

AGNs and rest AGNs are classified into type 1 Seyfert AGNs. However, this cloud is generally transparent in X-rays at energies greater than 4 KeV.

### *2.1 X-ray Instruments*

The study of astronomical objects at high energy regime (X-ray and $\gamma$-ray) began after 1970 when dedicated X-ray astronomy satellites, such as, *Uhuru*, *Ariel 5*, *SAS-3*, *HEAO-1* were launched. In the last couple of decades, several X-ray missions, such as, *EXOSAT*, *RXTE*, *ROSAT* etc. were launched. More recent ones are *Chandra*, *XMM-Newton* and *NuSTAR*.

*NuSTAR* mission is the first focusing high-energy X-ray telescope in orbit. This satellite operates in the energy band 3–79 KeV. One of the most important objectives to lunch *NuSTAR* is to probe the AGN activities in high energy regime. For details of the mission, see, Harrison et al. [16]. We use *NuSTAR* data for spectral analysis of NGC 4151 and the data from both *NuSTAR* and *XMM-Newton* are used for the spectral analysis of NGC 7469. Detail results are in [21] and [20].

## 3 Spectral Analysis of AGNs

Studying the spectral behaviour of an AGN and extracting the intrinsic properties of different physical parameters, like accretion rate, mass, size of Compton cloud have not been done before despite the presence of a large number of models in the literature. TCAF is capable of extracting in flow parameters as they evolve with time. But in case of other models, either they assume some of the parameters to fit a spectrum or depend on some previous surveys. This clearly shows huge advantage of TCAF over other models in understanding AGNs.

### *3.1 NGC 4151 and NGC 7469*

The nearby Seyfert 1 galaxies NGC 4151 (z = 0.003262; [10]) and NGC 7469 (z = 0.01639 de Vaucouleurs et al. [9]) have been a subject of extensive X-ray observations since 1970s. As NGC 4151 is the most bright nearby AGN, it has invariably been considered to be a prime target by major X-ray astronomy missions. This object has been extensively studied by missions such as *EXOSAT*, *Ginga*, *ROSAT*, *ASCA*, *CGRO* and more recently *RXTE*, *BeppoSAX*, *Chandra*, *XMM-Newton* and *NuSTAR*. The luminosity of this object in X-ray band is $L_{3.0\text{–}70.0\,\mathrm{KeV}} \sim 10^{44}$ erg/s. On the other hand, NGC 7469 is popular for its extreme behaviour in X-ray band. Evidences of excess soft emission in X-ray band were first observed by *EXOSAT* [1] of this AGN and subsequently confirmed by other X-ray observatories.

At high energy, *Ginga* observation revealed the evidence of Iron (Fe) line at 6.4 KeV and spectral flattening above 10 KeV [25]. The luminosity of this object in X-ray band is $L_{3.0\text{–}60.0\,\mathrm{KeV}} \sim 4 \times 10^{43}$ erg/s.

We will analyse the spectral behaviours of these AGNs by using TCAF model. For this, we use *NuSTAR* data at 3.0–70.0 KeV for NGC 4151 and 3.0–60.0 KeV for NGC 7469. After that, the background spectra are dominated over the source spectra (P18ab).

As both AGNs are nearby, the mass of the central black hole was estimated by various groups of scientists. For example, Hicks and Malkan [17] measured the dynamical mass of NGC 4151 is $M_{BH} = 3.0^{+0.75}_{-2.2} \times 10^7 M_\odot$ from the kinematics of the gas in the vicinity of the black hole. Onken et al. [23] measured the mass of the black hole to be $M_{BH} = 3.76^{+1.15}_{-1.5} \times 10^7 M_\odot$ by using stellar dynamical mass measurement. Also, many groups measured the mass of the black hole from reverberation mapping and find $M_{BH} = 4.57^{+0.57}_{-0.47} \times 10^7 M_\odot$ [2]. Using the slope and zero point determined by Tremaine et al. [28], the $M_{BH} - \sigma_*$ relationship predicts the black hole mass as $M_{BH} = 6.2^{+5.9}_{-3.0} \times 10^6 M_\odot$. This is a factor of 6 smaller than the other measurements. In case of NGC 7469, Peterson et al. [24] measured the mass of the black hole as $M_{BH} = 1.1 \pm 0.1 \times 10^7 M_\odot$ by using reverberation mapping.

We now carry out the spectral fit using TCAF for these objects. We use three *NuSTAR* observation ids for NGC 4151 and seven *NuSTAR* ids along with *XMM NEWTON* data for NGC 7469. In the literature, various groups of scientists were trying to determine the flow parameters [3]. They either consider mass or accretion rates etc. from other measurements to establish their results by using their models. We fitted all these observation ids by TCAF along with a power law tail. We also consider a Gaussian to fit the Fe line which arises at around 6.41 KeV. The spectra were fitted using 0% systematic error and the normalization kept free. Also, we do not consider any parameters determined by other groups. The fitting results of the spectra with $\chi^2$ are given in Table 1 and Fig. 1 [21] for NGC 4151 and in Table 2 and Fig. 2 [20] for NGC 7469 respectively. Here we see that our mass measurement of these AGNs are very precise as compared to other models and also its value agrees with most of the results which are discussed above.

**Table 1** TCAF + power law + Gaussian model fitted parameters in 3.0–70.0 KeV energy band for NGC 4151

| MJD | $\dot{m}_d$ ($10^{-3}\dot{M}_{EDD}$) | $\dot{m}_h$ ($10^{-2}\dot{M}_{EDD}$) | $X_s$ ($r_g$) | $R$ | $M_{BH}$ ($10^7 M_\odot$) | $N_{TCAF}$ ($10^{-2}$) | Photon index | $N_{pl}$ ($10^{-2}$) | $Fe$ $line$ (KeV) | $\sigma$ (KeV) | $N_{Fe}$ ($10^{-4}$) | $\chi^2/dof$ |
|---|---|---|---|---|---|---|---|---|---|---|---|---|
| 56243.26 | $1.77^{+0.4}_{-0.3}$ | $1.98^{+0.04}_{-0.03}$ | $150.87^{+22.0}_{-24.4}$ | $2.03^{+0.58}_{-0.73}$ | $3.10^{+0.27}_{-0.25}$ | $5.45^{+0.54}_{-0.54}$ | $1.47^{+0.01}_{-0.01}$ | $2.7^{+0.1}_{-0.1}$ | $6.24^{+0.07}_{-0.08}$ | $0.34^{+0.08}_{-0.07}$ | $3.26^{+0.2}_{-0.1}$ | 471.09/414 |
| 56243.79 | $2.29^{+0.29}_{-0.25}$ | $1.96^{+0.01}_{-0.01}$ | $152.735^{+16.25}_{-13.00}$ | $2.02^{+0.1}_{-0.01}$ | $2.99^{+0.27}_{-0.26}$ | $5.83^{+0.1}_{-0.1}$ | $1.43^{+0.01}_{-0.01}$ | $2.25^{+0.08}_{-0.09}$ | $6.31^{+0.19}_{-0.38}$ | $0.18^{+0.02}_{-0.03}$ | $3.90^{+0.3}_{-0.3}$ | 681.34/633 |
| 56245.34 | $2.21^{+0.3}_{-0.9}$ | $1.97^{+0.01}_{-0.04}$ | $152.67^{+26.20}_{-13.82}$ | $2.00^{+0.46}_{-0.45}$ | $2.99^{+0.2}_{-0.1}$ | $5.45^{+0.6}_{-0.6}$ | $1.64^{+0.06}_{-0.06}$ | $5.99^{+0.1}_{-0.1}$ | $6.27^{+0.03}_{-0.04}$ | $0.17^{+0.05}_{-0.05}$ | $7.40^{+0.1}_{-0.1}$ | 743.54/586 |

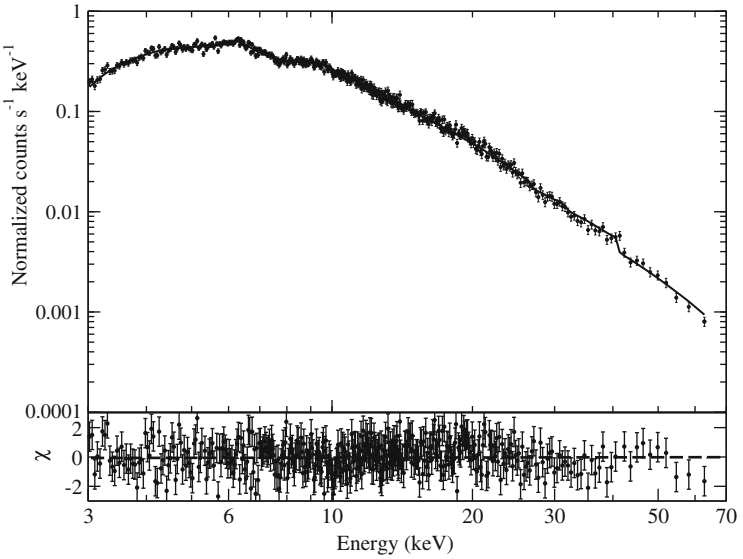



**Fig. 1** TCAF + power-law + Gaussian model is fitted for 3.0–70.0 KeV *NuSTAR* data and folded model spectrum of NGC 4151. The observation Id is 60001111002 (MJD 56243.26). The upper panel shows the fitted spectrum with corresponding model and the lower panel gives the variation of $\chi$. We consider systematic error as 0% and the final value of reduce $\chi^2$ is $\chi^2_r = 1.138$ [21]

From our fits, it is clear that spectral fitting of AGN by using TCAF solution produces reasonable value of mass along with various physical parameters. Also, this model does not require to refer the other sources and their details. The main advantage of this model is that it can show the dynamical variation of different parameters (accretion rates, shock location [namely, size of the Compton cloud], compression ratio etc.) naturally. If we continuously observed an object we can also determine the shock velocity, hence shock oscillation (if QPO is present there) precisely. So, this model is far better for use to determine accretion dynamics around AGNs. We will explore these aspects in future for other objects as well.

**Table 2** TCAF + power-law + Gaussian model fitted parameters in 0.8–60.0 KeV energy band for NGC 7469

| MJD | $\dot{m}_d$ ($10^{-2}\dot{M}_{EDD}$) | $\dot{m}_h$ ($10^{-2}\dot{M}_{EDD}$) | $X_s$ ($r_g$) | $R$ | $M_{BH}$ ($10^7 M_\odot$) | $N_{TCAF}$ | Photon index | $N_{pl}$ ($10^{-3}$) | $Fe$ $line$ (KeV) | $\sigma$ (KeV) | $N_{Fe}$ ($10^{-5}$) | $\chi^2/dof$ |
|---|---|---|---|---|---|---|---|---|---|---|---|---|
| 57185.78 | $3.10^{+0.1}_{-0.1}$ | $2.10^{+0.06}_{-0.05}$ | $10.001^{+0.14}_{-0.01}$ | $6.25^{+0.01}_{-0.01}$ | $1.00^{+0.01}_{-0.09}$ | $0.16^{+0.01}_{-0.01}$ | $1.77^{+0.01}_{-0.01}$ | $7.49^{+0.1}_{-0.2}$ | $6.33^{+0.01}_{-0.01}$ | $0.037^{+0.01}_{-0.03}$ | $2.89^{+0.4}_{-0.4}$ | 1461.50/1380 |
| 57350.69 | $3.07^{+0.1}_{-0.1}$ | $2.07^{+0.08}_{-0.08}$ | $10.001^{+0.002}_{-0.06}$ | $6.24^{+0.01}_{-0.006}$ | $1.09^{+0.03}_{-0.02}$ | $0.11^{+0.01}_{-0.01}$ | $1.71^{+0.01}_{-0.02}$ | $5.81^{+0.008}_{-0.01}$ | $6.33^{+0.01}_{-0.01}$ | $0.016^{+0.03}_{-0.04}$ | $2.69^{+0.3}_{-0.4}$ | 1312.16/1203 |
| 57371 | $3.08^{+0.1}_{-0.2}$ | $2.06^{+0.02}_{-0.01}$ | $10.087^{+0.26}_{-0.09}$ | $6.34^{+0.09}_{-0.01}$ | $1.04^{+0.01}_{-0.01}$ | $0.13^{+0.01}_{-0.01}$ | $1.73^{+0.01}_{-0.01}$ | $6.35^{+0.07}_{-0.07}$ | $6.35^{+0.09}_{-0.1}$ | $0.05^{+0.01}_{-0.01}$ | $3.09^{+0.3}_{-0.4}$ | 1585.08/1452 |
| 57378.43 | $3.08^{+0.1}_{-0.1}$ | $2.07^{+0.06}_{-0.06}$ | $10.006^{+0.24}_{-0.03}$ | $6.29^{+0.01}_{-0.01}$ | $1.01^{+0.01}_{-0.01}$ | $0.14^{+0.01}_{-0.01}$ | $1.74^{+0.07}_{-0.06}$ | $7.62^{+0.1}_{-0.1}$ | $6.35^{+0.01}_{-0.01}$ | $0.036^{+0.02}_{-0.01}$ | $2.64^{+0.3}_{-0.2}$ | 1678.43/1527 |
| 57381 | $3.24^{+0.1}_{-0.1}$ | $2.02^{+0.07}_{-0.08}$ | $10.001^{+2.97}_{-1.20}$ | $6.37^{+0.18}_{-0.01}$ | $1.06^{+0.01}_{-0.01}$ | $0.14^{+0.02}_{-0.02}$ | $1.74^{+0.01}_{-0.01}$ | $7.49^{+0.01}_{-0.01}$ | $6.37^{+0.01}_{-0.02}$ | $0.049^{+0.02}_{-0.01}$ | $3.06^{+0.5}_{-0.5}$ | 1489.58/1226 |
| 57383 | $3.17^{+0.01}_{-0.02}$ | $2.05^{+0.01}_{-0.01}$ | $10.001^{+0.003}_{-0.09}$ | $6.47^{+0.008}_{-0.01}$ | $1.10^{+0.02}_{-0.03}$ | $0.18^{+0.01}_{-0.02}$ | $1.7^{+0.01}_{-0.01}$ | $6.62^{+0.1}_{-0.1}$ | $6.36^{+0.01}_{-0.02}$ | $0.069^{+0.02}_{-0.03}$ | $3.26^{+0.5}_{-0.5}$ | 1375.96/1267 |
| 57384.94 | $3.11^{+0.1}_{-0.1}$ | $2.07^{+0.07}_{-0.07}$ | $10.001^{+0.24}_{-0.02}$ | $6.25^{+0.01}_{-0.01}$ | $0.99^{+0.01}_{-0.01}$ | $0.15^{+0.01}_{-0.01}$ | $1.72^{+0.01}_{-0.01}$ | $7.7^{+0.1}_{-0.1}$ | $6.35^{+0.01}_{-0.01}$ | $0.061^{+0.02}_{-0.02}$ | $3.23^{+0.5}_{-0.4}$ | 1670.33/1510 |

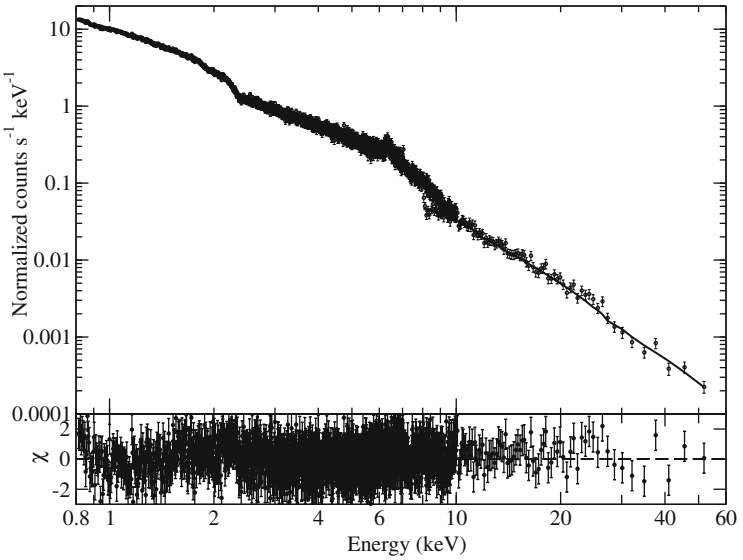



**Fig. 2** TCAF + power-law + Gaussian model is fitted for 0.8–60.0 KeV *NuSTAR* data and folded model of NGC 7469. The observation is done in MJD 57383.06. The upper panel shows the fitted spectrum with corresponding model and the lower panel gives the variation of $\chi$. We consider systematic error as 0% and the final value of reduce $\chi^2$ is $\chi^2_r = 1.07$ [20]

## References

1. Barr, P.: MNRAS **223**, 29P (1986)
2. Bentz, M.C., et al.: ApJ **651**, 775 (2006)
3. Beuchert, T., Markowitz, A.G., Dauser, T., et al.: A&A **603**, A50 (2017)
4. Cappelluti, N., Hasinger, G., Brusa, M., Comastri, A., Zamorani, G., Brunner, H., Civano, F., Finoguenov, A., Fiore, F., Gilli, R., Griffiths, R.E., Mainieri, V., Matute, I., Miyaji, T., Silverman, J.: ASPC **380**, 171C (2007)
5. Chakrabarti, S.K.: MNRAS **243**, 610 (1990)
6. Chakrabarti, S.K., Molteni, D.: ApJ **417**, 671 (1993)
7. Chakrabarti, S.K., Titarchuk, L.G.: ApJ **455**, 623 (1995)
8. Crummy, J., Fabian, A.C., Gallo, L., Ross, R.R.: MNRAS **365**, 1067 (2006)
9. de Vaucouleurs, G., de Vaucouleurs, A., Corwin, H.G. Jr., Buta, R.J., Paturel, G., Fouque, P.: Third Reference Catalog of Bright Galaxies, Version 3.9. Springer, New York (1991)
10. de Vaucouleurs, G., de Vaucouleurs, A., Corwin, H.G., Jr., et al.: AIP Conf. Proc. 183, Third Reference Catalogue of Bright Galaxies. AIP, Melville (1991)
11. Done, C., Davis, S.W., Jin, C., Blaes, O., Ward, M.: MNRAS **420**, 1848 (2012)
12. Gebhardt, K., Kormendy, J., Ho, L.C., et al.: ApJL **543**, L5 (2000)
13. George, I.M., Fabian, A.C.: MNRAS **249**, 352 (1991)
14. Gierlński, M., Done, C.: MNRAS **349**, L7 (2004)
15. Haardt, F., Maraschi, L.: ApJL **380**, L51 (1991)
16. Harrison, F.A., et al.: ApJ **770**, 103 (2013)
17. Hicks, E.K.S., Malkan, M.A.: ApJ **174**, 31 (2008)
18. Lynden-Bell, D.: Phys. Scr. **17**, 185 (1978)
19. Matt, G., Perola, G.C., Piro, L.: A&A **247**, 25 (1991)

20. Nandi, P., Chakrabarti, S.K.: (2018, submitted)
21. Nandi, P., Chakrabarti, S.K., Mandal, S.: (2018, submitted)
22. Narayan, R., Yi, I.: ApJ **248**, 13 (1994)
23. Onken, C.A., Valluri, M., Brown, J.S., et al.: ApJ **791**, 37 (2014)
24. Peterson, B.M., Grier, C.J., Home, K., et al.: ApJ **795**, 149 (2014)
25. Piro, L., Yamauchi, M., Matsuoka, M.: ApJ **360**, L35 (1990)
26. Rees, M.J.: ARA&A **22**, 471 (1984)
27. Shakura, N.I., Sunyaev, R.A.: In: Bradt, H., Giacconi, R. (eds.) IAU Symposium 55, X- and Gamma-Ray Astronomy, p. 155. Dordrecht, Reidel (1973)
28. Tremaine, S., et al.: ApJ **574**, 740 (2002)

# Spectral Study of Ultraluminous X-ray Sources with XMM-Newton




**Piklu Santra**

**Abstract** We study the spectral properties of ultraluminous X-ray (ULX) sources HOLMBERG IX X-1 and HOLMBERG II X-1 using the archival data of XMM-Newton (0.3–10.0 KeV) satellite. We use **Two Component Advective Flow (TCAF)** solution as an additive model in XSPEC for the spectral analysis. We extract parameters such as, Keplerian disk accretion rate ($\dot{m}_d$), sub-Keplerian accretion rate ($\dot{m}_h$), shock location ($x_s$), compression ratio (R) and mass of the black hole ($M_{bh}$). We fit the data from XMM-Newton satellite with **TCAF** model in the broadband energy coverage. From the spectral fit, we find that both sources contain an intermediate-mass black hole which accretes mass in sub-Eddington rate.

## 1 Introduction

Black hole is a region of space-time and its gravitational pull is so strong that no particle or electromagnetic radiation can escape from it. These objects do not produce any electromagnetic radiation and also no direct ways exists for the detection of these objects. To detect these objects, to understand the accretion flow dynamics (disk rate, halo rate etc.) and to measure important quantities such as mass and spin of the black hole, we need indirect ways. One important way is studying the accretion disk around these objects.

Three types of astrophysical black holes are present in literature: these are, Stellar Mass Black Hole (StMBH), Super Massive Black Hole (SMBH) and Intermediate Mass Black Hole (IMBH).

A. **StMBHs**: StMBHs are formed when normal stars die and their mass range is ($\sim$5–20$M_\odot$). Many galactic/extra galactic X-ray binary contain a StMBHs, other carry a neutron star or a white dwarf. The luminosity of these objects is

P. Santra (✉)
S. N. Bose National Centre for Basic Sciences, Kolkata, India
e-mail: piklusantra@bose.res.in

© Springer International Publishing AG, part of Springer Nature 2018

B. Mukhopadhyay, S. Sasmal (eds.), *Exploring the Universe: From Near Space to Extra-Galactic*, Astrophysics and Space Science Proceedings 53,
https://doi.org/10.1007/978-3-319-94607-8_26

typically less than $10^{39}$ ergs/s. Accretion processes on these objects are two types: Roche lobe overflow and wind accretion. Few ULX sources may contain massive stellar-mass black holes (20–100$M_{\odot}$).

B. **SMBHs**: Every galaxy is assumed to have a supermassive black hole ($10^{6}$–$10^{10}M_{\odot}$) at the centre and the luminosity is typically above $10^{42}$ erg/s. Accretion process is mainly from wind accretion. In case of the Milky Way, the SMBH is located at Sagittarius A*.

C. **IMBHs**: These are a new type of black holes. The mass of these type of black holes is ($10^{2}$–$10^{5}M_{\odot}$). Observationally, it has been found that IMBHs can exist in some ultraluminous X-ray (ULXs) sources. It is not known how these objects were formed. Different routes are thought of for their formation such as merging of a stellar-mass black hole (StMBH) with other compact objects, runaway collision of massive stars in dense stellar clusters (e.g., Globular cluster) or Primordial black holes (PBHs) of the early universe (Big Bang).

## *1.1 Ultraluminous X-ray (ULX) Sources*

ULXs are the astronomical objects whose X-ray luminosity ($10^{39}$–$10^{42}$erg $s^{-1}$) is below the luminosity of an active galactic nucleus (AGN) but they are more luminous than a Galactic X-ray binary. They are extra-galactic, non-nuclear point sources. It is unclear as to how these ULXs can produce such a high energy output. Different models suggest different processes. These include super-Eddington accretion [3] on stellar mass black holes or sub-Eddington accretion on intermediate-mass black holes [24]. It can also be due to relativistic jets beamed toward us [22].

Einstein satellite discovered these objects but due to the low resolution, it was not clear that whether they were galactic X-ray sources or not [11–13]. ROSAT and ASCA satellite confirmed that they were extra-galactic objects and their behaviours were different from galactic X-ray binary. Their luminosities were well above the Eddington limit of typical Galactic stellar mass BHs [11]. The black body temperature for a Galactic black hole is of the order of 1–2 KeV, but it is 0.1–0.4 KeV for ULXs. Low-temperature black body photon and high variability (few minutes to a few days) suggest ULXs harbour IMBH ($10^{2}$–$10^{5}M_{\odot}$) [24]. ULXs are found in an elliptical and spiral galaxies and also in a star-forming galaxy [16, see for review on ULXs].

In the energy interval 0.3–10.0 KeV, the energy spectra of ULXs can be divided into two groups: (1) simple power law dominated, (2) combination of soft excess below 2 Kev and a power law above 2 KeV. Some ULXs in the hard state show strong flux variability [15]. The spectra of ULXs can be modelled by the combination of power-law and low temperature (0.1–0.4 KeV) disk component [14]. This cool component was first identified by Fabian and Ward [10]. Most of the ULXs are persistence sources.

Galactic X-ray binaries show low-frequency Quasi-Periodic Oscillations (LFQPOs) [4, 26, 27] and it is ∼Hertz (Hz). Their masses have been calculated using Mass-QPO anti-correlation. Similarly QPO frequency (in MHz order) has been detected in ULX sources such as NGC 5408 X-1 [29], M82 X-1 [30], HOLMBERG IX X-1 [9], NGC 1313 X-1 [31], IC 342 X-1 [1] and the mass has been calculated from Mass-QPO frequency anti-correlation. Recently, it is reported that some ULXs contain neutron stars in their core and they are M82 X-2 [2], NGC 5907 X-1 [18, 19] and NGC 7793 P13 [18, 19].

Many models exist in the literature for explaining spectral and temporal properties of StMBHs, SMBHs and IMBHs. To study the spectral properties of BHs two components are needed, namely, multicolour black body component which emit from the thick Keplerian disk [34] around them and the power-law component which comes from the inner part of the disk (Compton cloud) [35, 36]. In this paper, we use Two Component Advective Flow (TCAF) solution [5] for spectral study which has both the components accreting simultaneously. Details of these results would be published in Santra and Chakrabarti [33].

## 2 Our Target Sources

### *2.1 HOLMBERG II X-1*

HOLMBERG II X-1 (HO II X-1) is a ULX source with luminosity $10^{40}$ erg $s^{-1}$. It resides near the edge of a dwarf star-forming galaxy and embedded in an H II region. He II emission-line cloud has been discovered at the position of HO II X-1 which indicates that it is actually photoionizing the surrounding gas [25]. ROSAT observation of HO II X-1 showed days to years variability (Grise et al. [17]). The spectrum is well described by a multicomponent disk (kT $\sim$ 170 eV) and a power law component (index $\sim -1.9$) observed by ROSAT and ASCA satellite [25]. XMM-Newton data showed a transition from brightest state to soft state in 2002 [8]. Radio observation showed collimated jets from HO II X-1 [7]. HO-II X-1 shows variabilities in infrared wavelength [23].

### *2.2 HOLMBERG IX X-1*

HOLMBERG IX X-1 (HO-IX X-1 or M81 X-9) is a bright ULX source with average luminosity $\sim 10^{40}$ erg $s^{-1}$ located near the galaxy M81. It was discovered by Einstein observatory [12] and later studied by many other satellites such as XMM-Newton, Chandra, NuSTAR. Swift observation of HOLMBERG IX X-1 showed that

the spectra can be fitted by the dual thermal model with cool blackbody and warm disk blackbody [21]. A QPO having frequency 202.5 MHz was detected with XMM-Newton observation [9]. Vierdayanti et al. [37] confirmed that source luminosity varies by a factor 3–4 using XMM-Newton and Swift data.

## 3 Observation and Results

Both the objects (HOLMBERG II X-1 and HOLMBERG IX X-1) are well studied by different authors since their discovery. Spectral and temporal properties are well studied by various models using data from various satellites (ASCA, Swift, XMM-Newton, Chandra, NuSTAR, Suzaku) in X-ray wavelength. Most mysterious things about these objects are the masses of the central object and the accretion processes. Masses have been calculated by several authors but those values vary from stellar to intermediate range. None of them have calculated the accretion rates. No precise value of the mass and no single model exists in the literature which can measure the mass of central black hole of ULXs till date. We use Two Component Advective Flow (TCAF) solution to calculate the mass of the central object (BHs). This model is also capable of determining the accretion rates.

Earlier, TCAF solution has been used to study accretion flow properties (i.e., the accretion rates, sizes of the Compton cloud, etc.) and to measure the mass of a few galactic stellar mass black holes such as H1743-322 (Bhattacharjee et al. 2016), MAXI J1836-194 [20], MAXI J1659-152 [26], GX 339-4 [28], J1543-564 [6]. This model successfully explained the flow properties around black holes and the measured mass by the TCAF lies within the mass range which is present in the literature. Inspired by these, we use TCAF model for the study of ULXs because it is generally believed that the central object of ULXs is a black hole.

For the spectral study, we use archival data of XMM-Newton satellite. We take all data of HOLMBERG IX X-1 and HOLMBERG II X-1 from XMM-Newton archive. We fit all the data (XMM-Newton data) with TCAF model in 0.3–10 KeV energy range and extract the parameters such as the mass of black hole, Keplerian disk accretion ($\dot{m}_d$), sub-Keplerian accretion rate ($\dot{m}_h$), shock location ($X_s$) and compression ratio R (ratio of density of post-shock flow to density of pre-shock flow). Details are presented in Santra and Chakrabarti [33].

The mass of HOLMBERG IX X-1 varies from $154.972 M_{\odot}$ to $335.956 M_{\odot}$, disk rate varies from 0.006495 to 0.007847 (in unit of $\dot{m}_{Edd}$) and halo rate varies from 0.004695 to 0.005055 (in unit of $\dot{m}_{Edd}$).

The mass of HOLMBERG II X-1 lies in intermediate region (2000 - 8000 solar mass), disk rate and halo rate vary in sub Eddington rate (of the order 0.001) (Figs. 1, 2).

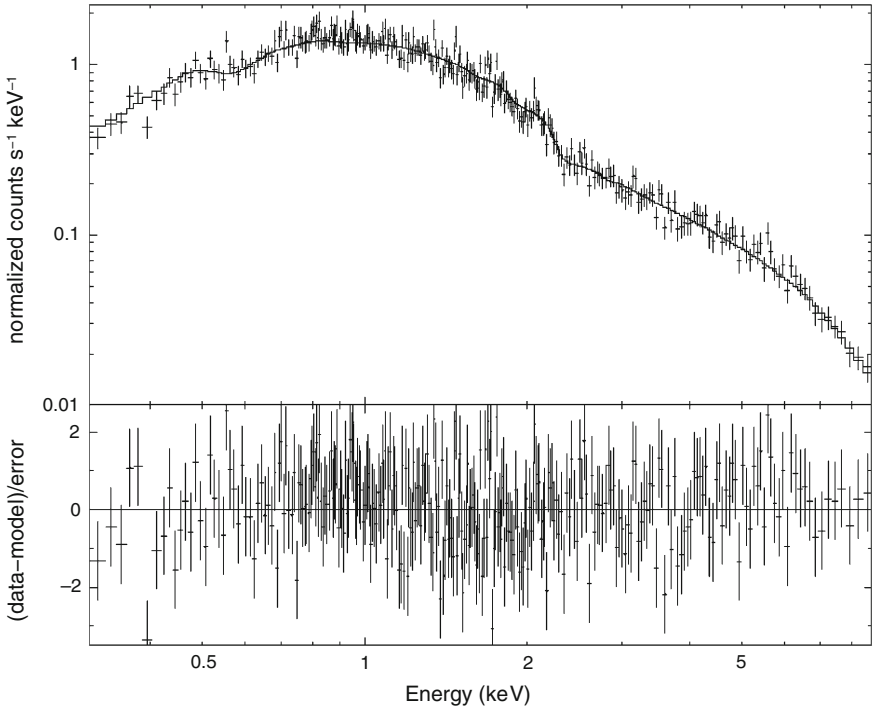



**Fig. 1** TCAF model fitted spectra of HOLMBERG IX X-1 in 0.3–10.0 KeV. Data taken from XMM-Newton data archive on 25th October 2012 (obs id. 0693850901). $\chi^2_{red} = 1.0644$ [33]

## 4 Conclusion

Our primary motive is to calculate the mass of the central object of ULXs. For ULX sources HOLMBERG IX X-1 and HOLMBERG II X-1, we find that TCAF fitted masses of these sources lie within intermediate ($10^2$–$10^5 M_\odot$) region and accretion rates lie within sub-Eddington region. This leads us to conclude that HO-IX X-1 and Ho II X-1 both ULXs contain an intermediate-mass black hole which accretes the matter in sub-Eddington rate. Details will be presented in Santra and Chakrabarti [33].

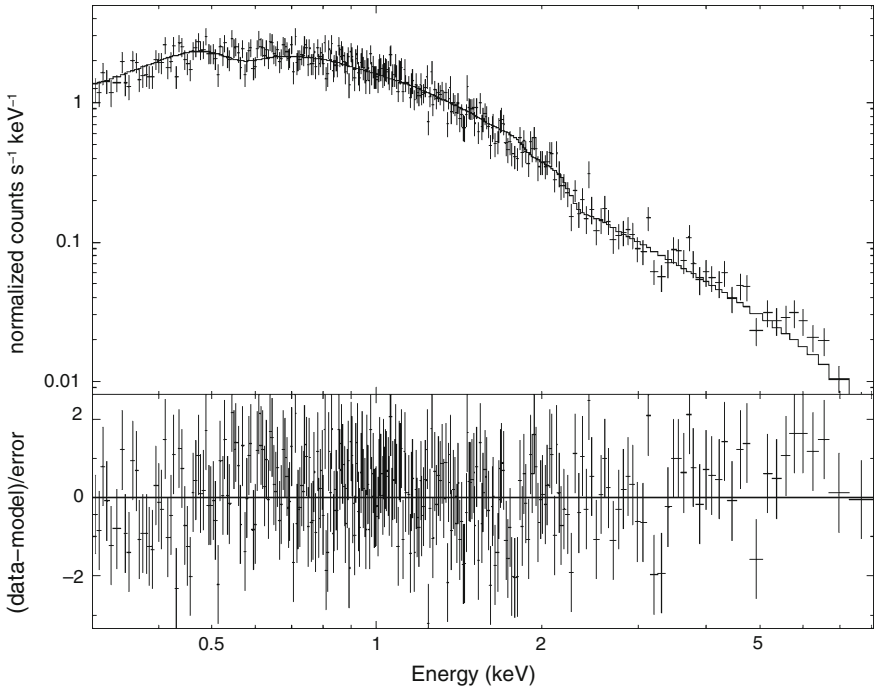



**Fig. 2** TCAF model fitted spectra of HOLMBERG II X-1 in 0.3–10.0 KeV. Data taken from XMM-Newton data archive on 16th April 2002 (obs id 0112520701). $\chi^2_{red} = 1.0854$ [32]

## References

1. Agrawal, V.K., Nandi, A.: MNRAS **446**, 3926 (2015)
2. Bachetti, M., Harrison, F.A., Walton, D.J., et al.: Natur **514**, 202 (2014)
3. Begelman, M.: ApJ **568**, L97 (2002)
4. Bhattacharjee, A., Chakrabarti, S.K.: MNRAS **466**, 1372 (2017)
5. Chakrabarti, S.K., Titachuk, L.G.: ApJ **455**, 623 (1995)
6. Chatterjee, D., Debnath, D., Chakrabarti, S.K., Mondal, S., Jana, A.: ApJ **827**, 88 (2016)
7. Cseh, D., Kaaret, P., et al.: MNRAS **439** (2014)
8. Dewangan, G.C., et al.: ApJ **608**, 57 (2004)
9. Dewangan, G.C., Griffiths, R.E., Rao, A.R.: ApJ **641** (2006)
10. Fabian, A.C., Ward. M.J.: MNRAS **263**, L51–L54 (1993)
11. Fabbiano, G.: ApJ **325**, 544 (1988)
12. Fabbiano, G.: ARA&A **27**, 87 (1989)
13. Fabbiano, G., Trinchieri, G.: ApJ **315**, 46 (1987)
14. Feng, H., Kaaret, P.: ApJ **633**, 1052 (2005)
15. Feng, H., Kaaret, P.: ApJ **696**, 1712 (2009)
16. Feng, H., Soria, R.: New Astron. Rev. **55**(5), 166 (2011)
17. Grise, F., Kaaret, P., et al.: ApJ **724**, 148 (2010)
18. Israel, G.L., Belfiore, A., Stella, L., et al.: Sci. **355**, 817 (2017)
19. Israel, G.L., Papitto, A., Esposito, P., et al.: MNRAS **466**, L48 (2017)
20. Jana, A., Chakrabarti, S.K., et al.: ApJ **819**, 107 (2016)

21. Kong, A.K.H., Yang, Y.J.: ApJ **722**, 1816–1820 (2010)
22. Kording, E., Falcke, H., MarkoA, S.: A&A **382**, L13 (2002)
23. Lau, R.M., et al.: ApJ **838**, L17 (2017)
24. Miller, J.M., Fabian, A.C., Miller, M.C.: ApJ **607**, 931 (2004)
25. Miyaji, T., Lehmann, I., Hasinger, G.: AJ **121**, 3041 (2001)
26. Molla, A.A., Debnath, D., Chakrabarti, S.K., Mondal, S.: MNRAS **460**, 3163 (2016)
27. Molla, A.A., Debnath, D., Chakrabarti, S.K., Mondal, S.: ApJ **834**, 88 (2017)
28. Mondal, S., Chakrabarti, S. K., Debnath, D.: ApSS **361**, 309 (2015)
29. Pasham, D.R., Strohmayer, T.E.: ApJ **753**:139 (2012)
30. Pasham, D.R., Strohmayer, T.E.: ApJ **771**, 101 (2013)
31. Pasham, D.R., et al.: ApJ **811**, L11 (2015)
32. Santra, P., Chakrabarti, S.K.: (under preparation)
33. Santra, P., Mondal, S., Chakrabarti, S. K.: (2018, to be submitted)
34. Shakura, N.I., Sunyaev, R.A.: A&A **24**, 337 (SS73) (1973)
35. Sunyaev, R.A., Titarchuk, L.G.: ApJ **86**, 121 (1980)
36. Sunyaev, R.A., Titarchuk, L.G.: A&A **143**, 374 (1985)
37. Vierdayanti, K., Done, C., Roberts, T.P., Mineshige, S.: MNRAS **403**, 120 (2010)

# Radio Observations of Galactic Compact Objects




**Sabyasachi Pal**

**Abstract** We discuss multi-wavelength observations of various compact objects giving emphasis in radio wavelengths. In this review, we will study spectral and timing properties of various Galactic compact objects, giving special attention to enigmatic compact object SS 433 and Galactic center black hole Sgr A*. Effort to search and discovery of transient radio sources from archival and pointed observations is also discussed. The method of determination of accretion rate of a black hole in quiescent state is discussed. We have also studied various properties of supernova and gamma-ray bursts and their host galaxies. The youngest supernova remnant in our galaxy G354.4+0.0 is discovered.

## 1 Introduction

As I am always curious about almost everything in life and love to explore different options in life, my trajectory in astronomical career also came across objects of different sizes (from extra-solar planets to galaxy clusters [29]) and energy bands (from very low radio frequencies [5, 6] to X-ray [19, 20] and $\gamma$ ray frequencies [29]). In this review, I will mostly be confined with study of compact objects (which was my PhD topic), but I will also touch upon some of my other loves like Galactic plane survey, search of transient radio sources, discovery of supernova remnants, study of radio galaxies and cluster of galaxies.

Compact objects are ultimate example of transient and variable sources. There are various examples of Galactic compact objects like neutron stars, white dwarfs, flare stars, brown dwarfs, radio emitting extra-solar planets. However, most compact sources are stellar black holes which have Schwarzschild radius of $r_g \sim$ few kilometers.

S. Pal (✉)
Indian Centre for Space Physics, Kolkata, India

© Springer International Publishing AG, part of Springer Nature 2018

B. Mukhopadhyay, S. Sasmal (eds.), *Exploring the Universe: From Near Space to Extra-Galactic*, Astrophysics and Space Science Proceedings 53,
https://doi.org/10.1007/978-3-319-94607-8_27

In this review, we will mention different spectral and timing properties of galactic compact objects, specially black holes. We have studied several black holes in past. Here we emphasis the study of three objects SS 433, Cygnus X-3 and A0620-00.

In the later parts of this review, I will touch upon Galactic plane survey and discovery of transient radio sources and youngest supernova remnants of our Galaxy. I also briefly mention some of the finding in extra-galactic astronomy.

## 2 Multi-Wavelength Observations of Galactic Compact Objects

Multi-wavelength observations are carried out with many Galactic compact objects to understand temporal and spectral evolution of these sources. We have used instruments in X-ray, IR, optical and radio wavelengths for doing the multi-wavelength campaign of several black holes and neutron stars.

We studied in detail the Galactic micro-quasar SS 433 [7]. For 2002 campaign (lightcurve in Fig. 1), we used the Giant Meterwave Radio Telescope (GMRT) for radio observations, the Physical Research Laboratory owned Infrared Telescope at Mt. Abu for infrared (IR), the ARIES telescope at Nainital for optical photometry, the telescope at the Vainu Bappu observatory for spectral measurements and the Rossi X-ray Timing Explorer for X-ray observations (3–25 keV). We find sharp

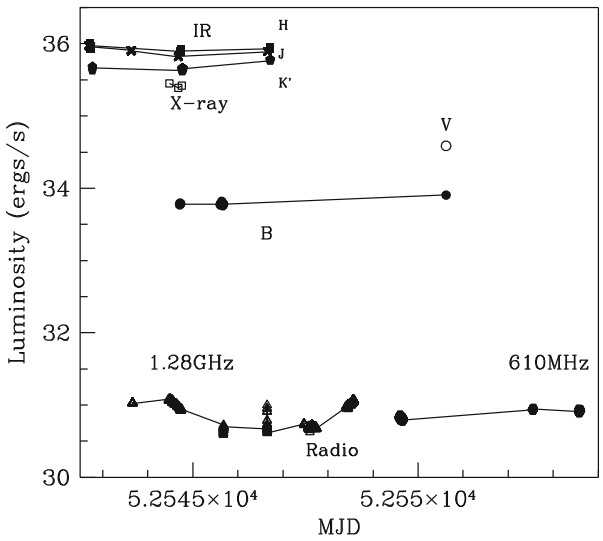



**Fig. 1** Multi-wavelength observation of SS 433 at 1.28 GHz (triangles) and 610 MHz (filled hexagons) in radio, at J (crosses), H (filled boxes), K′ (filled pentagons) bands in IR, B (filled circles) and V (open circle) bands in optical, and 3–25 keV (open squares) in X-ray during the campaign (from [5])

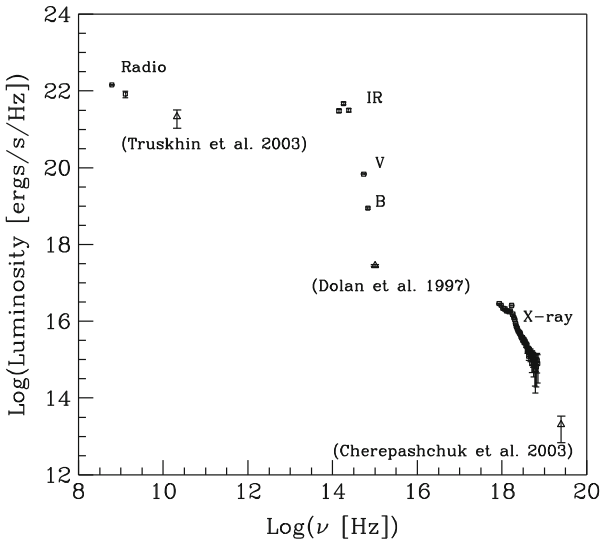



**Fig. 2** The multi-wavelength spectrum of SS 433 during 2002 campaign. Here, average luminosity (open boxes) over the available data has been plotted and the wave-bands are marked. For comparison, we include three points, marked by open triangles with error bars, from the literature (marked) which are not contemporaneous with our observation (from [5])

variations in intensity on time-scales of a few minutes in the X-ray, IR and radio wavelengths. Differential photometry in the J, H and K′ bands clearly indicates significant intrinsic variations on short time-scales of minutes. The broad-band spectrum showed evidence of very high extinction in the optical region, possibly due to a large scale obscuration of the central object by matter coming from the companion wind. Combining the results for these wavelengths, we find a signature of delay of about 2 days between the IR and radio signals. The X-ray spectrum yielded double Fe line profiles which corresponded to red and blue components of the relativistic jet. We also present the broad-band spectrum averaged over the campaign duration (Fig. 2).

SS 433 is an eclipsing binary black hole. We make multi-wavelength observation during a very rare occasion when the blue jet was pointing towards us (the precessional phase $\psi = 0$) and when the orbital phase $\phi$ of its companion was nearly zero (inferior conjunction) and compare this with the results obtained when $\psi \sim 0.5$ (superior conjunction) [8]. We used the RXTE for photometry and spectral study at 3–25 keV, the GMRT for the photometric observation at 1280 MHz and European VLBI Network (EVN) for photometry and imaging at 4990 MHz. During inferior conjunction, the companion totally blocked the disk and the base of the jet reducing the X-ray intensity by 20% with respect to the previous day, and the intensity went up by about 65% on the next day. The X-ray intensity is about one-third compared to RXTE results obtained during the superior conjunction. By taking the difference in the spectra between superior and inferior conjunctions, we obtained

the spectrum of the system core including the contribution from probable accretion shock that may have occurred during interaction between the accreting stream and the disk. The EVN observation clearly showed the separation of radio blobs. A clear dependence of X-ray intensity emitted from the base of the jet on the photon energy is seen. We find that the core is much brighter in hard X-rays.

The conjunctions have no effect on radio emissions observed by EVN showing that most of the radio emission is coming far from the core.

We have also made simultaneous Multi-Wavelength Observations of black-hole at the center of our Galaxy Sgr A* [34] and reported the detection of variable emission from Sgr A* in almost all wavelength bands (i.e., X-rays, near-IR, sub-millimeter, millimeter and centimeter) during campaign period. At millimeter wavelengths, detection of flare emission at 43 GHz using the Very Long Baseline Array with milliarcsecond spatial resolution indicates the first direct evidence that the hourly time-scale flares are localized within the inner $30 \times 70$ Schwarzschild radii of Sgr A*. We detected three moderate flares simultaneously in near-IR and X-ray bands. The ratio of X-ray to near-IR flux in the flares is consistent with inverse Compton scattering of near-IR photons by sub-millimeter emitting relativistic particles which follow scaling relations obtained from size measurements of Sgr A*. The flare statistics in near-IR wavelengths is consistent with the probability of flare emission being inversely proportional to the flux. From the cross-correlation plots between near-IR, millimeter, and sub-millimeter light curves, we found presence of time delays between the peaks of emission up to 5 h. The evidence for time delays at millimeter and sub-millimeter wavelengths are consistent with transition of the source of emission from optically thick to an optically thin regime. The correlation between the optically thin near-IR and X-ray flare and optically thick radio flare at 43 GHz on 2007 April 4 provides the first evidence of a radio flare emission at 43 GHz delayed with respect to the near-IR and X-ray flare emission. The time delay measurements support in favor of the expansion of hot self-absorbed synchrotron plasma blob and weaken the hot spot model of flare emission.

## 3 Broadband Radio Spectrum

We also studied broadband radio spectrum of the galactic micro-quasar SS 433 with the multi-wavelength campaign using the GMRT and the Effelsberg 100-m Radio Telescope [23]. The observations took place between 3rd January 2005 to 8th February 2005 using eight different frequencies. A flare is detected which appeared to have started prior to 18th January and lasted till 8th February. The light-curves of different frequencies show a progressively larger time-delay as the radio frequency goes down. The peak of the 6 cm light-curve is delayed by $\sim$3 days with respect to the peak of the 9 mm light-curve. There is an indication of the flattening of the spectrum with a possible turn-over at $\sim$1.5 GHz. If we interpret the turn-over to be due to synchrotron self-absorption, the required magnetic field would become too large, however, free-free absorption by hot thermal surrounding medium formed due to stellar winds is still a possibility.

## 4 Possible Photometric Evidence of Ejection of Bullet-Like Features in SS 433

SS 433 is a bright emission line compact system which is known to have a companion with an orbital period of 13.1 day, a large disk and two highly collimated relativistic jets moving at $v \sim 0.26c$. The velocity of jets are constant to within a percent or so [9, 15]. A very exciting observation, made within years of the discovery of SS 433, suggests that the jets of SS 433 are not continuous but are made of discrete and successive bullet-like entities, at least in the optical wavelengths [1, 10]. The $H_\alpha$ lines emitted from the source were seen to brighten up and fade away without changing their red/blue shifts, indicating that the brightened bullets are radially ejected and do not have any rotational velocity component. Using the results of numerical simulations involving oscillation of shocks in accretion disks, Chakrabarti et al. [3] concluded that in normal circumstances, a 50–1000 s interval is expected between successive bullet ejections. These bullets would be ejected from the X-ray emitting region and propagate through the optical, IR ($\sim 10^{13}$–$10^{14}$ cm), and finally to the radio-emitting region at $\geq 10^{15}$ cm (roughly the distance covered in a day with $v \sim v_{jet}$) or so. Thus, if the object is in a low or quiescence state, each individual bullet flaring and dying away in a few minutes time-scale should be observable not only in optical wavelengths [9, 15] but also in all the wavelengths, including X-ray, IR, and radio-emitting regions.

During the multi-wavelength campaign of SS 433 [7], a sharp rise in intensity in time-scales of a few minutes in X-ray, IR, and radio wavelengths were found through photometric studies. We interpret them to be possible evidences of ejection of bullet-like features from accretion disks [4]. Since the emitting regions of X-ray, IR, and radio are not well known, while duration of the flares lasts less than a few minutes, we could not prove beyond doubt that there are indeed correlations among the micro-flares observed in these wave-lengths.

## 5 Flare Activity from Compact Objects

Many flaring activities of compact objects were extensively studied using multi-wavelength instruments. For example, we discovered the second largest flare in the recorded history of Cygnus X-3 [24] in 2006 and studied radio and X-ray evolution of spectral and timing features of the black hole [25] using GMRT, VLA, RATAN and RXTE. We found that the radio spectrum is showing absorption towards lower frequency and after flare the turn-over frequency is shifting towards lower frequency region with time. It is shown that synchrotron self absorption may be the possible cause for such behavior. We examined the evolution of low frequency spectral index of the source and propose a possible model to interpret the observed behavior in terms of expanding blobs of plasma. We have also studied flaring events of SS 433 [23] and V 4641 Sgr [14].

## 6 Determination of Accretion Rate of a Black Holes

We have found a way to determine the accretion rate of a black hole in quiescent state assuming an equipartition of magnetic energy and the gravitational potential energy of accreting matter [22]. A micro-flare is detected from a Galactic black hole A0620–00 of mass $\sim 10 M_{\odot}$ with time-span $t = 192 \pm 32$ s using GMRT (Fig. 3).

If we assume that the flare is due to magnetic dissipation, with an energy density of $B^2/8\pi$, the expression for the total energy release is:

$$E_{mag} = \frac{B^2}{8\pi} V = 4\pi D^2 \nu_{obs} F_{\nu} t_{\mu f}. \tag{1}$$

Here, $B$ is the average magnetic field in the inflow where the flare forms. $V \sim r_g^3$ is the lower limit of the volume in the accretion flow that released the energy, $D$ is the distance of the source from Earth, $\nu_{obs}$ is the observation frequency and $F_{\nu}$ is the specific intensity of radiation. Re-writing Eq. (1) using the equipartition law,

$$\frac{B^2}{8\pi} \sim \frac{GM\rho}{r} = \frac{GM\dot{M}}{4\pi \upsilon r^3}, \tag{2}$$

where $\rho$ is the density of the flow, $\dot{M}$ is the accretion rate and $\upsilon$ is the velocity of inflow. In quiescent state, usually Keplerian disk does not form and one may assume the inflow to be generally like a Bondi flow, especially close to the black hole. Thus we use the definition of the accretion rate to be $\dot{M} = 4\pi\rho r^2 \upsilon$. More specifically, we assume, the free-fall velocity, $\upsilon \sim (2GM/r)^{1/2}$. Introduction of pressure and rotation effects do not change the result since the angular momentum is very low

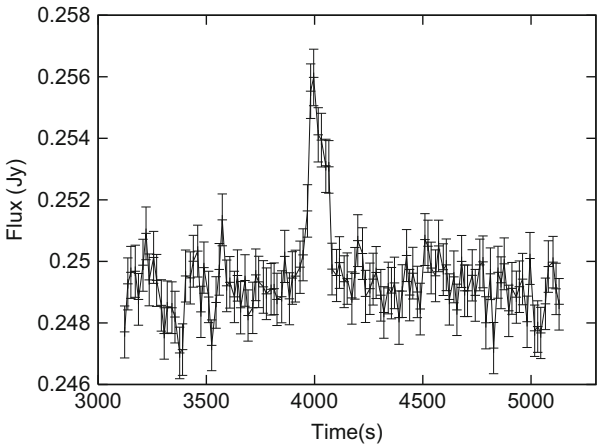



**Fig. 3** A micro-flare in A0620–00 observed in 1280 MHz by GMRT. For details, see Pal and Chakrabarti [22]

due to absence of Keplerian flow and the gas is tenuous. Thus one can obtain the upper limit of the accretion rate of the flow to be

$$\dot{M} \sim (3.5 \pm 0.58) \times 10^{14} x^{5/2} \mathrm{gm/s} = (5.5 \pm 0.91) \times 10^{-12} x^{5/2} M_{\odot} \mathrm{yr}^{-1}. \quad (3)$$

Here $x = \frac{r}{r_g}$, is the dimensionless distance of the flaring region from the center. From transonic flow models [2], the flow is expected to be supersonic only around $x \sim 2$–$3$ before disappearing into the black hole. This gives the accretion rate of A0620–00 in the quiescent state to be

$$\dot{M} = (8.5 \pm 1.4) \times 10^{-11} \left(\frac{x}{3}\right)^{5/2} M_{\odot} \mathrm{yr}^{-1}. \quad (4)$$

This is consistent with the other measurement of accretion rate of the black hole on the basis of X-ray observations [16].

## 7 Search for Transient Radio Sources

Transient Radio sources are ultimate compact objects. We are systematically looking for transient radio sources in our Galaxy using pointed observation by VLA and GMRT and study of different archival data. Earlier detection of two transient radio sources GCRT J1745–3009 [11, 12, 31] and GCRT J1742–3001 [13] were made from near Galactic Center region. The characteristics of GCRT J1742–3001 and GCRT J1742–3001 did not match with any known mechanisms of emission in transient compact sources. As a result, these sources seem to represent a member of a new classes of objects. GCRT J1745–3009 is a unique source which was detected only three times in 2002 [11], 2003 and 2004 [12]. All the three detections of the source were in 330 MHz. The behavior of the source changed significantly between three detections of the source. The source exhibited ∼10 min long, ∼1 Jy peaked bursts with a ∼77 min period in 2002. The emission from the source was coherent [11]. Extremely steep spectral index ($\alpha = -13.5 \pm 3.0$) [12] and high circular polarization [31] was found from the third detection of the source. GCRT J1742–3001 was active for a few months with ∼150 mJy flux density at the peak and its light-curve showed no periodicity in emission [13]. The source was detected in 235 MHz and exhibited steep spectral index ($\alpha < -2$). For both of these sources, no counterpart was discovered in high energy, ruling out the possibility of conventional follow-up radio observations after a high-energy detection.

Recently we have discovered another transient radio source [27] close to micro-quasar Cygnus X-1, some properties of which matches with GCRT J1745–3009 and GCRT J1742–3001.

## 8 Study of Supernova/GRB and Discovery of Supernova Remnants

We have studied temporal and spectral evolution of many supernovae and gamma-ray bursts and different properties of their host galaxies. We have studied in details two core-collapse supernova (SN) explosions SN 2008D and SN 2007uy in host galaxy NGC 2770 within 10 days of each other and 9 years after the first SN of the same type, SN 1999eh in the galaxy [33]. The star-formation history of host galaxy NGC 2770 is also studied.

The optically unbiased GRB host (TOUGH) survey at $z \leq 1$ is carried out [17] to determine the level of obscured star formation activity and dust attenuation in a sample of gamma-ray burst hosts, and to test the hypothesis that GRB hosts have properties consistent with those of the general star-forming galaxy populations.

We are carrying out a Galactic plane survey using GMRT at 330 MHz to systematically search hitherto undiscovered Supernova remnants. We discovered the youngest supernova remnant in our Galaxy G354.4+0.0 with an estimated size of 1.6 arcmin [30]. The remnant was hidden behind an extended HI region of size ∼4 arcmin. The estimated age of the remnant is 100–500 year. We have also discovered many pulsar candidates and variable radio sources as side product of this survey [28] (Fig. 4).

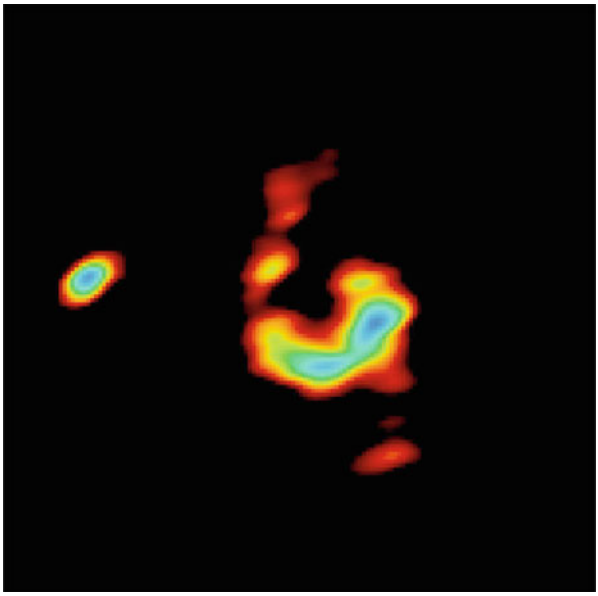


**Fig. 4** GMRT image of 354.4+0.0 in 330 MHz. For details, see Roy and Pal [30]

# 9 Study of Radio Galaxies and Galaxy-Clusters

## *9.1 Dwarf Galaxies*

Local Group dwarf galaxy, Leo T is studied using GMRT and Westerbork Synthesis Radio Telescope (WSRT) [32]. The total HI mass of the dwarf galaxy is $2.8 \times 10^5 M_\odot$, based on a distance of 420 kpc. Leo T has both cold ($\sim$500 K) and warm ($\sim$6000 K) HI at its core, with a global velocity dispersion of 6.9 km s$^{-1}$. We derive the dynamical mass within the HI radius to be $3.3 \times 10^6 M_\odot$, and a mass-to-light ratio of $>$50. Leo T is not only the lowest luminosity galaxy with on-going star formation discovered to date, but it is also the most dark matter-dominated, gas-rich dwarf in the Local Group.

## *9.2 Radio Galaxies*

Morphology and spectral properties of many giant radio galaxies is studied in detail [26]. For example, we studied large radio galaxies 3C46 and 3C452 [18] using GMRT and VLA. The primary objectives of these observations were to estimate spectral ages of different emission region of these galaxies and examining any evidence of diffuse extended emission at low radio frequencies due to an earlier cycle of activities.

## *9.3 Study of Cluster of Galaxies*

The radio, X-ray and $\gamma$-ray emission behavior of the Ophiuchus cluster of galaxies is studied in detail whose radio mini-halo has been recently detected at 1400 MHz. High-resolution 240 and 607 MHz GMRT radio observations was complemented with 74 MHz archival VLA radio observations [29]. We also studied archival Chandra and XMM-Newton data of the Ophiuchus cluster. Our observations do not show significant radio emission from the mini-halo. The XMM-Newton observations can be well explained by a two-temperature thermal model with temperatures $\sim$1.8 and $\sim$9.0 keV, respectively. This result confirms that the innermost central region of the Ophiuchus cluster is a cooling core. XMM-Newton and INTEGRAL data, along with GMRT and VLA data is used to create a detail model of emission mechanism from core and other parts of the cluster [29].

**Acknowledgement** I acknowledge support of my guide Prof. Sandip K. Chakrabarti for helping me during my PhD period [21] to do a good fraction of research published in present review.

## References


1. Brown, J.C., Cassinelli, J.P., Collins, G.W., II.: ApJ **378**, 307–314 (1991)
2. Chakrabarti, S.K.: Theory of Transonic Astrophysical Flows. World Scientific (1990). ISBN: 978-981-02-0204-0
3. Chakrabarti, S.K., Goldoni, P., Wiita, P.J., et al.: ApJL **576**, 45–48 (2002)
4. Chakrabarti, S.K., Pal, S., Nandi, A., et al.: ApJL **595**, 45–48 (2003)
5. Chakrabarti, S.K., Pal, S., et al.: IJP **76**, 693–697 (2005)
6. Chakrabarti, S.K., et al.: IJP **77**, 173 (2005)
7. Chakrabarti, S.K., Anandarao, B.G., Pal, S., et al.: MNRAS **362**, 957–965 (2005)
8. Chakrabarti, S.K., Pal, S., Nandi, A.: A&A **453**, 965–968 (2006)
9. Gies, D.R., McSwain, M.V., Riddle, R.L., et al.: **566**, 1069–1083 (2002)
10. Grandi, S.: Vistas Astron. **25**, 7–11 (1981)
11. Hyman, S.D., et al.: Nature **434**, 50–52 (2005)
12. Hyman, S.D., Roy, S., Pal, S., et al.: ApJL **660**, 121–124 (2007)
13. Hyman, S.D., Wijnands, R., Lazio, T.J.W., Pal, S., et al.: ApJ **696**, 280–286 (2009)
14. Ishwara-Chandra, P.S., Rao, A.P.: Low frequency GMRT observation of microquasar V4641 Sgr. In: Sixth Microquasar Workshop: Microquasars and Beyond - From Binaries to Galaxies, Como, Italy (2006)
15. Margon, B.: ARA&A **22**, 507–536 (1984)
16. McClintock, J.E., Remillard, R.A.: ApJ **531**, 956–962 (2000)
17. Michalowski, M.J., et al.: ApJ **755**, 11 (2012)
18. Nandi, S., Pirya, A., Pal, S., et al.: MNRAS **404**, 433–441 (2010)
19. Pahari, M., Pal, S.: MNRAS **409**, 903–912 (2010)
20. Pahari, M., Pal, S.: MNRAS **423**, 3352–3359 (2012)
21. Pal, S.: PhD thesis, Jadavpur University (2005)
22. Pal, S., Chakrabarti, S.K.: A&A **421**, 13–15 (2004)
23. Pal, S., Chakrabarti, S.K., Mondal, S, Kraus, A.: BASI **34**, 1–9 (2006)
24. Pal, S., Ishwara-Chandra, C.H., Rao, A.P.: The Astronomer's Telegram **809**, 1 (2006)
25. Pal, S., Ishwara-Chandra C.H., Rao, A.P.: Proceedings of the VII Microquasar Workshop: Microquasars and Beyond, 1–5 Sept 2008, Foca, Izmir, p. 109 (2008)
26. Pal, S., et al.: 36th Annual Meeting of the Astronomical Society of India (ASI), Hyderabad (2018)
27. Pal, S., Patra, D., Monique, H., Chakrabarti, S.K.: (2018, submitted)
28. Patra, D., Pal, S., Roy, S., Joshi, B.C.: (2018, submitted)
29. Perez-Torres, M.A., Zandanel, F., Guerrero, M.A., Pal, S., et al.: MNRAS **396**, 2237–2248 (2009)
30. Roy, S., Pal, S.: ApJ **774**, 150–156 (2013)
31. Roy, S., Hyman, S.D., Pal, S., et al.: ApJL **712**, 5–9 (2010)
32. Ryan-Weber, E.V., Begum, A., Oosterloo, T., Pal, S., et al.: MNRAS **384**, 535–540 (2008)
33. van der Horst, A.J., Kamble, A.P., Paragi, Z., Sage, L.J., Pal, S., et al.: ApJ **726**, 99–111 (2011)
34. Yusef-Zadeh, F., et al.: ApJ **706**, 348–375 (2009)

# From Black Holes to Earthquakes: Saga of a Long and Lovely Journey




**Asit K. Choudhury**

**Abstract** There are several sources of high energy radiations in the Universe. Each of them has a totally different emission mechanism. In this review, I concentrate on the study of the general properties of radiations emitted by matter which are accreted towards black holes and neutron stars. We also study the nature of X-ray radiation coming from the Sun in the form of energetic solar flares. These radiations are constantly bombarding the Earth's ionosphere changing its electron content and affecting the wave propagation through the Earth and the lower-ionosphere waveguide. We monitor Very Low Frequency (VLF) radio waves and correlate our observations with the presence or absence of the high energy radiations from space. Our results during solar flares, show how the number density of the ionosphere is enhanced by these celestial sources. The terrestrial high energy phenomena such as earthquakes are believed to affect the ionospheric properties and we have monitored VLF signals during earthquakes and found possible effects of seismic events on the VLF signals.

## 1 Introduction

Earths atmosphere is constantly being bombarded by hostile radiation and particles coming from all over the Universe. Out of them, the most prominent yet the most precarious source is the Sun. Other than this, there are Supernovae, gamma ray bursts, black holes, neutron stars and may other energetic sources present in our own galaxy and other galaxies. Because of these, the atmosphere is very dynamic and its vital parameters are constantly fluctuating. This review concentrates on three major studies in this Earth-Universe interaction scenario. First part tries to answer these questions: How does the extra-terrestrial high energy radiation sources behave? At what energy do they radiate? How to characterize these radiations in terms

A. K. Choudhury (✉)
Indian Centre for Space Physics, Malda, Kolkata, India

© Springer International Publishing AG, part of Springer Nature 2018

B. Mukhopadhyay, S. Sasmal (eds.), *Exploring the Universe: From Near Space to Extra-Galactic*, Astrophysics and Space Science Proceedings 53,
https://doi.org/10.1007/978-3-319-94607-8_28

of their spectral and temporal properties? As these radiations are necessarily also interacting with the atmosphere, studies of this type require going to space (beyond atmosphere) and observe these energetic phenomena. In the first part of my review, I study behaviour of some of these energetic sources as observed by both Indian and American satellites and try to understand their properties.

The second part of the review requires ground based observations with radio antennas and interpreting these results. Energetic radiations from the sources mentioned above and most importantly from the Sun ionize upper part of the atmosphere. This is a problematic zone because, satellites cannot survive in these heights of 90–150 km because of residual atmosphere of considerable density and at the same time balloon borne science cannot be carried out as the balloons fly up to a height of about 40 km. This part of the atmosphere must be studied by radio-sonde. Very Low Frequency (VLF) radio waves (3–30 kHz) are sent from standard transmitters to these layers and the reflected components (sky waves) along with surface waves are received by suitable antennas to 'feel' the pulse of the ionosphere. Naturally, whenever there are sudden disturbances in this ionosphere, the reflected signal is perturbed. So my work has been to monitor Earth's ionosphere and correlate the disturbances with satellite data mentioned above.

It has been found by several observers that when there are significant seismic activities on Earth, radon gas is emitted. This affects the ionosphere and consequently, the radio signal is perturbed. Third part of my activities under Prof. S. K. Chakrabarti thus include some work on ionospheric perturbation due to seismicity namely earthquakes.

Now I present the summary of some research activities in these three areas one by one.

## 2 Sources of High Energy Radiation and Their Analysis

Black holes are the end products of stellar evolutions. These black holes cannot be observed directly as they do not allow lights to come out of them. However, when they are in binary systems, matter from the companion is attracted by them which falls onto the black holes emitting significant radiation on the way. This matter forms a temporary reservoir called accretion disk whose properties can be analysed from the nature of radiation. Some of these black holes are in our own galaxy. I study properties of very well known black hole candidates, namely, GRS 1915+105, Cygnus X-1 and Cygnus X-3. Some other chapters of this volume discuss the properties of black hole accretion in detail.

### *2.1 Class Transition of the Compact Object GRS 1915+105*

GRS 1915+105 has been exhibiting different types of X-ray variability characteristics. PDS clearly shows evidence of quasi-periodic oscillations (QPO) of frequency 0.001–67 Hz.

Belloni et al. [2], based on colour-colour diagram, classified most of the light curves into 12 classes which are designated as $\chi$, $\alpha$, $\nu$, $\beta$, $\lambda$, $\kappa$, $\rho$, $\mu$, $\theta$, $\delta$, $\gamma$ and $\phi$.

One more independent class was identified by Naik et al. [21] and was designated as $\omega$.

As there are thirteen different classes, one class of light curve must change into another class of light curve at some point of time when an actual class transition takes place. Though RXTE pointed to GRS 1915+105 as many as thousand times it could not detect precisely the time when a class transition took place. But we observed that Indian X-ray Astronomy Experiment (IXAE) instrument had pinpointed such class transitions many times. When ISRO made the data public, we started working on it. We found that probably the source had a 'premonition' of class transition a few hundred seconds before the event.

In Fig. 1a–c light curves (upper panel) and time-frequency diagrams (lower panel) obtained by Fast Fourier Transform (FFT) of the data of three successive orbits of June 22, 1997, in the energy range of 6–18 keV [5, 17] are shown. In each panel, contours of constant normalized power (P) are plotted as a function of frequency and time. Contours are drawn for different normalized powers; highest power is shown with darkest shade.

In Fig. 1a, we show the light curve of the third orbit (June 22, 1997), which appears to belong to an unknown class. It is noted that in this unknown class the LFQPO frequency changes from $\log(\nu) = -1.987$ to $\log(\nu) = -1.73$.

In Fig. 1b we have seen a large spike in the light curve after about 750 s from the beginning of the observation. We can interpret this as a failed attempt of class transition. The power density spectra (PDS) in the pre- and post-transition regions are completely different and they produce a 'mixed' PDS in the transition region causing a large scale noise for ∼300 s. This is the size of our segments over which FFTs are taken. This would be further reduced if a dynamical FFT is taken.

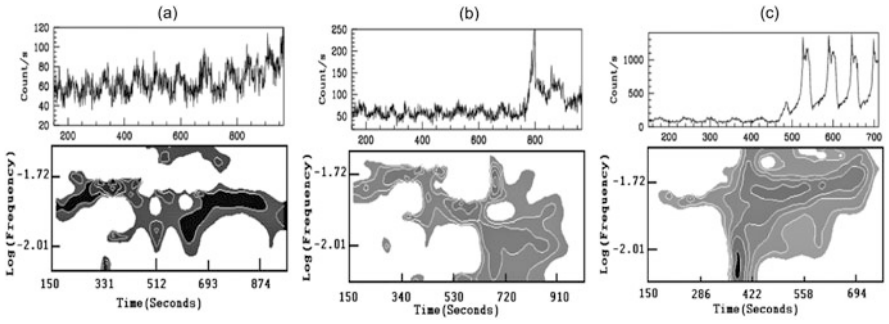



**Fig. 1** Light curves (top) and time-frequency plots (bottom) of GRS 1915+105, as observed by IXAE in three successive orbits on June 22, 1997. The light curves of (**a**) and part of (**b**) are of unknown classes. In (**b**), a failed attempt for transition was made where a "spike" is seen. In (**c**), a real transition to $\rho$ class is seen. This is also reflected in the time frequency plot [5]

In Fig. 1c the light curve clearly shows a transition from an unknown class to $\rho$ class for the final orbit. The LFQPO frequency at log $(\nu) \sim -1.75$ in the pre-transition 'unknown' class continues to drift towards higher value [log$(\nu)$ $\sim -1.664$] as the light curve enters into the well known $\rho$ class.

We present a few more examples of the class transition [6] in Fig. 2a–c, as seen by the observation of June 25, 1997. The light curves are plotted in the upper panel and the mean photon indices (MPIs) in the lower panel. The MPI $s_\phi$ is obtained using the definition [6, 16].

In Fig. 2a GRS 1915+105 is in the $\chi$ like class where the average photon spectra becomes soft as indicated by the gradual decrease in MPI. In Fig. 2b, the trend continued until a $\rho$ like class was achieved. Also the photon spectra went down. The count rate went up to four times after a full orbit and a $\rho$ class was achieved which is shown in Fig. 2c. The average photon index was $\sim$1.75 in Fig. 2a but it becomes $\sim$1.9 in Fig. 2c, this indicates the general softening of the spectrum. We found a clear evidence of transition of an unknown class to $\mu$ class (5) on August 9, 1997 for the 5th orbit. Unknown to $\rho$ class transition was observed in the 2nd orbit of June 22, 2000 (5).

It is interesting to note that for the IXAE observation of June 22, 1997 the light curve is in $\kappa$ class. In June 23, 24 and 25, 1997 the system was still in $\rho$ class after the transition on June 22, 1997. Subsequently, on June 25, 1997 there was another transition to $\chi$ and it returned back to $\rho$. It remained in $\rho$ class on June 26, 1997 before returning to $\kappa$ on June 27. Thus $\kappa \rightarrow< unknown >\rightarrow \rho \rightarrow< unknown >\rightarrow \rho \rightarrow< unknown >\rightarrow \kappa$ transitions had taken place in a span

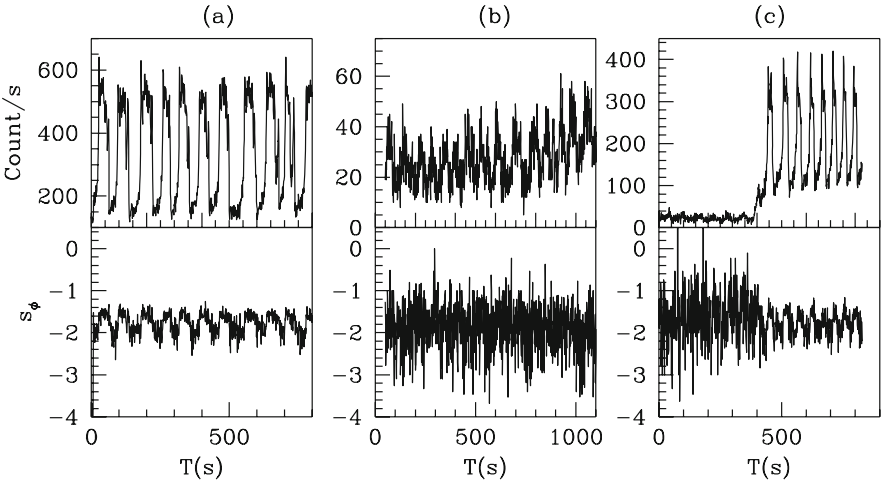



**Fig. 2** Class transition of GRS 1915+105 as observed by IXAE on June 25, 1997 in three successive orbits. (**a**) Unknown class similar to $\chi$. (**b**) Transition to $\rho$ type class with very low count rate. (**c**) $\rho$ class after stabilization in that class. The lower panels show the noisy behavior of $s_\phi$ during transition [6]

of 5 days [6]. Due to lack of observation, the exact time and duration of the last transition mentioned above could not be seen.

We presented a few examples of the class transitions in GRS 1915+105 especially using the IXAE data. The transitions are seen to take place through unknown classes. In all the cases, the class transition takes place within a very short time compared to the viscous time for a Keplerian disk, this indicates that the flow must be nearly freely falling i.e., a sub-Keplerian.

Similar time scale is also involved in state transitions in Cygnus X-1 and Cygnus X-3 [13]. Smith et al. [28, 29] also found observational signatures of nearly freely falling matter in several black hole candidates. More recently, Pal et al. [23] showed that the Comptonizing Efficiencies (EF) of the classes before and after the transition are also adjacent to each other, and they predict that similar transitions should be expected in a new source IGR 11791-3624 with similar variability classes [24].

## *2.2 Class Transition of the Compact Object Cygnus X-1 and Cygnus X-3*

Cygnus X-1, the brightest hard X-ray binary source, is considered to be one of the most firmly established persistent Galactic Black Hole Candidate (GBHC). Cygnus X-1 exhibits a bimodal behaviour with two distinct spectral states "hard" and "soft" and it is known to make transition from one state to the other irregularly [32]. It is observed that spectral transition of Cygnus X-1 from one state to the other is associated with a change in power density spectrum (PDS). In the soft state of Cygnus X-1 the intensity variations are less pronounced compared to that in the hard state. The upper panel of Fig. 3 shows the light curve (2–18 keV) of Cygnus X-1 in the 2nd orbit of May 7, 1996. For the first 550 s the object is seen to be in the hard class with an average photon count rate of 50 per second. After that it has suffered a rarely observed class transition from hard class to soft class corresponding to a mean photon count per second of more than 200. At the end (960 s) the light curve shows a tendency of attaining higher value (800 counts per second). It is seen from the lower panel of the Fig. 3 that the value of the mean MPI ($s_\phi$) changes from $-3.7$ to 0.2 before transition. But after the transition it varies between $-1.8$ and $-0.8$. Therefore, the hard to soft class transition is accompanied by a reduction in noise of $s_\phi$.

On transition dates, we detected an important feature in the power density spectra. Each of the observed power density spectra is characterized by a break in slope at a particular frequency. Above and below that particular frequency the PDS can be fitted by power-law of two different slopes. Figure 3b shows the PDS of Cygnus X-1 for the 2nd orbit of May 7, 1996. The power-law index for frequency below 0.1 Hz is fitted with power-low index 1.45 and above 0.1 Hz it is $-1.19$. We show the light curve of Cygnus X-3 for the 4th orbit of October 26, 1999 in the upper panel of Fig. 4a. We see that Cygnus X-3 suffers a transition from hard class to soft class after 600 s. In the hard class the average photon count per second is 20

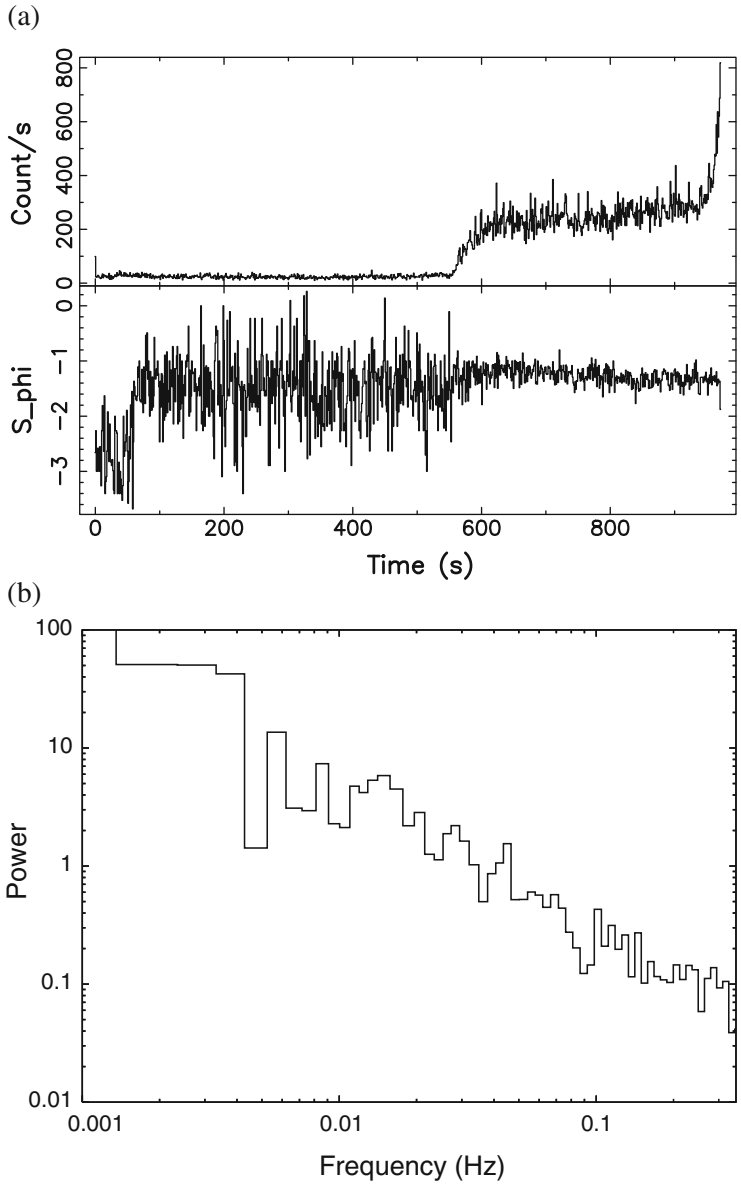



**Fig. 3** (**a**) 2–18 keV light curve of Cygnus X-1 as observed by IXAE (upper panel) and MPI ($s_\phi$) (lower panel) in the 2nd orbit of May 7, 1996. The compact object makes transition from hard class to soft class. Transition into hard class, $s_\phi$ becomes less noisy after the transition. (**b**) PDS of Cygnus X-1 for the 2nd orbit of May 7, 1996 [13]

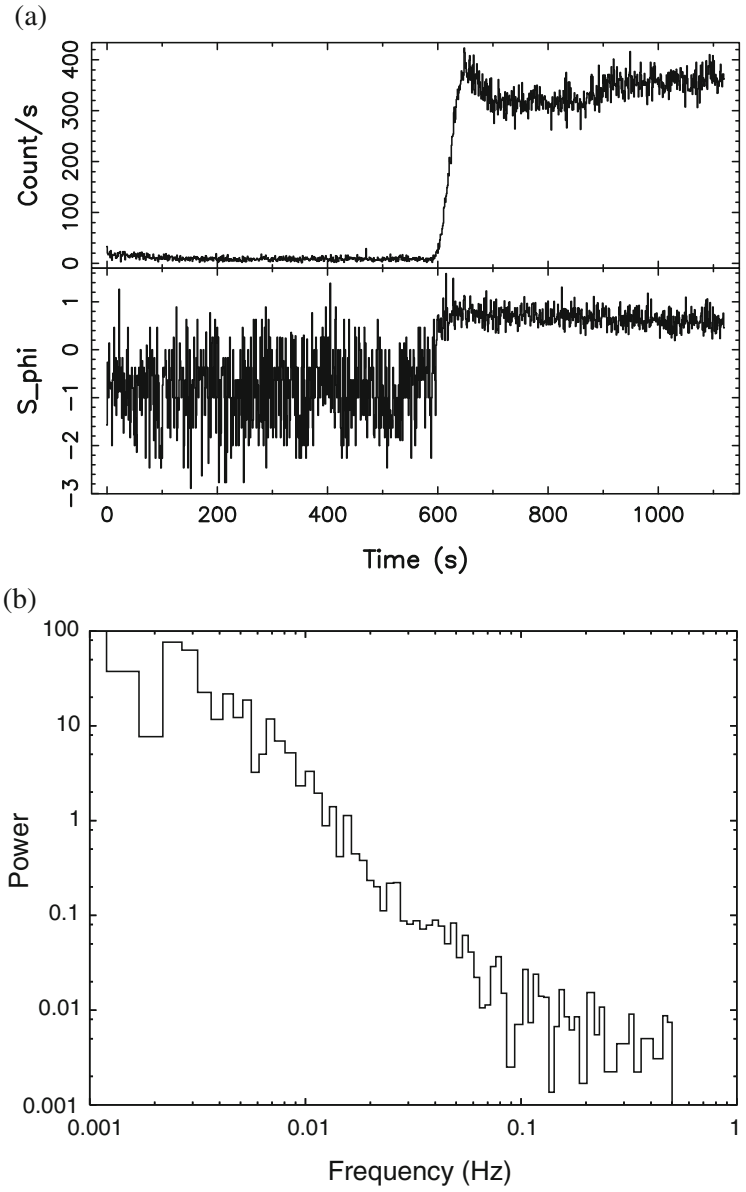



**Fig. 4** (**a**) 2–18 keV light curve (upper panel) and the corresponding variation of $s_\phi$ (lower panel) indicating a hard to soft class transition of Cygnus X-3 as observed by the IXAE on October 26, 1999 in the 4th orbit. (**b**) PDS of Cygnus X-3 for the 4th orbit of October 26, 1999 [13]

but in the soft class it becomes about 350. So there is a large difference of photon count rate in the two classes. Again the MPI ($s_\phi$) is found to become less noisy after the transition. The fluctuation of $s_\phi$ lies between $-2.9$ and 1.3 and it varies between 0.2 to 0.5 in the soft class.

The corresponding power density spectrum indicates a very prominent flattening after the break-up at 0.07 Hz as shown in Fig. 4b. For frequencies below 0.07 Hz the PDS has a power-law of index $-2.3$. But the index becomes $-0.65$ for frequencies above 0.07 Hz.

## 3 Detection of Sudden Ionospheric Disturbances Due to Solar Flares by Monitoring the VLF Signal

Sudden Ionospheric Disturbances (SIDs) are caused by ionizing sources external to the earth. By monitoring them, it is possible to locate these sources and a great deal of knowledge could be obtained about the rate at which these types of events occur in nature. Indian Centre for Space Physics (ICSP) has been monitoring the ionospheric disturbances for about a decade. Our goal is to study solar flares [4], meteor showers [3], lithosphere–ionosphere coupling and precursors to earthquakes [7, 8, 12, 27] and SIDs caused by high energy phenomena like Gamma Ray Bursts (GRB) and Soft Gamma ray Repeaters (SGR) [9–11, 20]. The latter study is very relevant not only to understand the ionospheric chemistry in presence of high energy photons, it also gives us an idea of how vulnerable the biosphere of the earth is. Please refer to several articles in the volume on ionospheric research.

### *3.1 Perturbation of VLF Signal Along VTX-MALDA Propagation Path*

During a solar flare, sudden release of electromagnetic radiation takes place in the solar corona which releases magnetic energy [31]. There is considerable perturbation of the D-layer of the ionosphere and changes in compositions [30]. Figure 5a (left) shows that the location of the peaks of the flares detected on July 13th 2005 exactly match with the GOES data. Figure 5b (right) shows the locations of the peaks of the flares detected on the same date but the peaks of the flares detected in afternoons by our receiver lag behind the peaks of the flare as detected by GOES spacecraft.

The main reason for this lag is the time taken by high energy X-rays from the Sun to carry out chemical reactions in the atmosphere at different layers. The duration of the lag depends on whether the whole path was illuminated by the Sun at the time of

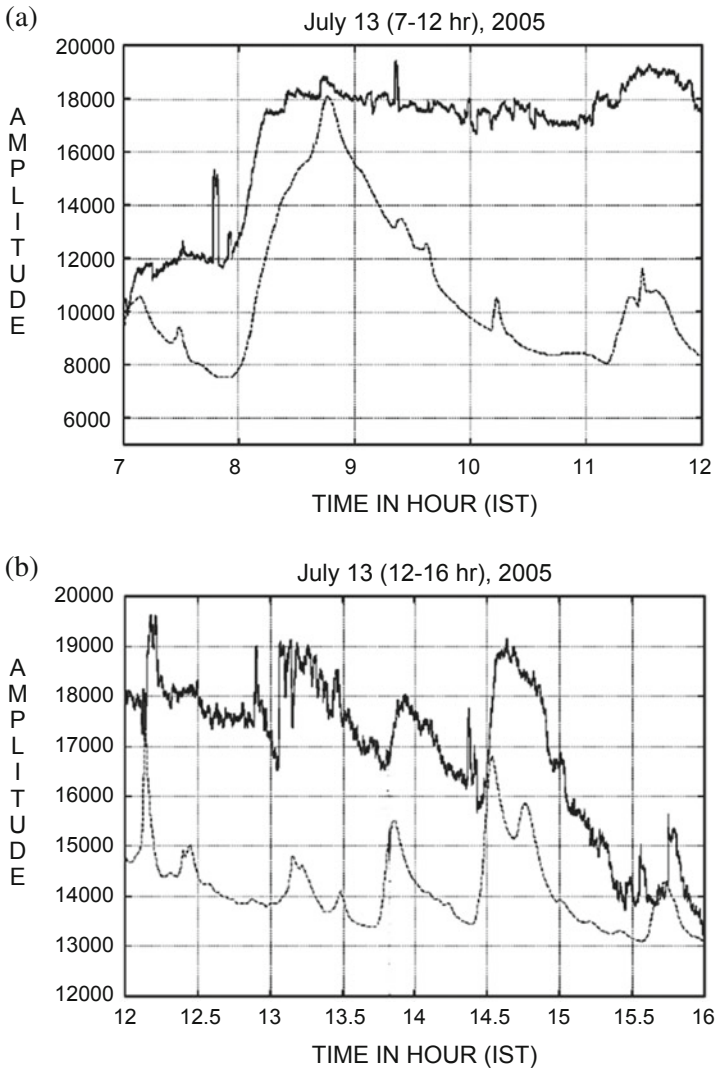



**Fig. 5** The five and four hours VLF data show the locations of the peaks of the flares detected on July 13th 2005, exactly match with the GOES data (top), but there is a time lag (bottom) of the peaks of the solar flare observed by our VLF receiver and GOES [22]

observation or not. The lags become very unpredictable if the path is only partially illuminated. Furthermore, lags due to weak flares (e.g., C-type) is longer than that due to stronger flares (e.g., X-type) as the high energy radiations in stronger flares quickly ionizes the atmosphere [1].

### *3.2 Study of Unusual Behaviour of VLF Signals During Solar Flares for Different Propagation Paths*

ICSP has VLF receiving systems both at Cooch Behar and Malda. We have observed over fifty solar flares during the months of October and November, 2014 for both receivers and found the following results. As per observation we have separated all the flares in different types. The types are (a) C2 to C8 flares, (b) C8.1 to M 3.4 flares, and (c) M3.5 to upper level flares. For (a) type of solar flares (C2 to C8) due to ionization in the ionosphere the sky wave intensity increases and ground wave became weaker, for which a path difference occurs in such a manner that resultant signal intensity get reduced for both receiving stations. In this case we have recorded a destructive interference pattern.

For (b) type of flares (C8.1 to M3.4) we have recorded different interference pattern in different receiving stations. Distance between Malda and Cooch Behar is 186 Km. The path difference between ground wave and sky wave occurs in such a manner that we got an increase of VLF amplitude during C8.1 to M3.4 flares at Cooch Behar. But as VTX- Malda we got a reducing of VLF signal amplitude at Malda. So we can say for these classes of flares we get constructive interference pattern at Cooch Behar and a destructive interference pattern at Malda for the same flare.

For (c) type of flares (M3.5 upwards) first there is a destructive interference pattern for a few minutes and then signal amplitude increases for both stations. This is due to the fact that the a path difference in such that the constructive interference dominates after few minutes over the destructive interference for Cooch Behar but for Malda the constructive interference occurs after few minutes but do not dominate the destructive pattern. This is because VTX-Malda propagation path is shorter than the VTX-Cooch Behar base line.

Figure 6a–c gives an example of how the VLF signals vary with solar flare class The 6 h plot of VLF data recorded on 20th October, 2014 shows three types flares for the same day data. The figure shows above natures of perturbation of VLF data of VTX at Malda and Cooch Behar during C5.4, C9.0, and M3.9 solar flares [15].

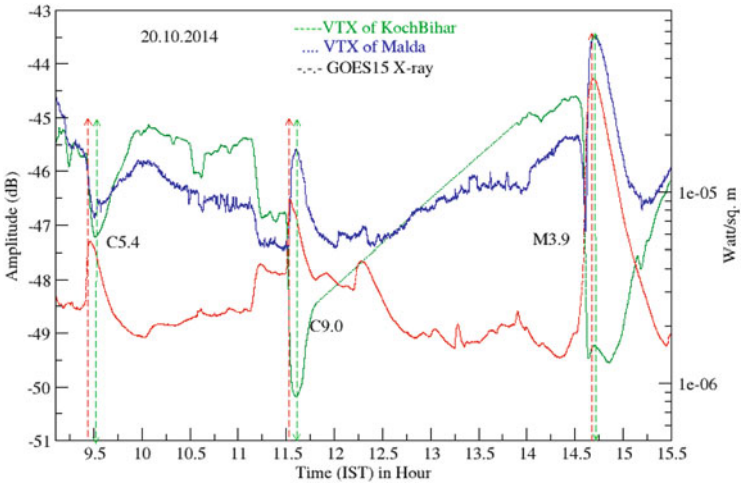



**Fig. 6** Results of observations of three solar flares by our detectors on 20.10.2014 for VTX-Cooch Behar and VTX-Malda base lines and comparison with GOES 15 X-ray data. Clearly there are lagging of time from GOES15 time. There are clearly opposite results for weaker flares and stronger flares [15]

## 4 Possible Relation Between VLF Signal Anomaly and Earthquakes

VLF signal anomalies have been long suspected to be precursors of earthquakes. The papers by Hayakawa et al. [19], Gufeld et al. [18], Chakrabarti et al. [12], Chakrabarti et al. [7], Ray et al. [25], have shown that anomalies are seen prior to earthquakes. In this part of my review, I study some of these anomalies which were detected by us and find evidences that these anomalies could be used as pre-cursors of Earthquakes.

### *4.1 Anomalies in Terminator Time and D-Layer Formation Time*

The VLF data obtained for a period of 3 months, from 14 April to 14 July 2008 has been analyzed in the present study. During this time, several earthquakes occurred on different dates in India and its adjoining region (www.imd.ernet.in).

The anomalies are seen in the sunrise terminator time and the D-layer preparation or formation time (DLPT/DLFT) before, during and after the days of earthquakes [14].

Figure 7 shows the plot of D-Layer Preparation time or DLPT versus day number of the year 2008. Mean DLPT is calculated excluding the data of those days on

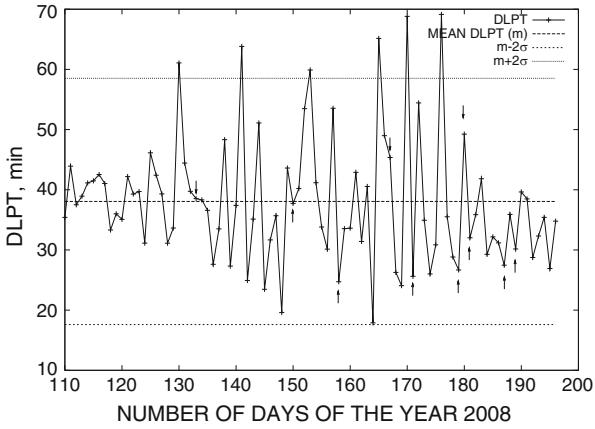



**Fig. 7** D-layer Preparation Time as a function of day number. The middle line represents the mean (m) DLPT and the one above and one below lines are respectively the $(m + 2\sigma)$ and $(m - 2\sigma)$, $\sigma$ is the standard deviation [14]

which there was an earthquake. The $(m + 2\sigma)$ and $(m - 2\sigma)$ lines are shown respectively above and below the mean DLPT line where m represents the mean DLPT and $\sigma$ is the standard deviation which were estimated based on the period of observation. The days of earthquakes are marked by arrow marks in Fig. 7. It is clearly seen that DLPT is fluctuating about the mean before and after seismically active days. In some cases the fluctuations in DLPT are very prominent where it is beyond m $\pm 2\sigma$ values. The observed values of DLPT on one day before, one day after and on the day of earthquake can be found. It is, thus, clear that there is a correlation of seismic activity with the anomalous behavior of DLPT. The exact cause of these anomalies is under investigation.

## *4.2 Cross Correlation Between VLF Anomaly and Earthquakes: A Statistical Study*

To find out a correlation with the seismic activity we took the seismic events which occurred in the neighborhood of the great circle path between the transmitter and the receiver. In the days when more than one earthquake occurs, we have calculated the total energy from the individual earthquakes and sum them up following Sasmal et al. [11]. Thus we have the deviation of the anomalous VLF day length from the mean and also the effective magnitude of each day. We then compute the correlation coefficient between these two quantities. We found a sharp peak 1 day before the earthquake [26].

Similarly, for DLPT, we computed the deviation of DLPT and studied the correlation coefficient between DLPT and the effective magnitude of earthquakes. We found that in case of DLPT, the peak of the correlation appears 2 days before the event day [26].

## 5 Concluding Remarks

In the first part of this review (i), we studied three very well known black hole candidates which undergo variability class transitions. We showed that they take very little time to change their emission pattern of X-rays and these could only be done only if the accretion flow is faster than Keplerian. We also show that there is a specific sequence in which these transitions occur. Later, further analysis of RXTE satellite data was carried out and it was shown that exactly in that sequence the variabilities should occur, indicating that our interpretation of the data was accurate.

In the second part of the work (ii), we discussed what is VLF propagation and how the standard signal from a given transmitter vary with propagation path. I also obtained signals of several solar flares and found that there are time lags between the solar flares and VLF signals. In yet another important work, we studied the VLF signal nature over two propagation paths and found direct evidences of interferences between the sky wave and the ground wave of the transmitted signal.

In the third part of the work (iii), I showed that some of the anomalies could be due to earthquakes and need not be due to the solar or extra-terrestrial source. Prior to earthquakes, there are mild vibrations of plates which may cause magnetic field fluctuations which, in turn, generate VLF/LF radio signals. The crevices formed before earthquakes are also known to produce Radon gas which in turn causes extra ionization of the ionosphere. This may cause terminator shifts and change the D-layer preparation time. We have observed several such anomalies and cross-correlated them with major seismological events. We found that typically terminator shifts occur 1 day before a major earthquake and anomaly in DLPT occur 2 days before a major earthquake. Exact cause of these effects is under active study. Some other chapters present these anomalies in more detail.

## References

1. Basak, T., Chakrabarti, S.K.: Astrophys. Space Sci. **348**(2), 315 (2013)
2. Belloni, T., Wolt, M.-K., Méndez, M., van der Klis, M., van Paradijs, J.: Astron. Astrophys. **355**, 271 (2000)
3. Chakrabarti, S.K., Pal, S., Acharyya, K., Mandal, S., Chakrabarti, S., Khan, R., Bose, B.: Indian J. Phys. **76B**, 693 (2002)
4. Chakrabarti, S.K., Acharya, K., Bose, B., Mandal, S., Chatterjee, A., Nandi, N., Pal, S., Khan, R.: Indian J. Phys. **77B**(2), 173 (2003)
5. Chakrabarti, S.K., Nandi, A., Choudhury, A.K., Chatterjee, U.: Astrophys. J. **607**, 406 (2004)
6. Chakrabarti, S.K., Nandi, A., Chatterjee, A.K., Choudhury, A.K., Chatterjee, U.: Astron. Astrophys. **431**, 825 (2005)
7. Chakrabarti, S.K., Saha, M., Khan, R., Mandal, S., Acharyya, K., Saha, R.: Indian J. Radio Space Phys. **34**, 314 (2005)
8. Chakrabarti, S., Sasmal, S., Saha, M., Khan, R., Bhowmick, D., Chakrabarti, S.K.: Indian J. Phys. **81**, 531 (2007)
9. Chakrabarti, S.K., Mondal, S.K., Sasmal, S., Bhowmick, D.: GRB Circ. Net. 8881 (2009)
10. Chakrabarti, S.K., Mondal, S.K., Sasmal, S., Bhowmick, D.: GRB Circ. Net. 8900 (2009)

11. Chakrabarti, S.K., et al.: GRB Circ. Net. 9316 (2009)
12. Chakrabarti, S.K., Sasmal, S., Chakrabarti, S.: Nat. Hazards Earth. Syst. Sci. **10**, 1751 (2010)
13. Chatterjee, A.K., Bari, W., Choudhury, A.K.: Indian J. Phys. **82**(11), 1429 (2008)
14. Chatterjee, A.K., Bari, W., Choudhury, A.K.: Indian J. Radio Space Phys. (India) **38**, 138 (2009)
15. Choudhury, A.K.: Sources of high energy radiation and their effects on the Very Low Frequency (VLF) radio signals, Dessertation, MAKAUT (2017)
16. Choudhury, A.K., Chatterjee, A.K., Nandi, N.: Bull. Astron. Soc. India **35**, 41 (2007)
17. Choudhury, A.K., Chatterjee, A.K., Bari, M., Chakrabarti, S.K.: Am. Inst. Phys. Conf. Proc. **1053**, 8 (2008)
18. Gufeld, I.L., Rozhnoi, A.A., Tyumensev, S.N., Sherstuk, S.V., Yampolsky, V.S.: Phys. Solid Earth (Russia) **28**, 267 (1992)
19. Hayakawa, M.: Atmospheric and Ionospheric Electromagnetic Phenomena Associated with Earthquakes, p. 996. Terra Scientific Pub. Comp., Tokyo (1999)
20. Mondal, S.K., Chakrabarti, S.K.: Am. Inst. Phys. Conf. Proc. **1286**, 61 (2010)
21. Naik, S., Rao, A.R.: Astron. Astrophys. **362**, 691 (2000)
22. Nandi, N.M., Chatterjee, A.K., Bari, W., Choudhury, A.K.: Am. Inst. Phys. Conf. Proc. **1286**, 205 (2010)
23. Pal, P.S., Chakrabarti, S.K., Nandi, A.: Proc.XII Marcel Grossman Conference, p. 969. World Scientific Pub. Co., Singapore (2012)
24. Pal, S., Chakraborty, S., Chakrabarti, S.K.: Adv. Space Res. **55**, 1190 (2015)
25. Ray, S., Chakrabarti, S.K., Mondal, S., Sasmal, S.: Nat. Hazards and Earth Syst. Science **11**(8), 2699 (2011)
26. Ray, S., Chakrabarti, S.K., Choudhury, A.K.: IEEE Conf. Publication (2011). https://doi.org/10.1109/URSIGASS.2011.6051047
27. Sasmal, S., Chakrabarti, S.K.: Nat. Hazards Earth Syst. Sci. **9**, 1403 (2009)
28. Smith, D.M., Heindl, W.A., Markwardt, C.B., Swank, J.H.: Astrophys. J. **554**, 41 (2001)
29. Smith, D.M., Heindl, W.A., Swank, J.H.: Astrophys. J. **569**, 362 (2002)
30. Whitten, R.C., Poppoff, I.G.: Physics of Lower Ionosphere. Prentice-Hall, Englewood Cliffs (1965)
31. Yashiro, S., Michalek, G., Akiyama, S., Gopalswamy, N., Howard, R.A.: (2007). arXiv:0710.3054v1 [astro-ph]
32. Zhang, S.N., Cui, W., Harmon, B.A., et al.: Astrophys. J. **477**, L95 (1997)

# Detector Development and Optimization for Space Based Astronomy from Satellites and Balloons




**Ritabrata Sarkar**

**Abstract** The field of experimental X-ray astronomy has undergone a long way since the first observation of extra-terrestrial X-ray dated back to sixties. Several techniques have been developed and used since then for detection of these radiations. There have been numerous missions with various kinds of detectors onboard sounding rockets, scientific balloons or satellite platforms. Several space agencies have been involved in such experiments world wide. In recent years a trend of using light-weight payloads has come through for this purpose, thanks to the technological advancements and miniaturization of instruments. Small payloads in the form of cubesats or nanosats are being used at the orbits. Also light-weight and specially designed payloads are being used onboard meteorological balloons for certain observations on X-ray astronomy. Here is a brief review of some recent developments in this field of instrumentation in X-ray astronomy, particularly in Indian context.

## 1 Introduction

Several decades have passed in X-ray astronomy since the first discovery of extra-solar X-rays [11], when gas filled detectors were carried outside the earth's atmosphere by a sounding rocket recorded X-rays from Scorpius-X1. Since then, X-ray emissions from such objects have been recorded and our understanding of high-energy processes in the Universe has improved significantly by the development of new experimental techniques and, in particular, new methods for X-ray detection. Nowadays more advanced energy sensitive X-ray detectors like semiconductor detectors, scintillator detectors and proportional counters have taken place of the gas filled Geiger counters. Longer observation time and larger photon collecting area are also achievable by the detectors onboard satellite missions.

R. Sarkar (✉)
Indian Centre for Space Physics, Kolkata, India

© Springer International Publishing AG, part of Springer Nature 2018

B. Mukhopadhyay, S. Sasmal (eds.), *Exploring the Universe: From Near Space to Extra-Galactic*, Astrophysics and Space Science Proceedings 53,
https://doi.org/10.1007/978-3-319-94607-8_29

The era started by the first satellite borne mission UHURU to explore the Universe in X-rays has been continued till date by the novel missions like RXTE [5], XMM Newton [13], NuSTAR [12], ASTROSAT [26] etc. ASTROSAT is the most recent X-ray astronomy venture by India covering a multi-wavelength band of electromagnetic radiation from space. There are several other indigenous missions dedicated to X-ray astronomy like Indian X-ray Astronomy Experiment (IXAE, on board IRS-P3 satellite [2] launched in 1996), RT-2 ([19] on board the CORONAS-PHOTON satellite) etc. The satellite experiments no doubt has the upper hand of the long term observation which cannot be achieved by the sounding rocket or balloon borne experiments. Though balloon experiments are useful to avoid the delay implicit to satellite experiments.

Balloon borne X-ray astronomy missions like PoGOLite [14], GRIP [7], EXITE [8] has brought forward many important scientific discoveries. But these kind of experiments have been accomplished using big payloads of several tons carried over by huge gas filled balloons of million cubic meters volume or more. These missions are mostly designed to float above the atmosphere for several days to gather scientific data from space. These huge balloon borne experiments along with satellite missions require a big budget, team of several manpower, planning and realization time which is out of grasp for small bodies who want to do space experiments. There are, of course, some other kind of balloon borne missions concerning small meteorological balloons. They carry small payloads of the order of few hundred grams, used mainly for the measurement of atmospheric weather parameters. There is a need to fill the gap between the mega-sized scientific balloons and meteorological balloons. So the micro-satellites carrying small scientific payloads of the order of few kilograms are introduced. For example, the UoSAT Spacecraft Engineering Research Unit in University of Surrey (UK) has designed, constructed and operated small, low-cost but sophisticated satellites in their the UoSAT spacecraft programme [27]. More recently the German Aerospace Center (DLR) and the Swedish National Space Board (SNSB) are collaborating in such kind of low-weight, low-budget space exploration programme REXUS/BEXUS [20].

Indian Centre for Space Physics has pioneered in carrying out low-cost experiments [6] involving small payloads of few kilograms onboard meteorological (both rubber and polythene) balloons for the exploration of space radiation which will be discussed later in this chapter.

## 2 Detector Optimization of Recent Satellite Borne Experiments

Space based telescopes are operated in a low signal-to-noise environment. Therefore an optimum shielding configuration to minimize the background counts and precise measurement of the background radiation for high energy X-ray detectors is

essential. Considering the scope of the work being discussed here, this section highlights the characterization of background noise, shielding optimization and detector response of some of the detectors onboard recent space borne missions.

## *2.1 ASTROSAT Experiment*

The ASTROSAT mission [3] is an Indian enterprise providing a simultaneous multi-band observations of electromagnetic wave from outer world for the spectral and temporal study of the sources in a broad energy range. On board ASTROSAT there are five astronomy payloads to accomplish the job (the following information about the instruments are taken from [3]):

1. Two modules of Ultraviolet Imaging Telescopes (UVIT) covering Far-UV to optical bands.
2. Three units of Large Area Xenon Proportional Counters (LAXPC) sensitive to 3–80 keV X-rays with an effective area of 8000 $cm^2$ at 10 keV.
3. One Soft X-ray Telescope (SXT) with conical foil mirrors and X-ray CCD detector working in 0.3–8 keV energy range with effective area of 120 $cm^2$. at 1 keV.
4. A Cadmium-Zinc-Telluride coded-mask Imager (CZTI), covering hard X-ray range in 10–150 keV, with an effective area of 480 $cm^2$ and an aperture of about 6° Field of View (FoV).
5. A Scanning Sky Monitor (SSM) system having three one-dimensional position-sensitive proportional counters with coded masks.

Here, in particular, we concentrate on our efforts to study possibilities of optimal shielding of two major instruments: LAXPC and CZT-Imager onboard ASTROSAT experiment [21].

LAXPC consists of three identical units of multi-wire proportional counters using Xenon gas (mixed with methane). This instrument is suitable for good timing analysis and have low spectral resolution of ∼20% FWHM at 6 keV and ∼10% FWHM at 22 keV. The collimator assembly made of tin, copper and aluminum provides $1^\circ \times 1^\circ$ FoV to the detector.

The detailed study of the shielding efficiency and detector response was done using the Monte Carlo (MC) simulation and can be found in [21]. The calculations provide an optimal shielding distribution and collimator configuration using tin and copper as the shielding material for the working energy range of the detector. Apart from the passive shielding surrounding the detector it also consists a veto layer of counter cells around the sensitive volume of the detector which excludes background counts using anti-coincidence technique.

Cadmium Zinc Teluride (CZT)—Imager is used to provide imaging and spectral study of X-ray in the ∼10–150 keV energy range. CZT is deployed to serve as the sensitive volume of the detector which can operate at the room temperature to provide high resolution (∼8% FWHM at 60 keV) X-ray and $\gamma$-ray spectroscopy.

This material also has an excellent detection efficiency of ∼100% in this energy range. The imaging capability of the detector is achieved by using the Coded Aperture Mask (CAM).

The main sensitive detector is made of CZT panel of 5 mm thick with total area about 1024 $cm^2$ divided into four quadrants. Underneath the CZT panel in each quadrant, there is a CsI crystal block providing the background exclusion due to Compton-scattered photons using anticoincidence method. The collimator made of tantalum and aluminum provide an aperture of 6° × 6°. The CAM made of 5.0 mm thick tantalum is fitted at the top of the collimator.

The passive shielding of the detector was realized using tantalum and the calculation for the optimum distribution of shielding material can be found in [21]. The detector efficiency and its response to the CDXRB was also calculated and given in the same work.

## *2.2 RT-2 Experiment*

The RT-2 (Roentgen Telescope-2) space astronomy experiment is a part of the Indo-Russian collaborative project on-board CORONAS-PHOTON mission [16]. The principal goal of this experiment is to study the solar hard energy X-rays in the energy range of ∼15–1000 keV through high resolution spectroscopy and imaging study. The detection of the Gamma-Ray Bursts (GRB) is also possible by the instrument in the range of its operation. The experiment consists three scientific payloads: RT-2/S, RT-2/G and RT-2/CZT and one processing electronic device: RT-2/E. The detector shielding optimization and response characterization of the scientific payloads onboard RT-2 experiment were exercised mainly using MC simulation and can be found in [23].

RT-2/S & G exploit scintillator detectors using NaI(Tl) and CsI(Na) crystals in phoswich combination and the signal read by a PMT and shares the same construction design except for the FOV (for RT-2/S FOV is 4° × 4° and for RT-2/G FOV is 6° × 6°). The detailed description and functionality of the detectors are given in [9].

While RT-2/CZT is a solid state imaging device which consists of Cadmium Zinc Teluride (CZT) and Complimentary Metal Oxide Semiconductor (CMOS) as the active detector materials [15]. The imaging capability of the detector is achieved by using the shadow casting technique by the implementation of the Coded Aperture Mask (CAM) and Fresnel Zone Plate (FZP) [17]. Using of CZT and CMOS as the active volume enables the detector to have a high resolution spectral and imaging capability in the energy range of ∼20–150 keV.

A detailed simulation was carried out to achieve the optimum distribution of the shielding material (tantalum) and is effective only for the low energy range (<150 keV) where efficient energy deposition in NaI crystal and CZT or CMOS is possible. The active shielding effect for RT-2/S&G is obtained by using the anticoincidence technique for the energy depositions in NaI and CsI crystals. For

this reason the shielding may be dropped out from the lower part of the detector as the CsI will guard the background from that direction. The FoV of the detector was also provided by a collimator using a square array of Ta plates. Ta was used also in RT-2/CZT as the shielding material but the whole box was needed to cover up since no active shielding is implemented in this case.

The background in these detectors may be divided into two major parts: counts due to external diffused space radiation and intrinsic secondary radiations from interaction of high energy particles with the constructing materials in the vicinity of the detector. Both kinds of background effects were considered to estimate the total background in the detectors (RT-2S/G/CZT). For the intrinsic background part an approximate mass distribution of the whole satellite was considered and the most abundant species (proton, neutron, gamma) of the high energy particles at the satellite orbit were used to generate the secondaries, while CDXRB photon distribution served the external diffused background part. However two other major components should be considered to make the whole background estimation up: background due to long term activation of the detector material by the CR and the trapped charged particles at the satellite orbit due to geomagnetic field.

The precise calculation of the detector response is very important for the faithful reproduction of the original source spectrum from that obtained in the detector. This response includes the varying efficiency of the sensitive detector with energy, change in the effective area of the detector with energy and also with position of the source w.r.t. the detector. Calculation of the response function was done by using detailed simulation of the detectors.

## *2.3 SPHINX Experiment*

A new concept of all sky monitoring payload for Spectro-photometry in X-rays (SPHINX) was given by Sarkar and Chakrabarti [22] which can be placed on a lander on the moon or in a space craft orbiting around the moon in future mission. There are several advantages of doing space Astronomy on lunar surface. The 27.3 days orbital period of moon is far longer than the period of an artificial satellite. Also moon has no rotational motion around its own axis. Thus, any celestial object can be viewed for at least 14 days at a stretch. Along with other advantages, such as low magnetic noise, stable platform, absence of atmosphere, moon is considered to be an ideal location for space astronomy experiment. SPHINX is considered to simultaneously provide high spectral and time resolution measurements of soft and hard X-rays in the energy range from $\sim$1 to 300 keV from Sun as well as from GRBs and other high-energy transient sources from all the directions, including X-ray Fluorescence (XRF) on the lunar surface when the Sun is active. In this respect, both the space science and lunar science could be carried out with the SPHINX detector. The wide energy range of the detector is realized by implementing two types of solid state detectors, namely Si-PIN and Cadmium-Telluride (CdTe) side by side. The details of the design and calculation of optimal parameters can be found

in [22]. Simulation of the effective background and response of the detector for the potential sources using CDXRB, Solar, GRB, SGR radiation spectra were calculated showing the capability of the concept.

## 3 Space Exploration with Smaller Balloons

X-ray astronomy relies on satellite based, scientific balloon borne or sounding rocket based experiments to explore the radiation sky. But this type of experiments are generally realized under a very high budget, using huge manpower and after a long preparation time. However, with the advent of new techniques in the electronics sector, miniaturization of astrophysical payloads is possible in the current era.

During the past decade, Indian Centre for Space Physics (ICSP), Kolkata has been involved in such a mission [6] to exploit these aspects to build small-scale, light-weight and cost-effective payloads. These payloads could be placed above most part of the atmosphere, to avoid X-ray absorption, with the help of meteorological balloons. So far a record total of 109 such missions have been completed under the leadership of Prof. Sandip K. Chakrabarti.

These kind of experimental techniques are particularly useful to study X-ray solar flares during solar activity, other X-ray activities from the point like sources and transients like pulsars and other X-ray binaries or radiations from high energy GRBs. Additionally it is also useful for in-situ measurement of the CR flux (secondary photons emission in the atmosphere) at various altitudes. Study of daily and seasonal variation of the CR data is possible using multiple mission data. As the CR fluxes are highly dependent on the geomagnetic-latitude, this kind of mission help us to know precise information of location dependence of the flux. Apart from the extra-terrestrial events, Terrestrial Gamma-ray Flashes (TGFs) from the cloud formation region of the atmosphere are other types of interesting and yet to be understood events which can be studied by these kind of experiments.

### *3.1 ICSP Mission Philosophy*

The key idea of these missions is to cut the budget cost by exploiting the idea of recoverable payload so that same payload can be used for multiple missions. The modular approach of the payload and mission design makes it possible to prepare for the mission in a very short time and also involving a few manpower.

The motivation is to carry payloads which are less than about 5 kg and to use light weight single or multiple rubber ($\sim$2 kg category) or plastic balloons (of about 7–9 kg category) which are generally used for meteorological purposes. To consider the study of the X-ray sky, the payloads typically fly up to the altitude of 35–42 km to avoid most of the atmospheric absorption. Similar procedure can also be exercised to study other energy bands using appropriate instruments in the payload.

The time and location of the mission flights are inter-dependent and strongly influenced by the local meteorological behaviour like wind pattern, geographical and demographic situations. For efficient recovery of the payloads, it is preferable to have a smaller range of flight which is possible to have when effective wind drift is minimum. The successful recovery of the payload also depends on the efficient tracking of the payload and prediction of the flight path. This is achieved by using onboard location communication system during the live mission and using flight path prediction calculation with the help of wind information.

The number and type of the carrier balloons mainly depends on the payload weight. Details are in [6]. When longer duration data at greater height of 35–42 km is needed, a single polythene balloon (made by TIFR, Hyderabad, India) is deployed which can stay about 4–5 h in flight with about an hour above 30 km. A picture of the payload and carrier balloon along with some of the mission team members and launch view of the balloon is shown in Fig. 1.



**Fig. 1** (Left) ICSP balloon team members (SKC with laptop) with the payload and carrier balloon before the launch of a mission. These 100 feet, TIFR made polythene balloons are about 7–9 kg in weight and can carry about 5 kg payload till 42 km height. (Right) Launching of a balloon

## 3.2 Payload Description

The payloads are designed to be compact, light-weight, reusable and most importantly of low-cost. For these missions, the payload has to undergo a change in the pressure like from ∼1000 mbar to ∼2 mbar and at certain stage it has to cope up with temperature as low as $\sim -70°$. Most of the general purpose electronic devices and power supplies are expected to fail and all circuits calibrations on ground are changed. The response of the detectors would also vary. But due the restriction on the payload weight it is not possible to provide the payload with any pressure vessel. Instead the payload components are designed to withstand the low pressure and tested properly under the same conditions. But the temperature change must be taken care of at least partially. Thus the payload box must be provided with a temperature shielding.

The payload components are arranged in a styrofoam (thermocol) box which provides thermal and mechanical shielding to the components and serves as the chassis for the payload. It has the ability to absorb some mechanical shock of possible impact with earth during landing. Typically, inside temperature of the payload remains at 10–15 °C throughout the journey.

The payload of a typical mission includes a Main Measurement Unit (MMU) which, for example, could be a scintillator type detector or Geiger-M*ü*ller (GM) counter. The MMU must be supported by some other essential/optional ancillary equipments discussed later.

### 3.2.1 Main Measurement Unit

The choice of the main measurement unit depends on the science goal to pursuit. The other constraints to consider in this regard are the effective energy range of the detector, restriction on the payload weight, mechanical robustness required for the mission etc. Scintillator detectors are reasonable candidate to fulfill these requirements. Sometimes to measure the integrated counts of secondary CR events in the atmosphere GM counters are used.

The experiments mostly used cylindrical crystals of NaI(Tl) and in some cases CsI(Na) optically mounted on a Photo-Multiplier Tube (PMT). Sometimes phoswich detectors are also used for better background elimination where two different kind of crystals (viz. NaI(Tl) and CsI(Na)) are optically coupled together with a single PMT. The details of the various scintillator detectors used in the experiments can be found in [6].

A collimator is provided to the detector to reduce the background counts. The FoV of the collimator depends on the observation purpose and constraints on the payload weight. Since there is no pointing device in the payload it will rotate at different rates at a different height and not necessarily always in the same sense. Thus in order to detect a specific target for a considerable amount of time, the FoV should not be too narrow. Depending on these restrictions of weight,

background count, source intensity under consideration, payload free rotation rate etc. calculation yields an optimum FoV of 10–15°. This collimator is realized by using materials like lead, tin or tantalum.

The high voltage bias to the detector is supplied from battery power supplied with the payload and the signal processing electronics process, digitize and store the signal information on to the memory cards in the payload.

GM counters are used in the experiment mainly for the purpose of measuring the integrated counts of secondary CR in atmosphere. Very light weight small cylindrical counters filled with Ne+Halogen are generally used as single or in multiple number to increase the detection area.

### 3.2.2 Ancillary Detectors

Several ancillary instruments support the mission which are used for live time mission control or for offline data analysis. Here brief descriptions of such modules are given.

AMU Attitude Measurement Unit (AMU) is used to record the instantaneous orientation of the payload and hence the direction of the detector. Since a conventional pointing device is not feasible to use in such missions due to the limitation on the weight, this device enables to tag the information in the main detector with the direction of its appearance. Inertia Measurement Unit (IMU) sensor which is a small micro-electro-mechanical module chip consisting of three axis Accelerometer, Magnetometer and Gyroscope is used for this purpose. This device needs to have a proper calibration to provide accurate data and calculations are done offline to convert the sensory data into directional information.

VCU Video Camera Unit (VCU) is a small and light-weight movie camera to record the overall mission operation. It also captures the extraterrestrial objects like Sun, Moon, bright stars and planets, meteorites etc. and an excellent areal view of the Earth from various altitudes.

SS Sun Sensor (SS) is a photo-sensor to capture the optical photons from the Sun. Especially used during the solar X-ray observation to cross-check if the Sun was indeed in the FoV when the data in MMU is sorted out as coming from the Sun.

GPSU Global Positioning System (GPS) Unit (GPSU) is used to obtain instantaneous payload location (latitude, longitude and altitude) which also may be used to derive the wind parameters at different levels through the atmosphere. The payload location information is very important for the later use during the data analysis as well as to track the payload for its recovery.

PITU Recovery of the payload largely depends on the anticipation of its landing location and on-the-go tracking feature handled by Positional Information Transmission Unit (PITU). This is a light weight and rugged device which

can give the real time positional information of a payload on board the carrier to the mobile ground base. Standard short range two way devices which are generally used for voice communication at the RF transmitter are used to transmit the location information collected from GPS to the receiver.

PASU To fail safe the recovery system another Position Alert System Unit (PASU) using cellphone network (GSM communication) is implemented. This is automatically activated upon landing when it is under GSM network coverage.

PTU Pressure and Temperature measurement Unit (PTU) is used to monitor the temperature inside and outside the payload box and the atmospheric pressure. These information are important for the payload health check as well as these high altitude information are important for the meteorological purposes.

PSU Power Supply Unit (PSU) consist of a stack of rechargeable batteries and are generally Li-Po type. Since the mission is expected to be of few hours, and could also be at night time, solar cells are not used to supply the power to the payload. Instead of a centrally powered system, separate units are used for different instrument modules to increase the chance of receiving some data in case of failure of some PSUs.

## *3.3 Test, Calibration and Responses*

Extensive tests of the detectors in the laboratory are required for the design and functional optimization of the detectors and proper execution of the experiments. Calibration of the detectors and calculation of their responses using laboratory tests and simulation procedures are needed to convert the detector signals into scientific information. More details of these procedures can be found in [6] and briefly discussed here.

**Detector Calibration**
Detector calibration is done by using several gamma ray radiation sources in the laboratory which have emission lines of fixed energies in the detector energy range. The channel to energy relation is subsequently used for the conversion of pulse heights into energy spectrum. The energy dependence of the detector resolution is used to calculate the response function of the detector.

**Atmospheric Response Calculation**
The incoming radiations from space suffer different absorption in the atmosphere for different height of the detector depending on the location of the payload during the course of flight. So to trace back the original spectra of the X-ray data it is necessary to calculate the absorbing nature of the varying residual atmosphere. This can be done by means of the simulation with a proper atmospheric model. For this purpose,

a simulation framework was developed using Geant4 toolkit [1] and considering the NRLMSISE-00 atmospheric model [18].

**Detector Sensitivity**
Sensitivity of the detector depends on the background counts. Due to the secondary generated CR, the background counts varies with the altitude for such balloon borne detectors. So it is necessary to estimate the detector background at different level in the atmosphere and calculate the corresponding sensitivity of the detector. This has been done by atmospheric simulation and from the knowledge of previous background measurements at different altitudes.

**Detector Response Calculation**
Geant4 toolkit is also used for the simulation of the detector response at different energies. The response function is necessary for the spectral analysis of the source radiation to convert the detector counts to absolute photon flux from the source. Other response calculations of the detector like effective area and angular dependence of the incident radiations are also important and also done by using the simulation procedure.

**Tests in Atmospheric Simulator**
The main detector and other payload components undergo a significant change in pressure and temperature during the flight. So the payload components are required to undergo some tests in the similar simulated environment. To simulate the low temperature effect on the payload, an insulated vessel is used to gradually decrease the temperature of the payload surrounding to about $-10\,^{\circ}\mathrm{C}$ from room temperature. The pressure variation may change the detector gain and/or may effect the electronics part especially on the high voltage biasing due to the change of dielectric constant of the medium. Proper insulation of the high voltage bias part is required to prevent this effect. Then the system is tested under low pressure condition using a pressure chamber where the pressure can be brought down to about 6–7 mbar (which corresponds to about 35 km height in the atmosphere) from the normal pressure at ground.

## *3.4 Science Outcomes*

Many important results have been obtained so far from this new paradigm of experiment. In situ measurement of secondary CR in the atmosphere at different altitude provides a great deal of information about its nature. This variation is again modulated by space conditions such as solar activity and is studied in detail by Sarkar et al. [24] and is briefly discussed below. The radiation data from other astrophysical objects such as the Sun or pulsars are prevalent only when the payload overcomes sufficient atmosphere (about above 30 km) so that the absorption is minimized. These results along with the information from the peripheral instruments can be found in [6].

### 3.4.1 Cosmic Rays

Primary CR interacts with the atmospheric nuclei to produce secondary cosmic-ray shower [10]. Intensity of the secondary X-ray depends on the altitude as the atmospheric density and composition varies with altitude. With the decreasing altitude the interaction of the primary CR gradually intensifies at lower heights producing more secondary particles. But the loss effect due to absorption and decay processes also become more at lower heights as the density gets higher. A maximum secondary intensity around 15–20 km arise due to the balance of these interactions. This maximum height depends on the geomagnetic latitude of the location [4] and is called Regener-Pfotzer maximum (RP-max). Figure 2 shows the spectral change of the secondary CR dynamically with altitude as recorded in one of the missions with scintillator detector.

The primary CR flux depends on the strength and spatial distribution of the terrestrial and Interplanetary Magnetic Field (IMF) which is again highly dynamic and is influenced by the plasma and magnetic field of the solar wind. So the observed secondary CR at the earth's atmosphere also vary with the solar activity. However, due the particular shape of the terrestrial magnetic field distribution, the CR variation is more prominent at the higher latitudes [4]. Though [24], using the results from these balloon borne missions, has found the CR variation with the

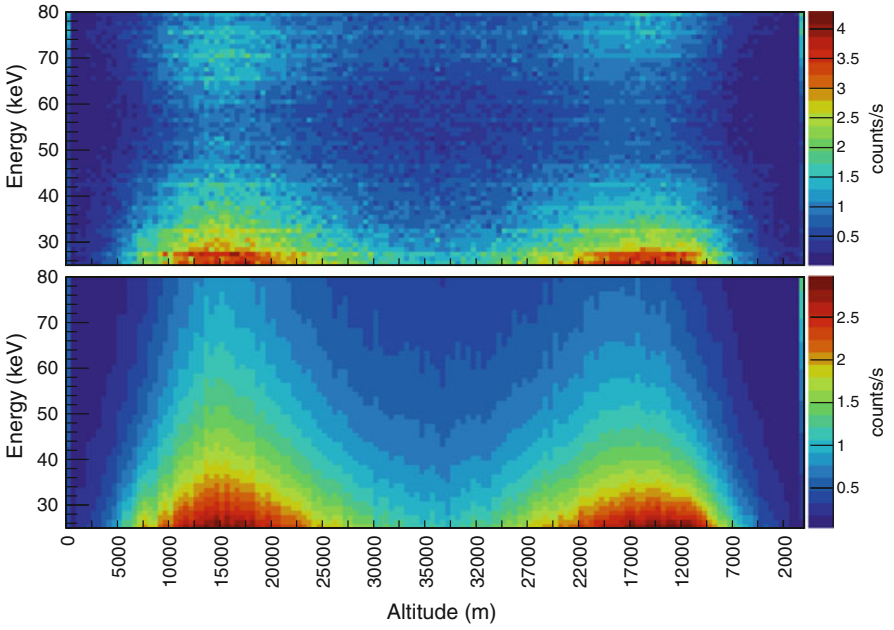



**Fig. 2** Dynamical variation of the secondary CR spectrum with altitude. (Upper panel) Detector data including emission effect from the lead collimator shielding. (Lower panel) Result after removing the emission effect (courtesy: [6])

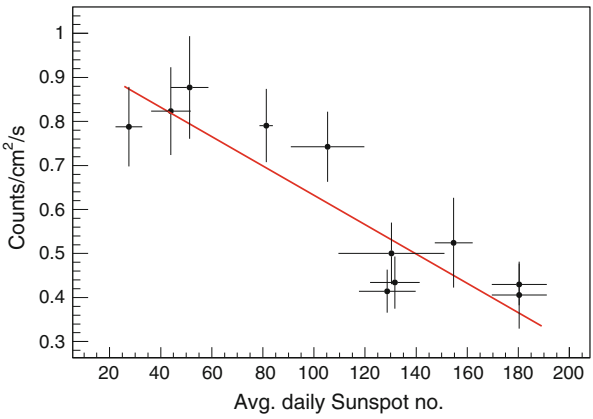



**Fig. 3** Correlation between the daily sunspot number averaged over previous 3 days and radiation counts at the RP-max. Data were taken during 24th solar maximum till next minimum (courtesy: [24])

solar activity even at low geomagnetic latitudes region near (∼14.5° N). The plot of radiation count rate at the RP-max with the sunspot number averaged over previous 3 days (which accounts for the solar activity) is shown in Fig. 3. This indicates a significant anti-correlation between the two phenomena.

### 3.4.2 Solar Flare

The high intensity of X-ray radiation from Sun during flares makes it possible to see them using small detectors even after the partial absorption in the residual atmosphere. Very short preparation time for the missions makes it possible to launch the mission during the predicted short duration solar activities.

### 3.4.3 Crab Radiation

Apart from the sun, one of the most bright and consistent X-ray radiation sources in the sky is the Crab pulsar. A 5″ diameter phoswich detector (with NaI(Tl) and CsI(Na) crystals) with proper collimator and shielding was deployed onboard a plastic balloon to detect the radiation from Crab. The sensitivity of the detector was just enough to detect the crab radiation from above 30 km. We get the lightcurve as in Fig. 4. The analysis of spectral information from the source requires precise knowledge of the background, detector response, atmospheric response etc. and considered during the analysis. The source spectrum fitted with the usual crab model of absorbed power law, along with the background spectrum is given in Fig. 5.

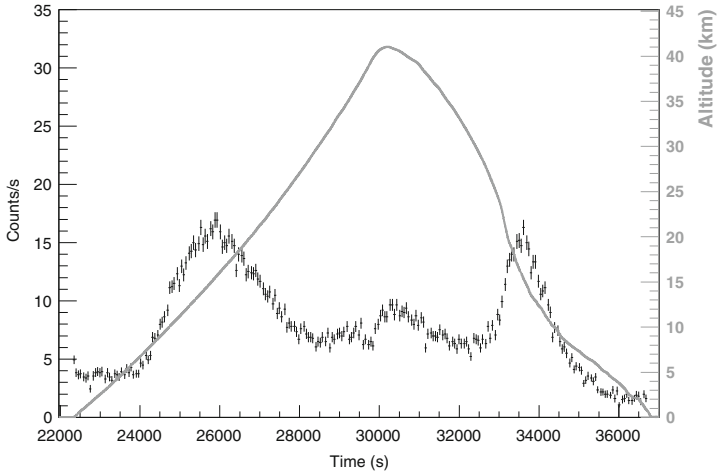



**Fig. 4** 25–60 keV light curve of the overall mission data showing the radiation from Crab above 30 km. Payload altitude is plotted simultaneously to show the detector position (courtesy: [25])

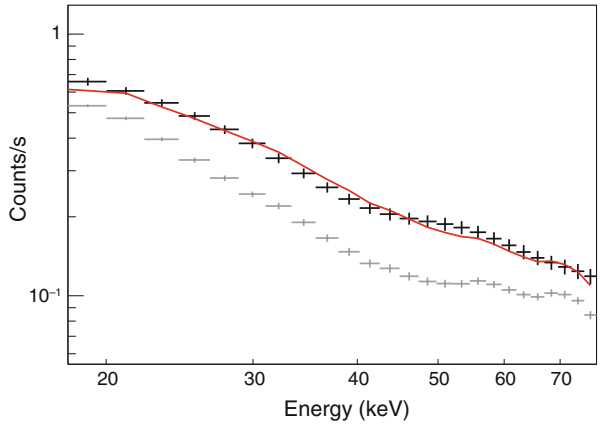



**Fig. 5** The detected (source + background) spectrum of Crab radiation (black) along with the calculated detector background (grey). The spectrum is fitted by using a absorbed power law modified by the atmospheric and detector responses (courtesy: [25])

## *3.5 Results from Peripheral Instruments*

Data from different ancillary units can also be used to provide important results. GPS data is mainly used for the location determination of the payload which aids the tracking and recovery of the payload. The wind velocity at different layers in the atmosphere up to a very high altitude of 40 km or more can also be synthesized from the GPS data and used to get a local picture of seasonal variation of wind profile.

Similarly, the data from the pressure and temperature sensors also provide important information which can be used for meteorological studies.

**Acknowledgements** The author wishes to express his most sincere gratitude to Prof. Sandip K. Chakrabarti for his continuous and invaluable guidance throughout the works. The author is also thankful to the LAXPC and CZT-Imager team of the ASTROSAT project and the RT-2 project team. Heartfelt thanks are also due to the members of the scientific ballooning team of Indian Centre for Space Physics.

## References

1. Agostinelli, S., et al.: Nuclear Instrum. Methods Phys. Res. **A 506**, 250–303 (2003)
2. Agrawal, P.C., Paul, B., Rao, A.R., et al.: JKASS **29**, S429 (1996)
3. ASTROSAT – A satellite mission for multi-wavelength astronomy. http://astrosat.iucaa.in/. Cited 12 Apr 2018
4. Bazilevskaya, G.A., Svirzevskaya, A.K.: SpScR **85**, 431–521 (1998)
5. Bradt, H.V., Rothschild, R.E., Swank, J.H.: A&A Supplement **97**, 355–360 (1993)
6. Chakrabarti, S.K., Sarkar, R., Bhowmick, D., Bhattacharya, A.: Exp. Astron. **43**(3), 311–338 (2017)
7. Cook, W.R., Grunsfeld, J.M., Heindl, W.A., et al.: ApJ **372**, L75–L78 (1991)
8. Covault, C.E., Grindlay, J.E., Manandhar, R.P.: ApJ **388**, L65–L67 (1992)
9. Debnath, D., Nandi, A., Rao, A.R., et al.: ExA **29**, 1–25 (2011)
10. Gaisser, T.K.: Cosmic Rays and Particle Physics. Cambridge University Press, Cambridge (1990)
11. Giacconi, R., Gursky, H., Paolini, F.R., Rossi, B.: PhRvL **9**, 439–443 (1962)
12. Harrison, F.A., Cook, W.R., Forster, K., et al.: ApJ **770**, 103 (2013)
13. Jansen, F., Lumb, D., Altieri, B., et al.: A&A **365**, L1–L6 (2001). System. Phys. Rev. Lett. **9**, 439–443 (1962)
14. Kamae, T., Andersson, V., Arimoto, M., et al.: APh **30**, 72–84 (2008)
15. Kotoch, T.B., Nandi, A., Debnath, D., et al.: ExA **29**, 27–54 (2011)
16. Kotov, Y.D.: SoSyR **45**, 93–96 (2011)
17. Nandi, A., Palit, S., Debnath, D., et al.: ExA **29**, 55–84 (2011)
18. Picone, J.M., Hedin, A.E., Drob, D.P., Aikin, A.C.: JGR **107**(A12), 1468 (2002)
19. Rao, A.R., Malkar, J.P., Hingar, M.K., et al.: SoSyR **45**, 123–134 (2011)
20. Rexus/Bexus - Rocket and Balloon Experiments for University Students. http://www.rexusbexus.net. Cited 12 Apr 2018
21. Sarkar, R.: Ph.D. Thesis, Kolkata (India) (2010b)
22. Sarkar, R., Chakrabarti, S.K.: ExA **28**, 61–77 (2010a)
23. Sarkar, R., Mandal, S., Debnath, D., et al.: ExA **29**, 85–107 (2011)
24. Sarkar, R., Chakrabarti, S.K., Pal, P.S., Bhowmick, D., Bhattacharyya, A.: AdSpRes **60**, 991–998 (2017)
25. Sarkar R., Chakrabarti, S.K., Bhowmick, D.: (2018, under preparation)
26. Singh, K.P., Tandon, S.N., Agrawal, P.C. et al.: ASTROSAT mission. Proc. SPIE **9144**, 15 (2014)
27. Underwood, C.I.: Annual AIAA/Utah State University Conference on Small Satellites, vol. 2, p. 18 (1990)

# Science with Small Telescopes




**Shyam Sarkar, Ashim Sarkar, and Pabitra Sil**

**Abstract** Indian Centre for Space Physics was founded by Prof. S.K. Chakrabarti about 20 years ago to have a space research facility in Eastern India. It has recently installed a 0.61 m telescope for observational Astronomy. This is added to already existing 0.25 m telescope. They are located at the Ionospheric and Earthquake Research centre and Otical Observatories (IERCOO) about 80 km from Kolkata. Various tests are being made to check the capabilities of the telescopes and the backend instruments. We present the test results of this new facility in terms of imaging and spectrometry by giving explicit examples of our study of the passage of the Asteroid 3200 Phaethon, the spectra of the Sun and Mizar system. We also give an example of our efforts to discover exoplanets as we scan unknown fields of stars.

## 1 Introduction

With a goal to generate manpower for mega projects such as Thirty Meter Telescope (TMT) on the horizon, it has become necessary to create manpower in Indian context at the grassroot level. To this extent, a 0.61 m reflector from Plane Wave Instruments (CDK-24) was added less than 6 months ago to the observatory of Indian Centre for Space Physics. This observatory is located at Sitapur (lat=22.511N, long=87.786E), a remote area of the State of West Bengal about 80 km away from Kolkata where the sky condition is acceptable. In this review, we discuss the present preliminary observations made during the winter period (December 2017 to January 2018). After the present monsoon period it would be fully operational. Apart from this, the

S. Sarkar (✉) · A. Sarkar · P. Sil
IERCOO, Indian Centre for Space Physics, Kolkata, India

© Springer International Publishing AG, part of Springer Nature 2018

B. Mukhopadhyay, S. Sasmal (eds.), *Exploring the Universe: From Near Space to Extra-Galactic*, Astrophysics and Space Science Proceedings 53,
https://doi.org/10.1007/978-3-319-94607-8_30

existing 0.25 m Meade reflector (SN10) was upgraded with a new mount (MyT). The 0.25 and 0.61 m telescopes were named by Prof. S.K. Chakrabarti as Arundhati and Vasistha respectively which are the Sanskrit names for Alcor and Mizar in Ursa major constellation (Saptarshi mandal or an 'Assembly of seven sages' in Sanskrit). Arundhati and Vasistha happen to be the most revered couple and sages described in Vedas in early Indian scriptures.

Major science which can be carried out by such telescopes would be very limited. However, for observations in survey mode or those requiring long follow ups such instruments are ideal. Thus the studies of variabilities, Gamma Ray bursts, exo-planet search etc., would be possible. Below, we present the system description and the peripheral instruments in this observatory. The observatory is known as the 'Ionospheric and Earthquake Research Centre and Optical Observatory' or IERCOO, in short.

## 2 Instrument Description

The main Telescope at IERCOO is Vasistha (CDK 24). Its optical design is of Corrected Dall-Kirkham type and is put on a German Equatorial mount. Diameter is 24 in (0.61 m) and the focal ratio and focal length are F/6.5 and 3.962 m respectively. Its limiting visual magnitude is 16.4. The plate scale is 52.055 arcsec/mm and the theoretical resolving power is 0.248 arcsec.

The smaller telescope at IERCOO is Arundhati (Meade SN10). Its optical design is of Schmidt-Newtonian type and is put on a German Equatorial mount. Diameter is 10 in (0.254 m) and the focal ratio and focal length are F/4 and 1.016 m respectively. Its limiting visual magnitude is 14.5. The plate scale is 203 arcsec/mm and the theoretical resolving power is 0.6 arcsec.

A major instrument of this facility is a spectrometer (LHIRES III): The grating element is 2400 grooves/mm. Its slit width is fixed at 25 μm. The highest resolving power is 0.4 Å. Resolution around $H_\alpha$ line is 16,000.

The observatory has three CCD cameras: (a) ATIK 314l+ for guiding in the spectrometer; (b) ATIK 460EX: for acquisition for spectrum by the LHIRES-III spectrometer and (c) SBIG - STF 1603M having 1.5k × 1k pixels and appropriate filters. In Fig. 1a, b we show the telescopes and the spectrometer mounted at the back of Vasistha with both ATIK cameras.

Apart from these we have an weather station which gives us in situ data as well as predictions based on such data.

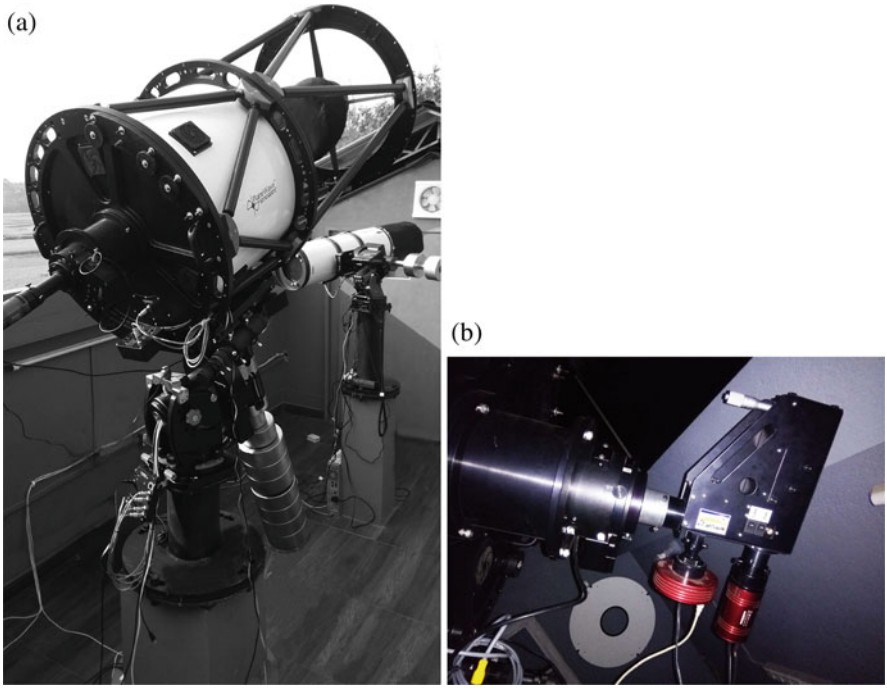



**Fig. 1** (**a**, Left) The Vasistha (nearer) and Arundhati (farther) telescopes at the Observatory with a roll-off roof. (**b**, Right) The mounting of the spectrometer with two CCD cameras at the back of Vasistha

## 3 Observations of 3200 Phaethon

3200 Phaethon is a potentially hazardous asteroid which is known to be the parent body of Geminid Meteor shower. Its distance with the earth was only 0.07 AU on December 15th, 2017. We observed the asteroid using both the telescopes and taken photographs at regular intervals. Vasistha observed this from 14th December, 2018 till 21st December, 2017. Arundhati observed this from 13th December, 2017 to 18th December, 2017. We used the astrometry software to obtain the RA/DEC of the asteroid and also obtained the magnitudes using IRAF. We saw some evidences of variation of apparent magnitude due to its rotation at ∼3.6 h. Figure 2 shows the 10 s exposure image of the asteroid showing how the appearance changes on a daily basis.

Figure 3a, b show the comparison of (Left) RA and (Right) DEC of 3200 Phaethon with that predicted by IAU's Minor planet center on 4th of December, 2017. Vasistha was used in this case.

In Fig. 4a, b, we show daily (IST) variation of the V-magnitude variation of 3200 Phaethon using (Left) Arundhati and (Right) Vasistha. We clearly note that the object became brightest at around 14.7th December, 2017 (IST). On 20th December,

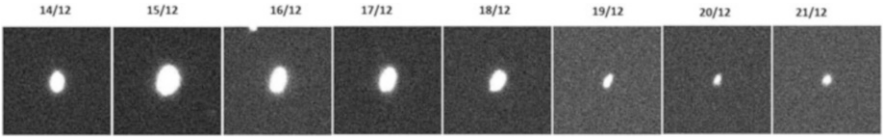



**Fig. 2** Images of the asteroid 3200 Phaethon taken by ATIK 460EX using Vasistha (0.61 m) telescope. It became brightest on 15th (IST) and then faded away. 10 s exposure makes the object look elongated

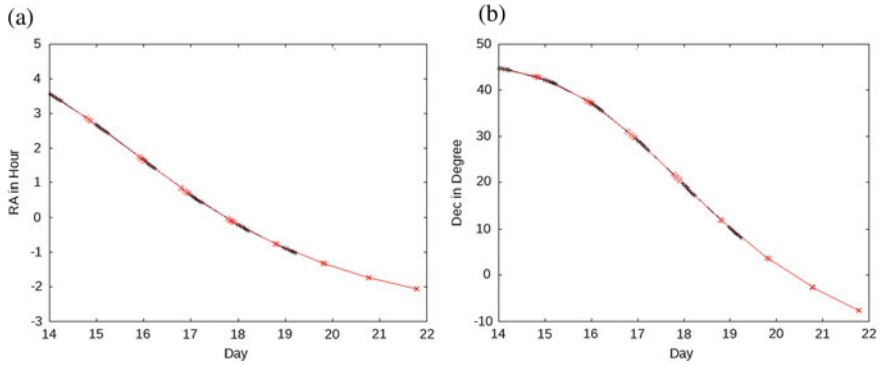



**Fig. 3** Observed (marked with 'x') (**a**, Left) RA and (**b**, Right) DEC of 3200 Phaethon compared with the RA/DEC (marked with '+') as predicted by IAU minor planet Centre based on 4th December, 2017 data. All times are in Indian Standard Time (IST=UT+5:30)

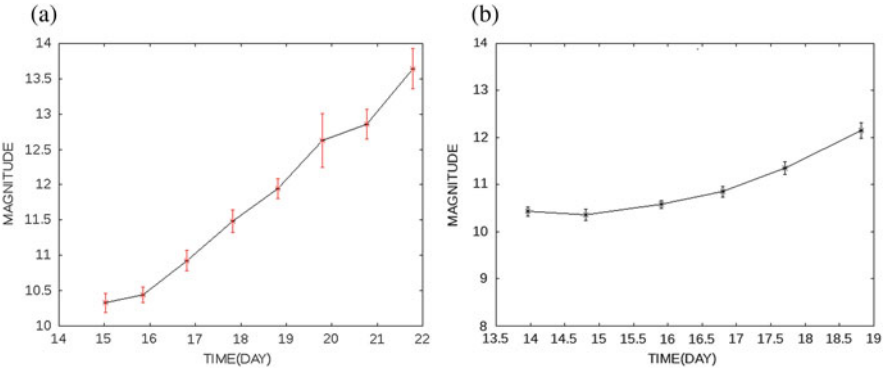



**Fig. 4** Daily variation of V-magnitude of 3200 Phaethon by (**a**, Left) Vasistha and (**b**, Right) Arundhati. See, text for details

2017, the sky condition was not good, giving rise to a large error. We did not use any V-filter. However, we used the V-magnitude of the standard star in the field to obtain the results.

It is known that 3200 Phaethon has rotational period of about 3.6 h [3]. Figure 5 shows our result using Arundhati on the variation of V-magnitude on

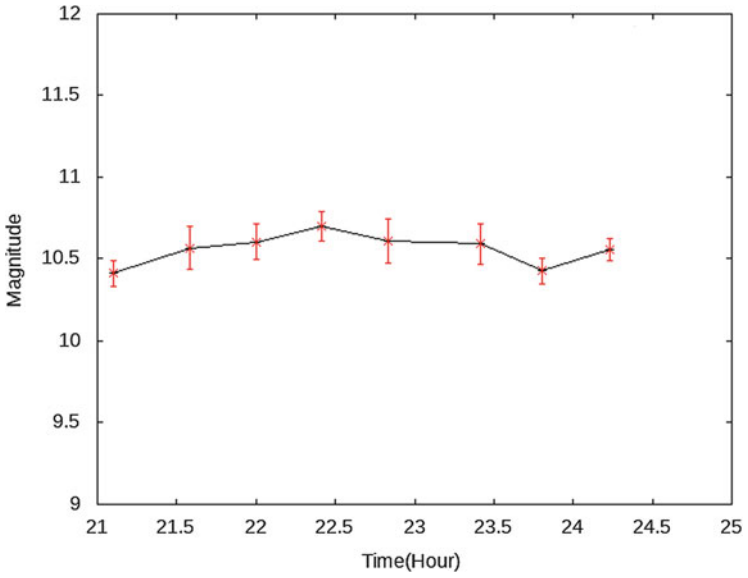



**Fig. 5** Variation of V-magnitude of 3200 Phaethon on 15th December, 2017. Time (IST) is along the X-axis. Arundhati telescope was used for this measurement

15th December, 2017. Variation in about 3 h scale could be seen. Our data is to be analysed in detail and more accurate result would be reported.

## 4 Solar and Stellar Spectrum

First test of LHIRES-III spectrometer was made by pointing at the Sun directly and identifying the known lines. An example of the capability of the image by ATIK 460EX is shown in Fig. 6. In the top part we show the spectrum with several Fraunhofer lines and also the Telluric O-bands. Splitting of lines in the O-band can also be seen.

As a test case, we pointed the spectrometer attached to Vasistha to the Mizar system. Both the ATIK CCDs were used for guiding and spectrometry. We align the slit with three stars namely: Mizar (GSC 3850:1385), Mizar (GSC 3850:1386), and a new suspected variable NSV6224 in between them. In Fig. 7, we show the spectrum as taken by ATIK 460EX as well as the calibrated results as obtained by IRAF.

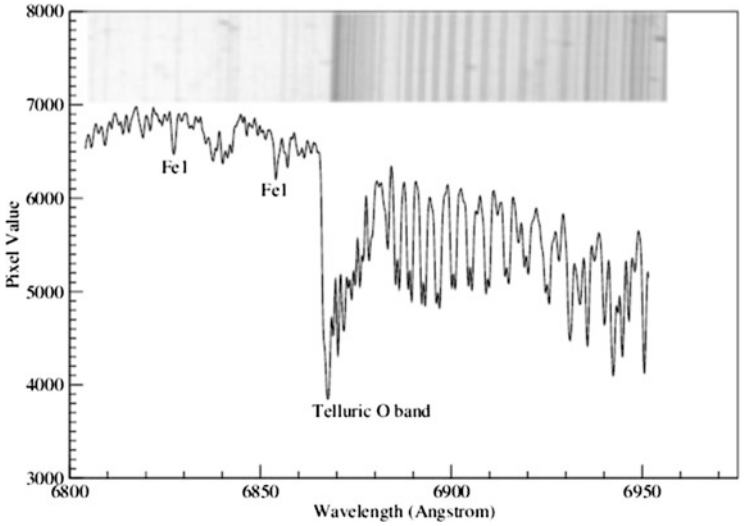



**Fig. 6** Direct spectrum of the sun taken by ATIK 460EX showing its capability. We notice several Fraunhofer lines, some of which are identified here, as well as the Telluric O-band lines

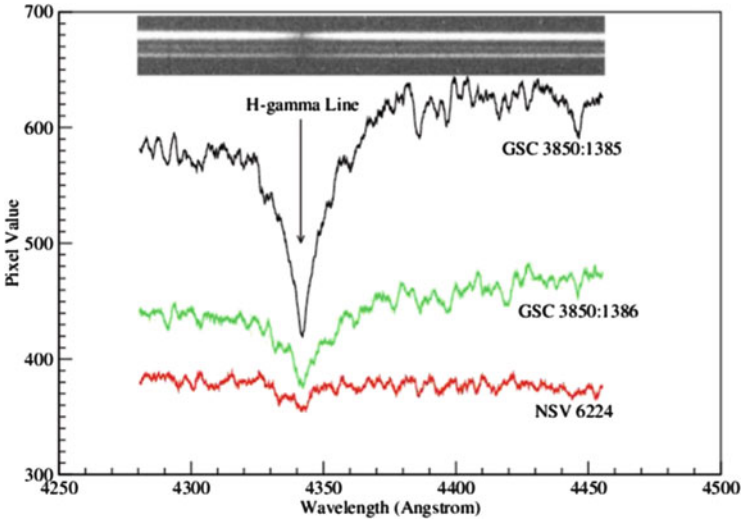



**Fig. 7** Spectrum of the Mizar system GSC 3850:1385, GSC 3850:1386 taken using Vasistha with the 25 µm slit aligned such that both the components of Mizar as well as a new suspected variable NSV6224 object is seen (marked). Note very faint spectrum in between the brighter Mizars in the photograph of the spectra

## 5 Search for Exo-planets

Exoplanets could be detected by several methods, such as transit photometry [2], Doppler spectroscopy (e.g. [4]), Gravitational microlensing [1] etc. At IERCOO, we have started to scan the sky to detect planets by the transit method. Two examples of the sky surveyed around HIP 31064 and GSC 1910:460 by Aurndhati and Vasistha are presented here. In Fig. 9a, b we show the relative fluxes of the stars shown in Fig. 8(a, b). Similar variabilities due to atmospheric and sky conditions could be seen for all the stars. Though we do not see any obvious candidate here, we will follow a similar procedure to scan the sky in future.

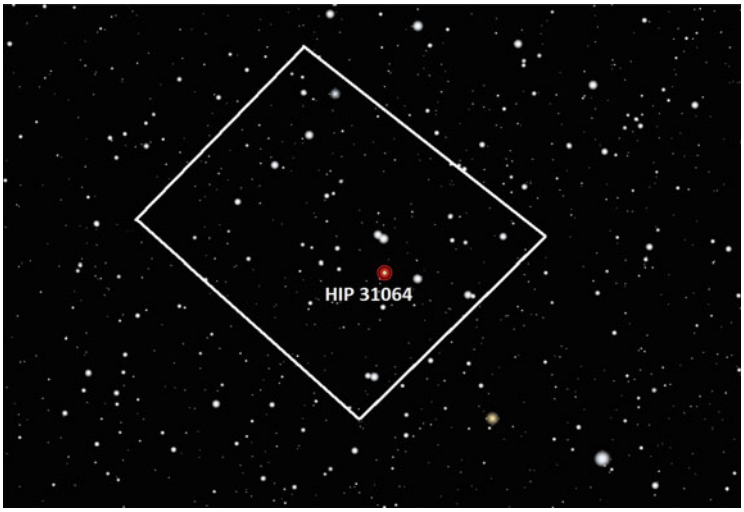



**Fig. 8** Starfield around (**a**, left) HIP 31064 scanned by Arundhati and (**b**, right) GSC 1910:460 scanned by Vasistha are marked by the box

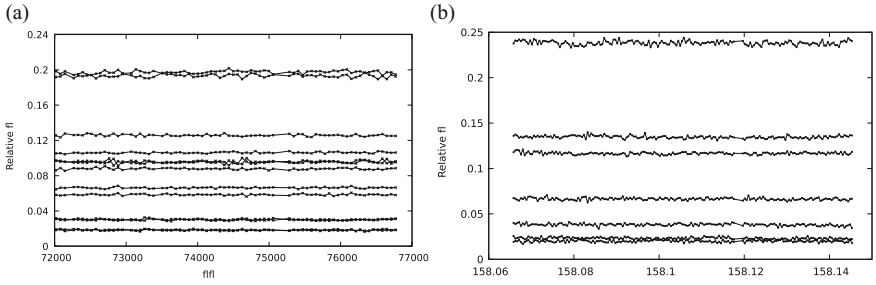



**Fig. 9** Two examples of processed light curves of several stars as taken by (**a**, left) Arundhati and (**b**, right) Vasistha. For Arundhati relative fluxes in arbitrary scale are plotted against time, given in IST on 21st January, 2018. For Vasistha, relative fluxes are plotted against Julian Day-2458000 (see text for details)

## 6 Concluding Remarks

The new facility of Indian Centre for Space Physics is expected to yield rich science in the field of variable stars, including variabilities due to exo-planets, dwarfs in binary systems, GRBs etc. Using the superb spectrometer we are able to probe the winds and outflows in star forming regions and also in compact systems.

**Acknowledgements** We are indebted to our Supervisor Prof. Sandip K. Chakrabarti for creating this telescope facility which is unique in eastern India. We acknowledge the engineering support from Mr. Debashis Bhowmick, logistic supports from Dr. Sudipta Sasmal and scientific support from Mr. Rana Khan and Mr. Soujan Ghosh. We thank Dr. S. Mondal, Dr. R.K. Das and Mr. S. Datta of SNBNCBS for helping us with initial supports in imaging software. PS and AS are supported by UGC NET Fellowship and SS is supported by CSIR NET Fellowship.

## References

1. Bond, I.A.: Astrophys. J. Lett. **606**, L155 (2004)
2. Henry, G.W., Marcy, G.W., Buter, R.P., Vogt, S.S.: Astrophys. J. **529**, L41 (2000)
3. Schmidt, R.E.: MPBu **45**, 131S (2018)
4. Wright, J.T., Gaudi, B.S.: In: Oswalt, T.D., French, L.M., Kalas, P. (eds.) Planets, Stars and Steller System, p. 489. Springer, Dordrecht (2013)

# A Classic Problem in Newtonian Dynamics: How Thick Are Saturn's Rings?




**Abhijit Bhattacharyya**

**Abstract** Saturn's ring system shows variation in opacity and spectral properties. Although water ice comprises the bulk of the Saturn's ring system, non-icy materials also play crucial role to understand the origin of the rings. Particles inside a planetary ring are subject to forcing due to the central planet, moons in the inclined orbits, self-gravity of the ring and other forces resulting from the radiation drag, collisional effects and the Lorentz force arising from the magnetic field of the planet. Study of the ring system got boost after gathering data from the Voyager flyby, the Cassini mission etc. Our study mainly composed of understanding of the C ring and the A ring. It was found that considerable amount of shear gets developed in the vertical direction even within the ring itself and the dissipation it causes can damp excitations due to moons within a couple of hundreds of kilometres. The study stressed mainly on the damping property of vertical bending waves.

## 1 Introduction

The physics of planetary ring system is interesting for its classical dynamic and evolving nature. In 1644, René Descartes introduced the idea that the whole space in the Universe is filled with vortices of invisible matter and there is no space left without vortex. Therefore, earth has a vortex extending to and including the Moon. Deducing from the Descartesian model, Huygens concluded [16] that Saturn must be surrounded with a ring system. In 1675, J.D. Cassini observed that the ring system was divided by a dark band which was later named as *Cassini's gap*. In 1785, Laplace showed that a solid ring, in uniform rotation, would break apart under the action due to centrifugal forces and the system would probably have to consist of a large number of independent "ringlets" [17]. In 1847, Roche determined

A. Bhattacharyya (✉)
PH-SFT Group (EP), CERN, Geneva, Switzerland

Nuclear Physics Division, Bhabha Atomic Research Centre, Mumbai, India

© Springer International Publishing AG, part of Springer Nature 2018

B. Mukhopadhyay, S. Sasmal (eds.), *Exploring the Universe: From Near Space to Extra-Galactic*, Astrophysics and Space Science Proceedings 53,
https://doi.org/10.1007/978-3-319-94607-8_31

that within a certain limit termed as *Roche Limit* from the planet [20], any satellite and presumably also any ring would be torn apart by the tidal forces. Saturn's ring system lie within that Roche limit [10].

In 1848, C ring was discovered. In 1857, Maxwell conjectured that Saturn's ring system could only consist of an indefinite number of very small particles [1]. The theory also conjectures that the stability of the system also requires countless independently orbiting satellites. In 1866, Kirkwood initially suggested resonant perturbations by Jupiter caused the radial gaps and clumps in the asteroid belts. In 1867, he extended the theory to the Cassini division and in 1871, it was extended to the *Encke's gap*.

Saturn's ring is divided into $A$, $B$, $C$, $D$, $E$, $F$ and $G$ rings containing particles of varying sizes from sub-micron to meter range. Forces acting on these particles are, namely, gravitational forces due to planet itself, the centrifugal force due to rotation in the orbit, the gravitational forcing due to satellites, Lorentz force due to planetary magnetic field and developed charge in the planetary magnetosphere on the micron and sub-micron sized particles [3], radiation loss as Poynting-Robertson drag, aerodynamic drag, self gravity of the disk and implicit collisional force.

Improved ground-based observations gradually revealed structural and orbital details, like topologically flat but spread out structures, optical transmission through the rings, structural variations with radius, different reflectivity depending on the wavelength and observed geometry. The concept of ring system changed with the availability of swarms of data transmitted by spacecrafts like Voyager, Pioneer, Ulysses, Cassini [15, 21, 24]. Satellite data points out some important features like subdivisions of rings into ringlets, existence of spokes, characteristic features of particle size spectrum and spiral waves like density and bending waves in the ring plane.

This article discusses modelling of particle dynamics to understand spiral bending wave in Saturn's A and C rings. The study was performed with both particle and fluid approach. The particle approach provides information on local ring properties viscosity of the ring and thickness while the fluid approach provides us information like surface mass density.

## 2 The Physics of Collective Effects

The variety and richness of features in the structure and dynamics of Saturn's rings manifesting the collective effects associated with the self gravity of the particulate disk have long fascinated astronomers [14, 19] since pre-Voyager era. In spherical systems with dissipation or inelastic collision, the high thermal velocity of particles decrease through friction or shock leading to the formation of the disk. Theoretical calculation on the disk modelling [4, 6, 7, 11, 12, 18, 22], usually consider thin disk approximation which signifies that the ratio of disk height '$h$' to its distance '$R$' from the central gravitating object like planet should be much smaller than unity i.e. $h/R \ll 1$. This approximation, in general, holds true for all galactic,

circum-stellar and circum-planetary rings. Physically this approximation means that the disk behaves as a "cold" disk and pressure gradient is comparatively much smaller than two main dynamic forces, viz. the gravitational and the centrifugal forces. Also the condition $h/R \ll 1$ limits the characteristic length scale $L$ of spatially regular structures as $L : h \leq L \leq R$. Hence, the smaller the ratio $h/R$, the more characteristic scales can be fitted into the range for $h$ and $R$ helping the structures formed in the astrophysical disk system to be much richer.

The astrophysical disk system becomes more interesting due to the presence of differential rotation [13] within the disk itself that causes different angular velocity due to different angular distance producing shear resulting in deformation. The ring system has viscosity which in conjunction of rotational shear of the disk is a constant energy source within the disk that transfers energy from this large-scale shear flow. This means the orbital energy of the particles is transferred into heat which is manifested as random motion of particles. The effect of viscosity means effect of collision among particles.

In combined presence of viscosity and differential rotation, a viscous stress is developed that leads to an outward transfer of angular momentum and a general radial spreading of the ring. The efficiency of transfer of angular momentum is determined by the kinematic viscosity $\nu$ which, in general, could be expressed as $\nu = \omega_c \lambda^2$. The timescale for spreading of particles in the radial direction is

$$t_v \simeq \frac{1+\tau^2}{\omega_c} \Omega^2 \left(\frac{\Delta r}{c}\right)^2, \tag{1}$$

where, $c$ is the velocity of dispersion, $\omega_c$ is collisional frequency, $\Omega$ is orbital frequency, $\Delta r$ is the radial spread and optical depth $\tau$.

Rings $A$, $B$ and $C$ contain far more material than the peripheral $D$, $E$, $F$ and $G$ rings as measured in terms of the optical depth as

$$\tau\,(\lambda) = \int\int n\,(r,\,z)\,Q_e\,(r,\,\lambda)\,\pi r^2 dr dz, \tag{2}$$

where, $z$ is the direction perpendicular to the rings, $n(r,\,z)$ is the number density per radial increment ($\mathrm{cm}^{-4}$) of particles of radius $r$ and $Q_e(r,\,\lambda)$ is the extinction efficiency of particles at wavelength $\lambda$.

If we consider two neighbouring particles having nearly circular orbits separated by a radial mean free path, the difference between their pre-collisional circular velocities is of the order $\lambda\Omega$. After collision, they will each acquire an orbital eccentricity of the order of $\lambda/c = c/\Omega a$. The energy change per unit mass associated with this gain in the eccentricity is of the order of $(\lambda/a)^2 = \lambda^2\Omega^2$. The rate of change of kinetic energy per unit mass associated with eccentric motion is $\dot{E}_t \simeq c^2\omega_c \simeq \lambda^2\Omega^2\omega_c$. In a differentially rotating disk, this viscous stress continually converts energy from that stored in the systematic shearing motion into

that associated with random motion at rate per unit mass as

$$\dot{E}_t = \nu \left( r \frac{\partial \Omega}{\partial r} \right)^2 , \tag{3}$$

which is of the order $\nu \Omega^2$ for the Keplerian orbits. In the absence of any dissipative process, particles would be "heated up" in the sense that the dispersion velocity would increase indefinitely. Typical collisions between particles within the ring are partially inelastic, resulting in the dependence of the coefficient of restitution of the matter of the ring particles. Also, it is natural to see that ring system would disperse after a long time while in reality rings have distinct boundaries. Shepherd's satellites, which are small satellites orbiting within the rings play the role of driver to drive the particles in the ring.

One of the most important features in the Saturn's ring due to satellite forcing is the formation of the density and bending waves. Density waves are spiral patterns of enhancement and depletion of ring materials, formed by particles coerced into coherently nested eccentric orbits. In-plane periodic forcing due to satellites at resonant locations in the rings can excite density waves. Bending waves are vertical corrugations of the disk, formed by the particles in coherently nested inclined orbits. Satellites in inclined orbits supply the necessary resonant vertical perturbations to ring particles to excite bending waves.

Let us consider a free particle orbiting in a circular orbit of radius $r$ with angular speed $\Omega(r)$ in the equatorial plane $z = 0$ of an axisymmetric planet with an associated potential $\phi_p(r, z)$. At the equatorial plane, centrifugal equilibrium is obtained from,

$$r\Omega^2 (r) = \left. \frac{\partial \phi_p}{\partial r} \right|_{z=0} , \tag{4}$$

where, $\Omega(r) = \left[ GM_p / r^3 \right]^{1/2}$, $M_p$ being the mass of the planet, $G$ being the universal Gravitation constant. If this test particle is displaced by an arbitrary small amount, it will freely oscillate in horizontal and vertical directions about the reference circular orbit with epicyclic frequency $\kappa(r)$ and vertical frequency $\mu(r)$ by Lindblad's theory [9]. The epicyclic $\kappa(r)$ and vertical $\mu(r)$ frequencies are given as

$$\kappa^2(r) = \frac{1}{r^3} \frac{d}{dr} \left( r^4 \Omega^2 \right) , \tag{5}$$

$$\mu^2(r) = \left. \left( \frac{\partial^2 \phi_p}{\partial z^2} \right) \right|_{z=0} , \tag{6}$$

such that

$$\mu^2(r) + \kappa^2(r) = 2\Omega^2(r). \tag{7}$$

If a satellite of mass $M$ orbits Saturn with a small eccentricity $e_M$ in a plane inclined by a small angle $i_M$ with respect to the planetary equator ($z = 0$), the contribution to the gravitational potential is

$$\Phi_M(r,\ \phi,\ z, t) = \\ -GM\left[r_M^2(t) + r^2 - 2r_M r\cos(\phi_M(t) - \phi) + (z_M(t) - z)^2\right]^{-1/2}, \tag{8}$$

where, suffix $M$ corresponds to the moon or satellite and terms without any suffix are for the test particle in the ring. If $a_M$ is the moon orbital radius, $\Omega_M$ is the Keplerian local velocity of the moon, parameters like $r_M(t) - a_M$, $\Theta_M(t) = \phi_m(t) - \Omega_M t$, $z_M(t)$ are small quantities and periodic in nature. To a sufficient degree of approximation, $r_M(t)$ and $\Theta_M(t)$ have periods $2\pi/\kappa_M$ and $z_m(t)$ has period of $2\pi/\mu_m$. Since $\Phi_m(r,\ \phi,\ z,\ t)$ is periodic in time $t$ and azimuthal angle $\phi$, its Fourier decomposition yield the nature of gravitation field due to forcing by moon as

$$F_M = \Re\left[\Phi_M(r,\ z)\exp\left(i\ (\omega t - m\phi)\right)\right], \tag{9}$$

where, the disturbing frequency $\omega$ due to forcing due to the moon being linear combination of integral multiples of the circular, vertical and epicyclic frequencies as perceived from the inertial frame is

$$\omega = m\Omega_M \pm n\mu_M \pm p\kappa_M, \tag{10}$$

so that $m$, $n$ and $p$ are non-negative integers. It was shown in [13] that most important horizontal force terms arise from $n = p = 0$, while the largest vertical force arise from the condition $n = 1$ and $p = 0$. In general, $n$ is 0 or even and $p$ is odd for horizontal forcing whereas $n$ is odd and $p = 0$ or even for the vertical forcing [23]. The forcing amplitude due to moon associated with disturbance frequency $\omega$ is proportional to $e_M^{|p|}\sin^{|n|} i_M$ [13, 23]. The test particle will undergo *horizontal* (Lindblad) resonance at $r = r_L$ [18] satisfying

$$\omega - m\Omega\ (r_L) = \pm\kappa\ (r_L), \tag{11}$$

while it will undergo vertical (inclination) if its radial position at $r = r_V$ satisfies

$$\omega - m\Omega(r_V) = \pm\mu(r_V), \tag{12}$$

where negative and positive sign refers to inner and outer resonances.

Larger satellites exist exterior to the main ring system and hence $\Omega_M < \Omega$ so that the inner resonances are important than outer ones. The satellite forcing associated with the resonances characterized by a ratio of integers which contain a difference $N$ between the numerator and denominator is proportional to a product of $(N-1)$ factors of small quantities, $e_M$ and $\sin i_M$. Thus the strongest inner horizontal resonances correspond to the ratio $m{:}m-1$, involving only the circular part of the satellite motion while the strongest inner vertical resonances correspond to the ratio $m+1{:}m-1$ involving one factor of the inclination of the satellite orbit. For example, the disturbance frequencies associated with 5:3 inner horizontal and vertical resonances of Mimas are given by

$$\omega_{horiz} = 4\Omega_M + \kappa_M, \tag{13}$$

$$\text{and, } \omega_{vert} = 4\Omega_M + \mu_M. \tag{14}$$

if $\Omega$, $\mu$ and $\kappa$ were all equal, $r_L$ would equal $r_V$ at a value $r$ where $\Omega(r)/\Omega_M = 5/3$. However, the degeneracy $r_V = r_L$ is split for $\mu > \Omega > \kappa$ due to the oblateness of Saturn.

Figure 1 suggests inner vertical and Lindblad resonances and the effect of oblateness on resonances. However, our work was mainly done on the Spiral bending wave and let us discuss the topic on the spiral bending wave in the next sections.

## 3 Spiral Bending Waves

Shu [22, 23] analysed the spiral bending wave as long density waves where Shu analysed the bending waves as a whole as observed from a stationary laboratory frame. However, it may also be interesting to carry out the analysis of motion of each particle within the warped ring since it may give us more detailed feature.

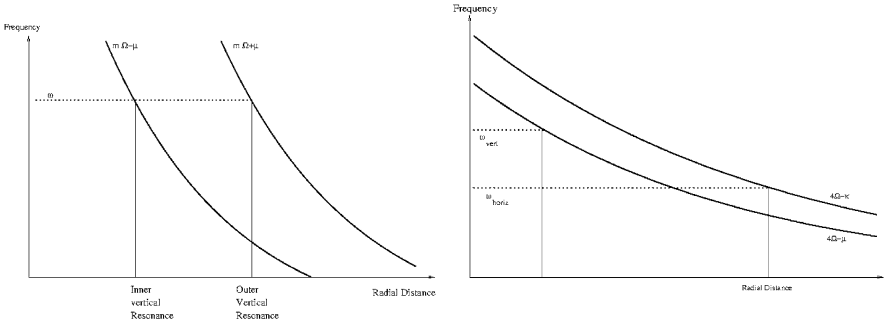



**Fig. 1** The first schematic shows that the oblateness of Saturn results in different radial locations for 5:3 inner vertical and 5:3 Lindblad resonance of Mimas. The second schematic shows that trailing spiral bending wave of frequency $\omega$ and angular mode $m$

Chakrabarti [6, 7] worked on the analysis of equation of motion of a single particle in the warped self-gravitating ring of finite thickness. The approach describes the equation of motion of test particle as seen from the frame placed atop the warped ring.

Figure 2 illustrates the mechanism of the bending wave. Let us consider a right handed Cartesian coordinate system $(X, Y, Z)$ at a radial distance $r$ from the center of the planet depicting the $X$ axis pointing radially outwards, $Y$ axis pointing to the azimuthal direction and the $Z$ axis pointing vertically upwards normal to the planetary equatorial plane. The frame is rotating around the planet with local Keplerian velocity $\Omega(r)$. Let the amplitude of the vertical oscillation be $\epsilon$ and a particle of mass $m$ is situated at $(x,\ y,\ z)$ in the $XYZ$ frame and at $(x',\ y',\ z')$ in $X'Y'Z'$ frame. Let $O'(x^*,\ y^*,\ z^*)$ be the origin of reference frame placed at the mid-plane of the ring. The difference between the phase of the particle and the phase of the propagating wave may be determined as

$$\phi - \phi^* = k_x\left(x - x^*\right) + k_y\left(y - y^*\right) = k_x x_1 + k_y y_1 = z_1 \epsilon \kappa^2 \sin\phi^*, \quad (15)$$

$$\text{where, } \phi = k_x x + k_y y - \omega t, \quad (16)$$

$$\text{and } \phi^* = k_x x^* + k_y y^* - \omega t. \quad (17)$$

The local gravitational acceleration ignoring the non-circular motion components can be written as $sg_z = g_P + g_M + g_D$. For $|z| \ll r$, the term $g_P = -\Omega^2 z$ is behaving as restoring force due to linear harmonic oscillator. Considering the contribution from planetary and satellite forcing, the vertical component of the equation of motion is

$$\ddot{z} = -\Omega^2 z + A\cos\left(k_x x + k_y y - \omega t\right), \quad (18)$$

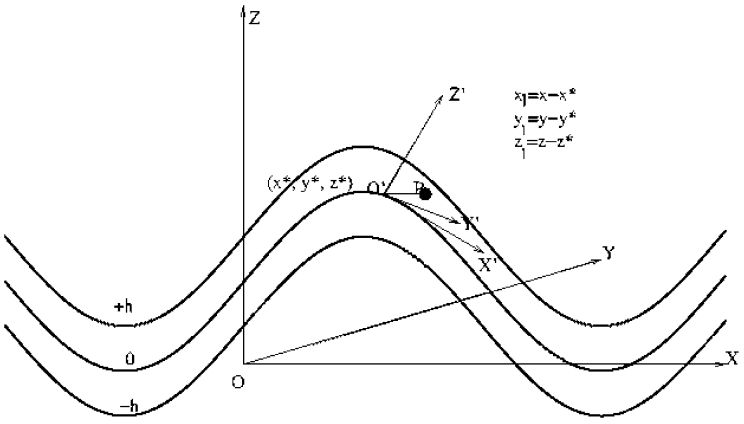



**Fig. 2** Geometry of spiral bending wave showing rotating of the frame of reference which oscillates vertically with frequency $\omega$

whose solution can be written as

$$z = -\frac{A}{\left(\Omega^2 - \omega^2\right)} \cos\left(k_x x + k_y y - \omega t\right). \tag{19}$$

For the perturbation due to the satellite forcing, we follow the prescription by Shu [22] to determine principal Fourier component of the un-damped disk using WKBJ formalism with $A(X) = A_0 \exp(\left[i \int k_x dx\right]$ as $A_0 = \epsilon\left(\Omega^2 - \omega^2\right)$. Therefore, the forcing component due to the satellite forcing is

$$z_{sat} = \epsilon\left(\Omega^2 - \omega^2\right) \cos\left(k_x x + k_y y - \omega t\right). \tag{20}$$

Therefore, the equation of motion of the test particle [4–8] can be determined as,

$$\ddot{x} = -2\Omega\dot{y} + 3\Omega^2 x - \nu^2 x_1 - \frac{\left(\Omega^2 - \omega^2\right)\epsilon^2 k_x \cos\phi \sin\phi^*}{\left(1 + \epsilon^2\kappa^2 \sin^2\phi^*\right)^{1/2}}, \tag{21}$$

$$\ddot{y} = 2\Omega\dot{x} - \nu^2 y_1 - \frac{\left(\Omega^2 - \omega^2\right)\epsilon^2 k_y \cos\phi \sin\phi^*}{\left(1 + \epsilon^2\kappa^2 \sin^2\phi^*\right)^{1/2}}, \tag{22}$$

$$\ddot{z} = -\Omega^2 z - \nu^2 z_1 + \frac{\left(\Omega^2 - \omega^2\right)\epsilon \cos\phi}{\left(1 + \epsilon^2\kappa^2 \sin^2\phi^*\right)^{1/2}}, \tag{23}$$

where, $\dot{\phi^*} = -\omega$.

It is assumed that the self-gravity of the disk on a particle is due to a flat disk of constant density $\rho$ so that the frequency of the vertical oscillations of a particle due to self-gravity would be

$$\nu^2 = 4\pi G\rho. \tag{24}$$

Equations (21)–(23) has been studied both analytically [2] and numerically [2, 4, 5, 8]. The solutions have been used to calculate the energy density of the spiral bending wave as

$$E_w = \frac{1}{2}\epsilon^2\Omega^2, \tag{25}$$

so that the rate of dissipation of energy density is

$$\dot{E_w} = \nu_k \left(\frac{\partial < v_x >}{\partial z_1}\right)^2, \tag{26}$$

where, the kinematic viscosity $\nu_k$ can be approximated as

$$\nu_k = \Omega \tau \max\left(R^2,\ R_{epi}^2\right), \tag{27}$$

where, $R$ is the size of the largest particle and $R_{epi}$ is the amplitude of the epicyclic motion which approximates as the half thickness of the disk $h$. The dispersion of the wave follows the group velocity

$$c_g = -\frac{\pi G\rho}{\omega - m\Omega}, \tag{28}$$

which yields the damping length of the spiral bending wave [2, 4, 5] as

$$\lambda_D = \frac{E_w}{\dot{E}_w} c_g. \tag{29}$$

The fluid dynamics approach to study the bending wave uses WKBJ approximation for the thin disk approximation which is valid for $R \gg h$ so that the vertical dynamics for a small vertical displacement $\xi(r,\ \phi,\ z,\ t)$ is given by

$$\left[\frac{\partial}{\partial t} + \Omega(r)\frac{\partial}{\partial \phi}\right]^2 \xi(r,\ \phi,\ z,\ t) = g_z, \tag{30}$$

where, $g_z$ is the local vertical force per unit mass which is the summation of all forces as $g_z = g_P + g_s + g_d + g_l + g_{rad} + \ldots$ so that $g_P$ is contribution due to planet, $g_s$ is due to satellite forcing, $g_d$ is due to self-gravity, $g_l$ is due to Lorentz force, $g_{rad}$ is due to radiation force etc. Since our work was related to the $A$ and $C$ ring of the Saturn, due to the larger size of particle, we considered only gravitation component due to planet and satellite and the self-gravity of the disk neglecting others which are considerable for micron and sub-micron sized particles like Saturn's $E$ and $F$ ring. Whenever, a particle is pulled above the normal ring plane by the force due to a satellite, the particle feels gravitational attraction from the portion of the whole disk which this particle can see from the top. Hence the test particle will feel a smooth surface density profile due to the whole disk and not a localised surface mass density. The density distribution corresponding to the pure bending of the disk is

$$\rho_d\,(r,\ \phi,\ z,\ t) = \sigma\,(r,\ \phi,\ t)\,\delta\,(z - \xi\,(r,\ \phi,\ z = 0,\ t))\,, \tag{31}$$

where the surface mass density is given by,

$$\sigma\,(r,\,\phi,\,t) = \Sigma(r)\exp\left[i\,(\omega t - m\phi)\right], \tag{32}$$

so that $\Sigma(r)$ is unperturbed disk surface density and $\delta(x)$ is Dirac Delta function. Following Shu [18], the ring was modelled as infinitesimally thin so that the gravitational potential due to the disk could be modelled as

$$\Phi_d\,(r,\,\phi,\,z,\,t) = \phi_d\,(r,\,z)\exp\left[i\,(\omega t - m\phi)\right], \tag{33}$$

which can lead us to write the Poisson's equation as

$$\nabla^2\phi_d(r,\,z) = 4\pi G\Sigma(r)\delta(z - \xi(r,\,t)), \tag{34}$$

so that the surface mass density at the ring mid-plane can be determined as

$$\Sigma(r) = \frac{1}{4\pi G}\left[\frac{\partial}{\partial z}\phi_d(r,\,z)\right]_{z=0^-}^{z=0^+}. \tag{35}$$

Solving Eq. (34), one may retrieve the dispersion equation for the spiral bending wave considering planetary and satellite forcing beside the self gravity of the disk itself as

$$D = -2\pi G\Sigma(r)s_k\,|\kappa(r)| = \mu^2 - \left[\omega - m\Omega(r)\right]^2, \tag{36}$$

where, $s_k = sgn(k(r))$ indicating the leading or trailing pattern of the spiral bending wave. The dispersion relation from Eq. (36) provides the group velocity as

$$c_g = -\frac{\partial\omega}{\partial\kappa} = -\frac{\pi G\Sigma(r)s_k}{(\omega - m\Omega(r))}. \tag{37}$$

To extrapolate the theory of infinitesimally thin disk for the disk of finite half-thickness $h$, a set of infinitesimal thin disk was considered in stack at a distance $z_i$ from the midplane $z = 0$.

## 4 Mimas 5:3 Resonance: A Ring

The 5:3 vertical resonance for Mimas is observed in the "A" ring. The perturbation frequency as observed from the rotating frame of ring is about $\omega = n - 4\Omega(r)$ which is exactly equal to $\Omega(r_v)$ at the vertical resonance [7]. Since the bending wave is launched inwards with the peak slope situated at around 100 km inside the resonance radius, the Keplerian frequency $\Omega(r)$ at the position of our interest $(r)$ is higher than $\Omega(r_v)$. The bending wave is damped within 150 km of launching.

Computation suggested that the average shear would be about $7 \times 10^{-5}\,\mathrm{s}^{-1}$ for half height $h$ about 10 m and about $5.0 \times 10^{-5}\,\mathrm{s}^{-1}$ for $h = 20$ m. The energy density of the wave $1/(2\epsilon^2\Omega^2)$ appears to be about 85 ergs $\mathrm{g}^{-1}$ which is transferred to the particles through infrequent collisions. This indicates an average kinematic viscosity $\nu_k \approx \Omega\tau h^2$ for $h = 10$ m would be around $64\,\mathrm{cm}^2\,\mathrm{s}^{-1}$ which gets dispersed with group velocity $c_g$ of about $0.026\,\mathrm{cm\,s}^{-1}$. The computed damping length ($\lambda_d$) suggested that observed length of bending wave of about 150 m could be achieved for total thickness for the A-ring turns out to be about 15 m (Fig. 3).

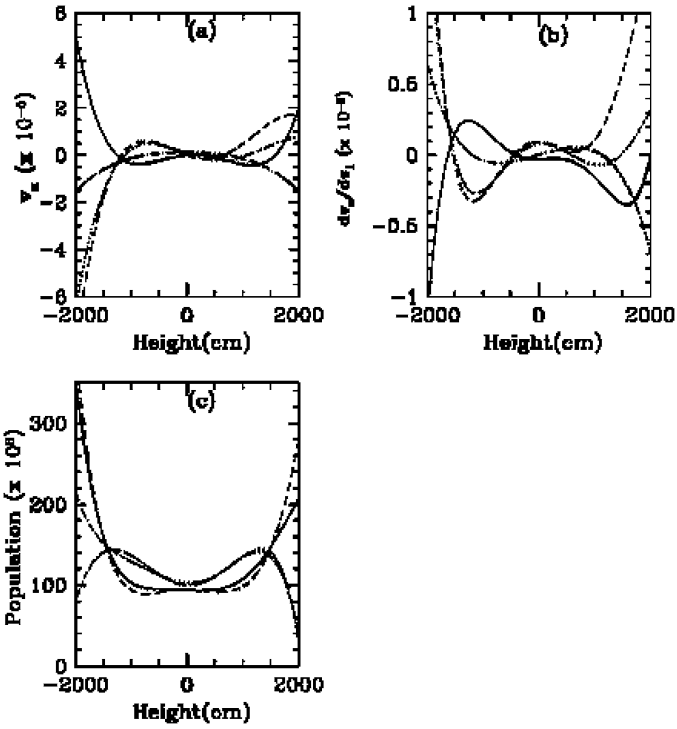



**Fig. 3** Numerical studies of particle behaviour near −1:0 resonance of Titan showing variation of (a) $x$ component of velocity $V_x$, (b) shear $dv_x/dz_1$ and the population of matter inside bending wave in C-ring. The solid, dotted, dashed and dot-dashed curves are drawn for wave phases $\phi^* = 0, \pi/2, \pi$ and $3\pi/2$ respectively [7, 8]

## 5 Titan −1:0 Resonance: C Ring

If a moon orbits the planet at a same rate as that of the nodal regression of the ring matter, a nodal bending wave is formed with a one-armed spiral. In case of Titan −1:0 resonance, the wave propagates outwards in C ring. Average optical depth variation at the location of this resonance clearly showed "W" pattern in the Voyager data those were interpreted as multiple passage of light through the ring bent out of the equatorial plane. Voyager data depicted that radio occultation data showed 28 oscillating waves those start at the inner vertical resonance (IVR) $r_v = 77{,}515 \pm 13$ km and die out at around 77,609 km. Near $r = r_v$, at constant local surface mass density ($\sigma$ gm/cm$^2$) rings, wave have wavelength of about

$$\lambda(r) = \frac{209\sigma}{(r - r_v)} \text{ km}, \tag{38}$$

taking $r$ and $r_v$ in kilometres while the amplitude of the bending wave is given as

$$|A_v| = \frac{334}{\sigma^{1/2}} \text{m}. \tag{39}$$

The linear theory of viscous damping would suggest the kinematic viscosity as

$$\nu = 4.76 \times 10^5 \left(\frac{\sigma}{\lambda_D}\right)^3 \text{ cm}^2/\text{s}. \tag{40}$$

Fitting of the "W" shaped feature as mentioned, suggested [21] $\sigma = 4.5$ g/cm$^2$ which indicated the value of the amplitude as 10 times larger than that suggested by Eq. (39). The wavelength obtained from Eq. (38) at $r - r_v = 20$ km is about 47 km. Using a more realistic value of $\sigma = 0.45$ gm/cm$^2$ Fig. 4 indicates an amplitude of 500 m. However, the wavelength obtained at a distance of 20 km from the IVR becomes around 4.7 km which does not match with observational data. Fitting of data [21] suggested that the surface mass density varies form $\sigma = 0.86 \pm 0.05$ gm/cm$^2$ near IVR to $\sigma = 0.39 \pm 0.02$ gm/cm$^2$. Using a damping length of about $\lambda_D \geq 50$ km, $\nu \sim 0.4$ gm/cm$^2$, the ring scale height turned out to be less than 2.6 m.

The analysis mentioned in [21] raised the following questions, such as: (a) is the amplitude of the wave at the launching site be around 1600 or 500 m? (b) Is the surface mass density 0.45 or 4.5 gm/cm$^2$? (c) Could the height of the ring be as small as 2.6 m?

We analysed numerically [4, 8] and theoretically [5] and discovered that complete dissipation of the bending wave at 85 km from the place of launching for the strongest component of shear as $dv_x/dz_1$. The ring half height determined in [2, 5] as 2.5 m as maximum value while the surface mass density ranges as 0.2–0.5 gm/cm$^2$. This means the C-ring total height appears to be about 5 m.

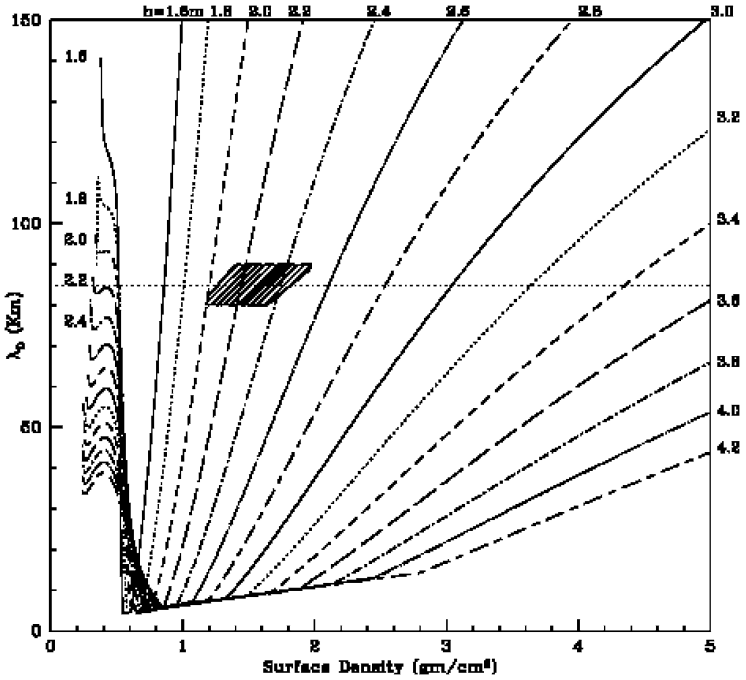



**Fig. 4** Variation of the damping length ($\lambda_D$) as a function of surface mass density. The shaded box indicates the prescribed parameter zone for the C-ring as obtained from the model [2, 5]

Cassini data suggested vertical thickness of the C-ring would be approximated as 5 m which is comparable to the analytical and theoretical data.

## 6 Conclusion

The physics of spiral bending wave in the Saturn's C-ring has been studied using Pre-Voyager and Voyager data. Using Newtonian mechanics, analytical equation of dynamics of the particles were solved analytically and numerically. The physical aspects considered are planetary and satellite gravitational force beside the self-gravity of the warped ring. A parameter space has been computed for estimation of surface mass density so that the bending wavelength could be computed to tally with the data. The kinematic viscosity computed using these parameters provided estimated ring height.

## References


1. Alexander, A.F.Ó.D.: The Planet Saturn: A History of Observation, Theory and Discovery. Faber and Faber, London (1962)
2. Bhattacharyya, A.: Doctor of Philosophy (Science). Thesis, Jadavpur University (2001)
3. Bhattacharyya, A., Basu, A.M.: Indian J. Phys. B **73**, 6 (1999)
4. Bhattacharyya, A., Chakrabarti, S.: 32nd Lunar and Planetary Science Conference, 1046 (2001)
5. Bhattacharyya, A., Chakrabarti, S.: Mon. Not. R. Astron. Soc. **357**, 156–164 (2005)
6. Chakrabarti, S.: J. Astrophys. **9**, 243 (1988)
7. Chakrabarti, S.: Mon. Not. R. Astron. Soc. **238**, 1381–1394 (1989)
8. Chakrabarti, S., Bhattacharyya, A.: Mon. Not. R. Astron. Soc. **326**, L23–L26 (2001)
9. Chandrasekhar, S.: Principles of Stellar Dynamics. University of Chicago Press, Chicago (1942)
10. Darwin, G.H.: Saturn's Rings. Harpers New Mon. Mag. **79**, 66–76 (1889)
11. Franklin, F.A., Colombo, G.: Icarus **12**, 338–347 (1970)
12. Franklin, F.A., Colombo, G.: Icarus **15**, 80–92 (1971)
13. Goldreich, P., Tremaine, S.: Icarus **34**, 227–239 (1978)
14. Goldreich, P., Tremaine, S.: Annu. Rev. Astron. Astrophys. **20**, 249–283 (1982)
15. Hedman, H.H., et al.: Icarus **223**, 105–130 (2013)
16. Huygens, C.: Systema Saturnium, sive de causis mirandorum Saturni phaenomenon, et comite ejus planeta novo. Adrian Vlacq, The Hague (1659)
17. Laplace, P.S., de Marquis: Mechanique Celeste, vol. III, p. 512. Hillard, Gray, Little, and Wilkins Publishers, Boston (1802)
18. Lin, C.C., Shu, F.H.: Astrophys. J. **140**, 646 (1964)
19. Pollack, J.B.: The rings of Saturn. Space Sci. Rev. **18**, 3–93 (1975)
20. Roche, R.A.: Akad. des Sciences et letters de Montpelier. Mem de la Section des Sciences **1**, 243–262 (1847)
21. Rosen, P.A., Lissauer, J.J.: Science **241**, 690–694 (1988)
22. Shu, F.H.: In: Brahic, A., Greenberg, R. (eds.) Planetary Rings. University of Arizona, Tucson (1984)
23. Shu, F.H., Cuzzi, J.N., Lissauer, J.J.: Icarus **53**, 185–206 (1983)
24. Zhang, Z., et al.: Icarus **281**, 297–321 (2017)

# From Test and Evaluation Till Onboard Performance of Indian Payloads: RT-2 Onboard CORONAS-PHOTON and LAXPC Onboard AstroSat




**Tilak Katoch**

**Abstract** I will briefly discuss my thesis work under guidance of Prof. Sandip Kumar Chakrabarti and the follow-up works I have been doing at TIFR. This includes my personal scientific involvements in development of an Indo-Russian collaborative satellite named CORONAS-PHOTON mission (RT-2 Experiment) and the Indian first multi-wavelength observatory named AstroSat mission (LAXPC), to study energetic phenomena of the Universe. I am presenting work done during the test and evaluation and calibration of each instrument before they were flown off to space. It includes discussion over the onboard performance, health parameters of the instruments and calibration of them, during Preliminary Verification (PV) phase. Finally, we present the analysis of some data received from these instruments such as flares, GRBs, etc.

## 1 Introduction

Solar flares are some of the most powerful energy bursts produced at the solar surface. This happens due to catastrophic merger of highly entangled magnetic fields beneath the surface near the active region. These explosions have energy of $\sim 10^{26}$–$10^{32}$ ergs within a very short interval of time ($\sim$10–$10^3$ s) and can achieve a height of $\sim 10^5$ km. The flares cover almost the entire electromagnetic spectrum from radio, visible, extreme ultraviolet, X-rays, Gamma-rays and particle emission. There are various models of solar flares [7, 11, 17], the flares are always associated with magnetic field. Due to instability the coronal loops expand, it opens up momentarily and expels plasmas. The solar spectrum is a thermal bremsstrahlung component coming from the hot plasma and a power law component coming from the non-thermal charged particle.

T. Katoch (✉)
Tata Institute of Fundamental Research, Colaba, Mumbai, India
e-mail: tilak@tifr.res.in

© Springer International Publishing AG, part of Springer Nature 2018

B. Mukhopadhyay, S. Sasmal (eds.), *Exploring the Universe: From Near Space to Extra-Galactic*, Astrophysics and Space Science Proceedings 53,
https://doi.org/10.1007/978-3-319-94607-8_32

## 1.1 The CORONAS-PHOTON Mission

The Complex Orbital Observations Near-Earth of Activity of the Sun (CORONAS-PHOTON) was a Russian solar-terrestrial science mission and was the second satellite of Russian Natalya series. The aim was to study the Solar radiation in the Extreme UV (EUV) up to high-energy gamma-ray radiation (Fig. 1). This mission had collaborators from Russia, India, Poland and Ukraine, where the Moscow Engineering Physics Institute (MEPhI, State University, PI: Yuri D. Kotov) was responsible for the mission payloads and NIIEM (Scientific-Research Electromechanic Institute), Istra, Moscow for the spacecraft.

The CORONAS-PHOTON satellite was launched from the Plestsk Cosmodrome, Russia, on January 30, 2009 over a Tsyklon-3 (Cyclone-3) vehicle, at the beginning of 24th Solar cycle. The satellite had a circular orbital period of 95 min having altitude equal to 550 km with an inclination angle of 82.5°. It had a mass of 1900 kg designed for a life of 5 years with data transmission link as a S-band with a rate of 62.5 or 125 kbit/s. It had three axis stabilizer systems with the Sun pointing accuracy of 0.1° continuously, having the angular drift of 0.0005°/s. A two solar panel employed for optimum power generation of 2 kW along with a GPS navigation (GLONASS receiver) to provide the orbit determination and timing services.

The scientific instruments onboard the CORONAS-PHOTON Satellite were: Natalya-2M (High energy radiation spectrometer), Penguin-M (Hard X-ray polarimeter), Konus-RF (X-ray and gamma-ray spectrometer), BRM (Fast X-ray monitor), PHOKA (Multi-channel ultraviolet monitor), TESIS (Telescope-spectrometer for imaging solar spectroscopy in X-rays), Electron-M-PESCA

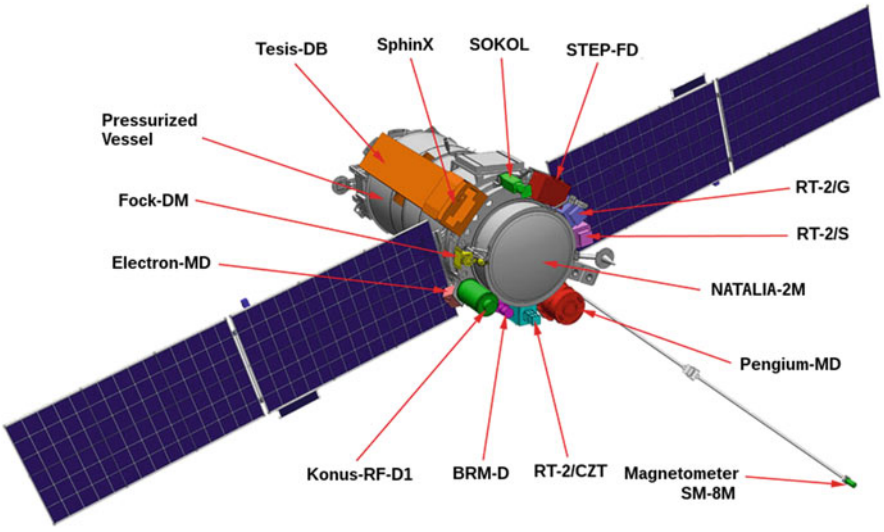



**Fig. 1** CORONAS-PHOTON satellite (directory.eoportal.org)

(Charged particle analyzer), STEP-F (Satellite telescope of electrons and protons) and RT-2 (Röntgen Telescope-2).

## *1.2 The AstroSat Mission*

The AstroSat mission is India's first multi-wavelength space observatory fully committed to astronomical studies (Fig. 2). It was launched on 28 September 2015 with five major astronomy payloads [1, 18] comprised of the Large Area X-ray Proportional Counter (LAXPC), Ultra Violet Imaging Telescope (UVIT), Soft X-ray Telescope (SXT), Cadmium Zinc Telluride Imager (CZTI) and Scanning Sky Monitor (SSM). The four major instruments (UVIT, SXT, LAXPC and CZTI) of Astrosat are co-aligned to point the same source for simultaneous observations. These multi-wavelength instruments have the capability to observe the object in the wide energy band ranging from Visible (320–550 nm) bands to FUV (130–180 nm) of UVIT, 0.3–8 keV of SXT, 3.0–80 keV of LAXPC and 20–100 keV of CZTI, whereas SSM to monitor the variability of known and new cosmic X-ray sources in 2–10 keV. The uniqueness of Astrosat lies in studying a cosmic source simultaneously in several spectral regions and their emission processes and correlation among them. It was launched from the Satish Dhawan Space Centre over PSLV-XL vehicle into a near-Earth equatorial orbit of 98 min with an inclination angle of 6°. It had a mass of 1513 kg designed for a life period of 5 years having the storage capacity of 420 Gigabits data per day.

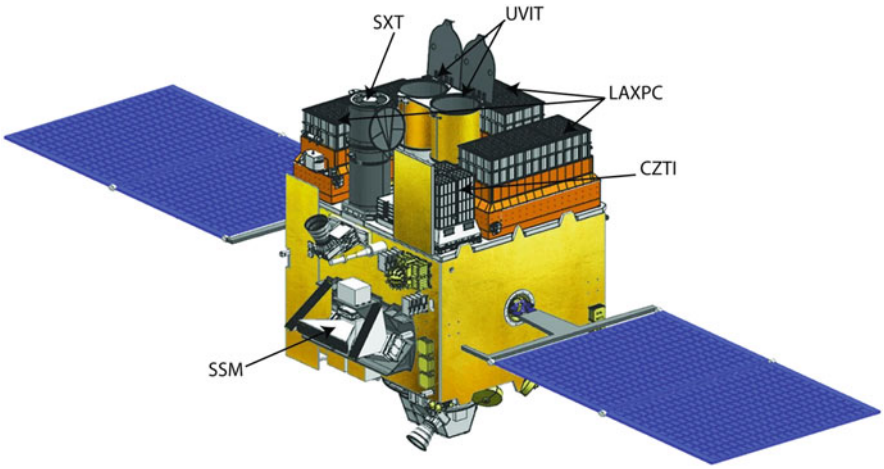



**Fig. 2** AstroSat satellite (https://phys.org/news)

## 2 RT-2 Experiment

An Indian payload Röntgen Telescope-2 (RT-2) Experiment, which consists of three scientific payloads, namely, RT-2/S, RT-2/G, RT-2/CZT and one processing electronic unit (RT-2/E) were built in India through a collaboration between the Tata Institute of Fundamental Research (TIFR), Mumbai and Indian Centre for Space Physics (ICSP), Kolkata with expert supports from Vikram Sarabhai Space Centre (VSSC), Trivandrum (PI: Prof. A.R. Rao and CO-PI: Prof. Sandip K. Chakrabarti).

The RT-2/S and RT-2/G were identical detectors made up of NaI(Tl) and CsI(Na) scintillation crystals in phoswich combination. Both have the same diameter (116 mm) but different thickness [6]. The RT-2/G detector had an Aluminum window as a filter to block low energy X-rays (<20 keV) and operational energy range from 25 to 150 keV to study solar flares up to class X (flux up to 20,000 counts/s) whereas RT-2/S had a detection energy range from 15 to 150 keV to study flares up to class M. A Field of View (FOV) for RT-2/S were $4^\circ \times 4^\circ$ and $6^\circ \times 6^\circ$ for RT-2/G. The effective area of these instruments were 100 $cm^2$ with an energy resolution of $< 25\%$ at 60 keV. In these crystals, NaI(Tl) detect lower energy range of 15–100 keV and CsI(Na) higher energies from 30 to 1000 keV along with detection capability of the charge particle background. These payloads were capable of detecting radiation in the higher energy limit extended up to 1 MeV.

The RT-2/CZT payload was a hard X-ray imaging instrument having two different types of a next generation solid state imaging detector, namely CZT (Cadmium Zinc Telluride) detector and CMOS (Complimentary Metal Oxide Semiconductor) detector [8]. These detectors were arranged in a configuration of $2 \times 2$ array having three CZT detectors and one CMOS detector employed with two different types of coders, a Coded Aperture Mask (CAM) and Fresnel Zone Plate (FZP), with a viewing angle ranging from $6'$ to $6^\circ$ [9, 10]. These coders cast the shadow of solar flares over the detector plane. It was the only imaging device onboard the CORONAS-PHOTON satellite to image solar flares in the hard X-rays region ranging 20–150 keV. This next generation CZT detector had a very good energy resolution (8% for 60 keV) and an excellent detection efficiency ($\sim$100%) up to 100 keV. The CMOS detector employed in the RT-2/CZT had an arc sec imaging capacity suitable for bright flares (brighter than 20 keV flux of $> 10^3$ photons $cm^{-2}\, s^{-1}\, keV^{-1}$) occurring roughly about once in 6 months during solar maximum. It is useful for hard X-ray imaging in the energy range of 20–150 keV. Each CZT detector consists of 256 individual pixels of size $2.5 \times 2.5$ mm and CMOS had a $512 \times 1024$ pixels of size $50 \times 50\,\mu m$.

The main scientific payloads were co-aligned with the Sun pointing axis and kept outside hermetically sealed vessel of the satellite. Figure 3 shows the RT-2 Experiment payloads of Flight model delivered to the Russian counterpart.

RT-2/E [19] was a main processing electronic unit of the RT-2 experiment which provides the interface between the satellite and detectors was placed inside the sealed vessel of the satellite. The RT-2 instruments had a time resolution of 100 ms in order to achieve faster spectral and image studies of solar hard X-ray flares.



**Fig. 3** Flight Model RT-2/S and G and Flight Model RT-2/CZT (www.csp.res.in)

The RT-2 payloads had two different modes of operation—Normal mode and Event mode. In Normal mode, where all the spectral data is accumulated and eight channel count rates are stored every 10 ms, whereas in Event mode, every event is time-tagged and correct to 0.3 ms and sent to RT-2/E in every second. Finally, Normal mode data were processed in RT-2/E and the best time resolution possible is 1 s for full spectrum.

## *2.1 Test and Evaluation of RT-2*

All the scientific payloads go through the extensive space qualification test on the ground in order to perform in space at the expected level and to sustain in the space environmental conditions. The RT-2 experiment each flight payload were independent space qualified on the basis of their performance at different environmental conditions: Thermal and Vacuum test, Vibration test, EMI (Electro-Magnetic Interference) test and Standard Room Condition (SRC) test. During these conditions, the payload performance was verified such as the High Voltage (HV) and Lower/Upper Level Discriminator (LLD/ULD) operation, stability of Pulse shape (PS) and Pulse height (PH), health parameters, quality of spectral (scientific) data etc.

During these laboratory tests, complete functioning of RT-2/S, RT-2/G and RT-2/CZT payloads were investigated and we calibrated HV, LLD, PS and PH variation with temperature, energy spectra, etc. For calibration, we used three radioactive sources: $^{241}$Am (with 59.5 keV), $^{109}$Cd (with 22.0 and 88.0 keV) and $^{57}$Co (with 122.0 keV).

The scintillator detectors have a medium energy resolution of about 18% at 60 keV. The measured NaI energy resolution is around 17.54% ± 0.55 and 17.68% ± 0.27 at 59.5 keV for the RT-2/S and RT-2/G instruments, respectively (Fig. 4a, b).

Three CZT modules and one CMOS detector were selected for the RT-2/CZT payload based on satisfactory performance during the space qualification tests and results obtained. To find the energy resolution at different temperatures, each of the CZT modules were exposed to a multiple radioactive sources to evaluate their spectrum and images. One such multiple source spectrum of 1024 channels and image of 256 pixels of CZT-1 modules at 10 °C is shown in Fig. 5a, b.

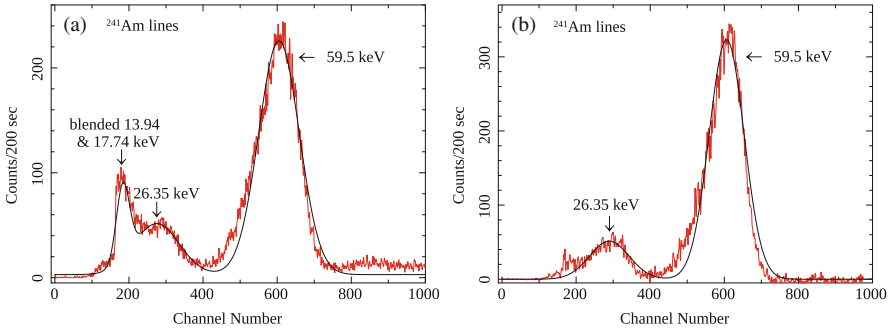



**Fig. 4** Flight Model RT-2/S and G: NaI spectrum obtained using a $^{241}$Am source [6]

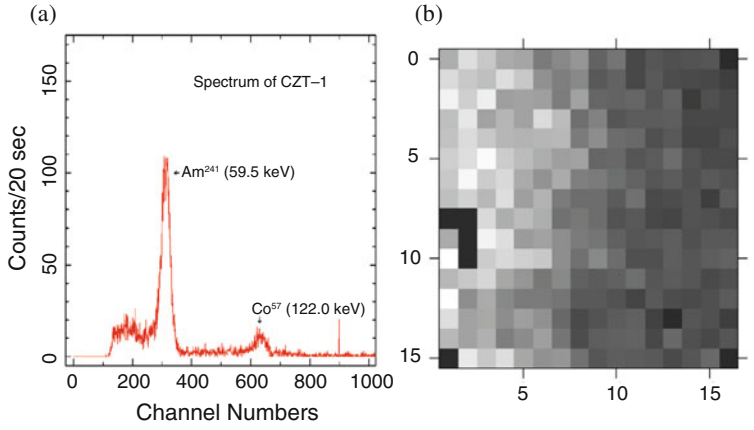



**Fig. 5** Spectrum and image of CZT-1 module of RT-2/CZT flight payload irradiated with radioactive source $^{241}$Am and $^{109}$Cd. Spectrum contains sum counts of all the 256 pixels of detector module [8]

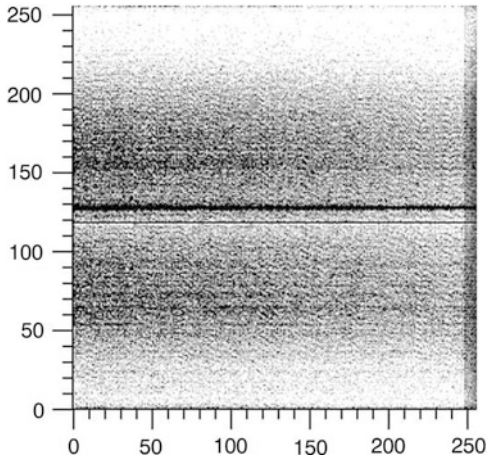



**Fig. 6** One bit background image (noise) as detected by CMOS [8]

The CMOS detector successfully cleared all the tests of space qualification process which were used for the CZT detector modules. We plot the one bit background image (noise) as detected by the CMOS detector as no significant change was found in the performance (Fig. 6). The horizontal bar shown in the image is the CMOS inherent reference line.

## *2.2 Onboard Performance*

RT-2 experiment onboard CORONAS-PHOTON mission was powered on during orbit No. 304 on 19th February 2009. Before switching ON, the temperatures of the payloads were monitored and maintained at around 16°C for RT-2/S and RT-2/G and −15°C for RT-2/CZT. The RT-2/S and RT-2/G payloads operational aspect were identical in comparison to complex operation of the RT-2/CZT payload. Onboard calibration of these detectors were carried out using the mounted calibration source $^{57}$Co (122 keV). It was observed that calibration source peak were stable throughout the period of all the detectors. A typical onboard background spectra observed by the Phoswich detectors of RT-2/S and G are shown in Fig. 7. Due to calibration source $^{57}$Co, the peak around 58 keV in background spectra is $^{121}$I decay peak of NaI crystal.

Similarly, the background spectrum and image of CZT-2 module of RT-2/CZT payload are shown in Fig. 8. The calibration source peak at 122 keV is clearly detected by the CZT-2 module with energy resolution around 5.6% @122 keV, whereas the other two CZT modules also detected the calibration source peak at around 127 keV and 124 keV with energy resolution 7.32% and 5.97% respectively. It was observed that the energy spectrum of all 3 CZT modules were background noise dominated below 40 keV.

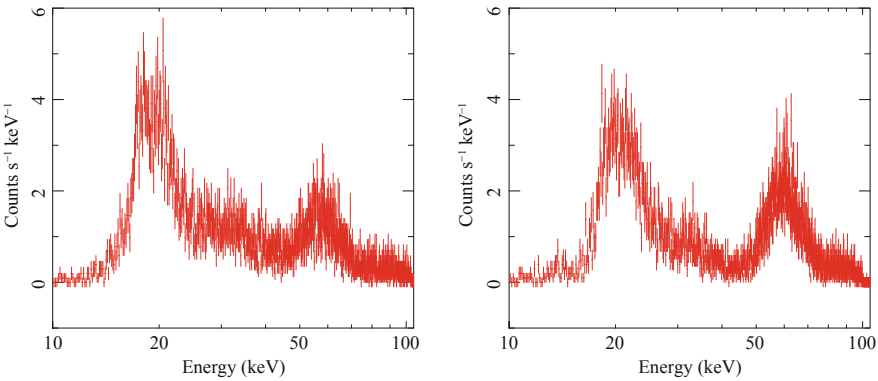



**Fig. 7** Flight Model RT-2/S and G background spectrum as observed from the satellite [6]

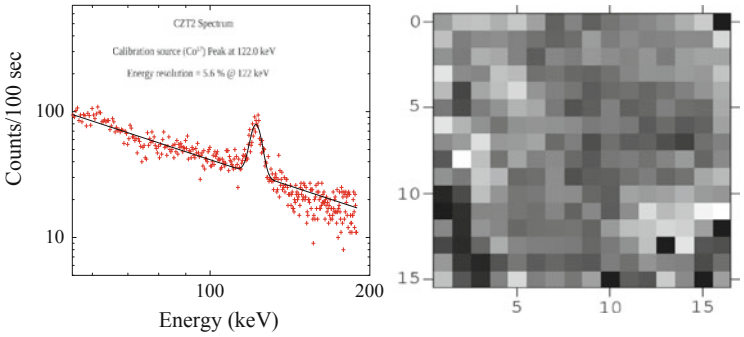



**Fig. 8** Background spectrum and image of CZT-2 module with data acquired for 100 s [9]

To find the threshold of CMOS background, it was calibration onboard during SHADOW mode (away from the Sun) at the different threshold values. At each threshold value, we have calculated the total number of events recorded by the CMOS pixels as a function of different satellite locations which are correlated to the total charge particle environment. Finally, it was set in operation at value 4F20. Figure 9 shows the onboard background images of CMOS detector during SHADOW mode for higher threshold value 4F20 having the reduced number of bright pixels to 154.

## *2.3 Observation*

The RT-2 instruments started a systematic collection of data from May 2009 onwards till December 2009. As unfortunate satellite power failure happened after which all the instruments could not function. During these 6 months of operations we were able to observe several solar flares and a few GRBs. A systematic analysis

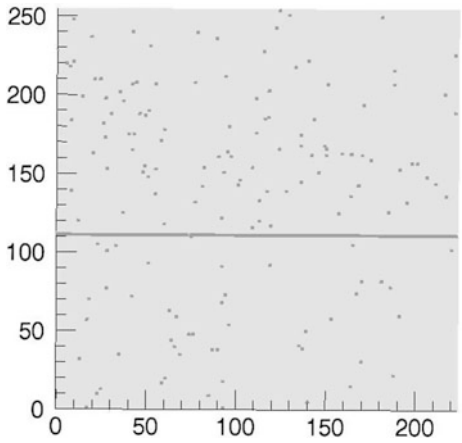



**Fig. 9** CMOS background image in shadow mode—4F20 [15]

of these solar flares detected by RT-2 payloads conducted during the period. The RHESSI satellite detected around 27 flares with counts recorded above 12 keV, whereas the RT-2 detectors RT-2/S and RT-2/G detected 29 and 7 flares respectively. Beside all these, RT2 Phoswich detectors had accounted huge data of X-ray background as it was viewing the X-ray sky during SHADOW mode (away from the Sun).

On 5 July 2009, a solar flare of the class C2.7 which occurred near the center of disk (S27W12) in NOAA 11024 peaked at 07:12 UT was detected by RT-2/S and RT-2/G is shown in Fig. 10. The impulsive nature of this flare was confirmed by X-ray light curve as observed from RT-2, GOES and RHESSI (Reuven Ramaty High Energy Solar Spectroscopic Imager). During the rising phase of the flare, a clear oscillating feature was noticed which in detail study reveal the evidence for Quasi-Periodic Pulsations (QPPs) at the periods of ∼12 s and ∼15 s [13]. The spectral fit was quite steep by a bremsstrahlung model with temperature kT of $3.43 \pm 0.30$ keV and found to be agreeing with RHESSI spectrum of this flare.

Due to the large viewing angle and the capability to act as an omni-directional detector [16] in the high energy range (>100 keV), the RT-2/S and G detectors have been able to detect at least 5 GRBs (in the energy band of 15–1000 keV), which were mostly incident on the detectors at a large off-axis angle. These were: GRB 090618, GRB 090719, GRB 090820, GRB 090926A, and GRB 090929A [3–5, 12]. Figure 11 represents the light curves in different energy bands of a very strong GRB 090618 detected by the RT-2/G detector when the satellite was in the SHADOW mode (in fact, the first event detected by RT-2). Both RT-2/S and G Phoswich detectors have registered the strong multi-peaked emission from this GRB during SHADOW (away from the Sun) and GOOD time (away from SAA and polar regions). It was triggered at T0 = 08:28:27 UT and lasted for almost 150 s. The burst profile with the emission peaks at T0 + 65 s, T0 + 85 s and at T0 + 115 s in the energy band of 59–215 keV, was fitted with the FRED function [14]. The spectrum was well fitted with the standard GRB Band model with peak energy at about 164 keV and integrated fluence of $2.8 \times 10^{-4}$ erg cm$^{-2}$ in the energy range of 20 keV to 1 MeV.

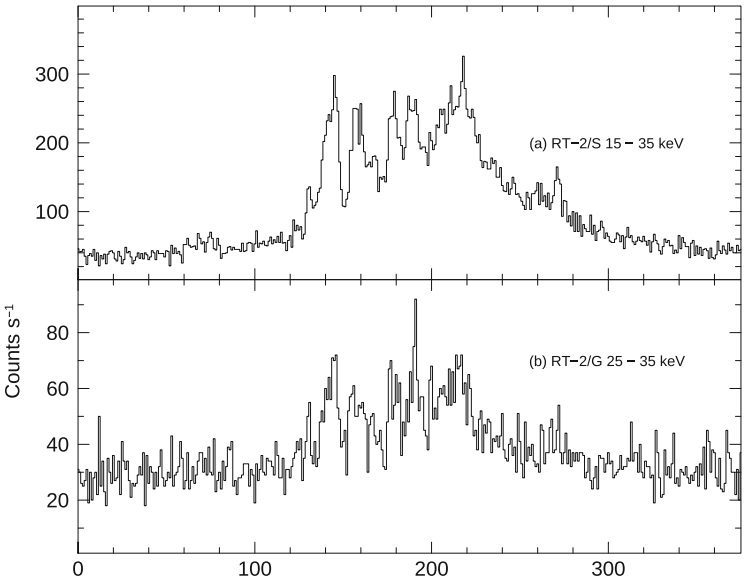



**Fig. 10** Light curve of 2009 July 5 solar flare. T0 = UT 07:08:50 [15]

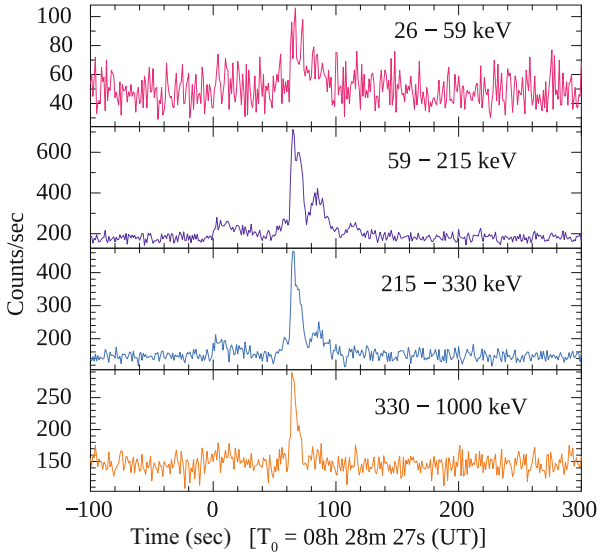



**Fig. 11** Light curve of GRB 090618, as observed by RT-2/G detector [15]

## 3 LAXPC—AstroSat

The Large Area X-ray Proportional Counter (LAXPC) is one among the five main payloads onboard the Indian Astronomy mission, AstroSat. It comprised of three co-aligned proportional counter detectors for timing and spectral studies in X-ray energy band of 3–80 keV. The individual LAXPC payload can be operated standalone with a time resolution accuracy of 10 µs during Event Analysis (EA) mode. These payloads contain a Xenon-Methane gas mixture having pressure of two atmospheres. The detectors have an FOV of about $1° \times 1°$. Each detector is accompanied by independent Processing Electronics (PE) unit. The characterizations of LAXPC detector and its design are discussed in [1]. The scientific goal of the LAXPC instrument is to achieve the periodic and irregular intensity variations, Quasi Periodic Oscillations (QPOs), binary periods and their evolution with time, etc.

### *3.1 LAXPC Payloads Design, Test and Evaluation*

LAXPC payloads are labeled in short as LX10, LX20 and LX30 (Fig. 12). Each instrument has a detection volume of $100 \times 36 \times 15\,\text{cm}^3$ consisting of five main anode layers and three Anti (veto) anodes. The main anode is further divided into



**Fig. 12** LAXPC flight payloads at ISAC, Bangalore [20]

12 cells having size $100 \times 3 \times 3\,\text{cm}^3$. The top two layers are further split in two sections connected alternately with cells. Therefore, there are total seven main anodes in each detector. The first layer consists of Anodes A1 and A2 from top, second layer having Anodes A3 and A4, and the following layers are Anodes A5, A6, and A7. These anodes are shielded by Anti anodes from three sides (Anti anode A9 guards the bottom area, whereas Anti anodes A8 and A10 guards the other two sides).

Each detector has its own inbuilt front-end electronics and command controlled High Voltage (HV) supply. They are also supported with independent signal processing electronic unit and onboard gas purification system. Beside these packages, there is one more additional unit known as STBG (System Time Base Generator) which provides a stable and accurate time reference for all the LAXPC as well as to all other payloads of the AstroSat with 10 μs resolution.

The LAXPC payloads have two main operational modes: Event Analysis (EA) mode and Fast Counter (FC) mode. In the default (EA) mode, each event generates five bytes of data which include incident time, anode ID where the event was registered and pulse height amplitude (PHA) giving energy information in the form of channel number. Simultaneously, along with EA mode, Broad Band Counting (BBC) mode data is also generated for diagnostic purpose with predefined time bin having four fixed different energy bins in three layers. During the FC mode, counts from only first layer are stored in a predefined time interval of 160 μs for four energy bands (approximately 3–6, 6–8, 8–12, and 12–20 keV).

LAXPC payload after going through various space qualification tests (Vibration, Thermal, Vacuum and EMI-EMC) successfully at ISRO Satellite Centre (ISAC), Bangalore. They were calibrated using three radioactive sources ($^{55}$Fe with 5.9 keV, $^{109}$Cd with 22.1 keV and $^{241}$Am with 59.6 keV) inside a Thermovac chamber, to measure the energy resolution and gain of the detectors, at three different temperatures such as 10, 20, and 30 °C respectively. A calibration source spectra and the LX30 background spectrum as observed at ground are shown in Fig. 13.

A complete calibration details of LAXPC payloads during ground and their comparison results with those obtained by GEANT4 simulations are discussed in detail by Antia et al. [2].

## *3.2 LAXPC Performance and Observation*

The LAXPC payload was made a fully operational from 19 October 2015 by setting the high voltage value during the ground calibration, after the launch of AstroSat on 28th September 2015. Initially, the gas purification of LAXPC detector was carried out. Following this, the onboard calibration such as tuning the gas gain and energy resolution of the instruments using a calibration source ($^{241}$Am with 59.6 keV) mounted in Anti anode A8 was done during the Performance Verification (PV) phase. The energy resolutions of LX10 after a gas purification improved from

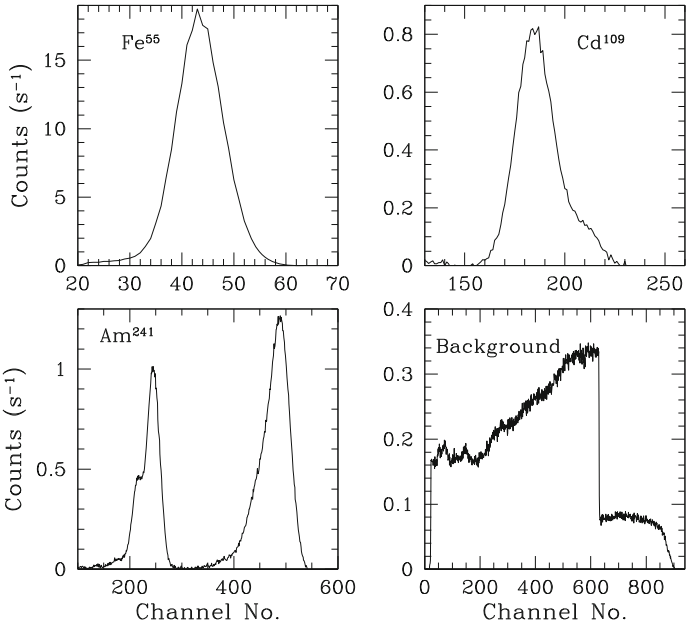



**Fig. 13** The LX30 spectra of radioactive sources and background as measured during ground calibration [2]

17% to 14% at 29.8 keV as shown in Fig. 14. Similar improvement was noticed in LX30 at 29.8 keV from 13% to 10%, whereas LX20 does not have significant improvement in resolution which remained almost stable to 12%.

During PV phase various celestial sources were observed to verify the instrument sensitivity at low energies, one such source named Cas A having an iron line at 6.62 keV [21] was observed on 4 January 2016. The spectral fit of this data found peak energies of 6.7 ± 0.1 for LX10, 6.8 ± 0.1 for LX20 and 6.7 ± 0.1 keV for LX30 as mentioned in [2] (Fig. 15). This observation confirms the channel to energy transformation used in the response of each instrument are within limits of 0.2 keV.

Figure 16 shows the observed background spectrum of LAXPC payloads at three different time intervals. This includes the first observation on 25 October 2015, the Earth occultation period and the observation on 23 November 2015. A simulated background spectrum calculated before launch for comparison which matches reasonably well is also presented. The LX10 has a higher background compared to LX20 and LX30 due to one of Anti anodes A10 has been disconnected at the ground. These background spectra were generated by integrating counts from the main anodes.

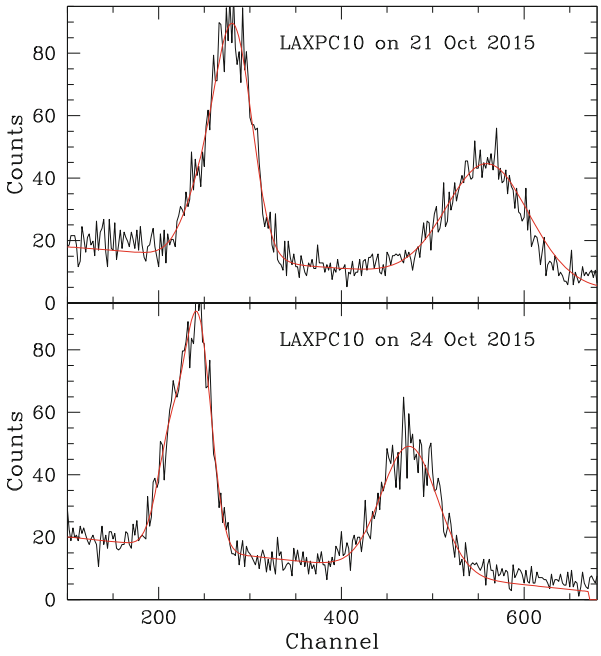



**Fig. 14** The LX10 spectrum of calibration source $^{241}$Am before (top) and after (bottom) onboard gas purification [2]

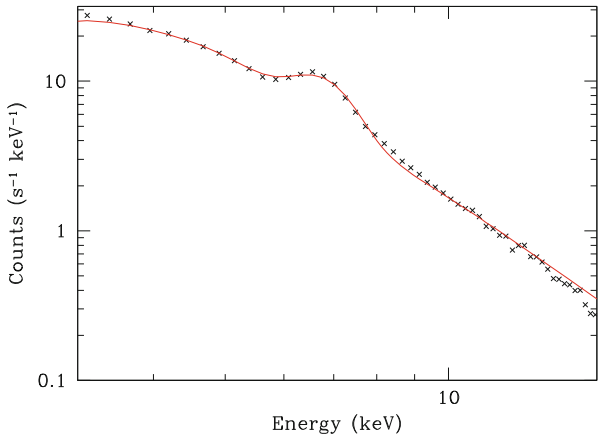



**Fig. 15** The LX10 spectrum of Cas A fitted by a power law along with a Gaussian line [2]

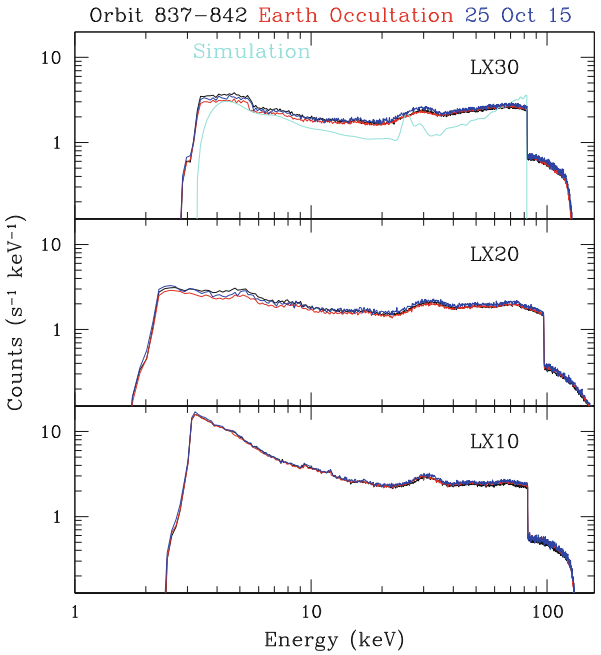



**Fig. 16** The LAXPC payloads background spectra at three different intervals along with simulated spectrum [2]

## 4 Summary

My contribution in these projects begins right from the proposal submission (RT-2 experiment only) to the final flight instruments delivery, till the data received from the satellite and analysed. I am fortunate to actively participate in design improvements, R&D discussion, laboratory test plan and setup, from space qualification testing to flight model evaluation.

All the three scientific detectors in the RT-2 experiment worked as expected with acceptable health parameters. However, the 24th solar cycle was anomalous instead of solar maximum, we could observe the sun only during solar minimum following 23rd cycle. A very few solar flares were detected by RT-2 experiment during its life of 10 months. RT-2/CZT was not able to register these faint flares due to higher threshold and having smaller effective area. The RT-2/S and G acted as omni directional gamma-ray detectors and registered a few gamma-ray bursts.

All the three LAXPC payloads performed as expected after launch of Astrosat including good health parameters. Lately, after a few months of launch, LX30 detector developed a fine leak due to which efficiency of the instrument drifted. The response of LAXPC payload is reasonably understood and has been used to produce scientific results. The LAXPC payloads have observed more than 250

distinct sources. Astrosat had completed more than 2.5 years of successful operation with more than 2100 pointing is carried out.

**Acknowledgements** I would like to thank Prof. Sandip Chakrabarti for his valuable support during my research work needed at any time of interval with his knowledge and feedback. Part of test and evaluation of RT-2 was carried out at the Indian Centre for Space Physics.

## References

1. Agrawal, P.C., Yadav, J.S., Antia, H.M., et al.: JApA **38**, 30 (2017)
2. Antia, H.M., et al.: ApJS **231**(10), 29 (2017)
3. Chakrabarti, S.K., Nandi, A., Debnath, D., Kotoch, T.B., Rao, A.R., et al.: GCN Circ., 9833 (2009)
4. Chakrabarti, S.K., Nandi, A., Debnath, D., Kotoch, T.B., Rao, A.R., et al.: GCN Circ., 10009 (2009)
5. Chakrabarti, S.K., Nandi, A., Debnath, D., Kotoch, T.B., Rao, A.R., et al.: GCN Circ., 10010 (2009)
6. Debnath, D., Nandi, A., Rao, A.R., Malkar, J.P., Hingar, M.K., Kotoch, T.B., et al.: Exp. Astron. **29**, 1 (2011)
7. Kopp, R.A., Pneuman, G.W.: SoPh **50**, 85 (1976)
8. Kotoch, T.B., Nandi, A., Debnath, D., et al.: Exp. Astron. **29**, 27–54 (2011)
9. Nandi, A., Palit, S., Debnath, D., Chakrabarti, S.K., Kotoch, T.B., et al.: Exp. Astron. **29**, 55 (2011)
10. Palit, S., Chakrabarti, S.K., Debnath, D., Rao, A.R., Nandi, A., Yadav, V.K., Girish, V.: Exp. Astron **27**, 77 (2009)
11. Priest, E.R., Forbes, T.G.: A&ARv **10**, 313 (2002)
12. Rao, A.R., et al.: GCN Circ., 9665 (2009)
13. Rao, A.R., Malkar, J.P., Hingar, M.K., et al.: RT2 detection of QuasiPeriodic pulsations in the 2009 July 5 solar hard Xray flare. Astrophys. J. **714**(2), 1142–1148 (2010)
14. Rao, A.R., Malkar, J.P., Hingar, M.K., et al.: Detection of GRB 090618 with RT2 experiment onboard the CoronasPhoton satellite. Astrophys. J. **728**, 42 (2010)
15. Rao, A.R., Malkar, J.P., Hingar, M.K., Agrawal, V.K., Chakrabarti, S.K., Nandi, A., Debnath, D., Kotoch, T.B., et al.: Sol. Syst. Res. **45**, 123 (2011). https://doi.org/10.1134/S0038094611020158
16. Sarkar, R., Mandal, S., Debnath, D., Kotoch, T. B., Nandi, A., et al.: Exp. Astron. **29**, 85 (2011)
17. Shibata, K.: Ap&SS **264**, 129 (1998)
18. Singh, K.P., Tandon, S.N., Agrawal, P.C., et al.: Proc. SPIE **9144**, 91441S (2014)
19. Sreekumar, S., Vinod, P., Samuel, E., Malkar, J.P., Rao, A.R., Hingar, M.K., Madhav, V.P., Debnath, D., Kotoch, T.B., Nandi, A., Begum, S.S., Chakrabarti, S.K.: Exp. Astron. **29**, 109 (2011)
20. Yadav, J.S., Agrawal, P.C., Antia, H.M., Chauhan, J.V., Dedhia, D., Katoch, T., Madhwani, P., Manchanda, R.K., Misra, R., Pahari, M., Paul, B., Shah, P.: SPIE **9905**, 1D (2016)
21. Yamaguchi, H., Badenes, C., Petre, R., et al.: ApJ **785**, L27 (2014)

# Part IV
# Astrochemistry of Biomolecules

# Renaissance of Astro-Chemistry in Indian Context




**Ankan Das**

**Abstract** Astrochemistry is a relatively new branch in Astrophysics. In the Indian context, some Astrochemistry related work is going on in some isolated pockets however, a visible community is still lacking. The Astrochemistry and Astrobiology department of Indian Centre for Space Physics (ICSP) has started this subject from the scratch and it is thus no surprise that ICSP has produced several scientists who are already well recognized worldwide. Manpower generated by this department of ICSP is enriching the Astrochemical community not only in the Indian context but also internationally. There were several attempts to study the presence of pre-biotic species in the ISM, however, they are yet to be identified with complete assurance. In this review, we explore the chemical evolution of interstellar pre-biotic molecules under various physical circumstances using various available tools. Our simulation suggests that even if the abundances of these pre-biotic species is not in the observed range it is better to look for their precursors which are equally relevant for inferring abundances of these pre-biotic species in the ISM. Physics and chemistry of the interstellar medium (ISM) are inter-related and thus interstellar species are very often used for the measurement of physical properties. Despite the lower elemental abundance of atomic deuterium, a high degree of deuterium fractionation is seen in the ISM. In our study, we used deuterium fractionation ratio of some interstellar ions as a tool in correlating the ionization degree of the ISM. Moreover, we performed quantum chemical calculations to find out spectral properties of the pre-biotic and deuterated species along with their precursors and performed radiative transfer modeling to predict various line parameters relevant for their future astronomical identification.

A. Das (✉)
Indian Centre for Space Physics, Kolkata, India

© Springer International Publishing AG, part of Springer Nature 2018

B. Mukhopadhyay, S. Sasmal (eds.), *Exploring the Universe: From Near Space to Extra-Galactic*, Astrophysics and Space Science Proceedings 53,
https://doi.org/10.1007/978-3-319-94607-8_33

## 1 Introduction

William Herschell in 1785 reported that there could be holes in the heavens. Later Barnard in 1919 argued using his deep photographs that many of these dark areas had obscuring bodies located between us and the distant stars. Bok [3] claimed that dark nebulae which are compact and roughly round in shape are the sites of the stellar birth. This is now reconfirmed with the advent of infrared and millimeter-wave technology. It is now well known that Dark cloud is mainly made up of molecular hydrogen and this is dark due to the presence of dust which is competent of absorbing starlight which leads to high visual extinction ($A_V > 1$). The start of notable chemical growth follows after the formation of molecular hydrogen, which is believed to result from the interaction of atomic hydrogen with dust grains. During the evolutions, molecules strongly influence environments. For example, inside a dense molecular cloud, cooling is mainly controlled by some molecular species, ionization balance is also controlled by some interstellar species which in turn can control the coupling of magnetic fields to the gas. These controls are very crucial to dictate the star formation rate. Since the molecules have controls on the star formation rates, tracing the evolutionary history of the molecules would broaden our understanding of the various stages of star-forming regions. With the advancement of the present observational facility, this highly inter-disciplinary field of Astrophysics (i.e., Astrochemistry) has observed notable changes. As many as new species identified in different regions, our understanding about the evolutionary history of these molecules were questioned. These new observations also put a compulsion on the existing physical-chemical models.

The interstellar medium (ISM) is a very dilute and tenuous medium where temperatures are low, radiation fields are intense and particle densities are exceptionally inadequate thus too extreme to prefer an active synthesis of chemical species. Despite this fact, near about 200 molecular species have been spotted in star-forming regions. This ranges from simple to very complex interstellar species. The life making primordial organic compound may also have been formed in the pre-solar nebula rather than on the early earth [5, 6, 9]. The presence of pre-biotic molecule [25] as well as chirality [33] were also spotted around various lines of sight which may solve the riddle of the origin of life on the Earth. The presence of these species in the interstellar space is believed to be due to cumulative outcome of gas-grain interactions.

Gas phase models can normally explain observed abundances of the smaller and many large radicals but they are unable to explain observed abundances of most of the stable and complex, partially organic species in space. It is now well established that dust particles play an essential role towards the chemical enrichment of the ISM. They act as a reservoir and catalytic sites for the formation of complex interstellar species. These dust particles are also the basic ingredients for planetesimal and finally planets. These icy grain mantles are exposed to the thermal, UV and atom bombardment which are extremely helpful for the chemical enrichment of the grain mantle. A summary of these gas-grain interaction process is shown in Fig. 1. Among

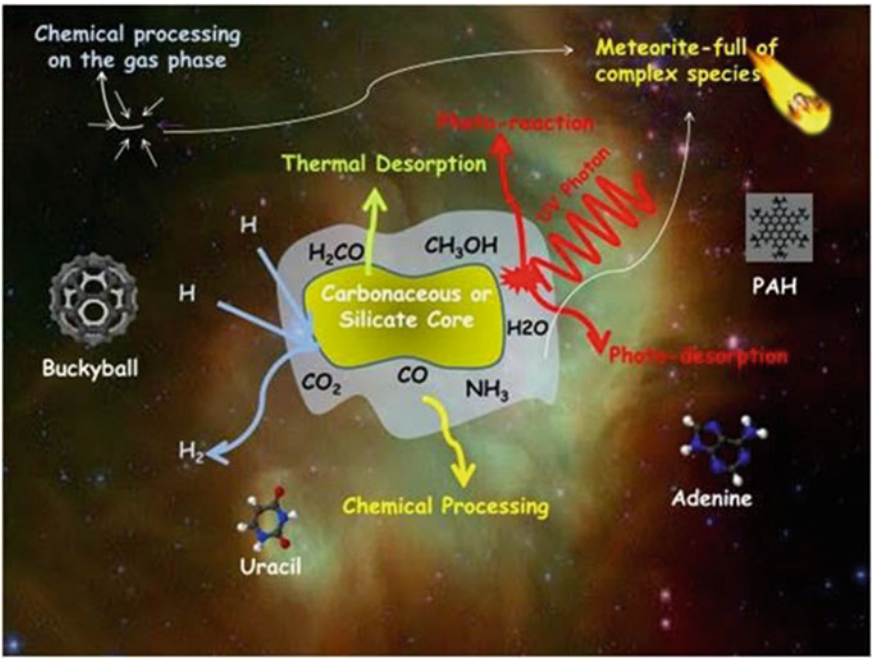



**Fig. 1** Chemical evolution by gas-grain interaction process

the observed molecules, some generic trend was obtained. For example, unsaturated or hydrogen-poor molecules were mostly identified around the cold regions whereas saturated or hydrogen-rich species were found around the young stellar object [25]. Interstellar dust is found to be made up of silicate or carbonaceous core along with the molecular ice layer [19, 22]. After the identification of several ice phase species, crucial contribution of interstellar dust towards the chemical evolution of the ISM is well understood.

For understanding the chemical composition of a molecular cloud it is not enough to study only the cloud chemistry. It is also crucial to understand the physical properties of the cloud. Stars are mainly formed in the comparatively densest part of the interstellar cloud called as the pre-stellar core. These regions are extremely cold (temperatures are about 10–20 K). At these temperatures and densities, gases are mainly in the molecular form. A proto-star is the central region of a collapsing cloud fragment which is in the process of formation of a star. This has not yet become hot enough and does not have enough mass to begin the process of nuclear fusion ($10^7$ K) in order to halt its gravitational collapse. When the density reaches a critical value, stars are formed. Star formation begins when the dense parts of the cloud core collapse under their own gravity. The cores are denser than the outer cloud. As a result, the cloud collapses rapidly. It is a long-standing aspiration to use chemical properties of various interstellar species for the measurement of physical properties of molecules clouds and star-forming regions. Molecules observed around the

Interstellar medium (ISM) derive the probes around their physical surroundings. For example, high resolution rotational and vibrational spectra of the observed species are utilized to demonstrate the density and temperature of the gas as well as any large-scale motions and vibrational spectra of molecules in dust give the information about the nature of the grain mantle. Study of the interstellar molecules helps to classify various evolutionary stages of star formation. This classification is mainly based on the observational evidences along the low mass stars because we have very limited understanding about the formation of higher mass stars. A complete knowledge about the chemical complexity requires a time dependent simultaneous study of physical and chemical properties of a collapsing cloud.

This article flows as following. In Sect. 2, we present detail methods which are implemented in explaining various astrochemical scenario. Obtained results are summarized and discussed in Sect. 3 and in Sect. 4 we conclude.

## 2 Methodology

### *2.1 Physical Properties*

The role of molecules in astronomy is now so convincing that the sizable portion of the Universe may be termed as "The Molecular Universe". A wide variety of molecules are seen in the interstellar space ranging from mono-atomic species to species containing dozens of atoms. The existence of much larger species is also feasible but it is quite difficult to trace the signature of these larger species with the present observational facilities. It is essential to study the origin of these species under various interstellar conditions. Over the years, we prepared/used various physical models to justify physical properties of the interstellar clouds. Some frequently used models are highlighted below.

- For simulating the collapsing cloud model, we considered an isothermal spherical gas cloud which is collapsing due to its self-gravity [16]. For the suitable physical condition, we often used Similarity solutions methods as described in [40] for the self-gravitating isothermal flow to find out the physical requirements [40].
- In order to study the dynamic behaviour during the collapse of a spherically symmetric isothermal gas cloud, we developed a numerical code [11]. This code often coupled with the chemical code to study the chemical evolution during these processes.
- Another numerical code is improved [15] by introducing two-dimensional flow. For this case, we solved the hyperbolic system of conservation equations by using total variation diminishing (TVD) scheme [26, 38].
- In order to verify the observational evidence of dark cloud or diffuse cloud region, we often used a constant value for the physical parameters, such as, density, temperature, visual extinction, grain size etc.

- In order to justify the observed abundances in the hot core region, we employed two-phase model [21, 23, 24, 41]. In the first phase, the cloud remains in isothermal ($T = 10$ K) phase for $10^5/10^6$ years which is then followed by a subsequent warm-up phase where the temperature can gradually increase up to 200 K in $10^4$–$10^5$ years. If in the isothermal phase collapse occurs then the cloud density, visual extinction and gas-grain temperature are also adjusted accordingly.

## *2.2 Chemical Model*

Chemical models were constructed in order to help our understanding of how molecules are synthesized in different regions of the ISM. There are several chemical databases around the world (OSU, UMIST, KIDA etc.) which contain several valuable reactions. These databases are normally used to study the chemical evolution around different regions of the ISM. Since the chemical species are used as a tracer of physical conditions around the ISM an accurate knowledge about the chemical abundances are essential. In order to appropriately model the chemical evolution, it is necessary to know the rate coefficients and several interaction energies with the dust grain accurately. For most of the chemical reactions, rate coefficients are measured at the room temperature and are then extrapolated for the astrophysical conditions of interest. This extrapolation often gives rise to misleading results. So it is customary to calculate the rate coefficients applicable to the astrophysical conditions. In this circumstance, we invoke the computational chemistry to find out the appropriate rate coefficients of several astrochemically important reactions of our interest for which rate coefficients were unknown [14, 23, 24, 27].

It is now fully recognized that interstellar dust behave as a catalyst for the chemical complexity. Composition of interstellar grain mantle could be studied by applying two different approaches: deterministic and stochastic. The Rate equation method which is very often used to determine the chemical complexity of interstellar ice belongs to deterministic approach. However, this method gives a good estimation when there is a notable surface coverage of the reactants. Since the interstellar medium is very dilute, very often this criterion is not fulfilled and this method cannot be applied. But this method is computationally faster and it can be used to study the chemical evolution in both phases simultaneously. The advantage of using the stochastic method is that here one can consider the statistical fluctuation. Since the interstellar medium is very dilute it is appropriate to use this method while simulating the composition of interstellar ices. Among the Stochastic method, Monte-Carlo method and the Master equation methods are widely used. The main disadvantage of this approach is that it is not economic in time and thus restrict us to continue this simulation for a much shorter network. Whenever, we required to model the ice chemistry more accurately, we used the stochastic method [7, 8, 10, 12, 13, 18].

We prepared a large gas-grain chemical network to iteratively study the chemical processes in a molecular cloud. Presently, our gas phase chemical network contains ∼7000 reactions in between 600 species. We mainly followed the UMIST 2006 [44] and UMIST-2012 databases [32] for the construction of our gas phase chemical network. In constructing the reaction network for the deuterium enrichment, we used some of the important reactions from databases and assumed that these reactions would also be possible for the deuterated isotopomers. To avoid long computational times, as well as the complexity of handling a large chemical network, we identified some dominant pathways for deuterium enrichment and focus on them. This selection is based on some of the earlier studies [2, 36, 37]. Gas-grain interactions are assumed by considering the accretion and evaporation (thermal/cosmic-ray/non-thermal) processes. Details of these processes were already presented in [14, 15].

## *2.3 Quantum Chemical Calculation*

There are multi-dimensional aspects of our quantum chemical calculation which supplements our chemical model and radiative transfer model. This includes calculation of rate coefficients, various interaction energies, spectral properties etc. Gaussian 09 program [20] is used for performing the quantum chemical calculations. The QST2 method is employed to calculate various energy barriers (activation barrier and Gibbs free energy of activation). Moreover, in order to determine the reaction pathways as well transition state structures we used QST2 method. Transition state (TST) calculations were performed to find out the formation route of any proposed chemical reactions. The outcome of the results were simultaneously coupled with the hydro-chemical and radiative transfer model to come up with the desired molecular transitions with the existing observational facilities. High-level quantum chemical calculations were employed in estimating accurate energies of various interstellar species. First of all, we optimized the geometry of the molecules, Gas phase vibrational frequencies of these molecules are also calculated. Ice phase vibrational frequencies of these molecules were obtained by using Polarizable Continuum Model along with the integral equation formalism variant as the default SCRF method. This is to be noted that the dielectric constant of ice is 85.5 whereas for the ice phase model Gaussian 09 consider a default value of the dielectric constant ∼78.5. For the computation of various electronic transitions of some interstellar species we use time dependent density functional theory. Most of the interstellar molecules were identified in interstellar space by their rotational transitions. It is proven that quantum chemical studies can provide reliable spectroscopic constants to aid laboratory microwave studies [23, 24, 41]. We used quantum chemical studies to provide the rotational and distortional constants of some relevant interstellar species. These spectroscopic constants were then used to generate catalog files of spectroscopic frequencies in the JPL/CDMS format.

### 2.4 Radiative Transfer Modeling

The main goal of radiative transfer calculation is to extract physical parameters from astronomical observations, however, in case of Astrochemistry, the main application of radiative transfer is the estimation of molecular abundances from line spectra at infrared and sub(millimeter) wavelengths [43]. Molecular spectral line may be analyzed in radiative transfer model in three ways: (a) single excitation temperature (LTE) model ($T_{ex} = T_{kin}$ ), (b) non- LTE model ($T_{ex} \neq T_{kin}$) and (c) non-local models. Using LTE approximation is comparatively easier as it requires minimal amount of parameters (spectroscopic data only) but not suitable to use at lower densities because at lower densities $T_{ex} < T_{kin}$. The non-LTE approximation is good but it often requires molecular collision data as an additional input which is often missing. The non-local method is the most sophisticated radiative transfer programs where consideration of local excitation is omitted and find out the molecular excitation as a function of position in the cloud. To estimate the possibility of detecting various isomeric and pre-biotic species with the present astronomical facilities, we employed radiative transfer model. For this calculation, we employed various molecular databases (CDMS, JPL, VAMDC, LAMDA, BASECOL, Splatalogue etc.). If the target molecule is missing in the available databases, we used the outcome of our quantum chemical calculations and invoke some educated estimation to set an observational guideline for the target species.

## 3 Results and Discussions

### 3.1 Deuterium Enrichment

Deuterium enrichment of the interstellar molecules draw a major attraction after the discovery of singly and multiply deuterated $H_2CO$ and $CH_3OH$ in the ISM. Interestingly, the fractionation ratios of these deuterated species often crossed the elemental D/H ratio. $H_2$ is the most abundant interstellar species, and its deuterated forms (HD and $D_2$) are also present in high abundance. The high abundance of these molecules could be explained by considering the chemistry that occurs on interstellar dust. We performed Monte-Carlo simulations to study the formation of $H_2$, HD and $D_2$ on interstellar ice [39]. We pointed out that a zero-point energy correction exists between hydrogenated and deuterated species, which is necessary to consider for performing the deuterium enrichment study. Difference between the rate equation method and Monte-Carlo method was highlighted for the formation efficiency of $H_2$ and its deuterated forms. We further implement our gas-grain chemical model to study the presence of the deuterated isotopomers of some recently observed complex interstellar species such as, Methyl acetate [17], cyanoformaldehyde [14], cyanomethyl anion [29], choloronium ion [30] etc.

Ionization degree of a cloud is the very crucial parameter as it controls the chemical evolution and also the star formation rate. Ionization degree can be estimated by observing the most abundant ions. However, it is very challenging to directly observe these ions. Thus, we need to depend upon some other chemical species which are influenced by the electron density to have an educated estimation of the ionization degree [4]. Despite the low elemental abundances of deuterium in space, extremely large amounts of deuterated species have been observed. In reality, f(e) depends on various parameters, however, some molecules can be used to diagnose this to some extent. Since the abundance of any species depends on various physical conditions and the age of the source, it is very difficult to present any generalized formula for predicting the ionization degree at any particular instant. A dependable method to assess the ionization degree of a molecular cloud is to use the fractionation of some deuterated molecular ions. The ionization estimation might vary due to the freezeout of the neutral molecules on the grain. $HCO^+$ is one of the abundant gas phase ions in the ISM. We used the deuterium fractionation of this ion $R1 = DCO^+/HCO^+$) to compute f(e). However, due to the heavy depletion of CO related molecules, $HCO^+$ and $DCO^+$ could be depleted at the dense interior which could severely affect $R_1$ to f(e) correlation. In order to justify the appropriate deuterium fractionation of an entire core, it is then essential to rely on some other molecules which can survive from the heavy depletion. In this regards, $N_2H^+$ is an ideal choice as nitrogen bearing spices normally have lower adsorption energy with the grain surface. Another benefit of observing N-bearing molecules is that their emission lines are split into hyperfine components, due to the non-zero nuclear spin of nitrogen. This enables the optical depths of the intervening medium to be measured. It is customary to study the ratio $N_2D^+/N_2H^+$ (hereafter $R_2$) to get a better approximation around that region. Based on the results obtained, we divided the entire zone of the molecular cloud into two parts. Outer zone is extending from 6000 to 20,000 AU and the dense interior extending from 100 to 6000 AU. We proposed to use $R_1$ used for estimating f(e) in the outer zone and $R_2$ for the inner zone [16].

Mote Carlo simulation were carried out to study the chemical composition of interstellar grain mantle and its deuterium fractionation under various physical conditions [18]. A comparison between the presence and absence of deuterium is shown in Fig. 2. It clearly depicts that the grain mantle is seen to be heavily fractionated when deuterium is considered in the chemical network. To have a realistic situation, we proceeded our simulation for diverse types of cloud. We noticed that in the diffuse cloud region, very limited number of layers were produced due to the effect of the strong interstellar radiation field. In the translucent cloud model, due to the attenuation of the radiation field, a notable number of layers were produced but the surface coverage of the grain mantle was dominated by the products of photo-dissociation. In the dense cloud region, interstellar radiation field is mostly attenuated and formation of complex species was favorable. For the better understanding, dense cloud region was further be subdivided into intermediate density and high-density region. We noticed that in the intermediate density region, grain mantle was dominated by water and methanol and their deuterated forms. For

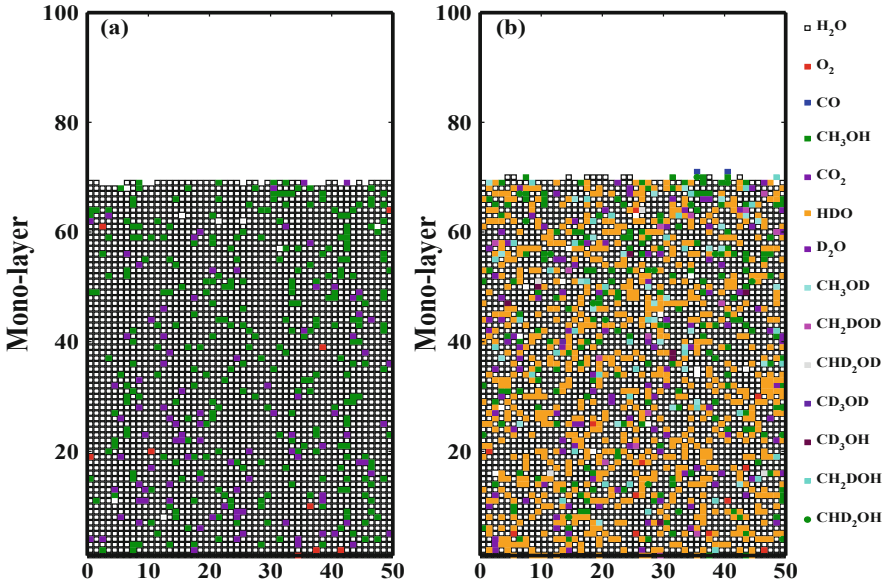



**Fig. 2** Cross sectional view of our simulated grain mantle by considering the presence and absence of deuterium: (**a**) without deuterium and (**b**) with deuterium

the high-density region, methanol and water production decreased and a striking increase of CO molecules and oxygenated species ($CO_2$, $O_2$, $O_3$) was found.

## *3.2 Complex Interstellar Species*

The origin of amino acids through pre-biotic chemistry of the early Earth has been a topic of long standing interest. However, complex pre-biotic molecules can also form inside a molecular cloud due to very complex and rich chemical processes. The production of amino acids, nucleobases, carbohydrates and other basic compounds can possibly start from the molecules like HCN, cyno compounds, aldehyde, and ketones [1, 34], which could lead to the origin of life in the primitive earth conditions.

The biggest obstacle in constructing a model to study the formation of these species is the use of approximate values of several chemical parameters. It is long debated if pre-biotic molecules are indeed present in the interstellar medium. Despite substantial works pointing to their existence, pre-biotic molecules are yet to be discovered with a complete confidence. In this attempt, we carried out extensive calculations to find out the potential formation of various complex and pre-biotic molecules and their possibility of detection around the interstellar analogues. We prepare a large gas-grain chemical network by considering various pathways for the

formation of these pre-biotic molecules. Rate coefficients of various reactions are estimated by quantum chemical calculations. As of now, we have pointed out to observe some of the most relevant complex interstellar species, like, propanethiol [24, 35], propargyl alcohol (precursor of benzene formation, [23], $C_4N_3OH_5$ (Z isomer of cytosine) [31], methyl propionate [42]. We found that for the formation of uracil by the reaction between cytosine and water require a high activation barrier which is quite challenging to overcome under the interstellar conditions. Thymine formation was studied by the reaction between uracil and : $CH_2$. Since the formation of uracil is blocked by the high activation barrier, thymine formation may not process along this path under the interstellar conditions. We implemented our computed reaction rates in our large gas-grain network to study the formation of interstellar cytosine.

Our model suggested that abundances of most of the bio-molecules are not in the detectable range even with the present observational tools. So it is hard to confirm the presence of any bio-molecules in the ISM. We can identify a few precursor molecules which eventually form bio-molecules in the interstellar space. Quantum chemical simulation is used to find out the spectral properties of these pre-cursor molecules. It is observed and experimentally verified that the spectral signature of a species significantly deviates between the gas phase and ice phase. So a theoretical study of the spectral properties of the precursors of some important bio-molecules in both the gas and ice phases could serve as benchmarks for the observations. We performed higher order quantum chemical simulations to provide detailed spectroscopical properties of the precursors of these bio-molecules for various vibrational, rotational and electronic transitions. Spectral properties significantly vary depending on the environment around these molecules. To reproduce the recent observational/experimental features, we continued our simulation for various astrophysical conditions to correlate resulting changes with the physical parameters. We prepare catalog files for the rotational transitions of these molecules, which could be useful for their future detection around the interstellar medium. We explored the infrared and electronic absorption spectra of various complex molecules, which could be treated as the precursors of adenine, glycine and alanine in several astronomical situations [28].

Almost half of the observed interstellar species have their isomeric counterparts. This isomerism was used as an instrument in confirming some observed aspects. A comparative study between various isomeric groups yield the most stable isomeric species in each isomeric group. This stability is not directly related to the observed abundances but it may influence the formation partially. So based on the stability, computed abundance around any particular source and computed dipole moment components and rotational constants, the most potential isomeric species from each isomeric group was proposed for observation. Moreover, we used Radiative transfer modeling to present the line parameters which may enable their future astronomical detection.

## 4 Conclusion

The work carried out over the past few years certainly enriched the Astrochemical community and this process will continue during the coming years. Successful observation of our proposed pre-biotic or the precursor of biomolecules would be a major clue to the origin of life. Our Monte-Carlo simulation is capable of studying the composition of the grain mantle around the various star forming region and protoplanetary disks. A detail analysis of the morphology of the grain mantle could be utilized as a pointer to find out the linkage between the cometary and interstellar ice. Observed band profile of the interstellar ice would be well explained after our theoretical modeling on the interstellar band profile. Our calculated synthetic spectra in the sub millimeter domain (LTE or non-LTE computation) would be extremely useful for explaining various unidentified interstellar bands and to observe new molecular species. Especially, the generated manpower are not only helpful in Indian context but also internationally.

**Acknowledgements** I would like to express my gratitude to Prof. Sandip K. Chakrabarti who had introduced me to this fascinating realm of astrophysics. I would also like to acknowledge the support of my two ISRO respond projects (Grant No. ISRO/RES/2/372/11-12 and ISRO/RES/2/402/16-17) and one DST project (Grant No. SB/S2/HEP-21/2013) and Government of West Bengal for the financial support.

## References

1. Abelson, P.H.: Proc. Natl. Acad. Sci. **55**, 1365 (1966)
2. Albertsson, T., Semenov, D.A., Vasyunin, A.I., Henning, T., Herbst, E.: ApJS **207**, 27 (2013)
3. Bok, B.J.: Centennial Symposia. Harvard Observatory Monograph, vol. 7, p. 53 (1948)
4. Caselli, P.: P&SS **50**, 1133 (2002)
5. Chakrabarti, S., Chakrabarti, S.K.: A&A **354**, L6 (2000)
6. Chakrabarti, S.K., Chakrabarti, S.: InJPh **74B**, 97 (2000)
7. Chakrabarti, S.K., Das, A., Acharyya, K.,Chakrabarti, S.: A&A **457**, 167 (2006)
8. Chakrabarti, S.K., Das, A., Acharyya, K.,Chakrabarti, S.: BASI **34**, 299 (2006)
9. Chakrabarti, S.K., Majumdar, L., Das, A., Chakrabarti, S.: Ap&SS **357**, 90 (2015)
10. Das, A., Chakrabarti, S.K.: MNRAS **418**, 545 (2011)
11. Das, A., Chakrabarti, S.K., Acharyya, K., Chakrabarti, S.: NewA **13**, 457 (2008)
12. Das, A., Acharyya, K., Chakrabarti, S., Chakrabarti, S.K.: A&A **486**, 209 (2008)
13. Das, A., Acharyya, K., Chakrabarti, S.K.: MNRAS **409**, 789 (2010)
14. Das, A., Majumdar, L., Chakrabarti, S.K., Saha, R., Chakrabarti, S.: MNRAS **433**, 3152 (2013)
15. Das, A., Majumdar, L., Chakrabarti, S.K., Chakrabarti, S.: NewA **23**, 118 (2013)
16. Das, A., Majumdar, L., Chakrabarti, S.K., Sahu, D.: NewA **35**, 53 (2015)
17. Das, A., Majumdar, L., Sahu, D., Gorai, P., Sivaraman, B., Chakrabarti, S.K.: ApJ **808**, 21 (2015)
18. Das, A., Sahu, D., Majumdar, L., Chakrabarti, S.K.: MNRAS **455**, 540 (2016)
19. Draine, B.T.: ApJ **598**, 1017 (2003)
20. Frisch, M.J., et al.: Ins. Wallingford CT, Gaussian 09, Revision E.01 (2009)
21. Garrod, R.T., Herbst, E.: A&A **457**, 927 (2006)
22. Gibb, E.L., Whittet, D.C.B., Boogert, A.C.A., Tielens, A.G.G.M.: ApJS **151**, 35 (2004)

23. Gorai, P., Das, A., Das, A., Sivaraman, B., Etim, E.E., Chakrabarti, S.K.: ApJ **836**, 70 (2017)
24. Gorai, P., Das, A., Majumdar, L., Chakrabarti, S.K., Sivaraman, B., Herbst, E.: MolAs **6**, 36 (2017)
25. Herbst, E., van Dishoeck, E.F.: Annu. Rev. Astro. Astrophys. **47**, 427 (2009)
26. Harten, A.: J. Comp. Phys. **49**, 357 (1983)
27. Majumdar, L., Das, A., Chakrabarti, S.K., Chakrabarti, S.: Res. Astron. Astrophys. **12**, 1613 (2012)
28. Majumdar, L., Das, A., Chakrabarti, S.K., Chakrabarti, S.: New Astron. **20**, 15 (2013)
29. Majumdar, L., Das, A., Chakrabarti, S.K.: A&A **562**, A56 (2014)
30. Majumdar, L., Das, A., Chakrabarti, S.K.: ApJ **782**, 73 (2014)
31. Majumdar, L., Gorai, P., Das, A., Chakrabarti, S.K.: AP&SS **360**, 64 (2015)
32. McElroy, D., Walsh, C., Marckwick, A.J., Cordiner, M.A., Smith, K., Millar, T.J.: A&A **550**, 36 (2013)
33. McGuire, B.A., Carroll, P.B., Loomis, R.A., et al.: Science **352**, 1449 (2016)
34. Orgel, L.E.: Biochem. Mol. Biol. **39**, 99 (2004)
35. Pavithraa, S., Sahu, D., Seth, G., Lo, J.I, Raja Sekhar, B.N., Cheng, B.M., Das, A., Mason, N.J., Sivaraman, B.: AP&SS **362**,126 (2017)
36. Roberts, H., Millar, T.J.: A&A **361**, 388 (2000)
37. Rodgers, S.D., Millar, T.J.: MNRAS **280**, 1046 (1996)
38. Ryu, D., Ostriker, J.P., Kang, H., Cen, R.: APJ **414**, 1 (1993)
39. Sahu, D., Das, A., Majumdar, L., Chakrabarti, S.K.: NewA **38**, 23 (2015)
40. Shu, F.: ApJ **214**, 488 (1977)
41. Sil, M., Gorai, P., Das, A., Bhat, B., Ethi, E.E., Chakrabarti, S.K.: ApJ **53**, 2 (2018)
42. Sivaraman, B., Radhika, N., Das, A., Gopakumar, G., Majumdar, L., Chakrabarti, S.K., Subramanian, K.P., Raja Sekhar, B.N., Hada, M.: MNRAS **448**, 1372 (2015)
43. Van der Tak, F.F.S., Black, J.H., Schoier, F.L., Jansen, D.J., van Dishoeck, E.F.: A&A **468**, 627 (2007)
44. Woodall, J., Agndez, M., Markwick-Kemper, A.J., Millar, T.J.: A&A **466**, 1197 (2007)

# The Interstellar Molecular Complexity




**Liton Majumdar**

**Abstract** One of the major questions of 'Cradle of Life' science theme of astronomy is how, when and where complex organic molecules, including the so-called prebiotic molecules, are formed. Key questions are: (1) which are the physicochemical processes that are involved in their production/destruction? and (2) whether grain surface processes or gas phase reactions prevail in their formation. Because of the success of large ground-based single dish telescopes (e.g. NRO 45 m, IRAM 30 m, GBT, ARO 12 m and NASA DSN) and interferometers (e.g. ALMA, NOEMA, and SMA) and space observatories (ISO, Spitzer, and Herschel), an interdisciplinary field has developed extending from astronomical instrumentation and observatories to laboratory astrophysics to theoretical chemical-dynamical modelings and to high level quantum computations. We are currently in an era to address the long-standing question of our 'chemical origins', that is, to understand the journey of organic molecules from pre-stellar cores to planet-forming disks, and finally to the Solar System bodies. Following this journey, which leads to the origin of life on Earth, is a Holy Grail of astronomy. I will review some of the significant results on the formation and detection of complex organic molecules, including prebiotic molecules and their organic precursors, towards star-forming regions.

## 1 Introduction

"Are we alone in the Universe?" This is a long standing question for the human being. The journey of life in the Universe starts with the chemistry of the elements and in particular, of those with a key role in life: hydrogen, carbon, oxygen, nitrogen, sulphur and phosphorous. Among them, hydrogen was formed during the creation of the Universe some 14 billion years ago in the so called 'Big Bang' era,

L. Majumdar (✉)
Jet Propulsion Laboratory, California Institute of Technology, Pasadena, CA, USA
e-mail: liton.majumdar@jpl.nasa.gov

© Springer International Publishing AG, part of Springer Nature 2018

B. Mukhopadhyay, S. Sasmal (eds.), *Exploring the Universe: From Near Space to Extra-Galactic*, Astrophysics and Space Science Proceedings 53,
https://doi.org/10.1007/978-3-319-94607-8_34

whereas nucleosynthesis during stellar evolution was responsible for the formation of other life making elements. These elements were then delivered to the interstellar medium (ISM) by means of stellar winds, planetary nebula ejection and supernova explosions, to be finally incorporated into the next generations of stars such as the Sun. By mass, 99% of the ISM is gas in any form (atomic or molecular), while 1% is micron sized dust particles or the so called grains. Interstellar grains act as a catalyst for organic molecule formation via reaction channels that cannot continue in the gas phase due to the high activation energy barriers [18]. For instance, $H_2$, which is the primary and most abundant molecule in the ISM, is formed on grains by the interaction of two neutrally charged H atoms trapped on grain surfaces. After $H_2$, CO is the second most abundant molecule with a fractional abundance of $CO/H_2 \sim 10^{-4}$. The production of more complex species begins effectively in molecular dark clouds where most UV radiation is attenuated (temperatures $\sim$10 K, $H_2$ densities $\sim 10^4$–$10^6\,cm^{-3}$ and visual extinction Av>10 mag). These clouds offer a shielded environment for the formation of larger species by gas-phase and grain-surface chemistry. To date, a large number of complex organic molecules (COMs) have been detected through infrared, radio, millimeter and sub-millimeter observations (almost 200 molecules listed by CDMS database [28]). Among them one can find nitriles, aldehydes, alcohols, acids, ethers, ketones, amines and amides, as well as long chain hydrocarbons.

All life on Earth is composed of water, proteins, lipids, nucleic acids, sugars and other minor substances, with proteins having the largest fraction in weight next to water. Amino acids bond together to make proteins, and this is why the search for amino acids and their precursors in the ISM is one of the exciting topics in modern radio astronomy and astrobiology. It has been suggested that comets may have delivered water, together with organic compounds, to a young Earth [15]. If amino acids were formed in the ISM, they could have been transferred to protoplanetary disks and, later on, to comets. In other words, interstellar amino acids could have been the seeds of 'life' on earth.

## 2 Recent Progress: From Astrochemistry to Astrobiology

An attempt to understand the origins of life must necessarily begin with detailed studies of the formation and evolution of complex organic molecules (COMs), products of a complex chemistry that most likely starts in molecular clouds and continues within the protoplanetary disk. The synthesis and evolution of organic molecules which form the building blocks of more complex biotic molecules is, however, not well understood.

The search of COMs in the ISM and the atmospheres of comets has made significant advancement in this filed. Among them, interstellar detections of aldehydes, namely propenal ($CH_2CHCHO$) and propanal ($CH_3CH_2CHO$) [20], and sugars like glycoaldehyde ($CH_2OHCHO$ [19] in Sgr B2(N) using GBT laid the foundation of the subject. Recently, propylene oxide ($CH_3CHCH_2O$) [26] has also been observed in the same source. This is the first COM identified in star-forming regions that

has the property of chirality (i.e., a molecule not superimposable on their mirror images), providing us the clues on the origin of homochirality of life. In the era of the Atacama Large Millimeter Array (ALMA), the detection of the branched alkyl molecule iso-propyl cyanide (i-$C_3H_7CN$) in Sgr B2(N) also gives clues to the presence of amino acids in the ISM due to its key side-chain structure [4]. Recently, volatile glycine ($NH_2CH_2COOH$) was detected in the coma of comet 67P/Churyumov-Gerasimenko by the ROSINA (Rosetta Orbiter Spectrometer for Ion and Neutral Analysis) mass spectrometer [1], also giving clues about glycine's interstellar origin. So far, several attempts have been made to detect glycine towards Sgr B2(N) and other high mass star forming regions (glycine is the simplest amino acid and the only non-chiral member out of 20 standard amino acids), but none of them has been successful [23]. Deep observations of complex organic molecules toward regions forming lower-mass stars (such as the Sun), have recently revealed that the level of chemical complexity in these regions is much higher than previously thought. Indeed, large complex organics such as methyl formate ($CH_3OCHO$), dimethyl ether ($CH_3OCH_3$) or vinyl cyanide ($CH_2CHCN$) have been detected in Solar-system precursors (the so called pre-stellar cores) and molecular dark cloud cores [2]. Methanol ($CH_3OH$) [34] and methyl cyanide ($CH_3CN$) [29] have also been identified in protoplanetary disks indicating that this chemical complexity is transferred from the initial to the last stages in the formation of a Solar system.

## 3 Formation of Prebiotic Molecules in the ISM

The major obstacle for studying the chemical evolution of complex prebiotic organic molecules is the unavailability of kinetic rate constants for various reaction channels which take place in the ISM.

Quantum chemical theory provides an important information for the search of different reaction potential energy surface (PES). By knowing stable structures of reactants and products, one can find information regarding the reaction kinetics as well as its thermochemistry of any reaction. Density Functional Theory (DFT) can be used explicitly to find out various reaction channels and branching ratios for the synthesis of interstellar pre-biotic organic molecules. Computations were performed in the past using B3LYP functional and 6-31G++ basis set using Gaussian 09W program [24, 25]. Total energies by optimizing the geometries of the species, ZPVE and electronic energies of all the reactants, products and transition states which are formed during the organic synthesis were also calculated [24]. Using these kinetic information, rate constants for a neutral-neutral/neutral-radical/radical-radical reactions at 30 K can be estimated by using semi-empirical relationship developed by [3],

$$K = 1 \times 10^{-21} A_r (6E_0 + N - 2)^{(3N-7)}/(3N-7)!\ \mathrm{cm}^3\ \mathrm{s}^{-1}, \quad (1)$$

where, $E_0$ is reaction association energy in eV, $A_r$ is transition probability (in $s^{-1}$) of stabilizing transition and $N$ is number of nuclei in the activated complex under consideration.

If calculated rate constants from Eq. (1) exceeds the limit set by following equation (Eq. (2)), then this limiting value can be adopted

$$K = 7.41 \times 10^{-10} \alpha^{1/2} (10/\mu)^{1/2} \text{ cm}^3 \text{ s}^{-1}, \tag{2}$$

where, $\alpha$ is the polarizability in Å$^3$, $\mu$ is reduced mass of reactants in $^{12}$C amu scale as suggested by Bates [3]. Bate's rate theory is not modern rate theory since it depends only on the association energy, not the activation energy barrier. Majumdar et al. [24, 25] consider this theory to get an educated estimation of the kinetic rate constants during the synthesis of pre-biotic molecules around the cold dark clouds.

As is [13] and references therein, rate coefficient for a chemical reaction having an activation barrier could be calculated by using transition state theory. According to this theory, the equation for calculating the reaction rates is:

$$k(T) = (K_B T / hC^0) exp(-\Delta G / RT) \text{ s}^{-1}, \tag{3}$$

where, $K_B$ is Boltzmann constant, $h$ is Plank's constant, $T$ is temperature, $C^0$ is concentration, $R$ is ideal gas constant, and $\Delta G$ is free energy of activation. It is clear from above equation that rate constant is strongly dependent on temperature.

Reactions among ions and molecules or those among open-shell atomic and molecular radicals often have no activation energy barriers in the potential energy surface between reactants and products. For these reactions, capture theory could be applied. According to [37], rate coefficients for this type of reactions could be computed by using Langevin rate formula given by,

$$k_{IN} = 2\pi e \sqrt{\frac{\alpha_d}{\mu}}, \tag{4}$$

where, $\alpha_d$ is polarizability of neutral reactant and $\mu$ is the reduced mass of the reactants. This theory predicts a temperature independent rate coefficient with a typical magnitude of $\sim 10^{-9}$ cm$^3$ s$^{-1}$. Polarizability of neutral reactants can be computed by using quantum chemical calculation (Gaussian 09W program) which is in units of Bohr$^3$ (1 Bohr= 0.529 Å).

## 4 Chemo-Dynamical Evolution of Prebiotic Molecules

### *4.1 Hydro-Chemical Model*

To study chemical evolution of prebiotic molecules during collapsing phase of a molecular cloud, [24] have developed a gas-grain chemical network. For the gas-phase, they adopted UMIST (2006) network. Formation of various pre-biotic species was included in their gas phase reaction network. However, rate constants for the formation of these pre-biotic molecules were unknown. They calculated all these rate coefficients by using either Bate's theory or conventional transition state theory using the output from Gaussian program and included in their gas phase

network. For grain surface reaction network, they followed [8, 10, 12, 17]. Their surface reaction network consists of various types of reactions and their associated reaction barrier energies as mentioned in [10] and references therein. Detailed discussions about their gas-grain chemical model were presented in [10]. Following 1D hydrodynamical model as discussed in [11], they consider density distribution of a collapsing cloud as an input physical condition for their gas-grain chemical code.

### 4.1.1 Chemical Evolution of Various Pre-biotic Molecules

I will now discuss and summarize the results of the most updated coupled one dimensional hydro-chemical model presented in [24]. We now present the outcome of most updated coupled one-dimensional hydro-chemical model discussed in [24]. They simulated a spherically symmetric isothermal ($T = 10$ K) molecular cloud for more than 4 million years. This is a typical age of a molecular cloud [10, 12].

In this model, density reaches its peak at the inner part of the cloud. They took density structure of the collapsing cloud as input parameters in their chemical model to explore the chemistry of star-forming regions. In Fig. 1, radial variation of final abundances of several interstellar pre-biotic molecules are shown from [24]. Along 'Y' axis, $n_X$ is denoted for prebiotic species and $n_H$ is denoted for total hydrogen nuclei in all forms. It is evident from their Fig. 1 that abundances peak inside around fourth to fifth shell (glycine peaks at around the first shell). For glycine, peak and final abundance both are shown. Glycine is found to decrease due to production of $C_2H_4O_3$ ($C_2H_5NO_2 + H_2O \rightarrow C_2H_4O_3 + NH_3$) by neutral-neutral reaction and production of $C_2H_4NO_3$ by fragmentation reaction ($C_2H_5NO_2 \rightarrow C_2H_4NO_3 + H$). Peak abundance obtained during their simulation time scales were $4.43 \times 10^{-25}$, $5.83 \times 10^{-16}$, $1.57 \times 10^{-18}$, $2.14 \times 10^{-15}$, $1.89 \times 10^{-22}$ for the interstellar

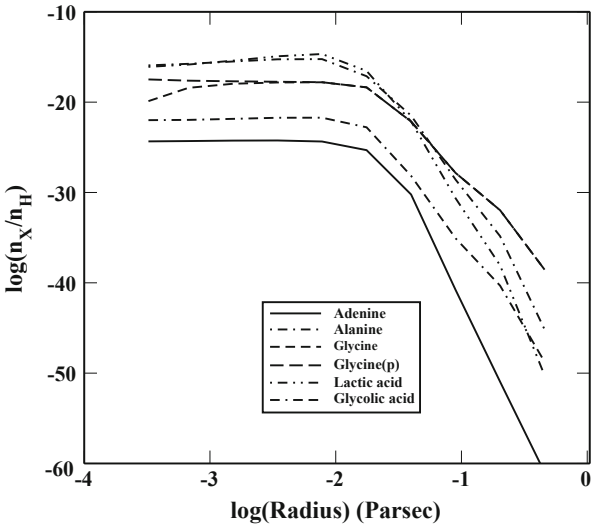



**Fig. 1** Radial distribution of abundances of various pre-biotic organic molecules during collapsing phase of a molecular cloud [24]

adenine, alanine, glycine, lactic acid and glycolic acid respectively. If they exclude radical-radical/radical-molecular reaction channels for formation of glycine and alanine, peak abundance obtained during simulation time scales were $4.43 \times 10^{-25}$, $8.85 \times 10^{-18}$, $1.96 \times 10^{-17}$, $2.35 \times 10^{-16}$, $1.36 \times 10^{-21}$ for the interstellar adenine, alanine, glycine, lactic acid and glycolic acid respectively at around fourth and fifth shells. Adenine abundance remains constant since excluded pathways do not involve any of its precursors, whereas the abundance of glycine and glycolic acid shows large deviation. The main reason behind this difference is the relative contribution of dissociation of $NH_2CH_2COOH$ as compared to its destruction channel with $H_2O$.

Time evolutions of several pre-biotic organic molecules are shown in Fig. 2 for fifth shell from [24] since most of them indicating their abundance peak at the intermediate shells. They start their simulation by assuming initial elemental abundances same as mentioned in [35]. In their simulation, all hydrogens initially were in atomic form. With time, all chemical species in the network channelized to form more complex species and some pre-biotic molecules as well.

First study to predict formation adenine in the ISM was made by Chakrabarti and Chakrabarti [5] (hereafter CC00a) who proposed successive addition of HCN for its formation. Since rate constants for these neutral-neutral addition reactions were unknown, they assumed a constant rate of $10^{-10}\,\mathrm{cm^3\,s^{-1}}$. Recently, based on the quantum chemical simulation, [24] have revised their hydro-chemical model and found that radical-radical/radical-molecular channels were the most dominant reaction pathways for the formation of adenine in the ISM.

In [6] (hereafter CC00b), they considered a parameterized rate theory whereas reaction proceeds via HCN addition, size of the product increases and thus the rate constant also increases as the square of the size. The parameterized rate constant varies as follows:

$$\alpha_i = f^{i-1}\alpha_{Ad}, \tag{5}$$

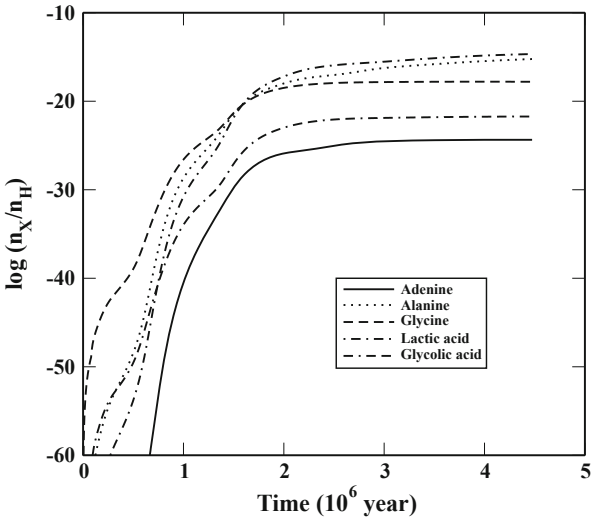



**Fig. 2** Chemical evolution of pre-biotic organic molecules at an intermediate shell of a collapsing cloud [24]

where, $i$ is the number of steps involved (in CC00ab adenine formation require four steps), $\alpha_{Ad}$ and $f$ were used to parameterized the reaction rates. They considered seven models by considering following parameters: Model A ($\alpha_{Ad} = 10^{-16}$ and f = 1), Model B ($\alpha_{Ad} = 10^{-14}$ and f = 1), Model C ($\alpha_{Ad} = 10^{-12}$ and f = 1), Model D ($\alpha_{Ad} = 10^{-10}$ and f = 1, same as CC00a), Model E ($\alpha_{Ad} = 10^{-16}$ and f = 100), Model F ($\alpha_{Ad} = 10^{-14}$ and f = 10), Model G ($\alpha_{Ad} = 10^{-12}$ and f = 5).

According to CC00a (i.e., Model D of CC00b), abundance of adenine was predicted to be $6.35 \times 10^{-11}$ when the effective rate, $10^{-10}\,\mathrm{cm^3\,s^{-1}}$ was used. In [24], by considering the same rate constant as in CC00a, they predicted that the abundance of adenine was $9.84 \times 10^{-15}$. The adenine abundance was reported to be $1.36 \times 10^{-34}$, $1.2 \times 10^{-22}$ and $1.8 \times 10^{-14}$ for Model A, E and G respectively in CC00b. On the other hand, by considering the same models and rate constants, [24] predicted the adenine abundances $1.1 \times 10^{-38}$, $1.1 \times 10^{-26}$, $1.65 \times 10^{-18}$ respectively. These values are several magnitudes lower. Majumdar et al. [24] have pointed out two primary reasons for this strong deviations. First, they assumed different density structures as their physical model. Second, they consider state-of-the-art gas-grain chemical model to compute the chemical compositions. Due to the presence of grains, HCN strongly depletes on the grains which in turn decreases adenine abundance as well. In Fig. 3a, the formation of adenine is shown from [24] based on quantum chemical calculations. In Fig. 3b, c, a comparison by assuming

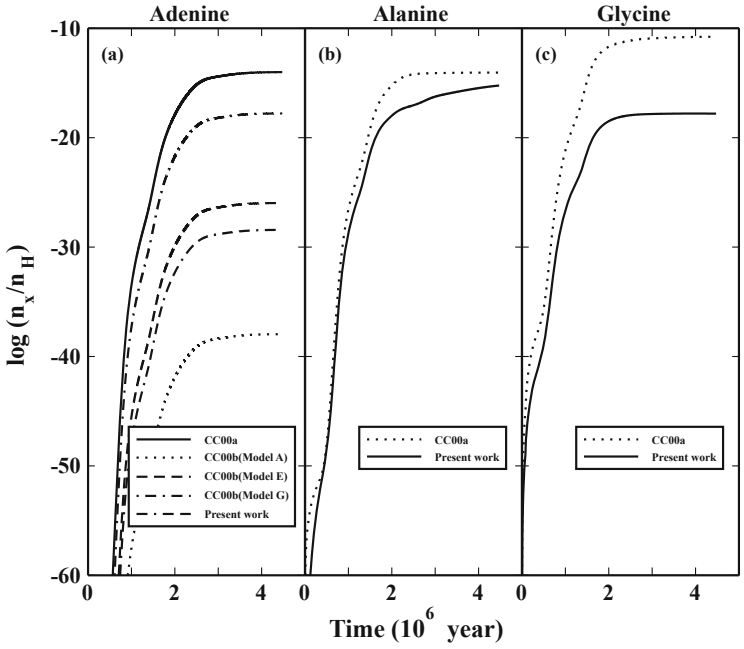



**Fig. 3** Abundance profiles of (**a**) adenine, (**b**) alanine and (**c**) glycine using various models reported in the literature [24]

parameters according to CC00a and [24] have been demonstrated for alanine and glycine respectively from [24] as well.

## 4.2 *Prediction of Precursor Molecules for Various Prebiotic Molecules*

### 4.2.1 Adenine

In the recent past, few authors have studied the formation of adenine in the ISM after the initial work of [5, 6] who proposed a neutral-neutral HCN addition reactions for the formation of adenine. According to them, the adenine could be formed by the following channels:

$$\mathrm{HCN} + \mathrm{HCN} \rightarrow \mathrm{CH(NH)CN}, \tag{6}$$

$$\mathrm{CH(NH)CN} + \mathrm{HCN} \rightarrow \mathrm{NH_2CH(CN)_2}, \tag{7}$$

$$\mathrm{NH_2CH(CN)_2} + \mathrm{HCN} \rightarrow \mathrm{NH_2(CN)C = C(CN)NH_2}, \tag{8}$$

$$\mathrm{NH_2(CN)C = C(CN)NH_2} + \mathrm{HCN} \rightarrow \mathrm{Adenine}. \tag{9}$$

Gupta et al. [16] have proposed following radical-molecular reaction network for the formation of adenine in the ISM:

$$\mathrm{HCCN} + \mathrm{HCN} \rightarrow \mathrm{C_3H_2N_2}, \tag{10}$$

$$\mathrm{C_3H_2N_2} + \mathrm{H} \rightarrow \mathrm{C_3H_3N_2}, \tag{11}$$

$$\mathrm{C_3H_3N_2} + \mathrm{NH_2CN} \rightarrow \mathrm{C_4H_5N_4}, \tag{12}$$

$$\mathrm{C_4H_5N_4} + \mathrm{CN} \rightarrow \mathrm{C_5H_5N_5}, \tag{13}$$

$$\mathrm{C_5H_5N_5} + \mathrm{H} \rightarrow \mathrm{C_5H_6N_5}, \tag{14}$$

$$\mathrm{C_5H_5N_5} + \mathrm{CN} \rightarrow \mathrm{Adenine} + \mathrm{HNC}, \tag{15}$$

$$\mathrm{C_5H_5N_5} + \mathrm{CN} \rightarrow \mathrm{Adenine} + \mathrm{HCN}. \tag{16}$$

Following new pathway has been proposed recently by Merz et al. [27], where adenine could be formed without using HCN as a precursor

$$\mathrm{C_3NH} + \mathrm{HNCNH} \rightarrow \mathrm{C_4N_3H_3}, \tag{17}$$

$$\mathrm{C_4N_3H_3} + \mathrm{HNCNH} \rightarrow \mathrm{C_4H_3N_3} + \mathrm{NH_2CN}, \tag{18}$$

$$C_4H_3N_3 + HNCNH \rightarrow C_4N_5H_5, \tag{19}$$

$$C_4N_5H_5 + HNCNH \rightarrow N_5C_5H_5 + NH_2CN, \tag{20}$$

$$N_5C_5H_5 + HNCNH \rightarrow \text{Adenine} + NH_2CN, \tag{21}$$

In the chemical model described in [24], the reactions (6)–(9) to (10)–(16) were included and it was concluded that the production of adenine is dominated by the radical-molecular reaction pathways. HCCN and $NH_2CN$ are the two important organic molecules, which are responsible for the production of adenine via radical-molecular reaction channels. So one could treat HCCN and $NH_2CN$ as the organic precursor for the formation of adenine in the ISM. Recently, [7] have included the new pathways from [27] in their gas-grain chemical model and concluded that the production of adenine through this pathways is also important in the ISM. They suggested that observers may look for the two new organic precursors ($C_3NH$ and HNCNH) in the star forming regions which are equally important for tracing interstellar adenine.

### 4.2.2 Glycine

One of the most fundamental debates in astrobiology concerns the possibility of finding glycine in the star forming regions. Astronomical observations of glycine are highly debated till date due to line confusions. Several gas-grain models as well as experiments were performed during past years. Chakrabarti and Chakrabarti [5] have proposed following pathways for glycine formation:

$$H_2CO + HCN \rightarrow C_2H_3ON, \tag{22}$$

$$C_2H_3ON + H_2O \rightarrow C_2H_5NO_2. \tag{23}$$

Quantum chemical calculations was performed by Woon [36] to evaluate viability of various pathways to formation of glycine, They considered following pathway:

$$HCN + H \rightarrow HCNH, \tag{24}$$

$$HCNH + H \rightarrow CH_2NH, \tag{25}$$

$$CH_2NH + H \rightarrow CH_2NH_2, \tag{26}$$

$$CO + OH \rightarrow COOH, \tag{27}$$

$$CH_2NH_2 + COOH \rightarrow C_2H_5NO_2. \tag{28}$$

According to [36], this reaction mechanisms is possible only when interstellar ices experienced thermal shocks. In the gas-grain chemical model described in [24], the reactions (22)–(23) and (24)–(28) were included and it was concluded that the production of glycine is dominated by the neutral-neutral reactions. They predicted $C_2H_3ON$ as one of the precursors of glycine formation in the ISM.

### 4.2.3 Alanine

According to [5], the alanine could be produced by the following reactions:

$$CH_3CHO + HCN \rightarrow C_3H_5ON, \tag{29}$$

$$C_3H_5ON + H_2O \rightarrow C_3H_7NO_2. \tag{30}$$

According to [36] production of alanine could follow the following reaction channels:

$$NH_2CH_2 + COOH \rightarrow NH_2CHCOOH + H, \tag{31}$$

$$NH_2CHCOOH + CH_3 \rightarrow C_3H_7NO_2. \tag{32}$$

But this mechanisms is possible only in the UV irradiated ice, which are much warmer. So this pathway is not important in the cold ISM. So neutral-neutral pathways as described by Chakrabarti and Chakrabarti [5] could be very useful. In this reaction channel, $C_3H_5ON$ reacts with highly abundant gas phase $H_2O$ to form alanine.

## 5 Survey Observations of a Glycine Precursor

Recently, [32] have reviewed the chemistry of glycine precursors in the ISM. Based on the reaction mechanism shown in Fig. 4, they identified $CH_2NH$ as a new precursor for the formation of glycine. Based on the above findings, [32]

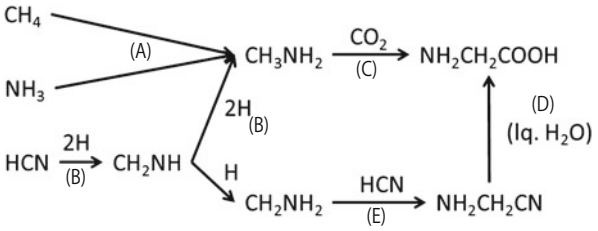



**Fig. 4** Various reaction channels for the formation of glycine [32]. "Iq" represents the hydrolysis process. References: (A)[22], (B)[33] and [36], (C)[21], (D)[30], (E) [9]

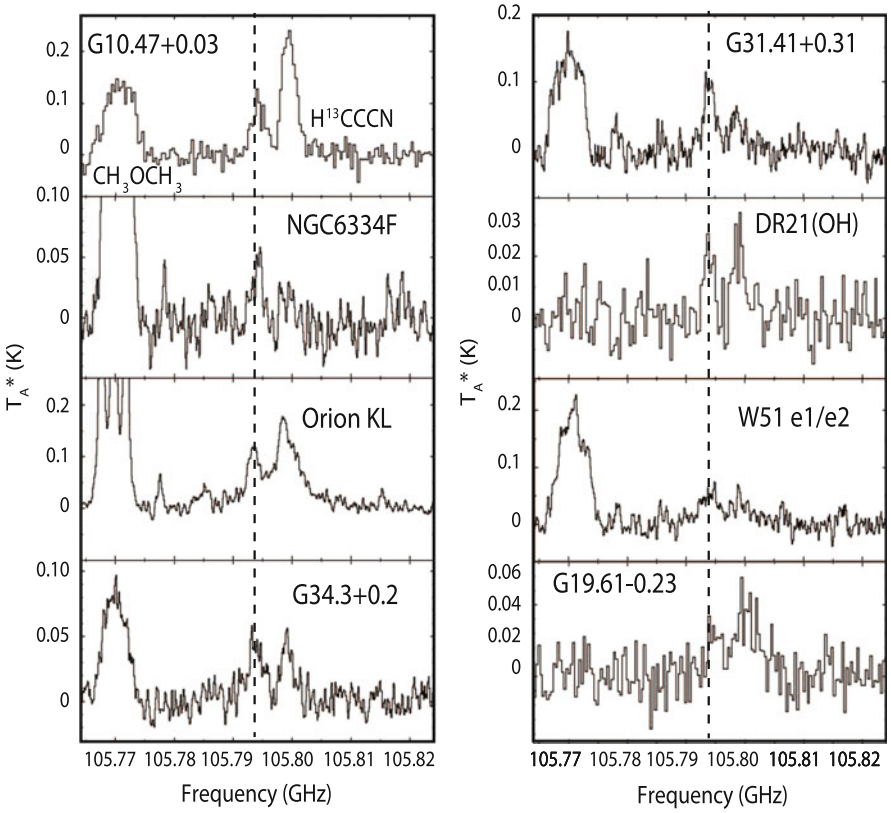



**Fig. 5** Detection of glycine precursor $CH_2NH$ towards eight high mass star forming regions from [32]. The vertical line shows the rotational transition $4_{04}$-$3_{13}$ at 105.794062 GHz

have conducted survey observations of $CH_2NH$ with the 45 m radio telescope at the Nobeyama Radio Observatory (NRO), National Astronomical Observatory of Japan in April, May, and December, 2013, and the Sub-Millimeter Radio Telescope (SMT), Arizona Radio Observatory in October, 2013. They detected $CH_2NH$ lines towards eight high mass star-forming regions as shown in Fig.5. Among them, Orion KL, W51 e1/e2, G34.3+0.15 and G19.61−0.23 are known $CH_2NH$ sources in the past surveys [14, 31]. However, [32] report the detection of the $4_{04}$-$3_{13}$ transition for the first time.

## 6 Conclusion

Chemical evolution of adenine, glycine, and alanine along with their precursor molecules are discussed in this review. Precursor molecules are within the

observational limit, and some of them were detected. It is very clear from this review that every collapsing interstellar molecular cloud would produce these biogenic molecules during their respective collapse phase. It is possible that during the planet formation, some of these biogenic molecules were destroyed due to high temperature. Subsequently, residuals of the planetary disk, such as comets which preserve these molecules deep inside their cores showered the planet much latter with these molecules and thus provided seeds of life in that planets which orbit inside so-called habitable zone. These speculations are very realistic and works are underway to quantify this line of thought.

**Acknowledgements** L. Majumdar acknowledges support from the NASA postdoctoral program. A portion of this research was carried out at the Jet Propulsion Laboratory, California Institute of Technology, under a contract with the National Aeronautics and Space Administration. L. Majumdar would like to thank Prof. Sandip K. Chakrabarti, Dr. Ankan Das and Dr. Taiki Suzuki for useful discussions on the manuscript.

## References

1. Altwegg, K., Balsiger, H., Bar-Nun, A., Berthelier, J.J., Bieler, A., Bochsler, P., Briois, C., Calmonte, U., Combi, M.R., Cottin, H., De Keyser, J., Dhooghe, F., Fiethe, B., Fuselier, S.A., Gasc, S., Gombosi, T.I., Hansen, K.C., Haessig, M., Ja ckel, A., Kopp, E., Korth, A., Le Roy, L., Mall, U., Marty, B., Mousis, O., Owen, T., Reme, H., Rubin, M., Semon, T., Tzou, C.Y., Waite, J.H., Wurz, P.: Prebiotic chemicals–amino acid and phosphorus–in the coma of comet 67P/Churyumov-Gerasimenko. Sci. Adv. **2**, e1600285–e1600285 (2016). https://doi.org/10.1126/sciadv.1600285
2. Bacmann, A., Taquet, V., Faure, A., Kahane, C., Ceccarelli, C.: Detection of complex organic molecules in a prestellar core: a new challenge for astrochemical models. Astron. Astrophys. **541**, L12 (2012). https://doi.org/10.1051/0004-6361/201219207
3. Bates, D.R.: Theory of molecular formation by radiative association in interstellar clouds. Astrophys. J. **270**, 564–577 (1983). https://doi.org/10.1086/161148
4. Belloche, A., Garrod, R.T., Müller, H.S.P., Menten, K.M.: Detection of a branched alkyl molecule in the interstellar medium: iso-propyl cyanide. Science **345**, 1584–1587 (2014). https://doi.org/10.1126/science.1256678
5. Chakrabarti, S., Chakrabarti, S.K.: Can DNA bases be produced during molecular cloud collapse? Astron. Astrophys. **354**, L6–L8 (2000)
6. Chakrabarti, S.K., Chakrabarti, S.: Adenine abundance in a collapsing molecular cloud. Indian J. Phys. B **74**, 97–99 (2000)
7. Chakrabarti, S.K., Majumdar, L., Das, A., Chakrabarti, S.: Search for interstellar adenine. Astrophys. Space Sci. **357**, 90 (2015). https://doi.org/10.1007/s10509-015-2239-1
8. Cuppen, H.M., Herbst, E.: Simulation of the formation and morphology of ice mantles on interstellar grains. Astrophys. J. **668**, 294–309 (2007). https://doi.org/10.1086/521014
9. Danger, G., Borget, F., Chomat, M., Duvernay, F., Theulé, P., Guillemin, J.C., Le Sergeant D'Hendecourt, L., Chiavassa, T.: Experimental investigation of aminoacetonitrile formation through the Strecker synthesis in astrophysical-like conditions: reactivity of methanimine ($CH_2NH$), ammonia ($NH_3$), and hydrogen cyanide (HCN). Astron. Astrophys. **535**, A47 (2011). https://doi.org/10.1051/0004-6361/201117602
10. Das, A., Chakrabarti, S.K.: Composition and evolution of interstellar grain mantle under the effects of photodissociation. Mon. Not. R. Astron. Soc. **418**, 545–555 (2011). https://doi.org/10.1111/j.1365-2966.2011.19503.x

11. Das, A., Chakrabarti, S.K., Acharyya, K., Chakrabarti, S.: Time evolution of simple molecules during proto-star collapse. New Astron. **13**, 457–467 (2008). https://doi.org/10.1016/j.newast.2008.01.003
12. Das, A., Acharyya, K., Chakrabarti, S.K.: Effects of initial condition and cloud density on the composition of the grain mantle. Mon. Not. R. Astron. Soc. **409**, 789–800 (2010). https://doi.org/10.1111/j.1365-2966.2010.17343.x
13. Das, A., Majumdar, L., Chakrabarti, S.K., Saha, R., Chakrabarti, S.: Formation of cyanoformaldehyde in the interstellar space. Mon. Not. R. Astron. Soc. **433**, 3152–3164 (2013). https://doi.org/10.1093/mnras/stt958
14. Dickens, J.E., Irvine, W.M., DeVries, C.H., Ohishi, M.: Hydrogenation of interstellar molecules: a survey for Methylenimine ($CH_2NH$). Astrophys. J. **479**, 307–312 (1997). https://doi.org/10.1086/303884
15. Ehrenfreund, P., Irvine, W., Becker, L., Blank, J., Brucato, J.R., Colangeli, L., Derenne, S., Despois, D., Dutrey, A., Fraaije, H., Lazcano, A., Owen, T., Robert, F., International Space Science Institute ISSI-Team: Astrophysical and astrochemical insights into the origin of life. Rep. Prog. Phys. **65**, 1427–1487 (2002). https://doi.org/10.1088/0034-4885/65/10/202
16. Gupta, V.P., Tandon, P., Rawat, P., Singh, R.N., Singh, A.: Quantum chemical study of a new reaction pathway for the adenine formation in the interstellar space. Astron. Astrophys. **528**, A129 (2011). https://doi.org/10.1051/0004-6361/201015557
17. Hasegawa, T.I., Herbst, E., Leung, C.M.: Models of gas-grain chemistry in dense interstellar clouds with complex organic molecules. Astrophys. J. Supp. **82**, 167–195 (1992). https://doi.org/10.1086/191713
18. Herbst, E., van Dishoeck, E.F.: Complex organic interstellar molecules. Annu. Rev. Astron. Astrophys. **47**, 427–480 (2009). https://doi.org/10.1146/annurev-astro-082708-101654
19. Hollis, J.M., Jewell, P.R., Lovas, F.J., Remijan, A.: Green bank telescope observations of interstellar glycolaldehyde: low-temperature sugar. Astrophys. J. Lett. **613**, L45–L48 (2004). https://doi.org/10.1086/424927
20. Hollis, J.M., Jewell, P.R., Lovas, F.J., Remijan, A., Møllendal, H.: Green bank telescope detection of new interstellar aldehydes: propenal and propanal. Astrophys. J. Lett. **610**, L21–L24 (2004). https://doi.org/10.1086/423200
21. Holtom, P.D., Bennett, C.J., Osamura, Y., Mason, N.J., Kaiser, R.I.: A combined experimental and theoretical study on the formation of the amino acid glycine ($NH_2CH_2COOH$) and its isomer ($CH_3NHCOOH$) in extraterrestrial ices. Astrophys. J. **626**, 940–952 (2005). https://doi.org/10.1086/430106
22. Kim, Y.S., Kaiser, R.I.: On the formation of amines ($RNH_2$) and the cyanide anion ($CN^-$) in electron-irradiated ammonia-hydrocarbon interstellar model ices. Astrophys. J. **729**, 68 (2011). https://doi.org/10.1088/0004-637X/729/1/68
23. Kuan, Y.J., Charnley, S.B., Huang, H.C., Tseng, W.L., Kisiel, Z.: Interstellar glycine. Astrophys. J. **593**, 848–867 (2003). https://doi.org/10.1086/375637
24. Majumdar, L., Das, A., Chakrabarti, S.K., Chakrabarti, S.: Hydro-chemical study of the evolution of interstellar pre-biotic molecules during the collapse of molecular clouds. Res. Astron. Astrophys. **12**, 1613–1624 (2012). https://doi.org/10.1088/1674-4527/12/12/003
25. Majumdar, L., Das, A., Chakrabarti, S.K., Chakrabarti, S.: Study of the chemical evolution and spectral signatures of some interstellar precursor molecules of adenine, glycine and alanine. New Astron. **20**, 15–23 (2013). https://doi.org/10.1016/j.newast.2012.09.002
26. McGuire, B.A., Carroll, P.B., Loomis, R.A., Finneran, I.A., Jewell, P.R., Remijan, A.J., Blake, G.A.: Discovery of the interstellar chiral molecule propylene oxide ($CH_3CHCH_2O$). Science **352**, 1449–1452 (2016). https://doi.org/10.1126/science.aae0328
27. Merz Jr., K.M., Aguiar, E.C., da Silva, J.B.P.: Adenine formation without HCN. J. Phys. Chem. A **118**, 3637–3644 (2014). https://doi.org/10.1021/jp5018778
28. Müller, H.S.P., Schlöder, F., Stutzki, J., Winnewisser, G.: The cologne database for molecular spectroscopy, CDMS: a useful tool for astronomers and spectroscopists. J. Mol. Struct. **742**, 215–227 (2005). https://doi.org/10.1016/j.molstruc.2005.01.027

29. Öberg, K.I., Guzmán, V.V., Furuya, K., Qi, C., Aikawa, Y., Andrews, S.M., Loomis, R., Wilner, D.J.: The comet-like composition of a protoplanetary disk as revealed by complex cyanides. Nature **520**, 198–201 (2015). https://doi.org/10.1038/nature14276
30. Peltzer, E.T., Bada, J.L., Schlesinger, G., Miller, S.L.: The chemical conditions on the parent body of the murchison meteorite: Some conclusions based on amino, hydroxy and dicarboxylic acids. Adv. Space Res. **4**, 69–74 (1984). https://doi.org/10.1016/0273-1177(84)90546-5
31. Qin, S.L., Wu, Y., Huang, M., Zhao, G., Li, D., Wang, J.J., Chen, S.: High-resolution submillimeter multiline observations of G19.61 - 0.23: small-scale chemistry. Astrophys. J. **711**, 399–416 (2010). https://doi.org/10.1088/0004-637X/711/1/399
32. Suzuki, T., Ohishi, M., Hirota, T., Saito, M., Majumdar, L., Wakelam, V.: Survey observations of a possible glycine precursor, methanimine (CH2NH). Astrophys. J. **825**, 79 (2016). https://doi.org/10.3847/0004-637X/825/1/79
33. Theule, P., Borget, F., Mispelaer, F., Danger, G., Duvernay, F., Guillemin, J.C., Chiavassa, T.: Hydrogenation of solid hydrogen cyanide HCN and methanimine $CH_2NH$ at low temperature. Astron. Astrophys. **534**, A64 (2011). https://doi.org/10.1051/0004-6361/201117494
34. Walsh, C., Loomis, R.A., Öberg, K.I., Kama, M., van 't Hoff, M.L.R., Millar, T.J., Aikawa, Y., Herbst, E., Widicus Weaver, S.L., Nomura, H.: First detection of gas-phase methanol in a protoplanetary disk. Astrophys. J. Lett. **823**, L10 (2016). https://doi.org/10.3847/2041-8205/823/1/L10
35. Woodall, J., Agúndez, M., Markwick-Kemper, A.J., Millar, T.J.: The UMIST database for astrochemistry 2006. Astron. Astrophys. **466**, 1197–1204 (2007). https://doi.org/10.1051/0004-6361:20064981
36. Woon, D.E.: Pathways to glycine and other amino acids in ultraviolet-irradiated astrophysical ices determined via quantum chemical modeling. Astrophys. J. Lett. **571**, L177–L180 (2002). https://doi.org/10.1086/341227
37. Woon, D.E., Herbst, E.: Quantum chemical predictions of the properties of known and postulated neutral interstellar molecules. Astrophys. J. Supp. **185**, 273–288 (2009). https://doi.org/10.1088/0067-0049/185/2/273

# One Supervisor and Three Different Topics to Choose from: My Choice and Subsequent Progress




**Kinsuk Acharyya**

**Abstract** Interstellar dust grains play a crucial role in the chemical evolution of star-forming regions. These grains exist in various sizes and also grow over time due to the formation of grain mantle. In recent times efforts were made to understand how different sized-grains take part in the formation of molecules. We considered two widely used size distributions from earlier models. To incorporate various grain sizes in the model, the distribution is divided into a number of logarithmically equal spaced ranges. Then each range is integrated to find its number density, and assigned that number density to the average size of that range. We started by studying the effect of size distribution in the production of molecular hydrogen in the diffuse interstellar medium. We found that $H_2$ formation efficiency is a function of grain radius and total effective surface area available for a given distribution. When we used fixed temperature for each size based on earlier works, we found that contribution from smaller grain is less since they have higher grain temperature, whereas when temperature fluctuation due to the stochastic heating of the grain is considered, smaller grains contribution increases significantly. We also found that $H_2$ formation rate strongly depends on the surface property and its topology, the mechanism for the reaction, as well as on the type of binding of H (e.g., without chemisorption sites $H_2$ formation at high temperature is very low). Molecular abundances of species, e.g., CO, $H_2O$, etc., in the dense clouds, are effected by the use of size distribution and grain growth over time. However, when the comparison between model abundances and observed abundances are made, it did not lead to the better agreement, and more study is needed.

K. Acharyya (✉)
Physical Research Laboratory, Ahmedabad, India
e-mail: acharyya@prl.res.in

© Springer International Publishing AG, part of Springer Nature 2018

B. Mukhopadhyay, S. Sasmal (eds.), *Exploring the Universe: From Near Space to Extra-Galactic*, Astrophysics and Space Science Proceedings 53,
https://doi.org/10.1007/978-3-319-94607-8_35

## 1 Introduction

It is a great pleasure to contribute to this special issue of Springer, in honour of Prof Sandip Chakrabarti, whose important research in accretion around compact objects, astrochemistry, and atmospheric sciences had a profound impact on these subjects. It was early days in Centre for Space Physics (presently called Indian Centre for Space Physics or ICSP), a newly established research institute by Prof. Chakrabarti; several important research topics were initiated. I had an opportunity to work in three different topics, namely, Very Low Frequency (VLF) observation of Leonid shower and Sudden Atmospheric Disturbance (SID), accretion around compact objects, and formation of molecules during star formation. First I briefly mention our work on the first two topics in the subsequent paragraphs of this section and then discuss the last topic in detail which eventually became my Ph.D. topic.

Ionizing sources external to the earth produces Sudden Ionospheric Disturbances (SID). By studying them, it is possible to obtain information such as the rate at which these types of events occur in nature and can also help to locate these sources. In one of the first experiments at ICSP, Very Low Frequency (VLF) signals were continuously monitored using loop Antenna for various events. In one such event, Leonid shower was observed. Mainly two types of signals were detected throughout the entire observation. One is 'bead'-like, and the other is exponentially decaying. Our observations were at a frequency far away from previously reported observations and confirmed that the meteors also generate VLF signals at 19 KHz during their entry into earth's atmosphere [3]. In another study, continuous observations of VLF signal due to solar flares were made. We compared the effects of solar flares of the VLF signal with those obtained by GOES Satellite of NASA monitoring X-rays and found excellent agreement [4]. We were also able to see substantial anomalous shifts in the sunset-terminator possibly due to the strong earthquake in another such continuous observation [6].

In another project, I got interested in finding oscillating behaviour of accretion disks. Accretion onto a black hole is assumed to be thin and axisymmetric. Non-axisymmetric instabilities can develop in an accretion due to the presence of a companion due to the self-gravity of the disk or to the gravity of the companion. Using numerical simulation, we demonstrated that a new kind of instability could be found in the accretion disk due to the interaction between the accreting matter and the outflowing wind generated from the accreting flow at the centrifugal barrier. The interface region between these two flows become unstable due to the shear instability or Kelvin-Helmholtz instability which is independent of the polytropic index or cooling mechanism in the flow. In the presence of rotation, this instability is not symmetric with respect to the equatorial plane [17, 18]. In a separate work, we found that due to both radial and vertical oscillation of shock waves in the accretion flow, the luminosity and average thermal energy content of the inner disk exhibit very interesting behavior. We found quasi-periodic variabilities between few Hz to hundreds of Hz in the power density spectra of a stellar-mass black hole,

whereas, the time scale for oscillations varies between few hours to the week for a supermassive black hole. The power density spectra have a flat top behavior with average RMS amplitude of a few percents. The major results appeared in [5].

I will discuss my research work in astrochemistry. Astrochemistry is 'the study of formation, destruction, and excitation of molecules in astronomical environments and their influence on the structure, dynamics, and evolution of astronomical objects" [9]. We have studied the formation of several molecules with an emphasis on the formation of molecular hydrogen which is by far the most abundant molecule. One important aspect that we introduced in the study is the effect of grain size distribution on the production of molecules. The remainder of the article will discuss this aspect, in which results were summarized primarily from [1, 2, 14]. In the next section, I will discuss various size distributions, and how it could be incorporated in the study of the formation of molecules in the star-forming regions. Then in Sect. 3, results found from such simulations will be discussed and finally, concluding remarks will be made in Sect. 4.

## 2 Size Distribution of Grains and Its Implementation in the Astrochemical Models

Interstellar dust grains are about 1% by mass compared to the gas and distributed in various sizes. However, most astrochemical models consider single size so-called "classical" grains, having a radius of 0.1 μm, posses $\sim 10^6$ binding sites, and with a number density of ($n_d$) $1.33 \times 10^{-12}$ $n_H$, where $n_H$ is the hydrogen number density in all forms. Grain surface chemistry is mostly handled by rate equations with a grain mass density of $3\,g\,cm^{-3}$. These grains can grow bigger with time due to accretion and formation of molecules on the grain surface. We developed a numerical simulation code to tackle such problems, and for the first time, we examined the effect of grain growth and grain size distribution on the chemical evolution of diffuse and dense interstellar medium (ISM). We considered two very well-known size distribution models as follows.

1. The Mathis, Rumpl, and Nordsieck (MRN) model: It is the simplest grain size distribution which can produce functional dependence of wavelength in the extinction. The normalized number density of grains having radii between a and a + da is given by the following expression:

$$dn_{gr} = Cn_H a^{3.5} da, \quad 50\,\text{Å} < a < 0.25\,\mu\text{m} \tag{1}$$

where $n_{gr}$ is the grain concentration, and C is the grain constant having a value of $10^{-25.11}\,cm^{2.5}$ for silicates and $10^{-25.13}\,cm^{2.5}$ for graphite according to [22]. Since there is almost no difference between the two constants, we utilized the one for silicates only and designated as MRN model in subsequent discussions [16].

2. Weingartner and Draine Model: In the Weingartner and Draine (WD) Model, silicate and carbonaceous distribution is different and covers the entire range. It is valid for grain sizes bigger than 3.5 Å and applicable for Milky Way, Large Magellanic Cloud (LMC), and Small Magellanic Cloud (SMC). The functional nature of the WD is complicated and contain many parameters such as reddening, carbon abundance, etc., with three humps for carbonaceous grains [22]. Since for WD model, silicate and carbonaceous distribution are different we considered them separately and designated WDs and WDc respectively throughout the discussion.

Along with a common gas phase, to study the effect of size distribution, one needs to consider chemistry on each differently sized grain which increases the computation time significantly especially when the various types of Monte-Carlo methods are considered. To manage computational time better we need to keep two things in mind. First, larger the size of the grains longer is the time to compute the abundance. Secondly, size distribution essentially refers to an infinite number of sizes hence one needs to consider a reasonable number of grains. In our first publication, we chose three major grain sizes where there are humps in WD distribution [1]. Subsequently, we used a different method in which we divided the entire grain size distribution to be studied into a number of logarithmically equally spaced regions ($n_{nr}$). To find the total grain number density, we integrated the relevant distribution in each range, and assigned that number density to the average size in that range. We decided the value for $n_{nr}$ based on regions we are studying [2, 14]. A similar approach is also considered by other authors [12, 19]. In Fig. 1a, we plotted the integral grain number density for various size ranges from a minimum radius of 0.005 μm to assorted maximum radii, using the WD size distributions when $n_H = 1\ cm^{-3}$. It is clear that the contributions of bigger grains are very small. Therefore, when we studied the $H_2$ formation in the diffuse clouds using the continuous-time random-walk Monte-Carlo technique, we neglected the grain sizes bigger than 0.25 μm. Considering the complexity of the WD distribution, we need to find an optimum number of grains ($n_p$) between the minimum and maximum radii without introducing error in the total integral number density of grains. To find $n_p$, we divided the entire range of sizes to be studied by various values of $n_{nr}$ (e.g., 5, 10, 15, 30 . . . 480) and determined the total grain number density in each range as shown in Fig. 1b. We found that for $n_{nr} \geq 60$ there is no appreciable change in the integrated grain number density. Therefore, it was concluded that at least 60 numbers of points should be considered while implementing the WD distribution. In some of our initial studies, we considered less number of points which overestimates total number density by a factor of 1.5–2.

In this context, a very important parameter is effective cross-section which is the product of actual grain cross-section for a given size and number density of that size. For example, bigger grains will have larger cross-section but much smaller in numbers whereas, the smaller grain will have a smaller cross-section, but they might be larger in number. Therefore, the product of these two quantities plays a crucial role. The total effective cross section for each distribution is the sum of

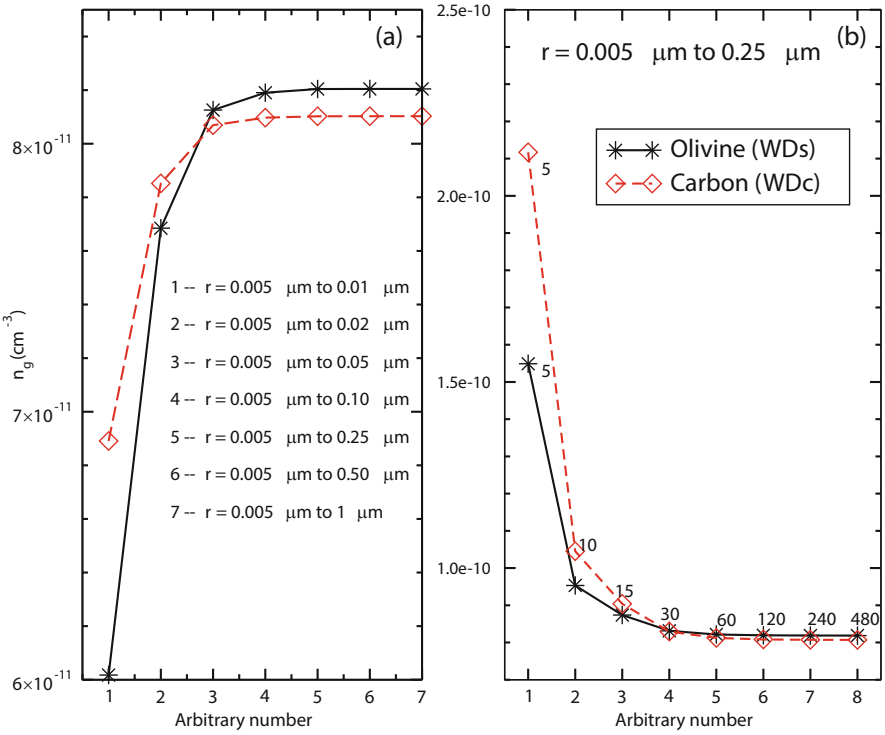



**Fig. 1** Panel (**a**) and (**b**) shows integrated grain number density ($n_{gr}(r)$) over various ranges marked as 1, 2 . . . , 7 and for various $n_{nr}$ in between 0.005 μm and 0.25 μm respectively [14]

the effective cross-section for each size. For MRN and WDc models, we found that the smaller grains are having, the larger effective area, whereas, for WDs grains, intermediate size grains have largest effective surface area. Regarding total effective cross-section, MRN models have largest followed by WDs and WDc [2, 14].

## 3 Results

We have studied the effect of several grain size distributions on the chemical evolution of diffuse and dense ISM. Results primarily consist of efficiencies, rates, and rate coefficients of $H_2$ formation as a function of grain sizes in the diffuse ISM. In the models for dense ISM, we have also studied effect of grain growth, and discuss abundances from various size distributions, relative contributions of various grain sizes, and finally, model abundances are compared with the observed abundances.

### 3.1 $H_2$ Formation

Molecular hydrogen is the most abundant molecular species in the Universe. In the diffuse and dense ISM, it primarily forms on the grain surface. Several different processes are possible. In Langmuir–Hinshelwood (LH) mechanism, a hydrogen atom adsorbs onto a grain surface and diffuses due to its thermal energy and forms molecular hydrogen when it meets another H atom. The newly formed $H_2$ molecule can be ejected to the gas phase immediately or via various thermal and non-thermal desorption processes. Molecular hydrogen can also be formed via Eley-Rideal (ER) mechanism, in which a hydrogen atom from the gas-phase directly hits another H-atom on the grains. There is also the hot-atom mechanism, in which H-atoms can recombine efficiently due to the non-thermal diffusion. The $H_2$ formation efficiency can be calculated as follows:

$$\eta = \frac{2\mathrm{N_{H_2}}}{\mathrm{N_H}}, \tag{2}$$

where, $\mathrm{N_{H_2}}$ is the total number of $H_2$ formed and $\mathrm{N_H}$ is the number of H-atoms striking the grain within a specific time, which is a function of grain cross-section. Therefore, efficiencies should be calculated for all grain sizes. Two other important parameters in this context are the rate constant and total rate. The rate coefficient $\kappa$ ($\mathrm{cm^3\,s^{-1}}$) is defined through the following equation:

$$\mathrm{d[H_2]/dt} = \kappa \mathrm{n(H) n_H}, \tag{3}$$

where, $\mathrm{n}(H)$ is the concentration of H-atoms and $\mathrm{n_H}$ is the overall concentration of protons. The value of $\kappa$ is calculated as follows:

$$\kappa = \frac{\int_{r_{min}}^{r_{max}} \frac{1}{2}\, v_H\, \eta\, \xi\, \sigma_{\mathrm{gr}}\, [dn_{\mathrm{gr}}(r)/dr]\, dr}{n_{\mathrm{H}}}, \tag{4}$$

where, $\mathrm{n_{gr}(r)}$ is the grain number density as a function of radius r, $\sigma_{\mathrm{gr}}$ is the cross section of grains, $\mathrm{v_H}$ is the thermal speed of gas-phase H-atoms, $\eta(r)$ is the efficiency of reaction as described by Eq. (2), $\xi$ is the temperature dependent sticking coefficient of H-atoms [11], and the integration is over all granular radii from a minimum to a maximum. Finally, the total rate $\mathrm{R_{H_2}}$ ($\mathrm{cm^{-3}\,s^{-1}}$) for $H_2$ formation is calculated via following equation

$$R_{H_2} = \int_{r_{min}}^{r_{max}} \frac{1}{2}\, n(H)\, v_H\, \eta\, \xi\, \sigma_{\mathrm{gr}}\, [dn_{\mathrm{gr}}/dr]\, dr. \tag{5}$$

It may be noted that the total rate contains the concentration of gaseous H-atom which is a function of time; hence total rate is also a function of time. However, $\kappa$ does not have explicit time dependence.

### 3.1.1 $H_2$ Formation in Static and Collapsing Clouds

In the first paper of the series, we studied $H_2$ formation following LH mechanism using rate equation (it tracks the average number of various species and less computationally intensive) and master equation (which follows the expectation values of various species and more computationally expensive) for static and collapsing clouds using three different grain sizes (0.001, 0.0034, and 0.022 μm). We have shown that above a critical accretion rate both the rate equation and master equation gives the same result. Then we studied $H_2$ formation during the collapse of a dense ISM for two different temperatures, masses (1 and 10 $M_\odot$), and for olivine (10 and 15 K) and carbonaceous grains (20 and 25 K) following WD model. We found that for olivine grains, 90% of $H_2$ can be formed between $10^5$ and $10^7$ years, whereas for carbon grains it is between $10^6$ and $10^7$ years [1].

### 3.1.2 $H_2$ Formation in Diffuse Clouds

Diffuse clouds are the relatively low density (number density varies between 1 and 100 $cm^{-3}$) regions of the ISM in which stellar UV radiation can penetrate. Although $H_2$ formation is studied extensively, it is still not fully understood. In presence of the distribution of grain sizes, the average number of hydrogen atoms on smaller grains will be less than unity; therefore, rate equation approaches break down, and also interstellar grain surfaces could be rough. We employed continuous-time random-walk (CTRW) Monte-Carlo technique to address these problems [13, 14].

The efficiency of $H_2$ formation is a strong function of different grain materials as suggested by the laboratory experiments and its subsequent analysis [15, 20, 21]. Therefore, we studied $H_2$ formation for three different grain materials, olivine, amorphous silicates and amorphous carbon. The diffusion and desorption barrier energy of hydrogen for olivine are 287 and 373 K respectively, for amorphous silicate it is 406 and 510 K, and for the amorphous carbon, they are 511 and 658 K [15]. Formation efficiency is also dependent on the nature of the binding sites involved. In our work, we used four different surfaces involving physisorbed and chemisorbed sites. The "flat" having only one type of binding sites due to physisorption, "rough" having five different types of binding sites for physisorption. Other two surfaces are having strongly bound chemisorption sites. In one, the hydrogen atom is first physisorbed then it goes to a chemisorbed site with a binding energy of 10,000 and 14,000 K for olivine and amorphous carbon, respectively. In other, it goes directly to a chemisorbed site for which we considered two different barriers, 25 meV (290 K) and 162 meV (1880 K), respectively. All the calculations were done for hydrogen atomic flux corresponding to three different number densities: $n_H$ = 1, 10 and 100 $cm^{-3}$.

We employed parallel computation and used 78 different grain sizes between 0.005 and 0.25 μm. Each grain size is run in a different CPU and information is exchanged using MPI (Message Passing Interface) scheme. All the grains were evolved simultaneously and interacted with each other after certain time step "dt"

for which gas phase abundances is assumed to be constant. Initially, we kept the gas temperature to be 90 K and fixed grain temperature depending upon grain size (smaller the grains higher is the temperature) from the available literature.

For the flat surface models with the different surface material, we found that the $H_2$ formation efficiency increases with the increase in grain size up to a certain extent and strongly dependent on the flux of H-atom. We found that both amorphous silicate and amorphous carbon grain surface show efficient $H_2$ formation. For bigger grains, efficiency can be unity. For olivine grains smaller than 0.02 μm, for $n_H = 1$ and $10\,cm^{-3}$ models does not show noticeable $H_2$ production even in $10^7$ years. For both the MRN and WD distributions and for both the olivine and amorphous silicate, the rate of molecular hydrogen formation becomes almost independent of grain size when grain radii are $\geq$0.1 μm. For amorphous carbon, this lack of size dependence comes at a lower grain radius. The integrated rate coefficient for olivine varies between $10^{-22}$ and $10^{-24}\,cm^3\,s^{-1}$, for amorphous silicates between $3.2 \times 10^{-19}$ and $2.4 \times 10^{-18}\,cm^3\,s^{-1}$, and for amorphous carbon $9.2 \times 10^{-19}$ and $4.1 \times 10^{-17}\,cm^3\,s^{-1}$. When these values are compared with the standardly used values of $10^{-17}\,cm^3\,s^{-1}$, these values lie between 5–7 orders and 1–2 orders of magnitude less for olivine and amorphous silicate grains respectively; whereas, amorphous carbon rates vary between a factor of five higher to one order of magnitude lower. Incorporation of rough surface models in which range of desorption energies and diffusion barriers are used can improve $H_2$ formation on the olivine grains; however, the rate is still not adequate to explain observed $H_2$ production for these types of grain surfaces. When we turned our attention to the total rate of recombination, we found that it decreases with decreasing grain size despite smaller grains having higher number density, due to its higher grain temperature.

To explain molecular hydrogen formation at high temperatures, one needs to take account of its formation via chemisorption processes. Cazaux and Tielens [8], showed that the molecular hydrogen formation is efficient until quite high (∼500 K) temperatures. However, they have used standard rate equation approach which breaks down in the low-density regions of ISM. A hydrogen atom can occupy chemisorption sites in two possible ways, in one it first lands on shallow physisorbed site which does not have a barrier, and then tunnels/hops to the chemisorbed site, and in the other, it directly lands on chemisorbed site by overcoming the barrier. Using the first method, we found $H_2$ production improved significantly even for low-density models ($n_H = 1$ and $10\,cm^{-3}$). This considerable improvement can be attributed to the fact that the residence time of H-atoms increased significantly due to the incorporation of chemisorption sites which resulted in an increase of $H_2$ formation efficiency, even for the smaller grain which has higher grain temperatures. It was also found that for the MRN and carbonaceous grains for WD distributions, the maximum contribution for $H_2$ production occurs for smaller grains; whereas, olivine grains for WD distribution, the maximum contribution is from medium-size grains. This is in contrast with grains having only physisorbed sites. For the second model where hydrogen atoms directly go to the chemisorbed site, we found a nearly constant efficiency of 0.6 when barrier for chemisorption is 25 meV and 0.13 when this barrier is 162 meV.

We examined $H_2$ formation when grains are stochastically heated instead of assuming fixed temperature as discussed in the earlier paragraphs. In reality, the temperature of the smaller grains in diffuse clouds will fluctuate significantly due to the interaction with stellar UV photons. When a photon hits a grain surface, the grain temperature will rise rapidly for a short period. Subsequently, the dust grain will cool down in much longer scale. We treated the photon interaction with the grains following [7]. Figure 2 shows the temperature variation of three different sizes of grains to illustrate this phenomenon. Two important aspects to note: (1) we see more temperature spikes on the bigger grains since the number of photons hitting the grain increases with its cross-section; (2) smaller the grain size higher is the temperature spike.

We found that this heating and cooling of the grains have a profound impact on the $H_2$ formation. The $H_2$ formation efficiency, rate, and the total recombination rate is shown in Fig. 3. We found that an increase in the efficiency for both silicate grains when compared with the efficiencies with only physisorption sites and grains

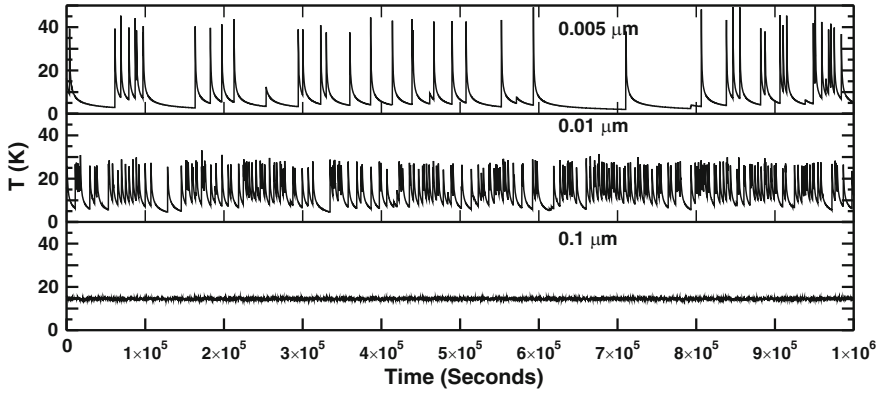



**Fig. 2** It shows temperature fluctuations for three different grain sizes in the diffuse interstellar medium [14]

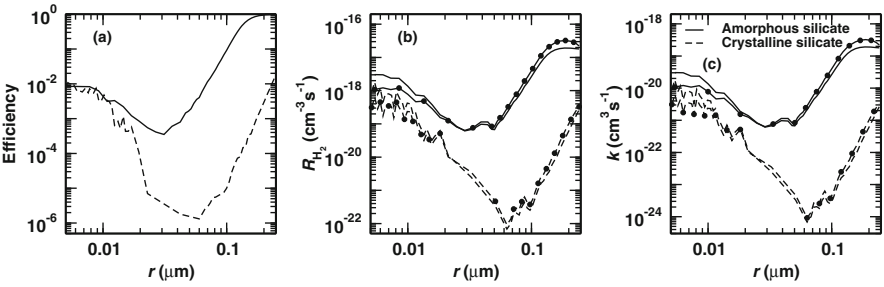



**Fig. 3** (**a**) Formation efficiency ($\eta(r)$), (**b**) total rate ($R_{H_2}$) and (**c**) rate coefficient ($\kappa$) for $H_2$ formation as a function of grain radius for models with temperature fluctuation ($n_H = 10\,cm^{-3}$) is shown. Flat surfaces for olivine and amorphous silicate are considered for the plot [14]

having a fixed temperature. When efficiency for different grain sizes are compared, a large increase in the efficiency for both olivine and amorphous silicate above 0.05 and 0.02 μm respectively can be seen. We have run models for physisorption mediated chemisorption process also but could not find any noticeable difference in the efficiency of $H_2$ formation, since once an H-atom reaches to a chemisorption site, it stays there up to a much higher temperature than the peak temperature generated from the temperature fluctuation.

### 3.1.3 Effect of Size Distribution in the Formation of Molecules in the Dense ISM

Dense interstellar medium is a rich reservoir of simple and complex molecules (having six or more atoms for this context). The grain surface chemistry is key to the understanding of the formation of these molecules. Therefore, incorporation of grain size distribution in the astrochemical models of dense ISM is essential. Motivated by this we introduce five different sized grains (0.008, 0.0175, 0.038, 0.0833, and 0.182 μm) for both the MRN and WD distribution, instead of a single so-called classical grain in the study of the chemical evolution of dense ISM [2]. It increased the total number of grain surface reactions by fivefold since all the grains are needed to be coupled separately to the gas phase. The abundance of each grain is summed up to find the total grain surface abundance. Then we compared our results with the observed abundances in L134 and TMC 1. For the WD size distribution, silicate (WDs) and carbonaceous (WDc) grains are studied separately since their distribution is different. We have chosen parameters from Table 1 of [22] which are suitable for a dense interstellar cloud: Rv = 5.5, Case A, and $b_c = 3 \times 10^{-5}$. We also incorporated the increase in grain size (or grain growth) due to the formation of grain mantle. We considered the so-called low metal elemental abundance, except $H_2$, all are atomic. We considered a density of, $n_H = 2 \times 10^4\ cm^{-3}$, visual extinction ($A_V$) = 10 mag, cosmic-ray ionization rate ($\zeta$) = $1.3 \times 10^{-17}\ s^{-1}$, sticking coefficient (S) = 0.5, and gas and grain temperature for all sizes to be 10 K. We do not expect temperature fluctuations since stellar UV radiation is blocked due to higher visual extinction in the dense ISM. We also assumed that the physical conditions remain constant and homogeneous throughout the entire time evolution of the chemical species. We restrain our discussion to carbon monoxide, which is formed mainly in the gas, and water, which is formed mainly on grains, to simplify the discussion. More detail discussion for a wide range of molecules can be found in [2]. All the abundances are relative to the total hydrogen density.

We found that due to mantle formation classical grains can grow by ∼35% and attains a steady size by $2 \times 10^6$ years, which causes greater depletion of CO-like molecules compared to the models without the grain growth. Higher depletion results in lower gas-phase abundance but higher grain surface abundance. Water surface abundances are almost not affected, but we found slightly higher water abundance in the gas-phase. When calculations were done with size distributions, we found that for all models (MRN, WDs, and WDc) size distribution is substantially

modified due to the growth of grains and in each size range, it differs among the three distributions because of differential accretion rates, although relative surface area remains similar. We found that the total effective area in the size distributions increased by factors of three to eight due to grain growth which is significantly higher when compared to the grain growth of classical grains. Therefore the change in abundance due to the grain growth should be more severe when a size distribution is used.

We found that the gas phase abundance of CO up to about $10^5$ years is similar for all the models, after that it begins to diverge when abundances begin to decrease due to the depletion. We found that peak gas-phase abundance of CO with and without grain growth comes for the WDs and WDc models respectively, whereas, MRN model have least peak abundance. It is mainly due to depletion of CO on grains since MRN model has the largest total effective area it has the largest depletion. Total effective surface area increases for models with grain growth, therefore, they show more depletion than the models without grain growth. We found that the gas phase abundances of molecules like CO are affected by grain-size distributions and their growth due to the coupling with grains via accretion and desorption. Figure 4 (top panel) shows the total abundance (circles) of surface CO as well as the contributions from all the five sizes of grain and for all the three size distributions in the presence of grain growth. For MRN model, it is clear that the grains having the smallest size

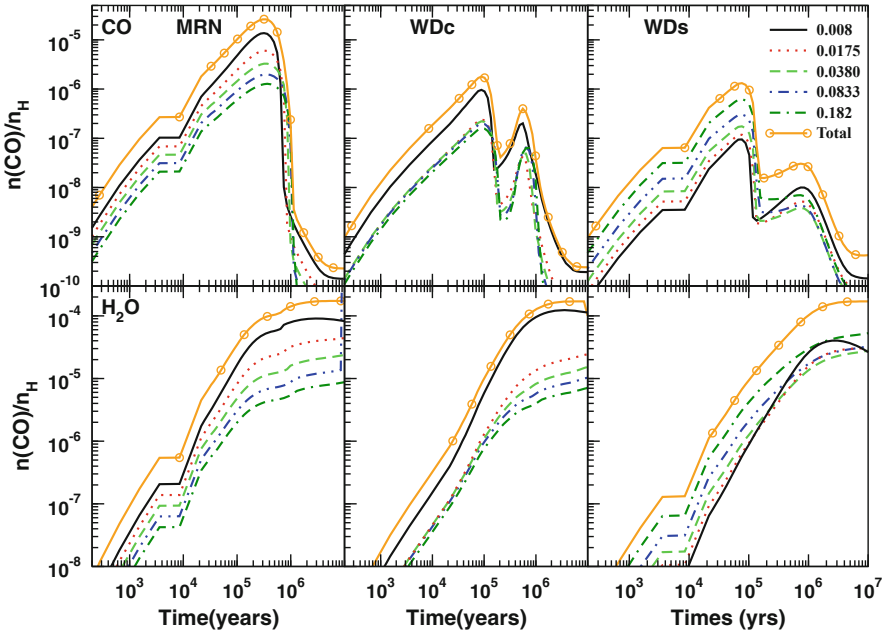



**Fig. 4** Grain-surface abundance of CO (top panel) and $H_2O$ (bottom panel) for different grain-size distributions with grain growth taken into account (radius is in μm). Both the panels have same legends [2]

have the largest contribution. Relative contribution goes down with the increase in grain sizes, primarily due to the lower effective surface area associated with them. However, at the late times, the pattern is more complex. For the Wdc models, for which number of small grains is the largest, its relative contribution to the total abundance is also significantly larger than the other sizes. Contributions from other sizes are very similar throughout the study. Finally for WDs grains for which, relatively larger size had the highest effective area gives the largest contribution, which decrease with the decrease in grain size.

Figure 4 (bottom panel) shows the abundance variation of surface water for all distributions and all the sizes. Water is abundantly formed in all the models, and peak surface abundance is very similar for all the models although at shorter times different distributions give different fractional abundances due to the difference in the total effective area, which goes away when the simulation is continued till $10^7$ years. In fact, we found that the effect of size distribution in the abundance of the surface species like water is relatively weaker. Then we have seen the contribution from each size, the similar trend is observed as for CO. Since surface species must be produced from the species need to be accreted to the grain first, the situation is more complex than the gas phase species.

Finally, we tried to see if incorporation of size distribution and grain growth can improve the model results towards better explaining the observed abundances. Model results were compared with the two sources called L134 and TMC1. To determine overall agreement between model and observed abundance, we used the "mean confidence level" method as described by Garrod et al. [10], where the "confidence" ($k_i$), calculated using error function. We found that, although individual species can be better matched with their observed abundance, overall agreement is about 0.3, and comes around $10^5$ years for all models. It was also difficult to distinguish between different models. Therefore, we concluded that the consideration of size distribution and grain growth is a more realistic approach; however, its effectiveness in explaining observed abundance better cannot be guaranteed. We need more such studies to understand the effect of size distribution better.

## 4 Concluding Remarks

In a series of publications, for the first time, the effect of size distribution in the production of molecular hydrogen, and other molecules are shown. We also provided a framework to incorporate grain size distribution in the astrochemical modeling. In this context, we found that total effective surface area is a key parameter in the understanding of the effect of size distribution. We found that the relative contribution in the total abundances of species from various grain size is different for different size distribution. We found that grain surface material, physical conditions, nature of binding sites, grain topology also play a crucial role in understanding molecular abundances. These studies also generated interest among

other groups to understand various aspects of size distribution better. Recently, the effect of grain size and temperature distributions on the formation of ice mantles was studied by Pauly and Garrod [19], and importance of cosmic-ray-induced desorption in determining the chemical abundances in the ISM has been studied using a multi-grain model by Iqbal and Wakelum [12].

**Acknowledgements** I wish to acknowledge Prof. Sandip K. Chakrabarti, for his constant guidance and inspiration during my Ph.D. and after that, I thank Prof. Eric Herbst, and my student Dr. Wasim Iqbal, who were my collaborators in the work that I presented in the article, without there help and active support, this work would not have been complete.

## References

1. Acharyya, K., Chakrabarti, S.K., Chakrabarti, S.: MNRAS **361**, 550 (2005)
2. Acharyya, K., Hassel, G., Herbst, E.: ApJ **732**, 72 (2011)
3. Chakrabarti, S.K., Pal, S., Acharya, K., Mandal, S., Chakrabarti, S., Khan, R., Bose, B.: Ind. J. Phys. **76B**, 693 (2002)
4. Chakrabarti, S.K., Acharya, K., Bose, B., Mandal, S., Chatterjee, A., Nandi, N.M., Pal, S., Khan, R.: Ind. J. Phys. **77B**, 173 (2002)
5. Chakrabarti, S.K., Acharya, K., Molteni, D.: Astron. Astrophys. **421**, 1 (2004)
6. Chakrabarti, S.K.,Saha, M., Khan, R., Mandal, S., Acharyya, K., Saha, R.: Indian J. Radio Space Phys. **34**, 314 (2005)
7. Cuppen, H.M., Morata, O., Herbst, E.: MNRAS **367**, 1757 (2006)
8. Cazaux, S., Tielens, A.G.G.M.: ApJ **604**, 222 (2004)
9. Dalgarno, A.: ARA&A **46**, 1 (2008)
10. Garrod, R.T., Wakelam, V., Herbst, E.: A&A **467**, 1103 (2007)
11. Hollenbach, D., McKee, C.F.: ApJS **41**, 555 (1979)
12. Iqbal, W., Wakelum, V.: A&A **615**, 20 (2018)
13. Iqbal, W., Acharyya, K., Herbst, E.: ApJ **751**, 58 (2012)
14. Iqbal, W., Acharyya, K., Herbst, E.: ApJ **784**, 139 (2014)
15. Katz, N., Furman, I., Biham, O., Pirronello, V., Vidali, G.: ApJ **522**, 305 (1999)
16. Mathis, J.S., Rumpl, W., Nordsieck, K.H.: ApJ **217**, 425 (1977)
17. Molteni, D., Fauci, F., Gerardi, G., Bisikalo, D., Kuznetsov, O., Acharya, K., Chakrabarti, S.K.: J. Korean Astron. Society **34**, 247 (2001)
18. Molteni, D., Acharya, K., Kuznetsov, O., Bisikalo, D., Chakrabarti, S.K.: ApJL **563**, L57 (2001)
19. Pauly, T., Garrod, R.T.: ApJ **817**, 146 (2016)
20. Pirronello, V., Biham, O., Liu, C., Shen, L.,Vidali, G.: ApJ **483**, L131 (1997)
21. Pirronello, V., Liu, C., Shen, L., Vidali, G.: ApJ **475**, L69 (1997)
22. Weingartner, J.C., Draine, B.T.: ApJ **548**, 296 (2001)

# Explaining Major Sources of Sulfur-Bearing Molecules in the Interstellar Medium




**Prasanta Gorai**

**Abstract** Despite the lower abundance of sulfur, it owns a pivotal part in the interstellar chemistry. Sulfur-bearing molecules are utilized to investigate the physical property and determine the age of a star-forming region. The major sulfur reservoir of the Interstellar medium (ISM) is a long-standing mystery. In the diffuse region, the abundance of sulfur seemed to be cosmic but in the dense cloud, it significantly deviates from the cosmic sulfur abundance ($\sim 10^{-5}$). In last few decades, various simple sulfur-bearing molecules were observed in different regions of the ISM or circumstellar shells. Among the complex sulfur yielding species, methanethiol (**$CH_3SH$**) has been firmly detected in the ISM. Investigations are going on for the discovery of the more complex sulfur species. Tentative detection of ethanethiol (**$C_2H_5SH$**) in the ISM has been recently reported. Based on this trend, we investigated the formation of higher order alcohols and their analogous sulfur species. Quantum chemical calculation has been employed to find out the most stable conformer of higher order alcohols and their sulfur analogues and their formation pathways under interstellar conditions. Kinetic information obtained from the quantum chemical calculations can be used in gas-grain chemical modeling to study the chemical evolution of these alcohols and thiols.

## 1 Introduction

After the Big Bang nucleosynthesis, within first 3 min, significant amount of hydrogen and helium and a trace amount of lithium were created. Later, all the heavier elements were formed during star formation process or by the supernovae explosions. Though sulfur is the tenth abundant element in the Milky Way, it has the significant impact on the Interstellar chemistry. CS is the first sulfur bearing molecule which was observed in space by Penzias et al. [33]. Charnley [6], Hatchell

P. Gorai (✉)
Indian Centre for Space Physics, Kolkata, India

© Springer International Publishing AG, part of Springer Nature 2018

B. Mukhopadhyay, S. Sasmal (eds.), *Exploring the Universe: From Near Space to Extra-Galactic*, Astrophysics and Space Science Proceedings 53,
https://doi.org/10.1007/978-3-319-94607-8_36

et al. [18] first proposed that $SO/SO_2$ and $SO/H_2S$ ratio can be correlated with different astrophysical contexts (such as dark cloud, hot-core, shocked region etc.). They suggested that these ratios can be used as a chemical clock. Later, [39] inquired the more realistic physical condition of hot core and concluded that none of the ratios involving these four most abundant sulfur species (SO, $SO_2$, OCS, and $H_2S$) could be useful to correlate the star formation scenario accurately rather each individual species itself could be used in estimating the ages of the core. They found that at the low temperatures, $H_2S$ production is efficient on ice phase, however, the non-detection of $H_2S$ in the interstellar medium may be due to its dissociation and formation of other products. Experimental studies reveal that $H_2S$ can easily be dissociated by UV photons and high energy radiation and can form other molecules like $CS_2$, polysulphanes $H_2S_n$ and $S_n$ on the grain surface [14, 21]. Using gas-grain chemical model, [10] found a significant amount of $H_2S_3$ and low abundance of solid $H_2S$ at temperature $> 10$ K. Woods et al. [41] studied the composition of sulfur yielding species in a hot core and compared with the observed sulfur abundances. Results showed a large variety of sulfur compositions observed towards different hot core i.e. no specific trend was observed.

Finding out the major sulfur reservoir in the dark cloud was a challenging job since 1970. Very recently, [38] reviewed the sulfur chemistry for dark cloud condition and they concluded that depending upon the age of the molecular cloud, either atomic sulfur is the major reservoir in the gas phase or HS and $H_2S$ are the major sulfur-bearing species in the icy phase. They reproduced the observed gas-phase abundance of simple sulfur-bearing species in dark cloud (Taurus Molecular Cloud (TMC)) by using the high cosmic elemental abundance of sulfur $X(S)_{ini}$ $\sim 1.5 \times 10^{-5}$. Very recently, [37] reviewed the sulfur chemistry in hot core and corino. Their result shows that pre-collapse chemical compositions are the critical parameters which could explain the observed sulfur compositions in a hot core. They also found a large difference (up to six orders of magnitude) in abundance for a given species between the static and dynamic models. Till date, around 200 molecules have been observed in the interstellar medium or circumstellar shells (https://www.astro.uni-koeln.de/cdms/molecules) and among them around 70 molecules are complex in nature which have greater or equal to 6 atoms. The presence of a large number of complex organic molecules (COMs) in space can resolve the long-standing mystery of the origin of life since the basic building block of life such as amino acid, sugar, lipid, proteins are very complex in nature. Synthesis of various COMs are discussed by various authors [3, 5, 8, 15–17, 19, 24, 35].

$CH_3SH$ is the first complex sulfur-bearing molecule detected in space by Linke et al. [23]. To date, methanethiol ($CH_3SH$) which is a complex sulfur bearing molecule was persistently observed in different regions of the ISM such as high mass star forming region (Sgr B2), outside the galactic center (G327.3-0.6), low mass protostar (16293-2422) etc. Recently, [22] reported the detection of ethanethiol ($C_2H_5SH$) towards Orion KL but [29] doubts about its detection. So, further investigations are required to confirm its presence in space. Pavithraa et al. [31] reported the first evidence of reversible phase change in an ethanethiol ice prepared under astrochemical conditions. Experiment suggests that SH stretching vibration

of propanethiol could be used for its identification in the interstellar icy mantles [32]. Recently, [17] studied the reaction pathways of higher order thiols and their monohydric alcohol analogue. The different molecular ratio obtained from their chemical model shows good agreement with the observed molecular ratio [17]. However, more in-depth studies are essential to find out the depletion of sulfur under various astrophysical environments.

This article is summarized as follows. In the next section (Sect. 2), major sources of sulfur bearing species are discussed. Section 3 describes the computational details. In Sect. 4, results are presented and discussed and finally, in Sect. 5, we conclude.

## 2 Sulfur Reservoirs

### *2.1 In Dark Clouds*

The abundance of sulfur seems to be cosmic $\sim 10^{-5}$ in diffuse region [13, 25]. But in the dense region, the observed abundance of sulfur-bearing species does not suit with cosmic sulfur abundance [30, 33, 36]. This is known as sulfur depletion problem. For explaining the missing sulfur problem, [38] proposed the depletion of sulfur-bearing species on the grain surface. The significant fraction of sulfur may be locked in the form of $H_2S$. But the presence of $H_2S$ is yet to be detected on the grain. $H_2S$ is the most abundant sulfur-bearing molecule observed in cometary ice [2]. The detection of $H_2S$ in the icy grain surface can solve the missing sulfur budget of the ISM. Only two sulfur-containing species, $SO_2$ and OCS were identified in the icy bulk. Vidal et al. [38] reviews the dark cloud model for sulfur chemistry and found that atomic sulfur is the main reservoir of sulfur in gas phase when the life time of the molecular cloud is below $5 \times 10^5$ years and whenever the age is greater than this value, HS and $H_2S$ are found to be the main reservoirs of sulfur in the grain phase. They considered a nearly cosmic abundance of elemental sulfur to reproduce the observed abundance of ice phase OCS and $SO_2$.

### *2.2 In Hot Cores*

Due to the inherent nature of sulfur-bearing species, sulfur-containing molecules are routinely used to trace the evolutionary history of the star-forming regions. A large variety of sulfur-bearing species have been observed in different hot cores [41]. Minh [27], Minh et al. [28] found a consistent fractional abundance of sulfur-bearing species in several massive star-forming regions for having a similar evolutionary history. It is believed that $H_2S$ and OCS are among the main sulfur reservoir on the grain surface. Detection of $H_2S$ in ice phase might solve the long-standing mystery

of missing sulfur budget of the ISM. Minh [27], Minh et al. [28] observed massive hot cores and studied the integrated emission of OCS, SO, and $H_2S$ to show different distributions. Their results show that OCS has a similar distribution like methanol. The reason behind is that they are mainly formed on the grain surface and populate the gas phase by various desorption mechanism. Distribution of $H_2S$ was found to be similar to the $^{13}CS$ and not like methanol or OCS. From this result, they suggested that $H_2S$ is not the major sulfur-bearing species on the grain surface instead it may synthesis on the gas phase and later it can deplete on the ice phase. Holdship et al. [20] studied the $H_2S$ formation in low mass protostar and observed that a large amount of $H_2S$ is locked in the grain surface prior to the evaporation in hot corino. Very recently, [37] studied the sulfur chemistry for hot cores. They used three types of simulations: extensive study of 0D simulation, 0D dynamic simulation, and 1D static simulation for major sulfur species, SO, OCS, CS, $H_2S$, $SO_2$, and $H_2CS$. They noticed a notable difference between sulfur bearing species for adopted physical conditions.

## 3 Computational Details

### *3.1 Quantum Chemical Calculation*

All the ab-inito quantum chemical results were carried out using Gaussian 09 program [12]. The suitable method and basis sets were used to study various conformers and reaction mechanisms. Here we use Density Functional Theorem (DFT) with the Becke three-parameter Exchange and the Lee, Yang, and Parr correlation (B3LYP) functional [1] with the 6-31+G(d) basis set available in Gaussian 09 program. For the influence of ice, we use water as a solvent using self-consistent reaction field method by default available in The Polarizable Continuum Model (PCM). We verify each optimized structure by harmonic frequency calculation having no negative frequency. For the transition state calculations, we use QST2 method. All the TS are verified with intrinsic reaction coordinate (IRC) calculation which connects reactants and product through the minimum energy path of the potential energy surface.

### *3.2 Chemical Modeling*

Gas-grain chemical network is used to study the chemical evolution of interstellar species under various astrophysical environments. The chemical model basically uses the rate equation approach to simulate both gas phase and grain phase chemistry. Kinetic data obtained either from theoretical study or from laboratory experiment are used as input parameters for chemical modeling. Interstellar dust

is used as catalyst for the synthesis of various surface species. Compositions of grain mantle were studied by various authors [4, 7, 9]. Various models have been developed for sulfur-bearing molecules in the last few decades by various authors [6, 10, 17, 18, 37–39, 41] to simulate physical and chemical properties of various types of interstellar sources and reasonable agreement with observations was seen. Our gas phase chemical network is principally adopted from the UMIST 2012 database [26]. For the grain surface reaction network, we primarily follow [34]. We also consider the exchange of chemical species from gas to grain and vice versa through various mechanisms such as thermal desorption, non-thermal desorption, and accretion. The model starts with initial conditions i.e., almost all hydrogen is in the atomic form and there are a few atoms and ions whose elemental abundances are known. Most of the complex molecules are formed in the denser regions of the cloud. Rate coefficients of the chemical reactions are very crucial to study the synthesis of the chemical species. Details of the gas-phase and grain-surface rate coefficients have been reviewed by Gorai et al. [16], Wakelam et al. [40].

## 4 Results and Discussion

To study the abundance of a chemical species it is essential to know the reaction mechanism of its formation because the kinetic data is essential for the chemical modeling. Gorai et al. [17] presented the potential energy surface scan (PES) to find out the most stable conformer of some complex sulfur-bearing molecules and their oxygenated analogues. For example, they considered: (1) methanol and methanethiol, (2) ethanol and ethanethiol, (3) 1-propanol and 1-propanethiol, (4) 2-propanol and 2-propanethiol etc. Though Interstellar chemical process far away from the thermodynamic equilibrium, isomerism can be used to initially select some most probable candidates from an isomeric group for astronomical detection [11, 35]. We calculate endothermicity or exothermicity of a chemical reaction to check that reaction can happen or not under interstellar conditions. Since some exothermic reactions are having activation barrier, it is always important to check the activation barrier of a chemical reaction. Rate coefficient of a chemical reaction plays a crucial role because it decides the fate of the product of that reaction. Activation barrier of a chemical reaction on the grain surface is used to calculate the rate coefficient which controls the ice phase synthesis, whereas, Gibbs free energy of activation can be used to calculate the rate coefficient of gas phase reactions. In Table 1, we have presented the kinetic data of propanol and propanethiol synthesis for both gas phase and ice phase. Figure 1 depicts the reaction mechanism of propanethiol synthesis via successive hydrogen addition reactions.

Gorai et al. [17] studied the formation and destruction pathways of complex sulfur-bearing molecules (methanethiol, ethanethiol and propanethiol) along with their monohydric alcohol analog. They used two-phase chemical model, where, the first phase belongs to the isothermal evolution and the other is during warm-up. Their modeling results suggested that gas phase methanethiol can efficiently

**Table 1** Kinetic data of propanol and propanethiol synthesis

| Reaction | Activation energy | | Gibbs free energy of activation | |
|---|---|---|---|---|
| | Gas phase (K) | Ice phase (K) | Gas phase (K) | Ice phase (K) |
| **1-propanol($CH_3CH_2CH_2OH$)** | | | | |
| $C_2H + H_2O \rightarrow HCCCHO + H$ | | | | |
| $O + C_3H_3 \rightarrow HCCCHO + H$ | | | | |
| $H + HCCCHO \rightarrow HCCHCHO$ | 1482 (2.946) | 1688[a] (3.354) | 4204 (8.354) | 4227 (8.401) |
| $H + HCCHCHO \rightarrow CH_2CHCHO$ | | | | |
| $H + CH_2CHCHO \rightarrow CH_2CH_2CHO$ | 807 (1.604) | 827[b] (1.644) | 3755 (7.462) | 3779 (7.511) |
| $H + CH_2CH_2CHO \rightarrow CH_3CH_2CHO$ | | | | |
| $H + CH_3CH_2CHO \rightarrow CH_3CH_2CH_2O$ | 2148 (4.268) | 2247[a] (4.466) | 5230 (10.394) | 5330 (10.592) |
| $H + CH_3CH_2CH_2O \rightarrow CH_3CH_2CH_2OH$ | | | | |
| $C_2H_5 + CH_2OH \rightarrow CH_3CH_2CH_2OH$ | | | | |
| **1-propanethiol**($CH_3CH_2CH_2SH$) | | | | |
| $C_2H + H_2S \rightarrow HCCCHS + H$ | | | | |
| $S + C_3H_3 \rightarrow HCCCHS + H$ | | | | |
| $H + HCCCHS \rightarrow HCCHCHS$ | 2082 (4.138) | 2167[a] (4.308) | 4818 (9.567) | 4897 (9.732) |
| $H + HCCHCHS \rightarrow CH_2CHCHS$ | | | | |
| $H + CH_2CHCHS \rightarrow CH_2CH_2CHS$ | 1217 (2.419) | 1248[b] (2.479) | 4220 (8.387) | 4284 (8.514) |
| $H + CH_2CH_2CHS \rightarrow CH_3CH_2CHS$ | | | | |
| $H + CH_3CH_2CHS \rightarrow CH_3CH_2CH_2S$ | 651 (1.293) | 734[a] (1.463) | 3543 (7.041) | 3648 (7.249) |
| $H + CH_3CH_2CH_2S \rightarrow CH_3CH_2CH_2SH$ | | | | |
| $C_2H_5 + CH_2SH \rightarrow CH_3CH_2CH_2SH$ | | | | |

Bracketed values are in Kcal/mol

[a]Presented in [17]

[b] Updated values

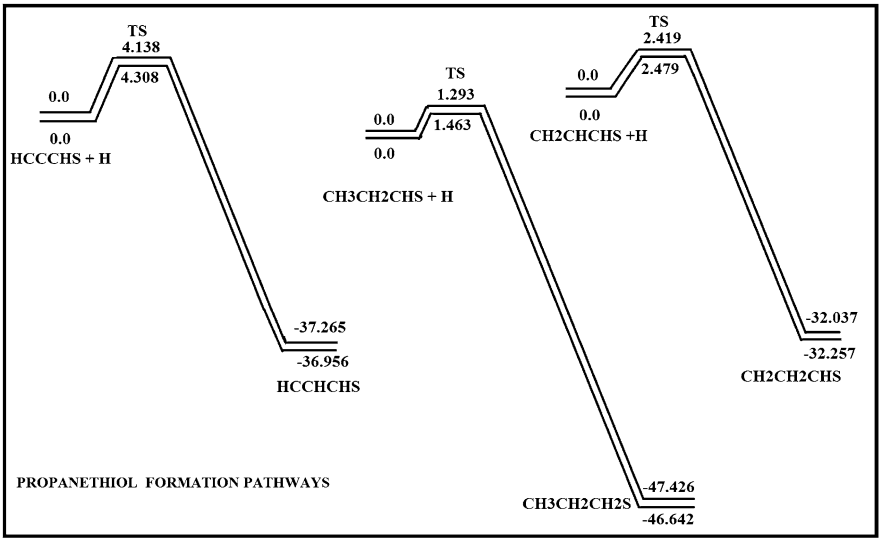



**Fig. 1** Schematic potential energy surfaces of propanethiol formation for various hydrogenation reactions indicating stable species and transition states (TSs). Energy differences in units of Kcal/mol are shown, referenced to reactant complexes calculated using B3LYP/6-31G+(d). The upper lines are the gas phase, while the lower line represents IPCM correction for the influence of ice

produce in the isothermal phase but the gas phase production of other higher order thiols (ethanethiol and propanethiol) are insignificant in the isothermal phase. In the hot core region, these higher order thiols can be produced in a reasonable amount and their peak gas phase abundance can reach up to $5.45 \times 10^{-9}$ and $3.71 \times 10^{-10}$ respectively. These peak abundances were obtained around 120–125 K [17]. High-resolution interferometry radio telescope like Atacama Large Millimeter Array (ALMA) and Northern Extended Millimeter Array (NOEMA) can reveal the presence of these complex sulfur species in the ISM.

Sulfur-containing molecules are used to probe the physical and chemical scenario of the ISM. The abundance of sulfur-bearing species varies in different regions such as high mass star-forming region, shock region, dark cloud, wind around protostar etc. Reservoirs of sulfur-bearing molecules in gas and grain phase are still a mystery. Using gas-grain chemical code, [17] obtained different molecular ratio such as methanol/methanethiol, ethanol/ethanethiol, methanethiol/ethanethiol etc. which are close to observed molecular ratio in hot molecular core Sgr B2. These ratios can be used to trace the evolutionary history of that molecular cloud. More observations, experimental, and theoretical results are needed to solve the puzzle of the total sulfur budget of the ISM. Most awaited high-resolution James Webb Space Telescope (JWST) can unfold the mystery of missing sulfur budget of the ISM.

## 5 Conclusion

Complex sulfur-bearing molecules are detected in interstellar space. It is expected that with the existing modeling results, more complex sulfur bearing species could be observed in near future. The brief outline of this report is highlighted below.

- A large variety of sulfur-bearing species were observed in the hot core regions and it is noticed that a very rich chemistry can process around this region.
- Propanol and propanethiol can be synthesized through successive hydrogen addition reactions. For some of successive hydrogen addition reactions, we carried out transition state theory (TST) calculations.
- Based on modeling results [17], we proposed to observe higher-order thiol such as ethanethiol and propanethiol in the hot core region.
- Indeed several modeling results, we think that more work is essential to explain the major source of the sulfur reservoir in the ISM.

**Acknowledgements** I wish to acknowledge ISRO respond project (Grant No. ISRO/RES/2/402/16-17) for financial support. I would like to express my special thanks and gratitude to Dr. Ankan Das and Prof. Sandip K. Chakrabarti for the continuous support and help to complete this work.

## References

1. Becke, A.D.: JChPh **98**, 5648 (1993)
2. Bockelée-Morvan, D., et al.: A&A **353**, 1101 (2000)
3. Chakrabarti, S., Chakrabarti, S.K.: A&A **354**, L6 (2000)
4. Chakrabarti, S.K., Das, A., Acharyya, K., et al.: A&A **457**, 167 (2006)
5. Chakrabarti, S.K., Majumdar L., et al.: APSS **357**, 90 (2015)
6. Charnley, S.B.: ApJ **481**, 396 (1997)
7. Das, A., Acharyya, K., Chakrabarti, S., et al.: A&A **486**, 209 (2008)
8. Das, A., Majumdar, L., Sahu, D., Gorai, P., et al.: ApJ **808**, 21 (2015)
9. Das, A., Sahu, D., Majumdar, L., et al.: MNRAS **455**, 540 (2016)
10. Druard, C., Wakelam, V.: MNRAS **426**, 354 (2012)
11. Etim, E.E., Gorai, P., Das, A., Arunan, E.: ASR **61**, 2870 (2018)
12. Frisch, M.J., Trucks, G.W., Schlegel, H.B., et al.: Gaussian 09, Revision D.01. Gaussian, Inc., Wallingford, CT (2013)
13. García-Rojas, J., Esteban, C., Peimbert, M., et al.: MNRAS **368**, 253 (2006)
14. Garozzo, M., Fulvio, D., Kanuchova, Z., et al.: A&A **509**, A67 (2010)
15. Garrod, R.: ApJ **765**, 60 (2013)
16. Gorai, P., Das, A., Majumdar, L., et al.: MolAp **6**, 36–46 (2017)
17. Gorai, P., Das, A., Das, A., Sivaraman, B., et al.: ApJ **836**,70 (2017)
18. Hatchell, J., Thompson, M.A., Millar, T.J., et al.: A&A **338**, 713 (1998)
19. Herbst, E., van Dishoeck, E.F.: Annu. Rev. Astron. Astrophys. **47**, 427 (2009)
20. Holdship, J., et al.: MNRAS **463**, 802 (2016)
21. Jiménez-Escobar, A., Muñoz Caro, G.M.: A&A **536**, A91 (2011)
22. Kolesniková, L., Tercero, B., Cernicharo, J., et al.: ApJ **784**, L7 (2014)
23. Linke, R.A., Frerking, M.A., Thaddeus, P.: ApJ **232**, L139 (1979)
24. Majumdar, L., Gorai, P., Das, A., et al.: APSS **360**, 64 (2015)

25. Martín-Hernańdez, N.L., Peeters, E., Morisset, C., et al.: A&A **381**, 606 (2002)
26. McElroy, D., Walsh, C., Markwick, et al.: A&A **550**, A36 (2013)
27. Minh, Y.C.: J. Phys.: Conf. Ser. **728**, 052007 (2016)
28. Minh, Y.C., Liu, H.B., Madrid, R.: ApJ **824**, 99 (2016)
29. Müller, H.S.P., Belloche, A., Xu, L.-H., et al.: A&A **587**, A92 (2016)
30. Palumbo M.E., Tielens A.G.G.M., Tokunaga A.T.: ApJ **449**, 674 (1995)
31. Pavithraa, S., Methikkalam, R.R.J., Gorai, P., et al.: Spectrochim. Acta A Mol. Biomol. Spectrosc. **178**, 166 (2017)
32. Pavithraa, S., Sahu, D., Seth, G., et al.: APSS **362**,126 (2017)
33. Penzias A.A., Solomon P.M., Wilson R.W., Jefferts K.B.: ApJ **168**, L53 (1971)
34. Ruaud, M., Wakelam, V., Hersant, F.: MNRAS **459**, 375 (2016)
35. Sil, M., Gorai, P., Das, A., et al.: ApJ **853**, 2 (2018)
36. Tieftrunk, A., Pineau des Forets, G., et al.: A&A **289**, 579 (1994)
37. Vidal, T.H.G., Wakelam, V.W.: MNRAS **474**, 5575 (2018)
38. Vidal, T.H.G., Loison, J.-C., Jaziri, A.Y., et al.: MNRAS **469**, 435 (2017)
39. Wakelam, V., Caselli, P., Ceccarelli, C., et al.: A&A **422**, 159 (2004)
40. Wakelam, V., Smith, I.W.M., et al.: Space Sci. Rev. **156**(1), 13 (2010)
41. Woods, P.M., Occhiogrosso, A., Viti, S., et al.: MNRAS **450**, 1256 (2015)

# Role of Interstellar Molecules on Evolution of Cosmic Deuteration: An ALMA Observation as a Case in Point




**Dipen Sahu**

**Abstract** The primordial atomic D/H ratio in the interstellar medium is $\sim 10^{-5}$. There is no known source in the Universe which produces atomic deuterium. Hence, the order of cosmic deuteration is similar to the primordial D/H ratio. Despite such low D/H ratio, many deuterated molecules are seen to be heavily fractionated compared to its hydrogenated counterpart. Interstellar chemistry and zero-point energy difference in deuterated species are the main cause of it. In this article, we discuss the deuterium fractionation of interstellar molecules under different molecular cloud condition, ranging from cold prestellar condition to hot protostar condition. We also discuss, how deuterium fractionation in interstellar molecules could be used as an evolutionary tracer of molecular clouds. As an example of an interstellar deuterated molecule, we discuss here an ALMA observation of deuterated formaldehyde in the low-mass protostar system HH212.

## 1 Introduction

Deuterium (D) is first produced during the Big-Bang. During the Big-Bang nucleosynthesis, deuterium appeared due to the fusion of proton and neutron within first few minutes since big bang. Big-bang nucleosynthesis ended with mainly producing the most stable light element $^4$He. The abundance of deuterium was very low as it was destroyed by the fusion reactions. There were several attempts by the astronomers to measure the deuterium to hydrogen (D/H) ratio. The observations towards high-redshift, low metallicity, quasar absorption systems (QAS) [12, 28, 29] with high-resolution spectra revealed the presence of D in the sources. The measurements from the earlier mentioned observations gives the D/H ratio to be $(D/H)_p = 2.6 \pm 0.2 \times 10^{-5}$. These observations at high-redshifts give a lower limit to primordial D/H value. Also, it reveals that in local interstellar medium,

D. Sahu (✉)
Physical Research Laboratory, Ahmedabad, India

© Springer International Publishing AG, part of Springer Nature 2018

B. Mukhopadhyay, S. Sasmal (eds.), *Exploring the Universe: From Near Space to Extra-Galactic*, Astrophysics and Space Science Proceedings 53,
https://doi.org/10.1007/978-3-319-94607-8_37

D/H value is around $1.56 \pm 0.04 \times 10^{-5}$. These measurements imply the depletion of D by a factor of two or so, due to stellar processes. There is no astrophysical source to produce atomic deuterium. This is because the deuterium may be produced during star formation process (nucleosynthesis), but it is destroyed immediately due to subsequent nuclear reactions. Hence, irrespective of the small differences by factors in deuteration (i.e., D/H) in different astrophysical sources, the order of D/H is $\sim 10^{-5}$.

Now consider a molecule XH in space and its deuterated form is XD. The ratio $f_D$= XD/XH is called deuterium fractionation. If we consider a simple statistical logic, then for the previous example, it is expected that $f_D$ should be $\sim 10^{-5}$, the cosmic deuteration. But it is observed that in dark clouds, the deuterium fractionation goes up to 0.3. Also, for doubly and triply deuterated molecules, for example $D_2CO$ and $ND_3$ [21, 23, 30], huge enhancement of $f_D$ has been observed. The observed $ND_3/NH_3$ is about $10^{-3}$ , which is $\sim$11 order of magnitude greater than what is expected from cosmic ratio, $(D/H)^3 \sim 10^{-14}$. The details about the interstellar chemical processes leading to enhanced deuterium fractionation are described in Sect. 2.

To understand the chemistry and thereby the deuteration in the interstellar medium (ISM), we have to know typical ISM conditions. Matter in the Universe located primarily in the Galaxies in the form of stars and interstellar material. Interstellar matter distributed in several light years in range (e.g., 100 light years or more). The matters consist of both gaseous and dust particle, typically of size 0.1 µm. Although 1% of total mass is in the form of 'grain' (dust/ice), it takes a major role for the interstellar chemistry. Dust components of the ISM are responsible for scattering and absorption of the external radiation. So, in the dense medium, visible and infrared cannot penetrate and these sources are dark to these wavelengths. Radio wave, mm-submm wave, and infrared can be used for study of these dense mediums as these wavelengths are larger than typical dust size. Also, observation is only possible if some source of radiation is available. It can be noted that most of the interstellar molecules have been observed through their rotational transition in radio and mm-submm wavelengths. In Sect. 3, I discuss one such observational result observed in the millimeter (mm) wavelength. Table 1 [22]

**Table 1** Properties of different interstellar medium and some of the molecular line tracers (Diagnostics) to study physical and chemical properties of these mediums

| Cloud type | Size (pc)[a] | T (K) | n ($cm^{-3}$) | $N_H$ ($cm^{-2}$) | $A_V$ (mag) | Diagnostics |
|---|---|---|---|---|---|---|
| Diffuse | 1–3 | 70–100 | 10–100 | $< 10^{21}$ | $< 1$ | 21 cm H line, $H_2$, UV abs, $C^+$ |
| Dark | 1–5 | 8–15 | $10^4$–$10^6$ | $10^{22}$ | 10–20 | CO, $H_2CO$, HCN, $HCO^+$ |
| Hot core | 0.01–0.1 | 100–300 | $10^7$–$10^9$ | $10^{24}$ | 5000 | CS, $CH_3OH$ $CH_3CN$, $NH_3$ |
| Giant molecular | 100–500 | 30–70 | $< 10^3$ | $>10^{25}$ | – | CO, HCN, $NH_3$ |

shows different ISM clouds and their properties. We will discuss some basic physical and chemical characteristics of the clouds subsequently.

Diffuse clouds are less dense, and the number density is of the order of $\sim 10^2$ cm$^3$. It is transparent to optical photons and visual extinction ($A_V$) typically less than 1 magnitude. Here, we have to note that in general, the ISM contains no photon with energies greater than 13.6 eV, the ionization potential of hydrogen. Far-ultraviolet photons (FUV) can penetrate through these clouds and can ionize atoms with ionization potential less than 13.6 eV. Because of the FUV-ionization, species like $C^+$, $S^+$ are present in these clouds. As the atoms like C are easily ionized by the photon field, the fractional ionization ($f_e$) is large; typically ($f_e = n_e/n$) is similar to $10^{-4}$ in these mediums. In this regard, it is important to mention that fractional abundance of $H_2$, $f_{H2} = n_{H2}/n$ varies from a small value $\sim 10^{-5}$ to a larger value $\sim$0.3 over a small range of $A_V$. It signifies that grains play a major role in $H_2$ formation (e.g., [11, 31]). Radiative association of two hydrogen atoms (H) to form $H_2$ is unlikely (spin-forbidden) and the gas phase route involving hydrogen ions ($H^+$, $H^-$) is rare and ineffective as the ions are not abundant in the diffuse medium. The dust surface acts as a catalyst where two H atoms can recombine to form an $H_2$ by providing a way to release excess energy during the recombination.

Dark clouds have density $\sim 10^4$–$10^6$ cm$^{-3}$ and it is called dark as these clouds are opaque to visible and UV radiation. Because of scarcity of UV photons, photo-dissociation and photo-ionization are negligible. Hence, in these clouds the gas temperature is $\sim$10 K and fractional ionization ($f_e$) is $\sim 10^7$–$10^8$; this is much less than their values in diffuse clouds. Also, due to lack of UV photons, all the $H_2$ molecules which are formed on grain surfaces survive. As most of the atomic H is converted to $H_2$, effectively it increases the atomic D/H ratio in the gas phase of dense molecular cloud. Presence of chemical species in these clouds can be detected through Millimeter and sub-Millimeter observations. The presence of chemical species in these clouds can be characterized as two types: firstly many polyatomic carbon species are observed and secondly, enormous increase in deuterium fractionation are observed. The deuterium fractionation is a kinetic process due to zero-point energy differences in deuterated species. Indirectly it can be used as a probe to understand physical and chemical evolution of molecular cloud (see below).

Hot-molecular cores are relatively small (few arc seconds) and very dense compared to the molecular clouds, n($H_2$) $\sim 10^7$–$10^9$ cm$^{-3}$. Hot-cores arise as an evolutionary stage of star-formation from dense molecular clouds. Depending on the mass, a star can be classified either as a low-mass or high-mass. Though the formation of low-mass stars such as our Sun is well understood but there is no general theory for massive star (>8–10 $M_\odot$) formation. The evolution process for the two types of stars are very different: massive stars form rapidly on a time scale $\sim 5 \times 10^4$ compared to $\sim 10^7$ year for the solar-type low mass star. Timescale greatly affects the presence of chemical species in these objects. Due to high temperature (>100 K), the molecular composition of a hot-core is significantly different as compared to the cold, dark molecular cloud. Hot-cores show a large abundance of hydrogenated molecules and especially complex molecules (>6 atom

molecules) and bio-molecules. Formation of complex molecules and deuteration in bio-molecules discussed in detail by Dr. Ankan Das in another article of this book. The hydrogenated molecules (e.g., $NH_3$, $CH_4$, $CH_3OH$, $C_2H_5OH$)) show increased fractionation by a few orders over those in dark clouds. The deuterium fractionation is not effective in (see Sect. 2) high-temperature hot-cores, so observed deuterium abundance is indicative of cold chemistry ∼10–20 K. Theoretical models suggest that molecules form in cold grain mantles (e.g., [11]) on dust grains and later it can evaporate into the gas phase in high-temperature regions such as hot-cores. The presence of gas-phase molecules can be observed via rotational transitions of molecules. Following a similar argument, we considered a two-phase model and showed that deuterated acetaldehyde could be produced in the hot-core region to an observable limit [10]. Historically, hot-core for low-mass stars with the signature of complex organic molecules is called hot-corino. Due to the presence of many complex molecules, the sub-Millimeter spectra are very bright and line rich. The NGC 1333 IRAS 4A is well known hot-corino, Fig. 1 shows one such rich molecular spectra towards A2 core of IRAS 4A.

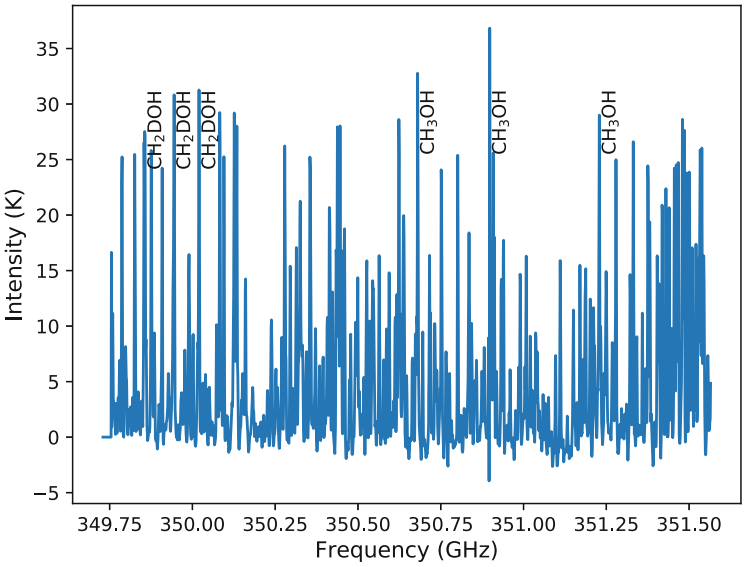



**Fig. 1** Forest of molecular spectra as observed using ALMA telescope towards the low-mass protostar NGC1333 IRAS4A2. Some transitions are identified as methanol and its deuterated form, $CH_2DOH$

**Table 2** Table shows most of the deuterated molecules that have been observed in the ISM

| Atom number | | | | | | | |
|---|---|---|---|---|---|---|---|
| 2 | 3 | 4 | 5 | 6 | 7 | 8 | 9 |
| HD | DCO+ | HDCO | c-$C_3HD$ | $CH_2DOH$ | $CH_3CCD$ | $HCOOCH_2D$ | $CH_2DOCH_3$ |
| ND | DCN | $D_2CO$ | c-$C_3D_2$ | $CH_3OD$ | $CH_2DCCH$ | $DCOOCH_3$(?) | |
| OD | DNC | HDCS | $NH_3D^+$ | $CHD_2OH$ | $DC_5N$ | | |
| | HDO | $D_2CS$ | $CD_3N$ | $CD_3OH$ | | | |
| | HDS | $NH_2D$ | $C_4D$ | $CH_2DCN$ | | | |
| | $D_2S$ | $NHD_2$ | $CH_3D$(?) | HDCCCC | | | |
| | $H_2D^+$ | $ND_3$ | | | | | |
| | $HD_2^+$ | l-$C_3D$ | | | | | |
| | $N_2D^+$ | | | | | | |
| | $C_2D$ | | | | | | |
| | $D_2O$ | | | | | | |

## 2 Interstellar Molecules and Deuteration

Typical condition of an interstellar medium and star formation is already described in Sect. 1 and a list of observed deuterated molecules are mentioned in Table 2 [22]. In the molecular cloud, the hydrogen and deuterium are mainly in the form of $H_2$ and HD respectively. The quasi-static molecular ion reactions are the key for the deuterium fractionation. In the dense cloud, HD is the major reservoir of the deuterium; the following reactions take place:

$$H_3^+ + HD \leftrightarrow H_2D^+ + H_2, \quad \triangle E_1 = 232K \tag{1}$$

$$CH_3^+ + HD \leftrightarrow CH_2D^+ + H_2, \quad \triangle E_2 = 352K \tag{2}$$

$$C_2H_2^+ + HD \leftrightarrow C_2HD^+ + H_2, \quad \triangle E_3 = 550K \tag{3}$$

These reactions are exoergic in the forward direction with the energy barrier given by $\triangle E_x$'s (w.r.t. ground state reactants). In the cold cloud, the typical temperature is 10 K, hence the backward reaction do not proceed. For this reason, the $H_2D^+/H_3$ abundance ratio can be much larger than the $HD/H_2$ ratio. To get a rough idea of the possible enhancement, let us consider the $H_2D^+$ ion and reactions involving it. The $H_2D^+$ ion can be lost by dissociative recombination with electrons and reactions with neutral species (say, N). Now,

$$R(H_2D^+) = \frac{f(H_2D^+)}{f(H_3^+)} = \frac{k_f f(HD)}{k_r + k_e f(e) + \sum K_N f(N)} = Fr * R(HD) \tag{4}$$

here, $k_f$ and $k_r$ are the forward and reverse rate coefficients of reactions (1), f(X) is the fractional abundance (= n(X)/n($H_2$)) , of a species X. For the typical condition of

cold dark molecular clouds, the third term (Eq. (4)) in the denominator is prominent and so the 'Fr' $\sim 1/\sum f(N) \sim 10^3$–$10^4$, which reduces to $R(H_2D^+) \sim 0.01$–$0.1$. For higher temperatures (e.g., room temperature, 300 K is very high temperature for astrochemistry) the back reaction is important and the $R(H_2D^+)$ decreases very fast (exponentially) with the temperature. So, in the hot-cores, the deuteration reaction is unimportant and would not help deuterium enhancement. Roughly, we can consider one-tenth value of the appropriate endothermicity as the critical temperature, below which the quasi-static deuterated ion can be significantly fractionated. The initial fractionation of ions such as $H_2D^+$ can be passed onto other species, e.g. CO:

$$H_2D^+ + CO \leftrightarrow DCO^+ + H_2 \tag{5}$$

$$H_2D^+ + CO \leftrightarrow HCO^+ + HD \tag{6}$$

Similar reactions can produce other ions, $N_2D^+$ and DCS etc. Observationally, $DCO^+/HCO^+$ ratio can be used to trace fractional ionization, f(e). Das et al. [9] discussed the role of $DCO^+/HCO^+$, $N_2D^+/N_2H^+$ for the measurements of degree of ionization. Alongside these reactions, the dissociative recombination reactions involving $H_2D^+$ directly increase atomic D/H ratio in molecular clouds. The enhanced presence of atomic deuterium leads to deuterium enrichment of some molecule, e.g., OD:

$$D + OH \leftrightarrow OD + H. \tag{7}$$

This reaction is exothermic by 800 K, thereby it should retain high deuteration in cold molecular cloud. In presteller condition condition, OD/OH ratio can be few percent and it was predicted by Croswell and Dalgarno [8]. Till now, we have discussed about singly deuterated species. Subsequent reactions, between already deuterated species can give rise to multiply deuterated species., e.g.:

$$H_2D^+ + HD \leftrightarrow D_2H^+ + HD \tag{8}$$

$$D_2H^+ + HD \leftrightarrow D_3^+ + H_2. \tag{9}$$

Since $D_3^+$ is the end product and does not react with other HD, the $D_3^+$ abundance in some extreme condition like complete depletion of heavy elements in grain surfaces (e.g., [36] and [5]), can lead to fractionation greater than 1.

Apart from the gas phase, ISM ice/dust takes an important role in deuteration of chemical species. It has already been mentioned that D atoms can be formed via dissociative recombination reactions of $H_2D^+$. These D atom can stick to grain surfaces via accretion from gaseous medium and starts new chemistry on ice surface. Mainly, three types of processes occur on dust-icy surfaces; accretion, diffusion and recombination. After accretion from gas surface an atom can stick to a bare site on the grain surface or it can directly recombine with a species already present on the grain surface. After sticking to a bare site on a grain surface, an atom

can hop to recombine with another species and may form a new molecule. These recombination processes are named as Eley-Rideal and Langmuir-Hinshelwood processes respectively. Sahu et al. [31], showed that HD and $D_2$ formation is effective in low temperature cold dense condition. Sahu et al. [31] considered only monolayer grain surface; to describe chemistry in dust-ice mantle [11] considered multi-layer grain surface (grain mantle) model. The model described deuteration of water and some other molecules including methanol. The results suggest that complex molecules can be heavily deuterated because of the surface recombination process. For example: $CO_{surface} \xrightarrow{H} HCO_{surface} \xrightarrow{H} CH_3O_{surface} \xrightarrow{H} CH_3OH_{surface}$, a typical recombination process by which molecules can form on grains. For a medium with high D/H ratio, severe deuterium fractionation possible in the same way with reaction involving D in place of H. Observational results also supports this assumption; deuterated methanol has been observed in prestellar core L1544 [33].

## 3 Stellar Evolution and Deuteration

The study of deuteration is extremely useful to understand the physical conditions of star-forming regions. Typical phases of star formation which are related to low-mass star formation are (1) Pre-stellar cores, (2) Protostellar envelopes, (3) Protoplanetary disks, (4) Planetesimal formation, (5) Planet formation. The deuteration in cold molecular cloud/prestellar condition is already discussed in Sects. 1 and 2. In prestellar cloud, temperature is typically $<20$ K and CO depletion is also high due to dense condition($>10^4\,cm^{-3}$). The $D_{frac}$ (D/H ratio) is high ($\sim 10^{-2}$ or higher) in prestellar condition and it changes with the evolution of the molecular core. Notably, for the low-mass case, [3] found a relation between deuteration and core evolution. The relation shows that $D_{frac}$ increases as the core evolves following the gravitational collapse; as the density increases, the CO depletion becomes more effective (thereby less destruction of $H_2D^+$) and the abundance of deuterated species greatly increases. Now, the temperature increases gradually as the young stellar object forms. Due to comparatively high temperature, CO evaporates from the grain which indirectly (e.g., destruction of $H_2D^+$) reduces deuteration of species, thereby $D_{frac}$ [14]. $D_{frac}$ can be considered as an evolutionary tracer for the low-mass star formation process.

High-mass star formation process is very different from that of the low mass stars. Early studies of HMPOs (high-mass protostellar objects) do not show consistent behavior of deuterium fractionation other than a common enhancement [13, 27]. The HMPOs generally have many cores at different evolutionary stages. Chen et al. [6] from the study of G28.34+0.06 found a moderate decreasing trend in the deuterium fractionation of $N_2H^+$ in one IRDC core compared to that from a massive starless core (MM9), a more evolved core with fragmentation and outflows (MM4) to a UC H II region (MM1). Fontani et al. [14] did a rigorous study with a

larger sample of 27 cores and revealed a similar trend across different evolutionary stages from HMSCs (High-mass starless cores) to HMPOs and H II regions. In general, in both of the cases of low-mass to high-mass star formation, $N_2D^+$, $DCO^+$ and ratio with their hydrogenated part—$N_2H^+$, $HCO^+$ respectively is a good tracer of evolutionary history.

### *3.1 Deuteration as a Fossil*

In the previous section, we mainly discussed the gas phase deuteration. Deuteration in ices are important as well. It can be thought of as a 'fossil' as the bulk ice mantle composition preserve the history of past physical and chemical conditions. In the inner warm region (>150 K) of deeply embedded protostars, all the ices are expected to sublimate [15]. The sublimated ices can take part in warm-gas phase chemistry resulting in a change of original species. But this situation is unlikely as the chemical time scale is much longer than the infalling time scale ($10^5$). For example, the ionization rate is ($10^{17}$ $s^{-1}$) of the warm gas onto central star. Though former argument relies on the spherical collapse of molecular clouds, the warm gas most likely is dominated by the ice-contamination formed during cold prestellar stages.

Ice formation during the stellar evolution can be divided into two stages, in the early stage $H_2$ dominates ice-layer formation and in later stages, as CO freeze out, mixed water ice consisting CO and other hydrogenated species (e.g., $H_2CO$, $CH_3OH$) are formed. Observations toward deeply embedded protostars show that methanol deuteration ($CH_3OH/CH_3OD \sim 10^{-2}$) is quite higher than $HDO/H_2O$ ratio ($\sim 10^{-3}$ ) in the warm ($\geq$150 K) gas around the protostar [23, 25, 26]. As the deuteration levels of icy molecules depend on gas phase atomic D/H ratio, the observation mentioned above indicates deuterium fractionation is more efficient in later stages of ice formation (i.e., CO depleted region) and also due to drop of $H_2$ ortho-para ratio [4, 35]. Then tracing the relative deuteration one can guess the relative timing of formation of icy molecules.

## 4 Deuteration in a Jet-Disk System: An ALMA Observation

We have already discussed about the deuteration in the molecular cloud and star-forming region. In this regard, I will discuss an ALMA (Atacama Large Millimeter Array) observation [32] of a typical jet-disk system, the HH212. With the advent of the ALMA, the sensitivity and spatial resolution have greatly enhanced to study the low-mass system in more detail. The spatial scale associated with a young stellar disk is limited to ~100 AU or even less. The ALMA's ability to detect molecules in disk systems surely reveal much more, that were previously unknown.

### 4.1 The HH212 System

A nearby (400 pc) object in Orion, can be associated with class 0 protostellar system. The position of HH212 protostar is given by the peak of continuum emission, $\alpha(J2000) = 05^h43^m51^s.41, \delta(J2000) = -01°02'53''.17$ [19]. The different class (e.g., 0, I, II etc) of stellar system in associated with the evolution of low-mass star-system, Class 0 is the early stage of star formation. Study of low-mass systems helps us to understand the evolution of the Sun like system and thereby our chemical heritage.

### 4.2 The Observation

The HH212 protostar system was observed with ALMA (Band -7) using 24 12 m antennas on 2012 December 1 (Early Science Cycle 1 phase [7, 19]. The field of view of the telescope is decided by the size of the single dish and the highest resolution depends on the baseline of the interferometer. In the observation, the shortest and the longest baselines were respectively 20 and 360 m. We reported [32] the deuterated formaldehyde line and compared with the $CH_3OH$, $C^{34}S$ and $C^{17}O$ lines to get physical and chemical conditions associated with the HDCO emission. The datacubes had a spectral resolution 488 KHz equivalent to $\sim$0.43 km s$^{-1}$. The typical synthesized beam size was $0.65'' \times 0.47''$ at position angle (PA) $\sim$49°. The observation was made for the spectral windows, 333.7–337.4 GHz and 345.6–349.3 GHz, the typical rms level was 3–4 mJy beam$^{-1}$ in 0.43 km s$^{-1}$ channels. We used CASA package for the data analysis; the calibration were made using quasars J0538-440 as flux calibrator, J0607-085 as passband calibrators, quasar J0607-085 as a gain calibrator, and Callisto and Ganymede as flux calibrators. To get the spectral properties, we generated spectral cubes by subtracting the continuum emission in visibility data.

### 4.3 Molecular Line Tracer and Kinematics of HH212

In the current day situation, astrochemistry and molecular astronomy is a quite wide spread field. According to [17]," ...the first attempt at the detection of a molecular line (OH) was made by Barrett and Lilly [1]," though the actual detection of OH was reported by Weinreb et al. [37]. The detection of OH is perhaps the first non-serendipitous detection of molecule in space. But, some serendipitous absorption features were observed towards the stars and later some of the features were identified as CH [34]. From the absorption features of CN, [16] concluded a rotational temperature 2.3 K. Penzias and Wilson [24] discovered the Microwave background radiation in 1965. So, molecular transitions may have some link with

cosmological constants. Though molecules could be observed in other wave lengths too, here we discuss primarily the mm-submm wave astronomy.

Among the telescopes in mm-submm wavelengths, ALMA is particularly very important; it has unprecedented spectroscopic capability throughout the spectroscopic windows for nearby as well as distant sources. While using a single dish one can study presence of molecules with a typical beam size ∼30 arcsecond. So, for young stellar objects (limited to a few arcsecond scale) we cannot study using a single dish observation. The ALMA, using higher base line can achieve images at 0.1 arcsecond (at 1 mm) or better that can be achieved by Hubble space telescope at visible wavelength. Some of the first discoveries in case of HH212 are discussed in this section.

Now, coming back to the molecular transition, a great discovery was the CO J=1→ 0 rotational line (2.6 mm) by Wilson et al. [38]. It was soon realized that CO J=1→0 transition arises from the collisions at fairly high interstellar density ($n \geq 10^2\,cm^{-2}$) with hydrogen as the collision partner. As, $H_2$ does not have a permanent dipole moment, it cannot be traced through rotational line transitions. Hence, CO can be effectively used as a measure of density. The abundance of CO relative to $H_2$ is $\sim 10^4\,cm^{-3}$. By converting CO column density to $H_2$, we can get the density of molecular clouds. Similarly, based on observational evidences, many molecular lines are effectively used as a tracer of different physical conditions of molecular cloud.

## *4.4 HH212 and as Seen by Molecular Line Tracer*

Stars are formed by means of gravitational collapse of molecular cloud core. Due to the presence of effects like magnetic field and angular momentum, the scenario becomes more complicated. For this reason, in addition to infall (or collapse), rotation and outflow are also seen in the star-forming region. Theoretical model prediction suggests that a rotationally supported disk is expected to form inside a collapsing core from which a part of matter is ejected as jets and outflows.

HH212 system is deeply embedded in a compact molecular cloud core in L1630 cloud of Orion at a distance of 400pc. The central source is a Class 0 protostar IRAS 05413-0104 and it drives a powerful outflow jet [18] as seen using SiO lines. The SiO line is a good tracer of shock and energetic outflow. The formation of SiO can be attributed to sputtering from Silicate grain mantle due to energetic interaction of shocks and outflows. Previous observations using SMA telescope ∼ 2.5″ resolution showed a flattened envelope around the central source using $^{18}$CO (J=2→1) and $^{13}$CO (J=2→1) lines as a tracer. The envelope is infalling with a rotation i.e. spiraling into the central source, thus it can be identified as a pseudo disk. A rotationally supported disk was not confirmed from the SMA (Sub-Millimeter Array) observation of the source [18]. High angular resolution observation in $HCO^+$ (J=4→3) and continuum (350 GHz) using ALMA shed light into this. Lee et al. [19] simultaneously modeled $HCO^+$ line and continuum emission and showed the

presence of flattened envelope around the central source extending out to ∼800 AU (2″). The $HCO^+$ kinematics show that the envelope is falling with a rotation. A disk ∼120 AU (0.3″) was predicted in the observation. However, the predicted disk with Keplerian distribution was a tentative one until later ALMA observation revealed more about it. From the same ALMA observation, Codella et al. [7] used $C^{17}O$ line to study kinematics of HH212. Different velocity components of $C^{17}O$ traces different physical property. Near systematic velocity (1.7 km/s) it shows the infalling envelope. At high velocity (> 3.6 km/s), it traces a disk ∼90 AU (0.2″) with Keplerian rotation around a stellar mass of $0.3\pm0.1\ M_\odot$. The $C^{34}S$ lines show a wide angle 'X' shaped outflow surrounding the bipolar-jet.

### *4.5 Formaldehyde(HDCO) and Deuteration in HH212*

The HDCO emission was found to be symmetric around the systematic velocity of HH212. It implies that the emission arises near the central hot-region. In the hot-region, the temperature is high enough and molecules on the grain surfaces (i.e., ice/dust) come out of it into the gas phase. To know the excitation temperature equivalent to rotational temperature under local thermodynamic equilibrium (LTE) condition of a molecule, one should observe multiple line transition of the same molecule. As, we observed a single line transition of HDCO, there was no scope to know the rotational temperature and derive the column density from that. To get column density and thereby the abundance of HDCO, we considered a range of temperatures for the line transition. The derived column density was in the order of $\sim10^{-14}\,cm^{-3}$. From Fig. 2, we see that HDCO emission is concentrated around the central hot region. This is probably due to high temperature (>100 K) thermal desorption into the gas phase, typical to the hot-corino environment. Except the emission near the central hot-corino, there is another outflow component which is similar to the large scale outflow as traced by $C^{34}S$ emission. HDCO can be produced on the grain surface in low-temperature (<40 K) and get out of the grain surface due to the energetic interaction with the outflow. Comparing the two emission components and $D_2CO$ emission as observed by Lee et al. [20], we speculate that the deuterium fractionation is comparatively higher than the methanol [2] deuteration. We guess there may be a gas phase route for HDCO production in the central hot-corino region of HH212. These kind of observations (high spatial resolution) using ALMA were previously unavailable. We can measure the deuteration more accurately without significant beam dilution of molecular line emission. Theoretical models are yet to describe the observed deuteration of the HH212 protostar.

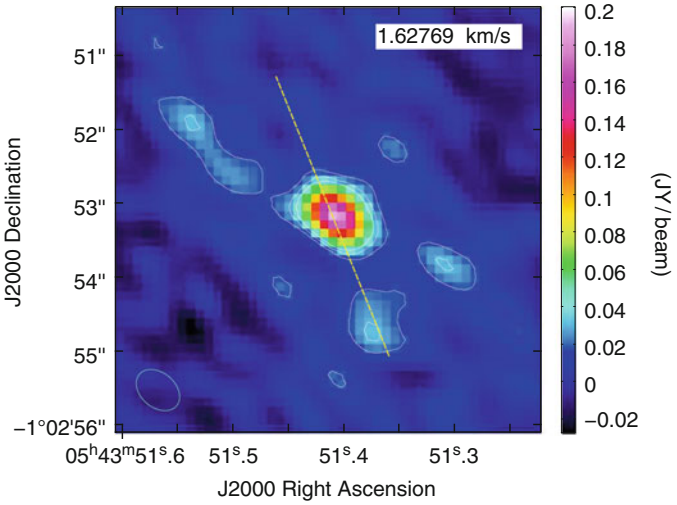



**Fig. 2** HDCO emission map of HH212 protostar system around systematic velocity. The line represents the direction of bipolar SiO jet. Strong HDCO emission can be seen in the central region. The faint emission features away from the central source are due the large scale outflow of the HH212 system. Adopted from [32] ©MNRAS

**Acknowledgements** I want to thank my supervisors Dr. Ankan Das and Prof. Sandip K. Chakrabarti for introducing me into the subject- Astrochemistry. I appreciate the effort of the Editors, for giving me a chance to write in this Festschrift.

## References

1. Barrett, A.H., Lilly, A.E.: AJ **62**, 5 (1957)
2. Bianchi, E., et al.: A&A **606**, L7 (2017)
3. Caselli, C., Stantcheva, T., et al.: Plan. and space sci. **50**, 1257 (2002)
4. Cazaux, S., Caselli, P., Spaans, M.: ApJ **741**, L34 (2011)
5. Ceccarelli, C., Dominik, C.: A&A **440**, 583 (2005)
6. Chen, H.-R., Liu, S.-Y., Su, Y.-N., Wang, M.-Y.: ApJ **743**, 196 (2011)
7. Codella, C., et al.: A&A **568**, L5 (2014)
8. Croswell, K., Dalgarno, A.: ApJ **289**, 618 (1985)
9. Das, A., Majumdar, L., Chakrabarti, S.K., Sahu, D.: New Astron. **35**, 53 (2015)
10. Das, A., Majumdar, L., Sahu, D., Gorai, P., Sivaraman, B., Chakrabarti, S.K.: ApJ **808**, 21 (2015)
11. Das, A., Sahu, D., Majumdar, L., Chakrabarti, S.K.: MNRAS **455**, 540–551 (2016)
12. Epstein, R.I., Lattimer, J.M., Schramm, D.N.: Nature **263**, 198 (1976)
13. Fontani, F., Caselli, P., Crapsi, A., et al.: A&A **460**, 709 (2006)
14. Fontani, F., Palau, A., Caselli, P., et al.: A&A **529**, L7 (2011)
15. Furuya, K., Drozdovskaya, M.N., Visser, R., van Dishoeck, E.F., Walsh, C., Harsono, D., Hincelin, U., Taquet, V.: A&A **599**, 40 (2017)

16. Herzberg, G.: Spectra of Diatomic Molecules, p. 496. Van Nostrand Reinhold, New York (1950)
17. Kraus, J.D.: Radio Astronomy, p. 101. Cygnus-Quasar, Powell (1986)
18. Lee, C.-F., Ho, P.T.P., Hirano, N., et al.: ApJ **659**, 499 (2007)
19. Lee, C.-F., Hirano, N., Zhang, Q., Shang, H., Ho, P.T.P., Krasnopolsky, R.: ApJ **786**, 114 (2014)
20. Lee, C.-F., Li, Z.-Y., Ho, P.T.P., Hirano, N., Zhang, Q., Shang, H.: ApJ **843**, 27 (2017)
21. Lis, D.C., Roueff, E., Gerin, M., Phillips, T.G., Coudert, L.H., van der Tak, F.F.S., van der Tak, F.F.S., Schilke, P.: ApJ **571**, L55 (2002)
22. Millar, T.J.: Plasma Sources Sci. Technol. **24**, 043001, 31pp. (2015)
23. Parise, B., Ceccarelli, C., Tielens, A.G.G.M., Castets, A., Caux, E., Lefloch, B., Maret, S.: A&A **453**, 949 (2006)
24. Penzias, A.A., Wilson, R.W.: ApJ **142**, 419 (1965)
25. Persson, M.V., Jørgensen, J.K., van Dishoeck, E.F.: A&A **549**, L3 (2013)
26. Persson, M.V., Jørgensen, J.K., van Dishoeck, E., Harsono, D.: ApJ **563**, 74 (2014)
27. Pillai, T., Wyrowski, F., Hatchell, J., Gibb, A.G., Thompson, M.A.: A&A **467**, 207 (2007)
28. Prodanovi'c, T., Fields, B.D.: Astrophys. J. **597**, 48 (2003)
29. Reeves, H., Audouze, J., Fowler, W., Schramm, D.N.: ApJ **179**, 909 (1973)
30. Roberts, H., Millar, T.J.: A&A **471**, 849 (2007)
31. Sahu, D., Das, A., Majumdar, L., Chakrabarti, S.K.: New Astron. **38**, 23 (2015)
32. Sahu, D., Minh, Y.-C., Lee, C.-F., et al.: MNRAS **475**, 5322 (2018)
33. Spezzano, S., Caselli, P., Bizzocchi, L., Giuliano, B.M., Lattanzi, V.: A&A **606**, 25pp. (2017)
34. Swings, P., Rosenfeld, L.: ApJ **86**, 483 (1937)
35. Taquet, V., Ceccarelli, C., Kahane, C.: ApJ **748**, L3 (2012)
36. Walmsley, C.M., Flower, D.R., Pineau Des Forêts, G.: A&A **418**, 1035 (2004)
37. Weinreb, S., Barrett, A.H., Meeks M.L., Henry, J.C.: Nature **200**, 829 (1963)
38. Wilson, R.W., Jefferts, K.B., Penzias, A.A.: ApJL **161**, L43 (1970)

# Binding Energy and Isomerism: Two Important Aspects of Astrochemistry




**Milan Sil**

**Abstract** Hydrogen is widespread in the universe and $H_2$, the precursor to more complex molecules, is mainly formed on the interstellar dust grain surface and binding energy dictates the surface chemistry. We review the adsorption energy of H and $H_2$ to find out the accurate formation efficiency of hydrogen molecules in the interstellar medium (ISM). Various types of substrate (carbonaceous, olivine, and water ice) were used to mimic interstellar dust grain. Interestingly we found that our calculated binding energy of H is always lower than that of $H_2$ for all types of adsorbent considered, whereas, some experiments found just the opposite trend. Though the ISM is far away from thermodynamic equilibrium, in some cases, isomerism of any specific group of molecules can be used as a way to determine the potential future observable candidates in interstellar space. Understanding the origin of life is a traditional mystery and it is curious to know how life emerged in the universe. We considered a set of molecules from various isomeric groups containing some probable precursors of the pre-biotic species to review their presence within ISM. For the selection of potentially observable molecules in between an isomeric group, we used some key tools such as enthalpies of formation, optimized energies, expected intensity ratio, and chemical abundances. According to our calculations, we proposed trans-ethylamine and (1Z)-1-propanimine as the most probable candidates from two different isomeric groups for future astronomical detection.

## 1 Introduction

Astrochemistry mainly studies the formation and destruction of molecules in space. The subject also includes chemical composition, evolution and fate of molecular clouds in the interstellar and circumstellar environments. According to the prediction of the big bang model of the universe, hydrogen is the most abundant, then

M. Sil (✉)
Indian Centre for Space Physics, Kolkata, India

© Springer International Publishing AG, part of Springer Nature 2018

B. Mukhopadhyay, S. Sasmal (eds.), *Exploring the Universe: From Near Space to Extra-Galactic*, Astrophysics and Space Science Proceedings 53,
https://doi.org/10.1007/978-3-319-94607-8_38

helium, a little bit of lithium and other volatile species. Stars, galaxies and clusters of galaxies were then formed by pulling the available matter together subsequently through Gravity and all of them emit light of different wavelength which gives information about the molecular story of the star formation and evolution. The star-formation cycle ends with a blast of supernova through which huge quantities of material spread out into space which are again used to form new stars. The interstellar material exists mainly in the form of different types of cloud, consisting of gas ($\sim$ 99% by mass) and tiny dust ($\sim$ 1% by mass) particles. These clouds are the birthplaces of stars like our Sun and planets like our living home Earth.

Hydrogen is known as the most abundant element in the whole Universe. The spectral characteristics of molecular clouds in the far-UV and near-IR region are strongly dominated by molecular hydrogen due to its very high abundance [43]. Since the possibility of one single hydrogen atom finding a larger grain surface is much higher than that of two hydrogen atoms finding each other in the gas phase, calculation of binding energy of H and $H_2$ with appropriate grain surface is essential to understand their synthesis in the gas phase as well as interstellar icy grain mantle. Incoming H atoms can stick with grain surfaces and form molecules via different acceptable mechanism like Langmuir-Hinshelwood (LH), Eley-Rideal (ER), and hot-atom mechanism.

According to https://www.astro.uni-koeln.de/cdms/molecules, around 200 atomic and molecular species have already been observed in the ISM or circumstellar shells indicating that the formation of biomolecules [8–10] takes place in collapsing clouds and star-forming regions. Majumdar et al. [33, 34] indirectly indicated that if the abundances of the life-forming bio-molecules are below the observable limit, there is a chance to observe their precursors for estimating the abundances of these bio-molecules. Though, no amino acid is successfully detected in ISM till date, according to [22], most of them have already been identified from meteorites bombarded on Earth indicating that there may be a link between the molecular composition of ISM and meteorites. Since most of the amino acids identified in meteorites are branched amino acids [7, 11], the observation of n-propyl cyanide [5] and i-propyl cyanide [6] (branched chain molecule) from $C_4H_7N$ isomeric group in ISM towards Sgr B2(N) further stresses the possibility of this link. However, in order to firmly establish this link, Etim et al. [23] proposed tert-butylnitrile from the $C_5H_9N$ isomeric group as the most probable candidate for future astronomical observation.

We target isomeric groups containing aldimines and amines as they are the basic building blocks of amino acids. Methanimine and formic acid react to form the simplest amino acid glycine [27] which indicate that the interstellar glycine could be formed from methanimine [41]. Holtom et al. [29] studied that glycine could have been produced by the reaction between methylamine and carbon-di-oxide under UV irradiation on an icy grain mantle. Again, production of methylamine could be possible by two successive hydrogen addition reactions with methanimine and by four successive hydrogen additions reaction with HCN on grain surface [27, 42]. Glycine may also be produced by the reaction between $CH_2NH_2$ and COOH radical [45] suggesting methylamine as an important precursor of glycine

formation. Similarly, ethylamine also performs the role of precursor molecule for glycine formation in ISM. Both these precursor molecules (methylamine and ethylamine) of glycine were already detected in comet Wild 2 [26] and in the coma of 67P/Churyumov–Gerasimenko [2]). Methanimine ($CH_2NH$), methylamine ($CH_3NH_2$) and ethanimine ($CH_3CHNH$) from $CH_3N$, $CH_5N$ and $C_2H_5N$ isomeric groups respectively were already observed in Sgr B2 [27], in both Sgr B2 and Orion A [24, 30] and again in Sgr B2 [32] respectively. It is essential to know the spectroscopic details and the chemical abundances of the species to find out the most probable candidate from the next $C_2H_7N$, $C_3H_7N$, and $C_3H_9N$) isomeric groups. The discovery of these molecules under astrophysical environment could be treated as important clues towards the origin of life.

This article consists of following sections. Section 2 describes the computational part of our work. Results are shown and discussed in Sect. 3 and based on the results finally conclusions are drawn in Sect. 4.

## 2 Computational Details and Methodology

We calculated the adsorption energy of a species on the grain surface using the mother equation,

$$E_{ads} = E_{ss} - (E_{surface} + E_{species}), \tag{1}$$

where, $E_{ads}$, $E_{ss}$, $E_{surface}$ and $E_{species}$ are the calculated adsorption energy of a particular species, the optimized energy for the complex containing both the species and grain surface, the optimized energies of the grain surface and species respectively.

### *2.1 Quantum-Chemical Calculations*

Quantum-chemical calculations play a significant role in interstellar chemistry by providing kinetic, thermodynamics, spectroscopic parameters that can guide laboratory detection or astronomical observation of molecules. Electronic structure theory is one of the main areas of computational chemistry devoted to the study of the optimized structure of molecules, their properties and their reactivity. We use the Gaussian 09 suite of programs [25] as main computational software for various quantum chemical studies. Gaussian 09 computational chemistry program is a general purpose electronic structure package based on quantum mechanics through solving the Schrödinger equation in order to compute a wide range of atomic and molecular properties such as reaction pathways, optimized energies, transition states, vibrational frequencies, rotational constants, dipole and higher order moments, excited states, thermochemical properties, rotational and distortional constants, off-diagonal nuclear quadrupole coupling constants etc. many

of which are not easily obtained via experimental methods. Accurate quantum-chemical studies have succeeded in providing reliable spectroscopic details to aid laboratory microwave studies and to detect interstellar species with confidence.

For various isomeric groups, here we supply in Table 2 the sum of electronic ($E_0$) and zero-point energy (ZPE) in hartree/particle and relative energy (in parentheses) in Kcal/mol using DFT B3LYP 6-31G(d) level of theory, total dipole moments ($\mu_{tot}$) and their components along the inertial axes ($\mu_a$, $\mu_b$, and $\mu_c$) in Debye using HF/6-31G(d) level of theory and rotational constants in GHz using Gaussian 4 (G4) composite method.

### *2.2 Chemical Modeling*

Chemical modeling is one of the most important parts of astrochemistry now-a-days which is used [15, 18, 19, 40] to probe the chemical abundance of the interstellar species under various interstellar astrochemical conditions. For constructing the chemical model, we need to consider the chemistry occurring on gas and dust (grain) both the phases. This is because, although by mass the dust consists of only 1% of the total ISM, it plays a significant role in the physics and chemistry of the ISM by helping to form many COMs, starting from hydrogen. So, it is necessary to incorporate gas-grain chemical interaction into the chemical model to explore actual physical processes going on the different interstellar cloud. Our large gas-grain chemical network [12–20, 28, 38, 40] is used for the purpose of chemical modelling where gas and grains both are coupled together.

## 3 Results and Discussions

### *3.1 Binding Energies of H and $H_2$*

Sil et al. [39] recently calculated the binding energies of H and $H_2$ using MP2/aug-cc-pVDZ method by considering different adsorbents presented in Fig. 1 using Eq. (1). Polarizability and diamagnetic susceptibility of H and $H_2$ were calculated using B3LYP/6-311g(d,p) method in order to calculate the binding energies of H and $H_2$ (268 K and 944 K respectively) on a graphite surface employing the relation from [3, 4]. Sil et al. [39] calculated the binding energy values for H and $H_2$ as 336 K and 1006 K respectively using benzene surface to mimic graphite as carbonaceous grain, 580 K and 1090 K respectively using silica cluster surface to mimic silicate grain and 1814 K and 545 K respectively using water cluster surface to mimic water ice interstellar grain mantle. For all the substrates they found a similar trend for all cases, which is, binding energy of $H_2$ is higher than that of H. Taking the average

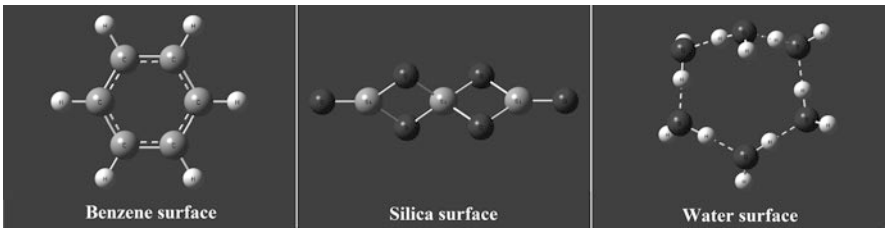



**Fig. 1** Different adsorbents used as interstellar grains

**Table 1** Available values of binding energies in kelvin of H and $H_2$

| Species | Set 1 Olivin [31] | Set 2 Amorphous carbon [1, 31] | Set 3 [44] | Set 4 [36] | Our calculated average value |
|---|---|---|---|---|---|
| H | 373 | 658 | 350 | 499 ± 3 | 341 |
| $H_2$ | 314 | 542 | 450 | 660 ± 6 | 896 |

(given in column 6 of Table 1) of all values of binding energy calculated by Sil et al. [39], we get 341 K and 896 K for H and $H_2$ respectively.

Table 1 presents different sets of already available theoretical and experimental values of binding energies of H and $H_2$. The desorption energies of H and $H_2$ are experimentally determined by Katz et al. [31] (Set 1) for olivine grain with values of 373 K and 314 K and for amorphous carbon (Set 2) by Katz et al. [31], Pirronello et al. [36] with values of 658 K for H and 542 K for $H_2$. Set 3 corresponds to a theoretical value obtained by Allen and Robinson [1]. Set 4 gives the estimated values of binding energies from an experiment. It is to be noted that the binding energy of $H_2$ molecule is less compared to that of H atom for Set 1 and Set 2 whereas, for Set 3 and Set 4, the trend is opposite. Interestingly, for all our calculations by Sil et al. [39] and also from our calculated average values of binding energy of H and $H_2$, we obtain a similar trend between H and $H_2$ as of Set 3 and 4. That is, the adsorption energy of $H_2$ is found to be always greater than that of H for all types of surfaces considered here. Recently, Das et al. [21] have calculated appropriate values of binding energy of some relevant interstellar species.

## *3.2 Isomerism*

Astrochemical study of different existing isomers from a specific isomeric group can predict the most probable isomer from that group for future astronomical observations. We consider total 34 isomers (presented in Table 2) from 6 different isomeric groups ($CH_3N$, $CH_5N$, $C_2H_5N$, $C_2H_7N$, $C_3H_7N$, and $C_3H_9N$) containing at least one aldimine or amine from each group to review the presence of them within ISM. Molecules are arranged in Table 2 according to their calculated relative

**Table 2** Calculated values of relative energies and spectral properties of different aldimines and amines from various isomeric group

| Sl. no. | Species | Astronomical status | $E_0$+ZPE in H/P (relative energy in Kcal/mol) | Dipole moment (Debye) | | | | Rotational constants (GHz) | | |
|---|---|---|---|---|---|---|---|---|---|---|
| | | | | $\mu_a$ | $\mu_b$ | $\mu_c$ | $\mu_{tot}$ | A | B | C |
| *$CH_3N$ isomeric group* | | | | | | | | | | |
| 1. | Methanimine | Observed[a] | −94.587165 (0.00) | −1.5558 | 1.6157 | 0.0000 | 2.2430 | 197.9741113 | 34.8777307 | 29.6535672 |
| 2. | $\lambda^1$-Azanylmethane | Not observed | −94.514481 (45.61) | 0.0000 | 0.0000 | −2.0486 | 2.0486 | 157.3550760 | 27.8196556 | 27.8196556 |
| *$CH_5N$ isomeric group* | | | | | | | | | | |
| 1. | Methylamine | Observed[b,c] | −95.788769 (0.00) | −1.4798 | 0.4108 | 0.0000 | 1.5358 | 103.0667143 | 22.7187286 | 21.8653216 |
| *$C_2H_5N$ isomeric group* | | | | | | | | | | |
| 1. | E-Ethanimine | Observed[d] | −133.883592 (0.00) | 0.7003 | 2.1103 | 0.0000 | 2.2235 | 53.6510872 | 9.7633679 | 8.7038309 |
| 2. | Z-Ethanimine | Observed[d] | −133.883093 (0.31) | −2.5834 | −0.5190 | −0.0025 | 2.6350 | 50.7326409 | 9.7860304 | 8.6405953 |
| 3. | N-Methylmethanimine | Not observed | −133.873740 (6.18) | 0.0803 | 1.7349 | 0.0000 | 1.7367 | 53.4385516 | 10.6582615 | 9.4010277 |
| 4. | Ethenamine | Not observed | −133.873496 (6.34) | −0.8935 | 0.0390 | 1.2642 | 1.5485 | 57.0958323 | 10.0011580 | 8.5864198 |
| 5. | Aziridine | Not observed | −133.848891 (21.77) | 0.0005 | 1.0105 | 1.6612 | 1.9444 | 22.9530891 | 21.2053212 | 13.4521489 |
| *$C_2H_7N$ isomeric group* | | | | | | | | | | |
| 1. | Ethylamine (trans) | **We proposed** | −135.077435 (0.00) | −1.0444 | −1.0691 | 0.0000 | 1.4946 | 31.9454882 | 8.7056210 | 7.7781645 |
| 2. | Ethylamine (gauche) | Not observed | −135.076779 (0.41) | 0.2399 | 0.7026 | 1.2549 | 1.4581 | 32.6271270 | 8.9000329 | 7.8134749 |
| 3. | Dimethylamine | Not observed | −135.069850 (4.76) | −0.0003 | −0.2370 | 1.1177 | 1.1425 | 34.6673787 | 9.2962535 | 8.2122396 |
| *$C_3H_7N$ isomeric group* | | | | | | | | | | |
| 1. | 2-Propanimine | Not observed | −173.177439 (0.00) | −1.3069 | −2.1673 | 0.0003 | 2.5308 | 9.64694 | 8.48897 | 4.78348 |
| 2. | (1E)-N-Methylethanimine | Not observed | −173.169746 (4.83) | 0.2751 | 1.6630 | −0.0005 | 1.6856 | 38.04146 | 4.07938 | 3.86089 |
| 3. | (1E)-1-Propanimine | Not observed | −173.167913 (5.978) | 0.9350 | −1.1103 | 1.6223 | 2.1769 | 23.30832 | 4.33503 | 4.20885 |
| 4. | (1Z)-1-Propen-1-amine | Not observed | −173.167911 (5.979) | 0.9366 | −1.1108 | 1.6212 | 2.1770 | 23.30833 | 4.33547 | 4.20908 |
| 5. | (1Z)-1-Propanimine | **We proposed** | −173.167428 (6.28) | −2.4803 | 1.0854 | 0.2029 | 2.7150 | 23.19882 | 4.28693 | 4.17097 |
| 6. | 2-Propenamine | Not observed | −173.165761 (7.33) | 0.2510 | −0.8774 | −1.1862 | 1.4966 | 9.54753 | 8.97855 | 4.79187 |
| 7. | (1E)-1-Propen-1-amine | Not observed | −173.162291 (9.51) | 1.0898 | −0.4583 | −0.2748 | 1.2138 | 38.31516 | 3.85080 | 3.59371 |
| 8. | N-Ethylmethanimine | Not observed | −173.161486 (10.01) | 0.2187 | 0.9274 | 1.3398 | 1.6440 | 24.05782 | 4.60272 | 4.48201 |
| 9. | N-Methylethenamine | Not observed | −173.153680 (14.91) | −1.0995 | −0.0800 | 0.8010 | 1.3627 | 32.00012 | 4.30235 | 4.04446 |
| 10. | Allylamine | Not observed | −173.149094 (17.79) | 0.9583 | −1.0362 | 0.0305 | 1.4118 | 23.65103 | 4.23494 | 4.17205 |
| 11. | Cyclopropanamine | Not observed | −173.141087 (22.81) | 0.5389 | −0.0002 | 1.3097 | 1.4162 | 16.28786 | 6.72692 | 5.80201 |

| | | | | | | | | | | |
|---|---|---|---|---|---|---|---|---|---|---|
| 12. | (2S)-2-Methylaziridine | Not observed | −173.140561 (23.1411) | −0.2420 | 0.6537 | 1.7124 | 1.8488 | 16.91889 | 6.53525 | 5.76592 |
| 13. | S-2-Methylaziridine | Not observed | −173.140560 (23.1417) | −0.2429 | −0.6533 | 1.7119 | 1.8484 | 16.91977 | 6.53608 | 5.76664 |
| 14. | 2-Methylaziridine (trans) | Not observed | −173.140559 (23.1423) | 0.2426 | 0.6522 | 1.7119 | 1.8479 | 16.92200 | 6.53613 | 5.76677 |
| 15. | 2-Methylaziridine (cis) | Not observed | −173.140051 (23.46) | −1.3360 | 1.1073 | −0.9894 | 1.9975 | 16.68599 | 6.56078 | 5.81794 |
| 16. | Azetidine | Not observed | −173.137487 (25.07) | 0.0000 | 0.4603 | 1.3597 | 1.4355 | 11.54225 | 11.36812 | 6.70581 |
| 17. | Methylaziridine | Not observed | −173.132935 (27.93) | 0.1215 | 0.0006 | 1.4692 | 1.4742 | 16.41594 | 7.25710 | 6.19112 |
| 18. | N-Methylethanamine | Not observed | −173.107533 (43.87) | 0.8499 | −1.1993 | 0.0025 | 1.4700 | 36.98588 | 4.14324 | 3.84501 |
| 19. | (Dimethyliminio)methanide | Not observed | −173.094985 (51.74) | −0.5473 | 0.0306 | −1.2990 | 1.4099 | 10.15847 | 9.14934 | 5.12560 |
| *$C_3H_9N$ isomeric group* | | | | | | | | | | |
| 1. | 2-Aminopropane | Not observed | −174.365796 (0.00) | | | | | | | |
| 2. | Propylamine | Not observed | −174.361745 (2.54) | | | | | | | |
| 3. | Ethylmethylamine | Not observed | −174.357863 (4.98) | | | | | | | |
| 4. | Trimethylamine | Not observed | −174.353287 (7.85) | | | | | | | |

[a]Godfrey et al. [27]
[b]Kaifu et al. [30]
[c]Fourikis et al. [24]
[d]Loomis et al. [32]

energies with respect to the most stable molecules having least electronic ($E_0$) with ZPE from each isomeric group.

Recently Sil et al. [40] already supplied the ice-phase formation pathways and gas-phase formation and destruction pathways of amines and aldimines both in ice and gas phase in which radical-radical (RR) reactions occur at each encounter but neutral-radical (NR) reactions possess activation barrier. They also performed a set of calculations such as Gibbs free energy of activation, transition state structures, enthalpies of formation, relative energies, total dipole moment and their components along the inertial axes, rotational constants, rotational partition function at $\sim$ 200 K temperature. The intensity of rotational transition is proportional to $\mu^2/Q(T_{rot})$, where $\mu$ is the electric dipole moment and $Q(T_{rot})$ is the partition function at the rotational temperature ($T_{rot}$). Sil et al. [40] also modeled for calculating the chemical abundances of various amine and aldimines in ISM. Initially, they assumed that the cloud remains in isothermal (at T = 10 K) phase for $10^6$ years and warm-up phase (temperature can gradually increase up to 200 K) for another $10^5$ years. So the total simulation time was used $1.1 \times 10^6$ years maintaining a constant density ($n_H = 10^7\,cm^{-3}$).

In this subsection, the results of high-level quantum chemical calculations and chemical modeling used by Sil et al. [40] are presented and discussed briefly.

Methanimine ($CH_2NH$) and $\lambda^1$-azanylmethane are the two isomers from $CH_3N$ isomeric group. Based on the relative energy values shown in Table 2, methanimine (already observed) appears to be stable candidate than $\lambda^1$-azanylmethane (not observed) having the energy difference 45.61 Kcal/mol. The total dipole moment of methanimine (2.2430 D) is slightly higher than that of $\lambda^1$-azanylmethane (2.0486 D). Our calculated rotational constants for both the molecules in this group are also shown in Table 2. According to [40], enthalpy of formation was not sufficient to dictate the abundance of methanimine. They calculated the abundances with respect to $H_2$ molecules for all the molecules of different isomeric groups. In the warm-up phase, the peak abundance of gas-phase methanimine was around $1.81 \times 10^{-09}$ compared with the recent hot-core observation of methanimine $\sim 7.0 \times 10^{-08}$ in G10.47+0.03 and $3.0 \times 10^{-9}$ in NGC6334F by Suzuki et al. [41].

Methylamine ($CH_3NH_2$), the known interstellar species, is the only candidate from $CH_5N$ isomeric group. According to [29, 45], it is the precursor of the simplest amino acid glycine. We have calculated optimized energy, dipole moments and rotational constants of methylamine shown in Table 2. As mentioned in [40], in the warm-up phase, methylamine attained a peak value of $5.54 \times 10^{-07}$ in the gas phase and $5.44 \times 10^{-07}$ in ice phase respectively which may be compared with the recent observation of methylamine [35] in G10.47+0.03 having abundance $\sim 1.2 \times 10^{-08}$.

There are five isomers belong to $C_2H_5N$ isomeric group, namely, E-ethanimine, Z-ethanimine, N-methylmethanimine, ethenamine, and aziridine. Both the conformers (E and Z) of ethanimine ($CH_3CHNH$) were already detected and remaining three candidates are yet to observe. From our calculation, we found that E-ethanimine is energetically slightly more stable (by 0.31 Kcal/mol) than Z-ethanimine. The effective total dipole moment of Z-ethanimine is higher than that of E-ethanimine. In Table 2, we point out the rotational constants and dipole moments. According

to [40], E-ethanimine had the minimum enthalpy of formation followed by Z-ethanimine and the predicted gas phase abundance of ethanimine had a peak value of $3.17 \times 10^{-08}$ during the warm-up phase. At the end of simulation (after $1.1 \times 10^6$ year), thay got an abundance of $1.27 \times 10^{-12}$ for Z-ethanimine whereas the predicted abundance of Z-ethanimine is $\sim 6.0 \times 10^{-11}$ by Quan et al. [37].

Three isomers (trans-ethylamine, gauche-ethylamine, and dimethylamine) belong to $C_2H_7N$ isomeric group from where no species is detected yet in the ISM. Ethylamine is the precursor of glycine. Between its two stable conformers, the trans conformer is slightly more stable by 0.41 Kcal/mol than the gauche conformer. According to [40], trans-ethylamine had the least enthalpy of formation and the highest expected intensity ratio ($\sim$ 1) and most stablity among all three candidates from this isomeric group. Thus from this isomeric group, trans-ethylamine has the highest possibility of its astronomical detection. In the warm-up phase, they got gas phase peak abundance of $3.98 \times 10^{-08}$. From a recent observation by Altwegg et al. [2], abundance ratio between methylamine and glycine is $\sim 1.0 \pm 0.5$ and ethylamine to glycine is $\sim 0.3 \pm 0.2$ in a comet 67P/Churyumov-Gerasimenko. In order to check the correlation between the cometary ice as observed by Altwegg et al. [2] and interstellar ice, [40] focused on ice phase evolution of the isothermal ($T = 10$ K) phase. From their modeling results, they found that in the isothermal phase, the methylamine to ethylamine abundance ratio to be $\sim$ 17.7 in the ice phase which is very close to the observed value ranges $\sim$ 1–15 [2] suggesting that more in-depth study is required to confirm this linkage between the interstellar and cometary origin of these molecules.

There are 19 isomers which belong to $C_3H_7N$ isomeric group from which no species has been detected yet in the ISM. In Table 2, we sort them according to their relative energies. Clearly, 2-propanimine (molecule no. 1) is the most stable and (Dimethyliminio)methanide (molecule no. 19) is the least stable isomer from this group. Sil et al. [40] also showed (Dimethyliminio)methanide (molecule no. 19) had the highest enthalpy of formation and least stablity among others in this group. Interestingly, (1Z)-1-propanimine (molecule no. 5) has the highest total effective electric dipole moment (2.7150 D) and the strongest a-type transition (2.4803 D) from this isomeric group. Sil et al. [40] found assuming same abundances of all these isomeric species, (Dimethyliminio) methanide and (1Z)-1-propanimine may be the most probable candidate for the astronomical detection from this group. Since (Dimethyliminio)methanide is not very stable species, it does not have a high probability of detection. Thus, based on the enthalpy of formation, stability, and expected intensity ratio, (1Z)-1-propanimine maintains its existence as the most probable species for the future astrochemical detection from this isomeric group. However, the available or proposed reaction pathways can ultimately decide the fate of this species. It was evident that the production of (1Z)-1-propanimine is only favourable in the hot core region where peak gas-phase abundance obtained as $2.20 \times 10^{-08}$ [40].

There are only 4 isomers (2-aminopropane, propylamine, ethylmethylamine and trimethylamine) from $C_3H_9N$ isomeric group. As mentioned in [40], We also find 2-aminopropane (a branched chain molecule) as the most stable isomer from this

group. According to them, trimethylamine had the maximum rotational intensity for its lower partition function in spite of its lowest total dipole moment value among others from this isomeric group. We do not calculate the rotational constants and dipole moments from this group since [40] indicated the production of propanimine from the very last isomeric group $C_3H_7N$, was very insufficient to product any species from this group.

## 4 Concluding Remarks

From our calculated physisorption energies of the hydrogen atom and molecule on different grain surfaces, we found an interesting trend that binding energy of $H_2$ molecule remains always higher than that of the H atom for all the cases whereas some early experimental works got the opposite trend. Based on this result, we would like to revisit the binding energy values of some other relevant interstellar and circumstellar species in near future. Detectability of some species in a few isomeric groups containing aldimine or amine in each group are discussed based on the enthalpy of formation, chemical abundance, rotational transition along with the radiative transfer modeling. We suggested trans-ethylamine and (1Z)-1-propanimine as the most probable candidate from $C_2H_7N$ and $C_3H_7N$ aldimines and amines isomeric groups respectively for future astronomical detection in the ISM. The spectroscopic results and dipole moments that could guide the future astronomical searches for these molecular species have been provided in this study.

**Acknowledgements** I thankfully want to acknowledge Department of Science and Technology, the Government of India for supporting me financially for continuing my work through DST-INSPIRE Fellowship [IF160109] scheme. I also want to thanks Dr. Ankan Das, Mr. Prasanta Gorai, and Prof. Sandip K. Chakrabarti for help and support to complete these works.

## References

1. Allen, M., Robinson, G.W.: ApJ **212**, 396 (1977)
2. Altwegg, K., Balsiger, H., Bar-Nun, A., et al.: SciA **2**, e1600285 (2016)
3. Avgul, N.N., Isirikyan, A.A., Kiselev, A.V., Lygina, I.A., Poshkus, D.P.: Russ. Chem. Bull. **6**, 1334 (1957)
4. Avgul, N.N., Kiselev, A.V., Lygina, I.A., Poshkus, D.P.: Russ. Chem. Bull. **8**, 1155 (1959)
5. Belloche, A., Garrod, R.T., Müller, H.S.P., Menten, K.M., Comito, C., Schilke, P.: A&A **499**, 215 (2009)
6. Belloche, A., Garrod, R.T., Müller, H.S.P., Menten, K.M.: Sci. **345**(6204), 1584 (2014)
7. Botta, O., Bada, J.L.: Surv. Geophys. **23**, 411 (2002)
8. Chakrabarti, S., Chakrabarti, S.K.: A&A **354**, L6 (2000)
9. Chakrabarti, S.K., Chakrabarti, S.: InJPh **74B**, 97 (2000)
10. Chakrabarti, S.K., Majumdar, L., Das, A., Chakrabarti, S.: Ap&SS **357**, 90 (2015)
11. Cronin, J.R., Pizzarello, S.: Adv. Space Res. **3**, 5 (1983)
12. Das, A., Chakrabarti, S.K.: MNRAS **418**, 545 (2011)

13. Das, A., Acharyya, K., Chakrabarti, S., Chakrabarti, S.K.: A&A **486**, 209 (2008)
14. Das, A., Chakrabarti, S.K., Acharyya, K., Chakrabarti, S.: New A **13**, 457 (2008)
15. Das, A., Acharyya, K., Chakrabarti, S.K.: MNRAS **409**, 789 (2010)
16. Das, A., Majumdar, L., Chakrabarti, S.K., Chakrabarti, S.: NEWA **23**, 118 (2013)
17. Das, A., Majumdar, L., Chakrabarti, S.K., Saha, R., Chakrabarti, S.: MNRAS **433**, 3152 (2013)
18. Das, A., Majumdar, L., Chakrabarti, S.K., Sahu, D.: New Astron. **35**, 53 (2015)
19. Das, A., Majumdar, L., Sahu, D., Gorai, P., Sivaraman, B., Chakrabarti, S.K.: Astrophys. J. **808**, 21 (2015)
20. Das, A., Sahu, D., Majumdar, L., Chakrabarti, S.K.: MNRAS **455**, 540 (2016)
21. Das, A., Sil, M., Gorai, P., Chakrabarti, S.K., Loison, J.-C.: ApJS **237**, 9 (2018)
22. Elsila, E., Dworkin, J.P., Bernstein, M.P., Martin, M.P., Sandford, S.A.: ApJ **660**, 911 (2007)
23. Etim, E.E., Gorai, P., Das, A., Arunan, E.: EPJD **71**(4), 86 (2017)
24. Fourikis, N., Takagi, K., Morimoto, M.: ApJL **191**, L139 (1974)
25. Frisch, M.J., Trucks, G.W., Schlegel, H.B., et al.: Gaussian 09, Revision D.01. Gaussian, Inc., Wallingford, CT (2013)
26. Glavin, D.P., Dworkin, J.P., Sandford, S.A.: M&PS **43**, 399 (2008)
27. Godfrey, P.D., Brown, R.D., Robinson, B.J., Sinclair, M.W.: ApJL **13**, L119 (1973)
28. Gorai, P., Das, A., Das, A., et al.: ApJ **836**, 70 (2017)
29. Holtom, P.D., Bennett, C.J., Osamura, Y., Mason, N.J., Kaiser, R.I.: ApJ **626**, 940 (2005)
30. Kaifu, N., Morimoto, M., Nagane, K., et al.: ApJL **191**, L135 (1974)
31. Katz, N., Furmann, I., Biham, O., Pironello, V., Vidali, G.: ApJ **522**, 305 (1999)
32. Loomis, R.A., Zaleski, D.P., Steber, A.L., et al.: ApJL **765**, L9 (2013)
33. Majumdar, L., Das, A., Chakrabarti, S.K., Chakrabarti, S.: RAA **12**, 1613 (2012)
34. Majumdar, L., Das, A., Chakrabarti, S.K., Chakrabarti, S.: NewA **20**, 15 (2013)
35. Ohishi, M., Suzuki, T., Hirota, T., Saito, M., Kaifu, N.: (2017). arXiv:1708.06871
36. Pirronello, V., Liu, C., Roser, J.E., Vidali, G.: A&A **344**, 681 (1999)
37. Quan, D., Herbst. E., Corby, J.F., Durr. A., Hassel, G.: ApJ **824**, 129 (2016)
38. Sahu, D., Das, A., Majumdar, L., Chakrabarti, S.K.: NEWA, **38**, 23 (2015)
39. Sil, M., Gorai, P., Das, A., Sahu, D., Chakrabarti, S.K.: EPJD **71**, 45 (2017)
40. Sil, M., Gorai, P., Das, A., Bhat, B., Etim, E.E., Chakrabarti, S.K.: ApJ **853**(2), 139 (2018)
41. Suzuki, T., Ohishi, M., Hirota, T., et al.: ApJ **825**, 1 (2016)
42. Theule, P., Borget, F., Mispelaer, F., et al.: A&A **534**, A64 (2011)
43. Tielens, A.G.G.M.: The Physics and Chemistry of the Interstellar Medium. Cambridge University Press, Cambridge (2010)
44. Vidali, G., Ihm, G., Kim, H.-Y., Cole, M.W.: Surf. Sci. Rep. **12**, 133 (1991)
45. Woon, D.E.: ApJL **571**, L177 (2002)

# Radiative Transfer Modeling of Some Relevant Interstellar Species




**Bratati Bhat**

**Abstract** Study of the formation of a star is immensely important as this holds clues to the matter abundance after Big Bang and also the subsequent evolution of chemical abundance of the Universe. Various evolutionary stages of the star formation could be probed by observing various molecules. The ability to track the evolution of key molecular tracers that have different critical densities for emission could be used to predict synthetic line profiles which can be compared to observed molecular line data and extract chemical diagnostics. It is also essential to apply radiative transfer model before proposing any line information for astronomical observation. Here, we have done radiative transfer modelling of Ethylamine and propanimine for their future detection in interstellar space. Line parameters are discussed to check the observability of these species with the ALMA facility.

## 1 Introduction

The spaces between stars and galaxies are not empty, it is full of a very dilute medium which is a mixture of gas (∼99%) and dust (∼1%). After Big-bang, hydrogen and helium molecules were formed with a trace amount of heavier elements. Complex molecules were formed from the recycling of the chemical soup for billion years. Molecular clouds are the birthplaces of a star. Dusts present in the ISM play a crucial role in the chemical evolution process of different complex molecules in the interstellar space [1–7, 9, 13]. Radiative transfer modelling calculation is a very useful tool for detection of astronomically relevant molecules which are forming in these regions.

There are various publicly available radiative transfer codes which can be utilized to calculate various line parameters. For example, the one-dimensional radiative transfer code RADEX is publicly available for non-LTE calculations. It is a very

B. Bhat (✉)
Indian Centre for Space Physics, Kolkata, India

© Springer International Publishing AG, part of Springer Nature 2018

B. Mukhopadhyay, S. Sasmal (eds.), *Exploring the Universe: From Near Space to Extra-Galactic*, Astrophysics and Space Science Proceedings 53,
https://doi.org/10.1007/978-3-319-94607-8_39

useful tool in rapidly constraining physical conditions such as kinetic temperature, velocity etc. on a large set of observational data. This programme can be used for optical depth ranging up to 100. RADEX can be used to calculate line ratios for a range of kinetic temperatures and $H_2$ densities. LTE and non-LTE methods are applicable in certain physical conditions [15]. An accelerated Monte-Carlo simulation may be implemented to consider the detailed balance between the energy levels of spherically symmetric source and lambda iteration process may be utilized to make the convergence faster [10]. CASSIS is a very useful interactive spectrum analyzer software (http://cassis.irap.omp.eu) which are very often utilized for the modelling purpose. Another radiative transfer code RATRAN is used to calculate molecular line excitations. The approach used in this code to solve the problem is based on the Monte Carlo method and incorporates accelerated lambda iteration. Radiative transfer code like RADMC3D (http://www.ita.uni-heidelberg.de/dullemond/software/radmc-3d) which can produce an image or spectral distribution. This image is generated from a given geometrical distribution of gas or dust and can simulate how it would look like when viewed from a certain angle. This allows modellers to compare their models with observed data. There are some more radiative transfer model like, CRETE (comet radiative transfer and excitation) which is an one-dimensional radiation transfer and water excitation code based on RATRAN [10]. It considers the transitions between the rotational level of water and produces fits file for image viewing [8].

A 3D non-LTE radiative transfer code LIME is publicly available and applicable for arbitrary geometries. It can predict profiles of molecular transitions, line strengths and also the intensity of the thermal continuum. It can model disks around young stellar objects, protostellar envelopes, giant molecular clouds etc. It was derived from RATRAN code by Michiel Hogerheijde and Floris Van der Tak and was written by Christian Brinch.

Parfenov et al. [11] performed line radiative transfer computations for a T Tauri protoplanetary disk assuming non-LTE excitation. They calculated LTE and non-LTE methanol line flux densities and compared it with the observational search for methanol.

There are many other radiative transfer models which are very often utilized to validate various observational aspects. Here, we use CASSIS spectrum analyzer software and RADEX program for the computation of line parameters. This article is arranged as following. In Sect. 2, methodology of the work is discussed. Discussion and results are discussed in Sect. 3 and finally in Sect. 4, we conclude.

## 2 Methodology

The main goal of observational astrochemistry is to extract the information from the telescopic data. Radiative transfer modelling is a very useful way to extract the spectroscopic information from the observational aspect. To extract various

line parameters and physical properties of the star-forming region, we need to know the detail chemical evolution pathways as the physical properties and chemical properties are interrelated to each other. Physical properties like density, temperature, velocity component etc. are the ancillary components of any observed line parameters. Radiative transfer modelling serves as the bridge between the experimental or theoretical results with the observational results. In this way, there are the growing needs of radiative transfer modelling to explain the observational results or to propose any line parameters before its observation.

## *2.1 LTE Model*

The easiest approach to continue the radiative transfer modelling calculation is to consider the Boltzmann distribution to estimate the level population and simply by considering the excitation temperature ($T_{ex}$) equal to the kinetic temperature ($T_{kin}$). This approximation is called Local thermodynamic equilibrium (LTE). But this approximation often deviates. This condition holds well around the high-density region where collision determines the excitation. To determine the ($T_{ex}$) from a range of energy levels where several lines are observed for a molecule, the relative intensities of lines are plotted as a function of upper-level energy. From the slope of the graph, we can determine $T_{ex}$ and the diagram is named as the rotational diagram for rotational energy levels.

## *2.2 Non-LTE Model*

In case of a low-density region, not only collision determines the excitation, both the radiative transition and collisional excitation takes place. In that case $T_{ex} < T_{kin}$, so the assumption of Boltzmann distribution as well as $T_{ex} = T_{kin}$ are very often violated. So a detail calculation is required both taking accounts of the radiative and collisional transitions and balancing between the excitation and de-excitation processes. As this method clearly deviates from the LTE condition, this formalism is named as non-LTE model. Problem with the non-LTE calculation is that it requires a handful information about the spectroscopic and collisional data. Collisional data is not available for all the astrophysically relevant molecules. There are mainly two methods of non-LTE calculation, the Sobolev approximation and the escape probability method. In Sobolev approximation, the cloud is assumed to have velocity gradient along the radius or distance of the cloud [15]. In case of escape probability method, the probability of escaping a photon from one grid to another (the cloud is assumed to divide into many grids for the computational purpose) is considered. This process depends on the geometry of the cloud. Both

these methods are iterative as molecular excitation and radiation intensity are interdependent.

## 3 Results and Discussions

Recently, Sil et al. [14] carried out a detail computation to find out some probable candidates for the astronomical detection. They altogether considered six isomeric groups for their study. From $CH_3N$ group Methanimine ($CH_2NH$), from $CH_5N$ group Methylamine ($CH_3NH_2$), from $C_2H_5N$ group Ethanimine ($CH_3CHNH$) are already observed in the ISM. According to some quantum chemical calculation like enthalpies of formation, optimized energies, expected intensity ratio and abundance they found that Ethylamine from $C_2H_7N$ group and from $C_3H_7N$ group (1Z)-1-propanimine are two relevant molecules for future astronomical detection. They found that these two species are efficiently synthesized in ice phase and can populate the gas phase in the hot core region. Sil et al. [14] continued radiative transfer calculations to find out the line parameters which are relevant under the hot core conditions. Here, we continue the radiative transfer calculations for these two molecules to find out the line parameters relevant in the cold region (10–20 K).

For the LTE calculation of Ethylamine and (1Z)-1-propanimine, we use CASSIS spectrum analyzer software. We point out some intense transitions of these molecules for the ALMA band 1–5 for the low temperature regime. The spectroscopic detail of ethylamine is already available in (https://www.astro.uni-koeln.de/cdms/catalog) but for propanimine it was absent. Sil et al. [14] computed the relevant spectral parameters for this molecule. By using their information, we use SPCAT [12] program to generate the spectroscopic data of the required format. This spectral file is then implemented in CASSIS for the LTE calculation. Here, we use the column density $H_2 = 10^{23}$ cm$^{-2}$, number density of hydrogen $n_H = 10^7$ cm$^{-3}$, excitation temperature $= 10$ K, FWHM $= 10$ km/s, $V_{LSR} = 64$ km/s, source size $= 3''$, Abundance of ethylamine $= 4.0 \times 10^{-08}$ and abundance of propanimine to be $2 \times 10^{-8}$. In Table 1, we list some of the intense transitions which are falling in the ALMA band 1 to 5. For each band we have pointed out five strongest transitions.

Based on the selection by LTE calculations shown in Table 1, we perform the non-LTE calculation using RADEX programme [16]. Since the collisional data files for these two species were not available in the literature, we prepared it by using the spectroscopic information we gathered (available or prepared by us). We assume $H_2$ as collisional partner here and use the similar method as used in [14] to estimate the collisional rates. In Figs. 1 and 2 we show the transitions for ethylamine and propanimine respectively for ALMA band $1 - 5$ using non-LTE calculation. We take the column density of ethylamine to be $10^{15}$ cm$^{-2}$ and column density of propanimine to be $5.0 \times 10^{14}$ cm$^{-2}$, $n_H = 10^7$ cm$^{-3}$, $T_{ex} = 10$ K, FWHM$= 10$ km/s for this calculation.

**Table 1** Identified intense transitions from LTE calculation

| Species | ALMA Band | Frequency (in GHz) |
|---|---|---|
| Ethylamine | Band1 (31–45 GHz) | 31.4005744 |
| | | 33.0673762 |
| | | 34.9850027 |
| | | 39.4293083 |
| | | 44.8063428 |
| | Band2 (67–90 GHz) | 80.241995 |
| | | 82.168784 |
| | | 82.674301 |
| | | 83.24287 |
| | | 84.980785 |
| | Band3 (84–116 GHz) | 101.886754 |
| | | 112.158369 |
| | | 114.294235 |
| | | 115.604884 |
| | | 115.9771874 |
| | Band4 (125–163 GHz) | 145.871741 |
| | | 149.11269 |
| | | 152.224777 |
| | | 159.753196 |
| | | 161.496431 |
| | Band5 (163–211 GHz) | 182.3234429 |
| | | 198.94447 |
| | | 198.945801 |
| | | 207.02715 |
| | | 208.053547 |
| Propanimine | Band1 (31–45 GHz) | 41.897946 |
| | | 42.2302861 |
| | | 42.2318919 |
| | | 42.2361126 |
| | | 42.5812455 |
| | Ban2 (67–90 GHz) | 67.5282969 |
| | | 76.0187663 |
| | | 84.44134587 |
| | | 84.4483753 |
| | | 84.4661717 |
| | Band3 (84–116 GHz) | 92.8959487 |
| | | 101.3005235 |
| | | 101.3444369 |
| | | 109.7449013 |
| | | 109.7938556 |
| | Band4 (125–163 GHz) | 126.6960852 |
| | | 143.6023263 |
| | | 152.0568371 |
| | | 160.4277999 |
| | | 160.5135369 |
| | Band5 (163–211 GHz) | 168.9718077 |
| | | 177.3269583 |
| | | 185.7821453 |
| | | 194.23659 |
| | | 202.6910348 |

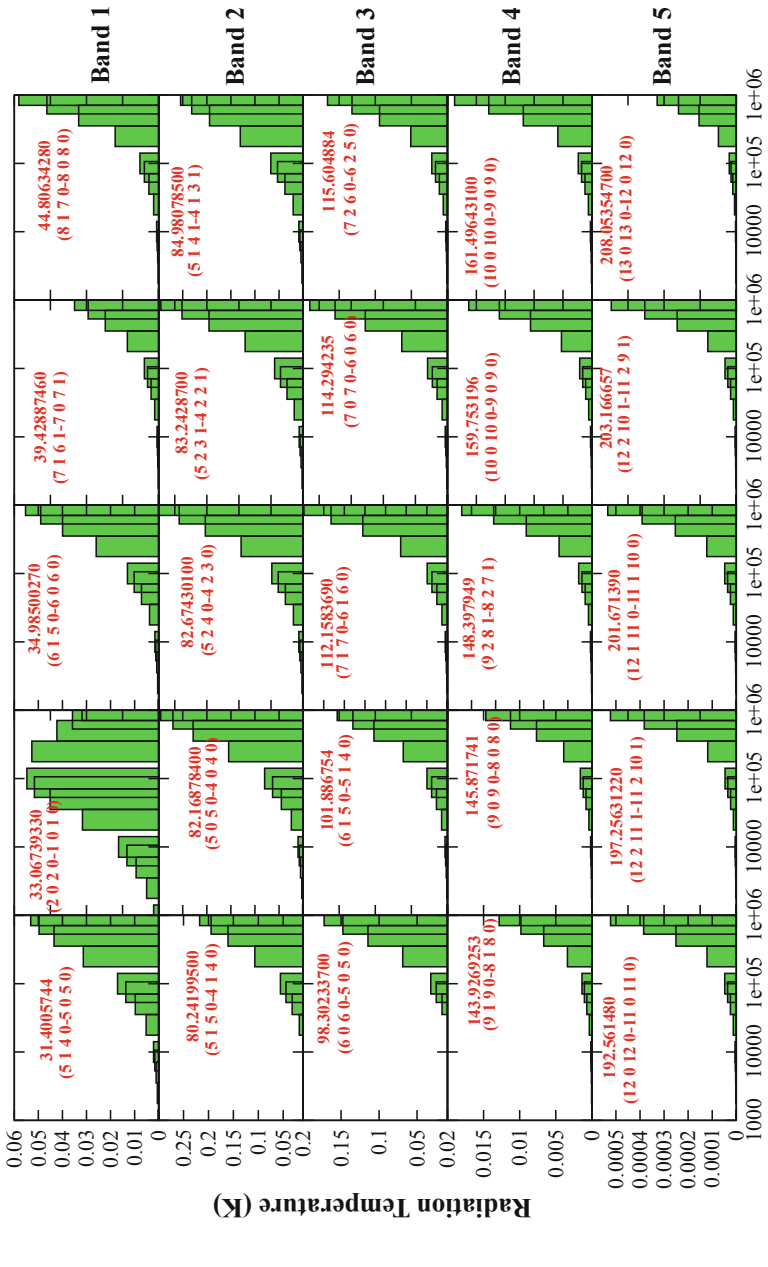



**Fig. 1** Density variation of the intensity of various transitions of ethylamine by considering non-LTE approximation at 10 K

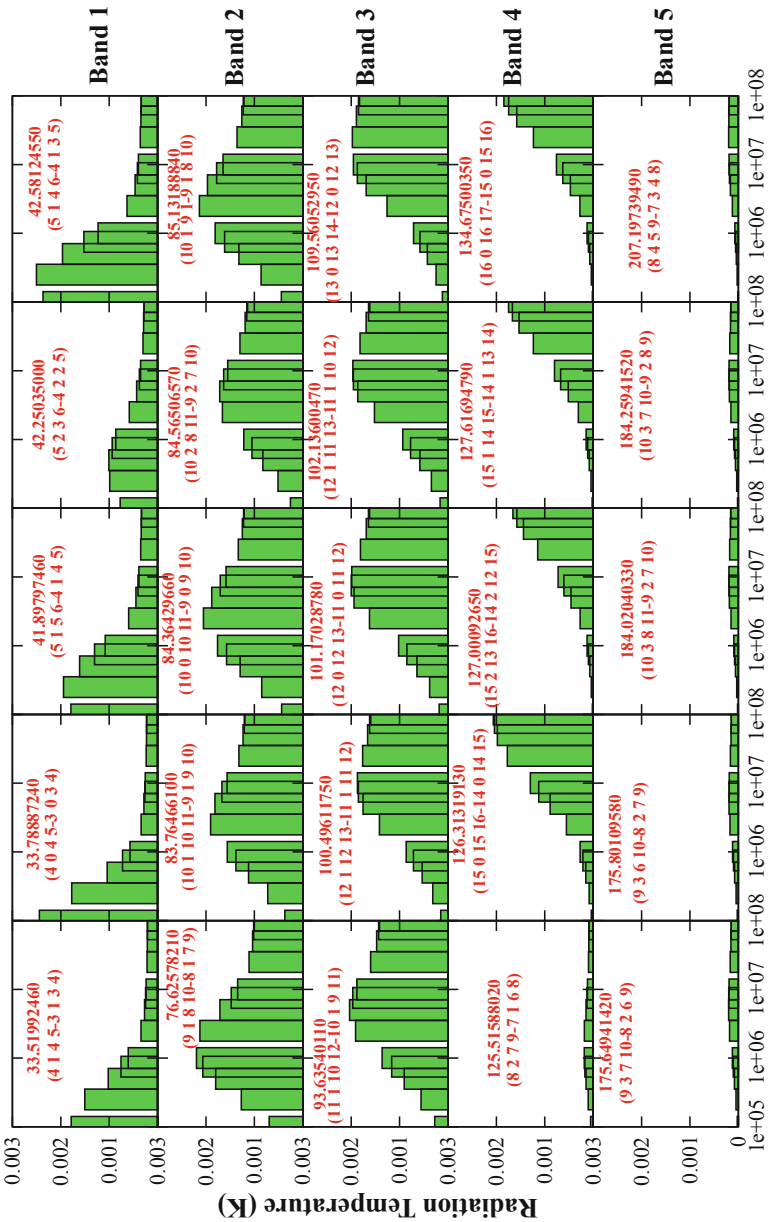



**Fig. 2** Density variation of the intensity of various transitions of ethylamine by considering non-LTE approximation at 10 K

## 4 Conclusion

Here, we have considered LTE as well as non-LTE computation to propose the line parameters for the ethylamine and propanimine. Our calculated parameters could be very useful for the detection of these two species in the cold core regime. Presently, ALMA band 3 is in full operational mode. From Cycle 5 onwards several new observational capabilities will be included. For example, including full polarization observations in Band 4 and observations in Band 5. So, our calculated parameters would be very timely.

**Acknowledgements** B.B. acknowledges DST-INSPIRE Fellowship [IF170046] for providing partial financial assistance. I also wish to acknowledge Dr. Ankan Das and Prof. Sandip K. Chakrabarti for providing a newcomer like me proper guidance to start research work in this exciting subject.

## References

1. Chakrabarti, S.K., Das, A., Acharyya, K., Chakrabarti, S.: A&A **457**, 167 (2006)
2. Chakrabarti, S.K., Das, A., Acharyya, K., Chakrabarti, S.: BASI **34**, 299 (2006)
3. Das, A., Chakrabarti, S.K.: MNRAS **418**, 545 (2011)
4. Das, A., Acharyya, K., Chakrabarti, S., Chakrabarti, S.K.: A&A **486**, 209 (2008)
5. Das, A., Chakrabarti, S.K., Acharyya, K., Chakrabarti, S.: New A **13**, 457 (2008)
6. Das, A., Acharyya, K., Chakrabarti, S.K.: MNRAS **409**, 789 (2010)
7. Das, A., Sahu, D., Majumdar, L., Chakrabarti, S.K.: MNRAS **455**, 540 (2016)
8. de Val-Borro, M., Wilson, T.G.: CRETE: Comet RadiativE Transfer and Excitation. Astrophysics Source Code Library (2016)
9. Gorai, P., Das, A., Das, A., et al.: ApJ **836**, 70 (2017)
10. Hogerheijde, M.R., van der Tak, F.F.: (2000). arXiv preprint astro-ph/0008169
11. Parfenov, S.Y., Semenov, D.A., Sobolev, A.M., Gray, M.D.: Mon. Not. R. Astron. Soc. **460**(3), 2648–2663 (2016)
12. Pickett, H.M.: JMoSp **148**, 371 (1991)
13. Sahu, D., Das, A., Majumdar, L., Chakrabarti, S.K.: New A **38**, 23 (2015)
14. Sil, M., Gorai, P., Das, A., Bhat, B., Etim, E.E., Chakrabarti, S.K.: Astrophys. J. **853**(2), 139 (2018)
15. van der Tak, F.: Proceedings of the International Astronomical Union **7**(S280), 449–460 (2011)
16. Van der Tak, F.F.S., Black, J.H., Schöier, F.L., Jansen, D.J., van Dishoeck, E.F.: A&A **468**, 627 (2007)

# Part V
# Earth's Ionosphere as a Gigantic Detector

# Renaissance of VLF Science in Indian Context




**Sudipta Sasmal**

**Abstract** This article briefly describes the evolution of research on lower ionospheric variabilities using VLF/LF radio wave propagation techniques in Indian scenario. We first emphasize on the importance of propagation characteristics and modulation techniques of the LF/ELF wave propagation through Earth-ionosphere waveguide. Next we present the scientific efforts made in India for the radio wave research. Finally, we describe the utility and application of this subject to understand the lower ionospheric irregularities.

## 1 Introduction

In 1864, the theory and characteristics of electromagnetic wave was published by James Clerk Maxwell. The first experimental application came through by Guglielmo Marconi by invention of Radio Telegraph system and its demonstration through transatlantic radio communications in 1901 [21]. As the waves could not penetrate the earth, the Marconi's experiment raised a question: "How could the radio signal reach a distant receiver where the electromagnetic wave travels in a straight line?". Soon after Marconi experiment, Kennelly and Heaviside published the idea that the only possible mechanism of getting back the radio signal is by reflection from an electrically charged layer of atmosphere. This concept of charged layer was initially known as Kennelly-Heaviside layer and presently, the entire ionized layer is known to us as "Ionosphere".

It was proposed that for any given time, a large portion of the air particles in the upper atmosphere are in ionized conditions and when a radio wave passes through it, the electric force of the EM wave accelerates the particles and this acceleration generates radiation. So an energy exchange happens between the EM wave and charge particle with a combined effect of reflection and refraction of the original

S. Sasmal (✉)
Department of Ionospheric Sciences, Indian Centre for Space Physics, Kolkata, India

© Springer International Publishing AG, part of Springer Nature 2018

B. Mukhopadhyay, S. Sasmal (eds.), *Exploring the Universe: From Near Space to Extra-Galactic*, Astrophysics and Space Science Proceedings 53,
https://doi.org/10.1007/978-3-319-94607-8_40

wave [17]. After successive radio experiments, it was found that the ionization features do not increase uniformly. As the chemical composition has varying distribution with height and as different gases have different absorption capabilities of solar radiation, the entire ionosphere must have a layered structure. The major ionization comes from the solar ultraviolet radiation. Due to the distribution of solar energy spectrum and the varying chemical composition and temperature, the ionized layers do not remain in the same height but vary diurnally and seasonally. The layers can be treated as permanent and semi-permanent. The E layer (90–150 km) and F Layer (150–800 km) are treated as permanent. During daytime, the F-layer is divided into F1 (150–220 km) and F2 regions where the F1 layer is present only in the daytime. A fourth layer, which was originally treated as "less important" namely D-layer, exists only during daytime (50–90 km).

The reason of the non-importance of the lowermost ionospheric layers originates from its own dynamic characteristics. First, the altitude range prohibits the experimental probing using balloon and satellite as this range is too far for balloon and too low for satellite. Rocket sounding experiments are also too transient to accumulate major time dependent information during its flight. Second, there was a lack of knowledge of the definite maximum of ionization distributions [32]. Absence of free electrons due to rapid recombinations, high collision frequency and presence of negative ions increase the electrical dynamics of the layer subsequently. The Low and Very Low Frequency (3–30 kHz) radio wave propagation is found to be the most fruitful exercise to study the characteristics of this layer. This attempt provides an estimation of major constituents of this layer which are electron number density, reflection height and reflection coefficients [1, 3].

Using the two key ingredients, number density and reflection height, LF/VLF radio propagation technique successfully delivers significant idea of D-layer variabilities but not in comparison to other layers. Since World War II, the usage of VLF communications started from the navigational aspects which later emerged with true ionospheric research worldwide. In India, specially in Kolkata (erstwhile Calcutta) radio research started in 1930 when the first experimental evidence was found by Prof. S.K. Mitra and after that publication of the famous book in 1947 'The Upper Atmosphere'. Significant and fruitful science on LF/VLF research programme accelerated in India to study the D-layer variability for a wide range of ionospheric irregularities starting from terrestrial (Lightning, Earthquakes, Cyclones) to extra-terrestrial (Solar energetic phenomena, Gamma Ray Bursts, Solar Eclipse) sources. In Kolkata, the original hotbed of the ionospheric research activities in India, the activities started in full swing once more in the last two decades. A group of young researchers/scientists from Indian Centre for Space Physics (ICSP) guided by Professor Sandip Kumar Chakrabarti (SKC), expanded the horizon of our understanding of the cause of various forms of VLF signal irregularities by treating the ionosphere as a gigantic detector. SKC developed a platform from scratch from where several new avenues of research opened up. This article is a brief review of the development of the VLF research in India and the past, recent and future outcomes of the subject.

## 2 Sub-ionospheric VLF Propagation

The surface of the earth together with the lower ionospheric boundary behave as a waveguide through which Very Low Frequency (VLF) radio wave having frequency range (3–30 kHz) can propagate with a very low attenuation rate 2–3 dB per mega meter. The higher frequencies experience a small fading due to their travel through upper ionosphere in F1 and F2 layers and thus suffer less due to ionization and turbulence. On the contrary, VLF reflects back from the D-layer and thus provides a very stable variation in both amplitude and phase. There are almost fifty active VLF transmitters around the globe which are mainly used for navigation and commercial purpose. Due to the large wavelength ($\sim$ 10–100 km), VLF transmitter require large wire antennas up to kilometer range and with a high transmitting power input. The receiving part is rather simple. Usually single or cross loop magnetic B-field antenna or single pole E-field electric antenna. The signal is amplified in both antenna and receiver end and fed into a data acquisition card or computer sound card for analog to digital conversion and then stored in the machine drive with time usually stamped by a GPS unit. ICSP uses four types of VLF systems. These are AWESOME, SoftPAL, SuperSID and UltraMSK. The top panel of Fig. 1 shows the schematic diagram of radio wave propagation methods and the bottom panel shows a typical diurnal signal amplitude as recorded from VLF receiver from VTX and NWC transmitters. The data shows drops in the signal during the local sunrise and sunset. These are known as sunrise and sunset terminator times.

## 3 Significant Research in the Context of Indian Scenario

Though the first radio communication experiment was communicated by Marconi, it was found in 1998 by Bondyopadhyay that the Marconi's Italian Navy Aotocohere had originated from an Indian, namely, Sir. J.C. Bose. Later Dr. S.K. Mitra became the pioneer of low frequency radio communication mechanism in India with significant discovery. The theoretical and experimental discoveries of D, E and F-layers came out from his research team. The first experimental evidence of E-Layer of the ionosphere came in 1930 by proposing the source of the ionization of the lower and middle (E-Layer) of the atmosphere is the solar ultraviolet radiation. In 1935, Mitra et al. first reported the echo radio pulse method at a height of 55 km. This is the first experimental validity of the presence of non-permanent Ionospheric D-Layer [35]. Further, it was proven that the photo-ionization in E and F layers are by Nitrogen and Oxygen [36]. By using the night sky airglow luminosity Mitra also established the fact that the emission of energy was due to ionized nitrogen in the F-layer. Based on the above theories, Mitra wrote the book on "The Upper Atmosphere" which became a milestone in ionospheric research. Later, his renowned PhD scholar Dr. A. P. Mitra played one of the leading roles in development of new ideas in ionospheric physics. Dr. Mitra developed the

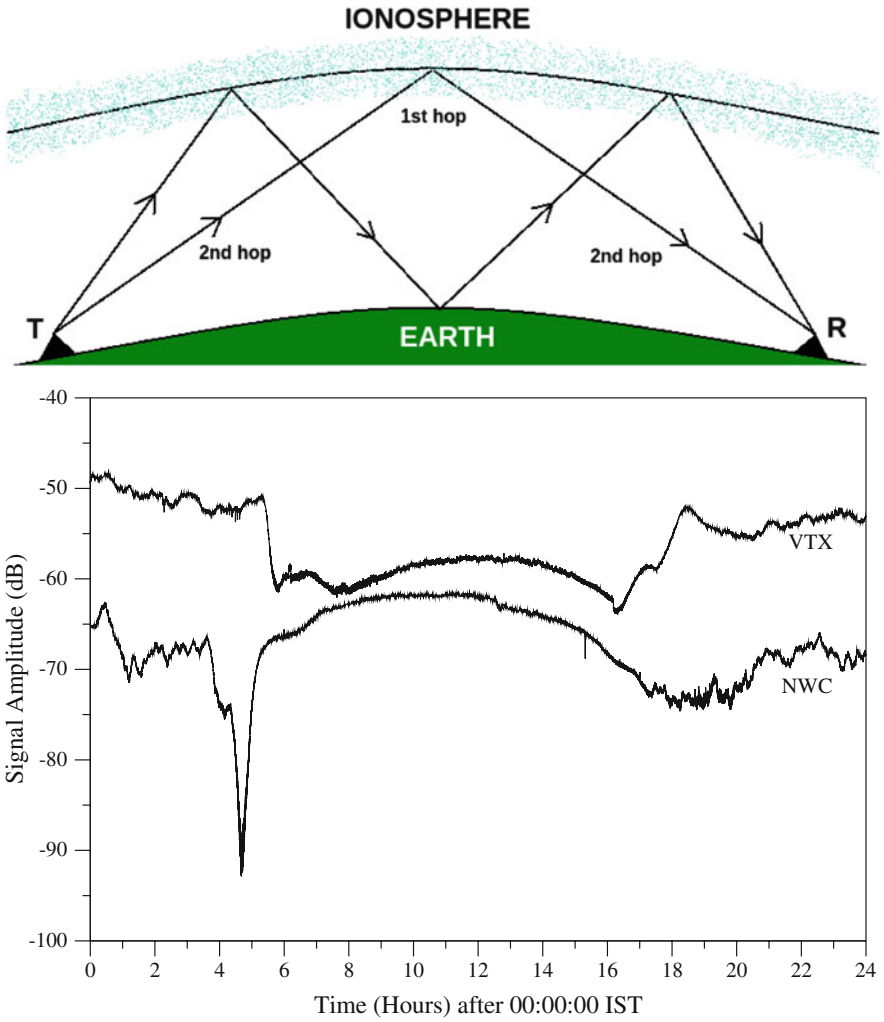



**Fig. 1** Top panel shows the schematic diagram of radio wave propagation. The bottom panel shows the diurnal variation of VLF signal amplitude profile as recorded from ICSP receiver from VTX and NWC transmitters

Cosmic Radio Technique (later called Riometer) which was highly useful to detect solar flares and solar proton events. He introduced the cosmic noise technique for estimating the temperature of F-layer. This technique was also used to study the D-layer by sending rockets [45].

Following the lead of the University of Calcutta, various groups in India started ionospheric low frequency radio research program. Initial works started with understanding of natural emission of VLF waves through lightning. Benaras Hindu University had several groups in 1963 who were working on this subject. Later the

subject slowly spreaded to National Physical Laboratory, New Delhi; Barkatulla University, Bhopal; R. B. S. College, Agra; Indian Institute of Geomagnetism, Mumbai; Tripura University, Physical Research Laboratory, Ahmedabad; Andhra University and many more. The first whistler recording system was installed in Gulmarg (1965–1972) and then in Nainital (1970–1975), Varanasi (1975), Agra (1980) and Bhopal (1990) [56]. Also, study of emission of EM wave in the Ultra Low Frequency (ULF) range from magnetometer started in Agra. In the first few years of current century, low frequency radio wave study got a significant boost after introduction of Stanford University SID (Sudden Ionospheric Disturbances) monitoring network where Very Low Frequency monitoring stations are developed throughout the world and also in India. Most of the VLF workers started using this facility to understand ionospheric variability using man-made signal from VLF transmitters. Later a new receiver named AWESOME from Stanford was launched which deals with both Narrowband and Wide-band spectrum of VLF signal. This monitoring scheme opened up a new scope to study lower ionospheric irregularities and also to model it using well known numerical models.

In 2002, ICSP started monitoring VLF signal from Indian Naval transmitter VTX3 (18.2 kHz) and from 2005 it entered in the AWESOME network. The initial projects started with Solar flares and meteor showers. Understanding of the seismo-ionospheric coupling was the next priority, the first evidence of which was observed during the great Sumatran earthquake in 2004 [6]. Judging from the past historical research [15, 16, 59, 60] and initial observation and signal quality, it was found that the VLF signal characteristics is an exclusive path dependent problem and in 2008, ICSP conducted an all India multi-station VLF campaign, first time done anywhere in such a large scale. The extensive usage of numerical simulation using Long Wavelength Propagation Capability (LWPC) [19] gave significant output of the signal characteristics and this made a test bed for understanding the signal characteristics under a quiet ionospheric condition. Later extensive observation and theoretical simulations were performed to understand the D-region variability during disturbed ionospheric conditions due to various sources. In 2012, ICSP started a dedicated VLF observatory named Ionospheric and Earthquake Research Centre (IERC), which is now known as IERCOO after Optical observatory was added to it. Completely new aspects of research, especially treating the Earth as a gigantic detector was given more emphasis. In this section, we give a brief overview of the recent progresses of the VLF studies by this group.

## 4 Significant Contributions from ICSP Ionospheric Group

ICSP has covered the studies of almost the entire regime of lower ionospheric irregularities as observed through VLF modulation technique. It follows most of the significant past researches on Solar Flares [4, 22, 26, 29, 34], Solar Eclipse [13, 14, 28, 30, 33, 55, 58] etc., Gamma Ray Burst [20, 25–27, 57] etc, Seismo-ionospheric coupling [23, 24, 37, 44] etc. and many more. The subject has been developed in both

the extensive analytical studies and detailed numerical simulations. In 2010, S.K. Chakrabarti organized an international conference on these aspects to synchronize ICSP performance with the rest of the world [5].

## *4.1 Solar Flares*

The intense hard and soft X-ray outbursts during the solar flares severely perturb the lower ionospheric D-region and can be studied by the VLF response. ICSP has monitored a huge number of solar flares during 23rd and 24th solar cycles. Almost every class of solar flares were recorded through VLF and for most of the cases the signal showed an enhancement in amplitude and phase. For a few cases, depending on the propagation path and strength of the flares, the signal amplitude got depleted. Extensive analytical study, satellite comparison and detail numerical modeling have been carried out for the last decade. The delay of ionospheric response named as "sluggishness" was studied with the strength of the flare and the solar zenith angle profile. Effective recombination co-efficients, enhanced electron density and variation of negative ion in D-layer have been thoroughly studied using LWPC code [2]. Later, true ionospheric condition due to solar flare was modeled by using Monte-Carlo Simulation and GPI ion chemistry model and the VLF response has been reproduced with great efficiency [42]. The ion chemistry model also has been used uniquely to reconstruct the source characterizations as incident radiation spectrum [43]. This ion chemistry model is well accepted in most of the reputed journals. The details of the works are in the article written by Sourav Palit and Tamal Basak.

## *4.2 Solar Eclipse*

Solar eclipse is a unique event to study controlled ionization experiment manifested by propagated VLF radio signal through earth-ionospheric waveguide. During the occultation of the sun by the lunar shadow, the ionization suffers from a depletion followed by an enhancement during and after the eclipse period. ICSP successfully observed this phenomenon several times during Total Solar Eclipse (TSE) 2009, Annular Solar Eclipse, 2010 (ASE) and the recent great American solar eclipse of 2017. Figure 2 shows the ionospheric response of TSE, 2017 for VLF signal transmitted from NML (25.2 kHz) transmitter and received at Tulsa and McBaine in USA. For the TSE 2009, a multi-station observation campaign was organized in India from more than a dozen of places and observed significant amplitude modulation, both enhancement and depletion, in the signal amplitude [9, 10]. The VLF response was modeled using LWPC and the pseudo night condition due to eclipse was achieved as the reflection height was increased by ∼4 km. In [41], the presence of atmospheric gravity wave (period ∼ minutes to hours) and planetary wave (period ∼ minutes to hours) was detected. In [12], the effects of eclipse were

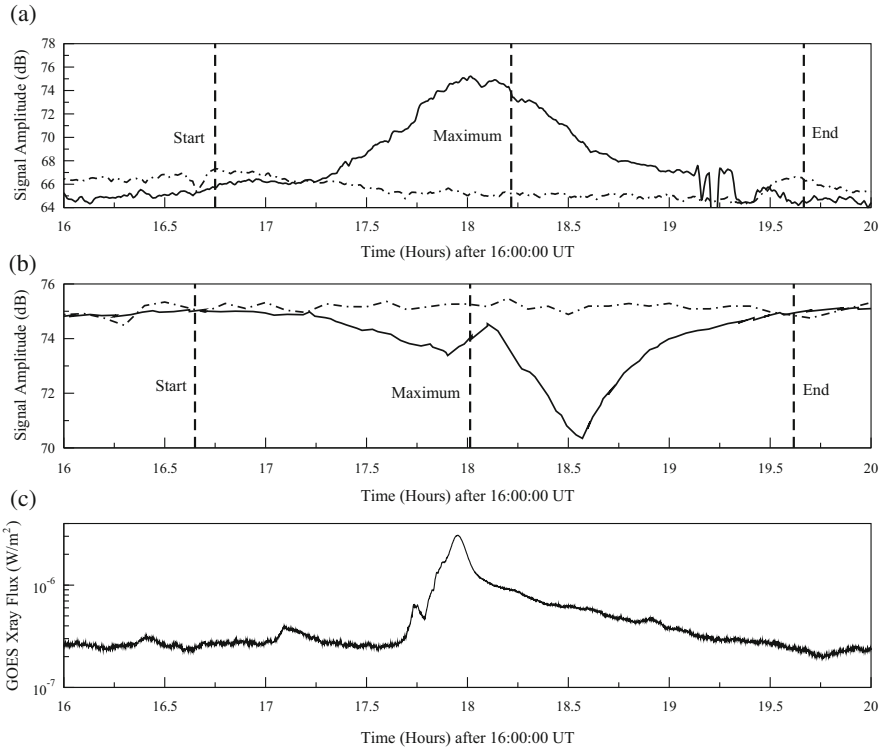



**Fig. 2** VLF signal amplitude variation as a function of time in hours in UT for (**a**) Tulsa and (**b**) McBaine during the total solar eclipse on August 21, 2017. The solid and dashed-dotted curves show the VLF response on the normal day and the eclipse day respectively. Three vertical dashed lines represent the starting, maximum and ending of the TSE. Panel (**c**) shows the GOES15 1Å–8 Å X-ray light curve of C3.0 class flare [11]

studied in detail by using advanced ion chemistry model by which the modulated electron number density was computed through Monte-Carlo Simulation. For ASE, 2010 and TSE, 2017, a unique event happened where during the eclipse, strong solar flare happened and the ionosphere suffered a combined effect of ionization due to the flare and recombination due to eclipse. Maji et al. [31], Pal et al. [40] and Chakrabarti et al. [11] reported these events which were successfully modeled using both the eclipse and flare using LWPC mechanism. The details of the analysis are in the articles written by Sujay Pal and Suman Chakraborty in this volume.

### 4.3 Gamma Ray Burst

Gamma Ray Bursts are the most energetic phenomena in the Universe where energetic gamma ray are produced by the violent explosions inside distant stars. Enormous energy is radiated for a short interval of time ranging from a few milliseconds to a few minutes. In this short time duration, the emission of radiation is so high that it can be compared with the whole radiation of the sun for its entire 10 billion years lifetime. The radiated gamma-ray interacts with the ionosphere and produces substantial ionization for a short interval of time and modulates VLF signal accordingly. ICSP successfully detected the ionospheric response of GRB090424 on April 24, 2009 and for Soft Gamma Repeater SGR J1550-5418 on January 22, 2009. For both the cases, VLF signal shows significant very sharp enhancement in signal amplitude due to the sudden excitation of huge ionization in the lower ionosphere. The multiple peak intense radiation for GRB090424 was detected by the Swift Burst Alert Telescope (BAT), SPIACS Integral satellite and Fermi Gamma ray Burst Monitor simultaneously. The VLF response of the ionosphere was also recorded from three recording stations, ICSP (Garia), Salt Lake and Malda [39]. The X-ray light-curve of the event matches exactly with the satellite responses [38]. For the SGR J1550-5418, a total of 76 events were detected from ICSP (Garia) VLF receiver. The ionospheric response was fitted with FRED function to compute the delays between satellite detections and ionospheric responses. The enhanced electron number density at a height of 80 km was numerically simulated using LWPC [38]. Details will be in the article written by Sushanta K. Mondal in this Volume.

### 4.4 Seismo-Ionospheric Coupling

It is well established that seismic hazards are not only the phenomena which are attached with the surface of the earth but the pre- and co-seismic effects can reach up-to lower ionosphere. There are three major channels, (a) Thermal, (b) Acoustic and (c) Electromagnetic through which the physical processes of seismic hazards can make a significant perturbation on the electron number density, reflection height, conductivity and temperature of the lower ionosphere. This phenomenon is named as lithosphere-atmosphere-ionosphere coupling (LAIC). VLF is one of the major tools to study such processes where there are direct or indirect evidences of consistent anomalies in the signal amplitude and phase. Three major methods are used where two of them deals with daytime variabilities (sunrise and sunset terminator times (SRT/SST) and D-layer preparation and destruction time (DLPT/DLDT)) where one deals with nighttime signal fluctuations. The works started from the great Sumatra earthquake where ICSP found significant shifts in the sunrise terminator time towards nighttime a few days before the earthquake. Later in 2009, Sasmal and Chakrabarti [49, 50] reported a statistical study of variation

of sunrise terminator times for more than 400 earthquakes and implemented a new idea of effective magnitude of earthquake which deals with combined effects of all earthquakes for a single day. It was found that the terminator time anomalies are well correlated with earthquake Richter scale magnitude and most of anomalies occurred on 1–2 days prior to earthquakes. In 2007 and 2010 Chakrabarti et al. [7, 8], showed a similar statistical study for D-layer preparation time (DLPT) and D-layer destruction time (DLDT) and found similar good correlations with maximum perturbation 1 day before the earthquake. In [47], the nighttime fluctuation was studied and it was equally correlated with earthquake magnitude with maximum perturbation 3 days prior to the main event. Later, in an extensive analysis, case-wise studies were made for various significant earthquakes such as Honsu, 2011 [51], Pakistan, 2011 [46, 48] and most recent Nepal, 2015 [13]. For the first two earthquakes, the concept of multi-path approach was studied to get an estimation of maximum earthquake perturbed area which can be identified through the radio wave technique. It has been found that the signal shows maximum anomalies for which the propagation path is closest to the earthquake epicenter or earthquake preparation zone [18]. For the Nepal earthquake, first time a numerical modeling was done using LWPC code to study the variation of electron density during seismically active days and it was found that for a long distance transmitter JJI (22.2 kHz) in Japan, the local ionospheric reflection height has been increased by 3 km. There was a strong presence of atmospheric gravity waves in the signal with period of 45–65 min three days prior to the earthquake. Presently an extensive numerical model is developed by this group which deals with the variation of ionospheric conductivity profile calculated from theoretical aspects. The increased lower ionization due to radioactive radon emission will be coupled with vapor-cluster/aerosol concentration. This will be coupled with the model conductivity profile to estimate the ionization potential and finally modulation of ion concentration will be computed which will provide the VLF anomalies numerically. For real time validation, a network of VLF receivers will be developed in India and its subcontinent shortly. The details of the results are in the articles written by Suman Ray and Suman Chakraborty of this Volume.

### *4.5 Lighting*

Lightning discharge generates a wide spectrum of EM wave frequency ranging from Hz to several MHz with a maximum spectral energy within the LF/VLF band. VLF signal traveled through the ionosphere suffers both direct and indirect perturbations. The lighting discharge causes heating and ionization of lower ionosphere and direct perturbation occurs within 20 ms of the associated lightning. This is known to be the early/fast events. Indirect perturbation occurs due to propagation of whistler mode wave through magnetosphere and precipitation of trapped electron in lower ionosphere producing a secondary ionization. This is known to be the lighting induced electron precipitation (LEP) events. In ICSP, around 120 such events were analyzed for two VLF propagation paths (VTX-ICSP and NWC-ICSP) with both

positive and negative amplitude modulation with a long recovery process. The details are given in the article written by Sujay Pal of this Volume.

### *4.6 Polar Ionospheric Study*

Long path radio wave propagation has a unique feature as the signal experiences large variation of solar irradiation and degrees of ionization. The dominating propagation modes and the modal conversion are completely different from that for the shorter (<3000 km) path. Study of VLF radio wave propagation in Antarctic region during summer period in southern hemisphere (November to February) gives a unique opportunity to explore such phenomena due to presence of whole day solar illumination. In 2007–2008 and 2015–2016 ICSP made a flag mark in the understanding of long path VLF radio wave research in Indian permanent base Maitri (Lat. 70°45′S, Lon. 11°40′E) and Bharati (Lat. 69°24′S, Lon. 76°10′E) research base in Antarctica. A consistent and stable diurnal signal variation has been obtained both in amplitude and phase. Signals from VTX (18.2) and NWC (19.8) have been recorded using AWESOME, SoftPAL and UltraMSK instruments. The long distance propagation has been modeled by three different approaches. In Sasmal et al. [51, 52], the signal amplitude was numerically reproduced by using IGRF model and LWPC. The modal attenuation was thoroughly examined during two specific time duration (a) when the entire path is sunlit and (b) when the entire path is dark. It was found that the signal suffered more modal conversion which appears in the signal as oscillations during the night time. In [53], the spatial distribution of the signal amplitude was examined by ion chemistry model. The entire long path for VTX-Maitri (∼10,000 km) has been divided into 20 segments, each of distance 500 km. The spatial distribution matches with Sasmal et al. [52] results. From observation and modeling, a very interesting features came out for VTX-Maitri path, where the stronger signal (1 MW) from NWC suffers huge attenuation in comparison to weaker signal (500 kW) from VTX. Figure 3 shows the spatial variation of VLF signal amplitude for VTX and NWC transmitters. The solid and dashed curves represent the time at 00:00:00 UT and 12:00:00 UT respectively. The dotted-dashed vertical lines show the location of Maitri with respect to VTX and NWC. It is clear that as soon as the NWC signal enters into Antarctic ice mass at around 6000 km, it suffers severe attenuation. This is why in Maitri, we never received a strong NWC signal. From modal attenuation it is found that the VLF signal suffers a huge attenuation during propagation over Antarctic land and sea ice. In [54] this outcome has been reestablished by studying the temporal profile of VLF signal using solar zenith angle model and LWPC. The ionospheric steepness parameters ($\beta$) and effective reflection height $h'$ has been computed from solar zenith angle profile and using LWPC, whole day VLF signal has been reproduced which matches with the observed results to a great extent. The simulated temporal

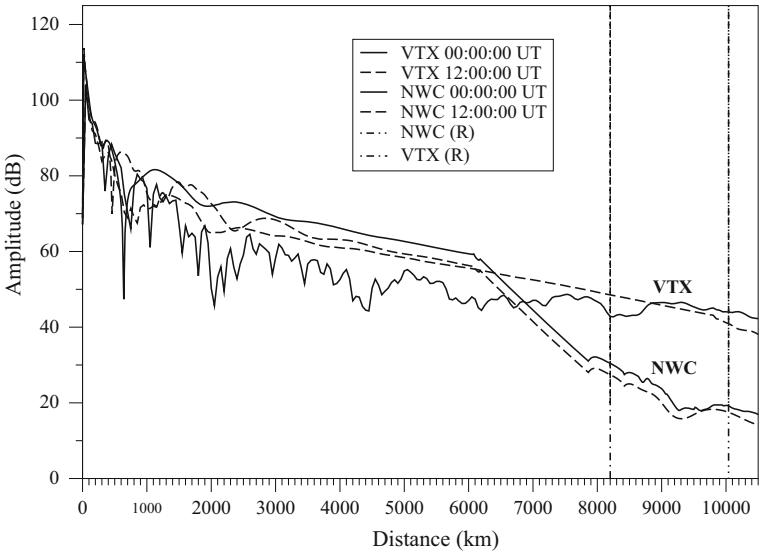



**Fig. 3** Spatial distribution of VLF signal amplitude variation as a function of distance in km from VTX-Maitri and NWC-Maitri paths. The NWC signal suffers strong attenuation after reaching the Antarctic ice mass [51]

profile of the signal also corroborates the Antarctic ice mass attenuation phenomena. This is the first time in Indian context where such an ice mass induced attenuation has been reported.

## 5 Conclusions

From the earlier stage of VLF radio communication to the present advanced era, the lower ionospheric D-region has always been critical to understand due to lesser number of probing equipments and its vast dynamics. VLF radio wave propagation methods in earth-ionospheric waveguide is a major source of study of these irregularities in normal and perturbed ionosphere. This article provides a brief overview of the development of the methodologies on this subject in the context of Indian scenario. In India, specially in Kolkata, the subjects emerged from 1930 from both experimental and theoretical ends. Later extensive and significant research was carried out by another Kolkata group from ICSP where almost every aspects of D-layer ionospheric irregularities are being studied. Starting from Solar high energetic flares, extra terrestrial gamma ray bursts to terrestrial lightning and seismic hazards, detailed understanding of the subject was achieved both from observation and simulation techniques. In this review we presented such processes where sub-ionospheric VLF signals show strong modulation and from this true

ionospheric condition can be modeled to a good extent. Though for real time D-layer monitoring is a tough job using VLF technique but to achieve such a platform two mandatory requirements are there. First need is a dense network of VLF radio receiving stations and second, an accurate software based numerical model which deals with complex ion chemistry and dynamics of D-layer. This exercise is under progress and hopefully will be implemented in near future for a clear understanding of lower ionospheric variabilities.

**Acknowledgements** I would express my very profound gratitude to Professor Sandip Kumar Chakrabarti without whom this subject could not have been developed in Kolkata. He was my PhD thesis supervisor, my present mentor and always my inspiration as 'SIR' to put myself in my scientific research area. I thank all my ionospheric research group members for building such a nice team to work as a family. I thank all the funding agencies during my entire research and working tenure to provide me supports to sustain my research. Finally I thank Dr. Banibrata Mukhopadhyay, Dr. Tamal Basak and Dr. Suman Chakraborty for the editorial supports. I dedicate this article to my father whom I lost few months ago.

## References

1. Anderson, N.: Proc. Inst. Radio Eng. **19**, 1150 (1931)
2. Basak, T., Chakrabarti, S.K.: Astrophys Space Sci. **348**(2), 315–326 (2013)
3. Budden, K.G.: Radio Waves in the Ionosphere. Cambridge University Press, Cambridge (1966)
4. Burgess, B., Jones, T.B.: Radio. Sc. **2**(6), 619–626 (1967)
5. Chakrabarti, S.K.: AIP Conference Proceedings, vol. 1053 (2010)
6. Chakrabarti, S.K., Saha, M., Khan, R., Mandal, S., Acharyya, K., Saha, R.: Indian J. Radio and Space Phys. **34**, 314–317 (2005)
7. Chakrabarti, S., Sasmal, S., Saha, M., Khan, M., Bhowmik, D., Chakrabarti, S.K.: Indian J. Phys. **81**, 531–538 (2007)
8. Chakrabarti, S.K., Sasmal, S., Chakrabarti, S.: Nat. Hazards Earth Syst. Sci. **10**, 1751–1757 (2010)
9. Chakrabarti, S.K., Pal, S., Sasmal, S., Mondal, S.K., Ray, S., Basak, T., Maji, S.K., Khadka, B., Bhowmick, D., Chowdhury, A.K.: J. Atmos. Sol. Terr. Phys. **86**, 65–70 (2012)
10. Chakrabarti, S.K., Mondal, S.K., Sasmal, S., Pal et al.: Indian J. Phys. **86**(5), 323–334 (2012)
11. Chakrabarti, S.K., Sasmal, S., Chakraborty, S., Basak, T., Tucker, B.: Adv. Space Res. **62**(3), 651–666 (2018)
12. Chakraborty, S., Palit, S., Ray, S., Chakrabarti, S.K.: Astrophys Space Sci. **361**, 72–87 (2016)
13. Chakraborty, S., Sasmal, S., Ghosh, S., Palit, S., Chakrabarti, S.K., Ray, S.: Adv. Space Res. **60**, 1787–1796 (2018)
14. Clilverd, M.A., Rodger, C.J., Thomson, N.R., Lichtenberger, J., Steinbach, P., Cannon, P., Angling, M.J.: Radio Sci. **36**(4), 773–788 (2001)
15. Crombie, D.D.: J. Res. Natl. Bur. Stand. D **65D**(5) (1961)
16. Cummer, S.A., Inan, U.S., Bell, T.F.: Radio Sci. **33**(6), 1781–1792 (1999)
17. Delliger B.H.: Natl. Bur. Stand. **19**, 111–141 (1937)
18. Dobrovolsky, I.R., Zubkov, S.I. Myachkin, V.I.: **117**, 1025–1044 (1979)
19. Ferguson, J.A.: Space and Naval Warfare Systems Center, San Diego (1998). Tech. doc. 3030
20. Fishman, G.J., Inan, U.S.: Nature **331**, 418–420 (1988)
21. Groves, K., Lee, M, Kuo S.: Radio signals traversing the ionosphere. J. Geophys. Res. **93**(A12), 14683–14687 (1988)
22. Grubor, D.P., Suliic, D.M., Zigmann, V.: Serb. Astron. J. **171**, 29–35 (2005)

23. Gokhberg, M.B., Gufeld, I.L., Rozhnoy, A.A., Marenko, V.F., Yampolsky, V. S., Ponomarev, E.A.: Phys. Earth Planet. Inter. **57**, 64–67 (1989)
24. Hayakawa, M., Molchanov, O.A., Ondoh, T., Kawai, E.M.: J. Comm. Res. Lab. Tokyo **43**, 169–180 (1996)
25. Inan, U.S., Lehtinen, N.G., Lev-Tov, S.J., Johnson, M.P., Bell, T.F., Hurley, K.: Geophys. Res. Lett. **26**, 3357 (1999)
26. Inan, U.S., Lehtinen, N.G., Moore, R.C., Hurley, K., Boggs, S., Smith, D.M., Fishman G.J.: J. Geophys. Res. Lett. **34**, 3357–3360 (2007)
27. Inan, U.S., Lehtinen, N.G., Moore, R.C., Hurley, K., Boggs, S., Smith, D.M., Fishman G.J.: Geophys. Res. Lett. **34**, L02106 (2007). https://doi.org/10.1029/2006GL028494
28. Kozlov, V.I., Karimov, R.R., Mullayarov, V.A.: Russ. Phys. J. **50**(6), 617–621 (2007)
29. Liu, L., WanYiDing, W., Le, C., Le, H.: Sci. Bull. **56**, 1202–1211 (2011)
30. Lynn, K.J.W.: Jour Atmos Terr Phys **43**, 1309–1316 (1981)
31. Maji, S.K., Chakrabarti, S.K., Mondal, S.K.: Earth Moon Planets **108**, 243–251 (2012)
32. Mitra A.P.: J. Geophys. Res. **56**(3), 373–403 (1951)
33. Mitra, A.P.: Ionospheric Effects of Solar Flares, vol. 46, p. 307. D. Reidel, Norwell, MA (1974)
34. Mitra, A.P., Rowe, J.N.: J. Atmos Terr. Phys. **34**, 795–806 (1972)
35. Mitra, S.K., Syam, P.: Nature **135** 953–954 (1935)
36. Mitra, S.K., Bhar, J.N., Ghosh, S.P.: Ind. J. Phys. **12**, 455–465 (1938)
37. Molchanov, O.A., Hayakawa, M.: J. Geophys. Res. **103**, 17489–17504 (1998)
38. Mondal, S.K, Chakrabarti S.K.: AIP Conf. Proc. **1286**, 311 (2010)
39. Mondal, S.K., Chakrabarti, S.K., Sasmal, S.: Astrophys. Space Sci. **341**, 259–264 (2012)
40. Pal, S., Maji, S.K., Chakrabarti, S.K.: Planet. Space Sci. **73**, 310–317 (2012)
41. Pal, S., Chakraborty, S., Chakrabarti, S.K.: Adv. Space Res. **55**, 1190–1198 (2015)
42. Palit, S., Basak, T., Mondal, S.K., Pal, S.: Chakrabarti, S.K.: Atmos. Chem. Phys. **13**, 9159–9168 (2013)
43. Palit, S., Basak, T., Pal, S., Chakrabarti, S.K.: Astrophysics Space Sci. **355**, 2190 (2014). https://doi.org/10.1007/s1050901421906
44. Pulinets, S., Boyarchuk, K.: Springer, Berlin (2004). ISBN 3-540-20839-9
45. Rao, B.R.: Indin J. Radio Space Phys. **16**, 1–4 (1987)
46. Ray, S., Chakrabarti, S.K.: Nat. Hazards Earth Syst. Sci. **13**, 1501–1506 (2013)
47. Ray, S., Chakrabarti, S.K., Mondal, S.K. Sasmal, S.: Nat. Hazards Earth Syst. Sci. **11**, 2699–2704 (2011)
48. Ray, S., Chakrabarti, S.K., Sasmal, S.: Indian J. Phys. **86**(2), 85–88 (2012)
49. Sasmal, S., Chakrabarti, S.K.: Nat. Hazards Earth Syst. Sci. **9**, 1403–1408 (2009)
50. Sasmal, S., Chakrabarti, S.K.: AIP Conf. Proc. **1286**, 270–290 (2010)
51. Sasmal, S., Chakrabarti, S.K., Ray, S.: Indian J. Physics **88**(10), 1013–1019 (2014)
52. Sasmal, S., Pal, S., Chakrabarti, S.K.: Adv. Space Res. **120**, 8872–8883 (2014)
53. Sasmal, S., Palit, S., Chakrabarti, S.K.: J. Geophys. Res. (Space Physics) **120**, 8872–8883 (2015)
54. Sasmal, S., Basak, T., Chakraborty, S., Palit, S., Chakrabarti, S.K.: J. Geophy. Res. **122** (2017). https://doi.org/10.1002/2016JA023812
55. SenGupta, A., Goel, G.K., Mathur, B.S.: J. Atmos. Tterr. Physic **42**, 907–409 (1980)
56. Singh.: R. Indian J. His. Scs. **52**(4), 407–419 (2017)
57. Tanaka, Y.T, Raulin, J.P., Bertoni, F.B., et al.: Astrophys. J. Lett. **721**, 24–27 (2010)
58. Thomson, N.R.: J. Atmos. Terr. Phys. **55**, 173–184 (1993)
59. Wait, J.R.: Electromagnetic Waves in Stratified Media, Pergamon Press, New York (1962)
60. Wait, J.R., Spies, K.P.: NBS Tech. Note U.S. 300. (1964)

# Remote Sensing of the Ignorosphere: Need for a Complete Earth-Ionosphere Radio Wave Propagation Model




**Sujay Pal**

**Abstract** We present a short review on retrieval mechanism of the D-region ionospheric plasma using sub-ionospheric VLF/LF data. First, we discuss importance of VLF/LF observation techniques and significant earth-ionosphere propagation models to diagnose electron-ion distribution in the lower ionosphere. Then we discuss about VLF/LF perturbations due to different geophysical phenomena and corresponding numerical simulations applied to retrieve the state of the D-region ionosphere.

## 1 Introduction

The ionosphere is mainly divided into three different regions based on peak electron density, namely the D-region extending from some 60–90 km, the E-region from 90–150 km and the F-region extending from 150 km and above. Electron-ion density in all of these regions show variation with time of the day, season, solar X-ray/UV flares, solar cycle and the level of magnetospheric and/or solar wind activity [17]. However, the lower part of the ionosphere approximately in 60–100 km region is highly variable as compared to other parts of the ionosphere with much lower electron density and increased neutral particles, negative ions and other hydrated ions. As a result, this lower part of the ionosphere causes considerable absorption of the medium and high frequency radio waves that pass through this region, but it reflects the Very Low Frequency (VLF) and Low Frequency (LF) waves (10–50 kHz). Historically, this lower part of the ionosphere has been studied much less compared to lower atmosphere and E- and F-region ionosphere, therefore received its nickname as the 'ignorosphere'. The main reason of ignoring is that this lower part of the ionosphere is far too thin to support research balloons or planes and thick enough to drag down spacecraft within few months. Ground-based high frequency

S. Pal (✉)
Department of Atmospheric Sciences, University of Calcutta, Kolkata, India

© Springer International Publishing AG, part of Springer Nature 2018

B. Mukhopadhyay, S. Sasmal (eds.), *Exploring the Universe: From Near Space to Extra-Galactic*, Astrophysics and Space Science Proceedings 53,
https://doi.org/10.1007/978-3-319-94607-8_41

RADAR observations are also not possible continuously due to lack of sufficient electron density for the observable echoes. Although some rocket experiments had been done and few satellites had taken measurements on their way back down to Earth, but that only produce some transient and spatially limited data with no continuity. Therefore the best way to monitor this 'ignorosphere' continuously is to record VLF/LF radio waves, that are originated by the lightning discharge naturally or by the man-made navigational transmitters, at the ground with some antenna-receiver system and to analyse recorded data accordingly. This process is known as remote sensing study of the so called 'ignorosphere'. Although lower part of the ionosphere was ignored compared to E and F-region, much of the studies were done before 1990s compared to present days. After the introduction of the satellite based navigational Global Position System (GPS) around 1992 with enormous future scopes, opportunities and applications, use of VLF/LF waves for navigation purpose has been reduced drastically. At present, only a few VLF transmitters are used for specific submarine communication purpose and many VLF transmitters are not operational. Scientists and researchers also find interest in using the GPS signals to study the ionosphere. As a matter of fact, at present a few research groups in the world work on the lower part of the ionosphere using VLF/LF remote sensing as a main diagnostic tool. Therefore, the name 'ignorosphere' is equally suited now a days as it was in the past.

VLF/LF remote sensing data alone are not sufficient to retrieve as much information about the ignorosphere. We need theoretical study and computer simulation as well. Significant discoveries about lower ionosphere came from observations followed by modeling of VLF/LF signal propagation within the earth-ionosphere waveguide. Recently, there has been much interest in modeling the propagation of VLF/LF signals over different radio paths from short, medium to long range paths including low to high latitude regions. This article will briefly review some recent developments on significant numerical models that are applied for simulation of VLF/LF signals to retrieve information about the state of the D-region ionosphere.

## 2 VLF/LF Remote Sensing Method

VLF/LF signals propagate a very long distance (~10,000 km) with sufficient energy to be recorded by the antenna-receiver system due to very low attenuation of the waves in the earth-ionosphere waveguide. They sample the information about the state of the ionosphere along the radio propagation path and thus are very significant tool for detection of various geophysical phenomena. Figure 1a illustrates a cartoon diagram of VLF/LF remote sensing methodology. The VLF/LF recording system is very simple and easy to handle. It has three main parts; one receiving antenna, one receiver/amplifier, one computer (Fig. 1b). The receiving antenna can be of two types, namely, the magnetic loop or B-field antenna which receives the magnetic component of the VLF signal and the electric field or E-field antenna which receives the electric component of the VLF signal. Depending on the local

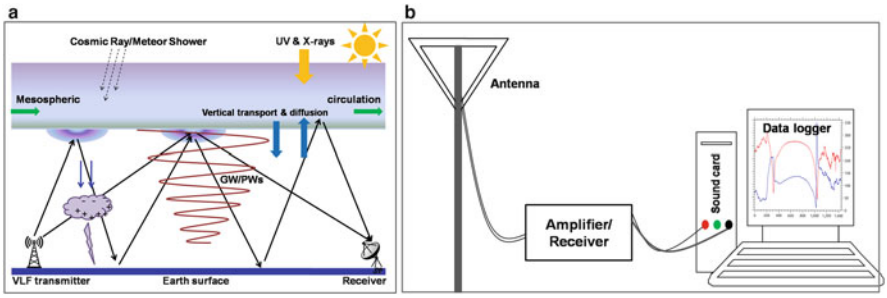



**Fig. 1** (**a**) Cartoon diagram of VLF/LF remote sensing methodology and (**b**) block diagram of a typical VLF/LF recording system

electrical environment, loop antenna or E-field antenna can be used. Since the dimension of antenna is very small compared to the wavelength of VLF waves, the time varying electro-magnetic field can be considered as uniform across the antenna, which induce open circuit voltage at the antenna terminals (see www.vlf.stanford.edu for details about VLF/LF remote sensing method). The output from the antenna is fed to the receiver where significant amplification of the signal amplitude is done by using suitable amplifiers. The receiver output is finally fed into the sound card of the computer where the analog signal is converted into the digital one and the data acquisition software continuously records (at sampling frequency) the variation of amplitude and phase of the signals with time.

## 3 VLF/LF Propagation Model

There is a renewed interest on VLF/LF research which comes with significant development of VLF/LF receiving technology along with increased dependence of near-earth space on human society. Long range radio wave propagation theory via multiple reflections between the earth and ionosphere has been known to us since 1930s and is a mature area of research. Propagation of VLF/LF waves between two points on earth can be represented either by ray theory or waveguide mode theory. The choice of representation depends on the frequency of the signal and the distance of propagation [86].

### *3.1 Ray Theory Propagation Model*

This method simply traces the different discrete ray paths (sky waves) that complete an integral number of reflections between a transmitter and a receiver. The total field is calculated as the sum of ground wave and the discrete sky-waves. Initially

short distance VLF measurements were explained using ray theory calculation of ionospheric reflection co-efficient matrix including the effect of earth's magnetic field also [2, 8]. In the later stage, with development of computer technology, the D-region electron density profiles were also derived by comparing the VLF observations with ray theory calculations [48, 55, 78]. Wakai [84] and Wakai et al. [85] used ray theory method to calculate the field strength of LF transmitter signal as a function of distance up to 2000 km at 40 and 60 kHz in Japan. They also calculated the diurnal variation of LF signals at a particular receiver. They compared their prediction with observed field data which generally agreed with each other. Pal and Chakrabarti [58] and Pal [57] successfully applied ray theory technique to calculate signal strength as a function of distance and diurnal variation of VLF signal at 18.2 kHz in Indian context. Effects of the total solar eclipse of July 2009 on VLF signal at various receiver locations have also been explained by ray theory code and corresponding D-region features have been derived [61]. Qin et al. [73] also used ray theory and transfer matrix based model to extract D-region ionospheric features from observation of lightning sferics in the earth-ionosphere waveguide.

### 3.1.1 Simulation of Diurnal Variation of VLF Signal

It is very challenging to predict accurately the diurnal variation of VLF/LF signal as it requires complete information about the lower and upper waveguide boundaries along the radio paths. In Fig. 2 (top panel), we present diurnal variations of VTX signal (18.2 kHz) in Indian sub-continent during summer (solid curve) and winter (dashed curve) calculated using the developed ray theory code (details can be seen in [57]). The corresponding observed results are also shown in bottom panel recorded at Indian Centre for Space Physics (ICSP), Kolkata. Diurnal features of simulation and observations are matching very well except for nighttime, because at night ray theory code assumes a uniform ionosphere over the propagation path. The difference between summer and winter daytime amplitude attributed the fact that in winter VLF signal experiences strong absorption in the lower D-region compared to summer. This phenomenon is also known as the D-region winter anomaly which may have direct correlation with the planetary waves in the lower atmospheric region [65, 77].

## *3.2 Mode Theory Propagation Model*

Another way to represent VLF propagation is in terms of infinite number of independent waveguide modes excited between the source and receiver according to the properties of upper and lower boundaries of the earth-ionosphere waveguide. The total field at any point in the guide is obtained by summation of fields from such waveguide modes. For VLF signal propagation at long distances, it is sufficient to consider only a few low order modes as the higher order modes attenuate at

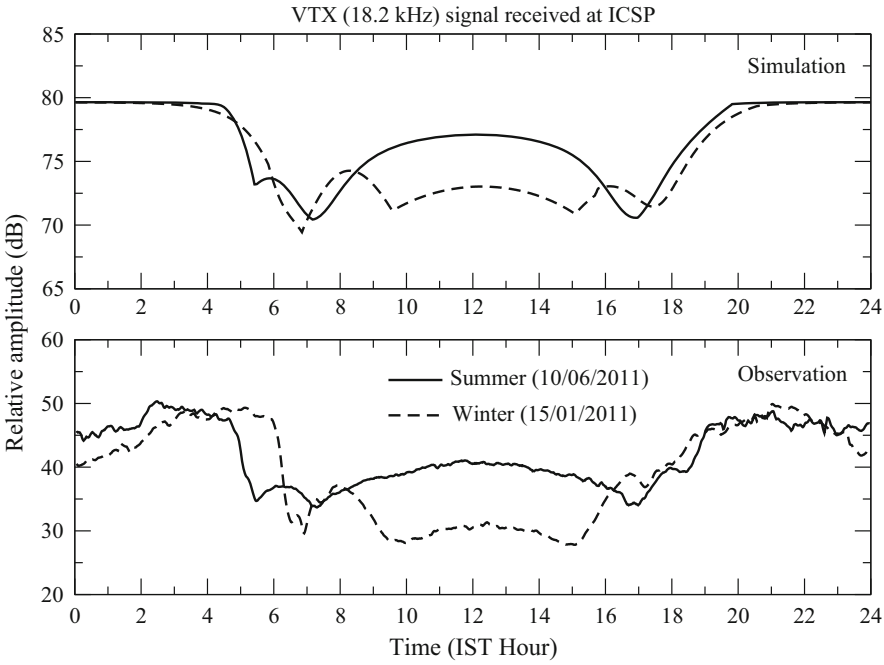



**Fig. 2** Simulation of diurnal variation of VLF signal for a medium range path using ray theory. Simulation results (top panel) for a typical summer and winter days are compared with the corresponding observations (bottom panel)

a faster rate. Thus the mode theory becomes an automatic choice of representation for relatively larger propagation distances. Mathematical formulations of waveguide mode theory for VLF propagation in the earth-ionosphere waveguide are pioneered by Wait [86] and Budden [8]. In Wait's formulation of mode theory, the upper and lower boundaries are specified by the conductivity, permittivity, and permeability of the boundary regions explicitly. However, effects of earth's magnetic field were not included in this formulation. Budden waveguide theory is the most general one, which includes the effects of geomagnetic field on VLF propagation resulting anisotropy in the medium. The first computer program for VLF propagation using mode theory was made by Pappert et al. [69] with exponential ionospheric profiles as defined by Wait and Spies [87]. The effects of mode conversion resulting from the inhomogeneity of the upper or lower boundary of the waveguide across the day night terminator and the land-sea boundary were also studied [1, 68, 79, 80]. A more general computer program, the Long Wave Propagation Capability (LWPC) code, was developed at the Naval Ocean Systems Center, USA [19] which computes field values for VLF signal propagation using the two-dimensional waveguide propagation formulation for an arbitrary propagation path and ionospheric conditions along the path, including the effects of the geomagnetic field. This program has been used by many researchers successfully for modeling of long-range VLF propagation.

With a modified LWPC, it was also possible to retrieve the average D-region electron density profile in presence of ionospheric anomalies ([16, 62, 72, 82, 83] and references therein).

### 3.2.1 Diurnal Variation of VLF Signal from LWPC

The default propagation model in LWPC, which uses two parameters model (sharpness factor of D-region electron density profile $\beta$ and effective VLF reflection height $h'$) to define D-region conductivity following Wait and Spies [87], is generally used for approximate prediction of diurnal behaviour of VLF signals at any place. The program has been used to predict the diurnal VLF signal behaviour in Indian subcontinent at various places which were found to agree with the VLF campaign results both in summer and winter during low solar activity period [9]. Comparative study has also been done between ray theory and LWPC code [60], where the field amplitude matches for both calculations but the VLF reflection height tends to be higher in ray theory code than the LWPC code. To get the day time variation of signal amplitude as a function of solar flux and to connect the LWPC propagation model with a realistic ionosphere model, Pal [57] coupled the FORTRAN code of the International Reference Ionosphere model [6] with the LWPC code. As a result, the electron-ion density profiles from the IRI-2007 model along the propagation path come as the inputs in the LWPC program to calculate the VLF diurnal variation in an automated way. In Fig. 3, we have presented the diurnal variation of the amplitude of VTX signal at 18.2 kHz as observed in Kolkata with the simulated variation as reproduced from the coupled IRI-LWPC code. The dotted curve is obtained assuming the electron-neutral collision frequency as described by Wait and Spies [87] which is also the default collision frequency as set in LWPC code. The solid curve is obtained assuming the temperature dependent collision frequency as described by Kelley [35]. In both of these calculations, only electron density profile has been used to characterise the D-region ionosphere. In third calculation (dot-dashed curve), we have used positive and negative ion density in addition to the electron density including the collision frequency between electron-neutral and electron-ions. From this calculation, we note that the effects of D-region ion density on VLF signal propagation can be neglected at daytime, but at nighttime significant difference in signal amplitude is observed. From the comparison of observed and simulated data, it is also to be noted that collision frequency profiles play a significant role in determining VLF diurnal variation. Wait's collision frequency produced higher daytime signal than Kelley's collision frequency, but at nighttime Wait's profile produced lower signal strength. This general behaviour is also seen in high mid-latitude region for NRK signal at 37.5 kHz received at Kiel observatory Germany (Fig. 4). Thus to model accurate diurnal behaviour of VLF signal and then to retrieve D-region profiles, it is better not to use constant collision frequency profile throughout day and night.

To check the effect of ground conductivity on the diurnal variation of VLF signal, we exercised the coupled IRI-LWPC model for two different ground conditions,

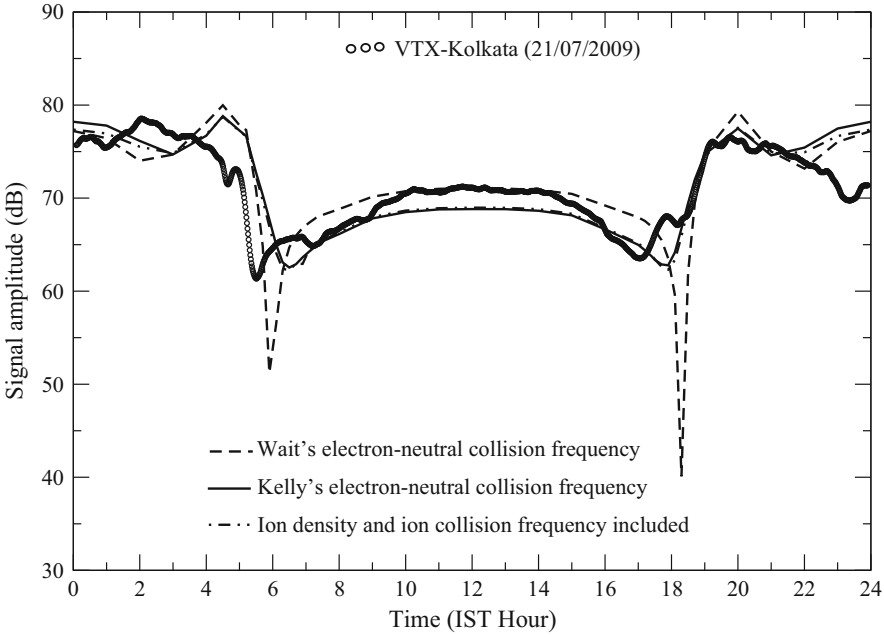



**Fig. 3** Simulation of diurnal variation using the coupled IRI-LWPC program for different collision frequency profiles compared with the observation at low latitude region

sea water ($\epsilon$:81, $\sigma$:4 S/m) and medium ground ($\epsilon$: 15, $\sigma$: 0.003 S/m) for constant ionospheric conditions. Solid line of Fig. 5 shows the diurnal variation of VTX signal at 18.2 kHz with ground path selected automatically (combination of sea water and medium ground) by the LWPC program. Dashed curve and dotted-dashed curve show the same variation for a complete sea water and medium ground path respectively. Daytime signal over the sea water path is more attenuated than medium ground path, while the nighttime feature is opposite. Another interesting feature is that the times corresponding to sunrise and sunset terminator minima shifted towards the daytime value (inset of Fig. 5) for increased ground conductivity. Therefore it is instructive to use proper ground conditions in LWPC program while modeling medium to long-range VLF propagation with variable terrain, for example signal propagating in Antarctic or Arctic region in summer and winter experiences different ground conditions in terms of variable ice mass, which can also be used to remotely sense the Antarctic/Arctic ice coverage. The current version of LWPC program (v2.1) includes the "Newmag85" (which calculates magnetic field for a model date of 1985) model for calculation of geomagnetic field at the ionospheric height. To check the effect of the International Geomagnetic Reference Field (IGRF-11) model on VLF signal, we have replaced the older magnetic model by the IGRF-11 model. It has been seen that the inclusion of IGRF-11 model in the LWPC program produced significant deviation of nighttime VLF signal from the original

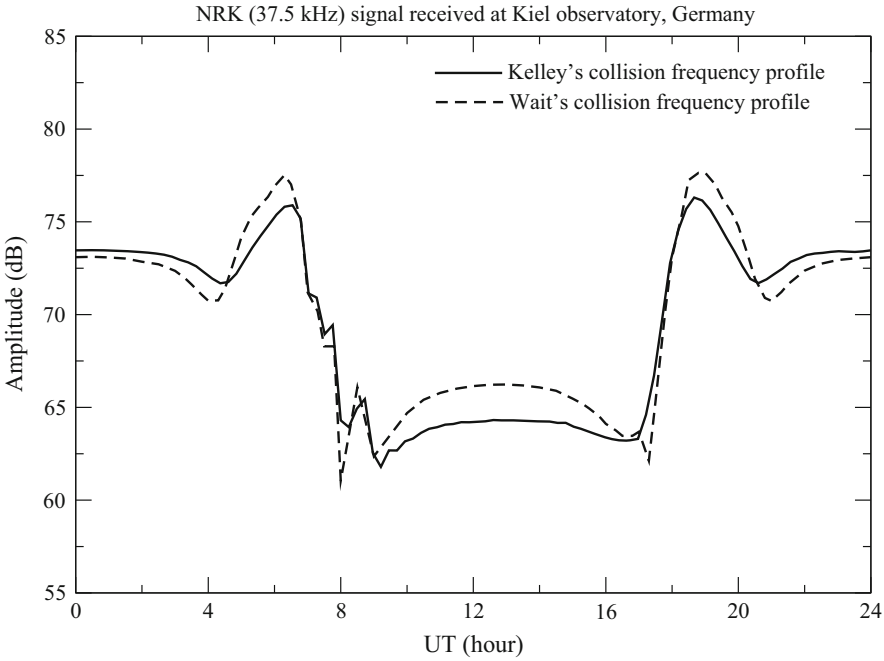



**Fig. 4** Effect of electron-neutral collision frequency profile on diurnal variation of VLF signal propagating over high mid-latitude region (NRK to Kiel, Germany)

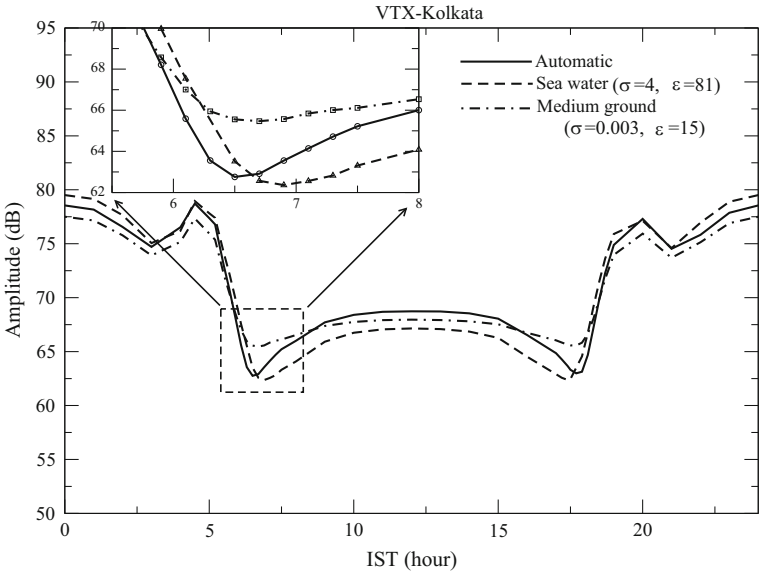



**Fig. 5** Effect of ground conductivity on diurnal variation of VLF signal

LWPC program [59]. Sasmal et al. [76] also used the revised LWPC program, which included the recent IGRF magnetic field model (IGRF-11), to calculate VLF signal strength for long distance propagation from VTX to Antarctica region as the south magnetic pole moves significantly in a year.

# 4 Perturbations on VLF/LF Signals and Retrieving the D-Region Information

## *4.1 VLF/LF Perturbations Due to Solar Eclipse*

Various geophysical phenomena disturb the normal D-region ionospheric plasma dynamics. As a result, VLF/LF signal propagation is also affected by the D-region ionospheric disturbances which makes VLF/LF signal as the most used diagnostic tool for this region. During a solar eclipse, D-region experiences a virtual sunrise followed by virtual sunset within a short time interval ($\sim$1–2 h) which set in a large-scale transient ionospheric perturbation. The UV and soft X-ray photons which are main ionizing sources for the D-region get totally or partially blocked in a predicting way giving an ideal opportunity to study the D-region processes. Significant studies on the D-region during solar eclipses have been done via their effects on the VLF/LF wave propagation in the earth-ionosphere waveguide.

Initial measurements of VLF amplitude and phase changes during solar eclipses were reported by Bracewell [7], Crary and Schneible [15] and many others. Lynn [46] showed that VLF phase response was a non-linear function of solar obscuration over three long VLF paths during the solar eclipse of 1976 and the effective time constant of ionospheric response was $4.3 \pm 1.5$ min. Noonkester and Sailors [56] first modelled the solar eclipse effects on VLF signal using a combined D-region aeronomy model and VLF propagation tool. Clilverd et al. [13] modelled the effects of total solar eclipse of August 11, 1999 on VLF signals in Europe using the LWPC program. They reported an 8 km rise in VLF reflection height during eclipse conditions over short paths, while over the medium-length paths, the estimation was 5 km increase in reflection height. A similar result was also reported by Fleury and Lassudrie-Duchesne [21], who found an increase of reflection height by about 5 km at mid-eclipse assuming ionospheric disturbance to be uniform along the whole radio path.

Later on, Chakrabarti et al. [10] took measurements on VLF signal during the total solar eclipse of July 22, 2009 at several places in Indian sub-continent. They found both increase and decrease in signal amplitude during the maximum eclipsed conditions depending on receivers location with respect to the eclipse totality belt. They also interpreted their results with the LWPC program. Pal et al. [62] took the opportunity to model the solar eclipse perturbations on VLF signal and to find the temporal variation of D-region electron density profile during the solar eclipse period. Assuming that the ionospheric perturbations are linearly related to the degree

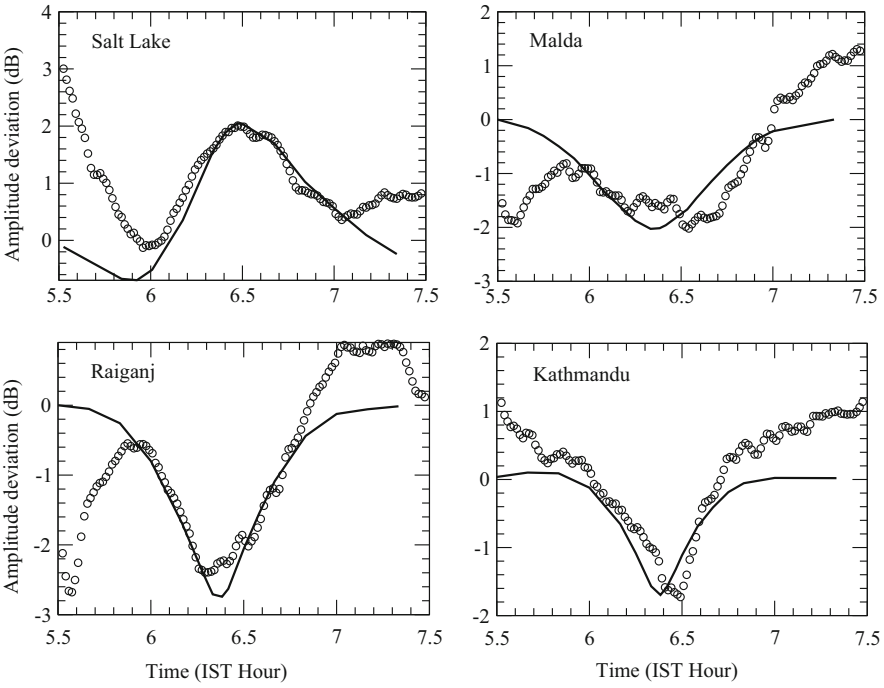



**Fig. 6** Temporal simulation (solid curves) of VLF signal disturbances along with observed (open circle) disturbances due to solar eclipse of July 2009 by LWPC code assuming a linear response of D-region ionospheric plasma to the eclipse obscuration

of solar obscuration along the propagation path, they created a 2D inhomogeneous time-dependent ionospheric perturbation model along the VLF wave propagation path to simulate temporal variation of VTX signal at frequency 18.2 kHz. Figure 6 shows the corresponding simulation (solid line) and observational (open circle) results at four places which match quite well, although the model assumed linear variation of ionosphere with respect to solar obscuration. During the annular solar eclipse of 2010, a C1.3 type solar flare occurred which was partly blocked by the Moon [47]. Following this, Pal et al. [63] deduced the effects of this occulted flare on D-region electron density profile along with the solar eclipse effects. This was the first report where the effects of two simultaneous events, namely the effect of solar eclipse and effect of a solar flare blocked by the moon during the eclipse, on the D-region electron density had been shown exclusively. Pal et al. [63] also showed that the ionospheric perturbation due to solar eclipse was indeed a non linear function of solar obscuration along the VLF propagation path. The ionospheric perturbations was found to vary according to $[S(t)]^n$ , where S(t) is the solar obscuration function which depend on time, latitude and longitude of places and the values of 'n' lie between 1.5–1.0 from the start of the observed deviation to the maximum deviation. Chakraborty et al. [12] also attempted to model the solar eclipse effects on VLF

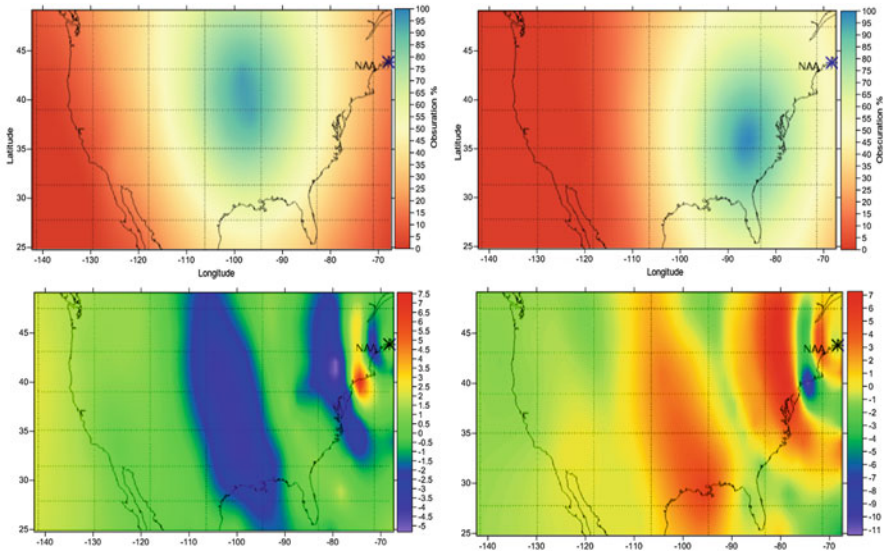



**Fig. 7** Prediction of the NAA signal (24 kHz) strength deviation in USA due to the great solar eclipse of August 21st, 2017. We note that signal could be enhanced by as much as 7 dB. The signal may be reduced by as much as 11 dB

signal using a D-region ion-chemistry model and LWPC program. Here in Fig. 7, we have presented prediction of the NAA signal strength deviation in USA due to the great solar eclipse of August 21, 2017 (published in ICSP report, www.csp.res.in) ahead of the event. The solar obscuration distribution (top panel) and corresponding spatial variation (bottom panel) of the NAA signal deviation due to the eclipse at 18:00 UT and 18:30 UT are shown respectively. For the calculation we followed the linear model of Pal et al. [62] and assumed that the NAA signal reflection height is increased by about 7.0 km at 100% obscuration zones and at rest of the places it varies according to obscuration percentage.

## *4.2 VLF/LF Perturbations Due to Lightning*

Tropospheric lightning couples the energy between troposphere and lower ionosphere via the mesosphere through quasi-electrostatic (QE) and electromagnetic pulsed (EMP) fields to produce small scale plasma disturbances in the D-region ionosphere. It is believed that the transient luminous events (TLEs) like sprites are formed due to QE field in the mesosphere following a +CG flash and elves are formed due to heating of the mesosphere by EMP [29]. Propagation of sub-ionospheric VLF/LF signal is also perturbed due to global lightning activities. Direct perturbations in the nighttime VLF signals occur within 20 ms of (i.e., early) the

associated lightning discharges. The onset duration of these events can be within a few milliseconds (<100 ms) and are called "early/fast" events or onset duration can be 1–2 s and are called "early/slow" events [31, 75]. They are caused by heating and ionization of the lower ionosphere by intense EMPs from lightning discharge. Typically early events are associated with +CG discharges with large charge-moment changes which produce sprites through large QE field in the mesosphere. Indirect perturbations on VLF signals due to lightning are delayed by ∼300 ms to 1 s relative to their parent lightning discharges. Indirect perturbations first studied by Helliwell et al. [28] and the transient perturbations in VLF signal were named as 'Trimpi' events. Trimpi events are caused by the interaction of lightning produced whistler mode wave with the trapped electrons in the magnetosphere causing them to precipitate in the ionosphere. Trimpi events are now commonly known as lightning induced electron precipitation (LEP) events. Lightning induced VLF perturbations and their modeling using LWPC program have been extensively studied mostly at the Stanford University [30, 32, 49, 70] and by many others [18, 29, 51, 54]. Mainly the LWPC program along with the simplified D-region chemical model namely Glukhov-Pasko-Inan model [23] have been successfully used to model the LEP events and also early events by most of the researchers. Recently, some early events are identified which take much longer time (several minutes ≥10 min) to recover to its pre-perturbation stages, termed as long recovery events (LORE) [14, 26]. LORE events tend to occur due to impact of intense EMP with very high peak current flashes, more than 100 kA [27, 36]. Using the LWPC program and a finite-difference time-domain (FDTD) technique for the calculation of D-region electron density profiles due to lightning peak current, Kotovsky and Moore [37] explained both the typical recovery (20–240 s) and long recovery (LOREs, >300 s) VLF events from conductivity changes associated with sprite halos. Chakraborty et al. [11] also reported LEP events including LORE events in low-latitude Indian region over the VTX-Kolkata and VTX-NWC propagation paths. It will be interesting to model the observed LEP and LORE events in such low-latitude region.

### *4.3 VLF/LF Perturbations Due to Solar Flares and GRBs*

The dynamics of the upper boundary of the earth-ionosphere waveguide is highly dependent on the solar radiation, cosmic rays, energetic electron precipitation and to lesser extent meteor shower. X-ray and hard UV components from solar flares produce large scale disturbances in the D-region conductivity resulting significant perturbations in the VLF/LF signals. The enhancement in ionization due to solar flares increases the VLF/lF phase velocity and lowers the VLF/LF reflection height. Effects of solar flares on VLF/LF signals and the variation of sharpness of the D-region electron density profile during solar flares have been extensively studied by Mitra [52], Thomson et al. [82], Zigman et al. [88], Grubor [25], Pal and Chakrabarti [58], Basak and Chakrabarti [3] and references therein. Mostly LWPC program was run to find a match between observed and calculated VLF amplitudes using a large

set of parameters ($\beta$ and $h'$) base which gave average electron density profile over the radio paths. However, this process may produce ambiguous results due to the degeneracy of the field amplitude with respect to the set of parameters. Due to this reason some researchers preferred to use both amplitude and phase of observed VLF signal to compare with the LWPC calculation. Palit et al. [67] first used the GEANT4 Monte-Carlo simulation code for the computation of ionization rate due to solar flares along with Glukov-Pasko-Inan ionospheric model and LWPC program to model VLF signal amplitude during solar flares. The powerful gamma ray photons from a distant galaxy associated with Gamma Ray Bursts (GRBs) also affect the D-region ionosphere modifying the electrical conductivity and produce detectable amplitude and phase changes in the VLF/LF signals. Transient VLF disturbances due to a GRB was first detected in 1983 [20]. Since then there are more detections using VLF signals as the main diagnostic tool (for e.g., [33, 34, 53, 81]). Mondal et al. [53] used only LWPC program to find the D-region sharpness changes due to GRB. Tanaka et al. [81] used Monte-Carlo simulations followed by D-region chemistry model to estimate the altitude profile of electron number density in presence of gamma-rays along with the Finite-Difference Time-Domain (FDTD) simulations to calculate VLF wave propagation.

### *4.4 VLF/LF Perturbations Due to Meteorological Events*

In addition to disturbances due to excess ionization associated with solar and geomagnetic activities, intense meteorological events (such as tropical cyclones, severe thunderstorms and polar stratosphere warming events) can cause significant large-scale disturbances in the ionosphere. Atmospheric gravity waves and planetary waves generated from such meteorological events may propagate upward under suitable background conditions up to the lower thermosphere where they break and deposit maximum momentum and energy. This mechanism can also act as a source of secondary atmospheric waves which could propagate further upward in the F-region ionosphere [42, 43]. Ionospheric disturbances in the F-region due to tropical cyclones have been studied in details for a long time by many researchers using ionosonde, HF Doppler and GPS TEC data [4, 45, 71]. The D-region ionosphere could be more influenced by the meteorological events [74] and therefore VLF/LF signals are expected to respond to such events [64]. Rozhnoi et al. [74] first investigated the effects of eight tropical cyclones over the Pacific ocean on VLF/LF signals and they found negative nighttime anomalies in the VLF/LF amplitude corresponding to six tropical events. Kumar et al. [38] also reported VLF signal perturbations corresponding to tropical cyclone Evan in 2012 and using LWPC program they estimated an average decrease in the nighttime D-region reference height by $\sim$5.2 km and increase in the daytime D-region by 6.1–7.5 km. Not only tropical cyclones or severe thunderstorm affects the ionosphere, but also the sudden stratospheric warming (SSW) event in the polar region of Northern hemisphere create large-scale perturbation in the ionosphere as well. During a SSW period polar

stratospheric temperature at 10 hPa level increases by at least 25 K within a week and the zonal mean wind at or near 10 hPa also reverses its direction for a major SSW event. This is a pure meteorological phenomenon believed to be caused by upward propagation of tropospheric transient planetary waves into the stratosphere and their interaction with the zonal mean flow [50]. Being a global event, it also affects the mid-latitude to low latitude ionosphere [22, 24, 39, 41, 44]. Ionospheric effects during SSW events have been extensively studied by ionosonde and GPS TEC method, however there are very few reports about the effects of SSW events on VLF/LF signal. Initial measurements of VLF signal during the SSW events were reported by Belrose [5] and Larsen [40], though their conclusions about the D-region electron density changes were not same. Pal et al. [66] first comprehensively studied the effects of a major SSW event on VLF/LF signal amplitudes and were able to model the variation of VLF/LF amplitude changes during the SSW period using the coupled IRI-LWPC program. Depending on the propagation paths, they found significant increase/decrease or both increase and decrease of VLF/LF amplitudes by ∼3–5 dB during the peak of the SSW event. Their simulation results indicated that VLF/LF anomalies associated with the SSW event were caused by increased electron density and slightly increased collision frequency in the lower ionospheric region. In Fig. 8, we present the observed (dotted) and simulated (solid) amplitude disturbances of the NRK signal during the SSW time period (for details see [66]).

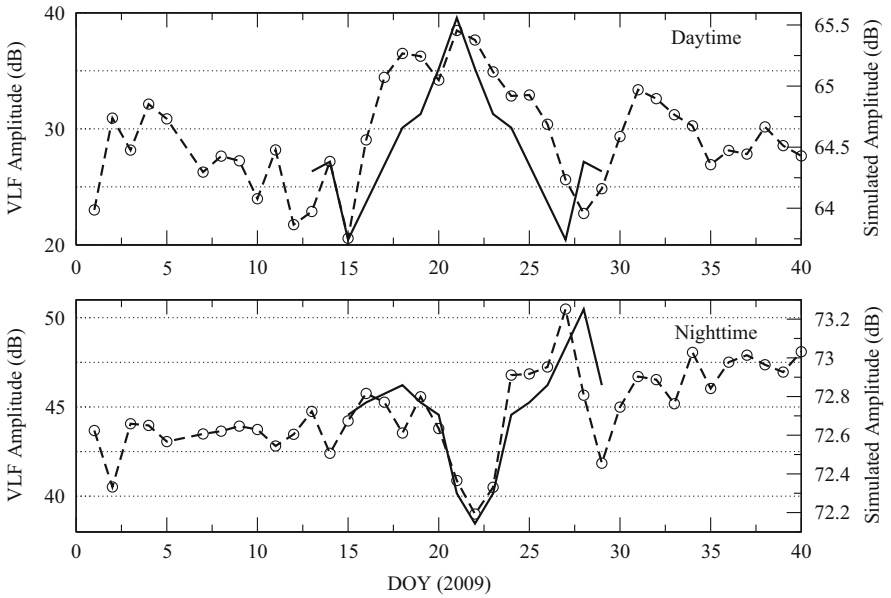



**Fig. 8** Relative comparison of the observed (dotted) and simulated (solid) amplitude disturbances of the NRK signal during the SSW time period (following [66])

## 5 Summary

This article briefly reviewed the significant developments in the earth-ionosphere propagation models from the view point of retrieving D-region information using VLF/LF remote sensing method. First we discussed about the developments of two different methods for modeling of VLF/LF signal propagation and hence to extract D-region electron density profile. Then we talked about modeling of VLF/LF perturbations due to solar eclipse, lightning, solar flares and GRBs using radio wave propagation model in combination with different ionospheric models. Finally, we discussed the impact of meteorological phenomena, such as tropical cyclones, polar stratospheric warming events on VLF/LF signals and corresponding D-region disturbances. As we mentioned, it is very challenging for any model to predict accurately the variation of VLF/LF signal and therefore to diagnose complete information about the D-region ionosphere. No matter how good the model is, there will always be some residual due to stochastic nature of the ionospheric plasma. Nevertheless, the VLF/LF remote sensing research is progressing towards greater accuracy. The subject needs a complete earth-ionosphere propagation model including the D-region chemistry and dynamics in a single software architecture which will be useful for modeling VLF/LF propagation in the earth-ionosphere waveguide under any geophysical conditions reducing VLF/LF navigational error significantly so that it could work as a back-up of GPS/GNSS navigational system. This will also allow to study the D-region ionospheric weather on day-to-day basis.

**Acknowledgements** Author acknowledges the support from the University Grants Commission (UGC) under the Dr. D.S. Kothari Post-doctoral Fellowship Scheme (No.F.4-2/2006 (BSR)/ES/17-18/0007). VLF data used here are from ICSP VLF network.

## References

1. Barr, R.: Proceedings of the 12th Annual Meeting of the International Omega Association, Hawaii, pp. 27.1–27.6 (1987)
2. Barr, R., Jones, D.L., Rodger, C.J.: J. Atmos. Sol. Terr. Phys. **62**, 1689–1718 (2000)
3. Basak, T., Chakrabarti, S.K.: Astrophys Space Sci. **348**(2), 315–326 (2013)
4. Bauer, S.J.: J. Geophys. Res. **63**, 265–269 (1958)
5. Belrose, J.S.: Nature, London **214**, 660 (1967)
6. Bilitza, D., McKinnell, L.A., Reinisch, B., Fuller-Rowell, T.: J. Geodesy **85**, 909–920 (2011). https://doi.org/10.1007/s00190-010-0427-x
7. Bracewell, R.N.: J. Atmos. Sol. Terr. Phys. **2**, 226–235 (1952)
8. Budden, K.G.: Radio Waves in the Ionosphere. Cambridge University Press, Cambridge (1966)
9. Chakrabarti, S.K., Mondal, S.K., Sasmal, S., Pal, S., et al.: Indian J. Phys. **86**(5), 323–334 (2012)
10. Chakrabarti, S.K., Pal, S., Sasmal, S., Mondal, S.K., Ray, S., Basak, T., Maji, S.K., Khadka, B., Bhowmick, D., Chowdhury, A.K.: J. Atmos. Sol. Terr. Phys. **86**, 65–70 (2012)
11. Chakraborty, S., Pal, S., Chakrabarti, S.K.: General Assembly and Scientific Symposium (URSI GASS). IEEE, New York (2014). https://doi.org/10.1109/URSIGASS.2014.6929559

12. Chakraborty, S., Palit, S., Ray, S., Chakrabarti, S.K.: Astrophys. Space Sci. **361**, 72 (2016). https://doi.org/10.1007/s10509-016-2660-0
13. Clilverd, M.A., Rodger, C.J., Thomson, N.R., et al.: Radio Sci. **36**(4), 773 (2001)
14. Cotts, B., Inan, U.S.: Geophys. Res. Lett. **34**, L14809 (2007)
15. Crary, J.H., Schneible, D.E.: Radio Sci. **69D**, 947–957 (1965)
16. Cummer, S.A., Inan, U.S., Bell, T.F.: Radio Sci. **33**, 1781–1792 (1998)
17. Davies, K.: Ionospheric Radio. Peter Peregrinus Ltd., London (1990)
18. Dowden, R.L.: Geophys. Res. Lett. **23**, 3421–3422 (1996)
19. Ferguson, J.A.: Technical document 3030, Space and Naval Warfare Systems Center, San Diego (1998)
20. Fishman, G., Inan, U.S.: Nature **331**, 418–420 (1988)
21. Fleury, R., Lassudrie-Duchesne, P.: In: Eighth International Conference on HF Radio Systems and Techniques. IET (2000). https://doi.org/10.1049/cp:20000208
22. Fuller-Rowell, T., Akmaev, R., Wu, F., Fedrizzi, M., Viereck., R.A., Wang, H.: Geophys. Res. Lett. **38**, L18104 (2011). http://dx.doi.org/10.1029/2011GL048985
23. Glukhov, V.S., Pasko, V.P., Inan, U.S.: J. Geophys. Res. **97**, 16971–16979 (1992)
24. Goncharenko, L., Zhang, S.R.: Geophys. Res. Lett. **35**, L21103 (2008). http://dx.doi.org/10.1029/2008GL035684
25. Grubor, D., Sulic, D., Zigman, V.: Ann. Geophys. **26**, 1731–1740 (2008)
26. Haldoupis, C., Cohen, M., Cotts, B., Arnone, E., Inan, U.: Geophys. Res. Let. **39**, L16801 (2012)
27. Haldoupis, C., Cohen, M., Arnone, E., Cotts, B., Dietrich, S.: J. Geophys. Res. Space Phys. **118**, 5392–5402 (2013). http://dx.doi.org/10.1002/jgra.50489
28. Helliwell, R.A., Katsufrakis, J.P., Trimpi, M.L.: J. Geophys. Res. **78**, 4679–4688 (1973)
29. Hobara, Y., Iwasaki, N., Hayashida, T., Hayakawa, M., Ohta, K., Fukunishi, H.: Geophys. Res. Lett. **28**(5), 935–938 (2001)
30. Inan, U.S., Carpenter, D.L.: J. Geophys. Res. **92**, 3293–3303 (1987)
31. Inan, U.S., Shafer, D.C., Yip, W.Y., Orville, R.E.: J. Geophys. Res. **93**, 11455–11472 (1988)
32. Inan, U.S., Bell, T.F., Pasko, V.P., Sentman, D.D., Wescott, E.M., Lyons, W.A.: Geophys. Res. Lett. **22**, 3461–3464 (1995)
33. Inan, U.S., Lehtinen, N.G., Lev-Tov, S.J., Bell, T.F., et al.: Geophys. Res. Lett. **26**, 3357–3360 (1999)
34. Inan, U.S., Lehtinen, N.G., Moores, R.C., Hurley, K., et al. Geophys. Res. Lett. **34**, 8103 (2007)
35. Kelley, M.C.: The Earths Ionosphere, Plasma Physics and Electrodynamics, Chapter 2.2, 2nd edn. Academic, New York (2009)
36. Kotovsky, D.A., Moore, R.C., Zhu, Y., Tran, M. D., Rakov, V.A., Pilkey, J.T., Caicedo, J.A., Hare, B., Jordan, D.M., Uman, M.A.: J. Geophys. Res. **121**, 5794–5804 (2016)
37. Kotovsky, D.A., Moore, R.C.: J. Geophys. Res. (2017). https://doi.org/10.1002/2017JA023996
38. Kumar, S., Amor, S.N., Chanrion, O., Neubert, T.: J. Geophys. Res. Space Phys. **122**(8), 87208732 (2017). http://dx.doi.org/10.1002/2017JA024023
39. Klimenko, M.V., Klimenko, V.V., Bessarab, F.S., Korenkov, Y.N., Liu, H., Goncharenko, L.P., Tolstikov, M.V.: J. Geophys. Res. Space Phys. **120** (2015). http://dx.doi.org/10.1002/2014JA020861
40. Larsen, T.R.: J. Atmos. Sol. Terr. Phys. **33**, 1251–125 (1971)
41. Laskar, F.I., Pallamraju, D., Veenadhari, B.: Earth Planets Space **66**, 94 (2014)
42. Lastovicka, J.: Phys. Chem. Earth **26**(Part C), 381–386 (2001)
43. Lastovicka, J.: J. Atmos. Sol. Terr. Phys. **68**, 479–497 (2006)
44. Liu, H.L., Roble, R.G.: Geophys. Res. Lett. **32**, L13804 (2005). http://dx.doi.org/10.1029/2005GL022939
45. Liu, Y.M, Wang, J.S., Suo, Y.C.: Adv. Geosci. **29**, 351360 (2006). http://www.adv-geosci.net/29/351/2006
46. Lynn, K.J.W.: J. Atmos. Sol. Terr. Phys. **43**, 1309–1316 (1981)
47. Maji, S.K., Chakrabarti, S.K., Mondal, S.K.: Earth Moon Planets **108**, 243–251 (2012)
48. Mambo, M., Nagano, I., Nakamura, K., Fukami, T.: Radio Sci. **18**, 119–127 (1983)

49. Marshall, R.A., Inan, U.S., Lyons, W.A.: J. Geophys. Res. **111**, D19108 (2006). http://dx.doi.org/10.1029/2006JD007219
50. Matsuno, T.: J. Atmos. Sci. **28**(8), 1479–1494 (1971)
51. Mika, A., Haldoupis, C.: Space Sci. Rev. **137**, 489–510 (2008). http://dx.doi.org/10.1007/s11214-008-9382-8
52. Mitra, A.P.: Ionospheric Effects of Solar Flares, Astrophysics and Space Science Library, vol. 46. D. Reidel Publishing Company, Boston (1974)
53. Mondal, S.K., Chakrabarti, S.K., Sasmal, S.: Astrophys Space Sci. **341**(2), 259 (2012)
54. Molchanov, O.A., Shvets, A.V., Hayakawa, M.: J. Geophys. Res. **103**, 23443–23458 (1998)
55. Morfitt, D.G., Shellman, C.H.: Naval Ocean System Centre, San Diego, California (1976)
56. Noonkester, V.R., Sailors, D.B.: Radio Sci. **6**, 871–878 (1971)
57. Pal, S.: Ph.D. Thesis, University of Calcutta (2013). arXiv preprint arXiv:1503.05789
58. Pal, S., Chakrabarti, S.K.: In: Chakrabarti, S.K. (ed.) AIP Conference Proceeding, vol. 1286. AIP, New York (2010)
59. Pal, S., Chakrabarti, S.K.: General Assembly and Scientific Symposium (URSI GASS) (2011). 978-1-4244-6051-9/11
60. Pal, S., Basak, T., Chakrabarti, S.K.: In: Satake, K. (ed.) Advances in Geosciences. Solar Terrestrial, vol. 27. World Scientific Publishing Company, Singapore (2011)
61. Pal, S., Basak, T., Chakrabarti, S.K.: General Assembly and Scientific Symposium (URSI GASS) (2011). 978-1-4244-6051-9/11
62. Pal, S., Chakrabarti, S.K., Mondal, S.K.: Adv. Space Res. **50**, 196–204 (2012)
63. Pal, S., Maji, S.K., Chakrabarti, S.K.: Planet. Space Sci. **73**, 310–317 (2012)
64. Pal, S., Chakrabarty, S., Chakrabarti, S.K.: Adv. Space Res. (2014). http://dx.doi.org/10.1016/j.asr.2014.11.023
65. Pal, S., Chakraborty, S., Chakrabarti, S.K.: Adv. Space Res. **55**, 1190–1198 (2015)
66. Pal, S., Hobara, Y., Chakrabarti, S.K., Schnoor, P.W.: J. Geophys. Res. Space Physics **122** (2017). https://doi.org/doi:10.1002/2016JA023813
67. Palit, S., Basak, T., Mondal, S.K., Chakrabarti, S.K.: Atmos. Chem. Phys. **13**, 9159–9168 (2013)
68. Pappert, R.A., Morfitt, D.G.: Radio Sci. **510**, 537–546 (1975)
69. Pappert, R.A., Gossard, E.E., Rothmuller, I.J.: Radio Sci. **2**, 387–400 (1967)
70. Pasko, V.P., Inan, U.S.: J. Geophys. Res. **99**(A9), 17523–17537 (1994)
71. Polyakova, A.S., Perevalova, N.P.: Adv. Space Res. **48**, 1196–1210 (2011)
72. Poulsen, W.L.: Ph.D. Thesis, Stanford University (1991)
73. Qin, Z., Chen, M., Zhu, B., Du, Y.: J. Geophys. Res. Atmos. **122**, 712–727 (2017). http://dx.doi.org/10.1002/2016JD025599
74. Rozhnoi, A, Solovieva, M., Levin, B., Hayakawa, M., Fedun, V.: Nat. Hazards Earth Syst. Sci. Discuss. **2**, 2789–2812 (2014)
75. Sampath, H.T., Inan, U.S., Johnson, M.P.: J. Geophys. Res. **105**(A1), 183–191 (2000)
76. Sasmal, S., Pal, S., Chakrabarti, S.K.: Adv. Space Res. (2014). http://dx.doi.org/10.1016/j.asr.2014.06.002
77. Schmitter, E.D.: Ann. Geophys. **29**, 1287–1293 (2011)
78. Shellman, C.H.: Radio Sci. **8**, 1127–1135 (1970)
79. Smith, R.: J. Atmos. Sol. Terr. Phys. **36**, 1683–1688 (1974)
80. Smith, R.: J. Atmos. Sol. Terr. Phys. **39**, 539–543 (1977)
81. Tanaka, Y.T., Raulin, J.P., Bertoni, F.CP., et al.: ApJ **721**, L24 (2010)
82. Thomson, N.R., Clilverd, M.A.: J. Atmos. Sol. Terr. Phys. **63**(16), 1729 (2001)
83. Thomson, N.R., Clilverd, M.A., McRae, W.M.: J. Geophys. Res. **112**, A7 (2007)
84. Wakai, N., Kurihara, N., Otsuka, A.: Electronics Letter **40**(5), 288–290 (2004)
85. Wakai, N., Kurihara, N., Otsuka, A., Imamura, K., Takahashi, Y.: Radio Sci. **41**, RS5S13 (2006). https://doi.org/10.1029/2005RS003344
86. Wait, R.J.: Electromagnetic Waves in Stratified Media. Pergamon Press, Oxford (1962)
87. Wait, J.R., Spies, K.P.: NBS Technical Note, U.S. 300 (1964)
88. Zigman, Z., Grubor, A.D., Sulic, D.: J. Atmos. Sol. Terr. Phys. **69**, 775–792 (2007)

# Ground-Based and Space-Based Studies of Lower Ionospheric Irregularities: Observation and Modeling




**Suman Chakraborty**

**Abstract** Ionosphere acts as a gigantic detector in studying the space weather effects on the Earth's atmosphere. The phenomena causing such impacts can be broadly classified as terrestrial/local perturbations and extra-terrestrial/non-local perturbations. Both ground-based and space-based studies of such ionospheric irregularities are being conducted for almost a century. Through such rigorous studies, a general picture of the ionosphere and its response to the hostile environment outside is understood. In this article, we will present a detailed historical review on the study of ionospheric irregularities using both ground-based and space-based technologies both from the observational point of view and from the theoretical point of view. At the end, the present scenario and the future aspects will also be discussed.

## 1 Basic Overview of the Topic

Earth's ionosphere, extending from a region of ∼60–1000 km is a highly dynamic region of the atmosphere that responds very effectively to the hostile environment both *'above'* and *'below'* it. The hostile environment *'above'* the ionosphere denotes perturbing events of solar and extra-terrestrial origin whereas that *'below'* it denotes perturbations of only terrestrial origin. This ionosphere has been a hotbed of research to the scientific community for almost a century but still a global unified picture is not available till date. This is because this particular region of the Earth's atmosphere can be studied neither by sending balloons as it is too high for them nor by satellites as it is too low for them. Rocket-borne experiments can be carried out but the data thus obtained would be of very short duration. Thus, the only effective technique left to study is through radio wave propagation. Propagation of radio waves through a medium is dependent on its properties. Presence of ions in a medium changes the dielectric constant and conductivity of that medium and

S. Chakraborty (✉)
S. N. Bose National Centre for Basic Sciences, Salt Lake, Kolkata, WB, India

© Springer International Publishing AG, part of Springer Nature 2018

B. Mukhopadhyay, S. Sasmal (eds.), *Exploring the Universe: From Near Space to Extra-Galactic*, Astrophysics and Space Science Proceedings 53,
https://doi.org/10.1007/978-3-319-94607-8_42

influences the propagation of radio waves through it. The ionosphere imposes different effects on the radio waves depending on their frequencies. Very Low Frequency (VLF) radio waves (3–30 kHz) propagate through the Earth-ionosphere waveguide (EIWG) by suffering multiple reflections from the lower ionospheric layer (D-layer during daytime and E-layer at night). They carry information of any anomalies in these layers and thus serve as useful experimental tools in probing the ionosphere. There are several antenna and receiver systems based on this working principle to monitor the lower ionosphere, such as, VLF receivers AWESOME, SoftPAL, UltraMSK, etc. There are some other ground-based techniques too for monitoring the upper ionosphere such as the Ionosonde, Digisonde, GPS receivers, etc. Among the space-based instruments lie several satellites installed in space by agencies like NASA, NOAA, CNES that monitor the ionosphere globally. Different useful parameters such as particle count in the radiation belts, columnar and total electron density, and other atmospheric parameters like measure of Outgoing Longwave Radiation (OLR), Surface Latent Heat (SLH), surface temperature, etc. can be derived from the procured data. With this basic framework in mind, in the scope of this present article, we will discuss how this particular area of understanding the lower ionosphere using both ground-based and space-based instruments evolved over the ages and what are their future aspects.

## 2 Observational Signatures of Ionospheric Irregularities: A Brief Review

The discovery of the existence of an ionized medium in the Earth's atmosphere dates back to 1839 when Gauss first speculated that the upper atmosphere might contain ionized medium. Marconi, in 1901 succeeded in sending wireless signals from Cornwall to Newfoundland round the curved surface of the Atlantic and in the very next year, Kenelly and Heaviside almost simultaneously postulated that Marconi's signal was propagated over the Atlantic by reflection from an ionized medium in the upper atmosphere. In 1926, Robert Watson-Watt first coined the term "ionosphere" and in the next year, its existence was confirmed by Appleton by sending continuous signals upwards and receiving echoes.

### *2.1 Ground-Based Observations of Lower Ionospheric Irregularities*

As discussed earlier, monitoring the received VLF signal amplitude/phase over a chosen propagation path between a pair of transmitter and receiver is a tool for studying the lower ionospheric response to certain irregularities. Now, such irregularities can be classified into extra-terrestrial/nonlocal ones and terrestrial/local

ones. Solar flares, solar eclipses, Gamma Ray Bursts (GRBs) are some of the extra-terrestrial perturbations while lightning, volcanic eruptions, earthquakes are some terrestrial perturbations.

### 2.1.1 Irregularities Due to Extra-Terrestrial/Non-local Events

1. **Solar eclipse effects on the lower ionosphere**
   Solar eclipses occur when the Moon comes in between the Sun and the Earth, thereby blocking the solar rays for a defined period of time over definite places on the Earth. Such events are beneficial to study because their time of occurrences are known beforehand and thus we can equip ourselves accordingly. The first ever effect of solar eclipse at VLF was reported in [5] during a partial eclipse in 1949 for the path GBR (Rugby, England) to Cambridge. The path under study experienced about 30% solar obscuration and the resulting phase change in the received signal was recorded to be 35° [5]. The next evidence of the effects of solar eclipse was reported during the total solar eclipse of October 23, 1976. VLF signals at frequencies 13.6 and 22.3 kHz from Omega Reunion, Omega, Japan and NWC were monitored at Melbourne and the effective time constant of ionospheric response was found to be $4.5 \pm 1.5$ min and independent of the reflection height. Next, the eclipse of February 26, 1979 was studied over the path Fort Collins, Colorado to Calgary, Alberta, Canada, having a path length of 1.3 mm using the 60 kHz WWVB transmitter [7]. Maximum amplitude change of 0.2 dB and maximum phase variation of 36° was observed and the increment in reflection height was estimated to be 2 km [18].
   During the total solar eclipse on August 11, 1999, amplitudes and phases of VLF signals were recorded from four transmitters having frequencies in the range 16–24 kHz at five receiving stations in Europe and significant variations in phase and amplitude were reported for almost 17 paths. The path lengths varied abruptly, ranging from 90 to 14,510 km, but most of the paths were $<2000$ km [18]. Although the path length was highly variable, typical changes observed in recorded signal amplitude and phase were $\sim 3$ dB and 50° respectively. The recorded changes were modeled using Long Wavelength Propagation Capability (LWPC) code and the changes in reflection height $h'$ and steepness parameter $\beta$ were obtained to be 8 km and 0.07 $km^{-1}$ respectively.
   During the total solar eclipse that took place in the Indian subcontinent on July 22, 2009, Indian Centre for Space Physics (ICSP) conducted a week long campaign under the leadership of Prof. Sandip K. Chakrabarti to collect VLF data before, during and after the eclipse from all over India and even abroad. VLF data were collected from both VTX (18.2 kHz) and NWC (19.8 kHz) but special emphasis was given to VTX because of its geographic location [13]. Both positive and negative deviations in the received signal amplitude was observed and [40] tried to numerically understand such signal modulations using LWPC code. It was found that an ionospheric reflection height change of 4 km was sufficient to explain the observations and it was also concluded that the negative

and positive shifts are due to constructive and destructive interferences between the sky wave and the ground wave. Later in 2015, [41] detected the generation of Atmospheric Gravity Waves (AGWs) at ionospheric altitudes using wavelet analysis method having periods of the order of few minutes to hours at the time of the maximum solar obscuration. It was for the first time that AGWs were detected using VLF technique. In the very next year, [15] theoretically reproduced the positive and negative deviations in the received signal amplitude using an obscuration function and the D region ion chemistry model. In the previous attempts, as those by Clilverd et al. [18] and Pal et al. [40], conclusions were drawn empirically based on observations, but this was for the first time that the VLF signal modulations during a solar eclipse were reproduced from a pure theoretical approach. In Fig. 1, we have shown the VLF amplitude deviation for the places (a) Kolkata and (b) Malda as obtained from both observation (dotted curve) and modeling (solid curve). We can see good agreement between the model outputs and the observation [15].

Most recently, a total solar eclipse took place in North America on August 21, 2017. Data were recorded by a number of receivers. Out of them two receiving stations YADA (McBain) and K5TD (Tulsa) procured good quality signal. A solar flare of class C0.3 happened during the eclipse. The signal at Tulsa was modulated due to the flare but that at Yada remained undeviated as it was inside the totality belt and could not experience the flare. Chakrabarti et al. (2018) numerically reproduced the signal variations at both the stations using Waits two-component D-region ionospheric model and LWPC code. The electron density as calculated was also found to match the true ionospheric condition quite satisfactorily.

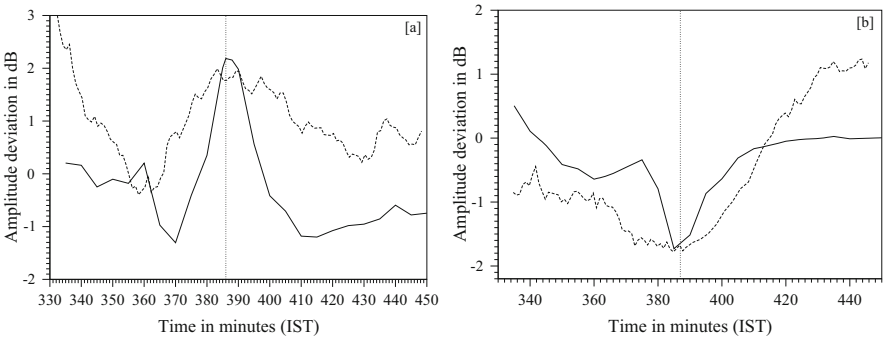



**Fig. 1** VLF amplitude deviation obtained by subtracting the eclipse day data from normal day data for (**a**) Kolkata and (**b**) Malda. Along x axis, we plot the time (IST) in minutes and along y axis, we plot the amplitude deviation in dB. The solid curve is obtained from simulation whereas the dashed curve is from observation. The vertical dotted line is the time of maximum solar obscuration [15]

2. **Effects of solar flare on the lower ionosphere**
   A solar flare is a sudden, rapid and intense enhancement in the Sun's brightness (especially in X-rays and soft gamma-rays) that occurs when the magnetic energy built up in the Sun's corona is released suddenly. The ionospheric disturbances associated with solar flares are called the Sudden Ionospheric Disturbances (SIDs) or the ionospheric solar flare effects [19] which affect the global radio wave communication abruptly.
   The solar flare effects on the ionosphere were recorded by the Absolute Phase and Amplitude Logger (AbsPAL) during the summer months of 2004–2007. The observed VLF signal amplitude and phase perturbations were simulated using the LWPC code and by varying the ionospheric parameters $h'$ and $\beta$. The altitude profile of electron density was also reconstructed for the entire flare duration and good agreement with the observed values were obtained. The response of the lower ionosphere to five different class of solar flares occurring on a single day was studied in [42]. The flares considered were of classes C2.04, C4.03, C8.57, C4.26 and M6.61. A theoretical model using a three step approach was developed for the study. The steps are (1) GEANT4 Monte Carlo simulation for ionization rate estimation, (2) GPI-scheme of ionospheric chemistry analysis and finally (3) LWPC modeling of subionospheric VLF signal propagation. The model was successful in reproducing the ionospheric response to the solar flares and it was concluded that as long as the electron densities produced by the X-rays from the flares dominate over the ambient electron densities due to regular ionization sources, such as the ultraviolet, Lyman-$\alpha$ photons, etc., the model should follow observed variations in the VLF data [42]. Basak et al. [2] examined the solar zenith angle effect on D-region ionosphere during flares. They monitored solar flare effects on the NWC (19.8 kHz) signal during January–September, 2011 and used the LWPC technique to simulate the data. They obtained a delay in the occurrence of peak of VLF amplitude after the X-ray peak of each flare and this delay depends on the class of the solar flare.
3. **Gamma Ray Burst (GRB) and the ionosphere**
   Gamma Ray Bursts (GRBs) are the most energetic events in the Universe that happen when a rapidly rotating, high mass star collapses to form a neutron star, quark star or black hole releasing huge amount of energy as gamma rays. These gamma rays interact with the upper atmosphere and the ionosphere and this excess ionization modulates the radio signal propagation through it. The effect of GRBs on the ionosphere was first detected on August 1, 1983 at the Palmer receiving station in Antarctica [22]. Some other significant events studied are the SGR $1900 + 14$ that occurred on August 27, 1998 at 10:20, X-ray transient XRF020427, GRB030329 ([49]; GCN-2176) and the mega hard x-ray/$\gamma$-ray flare from SGR1806–20 on December 27, 2004 at 21:30:26 UT. Indian Centre for Space Physics (ICSP) was the first to detect the signatures of GRB on VLF data from Kolkata/India [12]. The event monitored was a strong burst of SGR $J1550 - 5418$ that took place on January 22, 2009 at 00:53:52 UT. For more details, readers are requested to go through the article written by Sushanta K. Mondal.

### 2.1.2 Irregularities Due to Terrestrial/Local Events

1. **History of lightning-induced electron precipitation (LEP) research**
   It was in the early twentieth century that perturbations of VLF transmitter amplitude and phase were reported soon after the start of their use. Most authors correlated such perturbations with geomagnetic storms for several decades [6, 45] but numerous other authors [3, 35] suggested that such anomalies were generated due to the sudden local enhancements of nighttime D-region ionospheric parameters caused by the precipitation of radiation belt electrons having energies $>$ 40 keV. It was in 1973 that a direct correlation between VLF amplitude perturbations and lightning-induced electron precipitation events was presented by Helliwell et al. [28]. He suggested that cyclotron resonance between the whistler mode wave and the trapped radiation belt electrons was the main phenomenon triggering such events. Later in 1979, Kaiser reported phase perturbations that suggested a counterstreaming interaction between the radiation belt electrons and the whistler mode wave [36].
   Using a single-mode propagation theory for the VLF signal amplitude and phase perturbations, [30–32] inferred the precipitation flux to be $10^{-4}$–$10^{-2}$ erg $cm^{-2}\,s^{-1}$. Inan et al. [31] suggested that for same level of perturbations to be observed in the received VLF signal amplitude and phase, the ionospheric perturbation need to be $\sim$ 3 times larger for amplitude perturbation compared to phase perturbation. The first direct and extensive association between VLF perturbations and cloud-ground lightning events was provided by Inan et al. [33]. Burges and Inan [8, 9] showed that the same lightning event can result in VLF signal perturbations in both the Northern and Southern hemispheres. Dowden and Adams [20] observed that most of the LEP events resulted in positive phase change and negative amplitude change. They suggested that this is because of the fact that precipitation of additional electrons into the lower ionosphere enhanced the absorption of radio waves and reduction of reflection height, hence negative $\Delta A$. They also proposed a relation between phase change and amplitude change as: $\Delta p \approx -1/\Delta A$ so that negative amplitude change implies positive phase change. Dowden and Adams [21] also showed that the interferences in the Earth-ionosphere waveguide can result in positive and negative phase and amplitude variations.
   Indian Centre for Space Physics (ICSP) recorded signatures of such LEP events in the VLF signal amplitude and phase for both the NWC and VTX transmitters. Chakraborty et al. [14] used the LWPC code to detect the location and size of such disturbance region with respect to a chosen propagation path. It was concluded that if the perturbation region is close to the transmitter end, then it is most likely to produce maximum perturbation in the received signal amplitude/phase whereas if it is near the receiver end, it will impose almost negligible or no perturbation. It was also concluded that the amount of deviation depends on the size of the perturbation and the positive and negative deviations depend solely on its location with respect to the propagation path.

2. **History of research on seismo-ionospheric anomalies**

VLF signal anomalies due to seismo-ionospheric interaction was first reported by Gufeld and Marenko [26] during the Caucasus earthquake on December 30, 1983. They found significant anomalies in the nighttime VLF signal amplitude 2 days prior to the occurrence of the main event. Some other significant works are those by Calais and Minster [10], Afraimovich et al. [1], etc. The most reliable effect of the earthquakes on the ionosphere was presented by Hayakawa et al. [27] during the famous Kobe earthquake [27]. They used the terminator time (TT) method and found significant shift in the TTs few days before the occurrence of the quake. Molchanov and Hayakawa performed a detailed statistical study during 10 other strong earthquakes ($M > 6$) [38] and concluded from their extensive study that the effects of earthquakes on ionosphere can only be identified for crustal earthquakes and they prevail from a few days before the earthquake to few days after it. It was also concluded that generation of Atmospheric Gravity Waves (AGWs) during seismic activities is the possible reason behind such ionospheric anomalies [39]. During the great Sumatra earthquake in 2004, shifts in terminator times were reported in [11]. The VLF signal from four sets of propagation paths were studied during the Pakistan earthquake that took place on January 18, 2011 and presented in [46]. It was concluded that the proximity of a propagation path to the earthquake epicenter will result in greater anomaly in the received signal. The effect of 2011 Honshu, Japan earthquake on VLF signal was studied by Sasmal et al. [47]. Significant shifts in SRT beyond $2\sigma$ level was found to occur 2 days prior to the event. The D layer disappearance time (DLDT) was also found to exhibit unusual enhancements.

Recently, a severe earthquake took place in Nepal on May 12, 2015 with Richter scale magnitude $M = 7.3$ followed by several aftershocks, the major being on May 16 with magnitude $M = 6.7$. Indian Centre for Space Physics (ICSP) monitored the VLF signal transmitted from JJI transmitter at 22.2 kHz during the earthquake. Strong shifts in both SRT and SST were observed few days prior to the main event. The maximum increase in daylength was found to be 32 min on May 10, 2 days before the earthquake [16]. Numerical modeling using LWPC code was performed to understand the mechanism leading to such shifts in the terminator times. The path under study, namely, JJI-IERC had a high longitudinal variation and as a result, the solar illumination over the entire path was not uniform. Special attention was devoted to replicate the scenario and the ionospheric parameters, namely, the ionospheric reflection height ($h'$) and the steepness parameter ($\beta$) were varied accordingly over the entire path [16]. Later these parameters were both raised and lowered to determine under what condition the observed nightward shift in terminator times could be achieved and it was found that raising the ionosphere resulted in the observed increase in daylength. Figure 2 shows the simulated VLF signal amplitude during both SRT (left panel figure) and SST (right panel figure). It is found that raising the ionosphere created the desired nightward shift of both the terminator times [16]. The possible generation of AGWs during the earthquake was also checked and it

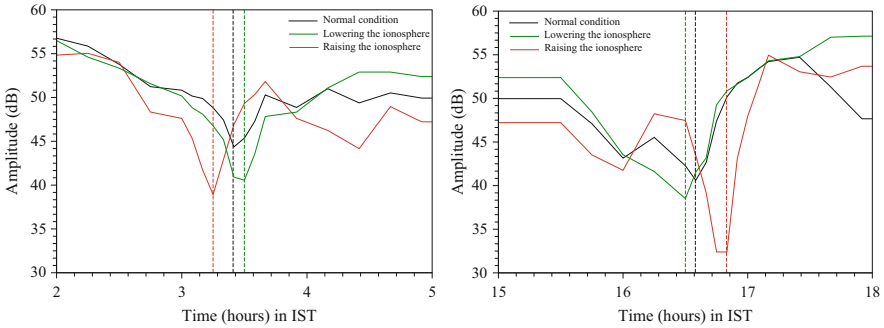



**Fig. 2** Simulated VLF signal amplitude around (left panel figure) sunrise terminator time (SRT) and (right panel figure) sunset terminator time (SST) under normal non-seismic situation (black curve: online version), lowering the ionosphere (green curve: online version) and raising the ionosphere (red curve: online version) within the EPZ (Earthquake Preparation Zone). Along x axis, we plot the time (IST) in hours and along y axis, we plot the simulated signal amplitude in dB. The three vertical dotted lines mark the corresponding terminator times [16] (Color figure online)

was found that waves with periods of about an hour was generated on May 8, four days prior to the earthquake day [17]. To check if the results got contaminated with any solar activity effects, the solar geomagnetic $Kp$ index was checked and it was found to be reasonably low. Hence it was concluded that the effects imposed on VLF signal amplitude were solely due to the earthquake on May 12 and its aftershock on May 16 [16, 17]. Another comparative study was also conducted in [24] to check the effects of location of the epicenter with respect to a VLF propagation path. One of the earthquakes was so chosen that its epicenter lies close to the transmitter end (the 2011 Honshu, Japan earthquake) while the other lies near the receiver end (the 2015 Nepal earthquake). It was found that for the earthquake near the transmitter end, the changes were more sudden but for the earthquake near the receiver end, the changes were rather gradual [24].

## *2.2 Space-Based Observations of Ionospheric Irregularities*

Space-based observations of ionospheric irregularities are rather less compared to ground observations. Yet there are several important ionospheric parameters that are derived from satellite observations. A detailed study of the high energy X-ray observations of the solar events on June 4 and 7, 1980 were performed with the Hard X-Ray Burst Spectrometer (HXRBS) on the Solar Maximum Mission (SMM) satellite. Recently, space weather forecasting, geomagnetic storm tracking and meteorology research are being conducted by the Geostationary Operational Environmental Satellite system (GOES) operated by the United States'

National Oceanic and Atmospheric Administration's National Environmental Satellite, Data, and Information Service division. GOES-12 and higher satellites have been equipped with Solar X-Ray Imager (SXI) and space environment monitoring (SEM) instruments. These instruments receive, monitor and interpret a wide range of solar-terrestrial data.

Sudden effects of lightning-induced electron precipitation (LEP) events can be observed directly by satellites [34, 54, 55]. The DEMETER (Detection of Electro-Magnetic Emissions Transmitted from Earthquake Regions) satellite was a French micro-satellite operated by CNES and devoted to the investigation of the ionospheric disturbances due to seismic and volcanic activities, but unfortunately, all the scientific operations ended on December 9, 2010. It was provided with an instrument for particle detection that measured the electron precipitation at low energies. It traversed the Earth in a sun-synchronous orbit at a height of 700 km and could see drift loss cone electrons through a majority of its orbits. With the data from DEMETER satellite and lightning location information from World-wide Lightning Location Network (WWLLN), the role of lightning in electron precipitation was examined. This satellite data was also used in studying the ionospheric response to the annular solar eclipse that took place on January 15, 2010 in [37]. In this paper, data measured by the ISL (Instrument Sonde de Langmuir) and IAP (Instrument Analyseur de Plasma) instruments on board the DEMETER satellite were used during the eclipse period over the low latitude ($\pm 40^\circ$) Indian ocean area. The maximum decrease in the electron density was found to be 35% and that in the ion density to be 40% from the reference orbits at the altitude of the satellite, i.e., 660 km [37]. The electron and ion temperatures were found to decrease by $\sim$200–300 K at the same altitude.

Recently, during the major Nepal earthquake on May 12, 2015, Outgoing Longwave Radiation (OLR) data obtained from NOAA satellites was analyzed during the earthquake days and presented in [17]. The data was downloaded from NOAA website with a spatial coverage of $6^\circ \times 7^\circ$ from 25°N to 31°N latitudes and 82°E to 89°E longitudes and a temporal extent of 45 days from April 16, 2015 to May 30, 2015. *'Eddy field calculation mean'* was calculated and singularities in the daily Eddy field around the earthquake epicenter was found to be prominent on May 10, just 2 days prior to the main event and to fade away after the main shock. Solar geomagnetic activity was also found to be reasonably low during the period of analysis and thus such intensification of the Eddy field just 2 days prior to the main event and its fading away after the event was attributed to nothing other than the earthquake on May 12 [17]. Figure 3 shows the daily Eddy field as calculated around the earthquake epicenter during the days May 1 to May 15, 2015. Intensification of the Eddy field around the epicenter on May 10, just 2 days prior to the main shock can be seen [17].

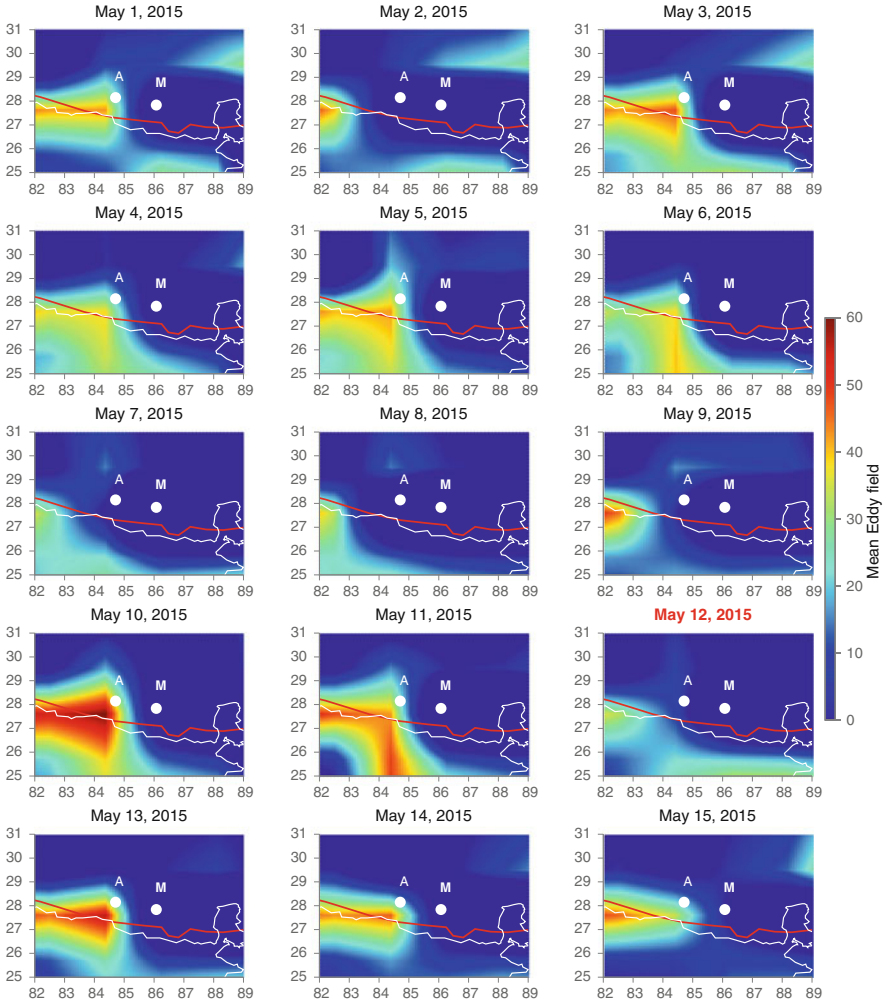



**Fig. 3** Daily Eddy field around the earthquake epicenters from May 1, 2015 to May 15, 2015 with a spatial extent from 25°N to 31°N and 82°E to 89°E. Longitudes are plotted along x axis and latitudes along y axis and the earthquake epicenters are denoted by white filled circles, A for April 25 EQ and M for May 12 EQ. The colorbar runs from values 0–60 which indicates the intensity of the mean Eddy field [17] (Color figure online)

## 3 A Brief Review on Ionospheric Models for Radio Wave Propagation

For the study of radio wave propagation through a medium, ample knowledge about the properties of the medium is required. For sub-ionospheric radio wave propagation, the most important factor is the electron density. Such studies require

different parameters depending upon their specific applications, such as, density maps for characteristic points, like the F-region peak electron density; or the whole electron density profiles; or the electron content along the propagation path; or a complete three-dimensional electron density map of the entire propagation medium [4]. An ionospheric model can be mostly of two types: Emperical model and Theoretical model. An empirical model is mostly based on observational data and uses mathematical functions to represent the characteristic variations in the data while a theoretical model considers the production, loss and transport of electrons and ions and determine the electron density by bringing a balance between these processes. Mostly, users use hybrid models, i.e., use both empirical and theoretical models [4].

## *3.1 Empirical Models*

Empirical models are based on statistical analysis of observed data. They are mostly models representing monthly or seasonal average conditions. In majority of cases, medians are calculated to check the variability of the data with respect to it. For ionospheric data, the most deviations can be seen in the F-region, with variations of upto 20–40% under quite conditions and even higher under perturbed state. Empirical models have the advantage of representing the ionosphere based on true observations rather than using assumptions of a developing theory. But the major disadvantage of it is its bias in terms of time and location. Historically, the initial empirical ionospheric models were the global maps for characteristic ionospheric parameters [4]. The most important empirical models for ionospheric electron-density profile are enlisted in Table 1.

## *3.2 Theoretical Models*

Theoretical models use numerical schemes to solve equations defining the true ionospheric physical processes using proper boundary conditions. Over the last few decades, successful modifications of self-consistent ionospheric models to ionospheric-thermospheric and to ionospheric-thermospheric-plasmaspheric models [50, 51] have been made in an attempt to reduce the dependency on empirical models for model input parameters [4]. The accuracy of such models depend on a number of factors, like, the correctness of the representation of the considered physical processes, the accuracy of the numerical scheme adapted, the applied boundary conditions, the implemented cross-sections and the input parameters. Also, they need good amount of computation time but instead of all these, they are excellent tools in understanding the real physical processes going on in the ionosphere. There are numerous theoretical models that are used widely such as the *Thermosphere-Ionosphere-Mesosphere-Electrodynamics General Circulation*

**Table 1** Empirical models for ionospheric electron-density profile (adapted from [4])

| Parameter | Region | Data base | Characteristics |
|---|---|---|---|
| ITS-79 | Below F2 | Ionosonde | Parabolic E and F2 |
| RAL | Below F2 | Ionosonde | Parabolic and linear segments, CCIR peaks |
| IONCAP | Below F2 | Ionosonde | Parabolic, linear, exp.segments, CCIR peaks |
| Rush-Miller | Full profile | Ionosonde | Chapman, parabolic, hyperbolic secant, CCIR peaks |
| Bent | Full profile | Ionosonde, satellite (TS, In situ) | Parabolic and exponential segments, CCIR peaks |
| ICED | Full profile | Ionosonde, satellite (TS) | Chapman profiles URSI-88 $foF2$ model |
| RIBG | Full profile | Composed of several models | ICED, Bent, Gallagher et al. (1988) models |
| IRI | Full profile | Ionosonde, Inc. scatter radar, satellites (TS, in situ), Absorp. Rockets | Recommended by URSI and COSPAR for international use ITU-R model |
| DGR | Full profile | Ionosonde | Epstein functions COST European model |
| NeQuick, COST prof, NeUoGplas | Full Profile and Plasmasphere | Ionosonde and VTEC | Epstein functions and plasmaspheric models COST European, ESA, and ITU-R models |
| Chiu | Full Profile | Ionosonde | Chapman layers, phenomenological peak model |
| Koehnlein | Full Profile | Inc.scatter radar, satellites (in situ) | Spherical harmonics |

*Model (TIME-GCM)* [52], evolved from the TGCM and TIGCM by progressively including a self-consistent formulation for the ionosphere, the mesosphere, and the electrodynamics of this region [4]; the *Time Dependent Ionospheric Model (TDIM)* developed in the mid-seventies [50] that calculates the densities of ions like $He^+$, $O^+$, $NO^+$, $N_2^+$, $N^+$, $O_2^+$, and the electron and ion temperatures over a geomagnetic region extending from 90 to 1000 km; the *Field Line Interhemispheric Plasma (FLIP) model* that solves the ion continuity and momentum, the ion and electron energy, and the photoelectron equations along entire magnetic-flux tubes; the *Global Theoretical Ionospheric Model (GTIM)* that calculates densities of ions like $O^+$, $H^+$, and $He^+$ along magnetic-field lines from 90 to 1600 km; and the *Coupled Thermosphere-Ionosphere Model (CTIM)* [23] that computes ion-densities like that of $H^+$, $He^+$, $N_2^+$, $O_2^+$, $NO^+$ and $O^+$ from 100 to 10,000 km [4]. Apart from these well-renowned theoretical models, there are some other models like the *IZMIRAN theoretical model* that is used to study the thermal structure of the ionosphere [44];

the *"Sami2 is Another Model of the Ionosphere" (SAMI2)* model developed by Huba et al. [29] that calculates the ion temperatures like $O^+$, $H^+$, and $He^+$ and includes the $E \times B$ drift of a flux tube; and the *Sodankkyl Ion Chemistry Model (SIC) model* that computes altitude profiles of 36 positive and 19 negative ions in the altitude range of 50–100 km [53].

A D-region ion-chemistry model was developed in [42] and later applied to study the ionospheric response to several perturbing phenomena including solar eclipses, solar flares and long to very long path propagation [15, 43, 48]. The D-region of the ionosphere is the most complex region as it contains different ion-species and hence to reduce complexity, this model considers the ionosphere to be comprised of only four types of ion-species, namely, the positive ions, the positive cluster ions, the negative ions and the electrons following the prescription as proposed in the Glukov-Pasko-Inan (GPI) scheme [25]. It then numerically solves the equations governing the rate of evolution of these ion-species using Monte Carlo simulation to compute the altitude profile of the electron density. This model is most effective at lower altitudes (60–90 km).

## 4 Present Scenario and Future Prospects

Presently, the main focus of studying the ionosphere has shifted to understanding the dynamics of the middle and upper ionospheric layers. Several phenomena such as the generation of plasma bubbles, scintillations in the radio signals, response of the ionosphere to space weather are attracting junior researchers in this field. Also as mentioned in the previous section, although numerous theoretical and empirical models are present in literature to understand the physical processes going on in the ionosphere, all of them present piece-wise discrete pictures. So there is a general urge to develop a model that can deliver a single unified picture of the ionosphere as a whole. Rigorous studies, both from observational point of view and theoretical point of view are going on to fulfill that aim. With better technologies being developed and better brains being involved, we hope to achieve that goal in near future.

**Acknowledgements** I would like to acknowledge Prof. Sandip K. Chakrabarti for introducing me to the subject. His continuous showering of new ideas helped me enrich my knowledge and potential. He was my guide during by Ph.D Thesis and I wish he remains my guide throughout my entire academic career. I could not have demanded having a better advisor and mentor besides me than him. I am also thankful to the editors for providing me a chance to contribute to this festschrift.

## References


1. Afraimovich, E.L., Kosogorov, E.A., Lesyuta, O.S., Ushakov, I.I., Yakovets, A.F.: Ann. Geophys. **19**, 723–731 (2001)
2. Basak, T., Chakrabarti, S.K.: Astrophys. Space Sci. **348**, 315–326 (2013)
3. Belrose, J.S., Thomas, L.: J. Atmos. Terr. Phys. **30**, 1397–1400 (1968)
4. Bilitza, D.: Ionospheric models for radio propagation studies. In: Stone, W.R. (ed.) The Review of Radio Science 1999–2002: Advances in 3G Mobile Communications, Cryptography and Computer Security, EMC for Integrated Circuits, Remote Sensing, Radio Astronomy and More, pp. 625–680. IEEE Press, Piscataway (2014)
5. Bracewell, R.N.: J. Atmos. Terr. Phys. **2**, 226–235 (1952)
6. Bracewell, R.N., Budden, K.G., Ratcliffe, J.A., Straker, J.W., Weekes, K.: Proc. Inst. Electr. Eng. Part 3 **98**, 221 (1951)
7. Buckmaster, H.A., Hansen, C.H.: J. Atmos. Terr. Phys. **48**, 393–397 (1986)
8. Burgess, W.C., Inan, U.S.: Geophys. Res. Lett. **17**(3), 259–262 (1990)
9. Burgess, W.C., Inan, U.S.: J. Geophys. Res. **98**(A9), 15643–15665 (1993)
10. Calais, E., Minster, J.B.: Geophys. Res. Lett. **22**, 1045–1048 (1994)
11. Chakrabarti, S.K., Saha,M., Khan, R.,Mandal, S., Acharyya, K., Saha, R., Indian J. Radio and Space Phys. **34**, 314–317 (2005)
12. Chakrabarti, S.K., Mandal, S.K., Sasmal, S., Bhowmick, D., Choudhury, A.K., Patra N.N.: Ind. Journ. Phys. **84**, 1461–1466 (2010)
13. Chakrabarti, S.K., Mondal, S.K., Sasmal, S., Pal, S., Basak, T., Chakrabarti, S., Bhoumik, D., Ray, S., Maji, S., Nandi, A., Yadav, V.K., Kotoch, T.B., Khadka, B., Giri, K., Garain, S.K., Choudhury, A.K., Patra, N., Iqbal, N.: Ind. J. Phys. **86**(5), 323–334 (2012)
14. Chakraborty, S., Pal, S., Chakrabarti, S.K.: URSI GASS, 2014 XXXIth URSI (2014). https://doi.org/10.1109/URSIGASS.2014.6929559
15. Chakraborty, S., Palit, S., Ray, S., Chakrabarti, S.K.: Astrophys. Space Sci. (2016). https://doi.org/10.1007/s10509--016-2660--0
16. Chakraborty, S., Sasmal, S., Basak, T., Ghosh, S., Palit, S., Chakrabarti, S.K., Ray, S.: Adv. in Space Res. **60** (2017). https://doi.org/10.1016/j.asr.2017.06.031
17. Chakraborty, S., Sasmal, S., Chakrabarti, S.K., Bhattacharya, A.: J. Geodynamics **113**, 43–51 (2018)
18. Clilverd, M.A., Rodger, C.J., Thomson, N.R., Lichtenberger, J., Steinbach, P., Cannon, P., Angling, M.J.: Rad. Sc., **36**, 773–788 (2001)
19. Dellinger, J.H.: Proc. IRE **25**, 1253 (1937)
20. Dowden, R.L., Adams, C.D.D.: J. Geophys. Res. **93**, 11543–15550 (1988)
21. Dowden, R.L., Adams, C.D.D.: J. Geophys. Res. **94**, 497–503 (1989)
22. Fishman, G.J., Inan, U.S.: Nature **331**, 418 (1988)
23. Fuller-Rowell, T.J., Rees, D., Quegan, S., Moffett, R.J., Codrescu, M.V., Millward, G.H.: Solar-Terrestrial Energy Program (STEP), Scientific Committee on Solar Terrestrial Physics (SCOSTEP), pp. 217–239 (1996)
24. Ghosh, S., Chakraborty, S., Sasmal, S., Basak, T., Chakrabarti, S.K.: J. Geodynamics (communicated)
25. Glukhov, V., Pasko, V., Inan, U.: J. Geophys. Res. **97**(16), 951–979 (1992)
26. Gufeld, I.L., Roznoi, A.A., Tyumentsev, S.N., Sherstyuk, S.V., Yampolskiy, V.S.: Phys. Solid Earth. **3**, 267–270 (1992)
27. Hayakawa, M., Molchanov, O.A., Ondoh, T., Kawai, E.: J. Comm. Res. Lab. Tokyo. **43**, 169–180 (1996)
28. Helliwell, R.A., Katsufrakis, J.P., Trimpi, M.: J. Geophys. Res. **78(22)**, 4679–4688 (1973)
29. Huba, J.D., Joyce, G., Fedder, J.A.: J. Geophys. Res. **105**(A10), 23035–23053 (2000)
30. Inan, U.S., Carpenter, D.L.: J. Geophys. Res. **91**(A3), 3106–3116 (1986)
31. Inan, U.S., Carpenter, D.L.: J. Geophys. Res. **92**(A4), 3293–3303 (1987)

32. Inan, U.S., Carpenter, D.L., Helliwell, R.A., Katsufrakis, J.P.: J. Geophys. Res. **90**(A8), 7457–7469 (1985)
33. Inan, U.S., Burgess, W.C., Wolf, T.G., Shafer, D.C.: Geophys. Res. Lett. **15(2)**, 172–175 (1988)
34. Inan, U.S., Piddyachiy, D., Peter, W.B., Sauvaud, J.A., Parrot, M., Geophys. Res. Lett. **34**(L07) (2007), https://doi.org/10.1029/2006GL029238
35. Lauter, E.A., Knuth, R.: J. Atmos. Terr. Phys. **29**, 411–417 (1967)
36. Lohrey, B., Kaiser, A.B., J. Geophys. Res. **84**(A9), 5121–5130 (1979)
37. Maji, S.K., Chakrabarti, S.K., Sanki, D., Pal, S.: J. Atmos. Sol Terr. Phys. **159**, 1–6 (2017)
38. Molchanov, O.A., Hayakawa, M.: J. Geophys. Res. **103**, 17489–17510 (1998)
39. Molchanov, O., Fedorov, E., Schekotov, A., Gordeev, E., Chebrov, V., Surkov, V., Rozhnoi, A., Andreevsky, S., Iudin, D., Yunga, S., Lutikov, A., Hayakawa, M., Biagi, P.F.: Nat. Hazards Earth Syst. Sci. **4**, 757–767 (2004)
40. Pal, S., Chakrabarti, S.K., Mondal, S.K., Adv. Space Res. **50**, 196–204 (2012)
41. Pal, S., Chakraborty, S., Chakrabarti, S.K., Adv. Space Res. **55**, 1190–1198 (2015)
42. Palit, S., Basak, T., Mondal, S.K., Pal, S., Chakrabarti, S.K.: Atmos. Chem. Phys. **13**, 9159–9168 (2013)
43. Palit, S., Ray, S., Chakrabarti, S.K.: Astrophys Space Sci (2016). https://doi.org/10.1007/s10509-016-2724-1
44. Pavlov, A.V., Abe, T., Oyama, K.I.: J. Atmos. Sol-Terr. Phys. **63**, 605–616 (2001)
45. Potemra, T.A., Rosenberg, T.J.: J. Geophys. Res. **78(10)**, 1572–1580 (1973)
46. Ray, S., Chakrabarti, S.K.: Nat. Hazards Earth Syst. Sci. **13**, 1501–1506 (2013)
47. Sasmal, S., Chakrabarti, S.K., Ray, S.: Indian J. Physics. **88**(10), 1013–1019 (2014)
48. Sasmal, S., Palit, S., Chakrabarti, S.K.: J. Geophys. Res. Space Physics **120**, 8872–8883 (2015)
49. Schnoor, P.W., Welch, D.L., Fishman, G., Price, A.: GCN 2176 (2003)
50. Schunk, R.W.: Solar-Terrestrial Energy Program (STEP), Scientific Committee on Solar Terrestrial Physics (SCOSTEP) (1996)
51. Schunk, R.W., Sojka, J.J.: Modern Ionospheric Science, Katlenburg-Lindau, FRG, European Geophysical Society, pp. 181–215 (1996)
52. Sharma, R.D., Roble, R.G.: J. Geophys. Res. **106**(A10), 21343–21350 (1995)
53. Turunen, E., Matveinen, H., Tolvanen, J., Ranta, H., Solar-Terrestrial Energy Program (STEP), Scientific Committee on Solar Terrestrial Physics (SCOSTEP), pp. 1–25 (1996)
54. Voss, H.D., Imhof, W.L., Walt, M., Mobilia, J., Gaines, E.E., Reagan, J.B., Inan, U.S., Helliwell, R.A., Carpenter, D.L., Katsufrakis, J.P.: Nature **312**, 740–742 (1984)
55. Voss, H.D., Walt, M., Imhof, W.L., Mobilia, J., Inan, U.S.: J. Geophys. Res. **103**, 11725–11744 (1998)

# Quantitative Modeling of Lower Ionospheric Response Due to Solar X-ray Flare: A Propagating Radio Wave Simulation Approach




**Tamal Basak**

**Abstract** The ionosphere is an expansive natural detector and it characteristically reacts to ionizing influences coming from sun and other extraterrestrial energetic sources. In this article, first we give a brief review of earlier works performed specifically on Very Low Frequency (VLF) radio signal interaction with D-region ionosphere. Those are mainly related to the D-region 'response time delay' as experienced by VLF signal ($\triangle t$), effective recombination coefficient ($\alpha_{eff}$) and its connection with the D-region electron density ($N_e$) and other essential parameters during X-ray solar flares. Further, we present the measurement techniques and the observed results regarding the same time delay ($\triangle t$) experienced by VLF signal with respect to the X-ray flux variation of solar flares. Several research groups have developed many lower ionospheric models based on theoretical and experimental results to deal with those above mentioned quantities. We follow a rather simplified model proposed by J. Wait for D-region through the Long Wave Propagation Capability (LWPC) numerical code to estimate the $N_e$ using flare induced amplitude-perturbation ($\triangle A$). Now, we use this $\triangle t$ and $N_e$-profile for estimation of the effective recombination coefficient ($\alpha_{eff}$). Lastly, we analyse the results and conclude.

## 1 Introduction

Solar flare was discovered by Richard Carrington in 1859. They form because of a sudden outbreak of large amount of magnetic energy through the solar-photosphere region. The irradiation emerged during the flares are generally spreaded over the entire range of the electromagnetic spectrum, i.e., from $\gamma$-ray (and X-ray) emissions to radio frequency emissions. The net amount of energy released during a typical solar flare is $\sim 10^{20}$ J.

T. Basak (✉)
Amity University, Rajarhat, New Town, Kolkata, India

© Springer International Publishing AG, part of Springer Nature 2018

B. Mukhopadhyay, S. Sasmal (eds.), *Exploring the Universe: From Near Space to Extra-Galactic*, Astrophysics and Space Science Proceedings 53,
https://doi.org/10.1007/978-3-319-94607-8_43

The flare energy emerging zones on the solar ball are concentrated primarily around its equatorial region due to the dynamic solar magnetic field orientations. The brighter coronal loops are situated near the stronger magnetic field region and are known as the 'active regions'. In general, the sunspots are neighbouring to those active regions. Hence, the solar flares are originated over there. The solar flare occurrence rate is closely associated to the '11-year solar cycle'. There are three phases of a solar flare. (1) The first phase is known as the 'precursor', when a sudden inception of energy burst takes place. Henceforth, some soft X-rays are emitted from the corona. (2) The second phase is the 'impulsive' phase, where streams of electrons and protons get energized. The hard X-rays and $\gamma$-rays are emitted in this stage, and in (3) the final 'decay' stage, the soft X-ray part starts to decay slowly.

The X-ray and Ultra Violet (UV) radiation components of solar spectrum affect the lower ionospheric D-region. Consequently, it perturbs the sub-ionospheric radio communication [5–7, 23, 27, 29, 38]. So, using the sub-ionospherically propagated Very Low Frequency (VLF) radio signal analysis, the characteristic ionospheric modifications can be mapped. This indirect research of the lower ionosphere, especially during solar flares is the main intent of this article.

The solar flares are classified, based on their peak-time X-ray flux in the following way: (1) A-class ($< 10^{-7}\,\mathrm{Wm}^{-2}$) (2) B-class ($10^{-7}$ to $10^{-6}\,\mathrm{Wm}^{-2}$) (3) C-class ($10^{-6}$ to $10^{-5}\,\mathrm{Wm}^{-2}$) (4) M-class ($10^{-5}$ to $10^{-4}\,\mathrm{Wm}^{-2}$) (5) X-class ($> 10^{-4}\,\mathrm{Wm}^{-2}$). The soft X-ray data taken in this work are recorded by Geostationary Operational Environmental Satellite-15 (GOES-15) (www.swpc.noaa.gov). The sub-ionospherically propagated VLF signal (under the influence of the flare induced ionosphere) closely follows the typical X-ray nature of the flare [3, 4, 38] (Fig. 1). Typically, a minimum C-class flare is detectable by VLF signal.

An extensive research on the modifications of the D-region ionosphere especially during solar flares using the radio signal as a tool already exists in the literature. Among them some fundamental theoretical and observational works on ionospheric changes were done by Wait [33], Wait and Spies [34], Mitra [15], Thomson and Clilverd [29], Thomson et al. [30] etc. A few of those aspects particularly which has already been closely followed, proposed and discussed by Basak [3] and Basak and Chakrabarti [4] are discussed in the later sections.

## 2 Solar Flare Impacts on D-Region Ionosphere

### *2.1 Ion-Recombination Mechanisms During Flares*

Some of the pioneering works on the recombination of ionospheric free electrons (and ions) in D-region were made by Appleton [1], Mitra and Jones [17], Mitra [15] etc. In a number of research works using the electron continuity theory, the (1) dissociative recombination coefficient ($\alpha_D$), (2) mutual ionic recombination coefficient ($\alpha_i$), (3) electron to negative ion ratio ($\lambda$) etc., which are the prime

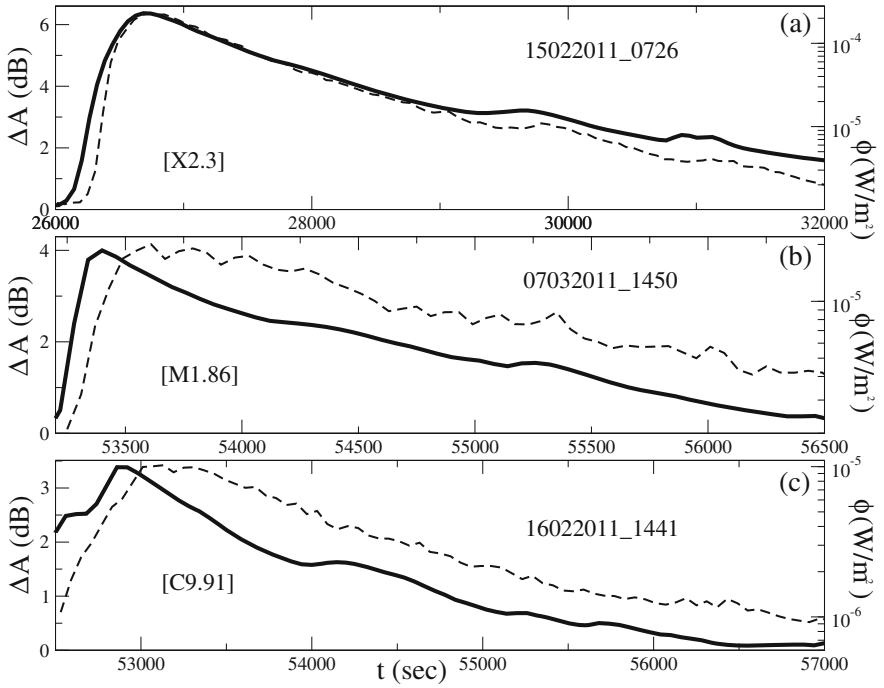



**Fig. 1** Examples of (**a**) X-class (**b**) M-class and (**c**) C-class solar X-ray flares (soft components) each as recorded by GOES-15 satellite (solid lines) along with corresponding VLF signal amplitude deviations ($\triangle A$) (dashed lines). Date and time (ddmmyyyy_hhmm) are marked in respective panels (adopted from [3, 4])

characterizing D-region parameters, were estimated and modelled [25, 35, 36]. Mitra [14] reported some alternative methods to obtain the recombination coefficients including the ionospheric height profile under different ionospheric conditions, e.g., (1) diurnal asymmetry method, (2) eclipse method and (3) solar decay curve method. The values of $\alpha_i$ and $\alpha_D$ obtained by using these methods resemble the direct measurements with a reasonable degree of accuracy. Whitten et al. [37], Parthasarathy and Rai [22] and Gledhill [10] proposed the empirical expressions keeping consistency with the physical models for D-region 'effective recombination coefficient ($\alpha_{eff}$)' (contains the proportionate contributions from (1) $\alpha_i$, (2) $\alpha_D$, (3) $\lambda$ and other dust capture coefficients which appear in the aerosol theory). Wagner and Thome [32] gave a different method altogether, namely, the 'Thomson Scatter Experimental Technique (TSET)' to physically simulate the electron density and $\alpha_{eff}$ during solar flares, relative to pre-flare condition at E-region.

Appleton [1] proposed the theory about the connection among the $N_e$, $\alpha_{eff}$ and the lower ionospheric response 'time delay ($\triangle t$)' to photo-ionization chemical reactions. The $\triangle t$ appears due to the 'collective inertial properties' having contributions

from each of those chemical reaction time scales of the D-region ionosphere. It can be said that, this $\triangle t$ is characteristically indifferent to the *sluggishness* Valnicek and Ranzinger [31] [1] and *relaxation time* [15]. Pozo et al. [26] computed the $\alpha_{eff}$ for night-time auroral ionosphere using EISCAT radar data and showed clearly that, $\alpha_{eff}$ is greatly dropped down with the increase in particle precipitation flux at higher energy. Same EISCAT radar observation was also used by Osepian et al. [21] to numerically model the $\alpha_{eff}$ during solar proton events (SPE). To take a comparative look on the experimental measurements of $\alpha_{eff}$ with the established theoretical formulations, Friedrich et al. [9] incorporated the temperature and pressure profiles of lower ionosphere in $\alpha_{eff}$ expression empirically. Using two same goal oriented yet different approaches of D-region electron-continuity theory, (1) Zigman et al. [38], Basak and Chakrabarti [4] etc. calculated $\alpha_{eff}$ during the flare peak (Fig. 4) and (2) Nina et al. [20] during the decaying phase of a solar flare.

## 2.2 Ion-Chemistry Models for D-Region

Chemical scenario in the D-region is complex. The out and out modeling of such diverse types of positive and negative ions as well as hydrated cluster ions, and several chemical reactions taking place among them is not easy and needs enormous theoretical framework. So it is effective and justified to choose among them the most chemically abundant ions and the commanding chemical reactions in presence of solar radiations. A number of them are there in the literature. A short discussion about them is as follows.

### 2.2.1 Mitra and Rowe 6-Ions+Electron Chemical Model

To deal with the D-region complex chemistry at lower heights (∼70 km) with simple and justified manner, Mitra and Rowe [18] proposed simplified model having six most abundant ions (including a few negative type ions) and free electron. After the thorough study of all the possible reaction channels among those components, Mitra and Rowe [18] concluded that at lower heights (∼70 km), the variation of positive and hydrated ions are less even during the strong solar flare induced ionization. In the D-region above 74–75 km, the negative ions are effectively not present. There, the main ion contents are $NO^+$ and $H_2O_5^+$. At 75–80 km height, the creation of $O_2^+$ is less than $NO^+$ under quiet and flare X-ray conditions [18] Mitra and Rowe [19]. Clustering of $O_2^+$ and $O_4^+$ are possible only during direct photo-ionization process under flare conditions. Thus, under X-ray flare conditions [$H_2O$] and [O] vary reasonably.

### 2.2.2 Glukhov-Pasco-Inan (GPI) Model

Another comprehensive model is Glukhov-Pasco-Inan (GPI) chemical model [11]. Here, three types of ion species are taken, namely, $N^+$, $N^-$, $N_x^+$ and $N_e$. It is a simplified one for the evolution of the D-region and at 65–70 km heights, this works efficiently [23, 24]. As an extended application of this model, [13] used this at an atmospheric height of 50 km, as they incorporated $N_x^-$ ions also to the model.

Apart from them, there are many other models in the literature, namely, (a) Low latitude ionosphere-plasmasphere model, (b) Global theoretical ionospheric model, (c) Coupled thermosphere-ionosphere model, (d) Mid-latitude ionospheric model (d) Sodankyla Ion Chemistry (SIC) and so on [28]. Brief discussions about them are included in [3].

## 3 Lower Ionospheric Response 'Time Delay ($\Delta t$)' During Flares

Due to the 'inertial' properties of the lower ionosphere, the response to the various photo-ionization driven reactions are not really instantaneous. Appleton [1] termed it as the 'sluggishness' of the lower ionosphere. Similar work on the ionospheric relaxation time was reported by Valnicek and Ranzinger [31]. Zigman et al. [38] estimated the time delay of VLF signal with respect to X-ray response of the solar flare and called it as the 'VLF amplitude time delay ($\triangle t$)'. Basak and Chakrabarti [4] defined it as the difference between the $APT$ and $FPT$, where, the $APT$ is the 'Amplitude Peak Time' of VLF signal and $FPT$ is the X-ray 'Flare Peak Time'. $\triangle t$ reduces significantly for stronger flares (Fig. 2) [4].

In connection with this observation by Basak and Chakrabarti [4], one can mention that Mitra [15] derived a relation between the 'ionospheric relaxation time ($\tau$)' with the flare-time maximum electron density ($N_{e,max}$). Mitra [15] concluded that, during a solar flare, the '$\tau$' is inversely related with $N_{e,max}$, i.e., during stronger flares the lower ionospheric response is more instantaneous. A similar result was reported by Valnicek and Ranzinger [31]. Using the X-ray data obtained by Intercosmos-1 satellite, they derived that the same 'sluggishness' ($\triangle t$) values go down with enhancing solar ionizing activity and vice-versa. Zigman et al. [38] calculated the temporal $N_e(t)$ profile for several classes of flares each using 'electron continuity theory' and $\triangle t$ as crucial parameters. Grubor et al. [12] observed the VLF response during flares for a comparatively shorter signal propagation path (GQD/22.1 kHz to Belgrade $\sim$2000 km) and they showed that, the 'solar zenith angle ($Z$)'-effect on amplitude and phase delay are in general not prominent enough, but the flares that occurred at higher zenith angles can cause amplitude and phase delay, only if they are strong (i.e. higher M or X-class).

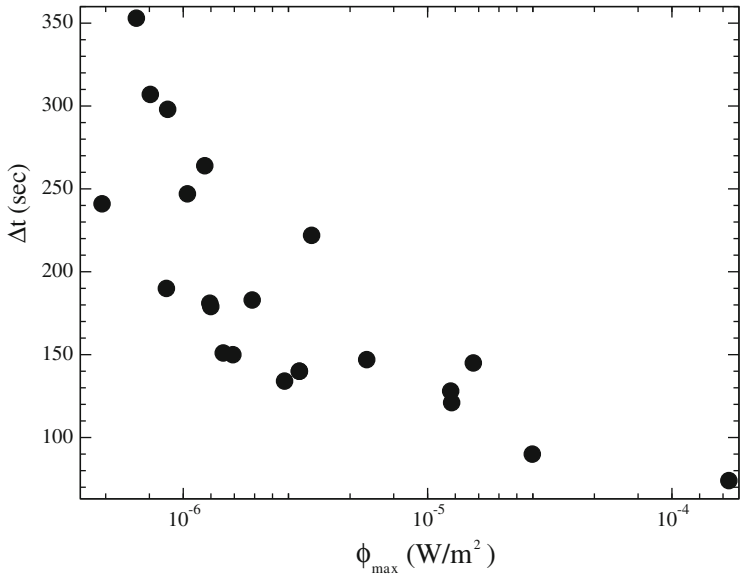



**Fig. 2** VLF response time delay ($\triangle t$) is plotted as a function of the corresponding peak flare flux ($\phi_{max}$, $\mathrm{Wm}^{-2}$) (adopted from [4])

## 4 Modulation of D-Region Effective Recombination Process During Flares

The 'recombination coefficient' means the time rate of recombination among positive ions, negative ions and neutral constituents per unit volume during an external ionizing action on the ionosphere. As mentioned in the Sect. 2.1 there are a number of types of recombination coefficients in the D-region ionosphere indicating respective recombination mechanisms. The dissociative recombination coefficient ($\alpha_D$) indicates the recombination among electrons, positive ions and positive cluster ions respectively. The mutual ionic recombination coefficient ($\alpha_i$) measures the recombination among positive and several negative ions in the D-region. The effective recombination coefficient ($\alpha_{eff}$) represents a combined effect of them [4, 20]. $\alpha_{eff}$-analysis is appropriate to replicate the overall recombining chemical actions across lower ionosphere through comparatively easier computations.

Basak and Chakrabarti [4] proposed an analytical formula to estimate the $\alpha_{eff}$ at low-latitude D-region ionosphere. The VLF amplitude time delay ($\triangle t$) and D-region electron density profile ($N_e$) (discussed in Sect. 4.1) during a solar flare are the key inputs in the above mentioned formula. The contribution from free $N_e$ has been primarily focussed in comparison to the positive and negative ions, because of heavier masses of positive and negative ions, they rarely influence the VLF propagation in lower ionosphere [4, 16, 20]. They also showed that $\alpha_{eff}$ has an inverse relation with 'peak flare flux' ($\phi_{max}$) [4] (Fig. 4). A broader description of

this topic has been elaborated in [3], as the discussions here are in a bit concise form of the same as in [3].

### 4.1 Numerical Simulation of D-Region $N_e$ During Flares

Thomson et al. [30], Zigman et al. [38], Nina et al. [20], Basak [3], Basak and Chakrabarti [4], Palit et al. [23] etc. emphasized on the maximum VLF signal amplitude perturbation ($\triangle A_{max}$), which is a crucial parameter for the D-region $N_e$ simulation. The $\triangle A_{max}$ is generally calculated by subtracting the mean of the available data of nearby solar-quiet days before and after the 'flare day' ($A_{quiet}$) from the maximum VLF perturbation for a given solar flare ($A_{perturbed,max}$). To minimize the possible error accumulated during direct measurements of the data, a polynomial fitting method was proposed by Basak and Chakrabarti [4].

Based on the Wait's theory [34], the Long Wavelength Propagation Model (LWPM) is a frequently used propagation model for the lower ionosphere [8] and it numerically simulates sub-ionospheric VLF signal propagation. It assumes an exponential increase in the altitude profile of $N_e$ and electrical conductivity in D-region. A sharpness factor ($\beta$) and effective reflection height ($h'$) are the main controlling factors of this ionosphere model [34]. Basak and Chakrabarti [4] etc. worked out the simulation over a single signal propagation path from NWC transmitter to IERCOO, ICSP, Sitapur, WB (22° 27′N, 87° 45′E) receiving station. For this analysis, they only accommodated those flares, which occurred when the sun was close to the zenith ($Z = 0$) with respect to VLF signal propagation path. Now, to authenticate $N_{e,unperturbed}$, they obtained the same unperturbed value (averaged over the entire propagation path) from 'International Reference Ionosphere (IRI)-2012' model of NASA. Lastly, the $\triangle A_{max}$ is being supplied to compute the $N_e(h)$ at a height '$h$' using very popular Wait's formula of 2-component exponential D-region profile (Fig. 3).

### 4.2 Estimation of Effective Recombination ($\alpha_{eff}$)-Profile Using Ionospheric Time Delay Method

Basak and Chakrabarti [4] analyzed a number of solar flares and analytically derived the expression for $\alpha_{eff}$ and from LWPC simulation, they estimated $N_{e,max}$ for each flare (Fig. 3). Also for verification of our LWPC simulation results, they again computed $N_{e,max}$ at $h = 74.1$ km height, using $\alpha_{eff}$ values taken from [38] (Fig. 3).

$\alpha_{eff}$ has been calculated from the relation derived by Basak and Chakrabarti [4]. The $\alpha_{eff}$ and $\phi_{max}$ are generally correlated with some exceptions [4]. That exception may be due to the zenith angle ($Z$) variation over propagation path during observation, which directly controls the ionization profile of the ionosphere. The obtained values of $\alpha_{eff}$ for low latitude D-region ionosphere generally agree with the results of [2, 22, 38] (Fig. 4). The recombination process is dominant near entire

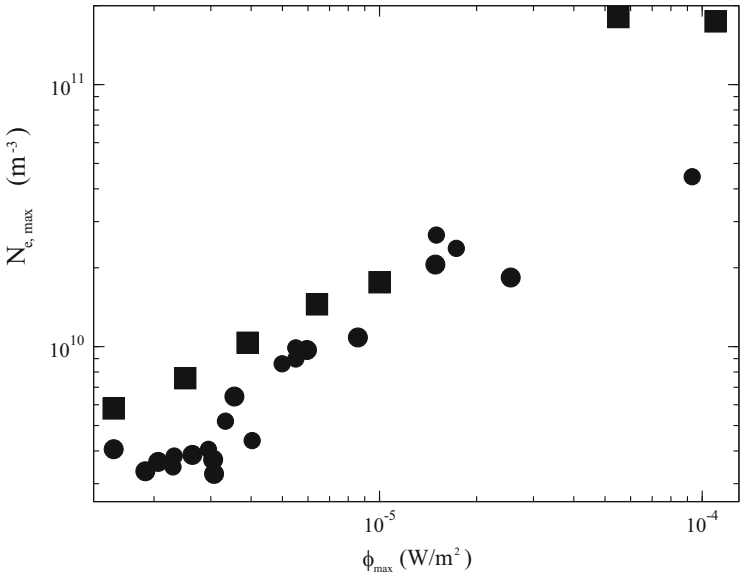



**Fig. 3** Simulated D-region electron density (circles) ($N_{e,max}$) ($m^{-3}$) at $h = 74$ km (ionospheric height) is plotted with corresponding peak flare flux ($\phi_{max}$) ($Wm^{-2}$). $N_{e,max}$ (squares) calculated at $h = 74.1$ km using $\alpha_{eff}$ values taken from [38] for a comparison (figure adopted from [3, 4, 38])

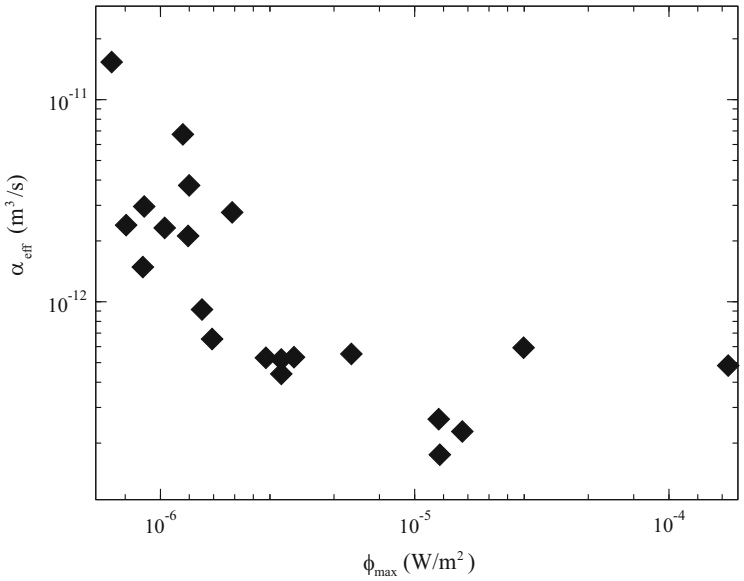



**Fig. 4** Effective reflection coefficient ($\alpha_{eff}$) ($m^3\ s^{-1}$) is plotted with corresponding peak flare flux ($\phi_{max}$) ($Wm^{-2}$) (adopted from [3, 4])

mesopause region, but it is reported that at 74 km in D-region the transformation occurs at a significant level and hence $\alpha_{eff}$ is reduced for stronger flares.

## 5 Conclusion and Future Plans

The topic of analysis here is focussed on the D-region ionosphere modulations during solar flares. The relevant parameters we studied are the response time delay ($\triangle t$) and $\alpha_{eff}$. The time delay $\triangle t$ decreases with increasing peak X-ray flux ($\phi_{max}$) [4] (Fig. 2). They moved towards a broader approach and we successfully analysed a good number of flares of all classes (Fig. 1). After analysing them, they earlier not only reported that the time delay of the VLF amplitude $\triangle t$ is anti-correlated with the flare energy flux $\phi_{max}$ (Fig. 2), but also that the relationship is not equally good at all times of the day (i.e. for different '$Z$'s), where, Appleton [1] anti-correlation formula related to $\triangle t$ has also been verified. Most importantly, the results of the effective recombination coefficient ($\alpha_{eff}$) at the peak of these flares of all possible classes are analysed according to the prescriptions of [4] (Fig. 4). The values of $\alpha_{eff}$ at 74 km altitude are generally in agreement with earlier results reported by several other workers [4, 38] (Fig. 4). As an extension of this work, now, we have been working on the simultaneous VLF signal multi-propagation path modeling of the solar flare induced D-region perturbation, where, a comparative discussions and conclusions will be drawn on the possible argumentative natures of $\triangle t$, $\alpha_{eff}$ on each of those propagation paths.

**Acknowledgements** Author is indebted to Prof. Sandip Kumar Chakrabarti for his guidance and kind contribution behind conceptualization of this work. Author acknowledges the contribution of Indian Centre for Space Physics, Kolkata for allowing him to use the data and their research facilities. Author is thankful to Dr. S. Sasmal (ICSP, Kolkata), Dr. S. Pal (CU, Kolkata), Dr. S. Palit (UPM, Brazil), Mr. S. Chakraborty (SNBNCBS, Kolkata), Dr. S.K. Mondal (SKBU, Purulia, WB) and Dr. S. Ray (ICSP, Kolkata) for their scientific advice.

## References

1. Appleton, E.V.: J. Atmos. Terre. Phy. **3**, 282–284 (1953)
2. Balachandra Swamy, A.C.: Astrophy. Space Sc. **185**, 153–164 (1991)
3. Basak, T, Ph.D. Thesis, University of Calcutta (2013). http://hdl.handle.net/10603/175305
4. Basak, T., Chakrabarti, S.K.: ApSS **348**(2), 315–326 (2013)
5. Chakrabarti, S.K., et al.: J. Atmos. Sol. Terr. Phys. **86**, 65–70 (2012)
6. Chakrabarti S.K., Sasmal S., Chakravorty S., Basak T., Tucker R.: Adv. Space Res. **62**(3), 651–661 (2018)
7. Chakraborty S., Sasmal S., Basak T., Ghosh S., Palit S., Chakrabarti S.K., Ray, S.: Adv. Space Res. **60**(8), 1787–1796 (2017)
8. Ferguson, J.A.: Version 2.0., Technical document 3030, Space and Naval Warfare Systems Center, San Diego (1998)
9. Friedrich, M., Torkar, K.M., Steiner, R.J.: ASR **34**, 1937–1942 (2004)

10. Gledhill, J.A.: Radio Sc. **21**(30), 399–408 (1986)
11. Glukhov V.S., Pasko V.P., Inan U.S.: J. Geophys. Res. **97**(A11), 16971–16979 (1992)
12. Grubor, D., Sulic, D., Zigman, V.: Serb. Astron. J. **171**, 29–35 (2005)
13. Lehtinen N.G., Inan U.S.: Geophys. Res. Lett. **34**, L08804 (2007). https://doi.org/doi:10.1029/2006GL029051
14. Mitra, A.P.: In: Landmark (ed.) Advances in Upper Atmosphere Research, pp. 57–87. Pergamon Press, Oxford (1963)
15. Mitra, A.P.: Ionospheric Effects of Solar Flares. D. Reidel Pub. Co., Holland (1974)
16. Mitra, S.K.: The Upper Atmosphere. The Asiatic Society, Calcutta (1992)
17. Mitra, A.P., Jones, R.E.: JGR **50**(3), 391–406 (1953)
18. Mitra, A.P., Rowe, J.N.: JATP **34**, 795–806 (1972)
19. Mitra, A.P., Rowe, J.N.: JATP **36**(11), 1797–1808 (1974)
20. Nina, A., Cadez, V., Sulic, D., Sreckovic, V., Zigman, V.: Nucl. Instrum. Methods Phys. Res., Sect. B **279**, 106–109 (2012)
21. Osepian, A., Kirkwood, S., Dalin, P., Tereschenko, V.: Ann. Geo. **27**, 3713–3724 (2009)
22. Parthasarathy, R., Rai, D. B., Scientific Report No. 1, Geophysical Institute of the University of Alaska (1965)
23. Palit, S., Basak, T., Mondal, S.K., Pal, S., Chakrabarti, S.K.: Atmos. Chem. Phys. **13**, 9159–9168 (2013)
24. Palit, S., Basak T., Pal, S., Chakrabarti, S.K.: Astrophys. Space Sci. **356**(1), 19–28 (2015)
25. Poppoff, I.G., Whitten, R.C.: JGR **67**(7), 2986–2988 (1962)
26. Pozo, C.F. del, Hargraves, J.K., Aylward, A.D.: JASTP **59**(15), 1919–1943 (1997)
27. Sasmal, S., Basak, T., Chakraborty, S., Palit, S., Chakrabarti, S.K.: J. Geophys. Res. Space Phys. **122**(7), 7698–7712 (2017)
28. Schunk, R.W. (ed.): CASS, Utah State University, Logan (1996)
29. Thomson, N.R., Clilverd, M.A.: J. Atmos. Terres. Phys. **63**, 1729–1737 (2001)
30. Thomson, N.R., Rodger, C.J., Clilverd, M.A.: J. Geophys. Res. **110**, A06306 (2005)
31. Valnicek, B., Ranzinger, P.: Bull. Astron. Inst. Czech. **23**, 318–322 (1972)
32. Wagner, L.S., Thome, G.D.: Radio Sc. **7**(4), 469–480 (1972)
33. Wait, J.R.: Electromagnetic waves in stratified media. Pergamon Press, Oxford (1962)
34. Wait, J.R., Spies, K.P.: NBS Tech. Note 300 (1964)
35. Whitten, R.C., Poppoff, I.G.: JGR **66**(9), 2779–2786 (1961)
36. Whitten, R.C., Poppoff, I.G.: JGR **67**(3), 1183–1185 (1962)
37. Whitten, R.C., Poppoff, I.G., Edmonds, R.S., Berning, W.W.: JGR **70**(7), 1737–1742 (1965)
38. Zigman, V., Grubor, D., Sulic, D.: J. Atmos. Terres. Phys. **69**, 775–792 (2007)

# Numerical Simulation of Equatorial Ionospheric Response to Extra-Terrestrial High Energy Phenomena Using Ion Chemistry Models




**Sourav Palit**

**Abstract** Ionosphere of earth is a giant natural plasma laboratory, which responses to various excitations from local and celestial radiation sources. Apart from the ever-present cosmic rays and the day-time ultraviolet radiation from the Sun, solar activities modify the plasma environment of the ionosphere with frequency regulated by the 11-year solar cycle. While incident energetic charged particles from events like solar flares and coronal mass ejections (CMEs), lead by geomagnetic field, affect only the high latitude part of the ionosphere, the equatorial ionosphere is readily modified due to ionization by the enhanced high energy photons, such as, extreme ultraviolet (EUV), soft X-ray fluxes etc. Evaluation of the modulation in ionospheric plasma properties by such events requires detailed estimation of the altitude-wise energy deposition/ionization rates and the subsequent ion-chemistry evolution. Particularly the least explored lowest part of the ionosphere (called the D-region during day time), for which direct evaluation of any physical parameters is almost impossible and radio frequency remote sensing is the only viable option, the task is quite challenging. A new computer model comprising of Monte Carlo simulation and a simplistic ion-chemistry scheme to evaluate the effect of extra-terrestrial ionizing radiation sources on D-region ionosphere is presented here. Rigorous validation of the model by comparing the outcome with Very Low Frequency (VLF) radio wave studies of several solar flares in a propagation path belonging to Indian subcontinent is done. The model is also extended to explore a reconstruction method to find source characteristics, like spectrum of incident photons by deconvolution of the observed plasma parameters. This is a significant stride along the path to establish earth's atmosphere as an astronomical detector.

S. Palit (✉)
Centro de Rádio-Astronomia e Astrofísica, Mackenzie Presbyterian University, Consolação, São Paulo, SP, Brazil

© Springer International Publishing AG, part of Springer Nature 2018

B. Mukhopadhyay, S. Sasmal (eds.), *Exploring the Universe: From Near Space to Extra-Galactic*, Astrophysics and Space Science Proceedings 53,
https://doi.org/10.1007/978-3-319-94607-8_44

## 1 Earths Ionosphere and Its Response to High Energy Phenomena

Earth's ionosphere is the part of its atmosphere consisting of ions and free electrons distributed over altitudes of ∼ 50–1000 km. High energy photons, mainly ultraviolet (UV) rays from the Sun and the galactic cosmic rays constantly ionize the atmosphere of earth, which subsequently goes through various chemical recombination processes. The rate of ionization decreases from above to below because of the gradual diminishing of the ionizing radiation flux due to absorption, whereas the rate of recombination increases downwards due to increase in atmospheric neutral density. In above altitude range, the rates of ionization and recombination balance each other to sustain a finite amount of free electrons and ions. In addition to the usual day-night and seasonal variations regulated by variation in solar UV radiation flux, the 11-year solar cycle, in which the solar ionizing radiation marches from lower to higher values during solar minima to solar maxima and the Forbush decrease of galactic cosmic rays lay their effects on the ionosphere [1–3]. During night, only the upper part of the ionosphere ($\geq\sim$ 150 km altitude), namely F layer and above, in which the ionization is due only to that of atomic oxygen by day time solar EUV (wavelength 10–100 nm) radiation and cosmic rays, remains heavily ionized. In the layer below this, i.e., in the E layer (∼90–150 km above earth's surface) the far-ultraviolet (FUV) and soft X-rays (1–10 nm) produce most of the ionization predominantly of molecular oxygen ($O_2$). The lowest part of the ionosphere (∼60–90 km altitude), called the D-region is formed by the ionization of nitric oxide (NO) by hydrogen Lyman-alpha series radiation (121.6 nm wavelength) during day time and vanishes in night time due to high chemical recombination rates.

Ionosphere, being the reservoir of naturally occurring plasma, is affected by various short-duration natural and anthropogenic sources of radiation. Among the natural terrestrial sources of interactions, the lightning induced electron precipitation, terrestrial gamma ray flashes (TGFs), seismo-electromagnetic emissions from earthquake and volcanic activities modify ionospheric electron and ion densities and temperature locally [4, 5]. The short-lived extra-terrestrial radiation events, which cause significant modification in the ionospheric plasma, are predominantly of solar origin. Energetic photons, in the form of EUV and X-rays from solar flares and energetic charged particles, mainly protons from solar eruptive events (such as, flares, CMEs) influence different ionospheric layers over a span of few seconds up to few days. Depending on the nature of disturbing sources and radiation agents they are termed differently, such as, the sudden ionospheric disturbances (SIDs, caused by flare ionization) [7–10], solar energetic proton (SEP, produced by high energy protons from earth directed flares or CMEs in height latitude/polar regions) [12–14] events, geomagnetic storms (generated by interaction of propagated solar magnetic field with geomagnetic field by magnetic reconnection process) [15–17] etc. Apart from solar origin, X-ray and $\gamma$ ray photons from extra-galactic transient sources

such as gamma ray bursts (GRBs), soft gamma repeaters (SGRs) etc. may also produce measurable perturbations in lower parts of the ionosphere [18–20].

The conducting nature of the ionosphere causes it to refract and effectively reflect radio waves. Waves with a broad range of frequencies starting from ultra low frequency (ULF $\geq$ 3 kHz) and VLF (3–30 kHz) up to very high frequency (VHF, 30–300 MHz) propagate in the space between the ionosphere and the ground of the earth by multiple reflections. The highest range of possible radio propagation varies in sync with the solar cycle owing to the variation in electron density over the heights. Various modifications in the plasma properties at the lower and the middle part of the ionosphere, as stated above, significantly affect the radio wave propagation, clear understanding of which is of utmost importance to estimate and nullify the disturbances created on the communication and navigation processes.

Most obvious outcome of solar flare interaction with earths atmosphere other than the polar region is due to the X-ray ionization of lower ionosphere and following electron density enhancement. It is also the least explored part due mainly to the constraint in direct observability. Large air drag obsoletes the possibility of satellite navigation and measurements while the scientific balloons cannot reach those heights. Radio signals at higher frequencies, such as those used in ionosondes and incoherent scatter radars do not usually get significant echoes there due to very small electron density ($\sim$10 $cm^{-3}$) [21, 22] and hence prone to be masked by interference and noises. The study of VLF signal modulation is the most effective mean of investigating lower ionosphere during the solar flare events [9, 10, 23–26]. The VLF signals transmitted by various stations situated worldwide for the purpose of submarine navigation provide us an excellent opportunity for such explorations.

## 2 Solar Flares, Equatorial Lower Ionosphere and VLF Wave Propagation

Enhanced incident fluxes of solar ultraviolet and soft X-ray photons during solar flare events lead to significant ionospheric modulation at middle and low latitude regions of earth. Highly energetic ($\sim$1–500 MeV) charged particles (mainly protons) during solar proton events (SPEs) following some solar flares and CMEs, though affect the atmospheric chemistry drastically by ionizing millions of molecules each, they are influential only at the polar latitudes due to geomagnetic cut-off. During flare enhanced UV and the EUV photons deposit most of their energies in the F and E layers respectively, whereas in the D layer mostly soft X-rays ($\sim$1–15 keV) deposit energy and cause most of the ionization. Photons of greater energies penetrate even lower heights (down to $\sim$30 km). The primary photo-ionizations by those photons are followed by consecutive electron ionizations. Chemical properties in a respective layer like neutral density, types and ambient concentrations of ions present in the layer and the reaction rate coefficients play a crucial role in how the extra ions and free electrons produced during the flare

stabilize. In the F layer, the chemistry is simpler with the presence of mainly $N^+$, $H^+$ and $O^+$ ions, with $O^+$ as the dominant species at higher heights (F2 layer) and $N^+$ and $O^+$ as the dominant ions in the lower heights (F1 layer) [27]. E layer is filled mostly with $O_2$, $N_2$ and NO molecules, which are ionized during flares by energetic X-ray photons to $O_2^+$ and $N_2^+$. The D layer has nearly similar light positive ion constituents along with hydrated positive cluster ions like $O_2^+(H_2O)_n$, $H^+(H_2O)_n$ etc. Variable percentage of different negative ions also exist in D-region. Various chemical reactions, causing electron exchange between all three species of ions and neutral molecules contribute to the production and loss of those ions and maintain equilibrium concentration of those along with free electrons.

Ionospheric refractive index is a complex quantity comprising of a reflective and an absorptive term. These are functions of many parameters, namely the plasma frequency ($\omega_p$), gyro frequency of electrons ($\omega_h$), effective electron-neutral collision frequency ($\nu$), angle between local magnetic field and wave propagation direction ($\theta$) and wave frequency ($\omega$). Oscillating electromagnetic fields of radio waves, while interacting with the free electrons and ions in the presence of ion (electron)-neutral collisions are absorbed and re-emitted mimicking the reflection of the waves. The reflection of the VLF wave is a continuous process over a range of ionospheric heights and so can not be pinpointed to a single height. According to Mitra [28], the reflection occurs at a height, at which the following condition satisfies

$$\frac{\omega_p^2}{\nu} = \omega sin^2\psi, \tag{1}$$

or

$$\frac{N_e(h)e^2}{\epsilon_0 m_e \nu} = \omega sin^2\psi, \tag{2}$$

where, $\psi$ is the angle of incidence during reflection, $N_e(h)$ is electron number density (in SI unit) as a function of height, $h$, $\epsilon_0$ is the permittivity of free space and $e$ and $m_e$ are charge and mass of an electron respectively.

In ambient conditions the electron density is approximated by Wait's formula [29]

$$N_e(h) = 1.43 \times 10^{13} exp(-0.15h')exp[(\beta - 0.15)(h - h')], \tag{3}$$

which is characterized by two parameters, namely, the reference height ($h'$) and an electron density gradient parameter ($\beta$). In the presence of ionizing sources the electron density evolves following the local continuity equation, given by [10]

$$\frac{dN_e(h)}{dt} = \frac{q}{1+\lambda} - \alpha N_e^2(h). \tag{4}$$

Here, $q$ is the rate of ionization per unit volume, $\lambda$ is the ratio of negative ion density to electron density and $\alpha$ is the effective recombination coefficient, all of which are functions of height. During a SID, lead by a solar flare, the electron density at any lower ionospheric height undergoes a sudden rise followed by a gradual fall due to chemical recombination of ions. For a steep ionization profile like a delta function (such as X-rays from SGR, GRB) the electron density at any given height will fall from the peak value $N_p(h)$ as

$$N_e(h) = \frac{N_p(h)}{1 + N_p(h)\alpha t}, \tag{5}$$

with a half time of decay, $T_{\frac{1}{2}} = \frac{1}{\alpha t}$. Although this is an ideal case, for actual solar flares the electron density at a given height should fall with a time scale inversely related to the respective effective recombination coefficient at that height. Another notable consequence of the finite chemical recombination time is the delay of the peak of the electron density value at a given height with respect to that of the ionizing X-ray radiation profile of the solar flare, detail of which will be discussed in a later section.

Together with the electron density values the height dependent collision frequency, like the most refined version, recently given by Kelly [30],

$$\nu_{ek} = 5.4 \times 10^{-10} n_n T_e^{\frac{1}{2}} \tag{6}$$

determines the effective reflection height of propagating radio waves. Here $n_n$ is the neutral density and $T_e$ is the electron temperature at respective heights. For a radio wave of certain frequency ($\omega$), combining Eqs. (2) and (6), it is very primitive to find a electron density value required in each height for effective reflection to occur at that height. Then from the intersection of the plot corresponding to these values with the actual electron-density vs. height plot (if known) at any given condition one can easily determine the effective reflection height. It is generally found that for VLF radio wave frequencies during night the effective reflection height remains in the range ~90–100 km of altitude, whereas in the day time it may degrade to as low as ~70 km.

For small distances ($\leq$1000 km) the Wave hop theory [31, 32] and for large distances ($\geq$1000 km) the Waveguide mode theory [23, 24, 33] describes the VLF wave propagation reliably. Stratified layers of the lower ionosphere and the earth's surface act as the upper and lower boundary of wave guide in mode theory. The electromagnetic field at any point is considered to be a superposition of 'modes', which are series of independent field structures, propagating with different velocities [34]. For a VLF wave of wavelength $\lambda_v$, the mode theory approximates the vertical electric field $E$ at a great circle distance $d$ from a source radiating with the power

$P$ as [35],

$$E \simeq \frac{300}{h_r}\left\{\frac{P\lambda_v}{asin(\frac{d}{r_e})}\right\}^{\frac{1}{2}} exp(-\alpha_v d), \tag{7}$$

where, $r_e$ is earth's radius, $h_r$ is the ionospheric effective reflection height and $\alpha_v$ is the attenuation factor. For each propagating mode, $\alpha_v$ is determined by the resonance condition involving the reflection coefficients at the upper and lower boundaries of the propagation path. For the complex refractive index of the form $n = \mu - i\chi$, neglecting the presence of the magnetic field, the absorption coefficient of the wave is given by

$$\kappa \sim \frac{\omega}{c}\chi \sim \frac{Ne^2}{2c\mu\epsilon_0 m_e}\left(\frac{1}{\frac{\omega^2}{\nu} + \nu}\right), \tag{8}$$

where, $c$ is the speed of light in free space. With the assumption that the whole propagation path consists of many small pieces (of length $\Delta d$) having their own value of local mean attenuation coefficient $\kappa_h$, and the region of nonzero electron density starting at height $h_0$ only contributes to the absorption, we have

$$E \simeq \frac{300}{h_r}\left\{\frac{P\lambda_v}{asin(\frac{d}{r_e})}\right\}^{\frac{1}{2}} exp(-\Sigma_{h_0}^{h_r}\kappa_h \Delta d). \tag{9}$$

The enhancement of the electron density causes the reflection height to decrease resulting in increase in measured field value due both to the $h_r^{-1}$ term in the coefficient and the $h_r$ dependent argument of the exponential decay term. On the other hand, this also leads to larger values of $\kappa_h$ and hence larger absorption and smaller measured field value. The combined effect determines the VLF amplitude modulation during any ionization event, which may either decrease or increase. To find the VLF signal modulation due to a given ionospheric condition thorough treatment of the waveguide mode theory with computer simulation program such as Long Wave Propagation Capability (LWPC) [36] code must be employed.

## 3 Estimation of Lower Ionospheric Plasma Properties During Solar Flares

Evaluation of the electron density modulation at different heights of ionosphere during solar flares requires extensive computer simulation to find the rate of ionization by enhanced high energy radiation from the Sun and modeling the subsequent ion-chemical evolution. Monte Carlo methods are best suited for the calculation of ionizing interaction of enhanced EUV and soft X-ray with the

D-region ionosphere. For the later part, proper knowledge of the ambient electron and ion density values i.e., those of undisturbed ionosphere is essential. These can be well approximated by the International Reference Ionosphere (IRI) model, the relevant features of which are discussed below.

## *3.1 The IRI Model*

The International Reference Ionosphere [37–39] is the standard model of ionospheric parameters, like electron and ion densities, temperature and velocities. It is jointly developed and updated by the Committee On SPAce Research (COSPAR) and the International Union of Radio Science (URSI) from 1968/1969. The model is based on experimental data from numerous ground and space based data sources along with theoretical and computational models. Regular solar dependence of ionospheric characteristics are incorporated by parameterization on solar zenith angle in lower altitudes (D and E region) and on the local (or UT) time in the higher altitudes (in the F region and above). 12 month running mean of the sunspot number ($R_{Z_{12}}$) and the global ionospheric index ($IG_{12}$, based on $F$ peak plasma density and linear regression with solar activity) are used to account for the 11-year solar cycle variation. The lower ionospheric electron density and other parameters are described based on very limited amount of rocket measurements, whereas the characteristics in the higher altitude regions, such as E and F layers are determined by various radar and ionosonde observations and extensive modeling efforts. Though IRI can provide satisfactory description of the electron-ion density values at different layers of the ionosphere in long term average, the short term variabilities or possible evolution of the ionospheric plasma characteristics to solar activities like flares, earth-oriented CMEs etc. can hardly be evaluated with IRI model.

## *3.2 Chemistry of the Lower Ionosphere*

As discussed earlier, the lower ionosphere consists mostly of neutral molecules, negative, positive ions, positive cluster ions and free electrons. The chemistry of the equatorial lower ionosphere is dominated by the ionization of solar photons (mainly UV and X-ray) and cosmic rays. In the shorter time span (few minute to few hours) of modulation during the solar flares, transport of ions or free electron by molecular or Eddy diffusion and convection or any other bulk motion is not important. An ion chemistry evolution dominated by ionization of mainly soft X-ray and EUV from solar flares is sufficient to determine the evolution of plasma properties during such events. There are few such ion chemistry evolution models [40, 41], which consider a broad list of ions and chemical reactions lead by the photo-ionization. A much simpler approach, in which all the ions and free electrons are grouped into four different categories of ion species (i.e., free electrons, negative ions, positive

ions and positive cluster ions) and all the chemical reactions are categorized into a few separate classes of interaction with their effective reaction rates, has been proposed by Glukhov et al. [42]; hereafter 'GPI model'. This is a less computer intensive model with extensively proven accuracy that deserves a somewhat detailed discussion.

### 3.2.1 The GPI Model

In GPI model of lower ionospheric ion-chemistry the positive ions with density $N^+$ (in SI units) comprise of mainly $O_2^+$ and $NO_2^+$. The negative ions ($N^-$) consist of $O_2^-$, $CO_3^-$, $NO_2^-$, $NO_3^-$ etc. The positive cluster ions ($N_x^+$) are of complicated structure, like $H^+(H_2O)_n$. A modified set of equations are used [43] for lower heights (∼50 km), where the inclusion of negative ion clusters (with density $N_x^-$) is necessary. For the heights, where VLF waves usually get reflected (≥∼ 70 km), the four species GPI model is sufficient. The time evolutions of the four species follow ordinary differential equations consisting of production (+ve) and loss (−ve) terms in the right hand side.

$$\frac{dN_e}{dt} = I + \gamma_e N^- - \beta_e N_e - \alpha_d N_e N^+ - \alpha_d^c N_e N_x^+, \tag{10}$$

$$\frac{dN^-}{dt} = \beta_e N_e - \gamma_e N^- - \alpha_i N^-(N^+ + N_x^+), \tag{11}$$

$$\frac{dN^+}{dt} = I - BN^+ - \alpha_d N_e N^+ - \alpha_i N^- N^+, \tag{12}$$

$$\frac{dN_x^+}{dt} = BN^+ - \alpha_d^c N_e N_x^+ - \alpha_i N^- N_x^+. \tag{13}$$

Also neutrality of the plasma ($N^- + N_e = N^+ + N_x^+$) at all the times is required. Here $\beta_e$ is the electron attachment rate [40], given by

$$\beta_e = 10^{-31} N_{O_2} N_{N_2} + 1.4 \times 10^{29} \left(\frac{300}{T}\right) e^{\left(-\frac{600}{T}\right)} N_{O_2}^2, \tag{14}$$

where the values of electron temperature ($T$) and densities of molecular Oxygen ($N_{O_2}$) and Nitrogen ($N_{N_2}$) for different heights can be obtained from NASA-MSIS atmospheric model [44]. The speculated value of effective detachment rate $\gamma_e$ varies widely from $10^{-23}$ to $10^{-16}$ N s$^{-1}$ [43, 45], where $N$ is the number density of neutral. The effective coefficient of dissociative recombination $\alpha_d$ has the value $10^{-7}$ to $3 \times 10^{-7}$ cm$^3$ s$^{-1}$ [40, 43]. The effective recombination coefficient of electron with positive cluster ions $\alpha_d^c$ has value $10^{-6}$ to $10^{-5}$ cm$^3$ s$^{-1}$. The effective coefficient of ion-ion recombination processes for all kind of positive ions with

negative ions $\alpha_i$ has value $10^{-7}\text{cm}^3\,\text{s}^{-1}$ [40]. The quantity B, i.e., the effective rate of conversion from positive ions to positive cluster ions has the value $10^{-30}\,\text{N}^2\,\text{s}^{-1}$ [40, 42]. For the exact choices of the values of the above parameters used in our calculation, readers are referred to [9]. While solving the equations during the model calculation, we divide each concentration term into an unperturbed and a time dependent term. The undisturbed values of the electron and ion densities can be inserted from IRI model. The unperturbed values of negative ion density $N_0^-$ can be obtained from that of unperturbed electron density ($N_{0e}$) with $N_0^- = \lambda N_{0e}$. We use GEANT4 Monte Carlo simulation to find the term $I$, the ionization rate per unit volume due to flare X-ray and EUV photons. The differential equations can be solved by time stepping algorithms, like Runge-Kutta method with variable step values to accommodate various reaction time-scales.

### 3.2.2 GEANT4 Monte Carlo Simulation for Ionization

We have used GEometry ANd Tracking 4 (GEANT4) Monte Carlo detector simulation software [46] for the calculation of ionization (electron ionization following photo-ionization) of neutral molecules at different altitudes in earth's atmosphere due to solar X-ray and ultraviolet photons from flares. For details of the set up of earths layered atmosphere in software geometry and necessary physics processes in GEANT4 readers are referred to [9]. To include the electron ionization process to the lowest level of electron energies possible, the lower energy threshold has to be extended down to a very small value (10 eV) in the code.

## 4 Forward and Inverse Modeling of Flare-Ionosphere Interactions

The calculated electron densities, when incorporated along with the collision frequency values in the LWPC code [36], give the temporal variation of VLF amplitude over a given propagation path. We applied the method in the modeling of the VLF amplitude modulation due to one M-class and another X-class solar flare. We call it forward modeling. In addition, we also develop an inverse modeling approach, in which we extract the flare spectral and timing information from the observed VLF signal modulation. As the photon absorption height in the earth's atmosphere is dependent primarily on their energies, the ionospheric ionization profile and hence the electron density distribution with height during the X-ray enhancement due to the flare should contain the spectral information of the incident photons. The peak time delay is found to contain the timing properties of the flare X-ray emission, such as the peak flux and the sharpness at peak, which can also be extracted.

### 4.1 Forward Modeling

Figure 1 shows the results of forward modeling of VLF amplitude during two solar flares previously presented in [9]. VLF data of NWC (19.8 kHz) transmitter received in IERC/ICSP (see [9]) station (propagation path of length 5691 km) during the X-class (15th Feb 2011) and the M-Class (24th Feb 2011) flares have been modeled. GOES and RHESSI satellite data for light curves and spectrum are used in the Monte Carlo simulation. In the upper panel of Fig. 1 the simulated electron density over different heights as function of time during the flares are presented. In the lower panel the modeled (dashed curve) and observed (solid curve) VLF amplitude variation during the two flares are shown. Reasonable matching between the simulated and observed values are obtained.

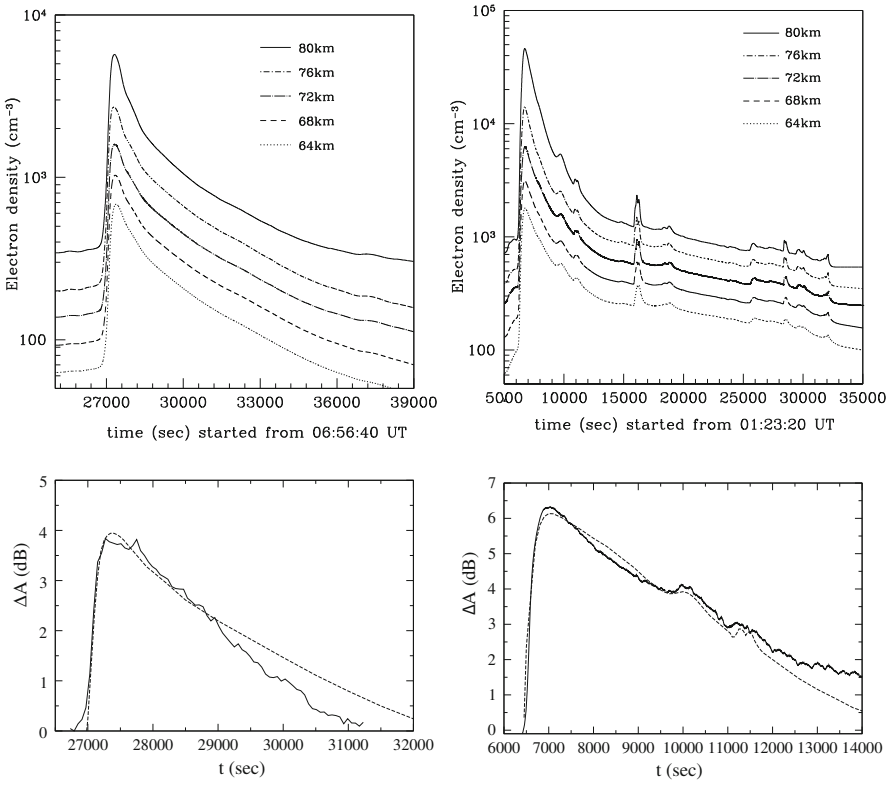



**Fig. 1** Simulated electron densities at different heights during the M-class (top-left) and X-class (top-right) solar flares. Modeled VLF amplitude perturbations (dotted line) and corresponding observed VLF data (solid line) are plotted with UT for the M-class (bottom-left) and X-class (bottom-right) solar flare (adopted from [9])

The approximate expression of the peak time delay ($\Delta t$) between the electron density at a certain height and the GOES soft X-ray light curve is found to be [10]

$$\Delta t^2 = \frac{(\frac{k'a}{\alpha})^{\frac{1}{2}} - \frac{3}{8\alpha\Delta t}}{\frac{b}{2}(\frac{k'}{\alpha a})^{\frac{1}{2}} + \frac{k'a}{2\Delta t}} \tag{15}$$

or, with some approximation for very sharp flare profile

$$\Delta t \sim \frac{2\eta}{(k'\alpha)^{(\frac{1}{2})}} \frac{1}{a^{(\frac{1}{2})}}, \tag{16}$$

where, $k'$ is the proportionality constant of modified Chapman's formula for X-ray ionization divided by $(1 + \lambda)$ (see [10]). $a$, the peak X-ray flux ($I_{max}$) and $b = \frac{1}{2}(\frac{d^2I}{dt^2})_{I_{max}}$ (sharpness of X-ray flux variation at peak) are both constants and characteristics of the flares. The corresponding peak time delay of VLF amplitudes are found to follow the delay in electron densities at approximate reflection heights.

## *4.2 Inverse Modeling*

One of the motivations in the modeling study of ionospheric and VLF modulation due to extra-terrestrial transient phenomena has been to establish the ionosphere or broadly the atmosphere as an ever-present nature-made detector or monitor of these radiation sources. To achieve this goal it is necessary to evaluate all the response characteristics of the so called ionospheric detector and to explore means to determine the source characteristics such as spectrum and timing information of the radiation. While the time delay in observed VLF peak can tell us approximate values of the peak intensity of the flare or how it may vary at peak, we found that up to a certain limiting accuracy, unique deconvolution of the observed VLF amplitude modulation can be done to get information on a part of the injected spectrum. A simplified modification of the Chapman's formula for obtaining the height dependent rate of ionization due to X-ray as a function of the spectrum (see [11] for details) is given by.

$$q(h,t) = \sum_j \int I_0(\nu,t) f(h,\nu,j) d\nu, \tag{17}$$

where, $I_0(\nu, t)d\nu$ is the irradiance or the solar flux at the top of the atmosphere in the frequency range $\nu$ to $\nu + d\nu$ and $f(h, \nu, j)$ is a function of absorption cross-section,

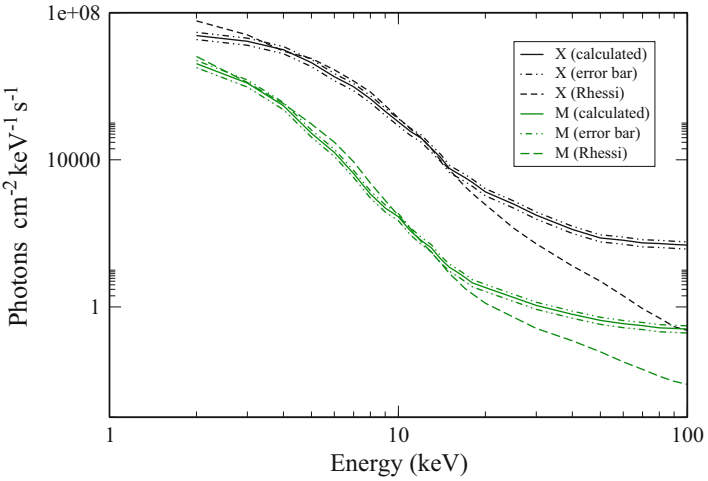



**Fig. 2** M-class gray and X-class (black) solar flare spectra during the peaks. Solid curves correspond to modeled spectra, which are plotted with calculated error bars (see Appendix 2 of [10] for details) and dashed ones are the corresponding spectra obtained from RHESSI data (Color figure online)

photo-ionization efficiency and concentration of $j$th neutral component in air. Combining with the continuity equation (Eq. (4)) it gives

$$\int I_0(\nu, t) f(h, \nu) d\nu = (1 + \lambda)(\frac{dN_e}{dt} + \alpha N_e^2). \tag{18}$$

This clearly corresponds to an integral transformation between two mathematical functions or spaces ($\nu$ and $h$ spaces) with the kernel $f(h, \nu)$. Knowing the values of the electron densities ($N_e(h)$) and rate of change of those ($\frac{dN_e}{dt}$), an inverse transform may provide us the irradiation values ($I_0(\nu, t)$).

The basis functions $f(h, \nu)$ are nothing but the height profile of electron density produced by a single photon in the energy range $\nu$ to $\nu + d\nu$. These can be calculated analytically or with Monte Carlo simulation. In [11] some of these functions are presented pictorially. In the same paper [11] we present one deconvolution method based on iterative maximum likelihood estimation using a modified version of Richardson Lucy algorithm to extract the spectrum information from the electron density values obtained from VLF observation using these basis function profiles. In Fig. 2 we present the result of such a spectrum reconstruction method corresponding to the same X and M-class flares. We use LWPC code to find the steepness parameter ($\beta$ in km$^{-1}$) and a reference height ($h'$ in km) from the VLF amplitude values during the flare and use the Wait's formula (Eq. (3)) to find the electron density values and the rate of change of those during the peak of the

flares. In the figure we plotted the modeled spectra in dotted curve and the actual observed spectra (from RHESSI satellite data) with solid curve. We find that there are reasonable resemblance of the modeled spectra with the observed ones in the range of (∼8–15 keV) for both the flares, as expected.

## 5 Accomplishment and Scope

We have done the first comprehensive simulation of the solar flare interaction with equatorial lower ionosphere and the effect on VLF propagation. Contrary to the conventional approach of study of solar influence on VLF radio waves, in which the Wait's parameters are extracted by purely trial and error method from observed VLF data and electron density is estimated using Wait's formula, this method is in-situ and close to actual physical and chemistry process occurring in the region. Direct and inverse modeling to extract lower ionospheric plasma parameter evolution from source radiation data and vice versa are developed. Currently with some improvements of the model chemistry to extend its applicability to atmosphere below the ionosphere we are in the process to simulate influence of extra-galactic transient sources, such as, GRBs, SGRs, etc. on the earth's atmosphere. Further improvements of the model in terms of inclusion of energetic particle interactions, geomagnetic field etc. are required to simulate the interaction of SEP events and geomagnetic storm with atmosphere. It may be extended to cover higher and lower parts of the atmosphere to account for the energy deposition by the entire spectral range of solar flare photons so that extraction of the whole spectrum is viable. We are gradually approaching to accomplish these goals.

## References

1. Gorney, D.J.: Rev. Geophys. **28**, 315336 (1990)
2. Liu, L., WanYiDing, W., Le, C., Le, H.: Chinese. Sci. Bull. **56**, 1202–1211 (2011). https://doi.org/10.1007/s11434-010-4226-9
3. Morrison, P.: Phys. Rev. **101**, 1397–1404 (1956)
4. Inan, U.S., Cummer, S.A., Marshall, R.A.: JGR **115** (2010). https://doi.org/10.1029/2009JA014775
5. Fishman, G.J., Inan, U.S.: Nature **331**, 418–420 (1988)
6. Whitten, R.C., Poppoff, I.G.: Fundamentals of Aeronomy. Wiley, New York (1971)
7. Mitra, A.P., Rowe, J.N.: JASTP **34**, 795–806 (1972)
8. Grubor, D.P., Suliic, D.M., Zigmann, V.: Serb. Astron. J. **171**, 29–35 (2005)
9. Palit, S., Basak, T., Pal, S., Chakrabarti, S.K.: Atmos. Chem. Phys. **13**, 9159–9168 (2013). https://doi.org/10.5194/acp-13-9159-2013
10. Palit, S., Basak, T., Pal, S., Chakrabarti, S.K.: Astrophys Space Sci. **356**, 19–28 (2015)
11. Palit, S., Ray, S., Chakrabarti, S.K.: Astrophys Space Sci. **361**, 151 (2016)
12. Mariska, J.T., Oran, E.S.: J. Geophys. Res. **86**, 5868–5872 (1981). https://doi.org/10.1029/JA086iA07p05868
13. McRae, W.M., Thomson, N.R.: J. Atmos. Sol. Terr. Phys. **66**,7787 (2004)

14. Thomson, N.R., Clilverd, M.A.: J. Atmos. Sol. Terr. Phys. **63**, 1729–1737 (2001)
15. Gonzalez, W.D., Joselyn, J.A., Kamide, Y., Kroehl, H.W., Rostoker, G., Tsurutani, B.T., Vasyliunas, V.M.: J. Geophys. Res., **99**, 5771 (1994)
16. Tsyganenko, N.A., Sitnov, M.I.: J. Geophys. Res. **110**, A03208 (2005). https://doi.org/10.1029/2004JA010798
17. Zhang, J., Richardson, I.G., Webb, D.F., Gopalswamy, N., Huttunen, E., Kasper, J.C., Nitta, N.V., Poomvises, W., Thompson, B.J., Wu, C.-C. Yashiro, S., Zhukov, A.N.: J. Geophys. Res. **112**, A10102 (2007). https://doi.org/10.1029/2007JA012321
18. Inan, U.S., Lehtinen, N.G., Moore, R.C., Hurley, K., Boggs, S., Smith, D.M., Fishman G.J.: J. Geophys. Res. **34**, L08103 (2007). https://doi.org/10.1029/2006GL029145
19. Tanaka, Y.T., Terasawa, T., Yoshida, M., Horie, T., Hayakawa, M.: J. Geophys. Res. **113**, A07307 (2008). https://doi.org/10.1029/2008JA013119
20. Raulin, J.P., Trottet, G., deCastro, C.G., Correia, E., Macotela, E.L.: J. Geophys. Res. **119**, 4758–4766 (2014)
21. Mathews, J.D., Breakall, J.K., Ganguly, S.: J. Atmos. Terr. Phys. **44**(5), 441–448 (1982). https://doi.org/10.1016/0021-9169(82)90050-2
22. Hargreaves, J.K.: The Solar-Terrestrial Environment. Cambridge University Press, New York (1992)
23. Wait J.R.: J. Res. Natl. Bur. Stand. Sect. D **64**(2), 153–203 (1960)
24. Wait J.R.: J. Geophys. Res. **67**(10), 3823–3828 (1962). https://doi.org/10.1029/JZ067i010p03823
25. Mcrae W.M., Thomson N.R.: J. Atmos. Sol. Terr. Phys. **66**(1), 77–87 (2003) https://doi.org/10.1016/j.jastp.2003.09.009
26. Zigman, V., Grubor, D., Sulic, D.: J. Atmos. Terr. Phys. **69**, 775–792,(2007). https://doi.org/10.1016/j.jastp.2003.09.009
27. Mitra, A.P.: Ionospheric Effects of Solar Flares. Astrophysics and Space Science Library. D. Reidel Publishing Co., Dordrecht, vol. 46, p. 307 (1974)
28. Mitra, A.P.: J. Geophys. Res. **56**(3), 355 (1951)
29. Wait, J.R., Spies, K.P.: NBS Tech. Note, 300 (1964)
30. Kelley, M.C.: The Earths Ionosphere, Plasma Physics and Electrodynamics, chapter 2.2, 2nd edn., Academic, New York (2009)
31. Davies, K.,: Ionospheric Radio. Peter Peregrinus Ltd., London (1990)
32. Poulsen, W.L.: Ph.D. Thesis, Stanford University (1991)
33. Budden, K.G.: Radio Waves in the Ionosphere. Cambridge University Press, Cambridge (1966)
34. Lyn, J.W.: AIP Conf. Proc. **1286**(3) (2010). https://doi.org/10.1063/1.3512893
35. Wait, J.R.: Geofisica pura e applicata **41**,73–85 (1958)
36. Ferguson, J.A.: version 2.0. Technical document 3030, Space and Naval Warfare Systems Center, San Diego, CA (1998)
37. Rawer, K., Bilitza, D., Ramakrishna, S.: Reviews Geophys. Space Sci.**16**(2), 177–181 (1978)
38. Bilitza, D.: International Reference Ionosphere 2000. Radio Sci. AGU. **36**(2), 261–275 (2001)
39. Bilitza, D., Altadill, D., Truhlik, V., Shubin, V., Galkin, I., Reinisch, B., Huang, X.: International Reference Ionosphere 2016: From ionospheric climate to real-time weather predictions. Space Weather **15**, 418–429 (2017). https://doi.org/10.1002/2016SW001593
40. Rowe, J.N., Mitra, A.P., Ferraro, A.J., Lee, H.S.: J. Atmos. Terr. Phys. **36**, 755–785 (1974)
41. Mitra, A.P.: J. Atmos. Sol. Terr. Phys. **43**, 737–752 (1981)
42. Glukhov, V.S., Pasko, V.P., Inan, U.S.: J. Geophys. Res. **97**, 16971–16979 (1992)
43. Lehtinen, N.G., Inan, U.S.: Geophys. Res. Lett. **34**, L08804 (2007). https://doi.org/10.1029/2006GL029051
44. Hedin, A.E.: Geophys. Res. Lett. **96**, 1159–1172 (1991)
45. Pasko, V.P., Inan, U.S.: J. Geophys. Res. **99**, 17523–17537 (1994)
46. Agostinelli, S., Allison, J., Amako, K., et al.: GEANT4 simulation toolkit. Nucl. Instrum. Meth. A **506**, 250–303 (2003)

# Earth's Ionosphere as a Detector for High Energy Extra-Solar Radiation




**Sushanta Kumar Mondal**

**Abstract** Earth's ionosphere is open to all kinds of radiation from all possible directions. The diurnal variation of the ionosphere is mostly controlled by the solar radiation and activity in the Sun. Occasionally strong, intense high energy radiation from extra-terrestrial sources disturb the ionosphere momentarily. The lower ionospheric disturbances could be measured by monitoring Very Low Frequency radio waves. This chapter presents studies of ionospheric effects in the narrow band very low frequency wave particularly due to various high energy photons of extra-terrestrial origin. The studies mostly include temporal sudden ionospheric disturbances over various propagation paths. The effort and contribution of Indian Centre for Space Physics in this regard is also discussed.

## 1 Introduction

Earth's ionosphere could be considered as a detector for high energy radiation. The ionosphere being very dynamic, the detector is noisy and its response will vary at different times of the day, at different seasons and different activity periods of the Sun. Very Low Frequency waves or VLF waves are used to probe the changes in the lower ionosphere. VLF waves (3–30 kHz) are transmitted by the world wide Navy for submarine communications since these waves can propagate long distance by reflecting back and forth in the Earth-ionosphere waveguide with very small attenuation. NWC (19.8 kHz, Australia), JJI (22.2 kHz, Japan), NPM (21.4 kHz, Hawaii), NLK (24.6 kHz, USA), VTX (18.3 kHz, India) are the call signs of a few operational transmitters. The ionospheric response to the enhanced solar UV and X-ray radiation during solar flares of various strengths have been studied quantitatively for many years by measuring the change in amplitude and phase of Very Low Frequency wave [34]. The Sun observing satellites, more specifically, the Reuven

S. K. Mondal (✉)
Sidho Kanho Birsha University, Purulia, West Bengal, India

© Springer International Publishing AG, part of Springer Nature 2018

B. Mukhopadhyay, S. Sasmal (eds.), *Exploring the Universe: From Near Space to Extra-Galactic*, Astrophysics and Space Science Proceedings 53,
https://doi.org/10.1007/978-3-319-94607-8_45

Ramaty High Energy Solar Spectroscopic Imager or the RHESSI satellite which became operational in 2002 provided great opportunity to study solar flares in great details [27]. Solar flares are regarded as irregular events and may extend from a few minute to few hours. Palit et al. gave an account of how solar spectra of various class of flares are absorbed at different altitudes in the ionosphere and how the ion-chemistry plays an important role in the prolonged recovery of the ionosphere [24, 25]. These studies are useful to characterize the sensitivity of the ionosphere detector to long recovery events.

There are another class of short impulsive events which are not originated from the Sun but more energetic than the solar radiation. Intense radiation from the extra-terrestrial sources such as X-ray transient, X-ray novae, Soft Gamma Ray repeaters (SGR), Anomalous X-ray Pulsars, Gamma Ray Bursts (GRB) are also found to disturb the ionosphere [1, 15, 16]. The whole subject and the discovery of high energy radiation from extra-terrestrial sources began in 1967, after the detection of a flash of gamma radiation of unknown origin by the Vela satellites. These satellites were originally deployed by the USA to hunt out nuclear detonations. After subsequent similar detections, the gamma ray flashes were confirmed to be Gamma Ray Bursts of cosmic origin [17].

Gamma Ray Bursts are the most violent phenomena in the universe releasing enormous amount of energy in a very short time. The total energy released during a GRB is greater than the energy output of the Sun over its whole lifetime. Space based gamma ray observatories are detecting on an average a new Gamma Ray Burst almost everyday since the first discovery. Most of these GRBs are located in the distant galaxies, the fluence that is reaching the Earth's ionosphere is too small to produce significant ionospheric changes which could be detected in VLF signal. Very few extremely bright events are detected in VLF.

## 2 A Brief History of VLF Astronomy

The first convincing result of detection of GRB in VLF came in 1988, detection of GRB830801, the strongest Gamma Ray Burst ever observed. VLF detection of two more GRBs, three SGRs and a few X-ray transients have been confirmed till date [22]. At least in two occasions the events were so powerful that the satellite detectors got saturated and stopped counting photons during the peak time of the event. The rare VLF discovery of these energetic events were so far prompted by the satellite detection of a powerful X-ray/$\gamma$-ray burst. From the last decade (last quarter of 1997) NASA maintains a GRB Circular Network (GCN, https://gcn.gsfc.nasa.gov) to alert the astronomy community with the coordinates of a new event immediately after detection by any of the operational $\gamma$-ray/X-ray satellite. The ionosphere absorbs the whole radiation and the ionospheric changes due to this are detected by observing sudden prominent changes in the VLF amplitude and phase coinciding with the satellite detection time. In the rest of this section above mentioned detections will be discussed in more details.

## 2.1 GRB830801

The Gamma Ray Burst GRB830801 was observed by the Prognoz-9, the International Comet Explorer and the Vela satellite on 1 August, 1983 at 22:14:18 UT. The burst with the total fluence of $2 \times 10^{-3}$ erg/cm$^2$ was resolved over 11 energy channels. Peak count was observed in the 68–110 keV and 110–165 keV energy range [19].

VLF discovery had to wait until the publication of the $\gamma$-ray detection result of the event, since GRB Circular Network type facility was not available then. Strong VLF disturbance was found in a receiving site at Palmer, Antarctica in GBR signal transmitted from Rugby, England. From the same receiving site weaker disturbances were observed in the NSS and NPM signal transmitted from Maryland and Hawaii respectively [8]. Figure 1 shows the three propagation paths, the sunset terminator and the sub-burst point (or the sub-flare point is the location on the Earth where the source was directly overhead at the time of burst) is indicated by the '+' symbol. In spite of the proximity of the NSS-Palmer and NPM-Palmer propagation paths to the sub-burst point the disturbance in both the signals is weak. Whether the GBR-Palmer propagation path being totally in the night side got affected more due to increased night time absorption can be seen from the right panel of Fig. 1.

## 2.2 SGR 1900+14

Soft Gamma ray Repeaters (SGR) are neutron stars with extremely high magnetic field of the order of $10^{15}$ Gauss. They are also called 'magnetars'. SGRs during the

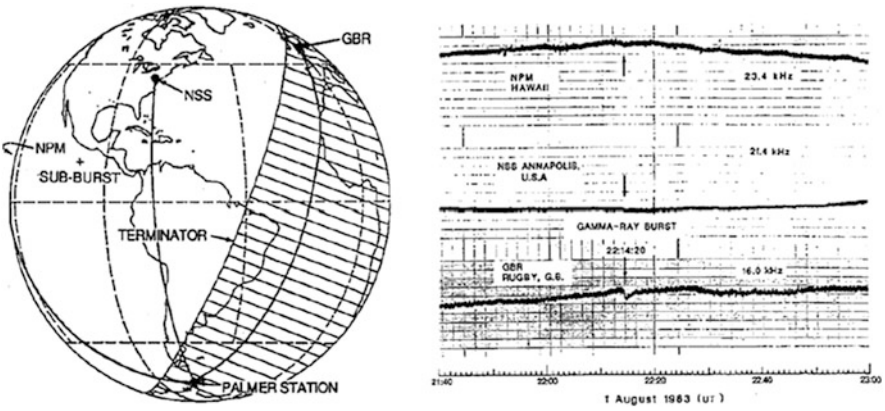



**Fig. 1** Left: The VLF propagation paths along with the day-night terminator is shown. The cross indicates the sub-flare point (103° $W$, 13° $S$). Right: VLF signal amplitude at Palmer from the three transmitters are shown. The arrow indicates VLF response at the time of the burst [8]

period of magnetic instabilities emit short, intense repeating pulse of soft or low energy gamma radiation. Unlike GRB, soft spectra and repeating nature of the pulse associated with the time period of spin of the magnetar is the unique characteristic of SGR bursts. The SGR 1900+14, first detected in X-ray in 1979 with a time period of spin 5.16 s, was emitting frequent low energy burst in X-ray from the month of April, 1998. It erupted with giant flares on August 27, 1998 at 10:22 UT. The event was observed by several space based gamma-ray experiments such as, Ulysses gamma-ray burst detector, BeppoSAX Gamma-Ray Burst Monitor in different energy ranges [10]. The giant flare also affected the ionosphere of the whole hemisphere facing the SGR.

The ionospheric changes were reflected in many VLF signals in various propagation paths in the exposed hemisphere. The NPM VLF signal recorded at Boston, Colorado in USA and at Palmer, Antarctica responded immediately. Amplitude change of ∼24 dB and phase change of ∼65° was observed at Palmer and is shown in Fig. 2 [12]. It could also be seen that during the peak of the flare Ulysses detector was saturated due to excess count but the VLF signal did not. In fact, the 5.16 s oscillation period was also extracted from the NPM signal amplitude. Similar changes were observed in VLF signals recorded at Chofu, Japan from three transmitters. The NWC, JJI and NPM signal showed ∼9 to 30 dB change in amplitude at the time of the flare [29]. Although the precursors to the giant flare of 27th August were not detected in VLF.

## 2.3 XRF020427

A wide field X-ray camera onboard BeppoSAX satellite detected an X-ray flash on April 27, 2002 at 03:48:40 UT [33]. The source, situated at a very high redshift of $z \sim 3.5$ [2], had an unusual flash profile unlikely to be an X-ray burst, it was

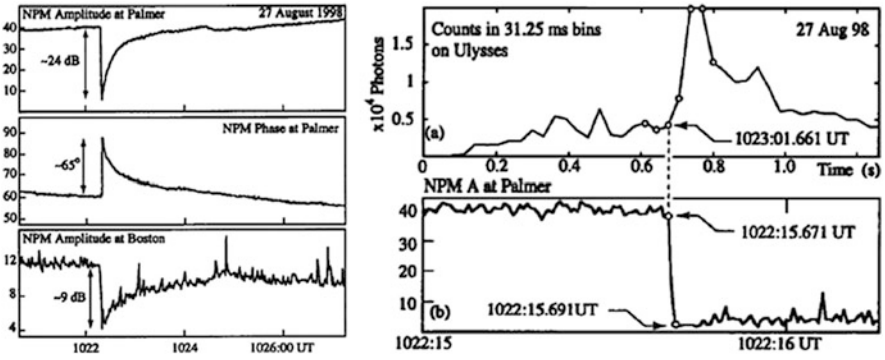



**Fig. 2** Left: Amplitude and phase of the NPM signal at Palmer and only amplitude in Boston is shown. Right: Ulysses light curve is shown with the NPM signal at Palmer [12]

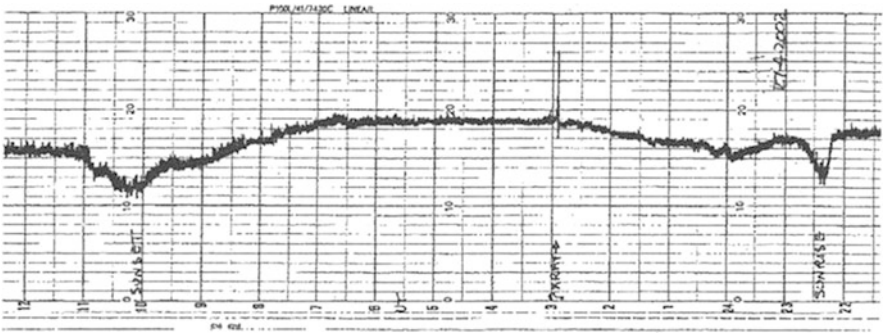


**Fig. 3** NWC signal variation over a whole day is shown in a strip chart recording. Time increases from right to left with a lag of 1 h. The disturbance could be seen clearly around 02:48 UT [9]

considered as a possible fast X-ray transient. Presence of high flux of low energy X-ray (<15 keV) in the flash produced sudden ionospheric disturbances which was detected in the NWC signal received in Perth, Australia [9]. The minute long disturbance is presented in Fig. 3. The strip chart recording did not allow to study the disturbance in finer details. It appears that the signal strength increased first and then decreased in contrast to the disturbance due to GRB830801 and SGR1900+14.

## *2.4 GRB030329*

The GRB was detected by the HETE satellite on 29 March, 2003 at 11:37:14.67 UTC. The long GRB triggered the FREGATE instrument onboard HETE in the 6–120 keV energy band [31]. Corresponding ionospheric disturbance was observed in a time signal (HBG, 75 kHz, Geneva) received in Kiel, Germany [28]. On that day two C-class flares occurred in a time difference of 2 h and the GRB occurred in between, about half an hour after the first flare. Fortunately, there was enough time for the ionosphere to relax from the effect of the flare. Figure 4 shows the double peak GRB profile and the VLF data. Sunrise, sunset time and the two flares are indicated by two downward arrows. The upward arrow indicates the disturbance due to GRB. Here also we see that signal strength increases during the disturbance. Although, double peak nature of the burst is not reflected in VLF data.

## *2.5 SGR 1806-20*

A giant flare from the SGR 1806-20 was observed on December 27, 2004 at 21:30:26 UT. The SGR, because of proximity from the Earth (only ∼15 kpc away, on the other side of the galactic center), the flare appeared to be the most brightest

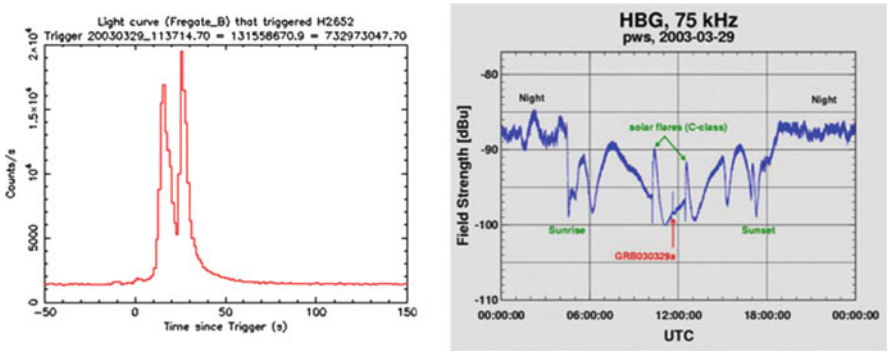



**Fig. 4** Left: HETE light curve during the event [31]. Right: VLF field strength over a full day is shown. The ionospheric disturbance due to the GRB is indicated by the upward arrow [28]

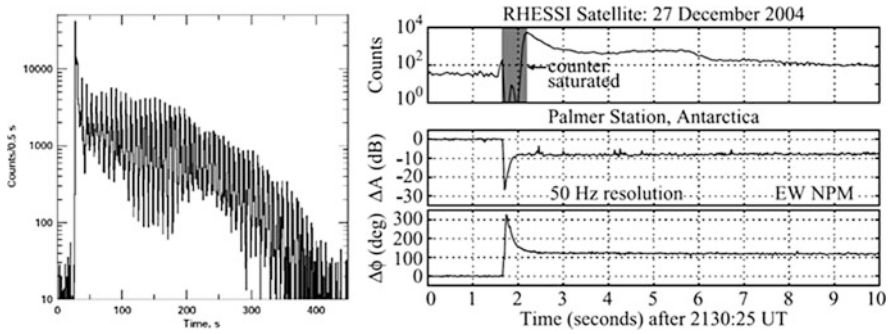



**Fig. 5** Left: Flare profile with initial spike and hard pulsating tail [11]. Right: Detectors onboard RHESSI satellite are saturated during the peak time of the flare. Change in amplitude and phase of NPM signal at Palmer [13]

X-ray source ever seen beyond the solar system. The main initial spike was followed by a tail extended for ∼380 s and oscillating at a period of 7.56 s as shown in Fig. 5 [11]. During the strong spike most of the X-ray $\gamma$-ray satellites were saturated. The gamma-ray flux was thousand times larger than the previous SGR and produced substantial amount of excess ionization in the ionosphere down to 60 km. Perturbation in the geomagnetic field was also observed over the duration of the flare. A modulated signal with 7.5 s periodicity, which is believed to be caused by the shock produced by the 'magnetar' flare, is measured by the high precision magnetometer onboard CHAMP satellite [21].

The VLF response to the giant flare was observed from many places in different VLF signals [4, 23]. In different propagation paths, various types of responses were found. Figure 5 shows NPM signal received at Palmer 10 s after the flare. About ∼26.5 dB change in amplitude and 328° change in phase was observed and it took an hour for the recovery of the signal to its normal value.

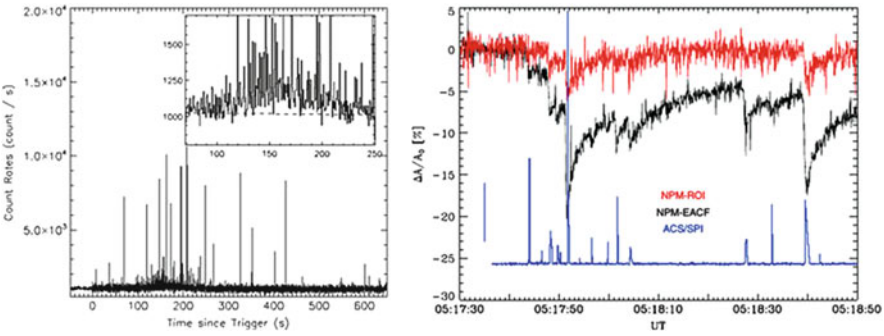



**Fig. 6** Left: Fermi GBM light curve of the SGR burst [14]. Right: The lower most curve represent the INTEGRAL SPIACS X-ray light curve. The vertical line indicates count rate of $2 \times 10^5$. The upper and middle curves are VLF response to the short bursts in two propagation paths of the SAVNET [26]

### *2.6 SGR J1550-5418*

On January 22, 2009 an anomalous X-ray Pulsar (AXP), another kind of magnetar, AXP 1E1547.0-5408 bursted into series of short $\gamma$-ray flares starting from 00:53:52 UT. The source, situated at only $\sim$10 kpc away, was initially discovered in 2008 in a relatively less active phase. But the active phase of January, 2009 was much stronger. Because of the similarity with SGR spectra the source later was renamed as SGR 1548-5418. More than 400 individual bursts were detected [14, 23] by various space based $\gamma$-ray observatories in various energy range, unlike the giant flares from the previous two SGRS i.e., a strong initial spike followed by a pulsating tail. The Fermi Gamma ray Burst Monitor (GBM) detected 286 bursts in the 8–200 keV band (Fig. 6, left). The SPIACS instruments onboard INTEGRAL satellite observed about 167 bursts above 50 keV over a period of 10 h. The peak count rate of the strong spikes vary from 30,000 to 170,000 s. Because of the large soft photon content, many of these bursts generated significant perturbation in the ionosphere. The most strongest burst occurred at 06:44:36 UT when the sub-flare point was located at 54.3°S, 14.0°E. The ionospheric disturbances were detected in VLF from various places such as, Palmer in Antarctica, Kolkata in India and by the South American VLF Network (SAVNET) [30]. VLF amplitude change corresponding to some of the not so intense spikes that occurred prior to the most intense burst is elegantly depicted in Fig. 6 along with the INTEGRAL SCIACS burst profile [26].

## 3 ICSP VLF Detections

The VLF group, working at Indian Centre for Space Physics (ICSP), Kolkata under the leadership of Prof. Sandip Kumar Chakrabarti, is involved in ionospheric studies since 2004. ICSP is continuously monitoring VTX signal (18.2 kHz) transmitted by

the Indian Navy using ICSP made indigenous single frequency VLF receiver. Except the SGR J1550-5418, ICSP receivers could not detect the other events being on the other side of the exposed hemisphere during the activity.

## *3.1 SGR J1550-5418*

During the first few hundred bursts, the sub-bursts points of the SGR were in the same hemisphere with the ICSP receiver at Salt Lake. At least 76 times detectable disturbances have been observed in the VTX signal coinciding with different satellite detection timings. With time the sub-flare point shifted and left the ICSP sky. During the strongest flare the source was over the southern American sky where the flare was observed by the SAVNET people using SOFTPAL receiver [30]. A few example of the effects of the repeated burst in VLF as recorded in Salt Lake are shown in Fig. 7 (left). The dashed lines indicate satellite detection of the burst and the dotted lines indicate onset of a VLF event. Several of these events lasted longer while others endured for few seconds only. Some more events are shown (Fig. 7, right) after background subtraction of the VLF signal. It could be seen that many a time successive events occurred even before the earlier one decayed completely [23]. The fast rise and exponential decay (FRED) feature of each of the events were recognized from the noisy VLF data above $3\sigma$ level. In order to study the impact of the individual burst and the energy deposition in the ionosphere each of these FRED type signals were fitted with a fast rise exponential decay profile (indicated by alphabets) developed by Kocevski et al. [18]:

$$F(t) = F_m(\frac{t}{t_m})^r[\frac{d}{d+r} + \frac{r}{d+r}(\frac{t}{t_m})^{(r+1)}]^{-(r+d)/(r+1)}, \quad (1)$$

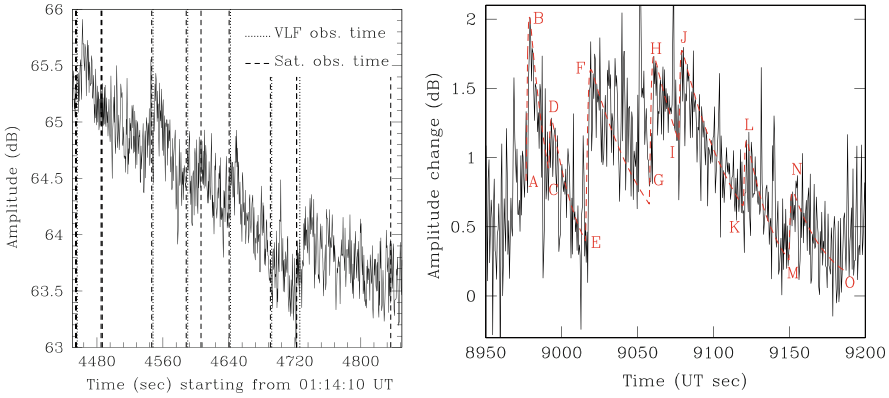



**Fig. 7** Left: VLF events associated with the SGR J15550-5418 bursts starting from 01:14:10 UT. Right: Events started from 02:29:10 UT. The FRED profile corresponding to each event is plotted in dashed line and indicated by alphabets [23]

where, each pair of alphabets indicates the time $t_m$ and the maximum flux at $t_m$ is given by $F_m$, r and d are the rising and decaying indices respectively. The FRED profile of the VLF signal indicates presence of huge flux of soft X-ray in the SGR radiation. Ionospheric changes were measured by calculating the Wait's exponential parameters [Wait], i.e., the ionospheric effective reflection height ($h'$) and the sharpness parameter $\beta$. Long Wave Propagation Capability (LWPC) code [7], which applies the earth-ionosphere waveguide mode theory, was used to calculate the VLF signal strength. The LWPC code provides one set of $h'$ and $\beta$ to fit with the observed amplitude at points marked by the alphabets in Fig. 7. This $h'$ and $\beta$ are then applied in the Wait's formula to obtain the electron density at a particular height $h$ [32]. The Wait formula is given by
$N_e(h, h', \beta) = 1.43 \times 10^{13} \exp(-0.15\, h') \exp[(\beta - 0.15)(h - h')]$, where $N_e$ is in $m^3$.

Repeating this process over the whole time range one can obtain two important information, namely, how the ionospheric reflection height changes with each of the burst and how the electron number density changes at the onset of each event. The result is shown in Fig. 8. Recurrent bombardment of the SGR increased the electron number density of different ionospheric heights. The electron density kept on increasing since the excess ion and electrons generated due to a flare did not get enough time to recombine before the next flare hits. Over the duration of 8950–9200 s the electron density at a particular height of 80 km enhanced by more than hundred times. Accordingly the lower ionospheric heights went down giving rise to enhancement in VLF signal amplitude.

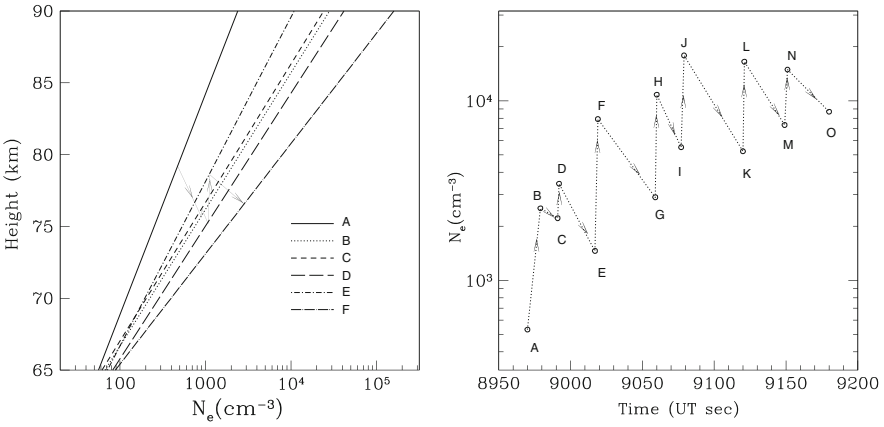



**Fig. 8** Left: Variation in electron number density at different altitudes during the time interval of 8950–9200 s. Right: Change of electron number density at the altitude of 80 km for each of the bursts [23]

### 3.2 GRB090424

The GRB090424 was detected on 24 April 2009. The GRB triggered the Swift Burst Alert Telescope (BAT) at 14:12:09 UT, the peak count rate reached ∼50,000/s in the 15–350 keV band within ∼3 s after the onset. SPIACS instrument onboard INTEGRAL satellite, the Fermi Gamma ray Burst Monitor (GBM) also detected the multi-peaked intense emission. The total fluence over ∼60 s duration of the event was $5 \times 10^{-05}$ erg/cm$^2$ [5]. Ionospheric disturbances due to this event were measured by the three receivers at ICSP, Salt Lake and Malda while recording VTX signal at the resolution of 2 Hz, 4 Hz and 1 Hz respectively [6]. Similar types of ICSP made receivers were installed in Salt Lake and Malda (10 and 200 miles away from ICSP respectively). The synchronization of all the three computers was made studying the correlation of the VTX signals at three receiving stations. Because of the similarity of the propagation paths all the signals were found to be correlated immediately after the burst for tens of seconds. VTX signal variation at three places are plotted with the X-ray light curves in Fig. 9. Salt Lake and ICSP receivers being only 10 miles away showed similar variations.

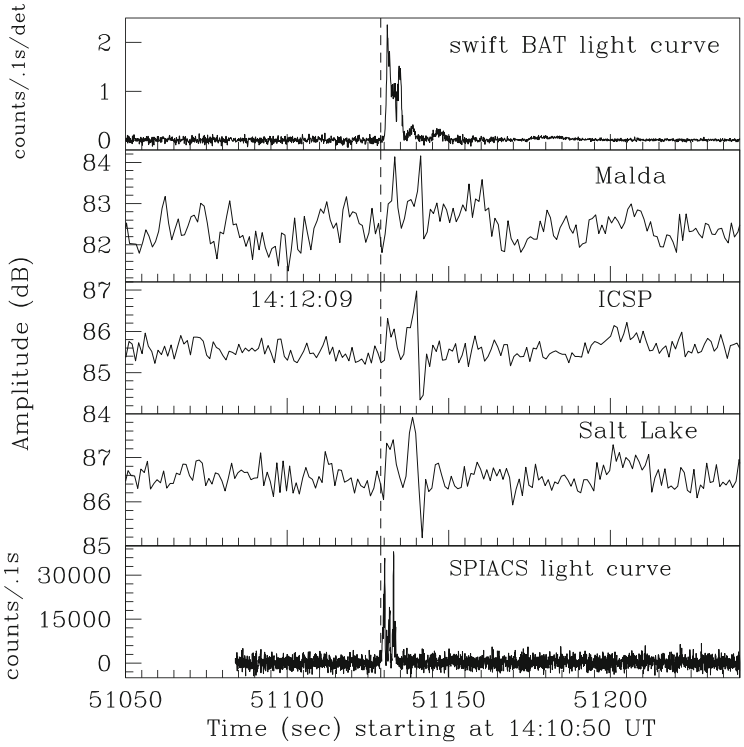



**Fig. 9** VLF response to the GRB090424 at three receiving stations are shown along with the BAT and SPIACS light curve. The dotted vertical line indicates the time of burst [5, 6]

## 4 Discussion

In this Chapter, VLF detections of high energy emissions from seven extra-terrestrial objects are discussed. The energy release during the events were so enormous that, even at a large distance, the Earth's ionosphere got affected. The giant flare of 2004 produced excess ionization six orders of magnitude higher than the normal at 60 km altitude. Any such nearby event can turn the atmosphere of the whole hemisphere facing the source into ionosphere, since the extent of ionization does not depend much on the zenith angle [3], and making it vulnerable to hostile radiation from outer space.

Various types of disturbances observed in VLF could be attributed to many factors. Firstly, different propagation paths such as, whether long or short, over the sea or land mass, East-West or West-East propagation, proximity to the magnetic equator etc. Secondly, the time of the event (presence or absence of the Sun), position of the day-night terminator. Thirdly and most importantly, soft photon content in the radiation. VLF propagation phenomena is still not well understood.

All the VLF observations were inspired by the satellite detection of very high energy events. Ionosphere may be affected even to the low energy events but VLF is sensitive to only the energetic ones, which causes substantial ionization in the lower ionosphere. A project was taken up by ICSP to search for GRB signature in the VTX-ICSP short propagation path from 2010 to 2012. More than 30 GRBs were found to have fluence in the range of $10^{-6}$–$10^{-7}$ erg/cm$^2$ and were available in the ICSP sky at the time of burst. No effect had been observed in VLF due to any of these GRBs. Other than the low fluence, another reason could be the position of the VTX transmitter ($8°23'N$, $77°45'E$) below the magnetic equator, the equatorial electro-jet is known to highly influence the equatorial short propagation path (<2000 km). Also, VTX signal is not stable. Except VTX, no other strong VLF transmitter is available in the Indian region, signal strength of NWC is not so strong and the JJI signal is too feeble.

More than three decades have passed since the first confirmed VLF discovery of an extra-terrestrial source. In the very first paper [8] it was proposed that the total energy absorbed by the ionosphere due to such an event could be calculated using a network of 'VLF burst monitors'. Also, a network is essential for the directional information. But the picture did not improve much since then. In between, only six more objects were detected in VLF. The various space borne observatories are detecting high energy radiation more efficiently in various energy bands. If the ionosphere detector is to be understood fully then more sensitive measurement techniques are needed to be developed. Up-gradation of VLF remote sensing technique with a highly sensitive receiver (with superior signal to noise ratio), powerful transmitters, and world wide network is essential. A recent publication revealed signature of the SGR J1550-5418, of the 2009 burst episode, in coherent ionospheric Doppler radar as a travelling ionospheric disturbance or TID [20]. Also, GPS based technique could be employed in such studies as GPS satellites have coverage of the whole ionosphere.

## References


1. Ananthakrishnan, S., Ramanathan, K.R.: Nature **223** (1969)
2. Bloom, J.S., et al.: Astrophys. J. **599**, 957 (2003)
3. Brown, R.T.: Nature **246** (1973)
4. Campbel, P., Hill, M.M, Howe, R., et al.: GCN 2932 (2005)
5. Cannizzo, J.K., Ukwatta, U.K., Palmer, D.M., et al.: GCN Report 221.1 (2009)
6. Chakrabarti, S.K., Mondal, S.K., Sasmal, S., et al.: Indian J. Phys. **84**(11), 1461–1466 (2010)
7. Ferguson, J.A.: Technical document 3030. Space and Naval Warfare Systems Center, San Diego (1998)
8. Fishman, G., Inan, U.S.: Nature **331**, 418–420 (1988)
9. Fishman, G., Woods, P.M., Hossfield, C., Anderson, L.: GCN 1394 (2002)
10. Hurley, K., et al.: Nature **434**, 1098–1103 (2005)
11. Hurley, K., et al.: Nature **397**, 41–43 (1999)
12. Inan, U.S., Lehtinen, N.G., et al.: Geophys. Res. Lett. **26, 22**, 3357–3360 (1999)
13. Inan, U.S., Lehtinen, N.G., Moores, R.C., et al.: Geophys. Res. Lett. **34**, L08103 (2007)
14. Kaneko, Y., Gogus, E., Kouveliotou, C., et al.: Astrophys. J. **710**, 1335 (2009)
15. Kasturirangan, K., Rao, U.R., Chakravarty, S.K., et al.: Astrophys. Space Sci. **42**, 57–62 (1976)
16. Kaufmann, L., Piazza, R., Ananthakrishnan, S.: Astrophys. Space Sci. **22**, 67–70 (1973)
17. Klebesadel, R.W., Strong, I.B., Olson, R.A.: Astrophys. J. **182**, L85 (1973)
18. Kocevski, D., Ryde, F., Liang, E.: Astrophys. J. **596**, 389 (2003)
19. Kuznetsov, A.V., Syunyaev, R.A., Terekhov, O.V., et al.: Pis'ma Astron. Zh. **13**, 1055–1060 (1987)
20. Mahrous, A.: Ann. Geophys. **35**, 345–351 (2017)
21. Mandea, M., Balasis, G.: Geophys. J. Int. **167**, 586–591 (2006)
22. Mondal, S.K., Chakrabarti, S.K.: AIP Conf. Proc. **1286**, 311 (2010)
23. Mondal, S.K., Chakrabarti, S.K., Sasmal, S.: Astrophys. Space Sci. **330**(2) (2012)
24. Palit, S., Basak, T., Mondal, S.K., Pal, S., Chakrabarti, S.K.: Atmos. Chem. Phys. **13**, 6007–6033 (2013)
25. Palit, S., Basak, T., Pal, S., Chakrabarti, S.K.: Astrophys. Space Sci. **355**, 2190 (2014)
26. Raulin, J.-P., et al.: J. Geophys. Res. Lett. Space Phys. **119**, 4758–4766 (2014)
27. Rhessi. http://hesperia.gsfc.nasa.gov/rhessi2/
28. Schnoor, P.W., Welch, D.L., Fishman, G., Price, A.: GCN 2176 (2003).
29. Tanaka, Y.T., Terasawa, T., Yoshida, M.: J. Geophys. Res. **113**, A07307 (2008)
30. Tanaka, Y.T, Raulin, J.P., Bertoni, F.B., et al., Astrophys. J. Lett. **721**, L24 (2010)
31. Vanderspek, R., et al.: Astrophys. J. **617**, 2 (2004)
32. Wait, J.R.: Proc. IRE **50**, 1624 (1962)
33. Zand, J., Reali, F., Granata, S., Lowes, P., Piro, L.: GCN GRB observation report, GCN 1383 (2002)
34. Zigman, V., Grubor, D., Sulic, D.: J. Atmos. Sol. Terr. Phys. **69**, 775 (2007)

# Study of Seismo-Ionosphere Coupling Using Perturbation in Very Low Frequency Radio Signal




**Suman Ray**

**Abstract** 'Very Low Frequency' (VLF) is one of the bands of Radio waves having frequencies lying between 3 and 30 kHz, with wavelengths of 100–10 km. It propagates through the Earth-ionosphere wave-guide which is formed by lower part of the ionosphere and upper part of Earth's surface. One of the most important application of this signal is that it could be used for predicting earthquakes. In this present article we shall mainly discuss how VLF signals could be used for predicting the seismic activities.

## 1 Introduction

Seismic events are one of the greatest natural disasters which may cause loss of lives and property damages. The physical processes leading to seismic activities are very complex. The occurrence of earthquake is connected to Earth's crustal dynamics which involves in movements of tectonic plates. The conventional way for the prediction of earthquakes is related to monitoring of crustal structure movements. However, this method has not yet yielded satisfactory results. Furthermore, this method failed to provide any short-term predictions. In the last few decades, scientists noticed that before any seismic event takes place, some disturbances in the ionosphere take place also. Thus, it is suggested that ionospheric disturbances may be used as precursors of earthquakes (e.g. [12]). In this context, the Lithosphere-Atmosphere-Ionosphere Coupling model (LAIC) has developed recently giving birth to hopes in developing the new ways in short-term earthquake prediction. In the previous attempts, developed in 1970–1980s, based on the so called physical precursors, every parameter was considered independently. But this model links different variations of geochemical, atmospheric and ionospheric parameters in

S. Ray (✉)
Gobardanga Hindu College, Gobardanga, West Bengal, India

Indian Centre for Space Physics, Kolkata, India

© Springer International Publishing AG, part of Springer Nature 2018

B. Mukhopadhyay, S. Sasmal (eds.), *Exploring the Universe: From Near Space to Extra-Galactic*, Astrophysics and Space Science Proceedings 53,
https://doi.org/10.1007/978-3-319-94607-8_46

logic chain of processes united by the common physical mechanism. This makes the process of prediction sensible and physically understandable. In support of this LAIC model, there are several evidences of having precursory effects in the 'Very Low Frequency' (VLF) radio wave signals. VLF signals propagate through the Earth-ionosphere wave-guide and hence it may be perturbed due to the ionospheric disturbances, associated with pre-seismic activities.

Scientific works regarding seismo-ionospheric perturbations started in 1960s. Among the largest earthquakes of the twentieth century is the Alaska Good Friday earthquake of 1964. It occurred on Friday, March 27, 1964. It happened at 17:36 local time (03:36 UT, 28th March) and had a magnitude M = 9.2. After this earthquake, Bolt [1] first reported possible seismo-ionospheric correlations. They used ionosonde method to find out this correlation. After that several papers have been published by Davis and Baker [5], Row [17], Yuen et al. [22] and Tanaka et al. [21]. Different workers had used different methods to find out relation between seismic events and ionospheric anomalies by using VLF signals. Gokhberg et al. [6] studied the signals received by Omega navigation transmitter (10.213.6 kHz) during 1983–1986, and they found that 250 out of 350 earthquakes with magnitude (M) greater than 4 were associated with phase and/or amplitude variations [6]. These studies on the ionospheric perturbations due to seismic events are mainly based on the anomalous variations of the phase and amplitude of the signals. In 1996, after the Kobe earthquake, Hayakawa et al. [7] (hereafter H96) introduced a new method, namely the terminator time method for earthquake prediction. They showed that both the sunrise and sunset terminators times shifted towards the nighttime a few days before the earthquake. Molchanov et al. [11] analyzed VLF signals around ten large earthquake (magnitude greater than 6) days and generally supported observations of H96. They found five cases where the terminator times were shifted a few days before the earthquake. According to them, the reasons for the absence of the terminator time shifts in the other five cases could be due to the long distance of the epicenter of the earthquakes from the propagation paths and also the larger depths of the earthquakes. This method was also examined by Clilverd et al. [4] who used the data of 6 years during 1990–1995. However, for a very few cases they found that the terminators of the VLF signals shifted before the earthquake, and in most of the cases they found no strong association between terminator time shifts and earthquakes. In a response to this conclusion, Soloviev et al. [20] performed the full-wave computation and showed that a perturbation in the lower ionosphere during day/night transmissions would exhibit a significant change in the terminator time.

Indian Centre for Space Physics has been monitoring the VLF signals from various stations to look for such ionospheric anomalies and to check if any correlations could be found among the ionospheric anomalies and the pre-seismic activities. Under the guidance of Prof. Sandip Kumar Chakrabarti, this group has already published several important publications on this topic ([2, 3, 13–16, 19], etc.). Under the leadership of Prof. Chakrabarti, this group successfully contributed to develop this subject and they are still trying to develop the subject further. In the

next section, first we shall discuss about the mechanism of LAIC model and then we shall discuss about the observational evidences of LAIC using VLF signals.

## 2 LAIC Mechanism

The Lithosphere-Atmosphere-Ionosphere Coupling model explains the possible mechanism for energy transport channels from the lithosphere to atmosphere-ionosphere. The proposed mechanism is shown in Fig. 1. In this model, several possibilities are mentioned for coupling mechanism. Among them, one possibility is that the ions are generated due to the radon emissions during the preseismic period. These ions may cause the atmospheric electric field which is generated on or near the ground surface during the preseismic period. The ionospheric anomalies may be caused by these atmospheric electric fields. Another possibility is that due to microfracturing prior to earthquakes, the positively charged holes are diffused from the focal zone to ground surface. This possibility is supported by a laboratory experiment. However there are no such observational evidence which supports the proposed possibility. In this LAIC model, it has also been proposed that the atmospheric gravity waves plays an important role to spread the pre-seismic disturbances in the ionosphere. Also there are some reports which claim rises of infrared radiation, surface latent heat flux and temperature due to pre-seismic effects. But it is difficult to explain how such anomalies disturb the ionosphere through the atmosphere.

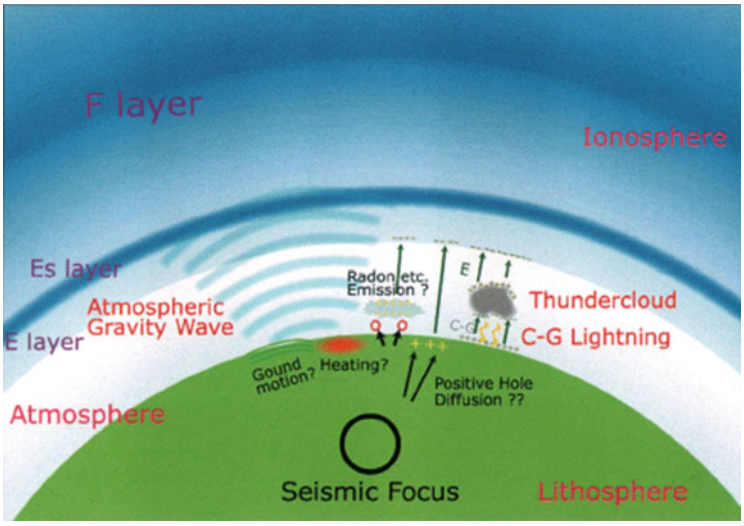



**Fig. 1** Diagram of pre-seismic lithosphere-atmosphere-ionosphere coupling model and proposed mechanism. This figure is taken from https://onlinelibrary.wiley.com/

## 3 Observational Evidences of LAIC Using VLF

In the present section, we shall mainly discuss about the observational evidences of LAIC mechanism using the VLF signal. If the LAIC mechanism is true then ionospheric disturbances must occur due to pre-seismic activities. These ionospheric anomalies could be identified by using VLF signals which propagate through the lower ionosphere. We shall now discuss several observational methods which explains how these VLF signals could be used to identify the ionospheric anomalies and hence to predict earthquakes, specially in the context of Indian sub-continent.

### *3.1 Possible Pre-seismic Effects on Night-Time VLF Signal Amplitude*

The Indian Centre for Space Physics (ICSP) has been monitoring VLF signals from various stations located in India. We have used ICSP-data to find out correlations, if any, between seismic events and ionospheric anomalies. Our study is particularly important since Indian sub-continent is an earthquake prone region and any reasonable prediction of earthquakes could save millions of lives. We have carried out year-long (2007) study of signature of VLF signal anomaly, as well as case studies of individual earthquakes. We have used the VLF signals transmitted from Indian Navy station VTX at 18.2 kHz and received at the ICSP, Kolkata. We analyzed this data to find out correlation, if any, between night time fluctuation and seismic events.

In Fig. 2, we present two typical examples of anomalous night time amplitude fluctuations, compared with normal night time amplitude variations of the VTX

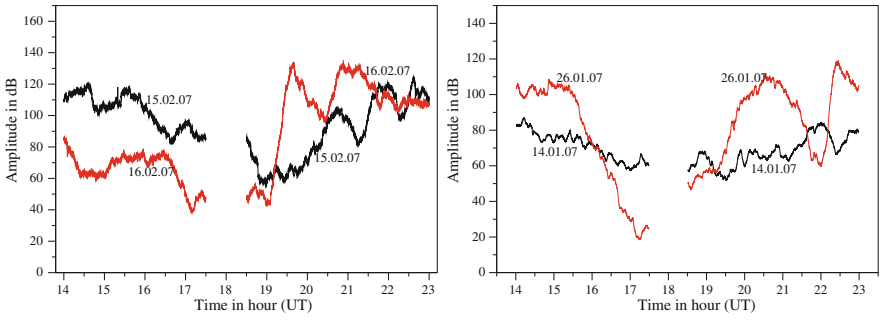



**Fig. 2** Left panel shows an example of a quiet night time (15/2/2007) data as compared with an anomalously fluctuating night time (16/2/2007) data. Here, high fluctuations in the signal amplitude on 16th February, 2007 are evident. Right panel gives another example where the quiet night time (14/01/2007) data is compared with an anomalously fluctuating night time (26/01/2007) data. Here the high fluctuations in the signal amplitude on 26th January, 2007 are evident [15]

signal as a function of time (UT). In the left panel of Fig. 2, the 'normal' data (black curve) of February 15th, 2007 with fluctuation below $1\sigma$ is compared with an 'anomalous' data (red curve) of February 16th, 2007 with higher night time fluctuation. On 19th February, 2007 there was a moderately strong earthquake ($M = 5.4$) at Southern Sumatra, Indonesia. The anomalous fluctuation of 16/2/2007 could be precursors of this earthquake. Another example is shown in the right panel of the same figure (Fig. 2) where we compare the 'normal' data (black curve) of January 14th, 2007 with an 'anomalous' data (red curve) of January 26th, 2007. On 29th January, 2007, an earthquake of magnitude 5.2 occurred at north of Camorta, Nicobar. Anomalous fluctuation of January 26th, 2007, could be the precursor of this earthquake.

To calculate night time fluctuations we used a new methodology, namely, the standard-deviation method. For the present purpose, we considered only the data of local night time which starts at 19:30 h (IST = UT + 5:30 h) and ends at 04:30 h of the next day. There are 1 h gap just prior to the midnight for maintenance purpose. We compute the mean and standard deviation ($\Sigma_i$) by using the data set on each day (denoted by $i$). This standard deviation is the measure of our signal fluctuation. To obtain the profile of mean fluctuation, it is necessary to eliminate the anomalous fluctuations from our collection of $\Sigma_i$s. This has been done by calculating mean and standard deviation $\sigma$ out of all $\Sigma_i$s eliminating those which are beyond $2\sigma$ level. By this way, we have obtained the mean fluctuations. We then subtracted the value of $\Sigma_i$s from this mean fluctuation. This would give us the deviation of night time fluctuation for each day. Also the effective magnitudes ($M_{eff_i}$) of seismic events on each day were computed. (The details of method for calculating the effective magnitudes are explained in Ray et al. [15]. Please refer this publication for detail study).

Thus we have now the deviation of the night time fluctuations of the VLF signals and the effective magnitude of the seismic events for each day. When we consider case by case basis, many of the strong quakes also show a correlation with $\Sigma_i$. In Fig. 3, we plot $\Sigma_i$s for a few days around six prominent earthquakes. (a) 18/1/2007 ($M = 5.8$) at Southern Sumatra, Indonesia; (b) 29/1/2007 ($M = 5.2$) at north of Camorta, Nicobar; (c) 11/2/2007 ($M = 5.6$) at off-coast of Sumatra; (d) 19/2/2007 ($M = 5.4$) at southern Sumatra; (e) 20/4/2007 ($M = 6.2$) at Southwestern Ryukyu Islands, Japan and (f) 24/7/2007 ($M = 5.4$) at northern Sumatra. In all these cases, we found that 3 days prior to an earthquake, $\Sigma_i$ became around 30 dB or more.

In order to see if this is true statistically for all the earthquakes, we have carried out a statistical analysis. For this, we have calculated the correlation coefficient between the deviation of the night time VLF signal amplitude and the effective magnitude of the earthquakes. In Fig. 4, we plot correlation coefficients between $\Sigma_i$ and $M_{eff_i}$. Histograms are drawn at 1 day interval. Here too, we find that the peak of the correlation is located at 3 days before the event day. The peak value is not unity, since the correlation is not true always. There are significant correlations in other nearby days also. However, we could interpret these coefficients as the probability for seismic events. Our prediction of an earthquake within 3 days is in line with pre-cursors discussed by several workers in 2–5 days [8–10, 18].

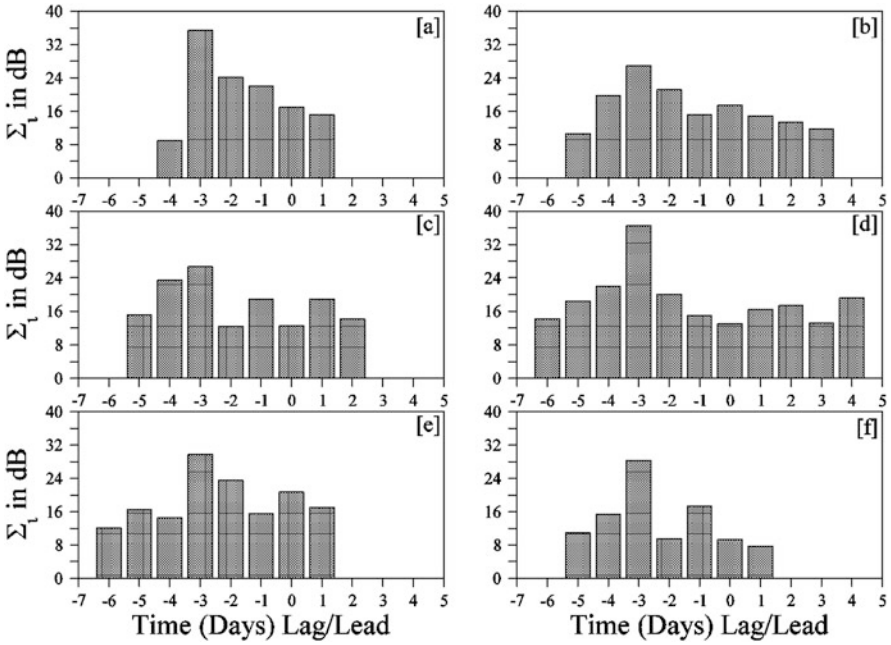



**Fig. 3** Examples of some cases where fluctuation measure $\Sigma_i$ became anomalously high 3 days prior to seismic activities. (**a**) 18/1/2007 ($M = 5.8$) at Southern Sumatra, Indonesia; (**b**) 29/1/2007 ($M = 5.2$) at north of Camorta, Nicobar; (**c**) 11/2/2007 ($M = 5.6$) at off-coast of Sumatra; (**d**) 19/2/2007 ($M = 5.4$) at southern Sumatra; (**e**) 20/4/2007 ($M = 6.2$) at Southwestern Ryukyu Islands, Japan and (**f**) 24/7/2007 ($M = 5.4$) at northern Sumatra [15]

## *3.2 Correlations Between Anomalous 'VLF-Day Length' and Seismic Events*

We have introduced a new parameter namely 'VLF-day length' defined as the time difference between sunrise terminator time (SRT) and sunset terminator time (SST) of VLF signals. After the Kobe-earthquake, Hayakawa et al. [7] showed that the terminators of the VLF signals are shifted towards night time before earthquake. Later this was supported by several other workers ([11], etc.). If it really happens then it will increase VLF-day length. We have carried out the year-long (2008) statistical analysis as well as the case-by-case studies to find out correlations, if any, between anomalous 'VLF-day length' and earthquakes.

We now present results of analysis of VLF signals transmitted from NWC (latitude 21.8° S, longitude 114.15° E) at 19.8 kHz and received at Salt Lake, Kolkata (latitude 22.56° N, longitude 88.4° E). We analyzed amplitude of VLF signals during 5–25th of June, 2010. During this time period, two major earthquakes of low-depth (∼10 km) and high magnitude ($M > 5$), occurred near the propagation paths of VLF signals. First one occurred on 13th of June, 2010 at Nicobar Islands,

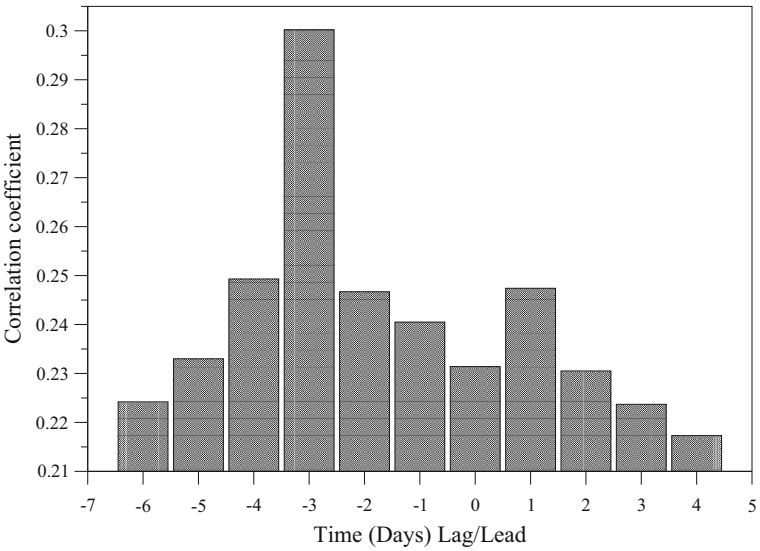



**Fig. 4** Correlation between effective magnitude $M_{eff_i}$ of the earthquake at the middle point between the transmitter and the receiver, and the standard deviation of the fluctuation measure $\Sigma_i$. Note that the correlation peaks 3 days before the event days [15]

India (latitude 7.8° N, longitude 92.0° E). Its magnitude was 5.1 (in Richter scale). The second one of magnitude 6.0 (in Richter Scale) occurred on 19th June, 2010 at Andaman Islands, India (latitude 13.4° N, longitude 93.0° E). For both of these two earthquakes, we found that the terminator times of VLF signals (mainly sunset terminator time), are shifted towards night time just 1 day before the seismic event and hence VLF-day-length, i.e., time difference between sunset terminator time and sunrise terminator time, became anomalously high 1 day before earthquakes. We claim that these were pre-cursors of the major earthquakes which occurred in Andaman and Nicobar Islands (Fig. 5).

It is interesting to study the trend of 'VLF day length' as a function of the day number. We calculate 'VLF day length' during 5th to 25th June, 2010 and plot variation in Fig. 6. Here 'solid' line represents 'VLF day-length' and 'dotted curve' represents mean value of these 'VLF day lengths'. 'Short-dashed ' and 'long-dashed' curves are for mean$\pm 2\sigma$ and mean$\pm 3\sigma$ plots. Two vertical lines indicate two different earthquake days. Note that on 12th of June, 2010 and 18th of June, 2010, the values of 'VLF day-length' crossed $3\sigma$ line. We believe that these two anomalous effects could be considered to be precursor effects of earthquakes which occurred on 13th of June, 2010 and on 19th June, 2010 respectively.

For the year-long (2008) statistical analysis we have used VLF signals collected at the Malda branch of ICSP, located in Malda, West Bengal and transmitted from VTX at 18.2 kHz. We calculate SRT and SST of VLF signals for each day and by subtracting SRT from SST we get 'VLF day length'. To obtain the mean variation

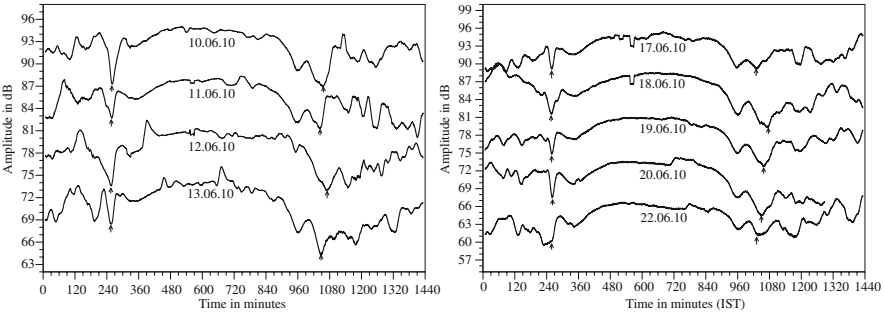



**Fig. 5** Variation of amplitude of VLF signal is plotted as a function of time in both plots. Signals are plotted in both left and right panel, around the earthquake day which occurred on 13th June, 2010 and also on 19th June, 2010, respectively. SRTs and SSTs of VLF signals are marked by 'arrow' symbols. Note that in left-panel, SST of data of 12th June, 2010 is shifted anomalously towards night time. In right-panel, an anomalous sunset terminator time shift is observed during 18–20 June, 2010, while the maximum shift occurred on 18th June, 2010

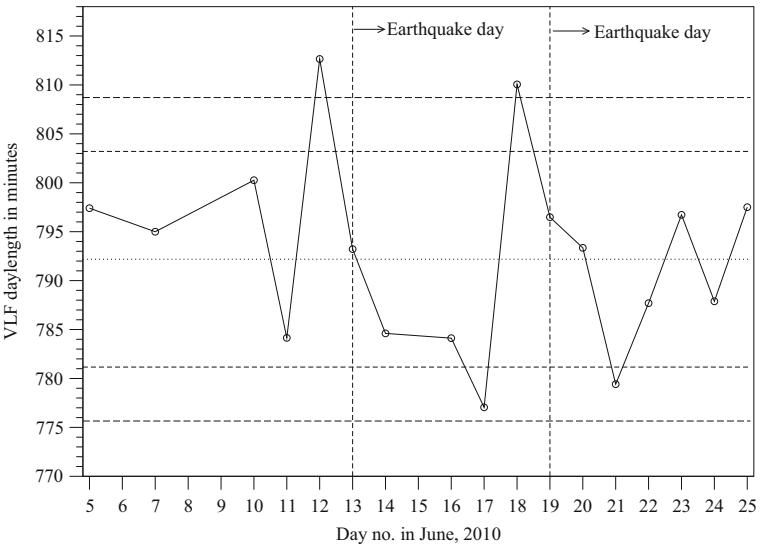



**Fig. 6** VLF day-lengths are plotted as a function of day number during 5–25 June, 2010. 'Solid' curve represents variation of 'VLF day-length'. 'Dotted' curve represents mean of these 'VLF day-length' while 'small-dashed' and 'big-dashed' curves represent mean$\pm 2\sigma$ and mean$\pm 3\sigma$ curves. Two vertical lines indicate two different earthquake days. Note that 'VLF day-lengths' of 12th June, 2010 and 'VLF day-length' of 18th June, 2010 crossed $3\sigma$ line. These could be precursor effects of earthquakes which occurred on 13th and 19th June, 2010

of this 'VLF day length' we first take the running mean of all calculated 'VLF day length' and calculate the standard deviation $\sigma$ and eliminate those which are beyond $\sigma$ level. After this, we compute the mean again. This mean is the actual mean variation of the 'VLF day length'. We then calculate the deviation of the

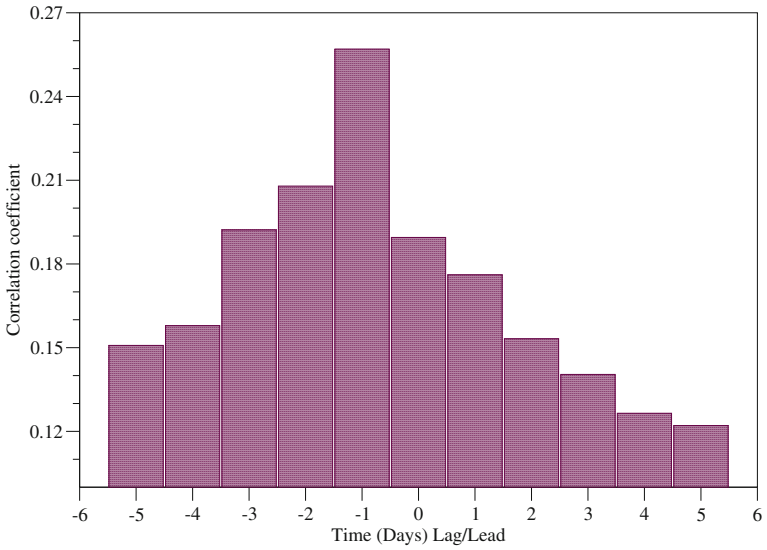



**Fig. 7** Correlation between effective magnitude of earthquake at mid-point between transmitter and receiver and variation of anomalous 'VLF day length'. Note that the correlation coefficient is highest 1 day before an earthquake

'VLF day length' from the mean variation for each day. Also, we calculate the effective magnitude of seismic activities. For this, we have followed the same process as mentioned in the previous sub-section. Thus we have now both the deviated 'VLF day length' and the effective magnitude of the earthquakes. We calculate the correlation coefficient between these two quantities and plot it in Fig. 7. We find a sharp peak 1 day before the earthquake. Thus anomalous deviation of 'VLF day length' may be used as a precursor effect of earthquake.

(Some parts of the above section are adopted from Ray et al. [14]. For details, please go through these publications.)

### *3.3 Precursory Effects in 'D-Layer Preparation Time' (DLPT) and 'D-Layer Disappearance Time' (DLDT)*

It is also reported that the 'D-layer preparation time' (DLPT) and 'D-layer disappearance time' (DLDT) become anomalous before the seismic events. This method was first introduced by Chakrabarti et al. [2, 3]. They used VLF signals transmitted from VTX and received at Kolkata. They analyzed signals for 16 months (from November 2006 to February 2008) and calculated DLPT and DLDT. This can be calculated by subtracting the morning terminator ($t_m$) from the time when the signal starts to attenuate towards $t_m$ and also by subtracting the evening terminator

($t_e$) from the time when the signal is fully recovered after sunset terminator. They also calculated correlation coefficient between this DLPT and DLDT with earthquake energy release and found that DLPT and DLDT become anomalous before earthquake. Later this method was also verified by Ray et al. [13]. They used the VLF signals for VTX-Malda propagation path. They found that the correlation coefficient between DLPT and DLDT with seismic events became high 1–2 days before the earthquake.

### *3.4 Path Dependency of Signal Anomalies due to Pre-seismic Effects*

So far, we have discussed several case-studies and year-long studies by analyzing signals for a single propagation path. Now we shall discuss results of analysis of VLF signals for multiple propagation paths.

On 18th January, 2011, at 20:23 UT, an earthquake of magnitude 7.4 occurred in Southwestern Pakistan (latitude 28°54′ N, longitude 64° E). We present results of analysis of Very Low Frequency (VLF) radio signals, received at three receiving stations located in India. We analyze VLF signal around this earthquake day and looked for possible precursory effects of this earthquake. For our analysis, we used four different VLF propagation paths. One of the important receiving locations was the Ionospheric and Earthquake Research Centre (IERC) under Indian Centre for Space Physics at Sitapur, West Bengal. These propagation paths were DHO-IERC, VTX-Pune, VTX-ICSP (Kolkata) and NWC-IERC. We observed significant shifts of 'sunrise terminator time' (SRT) for DHO-IERC/ICSP and VTX-Pune paths. For DHO-IERC path, SRT of VLF signals shifted towards night time 3 days before the earthquake day and in case of VTX-Pune path it shifted towards night time just 1 day before the earthquake day. For VTX-Kolkata path, shift of SRT was 4 days before the earthquake day, but here the shift was not so strong, somewhere between $2\sigma$ and $3\sigma$. For other two paths, namely, DHO-IERC and VTX-Pune, terminator shifts crossed $3\sigma$ line. We found no significant shifts of SRT for NWC-IERC propagation path. Higher deviation in VTX-Pune path as compared to VTX-ICSP path could be due to former's proximity to epicenter. Similarly, DHO-IERC path was over the epicenter while that of NWC-IERC path was away from the epicenter. This could be a reason why the effect in DHO-IERC path was stronger than that in NWC-IERC path. In Fig. 8, we have shown the propagation paths of VLF signals which we have analyzed along with the epicenter of the earthquake.

(In this section we have mainly summarized the results from Ray et al. [13]. Please refer this publication for detail study.)

In Figs. 9a, b and 10a, b we have plotted the behavior of the SRT as a function of day number around the earthquake day.

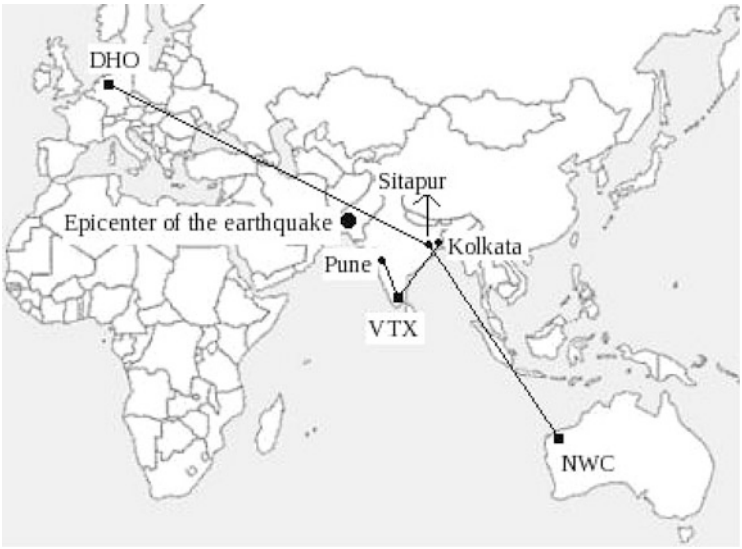



**Fig. 8** VLF propagation paths and the epicenter of the Pakistan earthquake considered for analysis. Transmitters and receivers are marked with filled squares and small filled circles respectively. The epicenter of the earthquake is marked by a large filled circle

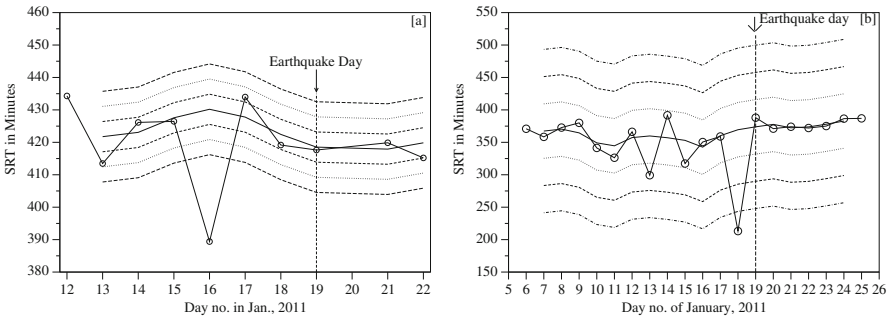



**Fig. 9** (**a**) SRTs of VLF signals for DHO-IERC propagation path are plotted as a function of day number. SRTs are marked by open circles connected with a solid line. Mean value of SRT is plotted as a solid line. Dotted and dashed curves represent $2\sigma$ and $3\sigma$ lines, respectively. Vertical dashed line is plotted to indicate the earthquake day. Note that SRT crossed $3\sigma$ line 3 days before the earthquake. (**b**) Variation of SRTs are plotted as a function of day number for VTX-Pune propagation path

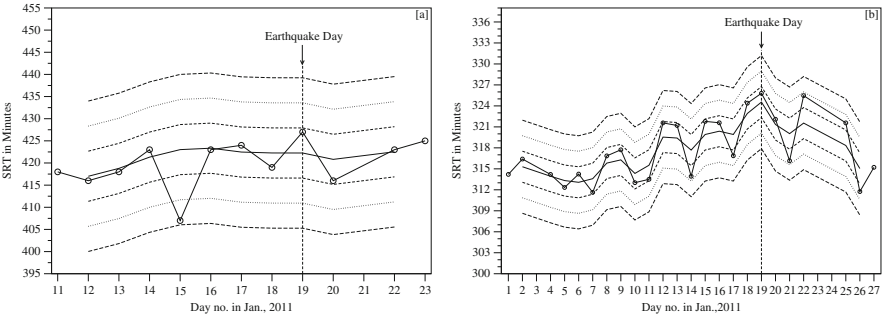



**Fig. 10** (**a**) Variation of SRTs are plotted as a function of day number for VTX-Kolkata propagation path. (**b**) Variation of SRTs are plotted as a function of day number for NWC-IERC propagation path

## 4 Summary

We have presented several types of VLF signal anomalies due to pre-seismic effects. These precursory effects in the signal amplitude associated with ionospheric anomalies due to pre-seismic activities may be considered as the observational evidences of 'Lithosphere Atmosphere Ionosphere Coupling' (LAIC) mechanism. We found several methods namely 'night time fluctuation', 'anomalous VLF day-length', 'DLPT and DLDT' to be effective for predicting seismic events by using VLF signals. We compared the effects of Pakistan-earthquake (that occurred on 18th January, 2011) in four paths and found very exciting results. We find, in particular, that anomalous terminator shifts are observed if distance of epicenter of earthquake and midpoint of the propagation path is lower and if this distance is very high then no significant shift could be observed for that particular path. This study indicates that it may be possible to predict the future location of the earthquake by analyzing the VLF signals for multiple propagation paths. For this simultaneous observations from several receivers and transmitters would be required.

## References

1. Bolt, B.A.: Nature **202**, 1095–1096 (1964)
2. Chakrabarti, S., Sasmal, S., Saha, M., Khan, M., Bhowmik, D., Chakrabarti, S.K.: Indian J. Phys. **81**, 531–538 (2007)
3. Chakrabarti, S.K., Sasmal, S., Chakrabarti S.K.: Nat. Haz. Earth. Sys. Sc. **10**, 1751–1757 (2010)
4. Clilverd, M.A., Rodger, C.J., Thomson, N.R.: J. Geophys. Res. **104**(A12), 28171–28179 (1999)
5. Davis, K., Baker, D.M.: J. Geophysical Res. **70**, 2251–2253 (1965)
6. Gokhberg, M.B., Gufeld, I.L., Rozhnoy, A.A., Marenko, V.F., Yampolsky, V.S., Ponomarev, E.A.: Phys. Earth Planet. Inter. **57**, 64–67 (1989)

7. Hayakawa, M., Molchanov, O.A., Ondoh, T., Kawai, E.: J. Comm. Res. Lab., Tokyo **43**, 169–180 (1996)
8. Kasahara, Y., Muto, F., Hobara, Y., Hayakawa, M.: Natural Hazards Earth System Sci. **10**, 581–588 (2010)
9. Maekawa, S., Horie T., Yamanuchi, T., Sawaya, T., Ishikawa, M., Hayakawa, M., Sasaki, H.: Ann. Geophys. **24**, 2219–2225 (2006)
10. Molchanov, O.A., Hayakawa, M.: Seismo-Electromagnetics and Related Phenomena: History and Latest Results, p. 189. TERRAPUB, Tokyo (2008)
11. Molchanov, O.A., Hayakawa, M., Ondoh, T., Kawai, E.: Phys. Earth Planet. Inter. **105**, 239–248 (1998)
12. Pulinets, S.A., Boyarchuk, K.A.: Ionospheric Precursors of Earthquakes, p. 316. Springer, Berlin (2004)
13. Ray, S., Chakrabarti, S.K.: Nat. Hazards Earth Syst. Sci. **13**, 1501–1506 (2013)
14. Ray, S., Chakrabarti, S.K., Sasmal, S., Choudhury, A.K.: AIP Conf. Proc. **1286**, 298–308 (2010)
15. Ray, S., Chakrabarti, S.K., Mondal, S.K., Sasmal, S.: Nat. Hazards Earth Syst. Sci. **11**, 2699–2704 (2011)
16. Ray, S., Chakrabarti, S.K., Sasmal, S.: Indian J. Phys. **86**(2), 85–88 (2012)
17. Row, R.V.: J. Geophys. Res. **72**, 1599–1610 (1967)
18. Rozhnoi, A., Solovieva, M.S., Molchanov, O.A., Hayakawa, M.: Phys. Chem. Earth **29**, 589–598 (2004)
19. Sasmal, S., Chakrabarti, S.K.: Nat. Hazards Earth Syst. Sci. **9**, 1403–1408 (2009)
20. Soloviev, O.V., Hayakawa, M., Ivanov, V.I., Molchanov O.A.: Phys. Chem. Earth **29**, 639647 (2004)
21. Tanaka, T., Ichinose, T., Okuzawa. T., Shibata, T., Sato, Y., Nagasawa., C., Ogawa, T.: J. Atmos Terr. Phys. **46**, 233–245 (1984)
22. Yuen, P.C., Weaver, P.F., Suzuki, R.K., Furumoto, A.S.: J. Geophys. Res. **74**(9), 2256–2264 (1969)

# Pre- and Co-seismic Irregularities in Ionosphere and Troposphere and Precursory Studies with Various Techniques




**Soujan Ghosh**

**Abstract** Earthquake is a very complex and multiparametric process. Earthquake occurrence is related to the earth's tectonic structure and crustal dynamics. The net energy released during an earthquake causes some irregularities at the different layers of the atmosphere. In this review work, we choose a complete different approach to discuss about the seismic mechanism and associated significant thermal, mechanical and electrical perturbation in ionospheric and tropospheric layers through the so-called Lithosphere-Atmosphere-Ionosphere Coupling (LAIC). The thermal, VLF, and critical frequency anomalies are analyzed as the tools respectively to probe the tropospheric, lower ionospheric and upper ionospheric perturbations. Respective data collected from different satellites and ground based receivers are analysed and the results are presented here.

## 1 Pre- and Co-seismic Irregularities in Ionosphere

### *1.1 Ionospheric D-Layer Irregularities and Modeling*

The study and existence of pre- and co-seismic irregularities in sub-ionospheric VLF signal has been established long ago through various works [2, 6–9, 16–22, 24, 27, 28, 41–44, 46, 47, 51, 52]. Several theories have been suggested for possible Lithosphere-Atmosphere-Ionosphere Coupling (LAIC) mechanism which is responsible for such anomalies [26, 32, 34]. There are various channels through which such coupling mechanism can happen such as electromagnetic channel, chemical channel, thermal channel, gravity wave channel, etc. [34]. It has been found that irrespective of the channel through which such coupling processes happen, the anomalies become evident from the received VLF signal amplitude/phase almost 0–4 days prior to the main event [6–8, 30, 41–44, 50–52]. Such anomalies in

S. Ghosh (✉)
Indian Centre for Space Physics, Kolkata, India

© Springer International Publishing AG, part of Springer Nature 2018

B. Mukhopadhyay, S. Sasmal (eds.), *Exploring the Universe: From Near Space to Extra-Galactic*, Astrophysics and Space Science Proceedings 53,
https://doi.org/10.1007/978-3-319-94607-8_47

VLF signal include shift of Sunrise/Sunset Terminator Time(s) (SRT/SST) towards nighttime thereby increasing overall daylength [20, 21], unusual enhancements of D-Layer Preparation Time (DLPT) and D-Layer Disappearance Time (DLDT) [7, 8, 51], unusual nighttime fluctuations (both positive and negative) before the earthquake [43, 44], etc. The effects of a particular earthquake on different VLF propagation paths have been presented in [41, 52]. We tried to find the effects of two different earthquakes on a single propagation path. Our primary focus is to reproduce the trend of VLF signal variation during the earthquake days: both before and after the main event. For this study, we have chosen JJI-IERC propagation path and the two earthquakes are 2011 Honsu earthquake ($M = 9.0$) and 2015 Nepal earthquake ($M = 7.3$). The Honsu earthquake is located near the transmitter end (JJI) whereas the Nepal earthquake is at the receiver end (IERC). For both the earthquakes the signal receiving location is within the preparation zone as prescribed by Dobrovolsky [11]. We considered an *'effective'* ionospheric condition defined by the parameters $h'_{eff}$ (effective ionospheric reflection height) and $\beta_{eff}$ (effective steepness parameter). These parameter values were then fed into the RANGE subprogram of the well known Long Wavelength Propagation Capability (LWPC) code [12] to obtain the VLF signal amplitude at that instant. The same process was repeated over a definite time interval around SRT to obtain the desired signal variation for a single day. Finally, the whole method was repeated to reproduce the trend of signal for few days both before and after the EQ days. We also calculated the electron density profile from the well known Wait's formula [57, 58].

### 1.1.1 Observation of VLF Signal

We have used the VLF data recorded by the SoftPAL (Software Phase and Amplitude Logger) VLF antenna/receiver system. We used electric field antenna coupled with pre-amplifier and service unit. The service unit provides the electrical power to the pre-amplifier and the Global Positioning System (GPS) unit. The data are being stored by a USB dongle and Lab-chart software with a time stamped by the GPS unit.

### 1.1.2 Numerical Simulation of Lower Ionospheric Parameters

To regenerate the VLF signal observed during both the earthquakes we coupled our observational data of VLF signal amplitude with the LWPC code [12]. The JJI-IERC propagation path is a typical example of mid-latitude path (22.5°N to 32°N), where it is justified to neglect the latitude variation of D-region ionospheric characteristics. Conversely, this path is significantly extended over longitude (87°E to 130°E). Hence, a notable contrast of solar irradiation induced net D-region ionization and electron content are present over the entire path, especially during sunrise and sunset terminator movements across it. To accommodate all these dynamic path variations of ionosphere using the Wait's exponential ionospheric model, we replace it with a

dynamic mean D-region ionospheric variation and accordingly it is represented by a set of $h'_{eff}$ and $\beta_{eff}$.

### 1.1.3 Possible VLF Anomalies During Seismic Events

The observed and simulated temporal variation of VLF-SRTs during both Honsu and Nepal earthquake are presented in the following figures. In Fig. 1a, b, VLF signal amplitude as observed from IERC as a function of time starting from 04:00:00 to 06:00:00 IST and corresponding simulated amplitude for the same time period for Honsu earthquake are presented. The gray curve indicates earthquake day whereas the black curves indicate the signal on normal days for both observation and simulation respectively. The arrows indicate corresponding VLF-SRTs. It can be clearly found that the SRTs are shifted towards nighttime and reach the maxima on 11th March 2011, i.e., the Honsu EQ day which satisfies our observation. The net shift of VLF-SRT observed on 11th March compared to 8th March (normal day) is ∼18.4 min, whereas the same obtained from simulation is ∼20.2 min.

In Fig. 2a, b the similar works for Nepal earthquake are presented. In Fig. 2a, the observational VLF signal amplitude is presented for the duration from 03:09:57 to 03:40:60 IST and in Fig. 2b the simulated counterpart of it for the same time period is presented. The VLF-SRT shift towards nighttime is more gradual in this case than Honsu earthquake and it reaches maximum on 11th May, 2015, i.e., a day before the Nepal earthquake. The net shift of VLF-SRT observed on 11th May compared to 9th May is ∼19.1 min, whereas, the same computed from simulation is ∼20.4 min. The net shift on the earthquake day, i.e. 12th May in VLF-SRT observed compared to 9th May is 16.2 min, whereas the same obtained from simulation is 16.6 min. It can be clearly seen that the shift is decreased by (19.1–16.2) = 2.9 min which indicates that the D-region ionospheric recovery processes are already initiated and

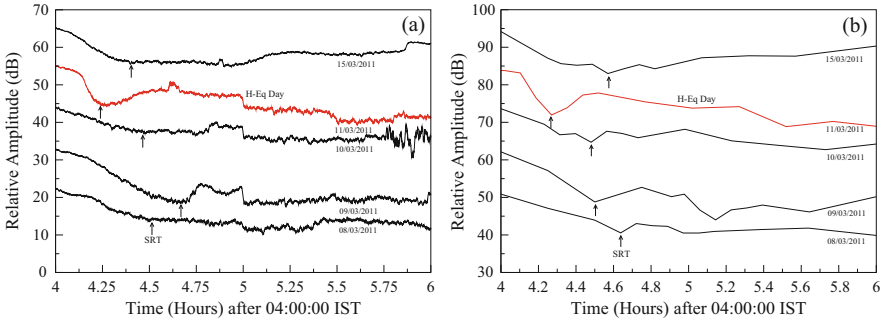



**Fig. 1** (**a**) Observed and (**b**) simulated amplitude variation around the SRTs during the Honsu EQ. Both the observed and simulated signal amplitude is plotted as a function of time in hours for an interval of 04:00:00 to 06:00:00 IST. The black curves and the red curve (Grey in print version) denotes the seismic quiet and active day respectively. The VLF-SRTs are marked with arrows. The simulated signal and especially the shift of the SRTs matches quite satisfactorily with the observed values. The shift in VLF-SRTs is maximum on the day of the Honsu EQ [15]

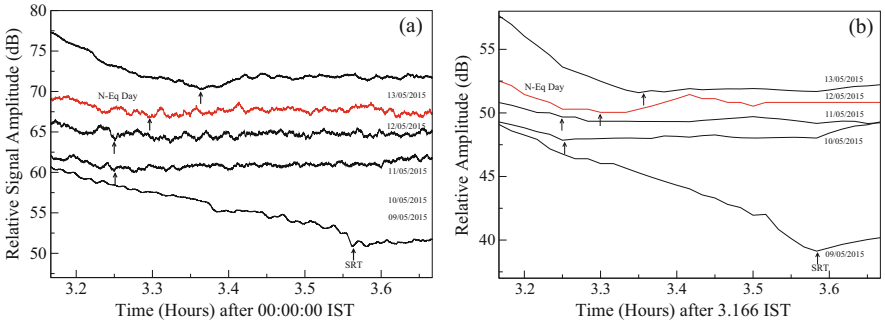



**Fig. 2** Comparison of (**a**) observed and (**b**) simulated amplitude variation around the SRTs during the Nepal EQ as a function of time in hours for 03:09:57 to 03:40:60 IST. The black curves and the red curve (Grey in print version) denotes the seismic quiet and active day respectively. The VLF-SRTs are marked with arrows. The simulated signal and especially the shift of the SRTs matches quite satisfactorily with the observed values. The shift in VLF-SRTs is maximum on 1 day prior to the Nepal EQ [15]

the VLF-SRT has started returning to its original value right from the earthquake day. This phenomenon is in contrary with Honsu EQ case, where the same recovery mechanism has started 2–3 days after the day of earthquake (Fig. 1a, b). The possible reason behind this contradiction may be associated with the locations of the epicenters in reference to the receiving location, IERC.

In Fig. 3 altitude profile of electron densities ($N_e(h)$) in $m^{-3}$ in logarithmic scale obtained from Wait's ionospheric model at VLF-SRTs on the days on and around Honsu and Nepal earthquake respectively are presented. In Fig. 3a, the ($N_e(h)$)s are calculated at VLF-SRT of 8th March 2011, which is treated as a quiet day for Honsu EQ. The ($N_e(h)$) change is sudden from 9th March to 10th March by an amount of ∼40% at a height of 82 km and interestingly the VLF-SRT change then is comparatively higher (∼20.4 min). The ($N_e(h)$) does not change much from 11th March 2011 to 15th March 2011 possibly because a series of aftershocks took place at that time and it did not allow the ionosphere to return to the so-called quiet or unperturbed state. In Fig. 3b, the electron density profile $N_e(h)$ as a function of reflection height is presented at the time of VLF-SRT of 9th May 2015, which is treated as normal day for Nepal EQ. In a similar manner, for altitude above 80 km, the electron density decreases gradually as one approaches to the earthquake day. The value of $N_e(h)$ became minimum on 11th May. After that it started increasing and on 13th May it reaches almost the same level from where it started initially. The maximum change of $N_e(h)$ from 9th May to 11th May in around 76%.

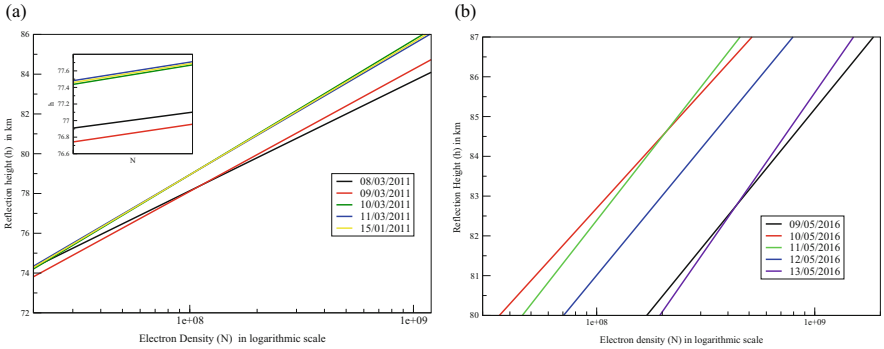



**Fig. 3** (**a**) The height profile of electron density (logarithmic scale) in $m^{-3}$ for a duration of 8th March to 11th March and 15th March, 2011 as calculated from effective ionospheric parameters and Wait's exponential formula. To understand the variation more clearly, the graphs are redrawn in the inset. (**b**) The height profile of electron density (logarithmic scale) in $m^{-3}$ for a duration of 9th May to 13th May, 2015 as calculated from effective ionospheric parameters and Wait's exponential formula. The values are calculated for the time of SRT of 9th May which is treated as a normal day. For a particular height, the electron density decreases gradually as one approaches the earthquake day. It became minimum on 11th May. After that it started increasing and on 13th May it reached almost the same level from where it started initially. The change is quite gradual rather than the Honsu EQ [15]

## *1.2 Ionospheric F-Layer Irregularities*

Pre- and Co-seismic evidence of ionospheric irregularities in D region and its study with VLF anomaly has already been discussed in the previous section. In this section irregularities associated with ionospheric F layer are discussed. To study F-layer irregularities two key parameters of Ionospheric F-layer, namely, critical frequency of $F_2$ layer and virtual height is used. The critical frequency is the highest frequency which could be reflected from ionosphere. Above this frequency, the radio wave penetrates into the upper ionosphere. The critical frequency of $F_2$ layer is denoted by $f_0F_2$. The virtual height of an ionized atmospheric layer is measured by the time interval between the transmission of a radio signal and the receipt of the return of its echo. The well-known Barbier formula establishes a direct relationship between the airglow intensity and the critical frequency of the $F_2$ layer. The variable part of this formula deals with the critical frequency and the virtual reflection height of F layer. The airglow intensity variation depends on the charge densities and types of ions which recombine to emit the radiation. As a whole, the critical frequency is associated with the charge density profile of the ionospheric layers. So it can be used as a tool to study the variabilities of the charge density profiles. LAIC mechanism predicts anomalous changes of charge density profile before seismic events. Correlations of seismicity with anomaly in F-layer were achieved using different methodologies from spectral analysis [59], satellite observation [31], equatorial ionization anomaly [48], etc. The first publications deal

with ionospheric characteristics variations as seismic precursors was Antselevich [1] study of the variations of $f_0E$ parameter before the Tashkent earthquake 1966. The peak electron density in the $F_2$ layer appears to be one of the most sensitive parameters connected to seismic activity. Spatial and temporal variation of electron concentration based on topside ionosonde data during seismic events was done by Pulinets et al. [35]. Several studies were carried out regarding the $f_0F_2$ variation by Gaivoronskaya and Zelenova [13], Pulinets et al. [36, 37], Liu et al. [25], Pulinets and Legen'ka [33], Pulinets and Boyarchuk [32], and Hobara and Parrot [23]. A variable parameter computed from Barbier equation using the $f_0F_2$ and virtual height profile and study of this parameter for a duration of ±15 days around five earthquakes in south American region and the obtained result are discussed in this section.

### 1.2.1 Data and Methodology

For entire analysis and to study F region, Jicamarca Ionosonde data is obtained from http://digisonde.com. The left side of ionogram shows a table of ionospheric characteristics scaled automatically by the ARTIST software [45]. The airglow intensity variation can be mathematically represented as,

$$airglow\ intensity \propto [f_0F_2]^2\ exp[-(z - z_0)/H].$$

Barbier [3, 4] was the first to establish a semi-empirical formula for OI 6300 Å airglow emission which is given by,

$$Q_{6300} = A\ (f_0F_2)^2\ exp[-\ (h'F - 200)/H] + B,$$

where, H is the scale height in terms of oxygen and was assumed by Barbier himself to be equal to 80 km. We only consider the variable part of this semi empirical formula and modified this equation to

$$Q_{6300} \propto [(f_0F_2)^2\ exp(h'F/H)].$$

We name the variable quantity as " F Parameter" and calculate this prior to the earthquakes to check possible correlations.

### 1.2.2 F-Parameter Anomaly During Seismic Activity

We computed F parameter for all the earthquakes under consideration using the formula mentioned above. Figure 4 shows variation of F parameter as a function of time in days for a span of 21 (10 days before and after) days around the earthquake. The thick curve is the average value of F parameter. We calculated the standard deviation from the mean value and plotted the $\pm\sigma$, $\pm2\sigma$ and $\pm3\sigma$ with the thick

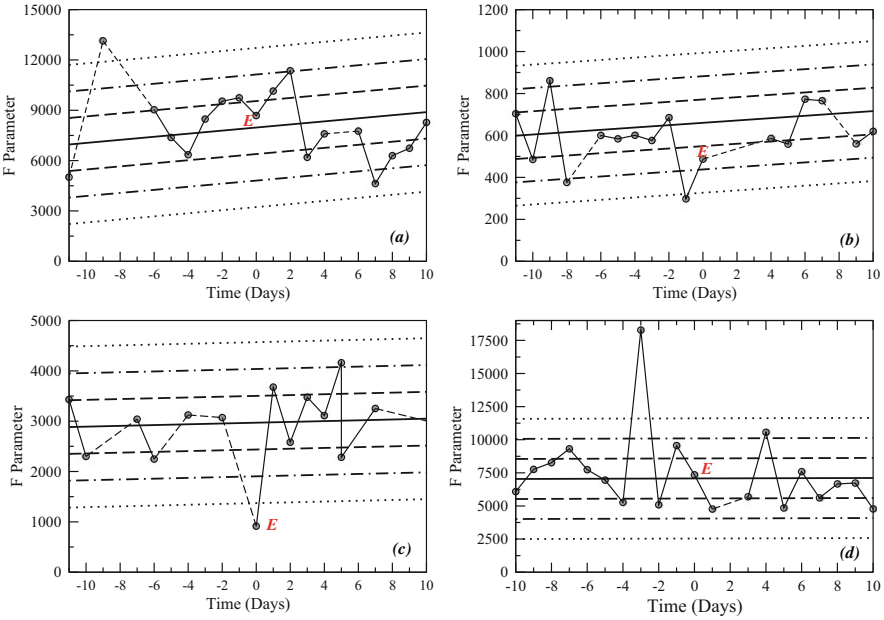



**Fig. 4** The variation of "F-Parameter" as a function of day number for the four earthquakes (**a**) 01/04/2014, (**b**) 15/08/2007, (**c**) 23/06/2001 and (**d**) 28/10/2011. The dashed, dotted-dashed and dotted curves are for $\pm\sigma$, $\pm 2\sigma$ and $\pm 3\sigma$ level respectively added with the average curve. $E$ is the day of the earthquake [14]

dashed, dotted-dashed and dotted curves respectively with the average value which shows an enhancement of the F parameter 6 days before the earthquake. The zero of the X-axis represents the day of the earthquake. It is clear that the F parameter increases anomalously with an order of more than $3\sigma$ from the average value. The zero represents the earthquake day marked as E.

Figure 4 shows an enhancement of F parameter for all the cases. For (a), (b) and (d), the F parameter suffers from an enhancement on 3–9 days before the earthquake. For the case of 28 October, 2011 (d), the maximum is quite sharp and reaches more than $7\sigma$ level. For (a) 1 April, 2014 and (b) 15 August, 2007, the enhancement is not so sharp but crosses $3\sigma$ and $2\sigma$ level respectively. For the case of (c) 23 June, 2001, the behavior of F parameter is still anomalous but rather different. The F value becomes minimum on the day of the earthquake. Before the earthquake the F value is quite higher than that for the earthquake day but the values just cross the $\sigma$ level. The value has a pre-seismic maxima on 11 days prior to the maxima but have significant secondary maxima on 2 to 5 days after the earthquake day. There are two possible reasons behind this post-seismic maxima. First, there were a series of aftershocks that occurred after this earthquake. Secondly, there was another strong earthquake with Magnitude ($M = 7.6$) occurring on 7 July, 2001. The secondary peak can be due to pre-seismic effects of the second quake as the second main shock

occurred within the next 14 days. So we believe the post-seismic shocks are due to the combined effects of these two factors.

## *1.3 Tropospheric Irregularities*

We present the effect of air ionization during and prior to large earthquakes. During and prior to large earthquakes, radon discharge from different cracks and faults is the primary source of air ionization. The newly formed ions coagulates with water molecules and drastic change in air temperature and relative humidity is observed. These changes extend up to the increment of surface latent heat flux also and can be observed though various remote sensing satellite as well as in many ground based measurements of surface air heat and other thermal parameters. We are presenting the change in relative humidity and surface latent heat flux parameters as a precursory phenomenon of Nepal 2015 earthquakes. Various kinds of precursory phenomena have been reported before large earthquakes. One of those phenomena is temperature anomaly.

Many scientists began to study this thermal anomaly with satellite data in China, Japan, India, Iran and Algeria during earthquakes [29, 39, 49, 54, 55]. Traditional seismic hazard monitoring deals with various geological parameters observed from various ground based stations. Satellite remote sensing has more advantages compared to ground based observations. High resolution spatio-temporal global remote sensing data can be obtained through modern advances in satellite technology. Continuous and stable TIR data can be obtained from satellite which makes it as a reliable data source to study thermal anomaly related to seismic events. Satellite remote sensing data can be obtained daily as well as 4-times daily, for this reason fast-changing seismic thermal anomaly can be studied using these dataset. Satellite can detect large scale as well as small scale anomaly in the active fault region. Satellite TIR data can reveal large scale linear structures and short-term (i.e., from days to weeks) variations of thermal anomalies over tectonic plate borders and active faults [53, 56]. Long term data from satellite measurement reveals thermal anomaly in seismogenic areas before medium and strong magnitude earthquake.

To study temperature anomaly before and at the time of large earthquakes, we chose two different meteorological parameters, namely, surface latent heat flux and relative humidity.

Surface latent heat flux (SLHF), a key component of the Earth's energy budget, representing the heat flux from the Earth's surface to the atmosphere has been proposed as a possible precursor of coastal earthquakes. Dey and Singh [10] have found an anomalous surface latent heat flux associated with coastal earthquakes up to 20 days prior to the earthquake. Cervone et al. [5] have developed a wavelet analysis approach for identifying peaks associated with an impending earthquake and demonstrating the atmospheric disturbances.

Surface Latent Heat Flux data obtained from satellite shows abnormal increment for coastal earthquake which is the result of the increase in surface temperature [38]. Various studies show SLHF anomaly is week on land surface due to the difference in humidity, wind speed and surface temperature. However, Qin et al. [40] found anomaly in Surface Latent Heat Flux for inland Pu'er earthquake (23.8092° N,101.15° E) on 2 June, 2007 approximately 10 days before. On the other hand Zhang et al. [60] found no significant anomalous variation for coastal earthquakes.

Cervone et al. [5] and Dey and Singh [10] studied soil moisture and linked that with Surface Latent Heat Flux anomaly before earthquake. According to Pulinets and Ouzonov [34], increase of water condensation on newly formed ions is mainly responsible for soil moisture and SLHF anomalies. In that paper authors also show that air ionization in the lithosphere-atmosphere-ionosphere coupling (LAIC) model may be responsible for the anomalous behaviour of those parameters.

### 1.3.1 SLHF and Relative Humidity Anomalies During Seismic Events

We take NOAA reanalysis data for Nepal and Honsu earthquake and analyze those data to study thermal anomaly. Here we are presenting the surface latent heat and relative humidity profile for Nepal earthquake. From Figs. 5 and 6 one can easily understand the sudden increase in Surface Latent Heat flux and Relative Humidity prior to Nepal earthquake in the epicentral region. The Surface Latent Heat flux is highest on 9th of May 2015 which is 3 days prior to the earthquake whereas the relative humidity is highest on 2nd of May 2015 which is 10 days prior to the earthquake.

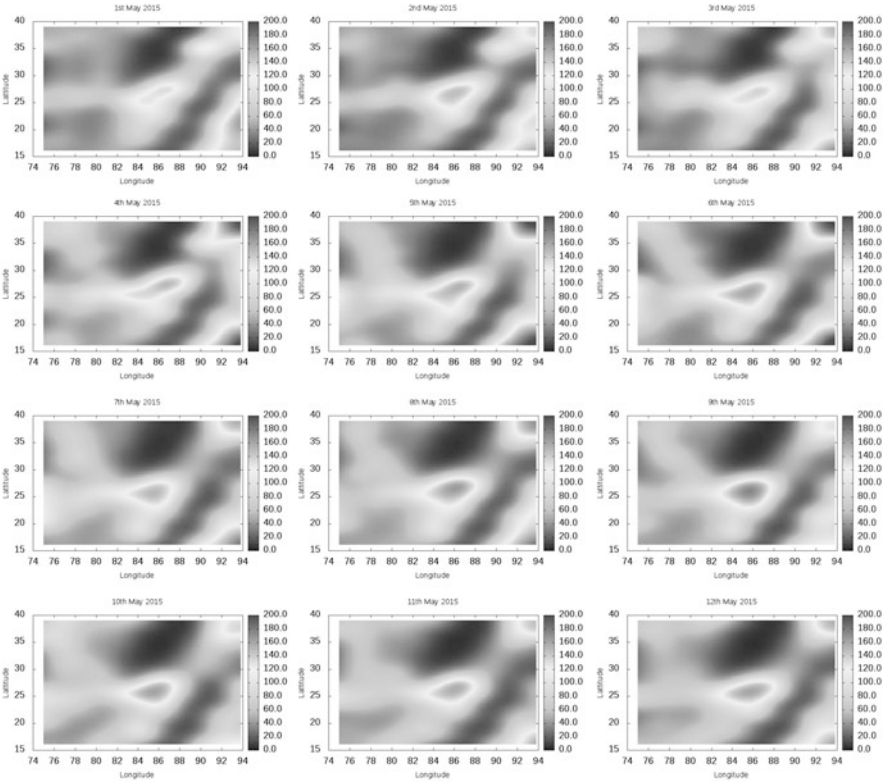



**Fig. 5** The variation of Surface Latent Heat Flux prior to Nepal Earthquake in a grid view from 1st May 2015 to 12th May 2015. On 9th May 2015 the Surface Latent Heat Flux is maximum near the epicentral region

## 2 Conclusion

The LAIC mechanism relates properties of apparently distant and distinct components of Earth system science ranging from lithosphere, lower ionospheric D-layer to upper F2 layer. Starting from the tropospheric thermal anomalies, lower ionospheric electron density variation to upper ionospheric critical frequency modulation, LAIC takes into account a wide range of geochemical and geo-physical phenomena which could be affected simultaneously. As yet, we have no clear idea of how and why exactly the lithospheric changes percolate into ionospheric changes. However, our study proves that such changes do occur. Study of physical mechanisms behind the LAIC mechanism and implementing acquired knowledge for future earthquake prediction and regular monitoring of such parameters is absolutely essential to achieve our goal. At the same time, we need to increase number of receiving stations so as to compare the anomalies from different points in order to locate the epicenter with accuracy.

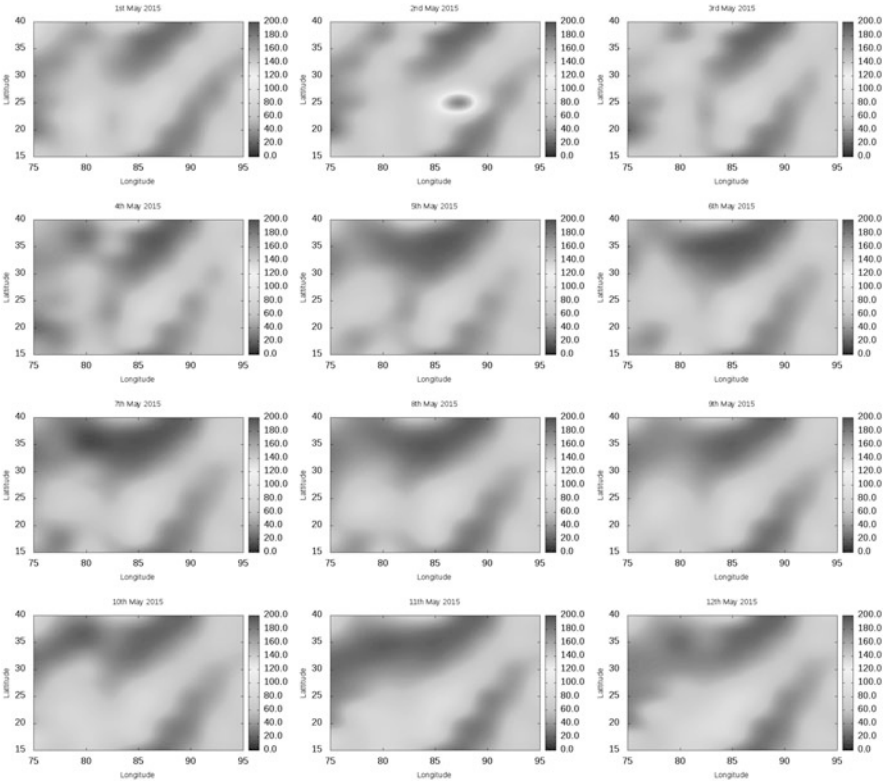



**Fig. 6** The variation of Relative Humidity prior to Nepal Earthquake in a grid view from 1st May 2015 to 12th May 2015. On 2nd May 2015 there is a sudden increase of Relative Humidity that is maximum near the epicentral region

**Acknowledgements** The author used the VLF data obtained at the Ionospheric and Earthquake Research Centre (IERC) of ICSP, Lowell Digisonde International, Prof. Bodo W. Reinisch and United States Geological Survey (USGS) for providing the ionogram and earthquake data respectively. The author also thanks to NCEP/NCAR. NCEP Reanalysis data provided by the NOAA/OAR/ESRL PSD, Boulder, Colorado, USA, from their Web site at https://www.esrl.noaa.gov/psd/~ .

## References

1. Antselevich, M.G.: FAN Publ., 187–188 (1971)
2. Baba, K., Hayakawa, M.: J. Geophys. Res. **101**, 10985–10993 (1996)
3. Barbier, D.: Compt. Rend. Acad. Sci. **245**, 1559–1561 (1957)
4. Barbier, D.: Ann. Geophys. **15**, 179–217 (1959)
5. Cervone, G., Kafatos, M., Napoletani, D., Singh, R.P.: Nat. Hazards Earth Syst. Sci. **4**, 359–374 (2004)

6. Chakrabarti, S.K., Saha, M., Khan, R., Mandal, S., Acharyya, K., Saha, R.: Indian J. Radio and Space Phys. **34**, 314–317 (2005)
7. Chakrabarti, S., Sasmal, S., Saha, M., Khan, M., Bhowmik, D., Chakrabarti, S.K.: Indian J. Phys. **81**, 531–538 (2007)
8. Chakrabarti, S.K., Sasmal, S., Chakrabarti, S.: Nat. Hazards Earth Syst. Sci. **10**, 1751–1757 (2010)
9. Clilverd, M.A., Rodger, C.J., Thomson, N.R.: J. Geophys. Res. **104**, 28171–28179 (1999)
10. Dey, S., Singh, R.: Nat. Hazards Earth Syst. Sci. **3**, 749–755 (2003)
11. Dobrovolsky, I.R., Zubkov, S.I., Myachkin, V.I. Pageoph. **117**, 1025–1044 (1979)
12. Ferguson, J.A.: Version 2.0 Technical document 3030, Space and Naval Warfare Systems Center, San Diego (1998)
13. Gaivoronskaya, T.V., Zelenova, T.I.: J. Atmos. Terr. Phys. **53**(6–7), 649–652 (1991)
14. Ghosh, S., Sasmal, S., Midya, S.K., Chakrabarti, S.K.: ojer **6**, 191–203 (2017). https://doi.org/10.4236/ojer.2017.64012
15. Ghosh, S., Chakraborty, S., Sasmal, S., Basak, T., Chakrabarti, S.K., Samanta, A.: Geomatics, natural hazards and risk (2018, under review). TGNH-2017-0087.R2
16. Gokhberg, M.B., Gufeld, I.L., Rozhnoy, A.A., Marenko, V.F.: Phys. Earth Planet. Inter. **57**, 64–67 (1989)
17. Hayakawa, M., Fujinawa, Y.: Electromagnetic Phenomena Related to Earthquake Prediction. Terra Scientific Publishing Co., Tokyo (1994)
18. Hayakawa, M., Molchanov, O.A. (eds.): Seismo-Electromagnetics: Lithosphere-Atmosphere-Ionosphere Coupling, p. 477. TERRAPUB, Tokyo (2002)
19. Hayakawa, M., Sato. H.: Ionospheric perturbations associated with earthquakes, as detected by subionospheric VLF propagation. In: Hayakawa, M., Fujinawa, Y. (eds.) Electromagnetic Phenomena Related to Earthquake Prediction, pp. 391–397. Terra Scientific Publishing Co., Tokyo (1994)
20. Hayakawa, M., Molchanov, O.A., Ondoh, T., Kawai, E.: J. Phys. Earth **44**, 413–418 (1996)
21. Hayakawa, M., Molchanov, O.A., Ondoh, T., Kawai, E.: J. Comm. Res. Lab. Tokyo **43**, 169–180 (1996)
22. Hayakawa, M., Ohta, K., Nickolaenko, A.P., Ando, Y.: Ann. Geophys. **23**, 1335–1346 (2005)
23. Hobara, Y., Parrot, M.: J. Atmos. Sol.-Terr. Phys. **67**, 677–685 (2005)
24. Horie, T., Maekawa, S., Yamauchi, T., Hayakawa, M.: Int. J. Remote Sens. **28**, 3133–3139 (2007)
25. Liu, J.Y., Chen, Y.I., Pulinets, S.A., Tsai, Y.B., Chuo, Y.J.: Geophys. Res. Lett. **27**, 3113–3116 (2000)
26. Molchanov, O.A.: Electromagnetic Phenomena Associated with Earthquakes, pp. 255–279. Transworld Research Network, Trivandrum (2009)
27. Molchanov, O.A., Hayakawa, M.: J. Geophys. Res. **103**, 17489–17504 (1998)
28. Molchanov, O.A., Hayakawa, M., Ondoh, T., Kawai, E.: Phys. Earth Planet. Inter. **105**, 239–248 (1998)
29. Ouzounov, D., Freund, F.: Adv. Space Res. **33**, 268–273 (2004)
30. Pal, P., Sasmal, S., Chakrabarti, S.K.: Geomatics, natural hazards and risk (2017). https://doi.org/10.1080/19475705.2016.1161666
31. Pulinets, S.A.: Adv. Space Res. **21**, 455–458 (1998)
32. Pulinets, S.A., Boyarchuk, K.A.: Ionospheric Precursors of Earthquakes, p. 315. Springer, Berlin (2004)
33. Pulinets, S.A., Legen'ka, A.D.: Cosm. Res. **41**(3), 1–10 (2003)
34. Pulinets, S., Ouzonov, D.: J. of Asian Earth Sciences **41**, 371–381 (2011)
35. Pulinets, S.A., Legen'ka, A.D., Karpachev, A.T., Kochenova, N.A., Fligel, M.D., Migulin, V.V., Oraevsky, V.N.: IZMIRAN **34a**(981), 25 (1991)
36. Pulinets, S.A., Kim, V.P., Hegai, V.V., Depuev, V.K., Radicella, S.M.: Geophys. Res. Let. **25**, 4143–4136 (1998)
37. Pulinets, S.A., Boyarchuk, K.A., Lomonosov, A.M., Khegai, V.V., Liu, J.Y.: Geomag. Aeron. **42**, 508–513 (2002)

38. Pulinets, S.A., Ouzounov, D., Karelin, A.V., Boyarchuk, K.A., Pokhmelnykh, L.A.: Phys. Chem. Earth **31**, 143–153 (2006)
39. Qiang, Z., Xiudeng, X., Changgong, D.: Chinese Sci. Bull. **35**(17), 1324–1327 (1990)
40. Qin, K., Wu, L.X., Ouyang, X.Y., Shen, X.H., Zheng, S.: Adv. Space Res. **53**, 266–271 (2014)
41. Ray, S., Chakrabarti, S.K.: Nat. Hazards Earth Syst. Sci. **13**, 1501–1506 (2013)
42. Ray, S., Chakrabarti, S.K., Sasmal, S., Choudhury, A.K.: AIP Conf. Proc. **1286**, 298–308 (2010)
43. Ray, S., Chakrabarti, S.K., Mondal, S.K., Sasmal. S.: Nat. Hazards Earth Syst. Sci. **11**, 2699–2704 (2011)
44. Ray, S., Chakrabarti, S.K., Sasmal, S.: Indian J. Phys. **86**(2), 85–88 (2012)
45. Reinisch, B.W., Galkin, I.A.: Earth Planets Space **63**(4), 377–381 (2011)
46. Rodger, C.J., Thomson, N.R., Dowden, R.L.: Journal of Geo. Research **101**(A6), 13369–13378 (1996)
47. Rozhnoi, A., Molchanov, O., Solovieva, M., Gladyshev, V., Akentieva, O., Berthelier, J.J., Parrot, M., Lefeuvre, F., Biagi, P.F., Castellana, L., Hayakawa, M.: Nat. Hazards Earth Syst. Sci. **7**, 617–624 (2007)
48. Ryu, K., Lee, E., Parrot, M., Oyama, K.I.: J. Geophys Res. **119**, 4767–4785 (2014)
49. Saraf, A.K., Choudhury, S.: Int. J. Remote Sens. **26**(13), 2705–2713 (2004)
50. Sasmal, S., Chakrabarti, S.K.: Nat. Hazards Earth Syst. Sci. **9**, 1403–1408 (2009)
51. Sasmal, S., Chakrabarti, S.K.: AIP Conf. Proc. **1286**, 270–290 (2010)
52. Sasmal, S., Chakrabarti, S.K., Ray, S.: Indian J. Physics **88**(10), 1013–1019 (2014)
53. Tramutoli, V., Cuomo, V., Filizzola, C., Pergola, N., Pietrapertosa, C.: Remote Sens Environment **96**, 409–426 (2005)
54. Tronin, A.A.: Int. J. Remote Sens. **17**, 1439–1455 (1996)
55. Tronin, A.A., Hayakawa, M., Molchanov, O.A.: J. Geodyn. **33**, 519–534 (2002)
56. Tronin, A.A., Molchanov, O.A., Biagi, P.F.: Int. J. Remote Sens. **25**, 2649–2655 (2004)
57. Wait, J.R.: Electromagnetic Waves in Stratified Media. Pergamon Press, New York (1962)
58. Wait, J.R., Spies, K.P.: Characteristics of the Earth Ionosphere Waveguide for VLF Radio Waves. Technical Note 300. National Institute of Standards and Technology, Gaithersburg, MD (1964)
59. Zelenova, T.I., Legen'ka, A.I.: Earth Phys. **25**, 848–853 (1989)
60. Zhang, W., Zhao, J., Wang, W., Ren, H., Chen, L., Yan, G.: Nat. Hazards Earth Syst. Sci. **13**, 2639–2647 (2013)

# Observation and Modeling of Ionospheric Response of Annular Solar Eclipse




**Surya K. Maji**

**Abstract** The ionosphere is a part of upper atmosphere where electrons and electrically charged atoms interact with electromagnetic fields. During a solar eclipse, the Sun's photosphere is shielded by the Moon, thereby decreasing the ionizing radiation from the Sun, causing changes in electron concentration of ionosphere. This causes noticeable effects on radio wave propagation as the wave guide itself changes its shape. Here we present a brief review of ionospheric effects of solar eclipses on the D-region ionosphere in low latitude Indian region. VLF signals from two transmitters (VTX and NWC) were used to diagnose the D-region effects due to the solar eclipses. We also present the solar eclipse effects on topside ionosphere and associated plasma transport effects using the data from DEMETER satellite.

## 1 Introduction

The ionosphere, an ionized region of the atmosphere extending from an altitude of about 60 km to more than 1000 km containing electrons, ions along with neutral atoms and molecules, is a natural and gigantic detector of different terrestrial and extra-terrestrial phenomena like lightnings, earthquakes, solar flares, solar energetic particle events, solar eclipses, gamma ray bursts etc. Researchers recently used VLF (3–30 kHz) signal, an inexpensive tool for bringing out the information from the ionosphere to study it. VLF signal is a part of electromagnetic wave that can reflect from both ground and ionosphere with very low absorption, hence propagates a long distance though earth-ionosphere waveguide along a zigzag path. Within earth-ionosphere waveguide the lower boundary ground is fixed for particular propagation path but the upper boundary is ionosphere which is not static, it changes its shape as the ionization changes. As VLF signals reflect from the ionosphere, it carries the information about the ionization and any changes occurring in ionization are

S. K. Maji (✉)
Indian Centre for Space Physics, Kolkata, India

© Springer International Publishing AG, part of Springer Nature 2018

B. Mukhopadhyay, S. Sasmal (eds.), *Exploring the Universe: From Near Space to Extra-Galactic*, Astrophysics and Space Science Proceedings 53,
https://doi.org/10.1007/978-3-319-94607-8_48

recorded in ground based VLF signal receiver. High energy particles and radiations from sun, extra-galactic and other sources when bombarded on the neutral atoms of the ionosphere detach electrons from neutral atoms and molecules and produce a collection of electrons, ions and neutral particles.

Also some of the electrons recombine with nearby positive ions to reproduce original neutral species. Thus production and loss of electrons and ions in ionosphere take place simultaneously and continuously. In equilibrium conditions, the number density of electrons and negative ions collectively equals that of all the positive ions to make ionosphere electrically neutral.

The structure and dynamics of the Earth's ionosphere are subject both to large spatial and frequent temporal variations, which can be periodic as well as irregular. The different physical processes also control the ionization at different heights. The lower ionosphere (up to 100 km) is a zone in which photo chemical processes mostly by solar UV is the main influence on its formation and ionization balance. The middle ionosphere (100–170 km) marks the limit of ionization-recombination processes together with thermal and dynamic processes. The upper ionosphere, is characterized by the transfer of charged particles in plasma by ambipolar diffusion, thermospheric winds, and ionosphere-magnetosphere interactions.

Ionosphere has different layers. At night ionization mainly made by extra-galactic radiation produces F-layer (upper) and E layer (lower). Day time ionosphere is mainly controlled by solar radiation. After sunrise due to extra and strong solar radiation, an extra layer produces below E layer called D-layer, the ionization and width of which increase with the increase of solar radiation. After sunset, due to recombination of electron with ion the D-layer gradually disappears. Thus we get a regular diurnal profile in both amplitude and phase of receiving VLF signal propagating through earth-ionosphere waveguide. We have also observed a seasonal variation in diurnal profile in VLF amplitude and phase as the solar radiation on ionosphere changes throughout the year. Apart from the regular variation of the ionization, the phenomena like lightning, earthquake, geomagnetic storm, solar flare, gamma ray burst etc., produce sudden increase in ionization which can be recorded by VLF signal.

## 2 Ionospheric Effects of Solar Eclipse

Unlike sudden increase in ionization solar eclipse is a unique opportunity to study the sudden decrease in ionization. During solar eclipse solar radiation is gradually blocked partially or fully by moon resulting decrease in ionization. Nowadays of ionospheric research, great interest has been taken in the effects of solar eclipses. The regular effects of solar eclipse on ionosphere are still not fully understood. During total solar eclipse, within very short time scale when the sun is fully blocked by moon, the ionosphere tries to configure itself into state similar to a night time situation where the photo chemical activity decreases almost at the night-time levels. The solar flux first rapidly decreases, causing a cooling of the atmosphere at all heights and cessation of the ionization processes at ionospheric

heights, then it increases yielding heating and return to a standard day state. However, the movement of the eclipsed region at supersonic speed clearly differs from that of regular solar terminators at sunrise and sunset times. Due to decrease in electron concentration VLF reflection height and the rate of change in ionization with height change. Apart from transition of moon during solar eclipse the change in ionization also depends on the various factors such as geographical condition, latitude, longitude and local time. Thus adequate ionospheric measurements during solar eclipses which enable the study and understanding of dynamical processes, mechanisms and propagation at work in the ionosphere, are still lacking

## *2.1 Total Solar Eclipse of July, 2009 and VLF Effects*

ICSP organized a summer campaign from 19th to 27th July of 2009 to study the effects of the total solar eclipse of 22nd July, 2009 [1]. This total solar eclipse took place just after the sunrise time with a magnitude (the ratio of apparent size of moon to the apparent size of Sun during eclipse) of 1.026 and width of about 280 km. It was the longest in the twenty first century and the maximum duration of totality was 6 min 39 s. Here we summarize VLF observational results from the receiving station at Khukurdaha. The time span of the eclipse was 05:28:43.8 h IST (Indian Standard Time, IST = UT + 5.30 h) to 07:30:16.9 h IST, where it started nearly 21 min after the eclipse. At 06:26:3.0 h IST eclipse acquired maximum obscuration of 90.7%. The details of the receiving stations are presented in Table 1. Time span of the eclipse at VTX transmitter was 05:31:09 h IST to 07:11:51.9 h IST. The total propagation path from VTX to Khukurdaha celebrate eclipse at equivalent time with separate percentage obscuration because the eclipse season of VTX continue between the eclipse season of Khukurdaha. Data from the receiving station Khukurdaha presented in Fig. 1 with time span 06:00 IST to 08:00 IST. The lower curve pictures the quotidian behaviour (average of the day before and after the eclipse) and the upper curve pictures the quotidian behaviour on solar eclipse day at Khukurdaha. Power outage which is beyond of our control makes a gap in our data. A detail report of geomagnetic storm was submitted by the Hyderabad station (Solar Geophysical Data Book NOAA). The beginning time was 07:26 h IST on 20th July, 2009 and the storm ended at 05:26 h IST 25th July, 2009, whereas the time span of eclipse was 05:28:43.8 h IST to 07:30:16.9 h IST 22nd July 2009, i.e., the eclipse come about almost during the mid-period of the storm. This storm was not detected

**Table 1** Details of Total solar eclipse at Khukurdaha

| Receiver lat long | Eclipse coverage | Coverage dist. (km) | Sunrise (IST) | 1st cont. (IST) (A°) | Max. (IST) (A°) | 2nd cont. (IST) (A°) |
|---|---|---|---|---|---|---|
| 22°27′N | Partial | 1894 | 05:07 | 05:28:43.8 | 06:26:3.0 | 07:30:16.9 |
| 87°45′E | 90.7 | | | 04 | 17 | 31 |

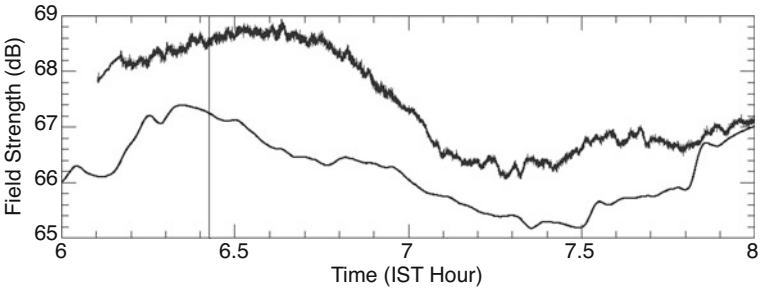



**Fig. 1** The data from 6 to 8 h (IST) at Khukurdaha. The lower curve represents normal behaviour (average of the day before and after the eclipse) and the upper curve represents diurnal behaviour on solar eclipse day at the same place. Vertical line at the time of maximum obscuration

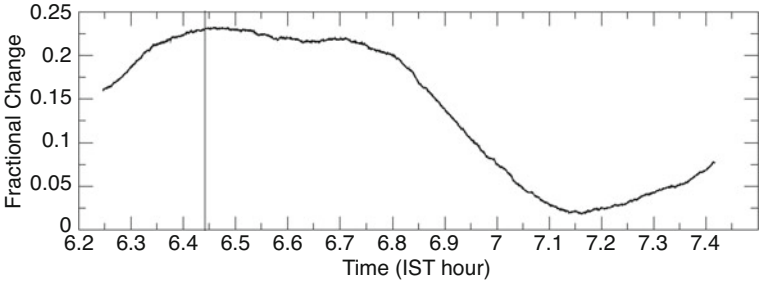



**Fig. 2** Fractional variations of the VTX (18.2 kHz) signal amplitudes with positive changes due to eclipse. The time is in Indian Standard Time (IST = UT + 5:30)

by other stations of the globe, so we concluded that the storm was not strong. It is specifying that the storm duration was about for 4 days whereas the duration of signal variation was about 2 h. It is good acceptance that the variation of signal duration with is in the duration of solar eclipse. The average amplitude and the signal amplitude of the eclipse day are denoted by $A_V(t)$ and $A_E(t)$ respectively. Data of 19th–21st and 23rd–25th of July, 2009 were used to compute the average amplitude. For the transmitter VTX, the fractional change was computed by $f(t) = [A_E(t) - A_V(t)]/A_V(t)$. The observed fractional change f(t) with time in IST presented in Fig. 2 where the vertical line at the time of maximum obscuration at the receiver site. Thus f(t) gives a mathematical measure of signal deviation on the eclipse day. Clearly, the deviation will be absent if $A_E = A_v$. The measurement of deviation in dB unit is $\triangle = 20log(1 + f)$. Due to the eclipse the changes in amplitude is positive is presented in Fig. 2. There is some residual in the primitive part of the eclipse during the construction of the D-region because the eclipse happened near to sunrise time (approximately 06:30 AM, IST). In total the signal is amplified by about 1.65 dB close to the maximum of the eclipse. In our observation this finding is consistent with the findings of [2].

## 2.2 Annular Solar Eclipse of January, 2010 and VLF Effects

An annular solar eclipse took place on 15th January, 2010 but the eclipse was partial from our receiving station Khukurdaha (22°27′N, 87°45′W). The receiving station is situated at about 400 km from the sector of total annularity. During the time of eclipse, a weak flare was in progress and was completely blocked at the places of total annularity. However, at the receiving station, the maximum coverage of the solar disk was 75%, and the flare was obstructed only partially. In this way the observation was a amalgamated effect of the eclipse and the partial occultation. This was the first such event that a solar flare was seen through lunar occultation during a partial eclipse. Here we summary the observational results of this unique event (following Maji et al. [4]). The parameters of the receiving station listed in Table 2. The last two columns give the starting and end times when the solar flare continued C-type (i.e., the flux was higher than $10^{-6}$ W/m$^2$).

The great circle path distance between transmitter and receiver is about 5700 km. Though the transmitter was far away from the eclipse belt, on the way from NWC to Khukurdaha, the 1st, 2nd and 3rd hop-points went through an eclipse coverages of 23%, 63% and 78% respectively as measured at 70 km above the ground. The whole propagation path experienced an average value of solar obscuration at the most 40% calculated using a numerical integration over the whole path. While the eclipse is in process and monitoring of VLF signal was going on, a C1.3 solar flare started at 07:22 UT (12:52 IST) and continued till 10:22 UT (15:52 IST) with a maximum at 08:41 UT (14:11 IST) which is about 15 min after the maximum obscuration of the solar disk. The peak energy flux in 1.5–12.5 keV was $1.3 \times 10^{-6}$ W/m$^2$ which is well above the detectability of ICSP's VLF antenna (typically, C1.0 flare). GOES Satellite was observing the sun unobstructed by the lunar occultation. The position of the lunar limb is superimposed on the magnetogram of the X-ray flaring region (No. 1040) at different times. Clearly, it is observed that a part of the active region (No. 1040) is blocked by the moon from the VLF receiving station. In Fig. 3, we have shown the exposed solar disk superimposed on the HINODE-XRT image of the solar flare during the solar eclipse at every 5 min (following [6]), starting from 13:50:00 IST to 14:25:00 IST (top-left to lop-right; bottom-left to bottom-right). Occultation of solar flare by the moon during the eclipse was recorded in the VLF data accordingly as a short time disturbances in the NWC signal amplitude.

**Table 2** Details of Annular eclipse event as seen from Khukurdaha

| Receiver lat long | Eclipse coverage % | 1st cont. (IST) Alt. (deg) | Max. (IST) Alt. (deg) | 2nd cont. (IST) Alt. (deg) | C 1.0 begins (IST) | C1.0 ends (IST) |
|---|---|---|---|---|---|---|
| Khukurdaha 22°27′N 87°45′E | Partial 75.1 | 12:05:30 +46 | 13:56:26 +36 | 15:28:28 +27 | 13:51:55 | 14:44:47 |

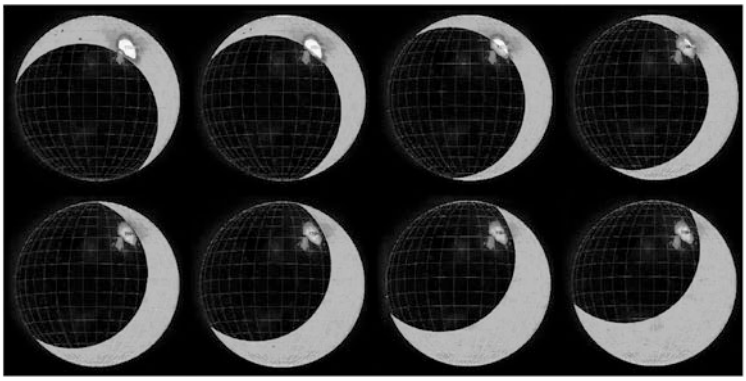


**Fig. 3** Exposed solar disk at every 5 min (from top-left to top-right; bottom-left to bottom-right), starting from 13:50:00 IST to 14:25:00 IST, are superimposed on the XRT image of the solar flare during the solar eclipse (following [6])

To analyse the effects of the eclipse the data of 3 days, from 14th January to 16th January, 2010 were considered. Normalization of VLF data had been done with the amplitudes in the midday and midnight as predicted by the LWPC code [3]. The data of these 3 days (marked) are plotted in Fig. 4. The data of 14th and 16th January are smoother as compared to that of the 15th January. The effects of the eclipse and the flare are analyzed in the following way.

In Fig. 5, they present three panels: in the top panel, they show GOES data of the solar flare in soft X-rays (upper curve) and hard X-rays (lower curve) of the 15th January, 2010 during the time of the eclipse. On the 14th and the 16th January, the solar disk was X-ray quiet at around B 1.1. Thus they subtract the average of the VLF data of the 14th and the 16th from the data of the 15th to obtain the combined effects of the flare and the eclipse. The subtracted result is shown in the middle panel. The net deviation from '0' by about $-1$ dB is due to the combined effect: a reduction due to the solar eclipse, and an enhancement due to the solar flare. In the lower panel, they present the fraction of the exposed disk of the sun as a function of time. This is to show that the VLF signal remains almost normal till the solar disk is covered by about 25%. It was noted that the observed minimum of the VLF signal is about 7 min after the maximum obscuration. This is on the larger side as compared to quantities observed for eclipse at a distance of 6000 km. This unusual shift, along with bumps in the signal profile in the recovery phase, is already an indication that the solar flare has modified the result expected from the eclipse alone. They correct the signal by removing the effects of the flare in the following way. The observed VLF signal is a composite effect that means the effect is neither due to the effect of the eclipse alone nor due to the flare alone. Maji et al. [4] separate the effects due to the solar flare and solar eclipse assuming that the composite effect is a linear superposition of the two effects. The curve (B) in Fig. 6 is the observed VLF signal same as in the middle panel of Fig. 5. Curve (C) is the flare signal received by the earth after lunar occultation centered at $t = 14.43$. The (D) is the resultant (=B-

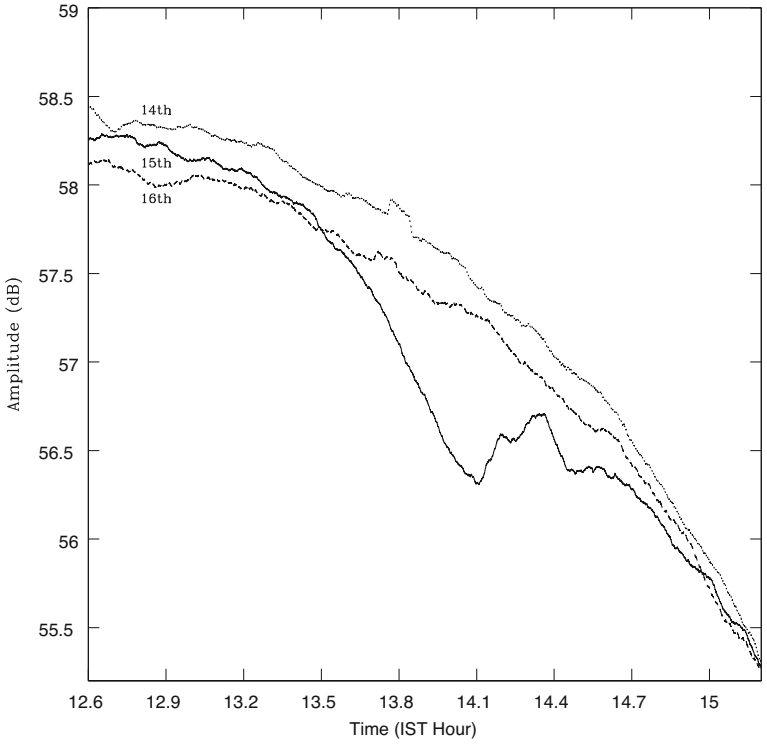



**Fig. 4** Comparison of VLF data of 15th January, 2010 with those of the 14th and the 16th (marked). The deviation from normal, smoother data in the 15th January is clear. The noise is $<0.05$ dB [4]

C) VLF amplitude which would have been expected if the flare was absent. The resultant curve became minimum only about 4 min after the maximum obscuration.

## 3 Topside Ionospheric Effects of the Annular Solar Eclipse

The response of the topside ionosphere during a solar eclipse is more complex than the bottom side ionosphere. During the solar eclipse, a decrease of electron and ion densities is observed in general in the bottom side ionosphere due to the decrease of ionizing radiation in all latitude. But the effect varies with geomagnetic latitude and time of occurrence of solar eclipse for the topside ionosphere. Maji et al. [5] studied the effects of annular solar eclipse of 2010 on the topside ionosphere using the data from DEMETER satellite over the low latitude Indian Ocean region. They used the orbits of 14th and 16th January in the vicinity of the same region to determine the reference ionosphere in the absence of solar eclipse.

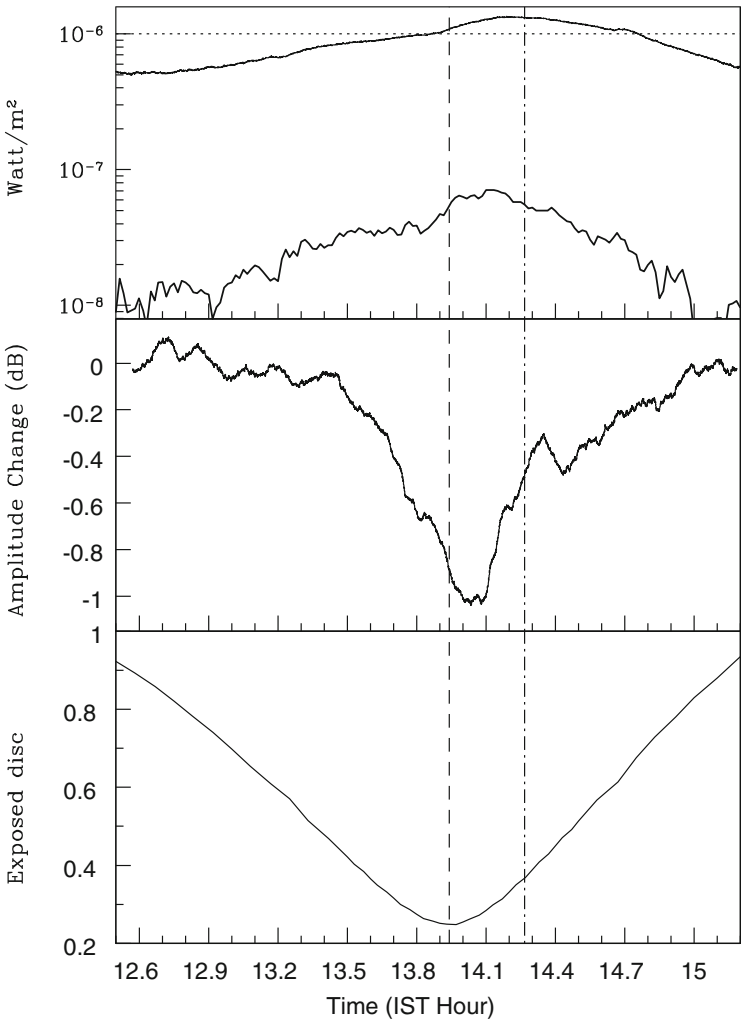



**Fig. 5** Upper panel: GOES data of the solar flares in soft X-rays (upper curve) and hard X-rays (lower curve) of 15th January, 2010. Middle panel: Difference of the average of the 14th and the 16th data from that of the eclipse day. Lower panel: Fraction of the unobstructed part of the solar disk as a function of time (IST) on the eclipse day as seen from Khukurdaha. The dashed vertical line indicates the time of the maximum eclipse and the dot-dashed vertical line indicates the time of the peak flare [4]

Figure 7 shows the path of annularity and contour lines of constant solar obscuration at the earth surface. The vertically curved lines are the tracks of the DEMETER satellite on 3 successive days from the day before and till the day after the eclipse day, i.e., 14th January, 15th January and 16th January respectively. The plotted orbit of 15th January corresponds to time 5.72–6.33 UT which crossed the

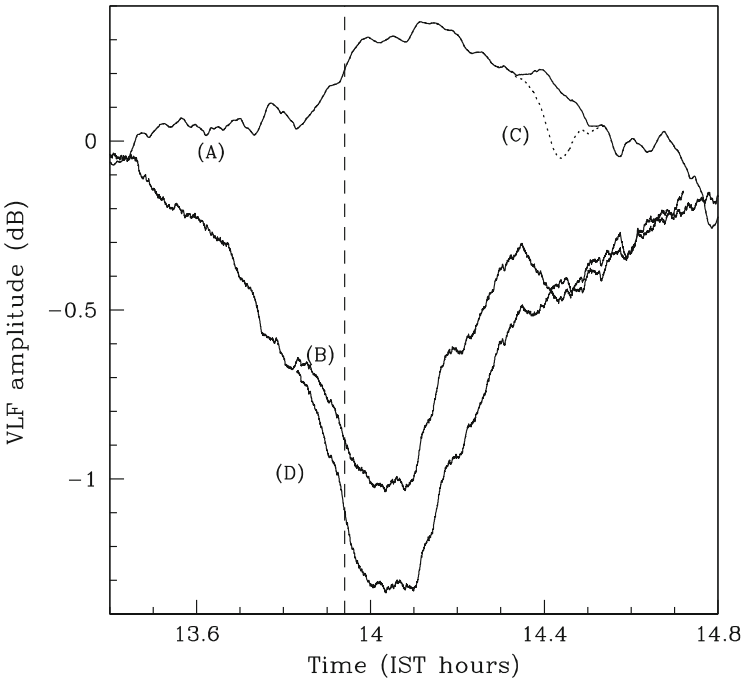



**Fig. 6** VLF signal of the eclipse after removing the effects of the flare which was partly occulted by the moon. (A) GOES flux (in log scale) in hard X-ray channel; (B) The observed VLF signal of eclipse day; (C) The model flare profile at the VLF receiving station after symmetric occultation by the lunar disk is included; (D) The expected VLF amplitude variation due to the partial eclipse alone, obtained from B-C [4, 6]

solar eclipse zone approximately ∼6 min before the time of maximum eclipse. The orbits of the 14th and 16th January are the closest available orbits to 15th January orbit as far as the time and spatial separation are concerned (see [5] for details).

Figure 8 represents variations of electron (top) and ion (bottom) densities as grey color coded line plot along the eclipse day orbit of 15th January with the orbits of 14th and 16th January as obtained by DEMETER satellite. Selected region corresponds to region from 30° N to 30° S, where eclipse day orbit experienced the solar obscuration larger than ∼20%. The orbit colours correspond to electron density number ($N_e$ in $cm^{-3}$). It is clear that the electron number density in eclipse day orbit (29641_0 denoted by 15) was lower than the reference orbits.

Solar eclipse effects have been found by subtracting the normal day data (average of 14th and 16th January data) of electron-ion densities and temperature from the eclipse day data and the same has been shown in Fig. 9 for electrons along with the solar illumination curves (dotted) along the orbit. Continuous with dotted lines are the illumination curves for the true satellite positions and dashed-dotted curves are for the corresponding conjugate points at the same height of the satellite during the same time frame of the solar eclipse. Figure 9 shows two minima approximately

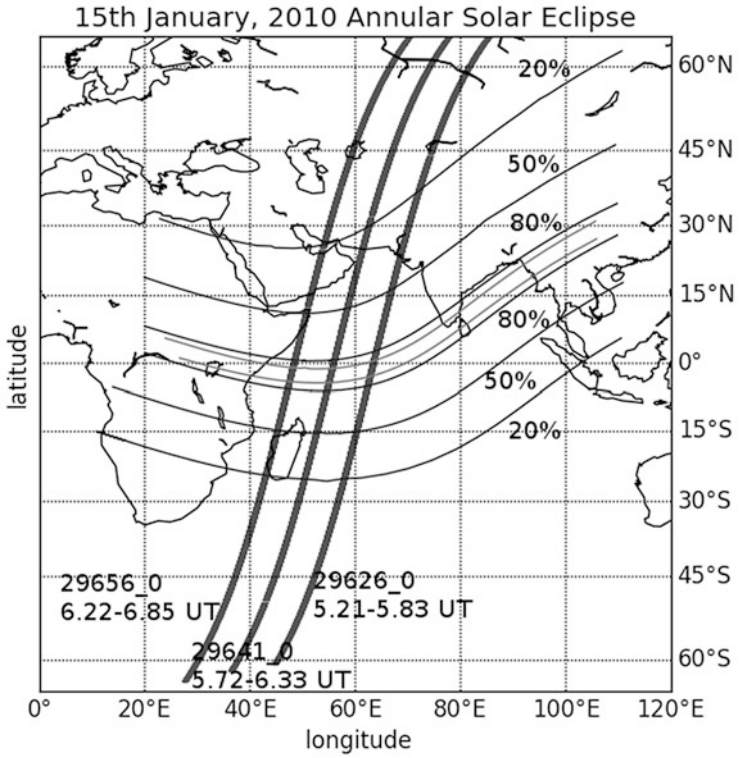



**Fig. 7** Path of annularity and partial eclipse zone of the annual solar eclipse of 15th January 2010 and the tracks of the DEMETER orbit on three successive days, including before and after the eclipse day [5]

around the $\pm 10^{\circ}$ with respect to the magnetic equator that matched well with the two solar illumination minima corresponding to conjugate point and the satellite position. The electron density was decreased by about 35% and ion density was decreased by about 40% near the geomagnetic latitude of $\pm 10^{\circ}$. Maji et al. [4] also reported that a very good correlation exists between the average solar illumination and decrease in plasma parameters ($r = 0.876$ and $r = 0.909$ for electron and ions) while electron temperature had poor correlation with the average illumination. Electron temperature did not exhibit gradual decrease with solar obscuration. Diffusive transport process could explain the observed temperature profile during the solar eclipse period.

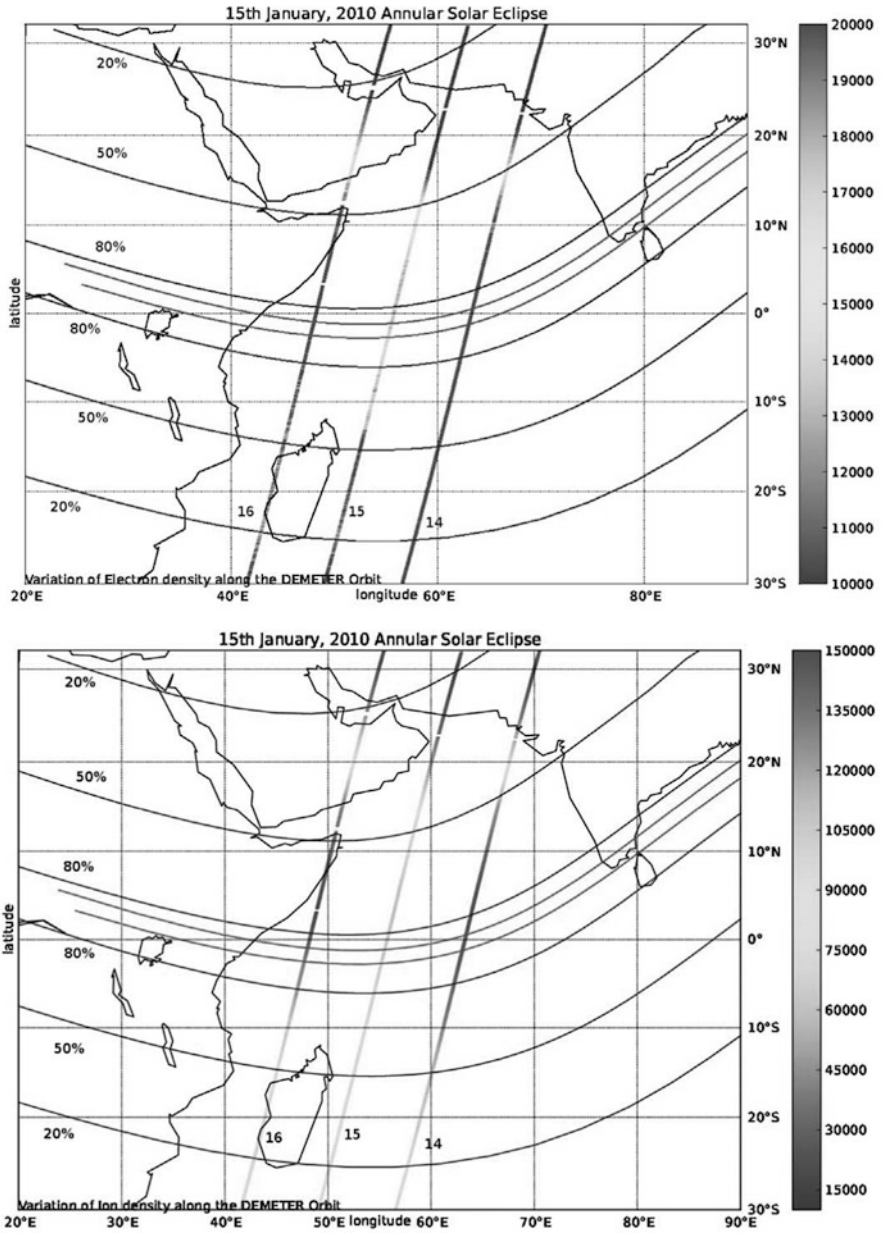



**Fig. 8** Variation of electron (top) and ion density (bottom) along the orbit of DEMETER satellite corresponding to solar eclipse of January, 2010 along with the nearest reference orbits before and after the eclipse day respectively [5]

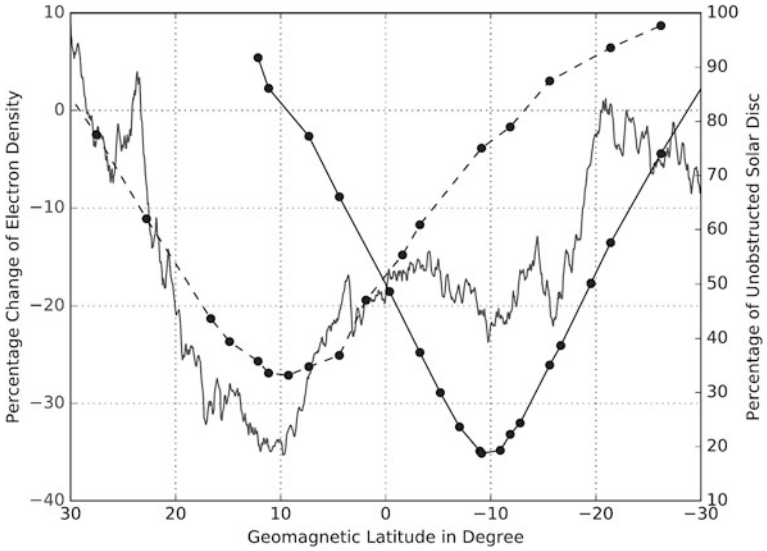



**Fig. 9** Difference of DEMETER baselines (in %) from eclipse day orbit of electron density. Variation of percentage of unobstructed solar disc (continuous with dotted line) along the DEMETER orbit and their conjugate points (dashed with dotted line) at 660 km altitude [5]

## 4 Summary

In this paper, we have reviewed the solar eclipse effects on VLF signal propagation over Indian sub-continent. Effects on VLF signals received from the same place for two solar eclipses are discussed. Simultaneous effects of solar eclipse and an occulted solar flare are also presented. We also discussed the effects of the annular solar eclipse of 2010 on topside ionosphere at an altitude of about 660 km. Changes in electron and ion density due to the eclipse followed the solar illumination variation averaged over the satellite orbit and its conjugate point. But change in electron temperature followed a complex wave-like oscillation having no detectable correlation with the average solar illumination curve during the eclipse period.

## References

1. Chakrabarti, S.K., Pal, S., Sasmal, S., Mondal, S.K., Ray, S., Basak, T., Maji, S.K., Khadka, B., Bhowmick, D., Chowdhury, A.K.: JASTP **86**, 65–70 (2012)
2. Clilverd, M.A., et al.: Radio Sci. **36**(4), 773 (2001)
3. Ferguson, J.A.: Technical document, 3030. Space and Naval Warfare Systems Center, San Diego (1998)
4. Maji, S.K., Chakrabarti, S.K., Mondal, S.K.: Earth Moon and Planets **108**, 243–251 (2012)
5. Maji, S.K., Chakrabarti, S.K., Sanki, D., Pal, S.: JASTP **159C**, 1–6 (2017)
6. Pal, S., Maji, S.K., Chakrabarti, S.K.: Planetary and Space Science **73**, 310–317 (2012)

# Space Weather: Response of the Atmosphere to Solar Activity and Its Implications for LEO Satellites Aerodynamic Drag




**Victor U. J. Nwankwo**

**Abstract** The atmosphere reflects the distinct signatures associated with long-term changes due to solar cycle, short-term changes related to solar phenomena such as solar flares, coronal mass ejections (CMEs), high solar wind streams (HSS) and corotating interaction region (CIRs), as well as changes related to latitude variation. The orbital trajectory of low Earth orbiting satellites (LEOSs) are affected accordingly, as direct consequence of the variability of atmospheric temperature (T) and density ($\rho$). Atmospheric perturbation increases drag on LEOSs leading to accelerated orbital decay. In this chapter we present a compact review of atmospheric responses to solar activity and how they impact the orbital trajectory of low Earth orbiting (LEO) satellites. This review includes the recent progress we made in the studies related to space weather effects on the ionosphere and LEO satellites trajectory.

## 1 Introduction

Space weather refers to variable and dynamic conditions in the Earth's magnetosphere and atmosphere that can affect the function and reliability of space-borne and ground-based systems and services that rely on them. This condition is caused by the collision and subsequent interaction of high-energetic charged particles and electromagnetic (EM) radiation (emitted during solar events—solar wind streams, coronal mass ejections (CMEs), solar flares etc.) with the Earth's magnetosphere. Interplanetary magnetic fields (IMF)fluctuation, shock waves, solar particle events (SPEs), relativistic electron precipitation events, geomagnetic storms and magnetospheric substorms etc. have been observed as a consequence of such interaction [e.g., 16, 20, 38]. The atmosphere respond to this solar-induced magnetospheric changes through magnetosphere-ionosphere coupling. Atmospheric responses manifest as fluctuation

V. U. J. Nwankwo (✉)
Department of Physics, Anchor University, Lagos, Nigeria
e-mail: vnwankwo@aul.edu.ng

© Springer International Publishing AG, part of Springer Nature 2018

B. Mukhopadhyay, S. Sasmal (eds.), *Exploring the Universe: From Near Space to Extra-Galactic*, Astrophysics and Space Science Proceedings 53,
https://doi.org/10.1007/978-3-319-94607-8_49

in parameters such as atmospheric temperature and density distribution, total electron content (TEC), ionospheric current system, ionization rates, conductivity gradient and reference height of the ionosphere [3, 4, 25, 30]. Although solar and geomagnetic activity contribute largely to atmospheric instability, the atmosphere can also be influenced by other phenomena including planetary tides, thermospheric tides, tropospheric tides, and stratospheric warming [7, 9, 10, 18, 20, 25–27, 37].

The atmosphere consists of the troposphere, stratosphere, mesosphere and the thermosphere. The ionosphere is embedded in the thermosphere and composed of the D, E, and F regions (also see, [11, 29]). From the troposphere to the thermosphere the atmosphere changes with time (e.g., diurnal, seasonal, solar cycle), location or latitude and solar activity [11, 19]. The extent of solar activity impact on the atmosphere depends on the intensity and duration of perturbing event (force). Geomagnetic storm induced effects on the atmosphere are more intense and almost promptly detectable in high latitude. The responses are usually delayed in the middle latitude, but minutely observed in low latitude and equatorial region [16, 23]. During storms, geomagnetic induced current (GIC) activity are enhanced at the equatorial regions [2, 5]. Moments of high solar wind (HSS) propagation and corotating interaction region (CIR) causes significant fluctuation in daytime vertical total electron content (VTEC) in low- and mid-latitude [32]. Also, the equatorial ionosphere promptly response to high-intensity, long-duration continuous auroral electrojet activity (HILDCAAs) events, which drive continuous penetration of planetary electric field [14, 31, 34]. In general, atmospheric responses at different heights, locations or latitudes vary in time and development, and reflect different mechanisms and aspects of the perturbing (or driving) forces [25].

## 2 Space Weather Induced Atmospheric Responses and It Effects on Radio Wave Propagation

One of the most important consequences of space weather in the lower atmosphere (e.g., ionospheric D-region) is sudden ionospheric disturbances (SID)—caused by sudden increase in ionisation rate of the atmosphere by solar flare associated EUV, X-ray and/or energetic particles. This scenario can change the reflection height for radio waves leading to abrupt shifts in the received frequency, amplitude and/or phase of the signals. The conductivity of the ionosphere increases during SID, and ionospheric electric currents intensify with their accompanying magnetic field disturbances [25, 29]. In addition to many other observational and experimental tools (e.g., ground-based GNSS receivers, vertical and oblique sounding, Riometers, coherent and incoherent scatter radars) very low frequency (VLF) radio waves have been extensively used to investigate ionospheric irregularities because the signal is sensitive to changes in the electrical conductivity of the ionosphere [1]. There is a correlation between X-ray flux induced SID and variations in daytime VLF signal amplitude and phase under solar flare condition. Such abrupt signal

shifts are rarely promptly detectable during geomagnetic storm induced ionospheric disturbances. However, studies have shown that VLF signals can be significantly affected during geomagnetic disturbances and storms due to ionosphere perturbations [e.g., 12, 15, 25, 28]. Anomaly in the phase of VLF signal was reported in trans-auroral propagation path during sub-storm of 13 November 1979 [12]. Depression in the signal's amplitude was observed in mid-latitude during storms of 7 April 2000 and 31 October 2003, and later observed in lower latitudes as delayed responses [28]. Reduction (or depression) in the signal's strength was also reported in low latitude during severe storm on 15 December 2006 [15]. In a recent study we investigated geomagnetic storm-induced magnetosphere-ionosphere dynamics in mid-latitude (40°–54°) D-region using VLF radio signal, to understand VLF propagation characteristics or signatures that are related to storms driven ionospheric changes [see, 25]. We found (and reported) that variation pattern of the signal metrics reflected the prevailing space weather condition (around the interval). In particular, we observed significant dipping of the mid-day amplitude peak (MDP), mean signal before sun-rise (MBSR) and mean signal after sun-set (MASS) within 1–2 days of strong geomagnetic disturbance or storm conditions. The observed pattern in variation of the signal metrics is shown in Fig. 1. The figure shows the mean deviation in Dst values and consequent variation of MDP, MBSR, MASS, sunrise terminator (SRT) and sunset terminator (SST) during 16 storm conditions for (a) GQD-A118 and (b) DHO-A118 propagation paths.

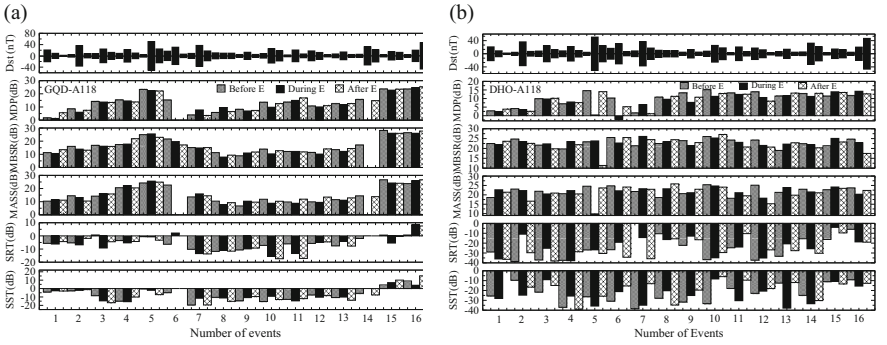



**Fig. 1** Daily deviation in Dst and corresponding variation of MDP, MBSR, MASS, SRT and SST (all in dB) signal metrics before and after each of the 16 storm conditions for (**a**) GQD-A118 and (**b**) DHO-A118 propagation paths. BE = 1-day before an event, DE = during an event, AE = after an event (From [25])

## 3 Space Weather Induced Atmospheric Perturbations and Its Effect on LEO Satellites Trajectory

Space weather drives thermospheric and ionospheric disturbances that can affect the performance and reliability of space-based satellite systems. Solar activity causes atmospheric expansion and subsequent increase in the density of the atmosphere due to Joule heating and precipitation of energetic particles. This temperature and density fluctuations adversely affect the motion or trajectory of low Earth orbiting satellites (LEOSs) via enhanced atmospheric drag (on LEOSs) that can accelerate their decay from orbit (e.g., [6, 13, 17, 21–24, 33]). Solar-induced increase in LEOSs aerodynamic drag can increase the probability of spacecraft collision due to the increased error margins in spacecraft positioning, which can result in significant uncertainties in the re-entry location of de-orbiting spacecraft. Also, satellites identification and tracking, maneuvering and lifetime prediction can be very challenging due to drag scenario [20, 24]. If not boosted or maintained (at scheduled interval), a satellite in orbit can gradually decay from its orbit and eventually re-enter or spiral into atmosphere under the influence of atmospheric drag force [20]. The orbital decay scenario of a LEO satellite due to atmospheric drag influence is depicted in Fig. 2.

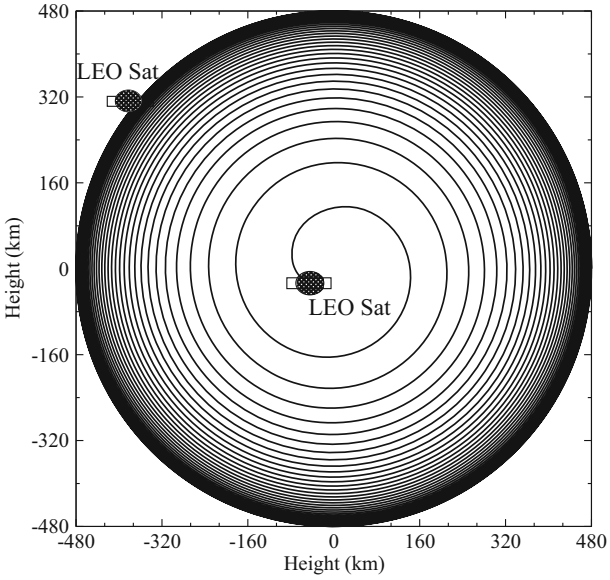



**Fig. 2** Orbital decay scenario of LEO satellite due to atmospheric drag

### 3.1 Drag Force Models

Atmospheric drag is the main force influencing the motion or trajectory of satellites in low Earth orbit. This force (drag) opposes the velocity vector of the satellites and take energy from the orbit at constant rate, leading to gradual decays (from orbit) due to this energy expense [20]. Drag force on LEOSs is given by the equation [20, 35, 36],

$$F_d = -\frac{a_d}{m_s} = -\frac{1}{2}\rho A_s C_d V_s^2, \tag{1}$$

where, $V_s$ is the velocity of the satellite with respect to the atmosphere, $A_s$ is the satellite projected area, $\rho$ is atmospheric density, $m_s$ is the mass of the satellite and $C_d$ is the dimensionless drag coefficient of the satellite.

The differential equation for changes in the mean radius of the satellite orbit per revolution is given by [6, 8, 24, 35, 36],

$$\frac{dr}{dt}(mrpr) = -\rho\frac{C_d A}{m}\sqrt{GMr}. \tag{2}$$

A set of coupled differential equations can be solved to obtain the instantaneous position and velocity components of satellites moving under the influence of atmospheric drag force. Assuming that the satellite always remains in the same plane (i.e., $\theta$ = constant) and changing its position through the azimuthal parameters ($\phi, \dot{\phi}$), the orbital decay due to atmospheric drag on the satellite can be computed (in spherical polar co-ordinate system ($r, \theta, \phi$)) from the following equations [21–24],

$$\dot{v_r} = -\dot{\phi}r^2(A_s C_d/m_s), \tag{3}$$

$$\dot{r} = v_r, \tag{4}$$

$$\ddot{\phi} = -\frac{1}{2}r\rho\dot{\phi}^2\frac{A_s C_d}{m_s}, \tag{5}$$

$$\dot{\phi} = v_\phi/r, \tag{6}$$

$v_r$ and $v_\phi$ are the respective radial and tangential velocity components, $r$ is the instantaneous radius of the orbit.

### 3.2 *Effects of Short- and Long-Term Atmospheric Variations of LEO Satellites' Orbital Trajectory*

The extent to which satellites are affected by atmospheric drag largely depends on the atmospheric (thermosphere) density. Although the precise density of the atmosphere at any given instant is difficult to determine (Chobotov 2002), many atmospheric models with good approximation have been developed over the years [20, 24]. Such models are usually incorporated into drag models for drag determination (e.g., JB2008, DTM-2000, NRLMSISE-00). The temperature, density, composition and winds of the thermosphere significantly show large solar activity variations, especially in the amount of absorbed solar radiation, and magnetospheric and ionospheric processes [33]. This include long-term changes due to solar cycle (∼11 years) and short-term changes associated with phenomena such as solar flares, CMEs, high solar wind streams (HSS) and corotating interaction region, CIR (formed by the interaction between high speed and preceding low-speed solar wind stream). The atmosphere (density) reflects the signature of both long- and short-term changes due to these phenomena. Consequently, the orbital trajectory of LEOSs are affected accordingly. A typical scenario of LEOSs orbital decay due to solar cycle variation is depicted in Fig. 3. Studies have shown that a typical satellite initially at a height of 500 km could have a lifetime of about 30 years under typical solar cycle minimum conditions and only about 3 years under the solar maximum conditions [33]. Strong CME-induced storms can cause large density perturbation and a resultant orbital decay during its main phase than CIR-induced storms [6, 17]. The orbit of a LEO satellite initially at $h = 450$ km can decay at the

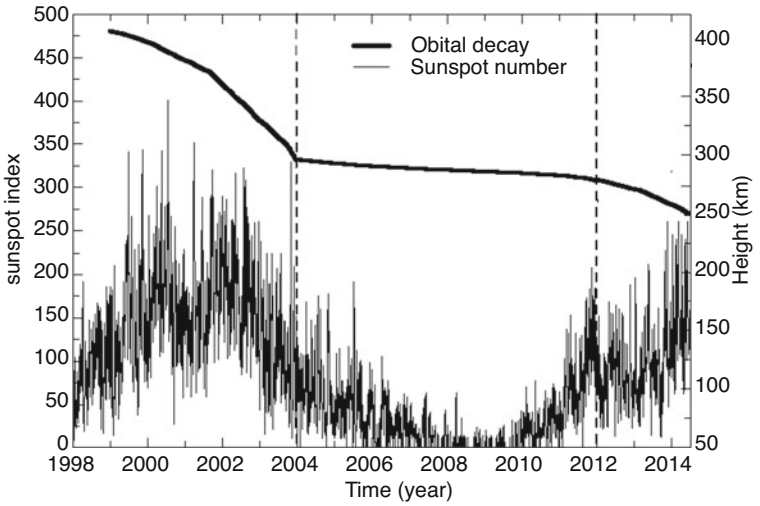



**Fig. 3** Typical orbit decay scenario of LEO satellites due to solar cycle variation during 1998–2014

rate of up to 41 km per year during solar maximum and 11 km per year during the solar minimum. However the decay rate would depend on their ballistic coefficient, intensity and duration of solar activity. Also, during solar minimum phase the subtle effect of CIR on thermospheric density can lead to additional decay rate of up to 3 km/year [20, 24].

Satellites in orbit are also affected by the time- and latitude-dependence variations of the atmosphere. Our recent investigation provided insight into how the orbital parameters of LEOSs varied in the equatorial, low and mid-latitude (EQL, LLT and MLT) during the notable storms of October/November 2003 [23]. The orbital radius ($r$) of a typical LEO satellite at $h = 450$ km can decay by about 4.20 km, 3.90 km and 3.20 km in EQL, LLT and MLT respectively during such interval of strong geomagnetic storms. The contribution of the storm to these decay values is about 3.80 km, 3.55 km and 2.95 km respectively. Similarly, storm-induced orbit decay rate ($ODR_m$) can be up to 124.3, 116.9 and 97.3 m/day. It has also been shown that such severe geomagnetic storms can lead to additional $ODR$ increase of about 117%.

## 4 Conclusions

In this chapter we presented a concise review of atmospheric responses to solar activity and how such responses affect the orbital trajectory of satellites in low Earth orbit. This review includes the recent progress we made in the studies related to space weather effects on the Earth ionospheric regions and LEO satellites trajectory. We conclude that the distinct signatures associated with long-term changes due to solar cycle, short-term changes related to solar phenomena such as solar flares, coronal mass ejections (CMEs), high solar wind streams (HSS) and corotating interaction region (CIRs), as well as changes related to latitude variation are reflected by the atmosphere. The orbital trajectory of low Earth orbiting satellites (LEOSs) are affected accordingly, as direct consequence of short- and long-term variability of atmospheric temperature (T) and density ($\rho$).

## References

1. Alfonsi, L., Kavanagh, A.J., Amata, E., Cilliers, P., Correia, E., Freeman, M., Kauristie, K., Liu, R., Luntama, J.-P., Mitchell, C.N., Zherebtsov, G.A.: J. Atmos. Solar-Terres. Phys. **70**, 2293–2308 (2008)
2. Alken, P., Maus, S.: J. Geophys. Res. **112**, A09305 (2007). https://doi.org/10.1029/2007JA012524
3. Buonsanto, M.J.: Space Sci. Rev. **88**, 563–601 (1999)
4. Burke, W.J.: J. Atmos. and Solar-Terres. Phys. **62**, 817–824 (2000)
5. Carter, B.A., Yizengaw, E., Pradipta, R., Halford, A.J., Norman, R., Zhang, K.: Geophys. Res. Lett. **42**, 6554–6559 (2015)

6. Chen, G., Xu, J., Wang, W., Lei, J., Burns, A.G.: J. Geophys. Res. **117**, A08315 (2012)
7. Chen, C.H., Lin, C.H., Chang, L.C., Huba, J.D., Lin, J.T., Saito A., Liu, J.Y.: J. Geophys. Res.: Space Phys. **118**, 3836–3845 (2013)
8. Chobotov, V.A.: Orbital Mechanics. AIAA Education Series, 3rd edn., pp. 193–213. American Institute of Aeronautics, Inc, Virginia (2002)
9. Forbes, J., Bruinsma, S.L., Zhang, X., Oberheide, J.: Geophys. Res. Lett. **36**, L15812 (2009)
10. Goncharenko, L.P., Coster, A.J., Plumb, R.A., Domeisen, D.I.V.: Geophys. Res. Lett. **39**, L08101 (2012)
11. Hunsuker, R.D., Hargreaves, J.K.: The High-Latitude Ionosphere and Its Effects on Radio Propagation. Cambridge University Press, Cambridge (2003)
12. Kikuchi, T., Evans, D.S.: J. Geophys. Res.: Space Phys. **88**, 871–880 (1983)
13. Klinkrad, H.: Symposium Proceedings (ESA SP-392), pp. 287–298. ESTEC, Noordwijk (1996)
14. Koga, D., Sobral, J.H.A., Gonzalez, W.D., Arruda, D.C.S., Abdu, M.A., deCastilho, V.M., Mascarenhas, M., Gonzalez, A.C., Tsurutani, B.T., Denardini, C.M., Zamlutti, C.J.: J. Atmos. Solar Terr. Phys. **73**, 148–155 (2011)
15. Kumar, A., Kumar, S.: Earth Planets Space **66**, 76 (2014)
16. Lastovicka, J.: J. Atmos. Terr. Phys. **58**, 831–843 (1996)
17. Lei, J., Chen, G., Xu, J., Dou, X.: Croatia: Intech Open Science, 253–263 (2013)
18. Leonard, J.M., Forbes, J., Born, G.H.: Space Weather **10**, S12003 (2012)
19. NGDC, 1996, NOAA, Boulder, CO
20. Nwankwo, V.U.J.: PhD thesis. University of Calcutta, Kolkata (2016)
21. Nwankwo, V.U.J., Chakrabarti, K.S.: Trans. JSASS Aerosp. Technol. Jpn. **12**, 47–53 (2014)
22. Nwankwo, V.U.J., Chakrabarti, S.: Indian J. Phys. **89**, 1235–1245 (2015)
23. Nwankwo, V.U.J., Chakrabarti, S.: Adv. Space Res. **61**, 1008–1889 (2018)
24. Nwankwo, V.U.J., Chakrabarti, S.K., Weigel, R.S.: Adv. Space Res. **56**, 47–56 (2015)
25. Nwankwo, V.U.J., Chakrabarti, S.K., Ogunmodimu, O.: J. Atmos. Solar-Terr. Phys. **145**, 154–169 (2016)
26. Oberheide, J., Forbes, J., Husler, K., Wu, Q., Bruinsma, S.L.: J. Geophys. Res. **114**, D00105 (2009)
27. Pancheva, D.V., Mukhtarov, P.J., Mitchell, N.J., Fritts, D.C., Riggin, D.M., Takahashi, H., Batista, P.P., Clemesha, B.R., Gurubaran, S., Ramkumar, G.: J. Atm. Solar-Terr. Phy. **70**, 101–122 (2008)
28. Peter, W.B., Chevalier, M.W., Inan U.S.: J. Geophys. Res. **111**, AO3301 (2006)
29. Prolss, G.W.: Physics of the Earth's Space Environment. Springer, Berlin (2004)
30. Simoes, F., Pfaff, R., Berthelier, J.J., Klenzing, J.: Space Sci. Rev. **168**, 551–593 (2012)
31. Tsurutani, B.T., Echer, E., Guarnieri, F.L., Gonzalez, W.D.: J. Atmos. Solar-Terr. Phys. **73**, 164–177 (2011)
32. Verkhoglyadova, O.P., Tsurutani, B.T., Mannucci, A.J., Mlynczak, M.G., Hunt, L.A., Runge, T.: Ann. Geophys. **31**, 263–276 (2013)
33. Walterscheid, R.L.: J. Spacecr. Rockets **26**, 439–444 (1989)
34. Wertz, J., Larson, W.J.: Space Mission Analysis and Design, 3rd edn., p. 145. Kluwer Academy, El Segundo (1999)
35. Wertz, J., Larson, W.J.: (3rd edn.), p. 145. Kluwer Academy, El Segundo (1999)
36. Xu, J., Wang, W., Lei, J., Sutton, E.K., Chen, G.: J Geophys. Res. **116**(A15), 2315 (2011)
37. Zhang, X., Forbes, J.M., Hagan, M.E.: J. Geophys. Res. **115**, A06316 (2010)
38. Zurbuchen, T.H., Richardson, I.G.: Space Sci. Rev. **00**, 1–15 (2005)

# Estimation of Wait's Empirical D-Region Model Parameters Based on Standard IRI Model




**Subrata Kundu and Swati Chowdhury**

**Abstract** Wait's 2-component ionospheric model is an appropriate tool for D-region modeling when it is investigated by Very Low Frequency (VLF) remote sensing technique. The 'effective reflection height' ($h'$) and 'sharpness parameter' ($\beta$) are the crucial parameters (called Wait's parameters) of this model, which are related to log-linear altitude profile of model D-region electron density ($N_e$). In this article, we took the standard altitude profile of D-region electron density ($N_e$) under ambient solar conditions from 'International Reference Ionosphere (IRI-2012)' model and fit it with its Wait's log-linear counterpart using Wait's parameters as fitting parameters. The Wait's parameters values corresponding to best fit gives a legitimate idea. We developed an automated computation mechanism to repeat this procedure under various ionospheric conditions to obtain the seasonal and diurnal variations of those parameters for different VLF propagation paths. The initial findings of our model are presented in this article.

## 1 Introduction

The ionosphere is a natural vast detector that characteristically responds to incoming ionizing radiation having wide range of energies and coming from terrestrial as well as extra-terrestrial sources. Ionosphere is divided into a number of permanent or semi-permanent layers and sub-layers based on their compositions and physical properties. These layers are perturbed by incoming radiation of different energies [7]. The lowermost and thinnest layer, yet extremely complicated to analyze in terms of its chemical and physical properties is the D-region of the ionosphere. It consists of electrons, different types of positive, cluster, hydrated ions and most importantly the negative ions, which are rarely available in other higher ionospheric layers. This D-region is situated within 60–90 km of ionospheric altitude. Hence the

S. Kundu (✉) · S. Chowdhury
Indian Centre for Space Physics, Kolkata, India

© Springer International Publishing AG, part of Springer Nature 2018

B. Mukhopadhyay, S. Sasmal (eds.), *Exploring the Universe: From Near Space to Extra-Galactic*, Astrophysics and Space Science Proceedings 53,
https://doi.org/10.1007/978-3-319-94607-8_50

direct satellite monitoring or balloon measurement techniques are not appropriate scientific approaches to explore this region. Sub-ionospheric Very Low Frequency (VLF) signal reflects back to earth by this D-region due to D-region critical frequency theory, after getting transmitted from various transmitters around the earth. Thus, this VLF signal are able to propagate a sufficiently large distance without suffering significant attenuation through this earth ionosphere waveguide (EIWG). The phase and amplitude of the VLF signal from a given transmitter are modified according to regular and irregular changes in the D-region due to external perturbations. They are measured to probe and explore the D-region dynamics under normal or perturbed conditions. The quantitative measure of the signal deviation helps us to estimate the fundamental characteristics of D-region, such as, free electron density profile, conductivity profile, several ionic profiles etc.

In this article, we probe this D-region using numerical modeling as a tool. Based on the primary D-region characteristics, a number of D-region numerical and analytical models are proposed. They serve different physical aspects of the D-region under different degree of external perturbations. Since the electrons have the least mass among all the charged particles in the D-region, the VLF signal gets affected mostly by the enhancement of free electron content as the solar Lyman $\alpha$ or X-ray incident on it. In this work, we use the 2-component Wait's model (Wait and Spies [19]) of the D-region as it deals with the altitude profile of D-region electron density and conductivity alongside. It justifiably assumes a log-linear profile of the mentioned quantities with height, and it is capable to estimate them with a good degree of accuracy. The main controlling parameters are called 'effective reflection height ($h'$)' and 'sharpness factor ($\beta$)'. Now the Wait's empirical formula leads us to estimate the electron density profile ($N_e$) using them. The popular numerical code Long Wavelength Propagation Capability (LWPC) code [4] is being used to numerically associate the VLF signal perturbations with respective changes in the D-region. In this code, the abovementioned Wait's parameters are extensively used to learn about the D-region local ionospheric conditions over the VLF signal propagation path, starting from the VLF transmitter location to signal receiving point. Within LWPC code, the grid-wise ground conductivity values are appropriately supplied in order to exclusively distinguish land-mass, sea-mass, ice-mass etc. at different segments of the path.

In this article, we have used a method to develop a database of ionospheric reflection parameters based on electron density profile and Wait's two component model which is compatible with LWPC. Our methodology will produce a set of $h'$ and $\beta$ for all possible transmitter-receiver paths for 'quiet' ionosphere ionized due to controlled solar illumination. This database can be used to extract the perturbed ionospheric characteristics through modulation in VLF signal. In Sect. 2, we present the goal of our work. In Sect. 3, the methodology is given. In Sect. 4, the results are given. Finally in Sect. 5, we conclude our works. This work summarises a more extensive work by Chowdhury et al. [3] (in preparation).

## 2 The 'Goal'

Earlier works using Wait's proposition and LWPC to investigate the D-region electron density enhancements during solar X-ray flares have been done by Thomson and Clilverd [17], Grubor et al. [6], Thomson et al. [18], Zigman et al. [20] etc. Schmitter [16] used the same mechanism to probe the planetary wave dynamics and diurnal variation over lower ionosphere. Nina et al. [8, 9] performed a deeper research on the similar context and gave a good estimation of effective recombination coefficient ($\alpha_{eff}$) at D-region heights during solar flare. During last decade, the VLF research team of Indian Centre for Space Physics, Kolkata, India has achieved a remarkable progress in the application and development of this model for D-region experimentation across a wide spectrum of fields under the guidance of Prof. Sandip K. Chakrabarti. Pal and Chakrabarti [10] started analyzing the flare induced ionosphere followed by Basak and Chakrabarti [1] who extended the work to different $\alpha_{eff}$ calculations for all classes of flares and also obtained the spatio-temporal dependency of VLF-X-ray correlations. Palit et al. [13, 14] has developed a complete multi-step model along with LWPC computation for theoretical representation of observed VLF amplitude profile. Pal et al. [11, 12] has extensively used the same LWPC, but for modeling the solar eclipse induced perturbations. Chakraborty et al. [2] and Ghosh et al. [5] extended this work to model the effects over ionosphere due to seismic events that happened in Nepal (2015) and Japan (2011). Sasmal et al. [15] did a unique work of applying LWPC technique for modeling long path signal propagation extended up to Antarctica, where the path variation of ionospheric profile through Wait's parameters was implemented to reproduce the VLF signal characteristics received at an Antarctica base. The VTX-Antarctica and NWC-Antarctica path are in the long path category ($>$9000 km), where, the ionospheric conditions change from point to point greatly due to wide variation of solar zenith angle ($Z$) which controls the solar illumination profile directly. It is a well established theory that the degree of ionization in every level of ionosphere has direct correspondence with the radiation flux rate coming from the sun. To perform this simulation, Sasmal et al. [15] performed a step by step setting of the Wait's parameters manually to corroborate with the spatio-temporal variation of solar radiation affected ionosphere.

In this context, we felt a lack of built-in database of Wait's parameters corresponding to D-region electron density and conductivity states due to all possible 'normal' and 'perturbed' conditions. As LWPC is the only tool which directly generates the VLF signal amplitude and phase with a direct coupling with ionospheric reflection parameters ($h'$ and $\beta$), a vast database of these two parameters for all possible transmitter-receiver baseline will have some special importance. The quiet ionospheric conditions both from diurnal and seasonal context will be easily computed and thus the knowledge of VLF signal amplitude profile will be known without having actual signal. Secondly, instead of arbitrary assumptions of reflection parameters in LWPC to model the perturbed VLF signal, it will be much easier as one has already the assigned values for a particular baseline. Thus for

D-layer modeling using LWPC will be easier with minimal manual iteration and one can exactly take the proper choice of input references of Wait's parameter from the database.

To begin with, we plan to compute true diurnal variation of the Wait's parameters for all possible VLF signal propagation paths globally. The Wait's parameters are directly connected with the electron density profile ($N_e$). The 'International Reference Ionosphere (IRI-2012)' gives us a legitimate distribution of electron and ion density altitude profiles of the entire ionosphere globally for ambient solar conditions. Fortunately, IRI-2012 estimations extended up to D-region. Up to now, the $N_e(h)$ obtained from Wait's analysis more or less agrees with IRI-2012. In this article, we adopt a fitting technique with the real-time electron density model and Wait's empirical log-linear profile to use $h'$ and $\beta$ as fitting parameters to obtain the parameter values corresponding to best fit. The detail procedure and results are described in later sections.

## 3 Methodology

A typical lower ionosphere electron density profile, frequently used in numerical modeling, is given by two parameter Wait's exponential formula [19].

$$N_e = 1.43 \times 10^{13} exp(-0.15h')exp(\beta - 0.15)(h - h'), \tag{1}$$

where, $N_e$ is the number density of electron in the unit of $m^{-3}$, $h'$ is the effective reflection height in km, $\beta$ is the steepness parameter in $km^{-1}$ and $h$ is the height in km.

Steepness parameter ($\beta$) is nothing but the gradient of electron density profile or we can say that it is the logarithmic linear slope of electron density profile as a function of height. Of course the value of steepness parameter is not constant but varies significantly both diurnally or seasonally. We give special importance to the calculation of $\beta$ as it can be directly computed from true electron density profile. We compute first the $N_e$ as a function of height.

We can now compute $\beta$ by reformatting Eq. (1) as a linear equation and then computing the slope. Equation (1) can be written as,

$$N_e = N_0 exp(-0.15h')exp(\beta - 0.15)(h - h'), \tag{2}$$

where, $N_0 = 1.43 \times 10^{13}\ m^{-3}$.

By taking $log_e$ on both side of Eq. (2), we get

$$log_e(N_e) = log_e(N_0 exp(-0.15h')exp(\beta - 0.15)(h - h')). \tag{3}$$

This can be written as,

$$log_e(N_e) = log_e(N_0) + (\beta - 0.15)h. \tag{4}$$

Equation (4) looks familiar with a linear equation $y = mx + c$. In our case $y = log_e(N_e)$, $m = \beta - 0.15$, and $c = log_e(N_0)$. By computing $N_e$ from IRI and using Wait's formula, we can theoretically estimate the values of $\beta$ and $h'$.

The International Reference Ionosphere (IRI) model is a unified Fortran code ionospheric model that provides computed global ionospheric parameters like electron and ion densities, electron and ion temperatures, total electron content (TEC), the occurrence probability of spread-F, vertical ion drift, etc. over a height range of 50–2000 km (https://omniweb.gsfc.nasa.gov/vitmo/iri2012_vitmo.html). Here, one has to provide the latitude and longitude of the desired location, select a height range for computed outputs and the desired output parameters. The model takes the input data from a wide range of receivers like ionosondes, incoherent scatter radars, the International Satellite for Ionosphere Studies (ISIS) and Alouette topside sounders, and in situ measurements on several satellites and rockets and provides outputs either in downloadable ASCII files or generate plots. The user has to choose from the options to get their outputs for further processing.

In this article, we study both the diurnal and seasonal variations of $\beta$ and $h'$ for the location of Ionospheric and Earthquake Research Centre & Optical Observatory (IERCOO) (Lat. 22.5°N, Lon. 87.48°E), Sitapur where presently all the VLF observations are being done by ICSP. We choose summer (June) and winter (December) and take the day 21st of each month to compute the abovementioned calculations. As our prime focus is to study the D-layer, we did our computations only for the day-time i.e. between the sunrise and sunset timings.

## 4 Results

We have developed an automated code to automatically download the electron number density from IRI model for the whole year. We also built another algorithm, where it automatically plots the raw electron density and fits with a linear equation to compute the slope as mentioned in the previous section. In this article, we concentrate only on two cases, one in summer and another in winter just to compare the values of the Wait's parameters. Figure 1 shows the variation of true electron density (per cubic meter) profile as computed from IRI model for 21st of (a) June and (b) December, 2016. The logarithmic electron density is plotted as a function of ionospheric height. The electron densities are computed for two specific times, one after the sunrise (solid) and another in the local mid-noon (dashed) 12:00:00 IST (IST = UT+05:30:00). It is evident that for the same reflection height, the electron density is larger in the mid-noon. Also, it is higher for the summer in comparison to winter season.

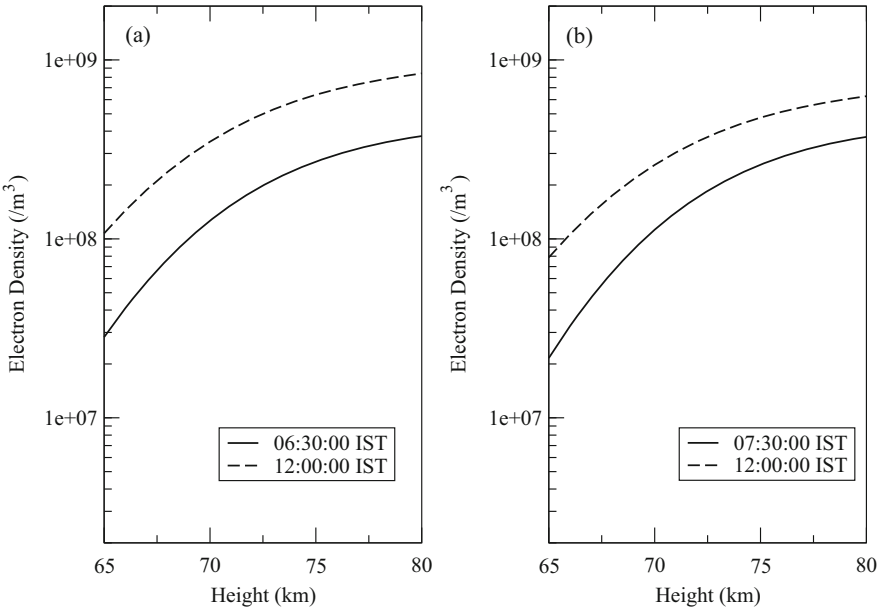



**Fig. 1** Variation of electron density (per cubic meter) profile as a function of height in km for (**a**) summer and (**b**) winter. The solid line represents the value just after sunrise and dashed for the local mid-noon

By the automated algorithm, we compute the $\beta$ and $h'$ for the abovementioned 2 days. Figure 2 shows the variation of (a) $\beta$ and (b) $h'$ as a function of hours for the daytime. We choose the time duration between 05:00:00 IST and 19:00:00 IST within which the D-layer is always present for all the seasons. The solid curves are for June and the dashed for December. The theoretical values of $\beta$ and $h'$ match satisfactorily with the conventional estimations. The minimum $\beta$ for both the seasons is $\sim 0.26\,\mathrm{km}^{-1}$ whereas the maximum value is $\sim 0.39\,\mathrm{km}^{-1}$ in winter and $\sim 0.38\,\mathrm{km}^{-1}$ in summer respectively. The slope changes sharply after the sunrise and before the sunset as the number of electron increases and decreases respectively. So the change becomes maximum during the sunrise and sunset times. During the mid-noon, as the number density gets saturated for a particular location, the change is almost zero. The $h'$ shows similar variation where it starts to decrease during sunrise and again increases during sunset. The maximum and minimum values of $h'$ for summer and winter ranges between $\sim$71–75.6 km and 72–76.7 km respectively.

For the summer season, both $\beta$ and $h'$ shows an asymmetry in their nature during daytime. Both the parameters attain high values in the sunset time from what they had at sunrise time. The main reason for this asymmetry is the difference in electron/ion production and recombination rate. During sunrise time, only the production rate dominates as there are no free electrons or ions before sunrise.

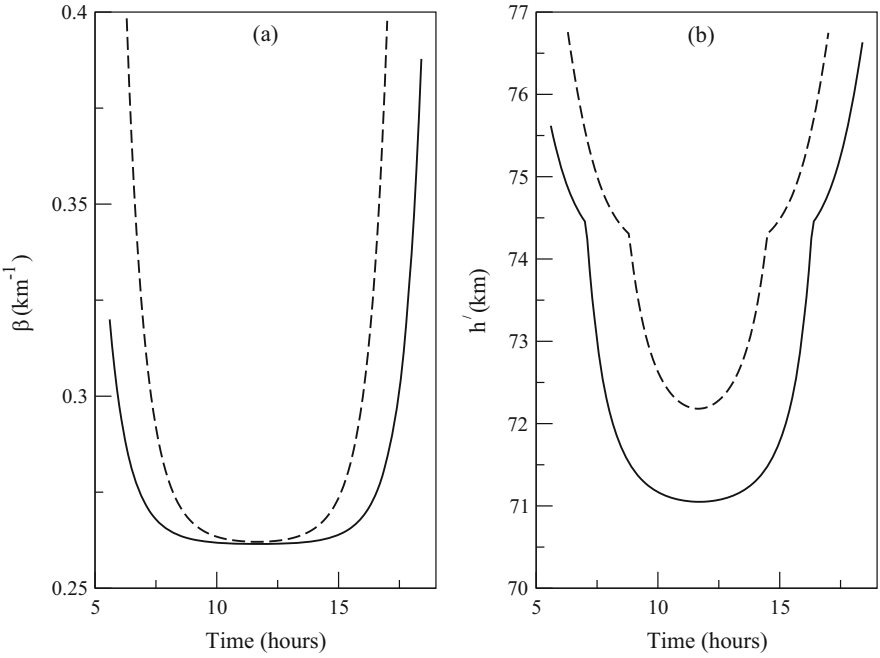



**Fig. 2** Variation of (**a**) $\beta$ and (**b**) $h'$ as a function of $km^{-1}$ and km respectively for June (solid) and December (dashed) as computed from IRI model and Wait's formula for IERCOO

During sunset, the recombination rate is different for different species of ions. Thus the number density is different which reflects in the value of $\beta$ and $h'$.

As mentioned in the Introduction section, the ionospheric characteristics are manifested by sub-ionospheric VLF signal. In Fig. 3, a typical diurnal VLF signal received from Australian transmitter NWC (19.8 kHz) and received at IERCOO is shown. The signal shows a sharp depletion and enhancement during sunrise and sunset respectively. This is due to the formation and destruction of D-layer which is responsible for the attenuation and enhancement of signal amplitude. If we ignore the daytime variation of signal amplitude that originates due to cosine nature of solar flux variation and treat this as constant, the signal amplitude exactly follows the same trend of $\beta$ and $h'$. First a sharp fall due to ion production ($h'$ and $\beta$ decreasing), a daytime variation and then a sharp rise ($h'$ and $\beta$ increasing) of amplitude. Thus our approach of making a database for Wait's parameter is correct and it corroborates the true ionospheric characteristics. Any perturbation over this due to terrestrial or extra-terrestrial sources can be easily modeled using the developed database and LWPC.

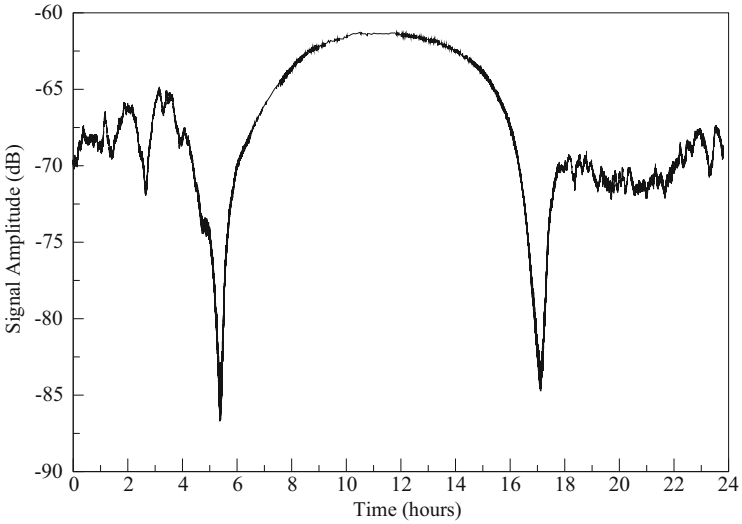



**Fig. 3** Diurnal variation VLF signal for NWC-IERCOO baseline

## 5 Conclusions

This article is the first attempt to develop a database containing Wait's D-region exponential parameters which are the most useful tool to model sub-ionospheric propagated VLF signal and its modulations due to quiet and perturbed ionospheric conditions. LWPC is absolutely needed for understanding of such VLF modulation as it directly deals with Wait's parameters $h'$ and $\beta$. The exercise of LWPC and VLF modulation can only estimate the deviation from normal scenario rather than its true value, thus one has to know the normal ionospheric behaviors before modeling it. Our approach exactly does the same where the parameters are computed from normal unperturbed ionospheric electron density profile. We have done this for the whole year and for various propagation paths. In this article we present only the two cases for June and December as observed from IERCOO, Sitapur. Our computation exactly matches with true ionospheric conditions and successfully manifested by the VLF signal amplitude received from the same location. Details would be presented in a more extended article Chowdhury et al. [3] (in preparation).

**Acknowledgements** We would like to thank Prof. Sandip K. Chakrabarti for giving us the opportunity to work in this field. We also sincerely thank Dr. Sudipta Sasmal, Dr. Tamal Basak and Dr. Suman Chakraborty for their consistent support. We thank DST-INSPIRE for financial supports.

## References


1. Basak, T., Chakrabarti, S.K.: Astrophys. Space Scie., **348**, 315–326 (2013)
2. Chakraborty, S., Sasmal, S., Basak, T., Ghosh, S., Palit, S., Chakrabarti, S.K., Ray, S.: Adv Space res. **60**, 1787–1796 (2017)
3. Chowdhury, S., Kundu, S., Chakraborty, S., Basak, T., Sasmal, S., Chakrabarti, S.K. (2018, in preparation)
4. Ferguson, J.A.: Technical document 3030, Space and Naval Warfare Systems Center, San Diego (1998)
5. Ghosh, S., Chakraborty, S., Sasmal, S., Basak, T., Chakrabarti, S.K.: Geomatics and Natural Hazards (under review, 2018). TGNH-2017-0087.R2
6. Grubor, D., Sulic, D., Zigman, V.: Serb. Astron. **171**, 29–35 (2005)
7. Mitra, S.K.: The Upper Atmosphere. The Asiatic Society, V (1992)
8. Nina, A., Cadez, V., Sreckovic, V.A., Sulic, D.: Balt. Astron. **20**, 609 (2011)
9. Nina, A., Cadez, V., Sreckovic, V.A., Sulic, D.: Nucl. Instrum. Methods in Phys. Res. B **279**, 110 (2012)
10. Pal, S., Chakrabarti, S.K.: AIP Conf. Proc. **1286**, 42–60 (2010)
11. Pal, S., Chakrabarti, S.K., Mondal, S.K.: Adv. Space Res. **50**, 196–204 (2012)
12. Pal, S., Maji, S.K., Chakrabarti, S.K.: Planetary and Space Sci., **73**(1), 310–317 (2012)
13. Palit, S., Basak, T., Mondal, S.K., Pal, S., Chakrabarti, S.K.: Atmos. Chem. Phys., **13**, 9159–9168 (2013)
14. Palit, S., Basak, T., Pal, S., Chakrabarti, S.K.: Astrophys. Space Sci. **356**, 19–28 (2015)
15. Sasmal, S., Basak, T., Chakraborty, S., Palit, S., Chakrabarti, S.K.: J Geophys. Res. **122**, 7698–7712 (2017)
16. Schmitter, E.D.: Ann. Geophys. **31**(4), 765 (2013)
17. Thomson, N.R., Clilverd, M.A.: J. Atmos. Solar Terr. Phys. **63**, 1729–1737 (2001)
18. Thomson, N.R., Rodger, C.J., Clilverd, M.A.: J. Geophys. Res. **110**, A06306 (2005). https://doi.org/10.1029/2005JA011008
19. Wait, J.R., Spies, K.P.: NBS Tech. Note U.S. **300**, 100 (1964)
20. Zigman, V., Grubor, D., Suli'Ąc, D.: J. Atmos. Solar Terr. Phys. **69**(7), 775–792 (2007)